

Transactions of the ASME®

Editor
L. S. LANGSTON (2006)
Associate Editors
Advanced Energy Systems
G. REISTAD (2005)
Fuels and Combustion Technologies
S. GOLLAHALLI (2004)
Internal Combustion Engines
D. ASSANIS (2002)
Nuclear
R. DUFFY (2004)
Power
D. LOU (2002)
International Gas Turbine Institute
IGTI Review Chair
D. R. BALLAL (2000)
R. NATOLE (2001)
E. BENVENUTI (2002)
Combustion and Fuels
P. MALTE (2003)
Structures and Dynamics
N. ARAKERE (2004)
M. MIGNOLET (2002)

BOARD ON COMMUNICATIONS
Chair and Vice-President
OZDEN OCHOA

OFFICERS OF THE ASME
President, **S. H. SKEMP**
Executive Director, **V. R. CARTER**
Treasurer, **R. E. NICKELL**

PUBLISHING STAFF
Managing Director, Engineering
THOMAS G. LOUGHLIN
Director, Technical Publishing
PHILIP DI VIETRO
Managing Editor, Technical Publishing
CYNTHIA B. CLARK
Managing Editor, Transactions
CORNELIA MONAHAN
Production Coordinator
JUDITH SIERANT
Production Assistant
MARISOL ANDINO

Transactions of the ASME, Journal of Engineering
for Gas Turbines and Power (ISSN 0742-4795) is published
quarterly (Jan., April, July, Oct.) by The American
Society of Mechanical Engineers, Three Park Avenue, New
York, NY 10016. Periodicals postage paid at New
York, NY and additional mailing offices. POSTMASTER:
Send address changes to Transactions of the ASME, Journal
of Engineering for Gas Turbines and Power, c/o THE
AMERICAN SOCIETY OF MECHANICAL ENGINEERS, 22
Law Drive, Box 2300, Fairfield, NJ 07007-2300.
CHANGES OF ADDRESS must be received at Society
headquarters seven weeks before they are to be effective.
Please send old label and new address.

STATEMENT from By-Laws. The Society shall not be
responsible for statements or opinions advanced in papers
or ... printed in its publications (B7.1, par. 3).
COPYRIGHT © 2002 by the American Society of Mechanical
Engineers. For authorization to photocopy material for
internal or personal use under circumstances not falling
within the fair use provisions of the Copyright Act,
contact the Copyright Clearance Center (CCC), 222
Rosewood Drive, Danvers, MA 01923, Tel: 978-750-8400,
www.copyright.com.
INDEXED by Applied Mechanics Reviews and Engineering
Information, Inc. Canadian Goods & Services Tax
Registration #126148048

Journal of Engineering for Gas Turbines and Power

Published Quarterly by The American Society of Mechanical Engineers

VOLUME 124 • NUMBER 3 • JULY 2002

TECHNICAL PAPERS

Gas Turbines: Advanced Energy Systems

- 441 Improved Gas Turbine Efficiency Through Alternative Regenerator Configuration**
P. A. Dellenback

Gas Turbines: Aircraft Engine

- 447 A Proposal for Integration of Wind Tunnel and Engine Test Programs for the Evaluation of Airframe-Propulsion Compatibility Using Numerical Simulations (99-GT-345)**
M. Davis, W. Baker, G. Power, and D. Beale

Gas Turbines: Ceramics

- 459 Rig and Engine Testing of Melt Infiltrated Ceramic Composites for Combustor and Shroud Applications (00-GT-638)**
G. S. Corman, A. J. Dean, S. Brabetz, M. K. Brun, K. L. Luthra, L. Tognarelli, and M. Pecchioli

- 465 Modeling the Thermostructural Capability of Continuous Fiber-Reinforced Ceramic Composites (00-GT-640)**
J. A. DiCarlo and H. M. Yun

Gas Turbines: Combustion and Fuels

- 471 Reaction Mechanisms for Methane Ignition (00-GT-145)**
S. C. Li and F. A. Williams
- 481 A Combined Eulerian and Lagrangian Method for Prediction of Evaporating Sprays (01-GT-047)**
M. Burger, G. Klose, G. Rottenkolber, R. Schmehl, D. Giebert, O. Schäfer, R. Koch, and S. Wittig

- 489 Analysis of the Effects of Water Injection on the Performance of a Gas Turbine**
K. Mathioudakis

- 496 On the Effect of Swirl Flow of Gas Turbine Exhaust Gas in an Inlet Duct of Heat Recovery Steam Generator**
B. E. Lee, S. B. Kwon, and C. S. Lee

Gas Turbines: Combustion and Fuels, and Cycle Innovations

- 503 Analysis Strategies for Tubular Solid Oxide Fuel Cell Based Hybrid Systems (00-GT-553)**
A. D. Rao and G. S. Samuelsen

Gas Turbines: Controls, Diagnostics, and Instrumentation

- 510 Dynamic Simulation of Full Startup Procedure of Heavy-Duty Gas Turbines (01-GT-017)**
J. H. Kim, T. W. Song, T. S. Kim, and S. T. Ro
- 517 Rolling Element Bearing Defect Detection and Diagnostics Using Displacement Transducers (01-GT-028)**
J. J. Yu, D. E. Bently, P. Goldman, K. P. Dayton, and B. G. Van Slyke

(Contents continued on inside back cover)

This journal is printed on acid-free paper, which exceeds the ANSI Z39.48-1992 specification for permanence of paper and library materials. ♻️
♻️ 85% recycled content, including 10% post-consumer fibers.

Gas Turbines: Controls, Diagnostics and Instrumentation, and Aircraft Engines

- 528 Simultaneous Short and Long Wavelength Infrared Pyrometer Measurements in a Heavy-Duty Gas Turbine (01-GT-026)
J. R. Markham, H. M. Latvakoski, S. L. F. Frank, and M. Lüdtkke

Gas Turbines: Electric Power

- 534 Kalaeloa: Combined Cycle Power Station Burning Low Sulfur Fuel Oil in Its Ninth Successful Year (00-GT-590)
Z. R. Khalaf and B. Basler
- 542 Advanced Gas Turbine Technology: ABB/BCC Historical Firsts (01-GT-395)
D. Eckardt and P. Ruffli

Gas Turbines: Heat Transfer

- 550 Evaluation of the Cross Corrugated and Some Other Candidate Heat Transfer Surfaces for Microturbine Recuperators
E. Utriainen and B. Sundén

Gas Turbines: Industrial and Cogeneration

- 561 Inverted Brayton Cycle Employment for Low-Temperature Cogenerative Applications (00-GT-315)
M. Bianchi, G. Negri di Montenegro, and A. Peretto

Gas Turbines: Industrial and Cogeneration, and Controls, Diagnostics, and Instrumentation

- 566 The μ Approach to Control of Active Magnetic Bearings (00-GT-408)
R. L. Fittro and C. R. Knospe

Gas Turbines: Manufacturing, Materials, and Metallurgy

- 571 Metallurgical Considerations for Life Assessment and the Safe Refurbishment and Requalification of Gas Turbine Blades (00-GT-642)
J. A. Daleo, K. A. Ellison, and D. H. Boone

Gas Turbines: Marine

- 580 Systematic Evaluation of U.S. Navy LM2500 Gas Turbine Condition (00-GT-667)
B. D. Thompson and B. Wainscott

Gas Turbines: Structures and Dynamics

- 586 A New Method for Dynamic Analysis of Mistuned Bladed Disks Based on the Exact Relationship Between Tuned and Mistuned Systems
E. P. Petrov, K. Y. Sanliturk, and D. J. Ewins

Gas Turbines: Structures and Dynamics, and Controls, Diagnostics, and Instrumentation

- 598 Active Control Algorithms for the Control of Rotor Vibrations Using Hybrid Squeeze Film Dampers (00-GT-564)
A. El-Shafei

Gas Turbines: Turbomachinery

- 608 Numerical Comparative Study of Compressor Rotor and Stator Blade Deposition Rates
D. Bouris, R. Kubo, H. Hirata, and Y. Nakata

Gas Turbines: Vehicular and Small Turbomachines, and Ceramics

- 617 Ceramic Turbine Engine Demonstration Project: A Summary Report (00-GT-532)
B. Schenk
- 627 Summary of CGT302 Ceramic Gas Turbine Research and Development Program (00-GT-644)
I. Takehara, T. Tatsumi, and Y. Ichikawa

Internal Combustion Engines

- 636 Analysis of the Combustion Process in a EURO III Heavy-Duty Direct Injection Diesel Engine
J. M. Desantes, J. V. Pastor, J. Arrègle, and S. A. Molina
- 645 Internal Combustion Engine Noise Analysis With Time-Frequency Distribution
G. T. Zheng and A. Y. T. Leung
- 650 A Study on the Knocking and Misfire Detection System Using Breakdown Voltage Characteristics
J. K. Park and J. O. Chae
- 660 Combustion and Emission Characteristics of Direct-Injection Compression Ignition Engines by Means of Two-Stage Split and Early Fuel Injection
K. Yamane and Y. Shimamoto
- 668 On Application of Nonlinear k - ϵ Models for Internal Combustion Engine Flows
G. M. Bianchi, G. Cantore, P. Parmeggiani, and V. Michelassi

- 678 Development of the Tracer Gas Method for Large Bore Natural Gas Engines—Part I: Method Validation
D. B. Olsen, G. C. Hutcherson, B. D. Willson, and C. E. Mitchell
- 686 Development of the Tracer Gas Method for Large Bore Natural Gas Engines—Part II: Measurement of Scavenging Parameters
D. B. Olsen, G. C. Hutcherson, B. D. Willson, and C. E. Mitchell
- 695 Multicode Prediction of the Influence of the Exhaust System on the Performance of a Turbocharged Engine
G. Chiatti and O. Chiavola
- 702 Use of Detailed Chemical Kinetics to Study HCCI Engine Combustion With Consideration of Turbulent Mixing Effects
S.-C. Kong and R. D. Reitz
- 708 Predicting Hydrocarbon Emissions From Direct Injection Diesel Engines
P. A. Lakshminarayanan, N. Nayak, S. V. Dingare, and A. D. Dani
- 717 A Model for Multicomponent Spray Vaporization in a High-Pressure and High-Temperature Environment
Y. Zeng and C. F. Lee

Nuclear Engineering

- 725 Dynamic Modeling of a Cogenerating Nuclear Gas Turbine Plant—Part I: Modeling and Validation
J. F. Kikstra and A. H. M. Verkooijen
- 734 Dynamic Modeling of a Cogenerating Nuclear Gas Turbine Plant—Part II: Dynamic Behavior and Control
J. F. Kikstra and A. H. M. Verkooijen

ANNOUNCEMENTS AND SPECIAL NOTES

- 744 Information for Authors
- 745 Preparing and Submitting a Manuscript for Journal Production and Publication
- 746 Preparation of Graphics for ASME Journal Production and Publication

Improved Gas Turbine Efficiency Through Alternative Regenerator Configuration

P. A. Dellenback

Department of Mechanical Engineering,
University of Wyoming,
P.O. Box 3295,
Laramie, WY 82071-3295

An alternative configuration for a regenerative gas turbine engine cycle is presented that yields higher cycle efficiencies than either simple or conventional regenerative cycles operating under the same conditions. The essence of the scheme is to preheat compressor discharge air with high-temperature combustion gases before the latter are fully expanded across the turbine. The efficiency is improved because air enters the combustor at a higher temperature, and hence heat addition in the combustor occurs at a higher average temperature. The heat exchanger operating conditions are more demanding than for a conventional regeneration configuration, but well within the capability of modern heat exchangers. Models of cycle performance exhibit several percentage points of improvement relative to either simple cycles or conventional regeneration schemes. The peak efficiencies of the alternative regeneration configuration occur at optimum pressure ratios that are significantly lower than those required for the simple cycle. For example, at a turbine inlet temperature of 1300°C (2370°F), the alternative regeneration scheme results in cycle efficiencies of 50 percent for overall pressure ratios of 22, whereas simple cycles operating at the same temperature would yield efficiencies of only 43.8 percent at optimum pressure ratios of 50, which are not feasible with current compressor designs. Model calculations for a wide range of parameters are presented, as are comparisons with simple and conventional regeneration cycles. [DOI: 10.1115/1.1451843]

Background

In recent years, ground-based gas turbine engine (GTE) applications have been appreciably expanded due to significant improvements in cycle efficiency. Simple cycle efficiencies of over 40 percent are now possible from some designs, making GTEs competitive alternatives to Diesel engines and Rankine steam cycles. Most ground-based GTE applications can accommodate the space and mass requirements associated with adding regeneration to a simple cycle, with the goal of even higher cycle efficiencies.

For many operating conditions, regenerators (heat exchangers) can improve ground-based GTE performance by recovering heat from high temperature exhaust gases. Numerous applications for the recovered heat have been devised, including combined cycle and cogeneration applications, but on stand-alone GTE cycles the recovered heat is usually used for preheating the air passing between compressor and combustor. In this way, a well-known goal of thermodynamic design is satisfied by increasing the average temperature at which heat is added to the air during combustion, resulting in increased cycle efficiency. Regenerators have traditionally ([1–3]) used product gases leaving the final turbine stage as the source of heat (referred to herein as “conventional regeneration”) so that the maximum amount of work is extracted from the high-enthalpy gas stream before any heat is recovered. However, such a regenerator location is inconsistent with a fundamental lesson from Carnot-cycle thermodynamics, which is that cycle efficiency is maximized by increasing the average temperature at which heat is added, and not necessarily by maximizing the work output. Thus, the overall efficiency of conventional regenerative GTE cycles can be improved through an alternative regenerator location, and to the author’s knowledge, this paper is the first discussion of such schemes.

Consider a GTE configuration with a high-pressure turbine (HPT) and a power turbine (PT). If a heat exchanger is located between the two turbines as shown in Fig. 1, then the cycle efficiency can be substantially improved beyond that available from the conventional regeneration configuration. The thermodynamic effect is to increase the amount of heat that is delivered to the compressed air beyond what conventional regeneration is able to achieve, resulting in a higher average temperature for the heat addition process in the combustor. Although there is less work produced by the PT in the “alternative regeneration” scheme due to decreases in pressure and temperature of the gas as it passes through the regenerator, the cycle efficiency is improved and the lower specific work output can be compensated for by using larger engine components.

Model Development

Computer models of simple, conventional regenerative, and alternative regenerative cycles were developed to examine the influence of various parameters on the performance of the cycles. The primary goal in developing the models was to demonstrate the enhanced performance of the proposed “alternative regeneration” scheme, and consequently, the models were not comprehensive in including all details of gas turbine engine performance. An economic analysis was beyond the scope of this paper, and would be difficult to implement in a general way for the wide variety of gas turbine engine applications that exist today. However, the case of continuous duty power generation is noteworthy since fuel costs over the lifetime of the plant are typically so high that it is commonly cost-effective to invest capital to improve cycle efficiency by even one percent. The following discussion will show that the alternative regeneration scheme has the potential to improve cycle efficiency by several percentage points in some scenarios.

Figure 2 depicts a simple GTE cycle in a two-turbine configuration having a gas generator and a power turbine (PT). The thermodynamic states have been numbered to be consistent with those in Fig. 1. The sole purpose of the high-pressure turbine (HPT) is to provide the compressor work requirement, so that the net work

Contributed by the Advanced Energy Systems Division of THE AMERICAN SOCIETY OF MECHANICAL ENGINEERS for publication in the ASME JOURNAL OF ENGINEERING FOR GAS TURBINES AND POWER. Manuscript received by the AES Division December 12, 2000; final revision received by the ASME Headquarters September 2001. Technical Editor: G. Reistad.

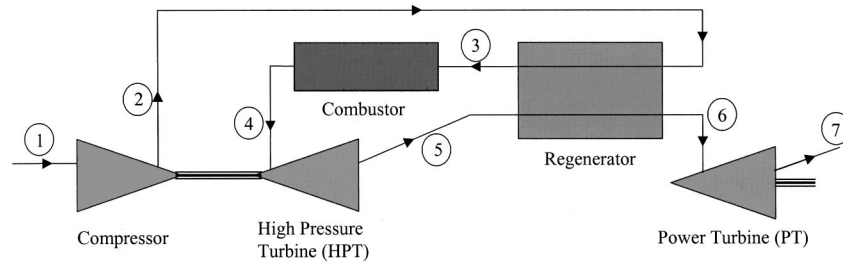


Fig. 1 Schematic of the alternative regeneration cycle

output by the cycle is proportional to the temperature drop across the PT. The simple cycle efficiency can be written as

$$\eta_{\text{cycle}} = \frac{\text{net work output}}{\text{external heat input}} = \frac{\dot{m} c_{pg} \eta_T (T_6 - T_{7S})}{\dot{m} c_{pg} (T_4 - T_2)} = \frac{\eta_T (T_6 - T_{7S})}{(T_4 - T_2)} \quad (1)$$

The “S” subscript in Eq. (1) refers to the temperature that is computed when an isentropic expansion is assumed:

$$\frac{T_{7S}}{T_6} = \left(\frac{P_7}{P_6} \right)^{\gamma_g / \gamma_g - 1} \quad (2)$$

For the simple cycle, the pressure at state 7 is assumed to be atmospheric and the temperature at state 6 is determined by writing an energy balance that equates the work input at the compressor to the work output by the HPT,

$$\dot{m} c_{pa} (T_2 - T_1) = \dot{m} c_{pg} (T_4 - T_6) \quad (3)$$

The simple cycle efficiency computed by Eq. (1) is used here as a comparison case for the regenerative cycle configurations. It is important to note that slightly lower values for simple cycle efficiency will be computed if the cycle is modeled as having only a single turbine that provides both the compressor work and net shaft work. Single and twin-turbine models give the same efficiency only when the turbines are modeled as isentropic. This modeling artifact also arises when modeling non-isentropic Rankine cycle turbines or multistage nonisentropic compression. There are no references known to the author that discuss this thermodynamic anomaly, but the calculation is so simple that it presumably has not warranted attention previously. The alternative regeneration cycle that is the focus of the present paper is modeled with a nonisentropic, twin-turbine configuration; hence it is more appropriate to compare those results to the larger values of simple cycle efficiency that are computed for the twin-turbine configuration by using Eq. (1).

Consistent with the prior comments, a two-turbine model of a conventional regeneration cycle was developed. In the conventional regeneration model, heat is added to the cycle between

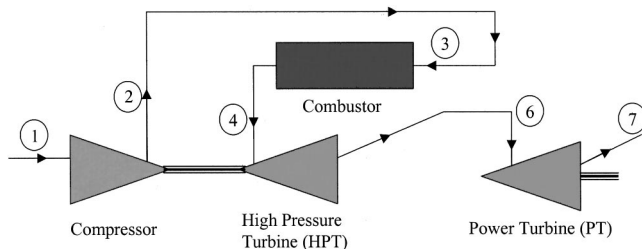


Fig. 2 Schematic of a simple cycle incorporating a gas generator and power turbine

states 2 and 3 of Fig. 2, and that heat is extracted from the exhaust gas stream leaving the PT at state 7. The resulting expression for cycle efficiency is given by

$$\eta_{\text{cycle}} = \frac{\dot{m} c_{pg} \eta_T (T_6 - T_{7S})}{\dot{m} c_{pg} (T_4 - T_3)} \quad (4)$$

State 6 is evaluated by an energy balance just as it was for the simple cycle. Temperature T_{7S} is again computed with Eq. (2), but the pressure at state 7 will be larger than atmospheric pressure by an amount equal to the pressure drop through the regenerator. The temperature at state 3 depends on the effectiveness of the regenerator in transferring heat from the exhaust gases to the compressed air stream, and can be evaluated from the regenerator effectiveness, defined as

$$n = \frac{\text{actual heat transferred}}{\text{maximum possible heat transferred}} = \frac{T_3 - T_2}{T_7 - T_2} \quad (5)$$

In Eq. (5), the heat exchanger effectiveness is defined for the fluid with the smaller product of mass flow rate and specific heat, which corresponds here to the compressor discharge air since it has the smaller specific heat. The increase in working fluid mass due to fuel addition at the combustor was ignored in the present models, but in real engine flows the mass flow rate of the air would be slightly less than that of the product gases, again supporting the idea that the minimum fluid for purposes of defining the heat exchanger effectiveness would be the compressed air stream between states 2 and 3. In Eq. (5), the temperature T_7 is the highest possible temperature that could be obtained by the air passing to the combustor, and this temperature could only be realized at state 3 if the heat exchanger had negligible heat transfer resistance or infinite surface area.

From the states identified in Fig. 1, an expression for the overall cycle efficiency of the alternative regenerative cycle can be written as

$$\eta_{\text{cycle}} = \frac{c_{pg} \eta_T (T_6 - T_{7S}) + c_{pg} \eta_T (T_4 - T_{5S}) - c_{pa} (T_{2S} - T_1) / \eta_C}{c_{pg} (T_4 - T_3)} \quad (6)$$

The second and third terms in the numerator of Eq. (6) cancel one another if the compressor work is supplied entirely by the HPT, but Eq. (6) is written in its full form because later discussion will consider a second approach to providing the compressor work.

The models for all three cycles assume that air is the working fluid between compressor and combustor inlets ($c_{pa} = 1.005 \text{ kJ/kg}^\circ\text{C}$, $\gamma_a = 1.4$), but that beyond the combustor inlet the chemical reaction and increased temperature alter the gas properties ([1]) so that they are better represented by $c_{pg} = 1.147 \text{ kJ/kg}^\circ\text{C}$ and $\gamma_g = 1.33$. All calculations further assumed the isentropic compressor efficiency was 86 percent, the isentropic turbine efficiencies were 89 percent, the combustor pressure drop was 13.8 kPa (2 psi), and that the compressor inlet conditions at state 1 were 21°C (70°F) and 101.4 kPa (14.7 psia). In addition, a reference case was established with moderate values estimated for the remaining parameters used in the calculations. The reference

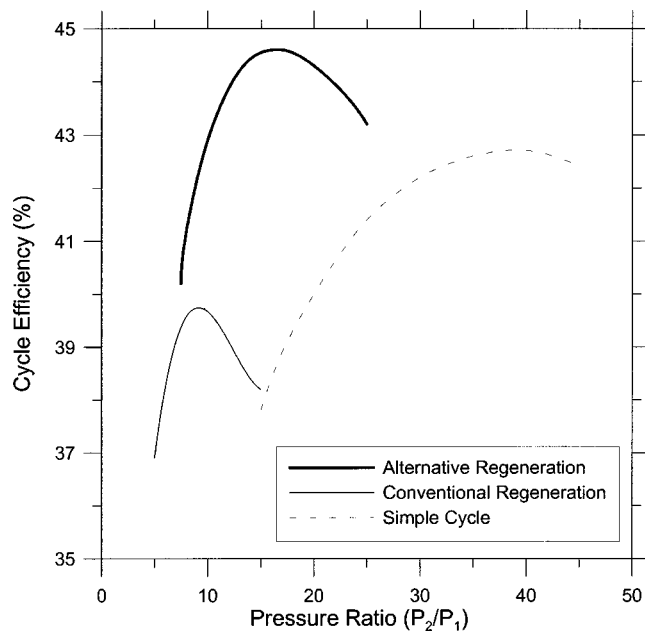


Fig. 3 Comparison of various cycle efficiencies for the reference case (turbine inlet temperature=1100°C, combustor and regenerator pressure drops=13.8 kPa, regenerator effectiveness=0.7)

case assumed that the regenerator effectiveness was 70 percent, that the turbine inlet temperature was 1100°C (2011°F), and that pressure drops associated with each pass through the heat exchanger were 13.8 kPa (2 psi) each. In the following discussion, the parameters used in the calculations were those associated with the reference case, unless otherwise specified.

Discussion

Conventional regeneration offers the benefit of improved cycle efficiency over simple cycles for the ideal case where there is no pressure drop through the regenerator. For example, for the reference case conditions, except with no pressure drops across the regenerator, a conventional regeneration cycle achieves cycle efficiencies of 43.0 percent at an optimum pressure ratio (PR) of 8, compared to the simple cycle's efficiency of 42.7 percent at an optimum, and fairly high PR of 37 (this small benefit of conventional regeneration improves as effectiveness increases—e.g., for an effectiveness of 90 percent, the efficiency improves to 50.4 percent at a PR of 4). In addition to the higher cycle efficiency of the conventional regenerative cycle, the lower optimum pressure ratio is attractive because the compressor requirements are less demanding. The alternative regeneration cycle represented in Fig. 1, with no regenerator pressure drops, achieves a peak efficiency of 45.9 percent at an optimum pressure ratio of 16, which is a substantial improvement over conventional regeneration.

Even small pressure drops through the regenerator, like those specified in the reference case, take a large toll on the performance of the conventional regenerative cycle, as shown in Fig. 3. In fact, for modest regenerator pressure drops of 13.8 kPa (2 psi), the performance of the conventional regenerative cycle is inferior to that of the simple cycle, illustrating one reason why conventional regeneration is frequently unsuitable for use on ground-based engines. Figure 3 shows that the peak efficiency of the alternative regeneration cycle (44.6 percent), with the regenerator pressure losses, is superior to either of the other two cycles, and this peak again occurs at the modest pressure ratio of 16.

Some GTE applications might impose severe space limitations on regenerator size, resulting in lower effectiveness or increased pressure drops. Figure 4 shows the effect of these two parameters

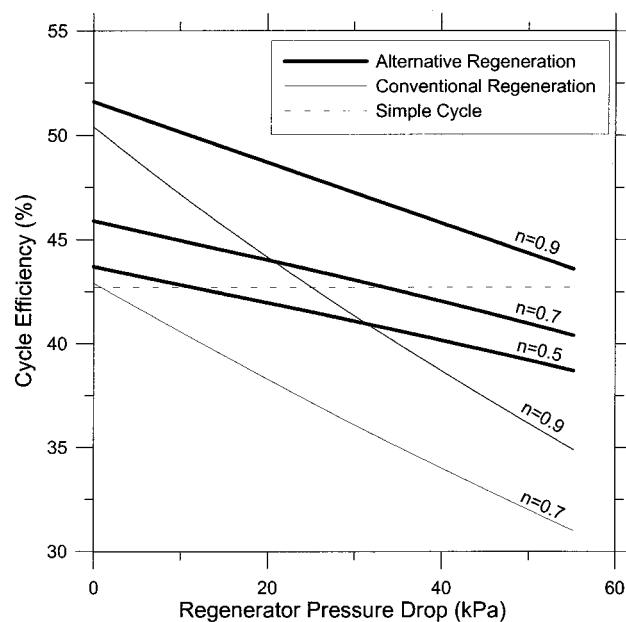


Fig. 4 Performance of various cycles as a function of regenerator pressure drop, with various regenerator effectivenesses (n) shown

on the performance of the cycles, where each point on the curve has been determined at the optimum pressure ratio for the particular operating condition. For the conventional regeneration cycle having heat exchanger effectiveness of 70 percent, there is actually a performance penalty when using a regenerator having any significant pressure drop. When the two regenerative cycles are compared at an effectiveness of 90 percent, it can be seen that the two curves are not parallel, but that the conventional regenerative cycle is degraded more abruptly than the alternative regenerative cycle as pressure drop through the heat exchanger increases. For the alternative regeneration cycle, there are various combinations of pressure drop and effectiveness that result in performance superior to the simple cycle. Finally, it is interesting to note that the optimum pressure ratio for the alternative regeneration scheme is only a very weak function of regenerator pressure drop. For example, for an effectiveness of 0.7, the optimum pressure ratio for the alternative regeneration cycle varies from 16 ($\Delta P_{\text{reg}} = 0$) to 18 ($\Delta P_{\text{reg}} = 55$ kPa).

It is well known that the maximum cycle temperature has a large effect on overall efficiency, and this is demonstrated in Fig. 5. In addition to the expected trends, Fig. 5 shows two important results. For the reference case pressure drops, the alternative regeneration cycle is superior to the other two for any turbine inlet temperature, and the conventional regenerative cycle performance falls further behind the that of the other two cycles as turbine inlet temperature increases. However, the simple cycle results shown in Fig. 5 could be misleading because they imply that a simple cycle could be useful at the higher turbine inlet temperatures, but the optimum pressure ratios required to achieve the efficiencies at higher turbine inlet temperature become excessive for a practical design. For example, the simple cycle requires optimum pressure ratios of about 37, 58, and 90 for turbine inlet temperature of 1100°C, 1300°C, and 1500°C, respectively. By contrast, the optimum pressure ratio of 30 for the alternative regeneration cycle operated at 1500°C is feasible with current compressor designs, and results in a cycle efficiency of 54.2 percent.

For engines that run continuously, cycle efficiency is likely to be the most important criterion used in designing the cycle because fuel costs over the lifetime of the engine will far exceed the initial capital costs. However, for some applications, the lowest

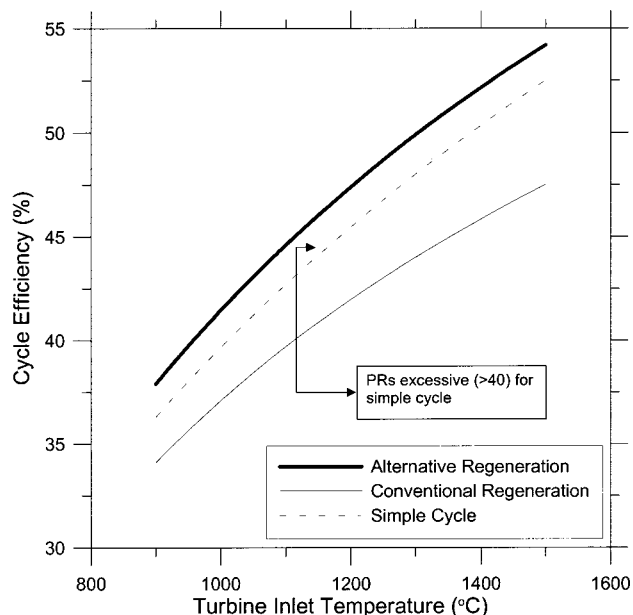


Fig. 5 Performance of various cycles as a function of turbine inlet temperature

specific cost or smallest engine size may be the more important criteria ([3]). The physical size and cost of an engine are directly related to the specific power output, and Fig. 6 shows that there is a penalty associated with the alternative regeneration scheme in this regard. To be consistent with this paper's theme of improved cycle efficiency, the operating points in Fig. 6 were determined by finding the pressure ratios that gave the highest efficiencies (alternatively, operating points could have been determined by finding the pressure ratios that resulted in maximum specific work output if that were the dominant concern driving engine design). For effectiveness between 52 percent and 75 percent, the alternative regeneration scheme has efficiency and specific work equal to, or

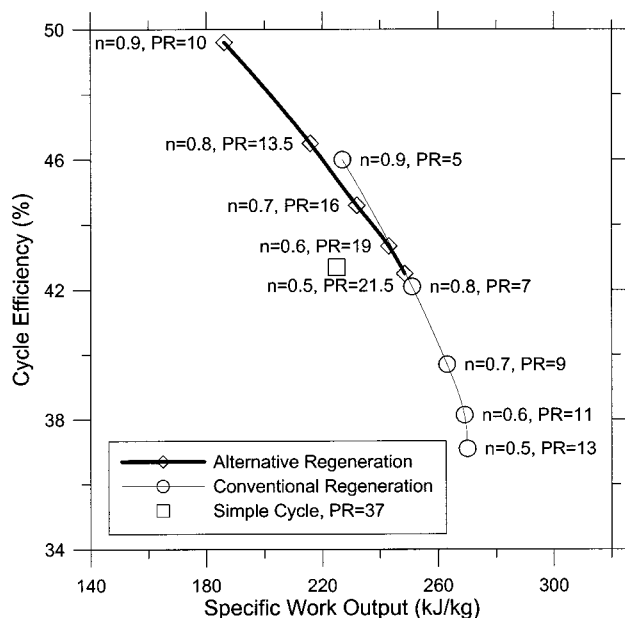


Fig. 6 The design compromise between engine size and efficiency is a function of regenerator effectiveness (n). The indicated pressure ratios (PRs) have been optimized to yield highest cycle efficiency for each effectiveness.

better than the simple cycle. For effectiveness greater than 75 percent, the cycle efficiency climbs sharply, but the specific work decreases below that of the simple cycle. The conventional regeneration cycle has specific work output superior to that of the simple cycle for any effectiveness, but the efficiency is inferior for effectiveness less than 82 percent. Also, for a particular effectiveness, the conventional regeneration cycle has better specific work output than the alternative regeneration cycle, but its cycle efficiency is 3.5 to 5.5 percentage points lower, depending on the particular conditions. Since a heat exchanger increases the overall size and cost of an engine, the Fig. 6 data would have to be weighted carefully for a particular application to determine which cycle would be preferable, especially for a space-limited or low-cost application where these characteristics are more important than cycle efficiency. To summarize, for the reference case effectiveness of 0.7, the cycle incorporating conventional regeneration yields about 13 percent more specific work output than the alternative regeneration cycle, suggesting that the engine components could be about 13 percent smaller than an engine utilizing the alternative regeneration scheme for a given power requirement, but the cycle with conventional regeneration would have much lower efficiency (39.7 percent versus 44.6 percent).

In order to design a suitable regenerator, the magnitude of the heat load in the device must be known. In the alternative regeneration scheme, the air preheating operation proceeds to a higher temperature than in conventional regeneration, but the hot side of the heat exchanger utilizes higher temperature gases to do the heating so that the overall surface area in the heat exchanger can be comparable to that in a conventional regeneration cycle. As one measure of heat exchanger size, a "regenerator heat ratio" was defined by

regenerator heat ratio

$$= \frac{\text{heat transferred in regenerator}}{\text{net work output from cycle}} \\ = \frac{c_{pa}(T_3 - T_2)}{c_{pg}(T_6 - T_7) + c_{pg}(T_4 - T_5) - c_{pa}(T_2 - T_1)} \quad (7)$$

For the reference case conditions, conventional regeneration results in a regenerator heat ratio of about 0.77, while the alternative regeneration cycle operated in the gas-generator configuration has a ratio of about 0.91, indicating that the heat exchanger would have to be somewhat larger to transfer about 18 percent more heat in the latter case.

Optimizing Performance Through a Single-Shaft Configuration. Figure 1 depicts the purpose of the HPT as providing power input to the compressor, consistent with many GTE configurations that have a gas generator (i.e., compressor, combustor, and HPT) and a power turbine. There are certain advantages to this arrangement, including the ability to operate the two turbines at different speeds. However, there is no thermodynamic reason why the optimum performance of the alternative regeneration cycle should correspond to this particular hardware configuration, and in fact, results discussed below will show that the best overall cycle efficiency usually occurs when the temperature drop across the HPT, and hence the HPT work output, is less than that required to drive the compressor. Thus, some work from the PT would also have to be directed to the compressor in the optimum efficiency, or "single-shaft" scenario. Figure 7 shows how the efficiency varies as a function of HPT outlet pressure. A vertical dashed line on Fig. 7 indicates the HPT outlet pressure when the cycle configuration is that of a gas generator with separate power turbine. HPT outlet pressures to the left of the dashed line correspond to cases where the HPT is supplying all of the compressor work and some net shaft work. Points to the right of the dashed line indicate that the HPT and PT are working together to supply the compressor work. The cycle efficiency peaks at an HPT outlet pressure slightly above that which would be required if the HPT

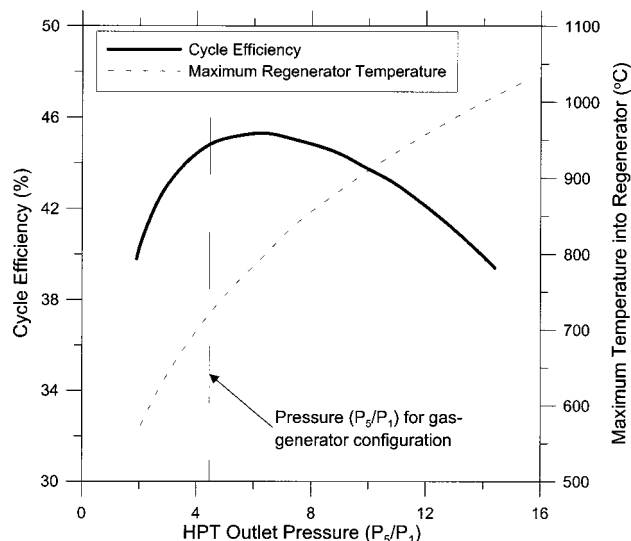


Fig. 7 Optimum performance of the alternative regeneration cycle usually occurs when the PT is used to supply some of the compressor work requirement in a single-shaft configuration. Calculation is for reference case conditions and overall PR = 20.

alone drove the compressor, and this is the usual case for the range of parameters considered here. In Fig. 7, the cycle efficiency increases from the reference case value of 44.6 percent to a maximum value of 45.3 percent when the PT is utilized to provide 26 percent of the compressor work requirement. The optimum cycle pressure ratio increases from 16 in the gas-generator configuration to 20 in the single-shaft case.

One important concern with the alternative regeneration scheme is the temperature experienced by the materials in the heat exchanger itself. Since the air preheating in the alternative regeneration scheme occurs at higher pressures and temperatures than in conventional regeneration, the heat exchanger requirements are more severe. However, for most of the operating conditions presented herein, the maximum heat exchanger temperatures (i.e., the peak temperatures at state 5) were in the range 700–900°C. Exceptions occurred for cases with higher turbine inlet temperatures and higher effectivenesses, where HPT outlet temperatures as high as 1100°C were computed for the single-shaft configurations. Modern gas/gas heat exchangers are capable of temperatures as high as 1100°C and pressures as high as 30 atmospheres ([4]), so the alternative regeneration scheme does not appear to pose any insurmountable problems in this regard. Figure 7 shows that for the optimum HPT outlet pressure and reference case conditions, the peak regenerator temperatures would be about 800°C. For contrast, if the HPT is used to provide all the compressor work in a gas-generator configuration, then the peak temperature in the regenerator is only about 690°C for the reference case conditions.

For consistency with other calculations presented herein, Fig. 7 was generated for the reference case conditions. However, Fig. 7 is somewhat misleading because the improvement in cycle efficiency when using the single-shaft configuration is much more significant when considering lower-technology regenerators having low values of effectiveness and/or large pressure drops. Figure 8 demonstrates how the single-shaft configuration is superior to the gas-generator configuration, as a function of regenerator performance parameters. As with previous figures, the overall cycle pressure ratio has been optimized to achieve the highest cycle efficiency for each point on the curve. The Fig. 8 data correspond to optimum PRs of between 8 and 33, with the larger values required for the lower effectivenesses. Figure 8 shows that the single-shaft configuration effectively decreases the slope of the efficiency curves, resulting in improved performance, especially

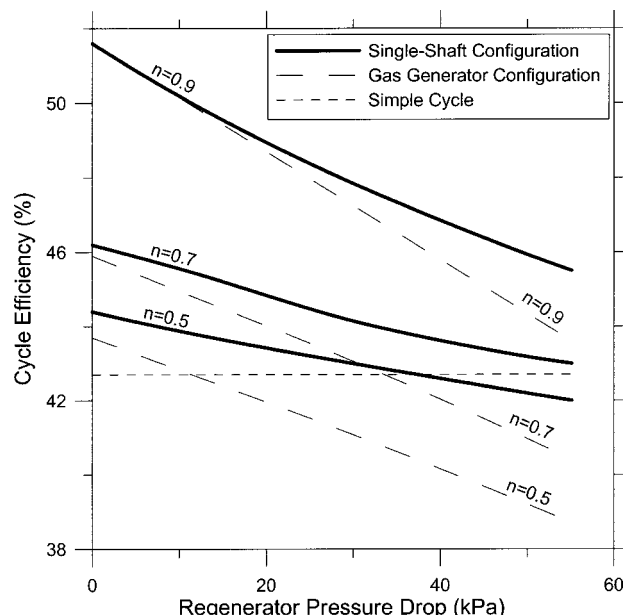


Fig. 8 For lower regenerator effectiveness (n) and larger pressure drops, it is particularly attractive to operate the alternative regeneration cycle in the single-shaft configuration which requires that the power turbine provide some of the compressor work. The overall PR has been optimized for each point shown.

for larger regenerator pressure drops. Consequently, there are more combinations of regenerator pressure drop and effectiveness that result in performance superior to the simple cycle. The maximum regenerator temperatures required for the single-shaft operating points shown in Fig. 8 lie between 760°C and 850°C, with the higher temperatures required for the higher effectivenesses.

For the single-shaft configuration, the peak in cycle efficiency is fairly flat and insensitive to overall cycle pressure ratio, as shown in Fig. 9. For each value of overall PR in Fig. 9, the cycle efficiency has been determined at the optimum HPT outlet pressure. Because the efficiency curve is fairly flat near its peak, it is conceivable that certain compromises might be attractive when designing a cycle's operating point. For example, Fig. 9 shows

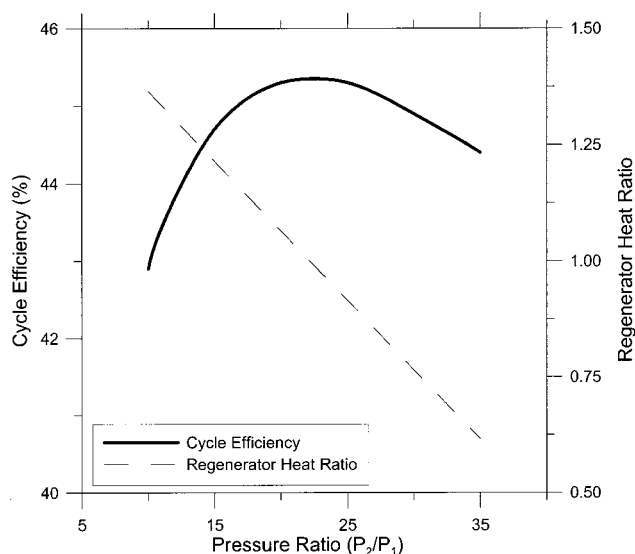


Fig. 9 Single-shaft alternative regeneration cycle performance for the reference case conditions

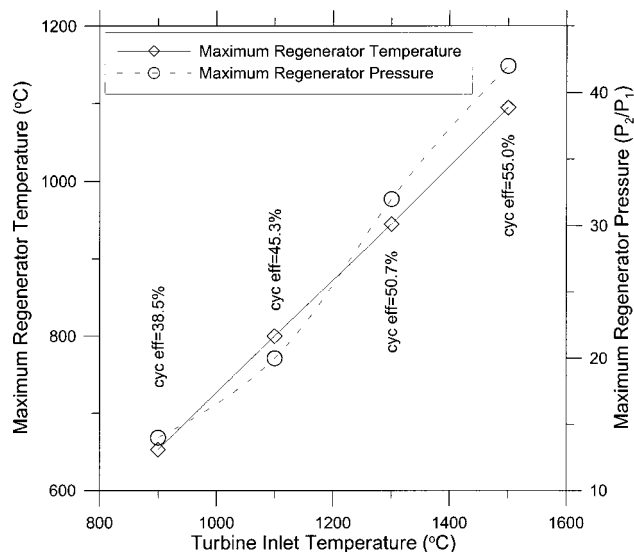


Fig. 10 Regenerator requirements for the single-shaft configuration at various turbine inlet temperatures, with resulting cycle efficiencies (cyc eff) shown

that if a designer were willing to use a larger compressor to increase the pressure ratio from the optimum value of 20 to a value of 30, then the cycle efficiency would drop from 45.3 percent to 44.9 percent, and the regenerator heat ratio would decrease by 30 percent. A 30 percent decrease in the regenerator heat ratio implies a corresponding reduction in size of the heat exchanger that is often the bulkiest component of a regenerative GTE. Hence the larger compressor and small reduction in efficiency might represent a tolerable design compromise for a compact engine where overall size is a critical issue.

Increasing the turbine inlet temperature obviously results in improved cycle efficiency, but the regenerator requirements become more severe at the same time. Figure 10 quantifies the maximum temperature experienced by the regenerator for the single-shaft configurations at various turbine inlet temperatures. All the temperature requirements shown in Fig. 10 can be satisfied by existing heat exchanger technology, even for turbine inlet temperatures approaching 1500°C.

Earlier discussion pointed out that the overall pressure ratio for the gas-generator configuration was feasible even for turbine inlet temperatures of 1500°C, whereas the simple cycle at the same temperatures requires PRs much higher than modern compressors can supply. The maximum regenerator pressure is the same as the compressor outlet pressure, so the PRs required for the gas-generator configuration (≤ 30) are feasible in the heat exchanger as well. However, the principle drawback of the single-shaft configuration is that optimum PR increases relative to the values required for the gas-generator configuration, with negative consequences on both compressor and heat exchanger requirements. For example, at a turbine inlet temperature of 1500°C, the optimum PR for the single-shaft configuration is increased to 42 (yielding $\eta_{\text{cyc}} = 55.0$ percent), and while this is essentially the limit of modern compressor designs, it is too high for modern high-temperature heat exchangers. At the same 1500°C turbine temperature, the gas-generator configuration has only a slightly lower cycle efficiency of 54.2 percent at a PR of 30, and this

would be feasible to implement. Figure 10 quantifies the maximum pressure requirements for the single-shaft configuration at various turbine temperatures. In summary, the chief attraction to the single shaft configuration appears to be in improving cycle efficiency at lower turbine inlet temperatures where optimum cycle pressure ratios are more modest.

Conclusions

An alternative configuration for a regenerative GTE cycle with numerous favorable operating characteristics is discussed. For practical ranges of operating parameters, the alternative configuration always results in a cycle efficiency superior to either a conventional regenerative cycle or a simple cycle. This performance improvement is robust and not limited to a narrow range of operating conditions or component efficiencies. Although the demands on the heat exchanger are severe, the regenerator temperatures and pressures are well below the limits of existing heat exchanger designs. The alternative regeneration scheme is particularly attractive at high turbine inlet temperatures. For turbine inlet temperatures as high as 1500°C, optimum PRs are only 30, whereas for the same conditions the optimum pressure ratio of a simple cycle is excessive (>40) for temperatures larger than 1115°C. When a power turbine and gas generator can be configured on the same shaft, operating at the same speed, then the alternative regeneration cycle efficiency can be improved even further and this situation is particularly useful if the heat exchanger is limited by low effectiveness or large pressure drops.

Nomenclature

- c_{pa} = specific heat of air
- c_{pg} = specific heat of product gases
- cyc eff = cycle efficiency
- HPT = high pressure turbine
- n = regenerator effectiveness = actual heat transfer / maximum possible heat transfer
- P = working fluid pressure
- PT = power turbine
- PR = cycle pressure ratio
- T = working fluid temperature

Greek

- ΔP_{reg} = pressure drop through regenerator
- η_{cycle} = cycle efficiency
- η_c = isentropic compressor efficiency = isentropic work / actual work
- η_T = isentropic turbine efficiency = actual work / isentropic work
- γ_a = specific heat ratio for air
- γ_g = specific heat ratio of product gases

Subscripts

- 1, 2, 3 . . . = thermodynamic states identified in Figs. 1 and 2
- S = state resulting from an isentropic compression or expansion

References

- [1] Cohen, H., Rogers, G. F. C., and Saravanamuttoo, H. I. H., 1996, *Gas Turbine Theory*, 4th Ed., Longman Group, Harlow, England.
- [2] Bathe, W. W., 1996, *Fundamentals of Gas Turbines*, 2nd Ed, John Wiley and Sons, New York.
- [3] Khartchenko, N. V., 1998, *Advanced Energy Systems*, Taylor and Francis, Washington, DC.
- [4] Wright, I. G., and Stringer, J., 1997, "Materials Issues for High-Temperature Components in Indirectly Fired Cycles," ASME Paper No. 97-GT-300.

M. Davis
W. Baker
G. Power
D. Beale

Sverdrup Technology, Inc.,
Arnold Engineering Development Center, AEDC,
Arnold Air Force Base, TN 37389-9013

A Proposal for Integration of Wind Tunnel and Engine Test Programs for the Evaluation of Airframe-Propulsion Compatibility Using Numerical Simulations¹

The current high-performance aircraft development programs, and the trends in research and development activities suggest a rapidly increasing level of aircraft subsystem integration, particularly between the airframe/inlet and the propulsion system. Traditionally these subsystems have been designed, analyzed, and tested as isolated systems. The interaction between the subsystems is modeled primarily through evaluating inlet distortion in an inlet test and simulating this distortion in engine tests via screens or similar devices. In the current paper, an overview of current techniques for inlet performance and distortion characterization and engine distortion testing is presented. A review of the current state of the art in inlet analysis is also presented along with a discussion of current engine analysis techniques, from a semi-empirical approach to high-fidelity full Navier-Stokes simulations. Finally, a proposal to coordinate the existing test techniques and analysis capabilities to provide a truly integrated inlet-engine test and evaluation capability is outlined. [DOI: 10.1115/1.1391279]

Introduction

A primary objective of the Arnold Engineering Development Center (AEDC) test and evaluation (T&E) mission is centered on integrating weapon system airframe and propulsion systems. Airframe-propulsion integration encompasses a number of issues ranging from aircraft stability and control to inlet-engine compatibility. Consequently, the integration involves a wide range of technical disciplines with implications to the T&E environment. Examples include external aerodynamics with the characterization of forces and moments, inlet performance, engine operability, engine performance, controls, and structures. To address the disciplines, the T&E process requires the application of a variety of test resources as well as analytical and computational tools. Testing for airframe-propulsion integration, and in particular inlet-engine compatibility, generally requires the coupling of component tests conducted in wind tunnels and engine altitude facilities.

The advent of technologies for providing controlled flight at extremely high angles of attack and sideslip have enabled weapon system developers to consider supermaneuver and post-stall maneuver capabilities as combat tactics. As a result, future fighter aircraft may be required to execute maneuvers containing drastic and transient changes in flight conditions at the high power settings demanded by combat. Such maneuvers present the issue of the role that the distortion time history might play in the inlet-engine integration task. Large and transient changes in angle of

attack can produce hysteresis and therefore deviations from the steady-state condition. As a result, future direct-connect engine or compressor tests may require distortion generators capable of producing a rapid sequence of distortion patterns to provide a time history corresponding to a transient maneuver.

Stealth has produced inlets highly integral with the airframe including blended inlets. Supercruise and stealth have both motivated designers to adopt bay-launched munitions in fighter aircraft designs. Together, these features have increased the proximity between the aircraft inlet and the weapon to be launched in flight. Furthermore, the use of the supermaneuver as a combat tactic in the point-and-shoot concept, will result in weapon launches at angles of attack and sideslip outside current flight envelopes. These factors increase the likelihood that hot weapon exhaust gases will enter the aircraft inlet.

Another type of inlet distortion that may appear in future operability and performance assessments involves flow angularity. The current total-pressure methodology neglects flow angularity as a separate distortion parameter. However, experience with a number of systems showed that flow angularity could affect both operability and performance. In an aircraft inlet, flow angularity generally appears in the form of swirling flow. A rotation of the entire flow about the engine or compressor hub constitutes a bulk swirl and either increases or decreases engine performance depending on the direction of rotation with respect to the machine. Localized swirl, in the form of vortices appearing in various regions of the aerodynamic interface plane (AIP), can affect surge margin. Engines lacking inlet guide vanes have demonstrated the highest sensitivity to inlet swirl. Inlet swirl can originate at the aircraft forebody or it can be generated in s-shaped inlet diffuser ducts. Therefore, the advent of stealth systems, with blended inlets and s-duct, may introduce requirements to address swirl in future inlet-engine compatibility tests.

¹The research reported herein was performed by the Arnold Engineering Development Center (AEDC), Air Force Materiel Command. Work and analysis for this research were done by personnel of Sverdrup Technology, Inc., AEDC Group, technical services contractor.

Contributed by the International Gas Turbine Institute (IGTI) of THE AMERICAN SOCIETY OF MECHANICAL ENGINEERS for publication in the ASME JOURNAL OF ENGINEERING FOR GAS TURBINES AND POWER. Paper presented at the International Gas Turbine and Aeroengine Congress and Exhibition, Indianapolis, IN, June 7–10, 1999; ASME Paper 99-GT-345. Manuscript received by IGTI, Oct. 1998; final revision received by the ASME Headquarters, Mar. 1999. Associate Editor: D. Wisler.

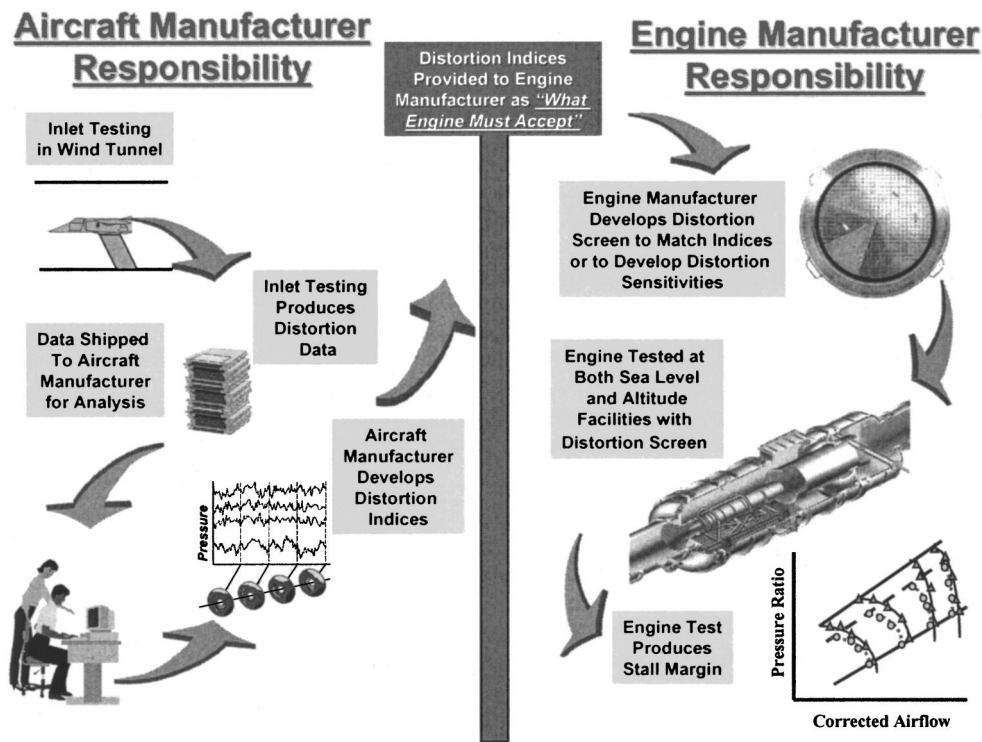


Fig. 1 Current inlet-engine integration test methodology

The AEDC T&E capabilities fulfill an essential role in the verification of the aircraft system performance. However, the need to evaluate the performance of a system often requires a number of separate test facilities. This requirement routinely arises in the integration of the airframe and propulsion system, particularly in the inlet-engine compatibility verification process. Although large propulsion wind tunnels such as AEDC 16T can accommodate complete cruise missile systems, fighter aircraft physical size generally exceeds wind tunnel capabilities. Therefore, fighter aircraft inlet-engine compatibility evaluations generally employ separate subcomponent tests. Subscale inlet model wind tunnel tests characterize inlet performance and distortion characteristics. Subsequently, direct-connect turbine engine tests, using inlet simulators, subject the engine to distorted flow representative of that experienced when coupled to the inlet.

The Inlet-Engine integration test methodology currently involves two separate processes that are loosely coupled as illustrated in Fig. 1. Wind tunnel experts and airframe developers conduct the inlet wind tunnel tests with little insight into the engine tests to follow. The subscale inlet tests determine the conditions that must be simulated at the face of a full-scale engine. These conditions, although a function of angle-of-attack, side-slip, and flight condition, are characterized by a distortion indexing methodology which may smear out the influences of each individual flight variable.

Similarly, the engine test teams must wait for an off-site analysis by airframe and engine developers to provide distortion patterns for test. Usually, the engine test team acquires little insight into the inlet distortion measurements and analysis that resulted in the particular selections. The engine test team measures the effect of a series of distortion patterns based upon distortion screens on engine operability and performance. Although efforts are proceeding to improve the inlet simulation devices placed in front of an engine, they presently neglect time history, flow angularity, and certain interactions such as the effect of the compressor face on the inlet characteristics. The true dynamic effect of an aircraft maneuver is not included in this test methodology.

The procedure of separating wind tunnel and engine test cell testing has perpetrated the evolution of separate wind tunnel and engine test cultures, with respect to airframe-propulsion integration, and resulting limitations in overall efficiency and cycle time. The test process limitations stem from the industry approach to test procedures.

Perhaps the latest assessment of the state-of-the-art airframe-engine integration methodologies is best summarized in the 1995 Wright Brothers Lectureship in Aeronautics ([1]). "In spite of all the improvements cited in this assessment, significant portions of the current state of the art for the airframe-engine integration process are still dependent on empiricism and scaling rules. Such dependencies always contain exposure to risks that the next configuration and/or next mission requirement will lie outside the bounds of applicability of the empiricism and/or scaling rules. These risks portend the possibility of a major negative surprise. The airframe-engine integration process has produced many such surprises in its history."

Through the use of modeling and simulation technology combined with the baseline information provided by the current wind tunnel and test cell test procedures, it is postulated that a virtual coupling of the wind tunnel facility with engine test cell information can be accomplished. The fusion of computational and experimental data will result in an increased level of information available to the design engineer for system development and potentially reduce the risk of a surprise in the next development cycle.

This paper reviews what constitutes the current practice for evaluating engine and inlet compatibility issues and highlights the potential for increasing the information available from current testing through the fusing of computational modeling and simulation and experimental data to provide a numerical simulation of the airframe-engine system. This paper also addresses the need and level of simulation technology that will be required for ground test facilities to provide a simulation capability for full inlet-engine compatibility evaluations.

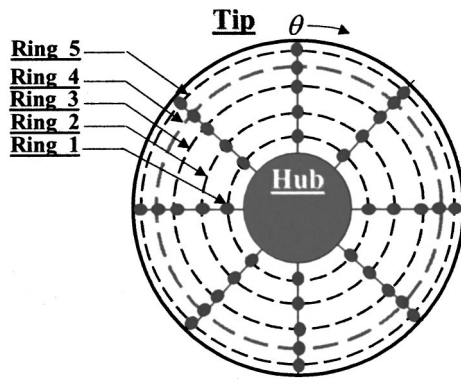


Fig. 2 Standard 40-probe rake

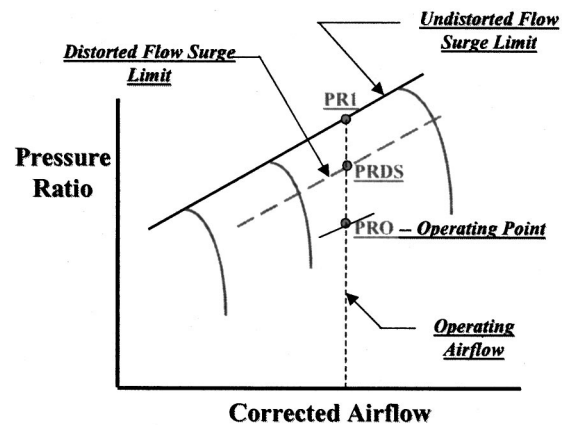


Fig. 3 ARP-1420 surge margin definition

Description of Existing Test Techniques²

Both inlet and engine ground and/or flight testing use a methodology developed by the S-16 committee of the Society of Automotive Engineers (SAE), the Aerospace Recommended Practice, ARP-1420 ([2]) and its companion document, the Aerospace Information Report, AIR-1419 ([3]) as guidelines for evaluating inlet and engine performance and operability with nonuniform inlet airflow. These documents are a recommended practice, derived by consensus of industry and government practices during the late 1970s and early 1980s. Over the last 25 years, these consensus practices have become established methodologies. A review of these methodologies is presented below.

The AIR-1419 ([3]) documents engineering information for use as reference material and for guidance. The document addresses the full spectrum of the methodology including definition of distortion descriptors, distortion test methods, instrumentation, data handling, performance assessments, and stability assessments. Inlet total pressure and other forms of flow distortion that can influence inlet-engine compatibility require examination to establish their effect on engine stability and performance. The report centers on inlet-generated total-pressure distortion measured at the aerodynamic interface plane (AIP), not because it is necessarily the sole concern, but because characterizing inlet distortion in terms of total-pressure parameters has historically proven adequate for integrating inlet and engine systems. The methodology assumes that total-pressure distributions, which can be readily measured during wind tunnel tests of inlets and direct-connect tests of engines, describes the distorted flow in sufficient detail to allow the aircraft developers to avoid surge problems. The report does not address the procedure for dealing with performance destabilizing influences other than those caused by total-pressure distortion, or with the effects of any distortion on aeroelastic stability.

The report advocates defining spatial total-pressure distortion using an array of steady-state and high-response probes distributed over the AIP as illustrated in Fig. 2. Standardizing the probe distribution provides a common basis for determining steady-state and dynamic distortion in wind tunnel tests, engine ground tests, and flight tests.

The selection of the 40-probe arrangement, shown in Fig. 2, is based on providing the spatial fidelity required for inlet-engine compatibility assessment objectives while avoiding excessive blockage. The probes are arranged on eight rakes spaced 45 deg apart to provide measurements of the circumferential distortion component. Each rake contains five probes spaced on five corresponding rings to provide measurements of the radial distortion

components. Each ring represents an equal area of the AIP to simplify the data reduction process. Thus each probe measures the pressure of an equal segment of the face area.

The concepts that are fundamental to the AIR-1419 methodology are

- inlet flow quality can be characterized, in a form relevant to engine distortion response, with numerical descriptors derived from an array of high-response total-pressure probes;
- propulsion system stability can be controlled by the aircraft and engine designers,
- engine stability can be demonstrated by tests using equivalent levels of steady state distortion, and
- the dynamic or time-variant distortion effects on engine stability are limited to events lasting longer than approximately one revolution of the machine and may be represented in test by a fixed peak distortion pattern selected from the distortion time history.

Surge margin and loss of surge pressure ratio are major concepts to the ARP-1420 methodology. The ARP-1420 defines surge margin at constant corrected airflow at the inlet of the compression component. Surge margin is the difference between the surge pressure ratio, (PR1), and the operating pressure ratio, (PRO), normalized by the operating pressure ratio as defined in Fig. 3 and the following equation:

$$SM = \frac{(PR1 - PRO)}{PRO} \times 100$$

The loss in surge pressure ratio caused by inlet total-pressure distortion is also measured at constant inlet corrected airflow and is defined as follows:

$$\Delta PRS = \frac{(PR1 - PRDS)}{PR1} \times 100$$

The loss in surge pressure ratio is normalized by the undistorted surge pressure ratio rather than by the operating pressure ratio because the operating pressure ratio may not have been defined when compressor rig tests are made to determine the effect of distortion on compression system stability.

Distortion Descriptor Element Definitions. Aerodynamic interface plane total-pressure probe data are used to describe inlet distortion directly in terms of the probe readings and numerically in terms of distortion descriptors that are related to the severity of the distortion. Distortion descriptors provide a means of identifying critical distorted inlet-flow conditions and a means of communicating distortion sensitivity during propulsion system develop-

²Information in this section was taken directly from the AIR-1419, Section 2—some of it has been paraphrased.

ment. Inlet spatial distortion is described in terms of circumferential and radial elements that are then linearly combined to provide a single-distortion description.

The requirement for a universal aerodynamic interface plane flow distortion descriptor which will

- define the quality of the air supplied by the inlet and
- describe the effect of the severity of the flow field upon engine stability,

is in direct contrast to the requirement for engine-specific information to predict the effect of any distortion pattern upon engine stability. This dichotomy exists, especially when both the inlet and engine development programs start about the same time. Ideally, an inlet development program would be structured such that distortion sensitivity data would be available from engine component tests prior to the start of inlet development testing. The largest impediment to a "universal inlet distortion factor" is that, a priori, the engine manufacturer cannot predict how the radial distortion will couple with the circumferential distortion, nor whether a compression component will be hub-or-tip distortion sensitive.

Current Testing Practices

Keeping with one of the fundamental precepts of the recommended practice set forth in the ARP-1420, namely, that engine stability can be demonstrated by tests using equivalent levels of steady-state distortion, the aircraft manufacturers, engine manufacturers, and testing organizations have implemented testing procedures which reflect that premise. A description of separate inlet and engine testing practices is presented in the sections below.

Wind Tunnel Testing for Inlet Performance. The primary objective of inlet test programs is to determine the suitability of the chosen inlet design for the airframe and engine installation. Primary data obtained for this evaluation are the steady-state and dynamic performance and stability data at the compressor face. Depending on the stage of development of the program, different configurations and inlet system operational variables may be tested to aid in the determination of the optimum contours of the inlet duct and configurations of various inlet subsystems (i.e. bleed, bypass, diverter) along with subsystem schedules. For some programs it is important to determine the vehicle (inlet pre-entry) and inlet flow fields (including boundary layer development) using flow-field survey rake assemblies. As the program matures, bleed and bypass configurations for the defined duct are optimized.

Tests involving aircraft with two inlet ducts often investigate cross talk effects of flow variations in one inlet duct on the performance of the other.

Model scale is a significant factor in correctly simulating the inlet performance of the full-scale flight vehicle. Although the scale of the model is quoted as a single number, there are often deliberate variations in scale of various inlet components. Some components are scaled differently because the model test Reynolds number is substantially different from the aircraft full-scale Reynolds number. The difference in Reynolds number causes the boundary layer thickness to be nonproportional from model scale to the actual full scale. For example, for the inlet duct to see a similar boundary layer from the fuselage, the diverter is sometimes scaled according to the expected boundary layer thickness at the model Reynolds number instead of by the model scale. Variations similar to this may be used as necessary on any inlet component. These scale differences usually will not impact the test program if the boundary layer height analysis is conducted correctly such that the flight vehicle boundary layer conditions are scaled properly on the test model.

Instrumentation. Although most inlet tests have similar instrumentation, there are no universal requirements. The primary instrumentation is usually a compressor face rake with combined steady-state/high-response total-pressure probes (Fig. 1). There

are usually static pressure taps near the compressor face station. Tests which use flow plugs to control mass flow through the inlet (most tests) usually have static pressure taps at the flow plugs. Each flow plug also has a potentiometer or LVDT (linear variable differential transformer) to measure its position.

For diagnostic purposes, some test articles have total-pressure rakes on the fuselage. Most models have diagnostic static taps both inside the duct and on the fuselage. Some have high-response pressure transducers mounted internally or externally, especially to monitor wakes from fuselage protuberances forward of the inlet. Models with additional flow passages are often instrumented with steady-state, and sometimes dynamic, total and/or static pressure instrumentation in the passages. Occasionally, model temperatures are monitored, especially if the model uses electronically scanned pressure (ESP) modules to measure steady-state pressures.

If separation inside the inlet duct is a concern, total-pressure rakes may be used inside the duct to measure pressure profiles. These rakes are usually removable since their wakes will invalidate pressure measurements at the compressor face station.

Flow Generation. An associated task of every inlet test is to provide the necessary flow through the inlet. At low Mach numbers there is insufficient pressure ratio across the inlet system to induce the desired airflow. There are two primary methods currently in use to overcome this problem. The more convenient method uses a high-pressure air-powered ejector ([4]). The ejector is mounted at the rear of the test article, behind the flow plug. High-pressure air is piped to the ejector and blows out through small sonic or supersonic nozzles in the ejector body. The high-speed flow exiting the nozzles reduces the ejector body pressure, inducing the flow through the duct.

The other primary system used to reduce the duct backpressure and thus produce airflow uses the suction scoop. The scoop is a tunnel system designed to remove exhaust gases from operating turbine engines or rocket motors. The scoop is directly connected to the aft end of the model and its pressure is reduced enough to induce airflow through the inlet duct. This system can often provide lower backpressure than is possible with an ejector and thus produce higher inlet mass flows which is useful when factors prohibit the use of an ejector system.

The most critical case for sizing any flow generation system is at static and low Mach number, high-pressure conditions. Inlets are tested statically and at low Mach numbers to determine performance for take-off and landing. These conditions often require high mass flow. In addition, the backpressure to which an ejector is exhausting is high and consequently the duct pressure ratio is minimal. This is usually the most challenging situation faced by the mass flow generator.

Flow Metering and Measurement. An important requirement of an inlet test is the accurate setting and measurement of the airflow through the inlet duct. In general, the best results have been obtained by using a device that is operated in a choked condition. (This requires that the throat of the entire inlet duct system be at the device itself rather than at an upstream or downstream location.) When the flow-metering device is choked, the actual corrected airflow is a function of area only. By varying the area, the flow can be varied, and for most devices the area is directly related to a measurable position of the choking device.

The most common device currently employed is a calibrated flow plug. The flow plug is a translating conical body that moves fore and aft in a pipe fitted with a diverging section matching the contours of the plug. As the plug translates within the conical area, the opening area changes. With sufficiently low backpressure, this translates to a change of flow through the duct. Typically, the plug is run with backpressure low enough that the plug remains choked.

An alternate method of mass flow determination involves the integration of the compressor face pressure measurements. The

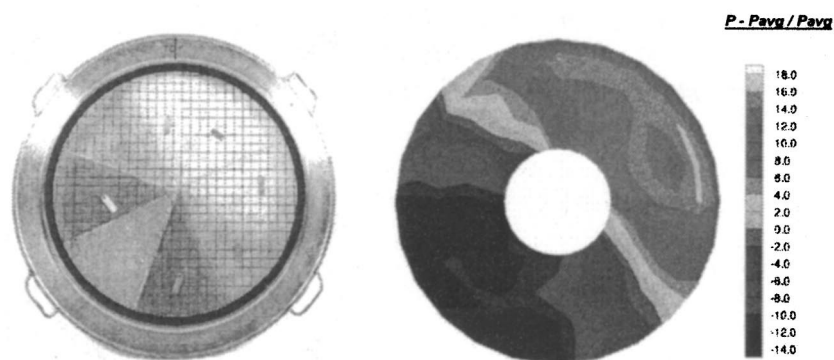


Fig. 4 Typical distortion screen and corresponding distortion pattern

compressor face total-pressure integration uses the average-static-to-total-pressure ratio at each total-pressure probe to calculate a local Mach. Once the Mach number is calculated it is converted to a velocity and used with the local air density and area to obtain a mass flow element. All of the individual mass flow elements are summed. The sum is then multiplied by a discharge coefficient to obtain the total mass flow at the compressor face station.

To use the integration of compressor face pressure method to measure inlet mass flow, there must be static pressure measurements at the station where the compressor face total-pressure probes are located. Integration of the individual total-pressure measurements at the compressor face provides a less accurate calculation that best serves as a check of the flow plug measurement.

Setting Model Attitudes and Plug Positions. There are several types of data variations that may be acquired during an inlet test. The most common variation is a mass flow sweep at constant angles of attack and sideslip. Others include an angle of attack sweep at constant mass flow and sideslip angle, mass flow sweeps of secondary flows, and angle of sideslip sweeps.

It is generally preferable to use computer control whenever possible for any positionable device which will be moved frequently during the test. This will usually result in more accurate and faster settings. Computer control is ideal for digital devices and very good for analog devices.

The usual mode of data acquisition during an inlet test is to first set model angles of attack and sideslip and follow with a mass flow/plug position sweep.

Engine Testing for Total-Pressure Distortion Effects. Compression systems can be tested for performance and operability characteristics using any of a number of techniques. These include wind tunnel tests, direct-connect tests, freejet tests, and flight tests. The choice of technique depends on such factors as the size of the vehicle, cost, and stage of development. Each technique employs a method of subjecting the compression system to distorted flows representative of the flight environment.

Smaller vehicles such as cruise missiles may be tested in large propulsion wind tunnels such as the AEDC PWT 16T/S. The complete inlet, airframe, and engine assembly can be evaluated as a system. The wind tunnel flow conditions simulate the uniform far-stream flight environment. The airframe and inlet modify the flow in a manner similar to that in flight subjecting the engine to steady state and dynamic distortion. This method is not limited to cruise missiles. The F-15 fighter aircraft development included full-scale tests of the inlet-engine assembly in both PWT 16T and 16S albeit at only moderate angles of attack. Although physical space prevented inclusion of the complete airframe, the test did include the entire inlet-engine assembly and the portion of the airframe most influential to the inlet flow.

The freejet technique also allows testing of the complete inlet-engine system. Unlike the wind tunnel, the freejet method uses a variable attitude and variable Mach number nozzle to provide a flow enclosing only the inlet opening and influential portions of the external airframe. Rather than change test article attitude, as in the wind tunnel, the technique changes the freejet attitude to simulate flight conditions. As a result, the method can simulate high flight angles of attack with fighter-size aircraft that physical size would prohibit in the wind tunnel.

The flight test method provides an evaluation of the complete inlet, engine, and airframe system. Often, the AIP is instrumented to measure inlet steady-state and time-variant distortion to allow correlation with other techniques. Generally, the flight test approach appears as the development of an aircraft system matures.

By virtue of being available early in the air vehicle development cycle, the direct-connect method has become the workhorse for testing compressors or engines in distorted flows. The method can readily be applied to engine components such as individual fans or compressors as well as to complete engines. In the direct-connect test, the component or engine is connected directly to an air supply duct that provides conditioned air at a pressure, temperature, and Mach number commensurate with a given flight condition. Thus, the duct conditions correspond to the flow output by the inlet after the diffusion process. With respect to the freestream, these conditions often include lower Mach numbers, higher static pressure, and higher static temperature. So, in a sense, the supply duct functions as an inlet simulator taking the place of the actual inlet.

In the absence of the inlet and airframe, the direct-connect approach must rely on additional techniques to simulate the distortion produced by the inlet. A number of methods have been applied to simulate steady-state inlet distortion as well as various aspects of time-variant distortion. The two most widely used inlet distortion simulators are the distortion screen and the air jet distortion generator.

The distortion screen ([5]) generates steady-state total-pressure patterns through flow blockage, a function of screen porosity and approach velocity. The screen consists of an assembly of various wire meshes with shape and porosity tailored according to the particular pattern of interest. When mounted forward of the compressor or engine and normal to the flow, the screen subjects the machine to distortion similar to that produced by the inlet. An example of a distortion screen appears in Fig. 4.

This particular screen produces a one-per-revolution, 180-degree circumferential pattern. As each screen produces a single distortion pattern, a particular test program may require a family of screen assemblies to satisfy inlet-engine compatibility verification objectives.

The air jet distortion generator ([6]) evolved as an approach to

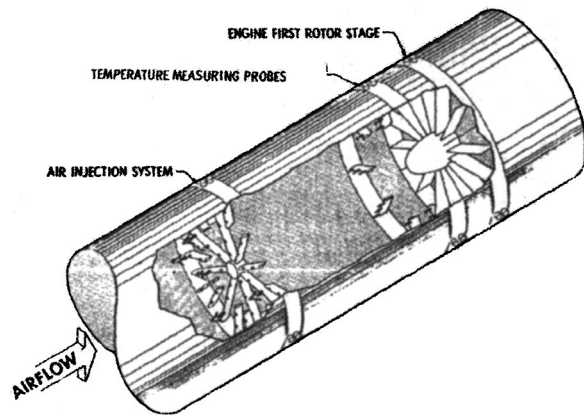


Fig. 5 Schematic of airjet distortion generator

avoiding the cost and cycle time needed to fabricate and install separate screens for each distortion pattern. The device uses the viscous mixing as a means of reducing the momentum in regions of the approaching flow. Forward-facing airjets exchange momentum with the approaching flow to effect pressure losses. An array of such jets, mounted on struts upstream of the test article, provides a means of spatially varying the pressure defects (Fig. 5).

By remotely adjusting the flow distribution among the jets, the tester can set desired distortion patterns without interrupting the test for hardware changes. Unlike the wind tunnel or flight test methods, the direct-connect method requires *a priori* definition of the flow distortion patterns to set in the inlet simulator whether screen or air jet distortion generator. As the direct-connect approach finds wide application throughout the vehicle development cycle, the patterns fall into two general categories: (1) classical distortion patterns and (2) composite or complex distortion patterns.

The so-called classical distortion patterns consist of standardized patterns that provide specific distortion features such as tip radial distortion, hub radial distortion, circumferential distortion with various multiple-per-rev specifications, or combinations. These patterns are generic in the sense that they do not necessarily correspond to a specific vehicle. The classical patterns generally find application earlier in the development cycle to establish the basic sensitivity characteristics of the engine or compressor system. A discussion of the classical patterns and sensitivity tests appears in the AIR-1419.

As the vehicle development progresses, the airframe-inlet design will be established. Or, if a specific compression system or engine is to be retrofitted to an existing aircraft, the airframe-inlet design will exist. The direct-connect test may then proceed with composite distortion patterns representing the environment that the engine will experience in the specific vehicle. These patterns are no longer generic. In general, subscale inlet model wind tunnel tests, such as those described in the previous section, provide measurements of the specific patterns expected with the full-scale vehicle in flight. The wind tunnel test must capture the effects of both the inlet itself and the influence of the external airframe on both steady-state and time-variant distortion. The prediction of the distortion patterns produced by the inlet-airframe system represents a key component of the integration of computation and experiment into a distortion evaluation methodology.

The screen and airjet distortion generator devices provide only steady-state distortion patterns. However, historical wind tunnel test results have shown that the time-variant distortion can be significantly higher than steady state. Over the years, a number of devices have been developed in an effort to simulate time-variant distortion in direct-connect tests. Examples of such devices can be found in the random-frequency generator ([7]), the discrete-frequency generator ([8]), and planar-wave generator ([9]). The

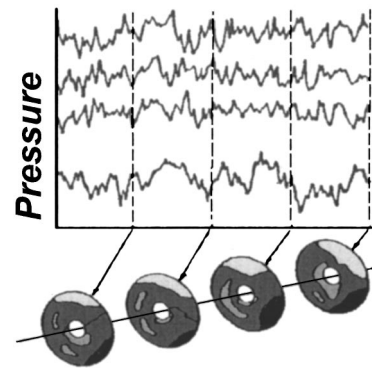


Fig. 6 Simulation of time variant distortion with steady-state patterns

random frequency generator devices generally used separated flow to produce fluctuations similar in nature to those encountered in an inlet duct. Discrete-frequency generators generally use a periodic pulsing of the flow to develop fluctuations at specific frequencies. These fluctuations may be produced by the air jet distortion generator with pulsed jets or by rotor-stator devices. However, these devices have yet to find general application.

To address time-variant distortion, the current methodology applies the following approach. The time-variant distortion measurements obtained in the wind tunnel, the distortion time history, is screened over the time recorded during the particular test point to identify peak levels of distortion. The wind tunnel data acquisition procedure must include a sufficient data record, typically 20 or 30 seconds, to capture peak distortion events. Experience has shown that turbomachines require a finite time, on the order of one revolution of the compression system, to respond to dynamic distortion events. Therefore, the screening process neglects events lasting less than approximately one revolution. The peak level of distortion is then applied in the direct-connect test using the screen or air jet distortion generator. The peak time-variant pattern becomes a steady-state pattern in the engine or compressor test neglecting the effects of time history. Figure 6 illustrates this approach.

The SAE methodology described thus far evolved over several decades and has been successfully applied to a number of systems up to current generation fighter aircraft. Recent years have brought forth new aircraft technologies that add new dimensions to the assessment of inlet distortion effects on engine performance and operability. The SAE and others have embarked on the investigation of methodologies necessary to address such technologies in the inlet-engine integration process. These issues will be discussed in the last section of this paper.

Computational Capability

For a numerical technique to become viable as a complementary test analysis tool, it must be able to provide solutions both quickly and accurately. Computational fluid dynamic (CFD) solutions for the inlets have been routinely done for many years, even with time-variant events. However, the complexity of the gas turbine engine makes CFD solutions of the full engine impractical at this time. At best, several blade rows of a turbomachinery component can be calculated in an "overnight" time frame. Thus, computational techniques must be used that use reduced grid complexity and levels of computer parallelization must be employed.

The computational simulation of inlets, especially for advanced fighter aircraft, requires modeling of complex geometries and physical phenomena. Inlets are often essentially part of the aircraft fuselage leading to highly nonuniform flow at the inlet entrance. The inlet duct transitions in cross-sectional area from a nearly oval or rectangular geometry to the required circular cross-section

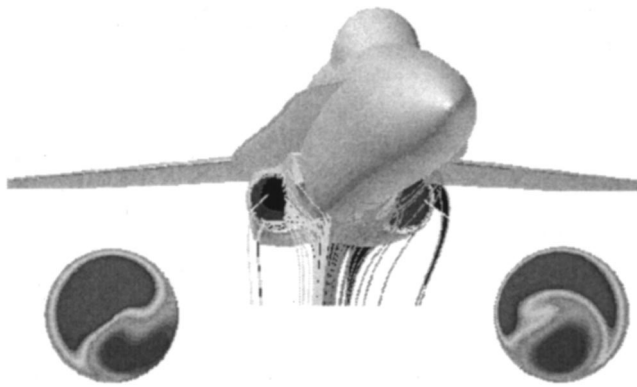


Fig. 7 Inlet flow distortions at high angle of attack on F/A 18A

at the engine face resulting in significant cross-flow velocities. Inlets for these advanced fighters are also highly curved to hide engine hot parts from infrared and radar detection. These highly curved ducts can result in flow nonuniformities, including flow separation. A fairly simple inlet configuration is shown for a F/A 18A High Alpha Research Vehicle (HARV) in Fig. 7.

This flow field was computed by Smith and Podelski [10] using the NPARC Code ([11]) at a Mach number of 0.2 and a 30-deg angle of attack. The Mach number contours shown in the figure indicate significant flow distortion at the AIP. Simulations of more complex inlets can be found in the recent papers by Mayer et al. [12] and Philhower et al. [13].

These advanced aircraft fly at speeds from low subsonic to supersonic, often at high angles of attack, resulting in complex flow structures in the vicinity and within the inlet, especially at transonic and supersonic conditions. Bleed systems and other mechanical devices are often employed to control shock location and flow conditions within the inlet. The engines are also subjected to other external influences, including rocket plume ingestion from air-launched missiles. Other phenomena, which are of concern, and thus must be adequately modeled, include inlet buzz and inlet unstart. Most, if not all, of these complex phenomena are at least partially influenced by the interaction between the inlet flow field and the propulsion system.

Simulating these complex geometries and the associated complex physical phenomena of engine inlets require simulation tools capable of capturing unsteady, three-dimensional, turbulent flow fields. Because of the highly three-dimensional nature of the flow and the potential for significant flow separation, full Reynolds-averaged, Navier-Stokes equations with sophisticated turbulence models must be solved. The Navier-Stokes solver must have the capability to model unsteady phenomena, such as unstart and buzz. Finally, the simulation tool must have the capability to solve for or model the effects of the engine, in particular the first stages of the compressor, on the inlet flow field.

Most Navier-Stokes codes in use today have the capability to model a majority of the flow phenomena required to adequately simulate the inlet flow field. The most challenging requirements are turbulence modeling, fast time-accurate simulation, and the modeling of the effects of rotating turbomachinery.

Current turbulence models that are based on the transport, production, and diffusion of turbulence quantities are capable of predicting flow separation in many situations. The most common models are k - ϵ models, such as the Chien low Re model ([14]), the k - ω model ([15]), hybrid models, such as the SST model ([16]) and one equation models, such as the Spalart-Allmaras model ([17]). Each of these has been shown to provide reasonable results in predicting separation, but none can be considered universally applicable.

Time accurate simulations of fluid dynamic processes are becoming more prevalent as computer power increases and algo-

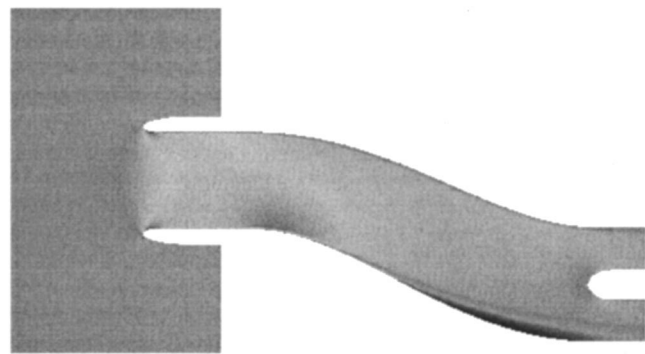


Fig. 8 Mach number in an S-duct inlet

rithms improve both the speed and accuracy of these simulations. Recent algorithmic advances in other fields of flow simulation, such as store separation ([18]), can be applied directly to simulation of the unsteady phenomena in inlet flow fields to allow larger physical time steps and, thus, faster simulations. The major limiting factor on speed is now the frequency of the unsteadiness that must be resolved, where significant computer resources are required for resolution of higher frequencies.

One approach to computationally modeling the effect of the engine on the inlet is to modify the flow at the compressor face through specialized boundary conditions. If a flow rate is known, this value can be set, allowing the static pressure to adjust at the compressor face to maintain this flow rate. The pressure may be a constant or may vary circumferentially and radially. If the pressure is known at the AIP, either at a point or over a region, this may be set directly. This technique would be applicable when modeling an inlet without an engine, where the pressure has been measured at various locations at the AIP.

Figure 8 shows the calculated Mach number through an S-duct inlet in a freestream flow at $M=0.21$, $p_0=14.68$ psi, and $T_0=527$ deg R. This configuration is the RAE Model 2129 inlet referred to as Test Case 3 by the AGARD FDP Working Group and was previously analyzed by Nichols [19]. The low speed flow in the region of adverse pressure gradient is shown as blue on the lower part of the duct.

In Fig. 9 the measured wall pressure distribution (symbols) along four circumferential stations is compared to the results of the WIND code ([20]). In this case, the static pressure at the exit of a straight duct extension of the S-duct was set to a constant value of 13.525 psi. The results compare very well with the data, indicating excellent prediction of the losses in the adverse pressure gradient region of the flow field.

An even more physical approach to modeling the compressor through boundary conditions has been developed by Paynter [21] and Paynter et al. [22] which models the effect of unsteady pressure or temperature distortions at the engine face as it affects the inlet flow field. This characteristic boundary condition is based on the small disturbance response to a time varying acoustic or convected disturbance.

A more physically realistic approach to modeling the effects of the engine on the inlet flow field is to model simultaneously the flow as it passes through the compressor stages as well as the inlet. This can be accomplished at various levels of empiricism. The most rigorous technique for simulating the effects of the rotating turbomachinery on the inlet flow is to simulate the engine hardware itself. This can be done by modeling the unsteady flow through the rotating blades for each row simultaneously using tools such as ADPAC ([23]) or to model each blade row, but approximate the interaction between the rows using an average-passage procedure, as outlined by Adamczyk [24]. While the average-passage approach is more efficient than modeling the

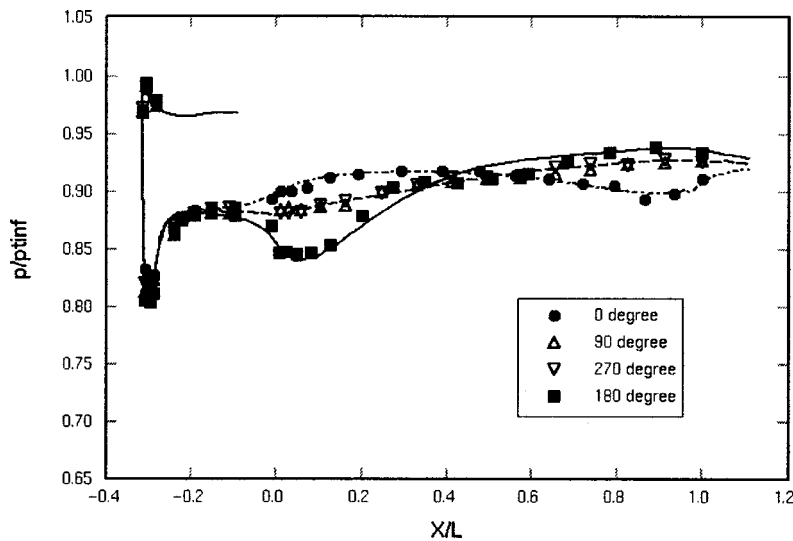


Fig. 9 Axial pressure distribution—S-duct

complete hardware and removes the time-dependency, both of these techniques require significant computer resources.

The choice of which approach to use to model the effects of the engine on the inlet flow field depends on the phenomena of interest, the required accuracy of the simulation, the turn-around requirements, and the computational resources available. Integrating a three-dimensional Navier-Stokes CFD inlet model with a corresponding complex three-dimensional CFD engine model for the study of inlet distortion is often not feasible for the required turn-around with the computational hardware of the 1990s, even with parallelization taken into account. Therefore, in order to compute time-dependent complex inlet distortion effects on the compressor flow field and vice versa, one must accept more empiricism in the modeling approach. One such approach is being developed by AEDC and is known as TEACC ([25]) (Fig. 10.)

A general-purpose three-dimensional flow simulation computer code ([11]) has been modified to accept turbomachinery source terms based upon semi-actuator disk theory. The governing equations used in TEACC were developed by applying the conservation of mass, momentum, and energy. TEACC allows for circumferential and radial control volumes to interact directly with each

other via the three-dimensional Euler equations with source terms representing a blade row. These source terms representing mass bleed, blade forces and shaft work are supplied by a streamline curvature code (a derivative of HTO300 ([26])).

TEACC was developed with complex patterns and dynamic capabilities in mind. Currently, TEACC has been operationally verified for steady operation with and without distortion present for compression systems up to three stages. Future versions of TEACC will be able to address applications of complex dynamic distortion and their effects on compression system operability and ultimately expanded to the full turbine engine.

Integration of Numerical Simulations Into the Test Environment

Clearly the volume of issues facing future integrations of inlet and engine into viable aircraft systems demands the development of new test and evaluation techniques along with numerical simulations capable of dynamic behavior. The techniques must couple experimental and numerical simulations to provide the most cost effective acquisition of information. Both experimental and the

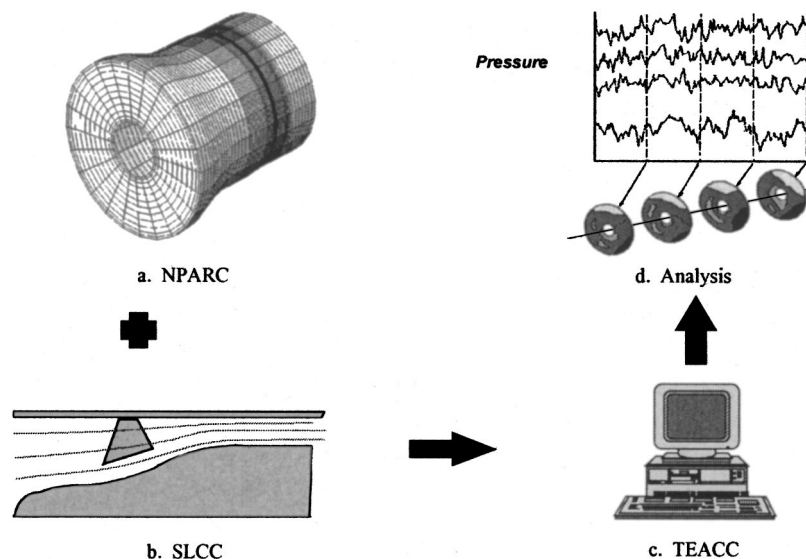


Fig. 10 Overall TEACC methodology

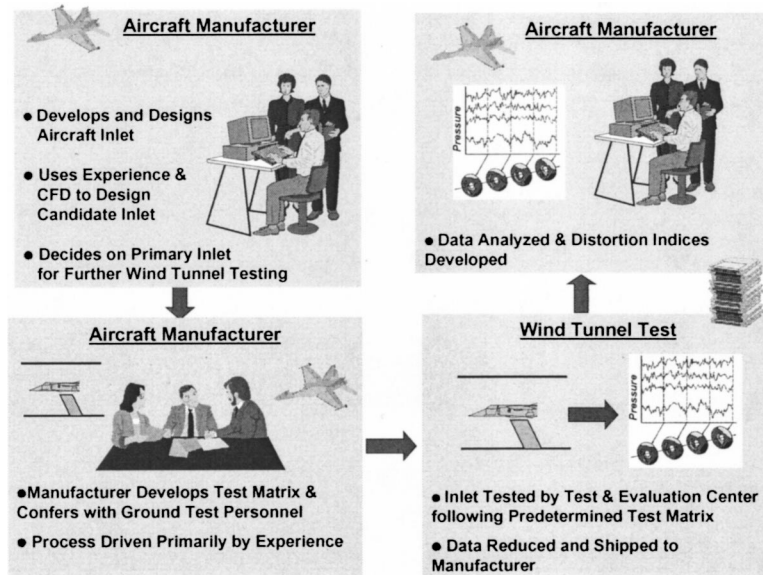


Fig. 11 Schematic of current process for inlet testing and analysis

corresponding numerical simulations require the development of methods for simulating inlet dynamic pressure distortion, swirl, and temperature distortion. It is the intent of this paper to suggest some ways that evolving numerical simulation capabilities can be utilized in conjunction with existing and new test techniques to address the issues outlined above.

We will examine each of the separate testing processes and suggest improvements that could be made using computational techniques. A schematic of the inlet testing process as it exists today is presented in Fig. 11. The aircraft manufacturer develops and designs the aircraft inlet based upon his experience and CFD calculations. The aircraft manufacturer decides on a primary inlet design and requirements for further wind tunnel testing. The aircraft manufacturer decides on what needs to be tested and how much test time will be required. This process is primarily driven

by the experience of both the aircraft manufacturer and the ground test provider. A matrix of test conditions is developed which includes flight conditions (altitude and mach number), angle of attack, side-slip, and roll. The wind tunnel test is conducted following the prescribed matrix. The data are stored and shipped back to the manufacturer for analysis. Very little interaction with the data is conducted during the testing process. If something was omitted in the process, the omission would persist until another test is conducted in the future to get that information.

One way to improve this process is to compute/predict inlet performance prior to testing. Such predictions would provide the means to optimize the test matrix and reduce the risk of a serious omission. The proposed new process is presented in Fig. 12.

In the improved process, the aircraft manufacturer and the ground test provider decide on the matrix of flight conditions not

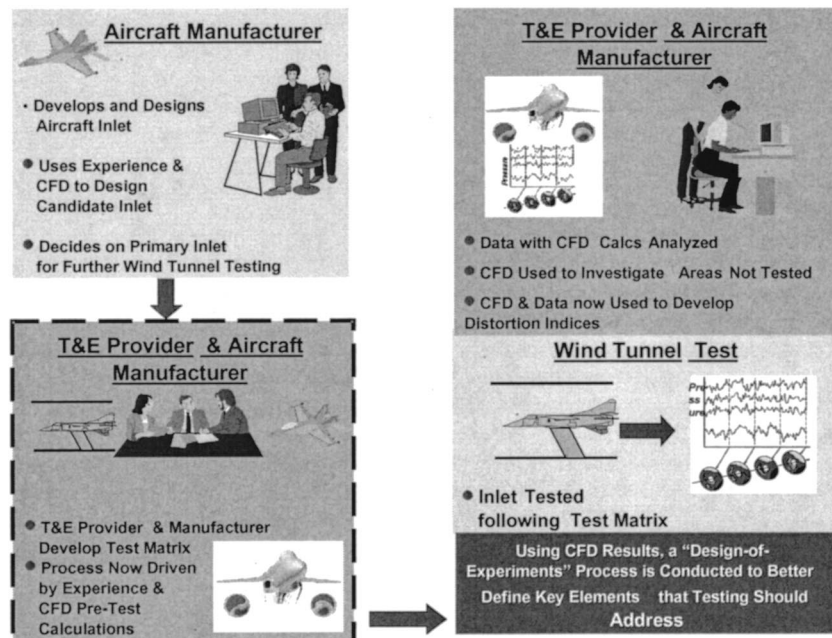


Fig. 12 Schematic of proposed improved process for inlet testing and analysis

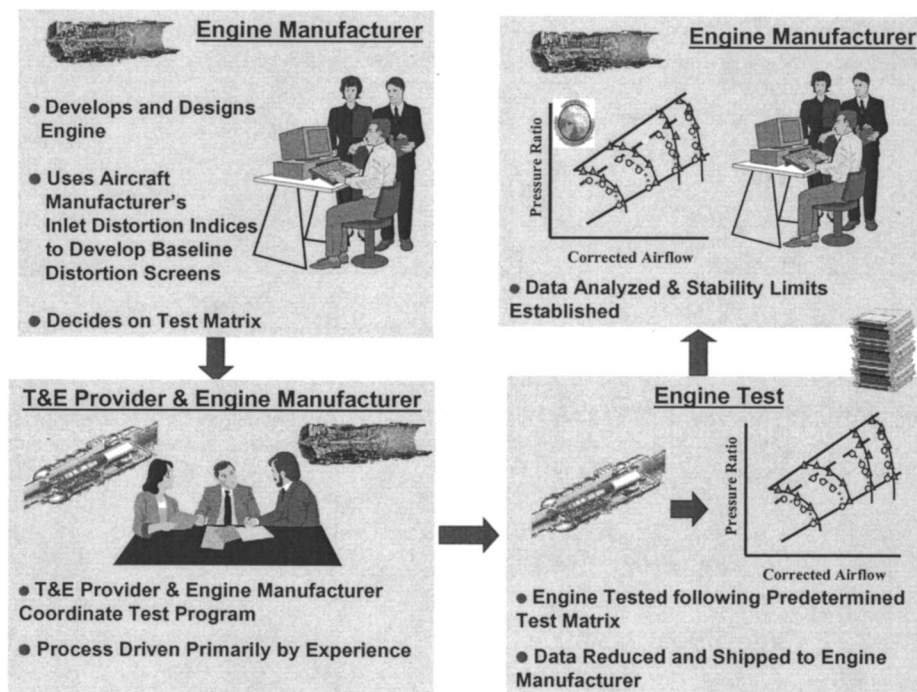


Fig. 13 Schematic of current process for engine testing and analysis

only based upon experience but on CFD calculations of the proposed test article. These calculations can be used in a "Design of Experiments" process to better define key elements that testing should address. In the improved process, both the test data and CFD calculations are used to develop the distortion indices. The experimental data provide a very coarse description of the flow at the AIP, while the CFD solutions provide the details of the flow between the data points. Validated computations provide the mechanism to fill in the data matrix for benign test conditions. Validated computations also allow the diagnostics of test conditions that result in high levels of distortion so that changes to the test article during the test can be made in an informed manner. When combined, the test data and computational simulations provide the needed information at the lowest cost.

The ultimate capability for inlet testing in the future will be to combine the fused data and CFD solutions for the inlet with a full three-dimensional engine model so that, while the inlet test is being conducted in the wind tunnel, the performance of the inlet can be determined as a function of the engine performance and stall margin changes rather than the nebulous values of distortion indices.

Looking at current engine testing, we see a process, as illustrated in Fig. 13, in place similar to the inlet process. The engine manufacturer uses whatever information that the aircraft manufacturer has provided about the nature of inlet distortion. Generally, the engine manufacturer plans distortion tests based upon previous experience and develops a test matrix using classical or baseline distortion patterns (180 deg circumferential distortion, hub radial, and tip radial distortion patterns). The engine manufacturer coordinates with ground test personnel and defines a specific test program and the length of testing required. The engine is tested to map out the compression system sensitivity to the prescribed classical distortion patterns. The data are shipped to the manufacturer who then analyzes the data and determines if the engine can tolerate the distortion patterns produced by the inlet based solely upon the classical distortion patterns.

In the improved engine test process, Fig. 14, the process is similar but by using a three-dimensional engine or compression system model, a prediction of the stability limit is obtained prior

to test. This prediction is used to streamline the test matrix by emphasizing critical regions of the flight envelope and omitting test conditions that contribute little to the evaluation. Again using a "Design of Experiments" approach, the test matrix is further refined to better define the key elements that testing should address. The engine is tested in the engine test cell based upon the test matrix defined previously. If something abnormal occurs, engine model calculations can be conducted to determine what is the most efficient way of obtaining additional test information. Once the data are obtained, analysis engineers can pool both the engine data and the model calculations to provide a better definition of the stability limit.

New engine test techniques are under development that, in the future, will replace the old distortion screen methods. The new techniques will allow a more realistic representation of both the static and dynamic pressure distortion patterns as well as the flow angles and temperature distributions at the face of the engine. Coupled with the new inlet test techniques that fully define the flow entering the engine, the new distortion devices will be able to accurately simulate the flight conditions seen by the engine.

In the near term, computational simulations of both the inlet and engine, used in a fully integrated manner prior to testing, can help to focus the test matrix on critical operating conditions and reduce the test matrix by identifying those conditions which are more benign. Computations also provide the test customer with more comprehensive information by filling in areas of the envelope that are not scheduled for testing or cannot be tested due to test facility limitations. In the long term, the combination of computational methods with new test methodologies will provide a much more realistic ground simulation of the static and dynamic conditions that an engine-airframe combination will encounter in flight.

Finally, once the accuracy of a simulation is established on a subscale test, computations provide an approach to extend the analysis to full-scale flight conditions, thus, providing a link between the measured subscale distortion from inlet testing to the distortion patterns utilized in full-scale engine testing.

In the final analysis, flight testing is conducted to operationally verify the mated inlet/aircraft with the propulsion system. Gener-

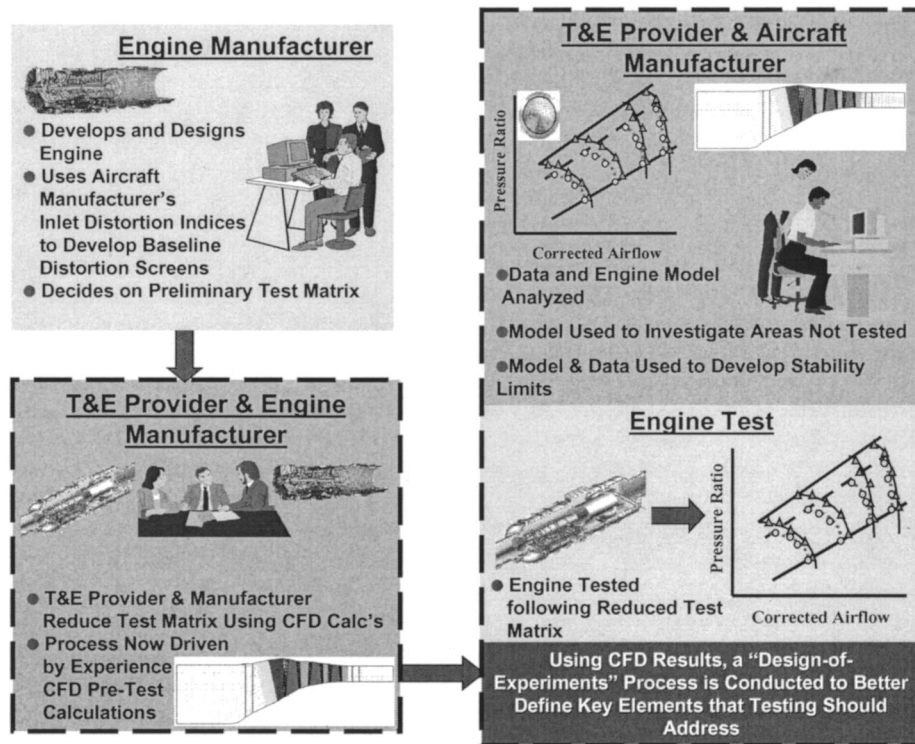


Fig. 14 Schematic of envisioned improved process for engine testing and analysis

ally, the flight test article is sparsely instrumented as compared to the ground test vehicle. In this environment, a go or no-go decision is all that can be made. With properly validated simulations of both the inlet and the engine, a virtual mating of the full propulsion system can be made and numerically flown at the desired flight condition prior to the actual flight test. The full spectrum of

the integrated test and evaluation process is illustrated in Fig. 15. The implementation of this vision has already begun with the development and application of one-dimensional engine-inlet simulations such as those reported by Garrard [27], Numbers [28], and Clark [29].

In the fully integrated test and evaluation process, system op-

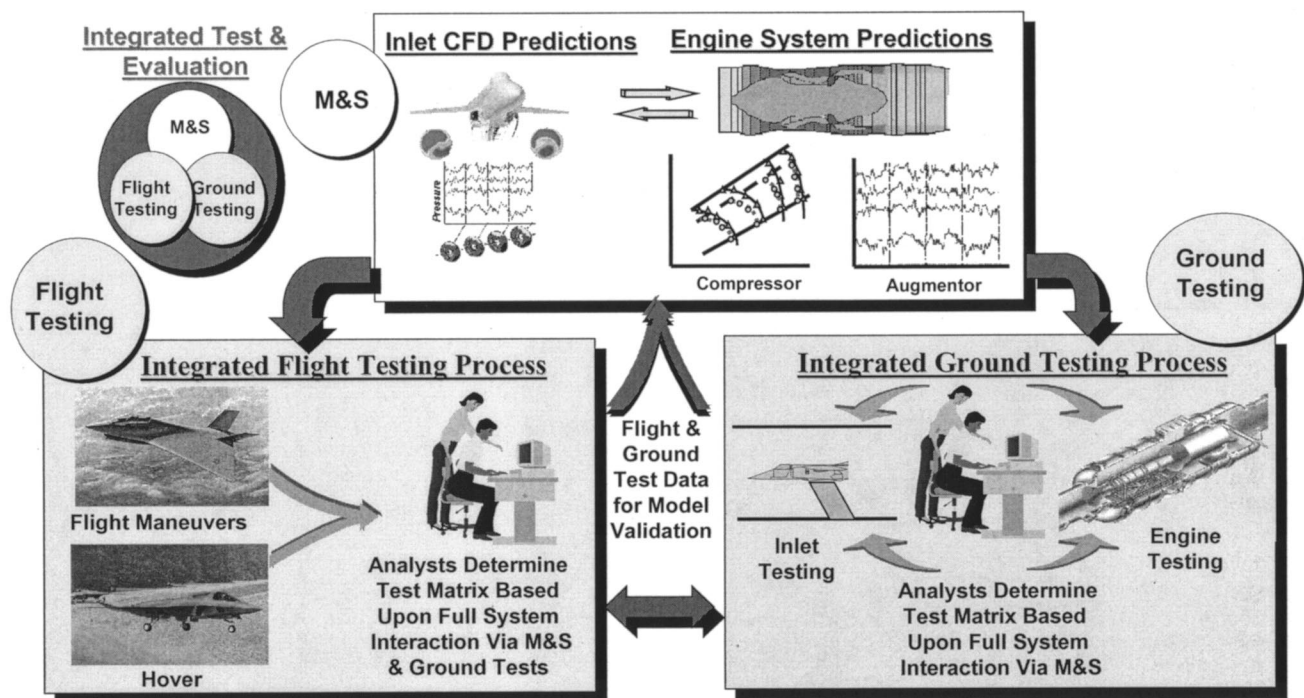


Fig. 15 Schematic of envisioned integrated test and evaluation for engine-inlet analysis

erability can be well known before the aircraft enters a flight test program. The inlet and engine models have been validated with ground test data, usually steady state in nature. However, during flight testing, dynamic distortion will be present. This dynamic nature will become more pronounced as inlets are constructed to become more "stealthy." Validation of both inlet simulations and engine simulations is an issue as stated by Benek and Kraft in their 1998 journal article ([30]). Among the issues raised by Benek and Kraft were

- the use of steady-state approximations to simulate time-averaged measurements of an intrinsically unsteady flow field.
- no systematic studies of the details of the computational procedures for time-dependent inlet flow have been made. The unsteady features prevent the use of usual steady-state convergence criteria that are based upon the reduction of the residual norms toward machine zero.
- time-accurate computations will be necessary for the simulation of unsteady (dynamic) distortion indices. Experiments must be carefully crafted from which to establish a validation database.
- CFD simulations are expensive in terms of computer resources and schedule and they must be used carefully to obtain the maximum benefit. A systematic study needs to be conducted to identify those parameters to which the simulations are most sensitive.

These issues must be addressed before a fully integrated test and evaluation process can be established.

Summary

This paper has reviewed the state of the art in inlet and engine testing procedures and has proposed an integrated test and evaluation process that provides additional information to the test customer at a reduced cost and schedule. That integrated test and evaluation process relies heavily on using computational simulations of both the inlet and the engine separately and in combination to provide guidance in the test process. Simulations can be used to reduce the test matrix to the absolute minimum required by providing calculations of areas not tested to a high degree of confidence. Finally, improved processes implementing advanced numerical simulations and advance test techniques are envisioned that will provide a test capability for inlets that allow modifications to the inlet during early wind tunnel tests. These inlet modifications will help ensure compatibility with the engine such that the performance of the combined inlet-engine system can be tuned to maximum system performance. Also, improved processes implementing advanced numerical simulations and advance test techniques are envisioned that will provide a test capability for engines that more accurately represent the static and dynamic conditions encountered in flight.

References

- [1] Smith, R. E., 1995, "Marrying Airframes and Engines in Ground Test Facilities—An Evolutionary Revolution," AIAA Paper No. 95-0950.
- [2] SAE Aerospace Information Report, AIR-1419, 1983, "Inlet Total-Pressure Distortion Considerations for Gas Turbine Engines," May.
- [3] SAE Aerospace Recommended Practice, ARP-1420, 1978, "Gas Turbine Engine Inlet Flow Distortion Guidelines," Mar.
- [4] Robinson, C. E., Smith, G. D., and Matz, R. J., 1969, "Evaluation of an Ejector—Powered Engine Simulator at Transonic Mach Numbers," Paper No. AEDC-TR-78-69.
- [5] Overall, B. W., 1972, "A Procedure for the Design of Complex Distortion Screen Patterns for Producing Specified Steady State Total-Pressure Profiles at the Inlet of Turbine Engines," Paper No. AEDC-TR-72-10.
- [6] Overall, B. W., 1976, "Evaluation of an Airjet Distortion Generator Used to Produce Steady-State Total-Pressure Distortion at the Inlet of Turbine Engines," Paper No. AEDC-TR-76-141.
- [7] Brimelow, B., Collins, T. P., and Pfefferkorn, G. A., 1976, "Engine Testing in a Dynamic Environment," AIAA Paper No. 74-1198.
- [8] Lazalier, G. R., and Tate, J. T., "Development of a Prototype Discrete Frequency, Total-pressure Fluctuation Generator for Jet Engine/Inlet Compatibility Investigation," Proceedings of the Air Force Airframe Propulsion Compatibility Symposium, June, Paper AFAPL-TR-69-103.
- [9] Reynolds, G. G., et al., 1973, "An Experimental Evaluation of Unsteady Flow Effects on an Axial Compressor—P³ Generator Program," Paper No. AFAPL-TR-73-43.
- [10] Smith, C. F., and Podleski, S. D., 1994, "Installed F/A-18 Inlet Flow Calculations at 30 Degree Angle-of-Attack: A Comparative Study," AIAA Paper No. 94-3213.
- [11] Power, G. D., Cooper, G. K., and Sirbaugh, J. R., 1995, "NPARC 2.2—Features and Capabilities," AIAA Paper No. 95-2609.
- [12] Mayer, D. W., Anderson, B. H., and Johnson, T. A., 1998, "3D Subsonic Diffuser Design and Analysis," AIAA Paper No. 98-3418.
- [13] Philhower, J. S., Robinson, D. E., and Brown, R. J., 1998, "Development of a Highly Offset Induction System for a Supersonic STOVL Fighter," AIAA Paper No. 98-3417.
- [14] Chien, K.-Y., 1982, "Predictions of Channel and Boundary-Layer Flows With at Low-Reynolds-Number Turbulence Model," AIAA J., **20**, No. 1, pp. 33–38.
- [15] Wilcox, D. C., 1992, "The Remarkable Ability of Turbulence Model Equations to Describe Transition," Fifth Symposium on Numerical and Physical Aspects of Aerodynamic Flows, California State University, Long Beach, CA, Jan. 13–15.
- [16] Menter, F. R., 1993, Zonal Two Equation $k-\omega$ Turbulence Models for Aerodynamic Flows," Paper No. AIAA-93-2906.
- [17] Spalart, P. R., and Allmaras, S. R., 1992, "A One-Equation Turbulence Model for Aerodynamic Flows," AIAA Paper No. 92-0439.
- [18] Tramel, R. W., and Nichols, R. H., 1997, "A Highly-Efficient Numerical Method for Overset-Mesh Moving-Body Problems," AIAA Paper No. 97-2040.
- [19] Nichols, R. H., 1991, "Calculation of the Flow in an Circular S-Duct Inlet," Paper No. AIAA-91-0174.
- [20] Bush, R. H., Power, G. D., and Towne, C. E., 1998, "WIND: The Production Flow Solver of the NPARC Alliance," AIAA Paper No. 98-0935.
- [21] Paynter, G. C., 1997, "Response of a Two-Dimensional Cascade to an Upstream Disturbance," AIAA J., **35**, No. 3, pp. 434–440.
- [22] Paynter, G. C., Clark, L. T., and Cole, G. L., 1998, "Modeling the Response from a Cascade to an Upstream Acoustic Disturbance," AIAA Paper No. 98-0953.
- [23] Hall, E. J., and Delaney, R. A., 1992, "Investigation of Advanced Counterrotation Blade Configuration Concepts for High Speed Turboprop Systems: Task V—Unsteady Counterrotation Ducted Propfan Analysis, Final Report," NASA CR 187126, NASA Contract NAS3-25270.
- [24] Adamczyk, J. J., 1985, "Model Equations for Simulating Flows in Multistage Turbomachinery," ASME Paper No. 85-GT-226.
- [25] Hale, A. A., and O'Brien, W. F., 1998, "A Three-Dimensional Turbine Engine Analysis Compressor Code (TEACC) for Steady-State Inlet Distortion," Journal of Turbomachinery, **120**, pp. 422–430.
- [26] Hearsey, R. M., 1970, "HTO300—A Computer Program for the Design and Analysis of Axial turbomachinery," Mar.
- [27] Garrard, D., Davis, M. W., Wehofer, S., and Cole, G., 1997, "A One-Dimensional, Time-Dependent Inlet/Engine Numerical Simulation for Aircraft Propulsion Systems," ASME Paper No. 97-GT-333.
- [28] Numbers, K., and Hamed, A., 1997, "Development of a Coupled Inlet-Engine Dynamic Analysis Method," AIAA Paper No. 97-2880.
- [29] Clark, L. T., 1995, "Dynamic Response Characteristics of a Mixed Compression Supersonic Inlet as Part of a Larger System," AIAA Paper No. 95-0036.
- [30] Benek, J. A., and Kraft, E. M., 1998, "Validation Issues for Engine-Airframe Integration," AIAA J., **36**, No. 5.

G. S. Corman

A. J. Dean

S. Brabetz

M. K. Brun

K. L. Luthra

GE Global Research Center,
P.O. Box 8,
Schenectady, NY 12301

L. Tognarelli

M. Pecchioli

GE Oil and Gas/Nuovo Pignone,
GE Power Systems,
Via Felice Matteucci, 2,
50127 Firenze, Italy

Rig and Engine Testing of Melt Infiltrated Ceramic Composites for Combustor and Shroud Applications

General Electric has developed SiC fiber-reinforced SiC-Si matrix composites produced by silicon melt infiltration for use in gas turbine engine applications. High temperature, high-pressure combustion rig testing, and engine testing has been performed on combustor liners and turbine shrouds made from such MI composites. Frame 5 sized combustor liners were rig tested under lean head end diffusion flame conditions for 150 hours, including 20 thermal trip cycles, with no observed damage to the ceramic liners. Similarly, 46-cm diameter, single-piece turbine shroud rings were fabricated and tested in a GE-2 gas turbine engine. The fabrication and testing of both components are described. [DOI: 10.1115/1.1455637]

Introduction

For the past eight years General Electric (GE) has been actively pursuing the development of melt infiltrated ceramic matrix composites (MI-CMC) for use in gas turbine engine applications under the Department of Energy (DOE) sponsored Continuous Fiber Ceramic Composite (CFCC) and NASA-sponsored High-Speed Civil Transport (HSCT) programs. MI-CMCs consist of continuous SiC reinforcing fibers in a matrix of SiC plus Si and are fabricated using a molten silicon infiltration process. Although many process variations can be used to fabricate such composites, GE has worked to develop two main processing routes: prepreg MI and slurry cast MI. Process flow diagrams for these two techniques are shown in Fig. 1. Details of the prepreg process and the resulting material properties have been described previously (Corman, et al. [1]).

The unique properties offered by MI-CMCs, such as high thermal conductivity, high matrix cracking stress, high interlaminar strengths, and good environmental stability (oxidation resistance) make them particularly suitable for gas turbine engine applications (Corman et al. [2]). Turbine shroud and small combustor liner components have undergone high-pressure high-temperature combustion rig testing (Dean et al. [3]) where the MI-CMC components clearly out-performed comparable metallic components. For instance, an HS-188 nickel-based superalloy shroud was found to fail by oxidation and thermal fatigue cracking after only 50 thermal trip cycles (sudden shutoff of fuel flow with full air flow maintained, resulting in a severe thermal quench from operating temperature to compressor discharge temperature) whereas the MI-CMC shrouds survived 200 thermal trip cycles and over 50 hours of steady-state exposure under the same conditions (1520°C gas temperature, gas velocity of mach 0.2, 1200°C shroud surface temperature) with only very minor edge cracking. A photograph of an HS-188 and a prepreg MI-CMC shroud after rig testing is shown in Fig. 2. Similarly, an MI-CMC combustor

liner was used in the shroud test rig for durability reasons after the initial stainless steel liner failed. The MI-CMC liner withstood combustor temperatures up to 400°C higher than did the metal liner with no observable damage.

GE has been following a stepwise approach to the testing and eventual commercial introduction of MI-CMC composite components. First engineering property data was collected and combined with analytical modeling to establish the viability of the material to meet the application requirements (Corman et al. [2]). Combustion rig testing was then conducted on subscale (combustor) or full-scale (shroud) components to demonstrate survivability of the components to turbine-like environments and duty cycles (Dean et al. [3]). The next step in this progression was to perform full-scale combustion rig tests of the combustor liner components and actual engine tests of the shrouds. This paper describes the fabrication and testing of these components.

Frame 5 Combustor Testing

GE has a worldwide fleet of about 3500 Frame 3 and Frame 5 gas turbines, most of which utilize fairly old diffusion flame combustion technology. This installed base represents a good opportunity to greatly reduce NO_x emissions with improved combustion technology. Consequently, a combustor uprate utilizing an MI-CMC liner, with its greatly reduced film cooling requirements, could prove to be an important vehicle to reduce NO_x. In addition, CO emissions can be reduced using MI-CMC liners by eliminating CO quenching reactions associated with liner cooling flows.

Test Rig Design. The goal of this effort was to rig test Frame 5-sized MI-CMC combustor liners. Initial testing was to be done under diffusion flame conditions using a standard "lean head end" (LHE) combustor configuration. This combustor is described in detail by Feitelberg et al. [4]. If successful, the liners would subsequently be tested in a different rig utilizing a premixed DLN combustion system.

A cross section of a normal Frame 5 LHE combustor is shown in Fig. 3. At the forward end of the combustor is a simple fuel injector consisting of a tube with eight holes drilled in a circular pattern. The injector is surrounded by a cast swirler and a cap assembly cooled by a series of louver openings. Just downstream of the cap mixing jets flow inward through holes in the liner and

Contributed by the International Gas Turbine Institute (IGTI) of THE AMERICAN SOCIETY OF MECHANICAL ENGINEERS for publication in the ASME JOURNAL OF ENGINEERING FOR GAS TURBINES AND POWER. Paper presented at the International Gas Turbine and Aeroengine Congress and Exhibition, Munich, Germany, May 8–11, 2000; Paper 00-GT-638. Manuscript received by the IGTI, November 1999; final revision received by ASME Headquarters, February 2000. Associate Editor: D. Wisler.

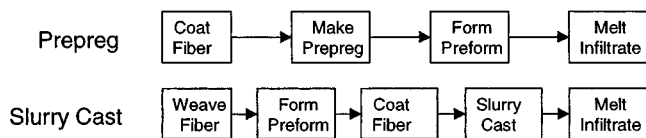


Fig. 1 Processing flow charts for fabrication of prepreg and slurry cast MI-CMCs

mix with the fuel and stabilize the flame. The metallic liner, which is cooled with louver cooling along its length, is roughly 28 cm in diameter by 91 cm long. Although this length is needed to ensure complete burning of liquid fuels under diffusion flame conditions,

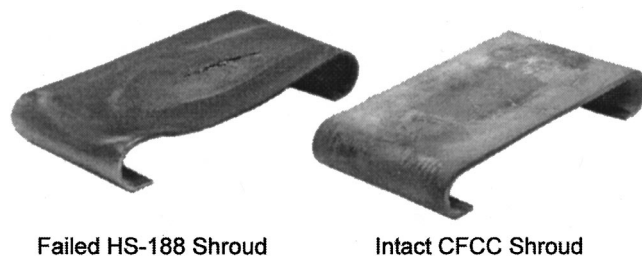


Fig. 2 Photograph of turbine shroud components following combustion rig testing

the region of maximum convective and radiative heat transfer from the flame to the liner wall is actually much smaller. Consequently the length of MI-CMC in the liner would not need to be the full 91 cm.

An additional goal of the rig tests was to allow for testing of two liner materials (the prepreg and slurry cast MI-CMCs). There were also questions about the proper design philosophy for the liner. GE Frame 5 engines have can-annular combustors where the compressor discharge normally convectively cools the outside of the liners before entering the combustion region. To allow similar convective backside cooling of the MI-CMC liner would keep material temperatures low, but would introduce significant thermal stresses in the liners from the through-thickness thermal gradients. Conversely, convective cooling of the MI-CMC liner could be eliminated by using an outer flow shield. This situation would minimize the thermal stresses in the liner by letting it run nearly isothermal, but the liner surface temperature would be greatly increased compared to the cooled concept. Thus it was desirable to be able to expose liners to both sets of conditions within the rig in order to evaluate the durability of the MI-CMC to both types of conditions.

The combustion rig liner configuration, which allowed for simultaneous testing of two MI-CMC materials under cooled and uncooled conditions, is also shown in Fig. 3. The preheated combustor inlet air is fed into the rear (right side) of the combustor casing and flows to the left along the outside of the liners. A portion of this air was used for convective and film cooling of the metallic sections of the liner. The air then reverses at the combustor cap and flows into the combustor liner where the natural gas

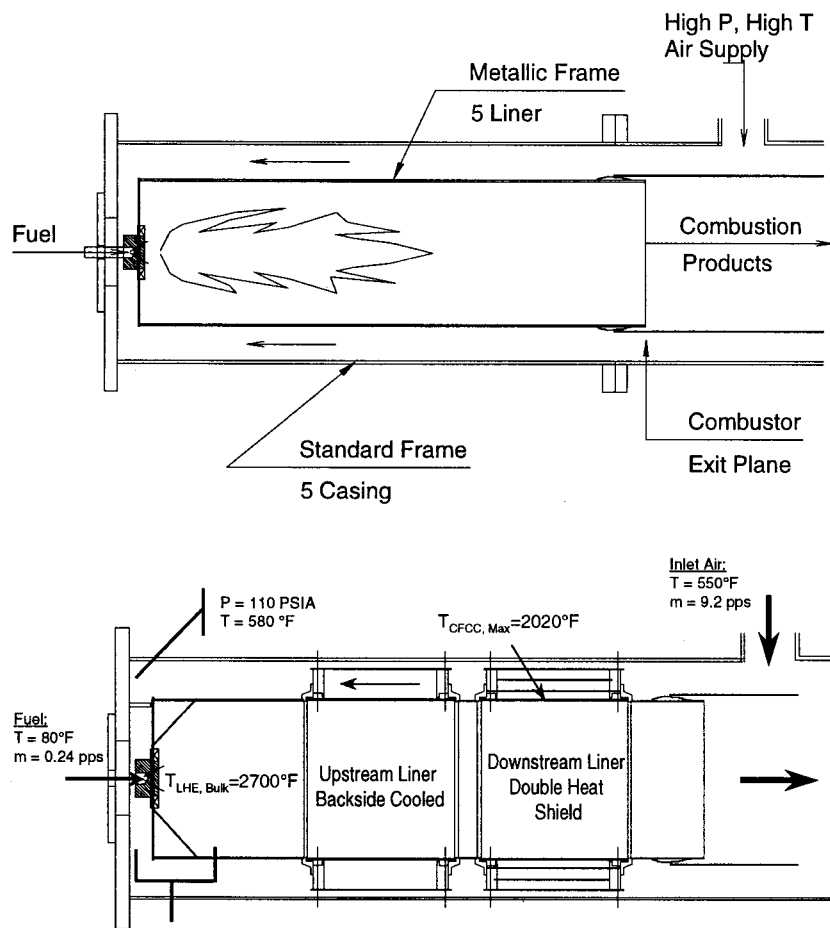


Fig. 3 Schematic of Frame 5 combustors mounted in the test rig. Top: metallic LHE liner. Bottom: test rig liner showing the location of the two MI-CMC liner sections.

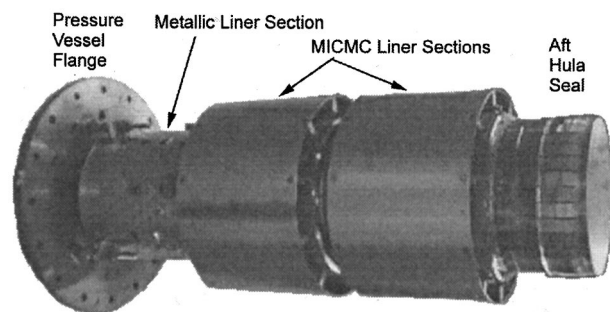


Fig. 4 Photograph of the liner assembly for the Frame 5 combustor test rig

fuel is injected and burned. The hot combustion gasses then flow left to right inside the MI-CMC liner sections and out an exhaust stack to the right. The upstream MI-CMC liner was left exposed on the back side so that it was convectively cooled by the compressed air whereas the downstream MI-CMC liner had two flow shields placed between it and the compressed gas flow. The two types of MI-CMC liner, prepreg, and slurry cast were swapped between the cooled and uncooled positions in order to accumulate the same net exposure under both sets of conditions.

The rig combustor liner was fabricated by cutting sections from an actual Frame 5 metallic combustor and welding in support rings for the MI-CMC liners. A metallic cylinder bolted to the outside of the support rings took up all structural loads through the liner, and thus the ceramic liners were not subject to mechanical loads. A photograph of the assembled rig combustor is shown in Fig. 4. The MI-CMC liners were held at each end by highly compliant seals. A benefit of this liner mounting scheme was that it allowed the geometry of the MI-CMC liners to be very simple with no complicated mounting flanges or holes. This simple geometry greatly aided liner fabrication.

The MI-CMC liners and support structure were analyzed using the ANSYS finite element modeling (FEM) code under steady-state conditions using the properties corresponding to each composite. The materials property data used for the analyses were from measurements done under the CFCC and HSCT programs. One key difference in the two types of MI composite are the thermal conductivity values. The thru-thickness thermal conductivity of the prepreg material is about 50 percent higher than the slurry cast material when using the same fiber. Values for the in-plane thermal conductivities were 10 percent to 20 percent higher than the thru-thickness values. Both composites were assumed to be transversely isotropic.

Thermal-mechanical FEM analysis of the combustor indicated that the frictional loads on the MI-CMC liners from the seals and the pressure loads were both negligible compared to the thermal gradient stresses. The stress calculations also revealed that having a uniform liner temperature is a key part of achieving low stress in the ceramics. However, the magnitude of the thermal gradients, and therefore the predicted stress levels, depended strongly on the thermal conductivity and gas leakage rate of the metal-to-ceramic seals. Uncertainty regarding these boundary conditions made accurate prediction of component stress levels impractical. Rather, strength limits of the MI-CMCs were used to derive bounds on the size of the temperature gradients in the region of the seals. Preliminary testing was then done with instrumented metallic liners in order to verify that the actual liner gradients would be within these bounds.

MI-CMC Combustor Fabrication. MI-CMC combustor liners were fabricated by both the prepreg and slurry casting processes. The liners were simple right cylinders nominally 27.8 cm outer diameter by 25.4 cm long. The slurry cast MI-CMC liner was fabricated by GE Power Systems Composites (formerly Hon-

eywell Advanced Composites) using 18 end per inch, 5 harness satin cloth of Hi-Nicalon™ fiber and a standard BN fiber coating.

The prepreg liner was fabricated at GE GRC, again using Hi-Nicalon fiber with a BN-based fiber coating. The liner was constructed of eight plies with a [0-90-0-90]_{2s} ply layout. The hoop-oriented fiber plies (0 deg) were continuously wound onto a cylindrical mandrel. The axially reinforced (90 deg) plies were laid up by hand over the hoop plies. In this way both the hoop and axial fibers were continuous through the piece with no fiber splices. Following infiltration a diamond saw was used to cut the liner to length. The final shape was within target so no machining of the ID or OD was necessary.

NDE evaluation of the two liners was performed at Argonne National laboratory using thermal diffusivity imaging. These tests confirmed that the liners were free of major defects. The prepreg liner showed a higher overall thermal diffusivity, but also showed some small delamination-like defects, primarily near the combustor edges, caused by wrinkles in the hoop fiber plies.

Test Rig Instrumentation. The test facility and test hardware were fully instrumented to measure combustor airflow, fuel flow, inlet pressure and temperature, combustor dynamic pressure, rig pressure drop (2 places), component temperature (surface-mounted and embedded thermocouples), and exhaust gas composition at the combustor exit.

Accurate measurement of the MI-CMC liner temperatures was challenging. The approach used in this program was to attach 0.040" diameter Type K thermocouples into grooves cut mid-thickness into the MI-CMC liner. The thermocouples were then bonded into the groove using a ceramic paste. Four thermocouples were attached to each liner. This method had the advantage of direct contact of the thermocouples with the parts. Unfortunately many thermocouples detached after only five hours of fired tests so bulk material temperature was not recorded for all tests. However, other measurements including fuel and air flows and temperatures of metal components showed that conditions were constant throughout the test program.

Liner Testing. Rig shakedown testing using instrumented metallic combustor liners provided detailed metal temperature information of the combustor liners and the interface to the metal support structure. Cooling air flows to the metallic components of the rig were modified as necessary to keep them within safe operating limits.

The liners were exposed to a bulk combustion gas temperature of 1480°C in cyclic and steady-state tests. Typical flows for these tests were 4.5 kg/s at 300°C inlet temperature and seven bar inlet pressure. Although the standard firing temperature of a Frame 5 engine is typically around 1065°C, the rig was run at the higher temperature to simulate a bulk gas temperature similar to a DLN combustor. Thus the overall heat load (a combination of temperature and surface heat transfer coefficient) to the MI-CMC liners was still somewhat higher than would be expected in an engine. A summary of the tests conducted is given in Table 1. The maximum liner temperatures observed were 890°C and 1100°C for the upstream (cooled) and downstream (uncooled) liners, respectively.

Cyclic testing simulated engine trip conditions with 20 flame-on, flame-off cycles. Figure 5 shows bulk gas temperature and MI-CMC temperature at four locations on the downstream liner as a function of time during the first cyclic test. Steady-state testing involved 150 hours of exposure at high temperature and pressure with hot combustion gases.

At the conclusion of this first phase of testing there was no visible damage to either liner. In the next phase of testing, the liners will be installed in a DLN combustor where the bulk temperature is similar to this set of tests but the temperature profile is more uniform, resulting in higher liner temperatures.

Table 1 Summary of Frame 5 combustor rig exposure test conditions

Test	Upstream Liner	Downstream Liner	Objective	Observations
1	Metal	Metal	Collect baseline temperature distributions	<ul style="list-style-type: none"> - Detailed temperature map and thermal paint images - Maximum metal temperature of 1010°C
2	Prepreg MI-CMC	Slurry Cast MI-CMC	1 st short-term exposure of MI-CMC liners; verify attachment operation	<ul style="list-style-type: none"> - Liner maximum temperature of 893°C upstream and 1110°C downstream - Oxidation color patterns on MI-CMC liners match thermal paint on metal liners - No indications of liner distress at attachments
3	Slurry Cast MI-CMC	Prepreg MI-CMC	2 nd short term exposure test with 10 trip cycles	<ul style="list-style-type: none"> - Liner maximum temperature of 871°C upstream and ~1100°C downstream - No damage from thermal cycles.
4	Slurry Cast MI-CMC	Prepreg MI-CMC	1 st long-term (75 hours) test	<ul style="list-style-type: none"> - Liner maximum temperature of ~871°C upstream and ~1093°C downstream (thermocouples failed early) - 3 shutdowns required to clean rig back-pressure plate
5	Prepreg MI-CMC	Slurry Cast MI-CMC	2 nd long-term test (75 hrs) with 10 trip cycles	<ul style="list-style-type: none"> - Same temperatures as Test 4 - No shutdowns required - No damage from thermal cycles

GE-2 Shroud Engine Testing

Following the successful shroud component rig tests described previously (Dean et al. [3]) it was desired to proceed with engine testing of a shroud component; however, the high level of financial liability, should a shroud failure occur, precluded testing in a large (>30MW) engine. Thus a small engine, the Nuovo Pignone GE-2, was chosen as the first test bed engine for an MI-CMC shroud. The second-stage shroud was chosen for the first engine tests again to reduce the overall risks of failure. The second stage represents a lower temperature, and therefore lower thermal stress, environment than the first stage shroud. The potential for engine damage is also much less in the event of a shroud failure.

GE-2 Engine/Shroud Design. The GE-2 is a 2 MW gas turbine engine with a two-stage centrifugal compressor, single-can silo combustor and two-stage axial turbine. Neither the first nor second stage shrouds are actively convectively cooled, rather they

rely on leakages and thermal conduction to the inner and outer turbine casings to keep shroud temperatures within operating limits of the alloys used. The current metallic second stage shroud consists of eight segments with leaf seals between the segments. A cross section of the engine turbine section, showing the positions of the first and second stage shrouds, is shown in Fig. 6. Bulk average combustion gas temperatures in the vicinity of the stage 2 shroud are about 780°C, with the temperature of the inner casings typically running about 450°C.

The size and geometry of the engine prevented the use of a ceramic shroud design of the type used in the previous rig tests. Moreover the segmented metal shroud design was known to have performance issues related to bucket tip clearance control and leakage such that reproducing the metal design with MI-CMC was not an attractive option.

The properties of the MI-CMC material did offer new shroud design opportunities. Because of its higher temperature capability relative to the metallic alloys, the MI-CMC shroud would not require a large thermal conduction path the turbine casing for cooling purposes. Also, the low coefficient of thermal expansion and high thermal conductivity of the MI-CMC would help to

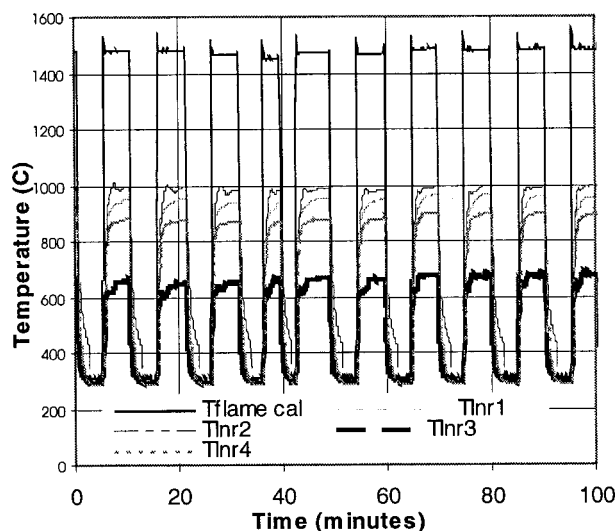


Fig. 5 Calculated bulk flame temperature ($T_{flame\ cal}$) and temperature readings of downstream liner (T_{lnr}) at four locations during cyclic testing in Test 3

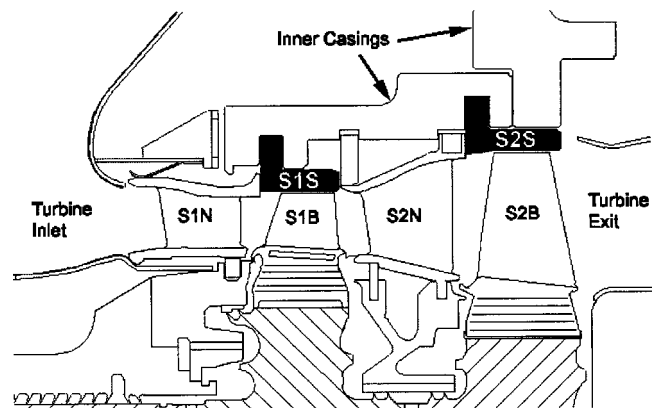


Fig. 6 Schematic of the turbine section of the GE-2 engine showing the positions of the stage 1 and stage 2 nozzles (S1N and S2N), buckets (S1B and S2B), and shrouds (S1S and S2S)

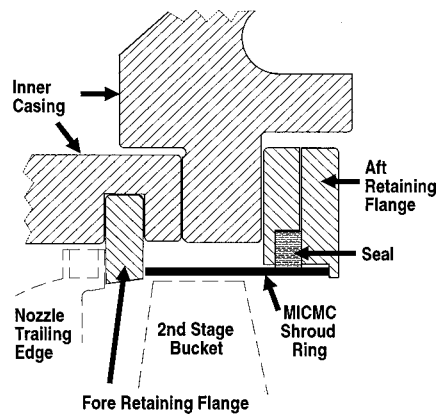


Fig. 7 MI-CMC second stage shroud design in the GE-2 engine

minimize thermal stresses, thus allowing for a single-piece shroud solution. Single-piece metallic shrouds had not been a viable option for this engine because the high thermal expansion of the metal caused high thermal gradient stresses and also prevented the attainment of the desired shroud tip clearances.

The shroud design that was developed consisted of a thin walled MI-CMC single piece ring nominally 466 mm ID by 57.5 mm long. The shroud ring is located axially in the engine between two metallic flanges and additional features were incorporated into the shroud to control its radial position. A seal, similar to that used in the Frame 5 combustor rig, was used on the back side of the MI-CMC shroud ring to prevent combustion gas leakage around the back side of the shroud. A schematic of the design is shown in Fig. 7.

MI-CMC Shroud Fabrication. Shroud rings for engine testing were fabricated from the prepreg MI-CMC. Fabrication procedures were similar to those used for the Frame 5 combustor liner discussed above. An eight-ply 0 deg-90 deg layup was used and the process adjusted to give a nominal 2.4-mm wall thickness.

The greatest challenge in fabrication of the shroud was meeting the desired dimensional tolerances. Bucket tip clearance has a large effect on engine efficiency and power output, especially for a small engine such as the GE-2, and therefore needs to be minimized as much as possible. This requirement in turn places tight tolerance limits on the rotor, bucket and shroud dimensions. Dimensional tolerances on the shroud ring were ± 0.3 mm for the ID dimension with a maximum out-of-roundness of 0.3 mm.

Three shroud rings were fabricated at GE-GRC. A coordinate measuring machine (CMM) was used to measure the dimensions of one of the as-fabricated rings. Overall the dimensional accuracy on the 466 mm ID ring was ± 0.5 mm. While this is an excellent tolerance for an as-fabricated piece of this size, it was still not within the desired range so that final grinding of the ring ID was necessary. Grinding of the ID proved to be rather problematic since the large size and thin wall of the shroud rings made it difficult for them to be fixtured for machining without distortion.

The rings were intentionally fabricated oversized in the length dimension so that the ends could be machined to the desired length and perpendicularity. All machining was done by diamond grinding. A photograph of one of the finished shroud rings is shown in Fig. 8.

Shroud Engine Testing. The MI-CMC shroud engine test plan was divided into three segments. In the first segment the engine was to be run under full speed full load conditions for only two hours, followed by a controlled shut-down and shroud inspection. The purpose of this test was to ensure that the shroud attachment system was working correctly up to the full operation temperature of the engine and that there were no early failures in the

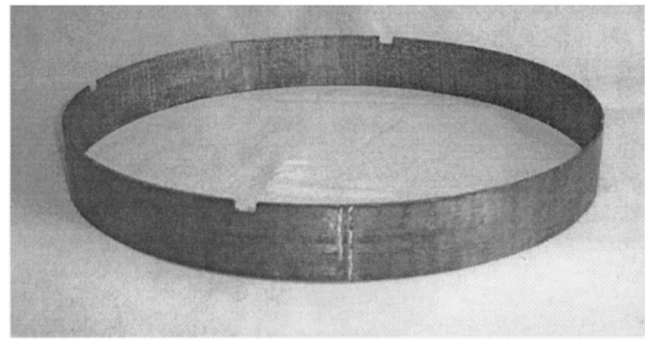


Fig. 8 Photograph of a finished prepreg MI-CMC GE-2 shroud ring. The dimensions of the ring were 466 mm ID×57.5 mm wide.

shroud. The design of the GE-2 is such that visual and boroscopic inspection of the shroud can be done via a removable expansion joint between the engine and exhaust stack.

During this initial test segment there were some control problems with the DLN combustion system that caused several turbine trips from full speed, no load conditions. Once these problems were resolved the engine ran the two hour test with no operational anomalies. However, during initial inspection it was discovered that a minor blade tip rub had occurred. The shroud section of the engine was disassembled and the MI-CMC ring removed for closer inspection.

Despite the blade tip rub, no significant damage was found in the shroud ring. In the region of the tip rub some of the blade tip alloy was smeared over the ID of the shroud ring, but the MI-CMC shroud showed only very limited wear and no signs of cracking. A photograph of the shroud in the location of the tip rub is shown in Fig. 9. Consequently this shroud was re-assembled into the engine and the test sequence was resumed.

To date the MI-CMC shroud has undergone over 66 hours of engine testing with no signs of distress. After 64 hours of "steady-state" testing (eight hours per day for eight days) the shroud was again disassembled and the shroud ring inspected. Despite indications of a second blade tip rub the shroud remained undamaged.

Additional thermal cycle testing of this MI-CMC shroud is planned in this test-bed engine at Nuovo Pignone. If the remaining

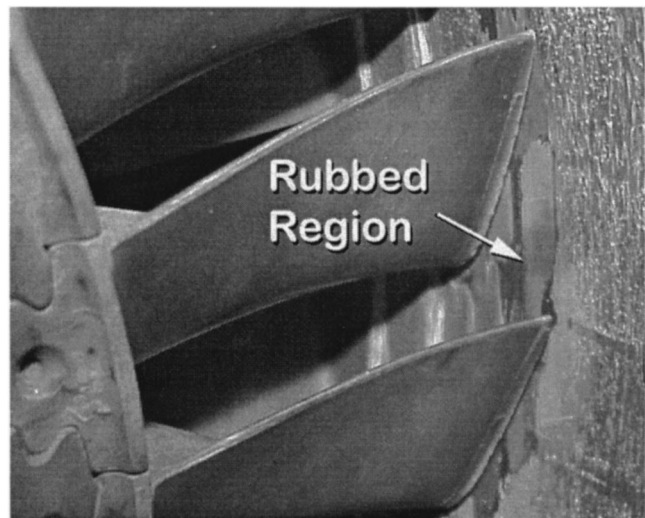


Fig. 9 Photograph of the MI-CMC stage 2 shroud in the GE-2 engine showing the blade tip rub region

testing proves to be as successful the shroud ring will be tested for an additional ~ 1000 hours in a field installation.

Conclusions

Several important milestones toward the demonstration of viable ceramic composite gas turbine components have been accomplished in this program, including the following:

- Simplified combustor liner and shroud ring designs were developed. FEM thermal/structural analysis verified that the major stresses in the liners and shroud were generated by thermal gradients and not by attachment or pressure loads.
- An effective ceramic-to-metal sealing system was demonstrated in both the combustor and shroud testing.
- Relatively large combustor liners were successfully fabricated using two variations of silicon melt infiltrated ceramic matrix composite (MI-CMC). Large shroud rings were also fabricated from prepreg MI-CMC with excellent as-fabricated tolerances.
- High-pressure combustion rig testing of the combustor liner components demonstrated excellent performance with no observed degradation of either material variant.
- To date, engine testing of the shroud ring has also proven to be very successful. The MI-CMC shroud has withstood multiple blade tip rubs with no indications of damage.

Acknowledgments

The authors are most grateful for the contributions of the following: H. McGuigan, G. Buczkowski, P. DiMascio, R. Orenstein, B. Bagepalli, V. Mezzedimi, D. Bianchi, P. Markatou, R. Camp-

bell, and M. Profeti. Part of this work was performed under DOE Contract DE-FC02-92CE41000, and we would like to thank DOE and the contract monitor, J. Mavee, for their support.

Nomenclature

ANSYS	=	finite element stress modeling code
CFCC	=	continuous fiber ceramic composites
CFD	=	computational fluid dynamics
CTE	=	coefficient of thermal expansion
CVI	=	chemical vapor infiltration
DLN	=	dry low NO_x
DOE	=	United States Department of Energy
FEM	=	finite element modeling
GE GRC	=	GE Global Research Center
LHE	=	lean head end
MI	=	silicon melt infiltration
MI-CMC	=	melt infiltrated ceramic matrix composite
NDE	=	nondestructive evaluation

References

- [1] Corman, G. S., Brun, M. K., and Luthra, K. L., 1999, "SiC Fiber Reinforced SiC-Si Matrix Composites Prepared by Melt Infiltration (MI) for Gas Turbine Engine Applications," ASME Paper 99-GT-234.
- [2] Corman, G. S., Heinen, J. T., and Goetze, R. H., 1995, "Ceramic Composites for Industrial Gas Turbine Engine Applications: DOE CFCC Phase 1 Evaluations," ASME Paper 95-GT-387.
- [3] Dean, A., Corman, G., Bagepalli, B., Luthra, K., DiMascio, P., and Orenstein, R., 1999, "Design and Testing of CFCC shroud and Combustor Components," ASME Paper 99-GT-235.
- [4] Feitelberg, A., Starkey, M., Schiefer, R., Pavri, R., Bender, M., Booth, J., and Schmidt, G., 1999, "Performance of a Reduced NO_x Diffusion Flame Combustor for the MS5002 Gas Turbine," ASME Paper 99-GT-058.

Modeling the Thermostructural Capability of Continuous Fiber-Reinforced Ceramic Composites

J. A. DiCarlo

H. M. Yun

NASA Glenn Research Center,
21000 Brookpark Road,
Cleveland, OH 44135

There exists today considerable interest in developing continuous fiber-reinforced ceramic matrix composites (CMC) that can operate as hot-section components in advanced gas turbine engines. The objective of this paper is to present simple analytical and empirical models for predicting the effects of time and temperature on CMC tensile rupture under various composite and engine conditions. These models are based on the average rupture behavior measured in air for oxide and SiC-based fibers of current technical interest. For example, assuming a cracked matrix and Larson-Miller rupture curves for single fibers, it is shown that model predictions agree quite well with high-temperature stress-rupture data for SiC/SiC CMC. Rupture models, yet to be validated, are also presented for three other relevant conditions: (a) SiC fibers become oxidatively bonded to each other in a cracked CMC, (b) applied CMC stresses are low enough to avoid matrix cracking, and (c) Si-based CMC are subjected to surface recession in high-temperature combustion gases. The practical implications of the modeling results are discussed, particularly in regard to the optimum fibers and matrices for CMC engine applications and the thermostructural capability of SiC/SiC CMC in comparison to nickel-based superalloys, monolithic ceramics, and oxide/oxide CMC. [DOI: 10.1115/1.1470480]

Introduction

The successful application of fiber-reinforced ceramic matrix composites (CMC) in advanced gas turbine engines will depend not only on selecting microstructural constituents that maximize rupture life of these CMC over a wide range of service conditions, but also on demonstrating that the maximized CMC rupture behavior is sufficient to outperform current bill-of-materials for the same conditions. Since the failure of CMC typically occurs simultaneously with fracture of the reinforcing fibers, the key to maximizing CMC life is the development of an understanding of the many factors that control fiber rupture within a complex engine environment. This can be a very difficult task since fiber behavior will not only depend on such CMC global variables as stress, temperature, and service environment, but also on how the fiber experiences these variables on the local level through mechanical, physical, and chemical interactions with each other, the interphase coating, the matrix, and the internal CMC environment. Nevertheless, because of the great potential CMC offer for increasing the efficiency of future turbine engines, research efforts are strongly needed in this area in order to develop at least some first-order understanding of their thermostructural capability. One approach toward gaining this understanding is to fabricate composite systems with the various fiber types available today and then to measure their mechanical behavior under simulated engine conditions. Although such CMC test efforts have and continue to be implemented, they are very costly and limited to only a few systems with limited test data.

The objective of this paper is to take a different and more cost-effective approach by developing simple analytical and empirical models for predicting CMC tensile rupture under various

composite and engine conditions. Because of their controlling role in composite fracture, emphasis is placed on the reinforcing fibers and their rupture behavior as measured on single fiber and single tow specimens. For example, one model assumes that the CMC contains a matrix with through-thickness cracks bridged by fibers that can fracture independently. Using simple rule-of-mixtures strength theory and Larson-Miller (LM) rupture strength curves for fibers of current technical interest, this model then predicts CMC rupture strength as a function of a single time/temperature-dependent parameter. It is shown that despite the simplifying assumptions and the complex fiber interactions that can occur in CMC, the model predictions agree fairly well with available data for the high-temperature stress rupture of SiC/SiC composites. Rupture models are also presented for three other potential conditions: (a) SiC fibers become oxidatively bonded to each other in a matrix crack, (b) the matrix remains uncracked due to low CMC stresses, and (c) SiC-based CMC are subjected to surface recession in high-temperature combustion gases. Although these models have yet to be fully validated, their predictive results can shed light on some important issues related to CMC engine application, such as the best fiber and matrix constituents for maximizing CMC rupture behavior, the detrimental effects of cracked matrices and moisture-containing combustion gases on Si-based CMC, and the degree to which SiC/SiC composites offer better thermostructural capability than state-of-the-art nickel-based superalloys and oxide/oxide CMC.

Results and Discussion

Fiber and Tow Rupture. In previous studies [1–5], the rupture strengths of a variety of continuous-length oxide and SiC-based fiber types were measured from 20 to 1400°C under ambient air conditions. The measurements were made on single fibers and on single multifilament tows across a time range from ~0.01 to over 100 hours using three types of tests: stress rupture (constant stress and constant temperature), slow warm-up (constant

Contributed by the International Gas Turbine Institute (IGTI) of THE AMERICAN SOCIETY OF MECHANICAL ENGINEERS for publication in the ASME JOURNAL OF ENGINEERING FOR GAS TURBINES AND POWER. Paper presented at the International Gas Turbine and Aeroengine Congress and Exhibition, Munich, Germany, May 8–11, 2000; Paper 00-GT-640. Manuscript received by IGTI, November 1999; final revision received by ASME Headquarters, February 2000. Associate Editor: D. R. Ballal.

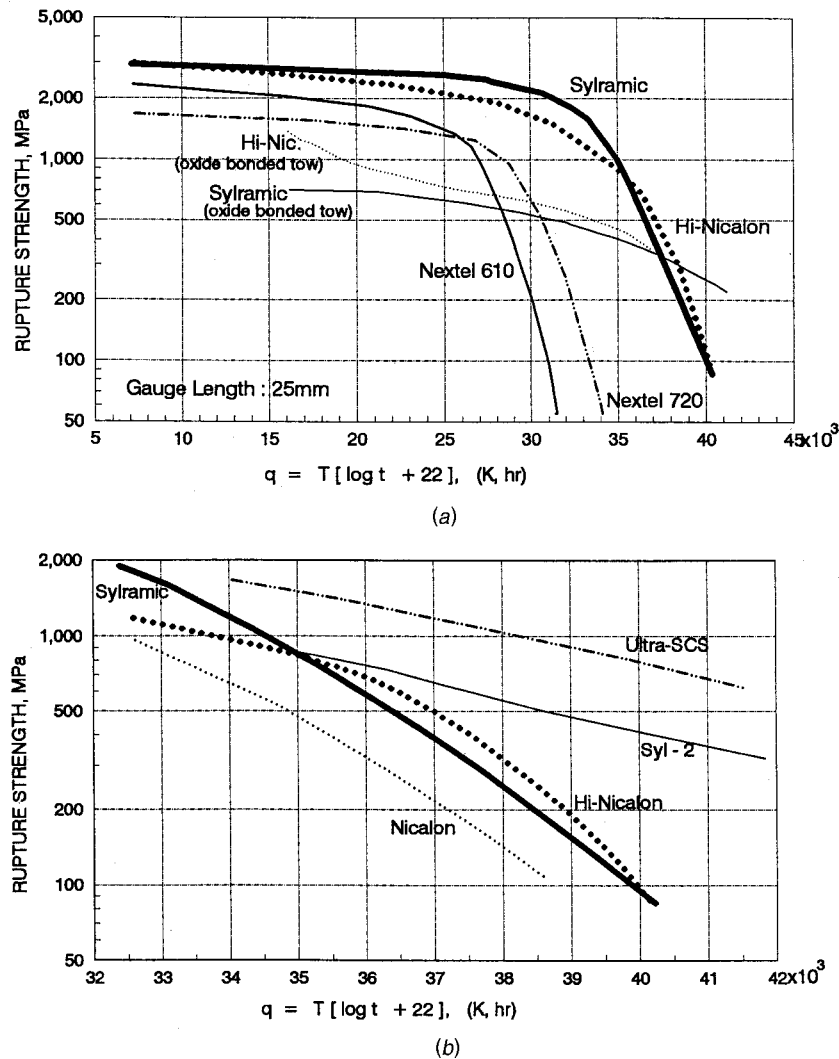


Fig. 1 Larson-Miller master curves for the time/temperature-dependent rupture strength of single-oxide and SiC-based fibers and single multifilament tows as measured in air (a) from ambient to high temperature and (b) at high temperatures

stress, constant rate of temperature change), and fast-fracture (constant temperature and constant rate of stress change). It was found that by simple thermal-activation theory ([6,7]), the rupture results of the three tests for each fiber and tow type could be combined into a single Larson-Miller (LM) master curve that plots the applied stress at rupture (or rupture strength) versus the time-temperature dependent parameter q given by

$$q \equiv Q_r / 2.3R = T(\log t_r + 22) \quad (1)$$

Here Q_r is the effective activation energy for fiber rupture; R is the universal gas constant (8.314 J/mol-K); T (Kelvin) is the absolute temperature for the rupture test; and t_r (hours) is the material rupture time. Thus for a 1000-hour test or service condition, $q = 25T$; so that at temperatures of 600, 1000, and 1400°C, q values are 21800, 31800, and 41800, respectively.

Figure 1 shows the LM master curves for various fiber types as measured in air using as-produced single fiber and single tow specimens. Figure 1(a) displays the average rupture strength behavior from room temperature to $\sim 1400^\circ\text{C}$ for two types of oxide-based fibers: Nextel 610 and Nextel 720, and for two types of SiC-based fibers: carbon-rich Hi-Nicalon fibers and stoichiometric Sylramic fibers that contain a trace amount of boron sintering aid. High-temperature strength curves are shown in Fig.

1(b) for five types of SiC-based fibers: Nicalon, Hi-Nicalon, Sylramic, Ultra SCS, and a developmental Sylramic fiber (Syl-2), which displays improved behavior over Sylramic due to a reduced boron content ([5]). These fiber types were selected because their creep and rupture properties are typical of other fiber types produced by the different commercial processing approaches used today ([8]), and because all are of current interest for reinforcement of CMC components for gas turbine engines. Figure 1(a) also shows LM strength curves for multifilament Hi-Nicalon and Sylramic tows measured in air after an oxide scale bonded the fibers within the tows to each other. All curves in Fig. 1 represent best-fit averages of single fiber or single tow rupture strengths as measured for a ~ 25 mm gauge length.

The results of Fig. 1 have many important basic and practical implications which are discussed in more detail elsewhere ([9]). For example, at low q values up to $\sim 25,000$, Fig. 1(a) shows that the average rupture strength of single fibers scales with average strength at room temperature ($q \approx 7000$). Thus the greater the as-produced tensile strength, the greater the rupture strength under low q conditions. In addition, the single SiC fibers clearly display greater thermostructural capability over the single oxide fibers both at low and high q values. At low q , this advantage is related

to the higher fracture toughness of SiC; while at high q the advantage is primarily related to slower diffusion processes in the SiC-based fibers ([9]).

Also to be noted in Fig. 1(a) is that SiC fibers lose their strength advantage at low q if they are allowed to oxidatively bond to each other within a tow. At q values below $\sim 30,000$, tow strengths for all fiber types are typically 60–80% of the average single fiber strength if the individual fibers within the tow can fracture independently. However, when SiC-based fibers bond to each other, Fig. 1(a) shows that this percentage degrades to $\sim 20\%$. However, as q increases above 30,000, the rupture strengths of bonded SiC-based tows change slowly, and at very high q can indeed be greater than the average strength of the individual SiC fibers. Thus in an oxygen environment, oxide fiber tows should outperform oxide-bonded SiC-based tows at low temperatures, but not at q values greater than $\sim 30,000$. Finally, it should be noted that the Fig. 1 curves can be used to predict the air rupture behavior of single fibers and bonded tows if any two of the following three application variables are known: stress, temperature, and time ([6]).

Composite Rupture, Cracked Matrix. One important CMC application condition is that in which the composite contains through-thickness or 0-deg bundle matrix cracks that are bridged by the load-bearing fiber reinforcement. These cracks could have developed during CMC fabrication due to a thermal expansion mismatch between the fibers and matrix or during CMC application due to some random overstress or to a design need for a high service stress. For the development of a simple rupture model for this condition, one might assume (1) that matrix cracks pre-existed or formed early during CMC service and (2) that the application requires the cracked CMC to experience a relatively constant uniaxial stress σ_c at a constant temperature T in an oxidizing environment. If V_f^* is the effective fiber volume fraction bridging the 0-deg bundle cracks in the stress direction, ultimate fracture or rupture of the CMC should then occur at time t_r when the following stress condition is satisfied:

$$\sigma_c = \sigma_c^r = V_f^* \cdot \sigma_B^r(t_r, T, L_e). \quad (2)$$

Here σ_c^r is the CMC rupture strength, σ_B^r is the average rupture strength of the fiber tows or bundles bridging the cracks, and L_e is the effective bundle gauge length within the cracks. Curtin [10] has shown that when the fibers are allowed to fracture independently (stable interfacial conditions), a good approximation for $\sigma_B^r(L_e)$ at room temperature is the average strength of single fibers measured at ~ 25 mm gauge length. Assuming this is the case at all temperatures and times, then the rupture strength of cracked CMC should be predictable from the following simple rule-of-mixtures relation:

$$\sigma_c^r \approx V_f^* \cdot \sigma_f^r(q, 25 \text{ mm}) \quad (3)$$

where $\sigma_f^r(q, 25 \text{ mm})$ is the average-fiber rupture strength as measured in a test environment that simulates the CMC application environment. Thus if the environment is oxidizing, one might simply equate $\sigma_f^r(q, 25 \text{ mm})$ to the Fig. 1 master curves measured in air on single fibers.

Obviously a key assumption in the above rupture model is that upon oxygen ingress into the matrix cracks, the bridging fibers are still able to fracture independently just as was the case for the single fibers used to generate the Fig. 1 curves. Although this is likely to be the case for the oxide-based fibers (at least up to $\sim 1200^\circ\text{C}$ where surface diffusion can cause self-bonding between contacting oxide fibers), it probably will not be the situation for the SiC-based fibers unless oxidation-resistant interphase coatings are developed. To model rupture for this particular condition of cracked composites with oxide-bonded SiC-based tows, it is suggested that one still use the same fracture theory employed for Eq. (3), but now assume the crack-bridging reinforcements, which fracture independently, are not a set of single fibers, but a set of

bonded tows that effectively act as monofilaments. This is a possible situation because in a typical woven CMC, the fibers within a tow are contacting each other, but the load-bearing tows are physically separated. Thus $\sigma_f^r(q, 25 \text{ mm})$ in Eq. (3) might now be interpreted as the time/temperature-dependent rupture strength of bonded tows measured at a 25-mm gauge length and as such can be estimated from the LM curves for bonded SiC-fiber tows shown in Fig. 1(a).

To verify the accuracy of the above rupture models, one can compare CMC rupture strength data in the literature against the predictions of Eq. (3) using the master curves of Fig. 1. To do this, one must (1) know the V_f^* for the CMC in the literature and (2) be assured that the tensile and rupture strengths of the fibers within the CMC microstructure are equivalent to those of the fibers used to generate the LM curves. Although fairly good estimates for V_f^* can be made, it is often the case that fiber strength characteristics are not equivalent. This can be the result of a variety of factors including spool-to-spool variation, fiber strength degradation during the CMC fabrication, and reduced load-carrying ability of the fiber tows due to architecture effects, such as weaving. To account for these issues, one needs to calibrate the fiber LM curves for each composite system by rewriting Eq. (3) as

$$\sigma_c^r \approx R_{FF} \cdot V_f^* \cdot \sigma_f^r(q, 25 \text{ mm}). \quad (4)$$

Here the calibration (or knockdown) factor R_{FF} can be determined from a fast fracture test on the CMC system to yield a composite ultimate tensile strength σ_c^{UTS} at temperature T . Because $q \approx 18T$ for a typical fast fracture test ([6]), it follows then that

$$R_{FF} = \sigma_c^{UTS}(T) / V_f^* \cdot \sigma_f^r(q \approx 18T, 25 \text{ mm}). \quad (5)$$

Figure 2 displays 1300 and 1315°C stress-rupture data that have been measured in air at stress from 70 to 150 MPa for SiC/SiC composites reinforced, respectively, by Hi-Nicalon fibers with a carbon interphase and a boron-containing matrix ([11]) and by Syl-2 fibers with a boron nitride interphase ([12]). Fortunately fast-fracture stress-strain measurements were performed on both of these CMC systems, yielding R_{FF} factors of 0.65 and 0.80, respectively, for the Hi-Nicalon ($V_f^* = 20\%$) and Syl-2 ($V_f^* = 16\%$) composites. Using these factors and assuming cracked matrices (0-deg bundle cracks typically form above 70 MPa in SiC/SiC), one obtains the two solid curves in Fig. 2. These curves predict the rupture strength behavior of these two CMC systems using Eq. (4) and the single-fiber master curves of Fig. 1. Also shown by the dashed line in Fig. 2 is the predicted rupture strength of the Hi-Nicalon CMC assuming the individual tows were oxide-bonded as in Fig. 1(a).

By comparing the data points and curves in Fig. 2, one finds good agreement between the single-fiber solid-line predictions and the test results for q values from $\sim 33,000$ to 38,000. This agreement indicates validity of the cracked CMC rupture model provided that under these test conditions, the carbon and boron-nitride interphases were sufficiently stable to allow the fibers to fracture independently. Indeed, microstructural observations on the Hi-Nicalon CMC showed that although some oxidation effects were observed at isolated creep-induced matrix cracks, the majority of the interphases were retained ([11]). This effect can be primarily attributed to matrix crack sealing by glasses created by the boron-containing matrix ([11]) and interphase ([12]) within the CMC. Although not measured in these CMC studies, matrix crack sealing due to boria and/or silica formation should not be as effective at lower q values and higher stresses. Thus one might expect that long-time rupture strengths of SiC/SiC composites at intermediate temperatures should be lower than those predicted by the single fiber LM curves. This behavior has indeed been observed for cracked SiC/SiC minicomposites ([13]). For very long times at intermediate temperatures, it is suggested here that the rupture strengths of woven and cracked SiC/SiC CMC should be

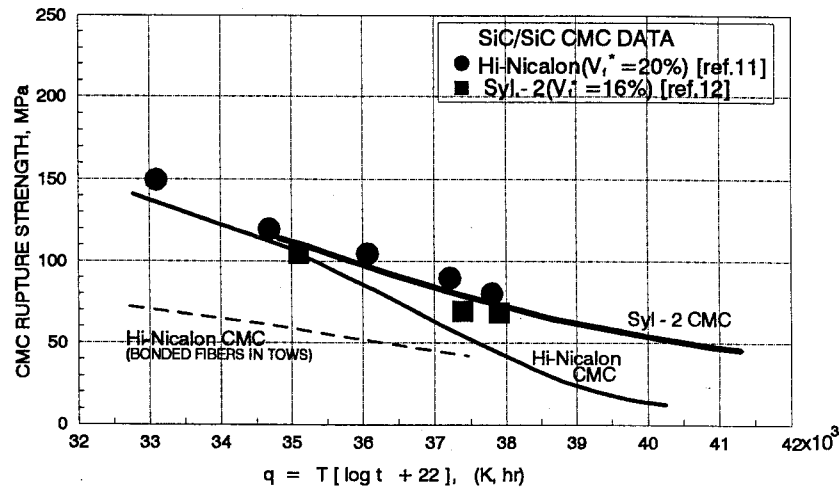


Fig. 2 Predicted rupture strength behavior and measured stress-rupture data for Hi-Nicalon and Syl-2 reinforced CMC tested at high temperatures in air. Solid and dashed curves are based, respectively, on the single-fiber and bonded-tow LM curves of Fig. 1.

predictable from the dashed curve in Fig. 2. Unfortunately, composite stress-rupture data to verify this bonded-tow model do not currently exist.

At stresses below ~ 100 MPa, the solid curve for the Hi-Nicalon CMC in Fig. 2 seems to underestimate CMC rupture life. As discussed in the next section, this deviation could be explained simply by the fact that at these stresses for the Hi-Nicalon CMC, matrix cracks through the 0-deg bundles did not exist during the test. In this case, the matrices would carry some of the applied load so that the internal fiber stresses were lower and lifetimes longer than assumed. Indeed, stress-strain and modulus measurements on the Hi-Nicalon CMC indicated that 0-deg bundle cracking did not occur until ~ 105 MPa ([11]). Thus it is concluded that the single-fiber data of Fig. 1 and the rule-of-mixtures model of Eq. (4) can yield fairly accurate predictions of the rupture strength of CMC provided the matrix is cracked and the fibers are able to fracture independently.

To demonstrate some practical advantages of the cracked CMC model, Fig. 3 employs Eq. (4) and the Fig. 1 curves for the Nextel

720 and Syl-2 fibers in order to predict the *maximum* high-temperature strength capability of cracked CMC exposed to an oxidizing environment and reinforced, respectively, by the most *creep-resistant small-diameter oxide* and SiC-based fiber types currently available. Here it is assumed that composites are operating in an oxidizing environment with stable interphases and with fiber strengths equivalent to those of Fig. 1 ($R_{FF} = 1.0$). It is also assumed (1) that the CMC contain 0/90 deg two-dimensional woven fiber architectures with a typical total volume fraction of 40 percent and (2) that the applied stress on the CMC is in the 0-deg direction so that $V_f^* = 20\%$. Also shown for comparison purposes is the rupture strength behavior for one of the highest-temperature nickel-based superalloys ([14]) as well as for two monolithic ceramics: siliconized-SiC ([15]) and AS-800 Si_3N_4 ([16]).

Figure 3 clearly projects that if the composites are cracked with stable interphases, CMC reinforced by the best available oxide fiber will not be able to outperform superalloys at any application temperature. On the other hand, CMC reinforced by the best available SiC fiber have potential for much better thermostructural be-

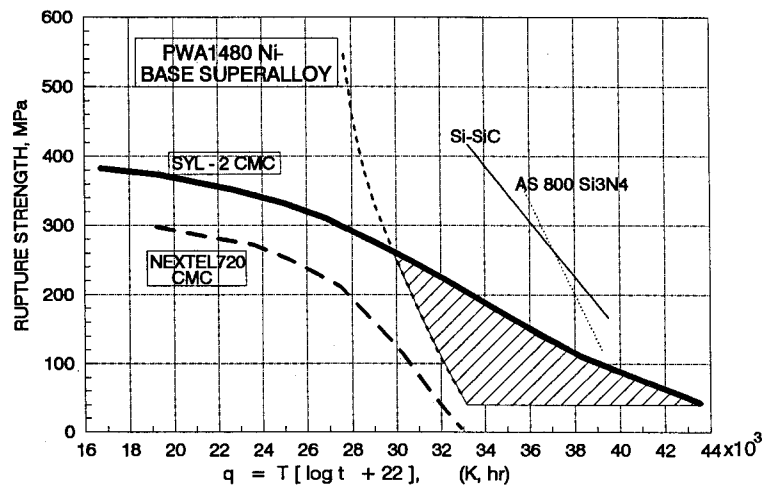


Fig. 3 Predicted maximum rupture strength capability for cracked 0/90 CMC reinforced by the most creep-resistant oxide and SiC-based fiber types currently available ($V_f^* = 20\%$). For comparison, measured strength curves are shown for a state-of-the-art nickel-based superalloy and for two types of monolithic ceramics.

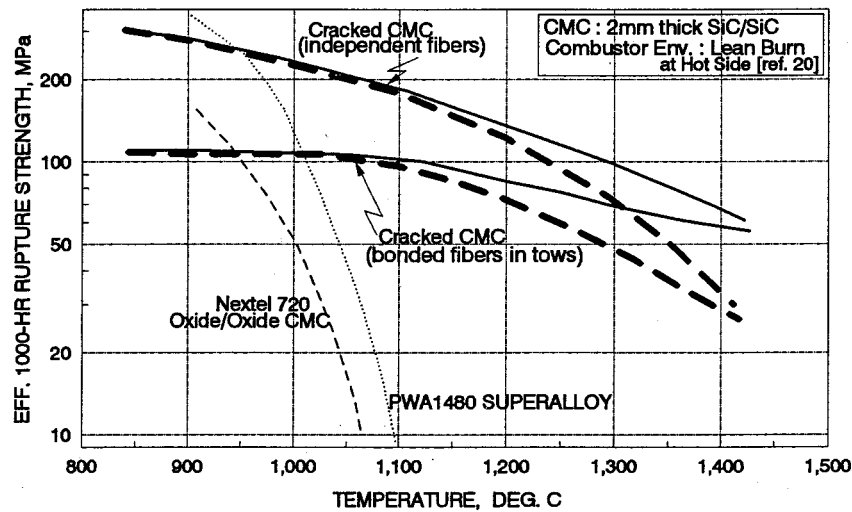


Fig. 4 Effective 1000-hour rupture strength predicted for cracked SiC/SiC CMC with Syl-2 fibers that fracture independently and a cracked SiC/SiC CMC with oxide-bonded Sylramic fibers. Solid curves=no recession; dashed curves=lean-burn combustion ([19]). For comparison, strength curves are shown for a nickel-based superalloy (measured) and an oxide/oxide CMC (predicted).

havior than both materials. In comparison to superalloys, this window of opportunity for SiC fiber-reinforced CMC exists only at high temperatures and at applied stresses no greater than ~ 200 MPa (see hatched area in Fig. 3). By comparison with Fig. 2, one could also conclude this opportunity would still exist, but at lower stress levels, even if the SiC-based fibers became bonded to each other during service. In addition, Fig. 3 indicates that the monolithic ceramics would show the best thermostructural capability provided the application conditions were benign enough to eliminate concerns over their reduced fracture toughness and tendency for catastrophic failure.

Thus an important benefit of the cracked-CMC strength model is that design engineers should now be able to select the best fiber reinforcement for their high-temperature application conditions without the need for CMC fabrication and testing. In addition, design engineers should also be able to estimate on an absolute basis the *maximum* thermostructural capability of their selected CMC. For example, for an application requiring 1000-hour service at 1200°C , that is, for $q = 36800$, one should not expect a cracked 0/90 deg composite with 40 percent Syl-2 fibers to display an ultimate rupture strength greater than ~ 140 MPa in the 0-deg direction.

Composite Rupture, Uncracked Matrix. For CMC containing expansion-compatible fibers and matrices, such as SiC/SiC, the as-fabricated composite is typically uncracked and generally requires a high tensile stress to form through-thickness matrix cracks. Morscher et al. [17] have shown that for a variety of two-dimensional woven SiC/SiC composites with SiC matrices produced by chemical vapor infiltration (CVI), the CMC threshold stress required for through-thickness cracks (0-deg bundle cracking stress) can be crudely approximated by

$$\sigma_c = E_o \cdot (0.00075) \quad (4)$$

where E_o is the CMC elastic modulus and (0.00075) is the average threshold elastic strain that has been observed for 0-deg bundle cracking. Because some SiC/SiC CMC can display moduli as high as 280 GPa at room temperature and 220 GPa at 1200°C , it follows for these composites that applied stresses as high as 210 MPa at room temperature and 165 MPa at 1200°C are required to form the 0-deg bundle cracks that eventually result in environmentally induced life reduction. Thus there can exist CMC components for which the maximum applied stress during service may

be low enough to avoid matrix cracking. For this situation, the CMC structural load will be shared in a time-dependent manner by both the fibers and the matrix. Since the fibers are not carrying the full CMC load, Eq. (4) and the LM curves of Fig. 1 would clearly underestimate fiber and presumably CMC rupture time. This appears to be the case for the Hi-Nicalon composite system discussed above (see Fig. 2).

To model this uncracked situation, it is clear that some knowledge is required of the matrix creep-rupture and geometric properties. In lieu of this information, the following model ([18]) has been proposed for the rupture life of uncracked CMC, that is, for CMC in which the matrix carries some portion of the composite load throughout the material cross-section. Assuming displacements for the fiber and matrix are the same (isostrain conditions), the creep rate of the composite, fiber, and matrix should be the same at any given time. Thus if one has knowledge of the CMC creep rate, one then should know fiber creep rate and thus could use Monkman-Grant (MG) plots ([19]) measured for the fiber in order to predict fiber and CMC rupture time. Although MG plots exist for various fiber types ([18]), this approach toward an uncracked-CMC rupture model has yet to be verified and also requires some a priori knowledge of CMC creep rate. Nevertheless, it does logically imply that one should seek matrices with high rupture and creep resistance not only to minimize the risk of time-dependent matrix cracking, but also to reduce internal stresses on the reinforcing fibers. Clearly more modeling work is needed in this area since practical situations can exist where CMC stresses are probably low enough to avoid matrix cracking, but still high enough to cause composite creep.

Si-Based Composites in Combustion Environments. The results of this study indicate that in an oxidizing environment, CMC reinforced by SiC-based fibers will display better thermostructural capability at high temperatures than state-of-the-art superalloys as well as CMC reinforced by oxide-based fibers. This appears to be the case even if the SiC fibers become oxidatively bonded to each other during service. However, it has recently been shown that when the oxidizing environment also includes moisture as in a gas turbine combustion environment, SiC and Si_3N_4 monolithic materials will oxidize in a parabolic manner due to volatile SiO and SiO_xH_y reaction products ([20]). This effect results in surface recession and cross-sectional area loss for the materials that depends primarily on temperature, moisture content,

system pressure, and velocity of the combustion gases. Thus oxide-based environmental barrier coatings (EBC) that are unaffected by moisture are currently under development for hot-section Si-based ceramic components in order that they retain sufficient structural capability during their designed engine lifetime.

Because of the importance of this environmental issue, it is of interest to understand how the thermostructural capability of Si-based CMC would be altered if EBC coatings were *not* utilized. To do this, one might assume a SiC/SiC CMC engine component with a material thickness of 2 mm and with a hot side surface which is continuously receding due to reaction with the combustion gases. For two generic combustor conditions, Smialek et al. [20] have calculated the amount of surface recession that would occur in a SiC material after 1000-hour service at various temperatures. Taking the case for the lean-burn condition, one can use these recession distances and the 2 mm CMC thickness to calculate a loss in material cross-section and thus in CMC effective rupture strength.

The results from these calculations are shown in Fig. 4, which plots, with and without recession, the predicted 1000-hour effective strength for a cracked SiC/SiC composite reinforced by fracture-independent Syl-2 fibers (~maximum intrinsic capability for a SiC/SiC CMC). The same property is shown for a cracked CMC reinforced by oxide-bonded Sylramic tows. Figure 4 also shows again the measured behavior of the state-of-the-art superalloy as well as the predicted behavior for a Nextel 720 CMC with an oxide matrix, two competing materials which are presumably unaffected by the combustion conditions. It can be seen that without an EBC, although a significant amount of CMC strength can be lost in a typical combustion environment, this loss occurs primarily at high temperatures. Also by comparing all the curves, one still arrives at the same conclusion that with or without EBC, and with or without fiber bonding, the Si-based CMC can still offer better thermostructural capability than the best available metallic alloys and oxide-oxide ceramic composites.

Summary and Conclusions

This paper has demonstrated that by using simple rule-of-mixtures composite theory and rupture strength data measured on single fibers, and tows, one can model with fair accuracy the time/temperature-dependent strength capability of cracked CMC at high temperatures. This modeling method should now allow design engineers to avoid costly CMC fabrication and testing programs in order to make key decisions concerning the best fiber type and fiber orientations for implementing CMC in such high-temperature applications as gas turbine hot-section components. For example, based on the measured fiber behavior, these models show that SiC-based fibers in general and stoichiometric SiC fibers in particular offer the best reinforcement choice for achieving CMC thermostructural performance better than nickel-based superalloys. From the other models presented here, this also appears to be the case if the CMC interphase is environmentally unstable, the CMC matrix is uncracked, or the CMC surface is unprotected from combustion gases. Although CMC with oxide fibers in oxide matrices would seem to offer solutions to all these environmentally related issues, this study has shown that these fiber types suffer intrinsically from strength-related problems associated with low fracture toughness and poor creep-rupture resistance. Also for engine components, they contribute to CMC with poorer thermal conductivity and higher density than SiC-reinforced CMC.

Because the models presented here are mechanism based, this paper has also offered some insights for the materials engineer in order to seek enhanced CMC thermostructural behavior by the judicious improvement of the CMC constituents and their geometries. For example, regarding the reinforcement, efforts should be focused on fibers with higher as-fabricated tensile strength and on the elimination of second phases in stoichiometric SiC fibers that reduce fiber creep-rupture resistance. Regarding fiber architecture, efforts should be directed toward understanding the application

requirements for tensile stress magnitude and direction and then providing architectures with sufficient volume fraction to meet these requirements. Regarding the interphase coating on the fibers, efforts should be focused on more stability in air and in moist environments in order to allow the fibers to fracture independently. Alternatively, the threshold stress for 0-deg-bundle cracking should be increased and maintained by developing dense matrices with high modulus and creep-rupture resistance. Finally, for gas turbine applications, efforts should be directed toward developing stable environmental barrier coatings for composites such as SiC/SiC in order to retain the maximum thermostructural capability available in the CMC microstructure for the service life of the component.

Acknowledgments

The authors gratefully acknowledge the support of the NASA Enabling Propulsion Materials (EPM) program under the High Speed Research Project and the NASA Advanced High Temperature Engine Materials Technology program.

References

- [1] Goldsby, J. C., Yun, H. M., DiCarlo, J. A., and Morscher, G. N., 1993, "Thermomechanical Properties of Advanced Polycrystalline Oxide Fibers," *HiTEMP Review 1993*, NASA CP 19117, Paper No. 85.
- [2] DiCarlo, J. A., Yun, H. M., and Goldsby, J. C., 1995, "Creep and Rupture Behavior of Advanced SiC Fibers," *Proceedings of ICCM-10, Microstructure, Degradation, and Design*, A. Poursartip, and K. N. Street, eds., Woodhead Publishing Ltd., Cambridge, UK, VI, pp. 315–322.
- [3] Yun, H. M., Goldsby, J. C., and DiCarlo, J. A., 1995, "Thermomechanical Behavior of Three Types of CVD SiC Monofilaments," *HiTEMP Review 1995*, Vol. III, NASA Conference Publication 10178, Paper No. 56.
- [4] Yun, H. M., and DiCarlo, J. A., 1999, "Comparison of the Tensile, Creep, and Rupture Strength Properties of Stoichiometric SiC Fibers," *Ceram. Eng. Sci. Proc.*, 20(3), pp. 259–272.
- [5] Yun, H. M., and DiCarlo, J. A., 1999, "Thermomechanical Characterization of SiC Fiber Tows and Implications for CMC," *Proceedings of ICCM-12*, Paris, Paper No. 594, and NASA/TM-1999-209283.
- [6] Yun, H. M., and DiCarlo, J. A., 1996, "Time/Temperature Dependent Tensile Strength of SiC and Al₂O₃-Based Fibers," *Ceram. Trans.*, 74, pp. 17–26.
- [7] DiCarlo, J. A., and Yun, H. M., 1998, "Thermostructural Performance Maps for Ceramic Fibers," *Proceedings of CIMTEC '98*, P. Vincenzini, ed., Techna Publishers, Srl, Florence, Paper No. SV-1: IL10.
- [8] DiCarlo, J. A., and Dutta, S., 1995, "Continuous Ceramic Fibers for Ceramic Composites," *Handbook On Continuous Fiber Reinforced Ceramic Matrix Composites*, R. Lehman, S. El-Rahaiby, and J. Wachtman, Jr., eds., CIAC, Purdue University, West Lafayette, Indiana, pp. 137–183.
- [9] DiCarlo, J. A., and Yun, H. M., 1998, "Microstructural Factors Affecting Creep-Rupture Failure of Ceramic Fibers," *Ceram. Trans.*, 99, pp. 119–134.
- [10] Curtin, W. A., 1993, "Ultimate Strengths of Fibre-Reinforced Ceramics and Metals," *Composites*, 24, pp. 98–102.
- [11] Zhu, S., Mizuno, M., Kagawa, Y., Cao, J., Nagano, Y., and Kaya, H., 1999, "Creep and Fatigue Behavior in Hi-Nicalon Fiber-Reinforced Silicon Carbide Composites at High Temperatures," *J. Am. Ceram. Soc.* 82(1), pp. 117–128.
- [12] Gray, P., 1999, Honeywell Advanced Composites, Inc., private communication.
- [13] Morscher, G. N., 1997, "Tensile Stress Rupture of SiC/SiC Minicomposites With Carbon and Boron Nitride Interphases at Elevated Temperatures in Air," *J. Am. Ceram. Soc.*, 80(8), pp. 2029–2042.
- [14] Nell, J. M., and Grant, N. J., 1992, "Multiphase Strengthened Nickel Base Superalloys Containing Refractory Carbide Dispersions," *Superalloys 1992*, S. D. Antolovich, R. W. Strusard, R. A. MacKay, D. L. Anton, T. Khan, R. D. Kissinger, and D. L. Klarstrom, eds., The Minerals, Metals & Materials Society, Warrendale, PA, p. 113.
- [15] Chuang, T.-J., Carroll, D. F., and Wiederhorn, S. M., 1989, "Creep Rupture of a Metal-Ceramic Particulate Composite," *Seventh International Conference of Fracture*, K. Salama, K. Ravi-Chandler, D. M. R. Taplin, and P. Ramo Rao, eds., Pergamon Press, New York, 4, pp. 2965–2976.
- [16] Li, C. W., 1996, Allied-Signal Ceramics, private communication.
- [17] Morscher, G. N., Gyekenyesi, J. Z., and Bhatt, R. T., "Damage Accumulation in Woven SiC/SiC Composites," *Mechanical, Thermal and Environmental Testing and Performance of Ceramic Composites and Components*, M. G. Jenkins, E. Lara-Curzio, and S. T. Gonczy, eds., American Society for Testing and Materials, West Conshohocken, PA, ASTM STP 1392.
- [18] DiCarlo, J. A., and Yun, H. M., 1999, "Factors Controlling Stress-Rupture of Fiber-Reinforced Ceramic Composites," *Proceedings of ICCM-12 Congress*, Paris, Paper No. 750.
- [19] Monkman, F. C., and Grant, N. J., 1956, "An Empirical Relationship between Rupture Life and Minimum Creep Rate," *Proc. ASTM*, 56, pp. 593–620.
- [20] Smialek, J. L., Robinson, R. C., Opila, E. J., Fox, D. S., and Jacobson, N. S., 1999, "SiC and Si₃N₄ Recession Due to SiO₂ Scale Volatility under Combustor Conditions," *Adv. Composite Mater.*, 8(1), pp. 33–45.

Reaction Mechanisms for Methane Ignition

S. C. Li

F. A. Williams

Center for Energy and Combustion Research,
University of California, San Diego,
La Jolla, CA 92093-0417

To help understand how methane ignition occurs in gas turbines, dual-fuel diesel engines, and other combustion devices, the present study addresses reaction mechanisms with the objective of predicting autoignition times for temperatures between 1000 K and 2000 K, pressures between 1 bar and 150 bar, and equivalence ratio between 0.4 and 3. It extends our previous methane flame chemistry and refines earlier methane ignition work. In addition to a detailed mechanism, short mechanisms are presented that retain essential features of the detailed mechanism. The detailed mechanism consists of 127 elementary reactions among 31 species and results in nine intermediate species being most important in autoignition, namely, CH_3 , OH , HO_2 , H_2O_2 , CH_2O , CHO , CH_3O , H , O . Below 1300 K the last three of these are unimportant, but above 1400 K all are significant. To further simplify the computation, systematically reduced chemistry is developed, and an analytical solution for ignition delay times is obtained in the low-temperature range. For most fuels, a single Arrhenius fit for the ignition delay is adequate, but for hydrogen the temperature sensitivity becomes stronger at low temperatures. The present study predicts that, contrary to hydrogen, for methane the temperature sensitivity of the autoignition delay becomes stronger at high temperatures, above 1400 K, and weaker at low temperatures, below 1300 K. Predictions are in good agreement with shock-tube experiments. The results may be employed to estimate ignition delay times in practical combustors.
[DOI: 10.1115/1.1377871]

Introduction

Knowledge of the chemistry of methane ignition is needed in various ways in power production, propulsion, and safety. Propulsion devices that have considered methane as a fuel include gas turbines, supersonic-combustion ramjets, ram accelerators, and dual-fuel diesel engines. In some applications, such as supersonic combustion and ram accelerators, it is important to achieve sufficiently rapid autoignition for the heat release to occur in the limited residence times. In other applications, such as gas turbines and dual-fuel diesel engines, for safety it is often desirable to prevent autoignition from occurring before flame propagation into the combustible mixture is complete, reducing relight overpressures and knock intensity ([1–3]).

Although methane chemistry has been studied for several decades, most of the published methane mechanisms were developed mainly for methane combustion and were tested by shock-tube experiments only for temperatures above 1400 K (e.g., [4]). In many cases, those mechanisms failed to predict ignition delay times correctly for temperatures below 1300 K ([5]). This is not surprising because the mechanisms were not designed for use at such low-temperature conditions. In the last five years, research on methane combustion has significantly advanced our knowledge of methane flame chemistry. As a result, we have developed a detailed reaction mechanism for methane combustion which consists of C_1 – C_3 chemistry and nitrogen-oxidation chemistry ([6]). Recently, Spadaccini et al. [7,8] and Petersen et al. [5] published experimental results on methane autoignition that provide valuable data for testing autoignition chemistry in both high and low temperature ranges. The present study extends our methane flame chemistry ([6]) to methane autoignition based on these shock-tube experiments ([5,7,8]).

In the present work, we present a detailed reaction mechanism that can be applied to a wide range of conditions. Short mechanisms

are then derived specifically for different initial conditions of interest. From the short mechanism, systematically reduced chemistry is obtained to further simplify numerical computations and to find an approximate analytical solution for ignition delay times. These mechanisms are then tested by comparing predicted ignition delay times with experimental results ([5,7,8]).

Detailed Reaction Mechanism

In predicting methane ignition, the present study employs a detailed C_1 – C_3 mechanism, consisting of 127 elementary reactions among 30 species, which are CH_4 , O_2 , HO_2 , H_2O_2 , CH_3 , CH_2O , CHO , OH , CO , H_2O , H , O , H_2 , CH_3O , CH_2OH , CO_2 , C_2H_6 , C_2H_5 , C_2H_4 , C_2H_3 , C_2H_2 , singlet CH_2 , triplet CH_2 , CH , HCCO , C_3H_7 , C_3H_6 , C_3H_5 , C_3H_4 , C_3H_3 . This reaction mechanism is derived from our published 177-step reaction mechanism ([6]) by deleting nitrogen chemistry (reactions 126–177) and adding two more reactions, $\text{CH}_4 + \text{O}_2 \rightleftharpoons \text{CH}_3 + \text{HO}_2$ and $\text{CH}_4 + \text{HO}_2 \rightleftharpoons \text{CH}_3 + \text{H}_2\text{O}_2$ with their rate parameters taken from the paper by Leung and Lindstedt [9] (reactions 122 and 123). These two reactions are important in the initiation stage of methane ignition but not in methane combustion.

24-Step Short Mechanism

The detailed mechanism can be significantly simplified when applied to predicting methane autoignition times for methane-air mixtures with equivalence ratios, Φ , leaner than 1.5, the principal range of interest. Under these conditions, the fate of C_2 – C_3 species generated from methyl recombination is not important, and species such as CH_2 , CH and CH_2OH contribute little to ignition processes. It is found from sensitivity and reaction-path analyses that 24 elementary reactions, listed in Table 1, then are most important to methane autoignition. This 24-step short mechanism retains the essential features of the detailed mechanism, clearly represents a very significant simplification over the 127-step mechanism and indicates that many elementary steps that are important in flames are not important in ignition.

In the 24-step mechanism, the initiation steps are steps 1 and 10. The former, where the CH_4 is attacked by O_2 to form CH_3 and HO_2 , has an activation energy half that of the latter, in which the

Contributed by the International Gas Turbine Institute (IGTI) of THE AMERICAN SOCIETY OF MECHANICAL ENGINEERS for publication in the ASME JOURNAL OF ENGINEERING FOR GAS TURBINES AND POWER. Paper presented at the International Gas Turbine and Aeroengine Congress and Exhibition, Munich, Germany, May 8–11, 2000; Paper 00-GT-145. Manuscript received by IGTI Oct. 1999; final revision received by ASME Headquarters Oct. 2000. Associate Editor: D. Wisler.

Table 1 The elementary reactions of the 9-step mechanism and the 24-step mechanism and their rate parameters, with the specific reaction-rate constants in the form $k = BT^m e^{-E/RT}$

No.	Reactions	B^a	m^a	E^a	Source
1	$\text{CH}_4 + \text{O}_2 \rightleftharpoons \text{HO}_2 + \text{CH}_3$	$3.98\text{E}+13$	0.00	238.0	[9]
2	$\text{CH}_4 + \text{HO}_2 \rightleftharpoons \text{H}_2\text{O}_2 + \text{CH}_3$	$9.04\text{E}+12$	0.00	103.1	[9]
3	$\text{CH}_4 + \text{OH} \rightleftharpoons \text{H}_2\text{O} + \text{CH}_3$	$1.60\text{E}+07$	1.83	11.6	[6]
4	$\text{CH}_3 + \text{O}_2 \rightleftharpoons \text{CH}_2\text{O} + \text{OH}$	$3.30\text{E}+11$	0.00	37.4	[6]
5	$\text{CH}_2\text{O} + \text{OH} \rightleftharpoons \text{CHO} + \text{H}_2\text{O}$	$3.90\text{E}+10$	0.89	1.7	[6]
6	$\text{CHO} + \text{O}_2 \rightleftharpoons \text{CO} + \text{HO}_2$	$3.00\text{E}+12$	0.00	0.0	[6]
7 ^b	$\text{CHO} + \text{M} \rightleftharpoons \text{CO} + \text{H} + \text{M}$	$1.86\text{E}+17$	-1.00	71.1	[6]
8 ^b	$\text{H} + \text{O}_2 + \text{M} \rightleftharpoons \text{HO}_2 + \text{M}$	$6.76\text{E}+19$	-1.40	0.0	[6]
9 ^b	$\text{H}_2\text{O}_2 + \text{M} \rightleftharpoons 2\text{OH} + \text{M}$	$1.20\text{E}+17$	0.00	190.4	[6]
10 ^c	$\text{CH}_4 \rightleftharpoons \text{CH}_3 + \text{H}$	$6.59\text{E}+25$	-1.80	439.0	[6]
	k_∞	$2.22\text{E}+16$	0.00	439.0	[6]
11	$\text{CH}_4 + \text{H} \rightleftharpoons \text{H}_2 + \text{CH}_3$	$1.30\text{E}+04$	3.00	33.6	[6]
12	$\text{CH}_4 + \text{O} \rightleftharpoons \text{CH}_3 + \text{OH}$	$1.90\text{E}+09$	1.44	36.3	[6]
13	$\text{CH}_3 + \text{O}_2 \rightleftharpoons \text{CH}_3\text{O} + \text{O}$	$1.33\text{E}+14$	0.00	131.4	[6]
14	$\text{CH}_3 + \text{O} \rightleftharpoons \text{CH}_3\text{O} + \text{H}$	$8.43\text{E}+13$	0.00	0.0	[6]
15	$\text{CH}_3 + \text{HO}_2 \rightleftharpoons \text{CH}_3\text{O} + \text{OH}$	$2.00\text{E}+13$	0.00	0.0	[6]
16 ^c	$2\text{CH}_3 \rightleftharpoons \text{C}_2\text{H}_6$	$1.27\text{E}+41$	-7.00	11.6	[6]
	k_∞	$1.81\text{E}+13$	0.00	0.0	[6]
17	$\text{CH}_3\text{O} + \text{O}_2 \rightleftharpoons \text{CH}_2\text{O} + \text{HO}_2$	$4.28\text{E}-13$	7.60	-14.8	[6]
18 ^b	$\text{CH}_3\text{O} + \text{M} \rightleftharpoons \text{CH}_2\text{O} + \text{H} + \text{M}$	$1.00\text{E}+13$	0.00	56.5	[6]
19	$\text{CH}_2\text{O} + \text{H} \rightleftharpoons \text{CHO} + \text{H}_2$	$1.26\text{E}+08$	1.62	9.1	[6]
20	$\text{CH}_2\text{O} + \text{O} \rightleftharpoons \text{CHO} + \text{OH}$	$3.50\text{E}+13$	0.00	14.7	[6]
21	$\text{H} + \text{O}_2 \rightleftharpoons \text{OH} + \text{O}$	$3.52\text{E}+16$	-0.70	71.4	[6]
22	$\text{H}_2 + \text{O} \rightleftharpoons \text{OH} + \text{H}$	$5.06\text{E}+04$	2.67	26.3	[6]
23	$\text{H}_2 + \text{OH} \rightleftharpoons \text{H}_2\text{O} + \text{H}$	$1.17\text{E}+09$	1.30	15.2	[6]
24	$\text{H}_2\text{O} + \text{O} \rightleftharpoons 2\text{OH}$	$7.60\text{E}+00$	3.84	53.5	[6]

^aunits: mol/cm³, s⁻¹, K, kJ/mol

^bchaperon efficiencies as given in the cited reference

^cfalloff included as given in the cited reference

CH_4 is thermally decomposed to CH_3 and H . Compared to step 1, the reaction rate of step 10 is negligible at temperatures below 1300 K in the range of meaningful equivalence ratios. As temperature increases, step 10 begins to compete with step 1; for instance, the reaction-rate ratio of step 10 to step 1 is about 10^{-4} at 1000 K and 8 at 2000 K for $\Phi=0.4$, so that step 1 is always of some importance, while step 10 is unimportant below 1300 K. These two reactions and the different steps that follow each of them lead to ignition times having a stronger temperature sensitivity in the high-temperature range and a weaker temperature dependence in the low-temperature range, largely because of the higher temperature dependence of step 10. Most other hydrocarbons behave differently.

With the 24-step mechanism, during the ignition delay, the radicals OH , H , and O are produced initially mainly by steps 4, 7, and 13, respectively. Because of their high activation energies, steps 7 and 13 are negligibly slow compared with step 4 at temperatures below 1300 K. The rates of steps 7 and 13 increase with temperature and become important competitors of step 4 at temperatures above 1400 K. The hydrogen-oxygen shuffle reactions, steps 21 through 24, are inconsequential at low temperatures but become important at high temperatures because of the increased participations of H and O . The concentration of OH is much higher than that of H and O at temperatures below 1300 K. The species HO_2 and H_2O_2 provide an additional source for creating OH radicals, although H_2O_2 decomposes to OH mainly at a later stage during the ignition process. In general, the radical OH plays a more important role than H or O in methane ignition at both high and low temperatures, although the latter two cannot be neglected at high temperatures.

Methyl radicals, CH_3 , are mainly produced by chain-reaction steps 2, 3, 11, and 12. Because of the dependences of H , O , and OH concentrations on temperature, reactions 11 and 12 are important at high temperatures but may be neglected at low temperatures. Methyl consumption by reactions other than step 4, namely by reactions 13, 14 and 15, becomes important at high temperatures, giving rise to the need for steps 17, 18, and 19. Methyl recombination (step 16) is included in the 24-step mechanism because it is important for reducing the CH_3 concentration and in-

creasing the ignition delay time when the methane mixture is rich. Since the products of C_2H_6 contribute little to the ignition processes, especially when $\Phi \leq 1.5$, it is treated as a product in the present ignition system, although all steps are allowed to be reversible.

9-Step Short Mechanism

The 24-step mechanism can be further simplified when applied to ignition for temperatures between 1000 K and 1300 K with equivalence ratio below 1.5. The species O , CH_3O , and C_2H_6 can then be neglected, and a number of steps involving H and CH_3 becomes unimportant. It is found from sensitivity analyses that nine elementary reactions, steps 1 through 9 listed in Table 1, are most important to autoignition of fuel-lean mixtures in the temperature range below 1300 K.

The nine-step short mechanism has as the initiation reaction step 1, which produces CH_3 and HO_2 . The chain-reaction step 2 starts to produce CH_3 and H_2O_2 as the HO_2 concentration builds up. When the CH_3 concentration is high enough, the main chain steps 3 and 4 become important and create CH_2O . The concentration of CH_2O increases rapidly because the rate of step 5, which consumes CH_2O , is slow in most of the induction period. The temperature of the system will run away, and ignition will occur, as the rates of steps 5 and 6 reach their maxima, since most of the thermal energy in the system is released through steps 5 and 6. Reaction 9 become significant only when the temperature in the system is high enough. Although all steps are allowed to be reversible in the computations, the reverses of all steps are entirely negligible, except for step 1, which starts to become of importance in removing radicals towards the end of ignition.

A Reduced Mechanism

The term "reduced mechanism" is employed here to signify a sequence of overall steps derived by systematically applying approximations such as chemical-kinetic steady states and partial equilibria to a mechanism consisting of only elementary steps. It thereby will distinguish the following approximations from the detailed and short mechanisms given above. From this type of reduced-mechanism viewpoint, the nine-step mechanism in fact involves only eight steps because it has only eight linearly independent differential equations containing nonvanishing chemical source terms; step 7 is not linearly independent, although its rate, of course, is present in the system of equations. With this terminology, there appears to be only one previous investigation of reduced mechanisms for methane ignition ([10]); in that work, a six-step mechanism was derived from 231 elementary steps by exercising a program of computational singular perturbations, with attention devoted to temperatures of 1300 K and above. The resulting reduced mechanism is quite different from that developed below, largely because the elementary rate data with which it began are different, but also because the concern here is mainly with temperatures below 1300 K, rather than above. A reason for the very sparse literature on systematically reduced chemistry for ignition is that steady states are less applicable to ignition than to flames, the ignition chemistry requiring special considerations of initiation processes, as will be seen.

The nine-step mechanism provides a basis for a reduced reaction mechanism in predicting methane autoignition for temperatures below 1300 K with equivalence ratios between 0.4 and 1.5. For simplicity, all nine steps are taken to be irreversible here. The species H and CHO are quite reactive in this system and are present in very small concentrations. Chemical-kinetic steady-state approximations therefore are accurate for these species during nearly all of the ignition process. The concentration of H_2O_2 also is small, and although its steady state is inaccurate, this inaccuracy is relatively inconsequential. These three steady states therefore are adopted and result in

$$\left. \begin{aligned} [\text{H}] &= (k_7/k_8)[\text{CHO}][\text{O}_2], \\ [\text{CHO}] &= k_5[\text{CH}_2\text{O}][\text{OH}]/(k_6[\text{O}_2] + k_7[\text{M}]), \\ [\text{H}_2\text{O}_2] &= k_2[\text{CH}_4][\text{HO}_2]/(k_9[\text{M}]), \end{aligned} \right\} \quad (1)$$

thereby reducing the system to a five-step mechanism consisting of elementary steps 1 through 5.

Numerical computations of the ignition process with the resulting five-step reduced mechanism agree well with those of the nine-step and detailed mechanisms for temperatures between 1000 K and 1300 K and pressures up to 150 bar, the range of interest in the applications. The five-step reduced mechanism is identical to steps 1 through 5, with the exceptions that step 2 is replaced by $\text{CH}_4 + \text{HO}_2 \rightarrow \text{CH}_3 + 2\text{OH}$ and step 5 by $\text{CH}_2\text{O} + \text{OH} + \text{O}_2 \rightarrow \text{CO} + \text{H}_2\text{O} + \text{HO}_2$ as the overall steps that proceed at the rates ω_2 and ω_5 ; ω_i denotes the rate of elementary step i .

In a homogeneous system, a set of independent equations describing this mechanism is

$$\left. \begin{aligned} d[\text{CH}_4]/dt &= -\omega_1 - \omega_2 - \omega_3, \\ d[\text{HO}_2]/dt &= \omega_1 - \omega_2 + \omega_5, \\ d[\text{CH}_3]/dt &= \omega_1 + \omega_2 + \omega_3 - \omega_4, \\ d[\text{OH}]/dt &= 2\omega_2 - \omega_3 + \omega_4 - \omega_5, \\ d[\text{CH}_2\text{O}]/dt &= \omega_4 - \omega_5. \end{aligned} \right\} \quad (2)$$

The concentrations of CO, H_2O , and O_2 can be obtained from the C, H, and O element balances along with Eq. (2), and by use of Eq. (1) expressions are found for the five rates in Eq. (2) in terms of the concentrations of the remaining species and temperature.

During most of the ignition period, the temperature and concentrations of the reactants CH_4 and O_2 change little by chemical reactions. If these changes are neglected, then many of the coefficients appearing in the rates in Eq. (2) become constant. The only nonlinearity in the system then comes from ω_5 , which exhibits a quadratic nonlinearity because of the occurrence of the product of the concentrations of CH_2O and OH. The term ω_5 is not important initially in the ignition process because these two species are not present initially and develop only as they are produced through steps 2 and 4. An initial stage therefore exists that is linear and that is described by Eq. (2) with ω_5 deleted.

A general solution to this linear system can be derived. The solution during this initial linear stage, with only CH_4 , O_2 and inert being present at time $t=0$, exhibits radical growth and exponential decays on two time scales, namely $(k_2[\text{CH}_4])^{-1}$ and $(k_3[\text{CH}_4] + k_4[\text{O}_2])^{-1}$. For example, it is found that $[\text{HO}_2] = (k_1/k_2)[\text{O}_2](1 - e^{-k_2[\text{CH}_4]t})$; the solutions for $[\text{CH}_3]$, $[\text{OH}]$, and $[\text{CH}_2\text{O}]$ are considerably more involved than this. After the decays have taken place, the solutions for the concentrations of the intermediates become

$$\left. \begin{aligned} [\text{HO}_2] &= (k_1/k_2)[\text{O}_2], \\ [\text{CH}_3] &= \frac{4k_1t[\text{CH}_4][\text{O}_2]}{1 + (k_4/k_3)([\text{O}_2]/[\text{CH}_4])}, \\ [\text{OH}] &= [\text{CH}_3(k_4/k_3)([\text{O}_2]/[\text{CH}_4])], \\ [\text{CH}_2\text{O}] &= \frac{1}{2}[\text{CH}_3][\text{O}_2]k_4t, \end{aligned} \right\} \quad (3)$$

showing that $[\text{HO}_2]$ approaches a constant value, $[\text{CH}_3]$ and $[\text{OH}]$ increase linearly with time, and $[\text{CH}_2\text{O}]$ increases quadratically with time.

Although this initial linear stage requires the initiation step, step 1, to get started, soon the chain steps 2, 3, and 4 become more important for all intermediates except $[\text{HO}_2]$. The OH concentration is found to remain low, and an OH steady state soon develops, approximated well by $\omega_3 = \omega_4$, a condition that is seen to apply in Eq. (3). The OH steady state in this approximation will be adopted for the remainder of this analysis.

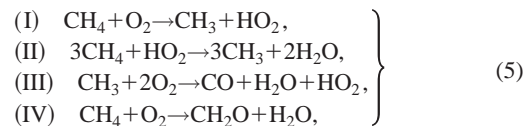
The quadratic nonlinearity of step 5 comes into play after the initial linear stage. The OH steady state did not apply during the

initial stage, the analysis of which was important, to obtain Eq. (3) as the initial conditions for treatment of the second stage. This second stage will be found to be a chain-branching stage of ignition, in contrast to the first stage, which was linear and nonbranching.

With the OH steady state, $[\text{OH}]/[\text{CH}_3]$ is small, so that in Eq. (3) the methyl concentration is approximately $[\text{CH}_3] = 4k_1t[\text{CH}_4][\text{O}_2]$. The OH steady state reduces the five-step mechanism to a four-step mechanism, equations for which can be written as

$$\left. \begin{aligned} d[\text{HO}_2]/dt &= \omega_1 - \omega_2 + \omega_5, \\ d[\text{CH}_3]/dt &= \omega_1 + 3\omega_2 - \omega_5, \\ d[\text{CH}_2\text{O}]/dt &= \omega_4 - \omega_5. \end{aligned} \right\} \quad (4)$$

Equation (4) replaces Eq. (2), having eliminated $[\text{OH}]$ and the fast steps; since the equation for $[\text{CH}_4]$, the first in Eq. (2), is not needed in the ignition analysis with $[\text{CH}_4]$ changes neglected, it is not included in Eq. (4). The four-step reduced chemistry can be written as



with the rates $\omega_{\text{I}} = \omega_1$, $\omega_{\text{II}} = \omega_2$, $\omega_{\text{III}} = \omega_5$, $\omega_{\text{IV}} = \omega_4 - \omega_5$.

An Analytical Solution for Methane Autoignition

A convenient nondimensionalization can be introduced for the problem defined by Eq. (4), subject to the initial conditions of Eq. (3). With the nondimensional time

$$\tau = 2t[\text{O}_2]\sqrt{k_1k_4k_5/k_3} \quad (6)$$

and concentrations

$$\left. \begin{aligned} x &= \frac{1}{2}(k_4k_5)/(k_1k_3)[\text{CH}_3]/[\text{CH}_4], \\ y &= (k_2/k_1)[\text{HO}_2]/[\text{O}_2], \\ z &= (k_5/k_3)[\text{CH}_2\text{O}]/[\text{CH}_4], \end{aligned} \right\} \quad (7)$$

the differential equations

$$\left. \begin{aligned} 4dx/d\tau &= 1 + 3y - 2\alpha xz, \\ \epsilon dy/d\tau &= 1 - y + 2\alpha xz, \\ dz/d\tau &= x(1 - z) \end{aligned} \right\} \quad (8)$$

are obtained, subject to $x \rightarrow \tau$, $y \rightarrow 1$ and $z \rightarrow \tau^2/2$ as $\tau \rightarrow 0$. The terms 1, y , xz , and x arise from the initiation step 1, the linear step 2, the quadratic step 5, and the linear step 4, respectively. Here the two parameters are

$$\left. \begin{aligned} \alpha &= \sqrt{(k_3k_4)/(k_1k_5)}, \\ \epsilon &= \sqrt{(k_1k_4k_5)/(k_2^2k_3)}[\text{O}_2]/[\text{CH}_4], \end{aligned} \right\} \quad (9)$$

and ϵ must be small for the time scale of the second stage to be long compared with that of the first. For small ϵ , the condition $y = 1 + 2\alpha xz$ is achieved quickly, and thereafter

$$\left. \begin{aligned} dx/d\tau &= 1 + \alpha xz, \\ dz/d\tau &= x(1 - z), \end{aligned} \right\} \quad (10)$$

with $z \rightarrow x^2/2$, $x \rightarrow \tau$ as $\tau \rightarrow 0$. Equation (10) is amenable to phase-plane analysis, showing z to increase with x and approach $z=1$ as $x \rightarrow \infty$. The long-time behavior, at the end of the explosion, has $x \sim y \sim e^{\alpha\tau}$. Thus, $[\text{CH}_2\text{O}]$ levels off first, while $[\text{CH}_3]$, $[\text{HO}_2]$, and $[\text{OH}]$ continue to grow, as was found in the full numerical integrations.

The histories of concentrations of intermediates predicted by these equations for the second stage are not exactly exponential in time but may be approximated as exponential over limited ranges of time. The nature of the approximation depends on the value of

α and the time period selected. Since, from the data in Table 1, $\alpha = 1.84 \times 10^{-3} T^{0.47} \exp(11,200/T)$ with T in K, it is found that α is larger than unity, so that the later-stage blowup is faster than at the beginning. For large α , the early-time behavior, which is appreciably slower and then controls the ignition time, can be approximated as

$$\left. \begin{aligned} x &= (2/\alpha)^{1/3} e^{(\alpha/2)^{1/3} \tau}, \\ y &= 4e^{2(\alpha/2)^{1/3} \tau}, \\ z &= (2/\alpha)^{2/3} e^{(\alpha/2)^{1/3} \tau}, \end{aligned} \right\} \quad (11)$$

in which a representative numerical value is $\alpha^{1/3} \approx 10$. Equation (11) shows that the time constant for the exponential HO_2 growth is half that for the CH_3 and CH_2O growth. From Eq. (11), the characteristic exponential growth time for CH_3 , OH , and CH_2O is obtained by use of Eqs. (6) and (9) as

$$t_e = \frac{1}{2^{2/3} [\text{O}_2] (k_4^2 k_5 k_1 / k_3^2)^{1/3}}, \quad (12)$$

which is a function of temperature and reactant concentrations, in general, although their changes are taken here to be negligible initially during ignition at early times.

The solutions in Eq. (11) in fact are not very accurate because the numerical value of the small parameter ϵ , about 0.3, is not sufficiently small. Especially because α is too large, a clear separation between the linear stage and that involving the quadratic term therefore does not exist. An expansion of the problem in Eq. (8) in powers of ϵ is then warranted. When this is done, it is found that y remains appreciably smaller than the value $1 + \alpha x z$ achieved for small ϵ , and Eq. (10) becomes inaccurate. The longest characteristic growth time then becomes appreciably longer than that of Eq. (12) and depends additionally (although typically not strongly) on the value of ϵ , that is, on the equivalence ratio, Φ , proportional to $[\text{CH}_4]/[\text{O}_2]$. When $2\alpha xy \gg 1$, the value of y obtained from Eq. (8) is reduced by a factor of approximately $[1 + (4\alpha)^{1/3} \epsilon]^{-1}$, more than an order of magnitude. A correction factor of $1 + c\alpha^{1/3} \epsilon$ also appears in the numerator of Eq. (12), with c being a constant. On the basis of comparisons with numerical integrations, the constant value $c\alpha^{1/3} \epsilon = 2$ is selected over the range of conditions for which the analysis applies. On substituting this revision and the rate parameters listed in Table 1 into Eq. (12), the t_e at $t=0$ can be written as

$$t_{e0} = \frac{8.6 \times 10^{-14} [\text{O}_2]_0^{-1}}{T_0^{-0.31} \exp(-12,000/T_0)}, \quad (13)$$

where the subscript 0 identifies initial conditions, and units are seconds, moles/cm³ and K.

Approximate expressions for concentrations during the initial exponential part of the second stage can then be written as

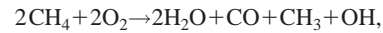
$$\left. \begin{aligned} [\text{CH}_3] &= [\text{CH}_4] \left(\frac{k_1 k_3}{k_4^2 k_5} \right)^{1/3} e^{t/t_{e0}}, \\ [\text{CH}_2\text{O}] &= [\text{CH}_4] \left(\frac{k_1 k_3^2}{k_4^2 k_5^2} \right)^{1/3} e^{t/t_{e0}}, \\ [\text{OH}] &= [\text{O}_2] \left(\frac{k_1^2 k_4}{k_3^2 k_5} \right)^{1/3} e^{t/t_{e0}}, \\ [\text{HO}_2] &= \frac{1}{3} [\text{O}_2] \left(\frac{k_1}{k_2} \right) e^{2t/t_{e0}}, \\ [\text{H}_2\text{O}_2] &= \frac{1}{3} \left(\frac{k_1 [\text{O}_2] [\text{CH}_4]}{k_9 [\text{M}]} \right) e^{2t/t_{e0}}, \\ [\text{CHO}] &= \left(\frac{k_1 [\text{O}_2] [\text{CH}_4]}{k_6 [\text{O}_2] + k_7 [\text{M}]} \right) e^{2t/t_{e0}}, \\ [\text{H}] &= \left(\frac{k_1 k_7 [\text{CH}_4] / k_8}{k_6 [\text{O}_2] + k_7 [\text{M}]} \right) e^{2t/t_{e0}}. \end{aligned} \right\} \quad (14)$$

Equation (14) maintains the previously identified steady states for H , CHO , H_2O_2 , and OH . It does not contain secondary dependencies on $[\text{CH}_4]/[\text{O}_2]$, and has coefficients selected to maximize simplicity, with values having magnitudes estimated from consideration of results of the expansion for small values of ϵ .

Figure 1 compares the prediction of Eq. (14) with results of numerical integrations under specified initial conditions. It can be seen from this figure that the concentration of CH_2O is the highest while that of CHO is the lowest among all intermediate species. This indicates the important role that is played by CH_2O in auto-ignition chemistry and helps to justify the steady-state approximation for CHO . As predicted in Eq. (14), the concentration slopes of HO_2 , H_2O_2 , and CHO are twice as high as those of CH_3 , CH_2O , and OH in a semi-log diagram. The concentration of the radical OH is almost two order of magnitude lower than that of CH_3 but has a similar slope of concentration history, which supports the OH steady state. The agreements are seen to be quite reasonable, in view of the many approximations involved.

Theory for Ignition Time

To estimate the ignition time, t_{ig} , based on the above analysis, we consider an overall step



derived by sequentially adding the fast steps 3, 4, 5, 6, 2, and 9 to eliminate the intermediates CH_2O , CHO , HO_2 , and H_2O_2 for the purpose of obtaining a one-step approximation to the three-step branching process of Eq. (8). This overall step is exothermic, having a heat release per mole of CH_3 produced, q , that can be calculated to be $q = 60$ kcal/mol at $T = 1000$ K, for example, and it is branching in that it involves net production of the radical CH_3 . It then becomes possible to apply a simplified theory of branched-chain thermal explosions ([11]) to estimate the ignition time. The relationship between T and $[\text{CH}_3]$ can be written as

$$T = T_0 + \frac{q}{\rho c_p} [\text{CH}_3], \quad (15)$$

where ρ and c_p are the density and specific heat at constant pressure, respectively, for the reactant mixture. The initial value of $[\text{CH}_3]$ at the beginning of the second stage is computed from Eq. (14) to be

$$[\text{CH}_3]_0 = [\text{CH}_4]_0 \left(\frac{k_1 k_3}{k_4^2 k_5} \right)^{1/3}, \quad (16)$$

and the corresponding initial temperature from Eq. (15) is $T_0 + (q/\rho c_p) [\text{CH}_3]_0$.

Considering

$$\frac{d[\text{CH}_3]}{dt} = \frac{[\text{CH}_3]}{t_e} \quad (17)$$

from Eq. (14), and making the Arrhenius approximation,

$$t_e = t_{e0} \exp(T_a/T - T_a/T_0), \quad (18)$$

we may define $\theta = (T - T_0) T_a / T_0^2$ and $\sigma = t/t_{e0}$ to obtain, in a Frank-Kamenetskii approximation,

$$\frac{d\theta}{d\sigma} = \theta e^\theta, \quad (19)$$

subject to $\theta = a = (q/\rho c_p) [\text{CH}_3]_0 T_a / T_0^2$ at $\sigma = 0$. The effective activation temperature, T_a , has a value of 12,000 K, according to Eq. (13). Integration of Eq. (19) to $\sigma = \sigma_{ig}$ at $\theta = \infty$ gives the nondimensional ignition time for small values of a as

$$\sigma_{ig} = \int_a^\infty \frac{d\theta}{\theta e^\theta} = \left[\ln \left(\frac{1}{a} \right) - \gamma \right], \quad (20)$$

where Euler's constant is $\gamma = 0.5772$.

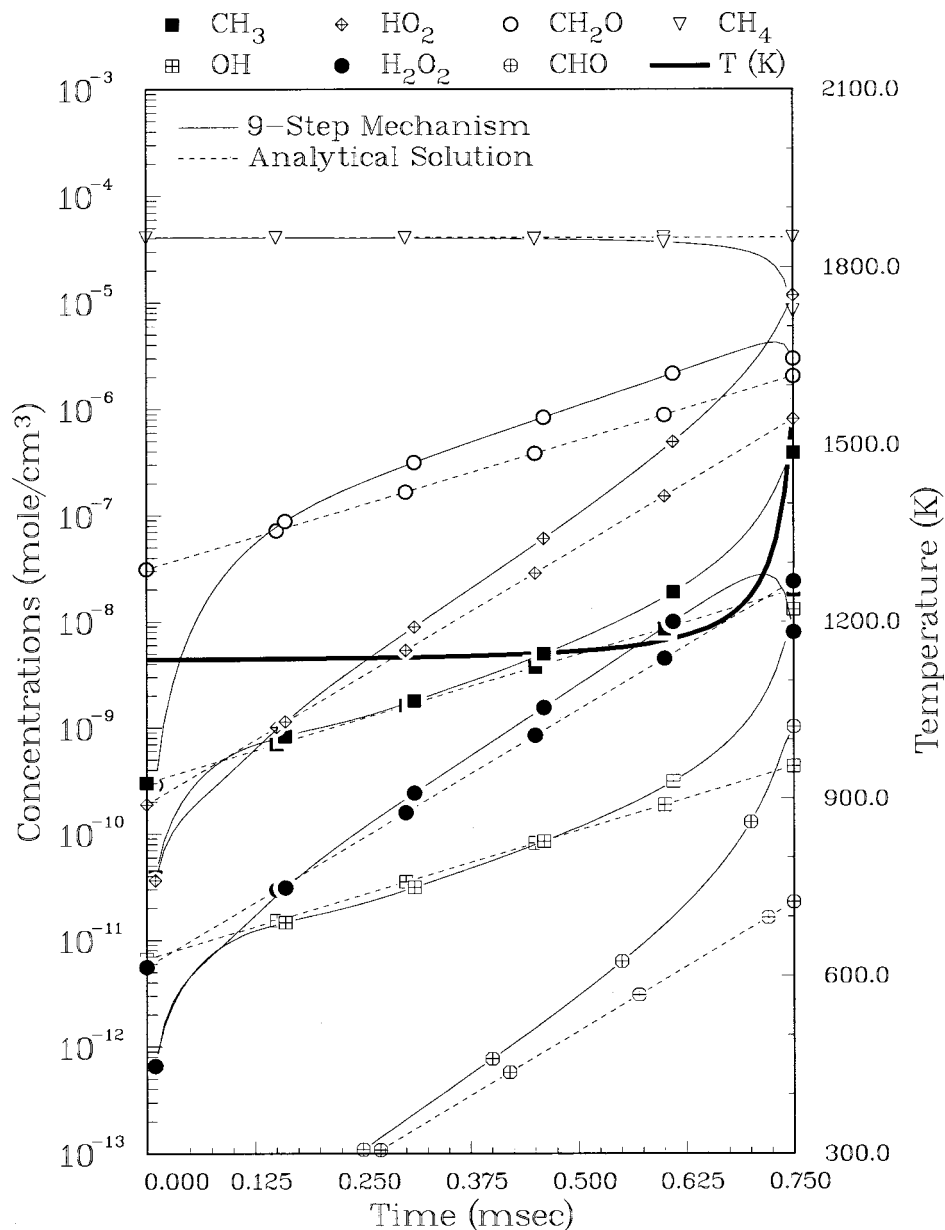


Fig. 1 Predicted histories of temperature and important species concentrations before ignition with $T_0=1136$ K, $p=100$ bar and $\Phi=0.4$.

In the present work, instead of including the secondary dependence on temperature and composition through a in Eq. (20), the value of σ_{ig} is taken to be constant. Values of a were found to range from about 0.02 to 0.05, giving σ_{ig} around 3.4 according to Eq. (20). From the definition of σ , the ignition time, t_{ig} , can then be written as

$$t_{ig} = \sigma_{ig} t_{e0} = \frac{2.9 \times 10^{-13} [\text{O}_2]_0^{-1}}{T_0^{-0.31} \exp(-12,000/T_0)}, \quad (21)$$

in view of Eq. (13).

Equation (21) is strictly limited to temperatures below 1300 K, as stated in the beginning of the analysis. It is seen from this equation that the ignition time is inversely proportional to pressure, p , through its proportionality to $[\text{O}_2]^{-1}$. The dependence on $[\text{CH}_4]$ is removed through the approximation of σ_{ig} . The dependence of the ignition time on temperature is approximately given by $t_{ig} \propto \exp(12,000/T_0)$. All functional dependences thus are predicted from the analysis.

Comparison With Experiments

Methane autoignition in practical combustors is similar in most respects to that in shock-tube experiments. In both cases, for example, the ignition delay times are much shorter than 1 ms under conditions of interest. Because of these features, the mechanisms developed above can be tested by shock-tube experiments before they are applied to practical combustors. Literature review reveals that shock-induced ignition of methane has been thoroughly investigated most recently by Spadaccini et al. [7,8] and by Petersen et al. [5]. In the former work, ignition delay times were measured over the temperature range of 1350–2000 K, the post-shock pressure range of 3–15 bar and equivalence ratio range of 0.45–1.25 while, in the latter, measurements of CH_4/O_2 autoignition were performed at elevated pressures (40–260 bar), temperatures (1040–1500 K) and three different equivalence ratios ($\Phi=0.4$, 3, and 6), in general covering a lower temperature range than the

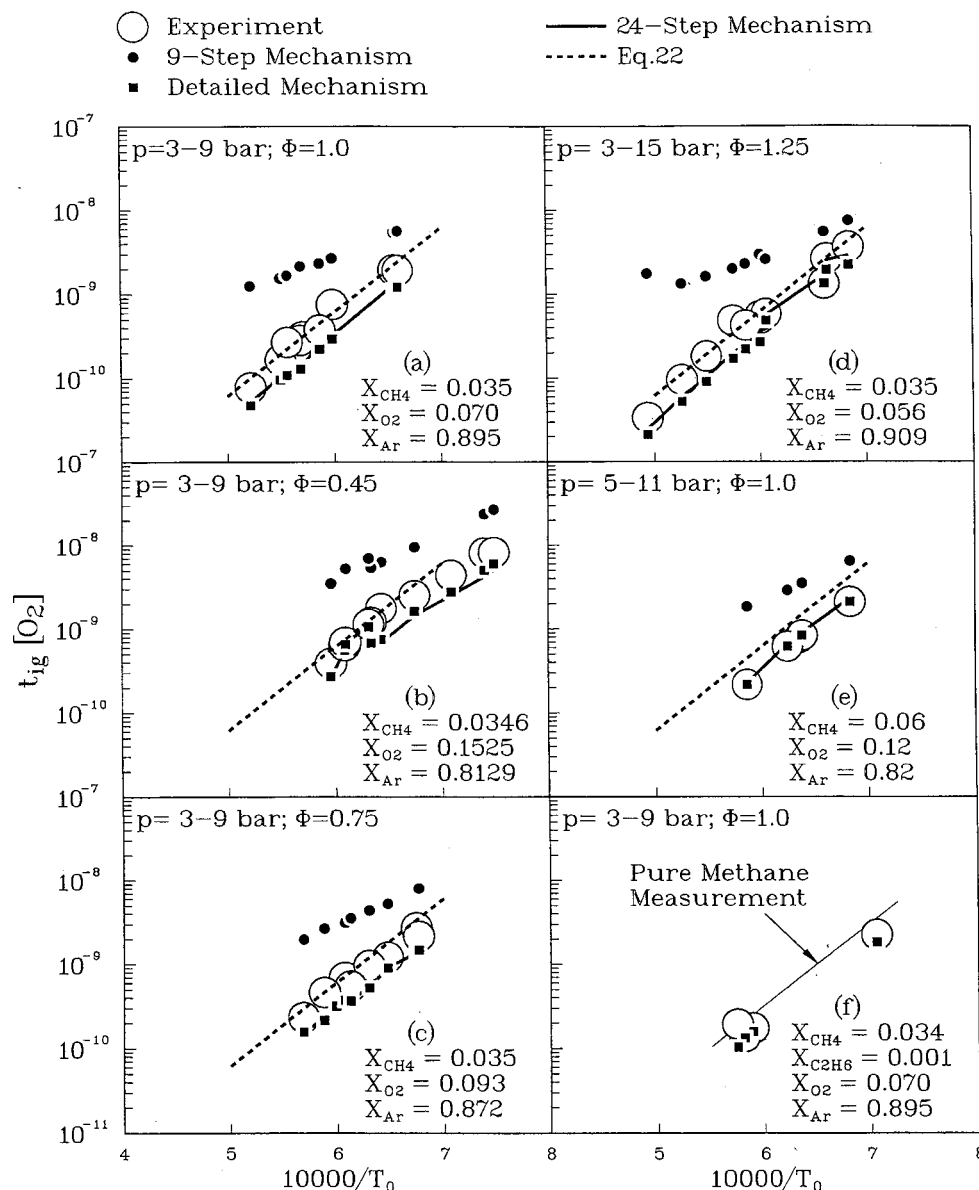


Fig. 2 Comparison of predicted and measured autoignition delays in shock-tube experiments (7)

former and a range more relevant to conditions in practical combustors. For completeness, comparisons will be made with both sets of data here.

Figure 2 compares measured ignition delay times, t_{ig} , with numerical computations using all three present mechanisms for the higher temperature range. The numerical code is based on the ideal-gas version of Chemikin [12]. Figures 2(a)–2(e) plot experimental and computational results for $\text{CH}_4/\text{O}_2/\text{Ar}$ mixtures with different equivalence ratios and dilution levels. Results in Fig. 2(f) are essentially the same as those in Fig. 2(a) except that three percent of the methane is replaced by ethane; this figure shows a negligible effect of replacing methane by ethane, to this extent, and has consequent implications for natural gas, although it certainly cannot be concluded in general that additives and natural-gas composition do not influence ignition times. There is in fact some evidence to the contrary, and in future work along present lines it would be of interest to investigate effects of additives.

The dashed line in each subfigure of Fig. 2 is a correlation in a form similar to Eq. (21). The dependence of t_{ig} on $[\text{CH}_4]$ and $[\text{O}_2]$ remains the same as in Eq. (21), but the temperature depen-

dence is different and is obtained by fitting this high-temperature experimental data. Here, points on all the dashed lines are calculated by $6.25 \times 10^{-16} \exp(23000/T_0)$ in the temperature range of 1400–2000 K. Units are the same as in Table 1. The agreements between experiment and prediction are very good for both the detailed and 24-step mechanisms, especially in terms of the temperature dependence, but the agreement with the nine-step mechanism is poor, indicating that reaction steps 10 through 24 are important at higher ignition temperatures.

The present high-temperature correlation,

$$t_{ig} = 6.25 \times 10^{-16} [\text{O}_2]^{-1} \exp(23000/T_0), \quad (22)$$

is similar to that suggested by Colket and Spadaccini [8] but has somewhat different concentration dependences. These new theoretical concentration dependences fit the data about as well as the older, empirical powers. Since Eq. (21) was based on the nine-step mechanism, it is interesting that the predicted dependence on pressure and reactant concentrations remains reasonable at higher tem-

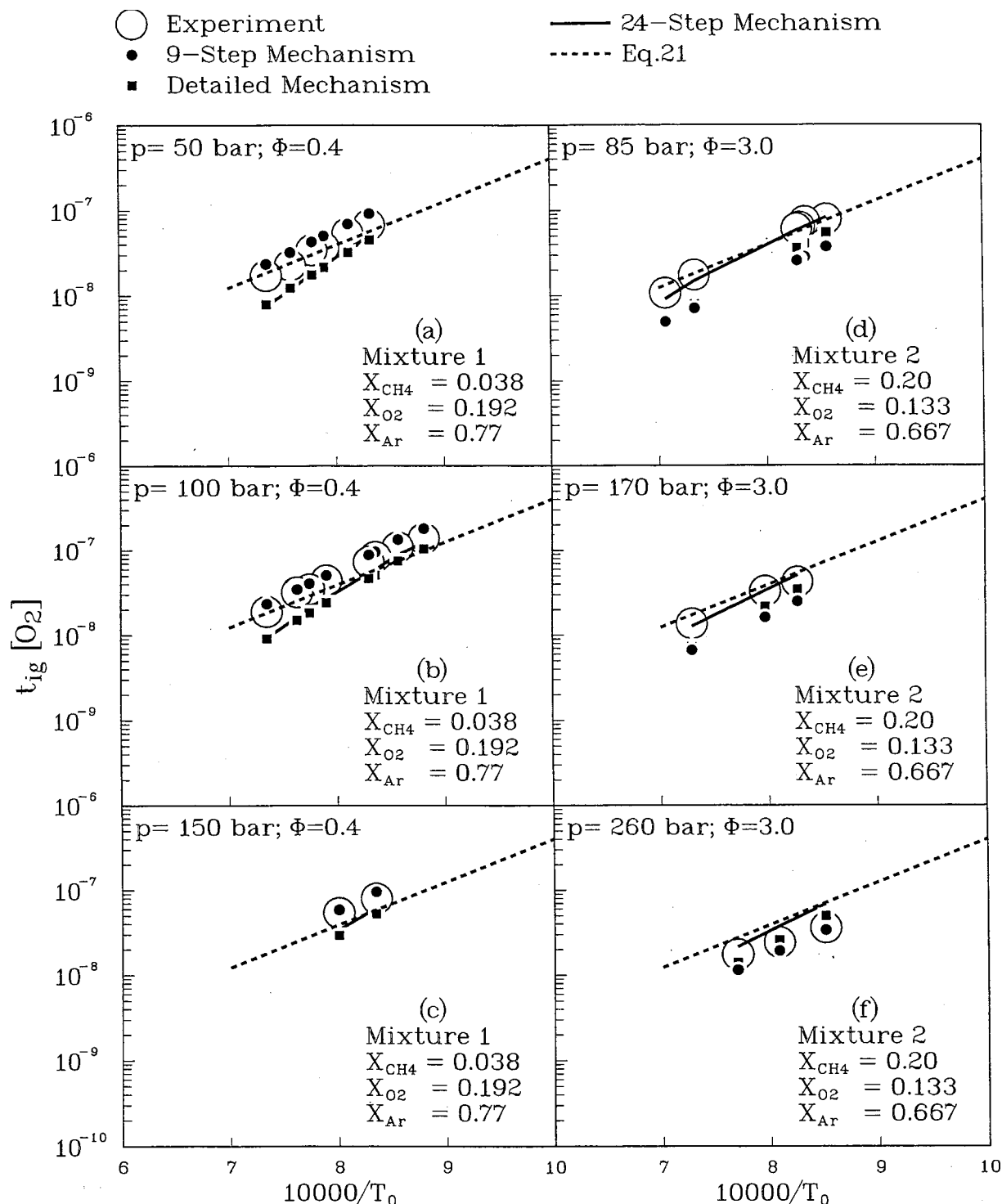


Fig. 3 Comparison of predicted and measured autoignition delays in shock-tube experiments ([5])

peratures even though the temperature dependence changes. The agreement of the data with predictions of the nine-step mechanism improves as temperature decreases, as expected.

Typical experimental ([5]) and computational results at high pressures and low temperatures are plotted in Fig. 3. Different from Fig. 2, the dotted lines in these figures are now given by Eq. (21). The detailed mechanism and its shortened versions are employed in the computations. Predicted ignition-delay times with different mechanisms agree with measurements well in most of cases and poorly in a few cases but generally are within a factor of

two. The agreement can be improved if the rates of steps 4 and 13 are reduced by a factor of 2, within the reported ([13]) uncertainties of a factor of 3. At this stage, however, such revisions are not recommended, considering the uncertainties involved in both measurements and shock-wave modeling.

Figures 3(a), 3(b), and 3(c) refer to fuel-lean conditions, which are of greatest practical importance. They show good agreement of predicted ignition delay times using the nine-step short mechanism with measurements. It is seen from Fig. 3 that, compared to predictions of the detailed mechanism, the ignition delay times

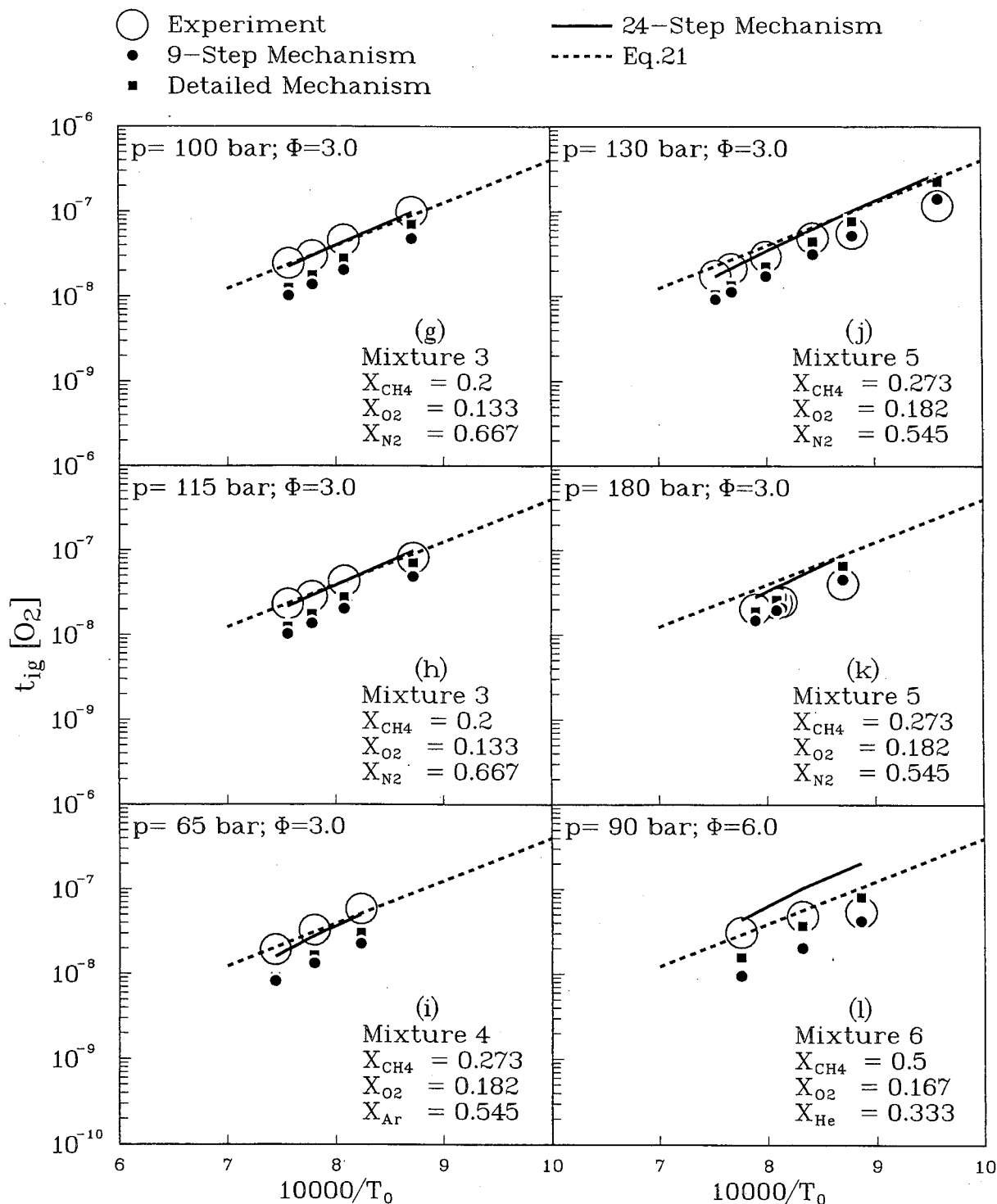


Fig. 3 (Continued)

predicted by the nine-step mechanism are slightly longer at $\Phi=0.4$ and shorter at $\Phi=3$ and 6. This is caused by the simplifications in the nine-step mechanism that exclude the methyl recombination ($CH_3+CH_3 \rightarrow C_2H_6$), which prolongs ignition delays, and consumption of CH_4 by H and O and of CH_3 by radicals, which shorten ignition delays. Under extremely fuel-lean conditions, the latter dominates and thus leads to the results shown in Figs. 3(a)–(c), while under very rich conditions, the former domi-

nates and leads to the results in Figs. 3(d)–(l). Further investigation shows that the predicted results agree with each other around $\Phi=1.5$, where the former is balanced by the latter.

The 24-step mechanism reproduces the prediction of the detailed mechanism for $\Phi=0.4$, as shown in Figs. 3(a)–(c). Predicted ignition delay times using the 24-step mechanism are longer than those from the detailed mechanism for $\Phi \geq 3$. This is because the products of C_2H_6 become important in very rich mix-

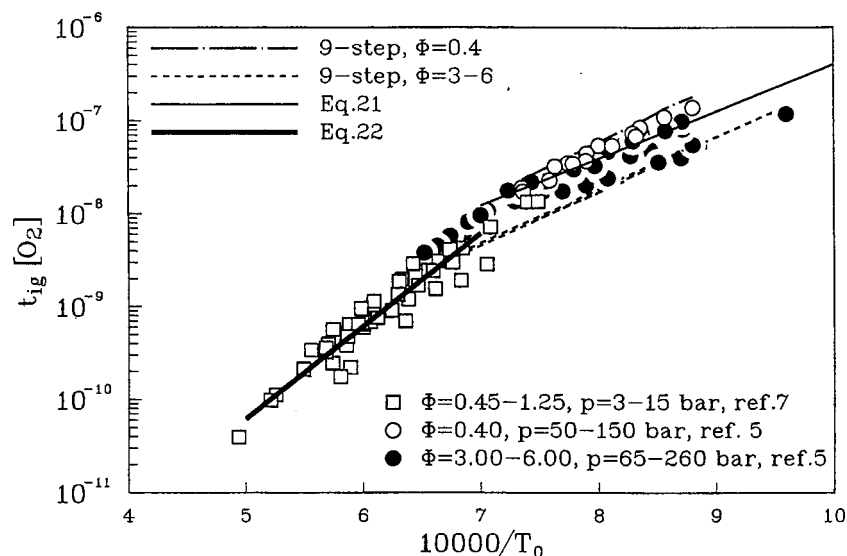


Fig. 4 Comparison of measured autoignition delays in shock-tube experiments with the predictions of Eqs. (21) and (22) and with the nine-step mechanism

tures. Comparisons with experimental results confirm that the 24-step mechanism can be applied to both high and low ignition temperature for $\Phi \leq 1.5$, while the nine-step mechanism can be applied to low temperatures only.

The agreement between prediction (dotted lines) by Eq. (21) and measurement is excellent for $\Phi=0.4$. It is expected that Eq. (21) predicts ignition times correctly up to $\Phi=1.5$. At higher equivalence ratios ($\Phi \geq 3.0$), the predicted temperature dependence remains consistent with experiment although the predicted t_{ig} is systematically higher. It is interesting that the augmentation by oxygen is predicted approximately correctly by the simplified theory. In general, therefore, the basis of Eq. (21) seems substantiated and the result useful.

Summary and Conclusions

A full reaction mechanism, a 24-step short mechanism, a nine-step short mechanism and five-step and four-step systematically reduced chemical mechanisms have been developed for predicting methane autoignition under different pressures, temperatures, and equivalence ratios. From these reaction mechanisms, the ignition time, t_{ig} , is found to be computed by Eq. (21) in the low-temperature range ($T_0 \leq 1300$ K) and by Eq. (22) in the high-temperature range ($T_0 \geq 1400$ K). The dependence of t_{ig} on T_0 is given by $t_{ig} \propto \exp(12,000/T_0)$ in the former range and by $t_{ig} \propto \exp(23,000/T_0)$ in the latter. These two equations predict that $t_{ig} \propto [O_2]^{-1}$, which is in reasonable agreement with experiment.

The degree of agreement that is achieved between these predictions and results from shock-tube experiments suggests that the present work can be applied to estimate ignition delay times in practical combustors. Future work would be desirable along the present lines to investigate effects of additives, as well as to study other fuels such as higher hydrocarbons. Although greater complexity may be anticipated in such investigations, in many respects good progress may be possible by building on the present results.

Figure 4 summarizes the agreements found here with all of the experiments. The predictions of Eqs. (21) and (22) are seen in Fig. 4 to be good over the ranges of conditions for which they were designed. Improvements can be obtained by introducing greater complexity; for example, the results plotted in Fig. 4 for the nine-step mechanism for the two different equivalence-ratio ranges, namely $\Phi=0.4$ and $3 \leq \Phi \leq 6$, show that better agreement for very lean and for very rich conditions is achieved with this mechanism

than with the formulas. The formulas have been designed only to cover conditions of greatest practical interest, namely $0.4 \leq \Phi \leq 1.5$, and they perform remarkably well over those conditions.

Although the pressure range selected for focus in the present study, $1 \text{ bar} \leq \Phi \leq 150 \text{ bar}$, was chosen with the applications in mind, available data prevented testing predictions below 3 bar but did allow some tests as high as 260 bar. The mechanisms may well be useful to even higher pressures and at subatmospheric pressures; pressure limitations have not been explored thoroughly here and could be studied further in future work. Temperatures below 1000 K and above 2000 K also could be of interest for future investigations.

The accuracies with which the various predictions agree with experiment typically are 10 percent to 25 percent in ignition time but occasionally worse than a factor of two; it is difficult to state firm and precise general conclusions about agreements, at least partially because of variability of the experimental data. Generally speaking, the detailed mechanism is best and gives some reasonable results even for $\Phi=6$. The 24-step mechanism is in reasonable agreement with the detailed mechanism, except that it is poor beyond $\Phi=3$. The nine-step mechanism is as good as the detailed mechanism below 1300 K, as is the five-step reduced mechanism, but the four-step reduced mechanism is less accurate and requires correction in deriving the analytical approximation. Further delineations of accuracies seem properly to be topics for future investigations.

Acknowledgment

This research was partially supported by the National Science Foundation under Grant No. CTS 98-12996.

References

- [1] Lefebvre, A. H., 1998, *Gas Turbine Combustion*, Taylor and Francis, Philadelphia, PA, pp. 57–62.
- [2] Prade, B., Streb, H., and Pyka, G., 1988, "Development of an Improved Hybrid Burner-Initial Operating Experience in a Gas Turbine," ASME Paper No. 96-GT-45.
- [3] Karim, G. A., and Zhaoda, Y., 1988, "An Analytical Model for Knock in Dual Fuel Engines of the Compression Ignition Type," SAE Trans., No. 880151.
- [4] Frenklach, M., Wang, H., and Rabinowitz, M. J., 1992, "Optimization and Analysis of Large Chemical Kinetic Mechanisms Using the Solution Mapping Method-Combustion of Methane," Prog. Energy Combust. Sci., **18**, pp. 47–73.

- [5] Petersen, E. L., Davidson, D. F., and Hanson, R. K., 1999, "Kinetics Modeling of Shock-Induced Ignition in Low-Dilution CH_4/O_2 Mixtures at High Pressures and Intermediate Temperatures," *Combust. Flame*, **117**, pp. 272–290.
- [6] Li, S. C., and Williams, F. A., 1999, "NO_x Formation in Two-Stage Methane-Air Flames," *Combust. Flame*, **118**, pp. 399–411.
- [7] Spadaccini, L. J., and Colket, III, M. B., 1994, "Ignition Delay Characteristics of Methane Fuels," *Prog. Energy Combust. Sci.*, **20**, pp. 431–460.
- [8] Colket, III, M. B., and Spadaccini, L. J., 2001, "Scramjet Autoignition Study," *J. Propul. Power*, **17**, pp. 315–323.
- [9] Leung, K. M., and Lindstedt, R. P., 1995, "Detailed Kinetic Modeling of C_1 – C_3 Alkane Diffusion Flames," *Combust. Flame*, **102**, pp. 129–160.
- [10] Treviño, C., and Méndez, 1992, "Reduced Kinetic Mechanism for Methane Ignition," *Twenty-Fourth Symposium (International) on Combustion*, The Combustion Institute, Pittsburgh, PA, pp. 121–127.
- [11] Varatharajan, B., and Williams, F. A., 2000, "Ignition Times in the Theory of Branched-Chain Thermal Explosions," *Combust. Flame*, **121**, pp. 551–554.
- [12] Kee, R. J., Rupley, F. M., and Miller, J. A., 1989, "Chemkin II: A Fortran Chemical Kinetics Package for the Analysis of Gas-Phase Chemical Kinetics," Sandia National Laboratories Report No. SAND89-8009.
- [13] Baulch, D. L., Cobos, C. J., Cox, R. A., Esser, C., Frank, P., Just, T., Kerr, J. A., Pilling, M. J., Troe, J., Walker, R. W., and Warnatz, J., 1992, "Evaluated Kinetic Data for Combustion Modeling," *J. Phys. Chem. Ref. Data*, **21**, pp. 411–734.

A Combined Eulerian and Lagrangian Method for Prediction of Evaporating Sprays

M. Burger

e-mail: matthias.burger@its.uni-karlsruhe.de

G. Klose

G. Rottenkolber

R. Schmehl

D. Giebert

O. Schäfer

R. Koch

S. Wittig

Institut für Thermische Strömungsmaschinen,
Universität Karlsruhe,
76128 Karlsruhe, Germany

Polydisperse sprays in complex three-dimensional flow systems are important in many technical applications. Numerical descriptions of sprays are used to achieve a fast and accurate prediction of complex two-phase flows. The Eulerian and Lagrangian methods are two essentially different approaches for the modeling of disperse two-phase flows. Both methods have been implemented into the same computational fluid dynamics package which is based on a three-dimensional body-fitted finite volume method. Considering sprays represented by a small number of droplet starting conditions, the Eulerian method is clearly superior in terms of computational efficiency. However, with respect to complex polydisperse sprays, the Lagrangian technique gives a higher accuracy. In addition, Lagrangian modeling of secondary effects such as spray-wall interaction enhances the physical description of the two-phase flow. Therefore, in the present approach the Eulerian and the Lagrangian methods have been combined in a hybrid method. The Eulerian method is used to determine a preliminary solution of the two-phase flow field. Subsequently, the Lagrangian method is employed to improve the accuracy of the first solution using detailed sets of initial conditions. Consequently, this combined approach improves the overall convergence behavior of the simulation. In the final section, the advantages of each method are discussed when predicting an evaporating spray in an intake manifold of an internal combustion engine. [DOI: 10.1115/1.1473153]

1 Introduction

Computational fluid dynamics (CFD) has evolved into a significant application for developing modern combustion devices. Of particular importance for the design process is the fuel-air mixture preparation, i.e., determining droplet and vapor distributions in the flow which are in turn influencing the combustion process. This study introduces an efficient approach for the simulation of complex two-phase flow fields. Two different conceptual approaches for the numerical description of dispersed two-phase flows are discussed: an Eulerian continuum model and a Lagrangian particle model. Both methods are employed to simulate fuel propagation in the intake manifold of an IC engine. Figure 1 shows a fuel distribution inside the intake manifold of a SI engine, 4 ms after the start of injection. The accurate discretization of the duct geometry requires a body-fitted mesh. An in-house three-dimensional compressible CFD code based on the finite volume method is used to calculate the gas flow field. In order to consider mutual influences of continuous (gas) and disperse (liquid) phases, the CFD code is coupled with the spray models. Two-phase flows are characterized by intense rates of interphase mass, momentum, and energy transfer. Typically, a major part of the interaction between droplets and gas phase due to dispersion and evaporation of fuel droplets occurs in the flow region near the nozzle.

Basically, two different conceptual approaches may be employed for the numerical description of dispersed two phase flows ([1]). In analogy to single-phase gas flow, the Eulerian approach is based on a continuum model of the spray, resulting in transport equations describing the propagation and evaporation of the droplet phase ([2,3]). In the Lagrangian approach, the spray is modeled by superposition of trajectories calculated for large numbers of

representative droplets. Each of the two basic approaches is characterized by specific advantages and restrictions. Although well established for the numerical calculation of complex disperse two-phase flows, Lagrangian methods for droplet tracking show a poor convergence behavior for this kind of flow. This is mainly due to the iterative solution of gas and droplet phases inevitably requiring strong relaxation of interphase source terms. Since the coupling between gaseous and liquid phase within the Eulerian method is realized in each iteration step, this method is inherently better suited to address the phase interaction problem. However, Eulerian methods can handle only a limited number of different droplet initial conditions and still have major deficiencies in predicting complex two-phase flow phenomena such as wall interaction. The pros and cons of each approach in simulating a two-phase flow of an intake manifold will be discussed in this study.

Incorporating the positive features inherent to each model, a combined computational "hybrid" scheme is presented in this study which achieves an accurate flow field prediction with lower computational effort. In the first stage of this procedure, the Eulerian method is used for the computation of an approximate two-phase flow field. A coarse discretization of spray boundary conditions at the nozzle limits the size of the system of transport equations to a practical dimension. In the following refinement stage, iterative cycles of single-phase gas flow computation and subsequent Lagrangian droplet tracking are employed to improve the accuracy of the precomputed two-phase flow field. Taking advantage of the stochastic nature of the tracking approach, a fine discretization of polydisperse sprays is achieved by random sampling of droplet initial conditions at the nozzle. The numerical description of the spray is enhanced by optional modeling of spray-wall interactions. Similar hybrid schemes have been developed for the computation of two-phase flows in combustor chambers ([4]) and rocket motors ([5]) for several years. This paper presents a hybrid scheme within a fully three-dimensional CFD code, demonstrating the applicability of the method for a complex computational domain discretized by a body-fitted grid as encountered in many practical engineering applications. The accuracy of

Contributed by the International Gas Turbine Institute (IGTI) of THE AMERICAN SOCIETY OF MECHANICAL ENGINEERS for publication in the ASME JOURNAL OF ENGINEERING FOR GAS TURBINES AND POWER. Paper presented at the International Gas Turbine and Aeroengine Congress and Exhibition, New Orleans, LA, June 4–7, 2001; Paper 01-GT-047. Manuscript received by IGTI, Dec. 2000, final revision, Mar. 2001. Associate Editor: R. Natole.

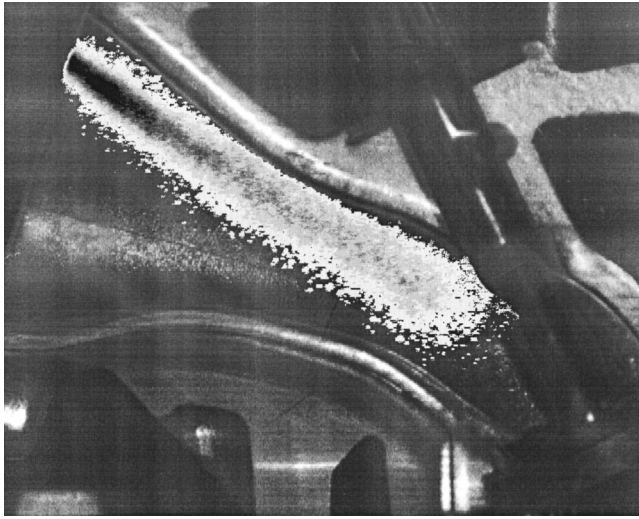


Fig. 1 Side view of fuel spray in intake manifold

this model in terms of droplet velocities, droplet size, and fuel vapor concentration has been investigated previously in the framework of an evaporating dodecane spray ([4]).

2 Eulerian Approach

The Eulerian approach for the numerical description of dispersed two-phase flows is based on the assumption that the liquid phase represents an additional continuum penetrating the gaseous phase. In analogy to the continuum approach of single-phase flows, each phase is described by a set of transport equations for mass, momentum, and energy extended by interfacial exchange terms. This set of transport equations can be recast into a universal formulation which is discretized by a conservative finite volume method and solved by a block-iterative scheme for the linearized equations.

2.1 Transport Equations of the Two-Phase Flow

2.1.1 Basic Equations. Except for the near region of the atomizer where the spray is dense, the volume fraction of the spray is low. For this dilute two-phase flow regime, interactions between droplets can be neglected. Starting from the Navier-Stokes equations, instantaneous transport equations for gas and droplet phase can be derived either by spatial, temporal ([6]), or ensemble averaging. However, these transport equations are only be used for the description of sprays in laminar gas flows. Since combustors generally operate in the turbulent flow regime, the system of transport equations is extended by introducing turbulent fluctuations of the transport quantities followed by Reynolds averaging of the equations. For the gaseous phase, the standard $k-\varepsilon$ model is employed to approximate the transport terms resulting from correlations of fluctuating quantities. This procedure has been described in detail by several authors ([7,8]). The turbulence terms in the droplet phase transport equations are approximated by an algebraic model which is based on a Boussinesq approach. The interacting flow fields are described by the following transport equations:

Gas phase:

$$\frac{\partial}{\partial t} \alpha_g \rho_g + \frac{\partial}{\partial x_j} \alpha_g \rho_g U_{g,j} = M_{\text{int},g} \quad (1)$$

$$\begin{aligned} \frac{\partial}{\partial t} \alpha_g \rho_g U_{g,i} + \frac{\partial}{\partial x_j} \alpha_g \rho_g U_{g,j} U_{g,i} = & -\alpha_g \frac{\partial}{\partial x_i} P_g + \frac{\partial \tau_{i,j}}{\partial x_j} + \alpha_g \rho_g f_i \\ & + I_{\text{int},g,i} \end{aligned} \quad (2)$$

$$\frac{\partial}{\partial t} \alpha_g \rho_g h_g + \frac{\partial}{\partial x_j} \alpha_g \rho_g U_{g,j} h_g = -\frac{\partial q_j}{\partial x_j} + S_{h,g} + H_{\text{int},g} \quad (3)$$

Droplet phase:

$$\frac{\partial}{\partial t} \alpha_d \rho_d + \frac{\partial}{\partial x_j} \alpha_d \rho_d U_{d,j} = \frac{\partial}{\partial x_j} \left(\frac{\mu_{t,d}}{Sc_{t,d}} \frac{\partial \alpha_d}{\partial x_j} \right) + M_{\text{int},d} \quad (4)$$

$$\begin{aligned} \frac{\partial}{\partial t} \alpha_d \rho_d U_{d,i} + \frac{\partial}{\partial x_j} \alpha_d \rho_d U_{d,j} U_{d,i} = & \frac{\partial}{\partial x_j} \left[\alpha_d \mu_{t,d} \left(\frac{\partial U_{d,i}}{\partial x_j} + \frac{\partial U_{d,j}}{\partial x_i} \right) \right] \\ & + \alpha_d \rho_d f_i - \alpha_d \frac{\partial}{\partial x_i} P_g + I_{\text{int},d,i} \end{aligned} \quad (5)$$

$$\frac{\partial}{\partial t} \alpha_d \rho_d h_d + \frac{\partial}{\partial x_j} \alpha_d \rho_d U_{d,j} h_d = \frac{\partial}{\partial x_j} \left(\alpha_d \frac{\mu_{t,d}}{Pr_{t,d}} \frac{\partial h_d}{\partial x_j} \right) + H_{\text{int},d} \quad (6)$$

$$\frac{\partial}{\partial t} \alpha_d \rho_d D + \frac{\partial}{\partial x_j} \alpha_d \rho_d U_{d,j} D = \frac{8 \alpha_d}{\pi D^2} \dot{m}_{\text{vap}} + \frac{\partial}{\partial x_j} \left(\alpha_d \frac{\mu_{t,d}}{Pr_{t,d}} \frac{\partial D}{\partial x_j} \right) \quad (7)$$

The volume concentrations α_g and α_d are a result of the averaging process and represent the local volume fractions of gas and liquid phase, respectively. Dilute two-phase flows are characterized by the conditions

$$\alpha_g + \alpha_d = 1, \quad \alpha_d \ll 1; \quad \alpha_g \approx 1. \quad (8)$$

Double and triple correlations involving fluctuations of α_d are neglected on the right-hand side of Eq. (5). In the present calculations a value of 0.9 is chosen for the turbulent Schmidt and Prandtl numbers, $Sc_{t,d}, Pr_{t,d}$. Using this value, Eq. (4) effectively is a transport equation of a scalar in the asymptotical case of a vanishing droplet diameter. A fundamental assumption of this approach is the dependence of the turbulent viscosity of the droplet phase $\mu_{t,d}$ on local mean flow properties ([9,10])

$$\frac{\nu_{t,d}}{\nu_{t,g}} = \frac{\mu_{t,d}}{\mu_{t,g}} \frac{\rho_g}{\rho_d} = \frac{1}{1 + \left(\frac{t_d}{t_g} \right)^{2n}} \quad (9)$$

Thus, the ratio of the kinematic viscosities of droplet and gas phase is postulated to be a function of the characteristic time scales of both phases. In Ref. [10] a value of 0.25 for the empirical parameter n is suggested. The time scale t_d , which is denoted as droplet relaxation time, characterizes the ability of a droplet to follow turbulent gas velocity fluctuations:

$$t_d = \frac{4}{3} \frac{\rho_d}{\rho_g} \frac{D^2}{C_D \text{Re}_d \nu_g} \quad (10)$$

Originally, the characteristic time of the gas flow turbulence t_g is taken to be the dissipation time scale given subsequently by Eq. (15). In this formulation, the droplet phase turbulence model fails to describe the crossing trajectory effect which has a significant influence on turbulent droplet dispersion ([11,12]). According to the turbulence modeling of the Lagrangian approach, the extended version of the model considers a second characteristic time scale. This crossing time t_c is the time required by a droplet to cross the turbulent eddies of integral scale.

$$t_c = \frac{L_e}{|U_g - U_d|} \quad (11)$$

Combining both time scales, the gas-phase time scale is now defined as

$$t_g = \min[t_e, t_c] \quad (12)$$

The validation of this enhanced turbulence model is based on the basic experiment described in Ref. [11]. In this flow regime, the

transport equations of the gas-phase approach the standard single-phase transport equations extended by additional interfacial exchange terms $M_{\text{int},g}$, $I_{\text{int},g}$, and $H_{\text{int},g}$.

2.2 Discretization of Polydisperse Sprays. To complete the numerical description of the spray, boundary conditions of the droplet phase have to be specified at the atomizer nozzle. However, most sprays of technical importance are characterized by a broad variety of initial droplet diameters and velocities. Since each individual droplet phase boundary condition theoretically requires the numerical solution of a separate set of transport Eqs. (4)–(7), a polydisperse spray has to be discretized by a limited number of representative droplet classes. In practice, the computational effort increases at least linearly with the number of droplet classes employed. As a consequence, the maximum number of classes is restricted by the CPU time and memory capacity available.

For dilute sprays, direct interaction between droplet classes can be neglected although each class is coupled to the gas phase.

3 Lagrangian Approach

The Lagrangian simulation of dispersed two-phase flow is based on the tracking of statistically significant droplet parcels in the gas flow. Each parcel is represented by one droplet and is determined by discretization of the continuous spectra of droplet initial conditions in the near field of the atomizer.

3.1 Equation of Motion. The tracking is based on the integration of the droplets equation of motion combined with an empirical correlation for the aerodynamic drag coefficient C_D ([13])

$$\frac{d\mathbf{u}_d}{dt} = -\frac{3}{4} \frac{\rho_g}{\rho_d} \frac{C_D}{D} |\mathbf{u}_d - \mathbf{u}_g| (\mathbf{u}_d - \mathbf{u}_g) \quad (13)$$

$$C_D = 0.28 + \frac{21}{\text{Re}_d} + \frac{6}{\sqrt{\text{Re}_d}}. \quad (14)$$

3.2 Spray Dispersion. In order to account for the effect of turbulent spray dispersion, the turbulence structure of the gas flow field is modeled by a random process along the droplet trajectories ([14,15]). In this concept, the local turbulence structure is characterized by the length scale l_e and dissipation time scale t_e of eddies representing the coherent flow structures

$$l_e = C_\mu^{1/2} \frac{k^{3/2}}{\varepsilon}, \quad t_e = \frac{l_e}{|\mathbf{u}'_g|}. \quad (15)$$

In addition to the life time scale t_e , a crossing time scale t_c is calculated from

$$\left\| \int_{t_0}^{t_c} (\mathbf{u}_g - \mathbf{u}_d) dt \right\| = l_e, \quad (16)$$

taking into account the droplet dynamics. Each time the smaller one of both time scales is elapsed, the droplet enters a new eddy. Consequently, the random process generates a new velocity fluctuation \mathbf{u}'_g from a Gaussian distribution which is determined by

$$P(\mathbf{u}'_g) = \frac{1}{\sigma \sqrt{2\pi}} e^{(\mathbf{u}_g - \mathbf{u}_d)/2\sigma^2}, \quad \mu = 0, \quad \sigma = \sqrt{\frac{2}{3}} k. \quad (17)$$

This velocity fluctuation remains constant for the period of droplet-eddy interaction and is added to the local value of the gas flow velocity.

3.3 Spray Evaporation. In this study, droplet evaporation is simulated by means of the uniform temperature model ([16–18]). This computationally effective droplet model is based on the assumption of a homogeneous internal temperature distribution in the droplet and phase equilibrium conditions at the surface. The analytical derivation of this model does not consider contributions

to heat and mass transport through forced convection by the gas flow around the droplet. Since diffusive time scales in the surrounding gas phase are much smaller than in the droplet fluid, a quasi-stationary description of the gas phase is applied. Using reference values for variable fluid properties (1/3 rule), an integration of the radially symmetric differential equations yields analytical expressions for the transport fluxes \dot{m}_{vap} , $\dot{Q}_{\text{cond},s}$ and $\dot{H}_{\text{vap},s}$. At this point, convective transport is taken into account by two empirical factors ([19]) resulting in the corrected fluxes \dot{m}_{vap}^* , $\dot{Q}_{\text{cond},s}^*$, and $\dot{H}_{\text{vap},s}^*$

$$\dot{m}_{\text{vap}}^* = \text{cfm} \dot{m}_{\text{vap}}, \quad (18)$$

$$\dot{Q}_{\text{cond},s}^* = \pi D^2 \alpha^* (T_d - T_g), \quad (19)$$

$$\dot{H}_{\text{vap},s}^* = \dot{m}_{\text{vap}}^* c_{p,\text{vap,ref}} (T_d - T_g), \quad (20)$$

$$\text{cfm} = 1 + 0.276 \text{Re}^{1/2} \text{Sc}^{1/3}. \quad (21)$$

Vapor mass flux and heat transfer coefficient are calculated as follows:

$$\dot{m}_{\text{vap}} = 2\pi D \rho_{g,\text{ref}} \Gamma_{\text{im,ref}} \ln \frac{1 - Y_{\text{vap},g}}{1 - Y_{\text{vap},s}}, \quad (22)$$

$$\alpha^* = \text{cfh} \frac{\frac{\dot{m}_{\text{vap}} c_{p,\text{vap,ref}}}{\pi D^2}}{\exp \frac{\dot{m}_{\text{vap}} c_{p,\text{vap,ref}}}{2\pi D \lambda_{g,\text{ref}}} - 1}, \quad (23)$$

$$\text{cfh} = 1 + 0.276 \text{Re}^{1/2} \text{Pr}^{1/3}. \quad (24)$$

The balance equations of the droplet reduce to ordinary differential equations,

$$\frac{d}{dt} m_d = -\dot{m}_{\text{vap}}^*, \quad (25)$$

$$\frac{d}{dt} (m_d h_d) = -\dot{Q}_{\text{cond},s}^* - \dot{H}_{\text{vap},s}^*, \quad (26)$$

which can be appended to the differential equations describing the droplet motion (Eq. (13)).

3.4 Wall Interaction. Interactions between droplets and flow boundaries have a decisive influence on the overall flow behavior. The model used in this study considers mechanisms for a dry wall based on experimental investigations by several groups ([20,21]). For a detailed simulation, the interaction mechanisms are classified in three characteristic wall temperature regimes: Cold wall—a temperature well below the fluid boiling temperature, moderate hot wall—a transition range up to a modified Leidenfrost temperature, and hot wall—a temperature well above the modified Leidenfrost temperature.

The cold wall interaction mechanisms are dominated by complete deposition of the droplet or splashing. In case of splashing, one part of the droplet mass is deposited on the wall whereas the other part is rebounded back into the gas flow decomposed into secondary droplets. Because of an insufficient comprehension of the splashing process, a stochastic model is used which reflects the experimental findings for this type of application. This spray-wall interacting model has been described in detail in previous publications by several authors ([4,21]).

Using the Reynolds and Laplace numbers, respectively, to distinguish between splashing and complete deposition, the following approach is employed.

The impact Reynolds number is based on a corrected droplet velocity normal to the wall $U_n = U_d \sin \alpha^{0.63}$. With respect to a Re-La map, an analysis of numerous droplet impact experiments indicates that splashing is separated from complete deposition by

$$\text{Re} = 24 \text{La}^{0.419} \quad (27)$$

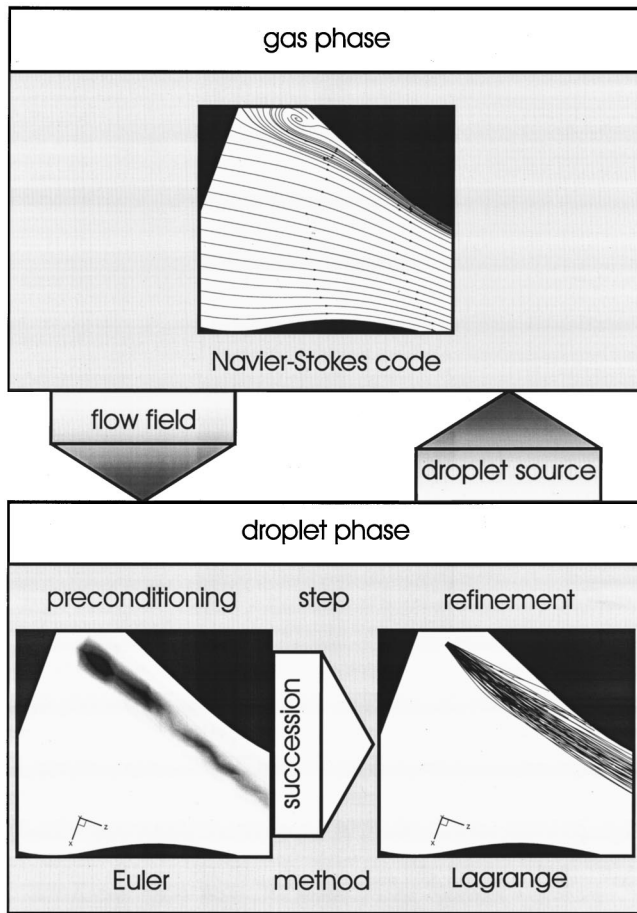


Fig. 2 Structure of the hybrid procedure

where

$$\text{Re} = \frac{U_n D}{\mu_d}, \quad \text{La} = \frac{D \sigma_d \rho_d}{v_d^2}. \quad (28)$$

Due to wall temperatures well below the fluid boiling temperature, only this mechanism was applied to account for droplet wall interaction in the present computation.

4 Interfacial Exchange Terms

The interfacial exchange terms describe the local rates of mass, momentum, and energy transfer across the liquid-gas interface. Equations (1), (2), and (3) contain interfacial exchange terms for the local rates of mass, momentum, and energy, transferred from the liquid phase to the gas phase.

4.1 Eulerian Model. Assuming a spherical shape of the droplets and a uniform internal temperature distribution, the transfer rates may be estimated from Lagrangian single droplet physics as discussed in the previous section. The following model expressions are derived from Eq. (13) and the heat and mass fluxes (18), (19), and (20) of an isolated droplet

$$M_{\text{int},d} = -M_{\text{int},g} = \frac{6\alpha_d}{\pi D^3} \dot{m}_{\text{vap}}^* \quad (29)$$

$$I_{\text{int},d,i} = -I_{\text{int},g,i} = \frac{6\alpha_d}{\pi D^3} \frac{\pi}{8} D^2 \rho_g C_D |U_g - U_d| (U_{g,i} - U_{d,i}) + \dot{m}_{\text{vap}}^* U_{d,i} \quad (30)$$

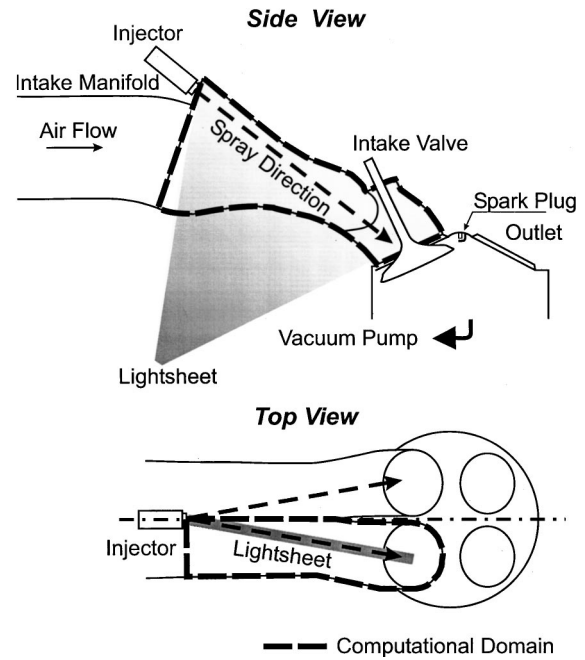


Fig. 3 Position of PIV light sheet

$$H_{\text{int},d} = -H_{\text{int},g} = \frac{6\alpha_d}{\pi D^3} \dot{H}_{\text{vap},s}^* + \dot{Q}_{\text{cond},s}^* \quad (31)$$

4.2 Lagrangian Model. As a result of the Lagrangian approach, source terms are calculated which are proportional to the droplet number density n_k of each class and the number of classes N present in the local control volume ([22])

$$M_{\text{int},d} = \int_V s_{\rho,d} dV = \sum_{k=1}^N n_k (m_d^{en} - m_d^{ex}) k, \quad (32)$$

$$I_{\text{int},d,i} = \int_V s_{U_i,d} dV = \sum_{k=1}^N n_k (m_d^{en} U_{d,i}^{en} - m_d^{ex} U_{d,i}^{ex}) k \quad (33)$$

$$H_{\text{int},d} = \int_V s_{h,d} dV = \sum_{k=1}^N n_k (m_d^{en} h_d^{en} - m_d^{ex} h_d^{ex}) k. \quad (34)$$

It is important to include the heat of evaporation with the droplet enthalpy: $h_d = h_{\text{vap}} + L$, where h_{vap} is the enthalpy of the vapor and L is the latent heat of vaporization.

5 The Hybrid Procedure

With artificial decoupling of the two-phase flow computation by separate solution schemes for each phase and iterative realization of phase interaction, total computation times are rather large ([4]). A reduction of computational effort is achieved by preconditioning the two-phase flow field by means of an Eulerian method in the first step. Following this approximate computation, the flow field and the droplet source terms are passed to the refinement step. In this second step, Lagrangian iteration cycles are performed which are characterized by a fine discretization of droplet injection conditions and wall interaction. This is in fact the basic idea of the hybrid procedure: A two-step combination of both methods in order to reduce total computation time. This approach is schematically illustrated in Fig. 2. Since the two-phase flow field calculated by the Eulerian method already accounts for spray effects on the gas flow, the droplet source terms recorded during subsequent tracking steps are rather close to the final flow result. Consequently, the number of iterations is significantly reduced compared to a complete Lagrangian simulation.

Table 1 Parameters at the inlet of the intake manifold ($z = 0$ mm)

Gas Flow (Air)		Fuel (Ethanol)	
\dot{V}_g	$0.029 \text{ m}^3/\text{s}$	\dot{m}_{fuel}	3.3 g/s
T_g	299 K	T_{fuel}	293 K
p_g	1 bar	U_{fuel}	24 m/s
Tu_g	5%	\angle_{cone}	10 deg

6 Sample Application

The performance and accuracy of the numerical methods presented is demonstrated by a simulation of the two-phase flow in the intake manifold of a SI engine. The experimental investigation has been part of an extended research project on mixture preparation for cold engine operating conditions.

The base engine is a four-cylinder four-valve production type. Ethanol is supplied by a sequential multipoint injection system. To study the fuel system at various engine conditions a test section was constructed. In order to gain optical access to the spray, the cylinder head of the engine was cut off in a plane through the middle of the intake port of the outer cylinder. Based on original CAD data the inner contour of the missing part was then machined from acrylic glass and fitted to the cylinder head. A detailed description of the test rig and the measurement techniques has been published ([23]). In the experiment, the air flow through

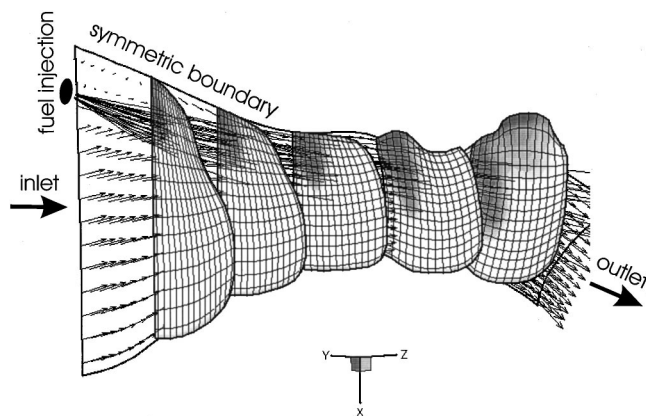


Fig. 4 Computational domain

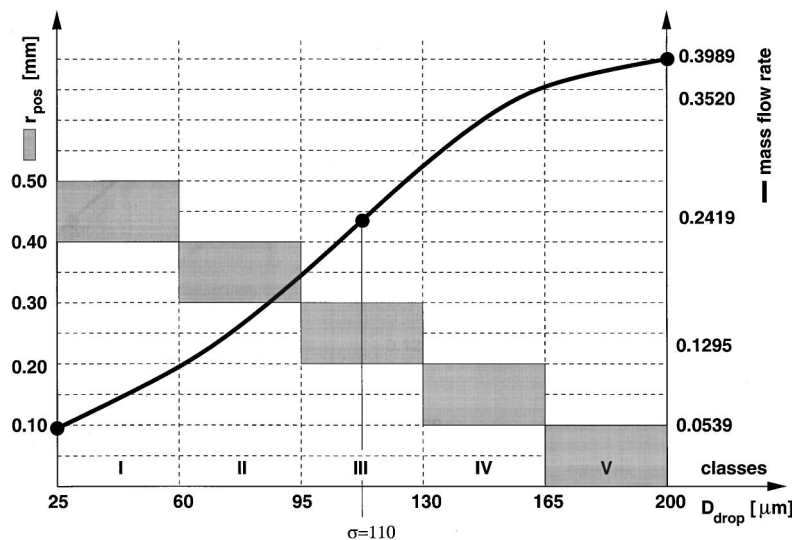


Fig. 5 Discretization of droplet initial conditions

the intake port and valves was generated by a vacuum pump. Fuel atomization was realized by a production two jet pintle type injector. The experimental setup is illustrated in Fig. 3. The operating point of the engine is specified by the stationary flow conditions summarized in Table 1.

The computational domain of the flow simulation is illustrated in Fig. 4, indicating the arrangement of discretized cross sections along the symmetry plane. Due to the symmetric design of the intake port only half is computed. To analyze stationary fuel-air mixing the valve is not considered in the present flow simulation. The position of the spray in the computational flow domain is indicated by representative trajectories originating from the simulated injection point.

6.1 Discretization of a Polydisperse Spray. The specification of spray boundary conditions (Euler method) and droplet initial conditions (Lagrangian method) depends on the inherent characteristics of the two disperse phase modeling approaches. Since primary atomization of the fuel is completed over a short distance of 1 mm, the spray properties can be specified close to the nozzle orifice. Furthermore, the experiment indicates that secondary atomization of droplets has no significant contribution in the evolution of the spray. With respect to the Eulerian method, the discretization of the spray boundary conditions has to be limited to a few classes. Each class is described by a specific combination of fixed numerical values for droplet diameter, velocity, and position.

One of the major advantages of the Lagrangian method is the possibility of a large number of different droplet initial conditions for a high-resolution discretization of the spray yielding an improved description of the primary atomization process ([24,25]) [21, 20]. In the Lagrangian method used for the present simulation, droplet initial conditions are stochastically sampled from distributions which have been determined from the PDA measurements of the spray. Based on experimental values of the characteristic diameters $D_{0.1}$, $D_{0.5}$, and $D_{0.9}$ the discretization of the droplet size spectrum is realized by five equally spaced diameter classes ranging from 25 to 200 μm as illustrated in Fig. 5. The distribution of the fuel mass flow rate on the diameter classes is approximated by a Gaussian function, an assumption which is based on a combined assessment of the PDA results D_{32} and number density. Neglecting effects of (a) primary atomization and (b) gas flow interaction on the droplet velocity closely behind the nozzle (1 mm), it is assumed that the initial velocity of the droplets in the computational model is directly inherited from the liquid jet leaving the nozzle. Thus, an averaged value of 24 m/s derived from PDA measurements at the nozzle orifice is assumed

Table 2 Required CPU times for a Athlon 800 MHz

Method	Euler	Lagrangian	Hybrid
Grid size (nodes)	14175	14175	14175
Droplet classes	5	5	5
Trajectories per class	-	5000	5000
CPU time (min)	232	849	345

for the initial velocity of all droplets. An overall cone angle of the spray of 10 deg is determined by a laser light sheet visualization. Due to the limited possibilities of the spray boundary conditions, the Eulerian continuum model does not consider the cone angle of the spray.

6.2 Results. The efficiencies of the three approaches used to calculate the given two-phase flow can be characterized by the CPU times required by the different calculations, shown in Table 2. The Eulerian model needs about three and a half times less computational effort than the Lagrangian counterpart. The hybrid method requires only insignificantly more computational effort than the Eulerian method. This minor increase is caused by the small number of Lagrangian iterations in the second step of the hybrid procedure.

In Fig. 6 the results of the predictions are compared with measurements. Obviously, the hybrid procedure yields the same result as the Lagrangian approach. Therefore, only Eulerian and Lagrangian results are shown. To compare the gas phase flow field the measured and predicted velocity vectors are shown. For characterizing the spray the number averaged velocity vectors are pre-

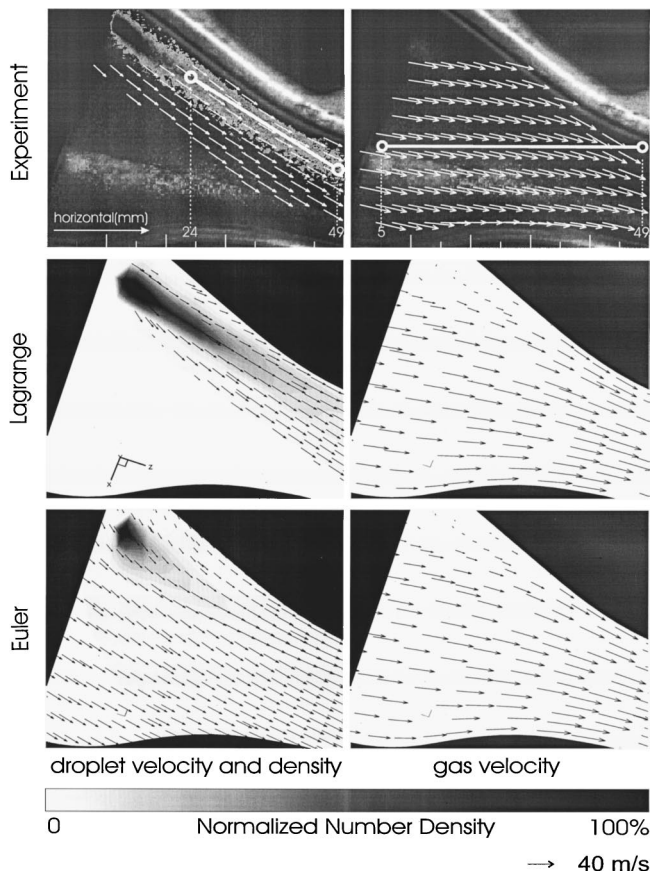


Fig. 6 Predicted and measured velocity vector fields and number density distributions

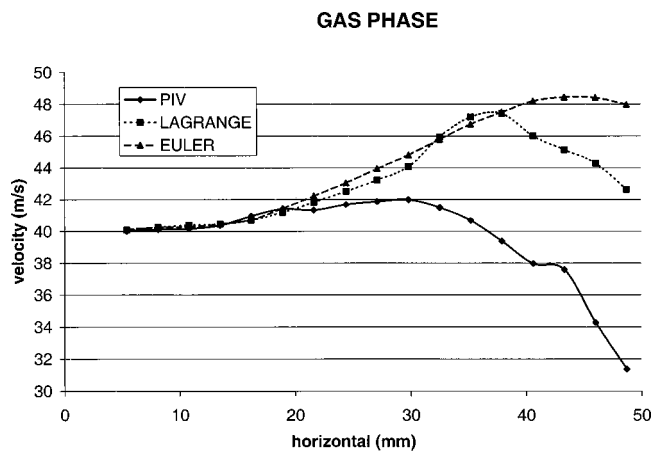


Fig. 7 Comparison of gas velocity

sented together with corresponding experimental data. Furthermore, the predicted number density distributions of the spray are compared with the visualization of the spray.

The direction and magnitude of the velocity vectors predicted by the Lagrangian model, as shown in Fig. 6 agree well with the experimental results. Due to the statistical nature of the Lagrangian droplet tracking method, dispersed phase velocity values are only available for spray regions of sufficiently high droplet number density. By comparing the predicted number density fields with the visualization of the spray it can be seen that the predictions based on the Lagrangian model again coincide well with the measurements. The higher result quality of the Lagrangian model is due to the finer discretization of the droplet initial conditions. A Lagrangian calculation based on the same coarse discretization of the droplet initial conditions as the Eulerian model reveals only insignificant differences.

The Eulerian and Lagrangian approaches are also quantitatively compared with the measurements. The magnitude of the droplet and gas velocities are compared with the measurement along the two straight lines, included in the two top illustrations of Fig. 6. The gas velocity in Fig. 7 is evaluated along the right horizontal line, whereas the mean droplet velocity in Fig. 8 is evaluated along the left transversal line. These results coincide with qualitative results presented before. Due to the coarse discretization of the droplet initial conditions, the Eulerian model deviates most from the measured values of the gas and droplet velocities.

As Figs. 7 and 8 demonstrate, both two-phase flow models have a significant influence on the prediction of the velocity fields of

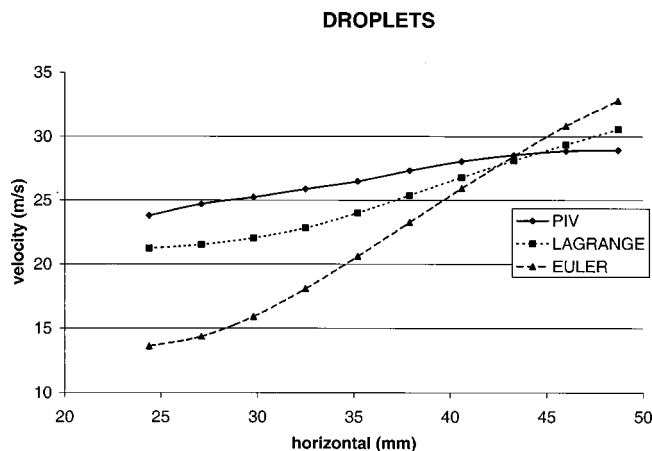


Fig. 8 Comparison of droplet velocity

continuous and dispersed phase. Compared to the experimental results, both models underpredict this influence. Even though the Lagrangian model is more accurate as the Eulerian model, an improved result quality can only be achieved by a more detailed droplet initial conditions. Since the Eulerian model is strictly limited to a few different droplet classes, a comparison of both models on the basis of a spray simulation with more classes is computationally not feasible.

7 Conclusions

In the present study, fuel injection, dispersion, and evaporation in an intake manifold of an IC engine is simulated by three different computational methods. In the first two approaches, Eulerian and Lagrangian two-phase flow models are used to describe the spray behavior. The third approach denoted as hybrid model, is a combination of the two fundamentally different models. To validate the flow simulation, the computed flow fields are compared with experimentally determined velocity flow fields of both phases. The results clearly support the concept of the hybrid scheme, showing that the Eulerian model reaches a solution of the coupled two-phase flow field comparatively quickly. However, this flow field is only of restricted quality due to the limitations imposed on the discretization of the polydisperse spray. The Lagrangian model on the other hand is highly accurate due to a refined discretization of droplet initial conditions, but requires significantly more computational effort to incorporate the coupling effects between both phases. Consequently, the hybrid model achieves an optimum in computational performance in terms of time and accuracy. Future studies on the present flow configuration are intended to focus on the evaporation behavior of the spray based on expected new experimental data.

Acknowledgment

The authors would like to thank Mr. P. Gorse for his valuable contributions to this project.

Nomenclature

cfm	=	convection correction factor
cfh	=	convection correction factor
c_p	=	specific heat capacity
D	=	droplet diameter
$D_{0,x}$	=	D at $x\%$ of total liquid volume
D_{32}	=	Sauter mean diameter
f	=	body force
h	=	enthalpy
\dot{H}	=	enthalpy flux
H	=	energy transfer rate
I	=	momentum transfer rate
k	=	turbulent kinetic energy
\dot{m}	=	mass flux
La	=	Laplace number
L	=	integral length scale
M	=	mass transfer rate
n	=	droplet number density
P	=	pressure, probability
Pr	=	Prandtl number
\dot{Q}	=	conductive heat flux
Re	=	Reynolds number
S	=	source term
Sc	=	Schmidt number
t	=	characteristic time scale
T	=	temperature
Tu	=	degree of turbulence
U	=	velocity component
Y	=	mass fraction

Greek Symbols

α	=	heat transfer coefficient
----------	---	---------------------------

α	=	volume fraction
β	=	off axis angle
ε	=	dissipation rate of k
Γ	=	diffusion coefficient
λ	=	thermal conductivity
μ	=	dynamic viscosity
ν	=	kinematic viscosity
ρ	=	density
σ	=	variance, surface tension
τ	=	shear stress

Subscripts

0	=	initial state
c	=	crossing
e	=	eddy
en,ex	=	entry, exit
g,d	=	gas, droplet
int	=	interface
k	=	class indicator
s	=	surface
n	=	normal
t	=	turbulent
vap	=	vapor

References

- [1] Crowe, C. T., 1982, "Review—Numerical Models for Dilute Gas-Particle Flows," *ASME J. Fluids Eng.*, **104**, pp. 297–303.
- [2] Klose, G., Schmehl, R., Meier, R., Maier, G., Koch, R., Wittig, S., Hettel, M., Leuckel, W., and Zarzalis, N., 2000, "Evaluation of Advanced Two-Phase Flow and Combustion Models for Predicting Low Emission Combustors," ASME Paper 00-GT-133.
- [3] Hallmann, M., Scheurlen, M., and Wittig, S., 1995, "Computation of Turbulent Evaporating Sprays: Eulerian Versus Lagrangian Approach," *ASME J. Eng. Gas Turbines Power*, **117**, pp. 112–119.
- [4] Schmehl, R., Roskamp, H., Willmann, M., and Wittig, S., 1998, "CFD Analysis of Spray Propagation and Evaporation Including Wall Film Formation and Spray/Film Interactions," *ILASS '98 Europe*, pp. 546–555.
- [5] Preclik, D., Estublier, D., and Wennerberg, D., 1995, "An Eulerian-Lagrangian Approach to Spray Combustion Modeling for Liquid Bi-Propellant Rocket Motors," AIAA, Technical Report 95-2779.
- [6] Ishii, M., 1975, *Thermo-Fluid Dynamic Theory of Two Phase Flow*, Eyrolles.
- [7] Launder, B. E., and Spalding, D. B., 1974, "The Numerical Computation of Turbulent Flows," *Comput. Methods Appl. Mech. Eng.*, **3**, pp. 269–289.
- [8] Rodi, W., 1984, *Turbulence Models and Their Application in Hydraulics—A State of the Art Review*, IAHR.
- [9] Mellville, W. K., and Bray, K. N. C., 1979, "A Model of the Two-Phase Turbulent Jet," *Int. J. Heat Mass Transf.*, **22**, pp. 647–656.
- [10] Krämer, M., 1988, "Untersuchungen zum Bewegungsverhalten von Tropfen in turbulenter Strömung in Hinblick auf Verbrennungsvorgänge," dissertation, Universität Karlsruhe.
- [11] Snyder, W., and Lumley, J. L., 1971, "Some Measurements of Particle Velocity Autocorrelation Functions in a Turbulent Flow," *J. Fluid Mech.*, **48**, pp. 41–71.
- [12] Klose, G., Rembold, B., Koch, R., and Wittig, S., 2000, "Comparison of State of the Art Droplet-Turbulence Interaction Models for Aero-Engine Combustor Conditions," *Proceedings of the Third International Symposium on Turbulence, Heat and Mass Transfer*, T. Tsuji, Y. Nagano, and K. Hanjalic, eds., Nagoya, Apr., **3**, pp. 763–770.
- [13] Wiegand, H., 1987, "Die Einwirkung eines ebenen Strömungsfeldes auf frei bewegliche Tropfen und ihren Widerstandsbeiwert im Reynoldszahlenbereich von 50 bis 2000," *Fortschrittberichte VDI*, **7**(120).
- [14] Gosman, A. D., and Ioannides, E., 1983, "Aspects of Computer Simulation of Liquid-Fueled Combustors," *J. Energy*, **7**(6), pp. 482–490.
- [15] Milojević, D., 1990, "Lagrangian Stochastic-Deterministic (LSD) Predictions of Particle Dispersion in Turbulence," *Part. Part. Syst. Charact.*, **7**, pp. 181–190.
- [16] Faeth, G. M., 1983, "Evaporation and Combustion of Sprays," *Prog. Energy Combust. Sci.*, **9**, pp. 1–76.
- [17] Sirignano, W. A., 1984, "Fuel Droplet Vaporization and Spray Combustion Theory," *Prog. Energy Combust. Sci.*, **9**, pp. 291–322.
- [18] Aggarwal, S. K., and Peng, F., 1995, "A Review of Droplet Dynamics and Vaporization Modeling for Engineering Calculations," *ASME J. Eng. Gas Turbines Power*, **117**, pp. 453–461.
- [19] Abramzon, B., and Sirignano, W. A., 1989, "Droplet Vaporisation Models for Spray Combustion Calculations," *Int. J. Heat Mass Transf.*, **32**, pp. 1605–1618.
- [20] Samenfink, W., 1997, "Grundlegende Untersuchung zur Tropfeninteraktion mit schubspannungsgetriebenen Wandfilmen," dissertation, Institut für Thermische Strömungsmaschinen, Universität Karlsruhe (TH).
- [21] Coghe, A., Cossali, G. E., and Marengo, M., 1995, "A First Study About

Single Droplet Impingement on Thin Liquid Film in a Low Laplace Number Range," *ICLASS-95, Nürnberg*, pp. 285–293.

- [22] Crowe, C. T., Sharma, M. P., and Stock, D. E., 1977, "The Particle-Source-In Cell (PSI-CELL) Model for Gas-Droplet Flows," *ASME J. Fluids Eng.*, **99**, pp. 325–332.
- [23] Rottenkolber, G., Kölmel, A., Dullenkopf, K., Wittig, S., Feng, B., and Spicher, U., 1999, "Influence of Mixture Preparation on Combustion and Emissions Inside an SI Engine by Means of Visualization, PIV and IR Thermography During Cold Operating Conditions," *SAE Tech. Paper Nr. 1999-01-3644*.

- [24] Schmehl, R., Maier, G., and Wittig, S., 2000, "CFD Analysis of Fuel Atomization, Secondary Droplet Breakup and Spray Dispersion in the Premix Duct of a LPP Combustor," *8th International Conference on Liquid Atomization and Spray Systems, ICLASS 2000*, Pasadena, CA, July 16–20.
- [25] Schmehl, R., Klose, G., Maier, G., and Wittig, S., 1998, "Efficient Numerical Calculation of Evaporating Sprays in Combustion Chamber Flows," *92nd Symp. on Gas Turbine Combustion, Emissions and Alternative Fuels*, RTO Meeting Proceedings 14, Lisbon.

Analysis of the Effects of Water Injection on the Performance of a Gas Turbine

K. Mathioudakis

Associate Professor,
Department of Mechanical Engineering,
Fluids Section,
Laboratory of Thermal Turbomachines,
National Technical University of Athens,
P.O. Box 64069,
15710 Athens, Greece

The effect of water injection in the combustion chamber of an industrial gas turbine is studied by means of analytic relations. Equations for the estimation of changes in the main performance parameters are provided. The relations are derived on the basis of an order of magnitude analysis and taking into account variation of gas properties due to water injection as well as changes in the interrelation of component performance parameters. It is shown that water/fuel ratio is the main parameter on which performance deviations depend. Data from the performance testing of an industrial gas turbine are used to check the validity of the proposed relations. The comparison of the predictions to the test data shows that the mechanisms of performance deviations are well modeled by the analysis presented. [DOI: 10.1115/1.1451755]

Introduction

Water injection has been used for many years in gas turbines in order to reduce NO_x emissions. It has been established that the amount of reduction of NO_x emission depends on the ratio of injected water to fuel flow rate. Dependence of emission levels on water/fuel ratio has been presented by many authors, as for example Shaw [1], Koch and Felix [2], and Schetter [3]. Lefebvre [4] reports analytical relations for estimating emissions reduction as a function of water/fuel ratio. Recent studies (Liever et al. [5]) have predicted such interrelation by using CFD techniques.

Apart from the effect on NO_x emissions, injection of water also affects the performance of a gas turbine. The effects of the injection on performance are qualitatively known, (see, for example, Walsh and Fletcher [6]), while dependence curves of performance parameters on the amount of injected water have been presented by various authors (Kreitmeier et al. [7] and Cloyd and Harris [8]). Such curves have been produced by running computational performance models of specific gas turbines. Numerical calculations of performance for gas turbines, when water content of the air or flue gases is high, have also been presented by other authors in different contexts (some recent examples being Camporeale et al. [9] and Jordal et al. [10])

A disadvantage of methods based on computational models is that although they provide information for a specific gas turbine, they do not give an idea about the generality of their predictions or about the factors governing the phenomena studied. Analytical studies, when they can be performed of course, are best suited for deriving this type of information. In the present paper the effect of water injection on the performance of a gas turbine is studied by a means of analytical relations. The analysis demonstrates which are the main parameters governing changes in performance variables and provides simple relations to estimate these changes. The use of analytic relations allows thus an understanding of the effect of water injection and provides a means for a quick estimation of such effects.

The results of the analysis are substantiated by comparison to data obtained from the performance testing of an industrial gas turbine.

Relations for Performance Parameter Deviations

The gas turbine layout considered in the present analysis is shown in Fig. 1. It is a single-shaft industrial gas turbine, with external cooling of the compressor exit bleed flow, prior to feeding it for turbine blade cooling. The possibility of water injection in the combustion chamber for NO_x control is foreseen. The station numbering shown in this figure will be used to characterize the various quantities mentioned in the analysis hereafter. This particular layout has been chosen since test data from a gas turbine of this type are available to substantiate the present analysis. On the other hand, it is general enough to cover simpler configurations (for example, engines with no external bleed cooling).

Injection of water results in the change of several operational parameters, affecting thus the power output and efficiency of a gas turbine. The analysis that follows has as a main purpose the evaluation of how much these two parameters change, when water is injected at the compressor exit and the control system acts to keep turbine inlet temperature unchanged.

Before proceeding to detailed analysis, it is useful to enumerate the factors on which power output depends and why it is expected to change when water is injected. For this purpose, it is useful to look at the equation relating power to component performance and individual cycle variables.

Power output results from the difference between the power produced by the turbine and that absorbed by the compressor:

$$P = \dot{m}_2 c_{pa} T_2 \left[\frac{\dot{m}_4}{\dot{m}_2} \frac{C_{pg}}{C_{pa}} \frac{T_4}{T_2} \eta_{Tis} \left(1 - \frac{1}{\pi_c \frac{\gamma_g - 1}{\gamma_g}} \right) - \frac{1}{\eta_{cis}} \left(\pi_c \frac{\gamma_a - 1}{\gamma_a} - 1 \right) \right]. \quad (1)$$

For this expression it has been assumed that the pressure loss in the combustion chamber and turbine exhaust is negligible, so that compressor and turbine pressure ratios are equal.

Water injection has the following effects:

- Mass flow through the turbine changes, and compressor-turbine flow matching results in a different compressor operating point, namely different pressure ratio and possibly mass flow rate.
- The gases through the turbine have now a different composition, therefore different specific heat. Consequently, for the same turbine inlet temperature and pressure ratio, a different amount of power is produced.

Contributed by the Combustion and Fuels Division of THE AMERICAN SOCIETY OF MECHANICAL ENGINEERS for publication in the ASME JOURNAL OF ENGINEERING FOR GAS TURBINES AND POWER. Manuscript received by the C&F Division, November 2000; final revision received by the ASME Headquarters May 2001. Associate Editor: S. Gollahalli.

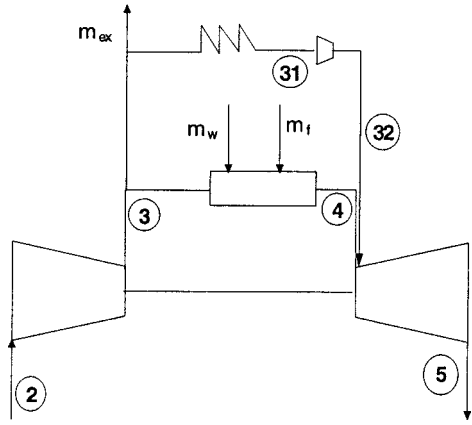


Fig. 1 Schematic of the gas turbine layout studied

• Fuel/air ratio also changes, as more fuel is added, in order to compensate for the heat absorbed for evaporation of the injected water, while keeping TIT constant.

In the following we will examine how changes in each one of these parameters can be evaluated.

At this point it should be commented that the fuel/air ratio f has a value, which is very small, typically around 0.02. The fact that this is a number with such a small value will be used to simplify several relations, by suitable approximation in the following. It should also be noted that according to current practice of water injection water/fuel ratio assumes values that are of the order of 1 or smaller.

Compressor Pressure Ratio. Pressure ratio is related to turbine and compressor capacities through the flow matching relations, given in the Appendix. We can apply Eq. (A2.3) to the two modes of operation, with and without water injection. It is realistic to assume that the bleed air fraction b and loss factor K_b do not change with water injection, namely the term $(1-b)(1-K_b)$ remains constant, while the turbine is choked (which means $q_4 = \text{constant}$). Writing Eq. (A2.3) once for operation without and once with water injection and dividing the two equations gives

$$\frac{\pi'_c}{\pi_c} = \frac{q'_2}{q_2} \frac{1+f'(1+w)}{1+f} \sqrt{\frac{R'_4}{R_4} \frac{\gamma_4}{\gamma'_4} \frac{T'_4}{T_4} \frac{T_2}{T'_2}} \quad (2)$$

This relation can be used to predict the pressure ratio at any operating condition once the pressure ratio at one operating point is known (e.g., at base load) and can be applied to both dry and wet operation. When applied to operating points with water injection it can be used to estimate the change in pressure ratio, which will result from the injection of water.

A simplification can be considered for operation with constant geometry, namely with no variation of stator vane angles. For modern compressors it is usual that the nominal constant speed characteristic is approximately vertical to the flow axis, namely $q_2 = \text{constant}$ for given speed. For a gas turbine used in electricity generation (constant rotational speed), operation at constant turbine inlet temperature ratio T_4/T_2 , allows further simplification of the previous relation:

$$\frac{\pi'_c}{\pi_c} = \frac{1+f'(1+w)}{1+f} \sqrt{\frac{R'_4}{R_4} \frac{\gamma_4}{\gamma'_4}} \approx (1+f'w) \sqrt{\frac{R'_4}{R_4} \frac{\gamma_4}{\gamma'_4}} \quad (3)$$

This relation shows that pressure ratio changes as a result of two effects: change of mass flow through the turbine and change of gas properties as a result of increased water content.

Fuel/air Ratio. The change in fuel/air ratio is derived by considering the heat balance of the combustion chamber for operation with and without water injection, for constant temperature at the

exit of the combustion chamber. The derivation is given in the Appendix. Relation (A3.4) relates the fuel/air ratio prior and after injection and can be written in the following form, to give directly the change caused by water injection:

$$\frac{\Delta f}{f} = \frac{f' - f}{f} = \frac{rwf}{1 - rwf} \quad (4)$$

Power Output. The following relation, as derived in the Appendix, will give the change in gas turbine output power for a given TIT:

$$\frac{\Delta P}{P} = \frac{\Delta \dot{m}_2}{\dot{m}_2} + 2 \frac{P_T}{P} f' w \quad (5)$$

P_T stands for the power produced by the turbine. The first term of the right-hand side represents the change in power caused by the change of the compressor operating point and the resulting change in inlet airflow. The second term represents the change in power produced by the turbine, as it swallows extra fluid, namely the steam produced by the injected water. This steam produces power twice the one produced by the same amount of combustion gas, when expanding over the same pressure limits. This happens because thermal capacity of steam is approximately double the thermal capacity of combustion gas.

For a modern single shaft turbine used in electricity generation, operation with fixed compressor geometry implies no change in inlet mass flow rate, as commented above. Therefore, the change in power will be a function of only the water/fuel ratio w , since the first term of the right-hand side of Eq. (5) will be equal to zero. When variable geometry exists and is used for engine control, mass flow changes will have to be taken into account according to this relation.

Efficiency. The relation for estimating efficiency deviation can be derived from the equation of definition of gas turbine efficiency:

$$\eta_{th} = \frac{P}{\dot{m}_f q_f} = \frac{P}{f \dot{m}_3 Q_f} \quad (6)$$

Efficiency change can be derived from this relation, by taking logarithms and then differentiating:

$$\frac{\Delta(\eta_{th})}{\eta_{th}} = \frac{\Delta P}{P} - \frac{\Delta f}{f} - \frac{\Delta \dot{m}_3}{\dot{m}_3} \quad (7)$$

Substituting for power output deviations from Eq. (5) and fuel/air ratio deviations from Eq. (4) we get

$$\frac{\Delta(\eta_{th})}{\eta_{th}} = \left(2 \frac{P_T}{P} - r \right) - \frac{fw}{1 - rf w} \quad (8)$$

Experimental Validation

The validity of the relations presented above and their capability to estimate the effects of water injection will be assessed by application to test data from an operating industrial gas turbine.

The tests are performed on a single-shaft gas turbine, the model V64.3 manufactured by Siemens, as a part of its commissioning at a power station. The layout of the turbine is the one presented in Fig. 1. The compressor is equipped with variable inlet guide vanes. They remain at a fixed position, for base load or loads below about 50 percent, while they are activated and moved for operation between these loads, in order to control exhaust gas temperature.

Testing is performed along the guidelines of the ISO 2314 standard [11], as to test procedure, measurement accuracy, etc. The quantities measured are indicated on Fig. 2. From these quantities it was possible to calculate the mass flow rate into the compressor, by applying a heat balance over the entire engine. ISO 2314 gives the guidelines for such calculations. They have also been discussed by Mathioudakis et al. [12]. Once the air mass flow rate

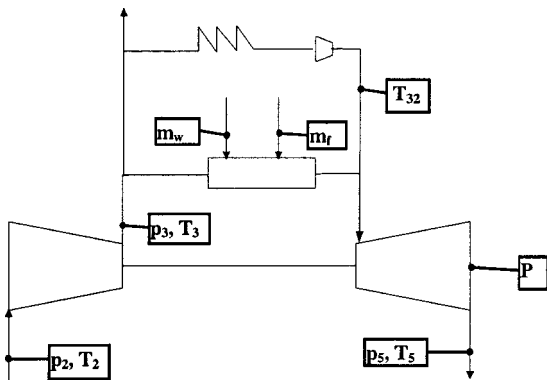


Fig. 2 Measured quantities on the single shaft gas turbine

has been calculated, it is possible to calculate turbine inlet temperature. Having thus a full set of data, all information needed for applying the previously derived relations is available.

Testing is accomplished for dry operation, at loads covering the full operating envelope of the engine, and operation with water injection. Different amounts of injected water were used to achieve different levels of emissions. For each load setting data were taken at several operating points, with small variations around the set point. The data give thus the possibility to derive all the information needed for isolating the deviations of performance parameters caused by water injection.

Compressor Pressure Ratio. Comparison of measured pressure ratio to values predicted by Eq. (2) is shown in Fig. 3. Measured and predicted values are in excellent agreement, for all operating points, from either dry or wet operation. Also, the operating points shown here come from conditions with either constant or variable geometry.

It is interesting to note here that taking into account the alteration of gas properties because of the changing amount of water content gives improved accuracy in the estimated pressure ratio. The magnitude of inaccuracy introduced if variable properties are not taken into account is demonstrated in Fig. 4. It is shown that when gas properties are considered constant, estimated pressure ratio is more than one percent lower than the actually measured value.

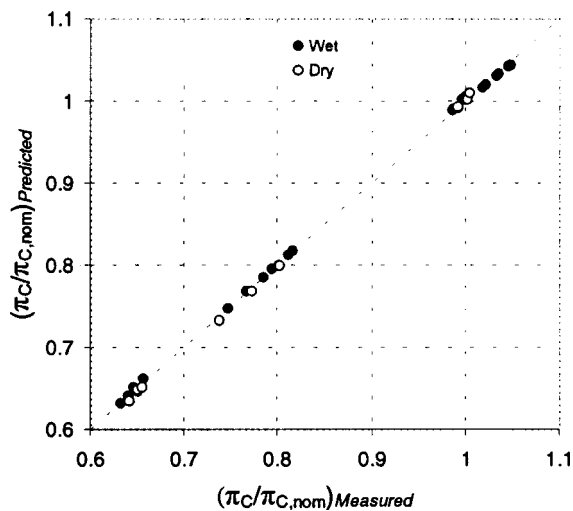


Fig. 3 Measured pressure ratio versus pressure ratio predicted by Eq. (2)

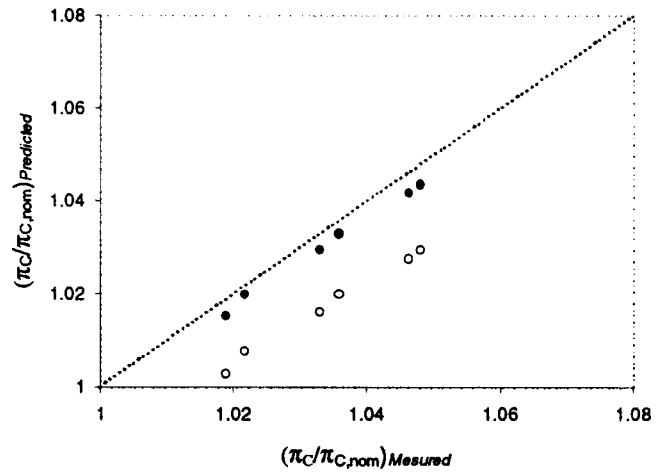


Fig. 4 Pressure ratio estimated using dry gas properties (○) and properties altered by water injection (●). Base load $w \approx 1.2$.

Fuel Air Ratio. Fuel flow rate is directly measured, while air mass flow rate is calculated from engine heat balance, giving thus the value of f for each test point. In order to check the validity of Eq. (4), values of f have to be compared for dry and wet operation, at the same TIT. Since TIT could not be kept strictly constant during the tests, data from several operating points were used for each condition and dependence of f versus TIT is established. Δf is then calculated by interpolating between the data, as shown in Fig. 5.

Comparison of fuel-air ratio deviations estimated from test data and values predicted by Eq. (4), using the amount of water flow rate as an input, is shown in Fig. 6. The very good agreement between measured and predicted values verifies that Eq. (4) gives a good estimation of water injection effect onto the fuel-air ratio of the gas turbine.

Power Output. Changes in power output when water is injected are evaluated from the measured power values. In order to evaluate changes at constant TIT, power is plotted versus TIT and deviations are calculated in the same way as for fuel air ratio, described above. This dependence for operating points around the base load condition is shown in Fig. 7.

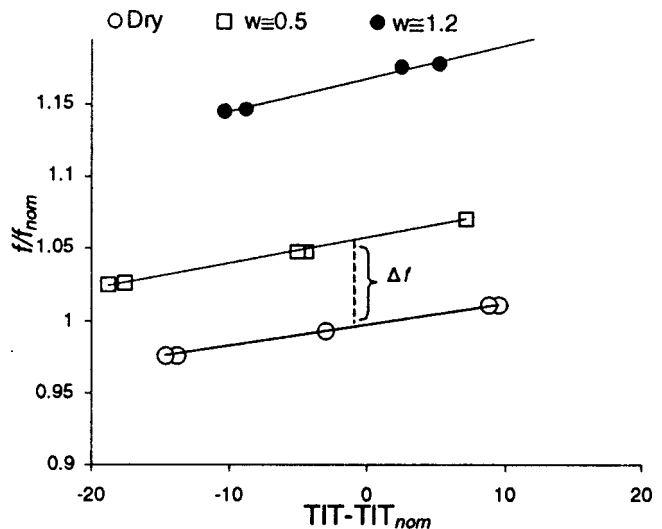


Fig. 5 Fuel/air ratio for different TIT and w values. Base load.

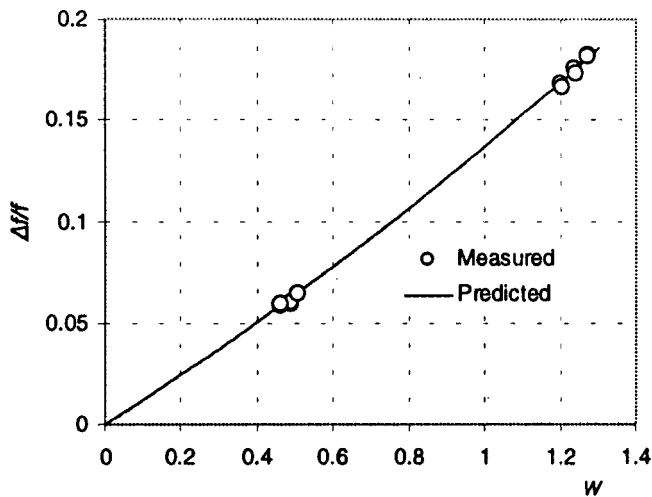


Fig. 6 Comparison of measured fuel air ratio changes to values predicted by Eq. (4)

Comparison of measured power output variations to the predictions, namely the line expressing the dependence on w , Eq. (5), is shown in Fig. 8. For operation at base load conditions the inlet guide vanes are kept at a constant setting angle. Compressor inlet air mass flow rate remains constant and the line shown in Fig. 8 represents the second term of the right-hand side of Eq. (5).

It is interesting here to see how the dependence changes when operation at part load is considered. For such operation, when water is injected, IGVs are also moved to adjust the turbine exit temperature. This means that air mass flow rate is also changed and power output deviation has to be estimated by using both terms of Eq. (5). Comparison of measured and predicted values for this load is shown in Fig. 9. The points representing only the term $2(P_T/P)f_w$ are also shown in the figure, which show no correlation with w . This demonstrates that the prediction has to take into account not only the water-fuel ratio, but also the changes in air mass flow resulting from the movement of IGVs.

Efficiency. The variation of efficiency as a function of the water to air ratio at base load operating conditions, is shown in Fig. 10. It is observed that the points derived from the test data are in very good correlation with the predictions of Eq. (8).

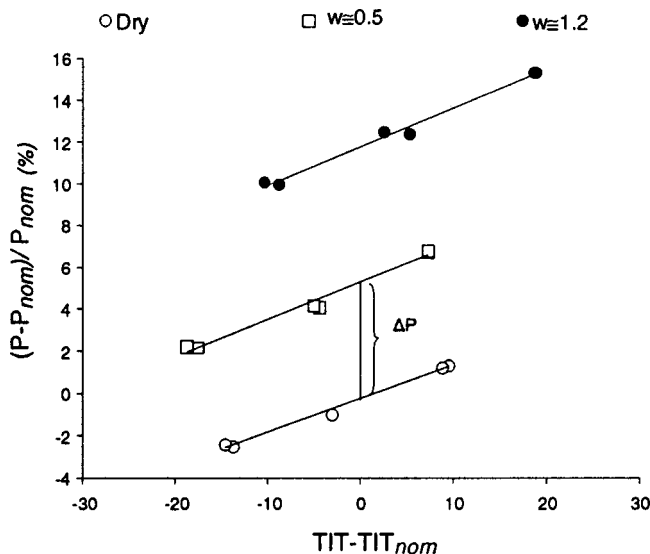


Fig. 7 Dependence of power output on turbine inlet temperature, for dry and wet operation

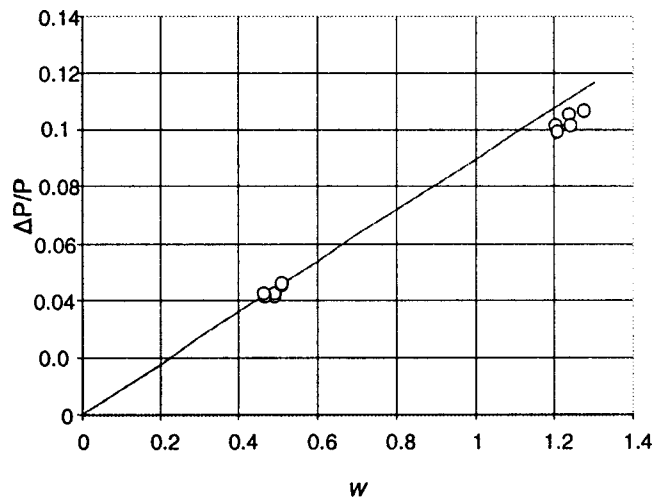


Fig. 8 Change in output power as a function of water/fuel ratio. Points from test data, line from Eq. (5) with $\Delta \dot{m}/\dot{m}=0$. Base load.

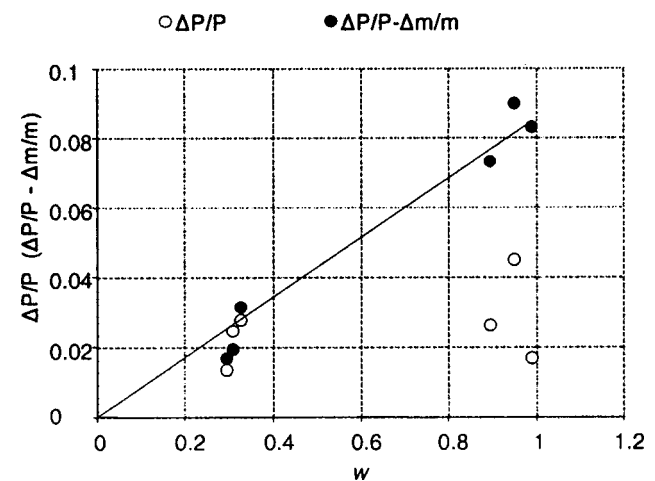


Fig. 9 Operation in the region where IGVs are activated. 75 percent load.

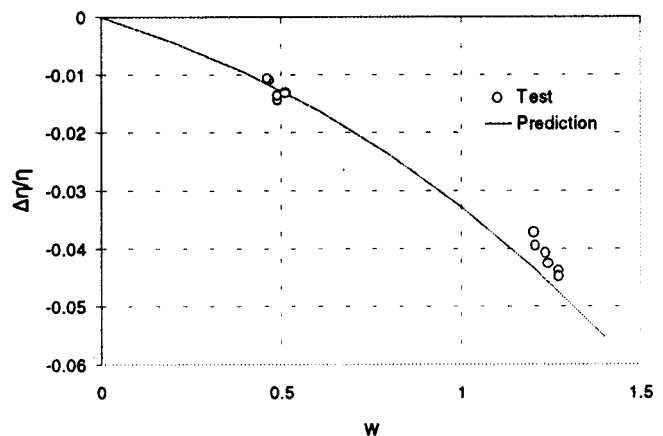


Fig. 10 Efficiency decrease due to water injection. Points from test data and line from Eq. (8).

Discussion

A feature of the equations derived for estimating the deviations of the different performance parameters is that the deviations at a given operating condition are functions of only the water to fuel

ratio. As mentioned in the Introduction, water-to-fuel ratio is the parameter which determines the amount of reduction in NO_x emissions as well. It is thus concluded that the same parameter is driving both emissions reduction and performance deviations. Although this has been tacitly assumed in the various publications reporting the effect of water injection on performance, it is here that analysis shows that this is the primary parameter determining the magnitude of the deviations.

The analysis presented above could be applied for the injection of steam. The difference is that injected water will absorb heat to evaporate and thus extra fuel is needed to keep TIT constant. Steam on the other hand does not need such extra heat but it can even offer some preheating thus reducing the necessary fuel. It is thus expected that in the case of steam injection thermal efficiency will increase. This is the trend observed in curves showing the effect of steam injection, as presented by various authors (Kreitmeyer et al. [7] and Cloyd and Harris [8]). This fact is reflected in the present analysis through the value of the parameter r . In the case of steam r will be much smaller than in the case of water, since enthalpy difference for changing the steam temperature will be much smaller as it does not include the heat of evaporation. This has as a result that the coefficient of w in Eq. (8) becomes positive and therefore the predicted deviations of thermal efficiency will also be positive.

In the analysis presented above the relations for fuel/air ratio, power output and efficiency have been derived for constant TIT. This is the usual way performance parameter deviations are evaluated (see Cloyd and Harris [8]). The approach presented here can nevertheless serve as basis in examining other types of operation, such as constant EGT, for example. The relation derived for π_c is of general validity.

The present analysis can also be useful in practical situations, when correction curves are provided by the engine manufacturer, accounting for the amount of water injected. Such curves may be used to refer data from performance testing to a certain amount of water injected. The formulas given above can be used for a check of the consistency of curves provided with gas turbine design data. They could even be used as basis for correction, if needed.

Conclusions

A method for estimating the deviation of performance parameters as a result of injection of water into the exit of the compressor for reduction of NO_x emissions, has been presented. Analytical formulas for estimating the deviations of compressor pressure ratio, fuel/air ratio, power output, and efficiency have been provided.

It has been shown that the main parameter determining the magnitude of deviation is the water to fuel ratio, which also happens to be the quantity determining the amount of reduction of nitric oxide emissions. The formulas provided highlight the performance quantities that determine the dependence of different parameter deviations, while they provide an insight in understanding the physics of the alterations resulting from the injection of water.

Data from testing of a single-shaft gas turbine, employed for electricity generation, have been used to verify that the proposed relations can give a very good tool for estimating performance parameter deviations.

Acknowledgments

The author would like to thank Public Power Corporation (Greece) for allowing the inclusion of the test data in the present paper.

Appendix

Specific Heat. The specific heat of the hot gases into the turbine changes, because of the increased steam content, produced

by the evaporation of the injected water. The new specific heat can be calculated if the gas is considered to be a mixture of water vapor and gas produced from dry combustion:

$$C'_{pg} = \frac{(1+f')C_{pg} + f'wC_{ps}}{1+f'(1+w)}. \quad (\text{A1.1})$$

An approximate expression can be derived from this relation, if certain features of practical experience are taken into account. Taking this into account and the fact that $f', f'w \ll 1$ we can write

$$\frac{C'_{pg}}{C_{pg}} \approx \left(1 + f'w \left(\frac{C_{ps}}{C_{pg}} - 1 \right) \right). \quad (\text{A1.2})$$

The specific heat of the dry combustion products can be considered to be the same as for the gas with no water injected, because fuel-air ratio does not change significantly. On the other hand, the specific heat of steam is roughly double the specific heat of the combustion gases, (example: for $T = 1100^\circ\text{C}$, $f = 0.02$, $C_{pg} = 1186$, $C_{ps} = 2532 \text{ J/KgK}$). The previous relation can thus be further approximated by the following one:

$$\frac{C'_{pg} - C_{pg}}{C_{pg}} = \frac{\Delta C_{pg}}{C_{pg}} \approx f'w. \quad (\text{A1.3})$$

Compressor-Turbine Flow Matching. The referred mass flow at the inlet of the turbine can be related to the referred mass flow at compressor inlet as follows:

$$\begin{aligned} \frac{\dot{m}_4}{P_4} \sqrt{\frac{R_4 T_4}{\gamma_4}} &= \frac{\dot{m}_2}{P_2} \sqrt{\frac{R_2 T_2}{\gamma_2}} \sqrt{\frac{R_4}{R_2} \frac{\gamma_2}{\gamma_4} \frac{\dot{m}_4}{\dot{m}_2} \frac{P_2}{P_4} \frac{P_3}{P_4}} \sqrt{\frac{T_4}{T_2}} \\ \Rightarrow q_4 &= q_2 \frac{\dot{m}_4}{\dot{m}_2} \sqrt{\frac{R_4}{R_2} \frac{\gamma_2}{\gamma_4} \frac{1}{\pi_c}} (1 - k_b) \sqrt{\frac{T_4}{T_2}}. \end{aligned} \quad (\text{A2.1})$$

It should be noted that the generalized expression for the referred mass flow rates is used, in order to take into account working fluid properties change, caused by water addition (Hensley [13], Gu and Palmer [14], Bird and Grabe [15], and AGARD [16]).

If the fraction of the total air flow bled from the compressor is b then

$$\frac{\dot{m}_4}{\dot{m}_2} = \frac{\dot{m}_4}{\dot{m}_3} \frac{\dot{m}_3}{\dot{m}_2} = (1 + f(1+w)) \cdot (1-b). \quad (\text{A2.2})$$

At combustion chamber outlet mass flow has resulted from the air mass flow to which fuel and water have been added. The previous relation can thus be written as follows:

$$\pi_c = \frac{q_2}{q_4} (1 + f(1+w))(1-b)(1-K_b) \sqrt{\frac{R_4}{R_2} \frac{\gamma_2}{\gamma_4}} \sqrt{\frac{T_4}{T_2}}. \quad (\text{A2.3})$$

Air-Fuel Ratio. We can evaluate the change in fuel/air ratio by applying the heat balance equation of the combustion chamber for dry and wet operation:

Dry operation:

$$(1+f)(h_{g4} - h_{g0}) = (h_{a3} - h_{a0}) + fQ_f. \quad (\text{A3.1})$$

Wet operation:

$$(1+f')(h_{g4} - h_{g0}) = (h'_{a3} - h_{a0}) + f'Q_f - wf'(h_{s4} - h_w). \quad (\text{A3.2})$$

Eliminating the quantity Q_f from the two relations gives

$$\frac{f'}{f} = rwf' + a \quad (\text{A3.3})$$

where

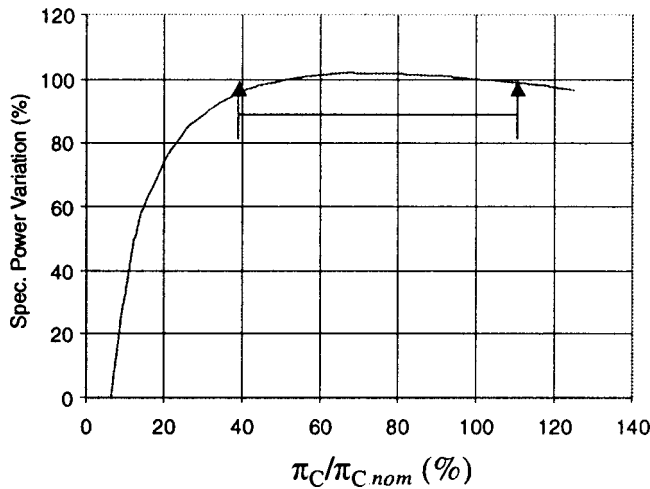


Fig. 11 Gas turbine specific power versus pressure ratio for constant TIT. The “flat” region is indicated.

$$r = \frac{h_{s4} - h_w}{(h_{g4} - h_{g0}) - (h_{a3} - h_{a0})}$$

$$a = \frac{(h_{g4} - h_{g0}) - (h'_{a3} - h_{a0})}{(h_{g4} - h_{g0}) - (h_{a3} - h_{a0})}$$

r expresses the ratio of the injected water specific enthalpy rise to the enthalpy rise of air in the combustion chamber. For the test case presented in the paper, base load operation, r has a value of about 5.30. a assumes a value close to unity, since the change in compressor exit temperature resulting from water injection is very small, compared to the temperature rise in the combustion chamber. We therefore have

$$\frac{f'}{f} = r w f' + 1 \Rightarrow f' = \frac{f}{1 - r \cdot w \cdot f} \quad (A3.4)$$

This equation has a physical interpretation: In order to have a certain temperature at the exit of the combustion chamber, the fuel/air ratio has to be increased by an amount such that it provides the heat needed to bring the water to the condition of steam at the turbine inlet temperature.

Gas Turbine Output Power. The effect of water injection can be analyzed by studying the gas turbine power balance Eq. (1). The basic mechanics can be revealed by using a simplified form of this equation, given as Eq. (1) in the main text. It expresses the fact that turbine power output is the difference between the energy produced by the turbine and the power absorbed by the compressor. To facilitate further derivations we will put

$$Y_C = \frac{1}{\eta_{cis}} \left(\pi_c^{\frac{\gamma_a - 1}{\gamma_a}} - 1 \right)$$

$$Y_T = \eta_{tis} \left(1 - \frac{1}{\pi_c^{\frac{\gamma_g - 1}{\gamma_g}}} \right) \quad (A4.1)$$

Equation (1) can thus be written:

$$P = \dot{m}_2 C_{pa} T_2 \left[\frac{\dot{m}_4 C_{pg} T_4}{\dot{m}_2 C_{pa} T_2} Y_T - Y_C \right] \quad (A4.2)$$

Considering that power output is a product of two terms, inlet enthalpy flow $\dot{m}_2 C_{pa} T_2$ and P_h , which is power per unit inlet air

enthalpy flow (specific power). For given ambient temperature and turbine inlet temperature, taking logarithms and differentiating, we obtain

$$\frac{\Delta P}{P} = \frac{\Delta \dot{m}_2}{\dot{m}_2} + \frac{\dot{m}_2 C_{pa} T_2}{P} \Delta P_h \quad (A4.3)$$

The second term can be further evaluated as follows:

$$\Delta P_h = \left[\frac{\dot{m}_4 C_{pg} T_4}{\dot{m}_2 C_{pa} T_2} \Delta Y_T - \Delta Y_C \right] + Y_T \cdot \Delta \left(\frac{\dot{m}_4 C_{pg} T_4}{\dot{m}_2 C_{pa} T_2} \right) \quad (A4.4)$$

The term in brackets expresses the rate of change of specific power with pressure ratio, if isentropic efficiencies of compressor and turbine do not change significantly. This term is very small and can be neglected for the following reason: gas turbine designers usually choose the design point of an engine in the “flat” region of the specific power versus pressure ratio curve, as shown in Fig. 11. The form of the curve shown in this figure is typical and the design point usually falls in the area indicated. In this area, the derivative is small and can be taken equal to zero in Eq. (A4.4).

The second term of the right-hand side can be evaluated, when ambient and turbine inlet temperature are constant, by using relations derived previously.

$$\Delta \left(\frac{\dot{m}_4 C_{pg}}{\dot{m}_2 C_{pa}} \right) = \frac{\dot{m}_4 C_{pg}}{\dot{m}_2 C_{pa}} \left(\frac{\Delta \left(\frac{\dot{m}_4}{\dot{m}_2} \right)}{\frac{\dot{m}_4}{\dot{m}_2}} + \frac{\Delta C_{pg}}{C_{pg}} \right)$$

The change of mass flow ratio between combustor inlet and outlet is easily evaluated by just taking into account the mass balance without and with water injection, using Eq. (A2.2), we get

$$\Delta \left(\frac{\dot{m}_4}{\dot{m}_2} \right) / \left(\frac{\dot{m}_4}{\dot{m}_2} \right) = \frac{f' w}{1 + f}$$

Substituting into the previous equation and using Eq. (A1.3) we finally get

$$\Delta \left(\frac{\dot{m}_4 C_{pg}}{\dot{m}_2 C_{pa}} \right) = \frac{\dot{m}_4 C_{pg}}{\dot{m}_2 C_{pa}} \left(\frac{f' w}{1 + f} + f' w \right) \approx 2 \frac{\dot{m}_4 C_{pg}}{\dot{m}_2 C_{pa}} f' w$$

Substituting into Eqs. (A4.4) and (A4.3), Eq. (5) of the main text is derived.

It must be pointed out here that the ratio P_T/P is a design feature of the gas turbine and does not exhibit a significant varia-

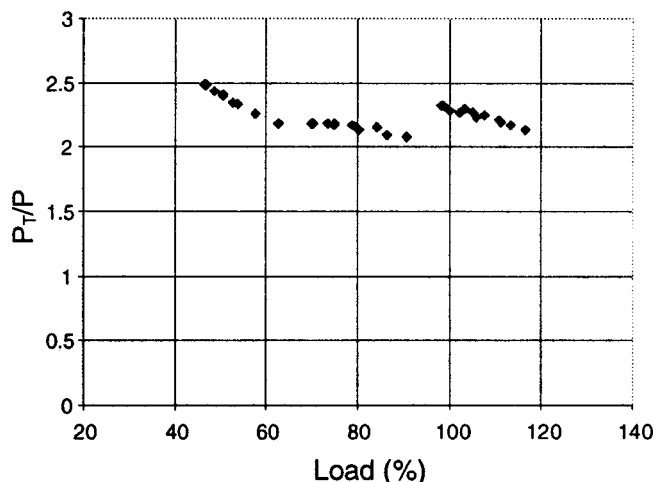


Fig. 12 Variation of the ratio of turbine power to output power, over a range of operating loads

tion over a wide range of operating conditions. This fact can be observed for the gas turbine used in the present tests, from the results shown in Fig. 12. It is observed that this ratio does not significantly change over a large range of operating conditions, while the change is even smaller when operation around a certain load is considered, as, for example, base load.

Nomenclature

b = compressor external air bleed as a fraction of inlet mass flow
 C_p, C_v = specific heat for constant pressure, volume
 EGT = exhaust gas temperature
 f = fuel/air ratio $f = \dot{m}_f / \dot{m}_a$
IGV = inlet guide vane
 K_b = total pressure loss in burner
 \dot{m} = mass flow rate
 P = gas turbine output power
 P_T = power produced by turbine
 P_h = specific power, Eq. (A4.2)
 p = pressure (total)
 q = reduced referred mass flow rate $q = \dot{m} \sqrt{(RT/\gamma)/p}$
 Q_f = Lower heating value of fuel
 r = enthalpy rise of water relative to air, Eq. (A3.3)
 R = gas constant
 T = temperature (total)
TIT = turbine inlet temperature
 w = water/fuel ratio $w = \dot{m}_w / \dot{m}_f$
 Y_C, Y_T = compressor, turbine specific power, Eq. (A4.1)
 γ = isentropic exponent $\gamma = C_p / C_v$
 η_{th} = gas turbine efficiency, Eq. (6)
 η_{Cis} = compressor isentropic efficiency
 η_{Tis} = turbine isentropic efficiency
 π_c = compressor pressure ratio $\pi_c = p_3 / p_2$

Subscripts

' = value changed because of water injection
2,3,4,5 = position along the gas turbine, Fig. 1
 a = quantity related to air
 C = compressor

f = fuel
 g = quantity related to the combustion gases
 s = quantity related to steam
 T = turbine
 w = quantity related to injected water

References

- [1] Shaw, H., 1974, "The Effects of Water, Pressure, and Equivalence Ratio on Nitric Oxide Production in Gas Turbines," *ASME J. Eng. Power*, **96**, pp. 240–246.
- [2] Koch, H., and Felix, P., 1977, "Exhaust Gas Emissions of Brown Boveri Gas Turbines," *Brown Boveri Rev.*, **64**, Jan., pp. 27–33.
- [3] Schetter, B., 1993, "Gas Turbine Combustion and Emission Control," *Combined Cycles for Power Plants*, Von Karman Institute, Lecture Series 1993–08.
- [4] Lefebvre, A. H., 1995, "The Role of Fuel Preparation in Low Emission Combustion," *ASME J. Eng. Gas Turbines Power*, **117**, pp. 617–654.
- [5] Liever, P. A., Smith, C. E., Myers, G. D., Hernandez, L., Griffith, T., 1998, "CFD Assessment of a Wet, Low-NO_x Combustion System for a 3MW-Class Industrial Gas Turbine," *ASME Paper 98-GT-292*.
- [6] Walsh, P. P., and Fletcher, P., 1998, *Gas Turbine Performance*, Blackwell Science Ltd., Oxford, UK.
- [7] Kreitmeyer, F., Fruttschi, H. U., and Vogel, M., 1992, "Economic Evaluation of Methods for Reducing NO_x Emissions of Gas Turbines and Combined Cycle Plants," *ABB Rev.*, **1/92**, pp. 29–36.
- [8] Cloyd, S. T., and Harris, A. J., 1995, "Gas Turbine Performance—New Application and Test Correction Curves," *ASME Paper 95-GT-167*.
- [9] Camporeale, S. M., and Fortunato, B., 2000, Aero-Thermodynamic Simulation of a Double Shaft Industrial Evaporative Gas Turbine, *ASME Paper 2000-GT-0171*.
- [10] Jordal K., and Torisson T., 2000, "Comparison of Gas Turbine Cooling With Dry Air, Humidified Air and Steam," *ASME Paper 2000-GT-0169*.
- [11] ISO 2314, 1989, Gas Turbine Acceptance Tests.
- [12] Mathioudakis, K., Stamatis, A., Tsalavoutas, A., and Aretaks, N., 2000, "Performance Analysis of Industrial Gas Turbines for Engine Condition Monitoring," *Proceedings of Institution of Mechanical Engineers, Part A: Journal of Power and Energy*, **215**, Mar., pp. 173–184.
- [13] Hensley, R. V., 1952, "Theoretical Performance of an Axial-Flow Compressor in a Gas Turbine Engine Operating With Inlet Water Injection," *NACA TN 2673*.
- [14] Gu, Y. G., and Palmer, J. R., 1986, "A Mathematical Model for Computing the Effects of Air Humidity, Fuel Composition and Gas Dissociation on Gas Turbine Performance and Its Application," *ASME Paper 86-GT-114*.
- [15] Bird, J., and Grabe, W., 1991, "Humidity Effects on Gas Turbine Performance," *ASME Paper 91-GT-329*.
- [16] AGARD-AR-332, 1995, "Recommended Practices for the Assessment of the effects of Atmospheric Water Ingestion on the Performance and Operability of Gas Turbines Engines," Sept.

B. E. Lee

Assistant Research Professor
Mem. ASME

S. B. Kwon

Professor

School of Mechanical Engineering,
College of Engineering,
Kyungpook National University,
1370, Sankyuk-Dong, Puk-ku,
Daegu 702-701, South Korea

C. S. Lee

Junior Researcher,
R&D Center, HANJUNG,
Korea Heavy Industries & Construction Co., Ltd.,
P.O. Box 77,
Changwon, 641-792, South Korea

On the Effect of Swirl Flow of Gas Turbine Exhaust Gas in an Inlet Duct of Heat Recovery Steam Generator

Computational and experimental studies are performed to investigate the effect of swirl flow of gas turbine exhaust gas (GTEG) in an inlet duct of a heat recovery steam generator (HRSG). A supplemental-fired HRSG is chosen as the model studied because the uniformity of the GTEG at the inlet plane of the duct burner is essential in such applications. Both velocity and oxygen distributions are investigated at the inlet plane of the duct burner installed in the middle of the HRSG transition duct. Two important parameters, the swirl angle of GTEG and the momentum ratio of additional air to GTEG, are chosen for the investigation of mixing between the two streams. It has been found that a flow correction device (FCD) is essential to provide a uniform gas flow distribution at the inlet plane of the duct burner [DOI: 10.1115/1.1473156]

1 Introduction

One of the important design parameters of the heat recovery steam generator (HRSG) is the flow distribution of the gas turbine exhaust gas (GTEG) at the duct plane immediately upstream of the duct burner for supplemental-fired HRSGs. This is because the possibilities of corrosion and rupture of heat exchange tubes of the HRSG are reduced dramatically as the uniformity of GTEG entering into superheater or duct burner increases. Additionally, a more compact HRSG can be designed if the GTEG is uniform, because the more uniform flow distribution of GTEG, the more precisely the temperature difference between the GTEG and tubes can be determined.

The flow in the HRSG is mainly governed by the swirl angle of the GTEG, the geometry of the HRSG, and the equipment installed within the HRSG, such as flow correction devices (FCD) and tube bundles. Each company manufacturing HRSGs has its own design requirement for the velocity distribution of the GTEG. However, the commonly used one, regardless of the design factors, is a velocity distribution of $\pm 20\%$ of the average freestream velocity over 90% of the duct cross section immediately upstream of duct burner for typical supplemental-fired HRSGs.

The additional ambient air, which contains more oxygen than the GTEG, may be required to provide additional oxygen in a supplemental-fired HRSG to produce higher amounts and temperatures of the steam in the HRSG. It is clear that both oxygen and velocity distributions at the inlet plane of duct burner should be uniform for a more stable reaction. However, it is difficult to find a specific design requirement for the oxygen distribution at the inlet plane of the duct burner. It may be assumed that uniform oxygen distribution can be provided by uniform velocity distribution of the GTEG if the additional air is mixed with the GTEG well. However, every company manufacturing HRSGs has its own additional air duct system. Therefore, the mixing between the GTEG and the additional air should be evaluated for each additional air duct system.

In this paper computational and experimental studies are performed to investigate both velocity and oxygen distributions at the inlet plane of the duct burner for a horizontal type of a supplemental-fired HRSG with a newly designed additional air

duct. The momentum ratio of the additional air to the GTEG, and swirl angle of the GTEG are chosen as major parameters in the present study.

2 Design of an Additional Air Duct System

Basically, an additional air duct system should be designed to promote mixing between the GTEG and the additional air to provide the desired oxygen level at the inlet of the duct burner section. The concepts employed in the design of the new additional air duct system are

1. The additional air duct system should be located at the front of the FCD to provide a more uniform oxygen distribution at the plane immediately upstream of the duct burner. Mixing between the GTEG and the additional air can be increased when the streams pass through the FCD because of strong turbulent fluctuations generated by the FCD.
2. Injection of additional air from opposite sides will help to generate a more uniform side-to-side oxygen distribution.

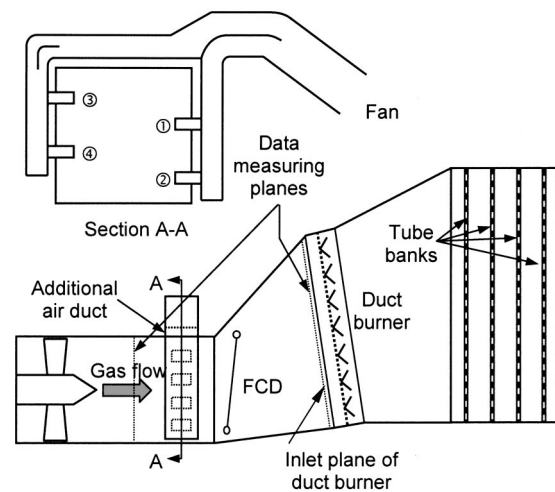


Fig. 1 A schematic diagram of a supplemental-fired heat recovery steam generator

Contributed by the Combustion and Fuels Division of THE AMERICAN SOCIETY OF MECHANICAL ENGINEERS for publication in the ASME JOURNAL OF ENGINEERING FOR GAS TURBINES AND POWER. Manuscript received by the CF Division Dec. 15, 2000; final revision received by the ASME Headquarters Jan. 28, 2001. Associate Editor: P. Malte.

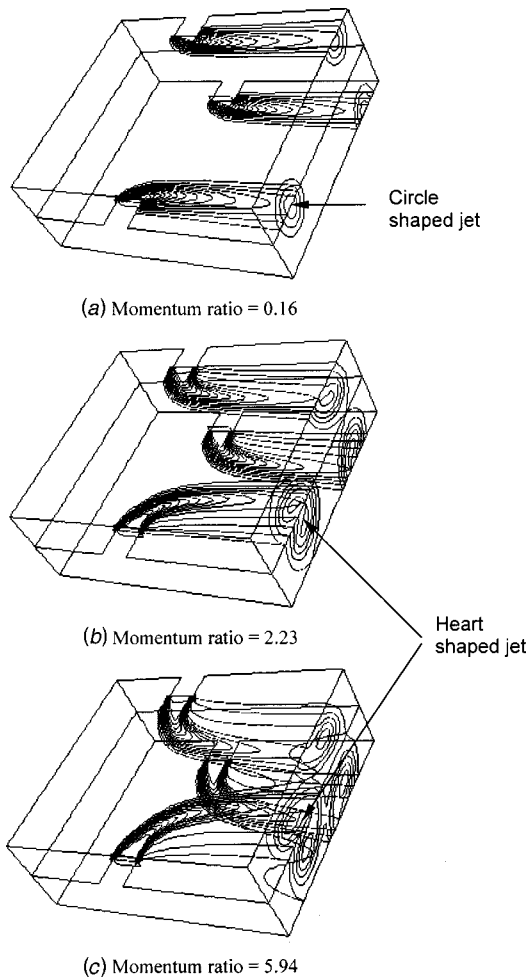


Fig. 2 Investigation of jet shapes with different momentum ratios

3. The injection of the additional air should be equally distributed along the height of the duct to increase the oxygen uniformity from top to bottom of the duct. Therefore, a staggered type of additional duct system is employed in the present study.

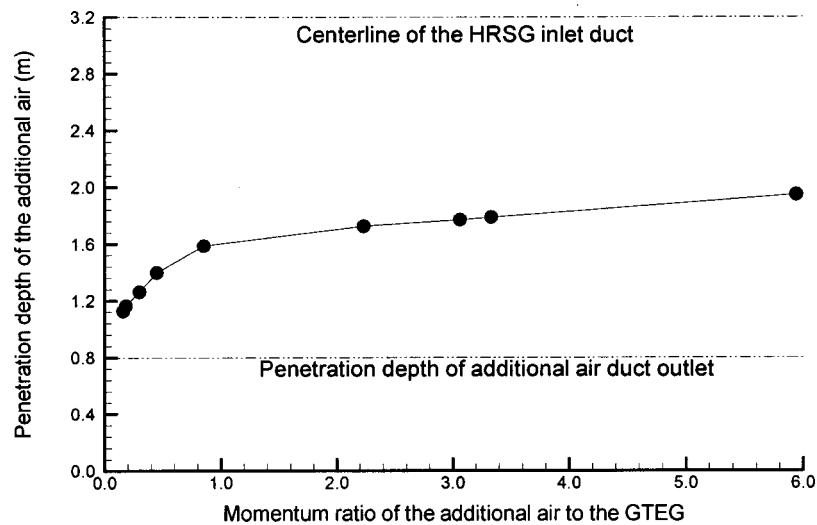


Fig. 3 Penetration depth of additional air into the main stream of gas turbine exhaust gas

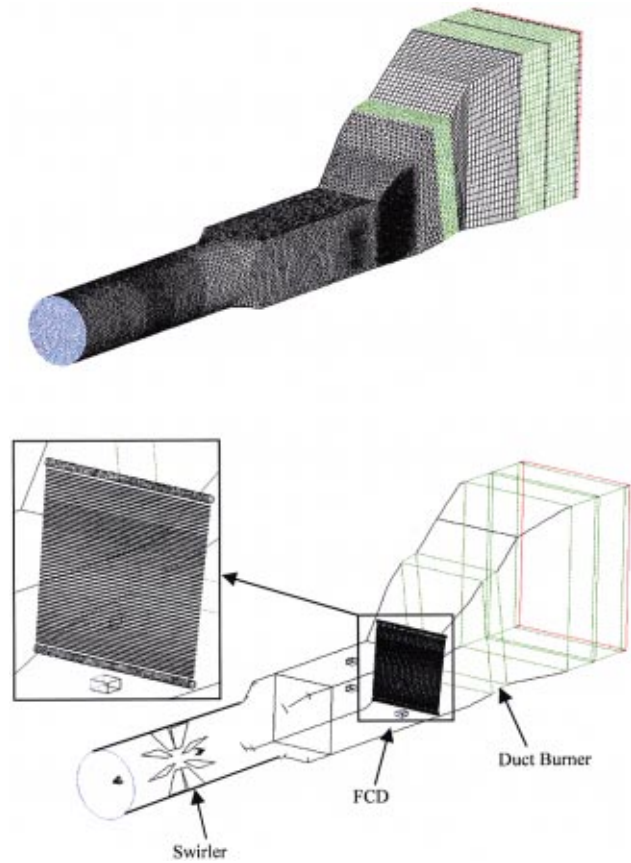


Fig. 4 Computational grid and outline of the heat recovery steam generator

4. The duct system should work well under part load conditions since the swirl angle of the GTEG is a function of gas turbine load.

Figure 1 represents the newly designed additional air duct system, with the concepts described above. In order to obtain the most effective side-to-side oxygen distribution, the penetration depth of additional air into the main stream of the GTEG

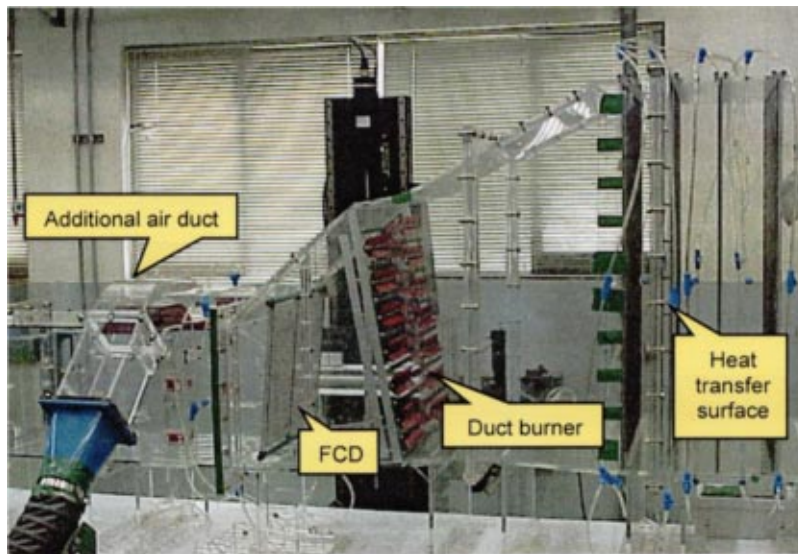


Fig. 5 Heat recovery steam generator air test model

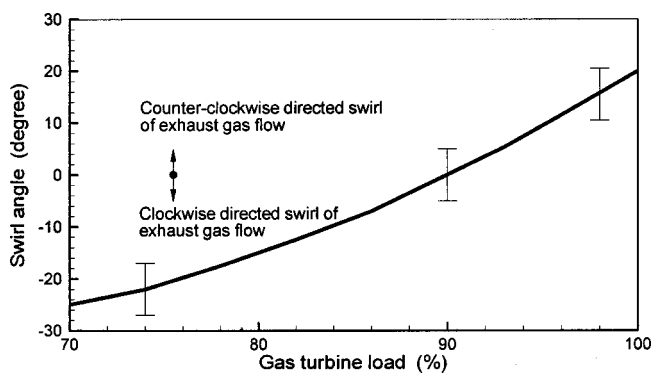


Fig. 6 Change of the swirl angle with gas turbine load (view from downstream)

is investigated using computational fluid dynamics (CFD) simulations. The quadrilateral shape of the additional air duct outlet, having an aspect ratio of 2, is considered in the present study. Figure 2 shows the penetration of the additional air into the main stream of the GTEG for different momentum ratios $((\rho V^2)_{\text{additional air}}/(\rho V^2)_{\text{GTEG}})$ without considering swirl in the GTEG. It is well known that the round type of jet becomes “kidney” type as it is deflected and distorted by the cross flow (Schetz [1]). It has been found in the present study, however, that a quadrilateral type of jet becomes circular when the momentum ratio is less than one, but it becomes “heart” type when the momentum ratio is greater than one.

Figure 3 presents penetration depth of the jet centerline as a function of momentum ratio. The penetration depths are determined 4.6 m downstream from air inlet. It can be seen from this figure that the penetration depth increases with the momentum

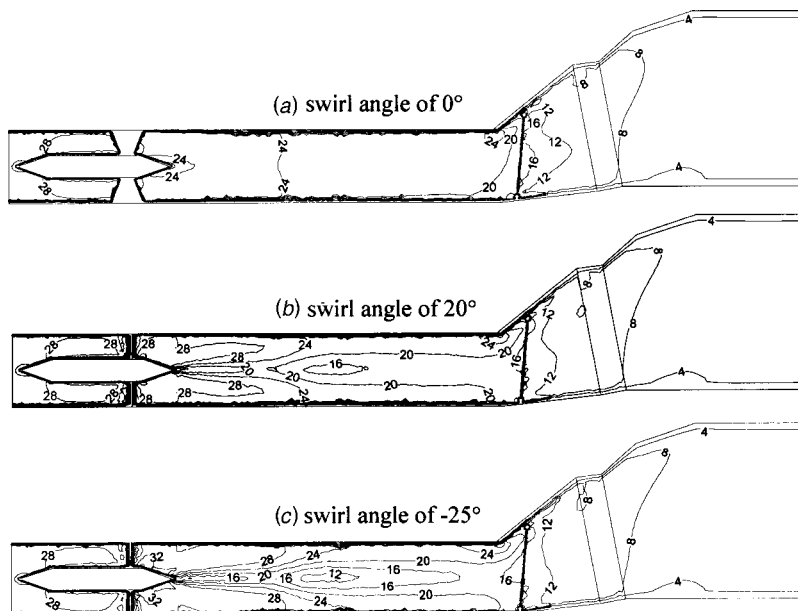


Fig. 7 Velocity magnitude (m) contours at the center plane of the heat recovery steam generator inlet duct

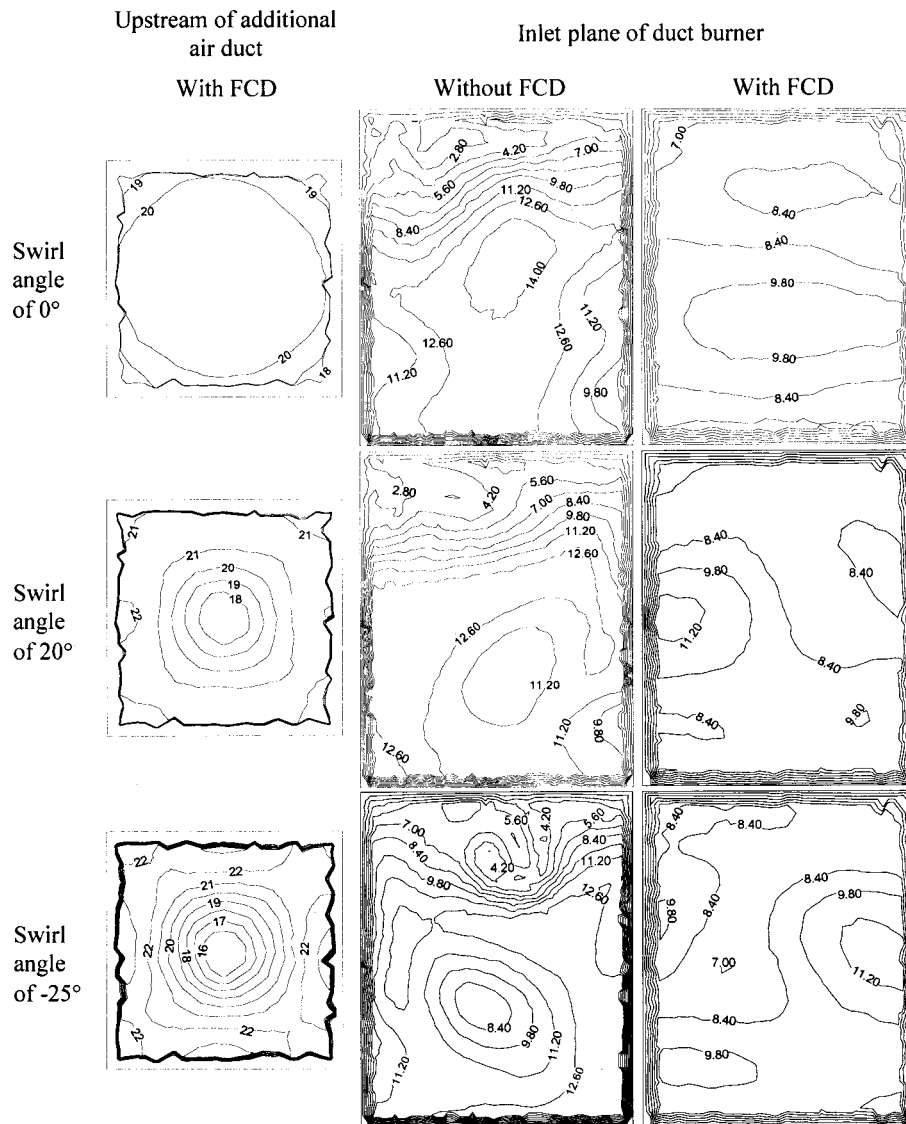


Fig. 8 Velocity magnitude (m) contours

ratio. It is clear from this figure that the penetration depth of the additional air duct into the interior of the HRSG inlet duct should be determined carefully if the plant is to be operated under the wide range of momentum ratio.

3 Computational Study

A commercially available CFD code, FLUENT, is used to investigate the flow behavior in the HRSG. An RNG $k-\varepsilon$ turbulence model is chosen to simulate the gas turbulent fluctuations. It is very difficult to simulate tube banks because the complex geometry requires huge computational memory. Therefore, a porous model (FLUENT Inc. [2]), which can predict the pressure drop with a small number of grid cells, is employed to simulate the tube banks. Two different types of gas are used to investigate the mixing between GTEG and the additional air supplied through the additional air duct. Figure 4 shows the computational grid and the outline of the HRSG. The number of grid cells is around 860,000.

4 Experimental Study

A 1/20th scale air test model (see Fig. 5) has been constructed to investigate flow behavior in the inlet duct of the HRSG. The

gas turbine exhaust diffuser and turning vanes, which can produce swirl flows, have both been included in the test model to simulate the flow of a prototype as closely as possible. Both the FCD and the duct burner are directly scaled down. Tube banks are replaced by perforated plates having the same pressure drop coefficients. The stack of the HRSG is not included in the test model because the flow upstream of the superheater is not affected greatly after the last tube bank. Two wind tunnels have been used for the supply of the GTEG and additional air. Ambient air has been used instead of GTEG.

A five-hole pitot probe and a PSI 8400 pressure system with 32-channel pressure scanner are used to measure the velocity distributions at the inlet plane of duct burner. A smoke tracer is used to study mixing between the GTEG and fresh air supplied through the additional air duct. The smoke generator is used to produce particles having a particle size range of 0.7–1.2 μm and a mean diameter of 0.9 μm . The source material of the smoke is glycerin which has a density of 1252 kg/m^3 . It is well known that small water droplets having particle size less than 3 μm can be used to determine gas velocity (Crowe [3] and Rudoff et al. [4]). This is because particles having very small Stokes' number follow gas streamline well. The particle concentration is determined by num-

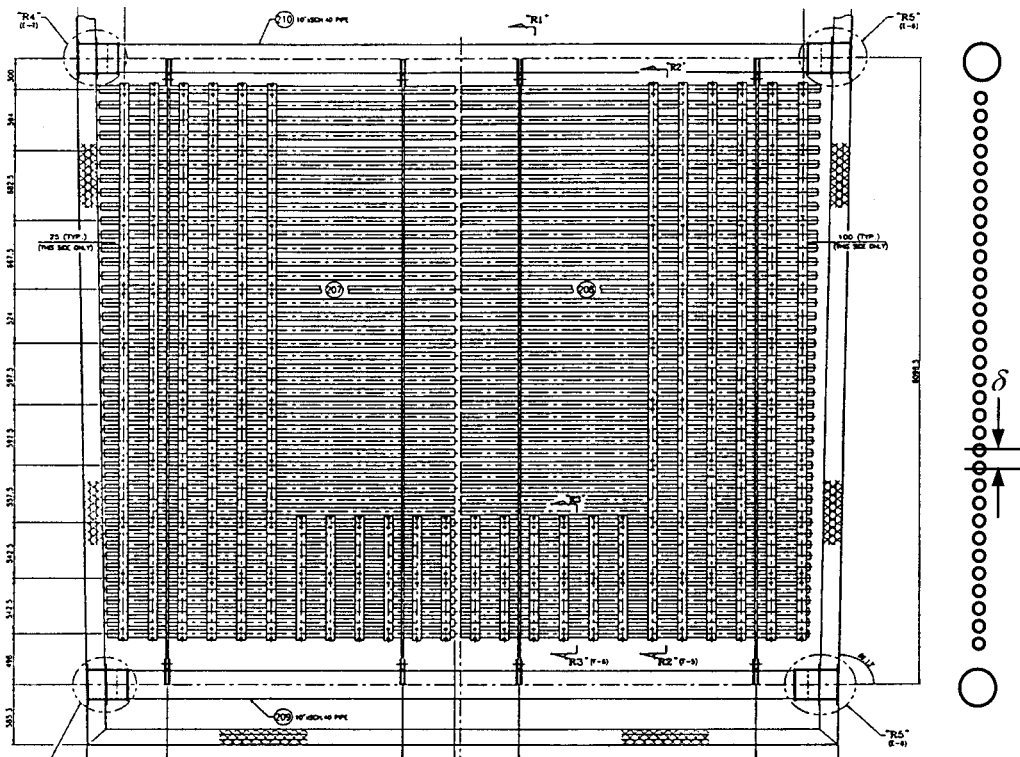


Fig. 9 A typical flow correction device

ber density. The number of particles is measured by using an Aerosizer LD (Amherst Process Instruments, Range of 0.2 to 700 μm).

5 Discussion of Test Results

The swirl angle of the GTEG is chosen as a major parameter to be studied for the investigation of both flow and mixing between the GTEG and the additional air within the inlet duct of the HRSG. This is because the gas turbine will be operated under wide conditions with different swirl angles of the GTEG, as shown in Fig. 6. The velocity of 20 m/sec, corresponding to the Reynolds number of 4.2×10^5 , is used as the inlet axial velocity of the main stream. This Reynolds number is much lower than that of the prototype. However, it is assumed that the physical model will produce gas flow profiles which represent those found in the prototype, as long as a Reynolds number greater than 10,000 is used. In this case, the model and actual HRSG are both operating in the fully turbulent gas flow regime.

GTEG swirl angles of -25° , 0° , and 20° deg corresponding to gas turbine loads of 70, 90, and 100%, respectively (see Fig. 6), are chosen to investigate flow and mixing. Figure 7 represents velocity magnitude at the center plane of the inlet duct of the HRSG. It can be seen from this figure that the velocity magnitude at the center of the duct decreases as the swirl angle increases because of the centrifugal force. Figure 8 also gives the velocity magnitude at cross sections just upstream from the additional air duct and at the inlet plane of the duct burner, as indicated in Fig. 1. It can be seen from this figure that the swirl angle affects velocity distribution significantly, if the FCD is not installed.

Basically, the role of the FCD is to provide a uniform flow before the GTEG enters into the duct burner in a supplemental-fired HRSG. A conventional type of FCD composed of many pipes, shown in Fig. 9, is employed in the present study. The most uniform flow distribution at the inlet plane of duct burner can be obtained by adjustment of distances between two adjacent pipes, δ (see Fig. 9). In general, better flow distribution can be obtained by more dense distribution of pipes at the bottom region of the

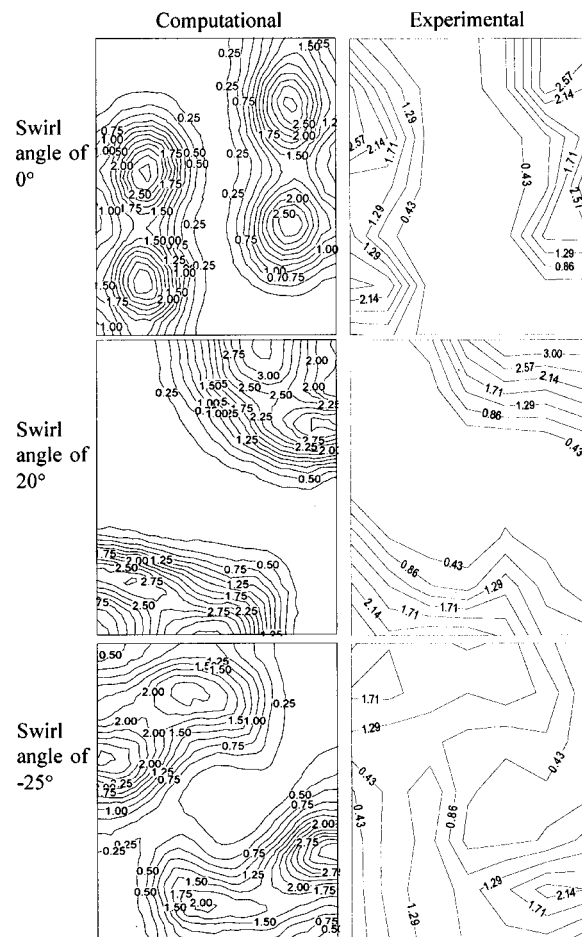


Fig. 10 Normalized oxygen concentration at the inlet plane of the duct burner

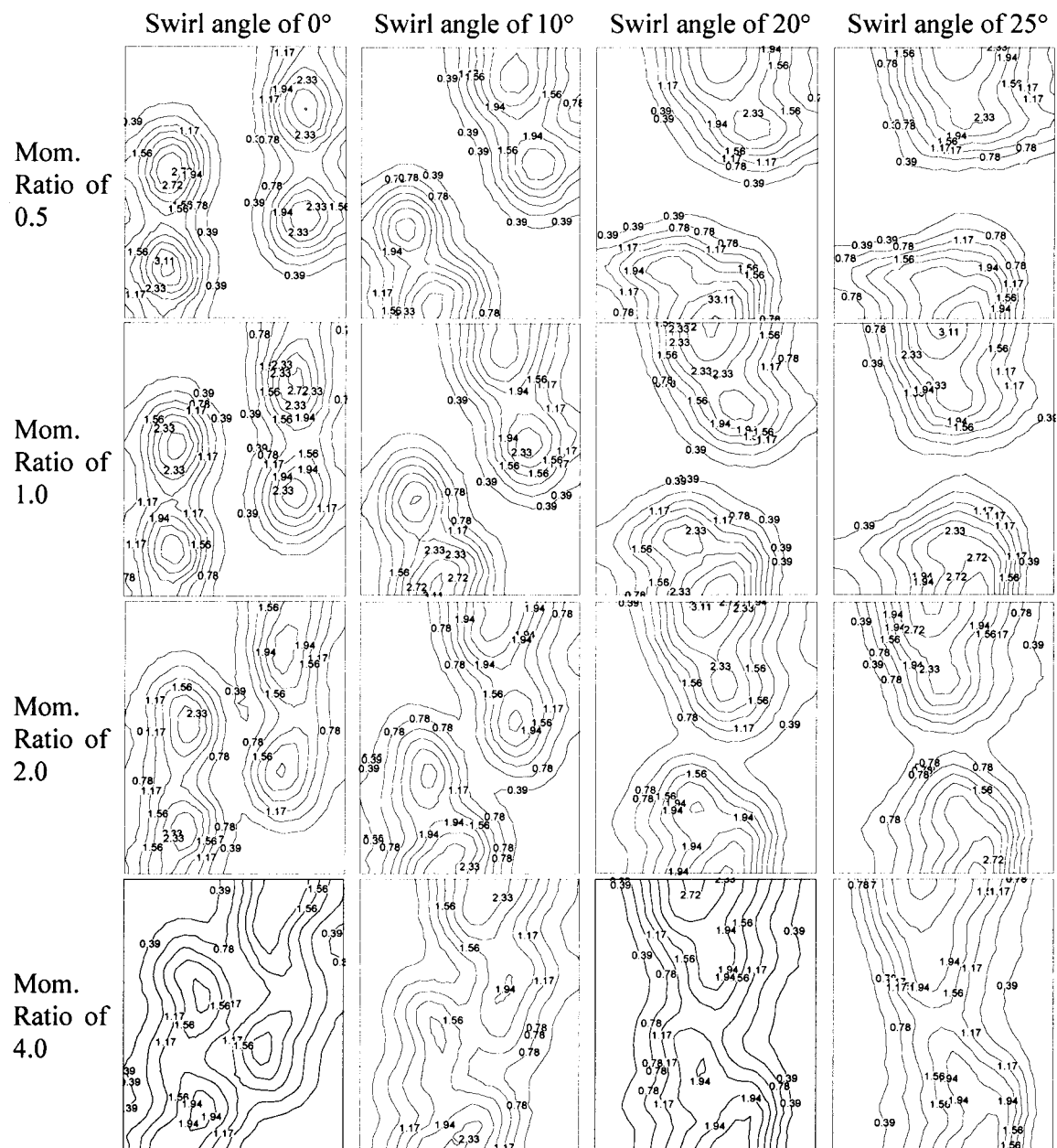


Fig. 11 Computationally predicted normalized oxygen concentration at the inlet plane of the duct burner

HRSR than at the top. However, the maximum number of pipes is restricted because the pressure drop through the FCD should be less than the value given in the design requirement. It can be seen from Fig. 8 that uniformity of the GTEG at the inlet plane of the duct burner is enhanced significantly and the effect of swirl angle of the GTEG almost removed when the FCD is employed.

The oxygen distribution at the inlet plane of the duct burner is one of the most important design parameters because stable reaction at the duct burner can be provided by the uniform oxygen concentration. Normally, ambient air having much higher content of oxygen than the GTEG is used as additional air. Therefore, the additional air and GTEG should be mixed very well before approaching the duct burner to produce uniform flame length, thereby avoiding tube failures caused by local overheating.

In order to investigate the mixing between the GTEG and the additional air at the inlet plane of duct burner, the experimental data are gathered at 49 points, 7 points in the horizontal direction and 7 points in the vertical direction. The oxygen distribution determined by aerosol particle number density is normalized

against the mean value. Figure 10 gives normalized oxygen concentration, supplied through only the additional air duct, simulated by the computational work and measured in the experimental work. The three cases shown represent the practical operating conditions of a plant. It can be seen from this figure that the computational simulations show good agreement with experimental data.

The effect of momentum ratio on the mixing is investigated both computationally and experimentally. Computationally simulated oxygen distributions are given in Fig. 11. Experimental results are not given because those are almost the same as the computational simulations. Two important features can be found in Fig. 11. The first one is that the mixing effect is improved under the same swirl angle as the momentum ratio increases. The second one is that the two additional air streams injected from the same sides of the HRSR inlet duct are unified quicker as the momentum ratio increases. However, the mixing quality is not significantly deteriorated by the unification of the two streams injected at the

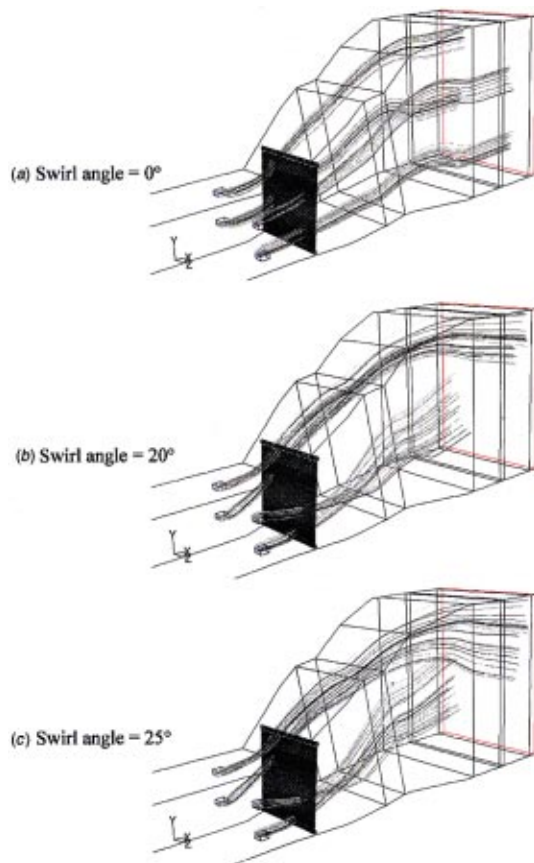


Fig. 12 Path line of additional air

same sides. Figure 12 gives path lines predicted by the computational method and shows the unification of the two streams injected from same sides of HRSG inlet duct.

6 Conclusions

The velocity distribution and mixing between the GTEG and the additional air at the inlet plane of duct burner are studied to evaluate the performance of a newly designed additional air duct for a supplemental-fired HRSG. Two parameters, the GTEG swirl angle and momentum ratio (additional air to GTEG), are studied. From the present study, the following conclusions can be drawn:

1. The uniformity of the velocity at the inlet plane of duct burner is not affected by the intensity of swirl of the GTEG, if the FCD is installed in the middle of transition duct of HRSG. However, this is not true when the FCD is not installed.
2. The mixing between the GTEG and the additional air is improved under the same swirl angle as the momentum ratio increases.
3. The two additional air streams injected from the same sides of the HRSG inlet duct are unified quicker as the momentum ratio increases. However, the mixing quality is not significantly deteriorated by the unification of the two streams injected on the same sides.

It should be mentioned that the conclusions obtained in the present study may be valid only when the FCD and additional air duct system discussed here are employed.

References

- [1] Schetz, J. A., 1980, "Injection and Mixing in Turbulent Flow," Vol. 68 *Progress in Astronautics and Aeronautics*, 68, AIAA, Washington, DC.
- [2] FLUENT Inc., 1998, *FLUENT 5 User's Guide*, pp. 6-103-121.
- [3] Crowe, C. T., 1993, "Modeling Turbulence in Multiphase Flows," *Engineering Turbulence Modeling and Experiments*, 2, Elsevier, New York.
- [4] Rudoff, R. C., Kamemoto, D. Y., and Bachalo, W. D. 1991, "Effects of Turbulence and Number Density on the Drag Coefficient of Droplets," AIAA Paper 91-0074.

Analysis Strategies for Tubular Solid Oxide Fuel Cell Based Hybrid Systems

A. D. Rao

G. S. Samuelsen

National Fuel Cell Research Center,
University of California,
Irvine, CA 92697

The emergence of fuel cell systems and hybrid fuel cell systems requires the evolution of analysis strategies for evaluating thermodynamic performance and directing design and development. A description and application of the recently developed tool for analyzing tubular SOFC based systems is presented. The capabilities of this tool include an analytical model for the tubular SOFC derived from first principles and the secondary equipment required to analyze hybrid power plants. Examples of such secondary equipment are gas turbine, reformer, partial oxidation reactor, shift reactor, humidifier, steam turbines, compressor, gas expander, heat exchanger, and pump. A "controller" is included which is essential for modeling systems to automatically iterate in order to meet the desired process or system design criteria. Another important capability that is included is to be able to arrange the various components or modules as defined by the user in order to configure different hybrid systems. Analysis of the hybrid cycle as originally proposed by Westinghouse (SureCell™) indicates that the thermal efficiency of the cycle is quite insensitive to the pressure ratio, increasing from 65.5 percent to 66.6 percent on a lower calorific value of the fuel as the pressure ratio decreases from 15 to 6.5. [DOI: 10.1115/1.1413462]

Introduction

Due to the projected increases in fossil fuel usage world wide, the greenhouse gas emissions of CO₂ to the atmosphere are expected to increase by about 60 percent by 2015 over the 1990 level. The CO₂ generated from a given fuel per unit of power produced is inversely proportional to the thermal efficiency of a power plant, assuming complete utilization of the fuel. In addition to CO₂, pollutants such as oxides of sulfur, oxides of nitrogen, and unburned hydrocarbons are introduced into the atmosphere when combustion is used to harness the chemically bound energy of the fuel. The amount of pollutants emitted to the atmosphere which depend on the degree of pollution abatement measures incorporated, typically increase the plant operating and capital costs. Thus, a need exists to develop energy efficient means of power generation while minimizing the environmental impact; fuel cells hold this promise.

Furthermore, distributed power generation which is gaining much attention from industry could be a niche market for fuels cells if configurations can be identified that are simple so that the plant capital cost and the process controllability are not compromised.

A fuel cell, as an electrochemical device is similar to a battery that converts chemically bound energy directly into electricity but unlike conventional batteries, the chemical energy to the cell is supplied on a continuous basis in the form of a fuel such as natural gas or synthesis gas while the oxidant (air) is also supplied continuously. Higher conversion efficiencies are achievable with a fuel cell when compared to heat engines since the fuel cell is not constrained by the Carnot cycle efficiency. In a fuel cell, where the chemical energy is directly converted into electricity, the intermediate step of conversion into heat as in a heat engine is eliminated. In a fuel cell, there are some heat effects that do limit the conversion of the fuel bound energy to electricity. These heat effects are due to

- 1 heating of the reactants to the reaction temperature and cooling of the products from the reaction temperature
- 2 the entropy change of the reaction
- 3 irreversibilities in the cell due to cell polarizations.

A schematic representation of a tubular SOFC stack is depicted in Fig. 1 while Fig. 2 shows the cross section of a tube. The oxidant is preheated in the central injector tube and then enters the annular section between the cathode layer and the injector tube while the fuel flows over the outer anode layer. Note that in the current design, the support tube depicted in Fig. 2 has been eliminated by Seimens-Westinghouse.

The electrochemical reactions occurring within the cell for H₂ as the fuel are

at the cathode: $\frac{1}{2}\text{O}_2 + 2\text{e}^- = \text{O}^-$

at the anode: $\text{H}_2 + \text{O}^- = \text{H}_2\text{O} + 2\text{e}^-$

with the overall cell reaction: $\frac{1}{2}\text{O}_2 + \text{H}_2 = \text{H}_2\text{O}$.

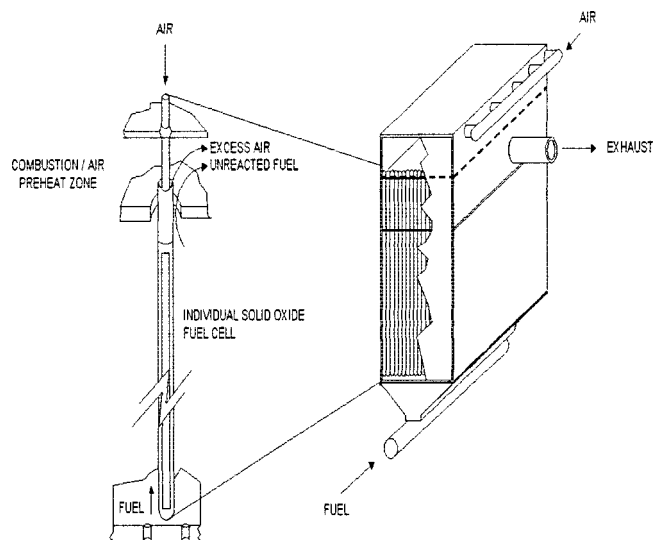


Fig. 1 Schematic representation of tubular SOFC stack ([2])

Contributed by the International Gas Turbine Institute (IGTI) of THE AMERICAN SOCIETY OF MECHANICAL ENGINEERS for publication in the ASME JOURNAL OF ENGINEERING FOR GAS TURBINES AND POWER. Paper presented at the International Gas Turbine and Aeroengine Congress and Exhibition, Munich, Germany, May 8–11, 2000; Paper 00-GT-553. Manuscript received by IGTI, Nov. 1999; final revision received by ASME Headquarters, Feb. 2000. Associate Editor: D. Wisler.

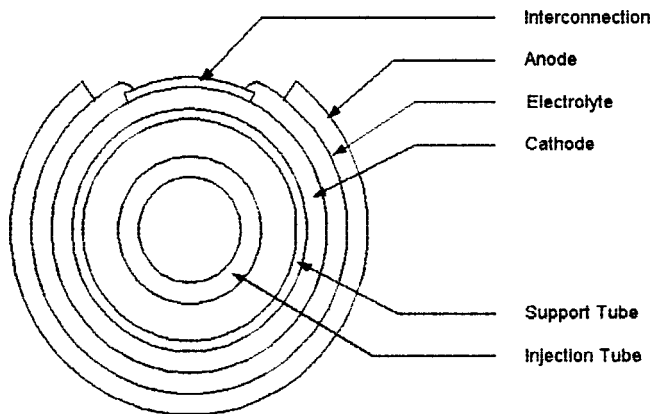


Fig. 2 Cross section of an individual cell ([1])

CO and hydrocarbons such as CH_4 can also be used as fuels in a SOFC. At the high temperatures within the cell, it is feasible for the following reactions to occur:

- 1 the water gas shift reaction: $\text{CO} + \text{H}_2\text{O} = \text{H}_2 + \text{CO}_2$
- 2 and the steam reforming reaction: $\text{CH}_4 + \text{H}_2\text{O} = 3\text{H}_2 + \text{CO}$ (in the case of natural gas and in the presence of a suitable catalyst).

The H_2 thus produced is easily oxidized at the anode. The direct oxidation of CO in fuel cells is well established while the direct oxidation of CH_4 has been investigated to a limited extent ([1]). The direct oxidation of CO and CH_4 occurs only at very low steam to carbon ratios. Potential for carbon formation, however, exists at the low steam to carbon ratios. Any sulfur compounds present in the fuel have to be removed prior to use in the cell to a concentration of <0.1 ppmV to avoid poisoning of the (conventional) reformer catalyst.

Solid Oxide Fuel Cell (SOFC) Hybrid Systems

A fuel-cell-based hybrid cycle consists of combining a fuel cell with a heat engine to maximize the overall system efficiency. One example of such a Hybrid cycle is the SureCell™ system as proposed by Westinghouse and depicted in Fig. 3 ([2]).

The cycle utilizes an intercooled compressor while the discharge air after preheating against the turbine exhaust is provided to the SOFC as its oxidant. Fuel is also preheated in the turbine exhaust, desulfurized, and then supplied to the SOFC as well as the gas turbine combustor(s). The exhaust from the SOFC is supplied to the high-pressure combustor of the gas turbine where additional fuel may be added and combusted by the SOFC exhaust. The exhaust from the combustor enters the high-pressure expander where it is expanded to a pressure that is higher than atmospheric and then supplied to a second combustor where additional fuel is fired. The hot exhaust from the second (low pressure) combustor is then expanded in the low-pressure expander to near atmospheric pressure and then supplied to the heat recovery unit. The power developed by the high pressure and the low-pressure expanders drives the compressors and the electric generator, respectively.

Existing Analysis Tools

Existing computer-based models for analysis of systems such as power cycles may be divided into two types (1) those developed for simulating chemical process plants (e.g., commercially available Hysis, Aspen, Pro II) and (2) those developed for simulating power plants (e.g., commercially available ThermoFlex and GATE/Cycle). Models in the first category have the capability for predicting the thermodynamic properties of nonideal systems but do not include detailed models for power cycle equipment such as gas turbines and fuel cells. The models in the second category have the capability of modeling gas and steam turbines in detail but not fuel cells nor the capability of predicting the properties of nonideal gases except for pure steam. Thus these models, for ex-

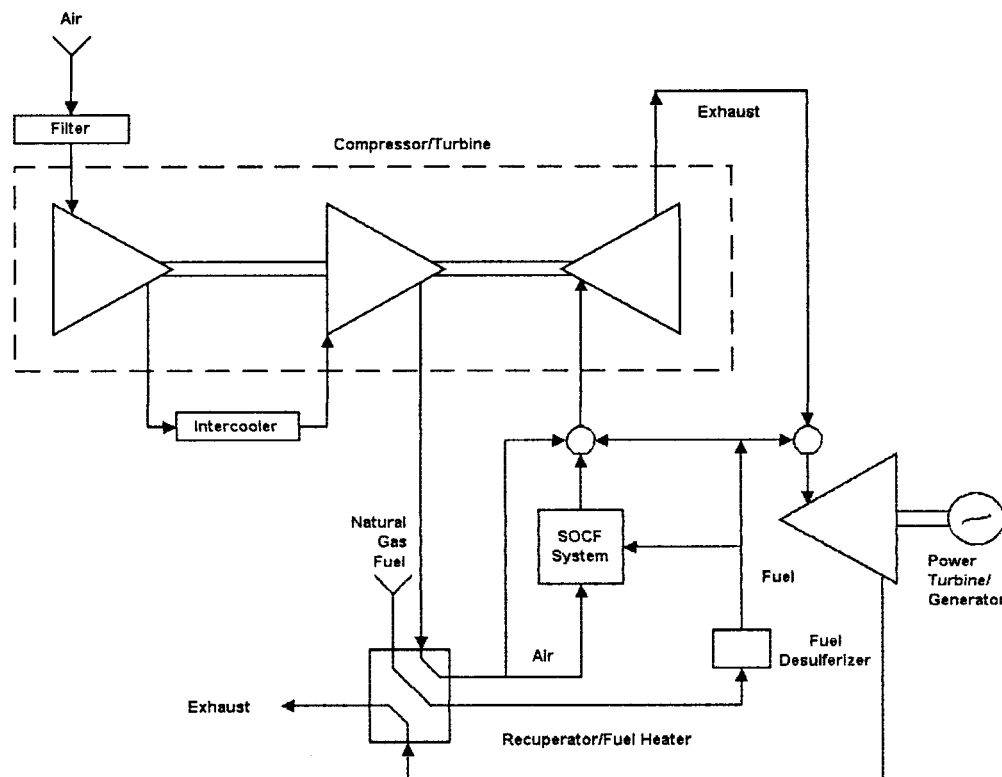


Fig. 3 SureCell™ system as proposed by Westinghouse ([2])

ample, cannot predict the Joule-Thompson cooling of natural gas when its pressure is reduced from typical pipeline pressure (50 bar) to the pressure required by a heavy frame gas turbine which typically operates at a pressure ratio in the neighborhood of 15. Furthermore, with greenhouse gas emissions becoming a more global concern, the proposed recovery and compression of the carbon dioxide to supercritical pressure is becoming a typical specification for disposal in many advanced cycle investigations, requiring the capability of predicting the nonideal behavior of carbon dioxide.

Models in the second category do not include modules for simulating reactors such as a shift reactor in cases where CO₂ removal and capture or production of H₂ for a PAFC or PEMFC is required. Simplified models are included for countercurrent multistage humidification which is being incorporated into advanced Brayton type of power cycles consisting of evaporating water into the working fluid, and for partial oxidation reactor which is utilized to convert a fuel such as coal or heavy fuel oil into synthesis gas suitable as fuel to a fuel cell.

Models for simulating fuel cell based plants have been developed by Ferguson [3], Haynes [4], and Bessette [5] but these models are limited either to systems consisting of ideal gases and pure steam or the models required for simulating many of the unit operations and processes that could make up a hybrid plant are not included such as a detailed gas turbine, a countercurrent multistage humidifier, a shift reactor, and a partial oxidation reactor.

In summary, the requirements for the analysis tools for the evaluation of SOFC fuel cell systems and SOFC hybrid systems performance are

- an SOFC model that accounts for the heat and mass transfer processes occurring within the cell as well as the electrochemistry such that the calculated performance reflects the particular system design conditions such as fuel composition, operating pressure, fuel utilization and geometric parameters such as tube dimensions.
- a gas turbine model that accounts for the changes in the cycle design conditions such as the operating pressure, turbine firing temperature, the fuel and oxidant temperature and composition. The gas turbine model must adjust the required turbine cooling flows or the firing temperature to correspond to changes in the temperature or composition of the working fluid or coolant based on the effective technology parameters that may be estimated from the gas turbine manufacturer's published data, in order to stay within the constraints of the maximum blade metal temperature.
- a humidifier model that accounts for the simultaneous heat and mass transfer rate-controlled processes.
- an equation of state capable of estimating the enthalpy and entropy corrections for nonideality of the gas streams is required in order to handle highly nonideal streams such as natural gas at pipeline pressures, and supercritical CO₂. A separate property package for steam and water is required (consistent with the ASME steam tables) including correction for the enthalpy of water due to pressure above its saturation pressure.

Thus a need exists for an analysis tool for evaluating tubular SOFC hybrid systems; the following describes the tool that was recently developed for such applications.

Analytical and Computational Strategy

Thermodynamic Property Basis. The Peng-Robinson equation of state ([6]) which is a modification of the van der Waal's equation is utilized to predict the deviations from nonideality of the specific volume, enthalpy and entropy of gases. Empirical correlations developed by Schnackel [7] are used for predicting the specific volume, enthalpy and entropy of pure steam. The properties of saturated water are predicted by empirical equations fitted to the ASME published data.

Tubular SOFC Model. An integral model for the heat and mass transfer and the electrochemical processes occurring in the various sections of the cell is developed although the model equations may be applied for zonal analysis of the SOFC when heat flux by conduction in the axial direction may be considered constant and interzonal radiation may be neglected. The integral model minimizes the computational time required to solve the SOFC module and thus the total time required by the computer to solve the entire hybrid plant. Note that a hybrid plant typically includes a number of other equipment modules and furthermore, a number of iterations have to typically occur not only within a module but also between the modules in order to arrive at a converged solution with all the user defined system design parameters satisfied.

The differential equations governing the various processes for a single cell are formulated and simplifying assumptions are made in order to solve these equations analytically. The resulting solutions to these equations are coded into the module. The net AC power output from the stack is estimated by applying an empirical factor to the product of the DC power generated by a single cell and the total number of cells calculated.

Heat Generation. The maximum power that may be developed by the cell is given by the Gibbs free energy change for the oxidation reaction of the fuel. However, the irreversibilities within the cell limit the conversion to useful work. The irreversibilities consist of concentration polarizations caused by a build up of reactants or products at the electrodes, activation polarizations that are caused by the sluggishness of the electrochemical reaction speeds and ohmic losses. The voltage drops due to each of these irreversibilities are taken into account. In addition to the heat generated by these irreversibilities, the cell generates heat on a net basis due to the entropy change of the overall H₂ oxidation reaction.

Solution Strategy. The solution strategy consists of starting the calculations at one end of the cell where the oxidant leaves the injector tube and enters the annular space between the cathode and the injector tube. For a given set of temperatures for the oxidant and the fuel at this cross section (boundary condition), a temperature drop for the air inside the preheat tube and the ratio of actual current flow to the limiting current flow are assumed. The heat and mass transfer equations are solved from section to section in the radial direction. Each of the heat generation terms due to the irreversibilities and the entropy change is utilized. The net DC electric power generated is calculated by subtracting the total heat generated due to the irreversibilities and those due to entropy change, from the overall enthalpy change for the oxidation reaction of the fuel with molecular oxygen. Next, an energy balance is made and the assumed temperature drop of the air inside the preheat tube is adjusted accordingly. Thus a solution is arrived at iteratively and the resulting voltage is calculated from the power produced and the current flow. Iterations are continued if the voltage calculated does not match the desired voltage by adjusting the ratio of actual current flow to the limiting current flow and repeating the entire iterative process defined above.

Compressor and Turbine Models. The outlet conditions from a compressor and expander (including a steam turbine) are calculated assuming an isentropic path and then applying the appropriate efficiency to determine the actual outlet conditions for a given inlet set of conditions. The efficiency is either user defined or is calculated by the computer program using empirical relationships ([8]) in the case of a compressor, while empirical correlations developed by Spencer et al. [9] for each of the sections (high pressure, intermediate pressure, and condensing) may be utilized for the steam turbine, depending on its size.

Gas Turbine Model. Two types of gas turbine models are developed, one that may be configured by the user to include multiple compression stages with intercooling between the stages

and multiple expansion stages with reheat (with combustors) between the stages, and the second consisting of a simple cycle (or conventional Brayton cycle) with no intercooling of the compressor or reheat during expansion.

The user defined gas turbine model is configured by utilizing a gas turbine compressor, combustor and gas turbine expander modules. The efficiency of the compressor and expander and the air required for cooling the blades of the turbine as well as its purge air requirements are determined by first calibrating a simple cycle engine based on data published by the gas turbine manufacturer, and then applying adjustments to the values determined for the "base line engine." The program estimates the necessary parameters for the base line engine and the adjusted values for use with the two gas turbine models when the manufacturer's overall gas turbine performance data is inputted.

The compressor and expander efficiencies are adjusted for flow through the compressor or expander. The turbine coolant requirement is adjusted in order to maintain the same metal temperature for the first stage blades of the turbine by utilizing the semi-empirical methodology proposed by El-Masri and Pourkey [10] which consists of modeling a combined convective/film cooled blade as a flat plate and developing nondimensional parameters relating the physical properties of the working fluid and the coolant. The turbine purge requirement is adjusted by maintaining the same velocity as that in the base line engine.

The second model, consisting of the simple cycle gas turbine, assumes that the gas turbine has the same geometry as the gas turbine used for calibrating the engine. The model makes adjustments to the compressor and expander efficiencies as well as the firing temperature and pressure ratio of the gas turbine for variations of flow rates and composition. The pressure ratio adjustment is based on the assumption that the Mach number for the flow in the first stage nozzle of the turbine is at unity ([11]). The firing temperature is adjusted in order to maintain the same metal temperature of the first stage blades as that for the base-line engine since the turbine cooling flows are not controlled.

Humidifier. The humidification column is divided into differential diffusional units= $k_x a dV/L$ [12] where k_x is the mass transfer coefficient on a mass basis, a is the interfacial area for mass transfer per unit volume, dV is a volume element for mass and heat transfer of differential thickness in the axial direction of the column per unit cross-sectional area, and L is the superficial liquid mass velocity (mass flow rate per unit cross-sectional area).

The heat and mass transfer differential equations for change in temperature of the liquid flowing down the column by gravity and the change in temperature of the gas flowing up the column counter-currently to the liquid are determined. A term was introduced to account for the heat transfer due to the sensible heat of the water vapor diffusing into the gas phase which was not included by previous authors. The Lewis analogy is invoked in deriving these equations and it is assumed that the gas and water flow through the humidifier column under plug-flow conditions.

Reactor Models. Models for the following reactors are included:

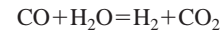
1. shift,
2. reformer, and
3. partial oxidation.

The reactor modules calculate the effluent composition and conditions for a given set of design parameters such as the feed composition and conditions of pressure and temperature, pressure drop through the reactor, and the outlet temperature in the case of an adiabatic reactor, and the required heat transfer rate in the case of a nonadiabatic reactor for a desired outlet temperature.

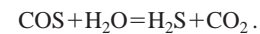
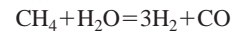
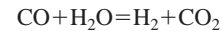
These calculations are made by solving a set of simultaneous

equations consisting of the elemental balances, energy balance, and the reaction quotients, which represent the approach to equilibrium at the outlet conditions of the reactor.

The thermodynamically independent reactions are for shift reactor:



for reformer and partial oxidation reactors:



Balance of Plant Equipment Models. The balance of plant equipment such as a valve, stream mixer, stream splitter, or divider and separator (of a single component from a stream or liquid water from gas/vapor phase) are modeled for an isenthalpic path. Two types of heat exchangers are available, one in which the outlet temperature may be specified to calculate the heat transfer rate, and the other where the heat transfer rate is specified to calculate the outlet temperature. For a pump, the power required is determined assuming the fluid is incompressible. A pipe module is also included to serve the important function of accounting for pressure and heat losses between the equipment in order to calculate the cycle performance more accurately.

Integrated Architecture. The system model or cycle is configured by identifying the desired equipment models and assigning numbers for the streams entering or leaving each of the equipment. The plant may be configured with multiple units of the same type of equipment. Each of the streams entering the plant such as fuel, water, and air is defined by its composition, flow rate, temperature, and pressure while the model predicts all the intermediate streams within the system and the streams leaving the system.

A special module, "controller" is included to define the special design parameters within the system. For example, in order to set the steam-to-carbon ratio in the stream entering the reformer at a predetermined value in order to avoid carbon deposition on the catalyst, the controller is included in the system definition to check if this ratio is being satisfied, as well as to make necessary changes in order to satisfy the design criteria. The controlled variable (dependent variable) and the controlling variable (independent variable) which has to be changed by the controller in order to meet a desired design criterion are identified. The type of variable (temperature, pressure, flow rate, steam-to-carbon ratio, etc.) and the stream or equipment containing these variables are also identified for the controller. The controller then forces the program to iterate while adjusting the controlling variable till the desired result is achieved. The controller may be used multiple times for defining different system design parameters.

In summary, the steps involved in developing the overall system performance are

- 1 a system model or cycle is configured by identifying desired equipment (graphical interface is currently not available).
- 2 assigning numbers for streams entering or leaving each equipment.
- 3 defining streams entering a system such as fuel, water, and air by specifying composition, flow rate, temperature, and pressure.
- 4 the "controller" is included to define cycle design parameters/targets within the system.
- 5 the model predicts intermediate streams within the system, streams leaving the system, power consumption (of pumps, compressors), power generation (of SOFC, gas turbine, turbo-expander), heat transferred in each of the heat exchangers.

The model also predicts the size of the SOFC (number of tubes for a specified tube diameter and length) and dimensions of the humidifier column (diameter and packed height). In this manner, systems may be identified that utilize these equipment having practical or realistic sizes.

Results and Discussions

A comparison of performance predictions made by the SOFC model (shown as discrete points) with curves published by Westinghouse ([13]) is presented graphically in Fig. 4. The bottom curve corresponds to an operating pressure of 1 atm while the top curve corresponds to an operating pressure of 10 atm. The tube length is 150 cm with 2.2 cm outside diameter. The fuel consists of a mixture of 89 mole percent hydrogen and 11 mole percent water vapor. Fuel utilization is held constant at 85 percent. The air used in the SOFC is six times the stoichiometric requirement.

As can be seen, the predictions made by the model are in agreement with the Westinghouse values. The curves are characteristic of fuel cells, where the power initially increases as the current also increases (since the oxidant and fuel flow to the tube are increased), reaches a maximum value and then decreases. The power decreases because the losses which increase with the current density become large enough to more than offset the gain made by the increase in the fuel and oxidant throughput.

A comparison of the single zone model predictions for the typical 85 percent fuel utilization with those obtained by applying the model with the cell subdivided into two zones in the axial direction, each with the same degree of fuel utilization (each at 42.5 percent utilization) is presented in Table 1 for a single tube. The

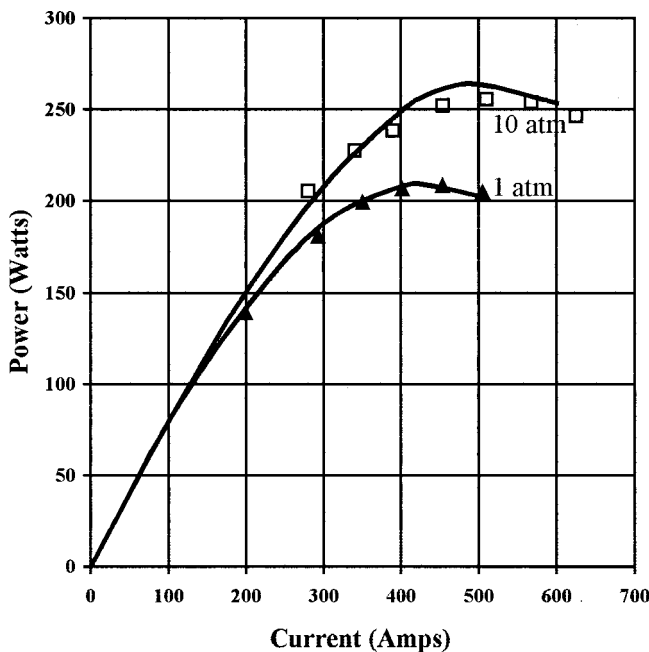


Fig. 4 Comparison between predicted performance and Westinghouse values

Table 1 Comparison of single and two-zone model predictions

	Single-Zone Model	Two-Zone Model
current density, mA/cm ²	310.0	311.2
power, Watts	243	242.8
cell length, cm	185.1	186.0

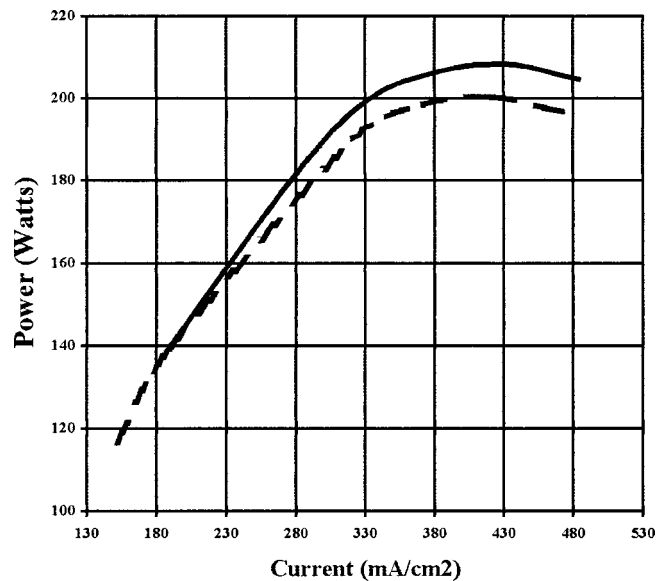


Fig. 5 Performance of SOFC with CO versus H₂ as fuel

current and power are essentially the same for the two cases while the cell length is within 0.5 percent showing that a single-zone (integral) model suffices.

Figure 5 compares the performance of the SOFC with CO versus H₂ as the fuel at 1 atm operating pressure with a mixture of 89 mole percent CO and 11 mole percent CO₂ versus the mixture of 89 mole percent H₂ and 11 mole percent H₂O. By choosing a mixture of CO and CO₂ the direct oxidation of CO may be compared with that of H₂ (ignoring the carbon formation potential for the CO fuel for this comparison). The current density and power produced by the cell are lower with CO because (1) the Gibbs free energy for the oxidation of CO is lower than that for H₂ at the operating temperature of the cell and (2) the diffusivity of CO is lower than that of H₂ which increases the anode concentration polarization.

Figure 6 shows the effect of pre-reforming (outside the cell) versus reforming the CH₄ fuel within the cell, i.e., assuming the anode section of the cell contains a reforming catalyst. When fuel reforming occurs within the cell, the heat released within the cell due to the various irreversibilities discussed earlier is absorbed directly by the endothermic reforming reactions while in the external reforming case, the heat rejected by the cell in the exhaust gas is utilized for the reforming reaction.

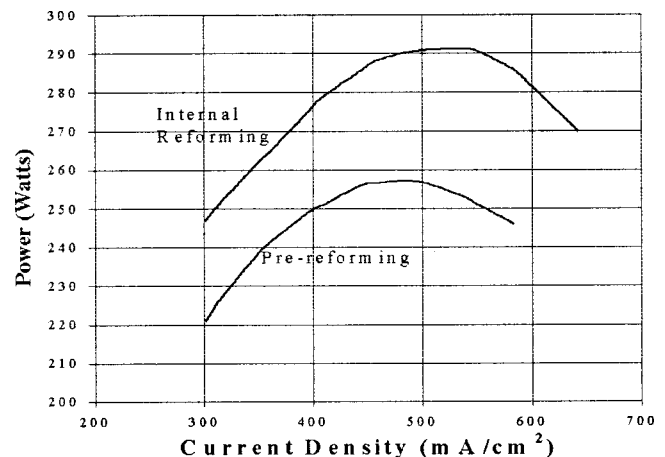


Fig. 6 Effect of reforming the fuel within the cell

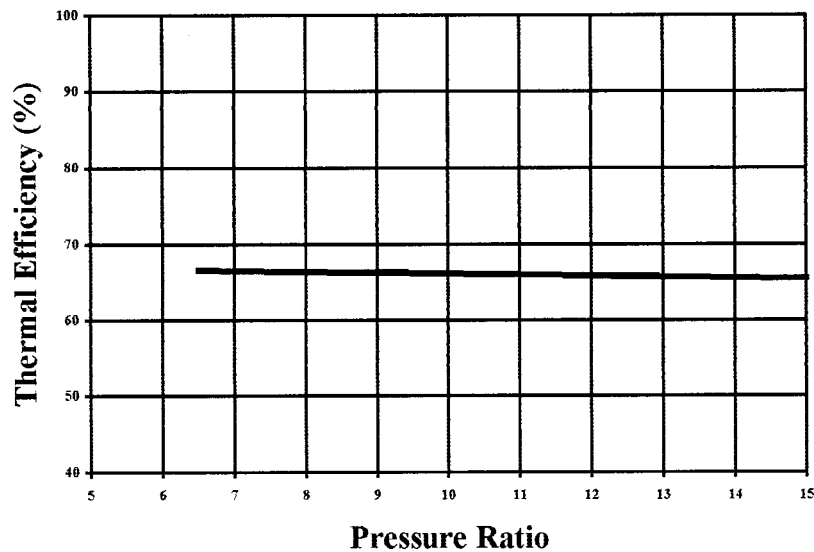


Fig. 7 Effect of pressure ratio on the performance of the SureCell™ hybrid cycle

The extent of reforming within the external reformer is limited by the concentration of water vapor contained in the fuel while in the case of internal reforming, the H_2O formed by the oxidation of the H_2 becomes available for continuing the reforming reaction within the internal reformer. Thus, the amount of CH_4 utilization is limited by the concentration of water vapor present in the fuel gas in the case of the external reformer. The cell performance is thus poorer for the external reformer case when limited amount of H_2O is added to the fuel.

Thus, internal reforming has the potential to minimize water consumption (or amount of recycle of the depleted fuel which may be used for water vapor addition to the fuel) as long as suitable reforming catalysts are developed that avoid carbon formation at low water vapor to carbon ratios.

Application of Methodology

An application of the system model to analyze the pressure dependence of the hybrid cycle configuration depicted in Fig. 3 is presented graphically in Fig. 7.

The entire air leaving the high pressure compressor was provided to the SOFC after preheating in the recuperator with an effectiveness of 90 percent. The individual cell voltage was maintained at 0.62 V. A portion of the depleted fuel was combined with the desulfurized natural gas in order to provide the water vapor required by the reformer within the SOFC. The high pressure turbine inlet temperature was maintained at 861°C , while the inlet temperature of the low pressure turbine was maintained at 863°C ([2]) by adjusting the fuel flow. The isentropic efficiencies of the compressors and the expanders were held at 85 percent and 87 percent, respectively.

The thermal efficiency of the cycle was found to be quite insensitive to the pressure ratio (ratio of SOFC inlet air pressure to low-pressure compressor inlet air pressure), increasing slightly with a decrease in pressure ratio in the range investigated; from 65.5 percent to 66.6 percent on a lower calorific value of the fuel as the pressure ratio was decreased from 15 to 6.5. As the cycle pressure ratio is reduced, the exhaust temperature from the low pressure turbine increases which in turn increases the temperature of the preheated air supplied to the SOFC. This increase in temperature more than offsets the decrease in efficiency of the SOFC operating at a lower pressure in the range of pressure ratios investigated. Furthermore, the irreversibilities in the low-pressure combustor are reduced at the lower pressure ratio because the tem-

perature of the oxidant stream entering this combustor increases as the expansion ratio of the high-pressure turbine decreases. Also, the contribution to exergy loss by the intercooler is reduced as the cycle pressure ratio is decreased since less heat is rejected in the intercooler as the compression ratio of the low-pressure compressor is reduced.

Selection of the optimum cycle pressure ratio requires performing an economic tradeoff between the calculated thermal efficiency of the cycle and installed cost of the equipment whose specifications may be established by this systems analysis tool. Note that as the pressure ratio is increased, the equipment becomes more compact.

Summary and Conclusions

The analysis capabilities required to perform tubular SOFC based hybrid cycles include an analytical model for the tubular SOFC as well as the secondary equipment required to analyze a hybrid power plant such as a gas turbine, reformer or partial oxidation reactor, shift reactor, humidifier, steam turbines, compressor, gas expander, heat exchangers, and pump. In addition to these equipment models, modules for functions such as separating a component from a stream, splitting a stream or combining streams and "controller" to automatically iterate in order to meet the desired design criteria are included. Another important capability that is included is to be able to arrange the various components or modules as defined by the user in order to configure different hybrid systems. With the help of this tool, it is possible to configure various hybrid cycle configurations in order to identify the more promising ones for further research and development.

Thus, the model may be used by cycle analysts from industry (e.g., equipment manufacturers, Engineering and Consulting firms, electric utility companies) for verifying performance of proposed cycles, as well as for developing new cycles. Current work is directed towards this activity of developing and identifying new tubular SOFC based hybrid cycles utilizing this tool. The ultimate goals for the capabilities of this tool are to have a user graphical interface for configuring the cycle and to have plant cost estimating capability.

Analysis of the hybrid cycle as originally proposed by Westinghouse (SureCell™) indicates that the thermal efficiency of the cycle is quite insensitive to the pressure ratio, increasing from 65.5 percent to 66.6 percent on a lower calorific value of the fuel as the pressure ratio decreases from 15 to 6.5.

References

- [1] Hirschenhofer, J. H. et al., 1950, *Fuel Cell Handbook* (Revision 3), U.S. Department of Energy (DE94004072), Jan.
- [2] Bevc, F. P., and Parker, W. G., 1995, "SureCell™ Integrated Solid Oxide Fuel Cell Power Plants for Distributed Power Applications," *PowerGen 1995*, PennWell, Tulsa, OK.
- [3] Ferguson, J. R., 1989, "Heat and Mass Transfer Aspects of SOFC Assemblies and Systems," *IEA Natural Gas Fueled Solid Oxide Fuel Cells and Systems*, Proceedings of Charnley Workshop, July 2–6, Swiss Federal Office of Energy, Berne.
- [4] Haynes, C. L., 1999 "Simulation of Tubular Solid Oxide Fuel Cell Behavior for Integration Into Gas Turbine Cycles," Ph.D. thesis, Georgia Institute of Technology, July.
- [5] Bessette, N. F., 1994, "Modeling and Simulation for Solid Oxide Fuel Cell Power Systems," Ph. D. thesis, Georgia Institute of Technology.
- [6] Peng, D., and Robinson, D. B., 1976, "A New Two-Constant Equation of State," *Ind. Eng. Chem. Fundam.*, **116**, No. 1, pp. 59–64.
- [7] Schnackel, H. C., 1958, "Formulations for the Thermodynamic Properties of Steam and Water," *Trans. ASME*, **80**, pp. 959–966.
- [8] Gas Research Institute Report, 1993, "Evaluation of Advanced Gas Turbine Cycles," Report No. GRI-93/0250, Aug.
- [9] Spencer, R. C., et al., 1974, "A Method for Predicting the Performance of Steam Turbine-Generators," General Electric Technical Bulletin GER–2007C, July.
- [10] El-Masri, M. A., and Pourkey, F., 1986, "Prediction of Cooling Flow Requirements for Advanced Utility Gas Turbines Part 1: Analysis and Scaling of the Effectiveness Curve," presented at ASME Winter Annual Meeting.
- [11] Electric Power Research Institute Report, 1983, "Gas Turbine Evaluation (GATE) Computer Program," Report No. AP-2871-CCM, Feb.
- [12] Kern, D. Q., 1950, *Process Heat Transfer*, McGraw-Hill, New York, pp. 563–621.
- [13] Bessette, N. F., and George, R. A., 1996, *Performance and Reliability of Westinghouse's Air Electrode Supported Solid Oxide Fuel Cell at Atmospheric and Elevated Pressures*, Mar., Denki Nagaku.

J. H. Kim

Senior Researcher,
Turbomachinery Department,
Korea Aerospace Research Institute,
Daejeon 305-600, Korea

T. W. Song

Graduate Student,
School of Mechanical and Aerospace
Engineering,
Seoul National University,
Seoul 151-742, Korea

T. S. Kim

Assistant Professor,
Department of Mechanical Engineering,
Inha University,
Inchon 402-751, Korea

S. T. Ro

Professor,
School of Mechanical and Aerospace
Engineering,
Seoul National University,
Seoul 151-742, Korea
Fellow ASME

Dynamic Simulation of Full Startup Procedure of Heavy-Duty Gas Turbines

A simulation program for transient analysis of the startup procedure of heavy duty gas turbines for power generation has been constructed. Unsteady one-dimensional conservation equations are employed and equation sets are solved numerically using a fully implicit method. A modified stage-stacking method has been adopted to estimate the operation of the compressor. Compressor stages are grouped into three categories (front, middle, rear), to which three different stage characteristic curves are applied in order to consider the different low-speed operating characteristics. Representative startup sequences were adopted. The dynamic behavior of a representative heavy duty gas turbine was simulated for a full startup procedure from zero to full speed. Simulated results matched the field data and confirmed unique characteristics such as the self-sustaining and the possibility of rear-stage choking at low speeds. Effects of the estimated schedules on the startup characteristics were also investigated. Special attention was paid to the effects of modulating the variable inlet guide vane on startup characteristics, which play a key role in the stable operation of gas turbines. [DOI: 10.1115/1.1473150]

Introduction

Gas turbines suffer transient operation due to startup, load change, shutdown, and other environmental disturbances. During most of the startup procedure, the performance of most components in particular is far lower than during operations around the design point. Operational characteristics are likewise often highly unstable. In addition, startup involves a fairly complicated series of rigid steps such as cranking, purging, and ignition. Accordingly, a good grasp of the details of gas turbine startup is very important to ensure safe operations until the base load point.

During startup, there is a high possibility for gas turbines to encounter critical situations such as compressor surge and stall, and hot start. In particular, instability due to compressor surge and stall at low shaft speeds often causes abnormal shutdown (trip) during startup. This situation can usually be avoided by modulating the angles of the inlet guide vane and/or by extracting some air from the midstages of the compressor. Meanwhile, if the starter is cut off before the net shaft power changes from negative to positive, the turbine decelerates and the temperature drastically increases. This start failure is known as a "hot start." To prevent such a situation, the schedule of fuel flow rate and starter cutoff time should be carefully determined. Consequently, sophisticated scheduling based on a precise prediction of dynamic operation is required.

Since it is not possible to intentionally pose unstable operations to engines during their startup procedures without endangering them, an analytical approach using numerical simulations is most effective in estimating the startup characteristics of gas turbines. However, related works using the numerical approach are hardly found except for those based on the quasi-steady methods ([1,2]). Furthermore, most of them are not perfect startup simulations by definition since the initial condition of their simulation does not

indicate zero speed but actually involves arbitrary midrange speeds. This appears to result from difficulties in obtaining low rpm component characteristics, especially those of the compressor.

In this study, a methodology for the simulation of full startup procedure of heavy duty gas turbines for power generation is proposed. Basic governing equations describing general transient operations and relevant component models are taken from the previous works of the authors of this paper ([3]), proved to be effective and applicable for the dynamic analysis of gas turbines. Speed-dependent characteristics of the compressor and startup sequences are modeled. Unsteady one-dimensional conservation equations are used and the sequences that dominantly affect startup characteristics are included in the startup scheduling. The startup characteristics of a typical heavy-duty 150MW class gas turbine are simulated. The results are then compared with field data. In addition, an analysis is carried out to investigate the effect of VIGV modulation on the startup characteristics. Even though the current analysis includes some specific models, only applicable to heavy duty gas turbines, its fundamental models and frame work can be applied to other types of engines with additional models, specific to each engine or group of engines.

Overview of Startup Procedure

In general, most engines share common startup sequences although details may differ from engine to engine. The two common steps are cranking and ignition. The gas turbine, like any internal combustion engine, is not self-starting and requires to be cranked from an external source. Although usually a diesel engine or an electric motor, the source may also be a steam turbine or a gas expander. The starter continues to assist the engine to reach a higher rpm even after the starter torque and the engine torque are equalized. It is only cut off when the turbine speed reaches a prescribed percentage of the rated speed, which varies from engine to engine. In general, turbine efficiency must be high enough, at a speed approximately 40% to 85% of its design speed, in order for the engine to sustain itself without starter power ([4]).

Contributed by the International Gas Turbine Institute (IGTI) of THE AMERICAN SOCIETY OF MECHANICAL ENGINEERS for publication in the ASME JOURNAL OF ENGINEERING FOR GAS TURBINES AND POWER. Paper presented at the International Gas Turbine and Aeroengine Congress and Exhibition, New Orleans, LA, June 4–7, 2001; Paper 01-GT-017. Manuscript received by IGTI, December 2000, final revision, March 2001. Associate Editor: R. Natole.

Table 1 Schedules of main starting sequences in various engines (% of the rated speed)

	Typical [5]	Solar Centaur [5]	Westinghouse 501F [18]	GE Typical [4,16]	GE 7F†
Ignition	10	20	25	10~15	15
Starter cutoff	40~60	60~70	64		
Bleed valve close		70~90	94		
VIGV open		70~90	100	83.5	80

†Field data from a combined cycle power plant

After cranking, purging (removal of combustible gas/fuel in flow paths) takes place before ignition. Simple cycle gas turbines with conventional upward exhaust do not require purging prior to ignition. The ignition sequence can proceed when the rotor speed passes through a designated firing speed. However, if a heat recovery equipment is present, gas path purging is required to ensure safe ignition. Fuel is supplied and ignition is initiated when the fuel pressure is high enough and turbine speed is above the preset minimum of the rated speed (10% typically, [5]). After ignition, the engine is accelerated up to the rated speed with a prescribed fuel flow schedule. During this acceleration, the VIGV angle and the bleed valve opening are modulated to secure stable operation.

Starting sequences of several engines are surveyed and shown in Table 1. Ignition is initiated at around 10–20% of the rated speed and the starter is cut off when the speed reaches around 60% of the rated speed. Bleed valves are kept open up to 70–90% of the rated speed and the VIGV angle is kept closed up to 70% or even 100% of the rated speed. At this moment, the front stage of the compressor is almost choked. Then, the VIGV angle is opened following a preset schedule.

The procedures stated above represent most of the current engines and are also considered the main sequence in the startup simulation carried out in this study.

Governing Equations

Unsteady conservation equations and the equation of motion for a rotating body describe the dynamic behavior of a gas turbine under transient operation. This paper adopts one-dimensional equations derived from the integral forms of conservation equations ([3]), which are continuity, momentum, and energy equations. They appear as follows:

Continuity equation:

$$V \frac{d\rho_{i+1}}{dt} = -\dot{m}_{i+1} + \dot{m}_i \quad (1)$$

Momentum equation:

$$V \frac{d(\rho u)_{i+1}}{dt} = -(\dot{m}_{i+1}u_{i+1} - \dot{m}_i u_i + p_{i+1}A_{i+1} - p_i A_i) + F \quad (2)$$

Energy equation:

$$V \frac{d(\rho H - p)_{i+1}}{dt} = -(\dot{m}_{i+1}H_{i+1} - \dot{m}_i H_i) + \dot{Q} - \dot{W}_s \quad (3)$$

The variables in the storage terms are represented by the control volume exit values. This study does not aim at capturing pressure fluctuation such as surge because the time scale of the analysis in this paper is not short enough to analyze pressure fluctuation inside the compressor. However, including the momentum equation may allow the possibility of simulating compressor surge, as exemplified in the previous work ([6]). Ordinary differential equations can be solved numerically using prescribed initial and boundary conditions. These equations are applied to each component with suitable F , \dot{Q} , and \dot{W}_s values, which must be specified

at each time step, i.e., given as input values. They can be derived from either characteristic maps or steady-state off-design models and are evaluated using the following equations:

$$F = \dot{m}_{i+1}^* u_{i+1}^* - \dot{m}_i u_i + p_{i+1}^* A_{i+1} - p_i A_i \quad (4)$$

$$\dot{W}_s = \dot{m}_i (H_i - H_{i+1}^*). \quad (5)$$

In these equations, * denotes the steady-state outlet conditions for the given inlet conditions at each time step. The heat transfer rate \dot{Q} appears only in the combustor and is equal to the fuel energy input.

Component Models

Compressors. The operational characteristics of modern compressors are very complicated due to the interstage air bleeding, and the active modulation of the variable inlet guide vane and stator vanes. An efficient method to calculate the performance of multistage axial compressors proposed by the authors of this paper ([3,7]) is used in the present analysis. It requires stage performance maps but differs from the conventional sequential stage-stacking method in that it adopts simultaneous calculation of all interstage parameters. Thus, it can be effectively utilized in a complicated system analysis such as the one used in the present study. Generalized stage characteristics ([8]) are used, which are represented by relations among flow coefficient, pressure coefficient, temperature coefficient, and efficiency. In case of variable vane setting angles, the stage characteristics evaluation is modified by adopting an analytical approach ([9]). The feasibility of the method can be found in previous works ([3,7]), where comparisons between analysis and field data for the performance of both fixed and variable geometry compressors were presented.

Turbine. With given inlet conditions, the expansion pressure ratio of a stage is obtained using the well-known Stodola equation. To obtain stage performances, a row-by-row prediction method for a cooled turbine proposed by Kim and Ro [10] is used, while a model of pressure loss caused by mixing is modified based on the model proposed by Kim et al. [11]. Coolant flow is driven by static pressure differences between points where the coolant is extracted and injected.

Combustor and Guide Ducts. The heating value of fuel is transferred to the combustor as the heat source \dot{Q} in the energy equation. In the combustor and inlet/outlet ducts, loss of total pressure is considered by assuming a quasi-steady flow.

Rotating Shaft. The rotational motion of the shaft can be presented by the following equation:

$$I \frac{d\omega}{dt} = G_t - G_c + G_{st} - G_l. \quad (6)$$

The first two terms on the right-hand side refer to the developed torque (net gas turbine torque) while the third term indicates the starter torque. The last term is the load torque and is maintained at zero during the acceleration period until full speed is reached.

Compressor Characteristics at Low Speeds

The performance of each component deteriorates at low speeds, and engines often cannot operate normally. Multistage axial flow compressors with a high design pressure ratio exhibit extremely low performance (low pressure ratio and low efficiency) and mechanical problems (vibration, etc.) at low speeds. Most of these problems are caused by discontinuities in the performance characteristics of the front stages. Such discontinuities may be due to stage stalling and deterioration of the stage performance ([12]). Therefore, careful attention should be paid to modeling low-speed operation characteristics of multistage axial flow compressors. The generalized stage performance characteristics mentioned in

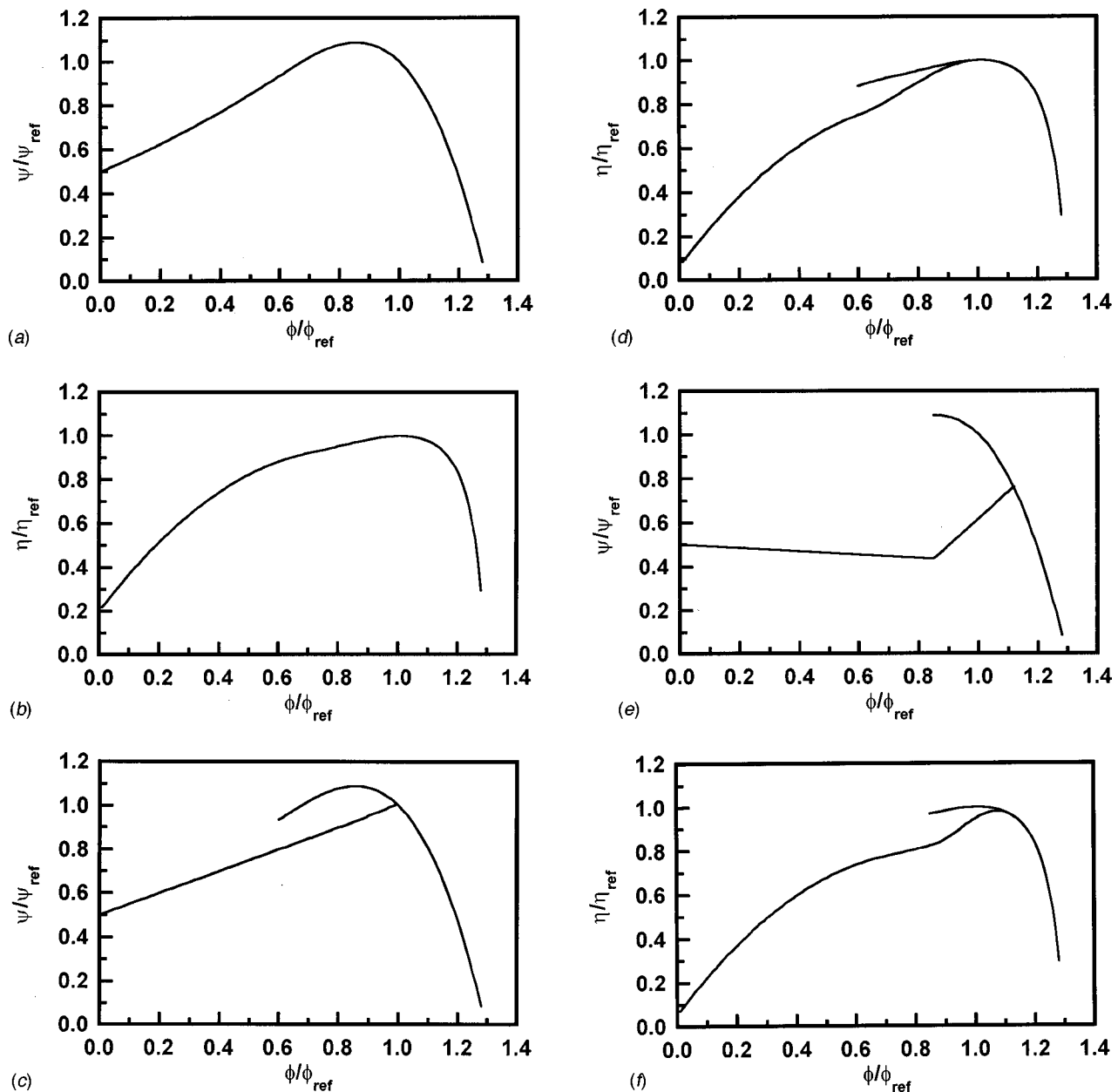


Fig. 1 Extended stage characteristics; (a) pressure coefficient (model 1-front stages), (b) isentropic efficiency (model 1-front stages), (c) pressure coefficient (model 2-middle stages), (d) isentropic efficiency (model 2-middle stages), (e) pressure coefficient (model 3-rear stages), (f) isentropic efficiency (model 3-rear stages)

the last section do not cover the low-speed region and should be modified to incorporate characteristics at low speeds, i.e., at low flow coefficients.

A couple of models have been proposed to obtain low speed characteristics. Agrawal and Yunis [1] developed a mathematical model to estimate gas turbine performance in the starting regime. Based on the general observation that characteristics at low-speed operation do not differ much from engine to engine, they estimated compressor characteristics using empirical observations from a number of engines. However, their model cannot be adopted in this study, based on a stage-by-stage model, since their work concerns the modeling of the performance of whole multi-stage compressors. The idea of Benser [12] is more appropriate for this work. He divided stage characteristics into three kinds using different definitions of stage stall: (1) progressive stall, a gradual but continuous decrease in stage performance as the flow

coefficient decreases below the stalling value, and (2) abrupt stall, a sudden or abrupt drop in stage performance at the stalling value of flow coefficient.

Since the basic concept of Benser is adopted in this work, three different models for stage characteristics are employed, and these are applied to the front, the middle, and the rear stages, respectively. While the generalized stage characteristics in the high flow coefficient region, mentioned in the last section, are used as they are, those in the low-flow coefficient region are generated based on experimental data ([13]). Then, all the operating range during startup, from very low to high flow coefficient, may be covered. The models used are shown in Fig. 1. As applied to front stages, only the progressive stall occurs in model 1, while only the abrupt stall occurs in model 3 as applied to rear stages. In model 2, applied to middle stages, a rather moderate abrupt stall occurs.

Table 2 Design specifications of the GE 7F engine

System	GE 7F
Speed, rpm	3600
Electrical power, MW	150
Cycle efficiency, %	34.5
Compressor	18-stage axial
Pressure ratio	13.5
Combustor	Reverse flow type
Turbine	3-stage axial
Exhaust air flow, kg/s	419
Firing temperature, °C	1260
Exit temperature, °C	600

Object of Analysis

The startup procedure of a 150 MW class gas turbine for power generation (GE 7F) is simulated, and the results are compared with field data. Design specifications are listed in Table 2. Some of the startup sequences should be assumed or estimated for the simulation because all of them are not specified from operating data. These are inferred from other engines and examinations of field data. The purging procedure before ignition is not considered in this study since such a procedure cannot be found from the field data. The estimated startup sequences and their detailed schedules are summarized in Table 3.

Sizing a starter system is difficult primarily because diverse contributing factors cannot be exactly quantified. This is normally done during the detailed system design phase. In general, it is known that the maximum starter power is obtained at about 20% of the rated speed ([14]), and the starter torque decreases linearly with rpm from its maximum value up to the cutoff speed ([5,15]). The maximum starter torque at zero rpm may be estimated approximately with this assumption. It is presumed that the starter cutoff occurs at 65% of the rated speed.

Modulation of VIGV angle follows the general rule of GE engines ([16]) and is listed in the table. During the modulating period, the opening is increased linearly with rpm. Since the schedule of air bleeding is not given from the field data, a reasonable assumption should be made. It is assumed that the total amount of bleed air is 15% of the compressor inlet airflow, and 5% of the bleed air is assigned to each bleed point (exit of 13th, 17th, and 18th stage—these are also coolant sources). At 95% speed, the bleed valve is closed and the extracted air is supplied to the turbine as coolant. The field data for fuel flow rate are not refined enough to be utilized as numerical input for the transient simulation. Thus, the schedule of fuel flow rate is determined so that the simulated turbine exhaust temperature values during full startup may match the measured data on the whole.

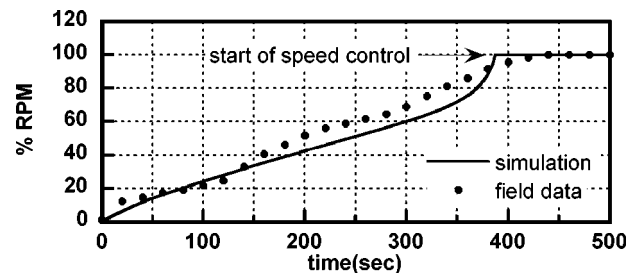
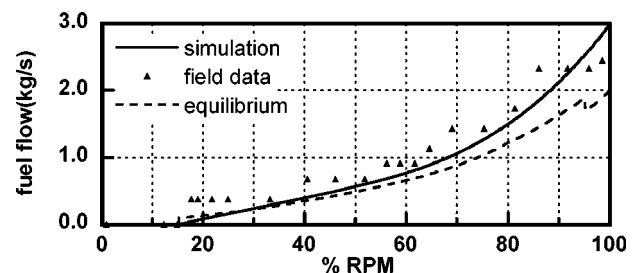
Numerical Treatment

A fully implicit method is introduced to solve a set of ordinary differential equations where the static pressure, temperature, and axial velocity for every control surface are variables. Therefore, all of $3(n+1)$ variables exist for n control volumes. Three of them are given as boundary conditions, and these are the inlet total temperature, pressure, and exhaust static pressure of the en-

gine. Consequently, remaining $3n$ variables can be obtained as solutions of the equation set since there exist $3n$ equations (continuity, momentum, and energy for n stages). The multivariable Newton-Raphson method is used to solve the equation set. During the main startup (acceleration) period, no special feedback control is used. Instead a kind of feed-forward control following fuel scheduling is applied. After the rated speed is reached, a feedback control to keep the rated shaft speed ([3]) is applied.

Results and Discussions

The variations in rpm and fuel flow rate during startup are shown in Fig. 2 and Fig. 3, respectively. The fuel supply schedule used as input in the simulation (the solid line of Fig. 3), which is determined using the criterion of a close agreement between predicted and measured exhaust temperatures, appears to reproduce the measured field data well enough. It should be noted that the field fuel flow data do not appear very reliable in the viewpoint of their local trends. Thus, the estimated input schedule is used as input in the simulation. The shaft speed development is well predicted. Furthermore, prediction of the time required to reach the rated speed is accurate enough. These results confirm that schedules for starter torque and fuel flow rate schedule were reasonably estimated. The dotted line in Fig. 3 represents the fuel flow rate, with which the turbine power equals the compressor power at each speed. This is usually called “equilibrium running.” This fuel flow rate for the equilibrium running is obtained by a steady state off-design performance analysis. To accelerate the system, more fuel than that corresponding to the equilibrium running should be supplied at each speed. This is confirmed in Fig. 3. The reverse effect at very low speeds (0 to 28% rpm) is due to the fact that the engine does not reach the self-sustaining point, and the starter supplies additional torque as will be shown later. The TET variation also matches the field data well, as shown in Fig. 4, because the fuel flow rate is scheduled so that TET prediction is as close as possible to the field data as stated earlier. The turbine exhaust temperature falls down at 80% of the rated speed when VIGV modulation begins. A sudden decrease of TET at that point can be clearly observed in Fig. 4(b), where TET variation is depicted with time. The decrease of TET is caused by the increase of combustor inlet airflow (low fuel-air ratio) by opening the VIGV.

**Fig. 2 Variation in shaft speed during startup****Fig. 3 Schedule of fuel flow rate during startup****Table 3 Estimated startup sequences of GE 7F**

Sequences	Detailed Schedule	Time(% RPM)
Ignition	On	15 [16]
Starter	$G_{st} = G_{st,max}(1 - \tilde{N}/0.65)$ cutoff	0–65 65
Air bleed	15% of compressor inlet Close	0–95 95
VIGV	closed 56° modulated 56°→33° opened 33°	0–80 [16] 80–90 [16] 90–100 [16]

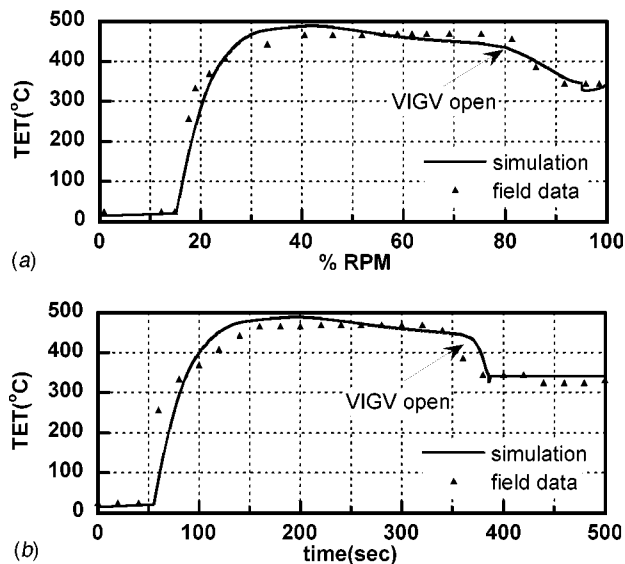


Fig. 4 Variations in turbine exhaust temperature during startup; (a) TET variation with % rpm, (b) TET variation with time

Meanwhile, a couple of typical characteristics during startup can be observed in the prediction results. It is known that the contribution of the turbine power during the first low-speed phase of starting may be neglected. This means that the developed power (the net power of the engine) has a negative value in the early stage of an engine startup. This is the reason why an additional power should be supplied externally by a starting device. As shown in Fig. 5, the developed (net) power decreases down to the negative scale with the rpm at the beginning stage. When fuel is supplied and combustion starts (15% rpm), however, the developed power begins to increase to reach the self-sustaining point (about 28% rpm). The increase of the developed power results from a rapid recovery of turbine efficiency as shown in Fig. 6. The prediction results are reasonable considering that the self-sustaining point is usually observed at 25% of the rated speed ([14]).

When a compressor runs at a speed lower than the design speed, the pressure ratio will be lower than the design values. The resulting effect of density reduction in rear stages will be to increase the axial velocity. Then, choking will eventually occur there and limit the mass flow ([17]). Such increases of axial velocities at rear stages can be observed from the prediction results shown in Fig. 7. At low speeds (10 and 50% rpm on the figure), axial velocities are higher in rear stages. Thus, the mass flow will be limited by choking in rear stages at low speeds. As speed increases, density at every stage approaches the design value, allowing the rear stages to pass the flow provided by the front stages. In high speeds, the flow coefficient of the first stage has the

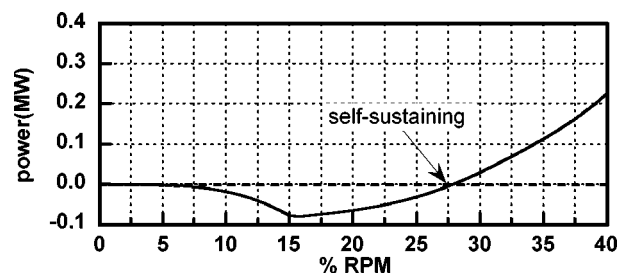


Fig. 5 Variation in developed power in low rpm region

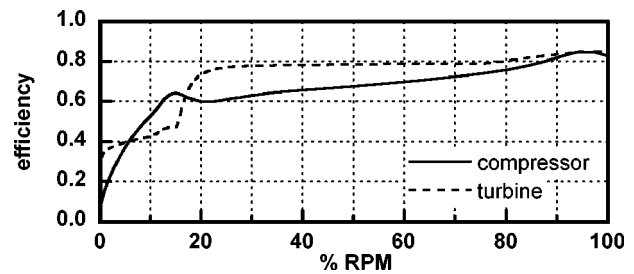


Fig. 6 Variations in turbine and compressor efficiencies during startup

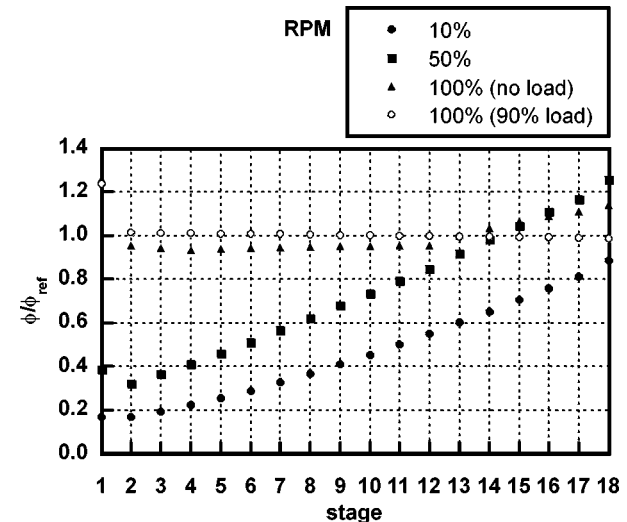


Fig. 7 Distribution of flow coefficient over the stages at various speed

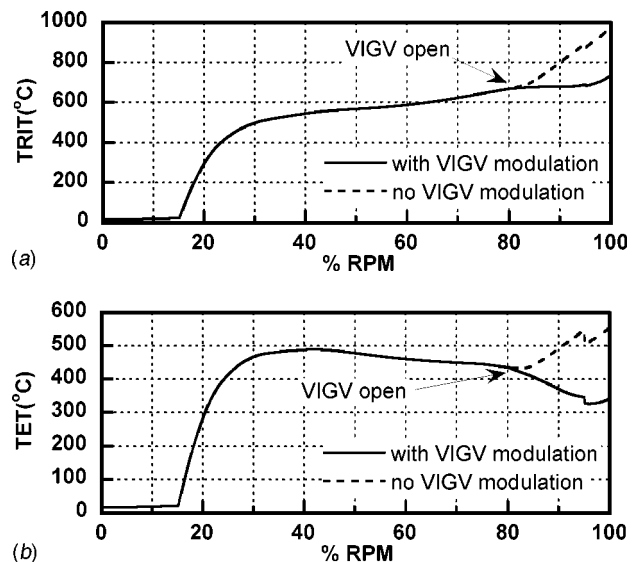


Fig. 8 Variations in firing temperature and exhaust temperature during startup: effect of VIGV modulation; (a) firing temperature, (b) turbine exhaust temperature

highest value, where choking occurs. This result also coincides with the fact that choking occurs at the front stage of the compressor in high rpm regions.

As mentioned earlier, gas turbines show different startup characteristics depending on the schedules of various sequences re-

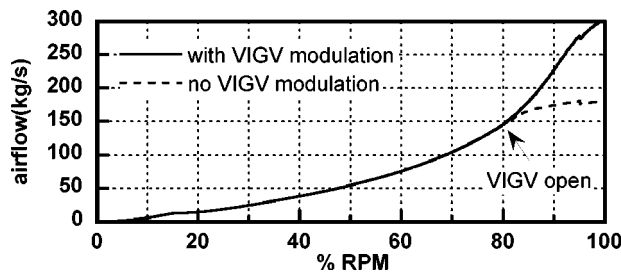


Fig. 9 Variation in combustor inlet airflow during startup: effect of VIGV modulation

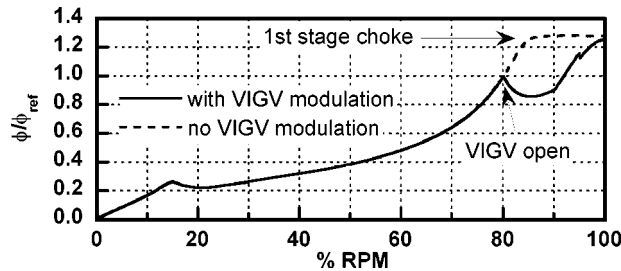


Fig. 10 Variation in first stage flow coefficient during startup: effect of VIGV modulation

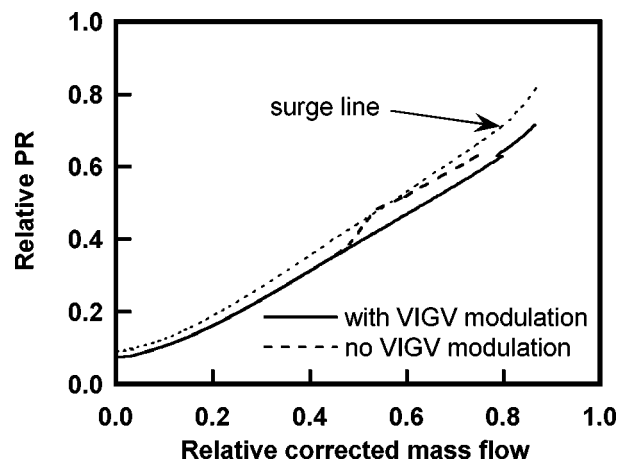


Fig. 11 Operating lines during startup: effect of VIGV modulation

quired. In this study, special attention is given to the effects of VIGV modulation on startup characteristics, which is very important for the stable operation of the compressor and, eventually, of the gas turbine. This investigation helps us to understand the reason why the schedule should be determined as such and to know how the sequence significantly affects startup characteristics. In addition, this procedure makes it possible to examine how a wrong schedule estimate (i.e., mismatching of sequences) can severely affect the startup characteristics estimate. To investigate the effect of VIGV modulation, the startup characteristics previously predicted are compared with those of the case without VIGV modulation (VIGV not opened even at speeds higher than 80%). In this case, the schedule is such that the rated speed is reached with VIGV fully closed and then opened at the rated speed. As shown in Fig. 8, the firing (turbine rotor inlet) and exhaust temperatures increase drastically after reaching 80% rpm without VIGV modulation. Increase of these temperatures is caused by the nearly constant air mass flow rate as shown in Fig. 9, which results in high fuel-air ratio at the combustor. The reason for this

result of nearly constant mass flow rate after 80% rpm is due to the 1st stage choking in the compressor. As shown in Fig. 10, the flow coefficient of the 1st stage does not change considerably after 80% rpm although the speed is increasing. Operating lines during startup for both cases are depicted in Fig. 11. The surge line is decided approximately based on the fact that the surge margin in gas turbines for power generation is about 15–20% ([14]) at every equilibrium running point. Evaluation of an exact surge line is beyond the scope of this work. In the absence of VIGV modulation, the operating line is closer to the surge line in high rpm regions. Thus, any mismatching between different sequences may cause very severe problems during startup. This simulation demonstrates the possible result of an extreme case of mismatching between fuel and VIGV modulation.

Conclusion

Transient behavior of a heavy duty gas turbine during startup was simulated and its unique characteristics were investigated. Typical engine starting sequences were examined and representative sequences were adopted in the simulation. Unsteady one-dimensional conservation equations were used, and models based on stage performance were adopted both for compressors and turbines. Special attention was made to model the operation of compressor stages at low speeds. The startup procedure of a 150 MW class gas turbine (GE 7F) was simulated with an estimated schedule of starting sequences including fuel supply, starter torque supply, VIGV angle setting, and air bleeding. All system parameters including shaft speed development and exhaust temperature are in good agreements with the field data during the whole acceleration period from zero to full speed. The time when the engine becomes self-sustaining matches the general observation. The possibility of rear-stage choking during low-speed operation is also confirmed. The effect of VIGV modulation was analyzed by performing a startup simulation without modulating the VIGV during the acceleration period. In the absence of VIGV modulation, the firing temperature increases drastically after 80% rpm due to high fuel-air ratio. This results in a high possibility of compressor surge. This analysis demonstrates the importance of a precise estimation of the startup schedule including the matching of diverse sequences.

Acknowledgment

This work was supported by the Brain Korea 21 project.

Nomenclature

- A = area
- F = force
- G = torque
- H = total enthalpy
- I = polar moment of inertia
- \dot{m} = mass flow rate
- N = rotational speed
- \tilde{N} = nondimensional rotational speed (N/N_{ref})
- p = static pressure
- PR = total-to-total pressure ratio
- \dot{Q} = heat transfer rate
- t = time
- TET = turbine exhaust temperature
- TRIT = turbine rotor inlet temperature (firing temperature)
- u = axial velocity
- V = volume
- VIGV = variable inlet guide vane
- \dot{W}_s = shaft power
- ϕ = flow coefficient (axial velocity/blade speed)
- η = isentropic efficiency
- ρ = density
- ω = angular velocity

ψ = pressure coefficient
(isentropic temperature rise/blade speed²)

Subscripts

c = compressor
 i = control volume index
 l = load
ref = reference
 st = starter
 t = turbine

References

- [1] Agrawal, R. K., and Yunis, M., 1982, "A Generalized Mathematical Model to Estimate Gas Turbine Starting Characteristics," *ASME J. Eng. Gas Turbines Power*, **104**, pp. 194–201.
- [2] Saravanamuttoo, H. I. H., and MacISAAC, B. D., 1973, "The Use of a Hybrid Computer in the Optimization of Gas Turbine Control Parameters," *ASME J. Eng. Power*, **95**, pp. 257–264.
- [3] Kim, J. H., Song, T. W., Kim, T. S., and Ro, S. T., 2001, "Model Development and Simulation of Transient Behavior of Heavy Duty Gas Turbines," *ASME J. Eng. Gas Turbines Power*, **123**, pp. 589–594.
- [4] Johnson, D., Miller, R. W., and Ashley, T., 1998, "SPEEDTRONIC™ MARK V Gas Turbine Control System," *GE Turbine State-of-the-Art Technology Seminar*, GER 3658D, pp. 459–477.
- [5] Beyene, A., and Fredlund, T., 1998, "Comparative Analysis of Gas Turbine Engine Starting," *ASME Paper 98-GT-419*.
- [6] Macdougall, I., and Elder, R. L., 1983, "Simulation of Centrifugal Compressor Transient Performance for Process Plant Applications," *ASME J. Eng. Power*, **105**, pp. 885–890.
- [7] Song, T. W., Kim, T. S., Kim, J. H., and Ro, S. T., 2001, "Performance Prediction of Axial Flow Compressors Using Stage Characteristics and Simultaneous Calculation of Interstage Parameters," *Proc. Inst. Mech. Eng., Part A, Power Energy*, **215**, pp. 89–98.
- [8] Muir, D. E., Saravanamuttoo, H. I. H., and Marshall, D. J., 1989, "Health Monitoring of Variable Geometry Gas Turbines for the Canadian Navy," *ASME J. Eng. Gas Turbines Power*, **111**, pp. 244–250.
- [9] Klapproth, J. F., 1958, discussion, "Effects of Stage Characteristics and Matching on Axial-Flow-Compressor Performance," *Trans. ASME*, **80**, pp. 1290–1291.
- [10] Kim, T. S., and Ro, S. T., 1997, "The Effect of Gas Turbine Coolant Modulation on the Part Load Performance of Combined Cycle Plants—Part1: Gas Turbine," *Proc. Instn Mech. Engrs, Part A*, **211**, pp. 443–451.
- [11] Kim, J. H., Kim, T. S., Lee, J. S., and Ro, S. T., 1996, "Performance Analysis of a Turbine Stage Having Cooled Nozzle Blades With Trailing Edge Ejection," *ASME Paper 96-TA-12*.
- [12] Benser, W. A., 1965, "Compressor Operation With One or More Blade Rows Stalled," *Aerodynamic Design of Axial-Flow Compressors*, I. A. Johnsen and R. O. Bullock, eds., NASA SP-36, pp. 341–364.
- [13] Copenhaver, W. W., 1993, "Rotating Stall Performance and Recoverability of a High-Speed 10-Stage Axial Flow Compressor," *J. Propul. Power*, **9**, pp. 282–291.
- [14] Walsh, P. P., and Fletcher, P., 1998, *Gas Turbine Performance*, 1st Ed., Blackwell Science Ltd., London.
- [15] Lindsay, D. H., 1995, *The Design of Gas Turbine Engines—Thermodynamics and Aerodynamics*, 2nd Ed., ASME, New York.
- [16] GE Industrial & Power Systems, 1993, *Fundamentals of SPEEDTRONIC™ MARK V Control System*, A00023 Rev.A.
- [17] Cohen, H., Rogers, G. F. C., and Saravanamuttoo, H. I. H., 1996, *Gas Turbine Theory*, 4th Ed., Longman Group Limited, London.
- [18] WESTINGHOUSE Power Generation Business Unit, 1994, *501F ECONOPAC Application Handbook*.

Rolling Element Bearing Defect Detection and Diagnostics Using Displacement Transducers

J. J. Yu¹

e-mail: john.yu@bently.com

D. E. Bently

P. Goldman

K. P. Dayton

B. G. Van Slyke

Bently Rotor Dynamics Research Corporation,
1631 Bently Parkway South,
Minden, NV 89423

This paper introduces the methodology of rolling element bearing defect detection using high-gain displacement transducers. The nature of defect influence on the outer race deflection in the vicinity of the transducer tip in time base has been established. Inner race, outer race, and rolling element (ball/roller) defects, which often occur sequentially, can be clearly identified according to spike signals on the time-varying outer race deflection curve along with known bearing frequencies. The developed techniques are fully corroborated by experimental data. Spike-to-deflection amplitude ratio, which is almost independent of changes in speed and load for a given defect, is used to judge the defect severity. Spectral characteristics due to these defects have also been found. It is shown that this direct measurement by using displacement transducers without casing influence, which would be inevitable by using accelerometers mounted on the casing, is a reliable approach to detect bearing defects as well as their severity and locations.

[DOI: 10.1115/1.1456092]

1 Introduction

Rolling element bearings are widely used in many machinery applications. Condition monitoring of rolling element bearings offers the advantages of reducing downtime and improving maintenance efficiency for critical rolling element bearing machinery. Therefore, it is very important for machinery maintenance engineers to understand the effective techniques and instrumentation used to monitor and diagnose problems associated with rolling element bearing machinery.

Most diagnostic techniques for rolling element bearings involve signature analysis of the data from acceleration or velocity probes mounted on the bearing housing or machine casing. Monk [1] diagnosed bearing damage by observing changes in the RMS (root mean square) level. Boto [2] used shock pulse measurement to detect bearing damage. Dyer and Stewart [3] introduced a statistical parameter Kurtosis value to measure bearing conditions. McFadden and Smith [4] discussed the high-frequency resonance technique (HFRT). Spectral analysis has been widely employed for the diagnosis of bearing conditions ([5,6]).

The above-mentioned techniques are related to the casing vibration instrumentation systems. As a result, vibration signatures from bearings can be obscured by other stronger components from the associated machinery and the foundation. For that reason, an eddy current transducer called REBAM[®] (rolling element bearing activity monitor), which directly measures outer race displacement of the bearing, was used by Bently [7], and Harker and Sandy [8]. Kim [9] also conducted experimental work using this type of transducer. Recently, Holm-Hansen and Gao [10] tried to obtain vibrational response of slotted outer race using a structurally integrated force sensor without casing influence. The nature of the outer race deflection in time base associated with bearing frequencies, however, has not been indicated for a bearing with inner race, outer race, or rolling element defects. It has often been misconstrued that this type of transducer, which measures only outer race displacement, may not detect an inner race defect.

This paper introduces new methodologies to detect inner race,

outer race, and rolling element defects with this type of displacement transducer. The nature of defect influence on the outer race deflection near the probe tip in time base has been established. Deflection of the outer race in a rolling element bearing is measured with these high-gain displacement transducers. Inner race, outer race, or rolling element defects can be clearly identified according to spike signals on the time-varying outer race deflection curve along with the known bearing frequencies. The methodology to detect an inner race defect, which moves relative to the

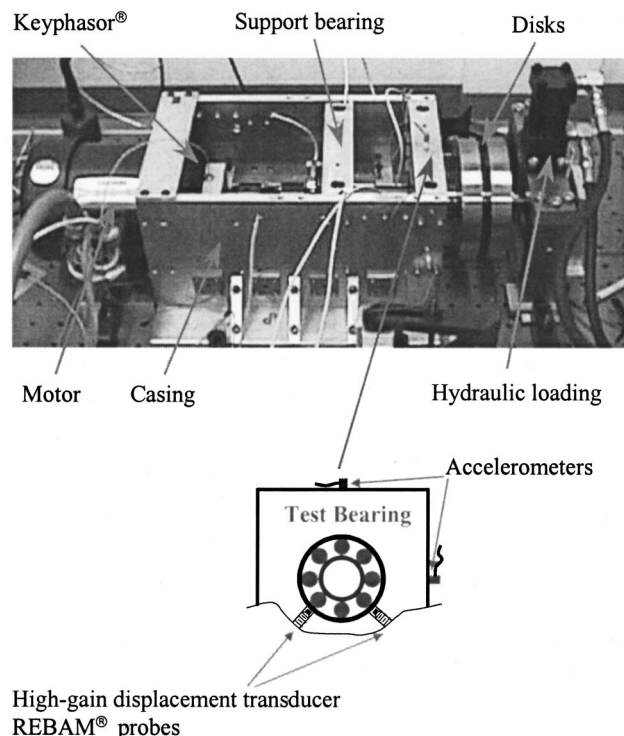


Fig. 1 Bearing test rig

¹To whom all correspondence should be addressed.

Contributed by the International Gas Turbine Institute (IGTI) of THE AMERICAN SOCIETY OF MECHANICAL ENGINEERS for publication in the ASME JOURNAL OF ENGINEERING FOR GAS TURBINES AND POWER. Paper presented at the International Gas Turbine and Aeroengine Congress and Exhibition, New Orleans, LA, June 4–7, 2001; Paper 01-GT-028. Manuscript received by IGTI Sept. 2000; final revision received by ASME Headquarters Mar. 2001. Associate Editor: D. Wisler.

Table 1 Approximate ratios of tested bearing frequencies to shaft speed

Approximate Ratio of Tested Bearing Frequencies to Shaft Speed	Ball Bearing	Roller Bearing
i_{IRBP} (=ratio of inner race ball pass frequency to shaft speed)	4.9	7.2
i_{ORBP} (=ratio of outer race ball pass frequency to shaft speed)	3.1	4.8
i_R (=ratio of rolling element spin frequency to shaft speed)	2.0	2.3
i_C (=ratio of cage frequency to shaft speed)	0.38	0.39

probe tip as it contacts balls/rollers, will be explicated more. Experimental data are presented to show detection techniques and their effectiveness.

2 Test Rig

The test rig used for detecting and diagnosing bearing defects is shown in Fig. 1. The test rig consists of a rotor with one support bearing and one test bearing.

The rotor includes a 746 W (1 hp) electric motor, which is connected to the main shaft through a laterally flexible coupling. The step main shaft is 419 mm (16.5 in.) long with diameters varying from 30 mm (1.181 in.) to 41 mm (1.6 in.). Attached to the shaft are two mass disks with 177.8 mm (7 in.) diameter and 25.4 mm (1 in.) thickness. The rotor is balanced by putting mass in one to several holes on the disks to compensate for unbalance.

A hydraulic pump with 25.4 mm (1 in.) diameter cylinder was used to apply the load to the shaft through a roller bearing with the number of elements much higher than the test bearing. In this way, the frequencies of the loading bearing would not interfere with the test bearing frequencies. The load on the bearing can be applied either in an upward direction or downward direction, and can be varied between -2224 N (-500 lbs.) and $+2224$ N ($+500$ lbs.). Note that the test bearing is loaded to some extent, even without hydraulic loading, due to the weight of the mass disks on this overhung rotor. The motor is connected to a variable frequency drive, which allows for ramped data collection at a controlled acceleration. The bearing housings are fixed to the casing, which is fixed to a large concrete foundation.

The displacement transducers, which had a gain of 78.7 mV/ μm (2 mV/ μ in.) compared to 7.87 mV/ μm (0.2 mV/ μ in.) for a generic eddy current proximity transducer, were used to measure the outer race deflection of the bearing. Accelerometers were also mounted on the casing to compare with these transducers.

Ball and roller bearings were used for the study of transducer response to raceway and rolling element defects, respectively. Approximate ratios of tested bearing frequencies to shaft speed, based on experimental data from good bearings, are shown in Table 1. Note that these values may change due to defect effects and vary with operating conditions. If a defect occurs on inner or outer race, balls/rollers will contact the defect at frequency $i_{IRBP} \times$ (i.e., i_{IRBP} times shaft speed) or $i_{ORBP} \times$. The sum of these two ratios is equal to the number of balls/rollers regardless of changes in speed and slip. If there is a defect on a ball/roller, inner or outer race will contact the defect at frequency $i_R \times$. Notice that since a

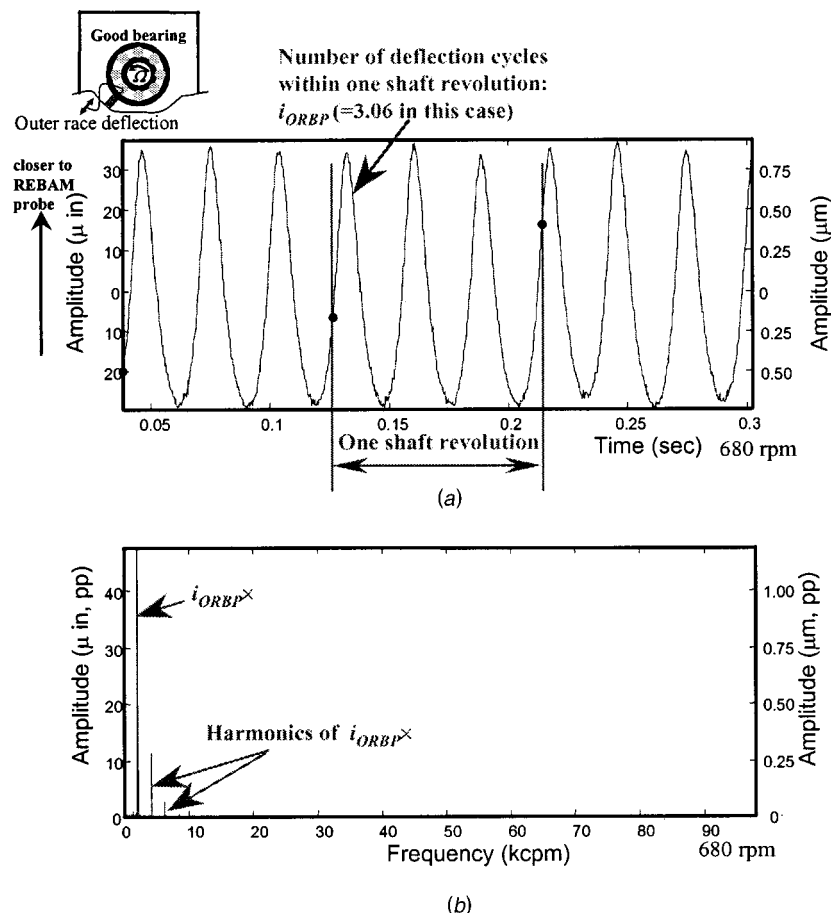


Fig. 2 Outer race deflection measured by displacement transducer; (a) time base, and (b) frequency spectrum

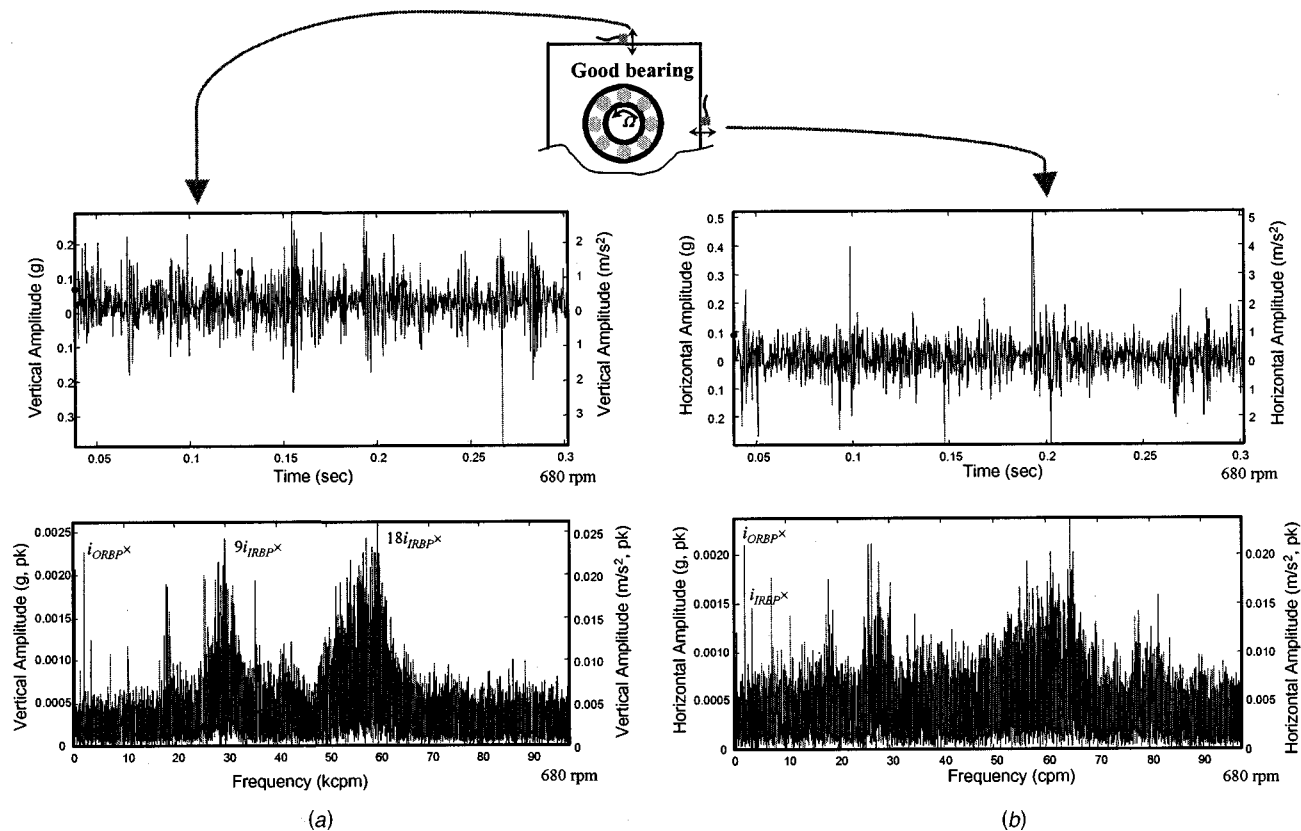


Fig. 3 Casing response in time base and frequency spectrum from accelerometers mounted in (a) vertical, and (b) horizontal directions

displacement transducer detects outer race deflection facing its tip, parameter i_C , the frequency ratio of the moving cage that holds balls/rollers is related to the detection of ball/roller defects.

3 Vibration Signature for Good Bearings

Both high-gain displacement transducers and accelerometers were installed to observe the corresponding vibration signature for a nondefective test bearing. The purpose was to find an effective sensor that clearly reflects the bearing operation, and an avenue that can expose bearing defects.

The high-gain eddy current transducer mounted in the hole of the housing can detect very small elastic deflection of the outer race penetrated by the transducer as each rolling element under load passes over the hole. For precaution, the strength of the outer race should be considered in order to prevent race failure through cyclic strain when determining the hole size in terms of the bearing size and loading. The deflection has a cycle of $360 \text{ deg}/i_{\text{ORBP}}$ shaft rotation. A good bearing possesses a smooth deflection curve in time base. Figure 2 shows vibration signature from the transducer mounted at the left side 45 deg from the bottom. Besides the weight of the whole rotor system, a hydraulic load of 1379 kPa (200 psi) downward is applied at the right end of the shaft as shown in Fig. 1. The test bearing has no defects on its inner race, outer race, or balls. No lubrication is supplied between the balls and raceways.

The localized deflection curve of the outer race, facing the probe, is clearly shown in time base where the shaft speed is 680 rpm (see Fig. 2(a)). The deflection has a peak-to-peak amplitude of about $1.65 \mu\text{m}$ ($65 \mu\text{in.}$). For each shaft rotation, the number of periodic waveform cycles due to the deflection is equal to i_{ORBP} ($=3.06$ in this case). When a ball is just being moved near the hole (left side 45 deg from the bottom) where the probe is mounted, the outer race around the hole, due to the ball pressing

on the outer race, deforms away from the bearing center (toward the probe). This case corresponds to all the high peak points in the time base shown in Fig. 2(a) and is the maximum deflection towards the probe. When two adjacent balls are just equally away from the probe hole, the deflection of the outer race around the hole is released so that the outer race is deflected away from the probe. This case corresponds to the low peak points in time base shown in Fig. 2(a). Due to surface roughness with lack of lubrication, ball tolerances, and ball undulations, there exists slight fluctuation on the deflection curve.

Figure 2(b) shows the deflection signal in frequency domain. Outer race ball pass frequency, i.e., $i_{\text{ORBP}} \times$ ($=3.06 \times$ in this case) component is dominant, accompanied by its harmonics, $2(i_{\text{ORBP}} \times)$, $3(i_{\text{ORBP}} \times)$, etc. The synchronous $1 \times$ component is almost negligible. Obviously, inner race ball pass frequency, i.e., $i_{\text{IRBP}} \times$ ($=4.94 \times$ in this case) component is not apparent in frequency domain.

Data from accelerometers give the casing vibration signals that include transducer response to rotor unbalance, foundation, and other frequency components in addition to the rolling element bearing operation. Figure 3 shows the signals in both vertical and horizontal directions for the same operating condition as shown in Fig. 2. Information from rolling element bearing operation is obscured or masked with the vibration signature from other sources in the rotor/bearing/foundation system. In the time domain as shown in Fig. 3, spikes or impulses occur although no defects exist in the bearing. In the frequency domain as shown in Fig. 3, vibration signals include components of $i_{\text{ORBP}} \times$, $i_{\text{IRBP}} \times$, and their harmonics for this nondefective bearing. As is known, these components often appear for a defective bearing, and for that reason are usually used to identify defects in the bearing. Applying this rule would misdiagnose the bearing. Therefore, it would be difficult to distinguish between defective and nondefective

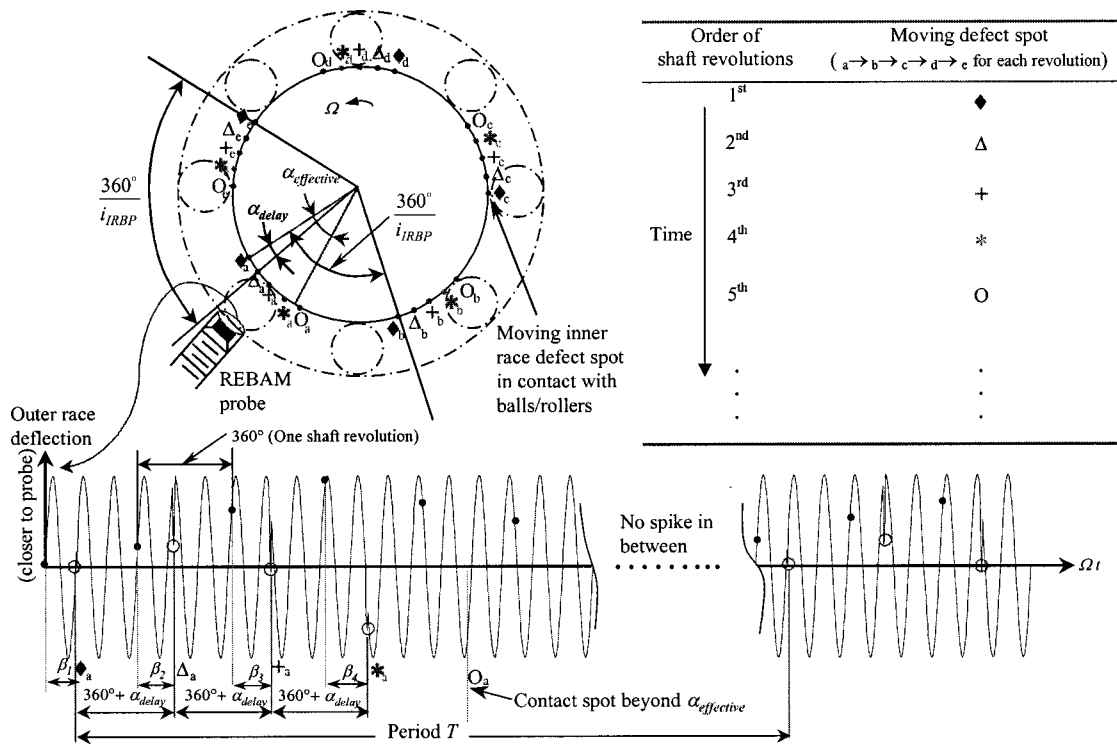


Fig. 4 Diagram of inner race defect detection methodology using high-gain displacement transducer

bearings by simply observing the advent of these fault frequency components with accelerometers. Besides, the response is to a great extent dependent on the casing. Harmonics of these bearing frequencies may or may not generate detectable casing vibrations. Although the number and magnitude of these components may be higher, as observed during experiments, it would be hard to establish a quantitative criterion for determining whether a bearing is damaged or not.

From these tests, it is clear that the high-gain displacement transducer detects only the deflection of the outer race of the rolling element bearing. If a defect in the rolling element bearing is related to the deflection, a detection technique using the transducer will be successful. Note that even for a good bearing without outer race defects, the spectral data of the deflection detected by the probe still gives the $i_{IRBP} \times$ component and its harmonics. No $i_{IRBP} \times$ component is present in the spectrum. However, as will be discussed, defects occurring in the inner race, the outer race, or a rolling element can be successfully detected by the high-gain displacement transducer.

4 Detection of Bearing Defects

As discussed previously, the outer race is deflected towards the displacement transducer each time an element under load passes over the transducer location. This produces a positive change in the displacement, relative to the low peak of the deflection curve where the least loading acts on the outer ring facing the probe. In spalling defects, material is actually removed from the raceway or ball/roller surface. The spalling defect produces a location of increased clearance, and ball/race contact over the defect spot is actually unloaded temporarily over a very short time period. The unloading makes the outer race spring back away from the transducer. The result is a short duration spike in the time base waveform.

4.1 Inner Race Defect. Detection of an inner race defect is often considered a difficult task in rolling element bearing monitoring. It is sometimes mistakenly believed that displacement transducers cannot detect inner race defects. Even though some

spikes might have been observed, the nature of these signals had not been explored when applying high-gain displacement transducers. Thus, it was difficult to diagnose the occurrence of inner race defects and to distinguish it from other defects.

The new detection methodology with the displacement transducer makes it possible to diagnose the inner race defect correctly. The nature and characteristics of observed signals can be fully understood. The accompanying real data validates the detection methodology.

4.1.1 Detection Methodology. If a defect occurs in the inner race, the defect spot will contact rolling elements i_{IRBP} times on average during each shaft rotation. The displacement transducer detects negative spikes when the moving defect spot is located within an effective zone near the probe. Figure 4 shows a diagram of the defect detection methodology. Assume that one defect occurs on the inner raceway.

Suppose that at one time (in the first shaft revolution) the defect spot in contact with a ball is entering the effective zone $\alpha_{effective}$ in which the probe can detect the negative spikes. Therefore, a negative spike occurs in the effective zone, marked with “◆_a,” which is also denoted in the time base with the same symbol. After $360 \text{ deg}/i_{IRBP}$ degrees shaft rotation from “◆_a,” where the defect spot contacts the next ball at “◆_b,” the probe cannot detect a negative spike because the contact occurs beyond the effective zone. For the following contact at “◆_c,” as shown in Fig. 4 when the defect contacts the following ball, the same situation occurs where the contact event is not within the effective zone of the probe. This situation exists until the defect spot contacts the j th (j is a round number for i_{IRBP}) ball within the effective zone again, as is indicated with “Δ_a” in the effective zone. Note that two conditions must be met for the probe to detect these negative spikes. One is that the inner race defect spot has to contact balls. The other is that the defect spot in contact with balls has to be within the effective zone.

A delay angle between the two contact spots within the effective zone “◆_a” and “Δ_a” can be given by

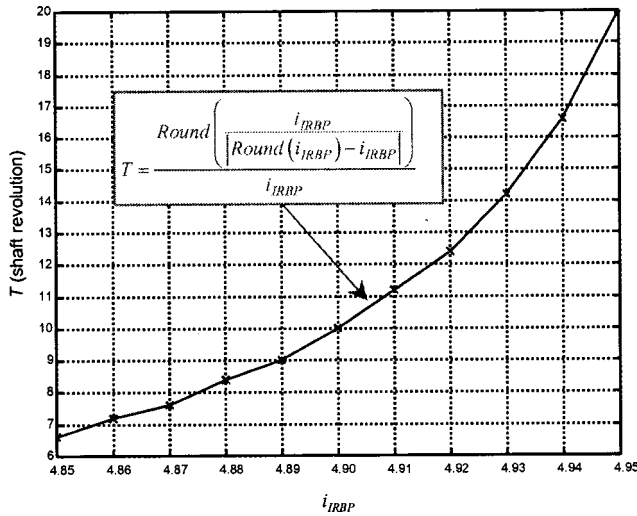


Fig. 5 Relation between i_{IRBP} and detected spike group period T

$$\alpha_{\text{delay}} = [\text{Round}(i_{IRBP}) - i_{IRBP}] \times \frac{360 \text{ deg}}{i_{IRBP}} \quad (1)$$

where $\text{Round}(i_{IRBP})$ represents a round number for i_{IRBP} (for example, $\text{Round}(4.9)=5$, $\text{Round}(4.1)=4$). In Fig. 4, the defect contact spot moves “forward” (from “ \diamond_a ” to “ Δ_a ,” the same direction as Ω) within the effective zone as α_{delay} is assumed to be greater than zero in this case. It would move “backward” in the

case of $\alpha_{\text{delay}} < 0$. In time base the two adjacent negative spikes have in terms of shaft rotations (degree) an interval

$$\alpha_{IR} = 360 \text{ deg} + \alpha_{\text{delay}} = \text{Round}(i_{IRBP}) \frac{360 \text{ deg}}{i_{IRBP}} \quad (2)$$

The interval α_{IR} will be longer than 360 deg shaft rotation for $\alpha_{\text{delay}} > 0$ and shorter for $\alpha_{\text{delay}} < 0$.

For the third and fourth shaft revolutions, the scenario will be similar to that for the first and second revolutions, as marked with “+” and “*” symbols. For the fifth shaft rotation, since the defect contact spot, marked with “ O_a ,” is beyond the effective zone, no spikes will be shown in time base.

This no-spike situation in time base will last until the defect contact spot in the left side marked with subscript “e,” as shown in Fig. 4, moves into the effective zone, thus making another similar cycle as is discussed above. From Fig. 4, such a spike group cycle T can be expressed in terms of shaft revolutions as

$$T \approx \frac{360 \text{ deg}}{i_{IRBP}} - \frac{|\alpha_{\text{delay}}|}{|\alpha_{\text{delay}}|} + 1 = \frac{1}{|\text{Round}(i_{IRBP}) - i_{IRBP}|} \quad (3)$$

Since the defect spot contacts a ball with a cycle of $360 \text{ deg}/i_{IRBP}$ shaft rotation, the following expression holds:

$$360 \text{ deg } T = n \frac{360 \text{ deg}}{i_{IRBP}} \quad (4)$$

where n is an integer. It follows that

$$n = \text{Round} \left(\frac{i_{IRBP}}{|\text{Round}(i_{IRBP}) - i_{IRBP}|} \right) \quad (5)$$

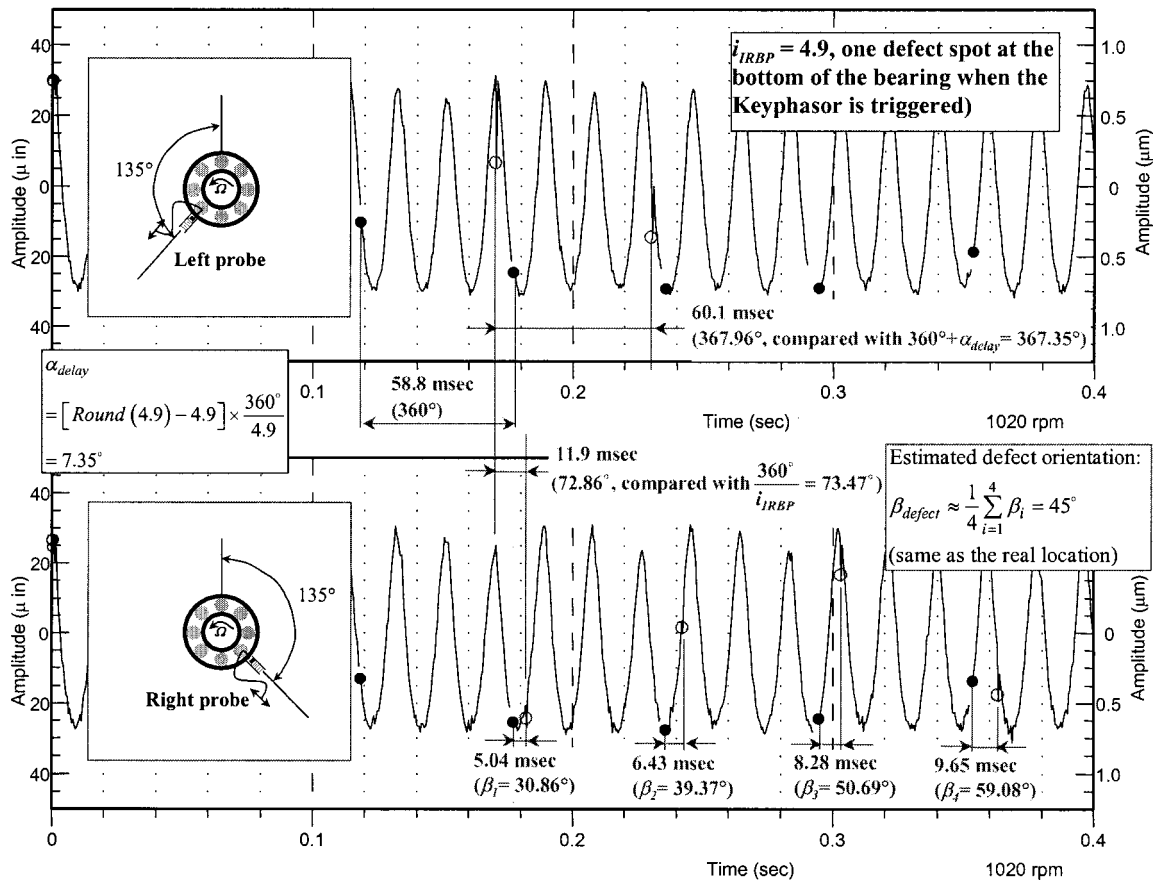
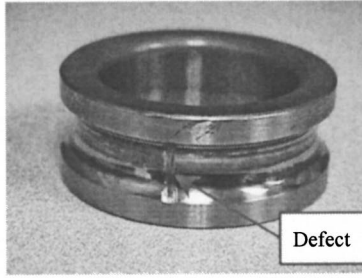
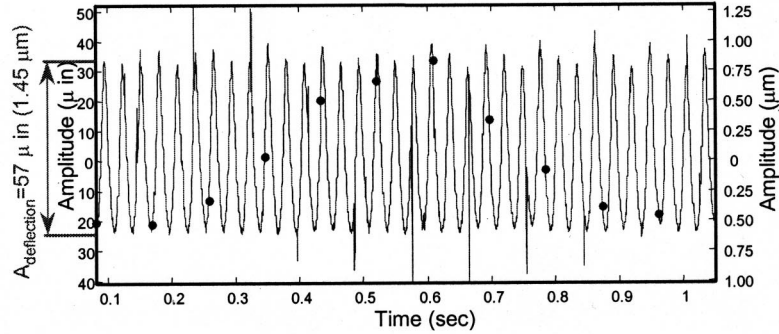


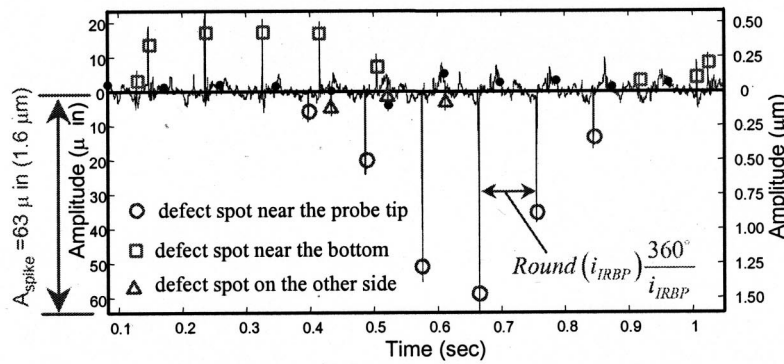
Fig. 6 Measured data in time base from displacement transducer



(a)



(b)



(c)

Fig. 7 More severe defect case ($A_{\text{spike}}/A_{\text{deflection}}=1.1$) at speed 680 rpm with hydraulic load 1379 kPa (200 psi); (a) real defect, (b) time base signal, and (c) time base signal after removing $i_{\text{ORBP}} \times$ and $2i_{\text{ORBP}} \times$ components

Thus the period T is given by

$$T = \frac{n}{i_{\text{IRBP}}} = \frac{\text{Round}\left(\frac{i_{\text{IRBP}}}{|\text{Round}(i_{\text{IRBP}}) - i_{\text{IRBP}}|}\right)}{i_{\text{IRBP}}} \text{ shaft revolutions.} \quad (6)$$

Note that a slight change in i_{IRBP} causes a much bigger change in detected spike group cycle T , as shown in Fig. 5. Therefore, a change in i_{IRBP} , which is related to slip, can be more accurately estimated from T .

During a cycle T in time base, the number of consecutive spikes n_{spike} is approximately equal to

$$n_{\text{spike}} \approx \frac{\alpha_{\text{effective}}}{\alpha_{\text{delay}}}. \quad (7)$$

Assume that the effective zone is symmetric about the probe location, and that the Keyphasor[®]—a shaft fixed timing reference

signal—is aligned with the probe. Thus, from Fig. 4, the location of the inner race defect spot (in terms of shaft orientation) can be estimated by

$$\beta_{\text{defect}} \approx \frac{1}{n_{\text{spike}}} \sum_{i=1}^{n_{\text{spike}}} \beta_i \quad (8)$$

where β_{defect} is a shaft rotational angle delayed relative to the probe.

If two probes are configured at an angle which allows two defect contact events to occur within their effective zones, spikes will appear in their corresponding time base response with an interval of $360 \text{ deg}/i_{\text{IRBP}}$ rotation within a single shaft revolution. That can be used additionally to confirm an inner race defect in the study. In the field, however, having one probe is enough to identify the defect.

4.1.2 Real Data Analysis. For the test ball bearing, an artificial spall was made on the inner race and oriented on the shaft so

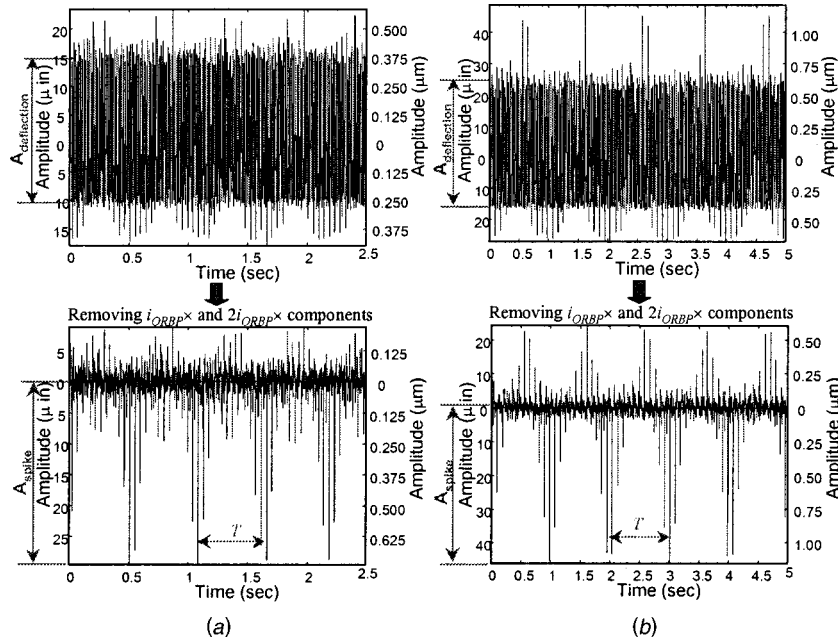


Fig. 8 Spike and deflection amplitude for the same defect shown in Fig. 7(a). (a) 1360 rpm without hydraulic load, and (b) 680 rpm with 689 kPa (100 psi) hydraulic load.

that the defect would be at the bottom of the bearing (180 deg from 0 deg) when the reference signal was triggered. The ratio of inner race ball pass frequency to shaft speed i_{IRBP} was found to be 4.9 (which could be determined from i_{ORBP} in spectrum and more accurately from T). Therefore, according to Eqs. (1) and (2), a delay angle within the detectable zone should be

$$\alpha_{\text{delay}} = [\text{Round}(4.9) - 4.9] \times \frac{360 \text{ deg}}{4.9} \\ = +7.35 \text{ deg (moving forward),}$$

and in time base the two adjacent negative spikes should have an interval of

$$\alpha_{IR} = 360 \text{ deg} + \alpha_{\text{delay}} = 367.35 \text{ deg} > 360 \text{ deg}$$

in terms of shaft rotation Ωt . Such a phenomenon should be repeated, according to Eq. (6), with a cycle of

$$T = \frac{\text{Round}\left(\frac{4.9}{\text{Round}(4.9) - 4.9}\right)}{4.9} = 10 \text{ shaft revolutions.}$$

Figure 6 shows experimental data from the displacement transducer for this case. A hydraulic force of 943 N (212 lbs) was applied to the nondrive end of the shaft. The rotor was running at about 1020 rpm. In time base, a time period of 58.8 msec within the two adjacent Keyphasor dots corresponds to one complete shaft revolution (rotation of 360 deg). Based on this ratio, two negative spikes apart by 60.1 msec have an interval of 367.96 deg. This is very close to the expected value of $360 \text{ deg} + \alpha_{\text{delay}} = 367.35 \text{ deg}$. The right probe once detects a spike 72.86 deg (11.9 msec) later than the left probe, which is also in good agreement with the expected value of $360 \text{ deg} / i_{IRBP} = 73.47 \text{ deg}$. Note that only 128 samples of data were taken for 360 deg shaft rotation in this case.

Using Eq. (8) along with the given β_i s in the time base for the right probe, as shown in Fig. 6, the location of the defect spot can be estimated in the following:

$$\beta_{\text{defect}} \approx \frac{1}{4} \sum_{i=1}^4 \beta_i = \frac{1}{4} (30.86 \text{ deg} + 39.37 \text{ deg} + 50.69 \text{ deg} \\ + 59.08 \text{ deg}) = 45 \text{ deg.}$$

The above value indicates that the defect spot had a 45 deg phase delay relative to the right probe, which was exactly the real defect location.

4.1.3 Severity Analysis. Since a bearing may run in various speed and load conditions, spike signals as well as deflection response can vary. As speed increases, the enhanced centrifugal forces of the balls along with the expansion of the inner race result in tight contact between balls and raceways. As loading increases, high pressing is maintained between the raceway and the balls. As a result, the outer race deflection and spike amplitude are increased, and smoothness of the deflection curve is greatly increased. Therefore, higher speed and load conditions make spike signals more noticeable. However, the spike signals reflecting defect occurrence are still present in time base at low speed and under light load, though not as obviously pronounced. Removing $i_{ORBP} \times$ and $2i_{ORBP} \times$ components due to normal loading deflection makes spikes pronounced without influence of their magnitude. For a given defect, the ratio of spike-to-deflection amplitude seems to have little change.

Figure 7 shows a more severe inner race defect case. The defect as shown in Fig. 7(a) is located at the horizontal position (90 deg from 0 deg) when the shaft reference signal is triggered. The left probe detects the corresponding response in time base as shown in Fig. 7(b). The spikes due to the defect become much pronounced after removing $i_{ORBP} \times$ and $2i_{ORBP} \times$ components due to normal loading deflection, as shown in Fig. 7(c). For this severe defect, more negative spikes are present as the defect contact spot passes near the probe tip. The spike-to-deflection amplitude ratio is

$$A_{\text{spike}} / A_{\text{deflection}} = 63/57 = 1.1.$$

In this case, positive spikes also appear. This is because the severe defect spot contacts a ball near the bottom where the maximum loading is located, thus impacting balls at other contact locations

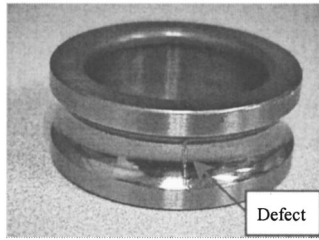


Fig. 9 Less severe defect case ($A_{\text{spike}}/A_{\text{deflection}}=0.4$)

including the one near the probe tip. Notice that small negative spikes occur due to a sudden loose contact when the defect is on the right side.

For the same defect as shown in Fig. 7(a), increases in speed yield slight increases in deflection amplitude $A_{\text{deflection}}$ and spike amplitude A_{spike} . As is expected, hydraulic loading is linearly proportional to the deflection amplitude $A_{\text{deflection}}$. Figures 8(a) and 8(b) show time base response in different speed and load conditions from those in Fig. 7. Notice that spike signals appear in a period T that is given by Eq. (3). In Fig. 8(a) a spike group cycle is $T=12.6$ shaft revolutions which correspond to $i_{\text{IRBP}}=4.921$, while in Fig. 8(b) it becomes $T=11.6$ shaft revolutions which correspond to $i_{\text{IRBP}}=4.914$, compared with $T=10.6$ shaft revolutions ($i_{\text{IRBP}}=4.905$) in Fig. 7. These variations are due to slippage between raceway and balls, which could be estimated. Regardless of changes in speed and load, ratio $A_{\text{spike}}/A_{\text{deflection}}$ remains almost the same (≈ 1.1).

For a less severe defect case as shown in Fig. 9, ratio $A_{\text{spike}}/A_{\text{deflection}}$ is decreased to around 0.4. This ratio, therefore, can be used to measure defect severity.

4.1.4 Fault Frequency Components. For spikes with an interval of $\text{Round}(i_{\text{IRBP}})360 \text{ deg}/i_{\text{IRBP}}$ shaft rotation in time base,

the corresponding multiple harmonic components of $i_{\text{IRBP}}/\text{Round}(i_{\text{IRBP}})\times$ can be seen in spectrum. Figure 10 shows these harmonics corresponding to spike signals due to the inner race defect as shown in Fig. 9. At speed 680 rpm, a frequency range of 10–20 kcpm is divided by about 15 intervals with harmonics of $i_{\text{IRBP}}/\text{Round}(i_{\text{IRBP}})\times (=0.98\times)$ for $i_{\text{IRBP}}=4.9$. Observing whether these fault frequency components occur is an additional tool to diagnose inner race defects in a rolling element bearing.

4.2 Outer Race Defect. An outer race defect spot in contact with balls/rollers does not move against probes for a rolling element bearing with its outer ring fixed to the casing. Figure 11 shows an outer race defect case at speed 680 rpm with 1379 kPa (200 psi) hydraulic loading. Since the defect spot faces the left probe, a sudden release of pressure between races and the passing ball leads to a negative spike on the outer race deflection curve. The number of spikes is the same as that of deflection cycles in time base. Thus, a spike interval for an outer race defect is given by

$$\alpha_{\text{OR}} = \frac{360 \text{ deg}}{i_{\text{ORBP}}} \quad (9)$$

Therefore, the fundamental frequency of spikes due to an outer race defect is equal to that of the outer race deflection, i.e., $i_{\text{ORBP}}\times$. Due to the defect, many of its harmonics are remarkable in a frequency range higher than $3i_{\text{ORBP}}\times$. Since ball sizes vary, harmonics of the cage (holding all the balls) frequency $i_{\text{C}}\times (=1/8i_{\text{ORBP}}\times)$ are also present as side bands.

It is found that spike magnitude and direction (positive or negative) due to an outer race defect vary with the defect orientation, as shown in Fig. 12. Numbers on the bearing indicate outer race defect orientations and correspond to the numbered spikes on the deflection curves on which spike magnitudes and directions are marked. The response for defect spots on the right side can be easily figured out based on Fig. 12. The discussed spots cover

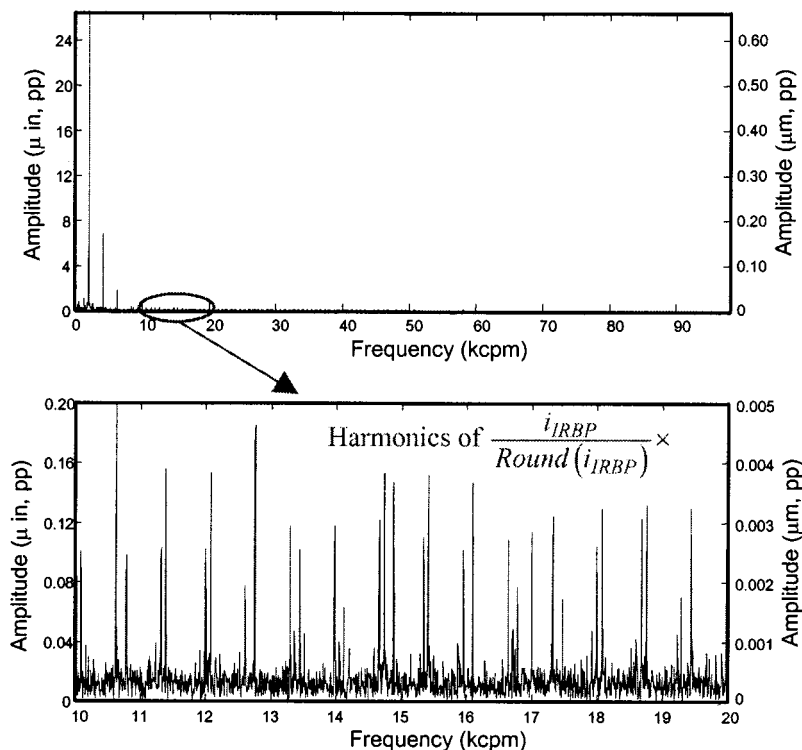


Fig. 10 Fault frequency components due to inner race defect using displacement transducer

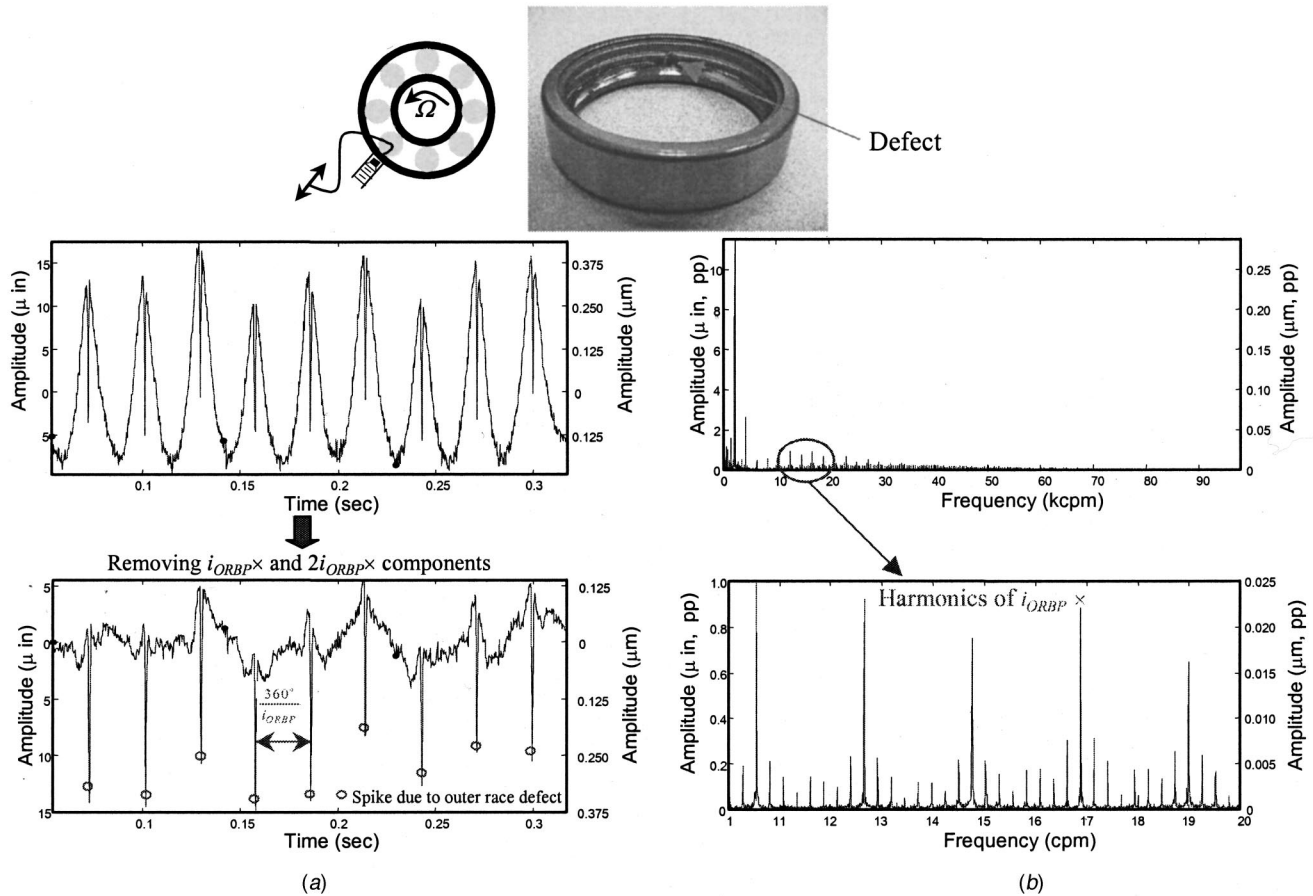


Fig. 11 Outer race defect signal measured by displacement transducer at speed 680 rpm without hydraulic loading; (a) time base, and (b) frequency spectrum

most of the loading zone where outer race defects usually occur. For a severe defect facing the probe, the fundamental frequency component $i_{ORBP} \times$ can decrease if the defect spot just faces the probe as in position "1," and can increase if the defect is at the bottom where maximum load is located as in position "5." However, many of its harmonics in the order higher than $3i_{ORBP}$ will become more pronounced than those without the defect. Having two probes is helpful to determine the defect orientation and severity.

4.3 Rolling Element Defect. If a rolling element (ball/roller) defect occurs, it will contact both the inner race and the outer race at its spin frequency $2i_R \times$. The probe detects a negative spike when the defect spot on the damaged ball/roller, which is held by the cage rotating at frequency $i_C \times$, contacts either the inner race or the outer race within the effective zone near the probe. Assume the probe detects spikes after k events of defect/raceway contacts. Thus, the following expression holds:

$$\frac{360 \text{ deg}}{i_C} \approx k \frac{360 \text{ deg}}{2i_R} \quad (10)$$

where k is an integer. It follows that

$$k = \text{Round} \left(\frac{2i_R}{i_C} \pm 0.5 \right). \quad (11)$$

Spike intervals due to a rolling element defect, detected by the probe in time base, are then given by

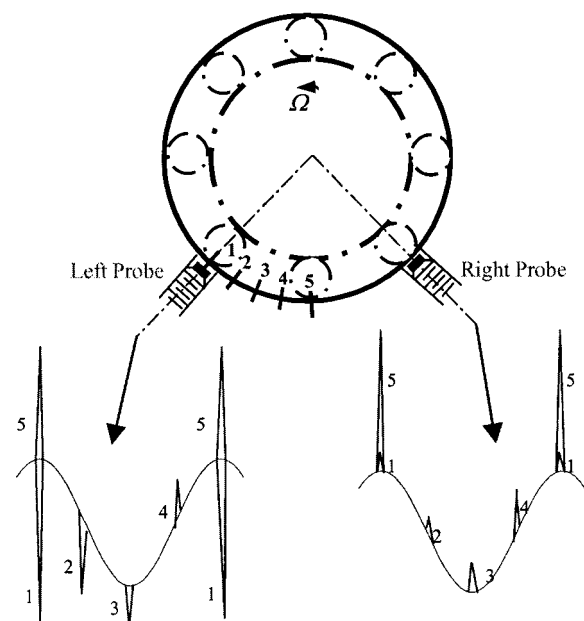


Fig. 12 Spike signal varying with defect orientation

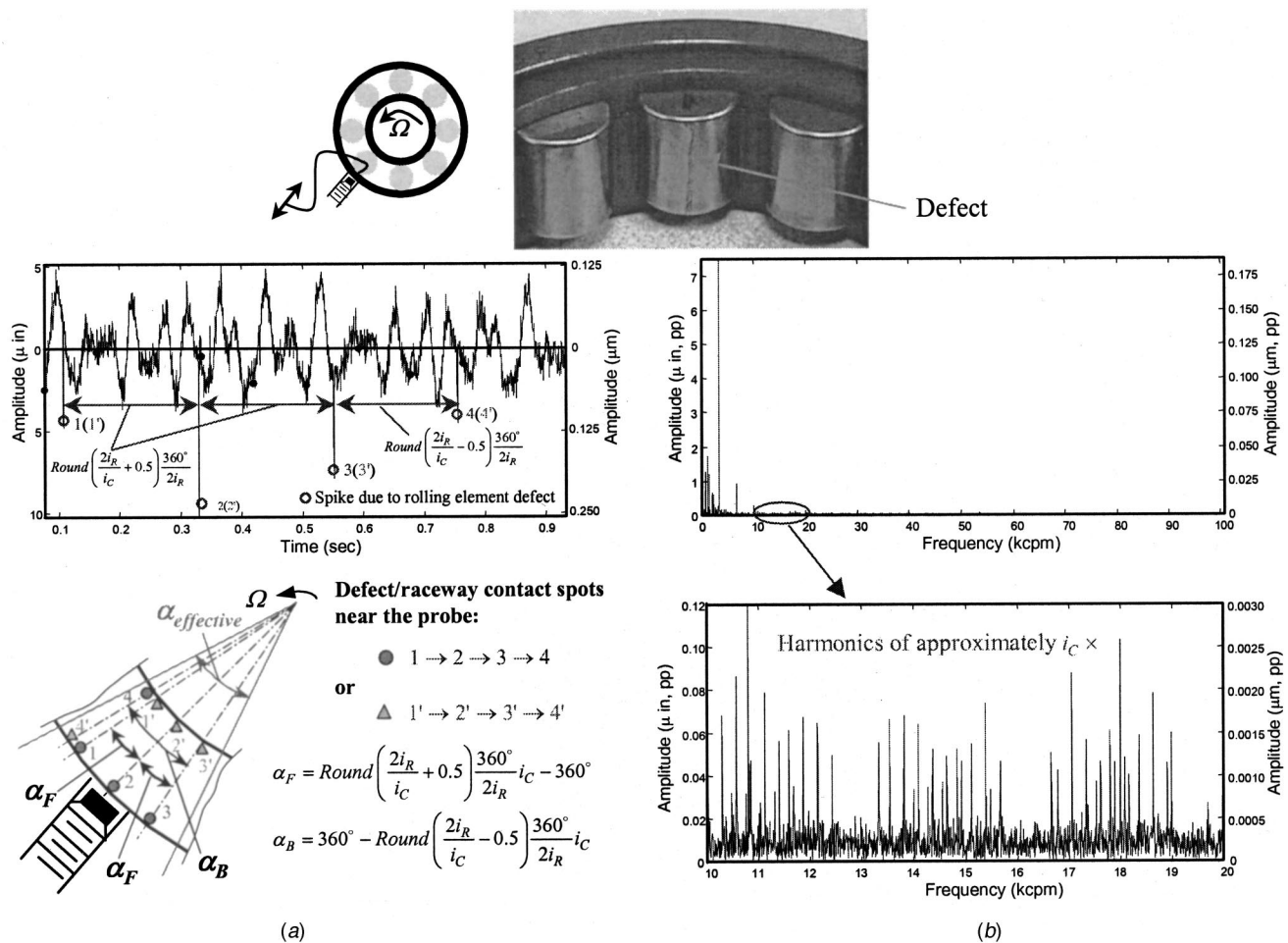


Fig. 13 Rolling element defect signal detected by the probe at 700 rpm with 1379 kPa (200 psi); (a) time base after removing $i_{ORBP} \times$ and $2i_{ORBP} \times$ components with corresponding defect contact locations near the probe, and (b) frequency spectrum

$$\alpha_{RE} = k \frac{360 \text{ deg}}{2i_R} = \text{Round} \left(\frac{2i_R}{i_C} \pm 0.5 \right) \frac{360 \text{ deg}}{2i_R} \text{ shaft rotations.} \quad (12)$$

Within the effective zone near the probe, real locations of defect contacts, detected by the probe, have intervals of

$$\alpha_{FB} = k \frac{360 \text{ deg}}{2i_R} i_C - 360 \text{ deg.} \quad (13)$$

The locations will move “forward” in the case of $\alpha_{FB} > 0$, and “backward” in the case of $\alpha_{FB} < 0$. An even number of k indicates that two contacts are on the same race, while an odd number means two contacts are on the different races. For spikes with intervals given by Eq. (12), many of harmonics of approximately $i_C \times$ are present in its corresponding spectrum. Figure 13 show a roller defect case, in which the defect is successfully detected in time base as well as in spectrum.

5 Summary and Conclusions

Inner race, outer race, and rolling element (ball/roller) defects, which often occur sequentially, can be successfully detected by directly measuring outer race deflection with high-gain displacement transducers. The defect signal is clearly present with spikes in the time base deflection facing the probe tip without casing influence, which would be inevitable by using casing-mounted accelerometers. Deflection amplitude is linearly proportional to radial load. An increase in speed makes a slight increment in

deflection amplitude. Spike amplitude due to defects usually varies with load and speed in the same way as deflection amplitude. Removing $i_{ORBP} \times$ and $2i_{ORBP} \times$ components due to outer race deflection makes spikes more evident. From the current study verified by experimental data, the following conclusions can be drawn:

1 For an inner race defect, negative spikes are seen in several consecutive shaft revolutions with an interval and then disappear intermittently or become positive, with a spike group cycle T . These parameters are uniquely determined by the inner race ball pass frequency ratio i_{IRBP} . A slight change in i_{IRBP} , which is related to slip, can be more accurately estimated from the corresponding big change in T . For a severe inner race defect, positive spikes appear along with more negative ones.

2 For an outer race defect, a spike occurs in each deflection cycle at a rate of outer race ball pass frequency $i_{ORBP} \times$. The spike amplitude and direction (positive or negative) vary with the defect location relative to the probe. Having two probes is helpful to determine the defect location and severity.

3 For a rolling element (ball/roller) defect, spike intervals are related to not only rolling element spin frequency ratio i_R but also cage frequency ratio i_C . Spikes occur at an average rate of cage frequency $i_C \times$ in time base.

4 Defect severity can be determined by spike-to-deflection amplitude ratio, which remains almost the same regardless of load and speed changes.

5 Defect location in the raceway can be determined from spike locations in time base along with known probe orientation.

6 Defect signals detected by displacement transducers can also be seen in spectrum. Inner race, outer race, and rolling element defects are characterized with harmonics of $[i_{IRBP}/\text{Round}(i_{IRBP})]\times$, $i_{ORBP}\times$, and $i_C\times$, respectively.

References

- [1] Monk, R., 1972, "Vibration Measurement Gives Early Warning of Mechanical Faults," *Process Eng.*, **Nov.**, pp. 135–137.
- [2] Boto, P. A., 1971, "Detection of Bearing Damage by Shock Pulse Measurement," *Ball Bear. J. S.K.F.*
- [3] Dyer, D., and Stewart, R. M., 1978, "Detection of Rolling Element Bearing Damage by Statistical Analysis," *ASME J. Mech. Des.*, **100**, pp. 229–235.
- [4] McFadden, P. D., and Smith, J. D., 1984, "The Condition Monitoring of Rolling Element Bearings by the High-Frequency Resonance Technique—A Review," *Tribol. Int.*, **17**, pp. 3–10.
- [5] Eshleman, R., 1980, "The Role of Sum and Difference Frequencies in Rotating Machinery Fault Diagnosis," *I. Mech Eng*, C272/80.
- [6] Mathew, J., and Alfredson, R. J., 1984, "The Condition Monitoring of Rolling Element Bearings Using Vibration Analysis," *ASME J. Vibr. Acoust.*, **106**, pp. 447–453.
- [7] Bently, D. E., 1982, "Monitoring Rolling Element Bearings," *Orbit*, **3**, No. 3, pp. 2–15.
- [8] Harker, R. G., and Sandy, J. L., 1989, "Rolling Element Bearing Monitoring and Diagnostics Techniques," *ASME J. Eng. Gas Turbines Power*, **111**, pp. 251–256.
- [9] Kim, P. Y., 1984, "A Review of Rolling Element Bearing Monitoring (III): Preliminary Test Results on Eddy Current Transducer Technique," *Proceedings of Third International Conference on Vibrations in Rotating Machinery*, The Institution of Mechanical Engineers, York, England, pp. 119–125.
- [10] Holm-Hansen, B. T., and Gao, R. X., 2000, "Vibration Analysis of a Sensor-Integrated Ball Bearing," *ASME J. Vibr. Acoust.*, **122**, pp. 384–392.

J. R. Markham
e-mail: Jim@AFRinc.com

H. M. Latvakoski

Advanced Fuel Research, Inc.,
87 Church Street,
East Hartford, CT 06108

S. L. F. Frank
e-mail: Stefan.Frank@blnh.siemens.de

M. Lüttke

Siemens Power Generation,
Huttenstrasse 12,
10553 Berlin, Germany

Simultaneous Short and Long Wavelength Infrared Pyrometer Measurements in a Heavy-Duty Gas Turbine

Advanced thermal barrier coatings (TBCs) are increasingly being used in high-performance turbine engines. For optimized use of the coatings, accurate surface temperature measurements are required in the combustion environment. Current on-engine pyrometers, which use short infrared wavelengths to accurately measure the temperatures of metal surfaces, show increased uncertainties when used on TBCs. Studies have suggested that long infrared wavelengths are a suitable alternative. Therefore, to evaluate the response of both wavelength regions, simultaneous measurements with short and long wavelength infrared pyrometers have been accomplished in the first stage turbine of a Siemens V84.3A 60 Hz 180 MW engine at the Berlin Gas Turbine Development and Manufacturing Center. [DOI: 10.1115/1.1473822]

Introduction

Manufacturers of gas turbine engines see a need to operate their engines at higher temperatures to increase power, improve fuel consumption, and lower emissions into the environment ([1–3]). This is leading to new designs and the use of new materials (ceramics instead of metal and ceramic thermal barrier coatings (TBC) on metal) inside the engines. Suitable diagnostic sensors are required for engine testing, for permanent monitoring of performance, and for identifying operation and maintenance problems when the advanced engines are installed for service. Measuring the surface temperature of engine components in the combustion environment is needed to ensure optimized engine performance while monitoring for signals of impending engine failures.

Radiation thermometry (optical pyrometry) has been successfully applied by Siemens [4] and others ([5–7]) on traditional engines for many years. Pyrometers that have been developed and utilized for measuring the surface temperature of 1st stage stationary and rotating airfoils detect hot part thermal radiation at wavelengths in the near-infrared spectrum, generally in the 1.0 μm region. These short wavelength infrared (SWIR) pyrometers provide for accurate surface temperature measurements from fully oxidized metal parts whose short wavelength radiative properties are conducive to such measurements (i.e., high emittance, low reflectance, and no transmittance).

However, studies by Advanced Fuel Research, Inc. (AFR) ([8]) and others ([9]) have shown that ceramics which show promise as thermal barrier coatings (TBCs) in turbine engine applications have low, variable emittance and significant reflectance, and transmittance at short wavelengths, which may cause increased uncertainties of measurement for SWIR pyrometry. Combustion reflection has been shown to contribute up to 70% of the measured SWIR signal in the worst case when used on TBCs ([10]). However, in the long wavelength infrared (LWIR), TBC emittance is high and stable (i.e., near blackbody), and transmittance is relatively low ([8,9]). The low transmittance provides for the measurement of temperature at the surface of the TBC ([11]).

The measurements were accomplished with two cylindrical probes of the Siemens standard pyrometer design ([12]) that are traversed between two vanes into the flow channel. One probe remains unchanged (SWIR) whereas the LWIR probe is modified to make it suitable for the long infrared wavelength sensor that is developed by AFR for use with TBC parts ([13–15]). A flexible, hollow waveguide is used to transfer LWIR energy from TBC parts to a pair of mercury-cadmium-telluride (MCT) detectors in order to simultaneously measure two LWIR regions, with radiance sampling at rates up to 1 MHz. Narrow-band filters select wavelengths centered around 10.5 and 11.8 μm . The SWIR is equipped with a silicon avalanche photo detector using the spectral region from 0.7 to 1.1 μm and sampling rates of up to 1 MHz.

The collaboration of AFR and Siemens Power Generation is an obvious benefit to the development of the LWIR pyrometer. The Siemens Gas Turbine Development and Manufacturing Center in Berlin has been supporting the development of heavy duty gas turbines for over 25 years and instrumentation has become highly sophisticated ([4,16]). SWIR pyrometry has been applied for over ten years ([17]). Turbine blade cooling designs have primarily been qualified through the results of SWIR pyrometry using a traversing device to position the pyrometer probe radially and by rotation about its axis ([18]).

This paper reports simultaneous measurements with Siemens' SWIR pyrometer and AFR's LWIR pyrometer from the turbine first stage under base load when fired with either natural gas or fuel oil.

Experimental Setup

The Siemens V84.3A 60 Hz 180 MW gas turbine is shown in Fig. 1. It is characterized by a disk-type rotor with central bolt, a 15-stage compressor, an annular combustor ring with 24 hybrid burners for natural gas and liquid fuel, and a four stage turbine. The first-stage turbine holds 80 blades, 73 with TBC and 7 uncoated. Figure 2 presents the relative orientation of the SWIR and LWIR pyrometer probes that intrude into the combustion flow near the first-stage turbine. These probes are water cooled and provide clean-gas purge for protection of the internal optics. The purge gas of each probe is automatically adjusted in order to keep the overpressure constantly higher than the turbine combustor op-

Contributed by the International Gas Turbine Institute (IGTI) of THE AMERICAN SOCIETY OF MECHANICAL ENGINEERS for publication in the ASME JOURNAL OF ENGINEERING FOR GAS TURBINES AND POWER. Paper presented at the International Gas Turbine and Aeroengine Congress and Exhibition, New Orleans, LA, June 4–7, 2001; Paper 01-GT-026. Manuscript received by IGTI, Dec. 2000; final revision Mar. 2001. Associate Editor: R. Natole.

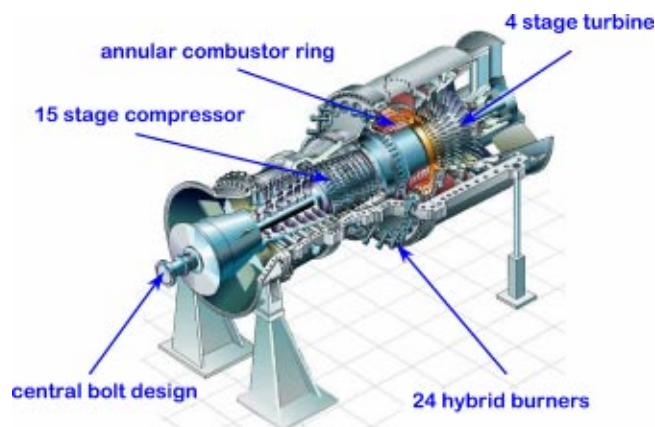


Fig. 1 Siemens Gas Turbine V84.3A 180 MW 60 Hz

erating pressure at any time. The Siemens' pyrometer probes are computer controlled and have the capabilities for radial scanning and rotation about their axis. The LWIR probe is inserted between the first stage vanes, and views downstream to the blades. The turbine rotation sweeps the field of view across the leading edge and most of the pressure side of the blade. The distance from the optical aperture of the probe to the blades varies from 65 mm at the optical focus on the leading edge to 130 mm near the trailing edge. The SWIR probe is inserted in the combustion flow prior to the first stage vanes, and views through to the blades. The distance from the optical aperture of this probe to the blades varies from 180 mm at the leading edge to 250 mm near the trailing edge. The SWIR probe and the LWIR probe are positioned such that the optical paths are parallel, thus allowing for the simultaneous collection of data at almost identical position on the blades. Table 1 provides a comparison of the pyrometers for geometries and data collection parameters used.

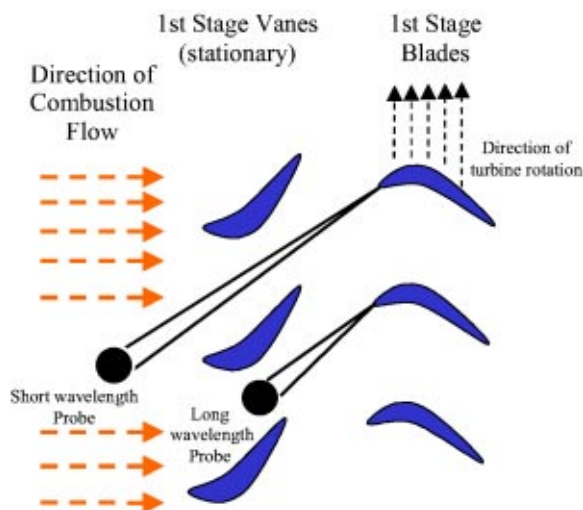


Fig. 2 Top view sketch showing orientation and view of intrusion probes in Siemens' V84.3A 180 MW turbine engine

Table 2 Measured emittance for test articles

	LWIR Pyrometer		SWIR Pyrometer
	11.8 μm	10.5 μm	0.9
"Brown" TBC	0.93	0.92	0.83
"White" TBC	0.97	0.95	0.48
Oxidized Blade	0.54	0.56	0.83

Here we report LWIR and SWIR pyrometer measurements with probes inserted to stationary positions of common depth into the combustion gas path and during radial scanning. During the pyrometer measurements, gas temperature was measured via thermocouple probes ([18]) and total gas pressure via static pressure tappings. All pyrometer measurements were performed when the engine was stabilized for output power (170 MW for natural gas firing, 180 MW for fuel oil). Before attachment to the engine each pyrometer was calibrated by the standard method of recording signal response as a function of well-known temperature when observing a blackbody radiation standard.

In preparation for the measurements, the spectral radiative properties of TBC and uncoated blade specimens were measured with AFR's high-temperature spectral emissometer ([8,19]). As a practical matter, an understanding of an object's emittance, as well as the related properties of reflectance and transmittance, benefits optical pyrometry of the object. Siemens provided AFR with two TBC on metal blade samples that would be representative of the TBC blade surfaces to be measured in the turbine engine. Combustion conditions had altered the initial "white" TBC to exhibit "brown" in the visible spectrum, as was observed by boroscope for V84.3A engine parts. A new or white TBC article was also supplied, and AFR had a representative uncoated metal blade that had been exposed to many hours of engine operation. The oxidized metal blade served as a qualitative indication rather than an absolute indication of the radiative properties of the uncoated metal surfaces on the Siemens turbine. Since the TBCs supplied were on metal substrates, transmittance data were not obtained and emittance was determined from reflectance. Table 2 summarizes the average emittance value in the wavelength regions of the two pyrometers for the test articles when heated in the emissometer to nominally 900°C (1650°F). The uncertainty in the emittance measurements is estimated to be within $\pm 3\%$ of the values indicated in the table ([19]).

In the bandpasses of the LWIR pyrometer, the white TBC is most near to blackbody (approaching 1.0), and the two brown TBCs present a slight drop but still are above 0.9. New TBC vanes removed after engine operation were previously observed for similar color changes in both the visible and LWIR ([11]). The oxidized metal exhibits a low LWIR emittance, or high reflectance. In the SWIR bandpass, the brown TBC emittance in the 0.85 range is much higher than the original white TBC. The oxidized metal blade exhibits a SWIR emittance similar to the discolored TBC.

The total radiation measured by a pyrometer consists of the blade radiation according to its temperature and emittance (ϵ , in the bandpass of the pyrometer) and the ambient radiation (i.e., especially combustor flame radiation) according to the ambient temperature and the reflectance (ρ) of the blade. Calculations have previously been reported for both the SWIR ([18]) and LWIR ([11]) that provide guidance as to the maximum temperature error

Table 1 Comparison of pyrometers

	Distance to Target	Measurement Spot Size	Sample Rate	Data Points per Blade	Center Wavelength(s) of Bandpass(es)
LWIR	65–130 mm	3.0–5.0 mm	500 KHz	104	10.5 μm , 11.8 μm
SWIR	180–250 mm	3.0–5.0 mm	500 KHz	104	0.9 μm

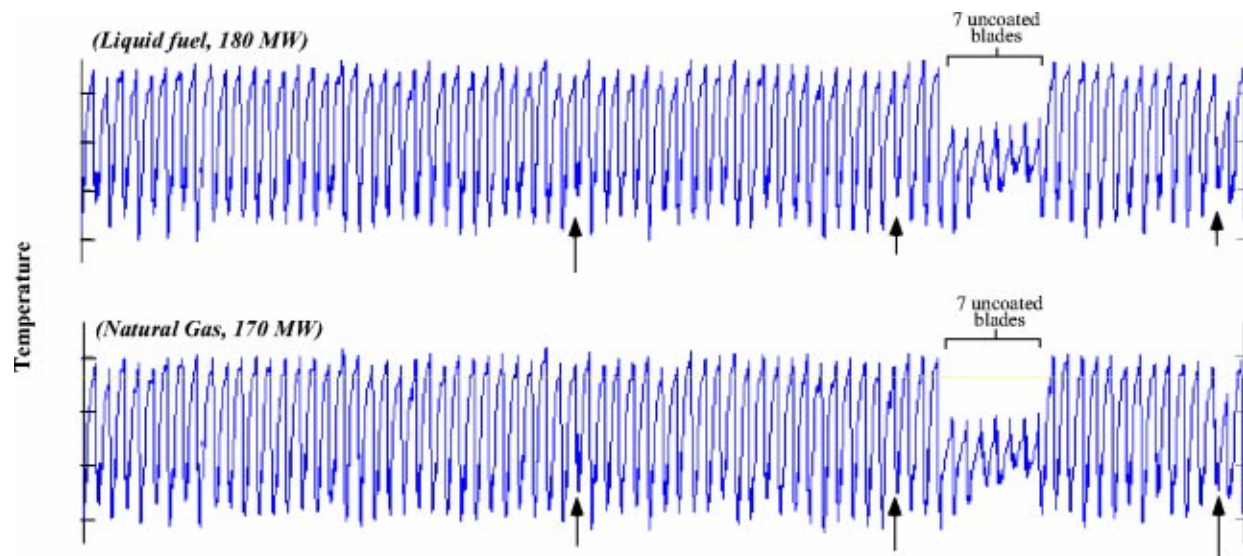


Fig. 3 LWIR pyrometer data: data traces obtained (average of 200 turbine revolutions) for liquid fuel and natural gas firing for the 80 blade turbine; a correction for gas interference has been applied

that can be imposed on a blade of $\varepsilon \geq 0.85$ ($\rho \leq 0.15$). These references point out that the view angles off the blade surface relative to the combustor outlet and vanes block a portion of combustor radiation and serve to significantly reduce the potential error. Recent analysis of SWIR measurements in the engine measured here have concluded that SWIR pyrometer measurements in the presence of natural gas flame radiation yield reasonable results, whereas a suitable flame radiation correction is essential for the more broad-band radiating sooty flame of fuel oil ([18]). In the LWIR, a suitable gas correction is necessary for either fuel since the combustion product gases H_2O and CO_2 contribute radiance, the largest concern being the direct radiance contribution to the pyrometer by the presence of these gases between the probe and the blade surface ([11]).

Results and Discussion

Since these are the first LWIR pyrometer measurements of turbine blades during engine operation, we first present the time-averaged temperature traces obtained with the LWIR probe at a

stationary position for 200 revolutions of the turbine. Figure 3 presents the data from the $10.5 \mu m$ bandpass, after a gas correction has been applied, for both fuel oil and natural gas firing of the engine. Blade-to-blade variations are observed to be consistent for both operating conditions of the engine. For examples, arrows in the figure are pointing to the leading edge temperature of three TBC blades that are consistently hotter during both operating conditions. One of these blades (second from the end on the right) consistently exhibits lower temperatures on its pressure surface than the other TBC blades. The group of seven uncoated blades is clearly distinguishable for each engine condition. Three of these present leading edge temperatures that are lower than the other four.

Figures 4 and 5 present thermal images generated from radiance data collected simultaneously during natural gas firing of the engine with the SWIR and LWIR pyrometers during continuous blade measurement. That is, each probe is traversed slowly from the tip of the hub at a rate of 2-mm per turbine revolution, and data is acquired continuously. Figure 4 is for one of the TBC

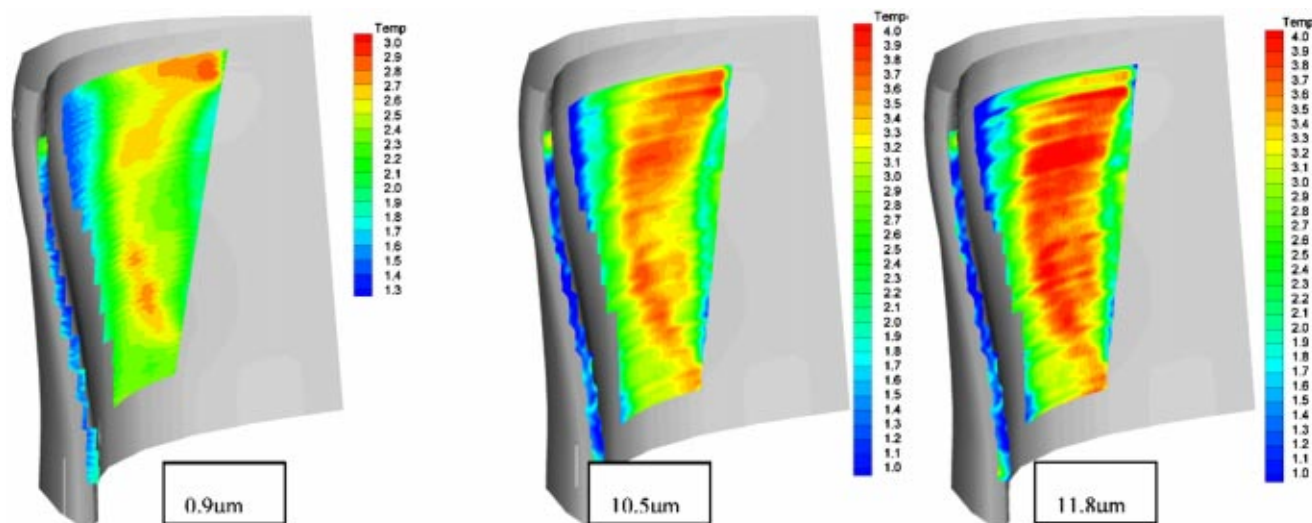


Fig. 4 SWIR and LWIR thermal images for a TBC blade during natural gas firing. The LWIR data has been corrected for hot gas radiation.

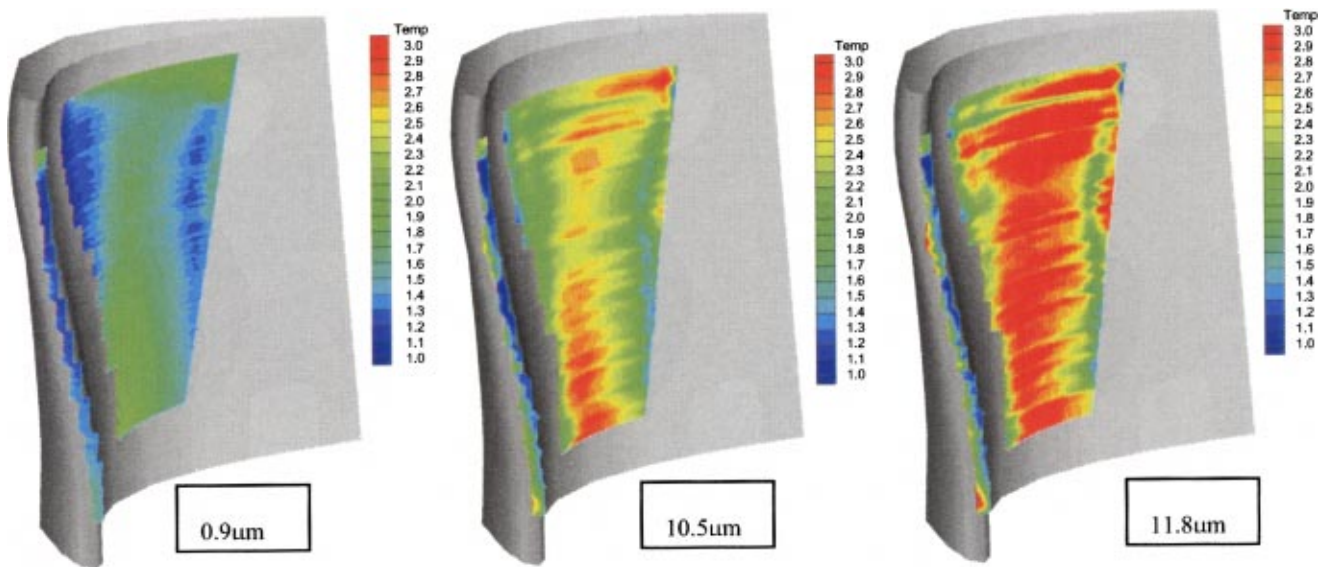


Fig. 5 SWIR and LWIR thermal images for a metal surface blade during natural gas firing. The LWIR data has been corrected for hot gas radiation.

blades and Fig. 5 is for an uncoated, metal surface blade. For the SWIR pyrometer, no corrections have been applied during the conversion of measured radiance signal to temperature. However, both bandpasses of the LWIR pyrometer have had a correction applied to account for the combustion gases in the optical beam path. The HITEMP spectral database of the wavelength dependent absorption/emission features for H_2O and CO_2 as a function of temperature ([20]) was used with the available gas temperature and pressures at the turbine to predict the extent of interference at both LWIR bandpasses. With these inputs, the model assumed that the magnitude of gas interference was only dependent on the distance from the probe to the point on the blade surface being measured. The combustion gas influence is readily apparent in the original signal recorded by the LWIR pyrometer during continuous data collection of multiple turbine revolutions. The standard deviations when measuring one particular point on a blade for multiple revolutions is about 2.7% for the $10.5\ \mu m$ LWIR bandpass and 4.3% for the $11.8\ \mu m$ LWIR bandpass, whereas it is 0.2% for the SWIR. Since simultaneous pyrometer measurements were obtained, the level of LWIR fluctuations can not arise from real temperature changes of the blade at each turbine revolution. Fluctuations in the gas radiance contribution can be caused by a combination of combustion dynamics and the interaction of the pressurized IR-inactive purge gas exiting the optical aperture of the pyrometer's intrusion probe.

In Figure 4 for the TBC blade, similar trends in temperature across the leading edge and pressure surface of the blade are observed for the one SWIR bandpass and the two LWIR bandpasses. The leading edge is the coolest with some temperature increase at top and bottom. The pressure surface presents a cool zone in the upper left, then presents a hotter band down the length of its center. In the center, the $0.9\ \mu m$ bandpass is consistently indicating temperatures $100\text{--}120^\circ C$ lower than the $10.5\ \mu m$ bandpass. The $11.8\ \mu m$ bandpass is generally indicating the highest temperatures, but within $10\text{--}15^\circ C$ of the $10.5\ \mu m$ bandpass.

Similar trends in temperature readings resulted from the uncoated, metal surface blade. Here again the $0.9\ \mu m$ bandpass is consistently indicating lower than the $10.5\ \mu m$ bandpass, but there is more disagreement between the $10.5\ \mu m$ and $11.8\ \mu m$ bandpasses ($\sim 50^\circ C$) with the longer wavelength providing the highest temperatures.

Comparisons between pyrometer measurement values and those from numerical calculations ([21]) of temperatures at midspan of

these two blades are exhibited in Figs. 6 and 7. The qualitative similarities and magnitude differences between the SWIR and LWIR measurements as described above are apparent. The numerical calculations represent the TBC surface temperature in Figure 6 and the surface temperature of the metal in Fig. 7. As mentioned above, the LWIR gas correction that relies on the HITEMP spectral database assumes that the combustion gas interferences are strictly the direct radiance contributions from between the probe and the blade surface. However, in the LWIR, laboratory measurements of the representative metal (engine oxidized) blade exhibited $\epsilon = 0.55$ and $\rho = 0.45$ (see Table 2). With these LWIR radiative properties, hot combustion gases directly in the probe's view as well as at any view angle off of the blade surface can contribute reflected gas radiance to the LWIR measurements. This can include radiance contributions from the hot-test gas upstream in the combustor to gas in the immediate vicinity of the metal blade. Therefore, the displayed disagreement between the LWIR bandpasses and the SWIR bandpass in Fig. 7 is

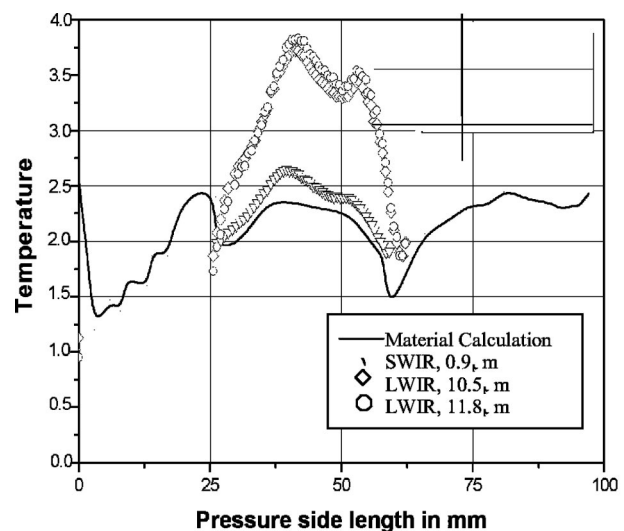


Fig. 6 Temperature traces for a TBC blade during natural gas firing. The LWIR data has been corrected for hot gas radiation.

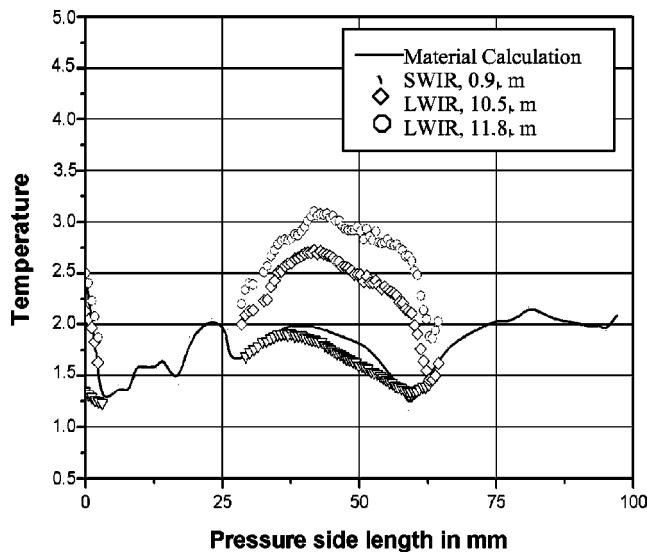


Fig. 7 Temperature traces for a metal surface blade during natural gas firing. The LWIR data has been corrected for hot gas radiation.

expected. The disagreement between the two LWIR bandpasses is also expected since the 11.8 μm bandpass is known to be more influenced by combustion gases than the 10.5 μm bandpass ([11]). For the TBC surface in Fig. 6, the TBC emittance (see Table 2) is much higher ($\epsilon=0.93$) and reflectance much lower ($\rho=0.07$), thus the reflected radiance contribution is much reduced and the two LWIR bandpasses show a close convergence of temperatures when using the HITEMP-based correction.

In the TBC data of Fig. 6, it is observed that the temperature data from both pyrometers converge at the minima in the calculation trace at the locations of ~ 30 mm and ~ 60 mm on the pressure side length. These minima correspond to locations of blade cooling air lines. The local cooling of the TBC in these regions by the escaping air flow may be serving to minimize the thermal gradient from the surface of the TBC to the bond coat on the metal substrate. It is known that new or fresh TBCs exhibit significant transmittance at SWIR wavelengths, so SWIR pyrometry would be measuring a distribution of temperatures through the depth of a fresh TBC. The TBC on this blade has had its SWIR emittance and reflectance altered by the environment of engine operation (see Table 2), but its transmittance properties have not yet been determined. Recent transmittance studies on TBC exposed to engine operation in locations other than the Siemens engine development center have demonstrated a transition to SWIR opacity in one case of a liquid fueled aircraft turbine engine ([11]), but opacity was not observed for TBC taken from a heavy duty power generating turbine engine after a few hundred hours of operation for one part, nor after several thousand hours of operation for another part. If the TBC on the turbine of this study is significantly transmissive at the SWIR bandpass and the thermal gradient through the TBC is much reduced at the blade's cooling air lines, the SWIR and LWIR pyrometers would be expected to indicate a similar temperature, as they do here. With the typical thermal gradient in place on the TBC, the LWIR pyrometer measuring surface temperature would be expected to indicate a higher temperature than the averaged depth temperature indication of the SWIR device. Of the data of Fig. 6, we still must reconcile the absolute highest temperatures provided by the LWIR pyrometer, which are higher than anticipated when compared to the calculation trace between the air cooling lines of the pressure surface. The SWIR pyrometer results from this TBC of relatively high emittance is in fairly close agreement with the calculation trace.

The spectral transmittance for this TBC is to be measured, analysis refined, and further simultaneous measurements are to be performed to complete the analysis.

Conclusions

Measurements on TBC parts in the SWIR with proven instrumentation are generally regarded as unreliable due to low emittance, semi-transmittance, and high reflectance of the coating. During this study, SWIR pyrometer measurements and calculations demonstrated a reasonable closure, but the transmittance of the altered TBC must be determined before expressing confidence that this is a surface temperature measurement. The new LWIR pyrometer demonstrated its ability to identify blade to blade temperature differences for TBC on the 80 blade turbine that were consistent for both firing conditions of the Siemens V84.3A engine. Distinct temperature profiles on individual blades were obtained. By subtracting the combustion gas contribution to the signal as calculated from known engine operating conditions and an available spectral database for high temperature gases, the two LWIR bandpasses were consistently within 10–15°C for the on-engine TBC data collected here.

The continuing focus of this study is to reconcile the agreement of the SWIR and LWIR TBC temperatures measured near the blade cooling air lines with the disagreement in measurements over much of the pressure surface in between these lines. If the combustion gas interferences are suitably accounted for, the near-blackbody emittance of TBC should provide the more accurate measure of surface temperature. On-engine testing will continue, including measuring the brightness temperature of the combustor with the LWIR pyrometer (as has been done previously with the SWIR pyrometer ([12])) to evaluate reflection sources and correction methodologies.

Acknowledgments

AFR's work in LWIR pyrometry during this collaboration was supported by funds received from the U.S. Department of Energy Small Business Innovation Research (SBIR) program under grant #DE-FG02-96ER82112. AFR also thanks Siemens Power Generation for additional support provided during the research reported in this paper. The authors express gratitude to Mr. B. Klix (Siemens) for calibration of the pyrometers and to Mr. H. Bals (Siemens) for the comparisons of calculated and measured values.

Nomenclature

Acronyms

LWIR = long wavelength infrared
SWIR = short wavelength infrared
TBC = thermal barrier coating

symbols

ϵ = emittance
 ρ = reflectance
 μm = microns (wavelength)

References

- [1] Gaul, G., McQuiggan, G., Southall, L., and Diakunchak, I., 2000, "The Siemens Westinghouse Advanced Turbine Systems Program," *Proceedings of the 1999 Advanced Turbine Systems Annual Program Review Meeting*, Pittsburgh, PA, U.S. Department of Energy Office of Industrial Technologies and National Energy Technology Laboratory, publication DOE/NETL-2000/1129.
- [2] Kayser, W. A., Kumpfert, J., Schulz, W., and Petters, M., 1999, "Advanced Materials and Coatings for Future Gas Turbine Technology," *Proceedings of AGARD-AVT Symposium on Gas Turbine Operation and Technology for Land/Sea/Air Propulsion Power Systems*, Ottawa, Canada, Advisory Group for Aerospace Research & Development (AGARD), Neuilly-Sur-Seine, France.
- [3] Czech, N., Schmitz, F., and Stamm, W., 1997, "Advanced Coatings for Gas Turbine Blades," *VGB Kraftwerkstechnik*, 77, 3.
- [4] Seume, J., 1997, "Valuable Experience Gained From 25 Years of Operating the Full-Load Gas Turbine Test Facility in Berlin," *Power Gen. Europe '97*, Madrid.

- [5] Kirby, P. J., Zachary, R. E., and Ruiz, F., 1986, "Infrared Thermometry for Control and Monitoring of Industrial Gas Turbines," ASME Paper 86-GT-267.
- [6] Suarez, E., 1994, "Turbine Pyrometry," NASA Conference Publication 10167.
- [7] Rooth, R. A., 1999, "Transient Pyrometer Shows Its Value," *Pyrometer News*, Issue 2, KEMA, The Netherlands.
- [8] Bonanno, A. S., Serio, M. A., and Markham, J. R., 1994, "High Temperature Radiative Property Measurements of Advanced Turbine Materials," NASA Conference Publication 10167.
- [9] Atkinson, W. H. and Cyr, M. E., 1990, "Evaluation of Sensors for Temperature Measurement of Ceramic Materials," NASA Conference Publication, 10051.
- [10] Suarez, E., 1994, "Temperature Measurements of Thermal Barrier Coated Turbine Blades," NASA Conference Publication 10167.
- [11] Markham, J., Latvakoski, H., Marran, D., Neira, J., Kenny, P., and Best, P., 2000, "Challenges of Radiation Thermometry for Advanced Turbine Engines," *ISA Trans.*, **397**, pp. 299–313.
- [12] Frank, S. L. F., Holt, T. O., Eisenlohr, H., and Raake, D., 2001, "Application of a High Resolution Turbine Pyrometer to Heavy Duty Gas Turbines," ASME/IGTI Paper 2001-GT-572.
- [13] Markham, J. R. and Kinsella, K., 1998, "Thermal Radiative Properties and Temperature Measurements From Turbine Coatings," *Int. J. Thermophys.*, **19**(2), pp. 538–545.
- [14] Latvakoski, H. M., Markham, J. R., Harrington, J. A., and Haan, D. J., 1998, "Sensor for Performance Monitoring of Advanced Gas Turbines," *SPIE*, **3535**, pp. 115–123.
- [15] Latvakoski, H., Markham, J., Borden, M., Hawkins, T., and Cybulski, M., 2000, "Measurement of Advanced Ceramic Coated Superalloys With a Long Wavelength Pyrometer," *AIAA Paper* 2000-2212.
- [16] Frank, S. L. F., Lechner, C., Mertens, B., and Warnack, D., 2001, "Testing of the V84.3A Gas Turbine in the Test Facility of the Siemens Gas Turbine Development and Manufacturing Center in Berlin," ASME/IGTI paper 2001-GT-0396.
- [17] Schulenberg, T., and Bals, H., 1987, "Blade Temperature Measurements of Model V84.2 100MW/60 Hz Gas Turbine," ASME Paper 87-GT-135.
- [18] Frank, S. L. F., 2000, "Surface Temperature Mapping of Gas Turbine Blading by Means of High Resolution Pyrometry," *ICHMT Turbine 2000 Int. Symp. Izmir/Turkey*.
- [19] Markham, J. R., Kinsella, K., Carangelo, R. M., Brouillette, C. R., Carangelo, M. D., Best, P. E., and Solomon, P. R., 1993, "A Benchtop FT-IR Based Instrument For Simultaneously Measuring Surface Spectral Emittance and Temperature," *Rev. Sci. Instrum.*, **64**(9), pp. 2515–2522.
- [20] Rothman, L. S., et al., 1998, "The HITRAN Molecular Database," *J. Quant. Spectrosc. Radiat. Transf.*, **60**(5), pp. 665–710.
- [21] Haendler, M., Raake, D., and Scheurlen, M., 1997, "Aero-Thermal Design and Testing of Advanced Turbine Blades," ASME Paper 97-GT-066.

Z. R. Khalaf

B. Basler

ALSTOM (Switzerland) Ltd.,
Baden, Switzerland

Kalaeloa: Combined Cycle Power Station Burning Low Sulfur Fuel Oil in Its Ninth Successful Year

This paper presents the O&M experience at the Kalaeloa Cogeneration Plant. Performance issues and other problems related to firing heavy oil in a combustion turbine are presented together with their long-term solutions leading to the current successful operation of the IPP power station in Hawaii, USA. [DOI: 10.1115/1.1447240]

Introduction

Finding people to work at Kalaeloa Cogeneration Plant is one of the easiest jobs in ALSTOM POWER O&M (formerly ABB). The plant is located at the southwest tip of the Island of Oahu, only 20 miles from Honolulu and Waikiki Beach. ALSTOM POWER has been operating Kalaeloa for nine years. As a combined cycle power plant operating in cogeneration mode, the plant provides approximately 20 percent of the electric power to the island, and approximately 120,000 lb/hr of steam to the refinery next door.

This paper describes the long term operating experiences at this plant, which operates on low sulfur fuel oil (LSFO), an uncommon fuel for combustion turbine applications.

Project Conception

The plant, Fig. 1, is a 200 MW turnkey power station built in 1991 by ABB under the then-new regulations of Independent Power Producers (IPP), made an excellent fit for the island's needs. The project started rather slowly, as the whole idea of IPP was still young in the late 1980s. The source of the idea was that Hawaiian Independent Refinery, Inc. (HIRI), a major producer of the island's transportation fuels, had to ship the heavy residue back to the mainland for disposal. At the same time, there was a need for power on the island and a conventional steam power plant was being on considered. ABB convinced the investors and the local businesses that a combined cycle plant would be more efficient, could be built in less time, and could burn the heavy oil as the primary fuel. The consortium of Southern Electric International Inc. (SEI), C. Itoh & Co. (ITOH), and ABB investigated the independent power producer rules and became convinced that this project was a good investment. In 1988, a power purchase agreement (PPA) was signed with the local utility, Hawaiian Electric Company (HECO). At the same time, a steam supply and fuel purchase agreement was signed with HIRI, the permits were secured, and a 25-year O&M contact was signed with ALSTOM O&M.

The project goal was to fulfil HIRI's needs for approximately 120,000-lb/h steam, while purchasing 1.8 million barrels of fuel annually. Additionally, the island's electricity needs, served by HECO, was to secure another step in its reserve capacity. The plant currently generates about 20 percent of the islands total electricity needs; and provides approximately one-third of the refinery's steam requirements.

In May 1996, ABB Energy Ventures acquired full ownership of the plant from SEI and ITOH; one year later a majority interest in the plant was sold to a partnership consisting of PSEG Global of New Jersey and Harbert Power of Alabama. The new owners recognized several areas for improvement in the plant and invested funds for their development. Some of these improvements are described in this paper.

Plant Description

Two Type 11N gas turbines, with silo combustors, single-burner design, rated at 74.6 MW at 76°F (24.4°C) each, including NO_x control by steam injection, are used as prime movers. Gas exhausts into individual horizontal dual pressure Deltak waste heat recovery steam generators (HRSG). The steam turbine, an ABB KT type, provides additional capacity of 51.5 MW. Steam is extracted and sent to the refinery at three pressure levels: 700, 450, and 230 psig. This combined cycle arrangement makes it possible to achieve an overall heat rate of 8310 Btu/kWh at design conditions. As a PURPA (Public Utility Regulatory Policy Act) qualified facility, the plant is required to maintain an annual operating efficiency of 42.5 percent or better, while exporting steam for process use equivalent to 15 percent of electrical output. Figure 2 is a simple schematic of the plant cycle. Figure 3 is a schematic of the process steam system.

The plant was built in two phases. GT1 was put into service first in a simple cycle configuration firing gas, and was declared commercial in March 1990. Installation of GT2 and the steam plant continued leading to full-plant commercial operation in May 1991.

The primary fuel for the facility is low sulfur fuel oil (LSFO). The fuel is treated at the refinery to meet low alkali requirements, then pumped through a permanent piping system to two LSFO tanks of one million gallon capacity each. Diesel is used as a secondary fuel for emergency operation, startup, and flushing procedures. Diesel is also supplied directly from the refinery through a permanent piping system, and stored in a 50,000 gallon tank. A

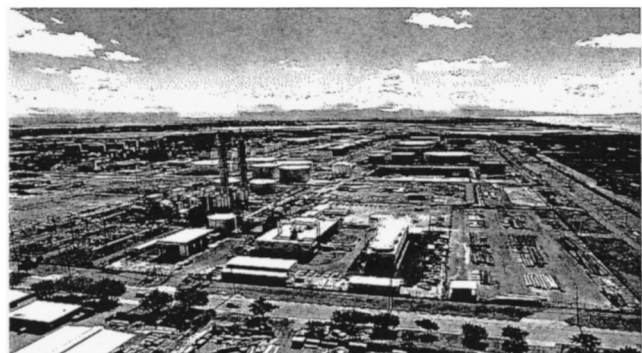


Fig. 1 Aerial view of Kalaeloa cogeneration

Contributed by the International Gas Turbine Institute (IGTI) of THE AMERICAN SOCIETY OF MECHANICAL ENGINEERS for publication in the ASME JOURNAL OF ENGINEERING FOR GAS TURBINES AND POWER. Paper presented at the International Gas Turbine and Aeroengine Congress and Exhibition, Munich, Germany, May 8–11, 2000; Paper 00-GT-590. Manuscript received by IGTI November 1999; final revision received by ASME Headquarters February 2000. Associate Editor: D. Wisler.

KALAELOA COMBINED CYCLE COGEN

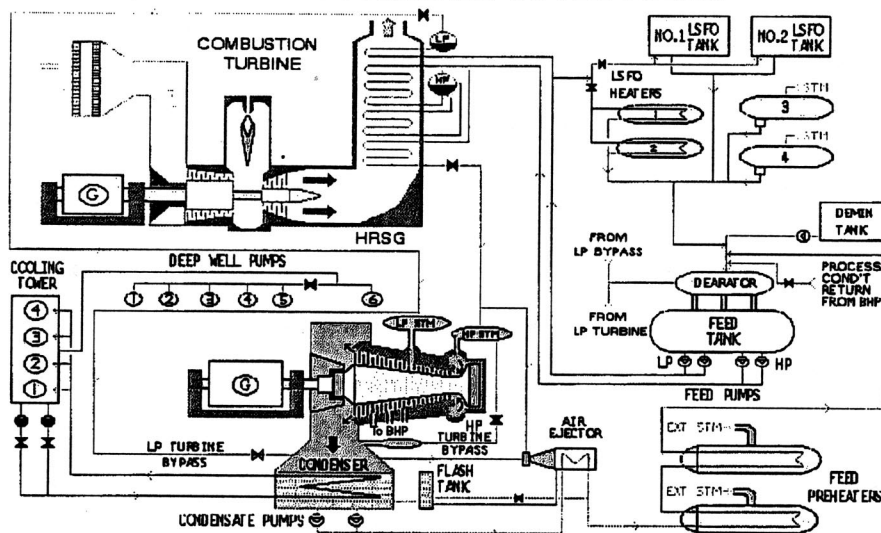


Fig. 2 Simple schematic of plant cycle

KALAELOA PROCESS STEAM TO BHP

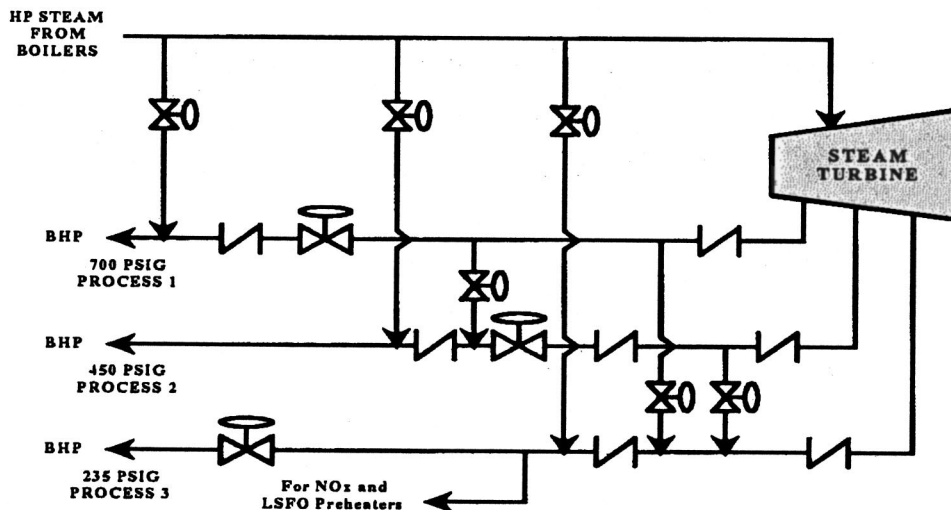


Fig. 3 Schematic of process steam system

simplified sketch of the fuel system is depicted in Fig. 4. From the fuel tanks, the fuel is moved via forwarding pumps. LSFO passes through preheaters that raise the temperature to 350°F (176.7°C), whereas diesel is not heated. Distribution headers split the fuel streams into three branches: one to each turbine fuel pump block and a third to the standby fuel pump block. A set of three-way valves allows the switchover between diesel and LSFO. Each fuel stream continues to a dedicated fuel pump that raises the pressure to 1400 psig and delivers it to the turbine fuel nozzle. The standby fuel block is common to both units, and is put into service whenever a dedicated fuel block needs to be removed from service for repair or maintenance. The switch to the standby fuel block is manual and requires the affected unit to be shut down.

A propane system provides ignition. Startup occurs on diesel oil, and the switch to LSFO occurs at approximately 20 MW.

Prior to the switch to LSFO, a corrosion inhibiting additive has to be introduced to the turbines. The additive system parallels that for fuel. A 13,000 gallon storage tank, forwarding pumps, dosing pumps and a piping/valve system is installed and allows additive

to be pumped directly to the fuel nozzle. The additive is mixed into the fuel stream in the nozzle (prior to atomization) and simultaneously enters the combustion zone.

Impact of Fuel on Plant Operation

A fuel specification and typical sample analysis are shown in Tables 1 and 2. The fuel is ash-bearing and in principle a heavy oil with a density of 19.8 API and a pour point >92°F (33.3°C). It requires preheating in the storage tanks, up to 180°F (82.2°C), in order to remain pumpable. Additional heating in a two-stage pre-heater, using hot water and LP-steam as a heat source, is necessary to allow pumping through the fuel nozzle. The viscosity of 45.7 cSt at 212°F (100°C) requires preheating to typically 350°F (176.7°C) at the burner tip for good atomization.

A maximum sulfur content of 0.50 percent is allowed by specification; the fuel typically has a 0.45 percent sulfur content as received. The trace elements listed in Table 1 show a rather a typical distribution for heavy oil. Whereas Vanadium is rather low

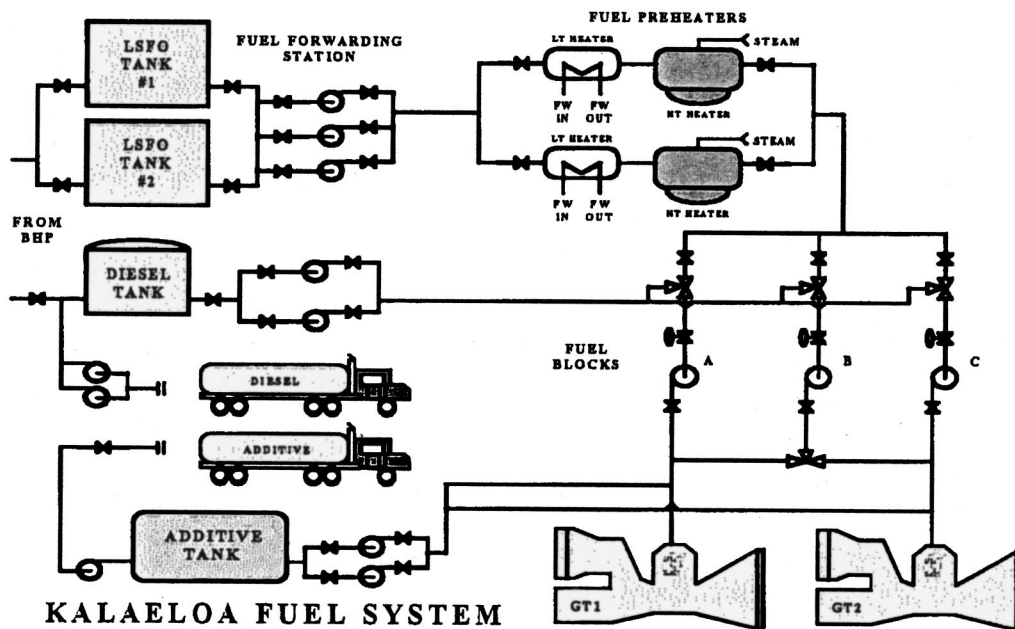


Fig. 4 Simplified sketch of fuel system

and in the range of 10–20 ppm, nickel reaches levels of up to 40 ppm. The washed fuel hardly shows any sodium and potassium and usually is considerably lower than 1 ppm.

The presence of Vanadium in the fuel requires the addition of a magnesium-based additive to avoid accelerated oxidation by low melting vanadates. When the fuel is burned, the vanadium forms an ash, Vanadium pentoxide V_2O_5 , which melts at approximately 1450°F and is a major contributor to high temperature corrosion. The additive, refer to Table 3 for typical analysis, contains 11 percent to 13 percent by weight magnesium in the form of magnesium sulfonate. This compound reacts in the flame zone to produce less harmful ashes with higher melting points such as $MgSO_4$, MgO , and $3MgO \cdot V_2O_5$ with melting points of approxi-

mately 2150, 5000, and >5000°F (1177, 2760, and >2760°C), respectively. With the turbine inlet temperature at 1854°F (1012.2°C), these newly formed ashes will pass through the turbine without melting or adhering to the blades.

Table 2 Typical sample analyze
BHP PRE-SHIPMENT REPORT
Product: Low Sulfur Fuel Oil

Method	Test	
D 4052	API Gravity, Avg.	19.8 API
D93	Flash Point, PMCC	330°F
D 97	Pour Point	33°C
D445	Viscosity@210°F	45.7cSt
D445	Viscosity@210°F	214 SUS
D4294	Sulfur	.45 Wt%
D1796	Water & Sediment	.30 Vol%
D482	Ash	
D240	Heat Content, Gross	19003.7 BTU/lb
D 240	Heat Content, MM Gross	6.216 BTU/Bbl
D4 629	Nitrogen, Total	
AES	Sodium & Potassium	<1 ppm
AES	Vanadium	5 ppm
AES	Nickel	35 ppm
AES	Lead	0 ppm
AES	Calcium	2 ppm
AES	Zinc	<1 ppm

Table 1 Fuel specifications
LSFO FUEL SPECIFICATION

Product Spec.	Test Method	Typical Range (Average)	Limits
API	ASTM D4052	14-23 (18)	14 min.
Density kg/liter	ASTM D1298	.97-.90 (.95)	.972 max.
Flash	ASTM D93 ASTM D445		150 °F
Viscosity SSU@210°F	ASTM D2161	100-450 (250)	450 max.
Pour Point °F	ASTM D97		130°F
Water & Sediment	ASTM D1796	.1% - 1%	1.0% vol. max.
Ash	ASTM D482	.01% - .06% (.02%)	.06% wt. max.
Gross (Higher) Heating Value	ASTM D240	6.0-6.40	6 MMBTU/BBL min.
Nitrogen	Dohrmann Chemiluminescence	.60%	.60 wt. max.
Sodium plus Potassium	AA*	20**	1 ppm max.
Vanadium	AA*	10-20 (10)	20 ppm max.
Sulfur	ASTM D4294	.50%	.50% wt. max.
Delivery Temperature			180 °F min.
Delivery Pressure			**25-50 lbs./sq. in. absolute

* To be tested by Automatic Absorption/Emission Spectroscopy (AAS/AES)

** Delivery Pressure may be adjusted by mutual agreement by both parties.

*** Untreated

Table 3 Additive analysis

Product:	Organic Overbased Mg Product
Quantity	44,040 LBS
Specific Gravity	1.151
Magnesium, Wt%	11.2
Flash Point, PMCC, C	60
Viscosity CST @ 100 C, CST	13.4
Water, Vol. %	1
Sodium, ppm	42
Calcium, ppm	1159
Lead, ppm	16
Vanadium, ppm	8

The amount of additive required is in the range of 3/1 Mg/V. A determination of additive flow is made each time a fuel delivery is made.

The chemistry of the deposition and corrosion prevention is quite complex. The formation of magnesium vanadates is actually happening, but the main buildup of deposits is magnesium sulfate and oxides. The presence of sulfates increases towards the cooler portions of the turbine and also Vanadium contents are increasingly higher there. In the front end of the turbine, one usually finds layer type structures changing from oxides to sulfates. Sulfates are usually water-soluble and can easily be washed off. Magnesium oxides form hard and hardly soluble rocky type deposits, mainly on the pressure side of the turbine blades.

The effect of nickel has been the subject of debate for quite some time. Whereas some people see it as an inhibitor, others see it as a potential melting point depressant and therefore, a corrodant. The phase diagram of nickel vanadates and nickel sulfates shows that at high Ni/V ratios, the melting points are high, hence the risk of corrosion due to such components is low. If, however, the ratio is lower, low melting Ni-vanadates, which could act as the very corrosive alkali-vanadates, could form. Therefore, the Ni/V ratio needs to be carefully watched. At a Mg/V ratio of 3, and the usually high Ni/V ratio, no accelerated corrosion is detected.

The use of ash-bearing fuel has operational consequences that have an impact on availability and performance. Fouling results in degradation of the gas turbines and HRSG performance, and consequently power and heat rate losses. In order to restore the performance, downtime is required to wash off deposits creating such degradation. Per the contractual agreement for Kalaeloa, once a week, each unit is shutdown for a 12-hour period for turbine washing. A typical schedule would have GT1 down Friday nights at 8:00 p.m. to Saturday mornings at 8:00 a.m. GT2 is similarly down Saturday evenings through Sunday morning.

The turbine wash process is fairly simple and short in duration. In most cases, a 45-minute wash is adequate. Demineralized water is used for the wash, and neither chemicals nor detergents are used. Water is injected through built in nozzles installed around the perimeter at the inlet of the turbine. The majority of the time during the 12-hour shutdown is used for unit cool down.

History of Plant Performance

Currently the plant is in its ninth year of operation. Operating hours and starts for each unit are shown in Table 4. The plant runs at an average load of 180 MW and is operated as a base load plant. Steam production is maintained at 20 to 25 percent of power production.

Since its inception, the plant has had its share of problems and challenges. Through hard work, experience, and smart investments by the plant owner, many problems have been resolved and the plant is now running at a high level of availability and efficiency.

Key performance parameters the plant is measured against and guarantee points are shown at Table 5.

Figures 5 through 9 graph key performance parameters since startup. As stated before, the early days were troublesome, but the plant has now achieved significant success and continues to do so. Some of the problems encountered early in the project can be attributed to factors described below.

Table 4 Operating hours and starts
ACTUAL DATA AS OF SEPTEMBER 1999

	GT1	GT2
Ops Hours	62200	62500
EOH	84200	81900
Starts	1100	970

Table 5 Plant design performance and guarantees

Basic Design:	Contractual Guarantees
2 GT11N rated at 74.6 MW at 76°F	180 MW Firm Capacity
1 ST rated at 51.5 MW	120000 lbs/hr Process Steam
2 Dual Pressure Deltak HRSGs	42.5% Plant Efficiency
Main fuel is LSFO w/Diesel as back up fuel	<12 Contractual Unit Trips/year
120000 lbs/hr of Process Steam	> 88% EAF
8310 BTU/KWH with nom. Process Steam	<4% FO
TIT 1854°F	> 15% Steam Export

Start Reliability

Start reliability is defined as the number of successful starts divided by the number of start attempts. A successful start is counted each time the unit is synchronized. Excluded from start attempts are repeated attempts to start without attempting corrective action. Although start reliability is not a guaranteed performance parameter, it has direct impact on most guarantees.

Figure 5 shows the annual start reliability trend since commercial operation. Problems with the fuel system, described below, were the main reason for the poor start reliability during the earlier years.

Unit Trips

A contractual trip is defined as the immediate removal of a unit from service, whether operator or control system initiated, which requires the host utility to start up one of their units to make up for part or all of the lost load. For Kalaeloa, the number of contract unit trips per year is guaranteed not to exceed 12, above that, liquidated damages are assessed. Contractual unit trips since start of project are shown at Fig. 6.

Availability

Availability is defined as the ratio of available MWh divided by plant contractual capacity. The availability guarantee per the O&M contract is 88 percent. The lowest availability recorded by the plant was 89.1 percent during the second contract year, most down time was primarily due to fuel system malfunctions. A maximum of 94.4 percent was achieved in the sixth contract year during which shortest C Inspection at 18.5 days, was achieved. Figure 7 shows the availability data since the start of project.

Forced Outage

A forced outage is defined as the immediate removal of a unit from service, or the inability to place a unit back into service due to equipment malfunction rendering the unit inoperable or unsafe to operate. The guarantee per the O&M contract is a forced outage rate not to exceed 4 percent. The highest rate achieved was 2.37 percent in the second contract year, and the lowest was 0.47 in the third contract year. Again, the fuel system was the primary cause of forced outage during the earlier years. Figure 8 shows the forced outage data since start of project.

Efficiency

In accordance with the rules established by PURPA, the facility is required to produce steam at a minimum rate of 15 percent of total output, and maintain efficiency at a minimum of 42.5 percent. The efficiency is calculated as the ratio of electrical output plus half the thermal energy output divided by the fuel input:

$$\text{PURPA eff} = \frac{\text{Electrical Output} + (\text{Steam Thermal Output}/2)}{\text{Fuel Input}}$$

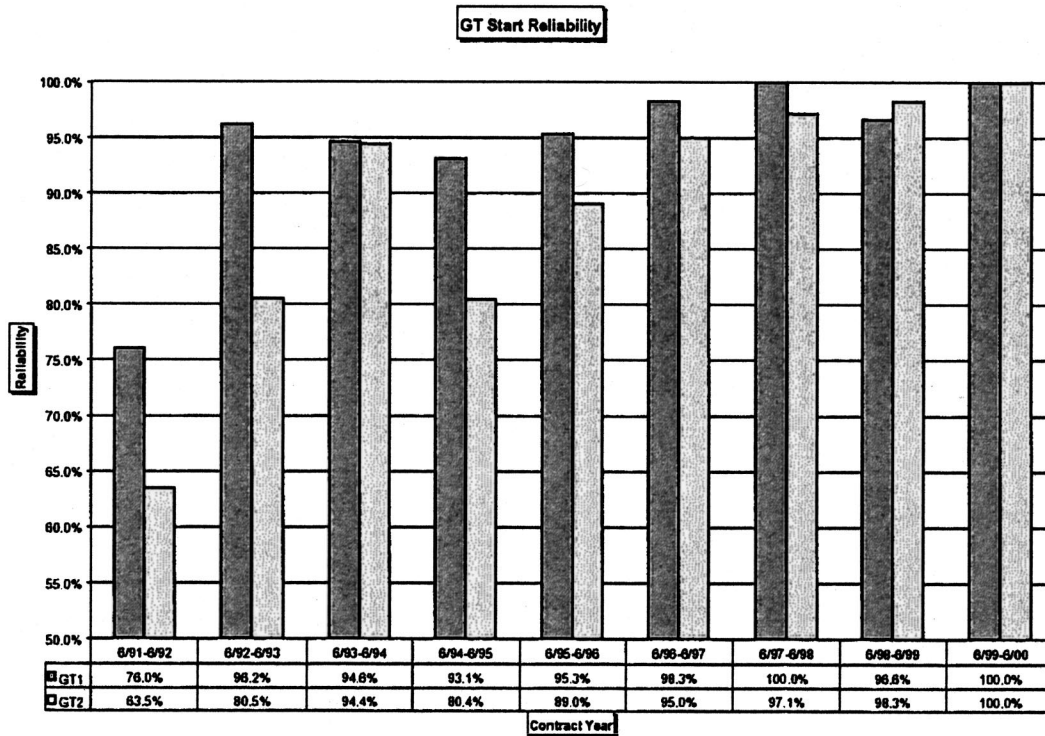


Fig. 5 GT start reliability chart

Figure 9 shows efficiency results since the start of project. While efficiency is not a contractual guarantee parameter, it must be met to maintain PURPA Qualifying Facility status. The efficiency of the plant has been controllable at the 42.5 percent level, however, with greater difficulty from year to year. This difficulty is the result of fouling in the HRSG, which causes deterioration of the steam cycle performance. The problem can be overcome by increasing steam export levels high enough thus causing the PURPA efficiency to come up, but at the same time, the heat rate suffers. Plant experience with boiler problems is discussed below.

Taming of the Fuel System

Much of the poor performance in the earlier years was attributable to the fuel system. Many trips, failed starts, and forced outage hours logged soon after start were the result of fuel system related issues. A re-evaluation of equipment specifications and process design led to many of the changes that helped bring the plant to its current state of high reliability. The following is a summary listing of some of the problems.

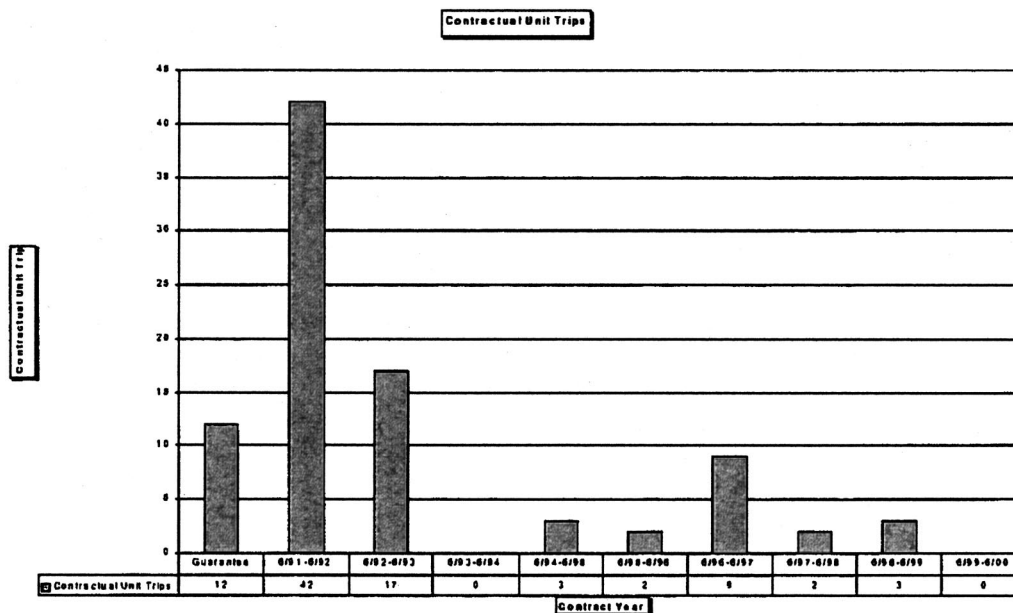


Fig. 6 Contractual unit trips chart

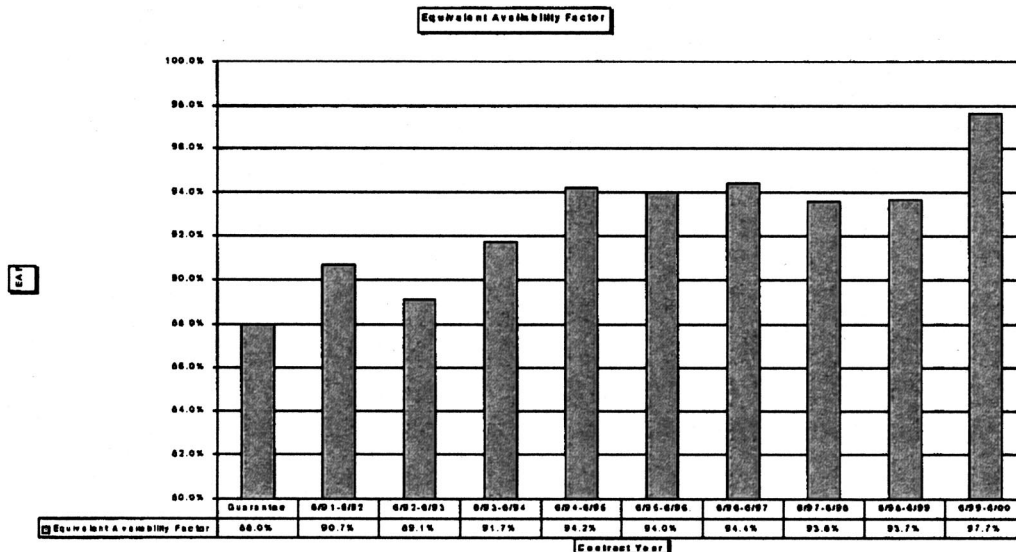


Fig. 7 Equivalent availability factor chart

Fuel Forwarding and Preheating System.

- Malfunctioning pressure relief valve caused fuel leakage tank to overflow. Tank high level generated a trip signal to fuel pumps on both units thereby taking the entire plant down. This problem was corrected by replacing the relief valve and replacing the trip due to high tank level with an alarm signal.
- Leakage in the fuel pre-heaters introduced LSFO into the steam cycle and water into the fuel system causing unstable combustion and flameouts. Pre-heaters tubes were seal welded to prevent further leakage. The addition of a constant pressure relief valve kept the pressure of the pre-heater steam always higher than the LSFO pressure; hence, a leak would allow steam into the fuel, but not fuel into the steam cycle.
- Improperly selected filters and contaminated fuel caused high-pressure drops in the lines resulting in unstable fuel delivery conditions. Problem was resolved by replacing filters with more suitable elements or removing them from service where possible.

- LSFO forwarding pumps experienced excessive wear and damage to the shaft seals. This was caused by the fuel leaving hard deposits when the seals cooled down. Heat tracing and insulation of the seals reduced the frequency of the problem. Excessive leakage of the pump seals was also caused by lack of expansion provisions in the original installation; the support system was corrected.
- LSFO forwarding pumps cavitated when the level in the LSFO tank fell below eight feet. The inlet strainers to the pumps were changed to a larger mesh and operation procedure was instituted to switch fuel tanks when one level dropped to ten ft. Fuel loading is done twice a week, which leaves at least one tank higher than minimum level at all times.
- LSFO forwarding pressure control was sluggish; causing plant trips and start failures. The entire pressure control system was re-evaluated and modified with new control valve, controller, and transducer.

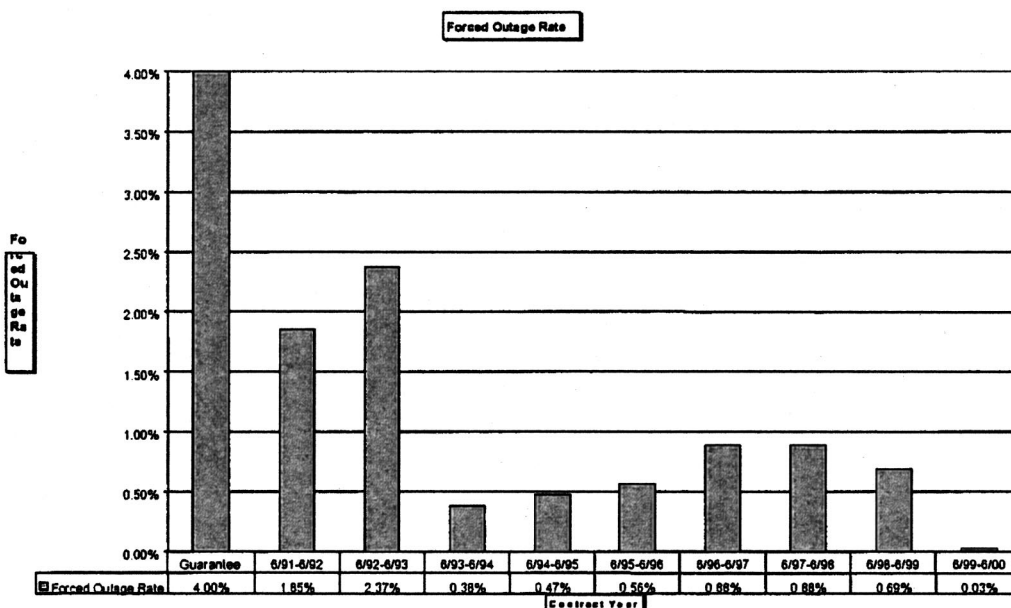


Fig. 8 Forced outage rate chart

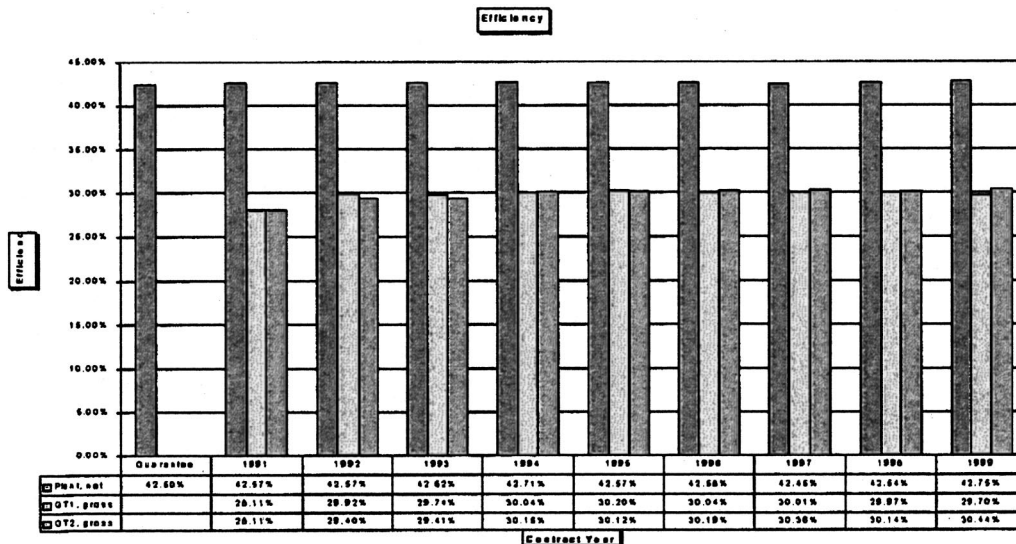


Fig. 9 Plant efficiency chart

- Original design called for two 100 percent fuel-forwarding pumps. Operationally, both were kept in service to reduce the risk of pressure loss. However, numerous problems were still experienced. A third pump, which was available in spare inventory, was installed to increase this system's availability.

Start-up of one LSFO pump while the other was in service caused a loss of suction pressure and both pumps tripped. This was resolved by installing variable speed drives.

- Loss of LSFO forwarding pumps due to electrical frequency variation was frequent for a period of time due to grid instability. The power supply to the pumps was changed to a UPS source.

Diesel Contamination

During the GT's ten-second ignition cycle, a self-sustaining flame needs to be established; otherwise the turbine shuts down. Diesel is used for normal startup and continues in service through synchronization and up to an appropriate load level in the range of 10 to 20 MW.

The original fuel switchover valves (three-way) allowed LSFO to leak back through the diesel line. This resulted in contaminated diesel going to the nozzle on start up affecting flow properties through the line, and ignition properties at the nozzle. Numerous failed starts occurred as a result. The valves were changed to a more robust type, and isolation valves were installed in both the LSFO and diesel side of each valve; the isolation valves allowed maintenance to be performed on these valves during weekend wash shutdowns. Currently, valve seals are replaced on a quarterly basis, and problems with contaminated diesel have not recurred.

Water in Fuel

Water from two different sources, which was present in the fuel, caused difficulties during startups. One source was the fuel supply. While the fuel specification is normally checked prior to delivery, it is suspected that occasionally water quantity higher than shown by lab analysis was present. Over time water collected at the bottom of the fuel tank and at some point entered the suction line to the transfer pumps eventually getting to the turbine. This problem was resolved by weekly water removal through installed drains, this procedure is still in use today. The amount of water removed each time varies from very little to several hundred gallons.

Another source of water was leakage through the fuel heaters. Once discovered, the heaters were taken out of service and modified to prevent recurrence.

Commissioning and Early Modifications

Commissioning work continued while the plant was in commercial operation. This work consisted primarily of troubleshooting various problems that were discovered as experience was gained with the plant. Solutions involved hardware and software changes. Due to load demand and contractual requirements, there were limited opportunities to perform the desired work. Signal simulations were performed to prevent loss of equipment while work was done on-line. Needless to say, things were occasionally missed and some loss of equipment was inevitable.

Some of the changes implemented by the commissioning team were not fully tested until the equipment was returned to service. Unfavorable results were occasionally encountered requiring removal of equipment from service to correct.

Redundancy built into the design of the plant had to be carefully reconsidered and improved where appropriate; particularly, protection schemes with 1 out of 2 logic had to be modified to 2 out of 3. "Bugs" were identified and eliminated, these were primarily in the fuel control system.

Ignition Torch

The original ignition torch was equipped with a conventional spark plug. Failure of the spark plug caused many failed starts and difficulty in accessing the spark plug caused the repair process to be very long. Several physical and procedural changes were made to reduce down time due to ignition problems, but eventually the spark plug was replaced with a glow plug. The glow plug consists of a metallic tip that heats up to glowing temperature as electric current passes through it. Once the glow plug design was fully developed, the start failures due to ignition torch became rare.

Operator Experience

Personnel hired to operate the plant came from various backgrounds. The majority had gained training and power plant experience while working with the U.S. Navy; some had worked at civilian power facilities, while others had no experience at all. Nevertheless, much of what was built at Kalaeloa was new to all operators. The project team conducted formal training, which was

supplemented by experience gained while working with the commissioning and construction teams. The real experience came by trial and error on the job.

Over the years, a concerted effort was put into developing operating procedures that included theory, practice, and lessons learned. Throughout this developmental process, mistakes were made leading to the poor performance numbers during the early years.

Fuel Nozzle Erosion

The fuel nozzle is composed of two sliding rings with a series of orifices that regulate fuel flow. At the switchover point, approximately 25 MW, the smaller ring closes and the larger one opens. As the orifices erode, severe load swings occur at the switchover point causing the turbine to trip. This problem was resolved by replacing the sensitive internal components of the fuel nozzle with hardened material and establishing a fuel nozzle overhaul frequency of six months.

Boiler Cleaning

Although the initial focus on reduction of degradation was toward the gas turbine, the HRSG became the focus soon thereafter.

The HRSG's are Deltak dual pressure design. The tubes are spiral-finned at four fins per inch. The two-inch tubes are at four-inch centers, with 52 tubes wide and 16 deep per bundle. Each HRSG is equipped with 15 steam rotary sootblowers. The source of the deposits on the tubes is the ash from the fuel, with contribution from the additive. The ash is of fine consistency and easy to blow off when hot, somewhat caked when cool. The stack design temperature under normal operation is 338°F (170°C). As the HRSG fouls, the stack temperature rises to as high as 400°F (204.4°C).

The sootblowers are capable of removing some ash, however, not enough to produce any significant drop in stack temperature for any reasonable duration. Experimentation with sootblowing techniques did not yield good results. Off-line cleaning methods were investigated producing mixed results.

- **Air Lancing:** This method involved the use of compressed air introduced to the HRSG by manually controlled hoses blown directly at the tubes. A small reduction in stack temperature was realized. The process was labor intensive and the units had to be placed on "unavailable" status while the cleaning was done.

- **Grit Blasting:** A copper slag, grit, was introduced into the air lancing process. The grit was conveyed through the air lines and blown against the tubes producing very good results on tube surfaces facing the cleaning media. Stack temperatures dropped down to 355°F (179.4°C) but quickly deteriorated back to high levels. In addition to the problems in common with the air lancing technique, there were added problems with this method: concern for accelerated tube erosion, and discharge of copper bearing particulate out the stack on start-up.

- **Sonic Systems:** A sonic horn was installed underneath an HRSG section. Initial observations revealed clean boiler bottom,

but no improvements on tube surface. An infrasonic device was then tested. This was installed in the stack and was designed to handle the entire volume of the HRSG. Cleaning results were not satisfactory. Continuation of the experiment by installing the infrasonic at another location was considered, but the concern for surrounding equipment, which vibrated as a result of the device's operation, led to the decision to terminate its use.

- **CO₂ Cleaning:** The CO₂ pellet blasting method was tested in 1998. Expected advantages over grit blasting included: less erosion and no cleaning grit discharge from the stack on startup. The cleaning process was much slower than with grit, and the cleaning results were not satisfactory. This process was not used again.

- **Water Washing:** With the change in plant ownership in 1997, new projects were explored; modification of the boiler for water washing was one. The boiler bottom was modified from ceramic insulation to refractory type insulation unlikely to be damaged by water. Drains were added and a containment area was built around the HRSG's to collect the wastewater. The first water wash was performed with fire hoses and nozzles spraying into the tube bundles. However, due to the high-density design of the HRSG, it was determined by use of a borescope, that the interior sections of each bundle were still not getting clean. Further consideration led to the currently used technique of washing the HRSG sections from the top. Access hatches were cut into the casing above each of the three sections, and wash nozzles were fabricated to facilitate the process. On the first wash attempt, water ran down the sidewalls of the HRSG causing failure of insulation in the sidewalls; this resulted in casing cracks on startup due to uneven expansion.

The current evolution of the water wash utilizes nozzle assemblies that essentially pour water between the HRSG headers. This method allows water onto the tubes without spraying into the sidewall insulation. The water then swirls down the tube fins, dissolving and removing deposits. Results have been very positive, with stack temperature dropping to 340°F after the wash.

This method is still under development. Future developments will include automation of the waste water collection, treatment and disposal system; automation of the spray system; and better control of pH of the process to avoid tube corrosion.

The boilers are now washed on an as needed basis based on stack temperature rise, but approximately every two months. Plant PURPA efficiencies have climbed to the 43 percent range with reduced steam export.

Summary

The Kalaeloa Cogeneration Plant has come a long way since startup, becoming a reliable power production facility for the island, and using a fuel that was not well understood for this application. Through strong commitments, by the various OEM groups and the Plant owners, to its success, problems have been resolved and are now under control. Room for improvement remains, and the commitment to achieve future improvement is there as strong as ever.

Advanced Gas Turbine Technology: ABB/BCC Historical Firsts

D. Eckardt

P. Ruffli

ALSTOM Power Ltd.,
Brown Boveri Strasse 7,
CH-5401 Baden, Switzerland

During more than 100 years engineers of the Swiss development center of A.-G. BBC Brown, Boveri & Cie., from 1988 onwards ABB Asea Brown Boveri Ltd., in 1999 ABB ALSTOM POWER Ltd., and now ALSTOM Power Ltd. in Baden, Switzerland, have significantly contributed to the achievement of today's advanced gas turbine concept. Numerous "firsts" are highlighted in this paper—ranging from the first realization of the industrial, heavy-duty gas turbine in the 1930s to today's high-technology gas turbine (GT) products, combining excellent performance, extraordinary low environmental impact with commercial attractiveness for global power generation. Interesting connections could be unveiled for the early parallel development of industrial and aero gas turbines. [DOI: 10.1115/1.1470484]

Introduction

In times of globalization, "new economy," and virtual stock market bonanzas it is worthwhile to reflect on the values of engineering ingenuity, enduring leadership, and technical substance. The historic contributions of ABB/BBC to the successful development of the present industrial gas turbines appear to be a grand example in this context.

Gas Turbine—Back to the Roots

BBC and ABB are part of the history of technology that gave rise to the greatest inventions of the past century. Gas turbines, more generally "turbomachinery," emerged in the wake of early electrification. Interestingly, the names of those pioneering companies are still today amongst the leading players:

In 1867 the German Werner von Siemens presented the first "dynamo" after having discovered the principle of electrodynamics. In 1879 Thomas A. Edison invented the light bulb, thus laying ground to create the powerful General Electric (1895). In 1891 Charles E. L. Brown succeeded in transmitting 220 kW of power the 175 km from Lauffen/Neckar to Frankfurt/Main, Germany. From this moment on, driving power no longer had to be generated and consumed at the same site. An electrical cable could now link the source of energy with the place at which it was utilized; centuries of limiting mechanical transmission equipment were over.

BBC GT Development—The First 50 Years:

Finding the Path

On Oct. 2, 1891 the following entry was made in the commercial register of the Swiss Canton of Aargau: "Charles E. L. Brown of Brighton, England and Walter Boveri of Bamberg, Germany, both resident in Baden, have established a limited partnership under the company name Brown, Boveri & Cie., Baden. The nature of the business: fabrication of electrical machines." The two founders complemented each other perfectly: Brown was the technical wizard and Boveri, the dynamic businessman (Fig. 1).

In retrospect the early years must not be viewed solely as a time of technical innovation and success; they were also rife with intense labor and social disputes. Shareholders, for their part, suf-

fered major disappointments in the 1920s and 1930s; economic difficulties have been as much a part of BBC's history as grand triumphs. From 1903 to 1914 AEG (Allgemeine Elektrizitäts-Gesellschaft) held a large part of the BBC shares. After WWI the BBC Group had no choice but to join forces for a short time with the powerful British Vickers Ltd. Paying out a dividend was out of the question from 1921 to 1924 and from 1931 to 1938 but in parallel, the technical innovative progress in the newly founded company appears having continued nearly not affected.

The internationalization of BBC was essentially shaped by one outstanding product: In 1900 the company made the courageous and momentous decision to include steam turbines in its range of products (Fig. 2). Watt's steam piston engines had triggered the first industrial revolution in the early 19th century; a hundred years later steam turbines, coupled with generators, were to play a role of similar importance. Rotating turboengines subject to constant impingement by jets of steam replaced the venerable piston steam engine. Consequently, the production of turbine generators soon became a major line of business at BBC. The fast-rotating alternating current generator, a stroke of genius on the part of Charles Brown, led to the breakthrough of turbine generators at the turn of the century and to an influx of orders for BBC from around the world. By 1902, BBC had delivered 17 steam turbines, one of them with an output of 3 MW. By 1905 the product was accounting already for half of total company sales, (Fig. 3).



Fig. 1 Charles E. L. Brown (1863–1924), J. Walter D. Boveri (1865–1924) as of 1891, the year of BBC's foundation

Contributed by the International Gas Turbine Institute (IGTI) of THE AMERICAN SOCIETY OF MECHANICAL ENGINEERS for publication in the ASME JOURNAL OF ENGINEERING FOR GAS TURBINES AND POWER. Paper presented at the International Gas Turbine and Aeroengine Congress and Exhibition, New Orleans, LA, June 4–7, 2001; Paper 01-GT-395. Manuscript received by IGTI, December, 2000, final revision, March, 2001. Associate Editor: R. Natole.



Fig. 2 Steam turbine assembly, Baden ca. 1902

In the context of the evolutionary move from piston to rotating engines, first exercised in the area of steam engines, the design target for the coming gas turbine became clearer: (partial) replacement of the (Otto or Diesel) combustion piston engines and consequently, no linearly accelerating/decelerating masses/pistons, cranks, and connecting rods, on the other hand, in view of the steam plant's complexity: no boiler, no condenser with circulating water, no water supply, no feed water pump, no water treatment, no air extractor, no condensate pump, no cooling tower, no other auxiliary equipment. However, already the first gas turbine (GT) patent of J. Barber in Great Britain and thereafter the development work of F. Stolze in Berlin at the end of the 19th century indicated a decisive difficulty on this path: A gas turbine with an useful, net power output is only possible if the total expansion work of the turbine(s) exceeds the compression work.

The first stand-alone, net power generating GT power plant was built by the French R. Armengoud and C. Lemàle at Paris, 1905–1906. While Stolze was in search of the all-axial-engine from the beginning, the French looked rather for a proven radial compressor design—from Brown Boveri (Fig. 4). This first experimental gas turbine consisting of a 25-stage radial compressor (System Rateau) with two intercoolers from BBC and a single-stage turbine (following as well Rateau's design) achieved self-sustained operation by adding some steam, generated in combustor cooling, and feeding it back to the turbine in a kind of early “steam injection” (STIG). The actual GT efficiency should have been between 2–3% only, or 6–10 kW of equivalent power produced.

The reason why the first turbine did not prove to become a success can be seen in Fig. 5 which shows GT thermal efficiency as a function of GT specific work—both for an early design stan-

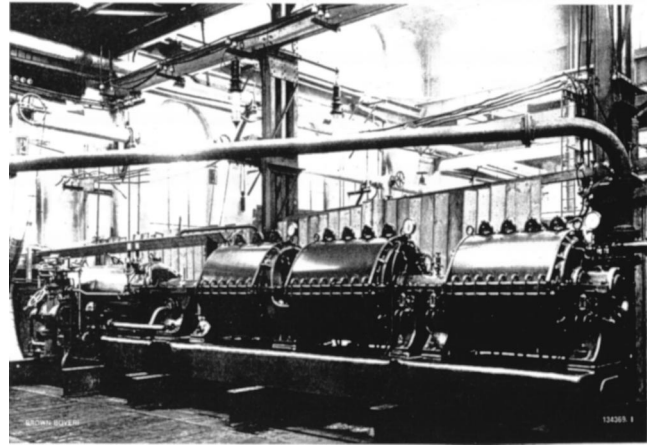


Fig. 4 BBC multistage centrifugal compressor for the Armengoud-Lemàle gas turbine, 1906

dard of 1920–1930 and for present state of the art. With a turbine inlet temperature (TIT) of about 830 K at the nozzles, obtained by injecting water into the combustion chamber, the turbine was just able to supply the mere power for compressing the air. The cause of this disappointing result must be sought in the great volume of compressed air required to reduce the combustion temperature of 2.200–2.270 K to the value admissible for the gas turbine blading.

The difficulty in designing and building an aerodynamic satisfying, i.e., “axial” compressor for large volume flows was insurmountable during the first decades of the 20th century. Consequently, an intermittently operating, discontinuous working process was selected, where the required pressure rise was achieved in a, for a short time, hermetically sealed combustion chamber by self-ignition of an explosive atmosphere. First operational gas turbines according to this “constant-volume” Holzwarth principle were introduced in the mid 1920s with steadily increasing output power up to 5 MW. In this turbine, the fuel (oil, blast furnace gas, or pulverized coal) was fed to this closed combustion chamber filled with compressed air, and the exploding mixture caused the pressure to rise approximately 4.5 times its original value. The combustion chamber, nozzles, impeller, and blades were water cooled. The power consumption of the compressor was only a fraction of that required for the combustion turbine and, consequently, a poor efficiency of the compressor no longer had such a disastrous effect; only a small amount of excess air was necessary for combustion (since water was used for cooling) and the air

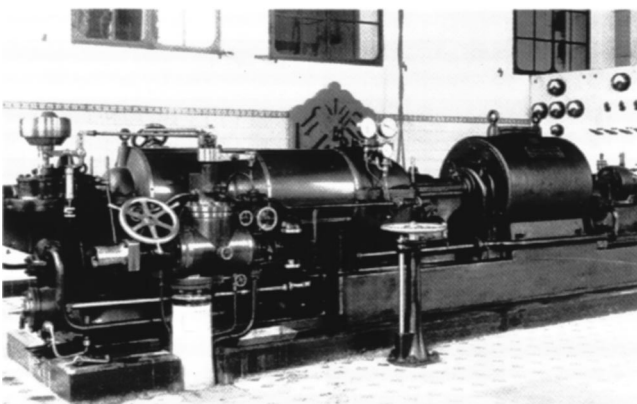


Fig. 3 BBC first “continental” steam turbine, Baden 1902

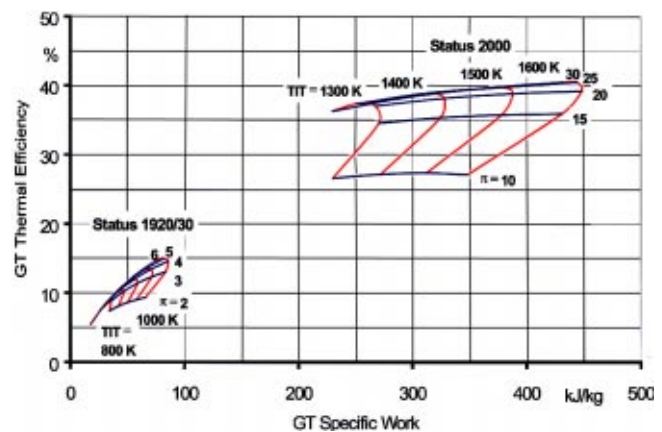


Fig. 5 Gas turbine thermodynamics (approximate performance model)

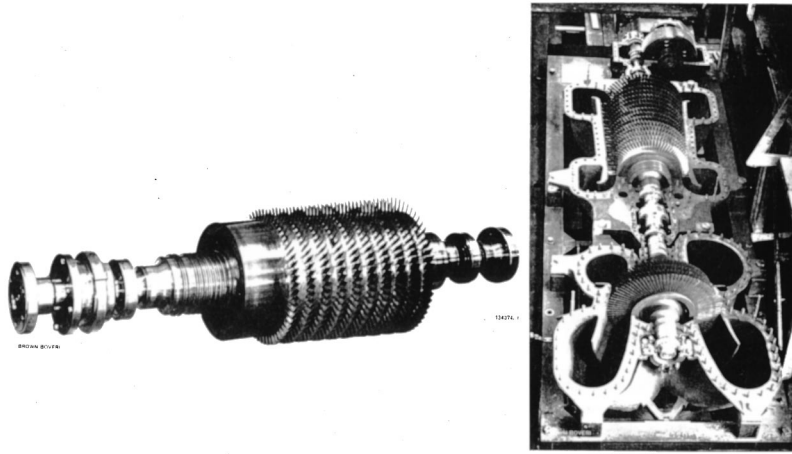


Fig. 6 BBC axial turbomachines for the Velox boiler, PR=2.4, 1931

needed only to be compressed to approximately one-quarter of the final explosion pressure. These straightforward advantages were, however, accompanied by considerable complication and increase in cost of the plant. BBC got involved in building several of those Holzwarth turbines, no. 2 as early as 1909–1913 and still, in a second approach in 1928. Brown Boveri proposed for it an improved two-chamber two-stroke cycle. This unit was installed in a Thyssen steel plant at Hamborn, Germany, where it has been several years in operation with blast furnace gas.

The explosion turbine might look as a dead-end development, but we are really only $1\frac{1}{2}$ development steps away from the “constant-pressure” gas turbine—the concept of today! The high heat transfer rates in the gas ducts of the Holzwarth turbine led to the concept of the BBC Velox boiler—with combustion under pressure, supercharged by gas turbine-driven air and gas compressors. This application of the gas turbine rendered essential the creation of a compressor set having a high efficiency. The problem was solved as early as 1932 by the development of a four or five-stage reaction turbine and a 10 to 12-stage axial compressor (Fig. 6), the design taking into account the results of the then latest research in the field of aerodynamics.

Wanted—The Efficient Axial Compressor

First ideas for an advanced compressor design were obviously introduced to BBC via its French daughter Cie. Electro-Mécanique (CEM), Paris. Between 1925–1931 CEM built under the supervision of G. Darrieus a series of windmills from 8–10 m wheel diameter, designed throughout according to modern aerodynamic principles. The practical transfer of single airfoil theory towards the design of a multistage axial compressor was carried

out at BBC by C. Seippel. The Göttingen airfoil no. 265 was selected as most appropriate, based on lift/drag polar plots published by L. Prandtl, transformed “conformal mapping” into a cascade flow and finally experimentally verified. The tests then allowed the reconstruction of the polar plot of the actual cascaded airfoil (Fig. 7) as a reliable design base ([1]).

In the light of the extensive von Ohain/Whittle discussion of recent years on the first turbine-powered flight in 1939, it appears to be beneficial still to investigate the role and contributions of potential 3rd players in this context/contest, e.g., it might be interesting to trace

- the dissemination of those key ideas, outlined above, applying airfoil theory for advanced compressor design, and
- the whereabouts of some advanced, in parts flightworthy compressor/turbomachinery hardware, delivered by BBC from Switzerland towards England, still during 1939–1940 (Fig. 8).

The whole excursion refers to the core assumption that advanced axial compressor designs finally became the key to the successful realization of the aero gas turbine—in and after 1940. All this happened in great secrecy before and during WWII, reflecting the fact that jet-powered flight was considered as, and actually played, a salient role in the war machinery of both sides. As a further footnote it is worthwhile to point out that both England and Germany went through early jet engine configurations with radial compressor designs; however, Germany managed to correct this detour, i.e., the necessary transition to an all-axial engine design much faster.

In strange contrast to this later development stands the fact that

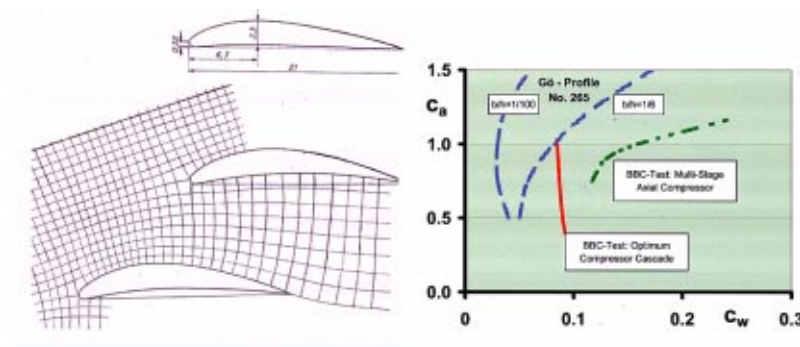


Fig. 7 Compressor cascade deduction/transformation and test of Göttingen compressor profiles, 1931

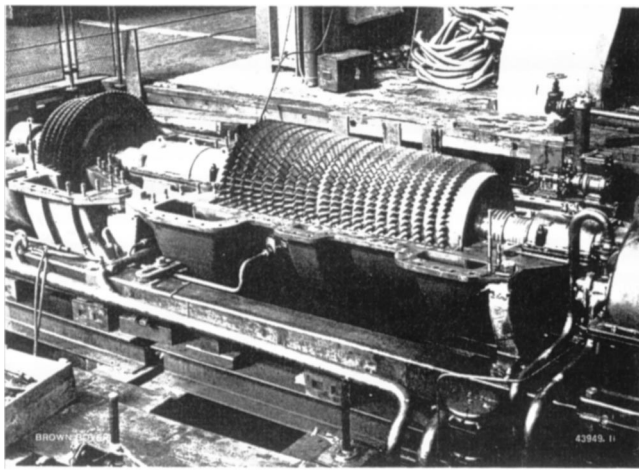


Fig. 8 First UK gas turbine (1.6 MW) at RAE, delivered by BBC in 1939

BBC openly sold advanced axial compressor hardware unrestricted to everyone, as early as 1931. Given the later importance, this ten-year-long dissemination period of axial compressor technology is rather astounding, not to mention today's short-term technology cycles.

The history of this specific development/flow of ideas and know-how has still to be written; within this context only a few notes shall be sketched. There appears to have occurred a steadily rising number of contacts on this subject within the triangular setup—Switzerland, Germany, and England—from 1925 onwards with some links to other European countries. Moreover, a fascinating row of (later) highly renowned names of scientists and industrial leaders were involved:

Switzerland (and Swiss abroad, in italics)

1921 *J. Ackeret, later on famous scientist of high-speed aerodynamics at ETH Zurich, hosted at L. Prandtl's AVA Aerodynamische Versuchs-Anstalt Göttingen; a planned one-year stay actually lasted seven years.*

1925 *CEM (G. Darrieus)—a Paris-based subsidiary company of BBC—successfully produces a series of windmills, based on airfoil theory design.*

1926 BBC, 4 st. axial test compressor, first with untwisted blades, later swirl adapted with $r=0.5$ and 1.0 reaction.

1932 BBC, sold a number of 11 st. axial compressors, $PR=3.4$, for the Mondeville project and high-speed windtunnels (acc. to J. Ackeret's design) at ETH-Zurich and Rome, $r=0.55$.

1934 C. Keller, assistant to J. Ackeret at ETH Zurich, designed one of the windtunnel blowers (2nd blower for the high-speed tunnel came from BBC), resulting in Keller's widely spread Ph.D. thesis "Axial Blowers in View of Airfoil Theory," detailing some axial compressor design know-how ([2]).

1939 A. Meyer, BBC Technical Director, presenting a comprehensive paper on GT design achievements (but also, e.g., on the

GT usage for compact and lightweight ship/destroyer propulsion) at the Institute of Mechanical Engineering, London.

1939 First commercial IGT from BBC operational at Neuchâtel (preserved still as an ASME Technical Landmark).

1939 BBC delivers 1st Industrial GT to RAE, 1.6 MW, 20 st. axial compressor and during 1940 axial aircraft superchargers 190 hp, $PR=2.5$ —in fulfilling a RR purchase order

1941 *High ranking Swiss delegation (J. Ackeret, C. Seippel, and C. Keller) retributing several foregoing visits from Germany by a tour to AVA Göttingen*

Germany (and Germans abroad)

1922 W. Bauersfeld suggests the use of airfoil theory for fluid machinery, VDI-Z

1928 A. Franz (later, Jumo 004 designer) at ETH-Zurich

1935(?) AVA Göttingen, 4 st. axial turbocharger, 7 st. compressor development, Encke et al. design, $PR=3.8$, $\eta_{ad}=83\%$ (in production $PR=3.1$, $\eta_{ad}=78\%$), reaction $r=1.0$

1935 H. P. von Ohain, secret turboengine patent no. 317/38

1937 H. P. von Ohain, test engine HeS3B running

1939 1st jet-powered flight He 178 aircraft with HeS3B, SUN Aug. 27, 1939, Rostock-Marienehe, test pilot E. Warsitz.

1939 R. Friedrich, Junkers Magdeburg, 14 st. axial compressor for RTO engine (Rückstoss-Turbine ohne Leistungsabgabe an Propeller), $r=0.5$, for HeS30 engine, based on Göttingen airfoil design.

1940 Jumo 004 with Gö derived compressor, 1st test run.

1941 BBC Mhm. design support for BMW 003C by providing a superior 7st. compressor, $PR=4$, $\eta_{ad}=84\%$, $r=0.5$.

1942 Me 262 fighter aircraft with $2 \times$ Jumo 004, 1st flight 18.07.42, test pilot F. Wendel.

England (and English abroad)

1926 A. A. Griffith "An Aerodynamic Theory of Turbine Design," GT as aircraft powerplant.

1929 Axial compressor test wheel, 10 cm diam., $PR=1.16$, $\eta=88.3\%$, according to A. A. Griffith.

1929 *H. Glauert stay with Th. von Karman, TH Aachen, in addition: AVA Göttingen publication.*

1930 F. Whittle, 1st patent for turbo aero engine.

1930 Tizard, Gibson & Glauert committee denies GT superiority relative to piston engine, in 1931 RAE finishes GT development for six years consequently.

1937 F. Whittle, radial compressor engine, test run 12.04.37.

1938 RAE delegation at BBC—result "Exclusivity on BBC (axial) compressor know-how could not be granted."

1941 Gloster E28/39 with Whittle engine, 1st flight.

1941 Testing of BBC delivered GT hardware at RAE, guarantees confirmed, but obviously no further consequences.

Soon, in the early 1930s, the efficiency of the turbocomponents applied at BBC for the Velox boilers made not only the turbine to drive the compressor, but in addition to generate excess power through the inverse operation of the electric starter motor. A further step in the direction of generating utility power (1 MW) was achieved as early as 1936 by an all-axial process gas turbine/blower group with $PR=4$ for a U.S. refinery, Houdry cracking process ([3]). Based on these practical experiences, BBC finally

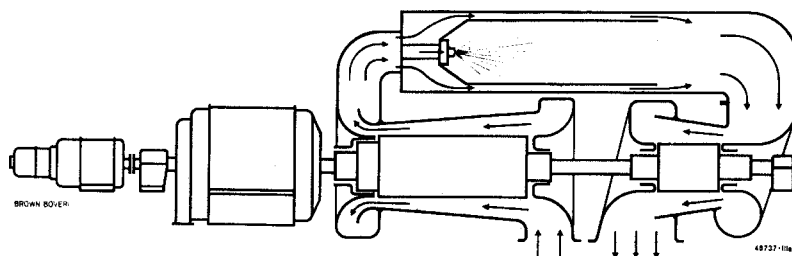


Fig. 9 BBC cross section of first gas turbine for public power generation, 1939

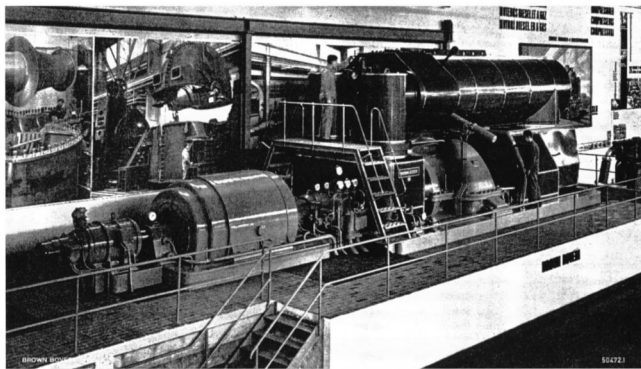


Fig. 10 BBC first utility GT powerplant, 4 MW, Neuchâtel, Switzerland, 1939

succeeded in July 1939 in putting the world's first utility gas turbine into operation at the Swiss town of Neuchâtel. The overall configuration was as simple as possible: One 23-stage axial compressor, one single-can combustor, one 7-stage axial turbine, and a synchronously operated generator on the same shaft (Figs. 9 and 10 of [3]).

This "constant-pressure" engine was able to generate 4 MW as peak load with a thermal total efficiency of 17%. Compressor pressure ratio was $PR=4.4$, adiabatic compressor efficiency approximately 85%, turbine inlet temperature $TIT=820$ K, turbine efficiency 88%, mass flow 62.2 kg/s. In the same year, 1939, the local competitor Escher Wyss from Zurich, later owned by ABB, put a 2 MW closed-cycle gas turbine into operation. The engine cycle was highly pressurized, striving for "carnotization," i.e., axial compressor with two intercoolers and one recuperator for indirect intake air heating, thus achieving at that time a record-high total plant efficiency of 31%.

During WWII advanced aero engine concepts belonged also to BBC's design background. C. Seippel already received in 1940 a Swiss patent on a turboprop engine configuration. A more detailed construction of such a geared turboprop gas turbine is illustrated in Fig. 11; BBC project studies of that period had outlined clearly the inherent advantages of mixed propeller/jet propulsion ([4]).

BBC/ABB GT Development—The 2nd 50 Years: Towards the Optimum

The GT evolution now progressed at a fast rate, already in 1945 a two-shaft gas turbine set with 10 MW output was taken into service. Another milestone in the development of the BBC gas turbine was the famous Beznau powerplant of the Nordost-Schweizerische Kraftwerke (Fig. 12). This plant was erected between 1945–1947. It contains gas turbines with three compressors, two turbines, and recuperators. Beznau station was the largest GT plant in the world at the time of its commissioning and

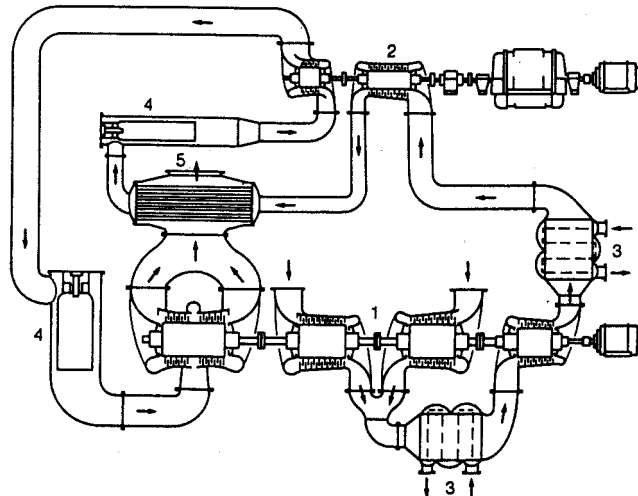


Fig. 12 BBC dual shaft gas turbine, 13+27, Beznau, Switzerland, 1948 (layout of the 27 MW turboset)

had a thermal output of 40 MW, two sets rated at 13 and 27 MW, both running on heavy oil and a total efficiency of more than 30% ([5]).

The following three decades were characterized by a fierce, performance-driven competition between steam and gas turbine. The simple cycle gas turbine appeared to be restricted to peak load and/or special, low fuel price operations only. The 1960s brought an essential simplification of the industrial gas turbine (IGT) towards high power density, accompanied by a single shaft/two bearings configuration, with the generator at the cold end. Multishaft units with intercooling and recuperation were no longer competitive. In the 1970s turbine inlet temperature was increased, first by introducing superalloys and then followed by especially designed alloys for the corrosive IGT fuels, e.g., IN 738, later by the introduction of air cooling in the first turbine stages, GT11B, 1970. Even with these increased temperatures the simple cycle gas turbine did not reach the efficiency of the steam turbines, while at the same time the oil crisis of 1975 re-emphasized the importance of low fuel consumption. A resolution of this dilemma was the introduction of the combined-cycle power plant (CCPP). When two thermal cycles are combined in a single powerplant the efficiency that can be achieved is higher than of one cycle alone. A combination of cycles with different working media allows to complement inherent advantages. The combination most widely accepted for commercial power generation is that of a gas "topping cycle" with a water/steam "bottoming cycle" ([6]).

The initial breakthrough of these cycles onto the commercial power generation market was possible due to the gas turbine—the key component of the combined-cycle plant—generating approximately 2/3 of the total output. Only since the late 1970s have

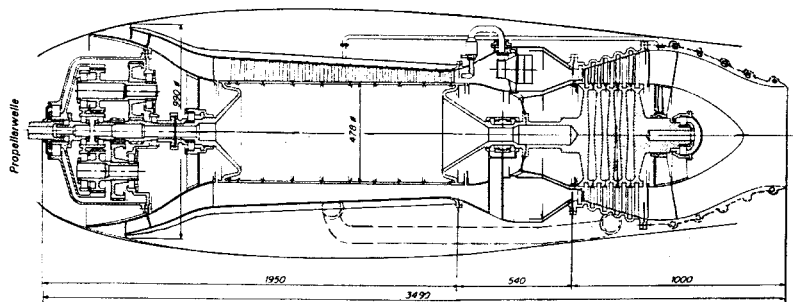


Fig. 11 BBC turboprop aeroengine design, 1944

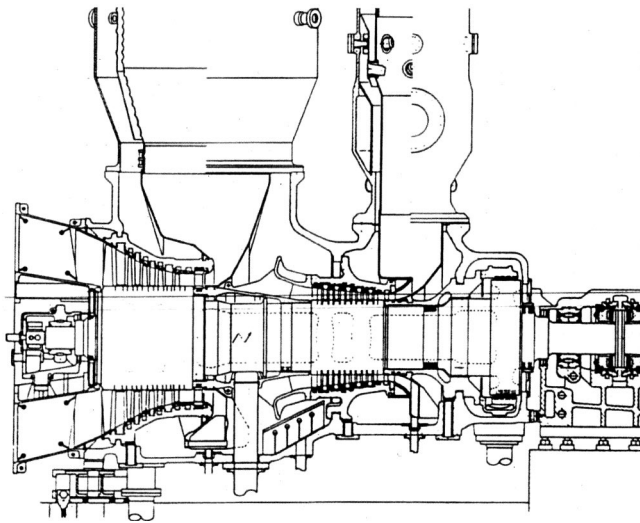


Fig. 13 Air storage GT powerplant, 300 MW, Huntorf, Germany, 1977

turbine inlet temperatures, and hence exhaust-gas temperatures, been sufficiently high for high-efficiency combined cycles. The result was a powerplant with high performance, low installation cost, and fast delivery time.

The development path to the present advanced gas turbine family GT24/GT26 of ALSTOM Power was already prepared relatively early. BBC had pioneered the reheat cycle already back in 1948 in two-shaft arrangements and had subsequently adapted this concept to the Huntorf plant in Germany. This unique air-storage GT powerplant, using 300.000 m³ of underground caverns, basically comprised a 300-MW compressed air plant with two silo combustors and two turbine expanders arranged on one shaft (Fig. 13).

IGT technology received a decisive boost in the early 1990s, not the least by a transfer of then available know-how and engineering capacity from the military aero engine side. All leading IGT manufacturers entertained at that time cross collaboration links to advanced aero technology, resulting, e.g., in a considerable increase in component performance and higher turbine inlet temperatures. Single crystal and directionally solidified materials were introduced for the first time for IGT turbine blading, challenging a highly specialized supply industry with respect to manu-



Fig. 15 GT 24/GT 26 rotor turbocomponents

facturing problems (dimensions, weight and complexity). In close cooperation between OEMs and relatively few selected high-technology suppliers considerable progress has been achieved mainly in the areas of precision cast parts and high temperature coatings. Computational fluid dynamics and improved understanding in high-temperature turbine cooling technology in combination with extreme lifing demands, unheard of in the aero regime, opened new technological frontiers. These were successfully addressed in concurrent engineering/ supply chain management (SCM) efforts.

With the introduction of the advanced GT24 (60 Hz) and GT26 (50 Hz) gas turbines between 1995–1997, ABB has provided a technology level to the power market which meets the requirements for extraordinary low emissions, high total efficiency, and unique operational flexibility in this very competitive market (Fig. 14). The GT cycle parameters (Fig. 5) illustrate the superior design principles of this GT family: PR=30, TIT>1.600 K, SC efficiency>37.5%.

Advanced turbocomponent development for the GT24/GT26 family was started at ABB in the early 1990s in close cooperation with MTU Motoren- und Turbinen Union, Munich and some resources from various research organizations ([7]). The subsonic compressor consists of 22 stages with controlled diffusion airfoils (CDA). The GT24/GT26 compressors, basically identical on a 1.2 scale basis, are operating at moderate relative inlet Mach no. <1.1 for rotor 1 tip. The CDA blading results in an improved behavior of the compressor also at part load, while providing an excellent surge margin (Fig. 15). Part load efficiency is further improved by three rows of variable guide vanes.

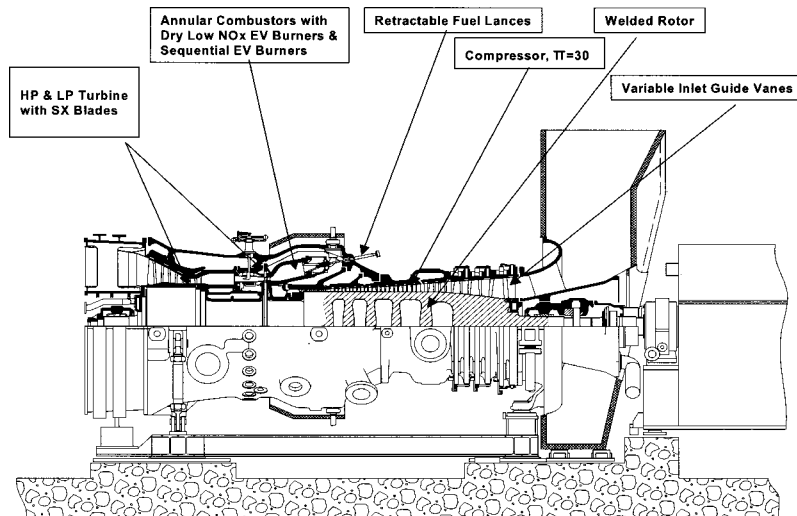


Fig. 14 Advanced GT 24/GT 26, 183/265 MW, unique design features

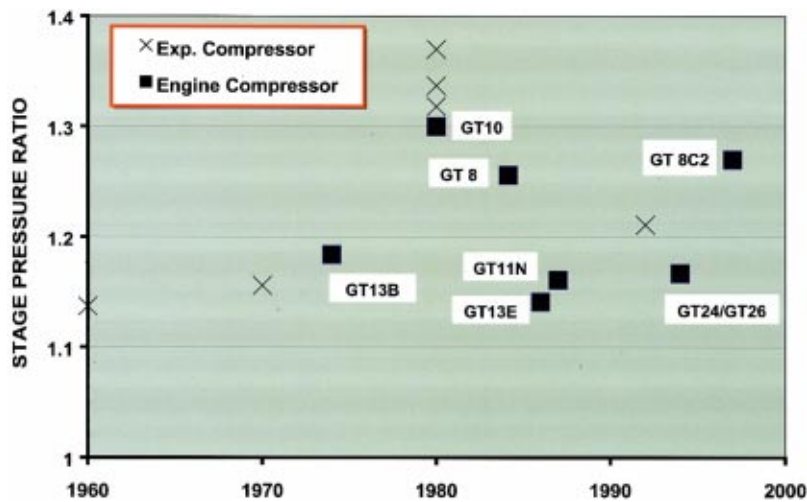


Fig. 16 BBC/ABB high-performance compressor development process

Beginning with the early design exercises of the 1930s the scientifically based, aerodynamic approach for improving the compressor performance has a long tradition at BBC/ Escher Wyss, both inherited by ABB. Figure 16 illustrates the progress achieved in the average stage pressure ratio during the past 40 years of axial compressor development. It becomes obvious that product innovation had been prepared in time by a number of very advanced test rigs. Especially the transonic compressor development of 1980 with relative tip Mach No. >1.3 represents a salient landmark, resulting in the unique products of GT10 and GT 8 compressors ([8,9]). This tradition of advanced transonic design is still preserved with the new 12 stage GT 8C2 compressor with $PR=17.6$. At the same time the $PR=30$ compressor for GT24/GT26 represents another unique and unprecedented "first" for a single-shaft configuration, though its stage pressure ratio was kept in a rather conservative regime. The high total pressure ratio was selected as optimum for sequential combustion.

The GT24 and GT26 utilize the unique sequential combustion system, which is based on the concept of two annular combustors in the gas turbine. The expansion process in a sequential combustion GT allows for an exhaust temperature of up to 640°C , which can be maintained over a wide part load range, thus representing optimum conditions for the subsequent steam section of the combined cycle. With the arrival of the annular combustor already in the GT13E2, ABB had introduced an important component for the sequential combustion technology employed in the GT24 and GT26 gas turbines. Sequential combustion with a still unsurpassed high-pressure ratio $PR=30$ results in a gas turbine with a higher

power density than conventional designs with the same overall power output. This design has the following benefits:

- high specific power/ a low air mass flow rate,
- low blade tip speed with lower thermomechanical stresses,
- smaller size for the steam/ water cycle plant, and
- lower turbine inlet temperature.

The GT24/ GT26 series of industrial gas turbines use a novel combustion technology based on two premixed combustion stages as part of a GT cycle with reheat at intermediate pressure level. The whole system is a continuously improved, stand-alone development originating from the early 1980s. The first high-pressure combustor uses dry-low NO_x Environmental (EV) swirl burners (Fig. 17), while a fuel-air mixing technique on the basis of "delta wing" vortex generators has been successfully implemented in the second (SEV) lean-premix reheat combustor. The EV burner provides the benefit of low- NO_x combustion without water/steam injection on natural gas, but alternatively can also be operated on liquid fuel. Extraordinary low NO_x emissions have been achieved in practical operation, both with natural gas and with oil.

As part of the very successful market introduction of the GT24/ GT26 family, ABB decided to build a GT26 Gas Turbine Test Center at Birr, Switzerland. It is equipped with a full-scale 300 MVA generator and is capable of firing both natural gas and diesel oil. This location is within 16 km from the ALSTOM Power engineering offices at Baden, so that direct feedback is possible during test runs as well as evaluation of actual engine operation at

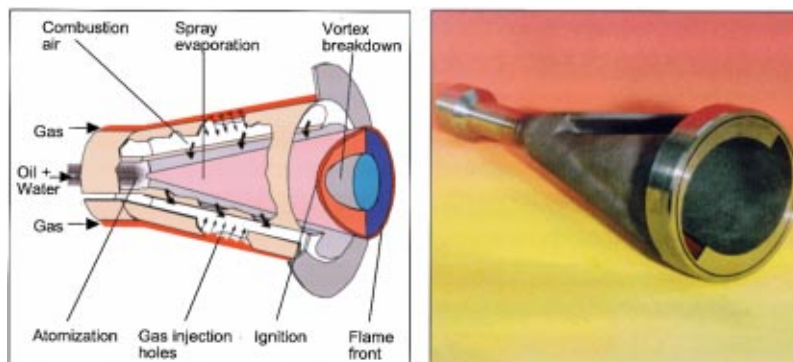


Fig. 17 Dual fuel low NO_x EV burner



Fig. 18 GT 26 rotor assembly at the ALSTOM Power GT Test Center, Birr, Switzerland

various conditions. Figure 18 illustrates the test turbine assembly process, highlighting the most paramount features of this unique GT concept:

- simple single shaft arrangement,
- rugged and reliable welded rotor design,
- an advanced compressor configuration, combining performance with operational flexibility, and
- sequential combustion, reflected by high and low-pressure turbines—a decisive asset in view of increasingly important environmental aspects.

Summary: ABB/BBC Gas Turbine “Firsts”

- 1905 BBC multistage centrifugal compressor (PR=4.5) for the Armangaud/Lemâle first experimental gas turbine
- 1910 First operative BBC gas turbine according to the Holzwarth principle
- 1923 First two-stage centrifugal compressor turbocharging a four-stroke diesel engine, PR=2.3
- 1931 All-axial compressor (ten stages, PR=2.4) and turbine set for commercial velox boiler with net power output (GT principle)
- 1933 Patent for BBC’s unique, welded gas turbine/steam turbine, and geno rotors
- 1935 Patent for closed-cycle gas turbine, granted to Akeret & Keller
- 1936 5 MW air/electricity gas turbine installed in a chemical plant (Houdry Oil Refinery Process), Philadelphia, USA
- 1939 4 MW first electricity generating, utility gas turbine, Neuchâtel, Switzerland
- 1940 First gas turbine powered locomotive (2,200 hp)
- 1945 10 MW electricity generating, two-shaft gas turbine with intercoolers and intermediate combustors, Bukarest, Roumania
- 1948 40 MW (13+27 MW)—world’s biggest all gas turbine

power station at Beznau, Switzerland

1955 6 MW mobile gas turbine powerplant

1957 4×27 MW world’s biggest all gas turbine power station, Port Mann, BC, Canada

1959 Introduction of first compact gas turbines in single and split shaft versions

1965 Gas turbine powered sea water distillation plant

1977 300 MW air-storage gas turbine powerplant with sequential combustion, Huntorf, Germany

1980 12 st. transonic compressor, $Ma_{via} = 1.3$, PR=16

1982 1200 MW (20×GT11) world’s largest crude oil GT powerplant, Riyadh, Saudi Arabia

1984 First commercial gas turbine operation with premix combustion first commercial application of a transonic compressor for GT 8, Shell, The Netherlands

1985 GT13E world’s biggest industrial GT>140 MW, >35% total efficiency, Hemweg, The Netherlands

1990 Nuclear powerplant repowered by combined cycle GT sets; 12×GT11N uprated, Midland, USA

1991 First vortex-breakdown dry low- NO_x EV environmental dual-fuel burner in annular combustor

1994 165 MW, 60 Hz, high-efficient (37.5+%) simple-cycle GT 24 gas turbine with single shaft, PR=30 compressor, low NO_x sequential combustion, two bearing welded rotor

1997 365 MW, 50 Hz, combined cycle powerplant GT 26 with 58+% total efficiency and low NO_x emissions

1999 World’s biggest 140 MW turbo gearbox from Renk AG, 60→50 Hz speed converter for GT11N2

Acknowledgments

The authors want to thank a number of colleagues for the generous help, digging deeply into their files/archives and memories to reconstruct the past; special thanks in this context to H.-U. Fruttschi and F. Farkas. To D. Carpenter, J. Dunham, and H. Schubert, we owe very valuable information on the early phase of axial compressor development history.

References

- [1] Seippel, C., 1940, “The Development of the Brown Boveri Axial Compressor,” *Brown Boveri Rev.*, **26**(6), pp. 86–91.
- [2] Keller, C., 1934, “Axialgebläse vom Standpunkt der Tragflügeltheorie,” dissertation ETH Zürich.
- [3] Meyer, A., 1939, “The Combustion Gas Turbine: Its History, Development, and Prospects,” *Brown Boveri Rev.*, **26**(6), pp. 67–80.
- [4] Pfenninger, H., 1970, “Die Gasturbinenabteilung bei BBC—Rückblick und heutiger Stand,” special print: *Schweizerische Bauzeitung*, Hefte 24 and 30.
- [5] Pfenninger, H., 1966, “Vergangenheit, Gegenwart und Zukunft der BROWN BOVERI Gasturbinen,” *MTZ*, **27**(11), pp. 449–461.
- [6] Kehlhofer, R., Bachmann, R., Nielsen, H., and Warner, J., 1999, *Combined Cycle Gas and Steam Turbine Power Plants*, PennWell Publishing Company, Tulsa, OK.
- [7] Meindl, T., Farkas, F., and Klusmann, W., 1995, “The Development of a Multi-Stage Compressor for Heavy Duty Industrial Gas Turbines,” ASME Paper 95-GT-371.
- [8] Farkas, F., 1986, “The Development of a Multi-Stage Heavy-Duty Transonic Compressor for Industrial Gas Turbines,” ASME Paper 86-GT-91.
- [9] Thoren, K. T. E., 1998, “Gas Turbine Development in Sweden after 1945-A Historical Review,” ASME Paper 98-GT-26.

Evaluation of the Cross Corrugated and Some Other Candidate Heat Transfer Surfaces for Microturbine Recuperators

E. Utriainen

e-mail: esa.utriainen@vok.lth.se

B. Sundén

e-mail: bengt.sunden@vok.lth.se

Division of Heat Transfer,
Lund Institute of Technology,
Box 118,
22100 Lund, Sweden

To achieve high thermal efficiencies, 30 percent and higher, for small gas turbines a recuperator is mandatory. As the recuperator represents 25–30 percent of the overall machine cost, efforts are now being focused on establishing new low-cost recuperator concepts for gas turbine engines. In this paper the cross corrugated (CC), also called chevron pattern, heat transfer surface is reviewed to assess its thermal and hydraulic performance and compare it to some other candidate surfaces for a 50 kW microturbine. The surfaces may be categorized into three primary surface types and one plate-fin type. Design calculations of a recuperator heat transfer matrix using these surfaces enable direct comparison of the recuperator matrix volumes, weights and dimensions. It is concluded that the CC surface has great potential for use in recuperators of the future.

[DOI: 10.1115/1.1456093]

Introduction

Following the deregulation of the electricity market in many countries around the world there has been a massive interest in micro and miniturbines (approximate output power ranges from 5 kW to 500 kW). The use of small power plants in the distribution network, known as embedded generation, allows distributors to relieve congested distribution networks and avoid transmission losses and costs. The small turbines enable small energy consumers to generate their own electricity to secure power supply even at peak load periods. In many geographical places the microturbine may produce power to a competitive cost. The small turbines must compete directly with reciprocating engines and the low maintenance cost of gas turbines is not enough to win the interest of presumptive customers. Gaining a low unit price cost of the gas turbine unit together with low emissions should be of highest priorities for the gas turbine manufacturers.

A recuperator is mandatory to achieve high thermal efficiency, 30 percent and higher for gas turbine units with output power from 5 kW. Thus design engineers face a challenge to establish low-cost heat exchangers that can be manufactured using high-volume production methods.

Further requirements on recuperators, of which low cost is already identified above, are the following:

- high thermal effectiveness and low pressure losses. These affect the gas turbine cycle efficiency.
- high reliability and durability give low maintenance cost and long operational life time.
- minimum weight and volume. The weight is directly proportional to material cost and a small volume of the unit makes the gas turbine packages easier to handle. Compact size of the integral GT package may also be a good sales argument.

These requirements may be matched with a heat transfer surface having passages with small hydraulic dimensions of primary surface or plate-fin types.

A goal of the recuperator unit cost of about 1.5 times the ma-

terial cost for production of recuperators in very large quantities has been suggested by McDonald [1]. Thus the minimum weight requirement is important. If the weight of a recuperator unit can be reduced it will save a considerable amount of money for the manufacturing company. To achieve the very low cost of a recuperator unit, technology transfer from fabrication of radiators in the automobile industry is mandatory.

At least three recent recuperator concepts amenable for automated production methods have been identified:

- A compact annular recuperator of plate-fin surface type has been demonstrated in the U.K. ([2]), see Fig. 1.
- An annular primary surface spirally wrapped unit is under development in Belgium ([3]).
- A spirally formed annular primary surface unit concept has been presented in the U.S. ([1]) see Fig. 2.

Common for all three concepts is the spirally wrapped configuration which is amenable to high-volume production in an automated continuous process of manufacturing. The heat transfer surfaces in these recuperator concepts are of the plate-fin and primary surface types. These are possible to manufacture with high compactness, i.e., high heat transfer surface area to volume ratio.

The cross corrugated (CC) surface, also called the chevron surface, has been identified as one of the best, i.e., giving small volume and weight for a small gas turbine recuperator ([4]). In the present study the performance of the CC surface is reviewed by compiling and comparing some results of previous studies published in the literature. Design calculations of a recuperator matrix for a 50 kW microturbine have been carried out for some selected surfaces. The presented results of the design calculations are focused on recuperator core volume and weight. Some aspects of design are also discussed.

The Candidate Heat Transfer Surfaces

The surfaces considered in this study have passive enhancement of the heat transfer process as opposed to active (surface vibration, electrical fields, etc.) enhancement techniques ([5]). In the passive techniques secondary flow structures are created by means of curved and interrupted duct surfaces. The secondary gas and air flow structures in heat exchangers disturb the insulating near wall layers and thus improve the thermal exchange process in the duct ([6]). As the low-pressure drop requirement is important in gas

Contributed by the IGTI Heat Transfer Committee of THE AMERICAN SOCIETY OF MECHANICAL ENGINEERS for publication in the ASME JOURNAL OF ENGINEERING FOR GAS TURBINES AND POWER. Manuscript received by the Heat Transfer Committee July 2000; final revision received by the ASME Headquarters Sept. 2001. Editor: C. MacArthur.

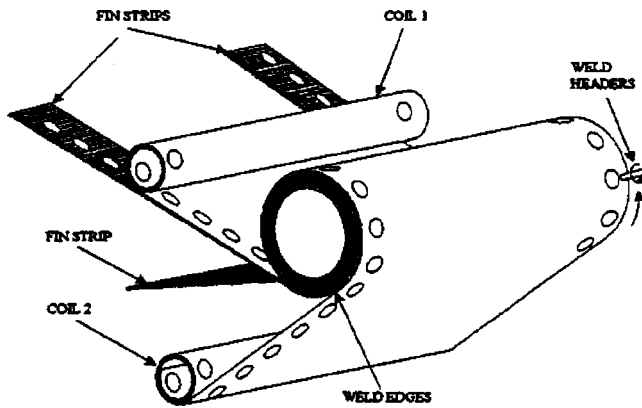


Fig. 1 Annular recuperator of plate-fin surface type (from Oswald [2])

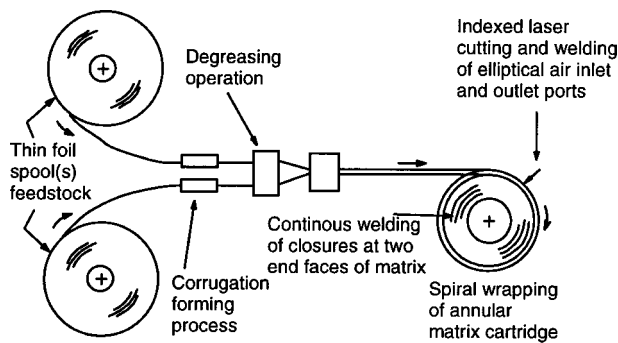


Fig. 2 Annular recuperator of primary surface type (from McDonald [1])

turbine recuperators the surfaces which show high heat transfer enhancement with an accompanying low increase of the pressure drop will successfully be integrated in actual recuperator designs. The four types of heat transfer surfaces, introduced below, all meet these requirements. Some surfaces presented in this study have been evaluated previously and they show competitive performance in terms of low weight and small volume of the recuperator matrix ([4]).

To provide comparison only of the thermal and hydraulic performances possible, the same hydraulic diameter has been used for all surface variants in the standard methods of comparison, the so-called volume goodness, area goodness diagrams, and in the design calculations for both air and gas sides in the recuperator. The hydraulic diameter chosen here is 1.54 mm. This passage size, or smaller, has already been demonstrated for three of the heat transfer surface types below. Whenever required, the available data have been used for extrapolation of Nusselt numbers and Fanning friction factors to low Reynolds numbers. The data of the CC surface has been extrapolated from $Re \approx 550$ down to $Re \approx 200$. Data of the other surfaces has been extrapolated less than that. Geometrical data and correlations of Nusselt numbers and friction factors, of all selected surface variants, are presented in Tables 1 and 2. The Nusselt (Nu) number and the product $f \cdot Re$ (Fanning friction factor · Reynolds number) are correlated by a linear least-squares method. All data obtained by the least square equations using the coefficients in Table 2 are within ten percent of the original data. This is illustrated by a plot of Nu numbers and friction factors of some selected surfaces, one from each group, in Figs. 3 and 4.

Cross-Corrugated (CC) Surface. The CC surface, also called the chevron plate, see Fig. 5, has been used in heat exchangers in the process industry and by tradition it has been classified as a plate-type heat transfer surface.

In the process industry the employed hydraulic diameter is bigger than 5 mm but for utilization in recuperators the CC duct

Table 1 Geometrical data of all surfaces

Type	Surface	Pitch P (mm)	Int. Height H_i (mm)	P/H_i	Length of Unitary Cell l_{uc} (mm)	Amplitude of Waviness A (mm)	C (m^2/m^3)	θ (Degrees)
CC	CC2.2-60	2.36	1.07	2.22	2.36	...	1298	60
CC	CC2.2-75	2.36	1.07	2.22	1.94	...	1298	75
CC	CC3.1-60	2.86	0.93	3.06	2.86	...	1298	60
CC	CC4-45	3.48	0.87	4.0	4.54	...	1299	45
CC	CC4-60	3.48	0.87	4.0	3.48	...	1299	60
CC	CC4-75	3.48	0.87	4.0	2.85	...	1299	75
CW	CW3-z3	1.38	2.28	0.61	2.98	0.79	1496	...
CW	CW3-z8	1.38	2.28	0.61	7.94	0.79	1343	...
CU	UCS-30	2.24, 3.17	1.30, 0.79	1.7, 4.0	6.33	...	1299	30
plate-fin	strip-fin	1.63	1.62	1.0	3.20	...	1192	...

Table 2 Coefficients of Nu and $f \cdot Re$ correlations in the form $(Nu, f \cdot Re) = C1 + C2 \cdot Re$

Type	Surface	Nu			$f \cdot Re$		
		C1	C2	R^2	C1	C2	R^2
CC	CC2.2-60	6.2884	0.1648E-01	0.9998	28.3023	0.3952E-01	0.9981
CC	CC2.2-75	8.8038	0.2307E-01	0.9998	38.7619	0.5413E-01	0.9981
CC	CC3.1-60	5.0307	0.1317E-01	0.9998	49.5291	0.6916E-01	0.9981
CC	CC4-45	2.9241	0.7655E-02	0.9998	21.3186	0.2948E-01	0.9978
CC	CC4-60	3.8988	0.1021E-01	0.9998	42.4535	0.5928E-01	0.9981
CC	CC4-75	6.1107	0.1478E-01	0.9995	85.6395	0.1362	0.9971
CW	CW3-z3	-0.5256	0.2309E-01	0.9993	51.7276	0.2524	1.0
CW	CW3-z8	1.8194	0.3878E-02	0.9990	26.1720	0.3131E-01	0.9982
CU	UCS-30	6.7538	0.1155E-02	0.9986	37.0463	0.1392E-01	0.9954
plate-fin	plate-fin	$f = 9.6243 Re^{-0.7422} \alpha^{-0.1856} \delta^{0.3053} \gamma^{-0.2659}$ $j = 0.6522 Re^{-0.5403} \alpha^{-0.1541} \delta^{0.1499} \gamma^{-0.0678}$					

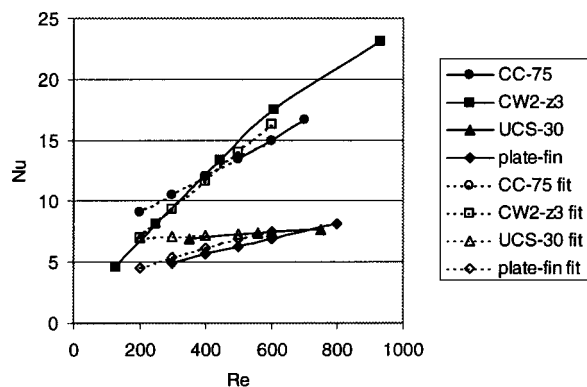


Fig. 3 Nusselt numbers and Nusselt number least square fits versus Reynolds number for some representative heat transfer surfaces

diameter must be much smaller and as it fulfills all requirements of a primary surface, it may be considered as a primary surface.

In an experimental study by Savostin and Tikhonov [7] of thermal and hydraulic performance of the CC surface, heat exchanger test modules having hydraulic diameters as small as 1.54 mm were fabricated for evaluation using a metallic material.

Another recuperator prototype was fabricated and tested in the late 1970s where a CC surface of stamped and folded design was used. The hydraulic diameter of the heat transfer test matrix was

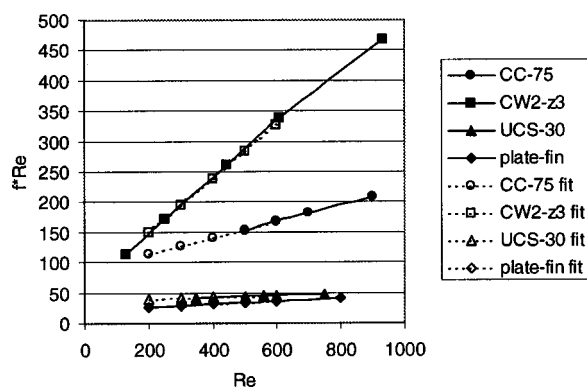


Fig. 4 Friction factors and friction factor least-square fits versus Reynolds number for some representative heat transfer surfaces

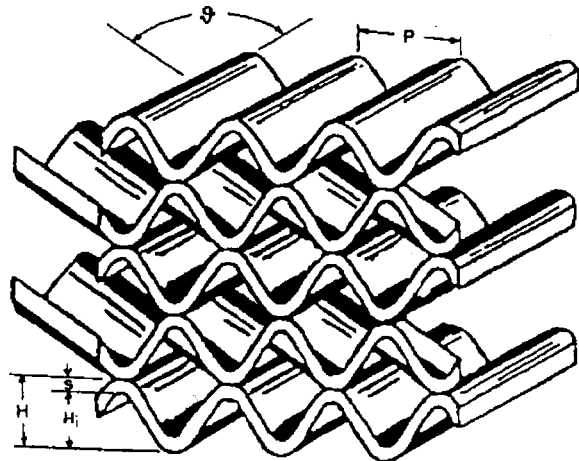


Fig. 5 The cross corrugated (CC) surface

1.24 mm and hydraulic diameters down to 0.6 mm were projected for different applications ([8,9]). This concept was not commercialized due to lack of application. The concept was re-evaluated recently for possible application in a low-cost annular microturbine recuperator ([10]).

Data of the thermal and hydraulic performance used in the present study have been retrieved from experimental work by Stasiek et al. [11]. The thermal and hydraulic performances of the CC surfaces having $P/H_i \approx 3$ and $P/H_i = 4$ were reported relative to a surface having $P/H_i = 4$ at $Re = 1000$.

Different pitch-over-height ratios ($P/H_i = 2.2, 3.1, 4$) have been considered in the present calculations and three different included angles ($\theta = 45$ deg, 60 deg, 75 deg), see Fig. 5, were evaluated.

The surface compactness (i.e., the ratio heat transfer surface area/enclosed volume) of all CC surfaces in this study, using the hydraulic diameter 1.54 mm, is about $1299 \text{ m}^2/\text{m}^3$.

Corrugated Undulated (CU) Surface. This is a variant, see Fig. 6, of the CC surface which also may be defined as a primary surface for the same reason as the CC surface above. It is only during the last decade that this type of surface has been presented in scientific papers for utilization in rotary air preheaters ([12,13]).

Production of this surface should be possible in the same manner as the CC surface, i.e., by stamping, pressing, or folding metal sheets/foil. The major disadvantage is that two different types of plates have to be fabricated which means more work for manufacturing and production specialists during the design phase.

The surface compactness, using the hydraulic diameter 1.54 mm, is about $1299 \text{ m}^2/\text{m}^3$. The data for the thermal and hydraulic performance, at low Reynolds numbers, have been obtained from a numerical work using direct laminar flow simulation ([14]).

Plate-Fin Surface. The offset strip fin (also called staggered fin), see Fig. 7, has been used in heat exchangers for decades. It consists of flow separating metal sheets with supportive offset strip fin secondary surfaces between them. The efficiency of thermal transport to the separating metal sheets from the secondary surfaces, the fins, depends on the fin height, fin material conductivity, etc. Good thermal contact is often secured by brazing the fin structure to the separating metal sheets. This configuration results in a higher mass of the recuperator unit than the primary surface types of surfaces. An advantage is the capability for operation with a high internal pressure difference (e.g., for an inter-cooled and recuperated gas turbine). In the results of the design calculations (in later sections) perfect thermal contact is assumed between the fin structure and the metal sheets but without the addition of the weight of the brazing material, which is not estimated in this study.

The offset strip fin surface considered here is the 1/10-19.74 which by Campbell and Rohsenow [15] was shown to give the smallest volume of a gas turbine (>5 MW) recuperator from a selection of the plate-fin surface configurations compiled in Kays and London [16]. This does not necessarily mean that this is the most efficient plate-fin surface but may only reflect that this surface has relatively good performance and the necessary small hydraulic diameter. All the plate-fin surface configurations having small hydraulic diameter perform well in the comparative study by Campbell and Rohsenow [15].

The correlations of the Nusselt number and the friction factor for the plate-fin configuration, see Table 2, are obtained from Manglik and Bergles [17].

The surface compactness for the strip fin surface considered in the present study, using the hydraulic diameter 1.54 mm, is about $1190 \text{ m}^2/\text{m}^3$.

Cross Wavy (CW) Surface. This is a commercially available primary surface concept, see Fig. 8, which consists of corrugated, flow separating, metal sheets where the corrugations are wavy in the main flow direction. These sheets are stacked in a manner that the waviness of the upper and lower duct halves are 180 deg out of phase relative to each other. A much higher volume flow rate of

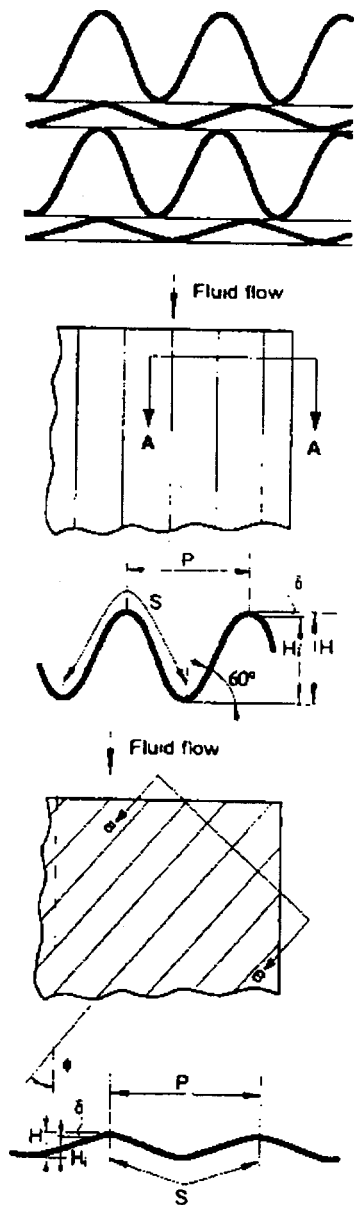


Fig. 6 The corrugated undulated (CU) surface (from Stasiek [12])

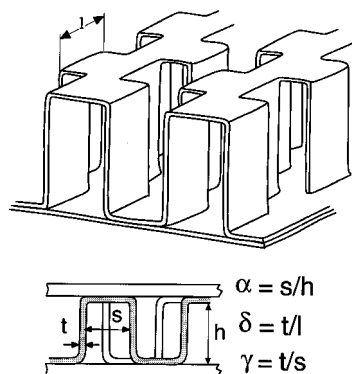


Fig. 7 The offset strip-fin surface

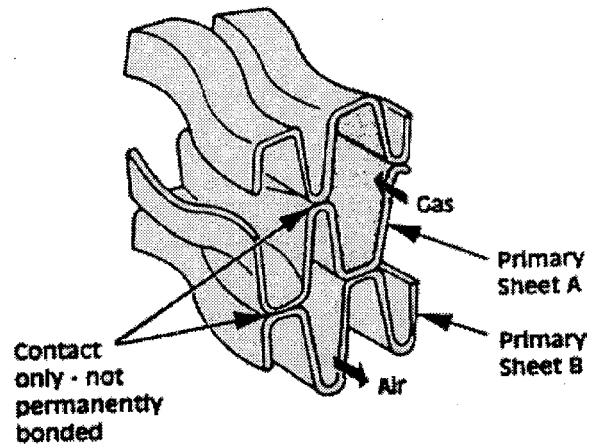


Fig. 8 The cross wavy (CW) surface

the noncompressed gas side flow lead to higher pressure drop and this is compensated for by having a bigger hydraulic diameter on the gas side and thus a lower velocity. In the present study the hydraulic diameters are equal, i.e., the same as for all other surfaces (1.54 mm), on both the gas and air sides, to enable a comparison of the thermal and hydraulic performances to the other heat transfer surfaces.

The wavy corrugation of the surface is obtained using a folding process. Pressing or stamping of the CW configurations in the present study is not possible, because of the very small pitch and relatively high height of the passage, see Table 1. This is due to, e.g., pressing tool and metal foil strength limitations. The data of thermal and hydraulic performance of the CW surface has been obtained from numerical work using direct laminar flow simulation [18].

The surface compactness, using the hydraulic diameter 1.54 mm, is about $1343 \text{ m}^2/\text{m}^3$ for the cw3z8 surface and about $1496 \text{ m}^2/\text{m}^3$ for the cw3z3 surface, see Table 1.

The Cross Corrugated (CC) Surface in the Literature

There are several investigations of the CC surface performance in the literature. In the present study the thermal and hydraulic performance of the laminar flow regime is of main interest as the design calculations, see later sections, show that the resulting Reynolds number is less than 550 for all selected surfaces. Several investigations are reviewed by Manglik [19]. However most of the results are only for turbulent flows. Several investigations reporting low Reynolds number results account only the thermal and hydraulic performance as depending on the included angle between the corrugations, i.e., influence of other surface geometry parameters such as pitch (P) and internal height (H_i) are not studied. The pitch (P) to internal height (H_i) ratio of the corrugation, see Fig. 5, has a great influence on the heat transfer and pressure drop ([11,20]).

Marriot [21], Heavner and Kumar [22], Wanniarachchi et al. [23], and Thonon et al. [24] report the dependence of the included angle (θ) but all other geometrical details of the CC surfaces are missing. Other investigations addressing the performance of the CC surface for relatively low Reynolds number flows include the Savostin and Tikhonov [7] report on experimental results for the Reynolds number range 200–4000, included angle range (θ) 0–145 deg and the surface P/H_i ratio from 0.8 to 2. Okada et al. [20] investigated the performance of the CC surface by experiments in the Reynolds number range 500–20,000, included angle range 0–150 deg and the P/H_i range 2–3.75. In that investigation the dimension of the reported pressure drop is not clear. Focke et al. [25] reported experimental work in the Reynolds number range (in the Reynolds number definition the equivalent diameter (D_{eq}) is twice maximum plate spacing, i.e., $2H_i$) 100–60,000,

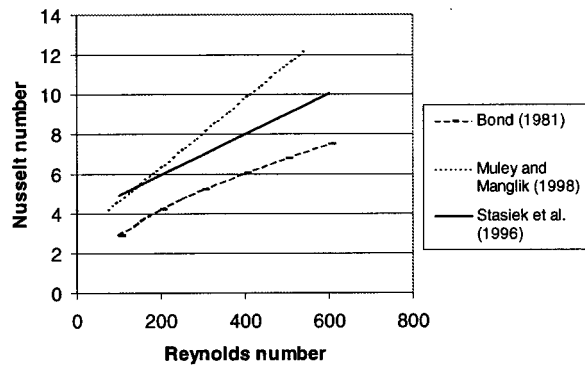


Fig. 9 Comparison of thermal performance in published literature for a CC surface with $\theta=60$ deg and $P/H_i \approx 4$

included angles 0–180 deg and $P/H_i=2$. Experimental work of Bond [26] reports thermal and hydraulic performance in the Re range 1–10,000, included angles 50–120 deg and the $P/H_i=4$. Muley and Manglik [27] report experimental results for the Reynolds number range (in the Reynolds number definition the equivalent diameter (D_{eq}) is twice maximum plate spacing, i.e., $2H_i$) 400–9000, included angle 60–120 deg and $P/H_i=3.6$. Muley and Manglik [28] report experimental results for the Reynolds number range (in the Reynolds number definition the equivalent diameter (D_{eq}) is twice maximum plate spacing, i.e., $2H_i$) 2–350, included angle 60–120 deg and $P/H_i=3.6$. Ciofalo et al. [29] report some sparse results from a numerical study. Predictions of thermal and hydraulic performance by computational fluid dynamics (CFD), in the Reynolds number range 500–10,000, included angle 30–150 deg and P/H_i range 2–4 were presented. Stasiek et al. [11] report experimental (thermal performance attained using liquid crystal thermography) results of the CC surface in the Reynolds number range 500–4000, included angles 45–75 deg and P/H_i in the range of 2.2–4.

All the CC surface characteristics reported in the present study are based on low Reynolds number data extracted from Stasiek et al. [11] because they investigated the influence of a suitable (for air/gas heat exchangers) range of the included angle between corrugations and also the influence of a practical range of P/H_i ratios. Their investigation is also one of the few papers reporting thermal performance for experiments using air as the working fluid. The others report their data in the form Nu^*Pr^n where n is -0.33 or -0.4 .

From all the above references it is difficult to extract performance characteristics having an equal (low) Reynolds number range, angles (θ) and P/H_i ratio and to plot Nusselt number (Nu) and Fanning friction factor (f). In Figs. 9 and 10 the results from three references are plotted. Muley and Manglik [28] ($\theta=60$ deg,

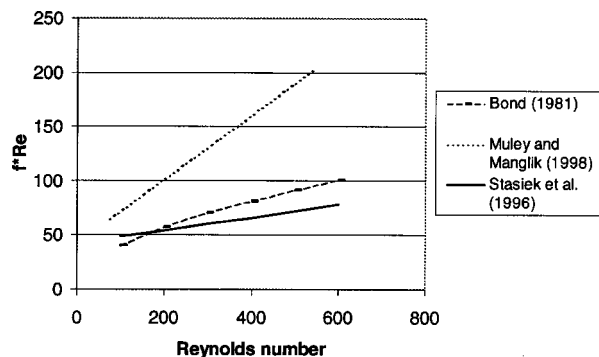


Fig. 10 Comparison of hydraulic performance in published literature for a CC surface with $\theta=60$ deg and $P/H_i \approx 4$

Table 3 Microturbine operating conditions

Gas turbine power output	50 kW
Thermal efficiency	29.5 percent
Turbine inlet temperature	900°C
Turbine flow	0.494 kg/sec
Turbine efficiency	84.0 percent
Compressor flow	0.49 kg/sec
Compressor pressure ratio	4
Compressor Efficiency	79 percent
Recuperator effectiveness	87 percent
Recuperator air temp. inlet/outlet	194°C/557°C
Recuperator gas temp. inlet/outlet	637°C/254°C
Recuperator $\Delta p/p_{tot}$	5 percent

$P/H_i=3.6$) reported thermal performance in the form $Nu^*Pr^{-0.33}(\mu_b/\mu_w)^{-0.14}$, where the viscosity ratio, in a recuperator for a representative gas turbine in Table 3, accounts for a maximal influence of 0.5 percent, on the Nusselt number, for the low Prandtl number fluid air ($Pr=0.7$). The Reynolds number was based on an equivalent diameter (D_{eq}) which was equal to twice the maximum plate spacing, i.e., $2H_i$. For the plots in Figs. 9 and 10 the Reynolds number was transformed to that adopted in the present study (see Nomenclature). Bond [26] also reported thermal performance in a similar form, $Nu^*Pr^{-0.33}(\mu_b/\mu_w)^{-0.17}$. The exponent for the viscosity ratio is different but will be negligible for air flow. The linear characteristics, in a log-log diagram, of the Nu number reported by Stasiek et al. [11] are extrapolated from $Re \approx 550$ down to $Re \approx 200$. This may be justified by searching for a change of slope in the reported thermal characteristics, i.e., for CC surfaces having the angle $\theta=60$ deg between the corrugations. Thonon et al. [24] reported no change of slope for Reynolds numbers in the range 50–13,000. In Focke et al. [25] one can detect a sudden but small change of thermal characteristics at $Re \approx 1000$ but the slope is unchanged (for a straight duct they reported a change from laminar to turbulent flow at $Re=6000$ –9000). In Bond [26] there is a small change of slope at $Re \approx 450$. The extrapolation of the Stasiek et al. [11] data seems not to contribute to any significant error of the low Reynolds number thermal performance.

For the plot of the Fanning friction factor (f), see Fig. 10, the Stasiek et al. [11] friction factor data were changed from Darcy friction factor (λ) to Fanning friction factor (f) and has been extrapolated from $Re=550$ down to $Re=200$. The Bond [26] and Muley and Manglik [28] Fanning friction factor data are also presented for comparison. A survey of the hydraulic performance of similar CC surface configurations, i.e., with the same included angle (θ), shows that there is a change in slope. Thonon et al. [24] show that this change occurs at $Re=500$. In Bond [26] there is a small change of slope at $Re=450$. The conclusion one may draw from the above is that there is a change of slope at $Re=500$ and the extrapolation of the Fanning friction factor data of Stasiek et al. [11] may lead to a slight underprediction of the pressure drop for $Re < 500$ (assuming the higher Reynolds number friction data coincide with the pressure drop in actual operating heat exchangers).

The comparison of the hydraulic performance, see Fig. 10, shows fair agreement between the Stasiek et al. [11] and Bond [26] data, while the Muley and Manglik [28] data show about 100 percent higher friction factors. An explanation for this discrepancy can not be found by the present authors except that their P/H_i ratio is slightly smaller than in the other data sets, which can not account for the large discrepancy. Comparison of the thermal performance, see Fig. 9, shows that there is about a 50 percent difference between the highest and lowest values of Nusselt numbers. The Stasiek et al. [11] results represent a median set of the data.

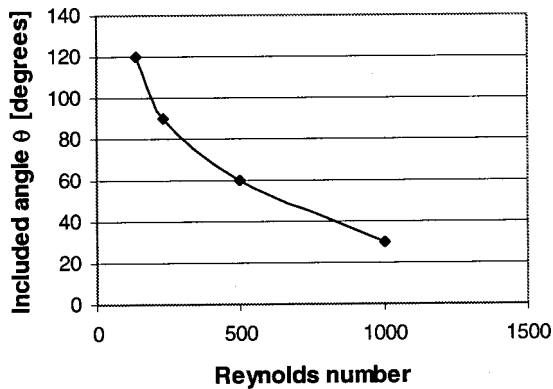


Fig. 11 Approximate occurrence of transition from laminar to turbulent flow, extracted from Thonon et al. [24]

The changes in slope discussed above are due to transition from laminar to turbulent flow. Bond [26] and Thonon et al. [24] show fair agreement on the occurrence of the slope change, i.e., when transition from laminar to turbulent flow occurs. The transition points of different included angles (θ) have been plotted in Fig. 11. These results show that when the included angle is increased from 30 deg to 120 deg the critical Reynolds number is decreased from about 1000 to 200.

As a matter of curiosity, the friction factor characteristics of the CC surface, as function of the P/H_i ratio only, is different from what might be expected. The Fanning friction factor (f) of the CC surface ($\theta=60$ deg) is higher for $P/H_i=3$ than it is for the surfaces having $P/H_i=2$ and $P/H_i=4$. This is confirmed by the results reported by Okada et al. [20].

Results

The selected heat transfer surfaces may be compared by standard methods of comparison in two diagrams [30]. Both methods consider only the performance of one side of the heat exchanger, i.e., gas or compressed air side. The first one is the volume goodness factor comparison, see Fig. 12, where the axes represent the heat transfer coefficient (h) and pumping power per unit heat transfer area ($\Delta p \cdot \dot{V}/A_{ht}$), respectively. Δp is pressure drop along the duct, \dot{V} is the volume flow rate and A_{ht} is the heat transfer surface area. A high position in this plot indicates a small volume of the recuperator core but it does not say anything of the shape of the volume. In the volume goodness factor diagram an equal hy-

draulic diameter for all surface variants is required for correct comparison. The second plot, see Fig. 13, shows the performance of the surfaces in a diagram for flow area goodness factor comparison where the ratio of the Colburn number and the Fanning friction factor (j/f) is plotted vs. the Reynolds number (Re). A high position in this plot indicates a small flow area of the recuperator. Combining these two diagrams gives an opportunity to find surfaces giving small physical recuperator size but also means to avoid very flat recuperators, i.e., large frontal area but small length in the flow direction.

A preferred way to compare different surfaces for a recuperator is to carry out recuperator design calculations and to compare, e.g., physical size, weight, etc. In this paper, recuperator heat transfer matrix calculations, see the Appendix, have been carried out for a representative microturbine having an output power of 50 kW. Operating conditions are given in Table 3 ([31]). In the calculations, some assumptions, based on experience from the industry, have been made:

- 90 percent of the total heat is transferred in the heat transfer matrix.
- 60 percent of the total pressure drop is over the heat transfer matrix, i.e., $\Delta p/p_{tot} \cdot matrix=3$ percent, see Table 3. All primary surface variants are suitable for the same kind of recuperator design, i.e., the pressure drop of the inlet and outlet manifolds may be regarded as equal for all surface variants.
- The metal sheet thickness is 0.08 mm except for the fin thickness in the plate-fin configuration where 0.05 mm is used.
- The hydraulic diameter is 1.54 mm for both the air and gas sides of the recuperator matrix.

The hydraulic diameter is the variable having the greatest impact on the recuperator core volume. A small hydraulic diameter will give a small recuperator volume, see Fig. 14 where the volume of the CC4-60 surface variant is plotted for different hydraulic diameters. In the calculations the transferred heat, recuperator effectiveness and total pressure drop are held constant. The volume is decreased to less than half the initial volume by decreasing the hydraulic diameter (D_h) from 2.0 mm to 1.0 mm. This shows the importance of achieving a fabrication method which gives small passage dimensions. The Reynolds number at design operating conditions in the recuperator matrix decreases from $Re=460$ (for $D_h=2.0$ mm) to $Re=200$ (for $D_h=1.0$ mm).

The gain in recuperator matrix volume by allowing greater total pressure drop, Δp_{tot} , is also worthwhile to consider. If the total relative pressure drop is allowed to be five percent instead of three percent over the matrix then the gain in volume would be approximately 11 percent, i.e., a decrease of the volume from 0.018 m^3 to

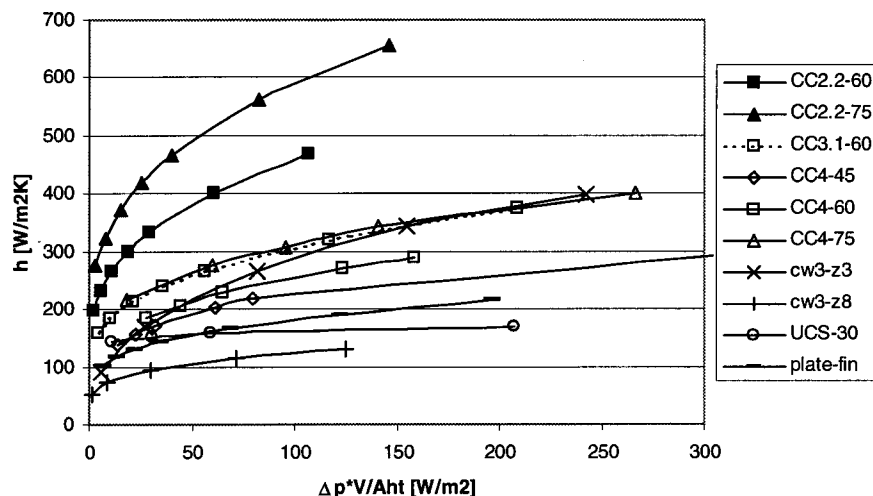


Fig. 12 The volume goodness diagram

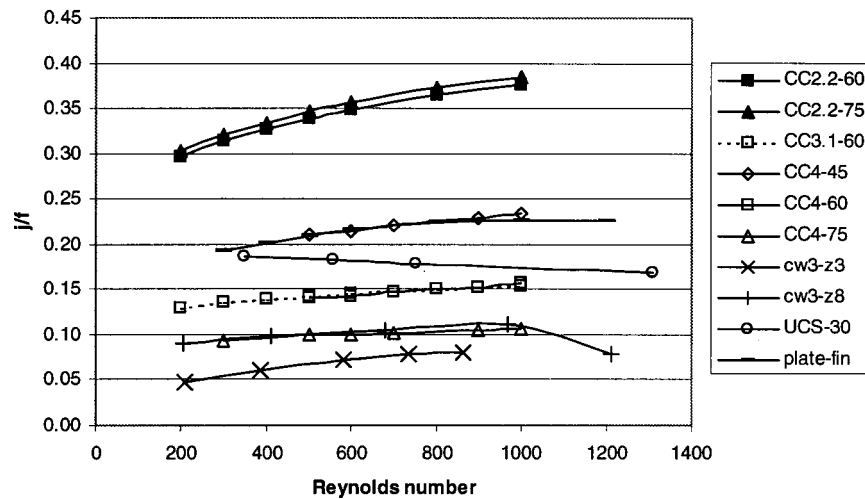


Fig. 13 The area goodness diagram

0.016 m³ for the CC4-60 surface, see Fig. 15. Economical gain (smaller cost of recuperator) by increasing pressure drop in the recuperator has to be balanced with the loss in overall cycle efficiency and the resulting higher fuel consumption.

In this study the hydraulic diameter of the different surface variants are all equal (1.54 mm) to compare only the thermal and hydraulic performances of the surfaces. The small dimensions give relatively high pressure drop at low Reynolds numbers. The resulting Reynolds number in the recuperator cores ranges from

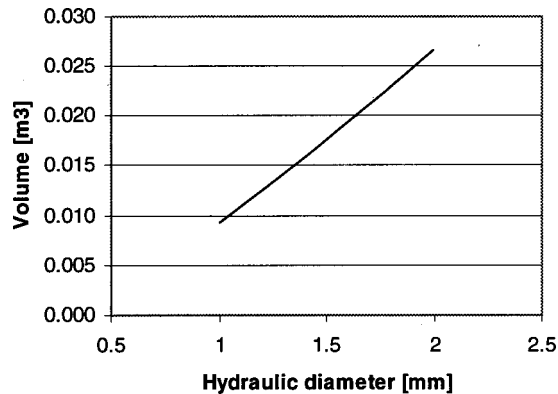


Fig. 14 Volume of the recuperator core, using the CC4-60 surface, for different sizes of the hydraulic diameter

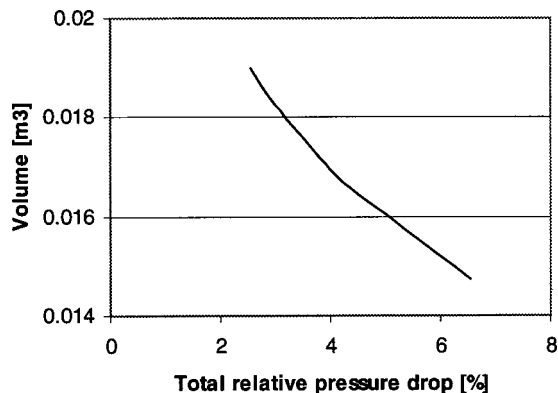


Fig. 15 Volume of the recuperator core, using the CC4-60 surface, for different total pressure drop in the matrix

270 to 540 (about equal on both air and gas sides of each heat exchanger), see Table 4, which may not be in the laminar flow regime for the higher Reynolds numbers, see discussion in previous section and Fig. 11. This will not be a problem when the gas turbine is operating at design conditions, i.e., turbulent flow in the recuperator matrix but may cause trouble if the turbine is operated at off-design conditions (part load). This is so if the turbine control is based on constant turbine inlet temperature. In such a control mode the volume and massflow rates are changing, which means that the Reynolds number in the recuperator core will change and the recuperator flow regime will go from turbulent to laminar flow and vice versa which may be difficult to handle for the control because of different pressure drop, (and maybe also thermal), characteristics in the laminar and turbulent flow regimes. This trouble may be avoided if the hydraulic diameter of the recuperator passages is decreased to be smaller than 1.54 mm. Then the resulting Reynolds number in the recuperator matrix will be lower for operation at the design conditions, see discussion above in connection with Fig. 14.

In Figs. 16 and 17 the resulting recuperator matrix volume and weight of each surface are shown. All the CC surfaces perform well compared to the plate-fin surface and the CW3-z8 surface. The CC surfaces having the smallest P/H_i ratios result in the smallest matrix volumes and lowest weights. Similarly, high values of the included angle (θ) give smaller volumes and weights due to better thermal performance but the higher friction factors (f) necessitate shorter length (L) of the matrix.

The CW surface is the only one that has been utilized in actual operating primary surface recuperators. The performance of the CW surface is improved significantly by decreasing the ratio, length of a unitary cell to amplitude of the waviness (l_{uc}/A_w), or in other words, by keeping the amplitude (A_w) of waviness (of the CW3-z8 surface) but decreasing the length of the unitary cell (which also is the "wave length"). Comparing the performance of the CW3-z8 surface to that of the CW3-z3, the shorter length of the unit cell (l_{uc}) results in a decrease of the matrix volume from approximately 0.044 m³ to 0.014 m³. This is a considerable improvement. The fabrication of the shorter one may not be possible in practice because of material strength limitations. It may result in cracking of the material, but any achieved length reduction, of a unit cell, should improve the performance of the CW surface.

The performance of the plate-fin surface is, relative to the others, not satisfactory. This surface has about four times the volume and weight of the CC2.2-75 surface. To the already high weight, the mass of the brazing material should be added.

The CU surfaces show relatively low values in both volume and weight but the major disadvantage of this kind of surface is that

Table 4 Results of design calculations

Surface	Re	Volume (m ³)	Weight (kg)	Width (B) (m)	Length (L) (m)	Inner Diameter (I/D) (m)	Outer Diameter (O/D) (m)
CC2.2-60	529	8.85E-03	7.2	0.310	0.092	0.500	0.610
CC2.2-75	534	6.29E-03	5.1	0.307	0.067	0.500	0.608
CC3.1-60	346	1.38E-02	11.2	0.383	0.094	0.500	0.661
CC4-45	409	2.19E-02	17.7	0.353	0.175	0.500	0.639
CC4-60	328	1.83E-02	14.8	0.393	0.118	0.500	0.669
CC4-75	274	1.30E-02	10.5	0.429	0.071	0.500	0.696
CW3-z3	376	1.43E-02	13.3	0.372	0.103	0.500	0.653
CW3-z8	283	4.37E-02	36.7	0.427	0.240	0.500	0.694
UCS-30	396	1.82E-02	14.7	0.359	0.141	0.500	0.644
plate-fin	415	2.25E-02	25.5	0.354	0.179	0.500	0.640

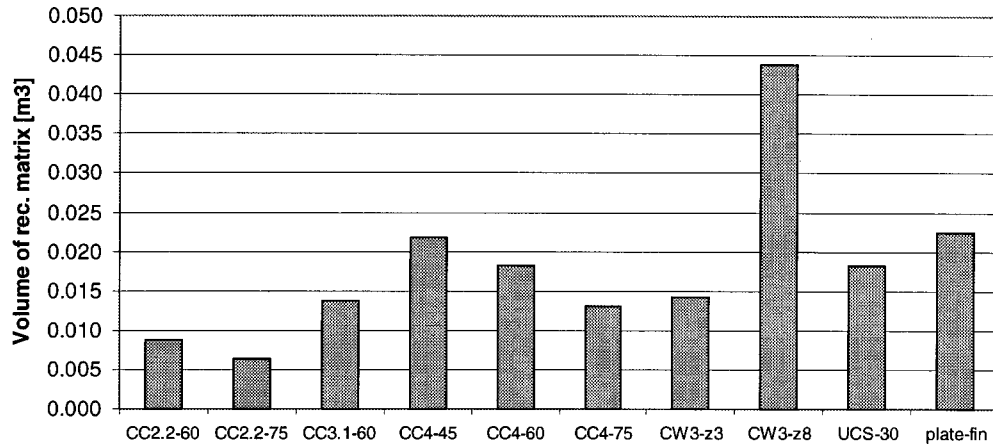
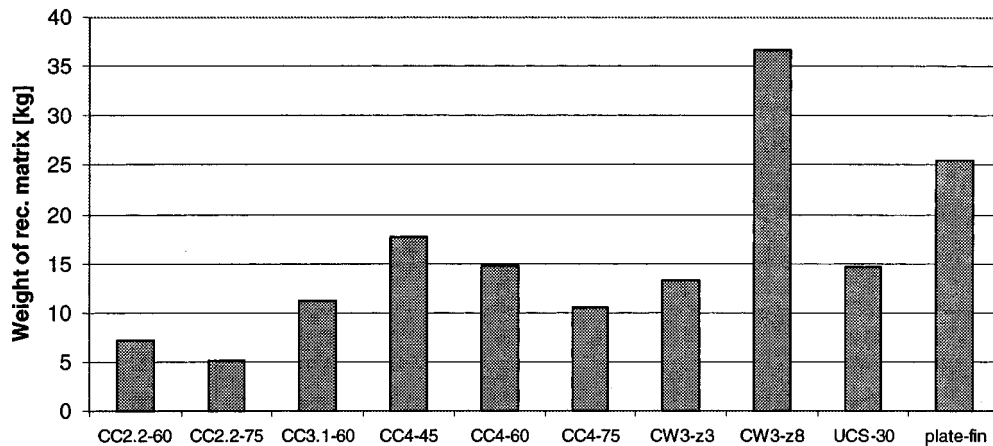
there is two different surfaces involved to form the matrix passages. This means extra cost for, e.g., tool development and fabrication.

All results in Figs. 16 and 17 are also presented in tabular form. The matrix dimensions presented in Table 4 correspond to the cube shaped recuperator configuration, see Fig. 18, and the annular configuration, see Fig. 19.

The inlet and outlet manifolds for each recuperator configuration will have about equal sizes, if they all have the same mass flow rate of gas and air flow. The total length of the recuperator will increase by 50–150 percent (depending on the length L of the recuperator matrix, see Table 4) and the weight will increase accordingly. Other concepts of air and gas flow management (which

do not include punching of inlet and outlet port holes on the actual metal foil) would probably give smaller addition to the integral recuperator volume.

For a comparison with actual operating gas turbine recuperators, four of the heat transfer matrixes in the present study were chosen (the ones having smallest volume of each surface group). To enable this comparison the sizes of air inlet and outlet manifolds for the cube shaped configuration, of Fig. 18, were roughly estimated. Using empirical algorithms, used for the CC surfaces (used in the process industry) by a heat exchanger manufacturer, the inlet and outlet port sizes were estimated. Also the hydraulic diameter had to be changed to a level that state-of-the-art heat exchangers have today, $D_h = 1.0$ mm (examples of this may be

**Fig. 16 Results of design calculations, volume of recuperator matrix****Fig. 17 Results of design calculations, weight of recuperator matrix**

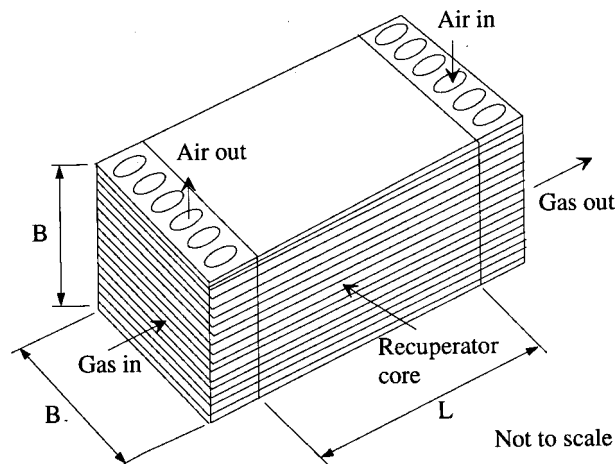


Fig. 18 Cube-shaped recuperator concept

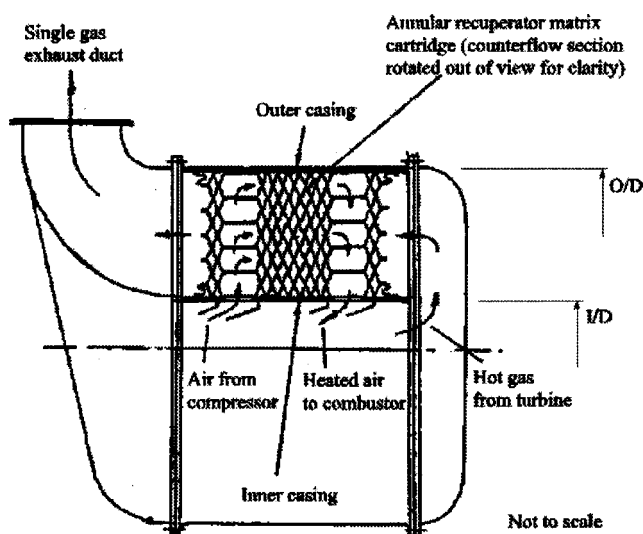


Fig. 19 Annular recuperator cartridge (from McDonald [1])

found in the literature, see, e.g., Parsons [32] and Kays and London [16]). The gas flow cross sectional shape of the cubic configuration had to be changed to allow for a reasonable pressure drop ($Dp_{\text{air ports}}/p_{\text{air}} \approx 0.5$ percent) and shape. The result is an individual shape for each of the four recuperators but they all have seven inlet and outlet ports, respectively. The port diameter is 39 mm. The resulting recuperator specific volumes are presented in Fig. 20, where the axes represent recuperator effectiveness and specific volume (recuperator volume/mass flow rate), respectively. The primary surface recuperators (CC, CW, and CU configurations) perform very well compared to the available examples of operating recuperators. Their volumes are approximately 30 percent less than what could be expected from primary surface recuperators of today (the gray zone in Fig. 20). Even the performance of the plate-fin configuration is surprisingly good. This may be explained by the small hydraulic diameter and the relatively efficient plate-fin heat transfer surface type.

Attention should also be focused on the pressure drop distribution between the air and gas sides of the recuperator. The volume flow rate, and therefore also the velocity, is much higher on the gas side because of the low pressure (close to atmospheric pressure) as compared to the four times higher pressure on the air side. The high volume flow rate leads to a high pressure drop on the gas side and a very low one on the air side. In present study, the air side pressure drop is only 0.2 percent (applies to all surfaces in the present study) of the total pressure drop which is 3 percent. This may cause poor distribution of the air between each pair of plates in the stack if the pressure drop is bigger in the port holes, see Fig. 18. There are two ways to change the pressure drop distribution, i.e., to increase the relative pressure drop for the air side. The first one is to change the respective cross sectional areas by, e.g., having different radius of the top of corrugations. Then the free flow area is larger for the gas side, see Fig. 21, which will decrease the velocity and therefore also the pressure drop. The other way is to distribute the pressure drops of the inlet and outlet areas on each side. The gas side inlet and outlet areas situated around the port holes consist of at least one and probably two flow area sudden contractions and expansions (due to passage strength and welding considerations) which are known to give relatively high pressure drop. The gas side inlet and outlet areas are subjected to similar flow contractions but distributed over a larger area (depending on the number of air port holes). By making a suitable tradeoff between these sources of pressure losses one may slightly redistrib-

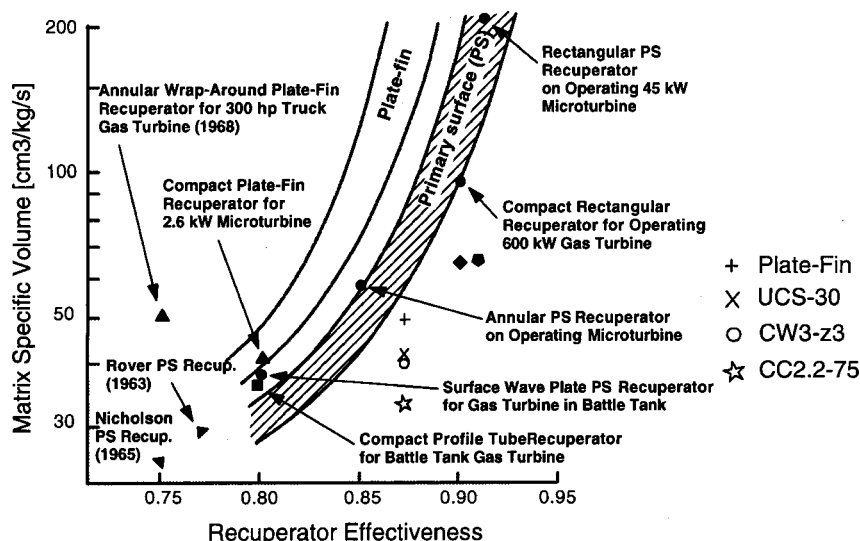


Fig. 20 Comparison of specific volume of some representative recuperators from present study with operating recuperators. (Diagram used with permission of C. F. McDonald, La Jolla, CA, USA.)

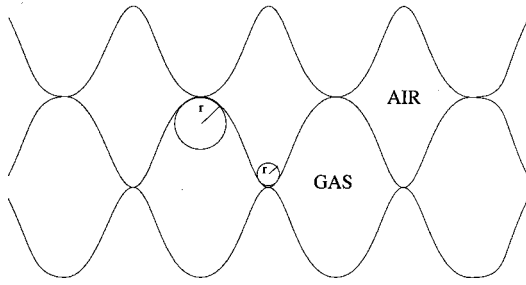


Fig. 21 Nonsymmetric CC surface passages to compensate for the mal distribution of pressure drop between gas and air sides

ute the pressure losses so that the air side pressure losses are increased. Both ways, briefly discussed above, may be utilized to ensure that severe mal distribution of mass flow is avoided.

The specific volumes, in Fig. 20, would not be significantly changed if the average of the air and gas side hydraulic diameters is kept around 1 mm. The thermal and hydraulic characteristics of the larger gas side passages should not be much different from the smaller air side passages if they have a similar shape of the flow cross section.

Conclusions

Thermal efficiencies of microturbines in excess of 30 percent a recuperator is mandatory. In this paper comparison, of three primary surface type of surfaces and an offset strip fin plate-fin surface, has been made for intended use in a recuperator heat transfer matrix.

Surface selection criteria as the volume goodness and the flow area goodness diagrams have been used for a first selection of surfaces. Results of recuperator heat transfer matrix design calculations are both shown in diagrams and tabulated to find the heat transfer surfaces giving the smallest volume and weight of the integral recuperator unit for a representative 50 kW microturbine. Dimensions of the corresponding recuperator matrixes were reported for a cube shaped unit and an annular spirally wrapped unit. If the total cost of a recuperator unit, fabricated in very large quantities, is a multiple of the material cost, as suggested by McDonald [1], then a small weight of the recuperator has highest priority.

It was shown that by allowing a bigger total pressure drop over the heat transfer matrix or decreasing the size of matrix passages the total volume of the matrix is reduced.

Some aspects of design and fabrication of recuperators using different kinds of heat transfer surfaces were also discussed.

The cross wavy (CW) and especially the cross corrugated (CC) surfaces show superior performance over the others giving a small volume and weight of the heat transfer matrix, but as the CC surface is well documented in the literature and probably is easier to manufacture with small passage dimensions this should be the first choice for further studies by recuperator manufacturers.

The design results show that a cross corrugated (CC) surface has the best potential for use in compact recuperators of the future as it will have smaller volume than any recuperator in operation today.

Acknowledgments

The authors wish to thank C. F. McDonald (McDonald Thermal Systems) for showing interest in our work and for the discussions through numerous e-mails and facsimiles. Financial support was received from STEM, the Swedish Energy Administration.

Nomenclature

- A = amplitude of waviness (mm)
- A_{ht} = heat transfer area (m^2)
- B = width of recuperator (m)
- C = coefficient of compactness, ratio of heat transfer surface/internal volume (m^2/m^3)
- c_p = specific heat (J/kg K)
- CC = cross corrugated heat transfer surface, also called chevron pattern
- CU = corrugated undulated heat transfer surface
- CW = cross wavy heat transfer surface
- D_h = hydraulic diameter $D_h = 4 \times \text{area of cross section} / \text{wetted perimeter}$ (m)
Other surfaces $D_h = 4 \times \text{internal volume of unitary cell} / \text{wetted surface}$ (m)
- D_{eq} = equivalent diameter, $D_{eq} = 2 \times H_i$, $D_{eq} = D_h^* \phi$
- f = Fanning friction factor, $4f = \text{Darcy friction factor}$
- H_i = internal height, see, e.g., Fig. 5 (mm)
- h = heat transfer coefficient ($W/m^2 K$)
- j = Colburn factor $St \times Pr^{2/3}$
- k = thermal conductivity (W/m K)
- l_{uc} = length of unitary cell (m)
- L = length of recuperator matrix (m)
- Nu = Nusselt number, $h \times D_h / k$
- P = pitch, see, e.g., Fig. 5 (mm)
- Δp_{tot} = total relative pressure drop over heat exchanger $\Delta p_{tot} = \Delta p_{gas}/p_{gas} + \Delta p_{air}/p_{air}$
- Pr = Prandtl number $Pr = \mu^* c_p / k$
- r = radius of circle (m)
- Re = Reynolds number $Re = D_h^* U_{av} / \nu$
- St = Stanton number $Nu / Re \times Pr$
- \dot{V} = volume flow rate (m^3/s)
- ϕ = developed heat transfer area/projected heat transfer area
- μ = dynamic viscosity (kg/m s)
- ν = kinematic viscosity (m^2/s)
- θ = included angle between corrugations (deg)
- α = see Fig. 7
- β = see Fig. 7
- γ = see Fig. 7
- μ_b, μ_w = dynamic viscosity at bulk conditions and wall conditions, respectively (kg/m s)

Appendix

The design calculations for each heat transfer surface are based on the following algorithm. Here is a simplified algorithm for primary surface configurations.

Input:

- dimensions of unit cell
- total heat (Q) transferred in the recuperator matrix, calculated with help of data in Table 3.

Step 1. Choose Re number for air side. Calculate velocity, W_{air} , for air side

$$W_{air} = \frac{Re_{air} \nu_{air}}{D_{h,air}}$$

Step 2. Calculate velocity of gas side from

$$W_{gas} = W_{air} \frac{\dot{m}_{gas} \rho_{air} A_{air}}{\dot{m}_{air} \rho_{gas} A_{gas}}$$

Step 3. Calculate Nu numbers and f factors, for both sides, using correlations in Table 2.

Step 4. Calculate heat transfer coefficients, for both sides. Here air side

$$h_{\text{air}} = \frac{\text{Nu}_{\text{air}} k_{\text{air}}}{D_{h,\text{air}}}$$

Step 5. Calculate the overall heat transfer coefficient from

$$\dot{U} = 1 / \left(\frac{1}{h_{\text{air}}} + \frac{1}{h_{\text{gas}}} + \frac{s}{k_{\text{wall}}} \right).$$

Step 6. Calculate the total heat transfer area:

$$A_{\text{tot}} = \frac{Q}{U \Delta T_{\text{log}}}.$$

Step 7. The compact coefficient (C) is calculated from a representative control volume of each heat transfer surface configuration:

$$C = A_{cv} / V_{cv}.$$

Step 8. The total volume of the recuperator can then be calculated using the following relation:

$$V_{\text{recuperator}} = A_{\text{tot}} / C.$$

Step 9. The total front area (flow area at inlet) is obtained from

$$A_{\text{front}} = A_{\text{air}} + A_{\text{gas}} + A_{\text{metall}}$$

where as an example the inlet flow area for air is

$$A_{\text{air}} = \frac{\dot{m}_{\text{air}}}{\rho_{\text{air}} w_{\text{air}}}.$$

Step 10. The total length of the recuperator heat transfer matrix is then obtained from

$$L_{\text{recuperator}} = V_{\text{recuperator}} / A_{\text{front}}.$$

Step 11. The pressure losses for both sides. Here the air side

$$\Delta p_{\text{air}} = 2 f_{\text{air}} \frac{L_{\text{recuperator}}}{D_{h,\text{air}}} \rho_{\text{air}} w_{\text{air}}^2.$$

Step 12. The total relative pressure losses:

$$\bar{\Delta p}_{\text{total}} = \Delta p_{\text{air}} / p_{\text{air}} + \Delta p_{\text{gas}} / p_{\text{gas}}.$$

Step 13. If the $\bar{\Delta p}_{\text{total}}$ is not equal to 0.03 (three percent, see assumptions at the beginning of the results section and Table 3) then go back to Step 1 and adjust the Re number.

References

- [1] McDonald, C. F., 2000, "Low Cost Recuperator Concept For Microturbine Applications," ASME Paper 2000-GT-167.
- [2] Oswald, J. I., Dawson, D. A., and Clawley, L. E., 1999, "A New Durable Gas Turbine Recuperator," ASME Paper 99-GT-369.
- [3] Antoine, H., 1997, "Echangeur de Chaleur Spirale," European Patent EP 0798527 B1.
- [4] Utriainen, E., and Sundén, B., 2001, "A Comparison of Some Heat Transfer Surfaces for Small Gas Turbine Recuperators," ASME Paper 2001-GT-0474.
- [5] Webb, R. L., 1994, *Principles of Enhanced Heat Transfer*, John Wiley and Sons, New York.
- [6] Jacobi, A. M., and Shah, R. K., 1995, "Heat Transfer Surface Enhancement Through the Use of Longitudinal Vortices: A Review of Recent Progress," *Exp. Therm. Fluid Sci.*, **11**, pp. 295–309.
- [7] Savostin, A. F., and Tikhonov, A. M., 1970, "Investigation of the Characteristics of Plate-Type Heating Surfaces," *Teploenerg.*, **17**, No. 9, pp. 75–78.
- [8] Kleeman, M., 1978, *Auslegung Eines Neuartigen Kompakten Rekuperators*, Doktor-Ingenieurs Genehmigte Dissertation, Technischen Hochschule Aachen.
- [9] Förster, S., and Kleeman, M., 1978, "Compact Metallic and Ceramic Recuperator for Gas Turbines," ASME Paper 78-GT-62.
- [10] McDonald, C. F., 2000, "Low Cost Primary Surface Recuperator for Microturbines," *Journal of Applied Thermal Engineering*, **29**, pp. 471–497.
- [11] Stasiek, J., Ciofalo, M., and Collins, M. W., 1996, "Investigation of Flow and Heat Transfer in Corrugated Passages—I. Experimental Results," *Int. J. Heat Mass Transf.*, **39**, No. 1, pp. 149–164.
- [12] Stasiek, J. A., 1998, "Experimental Studies of Heat Transfer and Fluid Flow Across Corrugated-Undulated Heat Exchanger Surfaces," *Int. J. Heat Mass Transf.*, **41**, Nos. 6–7, pp. 899–914.
- [13] Ciofalo, M., Collins, M. W., and Stasiek, J. A., 1998, "Flow and Heat Transfer Predictions in Flow Passages of Air Preheaters: Assessment of Alternative Modeling Approaches," *Computer Simulations in Compact Heat Exchangers*, B. Sundén and M. Faghri, eds., Computational Mechanics Publications.
- [14] Utriainen, E., and Sundén, B., 2001, "Numerical Analysis of Laminar Flow in Corrugated Undulated Ducts," *Compact Heat Exchangers and Enhancement Technology for the Process Industries—2001*, R. K. Shah, A. W. Deakin, H. Honda, and T. M. Rudy, eds., Begell House, New York.
- [15] Campbell, J. F., and Rohsenow, W. M., 1992, "Gas Turbine Regenerators: A Method for Selecting the Optimum Plate-Finned Surface Pair for Minimum Core Volume," *Int. J. Heat Mass Transf.*, **35**, No. 12, pp. 3441–3450.
- [16] Kays, W. M., and London, A. L., 1984, *Compact Heat Exchangers*, McGraw-Hill, New York.
- [17] Manglik, R. M., and Bergles, A. E., 1995, "Heat Transfer and Pressure Drop Correlations for the Rectangular Offset Strip Fin Compact Heat Exchanger," *Exp. Therm. Fluid Sci.*, **10**, pp. 171–180.
- [18] Utriainen, E., and Sundén, B., 2001, "A Numerical Investigation of Primary Surface Rounded Cross Wavy Ducts," *Heat and Mass Transfer-Wärme- und Stoffübertragung*, accepted for publication.
- [19] Manglik, R. M., 1996, "Plate Heat Exchangers for Process Industry Applications: Enhanced Thermal-Hydraulic Characteristics of Chevron Plates," *Enhanced and Multiphase Heat Transfer*, R. M. Manglik and A. D. Kraus, eds., Begell House, New York, pp. 267–276.
- [20] Okada, K., Ono, M., Tomimura, T., Okuma, T., Konno, H., and Ohtani, S., 1972, "Design and Heat Transfer Characteristics of New Plate Heat Exchanger," *Heat Transfer-Jpn. Res.*, **1**, No. 1, pp. 90–95.
- [21] Marriot, J., 1977, "Performance of an Alfaflex Plate Heat Exchanger," *Chem. Eng. Prog.*, **73**, No. 2, pp. 73–78.
- [22] Heavner, R. L., Kumar, H., and Wanniarachchi, A. S., 1993, "Performance of an Industrial Plate Heat Exchanger: Effect of Chevron Angle," *AIChE Symposium Series*, **89**, No. 295, pp. 262–267.
- [23] Wanniarachchi, A., Ratnam, U., Tilton, B. E., and Dutta-Roy, K., 1995, "Approximate Correlations for Chevron-Type Plate Heat Exchangers," *Proceedings of 30th National Heat Transfer Conference, HTD-314-12*, ASME, New York, pp. 145–151.
- [24] Thonon, B., Vidil, R., and Marvillet, C., 1995, "Recent Research and Developments in Plate Heat Exchangers," *Journal of Enhanced Heat Transfer*, **2**, pp. 149–155.
- [25] Focke, W. W., Zachariades, J., and Olivier, I., 1985, "The Effect of the Corrugation Inclination Angle on the Thermohydraulic Performance of Plate Heat Exchangers," *Int. J. Heat Mass Transf.*, **28**, No. 8, pp. 1469–1479.
- [26] Bond, M. P., 1981, "Plate Heat Exchangers for Effective Heat Transfer," *Chem. Eng.*, Apr., pp. 162–167.
- [27] Muley, A., and Manglik, R. M., 1999, "Experimental Study of Turbulent Flow Heat Transfer and Pressure Drop in a Plate Heat Exchanger With Chevron Plates," *ASME J. Heat Transfer*, **121**, pp. 110–117.
- [28] Muley, A., and Manglik, R. M., 1998, "Investigation of Enhanced Heat Transfer in Low Reynolds Number Flows in a Plate Heat Exchanger," *Proceedings ASME Heat Transfer Division*, **361-3**, ASME, New York, pp. 295–302.
- [29] Ciofalo, M., Stasiek, J., and Collins, M. W., 1996, "Investigation of Flow and Heat Transfer in Corrugated Passages—II. Numerical Simulations," *Int. J. Heat Mass Transf.*, **39**, No. 1, pp. 165–192.
- [30] Shah, R. K., 1978, "Compact Heat Exchanger Surface Selection Methods," *Proceedings 6th International Heat Transfer Conference, Toronto*, **4**, pp. 193–199.
- [31] Massardo, A. F., McDonald, C. F., and Korakianitis, T., 2000, "Microturbine/Fuel-Cell Coupling For High-Efficiency Electrical-Power Generation," ASME Paper 2000-GT-175.
- [32] Parsons, E. L., 1985, "Development, Fabrication and Application of a Primary Surface Gas Turbine Recuperator," SAE Paper No. 851254.

Inverted Brayton Cycle Employment for Low-Temperature Cogenerative Applications

M. Bianchi

e-mail: michele.bianchi@mail.unibo.it

G. Negri di Montenegro

A. Peretto

DIEM—University of Bologna,
Viale Risorgimento 2,
40136 Bologna, Italy

The employment of cogeneration plants for thermal and electric power production is constantly increasing especially for low power requirements. In most cases, to match these low power needs, the cogeneration plant is built up with diesel or gasoline engine or with gas turbine units. In this paper, the performance, in terms of the most utilized cogenerative indexes, of an inverted Brayton cycle working with the gas exhausted by the open power plant have been evaluated. Subsequently, the analysis of a cogenerative gas turbine equipped with IBC was carried out and the benefits numerically calculated. It resulted that the IBC employment may increase of about five percentage points the plant electric efficiency, making this solution particularly attractive for cogenerative applications. [DOI: 10.1115/1.1447237]

Introduction

Disposing of a hot gas at ambient pressure, a net positive specific work can be obtained first by expanding the gas, then by cooling it and, finally, by re-compressing it up to the ambient pressure. All these thermodynamic transformations may be performed by an expander, a heat exchanger and a compressor, and this “cycle” is commonly named inverted Brayton cycle (IBC). ([1]).

In this way, the existing power plant (for example, gas turbine) specific work and efficiency may be increased by expanding, below ambient pressure, cooling, and subsequently discharging to the ambient the plant exhaust gas.

The IBC employment results particularly suitable when the power plant is utilized for cogenerative applications in which a heat exchanger for the gas cooling is already present.

Moreover, this arrangement is especially convenient for low temperature thermal load, such as civil cogeneration, residential heating, etc. In fact, these cogenerative applications usually require maximum temperatures strongly lower than that of the gas exhausted by a gas turbine or a diesel engine.

The IBC engine may reduce the hot gas temperature producing additional electric power without any variation of the cold side temperature at the thermal utility inlet.

In this paper, a thermodynamic analysis of the IBC cycle is performed considering its employment in cogenerative application. Moreover, the performance variations of a cogenerative plant with and without IBC have also been evaluated.

Cogenerative Employment of the Inverted Brayton Cycle (IBC)

As it is well known ([1]), the inverted Brayton cycle is an engine “cycle” in which a gas is expanded from high temperature and ambient pressure to subatmospheric pressure, cooled at p_{low} constant pressure and finally recompressed to ambient pressure and discharged.

The employment of an IBC engine may result convenient when a free flow of hot gas at ambient pressure is available and when the heat exchanged, to cool the gas, is exploitable for cogenerative

applications: in this case the IBC is used as bottomer of an engine (diesel, gas or gasoline fueled) or of a gas turbine.

In particular, Fig. 1 and 2 represent the cogenerative power plant layouts without and with the employment of an IBC engine, respectively. It should be observed that, in the case of IBC (Fig. 2), thanks to the compression temperature increase, an additional heat exchanger, after the IBC compressor, may be used permitting to obtain additional thermal power by the exhaust gas before discharging to the stack.

The possibility to introduce the second heat exchanger depends on the temperature increase from 3 to 4 (due to the IBC pressure ratio, p_{amb}/p_{low}) and on the cold side required temperatures.

IBC Cycle Analysis. As mentioned above and as shown in Fig. 2 and 3, the IBC engine consists of an expansion below ambient pressure (1–2), an isobaric cooling at p_{low} (neglecting the heat exchanger pressure drops) in which the heat is supplied to the thermal utilities (2–3), a compression to the atmospheric pressure (3–4) and, finally, before the stack discharge, an optional new cooling at p_{amb} (4–5) to produce additional thermal power.

To obtain a net work output (Δw) from the IBC cycle, the turbine work should be greater than that absorbed by the compressor. In fact

$$\Delta w = (h_1 - h_2) - (h_4 - h_3). \quad (1)$$

The values of Δw and of the outlet expansion and compression temperatures, T_2 and T_4 , depend on the following quantities:

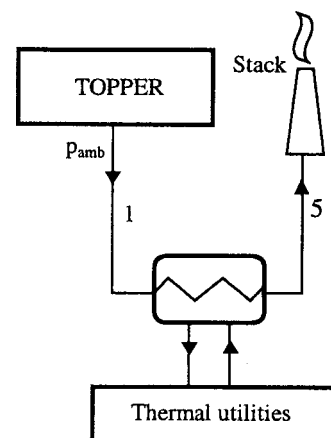


Fig. 1 Cogenerative power plant

Contributed by the International Gas Turbine Institute (IGTI) of THE AMERICAN SOCIETY OF MECHANICAL ENGINEERS for publication in the ASME JOURNAL OF ENGINEERING FOR GAS TURBINES AND POWER. Paper presented at the International Gas Turbine and Aeroengine Congress and Exhibition, Munich, Germany, May 8–11, 2000; Paper 00-GT-315. Manuscript received by IGTI, November 1999; final revision received by ASME Headquarters, February 2000. Associate Editor: D. Wisler.

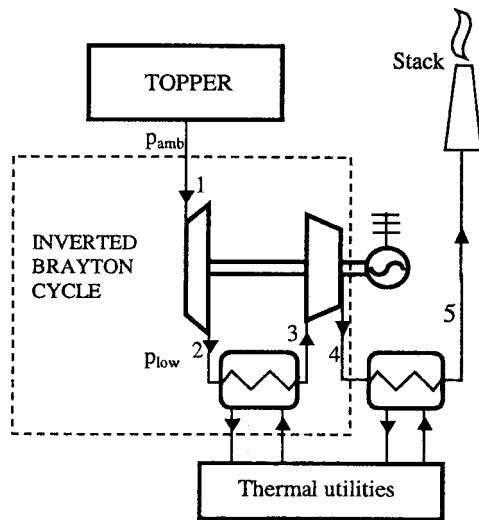


Fig. 2 Cogenerative power plant employing an IBC engine cycle

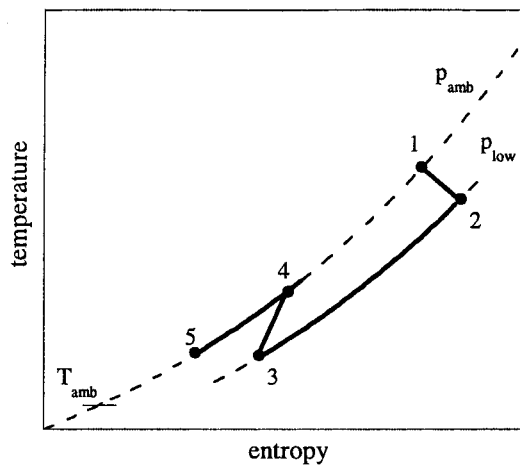


Fig. 3 IBC cycle temperature-entropy diagram

- inlet IBC cycle temperature, T_1 ;
- expansion and compression polytropic efficiencies, η_{pe} and η_{pc} ;
- subatmospheric pressure value, p_{low} ;
- after cooling temperature, T_3 .

For the influence evaluation of the above-mentioned quantities, a numerical analysis, whose results are reported in Figs. 4 and 5, has been carried out.

In Fig. 4, T_2 and T_4 values are reported as a function of p_{low} , for different T_1 , η_{pe} , and η_{pc} values and for fixed T_3 . In particular, the results are carried out assuming the inlet compressor temperature, T_3 , equal to 75°C, the polytropic compression and expansion efficiencies equal to 0.85 (dashed lines) and 0.90 (solid lines) and the inlet IBC temperature, T_1 , equal to 400°C, 500°C, and 600°C.

It should be highlighted that the outlet expansion and compression temperatures, T_2 and T_4 , are greatly influenced by T_1 and p_{low} and weakly by the polytropic efficiencies.

In Fig. 5, the IBC specific work output (Δw) is plotted as a function of p_{low} . Also in this case T_3 , η_{pe} , η_{pc} , and T_1 , are the same of the previous figure. It should be noted that the specific work decreases with T_1 , η_{pe} , and η_{pc} decreasing. As far as the p_{low} influence is concerned, in the p_{low} considered range, when T_1 is greater than 500°C, Δw increases with p_{low} decreasing while, when T_1 is equal to 400°C, Δw has a maximum.

The figure highlights that the net specific work obtainable by

the IBC is remarkable when the inlet IBC temperature is over 500°C and the IBC low pressure lower than 0.7 bar. High specific work (greater than 20 kJ/kg) may be reached also for IBC expander and compressor polytropic efficiencies equal to 0.85. Moreover, relevant values of Δw may be obtained also for inlet IBC temperature equal to 400°C but only with polytropic efficiencies equal to 0.9.

It should be noted that, in Figs. 4 and 5, the results for $p_{low} = 1.01$ bar are relative to the power plant without the inverted Brayton cycle.

IBC in Cogeneration. Since the IBC specific work is much greater when the inlet compressor temperature T_3 is low, the IBC employment results particularly convenient for low temperature cogenerative application.

Moreover, as Fig. 4 shows, the outlet compressor temperature, T_4 , is sufficiently higher than T_3 to permit an additional heat exchanger in which the exhaust gas is cooled from T_4 to T_5 (here assumed equal to T_3).

In spite of the second heat exchanger employment, the specific thermal power supplied to the cogenerative utilization is lower than that provided by the exhaust gas cooling from T_1 to T_5 at constant pressure without IBC (case, for example, of simple Brayton cycle gas turbine with an exhaust temperature equal to T_1). Furthermore, the employment of the IBC as bottom of a cogenerative power plant leads to a reduction of the heat exchanger inlet temperature from T_1 to T_2 .

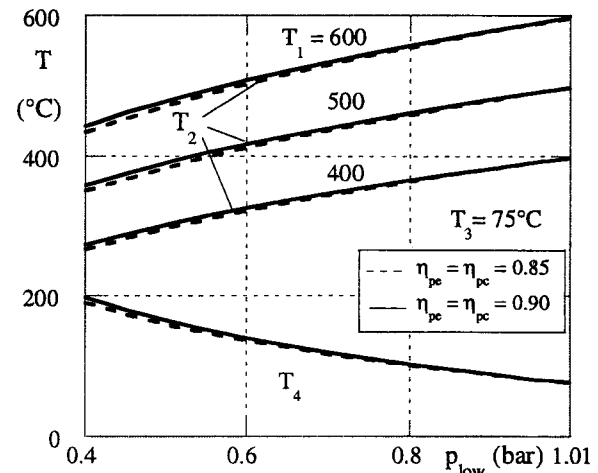


Fig. 4 Outlet expansion and compression temperature variations for an IBC engine cycle

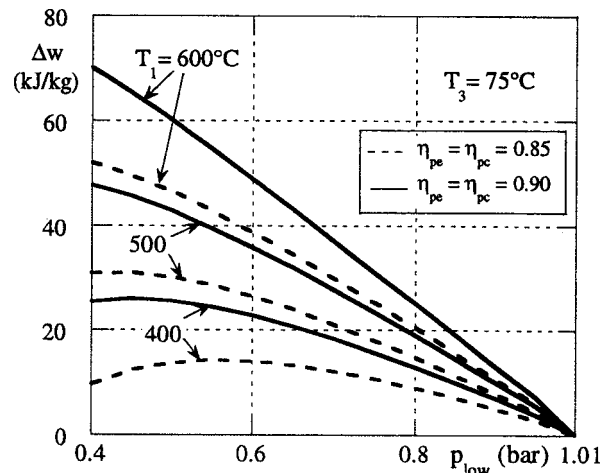


Fig. 5 IBC specific work output variation

Table 1 Reference electric and thermal efficiencies

	η_{el}^*	η_{th}^*	η_{el}^*/η_{th}^*
A	0.37	0.80	0.46
B	0.50	0.85	0.59

It should be observed that, supposing the same stack temperature T_5 (with and without IBC), the specific thermal power decrease (Δq) results (Fig. 3) equal to

$$\Delta q = [(h_2 - h_3) + (h_4 - h_5)] - (h_1 - h_5). \quad (2)$$

The comparison between Eq. (2) and Eq. (1) shows that the Δq decreasing is equal to the specific work produced by the IBC, Δw .

It should be noted that the specific work increase due to the IBC engine employment may represent a significant value with respect to the specific work of the topper engine (Fig. 5). This may be the case of a little size (<10 MW) Brayton cycle topper where, actually, the gas turbine specific work is usually lower than 300 kJ/kg.

Cogenerative Indexes

The indexes commonly utilized ([2]) to evaluate the cogenerative power plant performance are the following:

$$\eta_{el} = \frac{P_{el}}{F} \quad (3)$$

$$\eta_{th} = \frac{Q_{th}}{F} \quad (4)$$

$$\eta_u = \eta_{el} + \eta_{th} \quad (5)$$

$$ESI = \frac{F^* - F}{F^*} = 1 - \frac{1}{\left(\frac{\eta_{el}}{\eta_{el}^*} + \frac{\eta_{th}}{\eta_{th}^*} \right)} \quad (6)$$

where F is the primary energy (LHV fuel consumption) in the cogeneration plant to produce P_{el} and Q_{th} , and F^* is the primary energy consumption in two separated plants producing the same electric and thermal power output of the cogeneration plant.

The energy saving index, ESI, represents the difference between F^* and F , referred to F^* (fuel spent in two separated reference electric and thermal plants whose efficiencies are η_{el}^* and η_{th}^* , respectively). Then, the ESI depends on the reference efficiency values (η_{el}^* and η_{th}^*) that may be chosen considering the average efficiency (thermal and electric) of existing plants (scenario A of Table 1) or of future energy systems (case B of Table 1).

It should be observed that a cogenerative power plant upgrade may lead to an electric and thermal efficiency variation ($\Delta \eta_{el}, \Delta \eta_{th}$) and, consequently, to a new ESI' value expressed by:

$$ESI' = 1 - \frac{1}{\left(\frac{\eta_{el} + \Delta \eta_{el}}{\eta_{el}^*} + \frac{\eta_{th} + \Delta \eta_{th}}{\eta_{th}^*} \right)}. \quad (7)$$

Obviously, the ESI' is greater than ESI (before upgrading) if both $\Delta \eta_{el}$ and $\Delta \eta_{th}$ are positive. Nevertheless, even if $\Delta \eta_{el} > 0$ and $\Delta \eta_{th} < 0$, ESI' may be greater than ESI when (from Eq. (7)):

$$\left| \frac{\Delta \eta_{el}}{\Delta \eta_{th}} \right| > \frac{\eta_{el}^*}{\eta_{th}^*}. \quad (8)$$

This may be, for example, the case of the IBC employment where, since $|\Delta w| = |\Delta q|$, the electric efficiency increase is equal to the thermal efficiency decrease ($\Delta \eta_{el} = \Delta \eta_{th}$) being the IBC mass flow rate constant.

As a consequence, since the reference efficiency ratio (η_{el}^*/η_{th}^*) is lower than one (Table 1) the employment of the IBC leads to an ESI increasing as may be derived from Eq. (8). Moreover, as deducible from Eq. (7) imposing $\Delta \eta_{el} = \Delta \eta_{th}$, it emerges that the ESI' value, for a defined scenario, increases with $\Delta \eta_{el}$ growth. The reference efficiency ratio η_{el}^*/η_{th}^* is then an important parameter to establish the upgrading advantage.

Performance of Cogenerative Gas Turbine Power Plant With IBC

On the basis of the results obtained in the previous paragraphs, the effects of the IBC employment in cogenerative power plants equipped with existing gas turbines have been estimated.

The gas turbine units chosen for this analysis and their main features ([3]) are reported in Table 2.

The increase in the cogenerative gas turbine performance due to the IBC presence are evaluated by using the numerical results carried out in the previous paragraphs. In particular, it was here considered an IBC cycle engine with expansion and compression polytropic efficiencies equal to 0.9 and with a p_{low} equal to 0.6 bar. Also, in this case, the hot side outlet temperature (T_3) is imposed equal to 75°C (considering gas turbines fueled with natural gas). This assumption implies, in the four cogenerative power plants using the four gas turbine listed in Table 2, different heat exchanger effectiveness within 0.88 and 0.9 (this is due to different exhaust gas temperature values).

The performance variations obtained with the previous assumptions are presented in Fig. 6. In this figure, the full dots represent the cogenerative performance of a Brayton cycle gas turbine while the empty ones are the performance with the IBC employment. The reference electric and thermal efficiencies utilized for the ESI evaluation reported in Fig. 6 are the ones relative to the Case A of Table 1.

It can be noticed that, in all the considered power plants, the ESI_A increase is higher than 2.8 percentage points, reaching 3.3 points when the IBC inlet temperature is equal to 600°C (model a). These benefits are due to the remarkable growth in the electric efficiencies (up to 21 percent).

Considering the scenario B of Table 1, the ESI_B increase is higher than 2.3 percentage points, reaching 2.7 points for the model a.

Table 2 Gas turbine main features (Diesel & Gas Turbine Worldwide Catalog [3])

	Model and Manufacturer	P_{el} [kW]	HR [kJ/kWh]	T_{exh} [°C]	\dot{m}_{exh} [kg/s]
a	HURRICANE	1,725	13,870	600	7.4
b	Alstom PGT2	2,000	14,400	525	10.7
c	Nuovo Pignone ASE50	3,771	11,779	566	14.0
d	Allied-Signal TYPHOON 3.6 Alstom	3,540	13,215	527	15.4

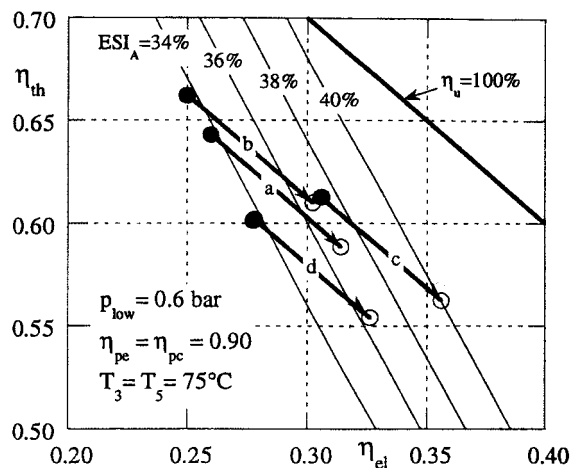


Fig. 6 Cogenerative performance variations of the gas turbines presented in Table 2, due to the IBC employment

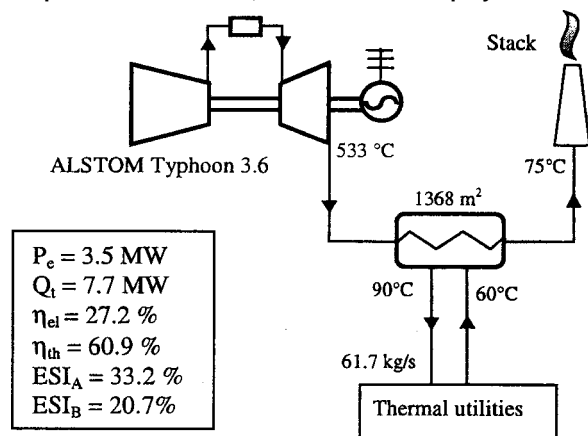


Fig. 7 Gas turbine cogenerative application without IBC

Moreover, also for polytropic efficiencies equal to 0.85, the ESI_A (ESI_B) and electric efficiency increases remain over 2.2 (1.8) percentage points and 12.8 percent, respectively.

As reported in Eq. (9), for each gas turbine model, the fuel utilization coefficient (η_u) is not dependent on the IBC employment:

$$\eta'_u = \eta_{el} + \Delta \eta_{el} + \eta_{th} - \Delta \eta_{th} = \eta_u \quad (9)$$

Consequently, the segments that link the solid with the empty dots of Fig. 6 have $\eta_u = \text{const.}$ (45 deg sloped) and, for the four considered gas turbine models (a, b, c, and d of Table 2) the η_u values are 0.90, 0.91, 0.92, and 0.88, respectively.

Application to an Assigned Cogenerative Power Plant. In this paragraph the comparison results between a Brayton cycle cogenerative power plant (CGT) and one employing IBC (IBC-CGT) are presented. The analysis has been performed with a computational code (Gate Cycle, Release 5.22 [4]) considering the gas enthalpy dependent on its composition and temperature.

The gas turbine used in the plants (Fig. 7 and 8) is a 3.6 MW engine with heat rate equal to 13,215 kJ/kWh and exhaust mass flow rate equal to 15.4 kg/s (Case d of Table 1). The exhaust gas turbine temperature (T_1), depending on the turbine discharge pressure, is 533°C for the CGT (the back pressure due to the heat exchanger and to the stack is equal to 1.04 bar) and 527°C for the IBC-CGT (where the pressure is assumed equal to 1.013 bar).

The IBC engine is designed for a sub-atmospheric pressure, p_{low} , equal to 0.6 bar. Moreover, the back pressure at the IBC outlet is assumed equal to 1.035 bar and the pressure drop in the first heat exchanger equal to 2 percent of the inlet pressure.

In both cases the cold fluid (water) temperature at the exchanger inlet is equal to 60°C and the stack temperature fixed to 75°C as assumed in the previous analysis. The water temperature at the exchanger outlet is imposed at 90°C (typical value for the civil cogenerative applications) and this permits the employment, in the case of IBC-CGT, of a second heat exchanger since the discharge IBC compressor temperature (139°C) is sufficiently greater than the highest thermal utilization temperature (90°C). The heat exchange diagrams for the CGT and for the IBC-CGT are shown in Fig. 9. The solid and dashed lines represent the exhaust gas temperature, while the dotted line the thermal utility fluid one.

On the basis of the evaluation carried out, the employment of IBC leads to

- an electric power increase (about 660 kW) and, consequently, an electric efficiency growth of about 20 percent (the fuel input power F is constant and equal to 12.7 MW in both cases).
- a thermal power decrease (about 660 kW) that leads to a water mass flow rate decrease (from 61.7 kg/s to 56.2 kg/s) and to a thermal efficiency decrease of 8.5 percent.
- finally, an ESI_A (ESI_B) increase of 3.2 (2.6) percentage points.

It should be noted that the employment of the additional heat exchanger leads to an increase of the surface area. Nevertheless, looking at the heat exchanger sizes, the heat exchanger used in the

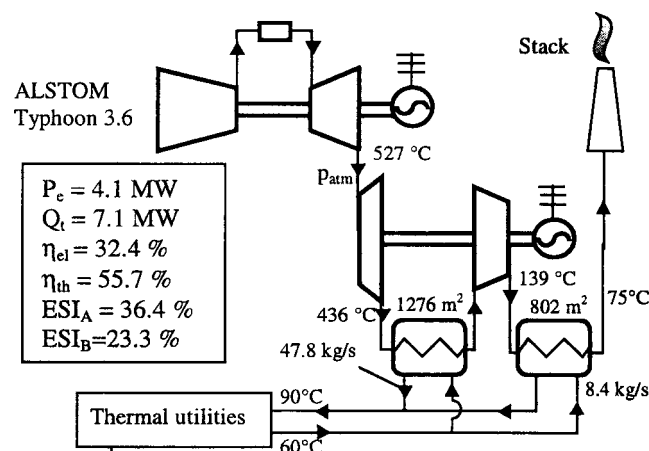


Fig. 8 Gas turbine cogenerative application with IBC

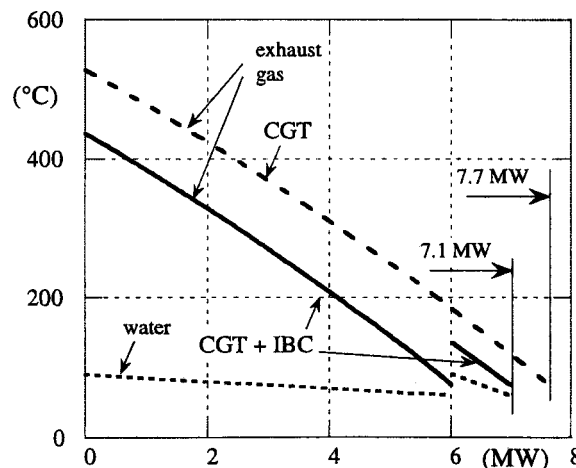


Fig. 9 Heat exchange diagram for the cogenerative gas turbine power plant with (continuous line) and without (dotted line) IBC

Table 3 Gas turbine cogenerative performances

	Typhoon 3.6	Typhoon 3.6 +IBC	Typhoon 4.35	Typhoon 4.35 +IBC
T_1 [°C]	533	527	518	512
T_2 [°C]	-	436	-	422
T_4 [°C]	-	139	-	139
P_{el} [MW]	3.5	4.1	4.2	4.9
Q_{th} [MW]	7.7	7.1	8.5	7.8
S_{exc} [m ²]	1,368	1,276 ⁽¹⁾ 802 ⁽²⁾	1,549	1,441 ⁽¹⁾ 919 ⁽²⁾
η_{el} [%]	27.2	32.4	29.0	34.0
η_{th} [%]	60.9	55.7	58.9	53.9
η_u [%]	88.1		87.9	
ESI_A [%]	33.2	36.4	34.2	37.2
ESI_B [%]	20.7	23.3	21.4	23.9

⁽¹⁾first heat exchanger surface area⁽²⁾second heat exchanger surface area

cogenerative plant without IBC (area of 1368 m²) may be employed as the main heat exchanger (1276 m²) in the plant with IBC.

As already mentioned, the utilization coefficient, η_u , is, for both power plants constant, and in this case equal to 0.88.

In order to obtain an equal thermal power Q_{th} (of the plant without IBC), the employment, in the IBC-CGT plant case, of a greater size gas turbine is necessary. It was then used the “Typhoon 4.35” gas turbine model at disposal on the market. This engine has an electric power equal to 4.2 MW, an electric efficiency of 29.04 percent, a turbine outlet temperature equal to 517°C, and the exhaust mass flow equal to 17.64 kg/s ([3]).

Table 3 shows the results of the comparison among the cogenerative applications of the Typhoon 3.6 and the Typhoon 4.35 with and without IBC. In the last column, Typhoon 4.35 with IBC, the thermal power produced is quite the same of that supplied by the simple CGT power plant employing the Typhoon 3.6.

From the table analysis it emerges that, in both engines, the IBC employment leads to an ESI increasing greater than three percentage points. As already mentioned, also in this case, the fuel utilization coefficient η_u is constant for each gas turbine model.

It should be observed that the IBC pressure and temperature operating values lead to increased compressor and turbine sizes with respect to the topper gas turbine components. In fact, for the IBC compressor, the inlet pressure and temperature are lower and higher than ambient values, respectively. All the same, for the IBC turbine, the discharge pressure is below the ambient one. In both cases, the volumetric mass flow rates at the compressor inlet and turbine discharge increase (about 90 percent and 70 percent, respectively) with respect to the topper ones.

Nevertheless, since small size gas turbines are considered, this fact does not cause relevant design problems because compressors and turbines, working with the new required volumetric mass flow rate, are at disposal on the market.

Conclusions

In this paper, the analysis of the inverted Brayton cycle for low-temperature cogenerative applications has been developed. The use of an IBC working with the gas exhausted from the topper power plant increases the specific work production and the cogenerative performance of the power plant itself.

The thermodynamic analysis of the IBC cycle has shown that the IBC specific work increases with the growth of the inlet temperature and polytropic efficiencies and with the reduction of the discharge pressure (up to 0.5 bar). In particular, the specific work may easily reach values over 20 kJ/kg working with IBC inlet temperatures higher than 500°C and discharge pressures lower than 0.7 bar.

Nevertheless, the employment of the IBC leads to a reduction of the heat supplied to the utilities that results equal to the IBC

work produced. Thanks to the equal value of the work increase and heat decrease, the fuel utilization coefficient, η_u , doesn't change with the IBC use.

On the contrary, the energy saving index (ESI) and the electric efficiency increase (evaluated with reference to existing gas turbines) up to 3.3 and 5.2 percentage points, respectively (when the reference electric and heat efficiencies are equal to 0.37 and 0.80, respectively). These results are obtained thanks to the secondary heat exchanger that supplies additional thermal power before discharging the exhaust gas.

Finally, the developed analysis of the IBC employment in a civil cogenerative application shows that, to obtain the same thermal power supplied by the power plant without IBC, a gas turbine model of greater size has to be chosen. In particular, for the assumed data, a 4.2 MW gas turbine is required when the IBC is used, to produce the same thermal power supplied by a 3.6 MW gas turbine without IBC. The electric efficiency and ESI differences between the 3.6 MW gas turbine without IBC and the 4.2 MW with IBC, are over 6.5 and 4 percentage points, respectively.

In conclusion, the inverted Brayton cycle may represent a viable way to increase the performance of a cogenerative power plant, especially for low-temperature applications, and consequently, an optimization of the gas turbine cycle, with the IBC employment, may be stimulating. Moreover, also on the basis of the encouraging numerical results, an economic investigation is worth of consideration.

Nomenclature

ESI	=	energy saving index (Eq. (6))
F	=	LHV fuel power supplied, (MW)
k	=	ratio of specific heats
h	=	specific enthalpy, (kJ/kg)
HR	=	heat rate (kJ/kWh)
m	=	mass flow rate, (kg/s)
P_{el}	=	electric power output, (MW)
p	=	pressure (bar)
q	=	specific thermal power (kJ/kg)
Q_t	=	thermal power (MW)
S_{exc}	=	heat exchanger surface area (m ²)
T	=	temperature (°C)
w	=	specific work output (kJ/kg)
β	=	pressure ratio
η_{el}	=	LHV electric efficiency (Eq. (3))
η_{pc}, η_{pe}	=	compression and expansion polytropic efficiencies
η_{th}	=	LHV thermal efficiency (Eq. (4))
η_u	=	LHV fuel utilization coefficient (Eq. (5))

Subscripts and Superscripts

A	=	referred to Case A of Table 1
B	=	referred to Case B of Table 1
amb	=	ambient
exh	=	exhaust gas
low	=	lowest IBC pressure
'	=	case with IBC
*	=	reference value

Acronyms

IBC	=	inverted Brayton cycle
LHV	=	lower heating value
CGT	=	cogenerative gas turbine power plant

References

- [1] Wilson, G. D., 1984, *The Design of High-Efficiency Turbomachinery and Gas Turbine*, The MIT Press Cambridge, MA.
- [2] Horlock, J. H., 1987, *Cogeneration: Combined Heat and Power*, Pergamon Press, Oxford.
- [3] *Diesel & Gas Turbine Worldwide Catalog*, 1999, Diesel & Gas Turbine Publications, Vol. 64.
- [4] *Gate Cycle*, Computational Code-Release 5.22, 1998, Enter Software, Menlo Park, CA.

R. L. Fittro
Mechanical and Electrical Engineering,
Aston University,
Aston Triangle,
Birmingham B4 7ET, UK
e-mail: R.L.Fittro@aston.ac.uk

C. R. Knospe
Department of Mechanical and
Aerospace Engineering,
University of Virginia,
Charlottesville, VA 22903
e-mail: crk4y@virginia.edu

The μ Approach to Control of Active Magnetic Bearings

Many important industrial problems in the control of rotating machinery with active magnetic bearings concern the minimization of the rotor vibration response to poorly characterized disturbances at a single or several shaft locations, these typically not corresponding to those of a sensor or actuator. Herein, we examine experimental results of a multivariable controller obtained via μ synthesis with a laboratory test rig. These indicate that a significant improvement in performance can be obtained with a multivariable μ controller over that achieved with an optimal decentralized PD controller.

[DOI: 10.1115/1.1417484]

Introduction

Many applications of active magnetic bearings (AMBs) have control requirements that may be considered as the minimization of the peak dynamic compliance of the rotor at a specified shaft location or locations. This is of particular interest in any application where an externally applied force is both highly localized and poorly (spectrally) characterized (e.g., cutting forces in machining, aerodynamic forces in gas turbines, fiber breaks in textile feeder rolls). Decentralized proportional-derivative (PD) and proportional-integral-derivative (PID) control systems are presently the standard in industrial magnetic bearings. However, the performance of these controllers is limited due to both their poor capabilities in loop shaping, their inherent lack of coordination between bearings, and the dearth of systematic design tools for obtaining a specified performance in spite of model uncertainties or plant variations. In contrast, μ synthesis provides a (relatively) systematic method for the design of multivariable controllers that includes both performance specifications and robustness guarantees. In this paper, we examine the effectiveness of a μ -synthesized controller in the reduction of rotor compliance on a laboratory test rig. The performance achieved is also compared to that of an optimized PD controller to indicate the benefits provided.

In our experiment, we seek to minimize the compliance of the rotor at its midspan (i.e., center) using only the actuators and sensors located at the rotor's ends. This task is interesting (and difficult) since the location of the disturbance is so far from the bearings. For a rigid rotor, the midspan compliance could be reduced using very stiff bearings (i.e., high gain decentralized PID control). However, this approach would be very ineffective if employed on our experiment, as the shaft is quite flexible.

μ Synthesis

μ -synthesis is a multivariable controller design technique for complex linear systems with norm-bounded uncertainties in their model descriptions, see [1] for a good introduction. Over the past decade, μ -synthesis has been applied to a number of AMB systems ([2–5]). Since a detailed discussion of μ -synthesis for rotor compliance reduction is discussed in detail elsewhere ([6–8]), it will only briefly be examined here. The *rotor compliance minimization problem* is stated as follows: design an AMB controller to reduce the maximum displacement that may occur at a particular rotor location in response to a unit sinusoidal force applied at that same location where the disturbance frequency is not specified. As

most readers will recognize, this problem is simply an H_∞ control problem where the force disturbance is collocated with the displacement performance signal. The problem of minimizing the compliance at a particular rotor location using actuators noncollocated with that location was first considered by Herzog and Bleuler [9]. This important theoretical result pointed out that dynamic compliance can not be made arbitrarily low via control for many rotor systems.

Experiment

The laboratory test rig, shown in Fig. 1, consists of a 685.8 mm (27 in.) long, 12.7 mm (0.5 in.) diameter steel shaft with a 0.82 kg (1.82 lbf.) disk mounted at the center. The shaft is horizontal and is supported by two active magnetic bearings at either end, each of which actively controls the position of the rotor in the horizontal and vertical directions. Journal disks composed of silicon iron laminations with a mass of 0.6 kg (1.32 lbf.) are attached at either end of the shaft resulting in a bearing span of 508 mm (20 in.). Each magnetic bearing stator consists of four solid (i.e., non-laminated) silicon iron horseshoe-shaped electromagnets arranged around the journals. The solid construction of the electromagnets foreordains that eddy currents in the bearing stators will have a profound effect on system performance. When levitated, the gap between the stator electromagnets and the bearing journals is 1.0 mm (0.040 in.).

A computer-controlled servomotor is connected to the shaft via a flexible coupling. The operating speed range of the rotor is 0 to 5000 revolutions per minute (rpm). Rotor position sensing is accomplished via noncontacting eddy current probes. Two sensors are located next to each of the magnetic actuators and measure the rotor's displacement along the horizontal and vertical axes. Two additional eddy current probes are located near the disk at the midspan of the shaft and are used for control performance evaluation purposes only. Before the feedback sensor signals are received by the system's digital controller, they pass through a first-order anti-aliasing filter with a bandwidth of 2.2 kHz. For this experiment, all of the power and control electronics were designed and built at the University of Virginia ([6]).

Modeling

μ -synthesis is fundamentally a model-based control design technique requiring a detailed mathematical model of the system including a characterization of system uncertainties. With a more accurate system model, higher performance can, in principle, be obtained. To this end, models for all of the test rig's components and uncertainty descriptions (see Fig. 2) were developed using a combination of analytical modeling and experimental identification.

Since the rotor was symmetric and is essentially nongyroscopic in the operating speed range ([6]) identical and independent mod-

Contributed by the International Gas Turbine Institute (IGTI) of THE AMERICAN SOCIETY OF MECHANICAL ENGINEERS for publication in the ASME JOURNAL OF ENGINEERING FOR GAS TURBINES AND POWER. Paper presented at the International Gas Turbine and Aeroengine Congress and Exhibition, Munich, Germany, May 8–11, 2000; Paper 00-GT-408. Manuscript received by IGTI Nov. 1999; final revision received by ASME Headquarters Feb. 2000. Associate Editor: D. Wisler.

Table 1 Uncertainty block description summary

Δ_{in}	Uncertainty in amplifier and K_i	2×2 diagonal	complex
Δ_{eddy}	Uncertainty in eddy current transfer function	2×2 diagonal	complex
Δ_{K_x}	Uncertainty in K_x	2×2 diagonal	real
Δ_{out}	Uncertainty in sensor gains	2×2 diagonal	real
Δ_p	Fictitious uncertainty—compliance	2×2 full	complex
Δ_c	Fictitious uncertainty—controller effort	2×2 full	complex

bandwidth of these sensors (approximately 10 kHz), they were modeled as constant gains.

Magnetic actuators when operated with transconductance amplifiers are typically characterized by their open-loop stiffness (K_x) and actuator gain (K_i). Since the experiment's actuators have solid stators, we must also consider the effect that eddy currents have upon the force produced. The open-loop stiffness and actuator gain are properties that can be determined by static tests of the actuators. Our experimental procedure to determine K_i was as follows. With the shaft levitated and centered, a known force was applied via a weight and pulley arrangement. A perturbation current was then injected into the system in order to bring the shaft back to the centered position. This procedure was performed several times with a number of known applied forces. A least-squares linear fit of the resulting force and current data then provided an estimate of K_i ([6]).

With the value of K_i already known, the value of K_x can be determined experimentally from the relationship between a change in perturbation current and the resulting change in rotor position. To this end, we injected a constant perturbation signal into the command input of each actuator amplifier while the rotor was levitated. Numerous amplitude perturbation signals were injected into each amplifier and the current and position readings were recorded. From the values for $\Delta i/\Delta x$ determined for each actuator from the slope of a least-squares linear fit of the resulting data, K_x can be determined ([6]).

We now examine the effect that eddy currents have upon the actuator's transfer function. These introduce a low-pass dynamic system into the actuator's force-current-position relationship:

$$F(s) = K_i G_{eddy}(s) i_p(s) + K_x x(s).$$

Previous research on eddy current effects in nonlaminated actuators has shown that they are difficult to model accurately from physical principles for typical actuator geometries ([10,11]). For this experiment, we identified the frequency response of the transfer function $G_{eddy}(s)$ and then fit it with a low-order system. The motor coupling was temporarily removed from the experiment and the rotor was then levitated using a nominal decentralized PID controller. A sine sweep test was conducted on this modified system. This resulted in the closed-loop system's frequency response (2×2 complex gain matrix) at discrete frequencies. From this data, the frequency response of the eddy current dynamics was determined at each discrete frequency by minimization of the 2-norm of the difference between the experimental closed-loop frequency response data and that of the model. In this fashion, the eddy current frequency response (complex gain) was backed out of the closed-loop experimental data. This discrete frequency response data could not be fitted with a stable rational transfer function due its significant magnitude attenuation at higher frequencies with little associated phase lag. To overcome this, the frequency response of the digital controller throughput delay was augmented to the eddy current discrete frequency response data. This combined eddy/delay frequency response could be accurately matched by that of a sixth-order stable transfer function. This model was assembled with that of the other system components to form a new closed-loop model. The frequency response of this compared very favorably with that of the experiment.

Next, the motor coupling was reattached and another closed loop sine sweep test was conducted to obtain new discrete frequency response data. The motor coupling stiffness and damping

coefficients were then chosen so as to obtain the best match between the model's closed-loop frequency response and that of the experiment. In this fashion, the motor coupling stiffness and damping coefficients were determined to be 22765 N/m (130 lbf/in) and 12.26 N·s/m (0.07 lbf·s/in), respectively.

Finally, to verify the system model developed, the test rig was levitated with several different decentralized PD controllers which effectively varied the system loop gain and bandwidth. Frequency response data obtained by sine sweep testing matched well that of the theoretical model in each case. When the uncertainties are omitted, this theoretical model is referred to as the *nominal system model*.

Uncertainty Representation

We now will consider the uncertainty blocks for each component depicted in Fig. 2. The details regarding each of these uncertainties as well as the philosophy guiding its construction is discussed in this section. Table 1 summarizes the characteristics of each of these uncertainty blocks.

Since the rotor model was very accurate as discussed above, no explicit uncertainty representation was assigned to it. In an effort to encapsulate the small errors in the model, the multiplicative uncertainty at the rotor inputs and those associated with actuator open loop stiffness K_x , were increased by five percent during synthesis. The additional uncertainty in K_x allows for minor errors in the rotor model's free-free natural frequencies.

The uncertainties in the amplifier and actuator gain (K_i) for each channel were combined together to form a single uncertainty block. Reducing the number of uncertainty blocks in the synthesis model should yield lower-order μ -controllers and decrease the time required for controller synthesis. The digital controller modeling error was judged to be negligible over the frequency range of interest, and therefore no uncertainty associated with it was necessary. The amplifier model was found to vary no more than three percent from the experimental data. Modeling errors for the actuator open-loop stiffness K_i were determined based upon the actuator's experimentally determined linearity and hysteresis as well as experimental repeatability.

The experimental values obtained for actuator gain K_i were found to be uncertain by approximately seven percent. Combining this with that of the amplifier to form a single multiplicative uncertainty for each input channel yielded a total uncertainty of ten percent. As described above, five percent uncertainty was added to ensure adequate multivariable input gain/phase margin, resulting in a total multiplicative input uncertainty of 15 percent.

The error in the anti-aliasing filter model was negligible and no uncertainty was attributed to this component. The experimentally determined position sensor gains, on the other hand, were viewed as uncertain. Based on the linearity and repeatability of the sensor calibration data, uncertainty in the sensor gains was estimated at two percent.

Since the values of actuator open loop stiffness K_x were calculated directly from experimental data used to determine K_i via $K_x = K_i(\Delta i/\Delta x)$, the uncertainty in K_x must be at least as great as that for K_i . Since, the additional error introduced by the experimental determination of $\Delta i/\Delta x$ was very small, the uncertainty in K_x is the same as that for K_i , ten percent. As described above, an additional five percent uncertainty was attributed to this term so as

to account for small uncertainties in the rotor's free-free natural frequencies. This resulted in a total K_x multiplicative uncertainty of 15 percent.

The greatest uncertainty in the system was due to the effect of eddy current effects upon the actuators' transfer functions. The degree of uncertainty attributed to this transfer function was computed from the difference between the actuator discrete frequency response data (backed out from the closed-loop experimental data as described above) and the frequency response of the fitted eddy/delay model $G_{ed}(s)$. A second-order filter was then chosen which over bounded this difference in magnitude.

$$W_{\text{eddy}} = 0.866 \frac{(s + 30)^2}{(s + 3000)^2}$$

This filter is the frequency-dependent weight for the additive uncertainty on this model component and has the following characteristics: negligible uncertainty below 5 Hz which increases quickly thereafter to a maximum variation of ± 86.6 percent in gain, ± 60 deg in phase for frequencies above 500 Hz.

The performance goal for our experiment is the minimization of the peak dynamic compliance of the shaft at its midspan with only the use of the position sensors and two magnetic actuators at the shaft's ends. Since the sensors at the shaft's midspan are not used in feedback, a large noncollocation (approximately 254 mm/10 in.) exists between the actuators/sensors and the compliance location. This goal may be formulated in the analysis/design system model used in μ -synthesis as a fictitious uncertainty block Δ_p between midspan displacement and a force applied at midspan (see Fig. 2). In controller design, we will also seek to accomplish this performance objective without excessive controller gain or bandwidth. This specification, too, may be represented by a fictitious uncertainty block, Δ_c , in the analysis/design system model. Simply stated, satisfaction of robust stability for the augmented system with these fictitious uncertainty blocks implies satisfaction of the compliance and controller effort specifications (via the Main Loop Theorem ([1])).

Controller Design

To assess the improvement achieved by the μ -controller, a decentralized PD controller was designed to minimize the maximum dynamic compliance. Since optimization of decentralized fixed-order controllers is notoriously difficult, the PD controller parameters were determined via an exhaustive search.

In μ -synthesis, the two fictitious uncertainty blocks that were augmented to the plant model were used for loop shaping design by adjusting the weighting functions associated with them. These weighting functions, W_p and W_c , are linked to the dynamic compliance and control effort specifications respectively (see Fig. 2). The weighting function W_c was used to limit the control effort and force the controller to roll-off at high frequencies. This was chosen to allow a maximum controller gain of 80 volts/volt and a roll-off beginning at 2.1 kHz and was motivated by the authors' previous experience with decentralized controllers for this experiment. If the specification is satisfied, the controller magnitude will be less than that of W_c^{-1} which is shown in Fig. 3. The compliance weight, W_p , was chosen to be a constant gain. The best obtainable compliance performance was determined via a bisection search over W_p to achieve $\mu \approx 1$. That is, a value of W_p was assumed, a controller was designed via μ -synthesis, and W_p was raised (lowered) if the achieved μ value was less than (greater than) one. In each case, we used the MATLABTM μ -Tools toolbox to perform the D-K iteration using the command *dkit*. For the final μ -controller, two D-K iterations were required to achieve a μ value of 1.02. Interestingly, the resulting 56th-order controller was open-loop unstable (discussed further below). The following procedure was then employed for controller reduction: (1) the unstable dynamics of the controller were removed; (2) the stable portion was reduced through balanced truncation; (3) the unstable dynamics were reintroduced; and (4) the stability and peak μ of

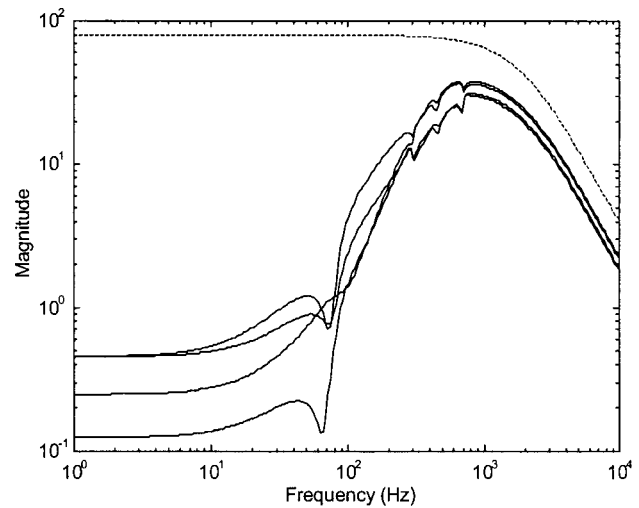


Fig. 3 Magnitude response of μ -controller (solid) and control gain limit W_c^{-1} (dashed), volts/volt

the closed-loop system was checked. In this fashion, the controller was reduced to 23rd-order while maintaining a peak μ of 1.02. The magnitude frequency response of this MIMO controller is shown in Fig. 3.

Experimental Results

Since the μ -controller was open loop unstable, the rotor was first levitated using PD control and then the control algorithm was switched to the μ -controller. The switch between the PD and μ -controller involved no timing delays and was virtually seamless. Both the PD and μ -controllers were implemented as discrete time, state-space systems with a sampling rate of 10 kHz. With the rotor levitated, the dynamic compliance at the midspan was experimentally determined by impact testing with an instrumented hammer. The resulting vibration was measured using the midspan position sensor.

Figures 4 and 5 show the midspan dynamic compliance results obtained with the PD and μ -controllers, respectively. In addition to the experimental data, these two figures also include the theoretical nominal compliance prediction. For both controllers there is excellent agreement between the theoretical compliance and the

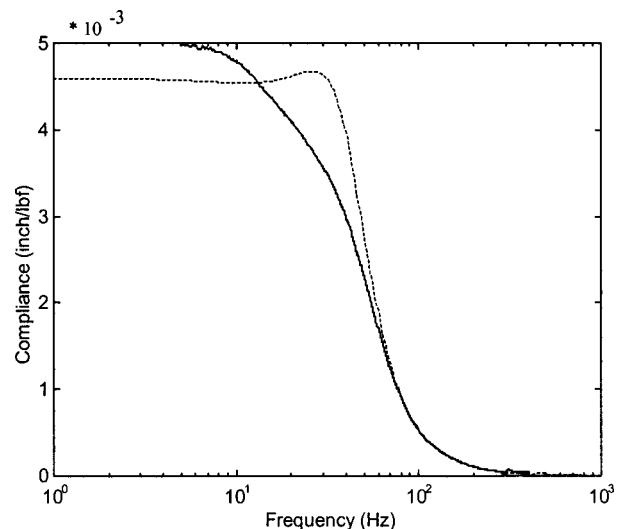


Fig. 4 Midspan compliance with the optimized PD controller—experimental (solid) and theoretical (dashed)

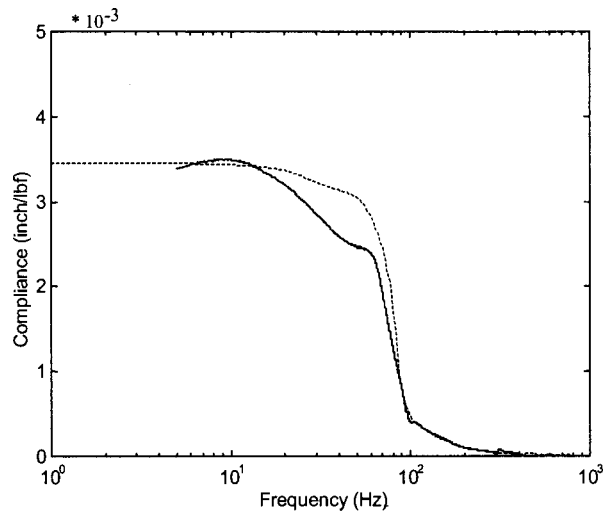


Fig. 5 Midspan compliance with the μ -controller—experimental (solid) and theoretical (dashed)

experimental data. (Note the linear magnitude scale used). The μ controller achieves a 30 percent reduction in maximum dynamic compliance over that achieved with the optimized PD controller. (Some readers may believe that this improvement is slight. However, for many applications this reduction is quite significant. For example, in a high speed milling spindle application this would translate to a 30 percent improvement in metal removal rate ([8])). For this application, the achievable performance was primarily limited by the uncertainty in the nonlaminated actuator model.

As an *ad hoc* test of system robustness, the amplifier gain for actuator #2 was varied from its nominal value to assess gain margin in this channel. For the PD controller, the system remained stable for variations from -48 percent to over +100 percent. The μ -controller's robustness to this parameter was also quite good: -28 percent to over +100 percent. We note for comparison that the μ -controller was designed with a 20 percent input uncertainty specification. As a final test of the μ -controller, the rotor was spun up to its maximum speed of 5000 rpm. It successfully supported the rotor over its entire operating speed range.

Conclusions

The theoretical and experimental results presented demonstrate the efficacy of μ synthesis for the design of controllers to mini-

mize the compliance of rotors supported by active magnetic bearings. Indeed, the problem examined was actually a very demanding application of the theory as the rotor was flexible, the compliance location was far from the sensors and actuators, and the actuators were not laminated. A significant improvement in performance was obtained by the μ -controller over that with the optimized PD controller.

Acknowledgments

This work was supported by Cincinnati Milacron, Inc. The authors would like to thank Dr. Stephen Fedigan for extensive assistance with the digital controller used.

References

- [1] Zhou, K., Doyle, J. C., and Glover, K., 1996, *Robust and Optimal Control*, Prentice-Hall, Englewood Cliffs, NJ.
- [2] Fujita, M., Matsumura, F., and Namerikawa, T., 1992, " μ -Analysis and Synthesis of a Flexible Beam Magnetic Suspension System," *Proceedings of the 3rd International Symposium on Magnetic Bearings*, Alexandria, VA, July, pp. 495–504.
- [3] Fujita, M., Namerikawa, T., Matsumura, F., and Uchida, K., 1993, " μ -Synthesis of an Electromagnetic Suspension System," *IEEE Trans. Autom. Control*, **40**, No. 3, pp. 530–536.
- [4] Löscher, F., Gähler, C., and Herzog, R., 1998, " μ -Synthesis Controller Design for a 3 MW Pump Running on AMBs," *Proceedings of the 6th International Symposium on Magnetic Bearings*, Cambridge, MA, Aug. Technomic, Lancaster, PA, pp. 415–428.
- [5] Nonami, K., and Takayuki, I., 1994, " μ Synthesis of Flexible Rotor Magnetic Bearing Systems," *Proceedings of the 4th International Symp. on Magnetic Bearings*, Zurich, Switzerland, Aug. pp. 73–78.
- [6] Fittro, R. L., 1998, "A High Speed Machining Spindle With Active Magnetic Bearings: Control Theory, Design and Application," Ph.D. dissertation, University of Virginia, Aug.
- [7] Stephens, L. S., 1995, "Design and Control of Active Magnetic Bearings for a High Speed Machining Spindle," Ph.D. dissertation, University of Virginia, Aug.
- [8] Stephens, L. S., and Knospe, C. R., 1996, " μ -Synthesis Based, Robust Controller Design for AMB Machining Spindles," *Proceedings of the 5th International Symposium on Magnetic Bearings*, Kanazawa, Japan, Aug.
- [9] Herzog, R., and Bleuler, H., 1992, "On Achievable H^∞ Disturbance Attenuation in AMB Control," *Proceedings of the 3rd International Symposium on Magnetic Bearings*, Alexandria, VA, July Technomic Publishing, Lancaster, PA pp. 485–494.
- [10] Meeker, D. C., Maslen, E. H., and Noh, M. D., 1996, "An Augmented Circuit Model for Magnetic Bearings Including Eddy Currents, Fringing, and Leakage," *IEEE Trans. Magn.*, **32**, No. 4.
- [11] Zmood, R. B., Anand, D. K., and Kirk, J. A., 1987, "The Influence of Eddy Currents on Magnetic Actuator Performance," *Proc. IEEE*, **75**, No. 2, pp. 259–260.

Metallurgical Considerations for Life Assessment and the Safe Refurbishment and Requalification of Gas Turbine Blades

J. A. Daleo

e-mail: daleo@bwdturbines.com

K. A. Ellison

D. H. Boone

BWD Turbines Ltd.,
1-601 Tradewind Drive,
Ancaster, Ontario L9G 4V5, Canada

Metallurgical analysis of rotating blades operating in advanced gas turbine engines is important in establishing actual operating conditions, degradation modes, remaining life, and most importantly, the proper repair and rejuvenation techniques to be used in developing optimum component life strategies. The elevated firing temperatures used in the latest engine designs result not only in very high metal surface temperatures but also in very high temperature gradients and concomitant thermal strains induced in part by the complex and efficient cooling systems. This has changed the primary function of today's superalloy-coating systems from one of hot corrosion protection to moderating high temperature oxidation reactions. Furthermore, as a result of the high thermal strains induced by the cooling systems, long-term metallurgical structural stability issues now revolve around optimizing both thermal mechanical fatigue (TMF) resistance and creep life. Thus the gradual change to directionally solidified (DS) and single crystal (SC) alloys throughout the industry. The use of DS and SC alloys coated with state of the art TBC, platinum modified aluminide and MCrAlY coatings with or without subsequent aluminizing applied by vacuum plasma spray (VPS), high velocity oxygen fuel (HVOF), physical vapor deposition (PVD), air plasma spray (APS), and by chemical vapor deposition (CVD) methods along with the widespread use of internal aluminide coatings have made today's rotating components prohibitively expensive to replace after only one cycle of operation. It is therefore, or should now be a high priority for all cost conscious gas turbine users to help develop reliable repair and rejuvenation strategies and techniques to minimize their operating cost. Traditional metallurgical considerations required for life assessment and the reliable refurbishment and requalification of gas turbine blades are reviewed along with some new exciting techniques. Examples of component degradation modes are presented. Appropriate attention to metallurgical issues allows turbine users to more successfully and economically operate their turbines. [DOI: 10.1115/1.1455638]

Introduction

Advanced D, E, and F technology turbines operate at very high firing temperatures primarily on relatively clean natural gas with high-grade distillate fuel used for back up. The realized maintenance period of the critical hot section gas turbine blades is usually determined by the life of the coating system and secondarily by the material's long-term metallurgical stability at the actual operating conditions encountered in service.

Specific operating conditions can dramatically affect the life of gas turbine hot section blades. An understanding of the original design parameters and their effect on component life is essential to understanding degradation modes, especially those resulting from invariable "off-design" operation. Today's advanced alloy and coating systems are expected to withstand very high temperatures and stresses for periods up to 48,000 hours. Steady-state centrifugal stresses range from a few MPa to 250 MPa, while the thermal stress in the airfoil as a result of temperature gradients can range from -350 MPa to 500 MPa. Typical steady state metal temperatures range from 760°C to 985°C. Specific conditions af-

fect the system balance, degradation modes, and hence the life. As longer hours of service are accumulated, maintenance considerations such as developing optimum component life strategies and repair processes become important.

When coatings applied to the external or internal surfaces do not perform satisfactorily, components can be quickly damaged and rendered no longer serviceable or repairable. If the coatings selected for the application perform as expected, the condition of the coating at the first overhaul period becomes an important consideration in the operator's decision to return the parts to service for another overhaul period in their present condition or to refurbish the components. Unexpected changes in microstructure and alloy properties as a result of higher than expected operating temperatures or stress can also result in diminished structural performance and consequently reduced life. Thermal mechanical fatigue (TMF) cracking in first-stage blades has been observed before and during the first scheduled overhaul of many of the advanced engine models.

Consequently reliable refurbishment techniques now need to address TMF and coating degradation. Methods to restore dimensional damage, such as welding, VPS powder build ups and brazing techniques are also important, but must be integrated around the following dominant coating and regenerative heat treatment issues:

Contributed by the International Gas Turbine Institute (IGTI) of THE AMERICAN SOCIETY OF MECHANICAL ENGINEERS for publication in the ASME JOURNAL OF ENGINEERING FOR GAS TURBINES AND POWER. Paper presented at the International Gas Turbine and Aeroengine Congress and Exhibition, Munich, Germany, May 8-11, 2000; Paper 00-GT-642. Manuscript received by IGTI, Nov. 1999; final revision received by ASME Headquarters, Feb. 2000. Associate Editor: D. Wisler.

- (a) the availability of a wider range of suitable non-OEM replacement coatings,
- (b) development of reliable techniques for removing internal aluminide coating systems without cracking the base metal or damaging the physical features cast into the components to promote cooling such as turbulators, pin fins etc.,
- (c) development of reliable techniques for removing complex TBC/MCrAlY coating systems on thin wall and controlled grain (DS, SC) material component designs,
- (d) development of suitable regenerative heat treatment cycles for DS and SC alloys that properly restore the microstructure and mechanical properties of the alloy without inducing unacceptable re-crystallization and grain growth, and
- (e) establishment of a reliable way of measuring, calibrating and maintaining the effectiveness of the component cooling scheme.

There is also a pressing need to develop reliable methods to repair structural cracks in rotating components and microstructure damage caused by TMF mechanisms. In order to accomplish this, DS and SC compatible repairs must be developed where the cracked or damaged areas of the component can be removed and replaced with suitable high-strength material. Potential repair technologies include VPS powder buildups and braze overlay techniques. More novel approaches may include replacing the damaged material with welded or diffusion bonded inserts.

General surface buildups to restore thin wall sections of DS and SC alloys may also be accomplished using electroplating technologies such as the PraxAir Tribomet (BAJ) process that is now used to apply MCrAlY overlay coatings and abrasive tips.

Refurbishment of Metallurgical Degradation

Metallurgical life assessment of service-exposed blades has proven to be the most effective means of identifying the important modes of material degradation affecting component life. In depth knowledge of what is really “wrong” with the components is the first and probably the most crucial step in determining suitable repair techniques to be used to restore the component to a safe condition.

A proper metallurgical analysis looks for service related deterioration and, combined with a mechanical analysis, evaluates the potential for continued safe service operation and/or identifies the need for repair. Methods are used that can detect all of the conditions that can lead to premature failure when combined with suitable nondestructive testing of the remainder of the components from the set. Detailed evaluation of representative sample blades allows the actual “state” of components to be determined and subsequently monitored. Note that the actual component temperature distributions are one of the least known and available parameters although they are undoubtedly one of the most important.

The basic modes of metallurgical degradation encountered in turbine airfoils along with the advantages of using combined mechanical and metallurgical evaluation techniques to perform metallurgical life assessments, failure analysis investigations and to calculate repair limits has been recently described by Daleo and Boone [1].

Repair of turbine blades is a multiple-step process involving coating removal using aggressive acids, high-temperature heat treatments, manual blending and welding operations, critical inspections, and carefully controlled recoating processes. The starting material for the repair process can be extremely variable as a result of variables in the initial manufacture of the components, as well as the different operating histories that the parts experience. In industrial turbine applications, no two sets of service run components are exactly alike.

The repair process must be capable of overcoming these variations in the incoming material with robust processes and excellent inspection techniques to ensure a high quality repair. Even a well-designed process may not provide an adequate component if ab-

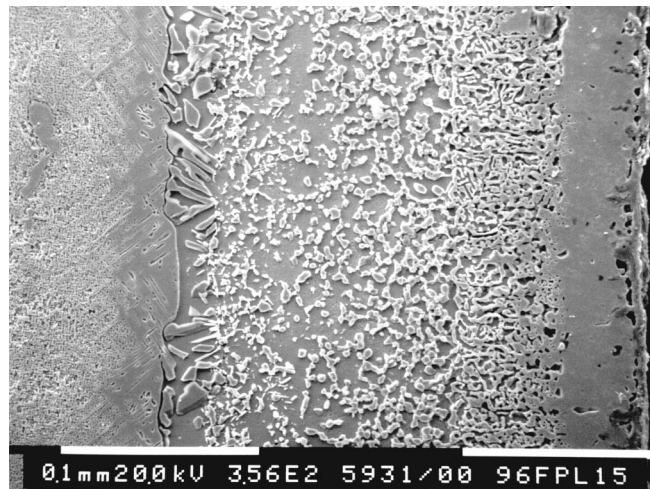


Fig. 1 A photomicrograph illustrating the microstructure of a service-run aluminized CoCrAlY coating applied to a directionally solidified GTD111 alloy component

normal conditions exist in the part. Final qualification of a sample component helps identify these abnormal conditions, as well as acting as a final check on the repair process.

Requalification consists of several steps that compare the sample part to typical new component standards. Metallurgical evaluation of surface condition can identify such problems as poor coating quality, incorrect coating thickness, and surface attack caused by chemical stripping or poor heat treatment atmosphere control. Microstructure evaluation using electron microscope methods can reveal unsuitable gamma prime structures and grain boundary morphologies due to inadequate heat treatment or pre-existing irreversible conditions.

Comparison of creep rupture properties of material taken from high temperature regions of the component and from the root form can demonstrate that the repair process has appropriately restored the mechanical properties. This testing can be done at several different test parameters to identify possible problems in different components of the microstructure. Inadequate heat treatments can also be identified from these tests.

Degradation Of Protective Coating Systems

In order to reduce the surface metal temperatures sufficiently to obtain acceptable coating life, complicated cooling schemes are mandatory, together with the now wide spread use of TBC coatings. The cooling systems can consist of turbulated cooling holes and/or serpentine cooling circuits with cast in airflow turbulators and pin fins. All of the new designs contain local areas where thin wall sections (0.020”–0.030”) are present. Where necessary, film cooling hole geometries present even more coating and refurbishment problems. This is in addition to the new and unique problems in removing both internal and external coatings.

One of the most commonly used IGT coating system was the General Electric aluminized CoCrAlY layer, GT29Plus (Rairden [2]). The coating is applied in two steps.

The GT29 (Co–29Cr–6Al–0.3Y) overlay layer is typically deposited using VPS or more recently HVOF spray methods, densified and diffused. The coating is then aluminized using standard pack aluminizing processes or optionally above the pack (ATP) or CVD processes when internal aluminizing coatings are to be simultaneously applied.

An aluminized CoCrAlY coating system applied onto a directionally solidified GTD111 alloy component that has been in service is illustrated in Fig. 1. The coating system is a non-homogeneous layer made up of discrete metallurgical phases. On the surface of the coating there is a very thin protective aluminum

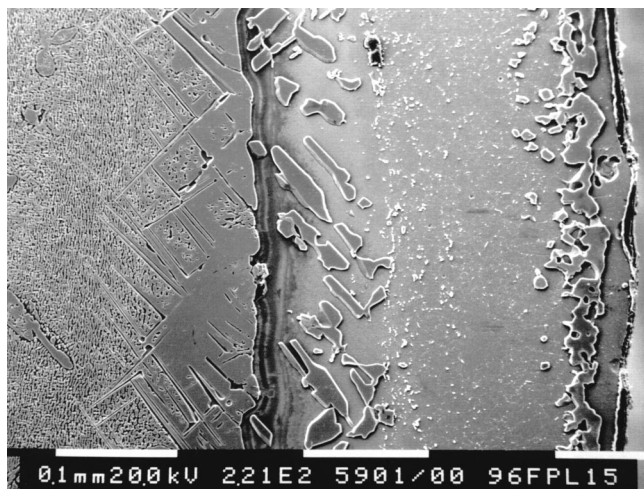


Fig. 2 A photomicrograph of a service-run aluminized CoCrAlY coating applied to a DS GTD111 alloy component illustrating data phase depletion and inter-diffusion with the base alloy

oxide (Al_2O_3) scale. Below the protective oxide there is a single-phase $\beta(\text{CoAl})$ layer that was formed during the aluminizing process together with the concurrent inter-diffusion zone. The composition of the CoCrAlY coating below the single-phase β layer has a graded aluminum concentration that is reflected in the microstructure by the changing volume fraction of $\beta(\text{CoAl})$ precipitates. The microstructure of the unaffected CoCrAlY layer consists of discrete (CoAl) precipitates in a γ matrix over the coating/GTD-111 alloy base metal diffusion zone.

In service the aluminized MCrAlY coating and base alloy combination act as one integrated system. Examination of service run components reveals a range of structures. In the hotter regions of the airfoil, the beta phase precipitates in the original CoCrAlY coating dissolve first as a result of inter-diffusion reactions that occur at the CoCrAlY/GTD-111 base alloy interface (Fig. 2). The aluminum concentration in the $\beta(\text{CoAl})$ additive layer is also simultaneously being reduced at the Al_2O_3 -aluminide-CoCrAlY interface as a result of the normal loss of aluminum through surface scale exfoliation and reformation. However, as a result of the increased reservoir of aluminum, this layer can remain intact long after the beta phase precipitates in the CoCrAlY coating have dissolved.

Once all of the beta phase in the as-deposited CoCrAlY has been depleted, what is left of the discernible aluminized CoCrAlY layer depletes. Even with depletion of all beta phase precipitates, this layer can continue to form an external oxide. Depending upon temperature, however, these oxides can be less protective and faster growing. Below some temperature and critical composition, the degradation mode can rapidly change over to internal oxidation. Once this occurs, the oxide is nonprotective and the substrate is rapidly consumed.

The inter-diffusion reactions between aluminized vacuum plasma sprayed CoCrAlY coatings and directionally solidified nickel-base superalloy such as DS GTD111 can be calibrated and used to estimate the operating temperatures of service-exposed combustion turbine blades. Recently a model developed by Ellison et al. [3] was used to estimate surface temperatures of service-exposed GE MS7001F first-stage blades. The metallurgical temperature estimates based on overlay coating inter-diffusion were in reasonable agreement with those obtained independently from an analysis of gamma prime precipitate coarsening and pyrometry data (Fig. 3).

A new nondestructive method of coating condition analysis was recently developed using advanced Eddy Current Test methods to examine degradation levels in service run coatings (Wells [4]).

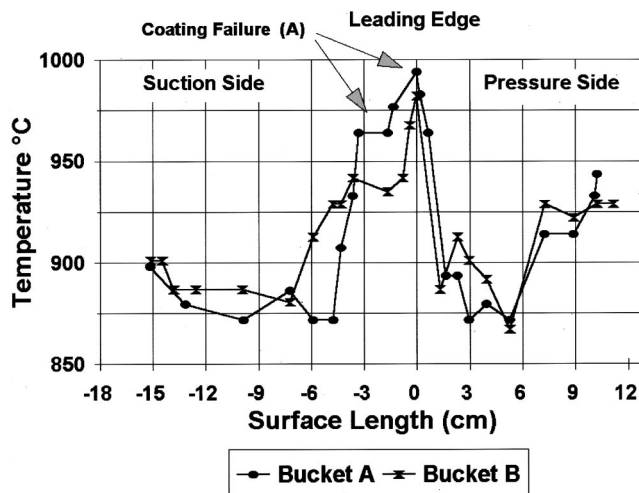


Fig. 3 Metallurgical temperature estimates of a service-exposed GE MS7001F first-stage turbine blade based on inter-diffusion rates between the aluminized CoCrAlY overlay coating and the directionally solidified GTD111 base alloy

Techniques such as this may allow coating performance to be monitored with the components in situ. Early detection of coating degradation may prevent expensive repairs if the parts can be removed before extensive base metal attack or the onset of cracking occurs as well as a potentially valuable measure of actual turbine conditions.

Removal of MCrAlY Coatings From Service Run Components

Ideally, the stripping procedure should attack only the coating and stop at the base alloy substrate. In most cases, TBC ceramic topcoats can be easily removed by grit blasting, MCrAlY coatings/bond coats on the other hand, have proven to be very difficult to remove because of the wide range of chemistries and microstructures (Daleo and Boone [5]).

Acid immersion techniques are the most widely used methods of coating removal and are based on selective attack of the aluminum rich phases. The dilemma is that MCrAlY coating systems have starting Al concentrations ranging from 6 to 12 percent and rapidly degrade at different rates over the airfoil to essentially nonacid strippable compositions. Thus problems that occur during the stripping process revolve around reliably removing the depleted areas of the coating without attacking the base metal. Consequently in practice, acid immersion methods are more effective in the cooler areas of the blade where the coating has retained most of its original structure and composition than in the hotter areas where almost complete coating consumption has occurred. In addition to coating depletion, extensive γ' film formation is frequently observed along severely aged grain boundaries in the hotter areas. This presents a real danger that the acid solution may attack the base alloy grain boundaries during coating removal.

Problems that occur during the stripping process revolve around reliably removing the depleted areas of the coating without attacking the base metal and detecting when the coating has been completely removed. Each vendor's stripping process is supposed to handle the service-induced microstructure variations adequately, although this is not always evident. In general, it is difficult to effectively remove all of the remaining coating from the substrate without causing base metal attack using acid stripping techniques alone. In practice, vendors invariably resort to repeated combinations of chemical stripping cycles and abrasive belt grinding steps. As a result of this, components are often rejected from the repair

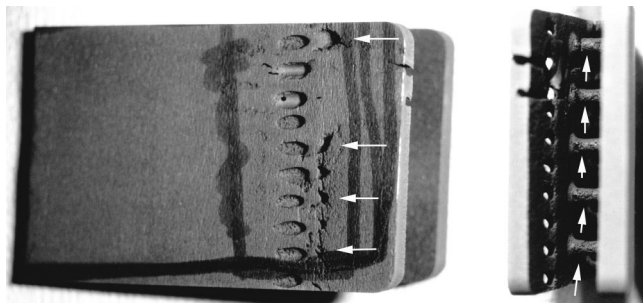


Fig. 4 A photograph illustrating irreversible stripping damage caused to a pin fin array

cycle because the blending limits are exceeded in the thin wall sections or because the internal airflow turbulators or pin fins have been preferentially attacked (Fig. 4).

Recently, more novel approaches to removing MCrAlY coatings have been developed, though they are not widely used. These include Siemens, Siclean procedure, aluminize and acid strip, and Sermatech's aluminize and grit blast process.

Microstructure Stability

Knowledge of the alloy microstructure is fundamental to understanding the mechanical property behavior of the material. Superalloy microstructures continually change with time at the operating temperatures experienced by gas turbine blades and vanes.

The starting microstructure of a blade is a product of the chemistry, the casting parameters and coating and heat treatment steps used to manufacture the component. In the new, heat treated alloy, the gamma prime (γ') particles are arranged in a structure, which results in an optimum balance of tensile, fatigue, and creep properties.

The microstructure of a directionally solidified GTD111 alloy blade in the standard heat-treated condition is illustrated in Fig. 5. Nickel-base alloys, such as DS GTD111 are primarily strengthened by a duplex mixture of ordered face-centered cubic, precipitated second phase particles γ' [$\text{Ni}_3(\text{Al,Ti})$] and by chromium and refractory element rich carbides that form during solidification and subsequently in the gamma (γ) solid solution strengthened matrix. The grain boundaries are often serrated and deco-

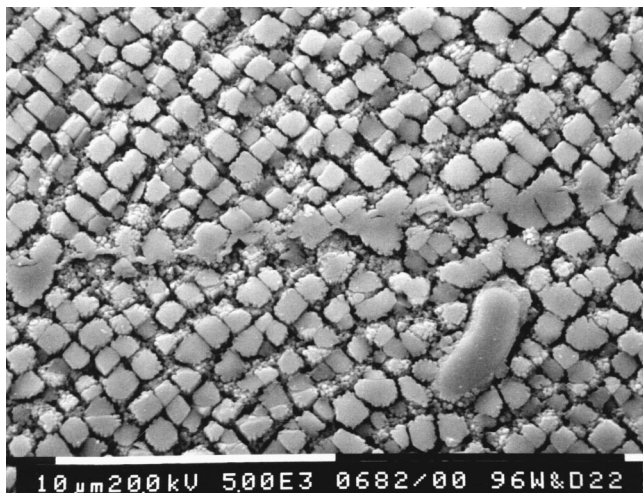


Fig. 5 A scanning electron micrograph of DS GTD111 alloy in the standard heat-treated condition illustrating the duplex γ' precipitate microstructure and the grain boundary carbide morphology

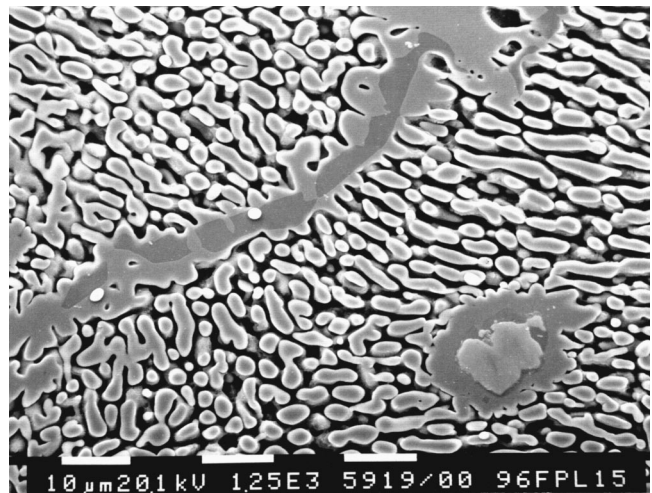


Fig. 6 A scanning electron micrograph of DS GTD111 alloy after 18,000 hours of service

rated with a very thin, discontinuous $\gamma'/\text{M}_{23}\text{C}_6/\text{M}_6\text{C}$ carbide layer. Minor additions of zirconium and boron are added to polycrystalline alloys to stabilize grain boundaries while additions of hafnium have several beneficial functions, particularly in columnar grain materials.

The stability of the various microstructural phases at the operating temperatures experienced by gas turbine blades is extremely important. As the alloy is exposed to the gas turbine operating conditions, changes in the microstructure occur resulting in reduced creep and fatigue strengths and ductility. In service the γ' phase increases in size with time and temperature, and complex carbide reactions occur.

The most important of the carbide reactions is the continued growth of the M_{23}C_6 carbide phase along the grain boundaries. The migration of chromium to the boundary leaves the matrix locally enriched in the γ' forming elements nickel, aluminum, titanium etc. allowing a film of γ' to form along the boundary. Degeneration of MC carbides into $\text{M}_{23}\text{C}_6 + \gamma'$ in the matrix and along the grain boundaries accelerates the process. Examples of these phase changes were observed in a DS GTD111 turbine blade removed from service after 18,000 hours (Fig. 6).

Reheat Treatment of Service Run Blades

Attempting to fully recover the aged microstructure to reestablish the mechanical properties by repeating the alloy's standard heat treatment sequence does not always work. For example, typical heat treatment cycles used for two of the most common industrial turbine rotating blade materials, polycrystalline GTD111 (Tien and Caulfield [6]) and IN-738LC (ASM Metals Reference Book [7]) are similar to the following cycle:

Vacuum Solution Heat Treatment. 1120°C for two to four hours followed by a rapid gas quench (25°C to 55°C/minute) to below 650°C.

Vacuum Precipitation Aging Cycle. 845°C for 24 hours followed by a rapid gas quench to room temperature.

Figure 7 illustrates a service run IN-738LC airfoil that was processed through this standard reheat treatment cycle. Note that the microstructure was only partially recovered by the heat treatment.

The reason why the standard heat treatment does not often work well is that the γ' solution temperature for IN-738LC and GTD111 alloys ranges from 1175°C to 1190°C. To fully restore the microstructure after service exposure, these alloys need to be solution treated at 1200°C. An effective way to incorporate the

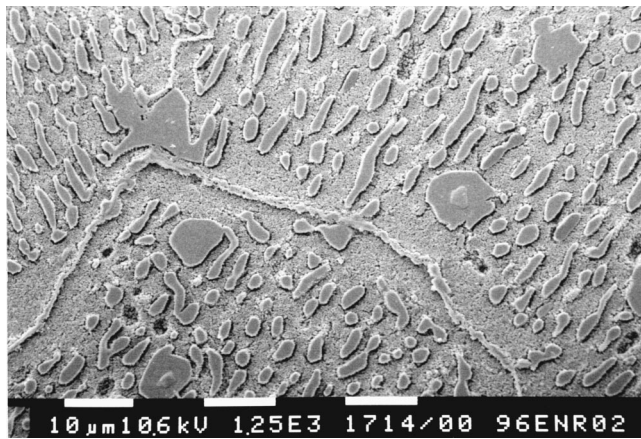


Fig. 7 A scanning electron micrograph of an IN-738LC turbine blade processed through the standard reheat treatment cycle. Note that the microstructure was not restored to its original condition.

high temperature cycle needed to restore the microstructure of service run blades is to hot isostatic press (HIP) the components, especially if the components were not hipped during the original manufacturing sequence. A typical HIP cycle used for the polycrystalline versions of IN-738LC and GTD111 alloys is similar to the following cycle:

HIP Cycle (Argon Atmosphere). 1200°C ± 10°C, 15,000 psi ± 100 psi pressure for two to four hours. Furnace cooled at a rate approximately 2.5°C/minute to 1120°C (Beddoes and Wallace [8]). Hold at 1120°C for one to two hours, then furnace cool.

The high temperature thermal cycle helps to homogenize the microstructure while the controlled cooling rate from 1200°C to 1120°C nucleates the optimum primary γ' distribution and increases the intermediate temperature creep rupture strength of the material by forming serrations in the grain boundaries. Where the components have been previously hipped, the above cycle can be performed in a vacuum furnace. A rapid gas quench (25°C to 55°C/minute) to below 650°C should be done from the final hold point at 1120°C.

The heat treatment steps performed after this cycle, will be alloy and coating specific, but similar to the following thermal sequence.

Internal Aluminide Coating Diffusion Cycle. 1000°C to 1080°C/two to eight hours, furnace cool.

MCrAlY Coating Diffusion Cycle. 1080°C to 1120°C two hours.

Solution Heat Treatment. 1120°C for two hours followed by a rapid gas quench (25°C to 55°C/minute) to below 650°C.

Precipitation Aging Cycle. 845°C for 24 hours followed by a rapid gas quench to room temperature.

Failure to correctly integrate the coating and heat treatment cycles can result in incompletely developed microstructures and properties (Fig. 8).

One precaution concerning regenerative heat treatment cycles above the γ' solution heat treatment temperature needs to be noted. Diffusion aluminide and MCrAlY coatings do not usually melt at the γ' solution temperatures, however, the coating-base alloy interdiffusion zone can melt in some coating alloy combinations doing irreversible damage. This is especially the case where internal aluminide diffusion coatings are present (Fig. 9). Additionally, exposure of the diffusionally controlled coating system to excessive temperatures can greatly degrade the coating protective-



Fig. 8 A scanning electron micrograph of an IN-738LC turbine blade not correctly processed through the modified high-temperature reheat treatment cycle

ity. Where possible, it is wise to remove both internal and external coatings before performing this type of refurbishment heat treatment.

In DS materials such as the GTD111 alloy, exposure at the 1200°C solution heat treatment cycle can induce re-crystallization in areas that have been plastically deformed. Impact damage on the surface of the airfoil and the contact areas of the root form are especially susceptible (Fig. 10). Since it may not be possible to fully recover the microstructure in all areas of these alloys, it is prudent to measure the resulting properties in the critical, hotter areas of the component as part of the material re-qualification process. Note that the new stress relaxation testing technique can be a very useful tool here for measuring creep properties in specific locations after reheat treatments.

Creep Damage

The firing temperatures used in the latest generation of gas turbines designs has forced engine designers to incorporate elaborate cooling component schemes. These are required to reduce steady state creep rates and TMF by reducing the average metal temperature and hopefully by reducing thermal gradients. In determining the remaining life of rotating blades and vanes, consid-

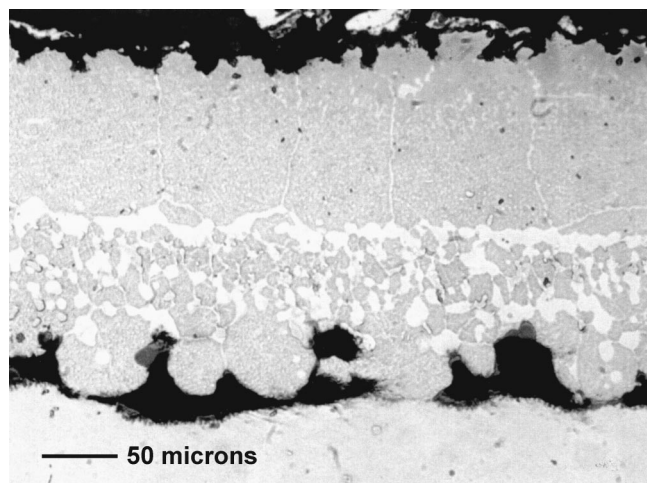


Fig. 9 A photomicrograph illustrating melting of the interdiffusion zone of an aluminide coated IN-738LC substrate

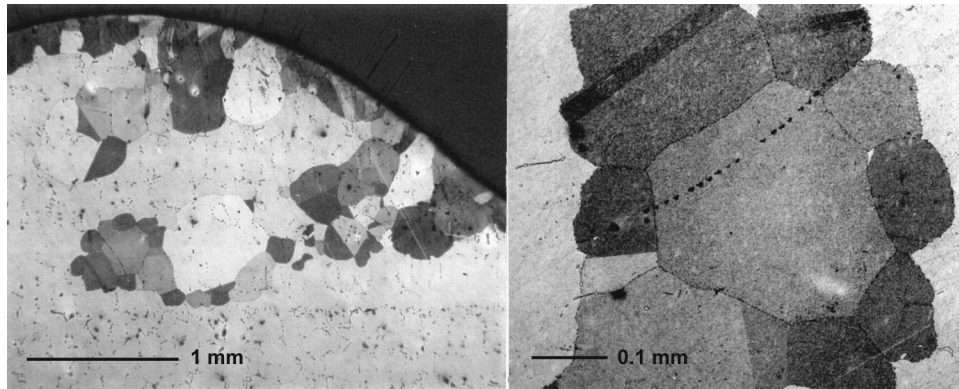


Fig. 10 Photomicrographs illustrating re-crystallization of the surface grains observed in the root form of a reheat treated DS GTD111 alloy blade

eration of both creep and thermal mechanical fatigue resistance are critically important, in that either degradation mechanism could lead to failure of the components.

The most effective method of determining the decrease in creep strength and ductility resulting from service exposure is to perform long-term mechanical stress rupture tests. Alternatively accelerated stress relaxation tests have shown considerable promise (Daleo et al. [9]). Traditional stress rupture testing is well known and understood, while use of the accelerated stress relaxation test method is not yet common practice. Thus, a brief review of the stress relaxation test method and its use follows.

Stress Relaxation Testing

Soderberg [10] originally described the fundamental methodology and mathematics of stress relaxation testing. Early examples of converting raw stress relaxation test data, (stress versus time) to stress versus strain rate and using it to compare creep properties of austenitic stainless steels were published by Oding [11]. As better strain gaging and high-speed digital data recording technology became available, methods of accelerating the test method using tensile testing machines were later developed and used (Lee and Hart [12]).

The use of stress relaxation test methods to help characterize the creep properties of service-run gas turbine components is a relatively new concept, first proposed by Woodford et al. [13]. The detailed test procedure has been described previously (Woodford [14]). The specimen is deformed to a fixed strain, which is held constant during a typical one-day test. The stress versus time response is converted to a stress versus creep rate response by differentiating and dividing by the modulus measured on loading. This is, in effect, a self-programmed variable stress creep test. Typically, a test lasting less than one day may cover up to five decades in creep rate. Thus, an enormous amount of creep data can be generated in a short time.

The data is best presented as a plot of stress versus the log of creep rate (Fig. 11). The test is meant to be performance based, i.e., it provides a measure of the current mechanical state in terms of creep strength, since time-dependent microstructure changes are deliberately minimized. Thus, the test allows a determination of the consequences of microstructure evolution and damage development. It does not attempt to incorporate these changes in the actual test as in the traditional creep rupture approach.

More detailed explanations of the stress relaxation data presented in this paper and how the methods are used for creep life assessment can be referenced found in the following papers (Daleo et al. [9] and Woodford and Daleo [15]).

Strain Rate Estimates of Design and Remaining Life

Once the operating metal temperatures and stress have been determined, an estimate of the design life can be calculated using a modified version of the Robinson Life Fraction Rule (Robinson [16]) that incorporates strain fractions.

$$\varepsilon_T / \dot{\varepsilon}_i - \sum O_i \quad (1)$$

where ε_T = the failure strain or alternatively the acceptable design strain criterion (strain to crack initiation 0.5%, etc.) of new material, $\dot{\varepsilon}_i$ = the strain rate at temperature and stress i , $\sum O_i$ = the sum of the operating hours at temperature and stress i .

In the case of a rotating gas turbine blade, the strain rate of the material changes with time, thus a refined estimate of remaining life can be calculated by measuring the current strain rate of the material at temperature and stress i , and recalculating a new life. If the new life is more than the next overhaul period, the component can be returned to service, if it is less, the component is repaired or replaced.

$$\left(\varepsilon_T \left(\sum O_i^* \dot{\varepsilon}_i \right) \right) / \dot{\varepsilon}_c > \sum O_{in} \quad (2)$$

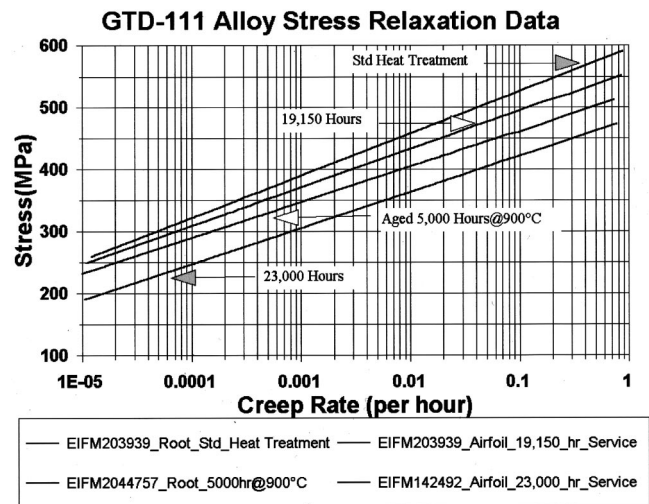


Fig. 11 A plot comparing strain rate data measured from polycrystalline GTD111 alloy samples in different conditions at 850°C and 0.8 percent total strain

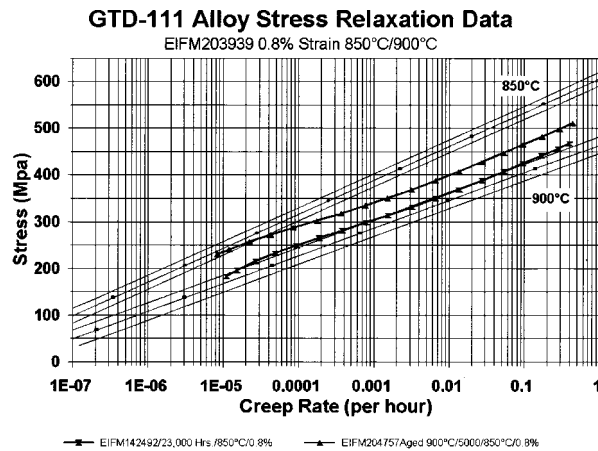


Fig. 12 A plot illustrating the drop in creep rate properties measured in a polycrystalline GTD111 alloy blade airfoil in terms of temperature capability of "new" material in the standard heat treated condition

Where $\dot{\epsilon}_c$ = the current strain rate of the material in condition c at temperature and stress i , $\sum O_{in}$ = the sum of the operating hours to the next overhaul at temperature and stress i .

The most conservative estimate would be to divide the failure strain or the acceptable design strain criterion of new material by the current the strain rate at temperature and stress i .

$$\epsilon_T / \dot{\epsilon}_c - \sum O_I \quad (3)$$

Temperature-Based Comparison Using Stress Relaxation Strain Rate Measurements

Stress relaxation creep rate data of material under different conditions can be compared directly in terms of temperature capability of the new material in the fully heat treated condition (Daleo et al. [9]). An example of this is presented in Fig. 12, where the material properties measured in the airfoil of a service run blade had deteriorated by the equivalent of almost 40°C.

To use this approach in life assessment applications, an estimate of the starting material properties generated by the original processing is needed. This would be obtained by measuring the material properties in the root form at three temperatures that bracket the service temperature range of interest. Service run airfoil samples would then be measured at two temperature levels of interest. Plotting the data all together on one graph provides a direct estimate of the drop in creep rate properties in terms of temperature. Once the drop in temperature capability is known, the extrapolation procedure of choice can be used to analyze the data. The creep rates of different materials tested in this manner can also be compared directly. This provides the material's engineer with a very powerful tool for new alloy development or in alloy selection for critical applications.

Estimates of Creep Rupture Life Based on Stress Relaxation Data

The mechanism resulting in fracture in the shortest time or after the lowest strain determines the failure characteristics of the material. In terms of creep mechanisms, time to failure is a function or a measure of the materials creep strength (i.e., creep rate) while strain tolerance at failure is primarily a function of the microstructure.

Creep strength can be best thought of in terms of changes in the steady state or average creep rate ($\dot{\epsilon}$) with respect to time, stress, and temperature.

$$\dot{\epsilon} = f(t, \sigma, T) \quad (4)$$

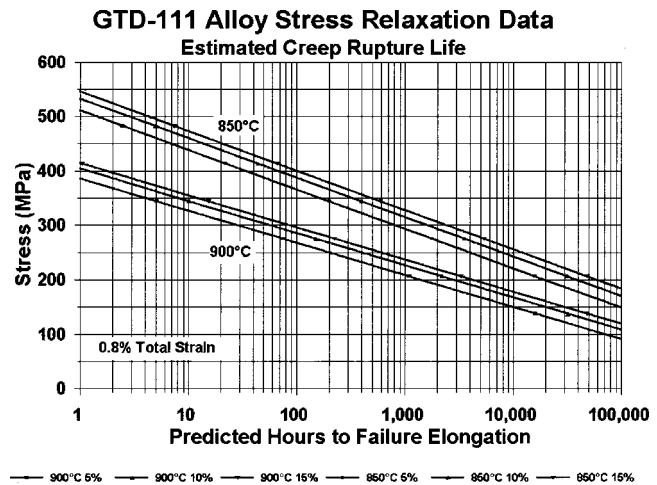


Fig. 13 A plot of stress versus estimated creep rupture life of polycrystalline GTD111 material in the standard heat treated condition based on 5 percent, 10 percent, and 15 percent failure elongation

The most widely accepted (used) expression for $\dot{\epsilon}$ is

$$\dot{\epsilon} = B \sigma^n e^{(-Q_c/RT)} \quad (5)$$

Where B and n are constants, σ = stress, Q_c is the activation energy for creep (KJ/mole), R is the universal gas constant (8.314 KJ/mole) and T = temperature in deg K.

Recognizing that the time for rupture, t_f , is also a function of the creep rate (Monkman and Grant [17] ($t_f \propto 1/\dot{\epsilon}$)) and many more sophisticated models to follow), the rupture life can then be expressed as

$$1/t_f \propto \dot{\epsilon} = B \sigma^n e^{(-Q_c/RT)}. \quad (6)$$

The stress relaxation test can be thought of as taking a cross section through a series of constant load creep rupture curves at a set total strain and temperature. At 0.8 percent total strain, in most constant load creep rupture curves, the steady-state creep rate has been reached. Thus in a single stress relaxation test an estimate of the steady-state creep rate is obtained over a large range of stress conditions. The time to failure at any given stress and temperature combination can therefore be estimated directly from the creep rates measured in the stress relaxation test runs. At the optimum total strain parameter of each alloy, the stress relaxation test provides a measure of the average steady-state creep rate. This allows a reasonable estimate of creep rupture life to be extracted from the data by dividing the expected or the minimum acceptable fracture elongation directly by the measured creep rate.

Polycrystalline GTD111 superalloy blades exhibit creep ductilities that range from a low of about 5 percent to approximately 15 percent when measured in standard constant load creep rupture tests (Daleo and Wilson [18]). A plot of stress versus calculated life based on 5 percent, 10 percent, and 15 percent elongation at any particular temperature therefore provides not only a measure of the expected life, but also an indication of the scatter to be expected (Fig. 13).

The data sets examined indicate that rupture lives can be estimated to within a factor of three, which is quite remarkable given that the data needed to estimate rupture properties can be generated and analyzed within a few weeks.

Correlation of Stress Relaxation Data With Time Temperature Parameter Approaches

A Larson-Miller curve was produced by converting the rupture time estimates generated by the stress relaxation data into Larson-Miller format (Larson and Miller [19]) and fitting the data into a

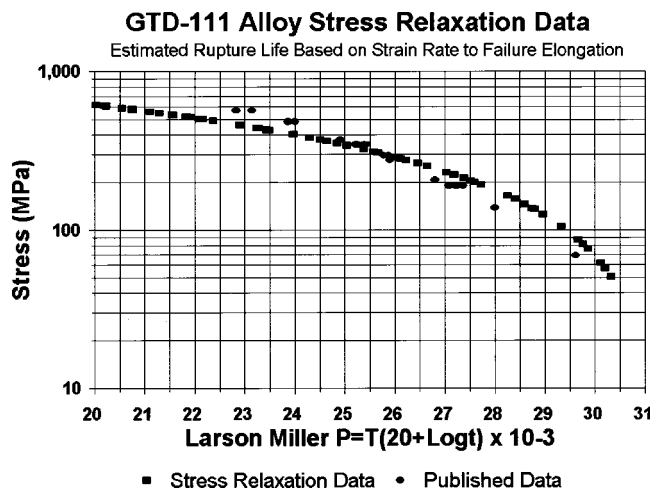


Fig. 14 A plot comparing a Larson-Miller curve created from estimated creep rupture life based on strain rate to failure elongation, to published GTD111 creep rupture data

best-fit curve using a least-squares regression model ($Y = \beta_0 + \beta_1 X + e$). Comparison of the plot made using the estimated data with published Larson-Miller plots in the open literature (Schilke et al. [20] and Daleo et al. [9]) indicates that this technique can rapidly produce these plots with reasonably good accuracy, Fig. 14. The technique was also used to produce Larson-Miller plots for two other widely used gas turbine blade alloys, IN-738LC and IN-939 (Daleo et al. [9]) for which stress relaxation data had been previously obtained (Woodford et al. [21]).

Thermal-Mechanical Fatigue Damage

Thermomechanical fatigue (TMF) damage is caused by a combination of strains resulting from mechanical loads together with high transient or steady-state temperature gradients in the part. When free expansion cannot occur as a result of the inherent part geometry, high stresses are generated. The highest combined strains usually occur in the hottest and coolest regions of the section.

Thermal fatigue life is generally correlated with the number of startup and shutdown cycles of the turbine where the shutdown and the induced tensile strains at the lower temperatures are more damaging, particularly to coatings. However, the number of actual cycles to failure can vary considerably from part to part and from engine to engine. The transient nature of the temperature changes makes thermal fatigue life very difficult to predict.

Since TMF cracking is almost always a surface related phenomena, the presence and type of protective coating plays a dominating role and must always be considered in the design and service analysis.

Often when problems occur, the only way to minimize the effect is through careful redesign of the component, change of coatings or materials or by changing engine operation. Startup cycles of the turbine employing quick light offs and/or rapid acceleration rates will tend to result in larger thermal gradients in the components and therefore higher thermal fatigue loads. The nature of shutdowns can often more significantly influence thermal fatigue life. Thermal fatigue loading is much higher under trip conditions than in controlled shutdowns. In addition, thermal fatigue resistance is significantly influenced by environmental attack. Elements in the hot gas path interact with the base alloy or with the coating system used to protect the base alloy.

In those instances where it is required to operate a turbine with cracked components to the next logical overhaul period, a defect tolerant design (fracture mechanics) analysis can be performed to assess the risks. A mechanical analysis of the component with the

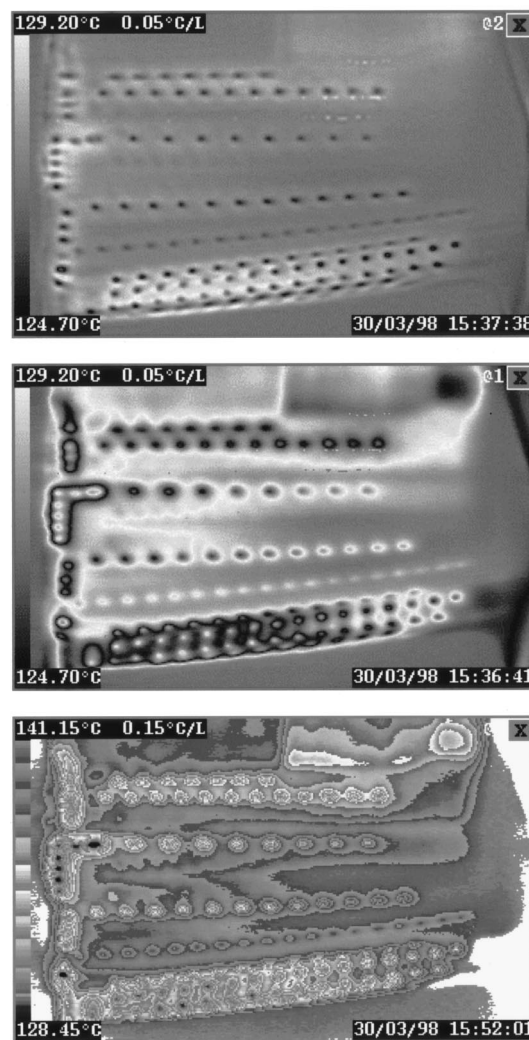


Fig. 15 A sampling of a series of transmission mode thermal inertia of images of a CF6 turbine blade

defect present is performed to calculate the stress, strains, and stress intensity factors. Knowing or measuring the relationship between the stress intensity factors and crack growth rates, the potential for crack growth to a critical size before the next overhaul can be evaluated. This often requires three-dimensional transient thermal stress analysis to determine the stress fields and the strain ranges in the defect zone under typical load cycles. Since the blades must be capable of withstanding abnormal operating conditions, the effect of high-cycle fatigue excitation may also have to be evaluated.

Thermal Inertia Analysis

Throughout this discussion, the importance of operating temperature on component life and reparability has been demonstrated. While designs are optimized and verified in an attempt to obtain the required temperatures, variations in theory and assumptions, manufacturing processes, and changes, which occur during operation, can result in actual service temperatures in excess of design limits.

Metallurgical techniques such as γ' and coating diffusion zone growth measurements have been very successfully used to determine actual temperatures Ellison et al. [3]. On several occasions they have been used to justify design changes. Since blade tem-

peratures are a strong function of cooling system design and reliability, a technique to monitor the function and service changes of the cooling system is extremely important.

In the past, direct NDE thermal analysis using sensitive infrared detectors has been successfully used, particularly to determine coating integrity. However, the recently introduced thermal inertia analysis (TIA) technique (Daniels et al. [22,23]) involving an integrated thermal source-measuring system and sophisticated data analysis, allows for the imaging and direct analysis of the cooling system performance and any changes that may have occurred. This new technique provides the ability to study and monitor thermal behavior changes to the components at various stages including; design, manufacture, coating (including actual thermal barrier effectiveness measurement), service changes resulting from contamination and deterioration, and most importantly verification of successful refurbishment such as impingement tube/core plug re-installation, correct hole diameters, and flow rates, etc. (Stiglish et al. [24]).

Essentially, a component can be analyzed after service to determine if the cooling scheme has been compromised, and hence if the component may have run out of specification (i.e., too hot) with possible structural damage. The presence of insulating deposits, blocked holes, tip cracks and leaks, etc., which change flows and cooling capacity can be detected. Based on this NDE information the run/ repair/ replace decision can be made with more confidence. When repair is warranted the component can be re-measured/certified prior to reinstallation with monitoring at overhaul. Obviously this technique can be a powerful tool for OEM design and manufacture.

The sensitivity of the thermal inertia analysis technique can be seen in a thermal image of a component showing cooling flow efficiencies and internal cooling design through the component and overlying TBC system (Fig. 15). Specific thermal insulation factors can also be measured and monitored.

The presence of nonmetallic deposits and residual core materials can be rapidly and economically detected compared with the more limited and complex techniques presently being explored.

Summary and Conclusions

In order for a user to more accurately predict and assess the remaining lives of critical components in their gas turbine engines, metallurgical evaluation and testing of select components should be performed in addition to careful NDE during hot gas path inspections and major overhauls. Metallurgical testing of representative components provides engine specific information regarding degradation mechanisms, safe refurbishment procedures and the proper requalification of repaired components. This database developed for the variety of service operating conditions experienced is necessary to make the proper component decisions.

When combined with the comprehensive metallurgical evaluation methods for gas turbine failure analysis and life assessment, the stress relaxation test methodology is a very powerful tool in helping to quantify degradation of creep properties in service run components and to properly re-qualify rejuvenation treatments. The speed at which the testing and analysis can now be performed makes realistic life assessment and repair replace decisions possible during normal turbine overhaul periods.

NDE techniques which can measure the "condition" of the coating and possibly substrate, and thermal inertia analysis which can determine the "efficiency" of the cooling system and hence propensity for damage, offer a new level of semi-quantitative in-

formation in the repair-replace-retire decision process. Use and integration of these techniques to support the range of new challenges of advanced gas turbines are being actively explored.

References

- [1] Daleo, J. A., and Boone, D. H., 1997, "Failure Mechanisms of Coating Systems Applied to Advanced Turbine Components," ASME Paper 97-GT-486.
- [2] Rairden, III, J. R., 1982, U.S. Patent, Re. 30,995, reissued July 13.
- [3] Ellison, K. A., Daleo, J. A., and Boone, D. H., 1998, "Metallurgical Temperature Estimates Based on Inter-diffusion Between CoCrAlY Overlay Coatings and a Directionally Solidified Nickel-Base Superalloy Substrate," *Proceedings of the 6th Liege Conference*, Vol. 5, Part III, Forschungszentrum Julich GmbH, p. 1523.
- [4] Wells, C., 1996, "Eddy Current Measurements of the In-Service Degradation of the GT29PLUS Coating System On GTD111 Turbine Blades," Final Report of Project GE96-20, Report number SIW-96-025, Structural Integrity Associates.
- [5] Daleo, J. A., and Boone, D. H., 1996, "Metallurgical Evaluation Techniques in Gas Turbine Failure Analysis and Life Assessment," *Failures 96, Risk, Economy and Safety, Failure Minimization and Analysis*, R. K. Penny, ed., A. A. Balkema, Rotterdam, pp. 187-201.
- [6] Tien, J. K., and Caulfield, T., eds., 1989, *Superalloys, Supercomposites and Superceramics*, Academic Press, San Diego, CA, p. 138.
- [7] *ASM Metals Reference Book*, 2nd Ed., 1983, ASM, Metals Park, OH, p. 415.
- [8] Beddoes, J. C., and Wallace, W., 1980, "Heat Treatment of Hot Isostatically Processed IN-738 Investment Castings," *Metallography*, **13**, pp. 185-194.
- [9] Daleo, J. A., Ellison, K. A., and Woodford, D. A., 1999, "Application of Stress Relaxation Testing in Metallurgical Life Assessment Evaluations of GTD111 Alloy Turbine Blades," *ASME J. Eng. Gas Turbines Power*, **121**, pp. 129-137.
- [10] Soderberg, C. R., 1936, "The Interpretation of Creep Tests for Machine Design," *Trans. ASME*, **58**, p. 733.
- [11] Oding, I. A., et al., 1959, *Creep and Stress Relaxation in Metals*, Academy of Sciences of the USSR (English translation by A. J. Kennedy, Oliver and Boyd Ltd.).
- [12] Lee, D., and Hart, E. W., 1971, "Stress Relaxation and Mechanical Behavior of Metals," *Metall. Trans.*, **2**, pp. 1245-1248.
- [13] Woodford, D. R., Van Steele, K., Amberg, K., and Stiles, D., 1992, "Creep Strength Evaluation for IN 738 Based on Stress Relaxation," *Superalloys 1992*, S. D. Antolovich et al., eds., The Minerals, Metals and Materials Society, pp. 657-664.
- [14] Woodford, D. A., 1993, "Test Methods for Accelerated Development, Design and Life Assessment of High Temperature Materials," *Mater. Des.*, **14**, No. 4, pp. 231-242.
- [15] Woodford, D. A., and Daleo J. A., 1999, "Life Assessment of Hot Section Gas Turbine Components," *Proceedings of a conference held at Heriot Watt University*, R. Townsend et al., eds., Edinburgh, UK, Oct. 5-7, IOM Communications, London, pp. 293-310.
- [16] Robinson, E. L., 1952, "Effects of Temperature Variations on the Long Time Rupture Strength of Steels," *Trans. ASME*, **74**, pp. 777-781.
- [17] Monkman, F. C., and Grant, N. J., 1956, "An Empirical Relationship Between Rupture Life and Minimum Creep Rate in Creep Rupture Tests," *Proc. ASTM*, **56**, p. 593.
- [18] Daleo, J. A., and Wilson, J. R., 1998, "GTD111 Alloy Material Study," *ASME J. Eng. Gas Turbines Power*, **121**, pp. 375-382.
- [19] Larson, F. R., and Miller, J., 1952, "Time-Temperature Relationships for Rupture and Creep Stresses," *Trans. ASME*, **74**, p. 765.
- [20] Schilke, P. W., Foster, A. D., Pepe, J. J., and Beltran, A. M., 1992, "Advance Materials Propel Progress in Land-Base Gas Turbines," *Adv. Mat. Processes*, **Apr.**, pp. 22-30.
- [21] Woodford, D. R., Daleo, J. A., and Wilson, J. R., 1996, "Analysis of Service Run Ruston TB5000 Components," 96Mpa/W&D01, Materials Performance Analysis, Wilson & Daleo, Inc., internal report.
- [22] Daniels, A., Bales, M., Bishop, C., Becker, E., and Van Dijk, M., "Infrared Testing of Turbine Blades and Vanes Using Both Transmission and Reflective Methodologies," presented at the 1995 ASNT Quality Testing Show, Dallas, TX.
- [23] Daniels, A., 1996, "Non-destructive Pulsed Infrared Quantitative Evaluation of Metals," *Thermosense XVIII: An International Conference on Thermal Sensing and Imaging Diagnostic Applications*, Apr. SPIE.
- [24] Stiglish J. J., Bishop C. C., Daleo J. A., Boone D. H., and Eelkema T. E., 1999, "The Thermal Inertia Analysis Technique in Gas Turbine Component Reliability Assessment," *Materials Solutions* 98, ASM International, pp. 138-144.

Systematic Evaluation of U.S. Navy LM2500 Gas Turbine Condition

B. D. Thompson

B. Wainscott

Fleet Technical Support Center,
Pacific, U.S. Navy

From an operational availability stand point, the U.S. Navy is interested in the short term reliability of its ship based LM2500 gas turbine engines. That is the likelihood that an engine will operate successfully through a six-month deployment (usually 1500 to 2000 operational hours). From a maintenance and cost of ownership standpoint both the short-term and long-term reliability are of concern. Long-term reliability is a measure in time (in operating hours) between engine removals. To address these requirements U.S. Navy Fleet support maintenance activities employ a system of tests and evaluations to determine the likelihood that an LM2500 will meet its short and long-term goals. The lowest level inspection is the predeployment inspection, which attempts to identify primarily mechanical faults with the engine. Gas Turbine Bulletin inspections are used to determine if predefined wear out modes exists. Performance evaluations can be performed which determine the ability of the LM2500 and its control system to meet expected power requirements. Lube oil system data can be analyzed to determine if excessive leakage or excessive scavenge temperatures exist. Engine vibration characteristics can be reviewed to identify the source of both synchronous and nonsynchronous vibration and determine if corrective measures need to be taken. This paper will discuss how the lowest level inspections feed the more sophisticated analysis and how these inspections and evaluations work to provide a systematic method of insuring both short and long-term LM2500 reliability. [DOI: 10.1115/1.1451716]

Introduction

The original maintenance philosophy of the LM2500 has evolved as a result of numerous factors, some of which are discussed by Hartranft in 1993 ([1]). As detailed by Thompson, Badgley, and Hartranft in 1989 ([2]), increases in mean time between removals, operational experience, and the development of in place maintenance and repair procedures took the LM2500 from an engine that was removed and repaired in the depot to an engine where problems were corrected in place. Since the LM2500 gas turbine in USN service typically does not see prolonged operation at or near design power levels, hot section degradation has not been an over riding factor in defining long term reliability. In fact long-term reliability has been a "moving target" in that with increased age of the engine new wear out modes have developed and have required assessment and resolution. Presently the mean time between removal is in excess of 16,000 hours with some engines now exceeding 30,000 hours. In order to obtain these levels of engine life, there has developed a refined understanding of the LM2500 and the propulsion and controls system. This coupled with the utilization of all aspects of the maintenance process has allowed the USN to meet both short and long-term goals.

Conditions which effect long term reliability of the LM2500 can be broken down into the following areas: engine vibration characteristics, ability to meet expected performance, lube-oil system performance, and the effects of "engine cleanliness" both internally and externally. This paper will discuss the tools developed for identification and assessment of LM2500 conditions and the in-place correction processes developed to ensure long-term reliability.

Contributed by the International Gas Turbine Institute (IGTI) of THE AMERICAN SOCIETY OF MECHANICAL ENGINEERS for publication in the ASME JOURNAL OF ENGINEERING FOR GAS TURBINES AND POWER. Paper presented at the International Gas Turbine and Aeroengine Congress and Exhibition, Munich, Germany, May 8–11, 2000; Paper 00-GT-667. Manuscript received by IGTI November 1999; final revision received by ASME Headquarters February 2000. Associate Editor: D. Wisler.

Marine Gas Turbine Inspectors

With the increased number of gas turbines used for propulsion and auxiliary systems in the U.S. Navy, it became apparent that the traditional method of engineering support, i.e., providing a technical representative to a ship to assess a problem and direct correction was ineffective in a maintenance scheme that dictated continuous maintenance. During this period, the U.S. Navy had a number of repair ships that would deploy to critical areas. Gas turbine repair shops were established and manned with personnel, tooling, and repair parts. The Marine Gas Turbine Inspector (MGTI) program was established that offered senior military personnel a qualification program where their skills gained from previous tours in maintenance facilities could be expanded and utilized. These personnel performed numerous inspections and repairs including changing out engines. As an outgrowth of this program and with the decommissioning of the repair ships, the talents of these personnel have been utilized as a vital link between the ship and traditional engineering support activities.

One of the key elements of the program is the predeployment inspection of both the propulsion and auxiliary gas turbine engines. The use of a predeployment inspection is to provide a uniformed inspector mainly looking at the mechanical condition and systems associated with the engines. These inspections are generally performed on a 24 month cycle focus on key items that help to ensure the Navy can meet both its short and long-term goals. On an as requested basis MGTI's will also perform inspections prior to an availability. Specifically these inspections lead to observations of the general engine condition, obvious signs of vibration, lube-oil system problems, variable stator vane (VSV) system problems, and assess input from the operators. Based on the severity of the items noted, these inspections will form the basis for more advanced systems testing

LM2500 Lube Oil System Performance

LM2500 lube-oil system performance can be characterized as lube-oil consumption rates and lube-oil scavenge temperature lev-

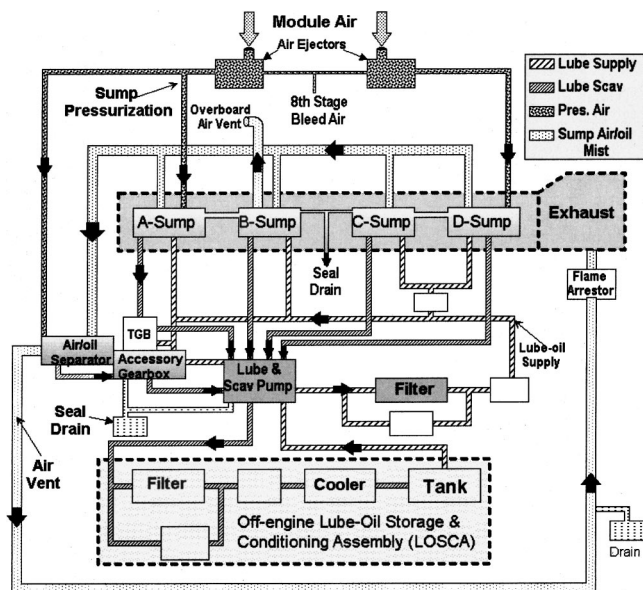


Fig. 1 LM2500 lube and scavenge system

els. There have been very few engine bearing failures on USN LM2500s. Therefore, lube-oil wear metal analysis has not yielded great benefits. The LM2500 lube-oil system is diagrammed in Fig. 1. Its basic feature is that compressor bleed air is used to provide a high-pressure blanket around each engine sump, thereby containing the lube oil. The difference in air pressure between the higher pressure air blanket and the pressure inside the sump is not great. The air from the blanket that does not enter the sump is usually exhausted in overboard seal vents. The air that enters the

oil sump gets separated from entrained lube-oil in the air-oil separator. The lube oil is scavenged from the sumps by a five or a six-element scavenge pump. The effective operation of the LM2500 lube system is determined by a balance of the pressure difference across the sump labyrinth seals, the rate at which the scavenge pump removes the oil from the sumps and the amount of lube oil extracted in the air-oil separator. When this system is operating normally (correctly) the engine does not leak oil externally, lube-oil scavenge temperatures are usually less than 250°F and total lube oil consumption should be less than 20 cc an hour.

Abnormal operation of the LM2500 lube-oil system is usually reported as "external lube-oil leakage," "high lube-oil consumption," or "high lube-oil scavenge temperatures." To help determine the cause of the abnormal condition, ship's force is requested to perform diagnostic tests. One test that is almost always run is a lube-oil survey, Fig. 2. In this test, the engine is started at idle and accelerated in increments to full power. How the individual parameters recorded behave as the engine goes to full power largely determines the direction of the troubleshooting. The parameters (such as compressor discharge pressure) taken in the lube-oil survey sheet can also be compared to engine performance model predictions to determine if an engine performance or a controls issue is the cause of the problem. In the example shown in Fig. 2, there is a rapid rise in "AGB" scavenge temperature as the engine nears full power. Previous investigative efforts have shown that the cause for this problem is a flooding accessory gearbox. It has been also determined that the real cause for the problem is the inability of the AGB scavenge element to keep up with the amount of oil entering the accessory gearbox. LM2500s entering Navy service prior to the early 1990s the oil discharge from the air-oil separator was piped to the accessory gearbox; this could potentially cause an oil flooding problem, particularly at high power. Another test that is typically performed is to connect specially configured bottles to the engines seal drains. The results

26.53 POWER BRIDGE 0730
27.31 GAS GENERATOR SERIAL NUMBER 330

GAS GENERATOR 1B SURVEY SHEET
SHIP GEORGE P
DATE 2 JUN
GAS GENERATOR TIME (TGA) POWER TURBINE TIME (TSA) ENGINE POSITION 1B AMBIENT TEMPERATURE G7

TIME AT POWER (DMP)	DESIRE O/GS RPM (2500)	ACTUAL LOG RPM (2500)	ACTUAL LPI RPM	COP	SCAV PRESS 2/9	MOD TEMP	LOSCA LEVEL	LUBE OIL		SCAVENGE TEMPERATURES						LEAKS	
								SUPPLY PRESS	COOLER DISCHARGE	GE	A SUMP	B SUMP	C SUMP	D SUMP	STOL STARTED	NO OIL DRAIN	
0907	15	5000	4970	700	14.6	16.6	151.6	27.31	24.85	129.4	134.3	150.7	163.2	151.5	146.1	0	0
0924	15	5000	5520	834	19.2	17.5	147.5	26.53	29.43	128.3	131.6	150.2	164.2	150.1	141.2	1 DEOP	
0941	15	5000	6000	993	25.9	18.2	149.2	26.53	33.59	130.7	135.6	154.2	168.1	153.9	143.0	0	
0957	15	5000	6510	1165	35.2	19.2	154.1	26.53	37.35	135.7	143.4	160.7	176.5	161.4	148.5	1 DEOP	
1013	5	7000	7000	1402	47.3	20.3	156.6	26.53	41.57	138.7	146.8	166.2	180.6	165.2	152.7	0	
1019	5	7250	7250	1667	61.5	20.9	161.8	26.53	43.48	141.7	151.4	170.1	176.9	172.1	158.6	0	
1025	5	7500	7500	1932	78.1	21.6	190.1	26.53	45.04	147.0	158.3	178.7	189.7	181.7	168.0	0	
1032	5	7750	7750	2282	98.3	21.8	192.1	26.53	45.70	153.5	164.0	182.4	202.5	191.3	174.9	1 DEOP	
1039	5	8000	8000	2657	122.3	22.5	195.7	27.31	47.38	159.3	171.1	188.6	210.3	203.1	188.9	3 DEOP	
1046	5	8250	8250	3041	150.0	23.1	202.9	26.53	49.70	165.0	178.7	197.4	215.3	215.3	205.7	0	
1052	15	8500	8500	3325	174.0	23.4	235.0	25.01	50.78	182.8	238.6	214.8	235.9	236.4	229.7	0	
1107	15	8750	8750	3510	196.5	23.7	245.1	25.07	51.34	194.3	276.4	274.9	254.6	249.7	247.1	0	
1129	15	8000	5060	1453	15.9	16.4	167.5	27.31	24.46	135.6	144.1	156.6	169.5	159.0	174.0	0	3cc's
DDTS																	

ByPASS PALMER DIS NOT OPEN - MANUALLY OPENED

* MARK LOSCA BULLS EYE
** DO NOT EXCEED TORQUE LIMITS
*** CHECK LOSCA BULLS EYE AND RECORD LEVEL (ABOVE OR BELOW)

Fig. 2 LM2500 lube-oil survey sheet (working document)

GAS GENERATOR SERIAL NR _____				POWER TURBINE SERIAL NR _____				SHIP USE VALVES FORGE 14-20 DATE 02 DEC 99						
GAS GENERATOR TIME (TSN) _____				POWER TURBINE TIME (TSN) _____				ENGINE POSITION _____		VIBRATION RUN NR _____				
TIME	GG RPM DESIRED	GG RPM ACTUAL	PT RPM ACTUAL	GG PICKUP PT GAS GENERATOR FREQUENCY		GG PICKUP PT POWER TURBINE FREQUENCY		LUBE OIL SUPPLY PRESSURE INLET TEMP		SCAVENGE TEMPERATURES GB A B C D				
	DDI	21	20	14	28	15	27	04	01	06	07	08	09	10
0130	5000	5000	850	.7	.6	.3	.6	21	136	151	163	151	138	125
0135	5500	5510	890	2	.6	1.2	.6	26	135	151	161	149	135	124
0140	6000	6010	960	2.2	.6	.8	.6	30	136	154	165	150	135	130
0145	6500	6500	1070	2.6	.5	1.3	.5	34	139	159	170	156	137	135
0150	7000	7000	1210	3.1	.5	2	.5	37	142	164	172	161	141	140
0155	7500	7500	1440	2.8	.5	2	.4	40	147	172	184	172	147	146
0200	8000	8000	1850	3.3	.5	2	.3	44	151	179	201	185	158	156
0205	8500	8490	2580	2.9	.7	1.6	.3	48	157	188	216	204	182	166
0210	8750	8490	2560	2.8	.6	1.6	.3	48	160	191	221	208	188	172
	9000**	8000												

DDI ADDRESSING: 1XX = 2A 2XX = 2B 3XX = 1A 4XX = 1B

NOTES: * = 5 MINUTES INTERVALS ** = DO NOT EXCEED TORQUE LIMIT

Fig. 3 Abbreviated LM2500 "self" vibration survey (working document)

of this effort can be seen in the far right-hand column of Fig. 2. This test is done to identify the location of either high lube-oil consumption or leakage.

To demonstrate the interdependencies of the LM2500 lube-oil system, consider a situation where on an older engine (20,000+ hour's time since installation) exhibit excessive seal drain leakage from one of the carbon seals in the accessory gearbox. The customary troubleshooting procedure is to install the above-mentioned bottles on all the engines seal drains and to instruct ships force to run the lube-oil survey, Fig. 2. The lube-oil survey reveals that high AGB scavenge temperatures that are just below the alarm level. The bottle test reveals that leakage is most prominent at higher engine powers. The conclusion of the investigation was that the accessory gearbox was flooding allowing liquid lube-oil to have direct contact with the carbon seals, thereby, causing them to leak. The solution to the leakage problem and to the scavenge temperature problem is to eliminate the accessory gearbox flooding. The real underlying problem was that more oil was being separated from air-oil mist going to the air-oil separator because of increased seal clearances around the engine main sumps (A, B, C, and D). This is probably due to engine age. But with the proper fix this engine can continue to operate satisfactorily for many thousands of hours.

LM2500 Vibration

The effects of LM2500 engine vibration can range from minor resulting in broken clamps and chaffed tubes, to major resulting in damage requiring engine change out. The installed vibration system allows monitoring of rotor-tracked vibration and alarm; it will trip (shutdown) the engine in a high vibration condition. It basically consists of installed vibration velocity pickups or accelerometers, signal processing, and analog (edge meters) or digital display (DDI) in mils peak to peak. Signal processing, which is part of the machinery control system, includes multiplex input, amplification, tracking filter with gas generator and power turbine speeds and integration from velocity to displacement.

Accelerometer based systems have an additional signal conditioner that pre-processes the vibration signal prior to uplink; it converts the signal from a charge signal (Pico-Coulombs) to voltage and has an additional stage of integration (acceleration to velocity).

The typical operating profile of a LM2500 on a USN ship tends to favor the 3000 to 10,000 BHP range. Although this is very good

for ultimate hot section life, it is unfortunately the speed range (both gas generator and power turbine) where several of the most structurally damaging vibration modes are, Thompson and Badgley [3]. Therefore the life of the engine is more likely to be based on damage or degradation that is the result of prolonged operation with high (3.5 to 5.0 mils peak to peak) or moderate (2 to 3.5 mils) vibration levels.

The gas generator with its long 16-stage high-pressure compressor rotor is susceptible to the effects of rotor unbalance and misalignment. Misalignment between the high pressure compressor and the high pressure turbine can be introduced during engine assembly. The unbalance can be a result of the engine assembly, or induced during in-place repairs such as when first stage compressor blades are changed for midspan damper wear, multiple blades are changed for foreign or domestic object damage, or multiple stages are changed for localized stall (as a result of VSV failure) or high speed compressor stall.

Typically, the ship expresses the concern for vibration when they see high vibration (or a large change in vibration level) on the installed system, or through Gas Turbine Bulletin engine inspection that reveal the results of high vibration. In the initial case of the ship seeing vibration, past maintenance is reviewed and the decision made as to whether the vibration is real or only an indication problem. Static testing of the monitoring system can be done by injecting a signal to observe the results. With the vibration monitoring system operating properly the second procedure is for the ship to perform a dynamic engine vibration survey during an underway period. This includes operation of the engine at various speed points, shown in Fig. 3. The results of the survey coupled with engine maintenance history will direct the maintenance approach. As discussed by Thompson [4], engine trim balancing may be required to reduce vibration level to enhance long-term reliability and arrest wear. This procedure requires special instrumentation, a minimum of one at sea vibration run, data analysis, and opening of the compressor case to install a trim weight.

LM2500 Performance Evaluation

In a typical scenario ships force will report that one engine "will not take the load" or one engine is "weak." Another situation is when the ships force knows they have an excessive torque split between two engines and they are concerned about making full power for an inspection. These types of requests will usually

GTM ENGINE PARAMETER SHEET - FFG			
SHIP: <u>USS George Philip</u>		DATE: <u>2-JUN</u>	
PRIOR TO STARTING GTE:			
DDI A/B	PARAMETER	1A	1B
130 / 131	T2	6.7	6.7
132 / 133	PT2	14.61	14.62
136 / 137	PT 5.4		
Torque Computer Test		VDC	
Main Fuel Control P#		P24	P25
Barometric Pressure & Outside Air Temp. (From Bridge)			
PLANT CONDITION: NGG > 8500			
DDI A/B	PARAMETER	1A	1B
130 / 131	T2	65.2	63.2
132 / 133	PT2	14.32	14.25
128 / 129	NGG	8760	8750
223 / 224	CDP	185.3	196.6
136 / 137	PT 5.4	42.7	49.7
145 / 146	TORQUE	20380	28070
143 / 144	HP	13820	19270
138 / 139	FMP	641	658
158 / 159	T5.4	1326	1385
134 / 135	NPT	3540	3510
TP 30 (see below)	NPT (T/C)		
047 / 048	PLA %	78.12	78.17
049 / 050	ENGINE BIAS		
053 / 054	GG PRESS. RATIO		
149 / 150	SHAFT RPM	174	
151/152 & Feet	PITCH	1	& 31.19 FT.
046	SHAFT TORQUE	971,000	
TP 9 / 10	TORQUE LIMIT VDC		
TP 21 / 22	PLA COM VDC		
	PLA FEEDBACK VDC		

TP 21 & 22 Voltage should match. If mis-matched, check TP 9 & 10
TP 9 7.5 - 11 VDC = Overtorque Control On. 0 - 2 VDC = Normal Ops.
TP 10 7.5 - 11 VDC = PT Speed Limiting On. 0 - 2 VDC = Normal Ops.

Fig. 4 Performance/torque split data sheet

result in an external inspection of the engine to insure that the variable stator vanes (VSVs) are rigged correctly, the compressor inlet temperature sensor inlet filter is not plugged, there no obvious leaks or damage to external engine control components. If these checks are passed satisfactorily, the ship is requested to operate the engine above a specific gas generator speed and provide the propulsion plant/engine performance parameters defined and shown in Fig. 4.

Performance deficiencies of the LM2500 propulsion engine in USN service can be separated into three categories: (1) a perceived problem that is caused by control system and/or sensor miscalibration, (2) a real performance issue that is the result of a control system malfunction, or (3) a real performance issue that is caused by the mechanical degradation of the engine. In practice the first two items are by far the most common occurrence.

In the past a variety of methods were used to resolve these issues. The most common was the comparison of performance data between two operating engines. This was accomplished by obtaining an "800" printout which contains all the machinery plants measured parameters. The appropriate data was then entered by hand in a data collection sheet and with the help of some approximate performance curves in the technical manual engine performance was analyzed. Needless to say this was trial and error and the success of which heavily depended on the experience of the trouble-shooter. Presently, at Fleet Technical Support Center Pacific, a computer program, described by Thompson and Raczkowski [5] is used to adjudicate discrepancies in the engine performance and sensor calibration. The assessment of the data provided in Fig. 4 by the Performance Diagnostic Program is shown in Figs. 5 and 6.

To perform this analysis a full engine performance model, adjusted for ships specific configuration, is used. Engine performance is computed three ways, using a different set of parameters for each method. If all the engine sensors had perfect calibration and accuracy the same level of performance should be computed

LM2500 Gas Turbine Performance Evaluation				
TIME		for		DATE
09:29:55 AM		USS George Philip FFG-12		GTM 1A
Ship Class - FFG-7		Gas Generator Type TST FFG-7		
Amb Pressure = 14.7		Amb Temperature = 67		
Parameter	Observed engine performance parameters Observed	Estimate of what engine performance "should be" Performance Map	Difference between observed and "what it should be" Delta	Status
T2 (degrees F)	65.2	65.2		OK
P2 (psia)	14.32	14.56	0.24	X
MFC type	P24	P24		
NGG (RPM)	8760	8760		OK
CDP (psig)	185.3	199	14	X
PI5.4 (psia)	42.7	49.7	7.0	X
FMP (psig)	641	667	26	in limits
NPT (RPM)	3540	3540		?
FSEE Torque	20,380	29,745	9,365	X
Torque (Formula)	22,067	29,586	7,519	X
FSEE BHP	13,820	20,029	6,209	X
BHP (Formula)	14,873	19,941	5,068	in limits
T5.4 (degs F)	1326	1323	3	in limits
CDP / PI5.4	4.34	4.00		
Pressure Ratio	2.98	3.41		
PLA (%)	78.1	78.2	0.1	in limits
Main Shaft Speed	174	177.0	3.0	X

Fig. 5 Diagnostics program output for GTM-1A

for each method. If the same level of performance is not computed for each method then control system correlation's are used to determine which sensor(s) need calibration, which controller needs adjustment or if engine performance has degraded. This provides the trouble-shooter with many tests of the data and provides him with the most likely problem area. In the past with the manual only method the interest was primarily on determining why an

LM2500 Gas Turbine Performance Evaluation				
TIME		for		DATE
09:45:33 AM		USS George Philip FFG-12		GTM 1B
Ship Class - FFG-7		Gas Generator Type TST FFG-7		
Amb Pressure = 14.7		Amb Temperature = 67		
Parameter	Observed engine performance parameters Observed	Estimate of what engine performance "should be" Performance Map	Difference between observed and "what it should be" Delta	Status
T2 (degrees F)	63.2	63.2		OK
P2 (psia)	14.25	14.56	0.31	X
MFC type	P24	P24		
NGG (RPM)	8750	8750		OK
CDP (psig)	196.6	199	3	in limits
PI5.4 (psia)	49.7	49.7	0.0	in limits
FMP (psig)	658	667	9	in limits
NPT (RPM)	3510	3510		?
FSEE Torque	28,070	30,037	1,967	X
Torque (Formula)	31,098	30,386	711	in limits
FSEE BHP	19,270	20,049	779	in limits
BHP (Formula)	20,783	20,307	475	in limits
T5.4 (degs F)	1385	1317	68	X
CDP / PI5.4	3.96	4.01		
Pressure Ratio	3.49	3.42		
PLA (%)	78.2	77.9	0.3	in limits
Main Shaft Speed	174	175.5	1.5	X

Fig. 6 Diagnostics program output for GTM-1B

engine was (or appeared to be) performing poorly. With the computer assisted approach an engine that may be performing “too well” for a given gas generator speed and can be more readily identified. This should reduce the number “high-speed” stalls (compressor surge) caused by misadjusted or worn-out fuel control components.

A too common problem with the performance of some LM2500s is its apparent inability to produce power. The symptom is characterized by low compressor discharge pressure (CDP), power turbine inlet pressure ($P_{5.4}$) and power turbine inlet temperature ($T_{5.4}$) indicating that the engine is actually not producing the power. But gas generator speed (N_2) is correct for the control setting. The result is a large torque split between engines and the inability of the ship to make rated speed. In the past, experience and a good knowledge of the relationship between N_2 , CIT, and CDP or $P_{5.4}$ has identified the cause for this problem as a “hot shifted” compressor inlet temperature sensor (CIT). The CIT sensor is reporting (hydraulically to the main fuel control) a higher compressor inlet temperature than is actually the case. This causes the main fuel control to schedule the variable stator vanes more closed reducing engine airflow and thereby power. The performance diagnostics program allows one to identify this problem quickly. In fact it can quite readily identify slight CIT sensor “hot shifts” or “cold shifts” that were very difficult to identify using experience. The case diagnosed in Figs. 5 and 6 is a “hot shifted” CIT sensor in GTM-1A on USS George Philip (FFG-12).

Using the LM2500 Diagnostic Performance Program, CIT sensor “cold shifts” or main fuel control “rich shifts” have been identified. This problem can be somewhat more difficult to diagnose because the engine produces plenty of power and ships force has no complaint with its performance. What will typically occur is the ship will complain about the “lack” of performance of its neighboring engine and the fact that power turbine inlet temperature on the “cold shifted” engine appears to be higher than normal. The risk with the “cold shifted” engine is that it will have a high-speed stall if it is not corrected. In most of these cases it has been found that the hydromechanical main fuel control (MFC) is the problem. Either its variable stator vane schedule is out of limits (on the open side) or its fuel schedule is “rich shifted.” The likely cause for both these problems is mechanical wear or degradation in a MFC that has been in service a long time.

Data Acquisition

Another aspect that affects the ability to trouble-shoot and diagnose engine and/or machinery plant control system problems is the availability of reliable machinery plant data. The diagnostic procedures discussed are performed under “real world” conditions. The control systems vary from the original DD-963 plant introduced 25 years ago to the latest DDG-51 plants, which include both Integrated Condition Assessment System (ICAS) and a machinery plant data archiving system (MCMAS). ICAS is described in Schreder et al. [6]. Therefore the trouble-shooter has to deal not only with sensor and signal conditioner calibration issues, but also the lack of data or data whose precision and reliability are in question, even on a perfectly “calibrated” system. In fact some important controlling parameters are not available at all through the ships propulsion control system. This is because the engine/propulsion control system is not integrated due to the different methods control. A classic example of this is the relationship between how engine fuel is scheduled and how engine power is controlled. Engine fuel is controlled by a hydromechanical main fuel control (MFC), whereas, engine power is set by a analog free-standing electronics enclosure (FSEE). One of the primary inputs into the fuel schedule is compressor inlet temperature (CIT) sensor; this sensor has no machinery control system display or readout. The torque computer in the FSEE calculates engine power; one of the primary inputs is gas turbine inlet temperature (T_2), which is not the same sensor as CIT. The link between the

FSEE and the MFC is what is known as the power lever actuator (PLA). A great deal of trouble isolation time is spent adjusting/calibrating this interface.

Obtaining repeatable, consistent data to perform the above mentioned analysis is essential. For some procedures hand-logged data from ships instrumentation is adequate, although not preferred. Hand-logged data can be susceptible to additional control calibration error as well as error introduced by the time lag effect in manually writing down the values of different parameters, that should be recorded simultaneously. For others, particularly performance analysis methods, it is not adequate at all. To obtain data from older control systems the “800 printout” is used. This provides an instantaneous readout of all the machinery plant parameters; this can be then manually entered into the analysis program. Some newer ships have MCMAS that was initially installed to provide consistent trial data, but has been retained because it is superior to the installed ship machinery control system for data trending. Some ships are equipped with ICAS, which can provide useful trend data if it specifically programmed to do so.

The ability to trend data, through the use of MCMAS, has become a valuable tool. It has been useful in diagnosing sensor and signal conditioner calibration drifts or failures. MCMAS acquires data at a once a second rate and is stored on large removable drives. It is portable (i.e., downloaded in a digital form), can be time or condition averaged, analyzed for any discontinuities (by an external program) and imported directly into the diagnostic procedures. Although, this greatly increases the validity and usefulness of the engine/plant performance data, it does complete the loop of providing automatically valid reliable data to a diagnostic analysis program.

The Future

The U.S. Navy is moving towards greatly increased automation at a rapid pace. A crew size of 100 men has been advertised for a ship the size of the DDG-51. It is clear that the present approach to trouble isolation and diagnostics will have to change to meet the new requirements. With greatly reduced machinery plant staff it is probable that the detailed trouble shooting and data acquisition that presently takes place will not occur manually. Therefore, the engine and propulsion plant controller must provide basic condition and fault diagnostics to the machinery plant manager (perhaps ICAS). It also must provide reliable engine data both at the time of the problem and historically. This is required, because when human intervention is required, as always, good data is essential. Investigative experience has shown that attempts to make exhaustive expert systems to automatically diagnose all plant problems is limited by the current state of knowledge (even at the OEM). The expert system can become quickly obsolete particularly on maturing systems. Therefore, an automated condition based maintenance system must not lead the crew astray and provide good data when engineering is called to resolve the problem.

Another aspect of automation is the tendency to add additional sensors to measure parameters that are considered critical from a maintenance and diagnostics point of view. These include sensors such as compressor discharge temperature (CDT), high-frequency accelerometers to measure gearbox vibration frequencies, fuel flow meters, individual thermocouple measurements and dynamic pressure sensors. One has to balance the additional maintenance load required to calibrate, maintain, and replace these devices (when they fail!) against the additional data provided and its usefulness in scheduling maintenance and diagnosing problems.

Kandl and Groghan [7] described efforts by the USN to develop condition based maintenance system for the LM2500. They found that the reliability of the electronics and data storage devices was poor, which essentially limited the usefulness of the system (i.e., the engine was much more reliable than the monitoring equipment). In addition, they found that the value of trending was of limited value because the engine was essentially very reliable during the time frame of the test. Practical experience with the

LM2500 has shown that this is relatively true. In the test described by Kandl and Groghan the computer hardware limited the capability of the system. Presently, the capability and reliability of computer hardware has increased 100 fold in the 20 years since this test. It is now incumbent on the software of a CBM system to sort through large amount of data that present systems (MCMAS) are capable of storing, to identify abnormalities and significant trends. This information should be provided to the operator along with recommendations on corrective action.

Conclusion

The present approach that has evolved to utilize the lowest level of inspections to feed the more sophisticated analysis has been extremely effective in ensuring both short and long-term reliability of the LM2500. However, this systematic method of inspections and evaluations essentially performs condition-based diagnostics that is heavily dependent on manual procedures (hand-logging data, etc.) and the idiosyncrasies of the installed propulsion control system (including add-ons such as MCMAS & ICAS). This makes a consistent diagnostic approach difficult because of the difficulty in acquiring data and historical information. Despite these shortcomings, significant trouble isolation procedures have been developed that are extremely successful. These include for the LM2500 lube-oil system trouble-shooting, perfor-

mance diagnostics, vibration diagnostics and trim balance, engine start trouble isolation, etc. The use of ICAS and MCMAS to automatically acquire data and to maintain historical data has begun. To obtain the desired automation for future ships will require selective integration of the trouble isolation procedures into future versions of ICAS that will alert the operators of changes, reflect the true picture of long-term degradation, direct maintenance and provide smart embedded technical manuals.

References

- [1] Hartranft, J., 1993, "Expansion of USN Gas Turbine Repair Into the Intermediate Level Repair Facility," ASME Paper 93-GT-152.
- [2] Thompson, B. D., Badgley, R., and Hartranft, J., 1989, "Experience From Expansion of On-Board Maintenance for Marine Gas Turbines," ASME Paper 89-GT-232.
- [3] Thompson, B. D., and Badgley, R., 1988, "Application of an Advanced Hybrid Rotordynamics Model to the Complete Structure of a Marine Gas Turbine Engine," ASME Paper 88-GT-123.
- [4] Thompson, B. D., 1991, "Optimization of Gas Generator and Power Turbine Trim Balance Techniques," ASME Paper 91-GT-240.
- [5] Thompson, B. D., and Raczowski, R., 1996, "Development of a Diagnostic Tool to Trouble Shoot LM2500 Performance and Controls Problems," ASME Paper 96-GT-213.
- [6] Schreder, D., Howell, I., Hardin, J., Mirilovich, R., and Hartranft, J., 1994, "A Gas Turbine Condition Monitoring System," *Proceedings of ASNE*, Sept. 7-9.
- [7] Kandl, M. G., and Groghan, D. A., 1980, "U.S. Navy, LM2500 Gas Turbine Condition Monitoring Development Experience," ASME Paper 80-GT-158.

E. P. Petrov
Imperial College of Science,
Technology and Medicine,
Center of Vibration Engineering,
Mechanical Engineering Department,
Exhibition Road,
London, SW7 2BX, UK

K. Y. Sanliturk
Faculty of Mechanical Engineering,
Istanbul Technical University,
80191 Gumussuyu,
Istanbul, Turkey

D. J. Ewins
Imperial College of Science,
Technology and Medicine,
Center of Vibration Engineering,
Mechanical Engineering Department,
Exhibition Road,
London, SW7 2BX, UK

A New Method for Dynamic Analysis of Mistuned Bladed Disks Based on the Exact Relationship Between Tuned and Mistuned Systems

A new method for the dynamic analysis of mistuned bladed disks is presented. The method is based on exact calculation of the response of a mistuned system using response levels for the tuned assembly together with a modification matrix constructed from the frequency response function (FRF) matrix of the tuned system and a matrix describing the mistuning. The main advantages of the method are its efficiency and accuracy, which allow the use of large finite element models of practical bladed disk assemblies in parametric studies of mistuning effects on vibration amplitudes. A new method of calculating the FRF matrix of the tuned system using a sector model is also developed so as to improve the efficiency of the method even further, making the proposed method a very attractive tool for mistuning studies. Various numerical aspects of the proposed method are addressed and its accuracy and efficiency are demonstrated using representative test cases.

[DOI: 10.1115/1.1451753]

1 Introduction

Small variations of individual blade characteristics in a bladed assembly inevitably arise during blade manufacture and assembly processes. It is well known that the dynamic response of a mistuned bladed disk can be altered significantly from that of its tuned counterpart so that the response of amplitudes of individual blades may vary widely within the same assembly ([1–3]). This situation has posed a very important practical problem for a long time and efforts of many investigators have been, and continue to be devoted to predicting and controlling these mistuning effects. Surveys of recent studies of mistuning are given in [4] and [5].

Most of the previous studies of mistuned bladed disks have been based on simple models, e.g., lumped parameter models, mainly in order to reduce the very high computational cost. In such models, each sector of a bladed disk is usually modeled using just one or a few lumped masses connected by springs. Qualitative results obtained using such models have been useful for gaining a general understanding of the influence of mistuning on the vibration of bladed disks, most notably the identification of critical blades and the increase in forced response levels which can be caused by mistuning ([6–10]). However, such simple models have limitations when quantitative predictions are of interest for specific practical applications, i.e., for a given bladed disk. Resorting to the lumped parameter model involves many approximations during the estimation of the model parameters, making the quantitative predictions based on such simple models quite unreliable. More representative bladed disk models incorporate beams and plates to simulate blades and disks, respectively ([6,11–13]). Such models can also be extended to include further practical features, e.g., pretwisted beams, shrouds and blade-disk joints in the analysis of bladed disk vibration ([14,15]). These models reflect vibration properties for a wider class of bladed disks although they still have a restricted range of applicability.

The current trend in the turbomachinery industry is to avoid the various simplifying assumptions during the modeling process and to seek quantitative answers to questions related to mistuning. Finite element based models are routinely used in industry for theoretical predictions. Using realistic finite element models for the complete bladed disk, including mistuning effects, is, however, still too expensive in spite of the advances in finite element modeling and computer hardware during recent years. The common practice in industry is to make use of the cyclic symmetry properties of the tuned system to obtain the natural frequencies and mode shapes of the whole tuned bladed disk assemblies. Although very desirable, there is no method readily available to extend the use of cyclic symmetry of a tuned bladed-disk assembly for mistuning studies.

Attempts at using detailed finite element models for mistuned bladed disks have been made recently. An original approach has been developed in [16] and [17] to reduce the size of the large-scale finite element models of mistuned bladed disks. The developed technique is similar to the Ritz procedure and is based on expansion of the mistuned bladed disk amplitudes into a series of mode shapes calculated for two specially chosen subsystems of the tuned bladed disk. An investigation of the validity of this technique can be found in references [18] and [19]. A different method is proposed in [20], where model reduction is carried out by representation of mode shapes as a limited sum of the system modes that are called “nominal” modes by the authors. These can be the modes of the tuned bladed disk or of the bladed disk with a specified mistuning pattern. Both of the above-mentioned approaches are dependent on the nominal mode shapes chosen for the expansions of the mistuned system response as well as on the number of these mode shapes, and incur approximation.

The present paper introduces a new method for the analysis of forced vibration of mistuned bladed disks. The method is based on an exact relationship between the response levels of the tuned and the mistuned bladed disks, the tuned system being described by a sector model using the cyclic symmetry properties of the assembly. An exact relationship between the tuned and the mistuned system is derived using Woodbury-Sherman-Morrison formula for the inverse of a perturbed matrix ([21,22]). This formula was ap-

Contributed by the Gas Turbine Division of THE AMERICAN SOCIETY OF MECHANICAL ENGINEERS for publication in the ASME JOURNAL OF ENGINEERING FOR GAS TURBINES AND POWER. Manuscript received by the GT Division, February 2000; final revision received by the ASME Headquarters September 2001. Associate Editor: M. Mignolet.

plied in reference [23] for response reanalysis of a simple linear system and was proposed and used successfully for calculations of modifications in the nonlinear analysis of systems with friction dampers in references [24,25]. The current paper proposes a further development of this approach for the analysis of mistuned systems. An important feature of the method proposed here is the reduction of the system model to a manageable size without introducing any loss of accuracy during the reduction process, such as is usually incurred when including only a subset of the model degrees-of-freedom reflecting the interest of the eventual application. Any subset of nodes of interest can be chosen from the whole set of assembly nodes for the mistuning analysis without any adverse effect. Accordingly, the method allows mistuning analysis of bladed disks using the large finite element models that are used at present only in the analysis of tuned bladed disks, based on a cyclic symmetry approach.

The first section of the paper describes an exact relationship between the response amplitudes of the mistuned and the tuned bladed disks as well as explaining how to perform the response calculations for the mistuned system at those coordinates where the system is mistuned. Also included is a recurrence procedure for the response calculation of a mistuned system which shows a better numerical performance when several patterns of mistuning are to be analyzed. The method presented allows the development of an expression for the response of a mistuned bladed disk using the response and the frequency response function (FRF) matrix of its tuned counterpart where the tuned system is modelled using finite elements based on its cyclic symmetry properties.

The second section explores how the tuned system properties can be used during the forced response analysis of a mistuned assembly. An original technique is presented for the calculation of both forced response levels and the frequency response function (FRF) matrix of tuned bladed disks using a sector model. This method allows one to obtain a tuned assembly's response properties under arbitrarily distributed harmonic loads over all bladed disk sectors, a feature essential for the analysis of mistuned bladed disks.

Various mistuning devices or "elements" are defined in the third section to facilitate simulation of the different mistuning conditions encountered in practice. An approach to establish a relationship between mistuning elements and blade-alone frequency mistuning is also described. The last section of the paper presents a comprehensive assessment of the numerical properties of the method proposed here, including several sample calculations of two practical bladed disks comprising a three-dimensional assembly model with solid elements and a pretwisted beam blade model. The results for the latter case are compared with an exact solution.

2 A New Method for Forced Response Analysis of Mistuned Bladed Disks

2.1 An Exact Relationship Between the Response of Tuned and Mistuned Bladed Disks. The equation of motion for forced vibration of a bladed disk such as that shown in Fig. 1 can be written in a customary form in the frequency domain as

$$(\mathbf{K} - \omega^2 \mathbf{M} + i\mathbf{D})\mathbf{q} = \mathbf{Z}(\omega)\mathbf{q} = \mathbf{f} \quad (1)$$

where \mathbf{q} is a vector of complex response amplitudes for nodal displacements; \mathbf{f} is a vector of complex amplitudes of harmonic nodal loads; \mathbf{K} , \mathbf{M} , and \mathbf{D} are stiffness, mass and structural damping matrices of the system, respectively; $\mathbf{Z}(\omega)$ is the dynamic stiffness matrix; ω is excitation frequency; and $i = \sqrt{-1}$. One can also include other terms representing gyroscopic and stiffening effects due to rotation in the dynamic stiffness matrix, if required.

It is proposed here to represent the dynamic stiffness matrix of a mistuned bladed disk as a sum of two matrices; a matrix corresponding to the tuned bladed disk, \mathbf{Z}_0 , and a mistuning matrix,

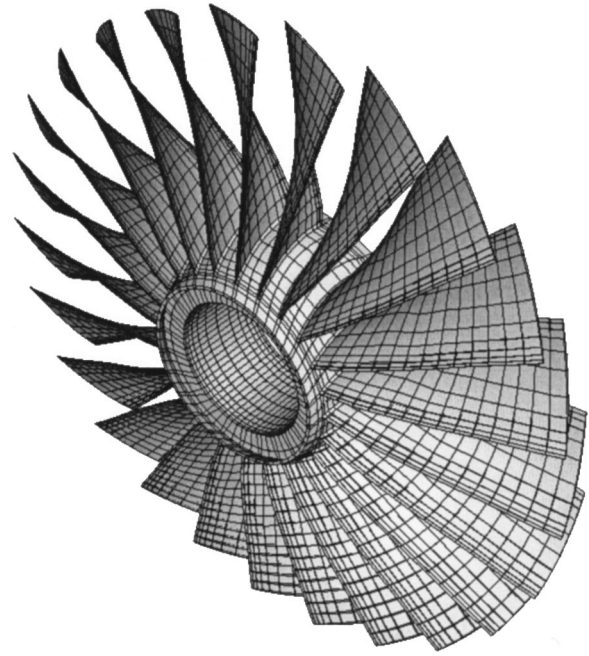


Fig. 1 Finite element model of a bladed disk

$\Delta\mathbf{Z}$, which reflects the deviation from the tuned system. As a result, the matrix equation for the forced response of a mistuned bladed disk (1) can be written as

$$[\mathbf{Z}_0(\omega) + \Delta\mathbf{Z}(\omega)]\mathbf{q} = \mathbf{f} \quad (2)$$

and so the response of the mistuned bladed disk is expressed as

$$\mathbf{q} = [\mathbf{Z}_0(\omega) + \Delta\mathbf{Z}(\omega)]^{-1}\mathbf{f} \quad (3)$$

However, calculation of the response levels by direct solution of Eq. (2), or using the inverse of a matrix as implied by the above equation, is extremely costly, especially for the analysis of a complete mistuned bladed disk assembly when a realistic finite element model is to be used. The major idea in this paper is to obtain the forced response levels for a mistuned bladed disk with high accuracy without the need for

- (i) a matrix inversion,
- (ii) a complete finite element model for the whole assembly, and
- (iii) inclusion of all the degrees-of-freedom in the response analysis.

It is shown in references [21] and [22] that the inverse of the sum of two matrices may be obtained using the so-called Sherman-Morrison-Woodbury identity which relates the inverse of the sum of two matrices to the inverse of one of the summands, transformed with the use of the second summand:

$$(\mathbf{Z}_0 + \mathbf{U}\mathbf{V}^T)^{-1} = \mathbf{Z}_0^{-1} - \mathbf{Z}_0^{-1}\mathbf{U}(\mathbf{I} + \mathbf{V}^T\mathbf{Z}_0^{-1}\mathbf{U})^{-1}\mathbf{V}^T\mathbf{Z}_0^{-1} \quad (4)$$

This identity is valid for any matrix \mathbf{Z}_0 ($N \times N$) and any matrix $\Delta\mathbf{Z} = \mathbf{U}\mathbf{V}^T$, expressed by multiplication of two rectangular matrices \mathbf{U} ($N \times n$) and \mathbf{V} ($n \times N$) if \mathbf{Z}_0 and $\mathbf{I} + \mathbf{V}^T\mathbf{Z}_0^{-1}\mathbf{U}$ are invertible. Here \mathbf{I} is an identity matrix, N is the total number of degrees-of-freedom for the system considered, and n is number of degrees-of-freedom where modifications are made.

For the mistuning problem addressed in this paper, the matrix \mathbf{Z}_0 is the dynamic stiffness matrix of the tuned bladed disk and the matrix $\Delta\mathbf{Z}$ represents the "mistuning matrix" which can itself be represented as a multiplication of two matrices. This representation can be done in various ways, one of which is to collect all nonzero rows into a matrix \mathbf{V}^T ($n \times N$) and to construct the matrix

$$\Delta \mathbf{Z} = \begin{matrix} (N \times N) \\ \begin{bmatrix} 0 & 0 & 0 & 0 & 0 & 0 & 0 \\ z_{21} & z_{22} & 0 & z_{24} & z_{25} & z_{26} & z_{27} \\ 0 & 0 & 0 & 0 & 0 & 0 & 0 \\ z_{41} & z_{42} & z_{43} & z_{44} & z_{45} & z_{46} & z_{47} \\ z_{51} & z_{52} & z_{53} & z_{54} & z_{55} & 0 & z_{57} \\ 0 & 0 & 0 & 0 & 0 & 0 & 0 \\ 0 & 0 & 0 & 0 & 0 & 0 & 0 \end{bmatrix} \end{matrix} = \begin{matrix} \mathbf{U} \\ (N \times n) \\ \begin{bmatrix} 0 & 0 & 0 \\ 1 & 0 & 0 \\ 0 & 0 & 0 \\ 0 & 1 & 0 \\ 0 & 0 & 1 \\ 0 & 0 & 0 \\ 0 & 0 & 0 \end{bmatrix} \end{matrix} \times \begin{matrix} \mathbf{V}^T \\ (n \times N) \\ \begin{bmatrix} z_{21} & z_{22} & 0 & z_{24} & z_{25} & z_{26} & z_{27} \\ z_{41} & z_{42} & z_{43} & z_{44} & z_{45} & z_{46} & z_{47} \\ z_{51} & z_{52} & z_{53} & z_{54} & z_{55} & 0 & z_{57} \end{bmatrix} \end{matrix}$$

Fig. 2 A scheme of decomposing the mistuning matrix into multiplication of two matrices

\mathbf{U} ($N \times n$) using unit vectors corresponding to nonzero rows of the matrix \mathbf{V} . This decomposition scheme is illustrated in Fig. 2.

Inserting Eq. (4) into Eq. (3), one can obtain an expression for the response of the mistuned bladed disk in terms of that of the tuned system and the modification matrices \mathbf{U} and \mathbf{V} as

$$\mathbf{q} = (\mathbf{Z}_0 + \mathbf{U}\mathbf{V}^T)^{-1}\mathbf{f} = [\mathbf{A}_0 - \mathbf{A}_0\mathbf{U}(\mathbf{I} + \mathbf{V}^T\mathbf{A}_0\mathbf{U})^{-1}\mathbf{V}^T\mathbf{A}_0]\mathbf{f} \\ = \mathbf{q}_0 - [\mathbf{A}_0\mathbf{U}(\mathbf{I} + \mathbf{V}^T\mathbf{A}_0\mathbf{U})^{-1}\mathbf{V}^T]\mathbf{q}_0 \quad (5)$$

where $\mathbf{A}_0(\omega) = [\mathbf{Z}_0(\omega)]^{-1}$ is the receptance (FRF) matrix for the tuned bladed disk, and \mathbf{q}_0 is a vector representing the amplitudes of the tuned assembly due to the external force vector, \mathbf{f} .

It should be noted that Eq. (5) is an exact expression and one of its very useful properties is the possibility it offers of obtaining the exact response of a mistuned system by considering only a small subset of the degrees-of-freedom. These degrees of freedom are: (i) those where the mistuning is applied and (ii) those where the forced response levels are of interest, and this combination is referred to below as the "active coordinates" all the other degrees-of-freedom constitute so-called "passive coordinates." Naming reflects here the fact that amplitudes of "active" coordinates are explicitly used in equations for forced response calculation of both the mistuned and tuned assemblies and "passive" coordinates are used only for calculation of response of a tuned bladed disk (when a sector model can be applied) and for the mistuned bladed disk analysis are not considered explicitly. The size of the matrices used in analysis of mistuned bladed disk can be reduced to any desired number of active coordinates without any loss of exactness of the description of the behavior. This significant feature can be achieved as follows. First, the vector of complex displacement amplitudes is partitioned into two: the part with the active coordinates (index a) and the part containing all the other, passive, degrees-of-freedom (index p), i.e., $\mathbf{q} = \{\mathbf{q}_a, \mathbf{q}_p\}^T$. The modification, or mistuning, matrix, $\Delta \mathbf{Z}$, is also partitioned accordingly, as illustrated below:

$$\Delta \mathbf{Z} = \begin{bmatrix} \Delta \mathbf{z}_{aa} & \Delta \mathbf{z}_{ap} \\ \Delta \mathbf{z}_{pa} & \Delta \mathbf{z}_{pp} \end{bmatrix} = \begin{bmatrix} \mathbf{U}_a \mathbf{V}_a^T & \mathbf{0} \\ \mathbf{0} & \mathbf{0} \end{bmatrix} = \begin{bmatrix} \mathbf{U}_a \\ \mathbf{0} \end{bmatrix} \begin{bmatrix} \mathbf{V}_a^T \\ \mathbf{0} \end{bmatrix} \quad (6)$$

Then, by partitioning the receptance matrix for the tuned system, \mathbf{A}_0 , the expression in Eq. (5) can be written in the following form:

$$\begin{bmatrix} \mathbf{q}_a \\ \mathbf{q}_p \end{bmatrix} = \begin{bmatrix} \mathbf{q}_a \\ \mathbf{q}_p \end{bmatrix}_0 - \begin{bmatrix} \mathbf{A}_{aa}^0 & \mathbf{A}_{ap}^0 \\ \mathbf{A}_{pa}^0 & \mathbf{A}_{pp}^0 \end{bmatrix} \begin{bmatrix} \mathbf{U}_a(\mathbf{I} + \mathbf{V}_a^T \mathbf{A}_{aa}^0 \mathbf{U}_a)^{-1} \mathbf{V}_a^T & \mathbf{0} \\ \mathbf{0} & \mathbf{0} \end{bmatrix} \begin{bmatrix} \mathbf{q}_a \\ \mathbf{q}_p \end{bmatrix}_0 \\ = \begin{bmatrix} \mathbf{q}_a \\ \mathbf{q}_p \end{bmatrix}_0 - \begin{bmatrix} \mathbf{A}_{aa}^0 \mathbf{U}_a (\mathbf{I} + \mathbf{V}_a^T \mathbf{A}_{aa}^0 \mathbf{U}_a)^{-1} \mathbf{V}_a^T \\ \mathbf{A}_{pa}^0 \mathbf{U}_a (\mathbf{I} + \mathbf{V}_a^T \mathbf{A}_{aa}^0 \mathbf{U}_a)^{-1} \mathbf{V}_a^T \end{bmatrix} \begin{bmatrix} \mathbf{q}_a \\ \mathbf{q}_p \end{bmatrix}_0 \quad (7)$$

where \mathbf{A}_{aa}^0 , \mathbf{A}_{ap}^0 , \mathbf{A}_{pa}^0 , \mathbf{A}_{pp}^0 are partitions of the matrix \mathbf{A}_0 according to the unmodified and modified coordinates. An important

feature of Eq. (7) is that it expresses the response of the mistuned system as that of the tuned system minus an expression which depends on (i) the FRF matrix of the tuned system, (ii) the mistuning matrix, and (iii) the response of the tuned system at the active coordinates. As a result, this feature allows calculation of the mistuned response levels at the active coordinates by considering only those rows in Eq. (7) which correspond to the active coordinates. The formulation in the next section deals with active coordinates only, hence the index a is dropped in subsequent development of the formulation.

2.2 Recurrence Update of the Forced Response. It is seen that Eq. (7) needs an inversion of a square matrix of order n which is the number of coordinates involved in modifications. In order to avoid the time-consuming matrix inversion, we have developed a recurrence technique for updating the forced response, which is reported below.

The modification matrix can be represented as a sum of individual modifications, $\Delta \mathbf{Z} = \sum_{j=1}^n \Delta \mathbf{z}_j$, such that each can be written as a multiplication of two vectors, i.e., $\Delta \mathbf{z}_j = \mathbf{u}_j \mathbf{v}_j^T$. For the scheme of matrix decomposition adopted here (as was illustrated in Fig. 2), \mathbf{u}_j is a unit vector with one nonzero component selected from j th column of matrix \mathbf{U} and \mathbf{v}_j is j th column of matrix \mathbf{V} . Then the influence of the considered part of the modification matrix, $\Delta \mathbf{z}_j$, on forced response can be calculated from the following expression, which is obtained from Eq. (5) with accounting for the structure of the vectors \mathbf{u}_j and \mathbf{v}_j :

$$\mathbf{q} = \mathbf{q}_0 - \frac{\mathbf{v}_j^T \mathbf{q}_0}{1 + \mathbf{v}_j^T \mathbf{a}_j^{(0)}} \mathbf{a}_j^{(0)} \quad (8)$$

where $\mathbf{a}_j^{(0)}$ is the j th column of matrix \mathbf{A}_0 , and the coefficient before $\mathbf{a}_j^{(0)}$ in Eq. (8) is a scalar value.

Successive accounting for the influence on forced response all the pairs of the vectors \mathbf{u}_j and \mathbf{v}_j (i.e., all individual rows of the mistuning matrix) yields an efficient formula for calculating the forced response levels of mistuned systems which does not need matrix inverse. The derived recurrence formula has the form

$$\mathbf{q}^{(j+1)} = \mathbf{q}^{(j)} - \frac{\mathbf{v}_j^T \mathbf{q}^{(j)}}{1 + \mathbf{v}_j^T \mathbf{a}_j^{(j)}} \mathbf{a}_j^{(j)}, \\ \mathbf{A}^{(j+1)} = \mathbf{A}^{(j)} - \frac{1}{1 + \mathbf{v}_j^T \mathbf{a}_j^{(j)}} [\mathbf{a}_j^{(j)} (\mathbf{v}_j^T \mathbf{A}^{(j)})], \quad j = 0 \dots n-1 \quad (9)$$

where the superscript indicates total number of the rows of the modification matrix which is being accounted for in the current recurrence update. As a result, $\mathbf{q}^{(n)}$ is a vector of responses when the whole mistuning matrix, $\Delta \mathbf{Z}$, is accounted for. As one can see

from Eq. (9), apart of the high computational efficiency following from avoiding the matrix inversion, there is another advantage of the recurrence update in the possibility it offers to calculate responses for the bladed assembly for many differently mistuned patterns introduced consequently during the recurrence update, i.e., the possibility to analyze the whole set, $\mathbf{q}^{(0)}, \mathbf{q}^{(1)}, \dots, \mathbf{q}^{(n)}$, of vectors of amplitudes of forced response, when appropriate (for example in statistical calculations or in search for the worst mistuning pattern). To start the recurrence update, the response amplitudes and the FRF matrix of the tuned bladed disk are used.

3 Response and Frequency Response Function Matrix for Tuned Bladed Disks

The method presented above allows us to express the response of a mistuned bladed disk using the response and the FRF matrix of a tuned assembly. As the calculations can be carried out at active coordinates only, and there are generally very small subset of the whole set of degrees-of-freedom, very detailed and realistic finite element models can be used to represent a bladed disk. Furthermore, a single-sector model can be used to describe the behavior of a complete tuned bladed disk and, hence, typical finite element models used in industry can be taken as a basis for the mistuning analysis method proposed in this paper. Accordingly, this section is devoted to the development of a technique for the calculation of forced response and the FRF matrix of a tuned bladed disk taking full advantage of the cyclic symmetry properties.

3.1 Response Calculations. Forced response levels of tuned bladed disks which are subjected to engine order (EO) type of excitation can be analyzed using a finite element model constructed from only one sector of the assembly. The equation of the motion for a single sector can be written as

$$(\mathbf{K}_S - \omega^2 \mathbf{M}_S + i \mathbf{D}_S) \mathbf{q}_S = \mathbf{f}_S + \mathbf{Q}_S \quad (10)$$

where \mathbf{K}_S , \mathbf{M}_S , and \mathbf{D}_S are the stiffness, mass, and damping matrices for one sector; \mathbf{q}_S and \mathbf{f}_S are the displacement and load vectors, respectively, for the considered, first sector; \mathbf{Q}_S is a vector of nodal forces for interaction of the considered sector with neighboring ones.

As a result of the cyclic symmetry properties of the tuned bladed disk, special boundary conditions can be applied to Eq. (10). In order to carry this out, the displacement vector in Eq. (10) is partitioned into the form $\mathbf{q}_S = \{\mathbf{q}_{\text{left}}, \mathbf{q}_{\text{internal}}, \mathbf{q}_{\text{right}}\}^T$, where \mathbf{q}_{left} and $\mathbf{q}_{\text{right}}$ are vectors of displacements at nodes lying on the left and the right boundaries separating the individual sector from the rest of the bladed disk; $\mathbf{q}_{\text{internal}}$ is a vector of displacements at internal nodes of the sector model. Correspondingly, the vector of interaction nodal forces takes the form $\mathbf{Q}_S = \{\mathbf{Q}_{\text{left}}, \mathbf{0}, \mathbf{Q}_{\text{right}}\}^T$. The symmetry properties and special excitation type result in the following relationships:

$$\mathbf{q}_{\text{right}} = e^{i\alpha k} \mathbf{q}_{\text{left}}; \quad \mathbf{Q}_{\text{right}} = -e^{i\alpha k} \mathbf{Q}_{\text{left}} \quad (11)$$

where k is the engine order; $\alpha = 2\pi/N_B$ is the sector angle, and N_B is the number of sectors in the bladed disk assembly. These relationships result in a reduced number of independent unknowns:

$$\begin{Bmatrix} \mathbf{q}_{\text{left}} \\ \mathbf{q}_{\text{internal}} \\ \mathbf{q}_{\text{right}} \end{Bmatrix} = \begin{bmatrix} \mathbf{I} & \mathbf{0} \\ \mathbf{0} & \mathbf{I} \\ e^{i\alpha k} \mathbf{I} & \mathbf{0} \end{bmatrix} \begin{Bmatrix} \mathbf{q}_{\text{left}} \\ \mathbf{q}_{\text{internal}} \end{Bmatrix} = \mathbf{T} \tilde{\mathbf{q}}_S \quad (12)$$

and, taking into account the relationship for the forces of interaction of the considered sector with the neighboring ones in Eq. (11), one can write the sector equation in the terms of nodal amplitudes of this sector only, i.e.,

$$\tilde{\mathbf{q}}_S = [\tilde{\mathbf{K}}_S^{(k)} - \omega^2 \tilde{\mathbf{M}}_S^{(k)} + i \tilde{\mathbf{D}}_S^{(k)}]^{-1} \tilde{\mathbf{f}}_S = \mathbf{A}_k(\omega) \tilde{\mathbf{f}}_S \quad (13)$$

where $\tilde{\mathbf{K}}_S^{(k)} = \mathbf{T}_k^* \mathbf{K} \mathbf{T}_k$; $\tilde{\mathbf{M}}_S^{(k)} = \mathbf{T}_k^* \mathbf{M} \mathbf{T}_k$; $\tilde{\mathbf{D}}_S^{(k)} = \mathbf{T}_k^* \mathbf{D} \mathbf{T}_k$; and $\tilde{\mathbf{f}}_S^{(k)} = \mathbf{T}_k^* \mathbf{f}_S$. $\mathbf{A}_k(\omega)$ is introduced here and is called the “wave FRF matrix” of the bladed disk, which corresponds to the k th engine order of excitation. The symbol \sim indicates that the relevant matrices are obtained after imposing the boundary conditions, and the symbol $*$ denotes Hermitian conjugate.

The condition that the excitation must be of the engine order type is important, meaning that the loads must be applied to different sectors with equal amplitudes and a specific monophasic shift between adjacent sectors, i.e.,

$$\mathbf{f}_j = \mathbf{f}_S e^{i\alpha k(j-1)} \quad (14)$$

where \mathbf{f}_j is the loading vector applied to j th sector.

Once the response levels of the reference first sector have been calculated, the response levels for any other sector, say the j th sector, can then be expressed in terms of the amplitudes of the first sector, using a rather simple relationship:

$$\mathbf{q}_j = e^{i\alpha k(j-1)} \mathbf{q}_S. \quad (15)$$

Equation (15) indicates that the circumferential distribution of amplitudes of the assembly is a discrete harmonic, k being the order of this harmonic, i.e., the number of displacement waves in the circumferential direction. The response levels of the whole tuned bladed disk are obtained by collecting the response levels of individual sectors as follows:

$$\mathbf{q} = \{\mathbf{q}_S, e^{i\alpha k} \mathbf{q}_S, e^{i2\alpha k} \mathbf{q}_S, \dots, e^{i(N_B-1)\alpha k} \mathbf{q}_S\}^T. \quad (16)$$

It is evident that the efficient calculation of the FRF matrix for a tuned bladed disk is quite important for the response calculation of a mistuned system. This efficiency is achieved by utilizing the wave FRF matrices introduced above, and as described in the next two sections.

3.2 Wave Frequency Response Function Matrix Calculation. The method proposed here for the efficient calculation of the wave FRF matrix is based on using the natural frequencies and mode shapes of the assembly obtained from a sector model. The attractive feature of this approach is that the wave FRF matrix can be calculated efficiently at the desired co-ordinates without any loss of accuracy due to coordinate reduction.

Natural frequencies and mode shapes of the complete bladed disk assembly can be determined by solving the eigenvalue problem for one sector:

$$\tilde{\mathbf{K}}_S^{(k)} \phi^{(k)} = \omega^2 \tilde{\mathbf{M}}_S^{(k)} \phi^{(k)}. \quad (17)$$

Matrices $\tilde{\mathbf{K}}_S^{(k)}$ and $\tilde{\mathbf{M}}_S^{(k)}$, obtained from Eq. (10) using cyclic symmetry boundary conditions Eq. (11) for a given number of the displacement waves along bladed disk circumference, k , are Hermitian for $k \neq 0$ and $N_B/2$. Hence the solution of the eigenvalue problem yields real natural frequencies but complex mode shapes, i.e.,

$$\phi_r^{(k)} = \phi_r^{(k)\text{Re}} + i \phi_r^{(k)\text{Im}} \quad (18)$$

where r is the mode shape number. The full set of natural frequencies and mode shapes for a tuned bladed disk can be obtained by considering all integer values for k ranging from 0 to $N_B/2$. The natural frequencies for $k \neq 0$ and $N_B/2$ are double (two modes with identical eigenvalues) and the two mode shapes corresponding to the same frequency are complex conjugates of each other.

Wave FRF matrices corresponding to forward traveling (wave number $+k$) and backward traveling (wave number $-k$) waves of engine order excitation can be expressed through the complex natural modes of one sector as

forward traveling wave

$$\mathbf{A}_k(\omega) = \sum_{r=1}^m \frac{\phi_r^{(k)} (\bar{\phi}_r^{(k)})^T}{(1 + i\eta_r)(\omega_r^{(k)})^2 - \omega^2};$$

back traveling wave

$$\mathbf{A}_{-k}(\omega) = \sum_{r=1}^m \frac{\bar{\phi}_r^{(k)} (\phi_r^{(k)})^T}{(1 + i\eta_r)(\omega_r^{(k)})^2 - \omega^2} \quad (19)$$

where η_r is the damping loss factor for the r th mode and a line over a symbol denotes complex conjugation. It should be noted that the matrices \mathbf{A}_k and \mathbf{A}_{-k} are not Hermitian conjugates due to the presence of damping in the considered system. Moreover, the following mode normalization for the mode shapes is assumed to be satisfied:

$$(\bar{\phi}_r^{(k)})^T \tilde{\mathbf{M}}_s^{(k)} \phi_r^{(k)} = 1. \quad (20)$$

As mentioned, the wave FRF matrices in Eq. (19) need to be calculated at the desired active coordinates only. The next section presents a technique for calculating the FRF matrix for tuned bladed disk using the wave FRF matrices described above.

3.3 Frequency Response Function Matrix for a Whole Bladed Disk From Wave Frequency Response Function Matrices. It is necessary to develop the FRF matrix for all sectors of the tuned bladed disk, without any assumptions imposed on load distribution, in order to analyze mistuned bladed disk using the approach developed in Section 2.

For this case we consider vibration under a set of arbitrarily distributed forces $\mathbf{f} = \{\mathbf{f}_1, \mathbf{f}_2, \dots, \mathbf{f}_{N_B}\}^T$ applied to all sectors. Forces can be different for individual sectors and they are not limited to the engine order type of excitation as previously assumed. We introduce a function $\mathbf{F}(\varphi)$ that allows us to represent loads in the following form:

$$\mathbf{f} = \begin{Bmatrix} \mathbf{f}_1 \\ \mathbf{f}_2 \\ \dots \\ \mathbf{f}_{N_B} \end{Bmatrix} = \begin{Bmatrix} \mathbf{F}(0 \leq \varphi < \alpha) \\ \mathbf{F}(\alpha \leq \varphi < 2\alpha) \\ \dots \\ \mathbf{F}(\alpha(N_B - 1) \leq \varphi < \alpha N_B) \end{Bmatrix} \quad (21)$$

where φ is an angle describing a sector position in the cylindrical coordinate system and this function has the form

$$\mathbf{F}(\varphi) = \sum_{j=1}^{N_B} [\chi(\varphi - \alpha(j-1)) - \chi(\varphi - \alpha j)] \mathbf{f}_j \quad (22)$$

where $\chi(\varphi)$ is an asymmetric step function, i.e., $\chi(\varphi) = \begin{cases} 1 & \text{for } \varphi \geq 0 \\ 0 & \text{for } \varphi < 0 \end{cases}$.

As derived in reference [26], and shown in detail in Appendix A, the function in Eq. (22) can be expressed exactly in terms of a finite series as

$$\mathbf{F}(\varphi) = \frac{1}{N_B} \sum_{j=1}^{N_B} \left(\sum_{k=-N_B/2}^{N_B/2} c_k e^{-iak(j-1)} \text{dexp}_{N_B}^{(k)}(\varphi) \right) \mathbf{f}_j \quad (23)$$

where $c_k = 1$ for all k , except $c_k = 0.5$ for $k = N_B/2$ when N_B is even. Here the following definitions for the introduced functions of discrete complex exponential functions, $\text{dexp}_{N_B}^{(k)}(\varphi)$, are used:

$$\text{dexp}_{N_B}^{(k)}(\varphi) = \sum_{j=1}^{N_B} [\chi(\varphi - \alpha(j-1)) - \chi(\varphi - \alpha j)] e^{iak(j-1)}. \quad (24)$$

For each vector of sector loads, \mathbf{f}_j , every term in the series over k in Eq. (23) satisfies relationship (14). As a result, the complex amplitudes for all bladed disk sectors caused by the k th term of the expansion for loads applied to the j th sector, $\mathbf{F}_k(\alpha(j-1))$, can be expressed (via Eqs. (13) and (15)) as

$$\begin{aligned} \begin{Bmatrix} \mathbf{q}_1^{kj} \\ \mathbf{q}_2^{kj} \\ \dots \\ \mathbf{q}_{N_B}^{kj} \end{Bmatrix} &= \begin{bmatrix} \mathbf{A}_k \\ e^{iak} \mathbf{A}_k \\ \dots \\ e^{iak(N_B-1)} \mathbf{A}_k \end{bmatrix} \mathbf{F}_k(\alpha(j-1)) \\ &= \frac{c_k}{N_B} \begin{bmatrix} \mathbf{A}_k \\ e^{iak} \mathbf{A}_k \\ \dots \\ e^{iak(N_B-1)} \mathbf{A}_k \end{bmatrix} e^{-iak(j-1)} \mathbf{f}_j. \end{aligned} \quad (25)$$

The expression for the FRF matrix of the tuned bladed disk is obtained by summing all the terms of the expansion for the loads applied to the j th sector, and then summing the responses caused by loads applied to all other sectors. The resulting coefficient matrix is the FRF matrix of the tuned bladed disk, i.e.,

$$\mathbf{A}_0 = \frac{1}{N_B} \begin{bmatrix} \sum_{k=-N_B/2}^{N_B/2} c_k \mathbf{A}_k & \sum_{k=-N_B/2}^{N_B/2} c_k e^{-iak} \mathbf{A}_k & \dots & \sum_{k=-N_B/2}^{N_B/2} c_k e^{-iak(N_B-1)} \mathbf{A}_k \\ \sum_{k=-N_B/2}^{N_B/2} c_k e^{iak} \mathbf{A}_k & \sum_{k=-N_B/2}^{N_B/2} c_k \mathbf{A}_k & \dots & \sum_{k=-N_B/2}^{N_B/2} c_k e^{-iak(N_B-2)} \mathbf{A}_k \\ \dots & \dots & \dots & \dots \\ \sum_{k=-N_B/2}^{N_B/2} c_k e^{iak(N_B-1)} \mathbf{A}_k & \sum_{k=-N_B/2}^{N_B/2} c_k e^{iak(N_B-2)} \mathbf{A}_k & \dots & \sum_{k=-N_B/2}^{N_B/2} c_k \mathbf{A}_k \end{bmatrix}. \quad (26)$$

It is important to note that the relationship given in Eq. (26) is exact since the series involved in its derivation are finite.

It is evident that rows of the FRF matrix for the whole tuned bladed disk can be formed by cyclic permutations of a vector combining the last and the first rows of the matrix \mathbf{A}_0 .

Moreover, this matrix is symmetric since its blocks disposed symmetrically in respect to the matrix main diagonal are the transpose of each other:

$$\begin{aligned} \left(\sum_{k=-N_B/2}^{N_B/2} c_k e^{-iak} \mathbf{A}_k \right)^T &= \sum_{k=-N_B/2}^{N_B/2} c_k e^{-iak} \mathbf{A}_k^T \\ &= \sum_{k=-N_B/2}^{N_B/2} c_k e^{-iak} \mathbf{A}_{-k} = \sum_{k=-N_B/2}^{N_B/2} c_k e^{iak} \mathbf{A}_k \end{aligned}$$

which is based on the relation between wave FRF matrices corre-

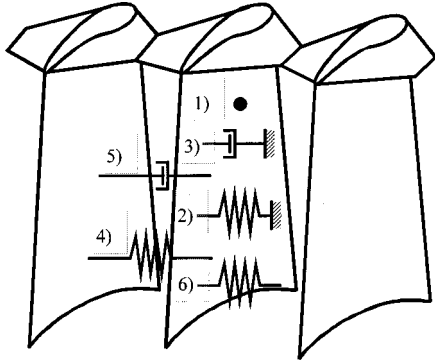


Fig. 3 Various mistuning elements: 1) lumped mass; 2) stiffness between a node and ground; 3) damping between a node and ground; 4) stiffness between nodes of different blades; 5) damping between nodes of different blades; 6) stiffness between nodes of the same blade

sponding to forward and back traveling waves, $\mathbf{A}_k = \mathbf{A}_{-k}^T$, following from Eq. (19).

These features of the matrix \mathbf{A}_0 avoid the need for computing $N_B \times N_B$ blocks of matrices. Instead, N_B blocks are sufficient to describe the FRF matrix fully.

The developed technique has advantages over other possible and more traditional approaches when the FRF matrix for the whole bladed disk is calculated from its mode shapes recovered from sector mode shapes. The main advantages of the proposed method are

- (a) the deduced expression (26) shows the structure of the matrix, and allows a drastic reduction in computation expense by calculating only one row of blocks in the matrix of Eq. (26); and
- (b) the expression (26) is much more general since it allows the use of wave FRF matrices obtained not only from mode shape generation but also by any another way, such as by direct calculation of Eq. (13).

4 Mistuning Modeling

4.1 Mistuning Elements. The method of analysis for mistuned systems proposed so far does not require any assumptions regarding the distribution or the magnitude of the mistuning matrix, $\Delta \mathbf{Z}$. However, it is useful to define, without any loss of generality, some simple mistuning elements that can be applied at desired locations in the bladed disk model. Various mistuning elements defined here have physical interpretation and their combination allows us to describe a wide range of mistuning patterns that might be encountered in practice. Some examples of such mistuning elements are illustrated schematically in Fig. 3, and include: lumped mass, stiffness, and damping mistuning applied between a node and ground or between two nodes. Each mistuning element is described by its matrix $\Delta \mathbf{z}^e$ and can be applied to any location desired.

The mistuning element matrix, $\Delta \mathbf{z}^e$, applied between a node and ground for the case of three degrees-of-freedom at a node can be expressed as

$$\Delta \mathbf{z}^e = \begin{bmatrix} \text{mass mistuning} & & \\ -\omega^2 m_x & 0 & 0 \\ 0 & -\omega^2 m_y & 0 \\ 0 & 0 & -\omega^2 m_z \\ \text{stiffness mistuning} & & \end{bmatrix};$$

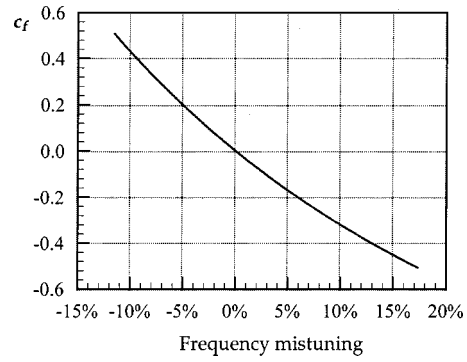


Fig. 4 A relationship between the mistuning coefficient and frequency mistuning

$$\Delta \mathbf{z}^e = \begin{bmatrix} k_x & 0 & 0 \\ 0 & k_y & 0 \\ 0 & 0 & k_z \end{bmatrix};$$

damping mistuning

$$\Delta \mathbf{z}^e = \begin{bmatrix} id_x & 0 & 0 \\ 0 & id_y & 0 \\ 0 & 0 & id_z \end{bmatrix} \quad (27)$$

where m_j , k_j ; d_j are mass, stiffness, and damping coefficients of the element in three orthogonal directions. These matrices may have all nonzero components for some other kinds of mistuning. For the specific types of mistuning elements expressed in Eq. (27), but applied between two nodes, j and k , the element matrix takes the form

$$\Delta \mathbf{z}_{jk}^e = \begin{bmatrix} \Delta \mathbf{z}^e & -\Delta \mathbf{z}^e \\ -\Delta \mathbf{z}^e & \Delta \mathbf{z}^e \end{bmatrix}. \quad (28)$$

4.2 Blade Frequency Mistuning. It is possible to describe quite a wide class of possible mistuning arrangements using the simple mistuning elements introduced in the previous section. One of the widely used measures of mistuning in practice is to refer to the “blade-alone” natural frequency scatter. This type of mistuning can easily be represented by establishing a relationship between individual blade frequencies and the properties of a set of mistuning elements applied to the blades. This can be achieved by conducting a preliminary analysis to determine a one-to-one relationship between the blade alone frequency scatter and the amount of mistuning introduced at specific locations. A possible approach is to express the mistuning matrix for a blade, $\Delta \mathbf{Z}$, as

$$\Delta \mathbf{Z} = c_f \Delta \mathbf{Z}_0 \quad (29)$$

where $\Delta \mathbf{Z}_0$ is a predefined mistuning matrix for a given set of mistuning element characteristics and c_f is a variable representing mistuning coefficient. Calculations are made for a sufficient number of values of c_f so as to establish a relationship with an acceptable accuracy between the mistuning coefficient, c_f , and the scatter in blade-alone frequency. This relationship is usually nonlinear but a very good description can be made using a spline approximation. A typical example demonstrating such a relationship is shown in Fig. 4 for a practical turbofan blade when lumped mass mistuning element was applied.

It should be stated that some preliminary blade-alone analysis may be necessary to determine the datum mistuning matrix ($\Delta \mathbf{Z}_0$), especially if the blade-alone frequency mistuning for more than one mode of vibration is of interest.

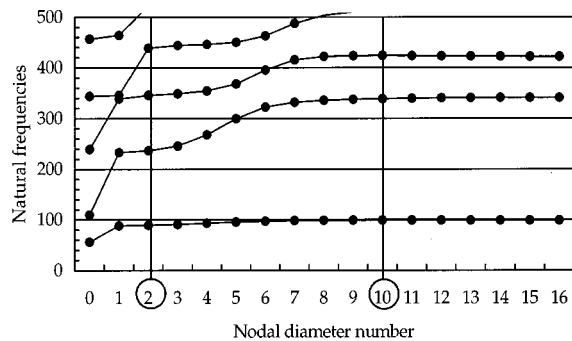


Fig. 5 Engine order harmonics and natural frequencies in the frequency range analyzed

5 Numerical Results

Two different bladed disk assemblies have been considered in a series of case studies to demonstrate the accuracy and the efficiency of the new mistuning analysis method proposed in this paper.

5.1 Bladed Disk With Midspan Shroud (Pretwisted Beam Blade Model). The natural frequencies and mode shapes obtained from any finite element package can be used to describe a tuned assembly and its sector finite element model may contain any types of finite elements. As the main purpose in this section is to illustrate the accuracy of the proposed method, results of the new method are compared with solutions obtained for a full finite element model of a mistuned bladed disk, in a case where the model size allows direct solution, i.e., without any reduction of degrees-of-freedom. The mistuned bladed disk model for a turbofan stage is considered, which comprises 33 pretwisted blades of variable cross section connected by a midspan shroud. The approach of reference [15] where pretwisted beam models are used for blades, has been used to obtain a direct solution of the finite element equations. Each blade consists of eight pretwisted beam elements and each shroud sector between adjacent blades consists of two curvilinear beam elements. Both types of the beam elements have six degrees-of-freedom per node and a total number of degrees-of-freedom in the considered system is 1980. The blade length is 78.5 cm, and the shroud is positioned at 47.5 cm from blade root.

The frequency spectrum for this tuned bladed disk is plotted in Fig. 5 for the frequency range of interest. Random mistuning was introduced into the bladed disk by applying mass mistuning ele-

ments to the blades. The level of mistuning was assumed to lie in the range of ± 5 percent of a first blade-alone frequency and a proportional structural damping level of 0.3 percent was used in the calculations.

As described in earlier sections of the paper, the proposed method is based on an exact relationship between the responses of the tuned and the mistuned bladed disks, the only sources of error being due to (i) the floating point arithmetic and (ii) residual effects in regenerating the FRF matrix for the tuned assembly as a result of the use of a limited number of natural modes for the sector model. The main attention in this section is therefore devoted to establishing the accuracy of the predicted results when different numbers of modes are included during the FRF matrix calculation for the tuned bladed disk. Forced response levels are calculated under second and tenth engine-order (2EO and 10EO) excitations using homogeneous distribution of loads along the blade and the results corresponding to the blade tip and shroud locations are presented below. The significance of these specific response locations was that the response levels were maximum at the blade tips and the worst accuracy in amplitude calculations was usually obtained at the shroud locations. The latter was caused by the fact that blade amplitudes at the blade-shroud joint were determined for the considered excitation mainly by the shroud elasticity. Natural modes of the bladed disk which are stipulated by shroud vibration had much higher natural frequencies than the modes stipulated by blade vibration. Because of that, calculation of the FRF coefficients at blade-shroud joints required a larger number of natural modes than for other points of the assembly.

Two examples are presented in Figs. 6 and 7 where the normalized forced response levels are plotted for individual blades of the mistuned assembly when excited by 2EO and 10EO, respectively, response normalization being made with respect to the maximum tuned response levels in the frequency range of interest. In contrast to the tuned system, it is immediately seen that there is a large scatter in blade response levels for the mistuned system, especially around the resonance frequencies. It is interesting to note the presence of two resonance frequencies where the distribution of individual blade response levels exhibits regular characteristics. For the 2EO case this is the resonance which is close to the tuned system natural frequency of the mode with two nodal diameters and the corresponding amplitude distribution has four waves. Such doubling of the number of waves comes from excitation of a mode shape with two dominant cycles when only positive amplitudes are shown. For the 10EO case, at the resonance

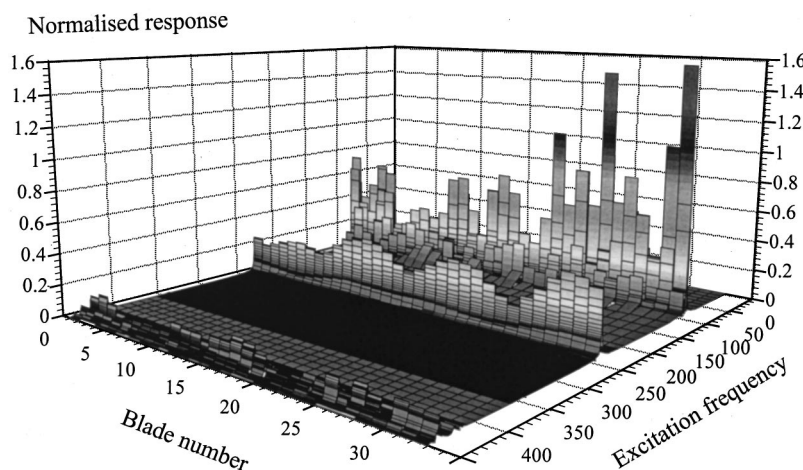


Fig. 6 Forced response for each blade of the bladed disk. Excitation by 2EO, amplitudes at blade tip.

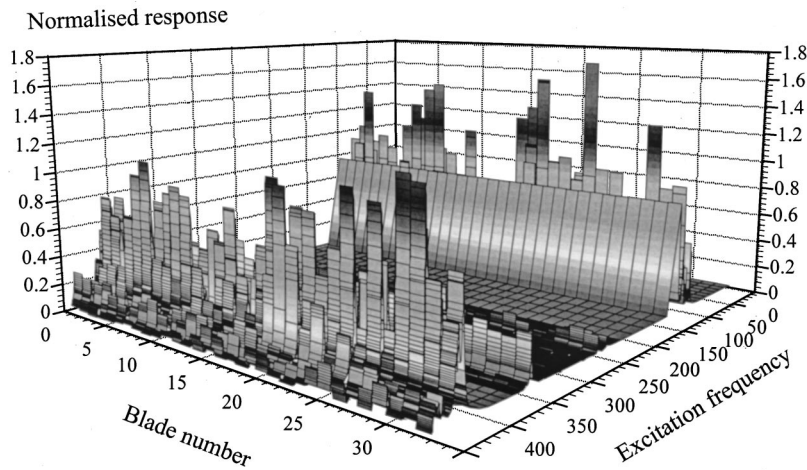


Fig. 7 Forced response for each blade of the bladed disk. Excitation by 10EO, amplitudes at blade-shroud joint.

corresponding to the mode shape with zero nodal diameters, the amplitudes are almost identical, as would be exactly the case for a tuned system.

In Figs. 8(a) and 9(a), the maximum response amplitudes found among all the blades of the mistuned bladed disk are compared with those of the corresponding tuned bladed disk. It can be seen that while the tuned system has a small number of resonances (four resonance regions for 2EO and three resonance regions for 10EO), the mistuned bladed disk has a large number of resonance peaks, as expected. The results obtained using the method of analysis proposed in this paper were compared with the exact solutions and the relative errors are presented in Figs. 8(b) and 9(b). It is seen that use of 16 mode shapes for each number of

nodal diameters results in less than two percent errors for all excitation frequencies in the range 0 . . . 450 Hz. Errors are minimum at resonance peaks and usually much less than the quoted value away from resonances.

In Fig. 10, maximum normalized response against resonance peaks and the associated errors are given. It is interesting to note that maximum error is about 0.65 percent when 16 modes are included and this maximum error belongs to the peak with the lowest amplitude. The maximum errors found among all identified resonance peaks are presented in Fig. 11 with respect to the number of modes included in the analysis. As expected, the error levels in the mistuned analysis decrease as more and more modes are included to describe the tuned assembly. It should be noted that

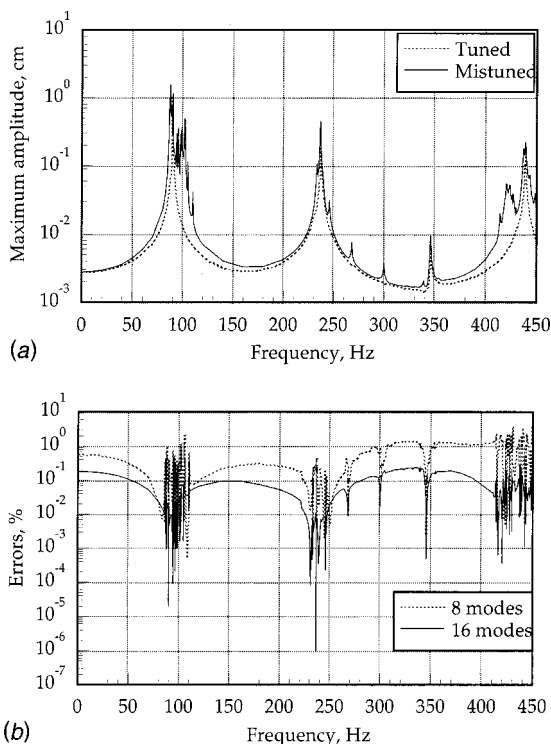


Fig. 8 The case of excitation of 2EO: (a) maximum amplitudes at blade tip searched among all blades for mistuned and tuned bladed disks; (b) errors in their determination

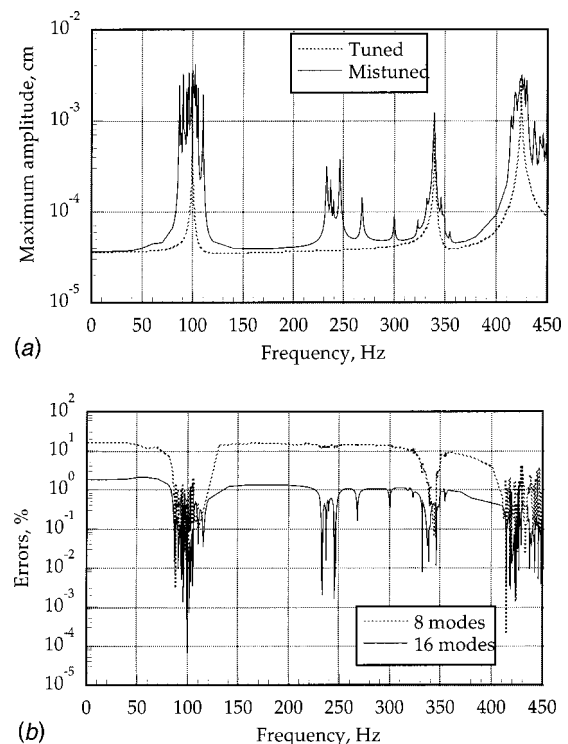


Fig. 9 The case of excitation by 10EO: (a) maximum amplitudes at blade-shroud joint searched among all blades for mistuned and tuned bladed disks; (b) errors in their determination

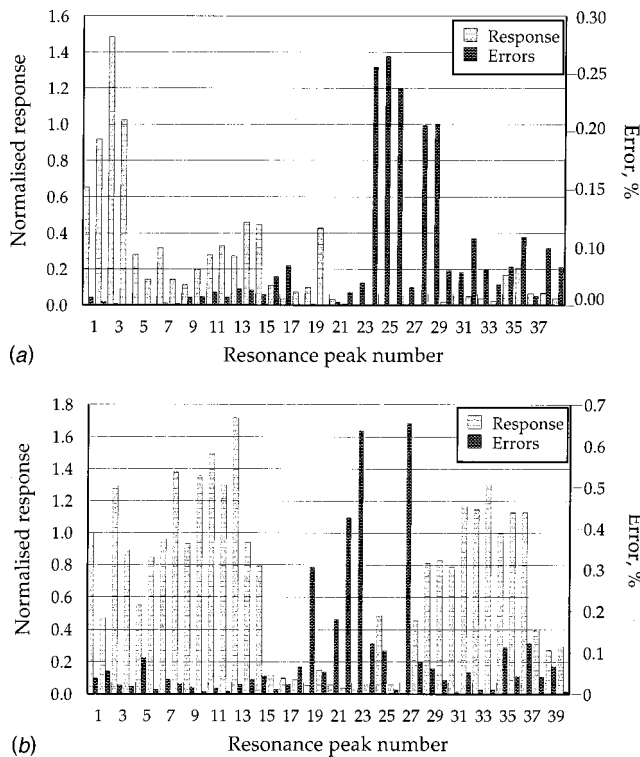


Fig. 10 Normalized response at found resonance peaks and errors in their calculations for the case when 16 modes are included: (a) the case of excitation by 2EO; (b) the case of excitation by 10EO

the relatively high error levels observed in Fig. 11 for the cases when only four modes for every nodal diameter number are included, refer to errors at resonance peaks with the lowest amplitude levels. Because of the existence of a very dense spectrum of resonance frequencies for the mistuned bladed disk, practically important resonances are those with higher amplitude levels, and they can be calculated with acceptable accuracy even with a small number of modes included (as demonstrated by the results below). It is quite important to be able to predict the distribution of maximum response levels for individual blades. Figure 12 shows a comparison of such results obtained using a direct (exact) solution and using the new method proposed here. It is seen that results are almost identical in spite of the fact that only four modes per nodal diameter were included to describe the FRF matrix for the tuned assembly. Another set of results, the maximum response ampli-

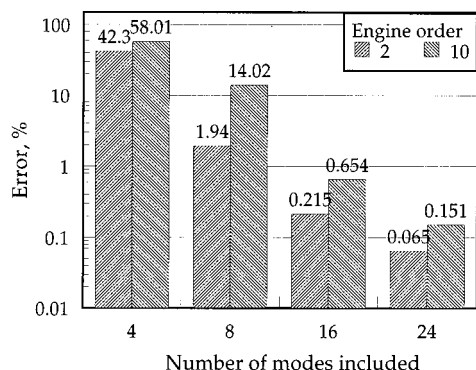


Fig. 11 Maximum error searched among all resonance peaks in the considered range in respect to number of modes included

tude of individual blades within the frequency range of interest, are presented in Fig. 13. It is evident that very high level of accuracy can be obtained even when a small number of tuned assembly modes are included to describe the tuned system.

5.2 Three-Dimensional Finite Element Model of a Bladed Disk Without Shroud. The second bladed disk studied here is a fan assembly (shown in Fig. 1) comprising 24 unshrouded blades. The complete three-dimensional finite element model shown in Fig. 1 had 47,808 nodes with three degrees-of-freedom per a node. A sector model was used in the predictions and 8 modes for each of 13 different nodal diameter numbers were used for calculating the FRF matrix of the whole tuned assembly.

Vibration amplitudes at nine nodes for each blade were included in the analysis, their locations being close to the blade tips. Excitation forces were uniformly distributed across 53 nodes on the lateral surfaces of individual blades and excitation by 1EO was considered.

In Fig. 14, the maximum response levels searched among all blades and all nodes included in the analysis are plotted against the excitation frequency and the results are compared with the response level of the corresponding tuned bladed disk. Also included in this figure are the modes included to describe the tuned assembly. It can be noted that the coupling between blades for this assembly is quite small due to high disk stiffness, hence the worsening effect due to mistuning is comparable to the blade frequency mistuning, i.e., ± 5 percent. In Fig. 15 the normalized forced response levels are shown for individual blades of the mistuned assembly in the vicinity of the first family resonance peaks. It is evident that each of the blades of the considered assembly has its own resonance peaks. At such resonances other blades have relatively very small amplitudes. The effect of damping level on resonance amplitudes of such a bladed disk is illustrated in Fig. 16. Two damping loss factors were considered here, namely: 0.3 percent and 3 percent. For the assembly with higher damping, resonance peaks are not as sharp as for the system with the lower damping loss factor and some weak resonance peaks disappeared although the damping did not affect the worsening effect due to the introduced mistuning.

6 Conclusions

An efficient method for the response analysis of mistuned bladed disks using detailed finite element models has been presented. The method proposed here allows exact calculation of the response of mistuned bladed disks using FRF matrices of the corresponding tuned system and a mistuning matrix. The distinct features of the proposed method are: (i) only a single-sector model is needed to represent the tuned and mistuned bladed disk, (ii) mistuning is treated as a structural modification problem, (iii) the computational cost for mistuning calculations does not depend on the size of the original sector model as the solution is obtained at active coordinates, and (iv) the reduced model corresponding to the active co-ordinates is as accurate as the initial sector model represented by its natural frequencies and mode shapes.

The effective method has been developed for calculation forced response of a tuned bladed disk under loads arbitrarily distributed along circumference (i.e., not necessarily engine-order type of excitation) and for calculation of the FRF matrix for a whole bladed disk assembly. The possibility of representation of the FRF matrix for the whole tuned assembly by a small subset of its components is proved. The method is based on a use of a sector finite model only and uses cyclic symmetry properties of the system.

A computer program for forced response analysis of mistuned bladed disks has been developed and various numerical aspects of the method have been studied. The accuracy and the computational efficiency of the new method have been demonstrated by performing forced response analyses of two practical mistuned bladed disks using large-scale finite element models.

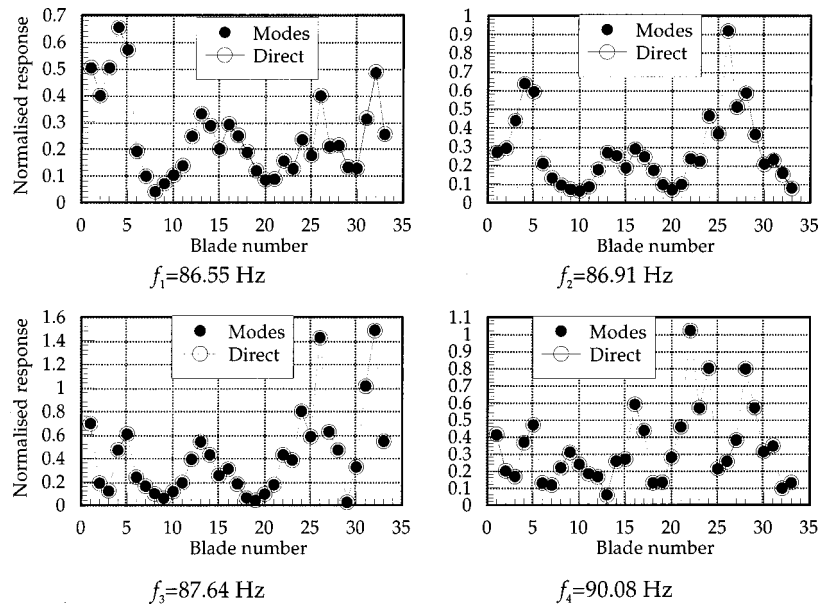


Fig. 12 Distribution of amplitudes at resonance peaks excited by 2EO for the case when four nodes are included

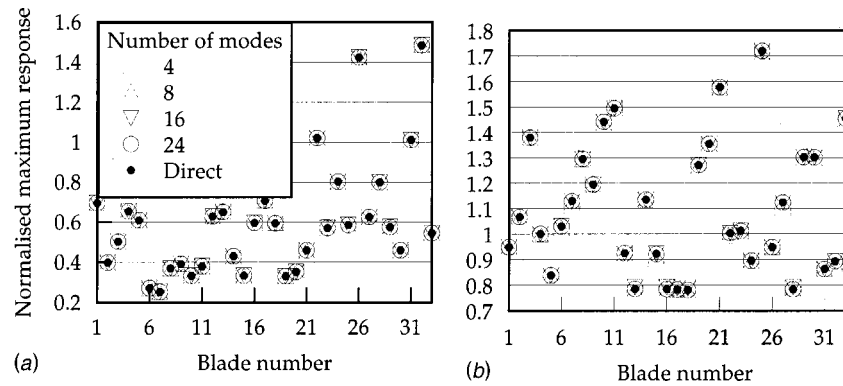


Fig. 13 Maximum amplitudes for each of the blade assembly for different numbers of modes included: (a) excitation by 2EO, (b) excitation by 10EO

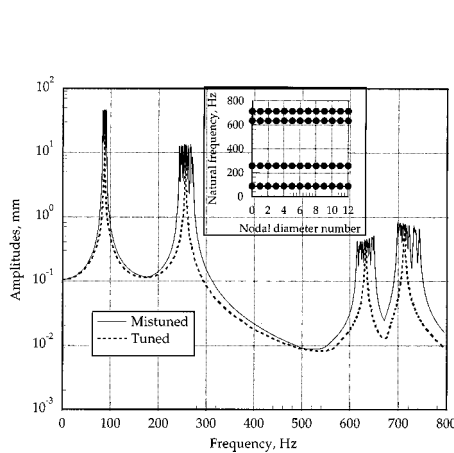


Fig. 14 Maximum amplitudes searched among analyzed nodes of all blades for the bladed disk shown in Fig. 1. Inset—all natural frequencies of the bladed disk.

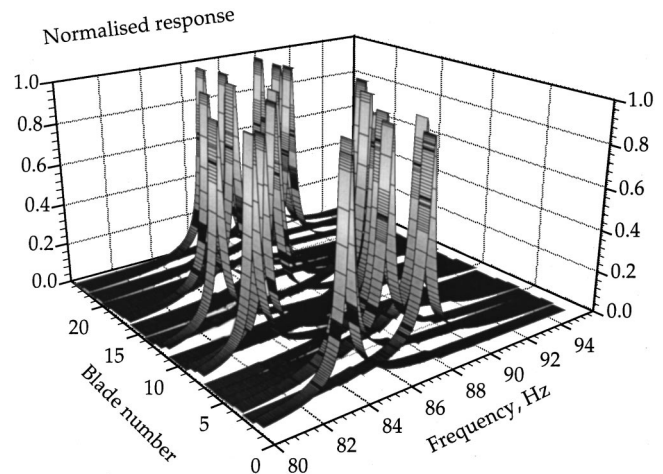


Fig. 15 Forced response for each blade of the bladed disk shown in Fig. 1

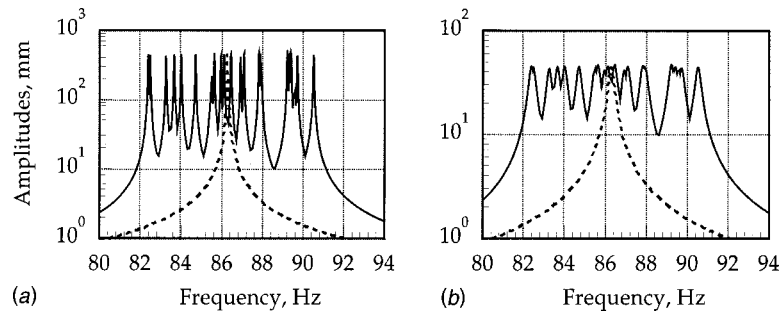


Fig. 16 Maximum amplitudes searched among analyzed nodes of all blades: (a) damping factor 0.003; (b) damping factor 0.03

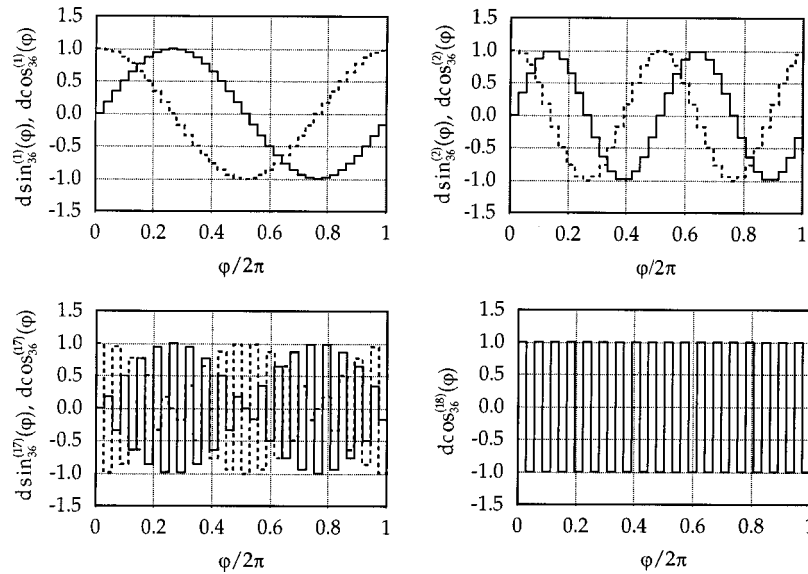


Fig. 17 Examples of the discrete harmonic function introduced

Acknowledgments

The authors are very grateful to Rolls-Royce plc. for providing the financial and technical support for this project and for giving us permission to publish this work. The authors thank Mr. M. Kim of UTC, Imperial College for providing the mesh for three-dimensional solid finite element model of one of the bladed disks analyzed in this paper.

Appendix

Expansion of an Arbitrary Load Distribution Into A Finite Discrete Series. This kind of expansion was specially developed in ([26]) for analysis of cyclically symmetric structures under loads arbitrary distributed over all sectors of the symmetric structure. The major idea here is representing the loads as finite series so that each term satisfies to condition (14) which allows calculation cyclically symmetric structures using only one sector model.

To make such expansion the function of discrete sine and cosine are introduced:

$$\text{dsin}_{N_B}^{(k)}(\varphi) = \sum_{j=1}^{N_B} [\chi(\varphi - \alpha(j-1)) - \chi(\varphi - \alpha j)] \sin \alpha k(j-1)$$

$$\text{dcos}_{N_B}^{(k)}(\varphi) = \sum_{j=1}^{N_B} [\chi(\varphi - \alpha(j-1)) - \chi(\varphi - \alpha j)] \cos \alpha k(j-1).$$

(30)

The total number of sectors in the structure, N_B , and wave number, k , are parameters of the discrete functions. Some examples of such functions are shown in Fig. 17.

From these functions discrete complex exponential functions are constructed:

$$\text{dexp}_{N_B}^{(\pm k)}(\varphi) = \text{dsin}_{N_B}^{(k)}(\varphi) \pm i \text{dcos}_{N_B}^{(k)}(\varphi)$$

$$= \sum_{j=1}^{N_B} [\chi(\varphi - \alpha(j-1)) - \chi(\varphi - \alpha j)] e^{\pm i \alpha k(j-1)}. \quad (31)$$

The function which is equal to unit for angle φ values corresponding to the j th sector and which is equal to zero for the others can be expressed as

$$\chi(\varphi - \alpha(j-1)) - \chi(\varphi - \alpha j) = \sum_{k=-N_B/2}^{N_B/2} c_k e^{-i \alpha k(j-1)} \text{dexp}_{N_B}^{(k)}(\varphi) \quad (32)$$

where $c_k = 1$ for all k , except $c_k = 0.5$ for $k = N_B/2$ when N_B is even.

Using Eq. (32) the arbitrary load distribution over all the structure sectors are expanded:

$$\mathbf{F}(\varphi) = \sum_{j=1}^{N_B} [\chi(\varphi - \alpha(j-1)) - \chi(\varphi - \alpha j)] \mathbf{f}_j$$

$$= \frac{1}{N_B} \sum_{j=1}^{N_B} \left(\sum_{k=-N_B/2}^{N_B/2} c_k e^{-i\alpha k(j-1)} \text{dexp}_{N_B}^{(k)}(\varphi) \right) \mathbf{f}_j. \quad (33)$$

References

- [1] Dye, R. C. F., and Henry, T. A., 1969, "Vibration Amplitudes of Compressor Blades Resulting From Scatter in Blade Natural Frequencies," *ASME J. Eng. Gas Turbines Power*, **91**, pp. 182–188.
- [2] Ewins, D. J., 1969, "Effect of Detuning Upon the Forced Vibration of Bladed Disks," *J. Sound Vib.*, **9**, No. 1, pp. 65–79.
- [3] Whitehead, D. S., 1966, "Effect of Mistuning on the Vibration of Turbomachines Induced by Wakes," *J. Mech. Eng. Sci.*, **8**, No. 1, pp. 15–21.
- [4] Ewins, D. J., 1991, "The Effects of Blade Mistuning on Vibration Response—A Survey," *IFTOMM 4th International Conference on Rotordynamics*, Prague, Czechoslovakia.
- [5] Slater, J. C., Minkiewicz, G. R., and Blair, A. J., 1999, "Forced Response of Bladed Disk Assemblies—A Survey," *Shock Vib. Dig.*, **31**, No. 1.
- [6] Ewins, D. J., 1973, "Vibration Characteristics of Bladed Disk Assemblies," *J. Mech. Eng. Sci.*, **15**, No. 3, pp. 165–186.
- [7] Ewins, D. J., and Han, Z. C., 1984, "Resonant Vibration Levels of a Mistuned Bladed Disk," *ASME J. Vib. Acoust., Stress, Reliab. Des.*, **106**, pp. 211–217.
- [8] Muszynska, A., and Jones, D. I. G., 1983, "A Parametric Study of Dynamic Response of Discrete Model of Turbomachinery Bladed Disk," *ASME J. Vib. Acoust., Stress, Reliab. Des.*, **105**, pp. 434–443.
- [9] Sanliturk, K. Y., and Imregun, M., 1992, "Statistical Analysis of Random Mistuning of Bladed Assemblies," *IMEchE Proceedings of the International Conference on Vibrations in Rotating Machinery*, University of Bath, UK, IMechE, London, C432/110, pp. 51–58.
- [10] Sanliturk, K. Y., and Imregun, M., 1994, "Vibration Analysis of Mistuned Bladed-Disk Assemblies-Inverse Approach," *AIAA J.*, **32**, No. 4, pp. 865–875.
- [11] Gu, J., and Gao, H., 1987, "Vibration Characteristics of Well-Modelled Mistuned Bladed Disk," *Vibrations of Bladed Disk Assemblies*, ASME, New York, pp. 55–59.
- [12] Irretier, H., 1983, "Spectral Analysis of Mistuned Bladed Disks by Component Mode Synthesis," *Vibrations of Bladed Disk Assemblies*, ASME, New York, pp. 115–125.
- [13] Rzadkowski, R., 1994, "The General Model of Free Vibration of Mistuned Bladed Disks. Part I: Theory, Part II: Numerical Results," *J. Sound Vib.*, **173**, No. 3, pp. 377–393, 395–413.
- [14] Petrov, E. P., 1993, "Large-Scale Finite Element Models of Blade-Shroud and Blade-Disk Joints and Condensation Technique for Vibration Analysis of Turbomachine Impellers," *Proc. of the 7th World Congress on Finite Element Methods: "FEM-Today and the Future"*, Monte Carlo, Monaco, pp. 507–513.
- [15] Petrov, E. P., 1994, "Analysis and Optimal Control of Stress Amplitudes Upon Forced Vibration of Turbomachine Impellers With Mistuning," *Proc. of the IUTAM Symposium: "The Active Control of Vibration"*, Bath, UK, pp. 189–196.
- [16] Bladh, R., Castanier, M. P., and Pierre, C., 1998, "Reduced Order Modelling and Vibration Analysis of Mistuned Bladed Disk Assemblies With Shrouds," *ASME Paper 98-GT-484*.
- [17] Castanier, M. P., Ottarsson, G., and Pierre, C., 1997, "Reduced Order Modeling Technique for Mistuned Bladed Disks," *ASME J. Vib. Acoust.*, **119**, pp. 439–447.
- [18] Kruse, M. J., Pierre, C., 1997, "An Experimental Investigation of Vibration Localization in Bladed Disks, Part 1: Free Response," *ASME Paper 97-GT-501*.
- [19] Frey, K. K., 1998, "Correlation of Reduced Order Model for the Prediction of a Mistuned Bladed Disk Response," *3rd National Turbine Engine High Cycle Fatigue Conference*, San Antonio, USA.
- [20] Yang, M.-T., and Griffin, J. H., 1999, "A Reduced Order Model of Mistuning Using a Subset of Nominal System Modes," *ASME Paper 99-GT-288*.
- [21] Sherman, J., and Morrison, W. J., 1949, "Adjustment of an Inverse Matrix Corresponding to Changes in the Elements of a Given Column or a Given Row of the Original Matrix," *Ann. Math. Stat.*, **20**, p. 621.
- [22] Woodbury, M., 1950, "Inverting Modified Matrices," *Memorandum Report 42, Statistical Research Group*, Princeton University, Princeton, NJ.
- [23] Level, P., Moraux, D., Drazetic, P., and Tison, T., 1996, "On a Direct Inversion of the Impedance Matrix in Response Reanalysis," *Commun. Numer. Meth. Eng.*, **12**, pp. 151–159.
- [24] Sanliturk, K. Y., Ewins D. J., and Stanbridge A. B., 1999, "Underplatform Dampers for Turbine Blades: Theoretical Modelling, Analysis and Comparison With Experimental Data," *ASME Paper 99-GT-335*.
- [25] Sanliturk, K. Y., Ewins D. J., Elliott, R., and Green, J. S., 1999, "Friction Damper Optimization: Simulation of Rainbow Tests" *ASME Paper 99-GT-336*.
- [26] Juravleva, A. M., and Petrov, E. P., 1981, "The Method for Forced Vibration Calculation of Cyclically Symmetric Structures," *Dynamics and Strength of Machines*, Kharkov, No. 33, pp. 66–74 (in Russian).
- [27] Griffin, J. H., and Hoosac, T. M., 1984, "Model Development and Statistical Investigation of Turbine Blade Mistuning," *ASME J. Vib. Acoust., Stress, Reliab. Des.*, **106**, pp. 204–210.
- [28] Hager, W. W., 1989, "Updating the Inverse of a Matrix," *SIAM Rev.*, **31**, No. 2, pp. 221–239.

Active Control Algorithms for the Control of Rotor Vibrations Using Hybrid Squeeze Film Dampers

A. El-Shafei

Department of Mechanical Design and
Production,
Faculty of Engineering,
Cairo University,
Giza 12316, Egypt

The hybrid squeeze film damper (HSFD) has proven itself to be an effective controlling device of vibration in rotating machinery. The critical stage in the development of the HSFD as an active vibration suppressant, is the development of the control algorithms for active control of rotor vibrations. This paper summarizes, evaluates, and compares the control algorithms for HSFD-supported rotors. Quantitative as well as qualitative measures of the effectiveness of the control algorithms are presented. The study includes the PID-type controllers, LQR, gain scheduling, adaptive and bang-bang controllers. The adaptive, gain scheduling, and nonlinear proportional controllers have proved to be quite effective in the active control of HSFD supported rotors, with impressive results. [DOI: 10.1115/1.1421058]

Introduction

A recent paper ([1]) presented a study on actively controlled bearing dampers for aircraft engine applications. They evaluated nearly seven nonmagnetic bearing devices that would be possible for aircraft engine applications. It was concluded that "weight, size, and cost penalties for all of the damper design candidates considered are probably unacceptable when compared to the passive squeeze film damper" ([1]).

In addition, it is now generally accepted that magnetic bearings will not find their way into aircraft engines for a few decades, for reasons of reliability, weight, size, and temperature considerations. Our group at Cairo University has been working with an active control device, the "hybrid squeeze film damper" (HSFD), which utilizes the inherent reliability of the squeeze film damper with the added capability of actively changing between various damping levels. The development of the HSFD was supported by the U.S. Air Force and several investigations, both theoretical and experimental ([2–4]), have confirmed the effectiveness and reliability of the HSFD as an active control device for rotor vibrations.

El-Shafei [5] introduced the HSFD and demonstrated its concepts both theoretically and experimentally. Later, El-Shafei and Hathout [6] presented a complete model of the HSFD, as well as the bang-bang controller. This nonlinear model was used to simulate the behavior of the open-loop, and to determine the damper parameters required for our test rig ([6]). Moreover, this mathematical model was later used by several of the cited papers in designing the closed-loop controllers.

Also, El-Shafei and El-Hakim [7] presented the first experimental results for the on-off controller. The theoretical development of the adaptive control was presented by Hathout and El-Shafei [8], while the PI control development was presented by the same authors the following year ([9]). Hathout et al. [10] presented the application of the on-off control to multimode rotors, while El-Shafei and El-Hakim [11] presented the experimental results of the adaptive controller. They also presented the experimental results for the PI control ([12]) and on-off control ([13]).

Since the introduction of the HSFD, it was clear that the control algorithms are critical to the successful implementation of HSFDs

to rotor systems ([14]). A major effort has been expended, with the support of the U.S. Air Force, to study the control algorithms for HSFD-rotor systems. This paper reports on the control algorithms used for the active control of rotors using HSFDs. It summarizes, evaluates, and compares the control algorithms for HSFD supported rotors. Quantitative as well as qualitative measures of the effectiveness of the control algorithms are presented. Both theoretical as well as experimental results are presented.

Basic Theory of the Hybrid Squeeze Film Damper (HSFD)

Most of the analyses of SFDs consider the short bearing approximation to Reynolds equation, which is justified if the damper is short in the axial direction such that the flow in the damper is axial rather than circumferential. On the other hand, the long bearing approximation to Reynolds equation, which is justified if the damper is long in the axial direction such that the flow in the damper is circumferential, has attracted comparatively very little attention (e.g. [15–17]). Usually open-ended dampers are considered short dampers and tightly sealed dampers are considered long dampers regardless of the actual physical length of the damper (which is usually short with respect to the diameter of the damper).

Short dampers and long dampers have very different characteristics ([18]). In general, long dampers are better at attenuating the amplitude response of the rotor, while short dampers are better at reducing the force transmitted to the support. Also it can be shown that the long damper provides more damping than a short damper. Thus if it is required to stabilize a rotor, then the long damper will remove more energy than the short damper. Also, because of the larger forces that are transmitted through a long damper, the long damper can be considered as a high load damper, i.e., it will be able to sustain high loads without executing large orbits ([19]), and thus the possibility of jump resonance is reduced. Table 1 summarizes the differences between short and long dampers.

Thus, if a squeeze film damper is designed to operate as a short damper when a small force transmitted to the support is desired, and to operate as a long damper when a small amplitude of vibration is desired, this would lead to a more effective squeeze film damper, and would allow rotors to operate safely at higher speeds. This can be accomplished by actively controlling the squeeze film damper to change its characteristics to either the long damper or the short damper. This implies that the control algorithm for such a hybrid damper would be as simple as just switching from long to

Contributed by the International Gas Turbine Institute (IGTI) of THE AMERICAN SOCIETY OF MECHANICAL ENGINEERS for publication in the ASME JOURNAL OF ENGINEERING FOR GAS TURBINES AND POWER. Paper presented at the International Gas Turbine and Aeroengine Congress and Exhibition, Munich, Germany, May 8–11, 2000; Paper 00-GT-564. Manuscript received by IGTI November 1999; final revision received by ASME Headquarters February 2000. Associate Editor: D. Wisler.

Table 1 Short versus long dampers

	Short Dampers	Long Dampers
Flow	axial	circumferential
Damping	low	high
Amplitude response	higher	low at critical speed
Transmissibility	low at running speed	higher
Fluid inertia	minimal	considerable
Load	low	high
Stability	fair	better
Jump resonance	possible	less probable

short dampers and vice versa. However, it may be required to obtain intermediate amounts of damping for better operation of the rotor.

This suggested that it is possible to develop an actively controlled hybrid squeeze film damper, which can operate as a long damper near critical speeds, such that it effectively attenuates the amplitude response of the engine and avoids the possibility of a jump resonance, and it also can operate as a short damper at the operating speed region, such that it effectively reduces the force transmitted to the engine frame. In addition, it can be used to provide intermediate amounts of damping. This is possible by designing the sealing on the damper, such that the damper becomes tightly sealed (i.e., long damper) or open-ended (i.e., short damper), or anything in between, according to the instructions of a controller. This is the hybrid squeeze film damper.

The HSFD

Figure 1 shows a cut-out of the HSFD. Two movable sealing rings (4) with sliding fit both to the end caps and to the housing, one on each end of the damper as shown in Fig. 1, are used as the controlling elements. The principle of the seals operation is simple. The damper oil film and the hydraulically actuated seals are supplied from independently variable sources. In order for the damper to operate as a long damper, the pressure to the seal chambers (12) is elevated above the internal pressure of the damper (5). The seal rings (4) will move in axially and seal the oil film inside

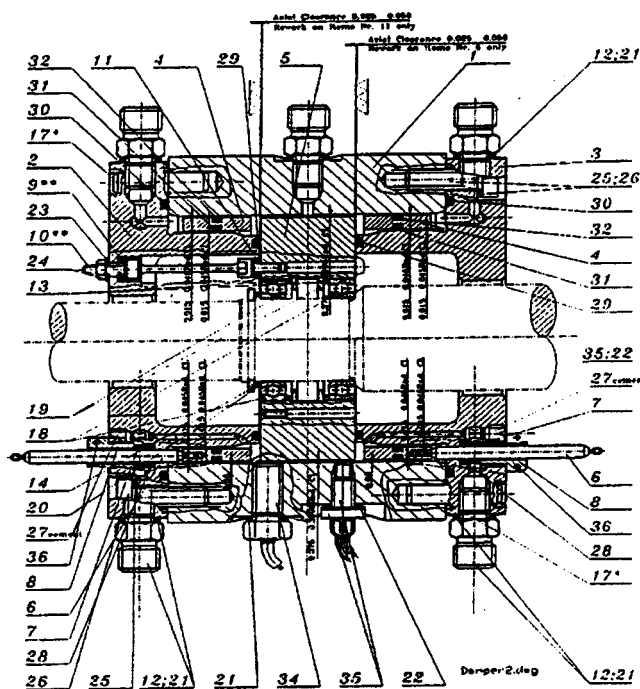


Fig. 1 Cutout of manufactured hybrid squeeze film damper (HSFD)

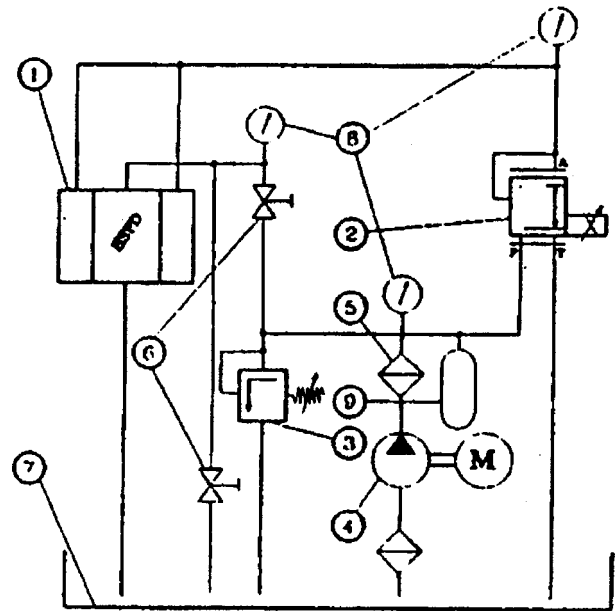


Fig. 2 Automated hydraulic circuit

the damper clearance. In order to return to the short damper configuration, the seal pressure is lowered until it is less than the internal pressure of the damper. This causes the seal rings (4) to return to their original positions.

It may be required to locate the sealing rings in intermediate positions, other than those for the short or long dampers, to provide for the required rotor control. Thus the sealing rings are connected to springs that would act to restrain their motion versus the applied pressure in the sealing chambers. As illustrated by the computer simulations of the system ([2]) this is quite an effective method of controlling the position of the sealing rings. The spring rods (10) shown in Fig. 1 allow for centering the journal in the damper, in addition to preventing the damper from rotation. The centering spring action provided by the spring rods (10) can be an important factor in the dynamics of the rotor bearing system ([20]).

HSFD Hydraulic Control Circuit

Figure 2 shows the automated hydraulic circuit used to control the HSFD. A three-way proportional pressure control valve (PPCV) 2 is used to control the pressure in the sealing chambers. The valve is normally closed, however, when it receives a current signal, it connects the supply line, through an orifice, to the sealing chamber, thus increasing the pressure in the sealing chamber. If, on the other hand, a reduction in pressure is required, the PPCV connects the drain, also through an orifice, to the sealing chamber, thus reducing the pressure in the sealing chamber. When the required pressure is achieved the valve is closed. It was shown by El-Shafei and El-Hakim [7] that the pressure in the sealing chamber should be at least twice as much as that in the damper to move the sealing rings. For our test rig, the damper supply pressure was 3 bar and the sealing chamber supply pressure was 6 bar.

Modeling of Open-Loop System

Figure 3(a) shows the open-loop block diagram. The input current actuates the PPCV thus applying the pressure on the sealing rings. The sealing rings control the amount of damping supplied by the HSFD to the rotor, thus providing the expected eccentricity ratio at the damper as the open-loop output.

A complete mathematical model of this open-loop system was developed by El-Shafei and Hathout [6]. This was a nonlinear model, in which the PPCV was modeled with a second-order transfer function, the sealing ring was also modeled with a

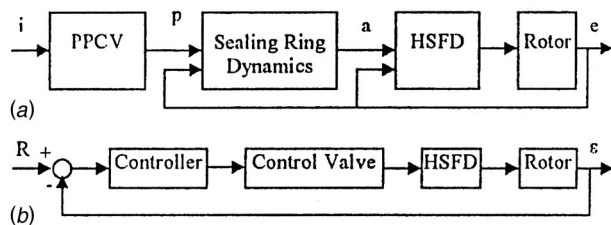


Fig. 3 (a) Open-loop system, (b) generic control loop for HSFD-rotor system

second-order transfer function with delay, and a linear HSFD model following Holmes and Dogan [16] was used. The pressure in the HSFD is controlling the damping which contributes to the rotor dynamics.

Although this was a nonlinear model, (neglecting some peculiarities such as saturation) this model behaved quite linearly. The PPCV had a bandwidth of about 250 Hz, the sealing ring was the slowest part of the open-loop controller with a bandwidth about 2.5 times the bandwidth of the rotor, which is slowest part in the system. In this case the sealing ring had a bandwidth of about 82.5 Hz and the rotor had a bandwidth of 30 Hz.

Based on this almost linear model and the relatively slow behavior of its mechanical components, it was decided to work with traditional common closed-loop controllers.

Control Algorithms

Several control algorithms have been applied to the HSFD. These vary from the simplest on-off control to the most demanding adaptive control. Other control algorithms include PID-type control, gain scheduling, nonlinear proportional, and LQR controllers. Most of these controllers have been investigated both theoretically and experimentally. These controllers were chosen because they are common controllers in the industry and are simple enough to be used in an applied environment. Moreover, based on the study of the open-loop system shown in Fig. 3(a), it is clear that these controllers should work, since there is a single output, and the system model and behavior is well defined ([6]).

For all the controllers, the feedback to the controller is the eccentricity of the journal in the damper. The only exception is the on-off control, which is based on switching at different speeds. Other states were considered for feedback, example pressure, or force in the damper, but early simulations indicated that the feedback on eccentricity is enough.

Basically, the control loop, for most controllers, is as shown in Fig. 3(b). The reference signal is compared with the eccentricity and an error signal is applied to the controller, which in turn applies the necessary control action to the control valve. The control valve provides the necessary pressure to the sealing rings in the HSFD, thus varying the damping acting on the rotor. The resulting eccentricity is the feedback, as shown in Fig. 4, and is compared with the reference signal, thus providing the error signal, until the reference signal is satisfied.

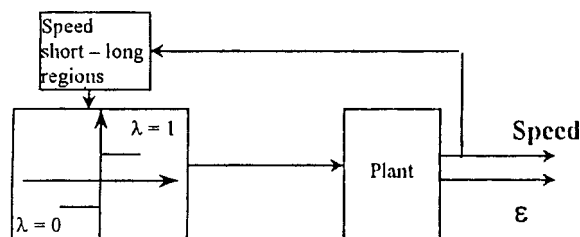


Fig. 4 On-off controller

The controllers were designed in several different ways. First the open-loop system was selected to simulate the behavior of our test rig. Then using a simple linear model and such well established design rules as the Ziegler-Nichols rules for the PID-controller, a preliminary set of design parameters are selected ([9]). Then using the nonlinear model ([6]), extensive simulations are used to tune the parameters of the controller to the required behavior [4]. These parameters were then used in the experiments, but it was found that a second stage of tuning experimentally was required ([3]).

On-Off Control

The basic concept of the typical on-off controller (see Fig. 4) is to switch between two modes of operation based on the error signal. In the active vibration control of the rotor system, the two modes of operations are the short and long damper modes. The criterion for tuning of the controller between its two modes is the major design implication. It is not quite straight forward to design the on-off controller based on the error signal. However, since the steady-state operation of the system in both the short and long modes are available at hand, a speed range can be chosen to be the switching criterion. This can be easily implemented as an on-off design. In summary, the controller is switched to either mode in a particular speed range as defined by the designer off-line. It was shown by Burrows et al. [21], that for some rotor systems only two levels of damping are required to control the behavior of the rotor-bearing system.

To implement the on-off controller to the HSFD-rotor system, basically one chooses the HSFD to be operating in the long damper mode at the critical speed and operating at the short damper mode away from the critical speed. Thus a critical speed analysis, as well as an unbalance response analysis, should be conducted before selecting the switching speeds. Figure 5 shows the experimental results of implementing the on-off controller in a coast-down test. It is clear from the figures that the controller succeeded in attaining the desired mode of operation in the given speed region. Switching between the two modes is not instantaneous and a time delay is observed in the response. However, this is not significant as the switching is designed off-line, and as a result one can include the delay in the design of the different regions.

Although the on-off control was quite successful in controlling the rotor system through a run-up or coast-down, yet it has the deficiency of not being able to accommodate varying operating conditions, or disturbances, such as sudden unbalance, because of no feedback on the rotor system. Only the damper is scheduled based on the speed of the rotor.

PID-Type Control

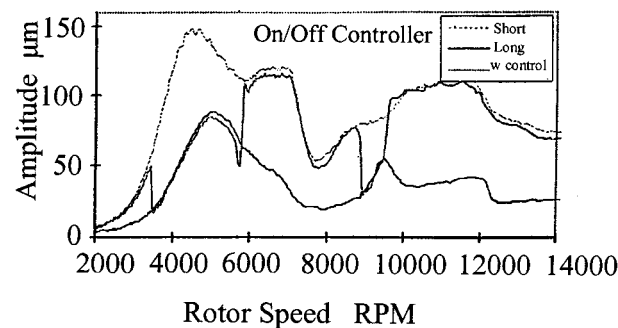
The first set of closed-loop controllers to be considered with the feedback on eccentricity, are the PID-type controllers. In this case, the controller in Fig. 3(b) is defined by the transfer function

$$\frac{U(s)}{e(s)} = K_p + \frac{K_i}{s} + K_d s \quad (1)$$

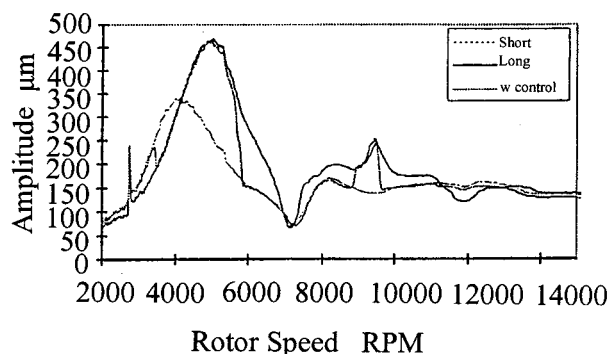
where

- U = is the control action
- K_p = is the proportional gain
- K_i = is the integral gain
- K_d = is the derivative gain
- e = is the error signal.

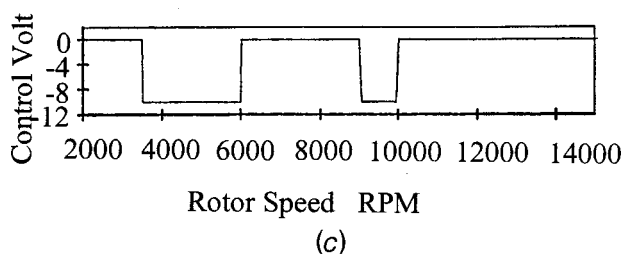
Several simulations were performed for the design of the appropriate PID controller for the HSFD-rotor system ([9]). However, early on, based on the simulations, it became apparent that the derivative control was providing chattering of the sealing rings, thus destabilizing the closed-loop system. This is due to the anticipatory nature of the derivative control, which in effect anticipates the damping needs based on trends, rather than actual



(a)



(b)



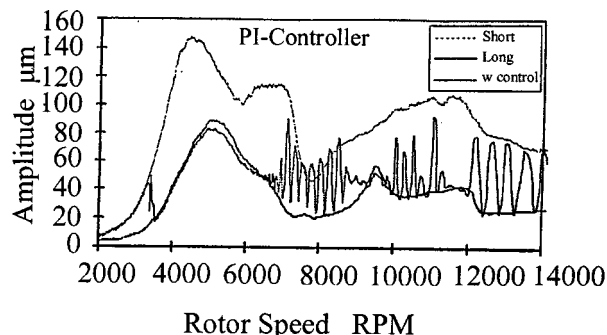
(c)

Fig. 5 Coast-down test of on/off controller; (a) experimental response of rotor at damper 2 for on/off controller, (b) Experimental response of rotor at CM2 for on/off controller, (c) actuating signal for on/off controller

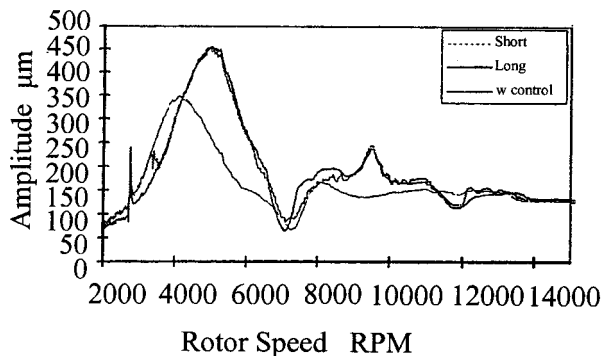
needs, resulting in the chattering action. Thus the derivative control was eliminated early on, and was not tested experimentally, while both the proportional and proportional-integral control were investigated thoroughly ([9]).

In the simulations, the PI-control behaved relatively well, with some minor chattering. However, experimentally, the P-controller and the PI-controller, both based on feedback of eccentricity in the damper, and both exhibited significant chattering in a coast-down test (as shown in Fig. 6), which can adversely affect the performance of the rotor. Even though the application of these controllers is simple, does not require pre-knowledge of the critical speeds, and can accommodate varying operating conditions, yet the chattering that occurred was not eliminated by extensive tuning, whether in theoretical simulations or experimentally. This leads to the conclusion that these control algorithms are not adequate for the control of the rotor-HSFD system. In fact, given the shortcomings of both the on-off controller and the P or PI-controller, one would choose the on-off controller to avoid the chattering problem.

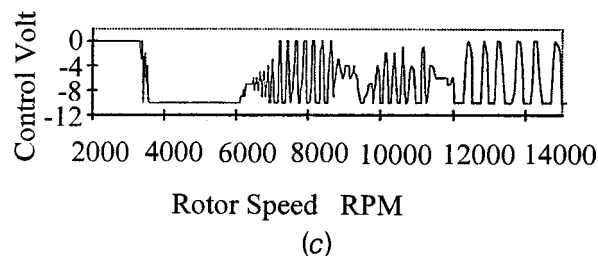
However, the simulations of the sudden unbalance (possible blade loss) showed that the PI-controller behaved well. Figure 7 shows the simulations of the sudden unbalance on the rotor using the PI-controller. In this case, the HSFD was able to accommodate



(a)



(b)



(c)

Fig. 6 Coast-down test of PI-controller; (a) experimental response of rotor at damper 2 for PI-controller, (b) experimental response of rotor at CM2 for PI-controller, (c) actuating signal for PI-controller

the sudden unbalance easily, and the controller behaved very well, changing the damper characteristics to provide more damping. It should be noted, that there is a limit to the ability of the HSFD in accommodating sudden unbalance: As soon as the HSFD reaches the long damper mode, it will not be able to provide any more damping, thus losing the capability to accommodate any larger unbalance.

No experimental data are available for sudden unbalance, since this would require a more elaborate test rig than the one available at Cairo University ([8]), and it would certainly require more elaborate safety precautions.

Nonlinear Proportional Controller

To overcome the problems encountered with the PID-controller, it was proposed to consider two alternatives, where the gains of the controller are changed based on the system requirements. These alternatives are the gain scheduling of the PI-controller (presented in the next section), and the nonlinear proportional controller. The basic idea in the nonlinear proportional controller is to change the proportional gain with the operating conditions. This controller has particular capabilities in high disturbance rejection and robustness to time delay. The original idea was proposed by Xu et al. [22] to design a nonlinear proportional-

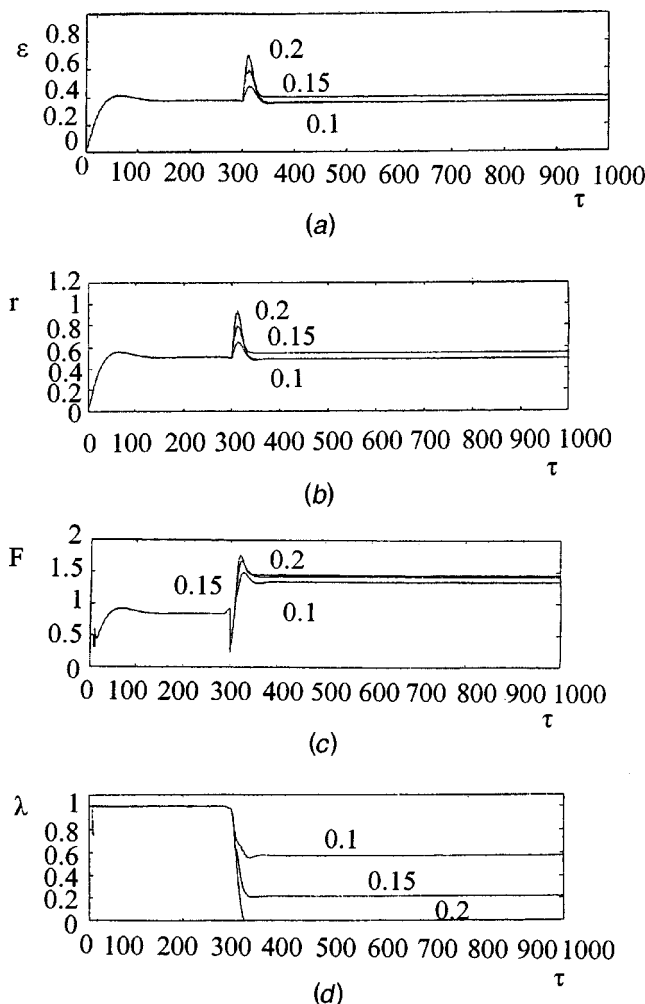


Fig. 7 Controlled sudden unbalance, $U=0.1, 0.15$, and 0.2 , PI-controller; (a) eccentricity ratio ε , (b) vibration amplitude at rotor center r , (c) transmitted force F , and (d) sealing ring motion λ

derivative controller to control the contact transients in robot systems. In the design and development reported here, only a proportional controller is suggested, mainly to improve the performance of the proportional controller. The derivative action was excluded from being used in the feedback because it responds to the rate of change of the error, and hence generates strong control actuating signal. Thus, it anticipates large errors and attempts corrective actions before they occur with high control signals. In summary, the control law is defined as

$$u = K_p e. \quad (2)$$

The proportional gain is defined based on the formula ([23]):

$$K_r = \frac{K_i}{1 + \beta \exp[\alpha \sin(\dot{e})e]} + K_0. \quad (3)$$

In principle the controller changes the gain nonlinearly based on value, sign, and rate of the error. When the error of the system increases, the gains are increased and vice versa. Thus, not only the error is used to modify the gains but also its rate of change. The gains are chosen based on two criteria. First, implementation and tuning the proportional controller guided the selection of the initial values of the proportional gain. Second, the factors characterizing the modification of the nonlinear gain were adopted from

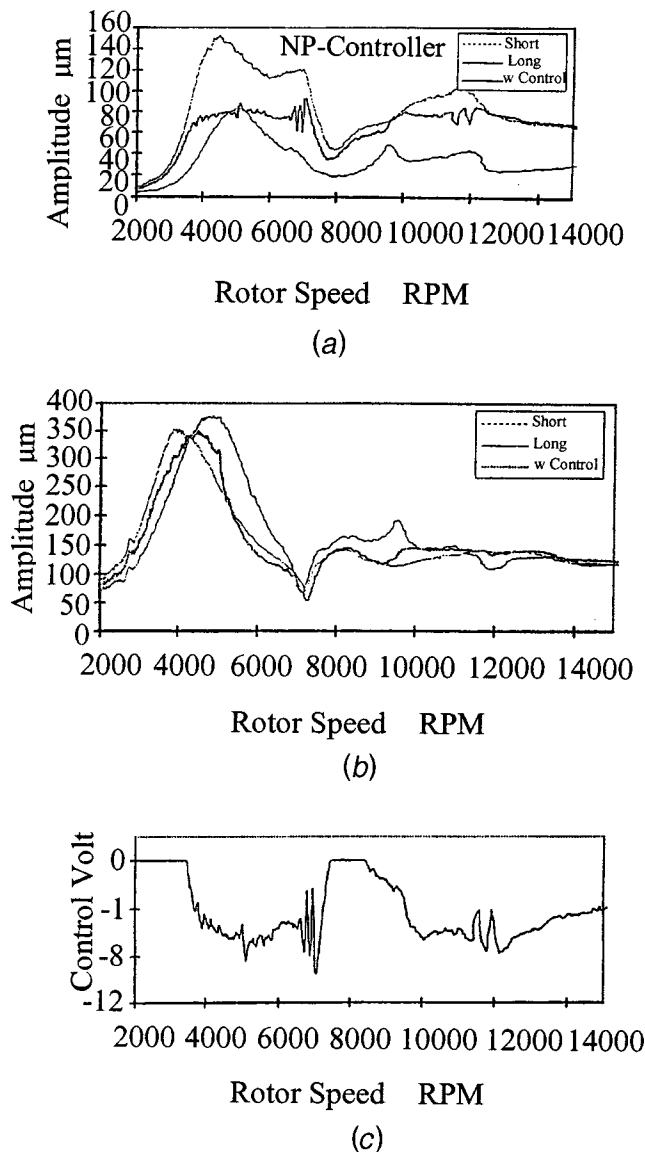


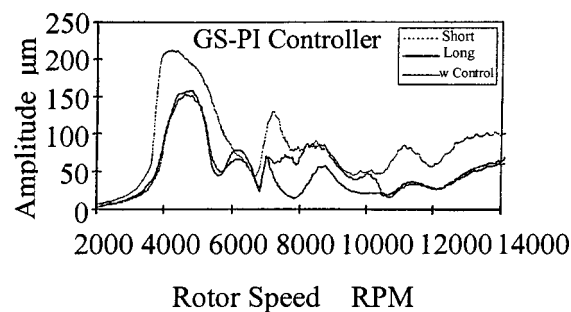
Fig. 8 Coast-down test of NP-controller; (a) (b) (c)

the work of Xu et al. [23]. For our experiments the following values for the NP-controller parameters were used: $K_0=0.2$, $K_1=0.7$, $\alpha=100$, $\beta=1$.

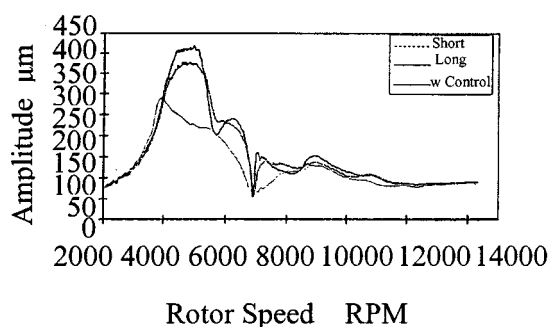
Figure 8 shows the experimental vibration of the rotor bearing and of the center mass and the actuating signal, respectively, in a coast-down test. These responses indicate that the updating of the proportional gain according to the nonlinear design presented managed to extensively reduce the chattering resulted from the implementation of the constant gain proportional control. Moreover, the actuation signal remained within its saturation limits. Thus, the nonlinear proportional controller achieved the least control activity and never saturated the output channel. This is a significant improvement over the previous controllers.

Gain-Scheduling Proportional-Integral Controller

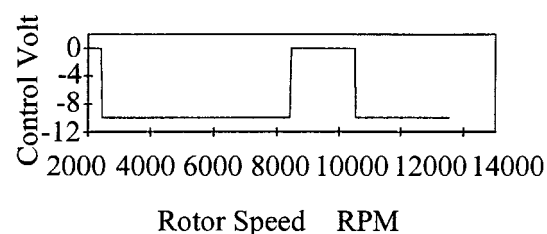
Applying linear control techniques to nonlinear systems can work efficiently at specific operating conditions. This is because a linear equivalent system to the original nonlinear system can be constructed at that particular operating condition. However, away from the linearization operating point, the linear controller with constant coefficients results in unacceptable performance and may lead to instability. Therefore, if for each linearized operating point



(a)



(b)



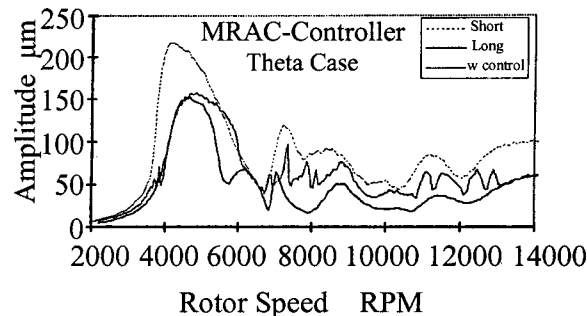
(c)

Fig. 9 Coast-down test of GS-PI controller; (a) experimental response of rotor at damper 2 for GS-PI controller, (b) experimental response of rotor at CM2 for GS-PI controller, (c) actuating signal for GS-PI controller

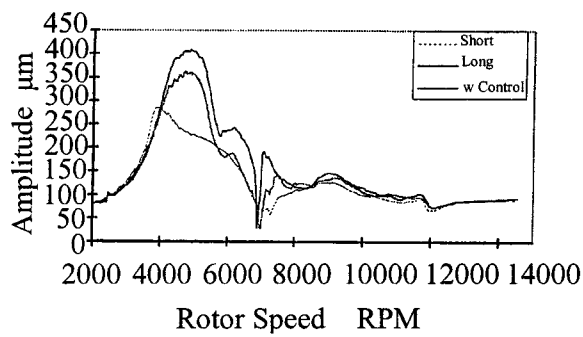
of the nonlinear system a specific linear controller gives desired performance characteristics then one can achieve the required performance for all operating regions by applying different controller gains for different operating regions.

The basic principle of the gain scheduling technique is that a linear controller (such as the proportional-integral controller) is designed, tuned, and tested for a particular region of the operating range. Then, the gain scheduler is to apply a particular set of the controller gains for a particular region of operation. The results obtained from experimental implementation of the proportional-integral controller encouraged using it in the gain scheduling technique ([24]). The basic performance parameter is chosen to be the reference input value for particular speed ranges. It was decided to only schedule the integral gain for the proportional-integral controller since it is the most effective parameter in controlling the run-up through critical speeds in the simulations.

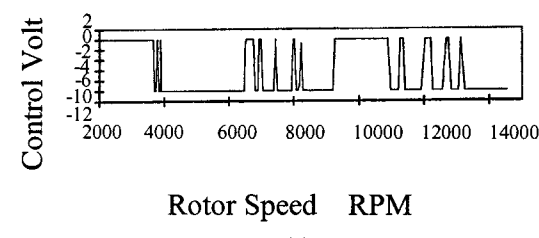
Figure 9 shows the experimental vibration amplitude at the bearing and at the center mass and the corresponding actuating signal, respectively. Investigating the vibration at the bearing in correlation with scheduled reference input indicates that the controller managed to regulate the vibration in different regions of the speed range. The response is smoother and does not have the chattering resulted from the proportional and the proportional-



(a)



(b)



(c)

Fig. 10 Coast-down test of MRAC-controller theta case; (a) experimental response of rotor at damper 2 for MRAC-controller theta case, (b) experimental response of rotor at CM2 for MRAC-controller theta case, and (c) actuating signal for MRAC-controller theta case

integral controllers. No significant changes appeared in the response of the center mass. The actuating signal shown in Fig. 9 indicates saturation of the output channel in most of the speed range. This is confirmed by the sealing ring, which assumed the short and long damper positions in those speed ranges.

It should be noted that each of the test runs with the control algorithms was preceded by coast-down tests of the test rig once in the short damper mode, and another time in the long damper mode, as shown in the figures. These measured data provided limiting conditions of the controller, and allowed visual evaluation of the controller performance. However, it should be clear from the figures that a deterioration in the test rig became apparent, as evidenced by the coast-down tests of Fig. 9 and 10. Actually, the characteristics of the earlier Figs. 5, 6, and 8 show distinctly different characteristics for the rotor-bearing system, from those shown in Figs. 9 and 10 although it is the same rotor. It was decided to continue testing, even though the test rig characteristics changed, either due to a bent shaft, a shaft crack or reduced balance quality, because this demonstrates the adaptability of the HSFD in controlling varying operating conditions, and also because there is no direct relationship between each of the proposed control algorithms that can inhibit the development of the controllers.

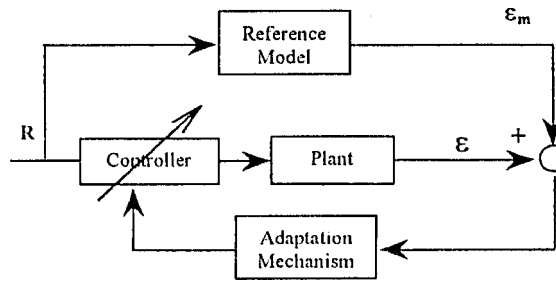


Fig. 11 Adaptive controller (model reference adaptive controller (MRAC))

Model Reference Adaptive Controller (MRAC)

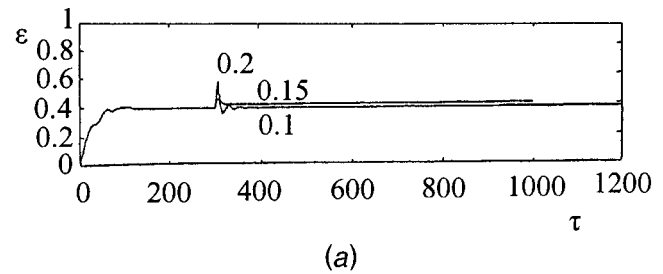
Adaptive control has a unique feature that distinguishes it from constant linear feedback control. An adaptive controller is usually composed of a controller and an adaptation mechanism. The adaptation mechanism is continuously updating the controller gains or parameters such that a specific performance criterion is maintained or achieved. As a result, the controller is able to perform in a wide range of operating conditions for which a constant gain controller either is unstable or does not perform satisfactorily. Another feature of adaptive control encouraged its application for the rotor system is that it can perform quite exceptionally even when the dynamic model parameters of the plant to be controlled are partially known. This is particularly true for the rotor system, since extensive identification is required to construct the full accurate dynamic model.

The principle of operation of the model reference adaptive control (MRAC) is that a reference model having the same order and structure of the plant is designed to achieve the desired performance. The adaptation mechanism compares the difference between the output of the plant and the output of the reference model then computes and updates the controller parameters in such a way that in the steady state the regulation error approaches zero ([8]). In other words, the output of the controller plant can track the output of the reference model.

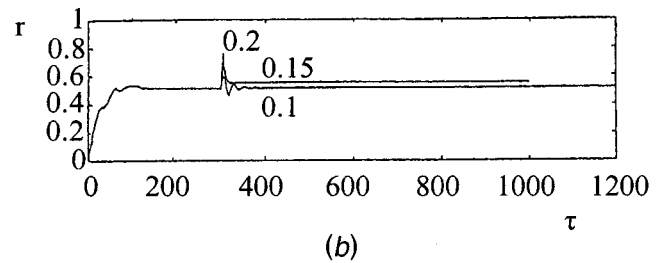
The complete MRAC strategy is based on the basic structure shown in Fig. 11. The output is chosen to be the amplitude of vibration at the bearing center. The desired performance is expressed in terms of the reference model. The three fundamental components that constitute the MRAC are the linear controller, the reference model, and the adaptation mechanism. Once these three components are designed then the MRAC can be tested ([11]).

The controller chosen is a simple proportional controller that aims at positioning the sealing ring infinitely between the short and long damper mode positions such that the vibration amplitude is regulated to the reference input. The proportional gain is updated according to the adaptation mechanism. The reasons a proportional controller is chosen to be the linear regulator, are its simplicity and the remarkable enhancement the nonlinear proportional controller achieved over the constant proportional controller. According to the analysis of the proportional controller and the definition of the model reference adaptive controller, one expects that the MRAC is continuously changing the dynamics of the system by changing the proportional gain. Thus, the closed-loop response is changing in such a way that the rotor vibration follows the reference model output.

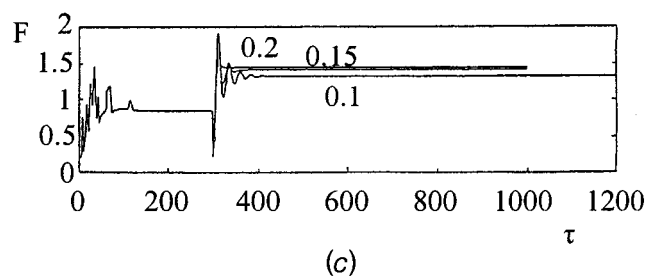
The experimental results of implementing the MRAC are shown in Fig. 10. It is clear from the figure that the adaptive controller succeeded in regulating the vibration amplitude at the bearing system to the reference value of 50 μm . Passing over the resonance, the adaptive controller preferred the short mode, which results in a smaller error in this range. The response of the center mass is also shown in Fig. 10. As the vibration of the center mass is not a directly controlled variable, its response is complementing the regulation of the bearing vibration. During the whole range the



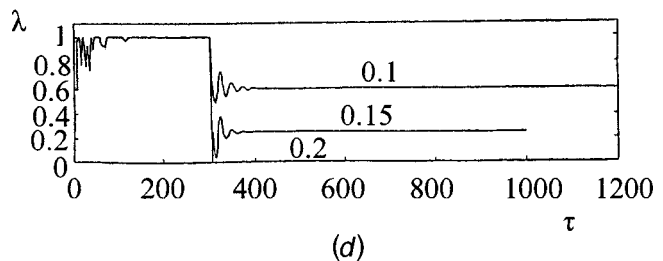
(a)



(b)



(c)



(d)

Fig. 12 Controlled sudden unbalance, ($u=0.1, 0.15$, and 0.2 , MAEC-controller; (a) eccentricity ratio ε , (b) vibration amplitude at rotor center r , (c) transmitted force F , and (d) sealing ring motion λ)

center mass amplitude remained between the short and long modes with less chattering than that of the bearing vibration.

Figure 12 shows the simulation results for the sudden unbalance with the MRAC controller. Here also, the HSFDF was able to accommodate the sudden unbalance easily, and the controller behaved very well, changing the damper characteristics to provide more damping.

Observations on the Coast-Down Tests

In all the coast-down tests reported here the reference value given to the controller was 50 μm . In all cases, all the controllers tried to achieve this 50 μm eccentricity at the damper location, away from resonance, with varying degrees of success.

It should be noted that in all the coast-down tests the results show only the amplitude response, but no force information. Unfortunately, we had problems in our pressure measurements, and are not reported here. One would expect the forces to be smaller in the short damper mode. However, a very important point is clearly identified in this paper. Although the long damper mode

provides more damping, thus giving smaller amplitude at the damper, yet this is a flexible rotor, thus the rotor deflection increases. In all figures, it is clear that the long damper mode provided smaller amplitude at the damper, but larger amplitude at the center of the rotor. Thus, actually the long damper mode increases the rotor deflection. There is an optimum amount of damping and the controller tries to vary the damping, to satisfy its objectives.

Qualitative Comparison

Qualitatively all of the advanced control algorithms behaved well, although the test rig changed its behavior. The nonlinear proportional controller was exceptional in that it never saturated which translates to available control effort to be used when needed. This also resulted in the rotor neither behaving as a short damper or a long damper for considerable time, but rather the controller tried to obey the reference value as much as possible. It was successful in avoiding the short damper mode at critical speeds, and avoiding the long damper mode away for critical speeds.

The gain scheduling controller also behaved extremely well although it was saturated most of the time and preferred the large damping capacity provided by the long damper mode. It is believed that more design effort could yield whatever required behavior because of the scheduling capabilities. Theoretically, the gain schedule controller behaved qualitatively as in the experiments.

The MRAC controller also behaved relatively well, although there was a bit of indecisiveness at higher speeds, changing frequently between the two extreme control signals. This could have happened because the reference model is only based on a single-degree-of-freedom system and does not contain any information on the higher modes ([11]). However, the MRAC controller was successful in avoiding either the long damper mode or the short damper modes for a long time except for crossing the first critical speed. Theoretically, the MRAC controller behaved much better than in experimentation, but there was the added complication of a nonlinear reference model ([8]). We believe that a reference model with at least as many degrees-of-freedom as the rotor exhibits critical speeds is necessary to obtain perfect performance from the MRAC controller ([11]).

Both the P and PI-controllers exhibited significant chattering both theoretically and experimentally. The nonlinear P-controller is an extension over the P-controller and performs much better, but has the disadvantage of ad hoc design. The gain-scheduling controller is an extension over the PI-controller and also performs much better but also requires a significant design effort in selecting the gain schedule.

Finally, the on-off controller behaved very much as expected. This controller has the advantage in that it precisely behaves as the designer wishes, and performs experimentally exactly as theoretically predicted. The only disadvantage that is worth mentioning is the inability of the on-off controller to accommodate varying operating conditions.

Quantitative Comparison Based on Indices

In this section a quantitative comparison of the experimental results, among the five feedback controllers is presented. It is necessary and deserves effort to compare the performance of the developed and tested control algorithms. The basic criterion for evaluating the performance of a controller can be its regulation error and associated control effort. For the rotor system, the regulating error indicates how close the controller succeeded in regulating the vibration amplitude to the reference desired level. Thus, the measure of the regulation performance is chosen to be the average integral square root of the error norm:

Table 2 Indices of five control algorithms

The Controller	I_e	I_c	Comments
Proportional controller	0.95	0.48	Chattering
Proportional-integral controller	0.96	0.36	Chattering
Gain scheduling controller	1.29	0.29	Saturation
Nonlinear/proportional controller	1.05	0.23	
MRAC controller	1.11	0.26	

$$I_e = \frac{\sqrt{\sum_{i=1}^N |e|^2}}{N}. \quad (4)$$

This normalized index can be used to compare the different control algorithms. Thus, controllers can be differentiated based on one single number.

The measure of the control effort reflects the energy the controller injected into the system. The index is also chosen to be the average integral square root of the control signal:

$$I_c = \frac{\sqrt{\sum_{i=1}^N |u|^2}}{N}. \quad (5)$$

Table 2 lists the error and control indices for the five feedback control algorithms developed and tested in this research work. From this table one can conclude that the proportional controller achieved the minimum error index followed by the proportional integral controller, while the nonlinear proportional controller has the minimum control effort followed by the MRAC controller.

For instance, if one chose a controller based on the error index, one would choose one of the elementary control algorithms, which would lead to the undesirable chattering, while if one chose the controller based on the minimum control effort one would definitely choose the nonlinear proportional controller.

Correlating the qualitative and the quantitative comparisons, one finds that both lead to nearly the same conclusions in ranking the controllers. The nonlinear-proportional controller passes with high colors in both the qualitative and quantitative analyses. A comprehensive comparison of the control algorithms is illustrated in Table 3 and represents the summary of the abilities of each controller.

It should be noted that some quantitative comparisons would not be quite meaningful given that the rotor characteristics have changed. However, it is believed that this comparison can be useful because:

(a) the controller should be able to respond to disturbances and to accommodate uncertainties. Among these uncertainties are the uncertainties in the plant. The performance indicators illustrate the behavior of the controllers within the framework of an actual rotor system, the same rotor in all cases, but its operating characteristics have changed (i.e., disturbances).

(b) the performance indicators illustrate more the behavior of the controller than of the actual plant (rotor system). Both indicators, the error indicator and the energy indicator, illustrate the abilities of the controller in responding to varying outputs.

Discussion and Conclusion

Several control algorithms were developed and applied to the active control of HSFD supported rotor systems. The on-off basic control algorithm with feedback on speed was developed to act as a long damper at critical speeds and short damper away from critical speeds. It was shown that this control algorithm is quite effective but requires preknowledge of the behavior of the rotor system and is not able to accommodate variable operating condi-

Table 3 Comparison between control algorithms

Controller	On-Off	P	PI	Nonlinear P	GS-PI	MRAC	LQR
Qualitative	-Follows design objectives -Effective	-Chattering -Saturation	-Chattering Saturation	-Excellent behavior -Available control effort	-Well behaved -Problem with saturation	-Well behaved -Reference model determines behavior	-Well behaved -Problem with estimator
Error Index	-	Good	Good	Good	Fair	Good	-
Control	-	High	High	Good	Good	Good	-
Effort Index							
Robustness	-Unable to accommodate any changes -Preselected	Sensitive to gain changes	Sensitive to gain changes	Good	Good	Good, but sensitive to the selection of reference model	Sensitive to design changes and operating conditions
Disturbance Rejection	Unable to reject disturbance	Possible but chattering problem	Possible but chattering problem	Excellent	Excellent	Excellent	Sensitive
Varying Operating Conditions	Unable to accommodate	Possible but chattering problem	Possible but chattering problem	Excellent	-Good -Needs redesign to schedule if changes are large	Excellent	Sensitive to changes
Sudden Unbalance	Unable to accommodate	-	Good	-	Good	Good	Fair
Design Effort	Minimal	Extensive tuning required	Extensive tuning required	Ad Hoc	Extensive design effort in selecting gain schedule	Effort in selection of reference model but simple design	Extensive effort in selecting gains and tuning

tions. A PI-control algorithm was developed and also shown to be effective. The enhancement of the PI-controller by gain scheduling provides one of the best control alternatives, both in controlling resonant conditions and sudden unbalance. The LQR-controller was not as effective as the PI-controller because of its sensitivity. The developed adaptive controller, with a unique nonlinear reference model, was also extremely effective both for controlling resonant conditions and sudden unbalance.

Experimentally, the on-off controller, the PI-controller (with and without gain scheduling), and the model reference adaptive controller were all applied. In addition a nonlinear-proportional controller was also developed and applied, and was shown to be the best overall controller of the HSFD. The experimental results, which involved elaborate set-up and verification and identification, confirmed the results of the theory and simulation and illustrated the power and utility of the developed algorithms, and of the HSFD itself as a robust controlling element of rotor vibrations. A comparison of the theoretical and experimental results of each of the developed controllers allows the designer to select the most appropriate algorithm for the desired application.

This study confirmed the capabilities of the hybrid squeeze film damper, as an efficient and powerful controlling element for high speed rotors, particularly of aircraft engines and rocket turbopumps. Specifically the results of this work establish that the HSFD:

1. improves the vibration isolation capability of the rotor support,
2. reduces the amplitude of vibration of the rotor at all speeds,
3. enhances the stability of the rotating machine,
4. allows the rotor and damper to operate at high-loads, and
5. results in a rotating machine that is capable of operating under varying and adverse conditions.

These results can be inferred from the various simulations and experiments presented that illustrate the adaptability of the HSFD

It is also the opinion of the author that the HSFD is now ready for engine testing. The control algorithms are sufficiently developed, the laboratory experimentation and verification were extensive and illustrate the strengths and adaptability of HSFDs.

In addition, the concept of HSFDs relies on a reliable and robust device that has been used extensively in aircraft engines for over thirty years, as a passive vibration controller. It is thus the

belief of the author that the results of this work should lead to full-scale engine testing for the active control of rotor vibrations using HSFDs.

Acknowledgment

The author would like to thank his students whose efforts contributed to this paper, in particular Dr. M. El-Hakim and Mr. J.-P. Hathout. This work was supported by EOARD, US Air Force office of Scientific Research, Grant No. F49620-92-J-0512, Dr. Charbel Raffoul and Dr. Nelson Forrester, program managers. This support is gratefully acknowledged. The U.S. government has certain rights to this material.

References

- [1] Vance, J. M., Ying, D., and Nikolajsen, J. L., 1999, "Actively Controlled Bearing Dampers for Aircraft Engine Applications," ASME Paper 99-GT-18.
- [2] El-Shafei, A., El-Hakim, M. M., and Hathout, J.-P., 1993, "Control of Rotor Vibrations Using Hybrid Squeeze Film Dampers," Report No. MDP-EOARD-1/93, Cairo University.
- [3] El-Shafei, A., El-Hakim, M. M., Hathout, J. P., and Youssef, R. Y., 1994, "Development of Hybrid Squeeze Film Damper for Active Control of Rotor Vibrations," Report No. MDP-EOARD-1/94, Cairo University.
- [4] El-Shafei, A., Massoud, A. T., El-Hakim, M., Hathout, J.-P. and Youssef, R., 1997, "Control of Rotor Vibrations Using Hybrid Squeeze Film Dampers," Report MDP-EOARD-1/97, Cairo University.
- [5] El-Shafei, A., 1993, "Experimental and Analytical Investigation of Hybrid Squeeze Film Dampers," ASME J. Eng. Gas Turbines Power, **115**, pp. 353–359.
- [6] El-Shafei, A., and Hathout, J. P., 1995, "Modeling and Control of HSFDs for Active Control of Rotor-Bearing Systems," ASME J. Eng. Gas Turbines Power, **117**, pp. 757–766.
- [7] El-Shafei, A., and El-Hakim, M., 1995, "Development of a Test Rig and Experimental Verification of the Performance of HSFDs for Active Control of Rotors," ASME Paper 95-GT-256.
- [8] Hathout, J.-P., and El-Shafei, A., 1996, "Adaptive Control of Rotor-Bearing Systems Using Hybrid Squeeze Film Dampers," Proc. Inst. Mech. Eng., pp. 671–690.
- [9] Hathout, J. P., and El-Shafei, A., 1997, "PI Control of HSFDs for Active Control of Rotor-Bearing-Systems," ASME J. Eng. Gas Turbines Power, **119**, pp. 658–667.
- [10] Hathout, J. P., El-Shafei, A., and Youssef, R., 1997, "Active Control of Multi-Mode Rotor-Bearing Systems Using HSFDs," ASME J. Tribol., **119**, pp. 49–56.
- [11] El-Shafei, A., and El-Hakim, M., 1999, "Experimental Investigation of Adaptive Control Applied to HSFD Supported Rotors," ASME Paper 99-GT-176.
- [12] El-Shafei, A., and El-Hakim, M., 2000, "Experimental PID Control of HSFD

Supported Rotors," ASME J. Dyn. Syst., Meas., Control, submitted for publication.

- [13] El-Shafei, A., and El-Hakim, M., 2000, "On-Off Control of HSFD Supported Rotors," presented at the International Conference on Vibrations in Rotating Machinery, Proc. Inst. Mech. Eng., Sept. 12–14, Nottingham, U.K.
- [14] Akin, J. T., 1990, private communication, Pratt & Whitney.
- [15] Feder, E., Bansal, P. N., and Blanco, A., 1978, "Investigation of Squeeze Film Damper Forces Produced by Circular Centered Orbits," ASME J. Eng. Gas Turbines Power, **100**, pp. 15–21.
- [16] Holmes, R., and Dogan, M., 1985, "The Performance of a Sealed Squeeze-Film Bearing in a Flexible Support Structure," Proc. Inst. Mech. Eng., **199**, No. C1.
- [17] El-Shafei, A., 1991, "Unbalance Response of Jeffcott Rotor Incorporating Long Squeeze Film Dampers," ASME J. Vibr. Acoust., **113**, pp. 85–94.
- [18] El-Shafei, A., 1989, "Long and Short Bearing Approximations for Squeeze Film Dampers," *Proceedings of the Vibration Institute*, Vibration Institute, pp. 145–151.
- [19] El-Shafei, A., 1991, "Hybrid Squeeze film Damper for Active Control of Rotors," U.S. Patent number 5,058,452, Oct.
- [20] El-Shafei, A., 1990, "Unbalance Response of a Jeffcott Rotor Incorporating Short Squeeze Film Dampers," ASME J. Eng. Gas Turbines Power, **112**, pp. 445–453.
- [21] Burrows, C. R., Sahinkaya, M. N., and Turkay, O. S., 1983, "An Adaptive Squeeze-Film Bearing," ASME Paper No. 83-Lub-23.
- [22] Xu, Y., Hollerbach, J. M., and Ma, D., 1995, "A Nonlinear PD Controller for Force and Contact Transient Control," IEEE Journal of Control Systems, Feb., pp. 15–21.
- [23] Xu, Y., Hollerbach, J. M., and Ma, D., 1993, "Nonlinear Proportional and Derivative Control for High Disturbance Rejection and High Gain Force Control," *Proc. IEEE*, May, pp. 924–930.
- [24] Astrom, K. J., and Wittenmark, B., 1989, *Adaptive Control*, Addison-Wesley, Reading, MA.

D. Bouris
R. Kubo
H. Hirata¹
Y. Nakata

Toshiba Corporation,
Power and Industrial Systems Research
and Development Center,
1 Toshiba-Cho, Fuchu-shi,
Tokyo 183-8511, Japan

Numerical Comparative Study of Compressor Rotor and Stator Blade Deposition Rates

Compressor fouling is generally accepted to be an important factor when monitoring the efficiency of an engine's operation. However, there are not many studies related to the local fouling behavior of the individual components of the compressor. In the present paper, the CFD-ACE software package is used for the flow field calculation and the results are utilized to calculate the deposition rates on the blade surfaces of a conventional compressor stator and rotor. The deposition model takes into account the particle and surface material properties and the energy balance at the point of impact. A discussion is presented regarding the various mechanisms that produce the final deposition rate distribution and how the flow field and blade geometry affect it.

[DOI: 10.1115/1.1454113]

1 Introduction

The purpose of the present paper is to present and discuss the mechanisms governing the local deposition process on the surfaces of a compressor stator and rotor blade. Atmospheric particles are inevitably drawn in through a compressor intake and some of them will eventually pass through the filters. These particles can build up on internal compressor surfaces and interfere with the airflow through the engine. Thus, the efficiency of the compressor is reduced and, since any change in the performance of the compressor will also have a chain effect on the performance of the turbine, the fuel consumption, operating temperatures, and emissions of the whole engine are increased.

The problem of fouling in turbomachinery has been known for a long time and various techniques to control it have been proposed in the past few decades. These usually involve washing the compressor surfaces with solid or liquid cleaners and recently ceramic-metallic coatings have been applied to the surfaces so that deposit formation is reduced ([1]). It is generally appreciated that it is important to understand the mechanisms with which deposits are formed so that the process may be dealt with more effectively. Nomura et al. [2] performed experimental measurements of the deposits formed on the surfaces of an air-cooled gas turbine blade to find that most deposits were formed on the suction surface since turbulent and thermal diffusion were the dominant mechanisms in the configuration they studied. Wenglarz [3] presented a numerical calculation of particle arrival rates to turbine blade surfaces that implemented data from a pressurized fluidised bed combustion plant. Adherence fractions were calculated from the measured deposit thicknesses. He noticed that inertial impaction is dominant on the pressure surface while for the suction surfaces it is diffusion that dominates and thus the particles sizes that deposit there are smaller. The two previous studies were aimed at understanding deposition mechanisms in turbine blades but no reference was made to the compressor, where thermal gradients are much smaller. Regarding overall performance, U1 Haq and Saravanamuttoo [4] introduced an aerothermodynamic model. This model uses geometrical dimensions of the compressor annulus and, by monitoring the mass flow rate, rotational speed, and ambient conditions, evaluates the performance deterioration due

to fouling. It is a functional approach that neglects the details of deposit formation, such as the flow field and the particle trajectories, to find only the overall effect. No discretion is made between rotor and stator or between pressure and suction side. However, the distribution of the deposit and the contribution of the particle sizes and materials is important for the performance of the engine since the deposit could change the shape of the blade and the level of surface roughness. Suder et al. [5] presented an interesting experimental and numerical study of the effect of adding thickness and/or roughness to the surface of a transonic axial compressor rotor. They found the effect of adding a rough coating to only the first 10 percent of the blade, near the leading edge, to be enough to induce a 9 percent loss in pressure ratio. What was surprising was that adding thickness or roughness to the rest of the blade had a minimal effect on the pressure loss. It seems that the distribution of the deposit's thickness and roughness is an important factor that should not be overlooked.

If modern techniques of ceramic or metallic coatings are to be applied in combination with cleaning then it is important to understand the local mechanisms of deposit formation on the compressor stator and rotor blades. Determination of optimum coating distribution and thickness must be a result of many influential factors such as deposit distribution and local mechanisms of deposition. These factors are also important in understanding the effects of local deposit formation on the individual efficiencies of the compressor components.

The present study aims to provide a discussion regarding the various mechanisms of particle deposition that are present in a conventional compressor rotor and stator blade cascade. Studies of compressor blade fouling are scarce in the literature and the application of the following numerical models to give deposited particle size distributions and effects of particle material properties has not been previously presented. The flow fields around the blade cascades are calculated using the CFD-ACE software package (CFD Research Corporation, 1998) that features compressible fluid flow calculation capabilities using a third-order TVD scheme. The detailed calculation of the flow takes into account the effect of the boundary layer as well as the presence of a shock wave and the thickening of the boundary layer that follows. The results are then used for the calculation of Lagrangian particle trajectories and, upon impact of a particle with a solid surface, an adhesion model considers particle arrival energy as well as particle and surface material properties to perform an energy balance at the point of impact. The energy losses will show if the remaining energy is enough to overcome the interfacial energy at the surface ([6,7]). Both the stator and the rotor blade cascade of a

¹To whom correspondence should be addressed.

Contributed by the Turbomachinery Division of THE AMERICAN SOCIETY OF MECHANICAL ENGINEERS for publication in the ASME JOURNAL OF ENGINEERING FOR GAS TURBINES AND POWER. Manuscript received by the Turbomachinery Division July 27, 1999; final revision received by the ASME Headquarters November 28, 2001. Editor: R. Abhari.

conventional compressor are considered close to the design condition. Deposition rates are calculated for various particle sizes using Al_2O_3 and CaCO_3 to represent a hard and soft particle material, respectively. The differences in the resulting deposit formations are discussed.

2 Description of Numerical Method

2.1 Fluid Flow. The CFD-ACE software package has been developed by CFDRC Corporation. The software is capable of solving compressible and incompressible flows and thus is well suited for the situations to be studied here which are a compressor rotor and stator blade cascade in transonic operating conditions. CFD-ACE is based on a finite volume methodology that uses the SIMPLEC pressure correction algorithm ([8]) to solve the Navier Stokes equations on body-fitted single or multidomain curvilinear grids in general curvilinear coordinates.

In the present applications, the third-order accurate Osher Chakravarthy TVD scheme ([9]) is used for convection term discretization, turbulence is modeled using the standard $k-\epsilon$ turbulence model with wall functions ([10]) and the fluid properties are considered temperature-dependent. The perfect gas law is used for fluid density, Sutherland's law for viscosity and the JANNAF tables are used for the calculation of the local variation of the specific heat coefficient.

The CFD-ACE software package was considered a reliable tool with which to obtain the flow field data. Transonic effects can be sufficiently modeled and yet unpublished calculations performed at the authors' company showed that the results regarding cascade total pressure loss, shock wave appearance, and wake behavior were in acceptable agreement with actual operation. Details regarding the numerical aspects of the software's implementation will be discussed later on.

2.2 Particle Tracking and Deposition Model. The particle tracking algorithm involved a stochastic Lagrangian tracking methodology through which a discrete spherical particle's trajectory is followed. The relatively small curvature of the blades to be studied, as well as the absence of recirculation zones permits the assumption of negligible streamline curvature effects on the particles. The particles are also considered noninteracting due to the low mass loading found in applications of this type. The methodology includes forces of aerodynamic drag, gravity, lift forces due to local velocity gradient ([11]) and thermophoresis ([12]).

$$\begin{aligned} \rho_p G_p \frac{\partial V}{\partial t} = & -\frac{3}{4} \frac{G_p}{d} \rho_f C_D (V-U)|V-U| + G_p (\rho_p - \rho_f) g \\ & + \frac{4.98}{\pi} G_p \frac{\rho_f}{\nu} \left(\frac{\tau_w}{\rho_p} \right)^{3/2} \\ & - \frac{12\pi\mu\nu r_p C_s (k_f/k_p + C_t \lambda/r_p)}{(1+3C_m \lambda/r_p)(1+2k_f/k_p+2C_t \lambda/r_p)} \frac{\nabla T}{T_o} \quad (1) \end{aligned}$$

More details on the forces acting on the particle can be found in Smoot and Pratt [13]. The particle drag coefficient in compressible flow (C_D) is expressed as a function of local particle Reynolds number $\text{Re}_p = |V-U|d/\nu$ and relative Mach number $\text{Mach} = |V-U|/(\gamma RT)^{1/2}$ ([14])

$$C_D = 24t_1^{-1} + t_2 t_3 \quad \text{Mach} < 1 \quad (2)$$

where $T_r = T_{\text{particle}}/T_{\text{gas}}$ (T is temperature) and $S_r = \text{Mach}(\gamma/2)^{0.5}$ and

$$t_1 = \text{Re} + S_r \{4.33 + (3.65 - 1.53T_r)(1 + 0.353T_r)^{-1} e^{(-0.247(\text{Re}/S_r))}\}$$

$$t_{21} = 0.03 \text{Re} + 0.48\sqrt{\text{Re}}$$

$$t_2 = \left\{ \frac{4.5 + 0.38t_{21}}{1 + t_{21}} + 0.1\text{Mach}^2 + 0.2\text{Mach}^8 \right\} e^{(-(\text{Mach}/2\sqrt{\text{Re}}))}$$

$$t_3 = 0.6S_r(1 - e^{-(\text{Mach}/\text{Re})})$$

and

$$C_D = t_2(1 + t_1)^{-1} \quad \text{Mach} > 1 \quad (3)$$

where $t_1 = 1.86\sqrt{\text{Mach}/\text{Re}}$, $t_2 = 0.9 + t_1(2 + 2S_r^{-2} + 1.058\sqrt{T_r S_r^{-1}} - S_r^{-4})$.

Equation (1) is in such a form that it can be analytically integrated and then discretized in first-order accuracy to find the particle velocity V at every time step. The tracking methodology considers the effects of turbulence on the particle motion and is the same that was used in Bouris and Bergeles [6,7]. Here, the Saffman lift force, and the compressible drag coefficient have also been added. Due to the low mass loading in the present applications, a one-way coupling is considered, i.e., only the effects of the flow on the particle and not vice versa. The flow field results on the multidomain grid are manipulated to be used as input for the particle tracking algorithm. Thus, the latter is in effect independent of the flow field calculation methodology so previous independent validations of both are valid.

The particle deposition model has been previously presented and validated in Bouris and Bergeles [6,7]. Through the stochastic Lagrangian tracking methodology, a particle's trajectory is calculated up to a point of impact with a wall where a boundary condition must be implemented to determine the adhesion or rebound of the particle from the solid surface. In the presently used model, this is done through an energy balance at the point of impact. The material properties of the particle and surface are taken into account to calculate the elastic and plastic deformations of the softer of the two. At the same time, the interfacial surface energy is used to determine the forces holding the particle to the surface. Thus, the particle's rebound velocity is given,

$$V_r = \left[\frac{2}{m_p} (Q_i - Q_p - Q'_A - Q_L + Q_{\text{lift}}) \right]^{(1/2)}, \quad (4)$$

where m_p is the particle mass. The initial kinetic energy of the particle at impact Q_i becomes plastic deformation energy Q_p and/or energy due to elastic wave propagation Q_L ([15]). The remaining energy (stored as elastic energy) is returned to the particle and, if it is larger than the energy due to attractive forces between particle and surface Q'_A , then the particle will rebound, otherwise it will stick to the surface. The attractive forces are mostly due to van der Waals-London dispersion forces ([16]). Q_{lift} is the aerodynamic lift energy that is gained by the particle due to hydrodynamic lift forces (Saffman lift force). For the tangential velocity component a similar analysis is performed using the method proposed by Bitter [17].

The expressions of the energy terms in Eq. (4) are quite complex and for a particle of known size and velocity they are functions of material properties of the particle and the surface to which it impacts: Young's modulus, Poisson's ratio, elastic yield limit of the softer of the two materials, particle density, and interfacial surface energy derived from the dispersive surface energies of the two materials. The expressions, used by Wall et al. [18], were originally introduced by Bitter [17,19] based on the Hertz theory.

The advantage of the present particle tracking and deposition modeling methodology is that it assumes discrete particle trajectories and impacts. The trajectories are affected by the most influential forces from the flow field while, for the impact, the impact velocity and angle as well as the particle and surface material properties are considered. This allows for consideration of quite a few physical mechanisms, whose individual behaviors often contribute in a rather complex way to the overall deposition phenomenon.

The calculation of the deposit growth from the deposition rates would lead to an asymptotic deposit height distribution. This would deform the shapes of the blades, necessitating reconstruction of the grid and recalculation of the flow field and particle deposition rates in a step-by-step manner. Furthermore, the calculation of deposit growth would have to include local removal

mechanisms such as erosion and shear stress that would have to be combined with a certain extent of measured deposition data in order to provide for the asymptotic local deposit height. This task has been performed in Bouris and Bergeles [7] for heat exchanger fouling but its complexity for the present application exceeds the scope of the paper. The only removal mechanism considered here is the hydrodynamic lift force included in Eq. (4).

3 Calculation of Deposition Rates on Compressor Blades

3.1 Configuration of Numerical Approach and Definition of Operating Conditions. The configurations that were studied were a compressor stator NACA65 type blade cascade (pitch-to-chord ratio $h/c=0.887$) and a rotor DCA type blade cascade ($h/c=0.776$). They were considered in two dimensions at the blades' midspan and general curvilinear multidomain grids were constructed for the passage between consecutive blades. For both the stator and the rotor, each grid had a total of 10,150 grid nodes and about 120 points on each blade surface. For the sake of numerical accuracy, care was taken so that the distance of the first grid point from the wall would give a y^+ value for the wall functions to be valid (here it was about $y^+ \sim 30-70$) while keeping the grid dense enough to correctly capture the details of the flow at the leading and trailing edge. The third-order accurate Osher Chakravarthy TVD scheme was used so that the compressible effects would be more accurately calculated. Numerical parametric studies of operating conditions were performed to find the design points of the stator and the rotor. Boundary conditions were: constant total pressure and temperature at the inlet and constant static pressure at the outlet. By regulating the outlet static pressure, the stator was found to be at optimum operating conditions regarding total pressure loss at an inlet Mach number of about $Mach_{in}=0.77$ while for the rotor it was $Mach_{in}=0.86$. For the case of the rotor, calculations were performed in the rotating frame of reference with the centrifugal forces acting in the plane normal to that being solved and thus neglected. The coriolis forces were also considered negligible in relation to the uncertainties of the widely applied two-dimensional assumption of the flow field calculation.

The solution of the flow field was used by the particle tracking algorithm for particle diameter sizes ranging from $0.1 \sim 2 \mu m$ and for particle materials Al_2O_3 and $CaCO_3$. The particles were injected into the flow, with the flow's instantaneous velocity, from 200 positions uniformly distributed along the inlet of the computational domain. The total number of particles used was 100,000 while a calculation with 300,000 showed the same general behavior proving statistical independence. The particle material properties, required for the deposition model were: (Al_2O_3): $\rho_p = 3900 \text{ kg/m}^3$, $\nu_p = 0.22$, $E = 370 \cdot 10^9 \text{ N/m}^2$, $k_p = 30 \text{ W/m K}$, $\Delta\gamma = 0.134$, $Y_{el} = 170 \cdot 10^6 \text{ Pa}$, ($CaCO_3$): $\rho_p = 2500 \text{ kg/m}^3$, $\nu_p = 0.3$, $E = 38 \cdot 10^9 \text{ N/m}^2$, $k_p = 2.75 \text{ W/m K}$, $\Delta\gamma = 0.15$, $Y_{el} = 38 \cdot 10^6 \text{ Pa}$. The surface was assumed to be steel and the required material properties were: (Steel): $\rho_s = 7800 \text{ kg/m}^3$, $\nu_p = 0.29$, $E = 210 \cdot 10^9 \text{ Pa}$, $Y_{el} = 9-15 \cdot 10^9 \text{ Pa}$. The mass distribution in the particle sizes was $m_p(d=0.1 \mu m)/m_{total} = 10$ percent, $m_p(d=0.5 \mu m)/m_{total} = 20$ percent, $m_p(d=1 \mu m)/m_{total} = 50$ percent, $m_p(d=2 \mu m)/m_{total} = 20$ percent. The choice of the two materials was based on evaluating the behavior of a hard material and a soft one while the diameter distribution's upper limit is one that is commonly found in compressor filters.

3.2 Results. The Mach number contours for the stator and the rotor at their respective operating conditions are presented in Figs. 1 and 2. The operating conditions considered here are of a relatively low inlet Mach number so that a clearly defined shock wave has not yet appeared, although the tendency towards it is evident. It is interesting to note that, although in the case of the stator the shock wave appears at about 25–30 percent of the chord

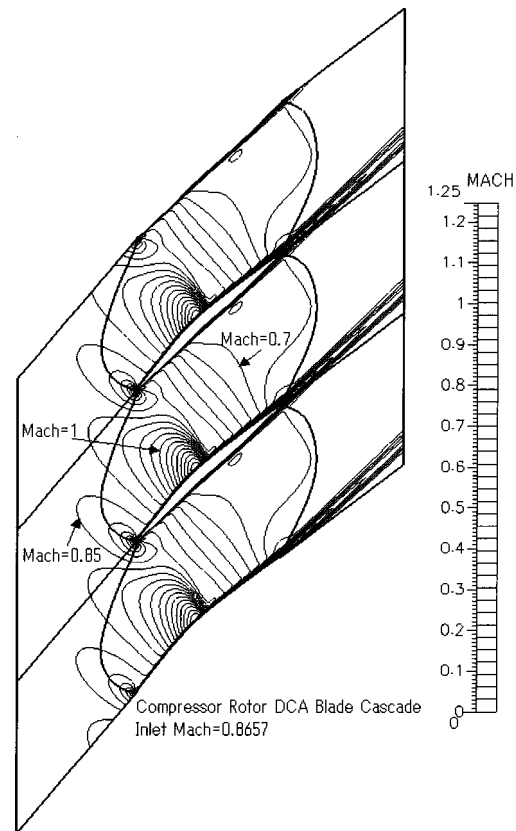


Fig. 1 Mach number contours for compressor rotor blade cascade with inlet Mach number 0.86

length from the leading edge, for the rotor it appears at about 45–50 percent of the chord length. This is obviously related to the geometry of the blade and the operating conditions but the point is made here because it will be called upon again during the discussion of the deposition rate distribution.

Figures 3, 4, and 5 show particle trajectories at the leading edge and the suction side of the stator and rotor while in Figs. 6–13 all the calculated deposition rate distributions for the stator and the rotor and for the two particle materials are presented. Care should be taken when observing the figures as the leading edge only has been plotted on the left axis while the rest of the graph follows the right axis. This was done so that the higher deposition rates present at the leading edge will not interfere with the analysis of the rest of the blade surface where the distributions' characteristics are on a much smaller scale. All the results presented here refer to deposition rates and not deposit heights or asymptotic deposits. If the removal mechanisms of erosion or fluid shear stresses were considered then the distribution of the final deposit might be different from that of the deposition rates, e.g., erosion on the leading edge would significantly reduce the growth rate of the deposit. Comments on the results of the deposition rate calculation will be made by comparing rotor-stator, then pressure side-suction side, and finally Al_2O_3 and $CaCO_3$.

3.2.1 Comparing Rotor-Stator. Although the deposition rates on the leading edge are an order of magnitude higher than on the rest of the blade surface in both the rotor and the stator and for both materials studied, it seems that the rotor's is generally lower. One must keep in mind that deposition on the leading edge is mostly related to the particles' inertia. This can be supported from the fact that the particle sizes at the leading edge are largely dominated by the 1 and $2 \mu m$ diameter particles. The behavior of the particle sizes near the leading edge is more clearly shown in Fig. 3 with the particle trajectories for Al_2O_3 particles of $d=0.1$ and 2

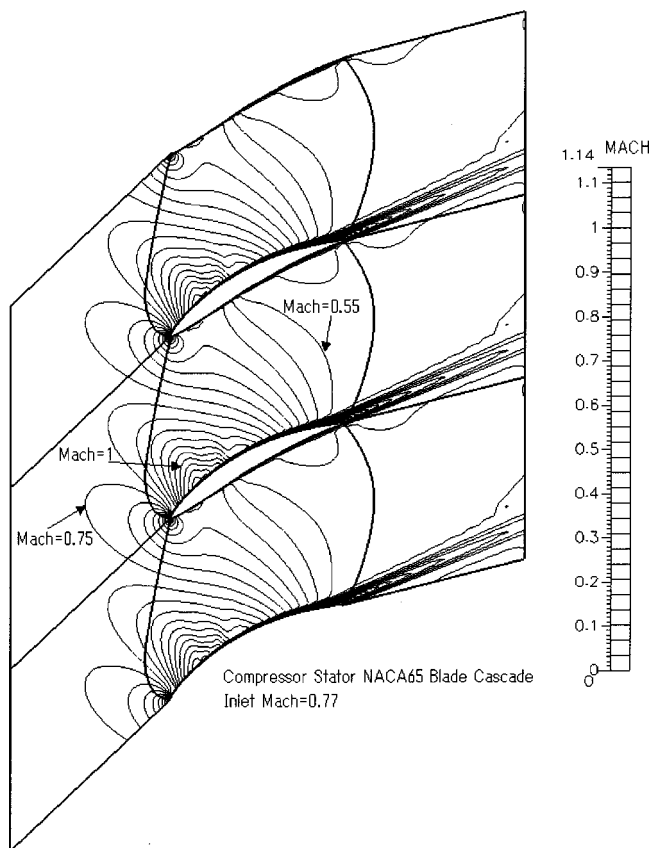


Fig. 2 Mach number contours for compressor stator blade cascade with inlet Mach number 0.77

μm near the stator leading edge. It is obvious that the smaller particles follow the streamlines, avoiding impact with the leading edge. Calculation of the particle Stokes numbers shows that only these two diameter sizes have Stokes numbers in the order of magnitude that indicates inertial behavior (the $1\ \mu\text{m}$ CaCO_3 has a Stokes number of 0.11 for the stator while the $2\ \mu\text{m}$ Al_2O_3 particle has a Stokes number of 1.03 for the rotor). Because of this inertial character of the leading edge deposition, the actual area of the leading edge that is perpendicular to the flow is important. The rotor is the thinner of the two blades and thus shows a smaller leading edge deposition rate. The effect of the thinner rotor shape can also be seen in Fig. 5 where the particle trajectories around the rotor suction side are shown to have a much smaller divergence from the flow than in the stator case (Fig. 4).

The dominance of the inertial impaction mechanism at the leading edge area was also noted by Wenglarz [3] for the case of a PFBC turbine. He also noted that for particle diameter sizes larger than around $1\ \mu\text{m}$, rebounds are not strong enough to carry particles across the passage and so the suction surface is usually free of particles larger than that size range. Grant and Tabakoff [20] performed numerical calculations in 1.5 stages of a compressor using $20\ \mu\text{m}$ diameter quartz particles and found that this size of particles do rebound off of the pressure surface or the leading edge and reach the suction side. In the present study, the particle sizes are not large enough for such behavior.

Some more observations can be made here regarding the particle sizes. On the pressure side, it is the stator blade that captures the heaviest particles and it is here where one observes the largest concentration of $2\ \mu\text{m}$ particles for both materials (compare Figs. 7 and 9 and Figs. 11 and 13). This is again related to inertial deposition phenomena since the relative impact angle of the flow for the stator is larger than that of the rotor. In Figs. 1 and 2, the lines defining the grid domains can still be seen and the symmetry

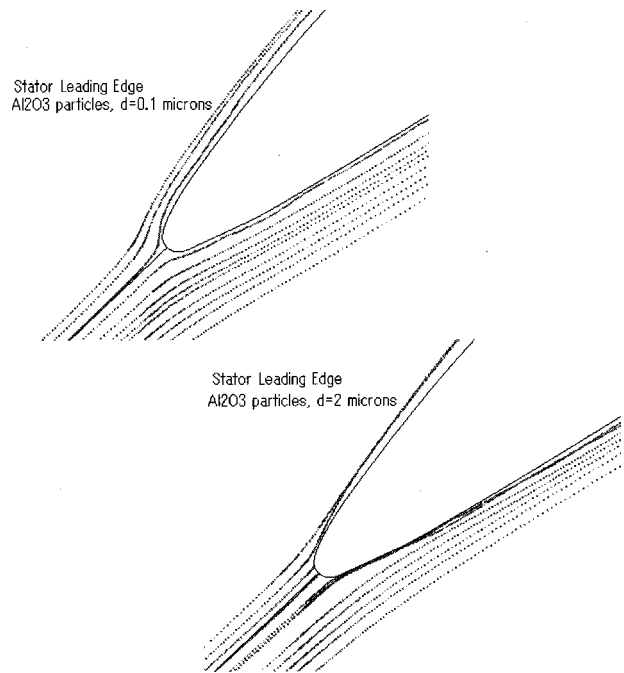


Fig. 3 Al_2O_3 particle trajectories near the stator leading edge for particle diameter sizes $d=0.1$ and $2\ \mu\text{m}$

line on the leading edge coincides with the flow direction. The difference in flow angle means that particles arriving at the stator pressure side will have a better chance of reaching the blade surface than in the case of the rotor who's thinner profile and positioning do not disturb the flow as much.

This effect of the flow angle and blade shape has a different effect on the suction side. There, the rotor's surface shows a larger

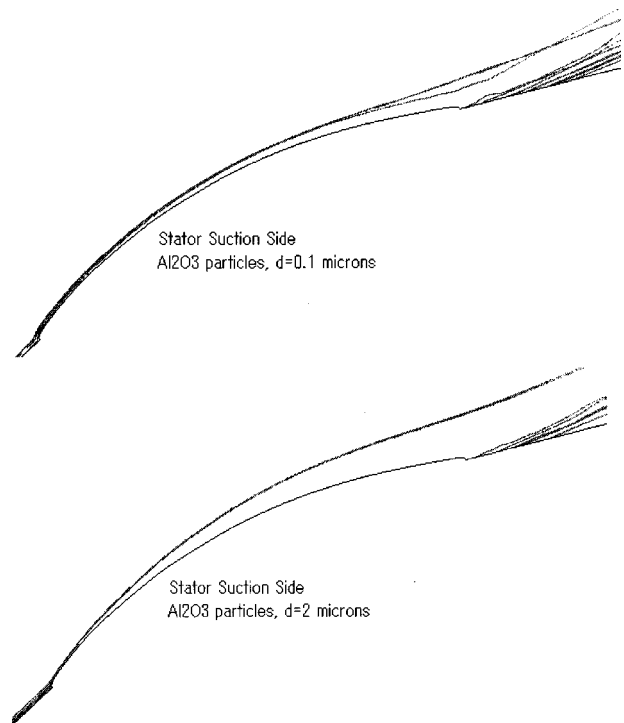


Fig. 4 Al_2O_3 particle trajectories near the stator suction side for particle diameter sizes $d=0.1$ and $2\ \mu\text{m}$

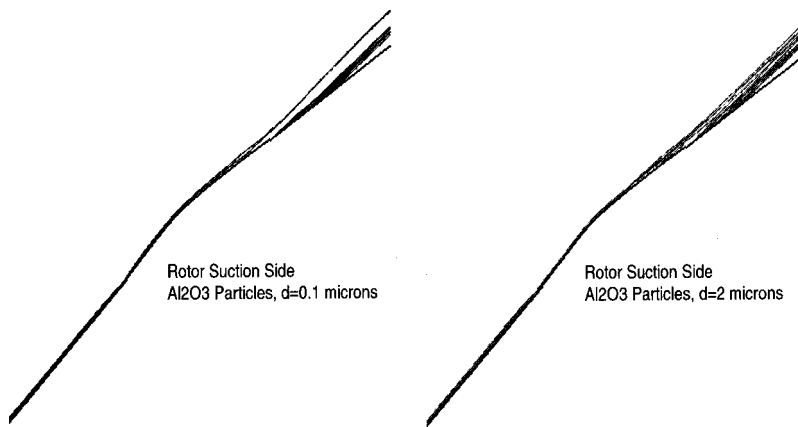


Fig. 5 Al_2O_3 particle trajectories near the rotor suction side for particle diameter sizes $d=0.1$ and $2\ \mu\text{m}$

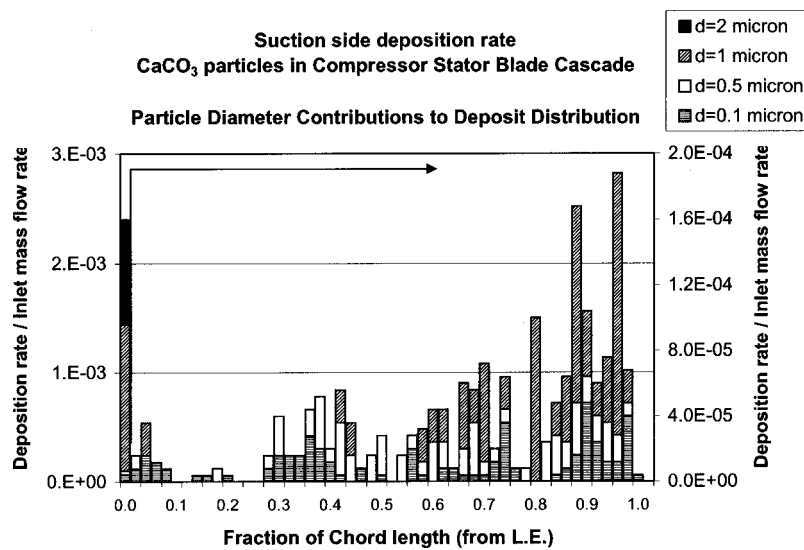


Fig. 6 CaCO_3 particle deposition rate distribution on suction side of compressor stator blade. (Arrow denotes graph area that follows right axis.)

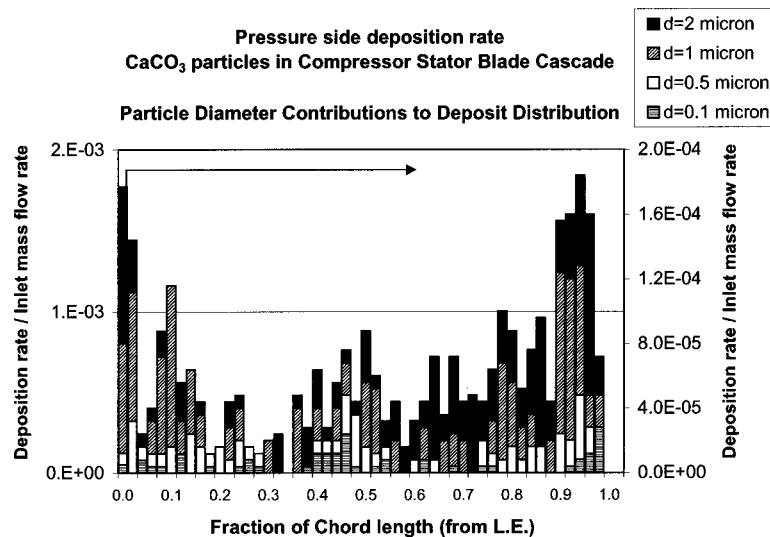


Fig. 7 CaCO_3 particle deposition rate distribution on pressure side of compressor stator blade. (Arrow denotes graph area that follows right axis.)

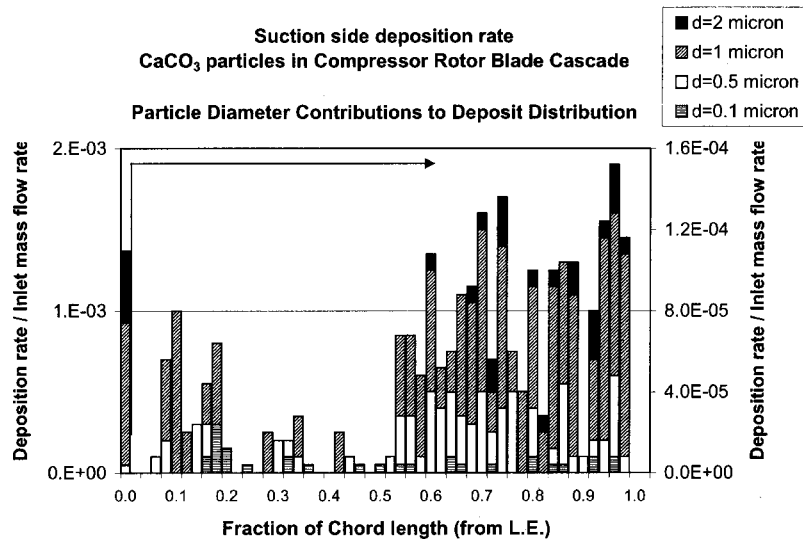


Fig. 8 CaCO_3 particle deposition rate distribution on suction side of compressor rotor blade. (Arrow denotes graph area that follows right axis.)

concentration of heavier particles (Figs. 6, 8, 10, and 12). The reason for this will be explained later in the comparison of pressure and suction-side surface deposition rates. It is pointed out here that the particle sizes found in the stator's deposition rate distributions are larger than the rotor's for the pressure side and smaller for the suction side.

The pressure sides of the rotor and the stator also have an interesting characteristic. Although that of the stator exhibits a relatively uniform distribution, the rotor's pressure side seems to show the highest deposition rate after the 30–40 percent chord length from the leading edge (Figs. 7, 9, 11, 13). Again, this must be attributed to the different mechanisms causing pressure side deposition in the rotor and the stator. For the case of the rotor, almost all deposition is due to diffusion processes and the turbulence levels in the boundary layer on the pressure side are not very high near the leading edge. In the case of the stator, the blade shape and positioning make it easier for particles to reach the surface and this is independent of the position on the chord of the blade.

3.2.2 Comparing Pressure Side–Suction Side. Regarding the differences between the pressure side deposition rate distributions and those of the suction side, it has previously been pointed out that the suction side of the rotor captures larger particles than that of the stator (compare Figs. 6, 8, 10, 12). This is due to the fact that the rotor blade's profile and positioning allow the larger particles to come closer to the suction surface thus allowing higher possibilities for them to be carried to the surface by turbulent diffusion. In the case of the stator, it can be seen from the trajectories in Fig. 4 that the highly curved suction side surface is very difficult to follow for particles with large inertia. One must keep in mind that the particle Stokes numbers for these cases are actually very close to the limit of $\text{Stk}=1$ between inertial behavior and “fluid particle” behavior. Therefore, even for the heavier particles used in the calculations, there will be some diffusion present and, in the case of the rotor suction side, this explains the presence of some larger particles.

As a general observation, for the reasons related to particle inertia that were mentioned above, the particles found on the suc-

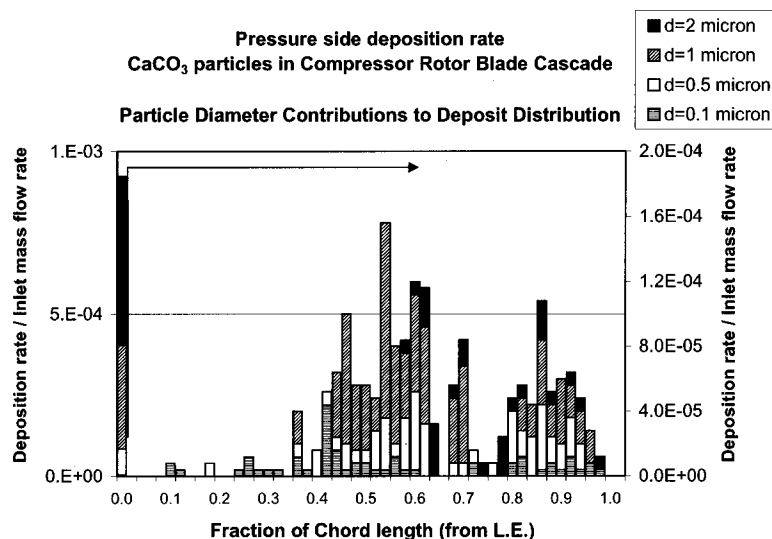


Fig. 9 CaCO_3 particle deposition rate distribution on pressure side of compressor rotor blade. (Arrow denotes graph area that follows right axis.)

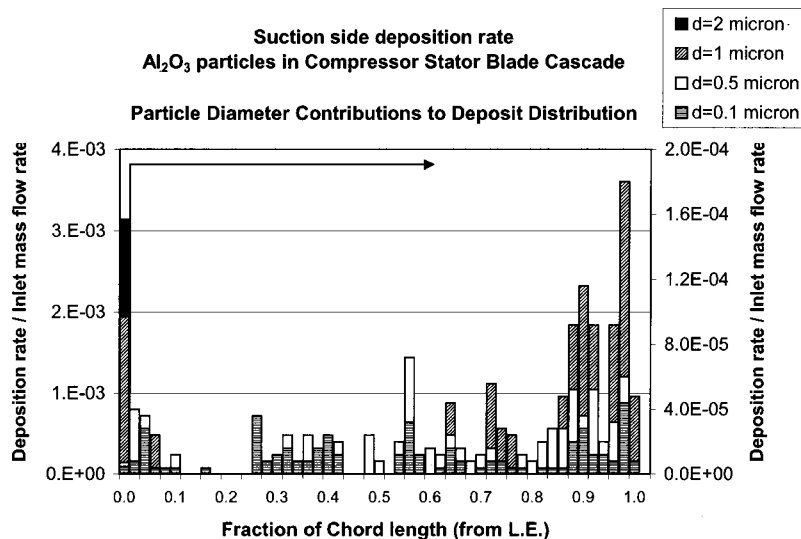


Fig. 10 Al_2O_3 particle deposition rate distribution on suction side of compressor stator blade. (Arrow denotes graph area that follows right axis.)

tion side are always smaller and lighter than the ones found on the pressure side. This applies to both rotor and stator and to both materials. It was also observed by Wenglarz [3] who states that in the industrial tests, virtually all the particles on the turbine suction surfaces were smaller than $1.5 \mu\text{m}$ in diameter.

Finally, attention is called to the effect of the presence of a shock wave, or more specifically speaking, of regions with $\text{Mach} > 1$. This effect is noticeable only on the suction side since, under the present operating conditions, the shocks are not strong enough to reach across the passage to the pressure side (Figs. 1 and 2). On the suction side of both the rotor and the stator a clear drop can be seen in the deposition rate distributions for both materials (Figs. 6, 8, 10, 12). In each case, the position is the region where the Mach number is close to, or over, unity. In these regions, there is an increase in velocities and turbulence kinetic energy with a decrease in local static pressure. The particles' velocities increase in the high Mach number regions and so, since diffusion is the major deposition mechanism on the suction side, they bypass the area without reaching the surface. On the other

hand, downstream of this region, the particle velocities are influenced by the reduction in flow velocity and the increase in turbulence kinetic energy. This facilitates deposition by turbulent diffusion and therefore the deposition rates are relatively uniform downstream of the high Mach number regions.

3.2.3 Comparing Al_2O_3 and CaCO_3 Particles. The differences that are at first obvious from the results are basically related to the different Stokes numbers of the particles. Calculations were made using the same particle diameters with different materials, resulting in different Stokes numbers so that the effect of material properties is not independent of the particle motion in the flow. It was decided to use the same particle diameters since the actual filtering procedure in compressors is usually based on size instead of mass. However, the results prove quite interesting if one considers that even for particles of totally different material properties, it is their behavior with respect to the flow that is the most important factor for deposition.

In previous work [21] calculations using the same deposition

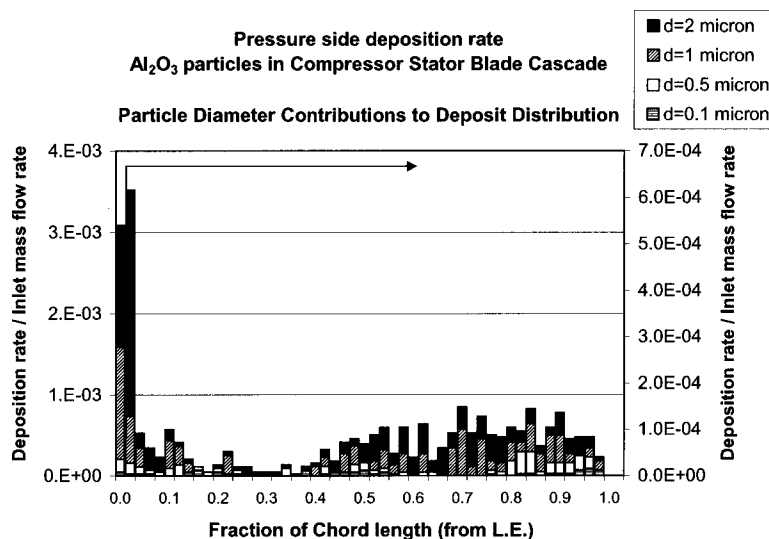


Fig. 11 Al_2O_3 particle deposition rate distribution on pressure side of compressor stator blade. (Arrow denotes graph area that follows right axis.)

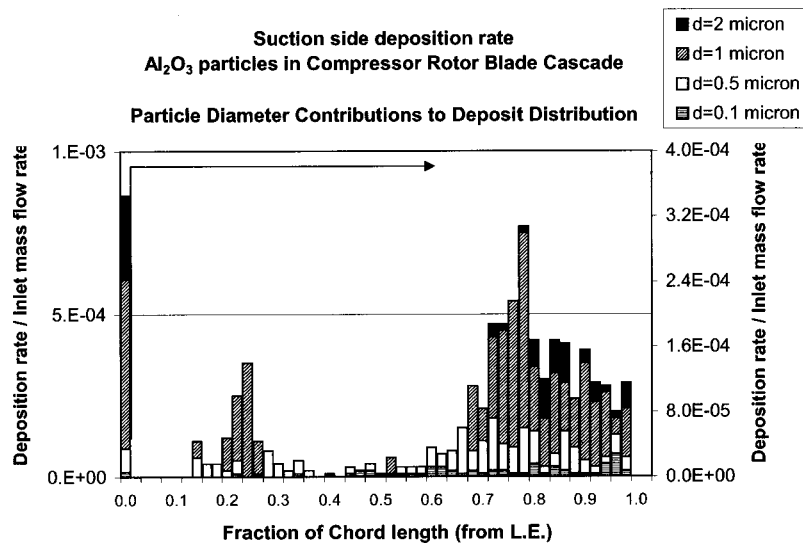


Fig. 12 Al_2O_3 particle deposition rate distribution on suction side of compressor rotor blade. (Arrow denotes graph area that follows right axis.)

model were performed for particles of various materials impacting vertically onto a flat plate and it was found that the results were in good agreement with experimental measurements of Wall et al. [18], indicating that the particle material is indeed an important factor for adhesion in that type of configuration.

4 Conclusions

Compressor stator and rotor blade fouling are considered important factors in assessing operational efficiency of turbomachinery. Many methods to deal with the problem of deposit formation have been proposed and are being applied. Since it is a subject that has direct impact on the operational costs, if further improvement is to be made, the mechanisms and the local phenomena present during fouling of the compressor's components should be fully understood. In an attempt to analyze the local deposit formation mechanisms, the CFD-ACE software package has been used in combination with a Lagrangian particle tracking method-

ology and an energy balance deposition model to calculate deposition rate distributions in conventional compressor stator and rotor blade cascades.

The numerical methodology that was applied allows the evaluation of the combined influence of many physical phenomena including the characteristics of the flow, the particle arrival mechanisms and the particle and surface material properties. Both a stator and a rotor blade cascade have been studied while the particle size range was $d = 0.1 \sim 2 \mu\text{m}$ allowing for inertial and diffusional mechanisms of deposition. Furthermore, two different particle materials were used.

The main conclusion that can be drawn is that the leading edge shows the highest deposition rate, being about one order of magnitude higher than the rest of the blades' surfaces, for both the rotor and the stator. The mechanism governing the leading edge deposition rate is inertial impaction while the same mechanism dominates the stator pressure side. These regions are prone to direct impact of larger and heavier particles making them vulner-

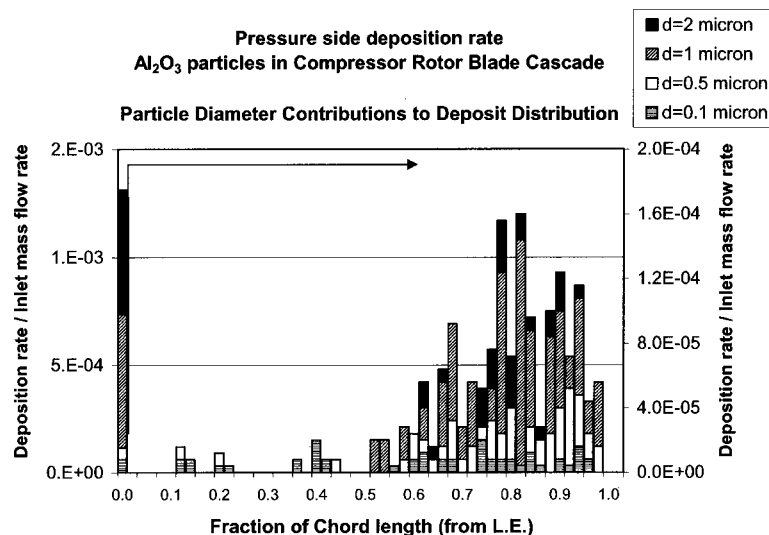


Fig. 13 Al_2O_3 particle deposition rate distribution on pressure side of compressor rotor blade. (Arrow denotes graph area that follows right axis.)

able not only to deposition but also to erosion. Furthermore, the larger particle sizes that deposit there will also increase the profile thickness and surface roughness of the blade, thus playing an important part in deviation from design condition operation. It is suggested that the effect of the leading edge and stator pressure side fouling and or blade profile change might warrant some further investigation as was done by Suder et al. [5] for a compressor rotor.

Turbulent diffusion is the main mechanism of deposition on the rest of the blades' surfaces. In the case of the stator, only the lighter particles are able to follow the highly curved suction side surface and therefore the deposit formed there will contain mainly the small particle size range. This is true for both sides of the rotor. The presence of a high Mach region and possibly a shock wave causes an increase in the turbulent kinetic energy near the blade thus facilitating deposition. This is in a slight contradiction with the fact that the boundary layer thickens after the shock and so further study might prove interesting.

Finally it is interesting to note that the effect of different material properties is not as important as the effect of particle motion in the flow. This is due to the dominance of diffusion as the deposition mechanism so that whether the particle will reach the surface and how becomes more important than how hard or soft the particle is.

It should be emphasized that all the results presented here refer to deposition rates and not deposit heights or asymptotic deposits. The difference is that most deposit removal mechanisms (i.e., erosion, centrifugal forces, fluid shear, turbulent bursts, etc.) have been left out of the calculation. These mechanisms could be important in some areas and might enhance the effect of, e.g., particle material since a hard particle would cause more erosion to the already formed deposit than a soft one. Also, during calculation of the flow field, three-dimensional effects were neglected. These could be influential to the whole phenomena especially in the case of the rotor where centrifugal and coriolis forces would cause the particles to move off the two-dimensional plane that was considered here. The authors realize that more detailed comparisons with experimentally or industrially observed deposit distributions would lead to much more general conclusions but measurements detailed enough to be compared with the numerical results are rare and even more so if one looks for clearly defined operating conditions. It was for this reason that the study was performed on both stator and rotor with different particle sizes and materials and using exactly the same numerical procedure. This allows reliable comparisons and conclusions to be drawn from the relational behavior of the various parameters. It is believed that the results presented here give many indications and directions for further and more detailed study and understanding of the fouling of compressor blade cascades.

Nomenclature

c	= mean molecular speed (m/s)
C_D	= particle drag coefficient
d	= particle diameter (m)
E	= Young's modulus (Pa)
g	= acceleration of gravity vector (m/s ²)
G_p	= is the particle volume (m ³)
k_p, k_f	= thermal conductivities of the particle and the fluid (W/m K)
$Mach = V - U / (\gamma RT)^{0.5}$	= particle Mach number
m_p	= particle mass (kg)
Q'_A	= particle-surface adhesion energy (J)
Q_i	= particle kinetic energy at impact (J)
Q_L	= particle energy lost to elastic wave propagation (J)

Q_{lift}	= aerodynamic lift energy (J)
Q_P	= particle energy lost to plastic deformation (J)
R	= universal gas constant (J/K/kg)
$Re_p = V - U / \nu$	= particle Reynolds number
r_p	= particle radius (m)
$Stk = \rho_p d_p^2 U_\infty / (18 D_{cyl} \mu)$	= Stokes number
T	= temperature of the gas (K)
t	= time (sec)
T_o	= fluid local temperature (K)
U, V	= instantaneous velocity of fluid and particle, respectively (m/s)
$y^+ = (\tau_w / \rho_f)^{1/2} y / \nu$	= nondimensional distance from a wall
Yel	= elastic yield coefficient (Pa)

Greek Symbols

$\partial / \partial t$	= temporal derivative along the discrete particle trajectory
ρ_f, ρ_p, ρ_s	= fluid, particle, and surface density (kg/s)
$\Delta \gamma$	= interfacial energy per unit area (J/m ²)
$\lambda = 2 \mu / \rho c$	= mean molecular path (m)
μ, ν	= fluid dynamic and kinematic viscosity, respectively (kg/m s), (m ² /s)
ν_p	= Poisson's ratio
τ_w	= shear stress (kg/m s ²)

References

- [1] Valenti, M., 1998, "A Drier Way to Clean Turbines," CME, Chart. Mech. Eng., Mar., pp. 98–100.
- [2] Nomura, M., Morishita, T., and Kan, S., 1977, "An Experiment of Deposit Formation on Surface of an Air Cooled Gas Turbine Blade," *Tokyo Joint Gas Turbine Congress*, May 22–27, Gas Turbine Institute of Japan, Tokyo, pp. 566–573.
- [3] Wenglarz, R. A., 1981, "An Assessment of Deposition in PFBC Power Plant Turbines," ASME J. Eng. Power, **103**, pp. 552–560.
- [4] Ul Haq, I., and Saravanamuttoo, H. I., 1993, "Axial Compressor Fouling Evaluation at High Speed Settings Using an Aerothermodynamic Model," ASME Paper No. 93-GT-407.
- [5] Suder, K., Chima, R., Strazisar, A., and Roberts, W., 1995, "The Effect of Adding Roughness and Thickness to a Transonic Axial Compressor Rotor," ASME J. Turbomach., **117**, pp. 491–505.
- [6] Bouris, D., and Bergeles, G., 1996, "Particle-Surface Interactions in Heat Exchanger Fouling," ASME J. Fluids Eng., **118**, pp. 574, 581.
- [7] Bouris, D., and Bergeles, G., 1997, "Numerical Calculation of the Effect of Deposit Formation on Heat Exchanger Efficiency," Int. J. Heat Mass Transf., **40**, No. 17, pp. 4073–4084.
- [8] Van Doormal, J. P., and Raithby, G. D., 1984, "Enhancements of the SIMPLE Method for Predicting Incompressible Fluid Flows," Numer. Heat Transfer, **7**, pp. 147–163.
- [9] Chakravarthy, S. R., and Osher, S., 1985, "A New Class of High Accuracy TVD Schemes for Hyperbolic Conservation Law," AIAA Paper 85-0363.
- [10] Launder, B., and Spalding, D., 1972, *Mathematical Models of Turbulence*, Academic Press, London.
- [11] Saffman, P., 1965, "The Lift on a Small Sphere in a Slow Shear Flow," J. Fluid Mech., **22**, p. 385; and Corrigendum, 1968, **31**, p. 624.
- [12] Talbot, L., Cheng, R. K., Schefer, R. W., and Willis, D. R., 1980, "Thermophoresis of Particles in a Heated Boundary Layer," J. Fluid Mech., **101**, pp. 737–758.
- [13] Smoot, L. D., and Pratt, D. T., 1979, *Pulverized-Coal Combustion and Gasification*, Plenum Press, New York.
- [14] Henderson, C., 1976, "Drag Coefficients of Spheres in Continuum and Rarefied Flows," AIAA J., **14**, No. 6, pp. 707–708.
- [15] Reed, J., 1985, "Energy Losses due to Elastic Wave Propagation During an Elastic Impact," J. Phys. D **18**, pp. 2329–2337.
- [16] Fowkes, F., 1964, "Attractive Forces at Interfaces," Ind. Eng. Chem., **56**, No. 12, pp. 40–52.
- [17] Bitter, J., 1963, "A Study of Erosion Phenomena—Part II," Wear, **6**, pp. 169–190.
- [18] Wall, S., John, W., and Goren, S., 1988, "Application of Impact Adhesion Theory to Particle Kinetic Energy Loss Measurements," *Particles on Surfaces 2*, K. L. Mittal, ed., Plenum Press, New York.
- [19] Bitter, J., 1963, "A Study of Erosion Phenomena—Part I," Wear, **6**, pp. 5–21.
- [20] Grant, G., and Tabakoff, W., 1975, "Erosion Prediction in Turbomachinery Resulting From Environmental Solid Particles," J. Aircr., **12**, No. 5, pp. 471–478.
- [21] Bouris, D., 1997, "Numerical Investigation of Flow Field and Fouling in Heat Exchangers," PhD. thesis, National Technical University of Athens, Department Mechanical Engineering, Athens, Greece.

Ceramic Turbine Engine Demonstration Project: A Summary Report

B. Schenk

Honeywell Engines, Systems & Services,¹
APU Technology Development,
111 S. 34th Street, M/S 503-319,
Phoenix, AZ 85034

Honeywell Engines, Systems & Services has successfully addressed critical concerns that are slowing commercialization of structural ceramics in gas turbines. The U.S. Department of Energy (DoE) sponsored Ceramic Turbine Engine Demonstration Project (CT-EDP) had the mission of advancing ceramic gas turbine component technology toward commercialization. The thrust of the program was to “bridge the gap” between ceramics in the laboratory and near-term commercial heat engine applications. Most of this mission has been achieved. The 331-200[CT] auxiliary power unit (APU) test bed featured ceramic first-stage nozzles and blades. Fabrication of ceramic components provided manufacturing process demonstration scale-up to the minimum levels needed for commercial viability. Through this program, design methods refinement and the development of new design methods unique to ceramic turbine components have been supported and validated in rig and development engine testing. Over 6800 hours of on-site endurance tests demonstrated component reliability. Additional field testing in APUs onboard commercial aircraft and stationary industrial engines has been initiated and will continue beyond completion of this program. [DOI: 10.1115/1.1417983]

Introduction

During 1993, the still ongoing Advanced Turbine Technology Applications Project (ATTAP), funded by the U.S. Department of Energy (DOE) and administered by the National Aeronautics and Space Administration (NASA) under Contract No. DEN3-335, was refocused to more effectively address the critical issues slowing the commercialization of structural ceramics in gas turbine engines, i.e., ceramic component reliability demonstration, ceramic design technology refinement, and cost-effective ceramic component fabrication. Honeywell Engines, Systems & Services changed the ATTAP ceramic engine test bed from the AGT101 automotive engine to utilizing the Honeywell Model 331-200[CT] auxiliary power unit (APU) as a test bed/demonstrator, with the first-stage turbine modified to incorporate ceramic nozzles and blades. The program was to provide the supporting experience, design methodologies, and fabrication capability by domestic U.S. ceramics manufacturers necessary for limited commercialization of ceramics in aeronautical applications, and provide a solid technological foundation supporting automotive ceramic heat engine applications.

During 1994, the former ATTAP was retitled the Ceramic Turbine Engine Demonstration Project (CTEDP), to indicate a new emphasis by the DOE's Office of Transportation Technologies in support of reductions in U.S. domestic oil consumption and vehicle emissions by hybrid vehicle development employing ceramic technology in advanced gas turbine engines. This work was sponsored by the U.S. DOE as part of the Turbine Engine Technologies Program to develop technology for an improved automobile propulsion system under Title III of U.S. Public Law 95-238, “Automotive Propulsion Research and Development Act of 1978.” Since 1997, the CTEDP has been administered by the DOE and authorized under DOE Contract No. DE-AC02-96EE50454.

The CTEDP strategy was developed to augment the maturing

ceramics technology by developing the infrastructure and engineering disciplines necessary to overcome those barriers which prevent its commercialization. At the beginning of this program, the principal barriers to the commercialization of ceramics were seen as

- immature supporting technologies,
- underdeveloped production capability, and
- inadequate demonstration.

The overall program plan provided an approach to resolve each of these issues. The following discussions summarize the progress to date in various project activities and outline the lessons learned under this program as well as recommendations to finally achieve commercialization of structural ceramic components in gas turbine engines. This work was initiated in 1993 and scheduled to be complete at the end of 1999. Over the course of this program, annual technical progress papers have been presented and published at the yearly ASME Gas Turbine and Aeroengine Technical Congress ([1–6]).

Background

The CTEDP is following a natural progression based on its predecessors. The focus is on near-term production capability, drawing heavily on “lessons learned” from the problems and successes on the previously completed ceramics development and demonstration programs.

The DARPA/Navy Ceramic Gas Turbine Engine Demonstration Program (1979 to 1982), and the USAF Ceramic Components For Turbine Engines Program (1979 to 1982), provided the foundation for the modern CTEDP. These programs utilized a test bed of similar design to the Honeywell production model 331-200 APU. Significant progress was successfully achieved in demonstration of ceramic axial inserted turbine blades, as well as initial exploration of ceramic design technologies, including contact failure, particle impact damage resistance, and pioneering computer-based probabilistic component life prediction.

The DOE/NASA Advanced Gas Turbine–AGT101 Engine Program (1980 to 1987), pursued several high-risk technologies, including ceramics for future automobile engine applications. The

¹Formerly AlliedSignal Engines & Systems.

Contributed by the International Gas Turbine Institute (IGTI) of THE AMERICAN SOCIETY OF MECHANICAL ENGINEERS for publication in the ASME JOURNAL OF ENGINEERING FOR GAS TURBINES AND POWER. Paper presented at the International Gas Turbine and Aeroengine Congress and Exhibition, Munich, Germany, May 8–11, 2000; Paper 00-GT-532. Manuscript received by IGTI, Nov. 1999; final revision received by ASME Headquarters, Feb. 2000. Associate Editor: D. Wisler.

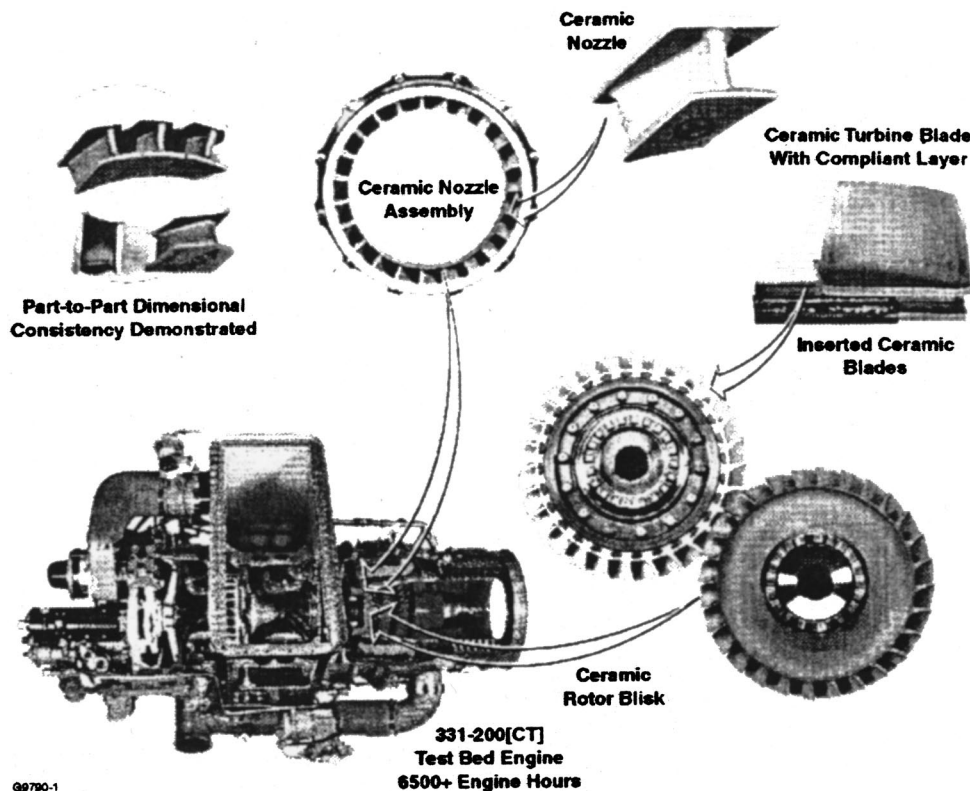


Fig. 1 Ceramic turbine engine demonstration test bed is based on proven model 331-200 auxiliary power unit with ceramic first-stage turbine components

AGT101 program succeeded in simultaneously demonstrating many related advanced engine technologies, and identified the most critical areas in ceramic engine technology needing further development.

The DOE/NASA Advanced Turbine Technology Project—ATTAP/AGT101 Program (1987 to 1992), emphasized the development of critical ceramics technologies, using the AGT101 automotive test bed. Significant progress was made in the ATTAP/AGT101 program toward successful impact-resistant ceramic turbine designs and ceramic component processing. However, the AGT101 engine proved to be inadequate as a test bed for the advanced ceramic technologies. This was because the AGT101 was designed as a demonstrator for several high-risk technologies, including the high-temperature ceramic regenerator, low-emission ceramic combustor, low-friction gas bearings, all-ceramic hot section structures, and impact-resistant ceramic turbine. As such, AGT101 reliability as a turbine test bed was not adequate for long-term endurance testing and evaluation.

The present DOE Ceramic Turbine Engine Demonstration Project continued refinement of ceramics technologies and design methods, and focused fabrication development on a scale up of demonstrated technologies to pilot-production levels. To adequately demonstrate ceramic technology, over 6800 hours of endurance testing have been completed, utilizing a reliable test bed based on the Honeywell Model 331-200/250 APU (Fig. 1). This APU is a fully developed gas turbine with current production applications in the Boeing 757 and 767 aircraft, as well as in the Airbus A300 and A310 aircraft. Thus, this APU has higher capability for successfully accomplishing not only long-term endurance testing, but also offers the opportunity for extended field evaluation of ceramic components which is currently progressing in several aircraft applications as well as in a ASE8-1000[CT] industrial engine, a derivative from the very reliable Model 331-turboprop and 331-200/250 APU engines.

The progress of the Ceramic Turbine Engine Demonstration Project toward commercialization of ceramic engine technology may be visualized with the chart in Fig. 2. This curve, based on cumulative experience in engine demonstration test hours and quantity of ceramic engine components achieved from 1980 to present shows the geometric trend in ceramic technology improvement. Figure 2 shows that ceramic engine technology is on the threshold of exploitation. The Ceramic Turbine Engine Demonstration Program has enabled very near-term commercialization in low volume, premium gas turbine applications such as airborne

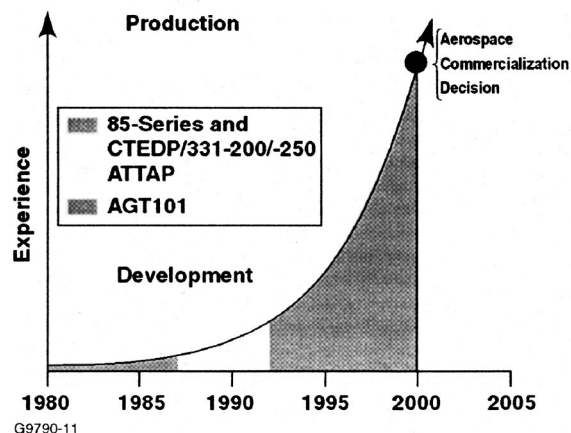


Fig. 2 CTEDP targets solutions for early ceramics commercialization

APUs, paving the way toward production of ceramic components for industrial microturbine applications for advanced distributed power generation.

Technology Development

All of the technologies described in the following section were identified as critical to the success of ceramics in commercial gas turbine applications. Only a very brief description of the major accomplishments of each development activity will be given in this paper. More detailed descriptions can be found elsewhere ([1–6]).

Impact Design Methods Refinement. The end goal of this activity has been the development of a method capable of accurately predicting structural impact damage for any ceramic component from carbon particles (combustor carbon), which resulted in design guidelines for impact-resistant, axial ceramic turbine blades. The development activities included

- incorporation of a newly developed carbon pulverization model into the DYNA3D finite element analysis computer code.
- computational fluid dynamics analyses using the RAMPANT code to predict carbon particle trajectories through the 331-200[CT] ceramic stator system, and to predict the resulting particle velocities and impact locations at the ceramic blade leading edges for various particle diameters and release velocities at the combustor exit.
- impact testing of ceramic axial turbine blades including blade strain measurements at the University of Dayton Research Institute (UDRI), in Dayton, OH. Results correlated well with the predictions.
- analytical study of various blade designs similar to the 331-200[CT] turbine blade, but differing in critical geometric parameters. A Taguchi L4 array was used in this study in which the effects of blade (tip) thickness, taper ratio, and twist on peak stress during impact were evaluated.
- integration of the dynamic impact stress predictions from the DYNA3D code with mechanical and thermal stress predictions from the ANSYS code.
- probabilistic life assessment of ceramic components subjected to these combined loading states using the CERAMIC/ERICA codes, ([7]).

Contact Design Methods Refinement and Blade Attachment Technology. The goal of this activity was to develop design tools to predict strength and life for ceramic/ceramic and ceramic/metal interfaces under gas turbine operating conditions, and to generate an improved understanding of the conditions within highly loaded ceramic interfaces. This knowledge is then used to derive useful tools for designing most cost-effective robust ceramic axial blade attachments for production gas turbines. These design solutions necessarily require a thorough understanding of the blade attachment contact stresses and the environmental and geometric factors that control these stresses. The development activities included

- design and fabrication of a contact rig for evaluation of ceramic contact interfaces of various configurations under extreme loads and elevated temperatures. Rig operation included the effects of normal contact stress, tangential contact stress, combinations of normal and tangential stresses (sliding motion), cyclic loading, and contact with high background stresses in the ceramic specimens.
- determination of the coefficient of friction for various material combinations.
- determination of the strength degradation which may have occurred as a result of contact damage.
- assessment of compliant layers, surface topography and tolerance effects, and surface strength with respect to machining direction.

- cyclic thermomechanical ceramic blade attachment subelement rig testing using a standard tensile testing machine which simulated engine disk and ceramic blade attachment deflection and load distribution characteristics.
- cyclic spin tests at room temperature and at elevated temperature in which various anti-friction treatments were applied to several types of blade compliant layers in order to evaluate wear characteristics and durability of the compliant layer systems.
- contact stress finite element analysis (FEA) in order to better understand the benefit of the compliant layer in the ceramic blade attachment system, including the effects due to plastic deformation of the compliant layer. The contact rig specimen geometries were modeled, so that a direct link between the analysis and the contact rig data could be established.

This work resulted in a proprietary compliant layer system developed by the Honeywell Laboratories, which demonstrated exceptional life and negligible wear.

Oxidation/Corrosion Characteristics of Ceramic Materials. Auxiliary power units and industrial engines are frequently used in high salt ingestion (e.g., coastal airport) operating environments, which can accelerate turbine component degradation. Surface recession and surface pitting associated with hot corrosion and water vapor attack have the potential to adversely affect the strength of silicon nitride components above 900°C. Environmental component life degradation therefore is of significant concern to the success of ceramic gas turbine applications.

In order to better recognize and avoid severe degradation conditions associated with hot corrosion and oxidation of ceramic components, Honeywell developed the CERSRL code ([8]) to predict the effects of duty cycle, environmental, and statistical scatter effects on tensile and stress-rupture lives. Predicted component life is dependent upon engine design (stress, temperature, pressure, fuel/air ratio, gas velocity, and inlet air filtration), mission usage (fuel sulfur content, location (salt in the air), and times at duty cycle power points), and material system parameters (Weibull modulus, characteristic strength, crack growth behavior, and coating (if any)). Additional experimental activities included

- burner rig testing of various coated (CVD zircon, CVD tantalum oxide, CVD and plasma-sprayed mullite) and uncoated silicon nitride materials in salt laden environment.
- burner rig testing of various uncoated silicon nitride materials in oxidizing combustion environment at different gas velocities, pressures, and temperatures.
- determination of fast fracture strength degradation, weight, and dimensional changes, following burner rig exposure.

The experimental results (symbols in Fig. 3) regarding water vapor accelerated oxidation of silicon nitrides were in close agreement with the empirical surface recession model (solid lines in Fig. 3) suggested by NASA ([9]).

Proof Test Techniques. The focus of this effort has been to identify cost-effective proof testing techniques to ensure the quality of ceramic hardware prior to engine installation. The goals were to develop proof testing methods that are accurate, yet inexpensive, that may potentially be used by ceramic component manufacturers and users. The study concluded that a simple flame impingement test is the preferred nozzle proof test method. The flame impingement stresses the vane trailing edges, which typically exhibit the highest stresses in the part during engine operation. The rig Fig. 4 creates thermal gradients on the ceramic nozzle by heating and cooling simultaneously. An infrared camera is used to measure the temperature distribution of the ceramic nozzle. Thin-film thermocouples were initially used to evaluate the thermal profile measured by the infrared camera. Repeatability of this proof test process has been assessed systematically and the system was found to be stable and measurement variation was adequate.

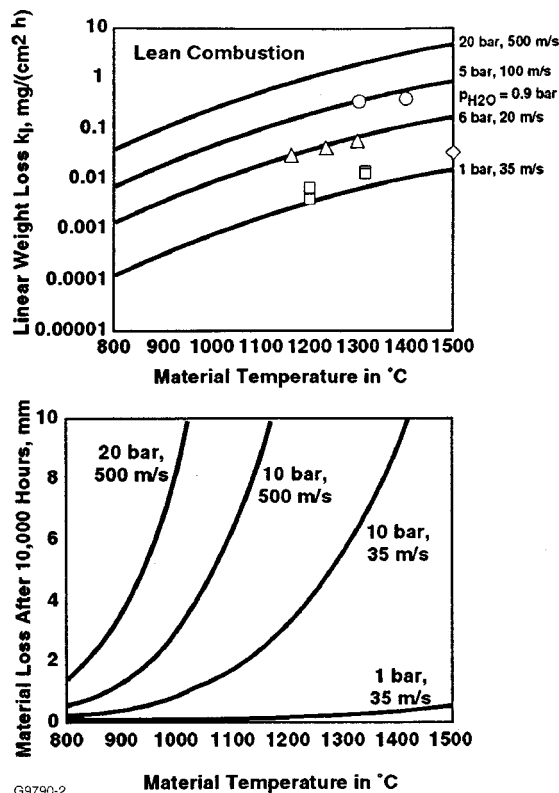


Fig. 3 Ceramic airfoil applications are extremely limited by surface recession. Extensive coatings research and development needed for successful ceramic gas turbine applications in aggressive environments.

Additionally, a mechanical test rig was designed and fabricated for proof testing the nozzle attachment features.

Thin-Film Instrumentation Development. Technology for chemical vapor deposition (CVD) methods to apply thin-film strain gages and thermocouples on silicon nitride gas turbine components has been developed and demonstrated. These efforts were the result of work performed in Honeywell's laboratories, subcontract work by the University of Rhode Island (URI, Providence, RI), and collaboration with the NASA Glenn Research Center (Cleveland, OH). The strain gage fabrication efforts used photo-

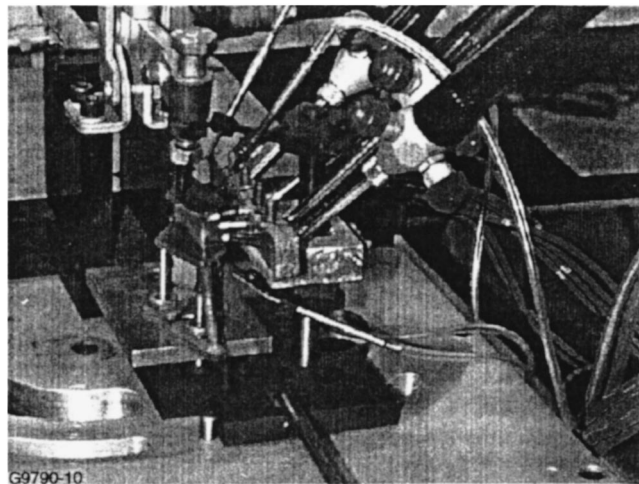


Fig. 4 Ceramic nozzle thermal proof test rig

Table 1 Ceramic component manufacturing scale-up goals

Item	Goal
Individual process capability	500 parts/month
Overall yield	75 percent
Demonstrated overall process capacity	100 parts/month
Cost	<\$300 per part

masking and sequential deposition methods to apply gage elements to the ceramic turbine blade airfoil surfaces and to attach the required leadfilms to the blade root area. Under in-house fabrication efforts, Honeywell Engines, Systems & Services has successfully deposited and fabricated thin-film palladium/chrome dynamic strain gages on SN252 and AS800 silicon nitride turbine blades.

Ceramic Components Quantity Fabrication Demonstration

The purpose of this activity has been to develop the capability of the domestic U.S. ceramic engine component suppliers to provide quality components in sufficient quantities to support scale-up to engine production, and to move the component fabrication process out of the laboratory and into an environment where components of consistent high quality can be made economically. Initiated in late 1993, two ceramics manufacturers, Norton Advanced Ceramics (NAC, in East Granby, CT) and Honeywell Ceramic Components (CC, in Torrance, CA), have been challenged to improve their demonstrated fabrication processes and develop methods and procedures to achieve the quantity production goal by building a pilot facility to demonstrate production of over 100 parts per month, on a continuous basis for several months (Table 1). Since NAC announced their business decision to discontinue production of gas turbine engine ceramics and terminated participation in this program by mid 1995, Kyocera Industrial Ceramics Company (KICC, in Vancouver, WA) initiated subcontract work during the third quarter of 1995.

During their rather short participation in the program, NAC focused their activities on the elimination of iron inclusions and demonstration of closed-loop processing (CLP) of NT164 silicon nitride components.

Already in 1994, CC demonstrated the feasibility of AS800 silicon nitride as a potentially lower cost turbine component material with respect to both material properties and shape capability, which enabled them to replace the glass-encapsulated, hot isostatic pressed (HiPped) GN-10 material with gas-pressure-sintered AS800 for the scale-up demonstration.

KICC initially focused on ceramic nozzle fabrication using their gas-pressure-sintered SN252 silicon nitride material and their proprietary hybrid molding process. By mid 1996, at the request of Honeywell Engines, Systems & Services, a material change to SN282 silicon nitride was initiated due to the intermediate temperature oxidation problems of SN252.

CC's and KICC's specific activities are described in more detail elsewhere ([4-6]). However, at the end of these subcontract activities in 1999, both suppliers have been able to demonstrate the capability of producing 331-200[CT] ceramic nozzles meeting all blueprint specifications at the rate of 100 parts/month. Both subcontractors also individually developed cost models accurately reflecting the production costs for ceramic nozzles across the supply chain. Overall yield for the complete process was 79.2 percent for CC, and 67 percent for KICC, respectively. Furthermore, it was demonstrated that the cost goal per part could be achieved. In order to further reduce the production cost, design modifications are necessary to reduce the required number of machined surfaces, setups, grinding operations, and/or close tolerance features.

Table 2 331-200[CT] ceramic turbine design cycle conditions

Parameters	Units	Value
Corrected flow	lbm/s (kg/s)	1.556 (0.7058)
Corrected speed	rpm	19,993
Physical speed	rpm	41,731
Turbine efficiency	...	85.7
Turbine inlet total pressure	psia (kPa)	129.8 (895)
Average turbine inlet total temperature	F (°C)	1800 (982)
Combustor pattern factor	...	0.18

CC also demonstrated their capability to fabricate MOD 2 ceramic blisks for the 331-200[CT] engine (see Ceramic Component Design section).

Engine Demonstrations

The ceramic engine demonstration activities required redesign and modification of the Model 331-200 APU into the ceramic test bed engine. Within the 331-200[CT] test bed, the first axial turbine stage was redesigned to incorporate ceramic turbine nozzle segments and inserted ceramic blades, and finally even a ceramic turbine blisk. This activity included detailed design of ceramic components and modified metallic support structure, test hardware fabrication, component testing to verify the component performance characteristics, and engine demonstration testing. These tasks are summarized in the sections below. The 331-200[CT] turbine design cycle conditions are summarized in Table 2.

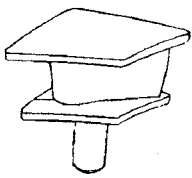
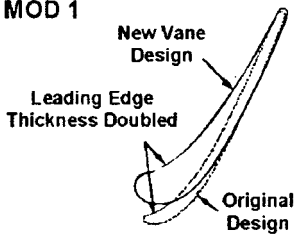
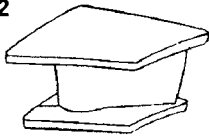
Ceramic Component Design. The design guidelines recognized that the redesigned components will be used in a later field evaluation program, in which ceramic-equipped engines replace production all-metallic engines; thus the ceramic-equipped engines must be aerodynamically similar to the metallic engines. In addition, to maintain the reliability of the test bed, modifications to the metallic support structures should be minimized.

The ceramic turbine nozzle segments and blades were designed with principal consideration given to component reproducibility, while also satisfying structural integrity and aerodynamic performance requirements.

Ceramic Turbine Nozzle Design. The ceramic nozzle assembly (Fig. 1) has 23 segmented ceramic vanes. For simplicity, the ceramic vane count was reduced to 23, from 29 vanes on the all-metallic engine. Nozzle surface geometry was kept as simple as possible to favor manufacturing, a result of concurrent engineering with the close collaboration of the ceramic component manufacturers. An attempt was made to maintain the aerodynamic performance of the ceramic nozzles at the level of the all-metallic design. The nozzle aerodynamic loadings were high, due to the low number of vanes and the envelope limitations, giving rise to concerns regarding increased losses due to flow separation on the suction side of the vanes. However, inviscid and viscous analyses of the nozzle loadings indicated acceptable suction side diffusion.

Over the course of the program the initial nozzle design (MOD 0) was redesigned twice for improved producibility of the ceramic nozzle system. The nozzle attachment features were simplified, and the performance and durability of the ceramic nozzle system was improved. Figure 5 shows the evolution of the 331-200[CT] ceramic nozzle through the three design iterations.

The MOD 1 design has thicker airfoils and platform sections than the initial MOD 0 design for decreased stress, as well as increased airfoil fillets and reduced platform slash angles. Also a draft angle was added to the platform gas path for improved castability. The MOD 2 design additionally has simplified attachment features for improved performance and manufacturability. The MOD 2 ceramic nozzle design resulted in a change in the way the ceramic nozzle segment is supported by the metallic structures. In the MOD 0 and MOD 1 designs, the ceramic nozzle

MOD	Features	Benefits
MOD 0 	Post mount ID Thin airfoil Thin platforms	Baseline configuration
MOD 1 	Post mount ID Thick airfoil Thicker platforms	Improved manufacturing Decreased stresses
MOD 2 	Clamp mount OD Thick airfoil Thicker platforms	Improved manufacturing Improved performance

G9790-3

Fig. 5 331-200[CT] ceramic turbine nozzle design evolution

mounting was cantilevered from a resilient attachment to the ceramic post on the nozzle hub platform. The design worked well from a structural perspective; but designing a robust seal for the outer shroud platform and machining the post feature on the ceramic nozzle presented difficulties. The MOD 2 nozzle is mounted on the outer shroud platform, which significantly improves the shroud and hub platform seals; and fabrication is eased by removal of the ceramic post feature from the hub platform. The MOD 2 design employs the MOD 1 airfoil geometry, for benefits in low airfoil stress and good formability.

Analyses were performed to predict the stresses induced in the MOD 2 ceramic nozzle airfoil at steady-state and transient operating thermal conditions. Table 3 shows a comparison of predicted stresses in the MOD 0, MOD 1, and MOD 2 ceramic nozzle designs. From these results, thermomechanical fracturing of the MOD 2 airfoil was not expected to present any problems during engine testing. Thermally induced cracks, found in several MOD 0 ceramic nozzles during proof tests and later during engine testing, indicated that the MOD 0 nozzle design was too highly stressed. The MOD 0 ceramic nozzle stress analysis, performed in prior years, had considered only nominal temperature conditions during the engine start transient and ignored any potential for temperature maldistribution (hot streaks) from the combustor dur-

Table 3 Predicted 331-200[CT] ceramic nozzle stresses

Nozzle Location	MOD 0 2D Nominal	MOD 1 3D Hot Streak	MOD 2 3D Hot Streak
Peak Transient Stress, ksi (MPa)			
Airfoil leading edge	44 (303)	8 (55)	8 (55)
Airfoil trailing edge	41 (283)	16 (110)	15 (103)
Post fillet	...	10 (69)	[N/A]
Peak Steady-State Stress, ksi (MPa)			
Airfoil leading edge	24 (166)	5 (35)	3 (21)
Airfoil trailing edge	20 (138)	8 (55)	6.5 (45)
Post fillet	...	4 (28)	[N/A]
[N/A]=not applicable.			

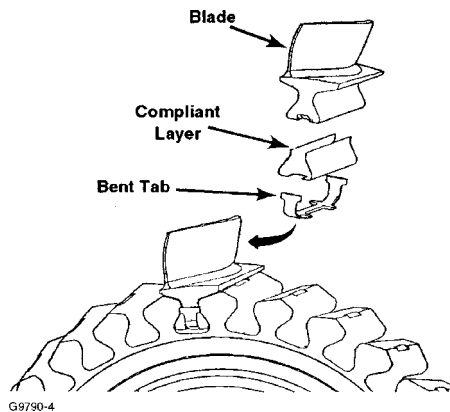


Fig. 6 331-200[CT] MOD 0 ceramic blade attachment scheme employed a compliant layer with a conventional metal bend tab retainer

ing the engine start. Additional studies revealed that such hot streaks can significantly increase the transient stress levels in the ceramic nozzles. Due to this finding, the stress analyses performed during the MOD 1 and MOD 2 ceramic nozzle redesign efforts employed worst-case light-off temperatures, to ensure more accurate modeling of actual transient engine operating stresses.

Ceramic Turbine Blade Design. The number of ceramic blades in the redesigned first-stage turbine wheel (Fig. 1) was reduced to 28 blades from 36 in the original all-metallic engine. This permitted an increase in the size of the ceramic blades, thickening the blade sections for better fabricability, and increasing the room available for a low-stress blade attachment scheme.

The initial MOD 0 blade design (Fig. 6) utilized a single-tang 60 degree attachment contact angle dovetail with a thin foil of compliant metal to distribute the compressive loads between the ceramic blade dovetails and the metallic turbine disk. Each blade assembly was held in place axially with a conventional metallic bend tab. Peak stress of 43 ksi (296 MPa) was predicted on the surface in the dovetail region near the edge of the contact zone.

While it was felt that the ceramic-equipped 331-200[CT] engine would meet its performance goals, aerodynamic performance of the ceramic blade may have been compromised, in favor of improved fabricability and mechanical integrity. Aerodynamic loading increased as a result of the reduced blade count and simultaneous restriction of the blade envelope. The largest loss occurred over the last 20 percent of the blade height, near the blade tip, attributed to tip leakage flow due to the increased tip clearance during operation.

A ceramic blade attachment redesign was initiated when it was learned that the contact stress levels, as a function of blade attachment bearing stress, were strongly affected by variations in the frictional coefficient of the attachment interface, especially during transient operating conditions. It was also considered desirable to move the blade resonant frequencies higher and to make the blade attachment features more robust. The redesign efforts included an appraisal of the shortcomings of the (baseline) MOD 0 ceramic blade design, which were

- the blade first resonant mode fell within the range of engine operating speeds,
- the blade attachment shank was thinner than good design practice suggested, and
- the specified 60-deg contact angle made the blade attachment feature bearing stresses sensitive to interface friction.

For the resulting MOD 1 ceramic blade design (Fig. 7), the airfoil was not changed from the MOD 0 baseline, and the MOD 0 design issues were addressed with revisions to the attachment geometry. The major features of the MOD 1 design include a

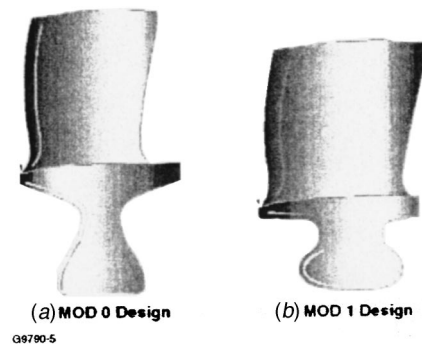


Fig. 7 331-200[CT] ceramic turbine blade attachment was redesigned to improve robustness (airfoils shown at different angles to emphasize changes in attachment geometry)

thicker, shortened blade shank, which serves to increase the shank section modulus, raising the blade resonant frequencies above the engine operating speed range. A second major change was a reduction in the attachment contact angle from 60 to 45 deg, which was intended to decrease the sensitivity of the attachment bearing stress to changes in interface friction. A peak stress of 42 ksi (210 MPa) is predicted to occur in the blade shank; this is approximately the same as the values for the baseline MOD 0 design. Design considerations for the MOD 1 metallic turbine rotor disk differed from the MOD 0 disk only in the geometry of the blade slots and the method for axially retaining the ceramic blades in the disk. An evaluation of various design options for retaining the ceramic blades in the metallic disk identified a bolted coverplate design as the favored concept. This design eliminated earlier problems with consistency of the bent tab retainer installation and ceramic machining difficulties encountered with the necessary features on the underside of the blade for alignment of the tab.

Ceramic Turbine Blisk Design. While the program progressed, ceramic turbine design philosophies have been formed which advocate peak design stresses in inserted blades be set much lower than in the present designs. The driver for this approach has been the realization that ceramic materials are more sensitive to the restrained conditions in the blade attachment than for conventional inserted metallic blades. Technology has been developed to improve the compliant layers for inserted ceramic blades; but the sense is that the combined effects of thermal stresses, inertial loads, friction, and contact stresses are not well enough understood at present (especially for transient operating conditions), to achieve successful ceramic turbine designs using the same margins assumed with metallic blades.

To this end, activity had been initiated to identify alternate ceramic turbine blade concepts, and to initiate a MOD 2 ceramic turbine design, based on the most promising candidate. As a result of this effort, an integrally bladed ceramic rotor ("blisk," see Fig. 1) version of the turbine rotor including an innovative ceramic/metal attachment scheme (Fig. 8) was designed. This component retains the airfoil geometry of the MOD 1 inserted ceramic blades, but integrates the 28 blades onto a single cast ceramic rotor disk. This design avoids the cost and durability issues associated with individual inserted blades.

All the blades on two different ceramic blisk rotors were tested in Honeywell's Acoustic Ring Signature Laboratory at room temperature and static conditions. The results from the testing were compared against the analytical predictions, and a favorable comparison was achieved. The test results indicated that the upstream and downstream vane excitation sources are outside of the operating range for the 331-200[CT] engine, as shown in the Campbell diagram in Fig. 9. Therefore, potential blade failure due to high-cycle fatigue (HCF) was not expected to be an issue during the

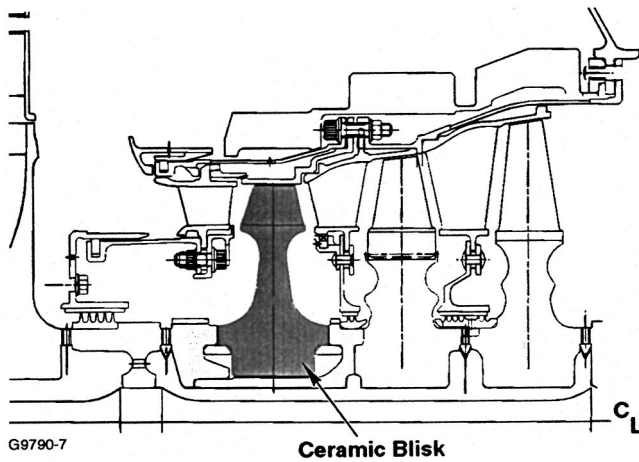


Fig. 8 Ceramic turbine blisk concept

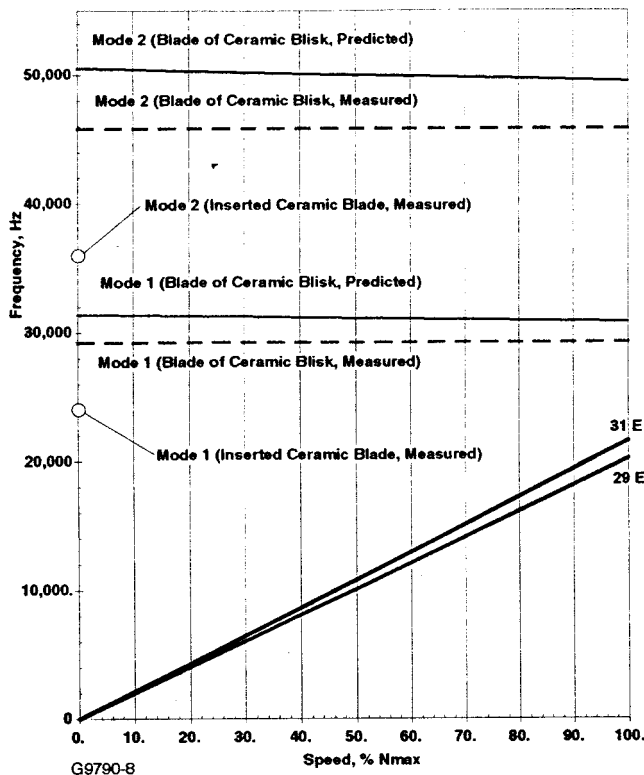


Fig. 9 Campbell diagram of MOD 2 AS800 ceramic blisk vibratory modes

validation engine testing, and represented a significant improvement compared to the MOD 1 inserted ceramic blade design.

The measured blade-to-blade frequency variation was very small. The one-sigma variation of the first mode measured 210 Hz, or less than one percent. Additionally, holography tests were performed on the blades and the mode shapes detected were the same as the analytical predictions.

Engine Testing Activities. Successful demonstration of engine operation with ceramic turbine components has served as the validation activity for the ceramic design methods and integrity of the actual ceramic components. Initial development engine testing activities have provided the environment for development and refinement of the ceramic component systems. Subsequent endurance testing and recently initiated field test activities were used to

Table 4 331-200[CT] ceramic turbine nozzle cumulative engine test experience

Ceramic Nozzle	Hours	Starts
MOD 0	897.6	2,481
MOD 1	9.8	22
MOD 2	4232.2	6530
Nozzle Total	5139.6	9033

establish the reliability of the ceramic components in both simulated and actual gas turbine operating service conditions.

Two production Model 331-200 APU engines were converted to the 331-200[CT] configuration for use as test beds for the development and endurance engine test activities. One engine was for evaluating the ceramic nozzles with metallic blades, and the other engine was for evaluating the ceramic blades with metallic nozzles. Using separate test beds reduced the risks and enhanced data collection for each ceramic component set.

Ceramic Nozzle Engine Testing. Initial MOD 0 ceramic nozzle engine testing revealed cracks in the trailing edge on 2 of 23 ceramic nozzle segments, similar to those seen earlier in proof testing. Both cracks were thermally induced, and initiated from the trailing edge and propagated halfway through the nozzle vanes. As discussed earlier, two redesign activities of the ceramic nozzles were initiated and resulted in successful engine testing since. Overall, endurance tests of the ceramic nozzles accumulated more than 5,100 engine operating hours (see Table 4). None of the MOD 2 ceramic nozzles ever failed during engine testing.

The CTEDP also reached a significant milestone by accumulating more than 2,500 hours of engine testing on a single set of MOD 2 AS800 ceramic turbine nozzles. Post-test inspections (Fig. 10) revealed no deterioration on the ceramic nozzles.

MOD 2 Ceramic Nozzle Field Testing. A standard Federal Aviation Administration (FAA) 150-hour engine block endurance test (required for certification of new APUs for commercial air transport service) was completed in 1997 on the ceramic nozzles. The test results, along with supporting data from the development testing and a summary of prior Honeywell ceramic gas turbine development experience was submitted in support of certification of the Honeywell Model 331-200 and 331-250 APUs for operation with ceramic turbine nozzles. FAA certification was granted to Honeywell in July 1999 and enabled the launch of a field demonstration of the ceramic nozzles under actual commercial air transport service conditions. The first 331-250 APU equipped with ceramic nozzles was built at Honeywell's Raunheim facility, Germany, in Dec. 1999, and entered service in a Lufthansa Airbus A300-600 in early Jan. 2000. Four additional APUs will subsequently be equipped with ceramic nozzles and enter service in early 2000. The five-field evaluation APUs will accumulate ap-

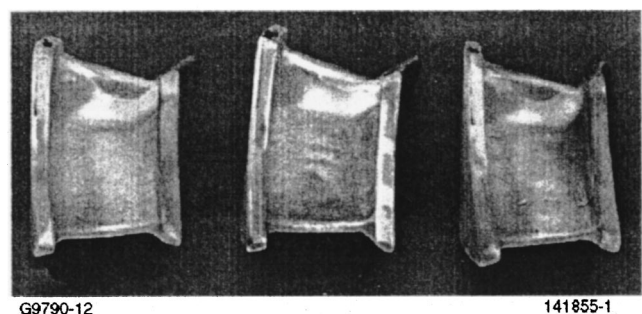


Fig. 10 MOD 2 AS800 ceramic nozzles were in excellent condition after completing 2519 hours of engine testing

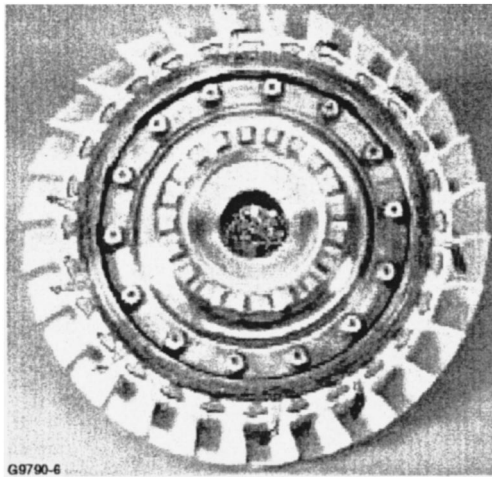


Fig. 11 MOD 1 AS800 ceramic turbine blades with thin-film instrumentation in metallic rotor

proximately 20,000 hours of commercial air transport service with ceramic turbine nozzles within the next two years.

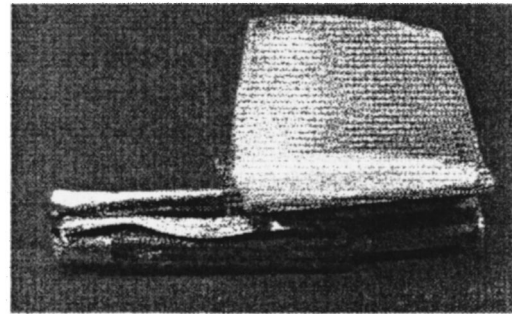
Ceramic Turbine Blade Engine Testing. The dual-test-bed strategy paid off during the first engine test on the MOD 0 ceramic blades. Approximately 86 seconds into the first engine test start in 1993, at 33,600 rpm, the engine suffered a failure. Subsequent disassembly, inspection, and analysis identified a number of possible causes. However, contact failure at the blade attachment was the most likely failure mode. Post-test inspections indicated that the compliant layer did not effectively spread the contact load over the attachment surfaces. Corrective actions were identified and implemented, with respect to this and other potential failure modes. During the subsequent operational testing, the engine successfully completed three starts and operated for a total of 1.5 hours at all load conditions prior to a blade fracture occurring. The engine ceased operation 16 seconds after unloading from the maximum load condition, at 39,500 rpm.

Extensive analysis identified blade vibration as the primary candidate for the cause of the blade fracture during the engine test. This conclusion was reached after an investigation which searched for and considered all the evidence supporting possible blade fracture conditions, including component overload, mechanical rub, foreign object damage (FOD), mechanical interference, contact loading, and vibration. The investigation eliminated each of the above causes, either by virtue of pretest inspections and proof test data, or post-test inspections, with the exception of excessive blade vibration at the blade resonant frequency, induced by an unknown driver.

As described earlier, a redesign of the ceramic blades was initiated which resulted in the MOD 1 ceramic blade design. Starting in 1996, development engine testing established “safe” operation of the test bed with the MOD 1 design ceramic turbine blades. Initial testing was performed to resolve the pending issues with respect to blade vibration. An engine test was performed in which MOD 1 ceramic blades were instrumented with thin-film gages for dynamic vibration strain measurement during operation. Figure 11 shows the metal rotor with instrumented ceramic blades. During this testing, the engine was operated up to 105 percent speed and at each of the design load conditions. The results showed that the ceramic blade strain levels did not exceed $150 \mu\epsilon$ under any engine operating condition. These strain levels were considered acceptable for further engine testing of the MOD 1 blade design without risk of vibration failure.

Subsequent engine testing then focused on evaluating and demonstrating the durability of various compliant layers. Several engine tests were run in blocks, approximating 100 hours each, at

Baseline Dual-Layer System



Latest Proprietary Compliant Layer System

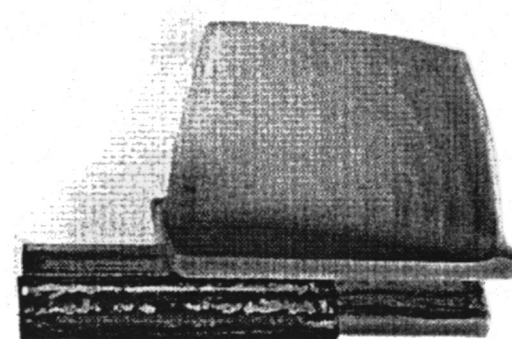


Fig. 12 Significant improvement in compliant layer durability could be achieved

Table 5 331-200[CT] ceramic turbine blade cumulative engine test experience

Ceramic Blades	Hours	Starts
MOD 0	1.5	4
MOD 1	1,043.5	1,027
Blades total	1,045.0	1,031

engine speeds and loads representative of typical APU operation. After each block test, the ceramic blades and compliant layers were evaluated and the configuration adjusted to improve durability. Finally, a compliant layer development breakthrough was demonstrated in the last engine test of 200 hours operation and 50 start-stop cycles, using an improved proprietary Honeywell compliant layer with a stable, high-temperature solid lubricant. Both the ceramic blades and the compliant layers were in excellent condition following the test, as shown in Fig. 12 (the compliant layers are shown partially pulled out for illustration purposes).

None of the MOD 1 ceramic blades failed during any of the engine testing activities. The CTEDP also reached a significant milestone by accumulating more than 1,000 hours of engine testing using inserted ceramic turbine blades (Table 5).

Ceramic Turbine Blisk Testing. As discussed earlier, an integrally bladed ceramic rotor (“blisk”) version of the Model 331-200/-250 APU first-stage turbine rotor was designed in 1997, which was designated as the MOD 2 ceramic blade design. A complete 331-200[CT] engine rotating group including a ceramic blisk was assembled and balanced in preparation for planned engine development testing, and in June 1998 testing was initiated. The test bed has since successfully accumulated over 1000 hours of full-speed operation in several test stages, using the same ceramic blisk (Table 6). The final 300 hours of blisk engine endur-

Table 6 331-200[CT] ceramic turbine blisk cumulative engine test experience

Ceramic Blisk	Hours	Starts
MOD 2	1,082	1,072

ance testing were run for the first time in an all-ceramic first stage (nozzles and blisk) configuration without any difficulties.

The purpose of the blisk endurance testing has been to evaluate the structural integrity of the rotating assembly including the ceramic blisk and its innovative metallic attachment scheme. The test objectives were to demonstrate the durability of the metallic attachment, and to evaluate the cumulative effects of time and cycles on the attachment system. Additionally, blisk cavity temperatures could be evaluated in order to estimate the ceramic/metal attachment temperature and to verify the secondary flow system. The testing successfully proved the feasibility and reliability of the plain friction drive concept without compliant layers (see Fig. 8) for use in the ceramic blisk field test activity.

During all the testing, the measured engine vibration levels were always normal, and there was no sign of any anomalies. The frictional (ceramic/metal) blisk to shaft attachment never showed any slippage. During two test blocks, the engine also experienced minor foreign object damage (FOD) events from metallic pieces, which had separated from an upstream thermocouple/pressure probe shield. The FOD only resulted in minor chips on the trailing edge of a few blades. However, the FOD damage was deemed to be minor, and did not interfere with continued engine operation during subsequent endurance testing of the very same blisk.

MOD 2 Ceramic Blisk Field Testing. In order to support one of the major objectives of this program, i.e., to provide extensive engine test experience and early field experience, a Honeywell Model IE831-800 industrial engine has been chosen for field testing of the ceramic rotor blisk during 2000. The IE831 engine models are derived from the very reliable AlliedSignal/Garrett Model 331 series turboprop and 331-200/-250 APU engines, with a robust gearbox suited for typical stationary industrial engine installations. Since the flowpaths of the IE831 industrial engine and the 331-200/-250 APU models are identical, the IE831 engine lends itself towards relatively simple introduction of a ceramic blisk in the first-stage turbine, as shown in Fig. 13.

Honeywell Engines, Systems & Services plans to field test the ceramic blisk equipped IE831 engine for possible use in an im-

portant new industrial turbine application. A variation of the IE831-800 industrial engine, designated as the model ASE8-1000, employs a modified combustor equipped with a proprietary catalytic converter, and is utilized for volatile organic compound (VOC) destruction. The ASE8-1000 provides VOC destruction with controlled, low environmental emissions, while simultaneously providing shaft horsepower for efficient electrical cogeneration and peaking, as well as a useful process heat source.

Since the ceramic rotor blisk has the potential to run at higher temperatures, and VOC destruction efficiency is substantially greater at elevated temperatures, there is good potential value to be achieved by using ceramic components in the VOC engine. Moreover, the reduction in secondary cooling air required resulting from the ceramic components will also enhance overall VOC destruction efficiency, due to less required bypass air, which yields greater flow through the combustor. At full power, the model ASE8 turbine generates 19 percent more torque than the test bed 331-200[CT] APU, so the planned field evaluation would also provide more aggressive testing for the ceramic blisk than in the completed 331-200[CT] APU endurance testing.

The ASE8-1000[CT] ceramic blisk field test engine is currently undergoing a 100-hour cyclic endurance test prior to shipment to the field test site in late 2001. The duration of the field test will be a minimum of 10,000 hours or a maximum of two years.

Summary and Conclusions

The DOE-sponsored Ceramic Turbine Engine Demonstration Project had the mission of advancing ceramic gas turbine component technology toward commercialization. Most of this mission has been achieved. Through this program, existing and newly developed design methods unique to ceramic components have been validated in rig end engine testing.

In addition, this program has enabled the transition of manufacturing processes for complicated ceramic turbine components from prototype processes of variable quality to successful batch manufacturing with controlled, fixed processes. This has resulted in the improvement of fabrication yields from less than 20 percent in 1995 to 79 percent at the end of the program. The transition of similar ceramic manufacturing processes from small turbine nozzle segments to larger, integrally-bladed turbine rotors with very high yields is evidence that the benefits are transferable to other ceramic components.

Engine testing performed under CTEDP has been invaluable in validating and augmenting design technologies for ceramic components. A combined total of over 6,800 hours of engine testing

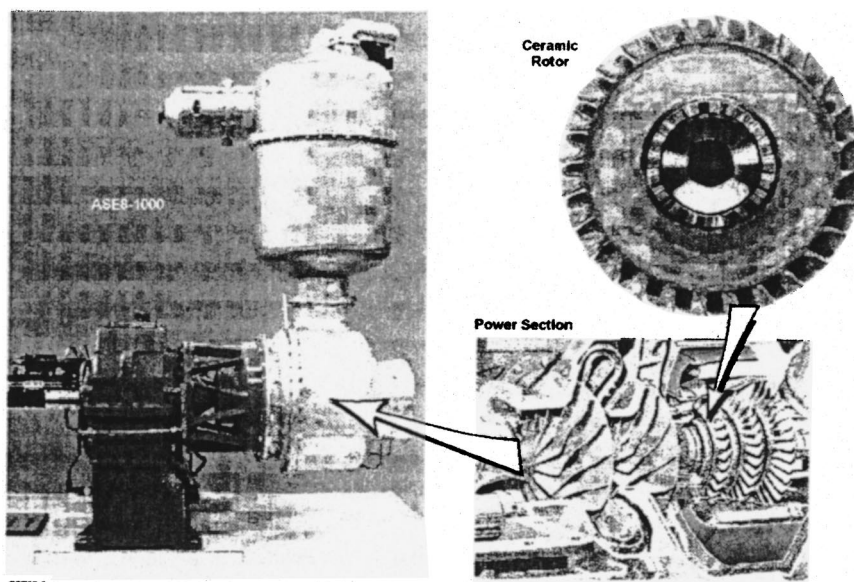


Fig. 13 ASE8-1000 ceramic blisk modification for industrial field evaluation

has been accumulated on ceramic turbine nozzles, blades, and blisks. During this work, performance data and evaluation information was gathered that has provided valuable feedback for technology development.

Field evaluation of ceramic nozzles in commercial air transport service has been initiated and work in 2001 will move the ceramic blisk demonstration into field testing.

Burner rig oxidation testing of current candidate silicon nitride materials confirmed that formation of surface recession pits, microstructural oxidation damage accumulation (grain boundary depletion), weight loss and dimensional changes already begin to limit the durability and reliability of structural ceramic components beyond 900°C material temperature. Extensive coatings research and development is needed for successful long-term operation of ceramic components in aggressive gas turbine environments.

Acknowledgments

The author wishes to thank the U.S. Department of Energy (DOE) for its financial support, and Mr. Thomas Strom, the NASA Program Manager, and Mr. Thomas Sebestyen, the DOE Program Manager, for their technical contributions toward the program goals. Significant technical contributions were made by the staff members at Honeywell Ceramic Components (Torrance, CA) and

Kyocera Industrial Ceramics Corporation (Vancouver, WA). Finally the author wants to thank his co-workers at Honeywell Engines, Systems & Services (Phoenix, AZ) and Honeywell Aerospace GmbH (Raunheim, Germany) for their contributions and Lufthansa for participation in the ceramic nozzle field evaluation.

References

- [1] Easley, M. L., and Smyth, J. R., 1994, "Ceramic Gas Turbine Technology Development," ASME Paper 94-GT-485.
- [2] Rettler, M. W., Easley, M. L., and Smyth, J. R., 1995, "Ceramic Gas Turbine Technology Development," ASME Paper 95-GT-207.
- [3] Easley, M. L., and Smyth, J. R., 1996, "Ceramic Gas Turbine Technology Development," ASME Paper 96-GT-367.
- [4] Kinney, T. K., and Easley, M. L., 1997, "Ceramic Gas Turbine Technology Development," ASME Paper 97-GT-465.
- [5] Easley, M. L., Schenk, B., and Cai, H., 1998, "Ceramic Gas Turbine Technology Development," ASME Paper 98-GT-554.
- [6] Schenk, B., 1999, "Ceramic Gas Turbine Technology Development," ASME Paper 99-GT-315.
- [7] Schenk, B., Brehm, P. G., Menon, M. N., Tucker, W. T., and Peralta, A. D., 1999, "Status of the CERAMIC/ERICA Probabilistic Life Prediction Codes Development for Structural Ceramic Applications," ASME Paper 99-GT-318.
- [8] Strangman, T. E., and Schenk, B., 2000, "Predicting the Deterministic Effects of Combustion Gas Environments on the Stress Rupture Life of Silicon Nitride Turbine Components," ASME Paper No. 00-GT-063.
- [9] Smialek, J. L., Robinson, R. C., Opila, E. J., Fox, D. S., and Jacobson, N. S., 1999, "SiC and Si₃N₄ Recession due to SiO₂ Scale Volatility Under Combustor Conditions," *Adv. Compos. Mater.*, **8**, No. 1, pp. 33–45.

Summary of CGT302 Ceramic Gas Turbine Research and Development Program

I. Takehara

e-mail: takehara_i@khi.co.jp

T. Tatsumi

Y. Ichikawa

R&D Department,
Industrial Gas Turbine Division,
Kawasaki Heavy Industries, Ltd.,
1-1 Kawasaki-Cho,
Akashi, Hyogo 673-8666, Japan

The Japanese ceramic gas turbine (CGT) research and development program (FY1988-1998) as a part of the New Sunshine Project funded by the Ministry of International Trade and Industry (MITI) was completed in March 1999. Kawasaki Heavy Industries, Ltd. (KHI) participated in this research program from the beginning and developed a twin-shaft CGT with a recuperator, designated as the "CGT302." The purposes of this program were (1) to achieve both a high efficiency and low pollutant emissions level using ceramic components, (2) to prove a multifuel capability to be used in cogeneration systems, and (3) to demonstrate long-term operation. The targets of this program were (i) to achieve a thermal efficiency of over 42 percent at a turbine inlet temperature (TIT) of 1350°C, (ii) to keep its emissions within the regulated value by the law, and (iii) to demonstrate continuous operation for more than a thousand hours at 1200°C TIT. The CGT302 has successfully attained its targets. In March 1999 the CGT302 recorded 42.1 percent thermal efficiency, and 31.7 ppm NO_x emissions (O₂=16 percent) at 1350°C TIT. At this time it had also accumulated over 2000 hours operation at 1200°C. In this paper, we summarize the development of the CGT302. [DOI: 10.1115/1.1451704]

Introduction

The CGT R&D program is one of many national projects promoted by the MITI with the aim of saving energy and protecting the environment. The program target and schedule are shown in Tables 1 and 2. The R&D program has three stages: (1) 900°C MGT (metal gas turbine), (2) 1200°C Basic CGT, and (3) 1350°C Pilot CGT, as shown in Table 2. The program was originally contracted for nine years but this was extended by two years in 1995.

KHI participated in this program and developed a CGT, designated the CGT302 (300 kW regenerative twin-spool ceramic gas turbine) jointly with both Kyocera Corporation (KC) for the ceramic components and Sumitomo Precision Products (SPP) for the recuperator.

The most difficult problem in the application of ceramics to a gas turbine engine seems to be how to support and attach ceramic components to a metal base frame. Ceramics are excellent heat-resistant materials, but generally they are extremely brittle and their thermal expansion rates are very low compared to metal. These characteristics make it impossible to attach ceramic parts with metal bolts as it creates a tensile spike. The different thermal expansion coefficients between metal and ceramics cause seal leakage of the combustion gas or air in the engine system. These problems must be overcome in order to operate a ceramic turbine engine without trouble and obtain the higher performance. Therefore proper integration of ceramic components into an engine is one of most important technologies of ceramic engine development.

Basic Design and Features of the CGT302

The CGT302 was designed only at a pilot condition (i.e., 300 kW of power and 1350°C of TIT) and so the target value of the basic CGT and the 900°C MGT are automatically fixed as a partial load. The component efficiencies of both the versions are de-

termined lower compared to the Pilot version because of developmental progress. In the cycle study of the basic design, KHI used a high-pressure ratio of eight, since it produces a low exhaust gas temperature, which allows the use of a conventional metal recuperator. The CGT302 specifications are shown in Table 3.

The CGT302 engine sectional view in Fig. 1, and Fig. 2 shows all the ceramic components except the coil springs, which were made of Si₃N₄ (Kyocera SN281/282). The coil springs are also made of Si₃N₄ and manufactured by NHK Spring Co.

The CGT302 has the following unique features used to solve the problems with the ceramic engines, mentioned above, and to achieve the target performance (see Ref. [1]).

1 Conventional Layout. KHI has manufactured over 5500 industrial gas turbine engine units for industrial use. The CGT302 followed a conventional small gas turbine layout, which KHI is accustomed to building, by using a single tangential combustion chamber, a turbine scroll and the conventional arrangement of compressor, turbine, and other parts.

Table 1 Program target

Item	Target
Efficiency	42 %
TIT	1350°C
Output Power	300 kW
NO _x Emission	< 70 ppm (16%O ₂)

Table 2 Development schedule

'88	'89	'90	'91	'92	'93	'94	'95	'96	'97	'98
Ceramic Component Fabrication Technology										
Component Technology (Turbine, Compressor, Heat Exchanger, etc.)										
Basic Design				Interim Appraisal						
900°C MGT										
				1200°C Basic CGT						
				1350°C Pilot CGT						

Contributed by the International Gas Turbine Institute (IGTI) of THE AMERICAN SOCIETY OF MECHANICAL ENGINEERS for publication in the ASME JOURNAL OF ENGINEERING FOR GAS TURBINES AND POWER. Paper presented at the International Gas Turbine and Aeroengine Congress and Exhibition, Munich, Germany, May 8-11, 2000; Paper 00-GT-644. Manuscript received by IGTI November 1999; final revision received by ASME Headquarters February 2000. Associate Editor: D. Wisler.

Table 3 Specifications of CGT302

Item	Unit	Target Pilot CGT	Target Basic CGT
Power	kW	300	140
Thermal Efficiency	%	42	30
Turbine Inlet Temp.	°C	1,350	1,200
Air Flow Rate	kg/s	0.94 *1	0.68
Pressure Ratio	—	8	5.9
Gas Generator Turbine (GGT) Speed	rpm	64,000 *2	68,400
Power Turbine (PT) Speed	rpm	47,800 *2	51,300
Compressor Efficiency	%	82	78
Turbine Efficiency (GGT+PT)	%	85.5	82.2
Heat Exchanger Efficiency	%	80	78

*1 original 0.89 kg/s

*2 original 76,000/57,000 rpm

2 Independent and Elastic Supporting by the use of Ceramic Springs. The CGT302 uses three types of ceramic springs, which are made of Si_3N_4 , to overcome ceramic problems (i.e., tensile spike and seal leakage, etc.). The first of the three spring types is a coil spring. This coil spring is used to attach ceramic components such as a turbine scroll, by pushing against the metal frame. The second type spring is a wave ring similar to a bent washer with the same purpose also applying force as the coil spring, and the last spring is an inner and outer seal ring, which is similar to the shape of a conventional piston ring. The actual application of these springs is shown in Fig. 3. In the CGT302 engine, main ceramic stationary components, which are a scroll, a combustor chamber, a CGT nozzle and PT nozzle assembly, are supported independently on different metal frames by ceramic springs, and these components can be slid along each other at any thermal condition (hot or cold). In addition to sliding, by using seal rings they can keep to seal each component. This concept was a different approach compared to other ceramic gas turbines such as the AGT101 by Garrett (Allied Signal) or the CGT301 by IHI.

3 Ceramic Fiber Binding System. Generally turbine nozzles in a gas turbine are divided into small segments with one (or a few) blade(s) to avoid thermal stresses. The CGT302 turbine nozzles were also divided into segments.

In order to solve how to assemble small segments, the ceramic fiber binding system was originally developed by KHI. The fiber



Fig. 2 All the ceramic parts of CGT302

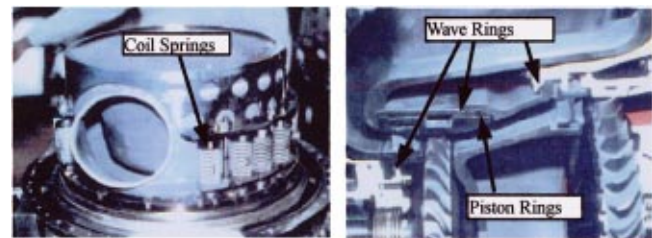


Fig. 3 Ceramic coil springs and pistonwave rings in CGT302

is made of SiC strings (SCS-6, Textron), which are reinforced by a carbon core and approximately 0.1 mm in diameter. KHI studied this binding system and created the fabricating process shown in Fig. 4. The SiC fiber is converted to a monolithic FRC binder by impregnating with organo-siliconpolymer (Polycarbosilane: PCS), and the thermal expansion rate of FRC binder is very close to that of the Si_3N_4 used in the turbine nozzles. Both the GGT and PT nozzles made by this process are shown in Fig. 5. To wind up nozzle segments, several hundred meters fiber was used.

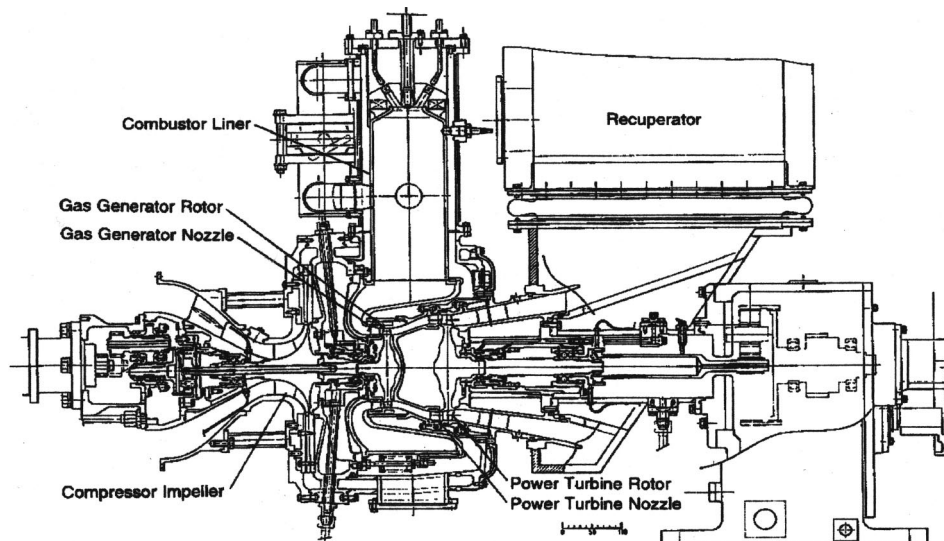


Fig. 1 Cross section of CGT302

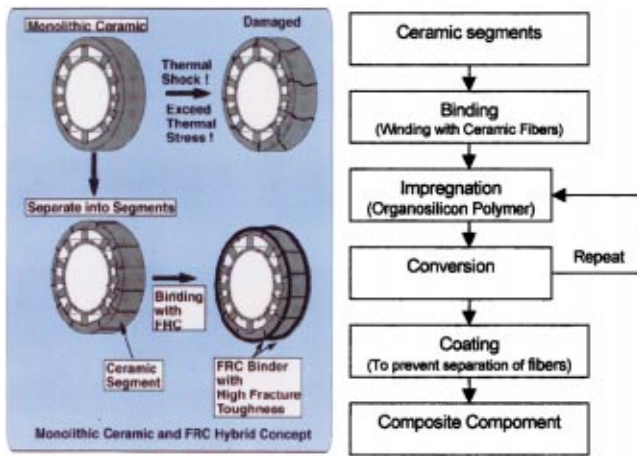


Fig. 4 Fabrication process FRC bound nozzles



Fig. 5 FRC bound GGT and PT nozzles

Table 4 Properties of abrasible Si_3N_4

Properties		Abradable Si_3N_4	Conventional Si_3N_4 (SN282)
Density (g/cm^3)		1.88	3.4
Flexural Strength (MPa)	RT	96	634
	1000°C	101	563
Coefficient of Thermal Expansion ($\times 10^{-6}/^\circ\text{C}$)	RT~400°C	2.0	2.5
	RT~800°C	2.5	2.9
	RT~1000°C	2.7	3
	RT~1200°C	2.9	3.1

4 Abradable Ceramic Shroud. Before installing an abrasible turbine shroud in the engine, a preliminary test was conducted to confirm its abrasibility. The abrasible shroud is made of porous Si_3N_4 and its material properties are shown in Table 4. This porous ceramic shroud was bonded to the base ceramic shroud. The engine test was successfully concluded and allowed us to obtain an initial turbine tip clearance of 0.1 mm without any trouble. This greatly contributed to the engine performance. The



Fig. 6 Abradable PT shroud after engine test

CGT302 was probably the first application of an abrasible shroud with monolithic ceramics in a gas turbine engine. Figure 6 shows the abrasible PT shroud after an engine test. The test results will be described in the next section.

Research and Development of Engine Components

1 Turbine. Before the ceramic turbine rotors and stationary components were installed in the basic CGT, these components were tested on a rig (i.e., cold and hot spin tests, and thermal shock tests). These tests were successfully completed in 1994.

All of the GGT and PT rotors, which were designed and fabricated under the development of the CGT302, are shown in Table 5.

(i) *Reducing Rotation Speed.* Throughout the engine tests, since the first use of the ceramic engine in 1994, the turbine blades of a GGT were occasionally chipped. Figure 7 shows a GGT with typical chipping. Chipping on the leading edge seemed to be caused by small foreign objects, such as carbon deposition or small debris (metals, ceramics and other materials), from the engine system or the air intake. But the chipping at the trailing edge was found to be caused by wave interference of foreign object damage (FOD) at the leading edge. This was confirmed in FOD rig tests (see Refs. [2, 3]).

To overcome this problem we designed a new GGT blade (No. 2), which had a blunt leading edge and a thick trailing edge (twice thickness as the original blade). But it could not expect good results against FOD (i.e., edge chipping) and also high turbine efficiency.

When we studied the GGT chipping data, it was found that chipping occurred usually when the rotor tip speed was over 480 m/s. We therefore decided to reduce the turbine rotation speed from 76,000 (rpm) to 64,000 for the GGT and from 57,000 to 47,800 for the PT, despite of the fact that the turbine performance would descend.

(ii) *Integrated Turbine Wheel and Redesign of Airfoil.* The airfoils of the GGT and PT were redesigned to accommodate to the reduced turbine rotation speeds (GGT: No. 3, PT: No. 2). None of the other turbine parts (i.e., nozzles, scroll, ducts, etc.) were changed and the same gas path was maintained. The reason

Table 5 Turbine rotor of CGT302

GGT (φ 144mm)			
No	Type	Speed (rpm)	Remarks
1	Original	76,000	
2	Anti-FOD	76,000	Blunt LE, Thick TE
3	Reduced speed	64,000	Blunt LE, Thick TE
PT (φ 192mm)			
1	Original	57,000	Hybrid Type
2	Integrated	47,800	Blisk, Blunt LE, Thick TE
3	Improved	47,800	Wide Code, Thin TE

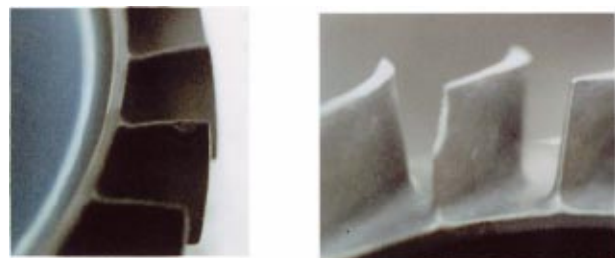


Fig. 7 Typical chipping of GGT

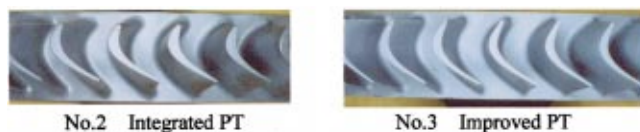


Fig. 8 PT rotors

Table 6 Tip clearance versus PT efficiency

T/C (mm)	PT Eff. (est.)
0.1	87.7
0.15	87.1
0.2	86.6
0.25	86.1
0.30	85.6
0.35	85.1

being that, if the gas path was changed it would require many ceramic parts to be redesigned and manufactured, and this would take too much time.

The GGT rotor is an integrated rotor and the original version of the PT rotor was a hybrid type (segment blades into a metal disk). Adopting a hybrid rotor, it becomes easy to manufacture the turbine blades, but obtaining a high efficiency becomes difficult. Because we could not expect to control proper turbine tip clearance and reduce gas leakage at the serration.

In 1996 the PT rotor was redesigned as an integrated rotor to obtain better efficiency as it became possible to manufacture an integrated (blisk) rotor due to progress in the ceramic fabrication technology. But the fabrication of such a blisk rotor is limited by the fact that a blade must be taken out from a mold with one direction, this meant that the blade performance would be reduced due to this restriction from the molding. This molding restriction similarly limited the GGT fabrication.

The integrated PT rotor, with the reduced rotation speed, was designed as an anti-FOD blade (No. 2). We were forced to redesign the blade again in order to obtain a better efficiency (No. 3). Figure 8 shows the improved and integrated PT blades.

(iii) *Nozzle Throat Area.* The throat area of turbine nozzles, especially the GGT nozzle, is very important because it decides the engine-matching point. Generally it is very difficult to precisely control the throat area while manufacturing turbine nozzles. A very small manufacturing error of the nozzle segments causes a very large change in the throat area. In the CGT302 Pilot engine, each throat area in the GGT and PT nozzle assemblies was measured with special gauges and the best combination of the nozzles was selected to obtain the best performance in the engine tests.

(iv) *Abradable Shroud.* In order to obtain higher turbine efficiency in the Pilot engine, an abradable PT turbine shroud was tested, and the engine was operated with a 0.2 mm initial tip

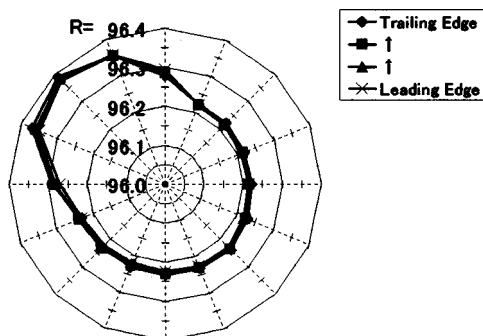


Fig. 9 Abradable shroud test result ($T/C=0.2$ mm)

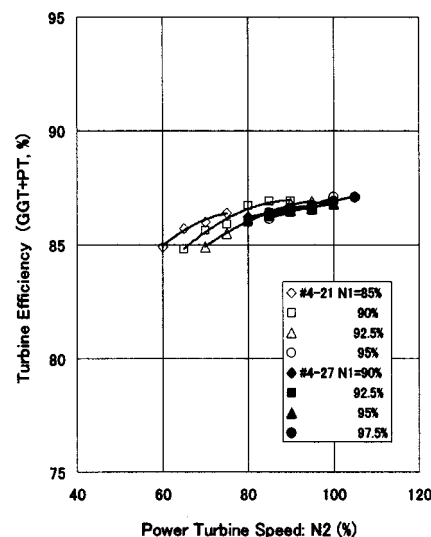


Fig. 10 Turbine performance

clearance in the first test. This test was successfully concluded and allowed us finally to obtain an initial turbine tip clearance of 0.1 mm. In the CGT302 we had been finding experimentally that the initial tip clearance must be within 0.35 mm, but the requirement from the turbine performance was under 0.2 mm. An estimated PT efficiency to tip clearance is shown in Table 6, and Fig. 9 shows the test result of using an abradable shroud with 0.2 mm initial tip clearance. Approximately 0.15 mm was shaved out in the 315 deg direction and our judgment of the operation limit was proved to be right. We think that this abradable shroud strongly contributed to achieving the program target of 42 percent engine efficiency.

(v) *Turbine Performance.* Turbine performance was evaluated in the engine tests and measured as total efficiency (GGT + PT) because it is difficult to measure parameters on the ceramic components (i.e., to attach sensors is very difficult). The final efficiency obtained was approximately 87 percent greater than the pilot target of 85.5 percent and this was very stable. Figure 10 shows the representative turbine performance measured during the engine tests (Engine No. #4-21, 27).

2 Compressor. The Compressor of the CGT302 is a single-stage impeller with a 0.89 kg/s airflow rate and a pressure ratio of 8 with an adiabatic efficiency of over 82 percent as the final target. During development the GGT, rotation speed (same as compressor speed) was changed and we changed the airflow rate from 0.89 to 0.92 (0.94) kg/s for the requirement of the matching of engine components. We designed eight types of impeller in this program, which have different airfoils, to obtain higher efficiency and to

Table 7 All the designed impellers for the CGT302

Type	Speed (rpm)	AirFlow (kg/s)	No. of Blade	Concept	Year
A	76,000	0.89	18	Full blade, Quasi 3D design	1989
B	76,000	0.89	14+14	Splitter blade with different line element from main blade, Rear loading, Q3D design	1989
C	69,000	0.89	14+14	Low speed back-up version, 3D Euler code design	1991
D	76,000	0.89	14+14	3D Euler code, Front loading	1991
E	76,000	0.94	14+14	Improved flow pattern from type D	1992
F	64,000	0.92	14+14	Redesigned engine speed, 3D Euler code	1995
G	64,000	0.92	14+14	3D N-S code	1996
H	64,000	0.92	9+9+18	Double Splitter Blade, 3D N-S code	1997



Fig. 11 Type H impeller

meet the GGT rotation speed. Also several angled diffusers were designed for each impeller. All of the impellers designed for the CGT302 are shown in Table 7, and the type H impeller, which is the latest version is, representatively, shown in Fig. 11.

In the rig test, the type F impeller proved to be the best, while the type E impeller was the best of the high-speed impellers (76,000 rpm). In 1998, we achieved the best efficiency of 79.1 percent using the type F impeller with a newly designed channel diffuser (CF21; C: Channel type, F: for the type F impeller, and the 21st design), in which the inlet angle distribution of the diffuser is adjusted to the measured impeller air outlet angle distribution. These results are shown in Fig. 12, compared with the type H, which was the latest version, and Fig. 13 shows the measured

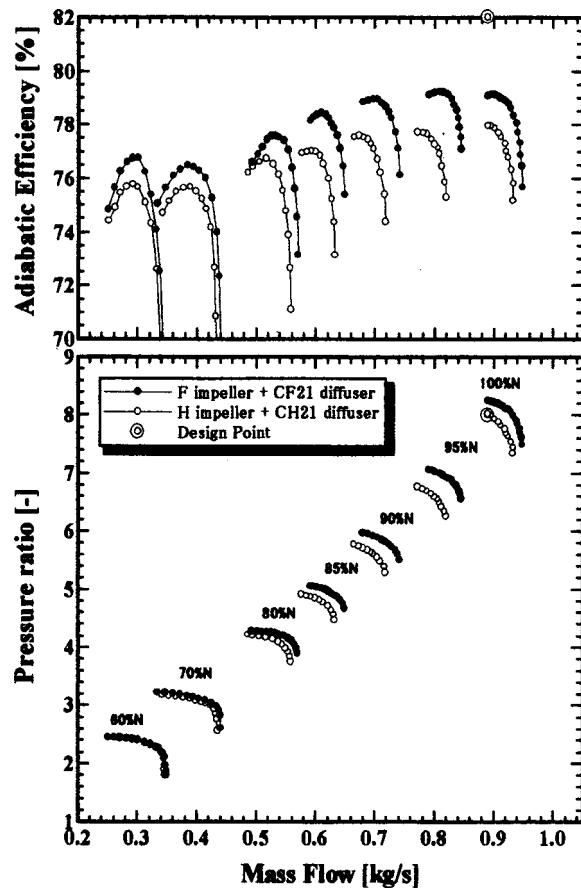


Fig. 12 Compressor performance

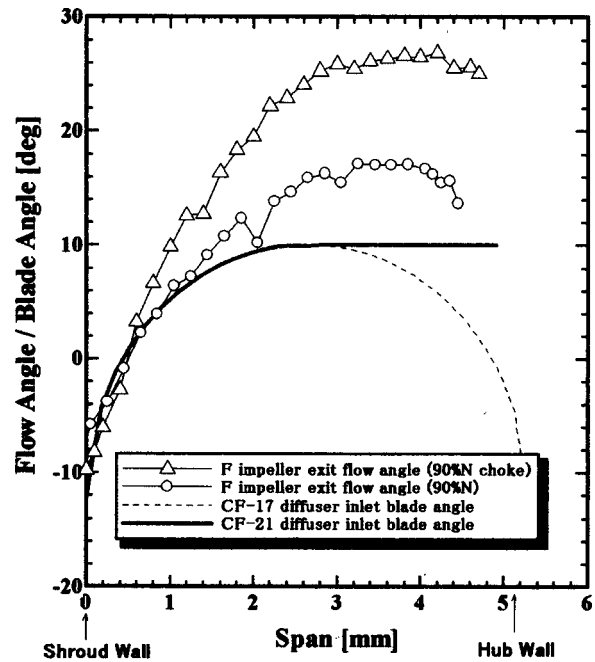


Fig. 13 Compressor performance

air outlet angle of the type F and the designed diffuser inlet angle. The performance of the type H was not so good, for the placement of splitter blades seems to be improper.

The compressor efficiency of 79.1 percent (Type F) is approximately three percent less than the target, but the target seems too difficult to achieve for such a small single stage impeller like the CGT302. Figure 14 shows the polytropic efficiency of commercial engines' compressor. It was found that the CGT302 achieved a top level of efficiency. The design target may have been slightly too ambitious.

3 Combustor. The CGT302 adopts a pre-mixed lean burn combustor to reduce NO_x emissions. This combustor is equipped with an air bypass line, which has an air bypass valve to control the air/fuel (A/F) ratio in the combustion zone to within a suitable

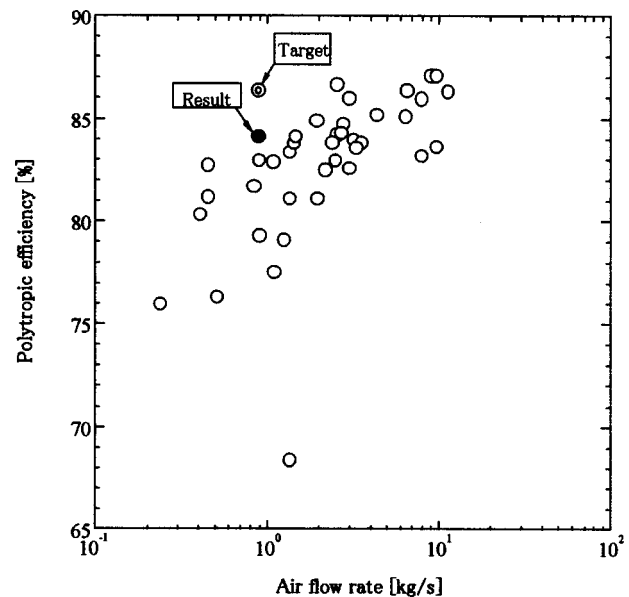


Fig. 14 Compressor polytropic efficiency

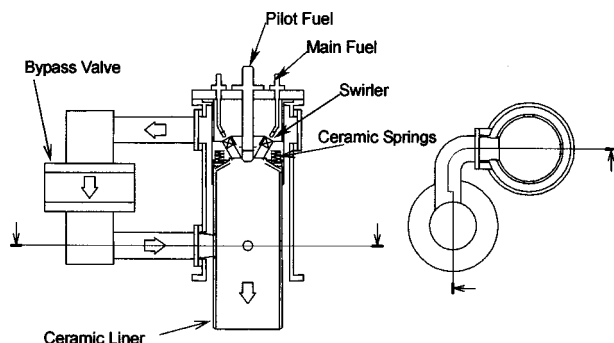


Fig. 15 Combustor schematic drawing

range, as the total A/F ratio changes widely over a broad operating range. Figure 15 is a schematic drawing of the combustor. The ceramic chamber is supported by ceramic coil springs, and these springs absorb the difference in thermal expansion between the ceramic chamber and the metal casing (see Ref. [4]).

Using this combustor, rig tests and engine tests at the rated condition of 1350°C TIT were carried out. The results of the rig tests are shown in Fig. 16. In Fig. 16, NO_x emissions and combustion efficiency without the pilot fuel (100 percent premixed) are plotted each as a function of the air valve opening rate of the bypass line, and the A/F of 60 corresponds to the rated value of 1350°C TIT. It was found that as the air valve opening ratio is closed NO_x emissions decrease. At the A/F ratio of 60 (i.e., 1350°C TIT), 8.9 ppm (O₂=16 percent) of NO_x emission was recorded against the target of 70 ppm.

The engine tests were conducted with the same configuration as the rig tests. The NO_x emission test results are shown as a function of TIT in Fig. 17. The CGT302 also cleared the target in the engine tests and the value of 31.7 ppm (O₂=16 percent) was achieved at the rated condition (1350°C). The combustion state was very stable with no flame out or other inconvenience was ever

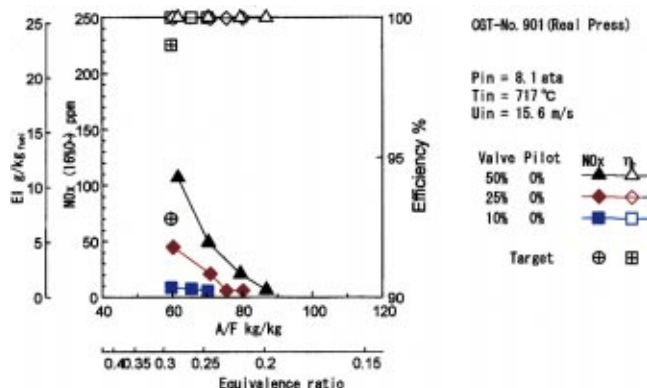


Fig. 16 Combustor rig test results

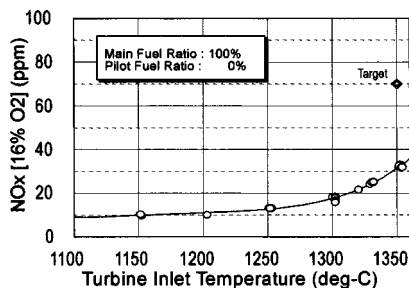


Fig. 17 Combustor engine test results



Fig. 18 Recuperator of CGT302 (49+49 fins for each core)

observed. The difference in performance between the rig and engine tests seems to arise from the different airflow conditions. In the rig tests, the air and gas flow are uniform ideally, but in the engine they are not, due to the complicated shape of the turbine scroll and other components. To solve this problem, it is considered to be effective that antiswirl vanes or guide vanes are placed on the outside of the chamber. We believe that a ceramic combustor chamber is very useful in reducing NO_x emissions for the following reasons:

- (i) no cooling air on the chamber wall reduces combustion temperature (i.e. to reduce NO_x), and
- (ii) higher radiation from chamber wall can keep combustion flame very stable, as the chamber wall can keep in high temperatures.

4 Heat Exchanger. The heat exchanger of the CGT302 is a plate-fin type recuperator, which has two cores with 79 fins on each core. The dimensions of this recuperator are 1060 mmW, 715 mmH, and 545 mmD. The component target of 82 percent effectiveness was successfully achieved in the engine tests by the end of FY 1997. But in order to meet the engine performance target, the recuperator required further improvement as the compensate performance found difficult to meet its target efficiency. In 1998 it was decided to add 20 more fins (i.e., 99 fins in each core), and in this improvement three percent and more effectiveness was expected. But this change was found difficult to fabricate and was modified to 49+49 fins by welding in each core. The depth of the recuperator was changed from 545 mm to 650 mm. Figure 18 shows the 49+49 fin recuperator.

Engine Test Results

Figure 19 shows an insulated CGT302 on the test bed.

1 Development History. Since the first run of the CGT302 with metal components in 1990 and ceramic components in 1992, engine tests had been carried out continuously until March 1999. The cumulative operation time on the performance bed reached approximately 370 hours, and 230 engine sets were tested.

In 1994 we achieved the second stage (Basic CGT: TIT = 1200°C) target of 30 percent thermal efficiency with 33.1 per-



Fig. 19 CGT302 on test bench

Table 8 Engine performance history

1st. 900°C MGT (1990-1992) stage	
Objective	To establish engine system as a base engine for the CGT.
Rotor Speed	80% of 76,000 (GGT) and 57,000 (PT) rpm
Achieved Eff.	23% and 59kW at 899°C (EG S/N #1-2)
Material	Metal
2nd. 1200°C Basic CGT (1992-1995) stage	
Objective	To establish "CGT" using conventional ceramic material and confirm 30% of thermal efficiency at 1200°C.
Rotor Speed	90% of 76,000 (GGT) and 57,000 (PT) rpm
Achieved Eff.	33.1% and 164kW at 1190°C (#3-22)
Material	Kyocera SN-252
3rd. 1350°C Pilot CGT (1995-1999) stage	
Objective	To demonstrate 42% of thermal efficiency at 1350°C of TIT.
Rotor Speed	64,000 (GGT) and 47,800 (PT) rpm
Achieved Eff.	42.1% and 322kW at 1396°C (#4-39)
Material	Kyocera SN-281/282

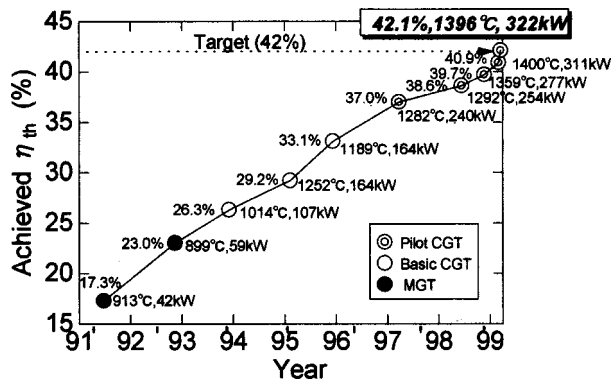


Fig. 20 Engine performance history

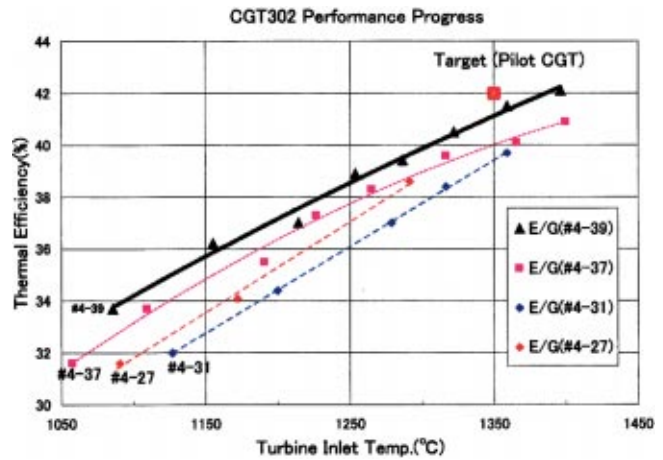


Fig. 21 Engine test results of CGT302

cent at 1190°C TIT. And in 1998, the CGT302 attained a 1350°C TIT and exceeded 40 percent thermal efficiency, but was still two percent below the desired efficiency. Finally in March 1999, with some improvements and modifications, the CGT302 successfully demonstrated 42.1 percent thermal efficiency at 1396°C (15°C-ISO condition), higher than the 42 percent program target. Table 8 and Fig. 20 show the performance history of the CGT302 (see Refs. [5,6]).

2 Performance Test Results in the Pilot Engine. Engine test results for the Pilot CGT are shown in Table 9 and Fig. 21. To achieve the Pilot engine target we attempted the following improvements and measures.

- improve aero-dynamic performance of engine components,
- improve engine matching,
- improve the recuperator,
- use an abradable PT shroud (reduced tip clearance),
- insulate the engine casing, and
- other measures.

Table 9 Test results of CGT302 (pilot engine)

Engine No.	Unit	Target	#4-27	#4-31	#4-32	#4-36
Inlet Air Temp.	°C	15	25.9	12.7	-7.9	8.6
corr.N1 (act.N1)	%	100	98.1 (99.9)	98.0 (97.6)	99.1 (95.1)	100.2 (99.1)
N2	%	100	105.0	103.2	103.9	108.0
corr.Output (act.)	kW	300	254.0 (257.1)	276.8 (276.5)	285.2 (275.7)	291.4 (287.9)
corr.TIT (act.)	°C	1350	1291.5 (1350.9)	1359.1 (1346.1)	1412.3 (1278.2)	1381.5 (1344.7)
Thermal Eff.	%	42	38.6	39.7	40.5	40.1
Pressure Ratio	—	8	7.32	7.59	7.61	7.93
Air Intake	—	—	Natural Intake	N2 Spray	N2 Spray	Natural Intake
Recuperator	—	—	79 Fins	←	99 Fins	49 × 2 Fins
Remarks	—	—			Heavily Air Leak	Original GGT/R, Abradable PT/S (T/C 0.2mm)

Engine No.	Unit	Target	#4-37	#4-39
Inlet Air Temp.	°C	15	5.3	4.3
corr.N1 (act.N1)	%	100	100.8 (99.0)	100.2 (99.2)
N2	%	100	106.1	105.0
corr.Output (act.)	kW	300	311.3 (305.7)	304.1 (302.4)
corr.TIT (act.)	°C	1350	1399.7 (1343.4)	1408.9 (1379.0)
Thermal Eff.	%	42	40.9	40.7
Pressure Ratio	—	8	8.25	8.09
Air Intake	—	—	N2 Spray	Natural Intake
Recuperator	—	—	49 × 2 Fins	←
Remarks	—	—	Original GGT/R (Use 76,000rpm turbine into 64,000rpm engine), Abradable PT/S (T/C 0.2mm)	Abradable PT/S (T/C 0.1mm), Improved PT/R



Fig. 22 Nitrogen spray unit

Aerodynamic performance (i) and engine matching (ii) were improved by designing and fabricating many different types of impeller blades and turbines, as well as selecting a range of GGT and PT nozzles. And the improved recuperator (iii) and the abradable turbine shroud (iv) were mentioned in previous sections.

We believe that the reasons we were able to achieve over 42 percent thermal efficiency (42.1 percent: Engine No. #4-39) were

- (i) Using ceramic components,
 - (a) no cooling air
 - (b) keeping small turbine tip clearance
 - (c) realizing uniform TIT spread (no cooling air in combustor and good combustion)
 - (d) Abradable ceramic turbine shroud
- (ii) latest aerodynamic analysis technology.

In the engine tests during the summer season, the air temperature rose and inevitably the turbine inlet temperature rose with it. Since the turbine inlet temperature is limited by ceramic material properties, it became impossible for the CGT302 to operate at the rated condition of 1350°C. To overcome this we built a nitrogen spray unit in 1998. The effect of the nitrogen was found to be negligible. In engine test S/N #4-31, nitrogen spray constituted seven percent of the airflow (N_2 ratio: 79.65 percent compare to 78.03 percent for normal air) and it was found that the following changes occurred:

- (i) air flow rate: -0.24% ,
- (ii) output power: -0.02% ,
- (iii) thermal efficiency: $+0.01\%$.

Figure 22 shows the nitrogen spray nozzle and engine test bed with the spray unit.

3 Premixed Lean Burn Test. On this program, the NO_x emissions must meet the value regulated by Japanese law (70 ppm or less, $O_2 = 16$ percent). The CGT302 also successfully cleared this target at the rated condition of 1350°C TIT, as is described in previous section.

4 Durability Test. The durability test, to demonstrate 1000 hours continuous operation at 1200°C TIT, was started in 1997. This test aimed to prove the reliability of the ceramic material for use in commercial engines, and the tests were done in the pilot plant with the enclosure unit shown in Fig. 23.

We tried three series of durability tests in WSS (weekly start stop) mode. These three tests were stopped after 592, 519, and 782 hours, respectively, and it is assumed that all tests were terminated due to the GGT rotor failure. But we could not specify this, and why they failed in such a short time also could not be determined. In a ceramic engine, when engine failure occurred, it was very difficult to specify the cause of the failure as the ceramic parts broke up into a lot of small debris.

As the GGT rotor failure, it seemed the following mechanism could have occurred.

- (i) ceramic material deterioration,
- (ii) blade resonance,



Fig. 23 CGT302 pilot plant (durability test unit)

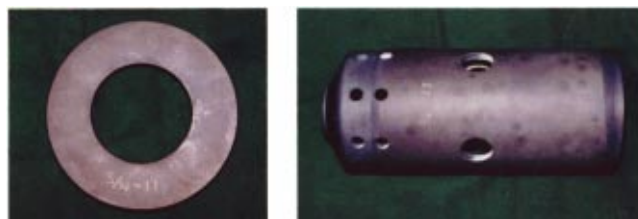


Fig. 24 Ceramic components after 1000 hours operation

- (iii) FOD or DOD (domestic object damage),
- (iv) re-assembling error, and
- (v) others.

As for (iv), troubles during the tests usually occurred within a few hours or a half day from restarting after de-assembling for an inspection.

In the third test, the combustor chamber, which is the hottest component, and some of the other small components were found to be able to withstand more in the inspection, so the test was continued and these components successfully attained 1000 hours operation at the target condition. Figure 24 shows the combustor chamber and support ring after 1000 hours operation. In the inspection after the test, no material defect was detected and these components were judged to use still more.

This durability tests proved reliability of ceramic components as stationary parts for 1000 hours, but could not confirm reliability as rotate parts.

5 Cumulative Operation Time. The operation time of the CGT302 on the performance test bench accumulated 370 hours on a total of 230 engine sets. This includes over 20 hours continuous operation at 1350°C TIT and approximately 30 hours were cumulated over 1350°C TIT. While in the durability tests, the CGT302 cumulated 2146 hours, including over 2117 hours at 1200°C TIT. The cumulated time of the durability tests is shown in Table 10.

Table 10 Cumulative time of durability test

Operating Temp.	Cumulative Time	Remarks
1200°C~	2,117 hr 57 min	
1100~1200°C	10 hr 40 min	
1000~1100°C	8 hr 04 min	
~1000°C	9 hr 29 min	
Total time	2,146 hr 10 min	
Start/ Stop	137	

Summary

1 The CGT302 successfully achieved the program's target of 42 percent thermal efficiency with 42.1 percent efficiency demonstrated and output power was 311.6 kW compared to the target of 42 percent and 300 kW.

2 The CGT302 achieved NO_x emissions of 31.7 ppm at the rated condition of 1350°C TIT compared to the target of 70 ppm.

3 The CGT302 accumulated over 2117 hours operation at over 1200°C TIT in the durability tests. The combustor chamber and some other parts were operated continuously for 1000 hours of the target condition.

Acknowledgments

This study was being carried out under the Japanese CGT R&D program conducted by NEDO. The authors wish to express their

gratitude to the Agency of Industrial Science and Technology of MITI and to NEDO for making this study possible and permitting this paper to be published.

References

- [1] Takehara, I., et al., 1996, "Research and Development of Ceramic Gas Turbine (CGT302)," ASME Paper 96-GT-477.
- [2] Yoshida, H., et al., 1998, "Experiment on Foreign Object Damage of Gas Turbine-Grade Silicon Nitride Ceramic," ASME Paper 98-GT-399.
- [3] "Research and Development on Ceramic Gas Turbine (300 kW class) FY 1998 Annual Report," 1999, NEDO Japan.
- [4] Okuto, A., et al., 1998, "Development of a Low NO_x Combustor for 300 kW-Class Ceramic Gas Turbine (CGT302)," ASME Paper 98-GT-272.
- [5] Tatsumi, T., et al., 1999, "Development Summary of the 300 kW Ceramic Gas Turbine CGT302," ASME Paper 99-GT-105.
- [6] Takehara, I., et al., 1999, "Development Summary of CGT302 Ceramic Gas Turbine," *IGTC '99*, Vol. I, Gas Turbine Society of Japan, pp. 57–64.

J. M. Desantes
J. V. Pastor
J. Arrègle
S. A. Molina

CMT—Departamento de Máquinas y Motores
Térmicos,
Universidad Politécnica de Valencia,
Apto. 22012,
46071 Valencia Spain
e-mail: cmt@mot.upv.es

Analysis of the Combustion Process in a EURO III Heavy-Duty Direct Injection Diesel Engine

To fulfill the commitments of future pollutant regulations, current development of direct injection (DI) Diesel engines requires to improve knowledge on the injection/combustion process and the effect of the injection parameters and engine operation conditions upon the spray and flame characteristics and how they affect engine performance and pollutant emissions. In order to improve comprehension of the phenomena inherent to Diesel combustion, a deep experimental study has been performed in a single-cylinder engine with the main characteristics of a six-cylinder engine passing the EURO III legislation. Some representative points of the 13-mode engine test cycle have been considered modifying the nominal values of injection pressure, injection load, intake pressure, engine speed, and injection timing. The study combines performance and emissions experimental measurements together with heat release law (HRL) analysis and high-speed visualization. Controlling parameters for BSFC, NO_x , and soot emissions are identified in the last part of the paper. [DOI: 10.1115/1.1456460]

Introduction

Heavy-duty turbocharged aftercooled (HDTCA) engines met EURO III emission regulations in 1999 incorporating the following technologies ([1–3]):

- Four valve cylinder head. This layout allows for centered combustion chamber and injector, being more efficient in the discharge coefficient-swirl number tradeoff, while reducing slightly pumping losses. A further potential of this layout is the variable swirl concept.
- Retarded injection with a precise control of timing as a function of the operating conditions. In this way, maximum combustion temperatures are reduced, followed by a reduction in NO_x emission, but with a penalty in engine efficiency (BSFC) as well as an increase in particulate emissions.
- High-pressure injection with increasing number of nozzle holes of decreasing diameter. This is probably the best known method to promote a fast fuel-air mixing, trying to control the combustion duration and thus, to reduce particulate emissions and to recover to a given extent the BSFC loss due to injection retardation.
- Combustion system matching. Proper combination of combustion chamber geometry, air movement (swirl and squish), spray number, and associated momentum is necessary to achieve an optimized compromise between NO_x , particulate emissions, and efficiency.

The incorporation of additional strategies, for instance EGR, particulate traps, exhaust catalysts, multistep injection, etc., was not essential at the EURO III stage, but they are currently being evaluated to overcome the targets of the more severe EURO IV standards.

The work reported in this paper is based on a parametric study carried out on a baseline engine with EURO III specifications to obtain a wide data base on the sensitivity of engine performance and emissions to the modification of some engine operating conditions. The methodology followed, which is described in detail in a later paragraph, includes single-cylinder engine performance

and emissions measurements, heat release law analysis from the instantaneous in-cylinder pressure, combustion visualization with a CCD camera, and the use of conceptual or phenomenological models.

A synthesis of the results has been also undertaken to improve the understanding of the combustion process in HDTCA Diesel engines with typical EURO III arrangements. This is a prerequisite to search for global solutions to overcome the EURO IV standards.

Methodology

Different information sources have been used in the analysis presented in this paper. The operating parameters to be analyzed are: engine speed, load, start of injection (SOI), injection pressure (IP) and boosting pressure (BP), according to the experimental matrix described later. From the engine tests, direct information of performance behavior can be obtained in terms of BSFC, pollutants (mainly NO_x and smoke, but also CO) and exhaust temperature. For each engine operating mode, the amount of fuel injected was kept constant, so that BMEP and BSFC are directly related.

Valuable additional information can be gained from the in-cylinder pressure, such as the heat release law (HRL) and several associated parameters as combustion duration, gravity center of combustion, premixed fraction, etc. For this purpose a combustion diagnosis code CALMEC ([4,5]) has been used. It is based on the solution of the energy equation in the cylinder on the assumption of uniform pressure and temperature over the instantaneous volume. This single-zone model approach allows for calculation of the instantaneous averaged temperature as well as the instantaneous heat released by the burned fuel. With additional simple hypothesis, the single-zone model can be extended to a two-zone model which provides information on the instantaneous temperature of both the burned and unburned gas fractions. The method and main assumptions are very similar to those described by Ishida et al. [6], reasonably validated against experimental data obtained with the two-color method.

Images obtained from in-cylinder visualization allow for further experimental qualitative and quantitative description of the injection and combustion processes. Spray tip penetration, liquid length, flame occurrence, flame luminosity, etc., are available parameters to be potentially correlated with engine operating condi-

Contributed by the Internal Combustion Engine Division of THE AMERICAN SOCIETY OF MECHANICAL ENGINEERS for publication in the ASME JOURNAL OF ENGINEERING FOR GAS TURBINES AND POWER. Manuscript received by the ICE Division, July 1999; final revision received by the ASME Headquarters, Nov. 2001. Editor: D. N. Assanis.

tions and engine performance. Finally, with theoretical arguments or modeling, new insights can be explored to compare with the experimental data.

Experimental Facilities and Setup

Single-Cylinder Engine. The engine used for this work is a single-cylinder engine with 123 mm bore, 156 mm stroke, and 16.3 compression ratio, equipped with a common-rail injection system capable of operating at an injection pressure up to 130 MPa. The cylinder head is a four-valve type one with an 8×0.18 mm hole nozzle central injector and low swirl number (SN=0.8).

To simulate the turbocharger, three root compressors supplied the compressed air, whose temperature at the engine inlet was controlled by an external heater. Air pressure and temperature were regulated in a stagnant chamber at the intake port. The restriction due to the exhaust turbine was simulated by a back pressure valve at the exhaust system. Fuel consumption was measured by a dynamic fuel meter based on the gravimetric measuring principle, and air flow rate by a hot wire anemometer based measurement device (SENSIFLOW). In-cylinder pressure has been measured with a Kistler 6067B pressure transducer and needle lift data were provided by a Hall-effect sensor.

The measurement of NO_x and CO was made with a HORIBA 7100 analyzer. Smoke emission was measured with a variable sampling smoke meter AVL 415 providing results directly in Bosch units that were transformed into dry soot mass emissions by means of a correlation by Christian et al. [7].

Optical Access and Visualization Systems. To allow optical access to the combustion chamber one of the exhaust valves was deactivated and replaced by two small quartz windows for endoscopic visualization and external illumination, respectively. To allow a proper visualization avoiding spray overlapping, the original 8×0.18 nozzle was replaced by a 2×0.18 nozzle to isolate two sprays and get unmasked images of one of them.

A flexible optical linkage is used to transfer the images from the endoscope to the recording camera avoiding the engine vibration. The layout of the system for image acquisition is shown in Fig. 1.

A color CCD camera (PULNIX TMC9700) with a spatial resolution of 768×484 pixels is used as the recording device. The system is triggered by TTL trains provided by an optical shaft encoder with a resolution of 0.1 CAD, though only one frame within a period of various cycles can be obtained. Shutter was selected at 1/4000 s⁻¹ to optimize the dynamic range of the camera in the combustion pictures. External illumination for spray imaging is provided by a stroboscopic Xe flash lamp (8 μs at 1/2 of the maximum intensity) and introduced into the combustion chamber through a fiber optics bundle. Thus, the effective shutter in the images without combustion corresponds to the flashlight duration.

Duration of the tests is limited by window contamination, which depends on the particular engine conditions tested. Before

and after each visualization test a calibration of the window transmittance was made to ensure that window contamination would not affect significantly the accuracy of the measurements on the images.

To perform statistical calculations ten pictures per instant of the combustion process have been taken at intervals of 2.5 CAD, and five pictures per instant for the injection images before the start of combustion at intervals of 0.2 CAD. To study geometrical features of the spray and the flame, a purpose-made image processing software has been developed which performs the correction of geometrical features of the images (including correction of the distortion introduced by the wide viewing angle of the endoscope), noise reduction in the image and automatic segmentation of the spray/flame from the background ([8]).

Maximum errors of the processing method used, with a careful choice of the thresholds for spray segmentation, have been estimated below ten percent for the visible spray tip penetration at the first stages of the injection process, and below two percent when the spray is further developed. Discrepancies between the values for penetration measured from different individual images and those obtained from the averaged pictures lie within these limits, though the variation of the injection process itself is included in this last case.

Regarding flame analysis, three different numerical parameters were estimated for each image: global flame luminosity (arithmetical addition of the digital levels of all the pixels in the average image above a given threshold, which gives an idea of the flame size and brightness), area of the flame (number of pixels in the average image with a digital level above the threshold, which gives an idea of the flame size, although the image is a two-dimensional representation of the flame) and weighted flame luminosity (ratio between both parameters, which provides information on the real averaged brightness of the flame, useful to compare different tests and the evolution within each test).

A preliminary sensitivity analysis of the combustion images showed that elastically scattered light from the flashlamp, shot noise and CCD read noise have a very low weight on the images for the camera settings used and can be neglected. Thus, recorded flame luminosity depends mainly on soot concentration and temperature though quantification is not possible at this stage of the research.

Experimental Matrix

Performance Tests. Three basic operating conditions, summarized in Table 1, have been chosen for this work. The nomenclature followed for the modes designation is consistent with the European steady-state cycle (ESC) implemented with the EURO III standard. The three selected engine operating conditions are relevant in the ESC cycle: A-100 and C-100 are full load modes with a weighting factor of 8 percent, while B-75 is a 75 percent load mode with a weighting factor of 10 percent ([9]).

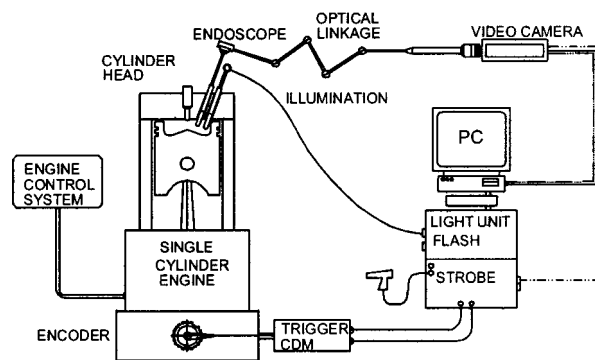


Fig. 1 Video-system layout

Table 1 Basic operating conditions

Mode	n (rpm)	IP (MPa)	m _{fcc} (mg/c)	SOI (CAD)	BP (MPa)	EP (MPa)	IT (°C)	F/A
A-100	1200	90	215	6 ATDC	0.25	0.200	35	0.62
B-75	1500	100	150	4 ATDC	0.22	0.205	35	0.49
C-100	1800	130	190	2 ATDC	0.30	0.315	40	0.48

EP = Exhaust back pressure IT = Inlet temperature

Table 2 First set of experimental conditions

Mode	SOI (CAD)	IP (MPa)	F/A
A-100	4, 6, 8, 10 ATDC	70, 80, 90, 100, 110	0.62
B-75	2, 4, 6, 8 ATDC	80, 90, 100, 110, 120	0.49
C-100	0, 2, 4, 6 ATDC	90, 100, 110, 120, 130	0.48

Table 3 Second set of experimental conditions

A100					
BP (MPa)	0.23	0.24	0.25	0.26	0.27
F/A	0.67	0.65	0.62	0.60	0.57
B75					
BP (MPa)	0.20	0.21	0.22	0.23	0.24
F/A	0.55	0.52	0.49	0.47	0.45
C100					
BP (MPa)	0.28	0.29	0.30		
F/A	0.53	0.50	0.48		

Table 4 Visualization tests

Mode	n (rpm)	IP (MPa)	SOI (CAD)
A-100	1200	70	10 ATDC
A-100	1200	90	6 ATDC
A-100	1200	110	4 ATDC
B-75	1500	80	8 ATDC
B-75	1500	100	4 ATDC
B-75	1500	120	2 ATDC
B-75	1200	100	4 ATDC
B-75	1800	100	4 ATDC
C-100	1800	90	2 ATDC
C-100	1800	130	2 ATDC
C-100	1200	130	2 ATDC

In a first set of tests 60 experimental conditions were considered. SOI and IP were modified according to Table 2.

A second set of 13 additional experiments was carried out for different BP values and their corresponding F/A, keeping the difference between BP and EP constant for each mode, according to Table 3. Values corresponding to the baseline conditions for each mode are indicated in boldface type in both tables. In the case of C-100 the experimental facility has a maximum BP limit of the order of 0.3 MPa and a maximum injection pressure limit of 130 MPa, so that only lower values could be tested.

Visualization Tests. Visualization tests were carried out injecting fuel with a two-hole nozzle at the operating conditions summarized in Table 4. All the conditions of this matrix were also tested in normal eight-hole operation.

Engine conditions for image recording were decided with the following criteria:

- Mode A-100: Together with the baseline case, two extreme conditions have been chosen with both low-pressure retarded injection and high-pressure advanced injection.
- Mode B-75: The first three cases for this mode have been chosen with the same arguments of the former mode. In addition, the effect of the engine speed has been tested, keeping constant all the other operating conditions.
- Mode C-100: The effects of the injection pressure and engine speed on the spray/flame development have been evaluated.

Comparison Between Eight-Hole and Two-Hole Nozzle Engine Operation

Fuel is injected in the cylinder through eight holes (8H) in the baseline case. As explained previously this arrangement does not allow a proper visualization of the in-cylinder processes. Instead, a two-hole arrangement (2H) was selected. The first question to be answered concerns the similarities and differences between the engine operating conditions with this two arrangements, in order to evaluate to which extent the recorded images can represent the baseline conditions.

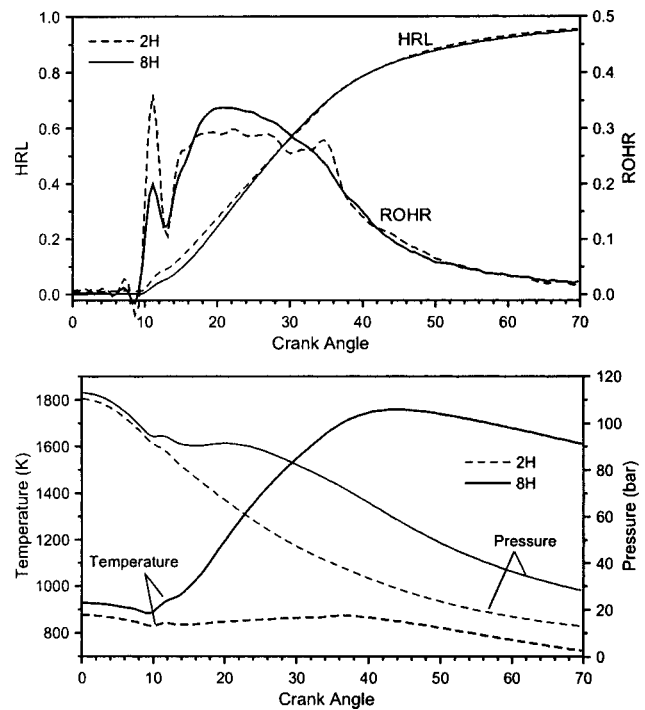


Fig. 2 HRL analysis for 2H and 8H arrangements. A-100.

Fuel Delivery. Nozzle hole diameter and injection pressure have been the same for equivalent 2H and 8H test conditions and the fuel quantity per cycle has been reduced to 1/4 of the original case. Despite these analogous conditions, the injection rate is not exactly the same due to the higher overall discharge coefficient of the 2H injector. As expected, the difference is more appreciable at low needle lifts, where the injected fuel quantity is controlled by the needle position. The measured injection duration difference increases for lower injection quantities, being less than eight percent for mode B-75.

Heat Release Law Shape. Figure 2 shows a comparison of the measured in-cylinder pressure, the calculated HRL and the calculated average temperature for nominal test condition A-100 in the 2H and 8H arrangements.

In-cylinder pressure during the combustion process is much lower in the 2H arrangement as expected, as well as the average temperature with a reduction of the maximum values from 1400°C down to 600°C. Focusing on the rate of heat release (ROHR) it can be noticed that the start of combustion (SOC) is very similar in both cases, but the amount of fuel burnt in premixed conditions has increased from five percent in the 8H arrangement up to eight percent in the 2H case. The reason for this increase seems not to be associated with a longer ignition delay but to an increase of the injection rate at early injection stages as commented.

Concerning the diffusion controlled combustion fraction, the shape of the ROHR curve shows some differences also. The 2H arrangement presents a more "rectangular" profile with a sudden increase after the premixed spike, an almost constant value over a long crank angle interval and a sudden decay at about 35 CAD ATDC for this operating mode. On the other hand, the 8H arrangement shows a more conventional "rounded" shape with smaller increase and decay slopes but higher combustion rate over most of the diffusion controlled combustion fraction. The higher combustion rate for the 8H arrangement seems to be associated with a higher flame temperature due to a higher compression temperature and lower percentual heat losses of diffusive and radiative type. The higher flame temperature implies consequently a

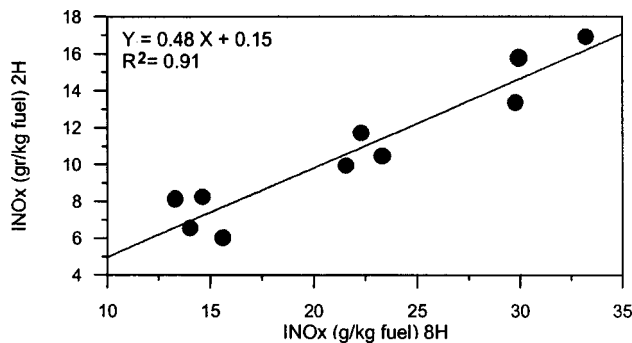


Fig. 3 NO_x relationship between 2H and 8H cases

higher evaporation rate and a higher combustion velocity. The situation changes at the later stages of the combustion process where fresh air entrainment into the spray is warranted in the 2H arrangement while burnt gases are also entrained in the 8H case, slowing down the late diffusion controlled combustion.

NO_x Emissions. NO_x emissions in ppm follow the same trend in both arrangements with lower values for the 2H arrangement than for the 8H nozzle as expected. Assuming similarity between both combustion processes, a reduction of NO_x by a factor of 4 measured in ppm or, in other words, similar INO_x values (gNO_x/kg fuel) could be expected. Figure 3 shows a plot of the INO_x emission obtained with the 2H arrangement versus the INO_x emission obtained in the 8H case. A quite acceptable linear relationship can be observed being the slope of the linear fit 0.48. Lower flame temperature during the combustion process in the 2H arrangement is responsible for this 50 percent reduction in INO_x as can be expected.

Smoke Emissions. Smoke emissions follow also a similar trend in both configurations with much lower values for the 2H arrangement in smoke units due to a lower F/A ratio. Figure 4 presents a plot of the dry soot emissions in gC/kg fuel (Isoot) in both arrangements. An almost linear relationship can be stated with a slope of 1.97 or, in other words almost twice dry carbon emissions have been obtained per kg of fuel in the 2H arrangement, despite the much lower F/A ratio. The reason for this behavior could be related to the lower end cycle temperatures for this arrangement as explained later. The test condition A-100 with the latest SOI and the lowest IP deviates significantly from this behavior and it has been excluded from the linear fit. This test condition presents higher soot emissions for the 8H arrangement (it is the last point on the right side of Fig. 5) for reasons which will be explained later.

As a summary, it can be said that despite the fact that the in-cylinder boundary conditions at the injection beginning and the injection parameters for a single spray are almost identical, there

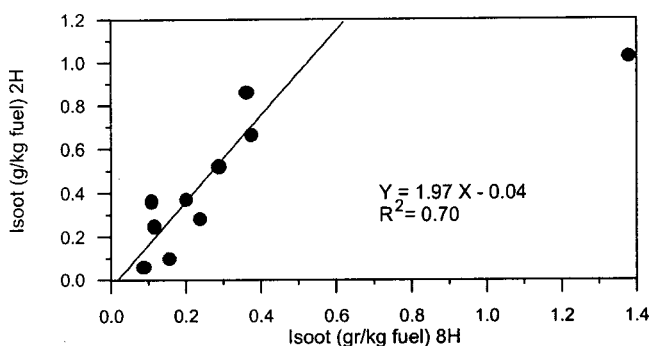


Fig. 4 Soot comparison between 2H and 8H cases

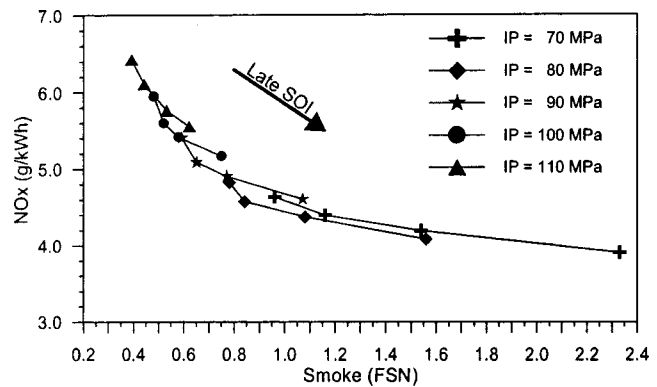


Fig. 5 NO_x—Smoke tradeoff. Mode A-100.

are differences in both arrangements related to the injection rate, flame temperature and spray-air entrainment that conditions the combustion process in terms of both ROHR and emission production. Being careful and knowing these differences, the comparison of information obtained from the images can be extrapolated, at least qualitatively, to the real 8H operation.

Analysis of Results

The analysis of results has been organized as follows.

A first part is devoted to the results obtained from the engine in the performance version focusing on BSFC, NO_x, and smoke emissions. Results are presented separately for each experimental set. Table 5 shows, as a summary, the variations found (in percent) in the measurement of BSFC, NO_x, and smoke for the three modes considered when the operating parameters indicated in the second column of the table (labeled as "variation of") are increased in the quantities stated into brackets.

In a second part of the analysis, the results obtained from visualization are presented and correlated with the performance tests.

Analysis of Results. Performance Tests. Set 1. Later SOI during the engine cycle means that fuel is injected against compressed air at lower density and temperature. Higher spray penetration is achieved but air mass entrainment is reduced. The typical size of the atomized droplets is also reduced ([10]). The combustion process will take place at lower in-cylinder temperature and pressure.

On the other side, the increase in IP shortens injection duration and so a quicker combustion process is expected with higher cycle temperature and pressure histories. In addition, larger spray penetrations are achieved but also higher air entrainment and reduced drop size. High injection, mixing, and evaporation rates produce a fast combustion process development at high temperature.

The measured effect of SOI and IP on the engine performance can be summarized as follows:

Table 5 Performance sensitivity to operating parameters

	Variation of:	A-100	B-75	C-100
BSFC (g/kW h)	SOI [1 CAD]	1.92	1.83	2.13
	IP [100 bar]	-2.75	-1.75	-2.50
	BP [100 mbar]	-1.12	-1.01	-1.27
NO _x (g/kW h)	SOI [1 CAD]	-1.9	-3.0	-3.4
	IP [100 bar]	7.20	8.60	12.80
	BP [100 mbar]	1.07	1.03	2.23
SMOKE (FSN)	SOI [1 CAD]	12.50	~ 0	5.9
	IP [100 bar]	-18.75	-12.62	-18.25
	BP [100 mbar]	-12.31	-24.85	-3.00

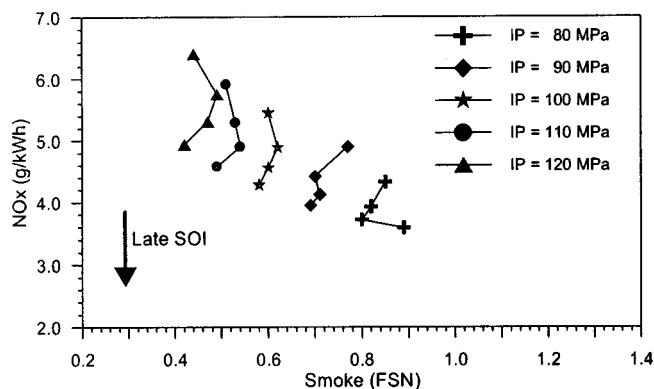


Fig. 6 NO_x—Smoke tradeoff. Mode B-75.

Brake Specific Fuel Consumption. BSFC increases with later SOI, with a two percent increment each crank angle degree, independently of the engine operating conditions (see Table 5).

Higher IP produce a BSFC reduction between two and three percent for each 100 bar increase. The most sensitive mode is A-100.

NO_x Emissions. NO_x emissions both in ppm and in g/kWh are reduced for late injection. The measured benefit is quantified in two–three percent each CAD with higher benefits for earlier nominal SOI angle. This small reduction of NO_x shows that in late SOI arrangements a further injection retardation is not efficient for NO_x reduction.

As expected, higher NO_x emissions were measured at higher IP. The amount of this increase lies in the range of 7–13 percent for each 100 bar increase, being larger at higher engine speed.

Smoke Emissions. The smoke emission trend as a function of SOI differs from one mode to another. Mode A-100 shows a systematic increase of the order of 12 percent each retarded crank angle. This trend is consistent with the results obtained from the literature, for instance Feola et al. [11]. Mode C-100 is much less sensitive to SOI, mainly at low injection pressure. Finally, in mode B-75 SOI does not affect substantially the smoke emission independently of IP. An additional short test was performed for mode B-75 increasing the explored range from 4 CAD BTDC to 11 CAD ATDC. The measured smoke emission showed an increasing-decreasing trend with peak values of 0.9 F.S.N. around 4 CAD ATDC. Khan [12] and Khan et al. [13] observed also this trend.

The engine is also very sensitive to IP as far as smoke emissions are concerned. A reduction ranging from 12 to 19 percent each 100 bar has been experimentally confirmed. Higher reduction was achieved at high load conditions.

NO_x—Smoke Tradeoffs. Figures 5, 6, and 7 show the NO_x—smoke tradeoffs for the three operating conditions considered. For mode A-100, NO_x and smoke are well correlated for the whole test matrix conditions. However, for modes B-75 and C-100 a different family of tradeoff curves is obtained for each injection pressure value.

From an overall point of view, analysing all the results obtained in this first set of the parametric study, it can be stated that BSFC is mainly controlled by the placement of the combustion process with respect to TDC, with AQ-75 (CAD at which a 75 percent of the heat has been released) being a good parameter to correlate.

Figure 8 shows the INO_x emissions versus the inverse of the maximum burnt gas temperature. The correlation between these two parameters is quite good for the three engine operating conditions, showing that NO_x exhaust gas emission level is mainly controlled by the peak burnt gas temperature ([14–17]). The slope of the fits to the experimental points is very similar for modes

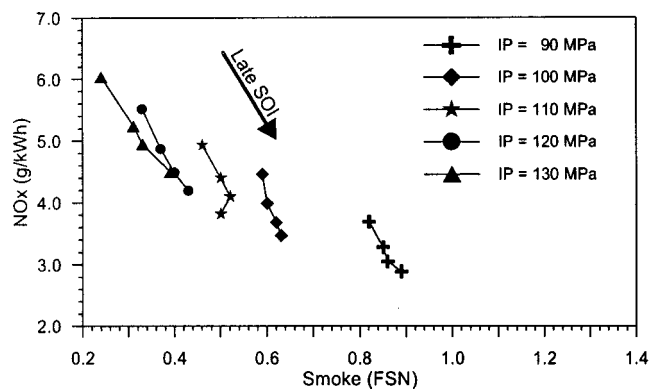


Fig. 7 NO_x—Smoke tradeoff. Mode C-100.

A-100 and C-100 with lower values in the last case at equal maximum burnt gas temperature. The shorter characteristic time at higher engine speed could explain this trend ([17]). Mode B-75 shows a higher slope with values similar to those of A-100 at high burnt gas temperatures and similar to those of C-100 at low burnt gas temperatures.

Smoke emissions are not so easy to correlate with a single parameter up to this stage.

Analysis of Results. Performance Tests. Set 2. When intake pressure (BP) is modified from the nominal value keeping a constant ΔP between intake and exhaust, the air mass entering the engine varies almost linearly with the intake pressure. The in-cylinder pressure at the end of the intake process is also proportional to the intake pressure and the pressure history during compression increases consequently. Temperature during compression is almost independent of the intake pressure due to the proportionality between mass and pressure, and it is controlled by the intake temperature, that has been kept constant for each operating mode. During combustion, obviously higher maximum in-cylinder pressure is obtained but single-zone combustion analysis predicts lower averaged temperature profiles due to a higher amount of gas not participating in the combustion process and acting in fact as a nonreacting dilutant gas. Gas density increases linearly with intake pressure reducing spray penetration and increasing the SMD of the spray droplets, but promoting higher air mass entrainment. From another point of view, of course a reduction in the overall F/A ratio is achieved when BP is increased. The following trends have been found increasing BP:

Brake Specific Fuel Consumption. A consistent reduction of BSFC has been measured for all the modes. This reduction can be estimated to one percent each 100 mbar (Table 5) and is due to an

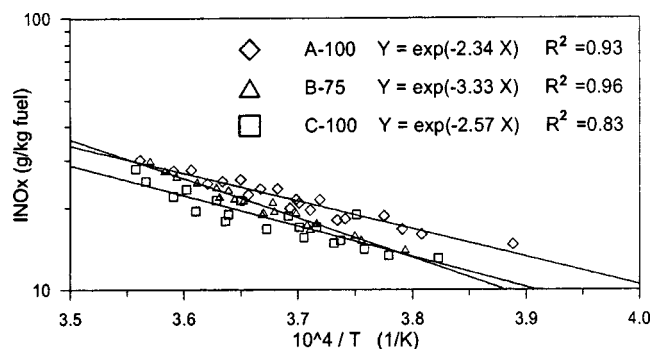


Fig. 8 INO_x emissions versus maximum burnt gas temperature

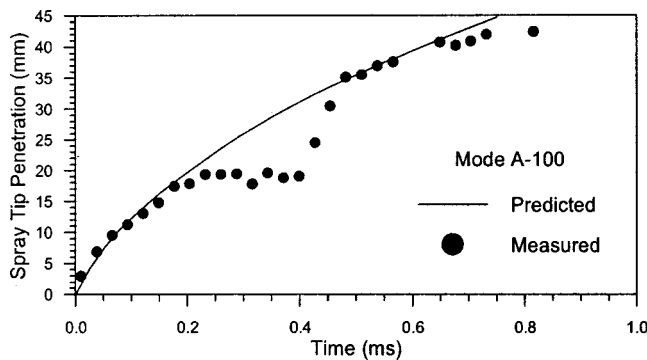


Fig. 9 Spray tip penetration. Mode A-100 nominal.

experimentally confirmed reduction of the combustion duration when BP is increased. This result is consistent with the statement made on the set 1 analysis.

NO_x Emissions. NO_x emissions are almost independent of BP (see Table 5), which is consistent with the statements made on regards of Fig. 8 at the end of the analysis of set 1 results, taking into account that maximum burnt temperature is independent of BP.

Smoke Emissions. Smoke is reduced in all the modes for increasing intake pressure, being the effect much more pronounced for mode B-75 and almost negligible for mode C-100 (Table 5). The reduction of smoke emissions when F/A is reduced can be expected, but it is interesting to note the large difference observed among modes.

CO Emissions. The trends of emitted CO versus intake pressure are very similar to those of smoke. This similarity allows to guess that CO emissions in this engine are mainly due to a rich combustion process, while overlean CO emissions have less importance.

Analysis of Results, Visualization Tests. Results from visualization tests are available in the bibliography, but usually for rapid compression machines (e.g., [18,19]) or transparent engines (e.g., [20,21]) and quite few with actual engine geometry (e.g., [22,23]). Injection and combustion in-cylinder visualization through endoscopy with actual engine geometry allows a qualitative analysis of its evolution, but also a quantitative description of some processes relevant to the understanding of the engine behavior.

Spray Penetration. Figure 9 shows the spray penetration obtained from the recorded images for nominal A-100 engine operating conditions. When there is not combustion, dots represent the maximum axial position of the liquid fuel; when flame appears the measurement corresponds to the maximum distance of the flame on the spray axis. During the first 0.2 ms after SOI the spray penetrates in the combustion chamber and the visible liquid part of the spray grows up to approximately 19 mm, remaining constant during the next 0.2 ms in the considered test case. During this period the evaporation rate and the injection rate are similar, and the plateau region of the curve is in agreement with the observations by Espey and Dec [24]. Approximately after 0.4 ms from SOI, flame appearance occurs with a sudden enlargement of the visible penetration that is supposed to be approximately coincident with the maximum flame length. After this abrupt change, spray tip penetration further grows up with time until wall impingement. The length of the spray path until bowl wall impingement is around 43/44 mm, being impossible to extract quantitative information about the wall spray evolution from the images. The solid line in Fig. 9 is the spray tip penetration predicted by a phenomenological spray evolution model, DIES ([25,26]), based

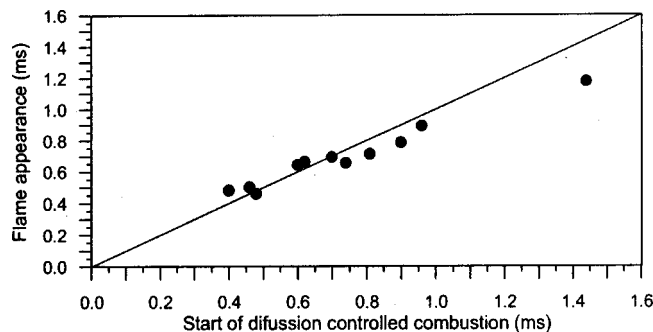


Fig. 10 Time of flame appearance versus start of diffusion-controlled combustion

on the mass and momentum conservation, and assuming similarity between a Diesel spray and a turbulent gaseous jet. The agreement between the experimental data and the model prediction is quite good in all cases, showing on the one hand that Diesel-type sprays injected in a high density environment behave macroscopically in a similar way to gaseous jets and, on the other hand, that the image processing procedure used is accurate to follow the time evolution of the spray-combustion process.

Ignition Delay and Flame Appearance. A correlation of the ignition delay time (IDT) has been tried with all the available tests as a function of in-cylinder pressure, in-cylinder gas temperature during IDT and injection pressure with the result

$$IDT \propto \exp[4090/T_a] \cdot P^{-0.57} \cdot IP^{-0.21} \quad (R^2 = 0.97). \quad (1)$$

This expression is similar to others found in the literature concerning the effect of the gas temperature and pressure ([27–29]). A new relevant parameter included in this correlation is the injection pressure that appreciably influences the value of IDT, reducing it when IP increases. This dependence has also been noticed previously ([30]). The result indicates that for air density and IP reflective of current heavy duty Diesel engines the physical ignition delay is not negligible.

Flame appearance occurs after the heat release initiation, and correlates quite well (Fig. 10) with the start of the diffusion controlled combustion defined arbitrarily at the minimum of the ROHR curve after the premixed spike. The point outside the correlation is A-100, with late SOI and low IP, where the visible flame starts before the end of the premixed combustion fraction showing that premixed combustion phase is a sooting process at these conditions.

Evaporation Characteristic Length. As explained before, the liquid visible spray length grows to a given penetration and remains constant until flame appearance. The maximum liquid spray length, or the associated characteristic time, fulfils the condition that the injection rate and the evaporation rate up to this point are identical. Some recent research in closed bombs ([31,32]) with injection pressures and air densities similar to that used in our experiments found that the evaporation length is a function of the air density, the air temperature, and almost independent of the injection pressure. These results are consistent with previous data of Espey and Dec [24] in an optical engine while an additional small dependence of the injection pressure has been found by Verhoeven et al. [33] with increasing liquid lengths at higher injection pressures. In all the test cases reported in this paper the flame appearance occurs well after the liquid length stabilization, which means that the primary source of energy for fuel vaporization is the hot air entrained by the spray and not the energy from the combustion process. The evaporation process can then be controlled either by the rate of air entrainment (mixing controlled) or by the rate of heat and mass diffusion (diffusion controlled).

With our set of experiments we tried a general correlation of the liquid length (LL) with the air density, the air temperature and the

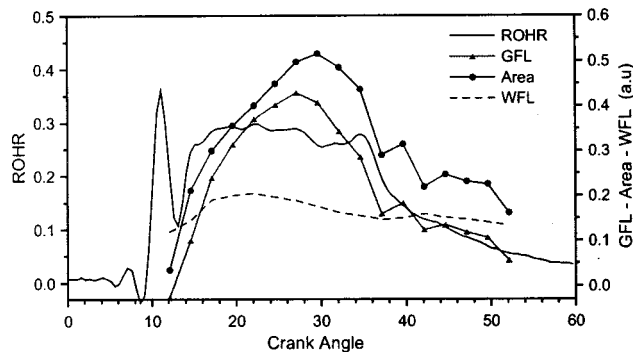


Fig. 11 GFL, area, WFL and ROHR versus angle. A-100.

injection pressure (covering the ranges 31 to 52 kg/m³, 800 to 1050 K and 70 to 130 MPa, respectively) with the following results:

$$LL \propto \rho_a^{-0.71} T_a^{-2} IP^{0.53} \quad (R^2 = 0.94). \quad (2)$$

This equation shows a decrease of the evaporation length when the air density and the temperature increase, and an increasing trend with the injection pressure.

Air entrainment normalized to the fuel mass flux in completely atomised sprays ([34–36]) follows the relationship

$$\frac{\dot{m}_a}{\dot{m}_f} \propto \frac{x}{d_o} \sqrt{\frac{\rho_a}{\rho_f}} \quad (3)$$

while from an energy balance the amount of entrained air mass flow normalized to fuel mass flow to completely vaporize the fuel should be

$$\frac{\dot{m}_a}{\dot{m}_f} = \frac{C p_f \cdot (T_{boi} - T_f) + H_{vap}}{C p_a \cdot (T_a - T_{boi})}. \quad (4)$$

Combining Eq. (3) and Eq. (4), a first estimation of the liquid length in a mixing controlled situation should give $LL \propto \rho_a^{-0.5} T_a^{-1}$. However, the exponents found in the experimental correlation for air density and temperature and the dependence upon the injection pressure show that in the engine operating conditions under study the evaporation process is definitively not mixing controlled.

Flame Luminosity. Figure 11 shows a superposition of the HRL, the ROHR, the global flame luminosity (GFL), the area of the flame and the weighted flame luminosity (WFL) for nominal A-100 test conditions.

Flame appearance is almost simultaneous with the start of the diffusion controlled combustion in all the test cases (see also Fig. 10). Flame area grows when diffusion combustion starts showing a maximum at a crank angle at which the amount of heat released is between 50 and 60 percent in all the tested cases. After peaking, the flame area decays first quickly and later slowly with patterns that depend on the operating conditions. WFL has a smooth evolution with crank angle with a systematic maximum around 30 percent of heat released, decaying later with patterns that are also engine operating dependent.

WFL correlates quite well with burnt gas temperature at different crankangles. Focusing on the crankangle at which a 75 percent of the heat has been released, a good correlation (Fig. 12) can be also found between the WFL and the emitted ISoot.

This result shows that in the overall lean conditions (as is the case of the 2H operation) the ISoot controlling parameter is the end combustion temperature, independently of the engine operating conditions. Low emissions are achieved keeping a high temperature in the final part of the combustion process, i.e., bright flames. Burnt gas temperatures below 2200 K increase dramati-

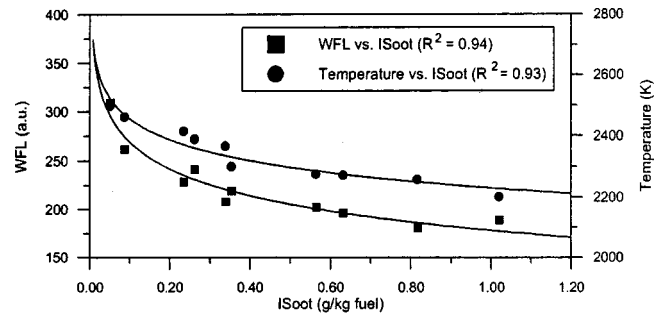


Fig. 12 WFL and burnt gas temperature versus smoke at a crank angle where 75 percent of the total heat has been released

cally the ISoot emission. Lower end combustion temperatures can explain the higher ISoot emissions observed in the 2H operation (see Fig. 4).

Soot Emission. Figure 13 represents the dry soot emission versus the inverse of the burnt gas temperature for all the tested cases of set 1 and set 2. The increasing trend with decreasing end combustion temperature is apparent for the three engine operating modes as explained in the previous paragraph, but the sensitivity and the emission level is different for each mode.

Mode C-100 shows the lowest soot emission levels and it is able to keep this trend even in the low temperature range. Compared with the other two modes, in mode C-100 the in-cylinder air during the injection-combustion process has a high density (due to a high BP and early SOI) and a high temperature (due to a higher intake temperature and lower heat losses). Liquid spray lengths are small (15 mm at nominal conditions) and flame develops far from the bowl wall (at 20 mm from the nozzle). In addition higher swirl velocities are expected due to the high engine speed. Smoke emissions are not sensitive to the intake pressure, and the tested operating conditions modifying SOI, IP, and BP lay on the same correlation curve, which allows to think that the spray air entrainment is high enough in all the explored range, and the evaporation process is diffusion controlled. The calculated SMD of the spray droplets according to the equation proposed by Hiroyasu and Arai [10] is 41 μ m at nominal conditions.

Mode B-75 shows higher soot levels but, on the contrary, the sensitivity to the end gas temperature is lower than in the former case. In-cylinder conditions characteristic of this operating mode are much lower density and lower air temperature than for C-100. Relative high-injection pressure and low gas density allows for small spray droplet diameter (37 μ m at nominal conditions). BP influence on the soot emissions is evident from Fig. 13 with a sharp increase for reduced BP or, in other words, reduced in-

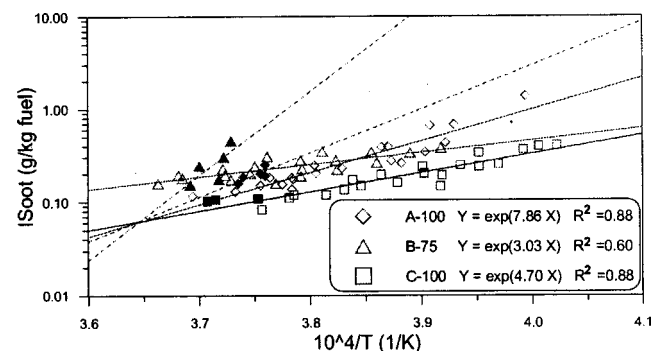


Fig. 13 ISoot emissions versus burnt gas temperature at 75 percent of heat released. Set 1 (hollow symbols, solid line). Set 2 (filled symbols, dashed line).

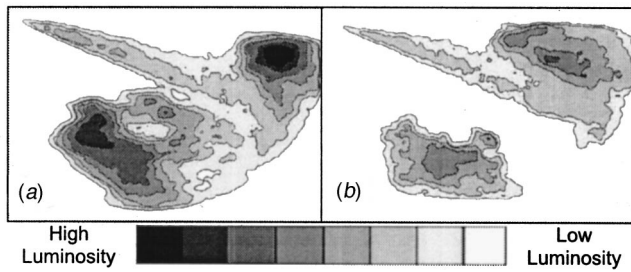


Fig. 14 Flame just before end of injection; (a) C-100, nominal conditions (b) A-100, late SOI, low IP

cylinder air density, even for quite high-end combustion temperature. These statements allow to guess that the evaporation process is mixing controlled for this mode that shows liquid spray lengths of the order of 18 mm and flame development at about 30 mm from the injector for nominal conditions. Mode A-100 is the most sensitive one according to Fig. 13. At high end combustion temperatures the soot emission is similar to that of mode C-100 while at low temperatures it is largely higher. Mode A-100 is characterized by intermediate air densities compared with the other two modes but lowest air temperatures due to a late SOI and higher heat losses. On the other hand air swirl velocity should be small and estimated SMD of the droplets is 40 μm . Liquid spray lengths at nominal conditions are about 20 mm and flame development at 35 mm. The sensitivity to BP, and so to the air density, is clearly lower than for mode B-75.

At high end combustion temperatures that correspond to early SOI and high IP, the evaporation process is probably diffusion controlled while at lower end combustion temperatures the process turns to be mixing controlled.

Figure 14 shows a comparison of pictures of the spray flame situation just before the end of injection for nominal C-100 and low IP, late SOI A-100. In both cases the picture corresponds to a crank angle at which 70 percent of the heat has been released. While picture (a) shows a continuous flame around the spray with large high luminosity (and so high temperature or high soot concentration) areas, picture (b) shows that the jet impinges against the bowl wall and the flame develops later. Unburned wall jet impingement promotes turbulence and thus combustion duration is shortened, but flame quenching is usual ([37]). A poor air entrainment retarding the evaporation process and forcing a rich combustion process, together with a low end combustion temperature and relatively high F/A ratios increase drastically the ISoot emission. It should be noted that picture (b) corresponds to the point which deviates from the linear fit of Fig. 4 where a comparison of soot emissions between the 2H and 8H arrangements was made. It implies that, since this effect is evident with the 2H arrangement used for visualisation, it should have been much more marked if visualization tests could have been performed with the real 8H arrangement.

Summary and Conclusions

The injection-combustion process of a HDTCA single cylinder engine with EURO III specifications was analyzed at three operating modes relevant to the ESC testing cycle through a parametric study focusing on engine performance and emissions as well as through in-cylinder visualization. A comparison has been carried out between the behavior of the 8H and 2H arrangements, characteristic of the actual engine and the visualisation operating conditions, respectively, discussing the analogies and differences between them.

The sensitivity of engine performance to operating parameters like SOI, IP, BP and engine speed has been quantified (Table 5). Several parameters characterizing the injection-combustion process have been correlated with statistically relevant engine param-

eters, ignition delay is controlled by in-cylinder gas temperature and pressure, but also by the injection pressure, showing that the physical delay is not negligible in current HD engines. Visible flame appearance occurs at the end of the premixed combustion process with the exception of a very high sooting combustion process where visible flame is advanced.

The correlation found for the liquid spray length (Eq. (2)) show that the combustion process all over the operating conditions tested is not always mixing controlled.

BSFC is determined by the relative position of the combustion process in the cycle and correlates quite well with the crank angle at which a 75 percent of heat has been released.

INO_x emissions are mainly controlled by the peak burnt gas temperature for the three explored engine modes. At the same peak burnt gas temperature lower emissions are obtained when engine speed increases due to a reduction in the cycle characteristic time.

ISoot emissions are mainly controlled by the end burnt gas temperature, decreasing with higher values of this one. Lower emissions have been measured at engine operating conditions where the evaporation process is guessed to be diffusion controlled, while higher values appear when a mixing controlled process is guessed. ISoot emissions increase dramatically when the air-fuel jet impinges against the bowl wall before burning.

Acknowledgments

The authors would like to thank RVI for the financial support of this research work and their permission for publication of this paper.

Nomenclature

2H	= two hole
8H	= eight hole
ATDC	= after top dead center
BP	= boosting pressure (MPa)
BMEP	= brake mean effective pressure (MPa)
BSFC	= brake specific fuel consumption (g/kW h)
CAD	= crankangle degrees
C_p	= constant pressure heat capacity (kJ/kgK)
EP	= exhaust pressure (MPa)
F/A	= fuel air ratio
FSN	= filter smoke number
GFL	= global flame luminosity (a.u.)
H	= latent heat of evaporation (kJ/kgK)
HRL	= heat release law
IDT	= ignition delay time (ms)
IP	= injection pressure (MPa)
IT	= inlet temperature (K)
LL	= liquid length (mm)
P	= in-cylinder pressure (MPa)
ROHR	= rate of heat release
SOC	= start of combustion (CAD)
SOI	= start of injection (CAD)
SMD	= Sauter mean diameter (μm)
T	= temperature (K)
WFL	= weighted flame luminosity (a.u.)
a.u.	= arbitrary units
d_o	= nozzle diameter (mm)
m	= mass flow rate (kg/s)
x	= axial coordinate of the spray (mm)
ρ	= density (kg/m ³)

Subscripts

a	= air
boi	= boiling
f	= fuel
vap	= vaporized fuel

References

- [1] Herzog, P. L., Buerger, L., Winklhofer, E., Zelenka, P., and Cartellieri, W., 1992, "NO_x Reduction Strategies for D.I. Diesel Engines," SAE Paper 920470.
- [2] Knecht, W., Amann, G., and González-Balmás, F., 1992, "Truck Diesel Engine Development for Future Emission and Noise Standards," *Proceedings of the International Congress "The Powertrain: Development and Future,"* Société des Ingenieurs de l'Automobile, pp. 290–298.
- [3] Havenith, C., Needham, J. R., Nicol, A. J., and Such, C. H., 1993, "Low Emission Heavy Duty Diesel Engine for Europe," SAE Paper 932959.
- [4] Payri, F., Desantes, J. M., Leiva, A., and Armas, O., 1997, "Thermodynamic Model for the Experimental Diagnostics of the Combustion Process in D.I. Diesel Engines," *Proc. III Congreso Iberoamericano de Ingeniería Mecánica*, La Habana, Cuba, Instituto Superior Politécnico José Antonio Echeverría (in Spanish).
- [5] Lapuerta, M., Armas, O., and Hernandez, J. J., 1999, "Diagnostic of D.I. Diesel Combustion From In-Cylinder Pressure Signal by Estimation of Mean Thermodynamic Properties of the Gas," *Appl. Therm. Eng.*, **19**, pp. 513–529.
- [6] Ishida, M., Ueki, H., Matsumura, N., Yamaguchi, M., and Luo, G. F., 1996, "Diesel Combustion Analysis Based on Two Zone Model (Comparison Between Model Analysis and Experiment)," *JSME Int. Journal, Series B*, **39**, No. 1, pp. 185–192.
- [7] Christian, R., Knopf, F., Jasmek, A., and Schindler, W., 1993, "A New Method for the Filter Smoke Number Measurement With Improved Sensitivity, (in German)," *Motortechnische Zeitschrift*, **54**, pp. 16–22.
- [8] Pastor, J. V., Arrègle, J., and Palomares, A., 2001, "Diesel Spray Image Segmentation With a Likelihood Ratio Test," *Appl. Opt.*, **40**, No. 17, pp. 2876–2885.
- [9] Chmela, F., 1996, "Test Cycle Development EURO III for Heavy Duty Diesel Engines," FISITA Congress, Prag.
- [10] Hiroyasu, H., and Arai, M., 1990, "Structures of Fuel Sprays in Diesel Engines," SAE Paper 900475.
- [11] Feola, M., Pelloni, P., Cantone, G., Bella, G., Casoli, G., and Toderi, G., 1992, "Optimization of Injection Law for a D.I. Diesel Engine," ASME Paper 92-ICE-4.
- [12] Khan, I. M., 1970, "Formation and Combustion of Carbon in a Diesel Engine," *IME Symposium*, **184**, Part 3J.
- [13] Khan, I. M., Greeves, G., and Wang, C. H. T., 1973, "Factors Affecting Smoke and Gaseous Emissions From Direct Injection Diesel Engines and a Method of Calculation," SAE Paper 730169.
- [14] Ahmad, T., and Plee, S. L., 1983, "Application of Flame Temperature Correlations to Emissions From a Direct-Injection Diesel Engine," SAE Paper 831734.
- [15] Yu, R. C., and Shaded, S. M., 1981, "Effects of Injection Timing and Exhaust Gas Recirculation on Emissions From a D.I. Diesel Engine," SAE Paper 811234.
- [16] Iida, N., and Watanabe, J., 1990, "Surrounding Gas Condition Effects on NO_x and Particulates," *Proc. International Symposium COMODIA 90*, Japan Society of Mechanical Engineers, Tokyo, pp. 625–632.
- [17] Desantes, J. M., Lapuerta, M., and Salavert, J. M., 1996, "Study on Independent Effects of Diesel Engine Operating Conditions on Nitric Oxide Formation and Emissions Through Schematical Combustion Simulation," *Proc. Inst. Mech. Eng.*, **210**, pp. 71–80.
- [18] Matsuoka, S., Kamimoto, T., and Kobayashi, H., 1984, "Photographic and Image Analysis Studies of Diesel Spray and Flame With a Rapid Compression Machine and a D.I. Diesel Engine (Interpretation and conceptual image)," SAE Paper 845009.
- [19] Balles, E. N., and Heywood, J. B., 1989, "Spray and Flame Structure in Diesel Combustion," *Basic Processes in Internal Combustion Engines, ICE-Vol. 6*, ASME, New York, pp. 1–7.
- [20] Gartner, U., Oberacker, H., and König, G., 1998, "Combustion Analysis of Modern HD Diesel Engines Using Pressure Indication and Film Technique," 3 Internationales Indiziersymposium AVL Germany.
- [21] Arcoumanis, C., Hadjiapostolou, A., and Whitelaw, J. H., 1991, "Flow and Combustion in a Hydra Direct-Injection Diesel Engine," SAE Paper 910177.
- [22] Werlberger, P., and Cartellieri, W. P., 1987, "Fuel Injection and Combustion Phenomena in a High Speed Diesel Engine Observed by Means of Endoscopic High Speed Photography," SAE Paper 870097.
- [23] Payri, F., Pastor, J. V., and Arrègle, J., 1996, "Endoscopic High Speed Visualisation of Injection and Combustion Processes in a D.I. Diesel Engine," *Entropie*, **200**, pp. 7–15.
- [24] Espey, C., and Dec, J. E., 1995, "The Effect of TDC Temperature and Density on the Liquid-Phase Fuel Penetration in a D.I. Diesel Engine," *Transactions of the SAE*, **104**, Section 4, pp. 1400–1414.
- [25] Correias, D., 1998, "Experimental and Theoretical Study of a Diesel Type Free Spray," PhD thesis, Universidad Politécnica de Valencia, Spain (in Spanish).
- [26] Pastor, J. V., Encabo, E., and Ruiz, S., 2000, "New Modelling Approach for Fast Online Calculations in Sprays," SAE Paper 2000-01-0287.
- [27] Wolfer, H. H., 1938, "Ignition Lag in Diesel Engines," *VDI-Forschungsheft* 392 (translated by Royal Aircraft Establishment, Farnborough Library, No. 358, UDC 621-436.047, Aug. 1959).
- [28] Stringer, F. W., Clarke, A. E., and Clarke, J. S., 1969–1970, "The Spontaneous Ignition of Hydrocarbon Fuels in a Flowing System," *Proc. Inst. Mech. Eng.*, **184**, Part 3J.
- [29] Hiroyasu, H., Kadota, T., and Arai, M., 1980, "Supplementary Comments: Fuel Spray Characterization in Diesel Engines," *Combustion Modeling in Reciprocating Engines*, J. N. Mattavi and C. A. Amann, eds., Plenum Press, New York, pp. 369–408.
- [30] Pischinger, F., Reuter, U., and Scheid, E., 1988, "Self Ignition of Diesel Sprays and Its Dependence on Fuel Properties and Injection Parameters," *ASME J. Eng. Gas Turbines Power*, **110**, pp. 399–404.
- [31] Naber, J. D., and Siebers, D. L., 1996, "Effects of Gas Density and Vaporization on Penetration and Dispersion of Diesel Sprays," SAE Paper 960034.
- [32] Siebers, D. L., 1998, "Liquid-Phase Fuel Penetration in Diesel Sprays," SAE Paper 980809.
- [33] Verhoeven, D., Vanhemelryck, J. L., and Baritaud, T., 1998, "Macroscopic and Ignition Characteristics of High-Pressure Sprays of Single-Component Fuels," SAE Paper 981069.
- [34] Ricou, F. P., and Spalding, D. B., 1961, "Measurements of Entrainment by Axisymmetrical Turbulent Jets," *J. Fluid Mech.*, **11**, pp. 21–32.
- [35] Wakuri, Y., Fujii, M., Amitani, T., and Tsuneya, R., 1960, "Studies on the Penetration of Fuel Spray in a Diesel Engine," *Bull. JSME*, **3**, No. 9.
- [36] Chikahisha, T., and Murayama, T., 1995, "Theory and Experiments on Air-Entrainment in Fuel Sprays and Their Application to Interpret Diesel Combustion Processes," SAE Paper 950447.
- [37] Kamimoto, T., and Kobayashi, H., 1991, "Combustion Processes in Diesel Engines," *Prog. Energy Combust. Sci.*, **17**, pp. 163–189.

Internal Combustion Engine Noise Analysis With Time-Frequency Distribution

G. T. Zheng¹

School of Astronautics,
Beijing University of Aeronautics
and Astronautics,
Beijing, China 100083
e-mail: gtzhengtu@yahoo.co.uk

A. Y. T. Leung

School of Engineering,
Manchester University,
Manchester, UK
e-mail: Andrew.leung@cityu.edu.uk

An analysis procedure, using the time-frequency distribution, has been developed for the analysis of internal combustion engine noise signals. It provides an approach making use of advantages of both the linear time-frequency distribution and the bilinear time-frequency distribution but avoiding their disadvantages. In order to identify requirements on the time-frequency analysis and also correlate a time-frequency analysis result with noise sources, the composition of the noise signal is discussed first. With this discussion, a mathematical model has been suggested for the noise signal. An example of identifying noise sources and detecting the abnormal condition of an injector with the noise signal time-frequency distribution for a diesel engine is also provided.

[DOI: 10.1115/1.1455639]

1 Introduction

Internal combustion (IC) engine noise has been drawing significant attention from automotive manufacturers. To effectively reduce the noise level, the first step is the identification of noise sources, which relies on the noise signal analysis. From the aspect of condition monitoring or manufacture/assembly quality assessment, abnormal noise signals usually indicate abnormal conditions or problems in the manufacture quality. To pick up the problem, the abnormal signal source should be found first. This also depends on the signal analysis.

Traditionally, noise signals are mainly analyzed with spectral analysis, i.e., the Fourier transform. However, the Fourier transform is not a proper tool for the analysis of internal combustion engine vibration and noise signals, as they are nonstationary and consist of many transient components. In recent years, a new signal processing technique especially suitable for the nonstationary signal analysis, time-frequency distribution, has been developed ([1–5]). It is a technique of displaying a signal over a time-frequency plane and showing the variation of frequency content versus the time or the evolution of a time signal with respect to the frequency. Methods include linear time-frequency distribution (LTFD) and bilinear time-frequency distribution (BLTFD). Constrained by the uncertainty principle ([1]), an important drawback of the LTFD is that it cannot have simultaneous high resolution in both the time domain and the frequency domain. As a consequence, when it is applied to engine noise signal analyses, it may not separate neighboring transient components and present major frequencies of each transient component. Although the BLTFD can have a higher simultaneous resolution than the LTFD ([2]) and much effort has been devoted to develop better methods ([5]), it has problems such as cross terms in the distribution, complexity of the algorithm, and low speed of the calculation. Nevertheless, because the BLTFD can achieve a higher simultaneous resolution, it has been widely applied to noise signal analysis ([6,7]) and engine vibration and pressure signal analysis ([8]).

In this paper, in order to identify requirements of the noise signal analysis and also correlate a time-frequency analysis result with noise sources, the composition of the noise signal is discussed first. With this discussion, a mathematical model has been

suggested for the noise signal. In the third section, an analysis procedure has been developed for making use of the advantages of the LTFD and the BLTFD, but avoiding their disadvantages, in this section, an analysis procedure with the time-frequency distribution has been developed. Another important purpose is to develop a signal processing procedure especially for mechanical engineers of such merits as simplicity and practicality. An example of identifying noise sources and detecting the abnormal condition of an injector with the noise signal time-frequency distribution for a diesel engine is provided in the fourth section. The last section of the paper is the Conclusion.

2 Internal Combustion Engine Noise Signal Components

An IC engine noise signal is composed of many components from different sources. These sources include combustion, mechanical, and the combination of both. To identify the requirement of noise signal analysis, we begin with a discussion on the noise signal components.

The combustion noise is produced by a rapid rate of pressure rise, which besides being a source of engine structural vibrations also excites resonance in the gas inside a combustion chamber cavity. The latter is also a source of vibration and noise. The contribution of the combustion to the whole noise signal is some transient components. In a normal condition, the combustion noise is mostly in a frequency range above a few 100 hertz as the combustion energy below this range is mostly transformed into useful work by pushing pistons forward. In the case of abnormal conditions, degradation in the combustion quality may produce some low frequency content in the combustion noise.

A rise in the cylinder pressure pushes the piston from the top dead center (TDC) advancing to the bottom dead center (BDC). In this movement, the clearance between the piston and the cylinder or damage to piston rings can cause the piston to impact with the cylinder, the phenomenon of piston slap, which is another major source of engine noises. As the piston slap is caused by both the combustion and the clearance, the noise level reflects the combustion quality and changes in the clearance. The impacts will add transient components to the engine noise signal. As piston slap happens on the way from the TDC to the BDC, it can be identified by referring to the time axis.

An important feature of IC engines is that they have both reciprocating and rotating parts. Different type of parts will produce different signal components. Rotating parts, such as the flywheel and front pulley, can excite harmonic components to the noise.

¹To whom all correspondence should be addressed.

Contributed by the Internal Combustion Engine Division of THE AMERICAN SOCIETY OF MECHANICAL ENGINEERS for publication in the ASME JOURNAL OF ENGINEERING FOR GAS TURBINES AND POWER. Manuscript received by the ICE Division, June 2000; final revision received by the ASME Headquarters, August 2001. Editor: D. N. Assanis.

Decided by the engine speed, these harmonic components mainly distribute in the low-frequency range. An increase in the amplitude of the harmonic components indicates condition variations of these rotating parts. Contributions of different rotating parts to the noise can be identified with reference to their speeds. The timing gear chain is another source of mechanical noise. Any damage to the gears will produce impacts and thus adds extra transient components to the signal or increase the amplitude of corresponding transient components.

Injectors and valves are reciprocating moving parts. They produce impacts to the engine structure and hence contribute transient components to the noise. In a normal condition, there are two major impacts generated in the operation of an injector. The first impact is the needle of the injector striking the backstop, and the second impact occurs when the needle sits back in its seat. In an injector, the needle is held onto its seat by a high rate spring. This spring also serves to control the injection pressure and regulate the injection time. A decrease in the stiffness of the spring will bring forward the injection time. As a consequence, the combustion quality will be degraded. Low spring stiffness may also fail to push the needle onto its seat against the combustion pressure. In some other abnormal conditions, the needle may remain open because of the deterioration of the guide or the seat. In such cases, there will be no impact at all. Degradation in fuel pumps, such as low pressure and piston leakage, will also result in a change in the injection time and pressure. In summary, time and amplitude of some transient components are indications of the condition of an injection system.

An engine has many inlet valves and exhaust valves. A valve is opened by a camshaft and pushed back to its seat by a valve spring. Any problems with valve seats, tappets, and mechanisms can cause a change to the transient vibrations produced during opening and closing, and thus the corresponding transient components of the noise signal. These valves open and close at different times, and so the contribution of different valves to the noise can be identified from the times of events.

Fluid-induced noise, such as exhaust and inlet noise, is also an important part of the noise. Along with the sudden release of gas into the exhaust system or the rush of a sharp pulse of fresh air into the cylinder, oscillation of the air volume in the cylinder and the exhaust system is excited and hence noise is produced. When inlet and exhaust valves close, noises will also be generated for a change in the fluid field. The fluid-induced noise contributes transient components to the whole noise. Some early research shows that fluid-induced noise usually has high frequencies. With modern fluid passage designs, the level of fluid-induced noise is normally very low. Damage or problems with the exhaust and inlet system will increase the magnitude of the fluid-induced noise.

Referring the above discussion on the composition of the engine noise, a noise signal can be mathematically described as

$$x(t) = \sum a_i \cos(\omega_i t + \alpha_i) + \sum \sum b_{ij}(t)u(t-t_j) \times \cos(\omega_{ij}t + \alpha_{ij}) \quad (1)$$

where a_i and $b_{ij}(t)$ denote the amplitude of a signal component, ω_i and ω_{ij} represent the frequency, $u(t)$ is the step function, t_j is the instant at which an event occurs, and α_i and α_{ij} are phases of signal components. That is, a noise signal component can be characterized with four quantities: amplitude, frequency content, time, and phase. Figure 1(a) is a noise signal from a four-cylinder diesel engine. The signal is dominated by harmonic components. When major harmonic components, i.e., the first term of Eq. (1), are removed, as shown in Fig. 1(b), it can be seen that the signal contains many transient components which are the second term of the equation.

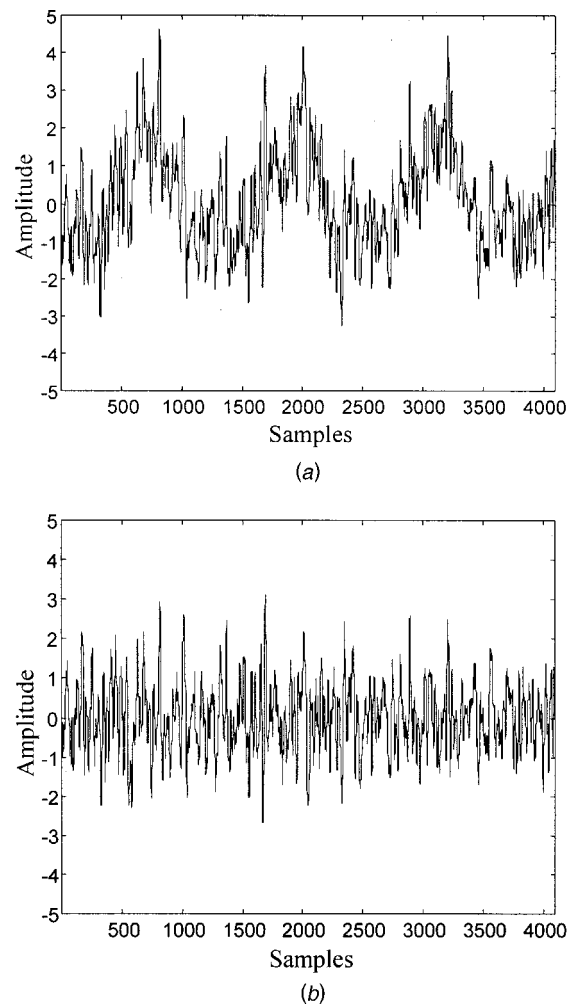


Fig. 1 A diesel engine noise signal. (a) diesel engine noise signal, (b) residual diesel engine noise signal

3 Signal Processing Procedure

It is known from the discussion in Section 2 that a basic requirement on a signal processing technique is that it should at least reveal information on the amplitude, the time, and the frequency content of an event. To satisfy the requirement, a signal processing technique should be two-dimensional, in the time-frequency domain.

The LTFD and the BLTFD both have advantages and disadvantages. Apparently, an ideal transform is the one that has both their advantages but not their disadvantages. In this section, a new signal processing procedure with the time-frequency distribution will be developed from the linear transform and the bilinear transform.

The LTFD of a measured signal sequence $x(n)$ uses the following formula ([4]):

$$A(t, f_k) = \sum_n [x(n)w(\alpha, t-n)]e^{-j2\pi f_k n} \quad (2)$$

where f_k is the central analysis frequency (carrier frequency), $w(\alpha, t-n)$ is the time domain window for localizing the analysis in the time domain at the instant t and parameter α defines the width of the time domain window ([1]). The LTFD provides a bank of band-pass filters. The real part of the transform $A(t, f_k)$ is the frequency component going to be picked out. With a given carrier frequency, the transform can give an approximation to the

envelope for the corresponding frequency component directly, i.e., the sound pressure variation for the f_k frequency component, which is

$$E(t, f_k) = |A(t, f_k)|. \quad (3)$$

An advantage of the LTFD is that it can be easily realized with the fast Fourier transform (FFT).

The BLTFD is generally defined with the following equation of the Cohen class ([2]):

$$B(t, f_k) = \int \int \phi(\theta, \tau) e^{-j\theta t - j2\pi f_k \tau} \left[\int x\left(u + \frac{\tau}{2}\right) \times x^*\left(u - \frac{\tau}{2}\right) e^{j\theta u} dtu \right] d\theta d\tau \quad (4)$$

where all integrations are from $-\infty$ to ∞ and $*$ denotes the complex conjugate. In Eq. (4), the weighting function $\phi(\theta, \tau)$ is called kernel of the distribution. However, it can be found from Eq. (4) that a BLTFD may produce spurious interference artifacts in frequency and time by the product of $x(a)x(b)$, which bring difficulties to the interpretation of the signal analysis result and may result in the misunderstanding of the system condition. Even with some knowledge about the frequency content of a signal, the BLTFD should be applied with caution as some crossterms may have same positions as some autoterms in the frequency domain. In practical applications, a discrete form often used is

$$B(t, f_k) = \sum_n e^{-j2\pi f_k n} \left[\sum_m \psi(t-m, n) x(m+n/2) x^*(m-n/2) \right] \quad (5)$$

where

$$\psi(t-m, n) = \int e^{-j(t-m)\theta} \phi(\theta, n) d\theta \quad (5a)$$

$\psi(t-m, n)$ is the correlation weighting function.

A measured engine noise signal is usually contaminated by noises from the environment and the measurement system. Mathematically, the measured signal sequence should be expressed as

$$x(n) = y(n) + \varepsilon(n) \quad (6)$$

where $y(n)$ is the unknown engine noises and $\varepsilon(n)$ represents all other noises. Unless the frequency band of the noise is different from the frequency band of the interested signal, the LTFD cannot suppress the noise. To reduce the influence of these noises on the result, the measured signal should be pre-processed, such as with time-domain averaging or other methods ([9]). It can be seen from Eq. (5) that the BLTFD is the Fourier transform of the weighted correlation function. Therefore, if these noises are white noises and are independent of the engine noises, the bilinear transform can suppress their influence on the analysis result. This is another advantage of the BLTFD.

To make use the advantages of the BLTFD, a new signal processing procedure can be derived from the BLTFD. By substituting the coordinate transform

$$m+n/2=s \text{ and } m-n/2=p \quad (7)$$

into Eq. (5), Eq. (5) can be rewritten as

$$B(t, f_k) = \sum_s e^{-j2\pi f_k s} x(s) \times \sum_p \psi(t-(s+p)/2, s-p) \times e^{j2\pi f_k p} x^*(p). \quad (8)$$

In Eq. (8), if the function $\psi(t, (s+p)/2, s-p)$ is so chosen that it can be decoupled with respect to variables s and p as

$$\psi(t, (s+p)/2, s-p) = u(\alpha, t-s) v(\beta, t-p), \quad (9)$$

then Eq. (8) becomes

$$B(t, f_k) = \left[\sum_s x(s) u(\alpha, t-s) e^{-j2\pi f_k s} \right] \times \left[\sum_p x(p) v(\beta, t-p) e^{-j2\pi f_k p} \right]^*. \quad (10)$$

To calculate the sound pressure, the transform is

$$E(t, f_k) = |B(t, f_k)|^{1/2}. \quad (11)$$

This is the general form of the transform. With reference to the general form of the linear transform expressed by Eq. (2), the transform is the multiplication of two linear transforms. With the FFT, the transform can be calculated with high speed. The algorithm is also simplified.

The above discussion also gives an explanation why a bilinear distribution can have a simultaneously high time and frequency-domain resolution. If one linear transform has a high time-domain resolution, or a narrow time-domain window, and the other has a high-frequency-domain resolution, or a narrow frequency-domain window, the multiplication of their windows will only occupy a very small area on the time-frequency plane.

In the transform, the Gaussian function is often as the time-domain window.

$$e^{-0.25n^2/\alpha/\sqrt{4\pi\alpha}} \quad (12)$$

A property of the Gaussian function is that its Fourier transform has the same form as its time-domain function. This is useful for both avoiding the problem of energy leakage and conducting the transform in the frequency domain [4].

In summary, the new signal processing procedure is as follows.

1. conducting the LTFD twice, one transform with a narrower window and the other with a wider window,
2. multiplying one transform with the complex conjugate of the other transform, and
3. the result is the square root of the modulus of the multiplication.

4 Example

The following example is a practical application of the signal processing procedure developed in Section 3 to the analysis of diesel engine noise signals. It is the condition monitoring of diesel fuel injectors from engine noise signals. This example will also show contributions of different sources to a noise signal.

Fuel injectors are important parts of a diesel engine. One of factors defining the condition of an injector is the stiffness of the spring holding the needle onto its seat. Any decrease in the stiffness will change the injection time and therefore degrade the performance of the engine. In this application, the stiffness was artificially reduced. This action decreased the injection pressure. As a result, an earlier injection was expected. The beginning and ending time of the injection, which are represented by signal transient components generated by impacts between the needle and the seat/backstop, can be found from the time-frequency distribution of the noise signal. Although the impacts between the needle and the seat/backstop are weak compared with many impacts among other engine components, the time-frequency distribution can still reveal them by localizing the signal analysis. This is an important advantage of the time-frequency distribution.

The diesel engine has four cylinders. It was installed on a test rig in the Engine Laboratory, School of Engineering, Manchester University, UK. In the experiment, the engine speed was around 2010 rpm. A microphone (B&K 4130), located at a short distance toward the injector, in which the stiffness of the spring was artificially reduced, was used to measure the noise signals. A measured noise signal is shown in Fig. 1(a) (the time axis is samples).

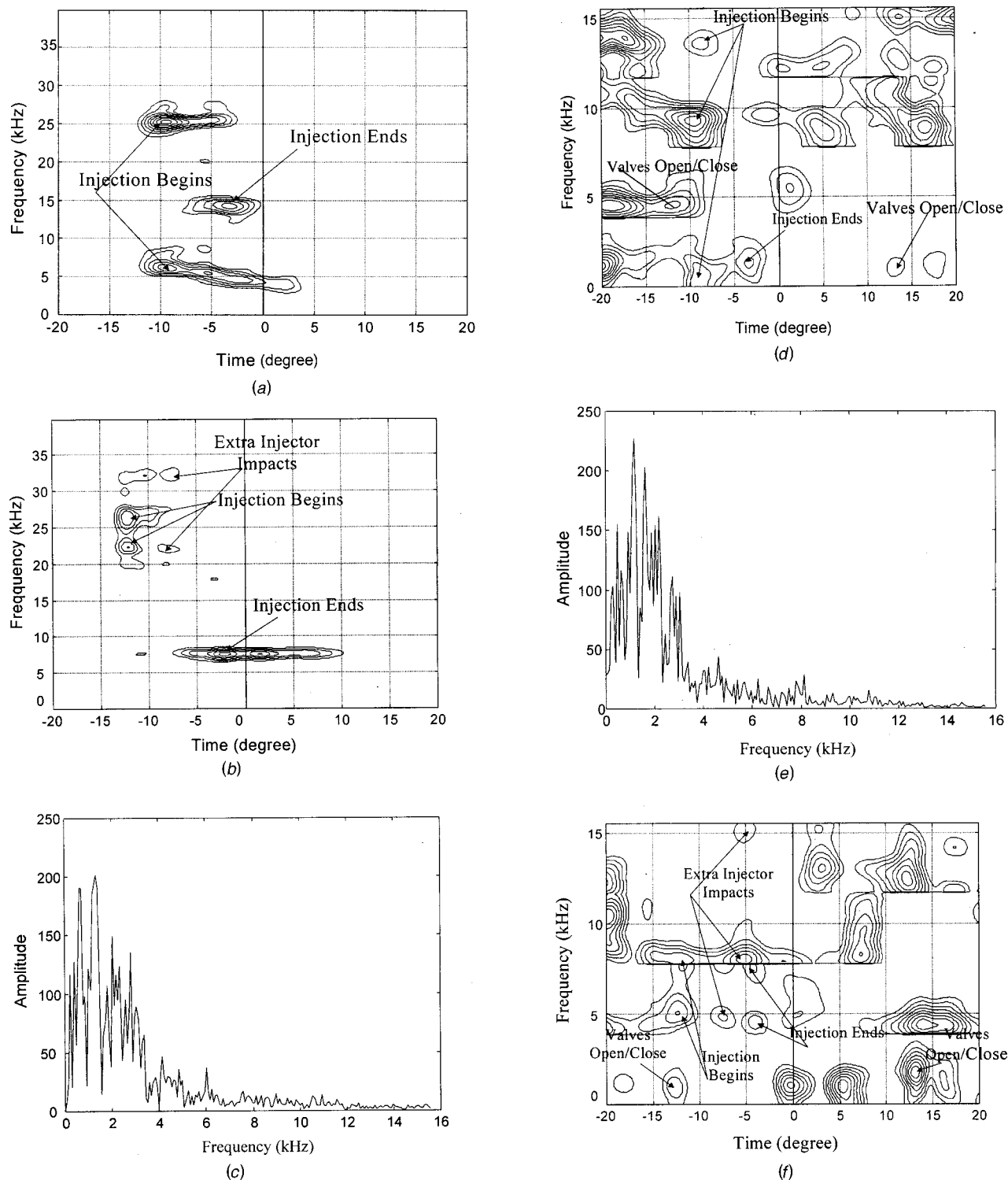


Fig. 2 Diesel engine noise signal time-frequency distributions; (a) time-frequency distribution of injector vibration signal (without fault), (b) time-frequency distribution of injector vibration signal (with fault), (c) spectrum of residual noise signal (without fault), (d) time-frequency distribution of residual noise signal (without fault), (e) spectrum of residual noise signal (with fault); (f) time-frequency distribution of residual noise signal (with fault)

In the signal processing, dominant harmonic components were removed from the signal with the Fourier transform. Figure 1(b) is the residual signal. To verify the result from the noise signal analysis, a specially designed (acceleration) sensor was arranged inside the injector for measuring vibration signals of the injector ([10,11]), which can exactly measure the injection time. Data was sampled in the time domain. In Fig. 2, where degree from the

TDC is used as the x -axis, the time interval was transformed into the angular interval by supposing that the engine speed was constant during the time interval of sampling. To provide reference for events, the time of the TDC was also recorded.

In the transform, the time-domain window is the Gaussian function. For the narrow window, $\alpha=115$, and for the wide window, $\alpha=390$. To show the effectiveness of the proposed method in

detecting injection times, only those parts of signals around the top dead center (TDC) are displayed in Fig. 2.

The residual noise signals are dominated by low-frequency components, whose frequencies are lower than 3 kHz. The effective measurement range of the microphone is 10 Hz–12.5 kHz. In this frequency range, if the time-frequency distribution of the signal is directly put on the time-frequency plane by a contour plot or other type of three-dimension diagram, those high-frequency components could not be shown clearly for a high contrast ratio. To exhibit all frequency components on one diagram, and also to eliminate the interference of the low-frequency components to their neighbor high-frequency components, the transform was carried out with respect to different frequency ranges of the signal. With high pass filters, a signal was first redefined as four signals, whose lowest frequencies are 0 Hz, 3.98 kHz, 7.89 kHz, and 11.80 kHz, respectively, and then these signals were transformed with the procedure suggested in the present paper. By setting the highest amplitude of each transform result to 1, the time-frequency distribution of these signals in frequency ranges [0, 3.98 kHz], [3.98 kHz, 7.89 kHz], [7.89 kHz, 11.80 kHz], and [11.80 kHz, 15.20 kHz] are shown together on one contour plot. Figure 2 shows that major transient components of different frequencies can be clearly displayed in this way.

Because the effective measurement range of the microphone (10 Hz–12.5 KHz) and that of the acceleration sensor (1 Hz–80 kHz) are different, in Fig. 2, the frequency range of the noise signal analysis is [0, 15.20 kHz], but the frequency range of the vibration signal analysis is [0, 40 kHz].

The exact injection time can be found from the time-frequency distribution of the injector vibrations in Figs. 2(a) and 2(b). In the case of abnormal condition, because of the decrease in the spring stiffness, the injection time is brought forward about two degrees. Another consequence is that there are more impacts between the needle and the seat/backstop ([10,11]).

With the noise signals, the time-frequency distribution of the signal from the abnormal condition also indicates that the injection time is advanced about two degrees with respect to the normal condition. Some extra noise signal transient components, which are the results of impacts between the needle and the seat/backstop, can also be found. As a result of the weakness in the spring stiffness, the impact energy thus generated is lower and the corresponding signal components have higher carrier frequencies than those under the normal condition. Comparing with that of the injector vibration signal, as shown in Figs. 2(d) and 2(f), the time-frequency distribution of the noise signal can provide more rich information on the engine condition. In the duration [−20 deg, 20 deg], besides the fuel injection operation, other events of the engine are: inlet valves open (13 deg before the TDC), inlet valves close (13 deg after the BDC), exhaust valves close (13 deg after the TDC), exhaust valves open (13 deg before the BDC), and combustion in the cylinder whose injector being monitored. With the timing of the engine as a reference, in Figs. 2(d) and 2(f), noise signal components generated by inlet and exhaust valve operations can be located. As some valves open or close at the same time, the contribution of an individual valve to the noise signal cannot be identified.

Because of the difference in the injector conditions, dominant noise sources are also different. Under the abnormal condition, in all frequency range, the signal is dominated by those components between [−2 deg, 15 deg] generated by other sources, particularly in the low-frequency range. Degradation in the combustion quality is a reason for this phenomenon. Such changes in the engine condition cannot be detected with the spectra.

5 Conclusion

As an engine noise signal requires at least three parameters to describe, i.e., amplitude, frequency, and time, the time-frequency distribution is a suitable means for analyzing the signal. With the time-frequency distribution of a noise signal, contributions of different noise sources can be identified. Although impacts between some small components are weaker than those between other engine components, the time-frequency distribution can still reveal them by localizing the signal analysis. This provides an effective tool for improving the engine design. An important application of the noise signal time-frequency analysis is the condition monitoring. It can be seen from the example of the present paper, with the knowledge of timing, problems with reciprocating components can be detected.

Although the signal processing procedure developed in the present paper can avoid problems of the BLTFD, care should still be taken in applications. As a narrow time-domain window means a wide frequency-domain window, and vice versa, an over-narrow or over-wide window will cause significant interference to other signal components nearby. Therefore, the choice of window width should depend on the situations of signal components, such as time intervals and frequency separations.

As a window width should be always chosen in a reasonable range, i.e., not too narrow or too wide, the existence of some strong harmonic signal components might disturb and smear the distribution of transient components. To improve the result, in processing an engine noise signal, it is recommended that strong harmonic components should be removed from the signal.

Acknowledgment

The authors are grateful to Prof. A. D. Ball and Dr. F. Gu of school of Engineering, Manchester University, for supplying the engine vibration and noise data.

References

- [1] Chui, C. K., 1992, *An Introduction to Wavelets, Volume 1: Wavelet Analysis and Its Applications*, Academic Press, San Diego, CA.
- [2] Cohen, L. 1989, "Time-Frequency Distributions—A Review," *Proc. IEEE*, **77**, No. 7, pp. 941–981.
- [3] Atlas, L., and Duhamel, P. eds., 1999, "Recent Developments in the Core of Digital Signal Processing," *IEEE Signal Process. Mag.*, **16**, No. 2, pp. 16–31.
- [4] Zheng, G. T., and McFadden, P. D., 1994, "Windowed Fourier Transform of Mechanical Vibration Signals," Technical Report of Oxford University, Report No. OUEL 2036/94.
- [5] Zheng, G. T., and McFadden, P. D., 1996, "A Time-Frequency Distribution for Analysis of Signals With Transient Components and Its Application to Early Gear Failure Detection," Report OUEL 2088/96, Department of Engineering Science, University of Oxford, Oxford, UK.
- [6] Azzoni, P., Moro, D., and Rizzoni, G., 1998, "Time-Frequency Signal Analysis of the Acoustic Emission of Formula 1 Engines," *Proceedings of the IEEE SP International Symposium on Time-Frequency and Time-Scale Analysis*, IEEE, Piscataway, NJ, pp. 441–444.
- [7] Mossing, J. C., and Tuthill, T. A., 1996, "Reduced Interference Distributions for the Detection and Classification of Outside Sound Source Acoustic Emissions," *Proceedings of 1996 IEEE International Conference on Acoustics, Speech, and Signal Processing*, Vol. 5, IEEE, Piscataway, NJ, pp. 2758–2761.
- [8] Samimy, B. and Rizzoni, G., 1996, "Mechanical Signature Analysis Using Time-Frequency Signal Processing: Application to Internal Combustion Engine Knock Detection," *Proc. IEEE*, **84**, No. 9, pp. 1330–1343.
- [9] Lee, S. K., and White, P. R., 1998, "The Enhancement of Impulsive Noise and Vibration Signals for Fault Detection in Rotating and Reciprocating Machinery," *J. Sound Vib.*, **217**, No. 3, pp. 485–505.
- [10] Gu, F., and Ball, A. D., 1996, "Diesel Injector Dynamic Modelling and Estimation of Injection Parameters From Impact Response, Part 1: Modelling and Analysis of Injector Impacts," *Proc. Inst. Mech. Eng., Part D (J. Automob. Eng.)*, **210**, pp. 293–302.
- [11] Gu, F., and Ball, A. D., 1996, "Diesel Injector Dynamic Modelling and Estimation of Injection Parameters From Impact Response, Part 2: Prediction of Injection Parameters From Monitored Vibration," *Proc. Inst. Mech. Eng., Part D (J. Automob. Eng.)*, **210**, pp. 303–312.

A Study on the Knocking and Misfire Detection System Using Breakdown Voltage Characteristics

J. K. Park

J. O. Chae

Department of Mechanical Engineering,
Inha University,
253 Yonghyun-Dong,
Nam-Gu,
Inchon, South Korea

Engine knocking and misfire cause a negative effect on the engine power and the exhaust emissions such as HC, CO and NO_x. They also cause permanent damages to the three way catalyst (TWC) system. And a heavy knock can cause severe damages to the engine itself, which gives more reason why it must be detected and corrected. This study introduces a new system concept for detecting combustion misfire and knocking using breakdown voltage (BDV) characteristics between spark plug electrodes. This system detects and evaluates the degree of combustion by measuring the breakdown voltage which predicts that the breakdown voltage depends on the pressure and the temperature.

[DOI: 10.1115/1.1470486]

Introduction

In recent years, the demand for automobiles has increased abruptly over the world, contributing to serious environmental and energy problems. Many governments have intensified the environmental and energy regulations to check this growth and monitor these problems. On that account, advanced automotive manufacturers over the world have also conducted research concerning engine technology in hopes of achieving better efficiency and reducing emissions, and to meet environmental regulations. An example of such research is the study of real-time control of spark ignition and fuel mixture quantities for improving engine performance. Another hot research topic is the detection of abnormal and incomplete combustion which results in noxious gas emission. A classic example of the latter is the knock and misfire, which raise noxious exhaust gas levels, deteriorate the three way catalyst (TWC), increase fuel consumption, and decrease performance and life of the engine.

So, for the last several years, automobile manufacturers and their suppliers have been working on various solutions to meet the misfire and knocking detection challenge. The crankshaft velocity fluctuation (CVF) method has been used in the past for misfire detection and the crank angle sensor input to calculate the variation of the crankshaft rotational speed. But this approach has a limit due to the fact that there could be problems under certain engine condition like deceleration or high speed condition ([1]). The most difficult problem is identifying which cylinder has misfired. Moreover, the accuracy of sensing is affected by crankshaft torsional vibrations and overlapping of the firing pulses in multi-cylinder engines. Rigid crankshaft, constant load torque, and non-overlapping firing pulse assumption remain as the major obstacle to developing nearly 100 percent effective technique for identifying the misfiring cylinder. Another approach to the misfire detection is the torque measurement method using the torque sensor. However, the torque measurement on idling not always provides useful information, for the torque itself is very small. Moreover, such additional loads as the alternator and the air conditioner may affect the measurement ([2]).

The other method for the misfire detection is based on monitoring the combustion process rather than the engine's external parameters such as speed and torque. There are three common meth-

ods to obtain information from inside of a cylinder. The first method, in-cylinder pressure monitoring, is the oldest one. It is very informative, but it is very difficult to commercialize this method due to the high price of pressure sensor. The second is a method to obtain the image of the combustion process through a window or a fiber optics. It is still for the research purpose, and will not be applied to automobiles in the near future. The third, known as a method employing an ion probe, is based on a primary effect of flame ionization. Free ions are generated in the flame and these ions will be drawn to the electrodes according to their polarity when bias voltage is applied to the electrodes. This method utilizes the spark plug in cylinder, so there is no need for another sensor to detect the misfire phenomenon. However, the ion current has very low value, so it is necessary to install the amplifier, and complicated signal processing should be followed ([3,4]).

There are also several methods, for knocking detection. Using remote measurement sensors is one of them. The sensors detect vibrations transmitted through the structure of the engine to diagnose knock in the combustion chamber. The signal received by remote sensors can be contaminated by sources other than engine knock, which increases the difficulty of signal diagnosis. This is especially true at higher engine speeds in which background mechanical vibrations are much higher. One advantage of using remote sensors is that, with careful placement, only one or two sensors are required to monitor all cylinders. In addition, the sensors are less expensive, primarily due to a less harsh operating environment.

There is another method using a flat frequency response sensor. However, the common problems of all the vibration sensors, namely that acceleration input includes engine noise as well as knock signals, require a quite complicated signal proceeding in order to be solved completely. Special microchips are available for piezo-sensor signal processing as well as dedicated control systems. Pressure sensors can also diagnose the knock phenomena in-cylinder. This direct measurement of the combustion process provides the best signal to analyze in detecting the engine knock. However, each cylinder requires its own sensor, and the cost of an individual sensor is still relatively high. As a result, pressure sensors are used primarily in research settings. The other method for the knocking detection is the ion current measurement method which was also used in misfire detection. As already mentioned in misfire detection, the ion current method uses the spark plug. Therefore, unlike the other methods, there is no need to install another sensor in the cylinder. But it is necessary to install an amplifier and complicated signal processing should be followed because its current is very low ([5]).

Contributed by the Internal Combustion Engine Division of THE AMERICAN SOCIETY OF MECHANICAL ENGINEERS for publication in the ASME JOURNAL OF ENGINEERING FOR GAS TURBINES AND POWER. Manuscript received by the ICE Division, Dec. 4, 2000; final revision received by the ASME Headquarters, Oct. 6, 2001. Editor: D. N. Assanis.

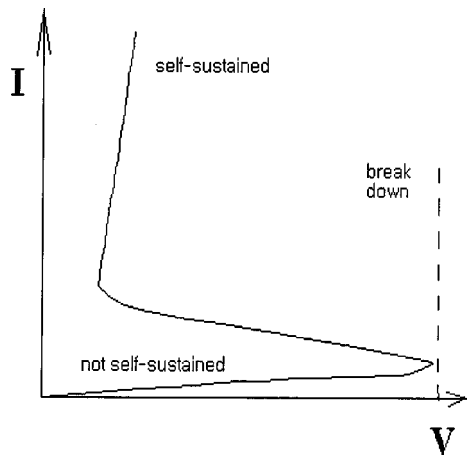


Fig. 1 A simplified volt-ampere characteristic

This study introduces the new method of misfire and knocking detection. This method uses the breakdown voltage (BDV) between the electrodes of the spark plug. As already mentioned above, the ion current measurement system also uses the spark plug for detection of abnormal combustion phenomena. But the BDV system for the engine diagnostics is based on the electrical breakdown in gas while the ion current method measures only ion density which has a rather weak signal. The breakdown voltage is very easy to distinguish between the normal combustion and abnormal combustion because the signal is very clear. Besides, in this breakdown voltage method, there is no need for an amplifier and complicated signal processing like in the ion current method. In this respect, the breakdown voltage method is completely different from the ion current method except that both use a spark plug for detection of abnormal combustion ([3,4]).

Theory of Breakdown Voltage

As far as conditions of the gas in the spark gap are subject to vary in the course of the engine operation, the voltage necessary for initiating a spark (breakdown) in the gap will vary accordingly. Among the factors determining the breakdown voltage, the following are major factors: gap width, gas nature, gas pressure, and gas temperature. Such factors as the shape of the electrodes, their material, gas humidity and initial ion concentration play a role too, but far less significantly than the major four.

The gap width and the pressure are frequently considered together, since both of them affect the breakdown voltage in a similar fashion. That is why the product Pd (where P is pressure and d is the gap width) is widely used as a parameter when comparing

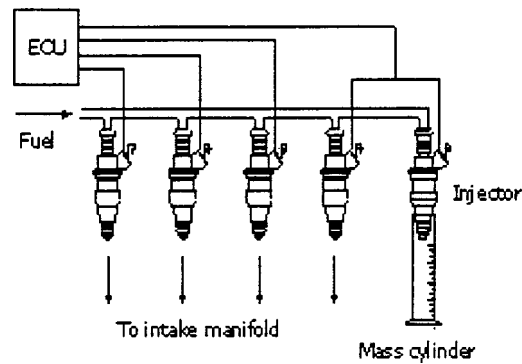


Fig. 2 Experimental setup for measurement of fuel injection quantity

different gaps. In the case of a given gap, the pressure is, therefore, the controlling parameter of the breakdown voltage.

All the gases occurring in nature are dielectric (insulators). It means that no current flows in the gas when voltage is applied. No measurable electric current can flow in a gaseous media with reasonable levels of applied voltage. However, if you apply exceedingly high voltage, you can get a very high current in gas media. This effect is called "gas discharge" and indispensably preceded by a very interesting phenomenon termed "gas breakdown." So we called the bias voltage which brings the breakdown between the electrode gap the breakdown voltage. Fortunately, this breakdown voltage varied with the pressure and temperature between the electrode gap. This means if we know the breakdown voltage characteristics of gases we can estimate the pressure or temperature by appropriate signal process. As the pressure increases, it becomes difficult to break the isolation between the electrode gap due to high density. Therefore the breakdown voltage is very high at high pressure. In the case of temperature, the tendency is adverse. As the temperature increases at the same pressure, the density decreases between electrode gaps, so it becomes easy to break the isolation. That means the breakdown voltage becomes low at the high temperature.

Operating with d (gap width) and n (gas density), we can express the breakdown voltage as V_s :

$$V_s = f(nd). \quad (1)$$

Table 2 The relation between MOTEC index and equivalence ratio

MOTEC index	0	-10	-20	-30	-40	-50
Equivalence ratio	1	0.9	0.8	0.75	0.7	0.6

Table 1 Specification of test engine

Description			Specification
Number of Cylinder			4
Valve Timing	Intake Valve	Open	BTDC 20°
		Close	ABDC 64°
	Exhaust Valve	Open	BBDC 64°
		Close	ATDC 20°
Fuel Supply System			MPI
Bore×Stroke			85×88
Total Displacement			1997 cc
Compression Ratio			8.6

Table 3 Experimental parameters

Engine Coolant Temperature	89±1°C
Intake Air Temperature	15±1°C
Engine Speed	1200, 1800, 2400 (rpm)
Engine Torque	0, 2, 6 N·m
Fuel Trim (for misfire)	0, -10, -20, -30, -40, -50 Fuel-cut (MOTEC ECU)
Ignition Timing (for knocking)	BTDC 20°, 25°, 30°, 35°, 40°, 45°

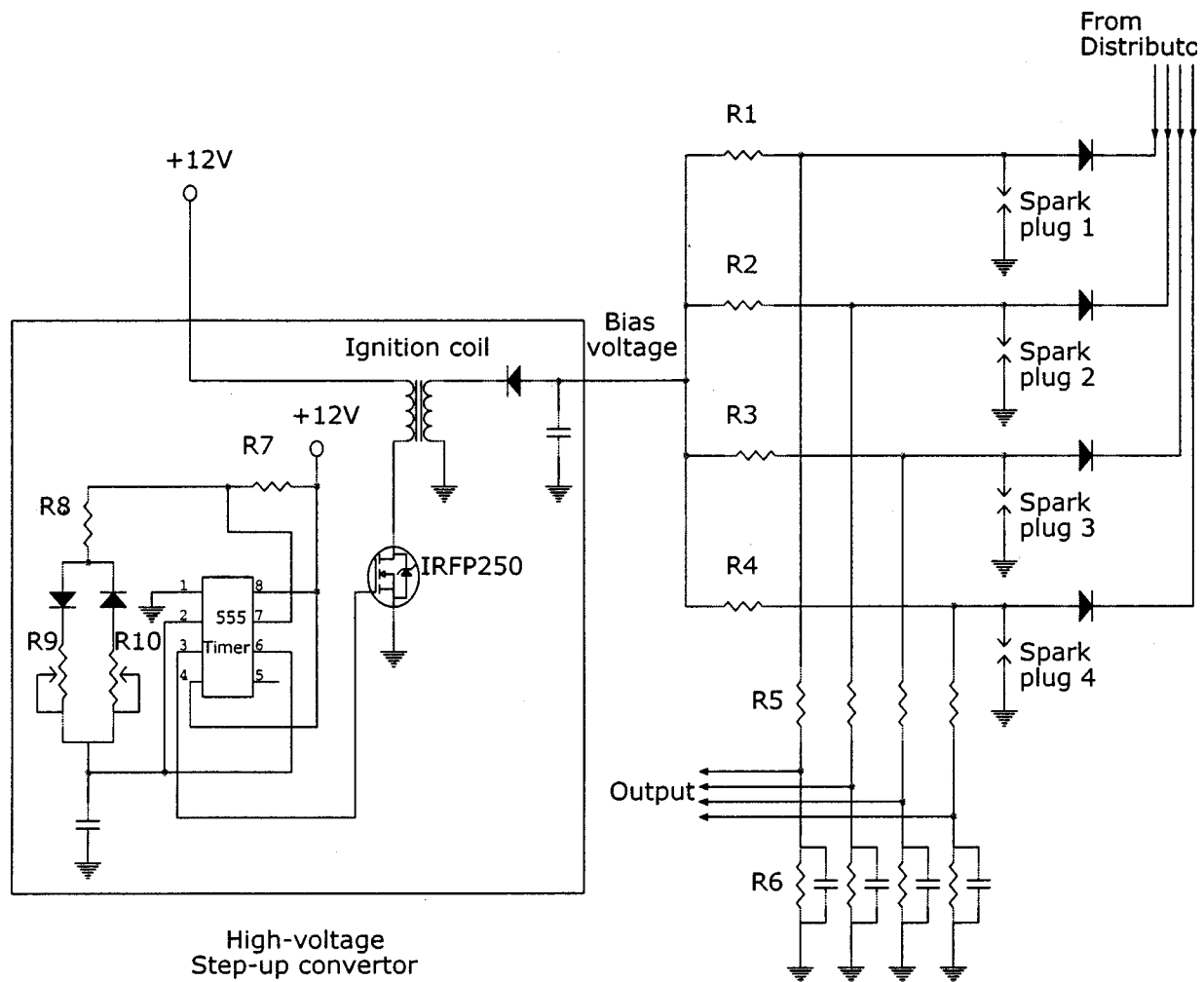


Fig. 3 Four-cylinder breakdown voltage measurement circuit

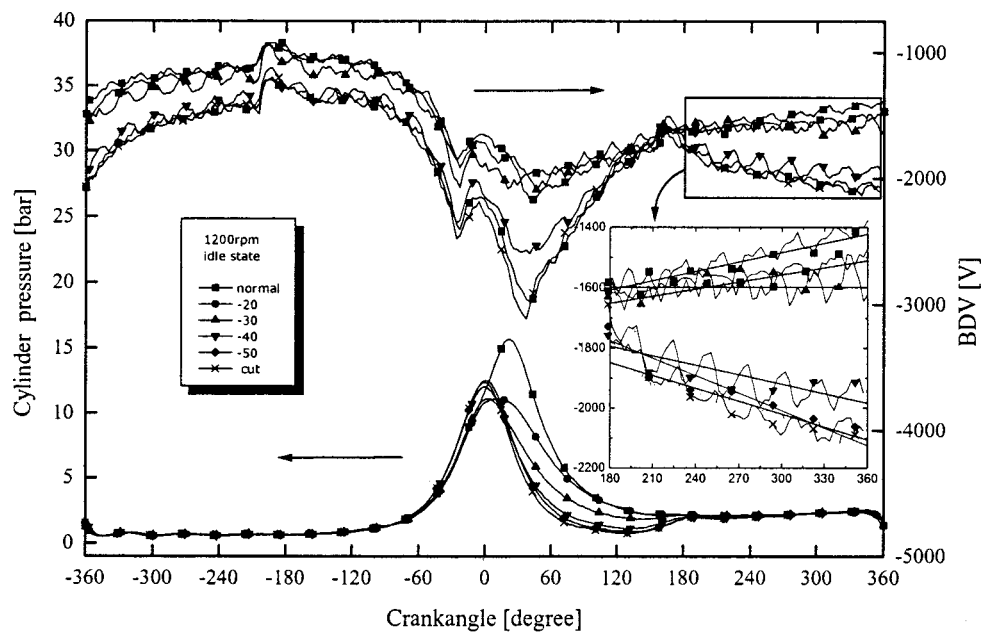


Fig. 4 Breakdown voltage and pressure according to the crankangle at 1200 rpm and idle state

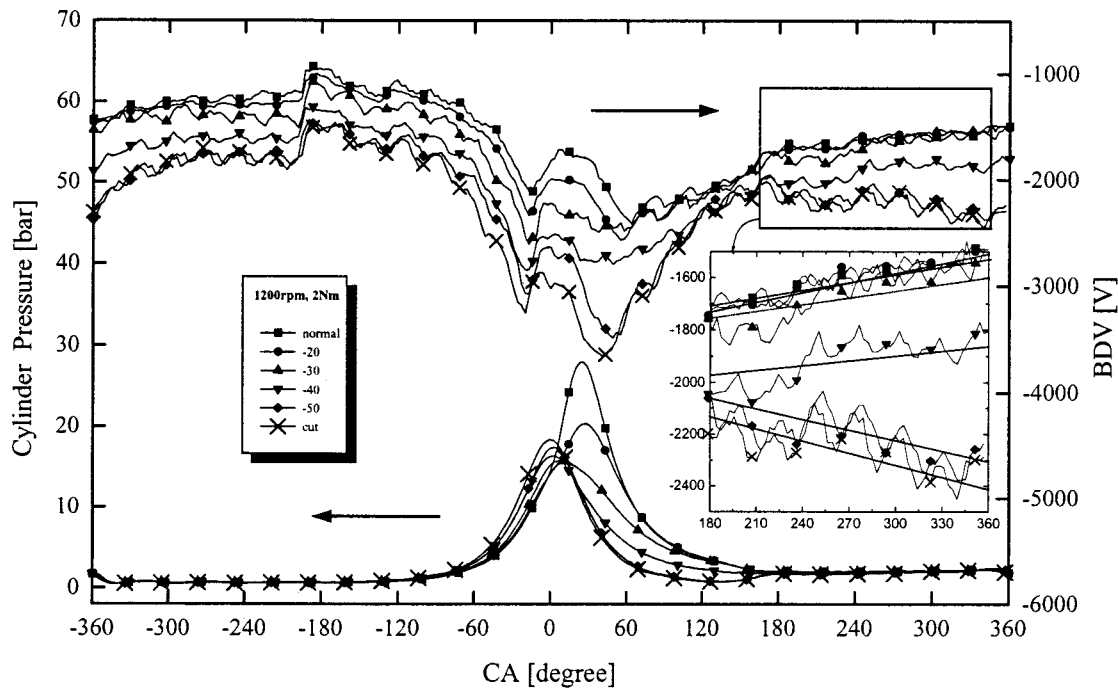


Fig. 5 Breakdown voltage and pressure according to the crankangle at 1200 rpm and 2N-M

The formula (1) represents the Pashen's law. In a very wide range of n and d , it is the value of nd which determines the breakdown voltage ([6,7]). The function (1) in the area of gas densities typical for a combustion chamber is linear. The method described in this paper is a further development of the approach introduced by the authors earlier ([8,9]).

The spark gap volt-ampere characteristic is nonlinear. The gap does not conduct electricity (barring a small ion current, if any) while the applied voltage is lower than what is known as the

breakdown threshold. Because this small current is carried by charged particles generated by other means than the discharge itself, this region of the volt-ampere characteristic of the gap is called "not self-sustained discharge."

After a breakdown is achieved, the current through the gap may be very large whereas the voltage drop is small. In this case, the charged particles (electrons and ions) are generated by the processes of gas ionization in the discharge. That is why it is called "self-sustained discharge." The type of volt-ampere characteristic

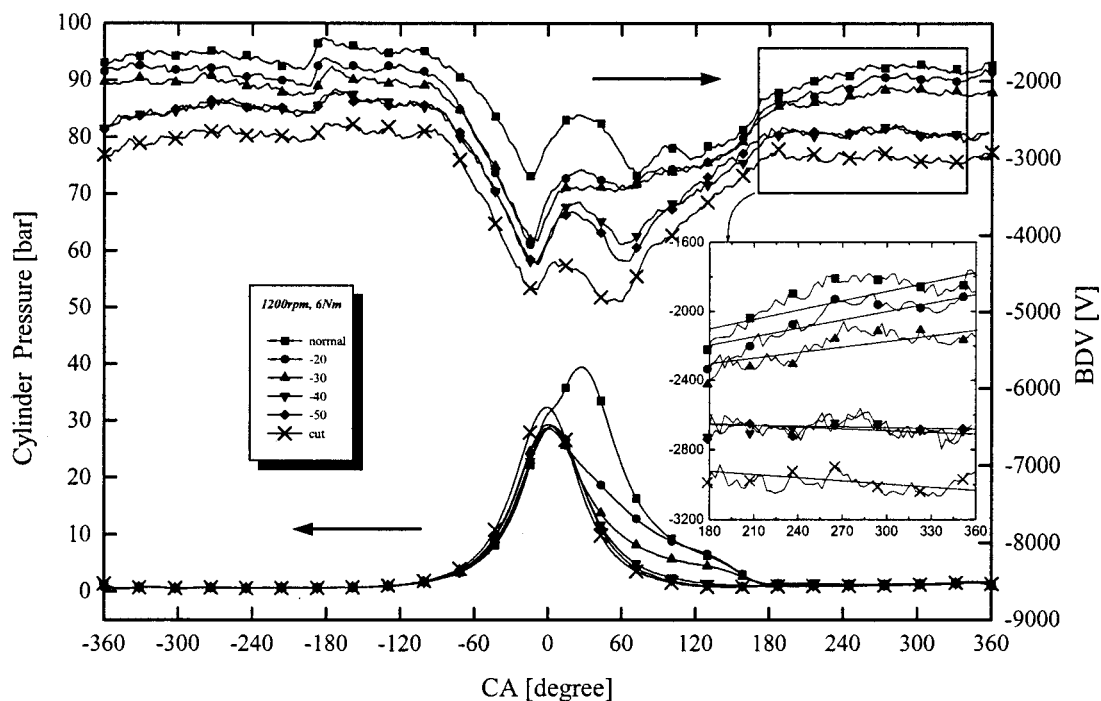


Fig. 6 Breakdown voltage and pressure according to the crankangle at 1200 rpm and 6N-M

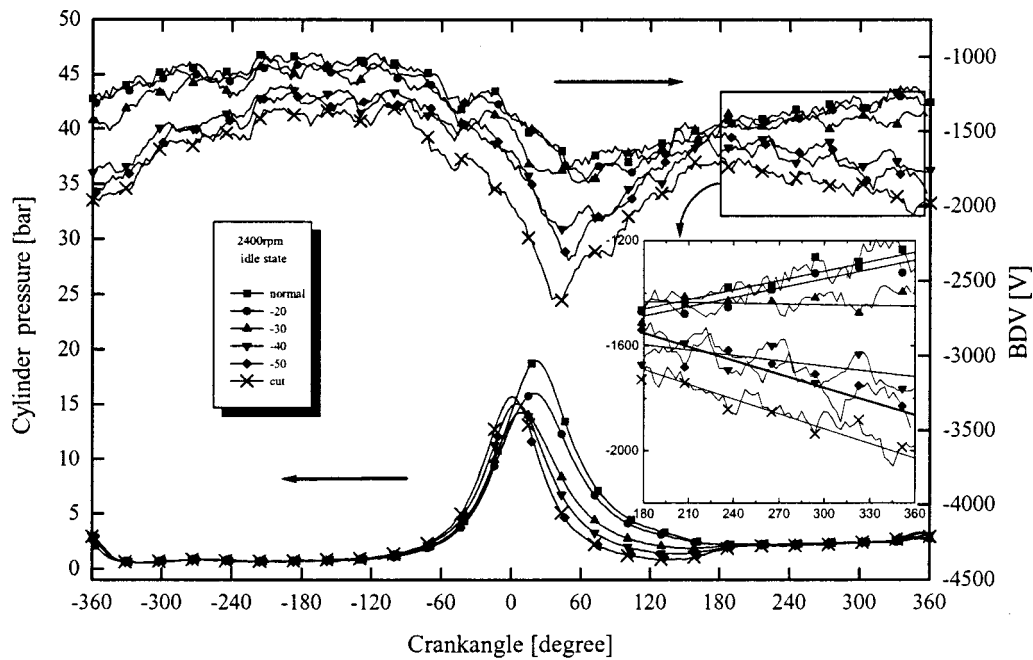


Fig. 7 Breakdown voltage and pressure according to the crankangle at 2400 rpm and idle state

shown in Fig. 1 is called the *S*-type characteristic. Neon lamps and thyristors are other common examples of elements with *S*-characteristics.

In this study, we applied 30 kV as a bias voltage. This voltage can be included in a “self-sustained region” or a “not self-sustained region” by the condition of the gas. For example, at the atmosphere pressure, the breakdown can occur between electrode gaps when this bias voltage is applied. But, at the state of 100 bar, the breakdown cannot occur due to high density, which means it is very difficult to break the isolation between the electrode gap in high pressure. Of course, if a more powerful bias voltage is applied, it is possible to break the isolation even at 100 bar. So the

breakdown voltage, which is the border of two regions (not self-sustained and self-sustained), is more dependent on the gas condition than the voltage itself. The 30 kV, which is applied in this study, can break the isolation between spark gap during engine stroke.

Experimental Setup

The engine used in our experiments was a modern four-stroke, four-cylinder OHC gasoline engine. The specification of the engine is shown in Table 1.

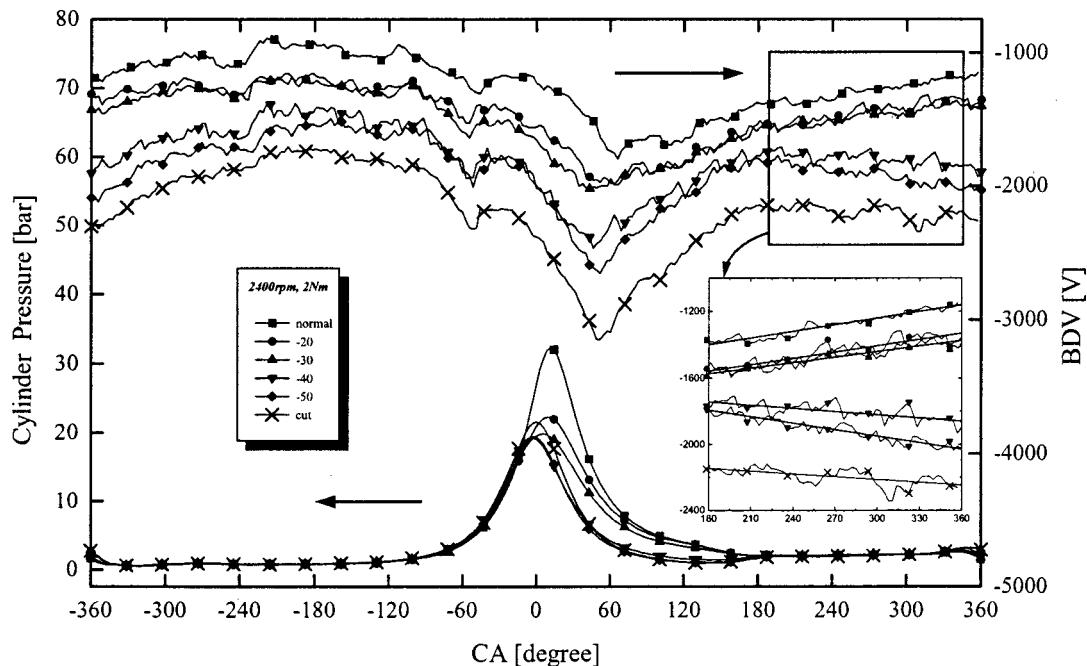


Fig. 8 Breakdown voltage and pressure according to the crankangle at 2400 rpm and 2N-M

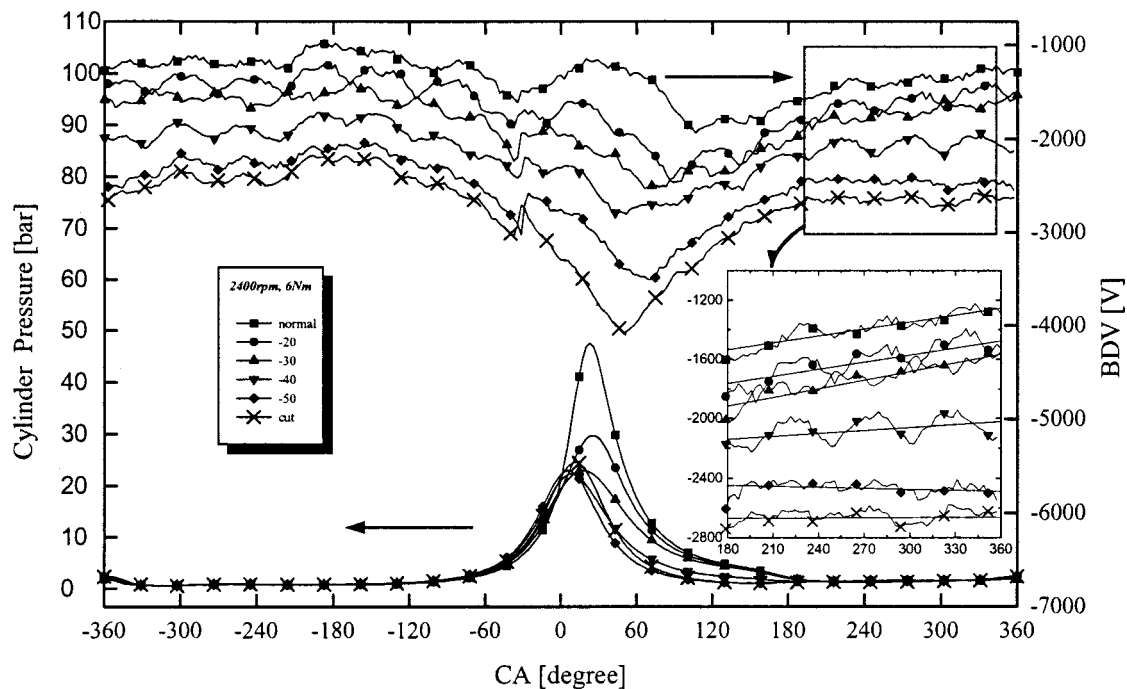


Fig. 9 Breakdown voltage and pressure according to the crankangle at 2400 rpm and 6N-M

In order to simulate misfire and knocking events, the engine's original ECU was replaced with a MOTEC research ECU which has the function of fuel trim and ignition timing control. The fuel quantity of MOTEC ECU can be ranged from -50 to 50 , in which 0 means the equivalence ratio state, negative means lean state, and positive means rich state. So, in this experiment, it is focused on the range from -50 to 0 in order to make a misfire. To verify the relation between MOTEC index and equivalence ratio, we measured the fuel quantity by MOTEC index. Figure 2 shows the experimental setup for this measurement. And the relation between MOTEC index and equivalence ratio is shown in Table 2. And the knocking in the engine was provoked by means of ad-

vancing the ignition timing. The onset of knocking was judged by its sound and by the appearance of characteristic waves on the in-cylinder pressure traces. The condition of this experiment is shown in Table 3.

The current flowing between the spark gap is to be small enough to avoid pre-ignition from the corona discharge. Ignition occurs, as usual, due to spark discharge generated by an ignition system. The full electric diagram of the breakdown voltage measurement circuit for a four-cylinder engine is shown in Fig. 3. The system consists of a DC to DC setup converter (high-voltage source) and the measurement circuitry itself. The high-voltage converter is made of an ignition coil which serves as a stepup

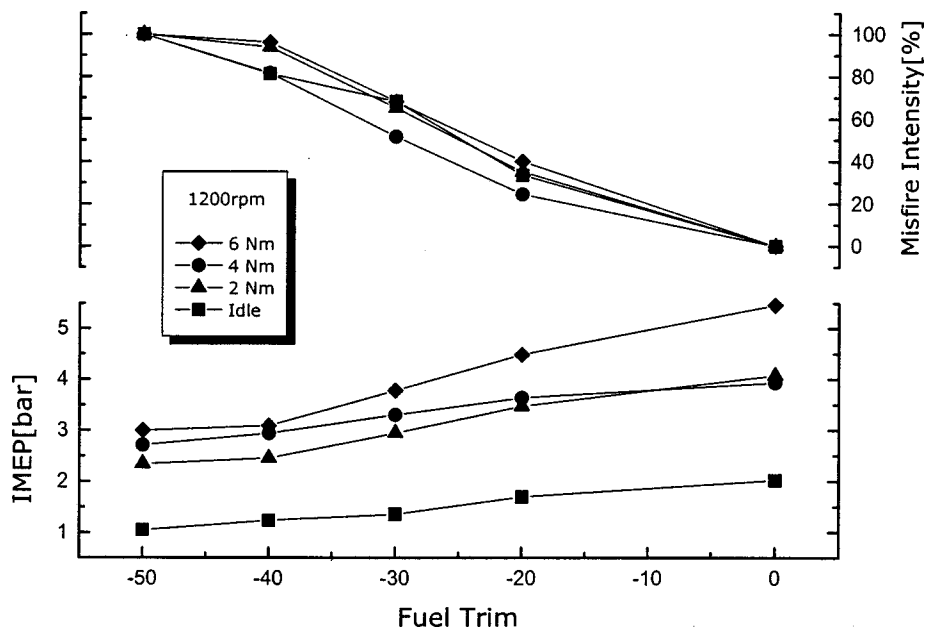


Fig. 10 Indicated mean effective pressure and misfire intensity according to the fuel trim at 1200 rpm

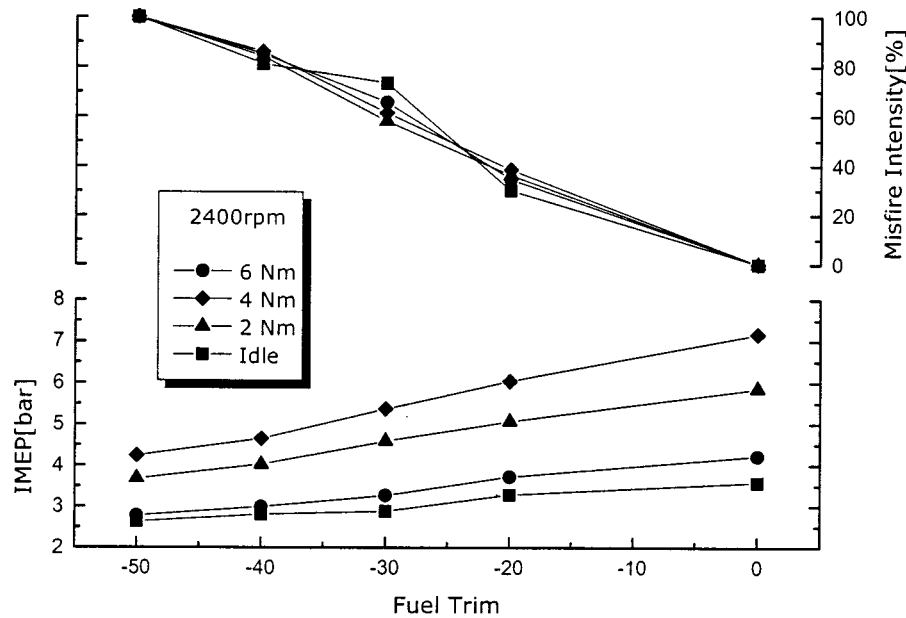


Fig. 11 Indicated mean effective pressure and misfire intensity according to the fuel trim at 2400 rpm

transformer. The bias voltage (negative) formed on the capacitor is then distributed among the channels (four, for the number of the cylinders is four) by means of equal resistors of 600 MOhm. To eliminate the interference between ignition and measurement systems, a diode for high voltage is used. The output signal is obtained from the four voltage dividers connected in parallel to the spark plug gaps.

Results and Discussions

Figures 4–9 show the breakdown voltage (BDV) and pressure signals with decreasing fuel trim at the same rpm and load. In

these figures, upper curves show the BDV signal and lower curves show the pressure signal in the cylinder. In these figures, it is noted that the BDV is applied by negative bias voltage. As shown in Eq. (1), BDV is dependent on the pressure and temperature; hence a lower value of BDV corresponds to a higher pressure or a lower temperature. As the fuel quantity injected to the cylinder decreases, the temperature of the combustion chamber also decreases and it becomes more difficult for breakdown to occur between the electrodes of the spark plug. This means that the value of BDV across the electrodes is higher at low fuel quantity injected than at high fuel quantity injected. In the com-

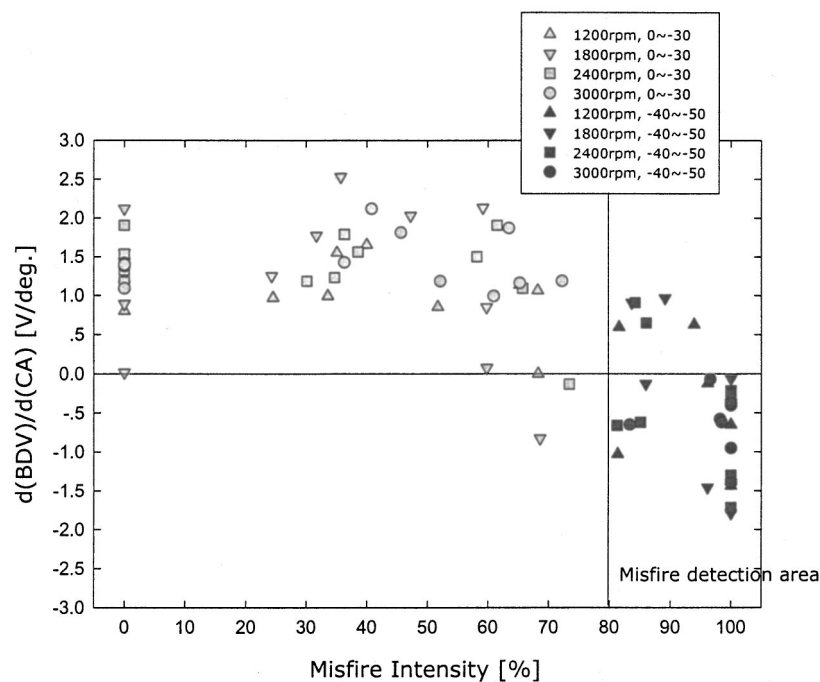


Fig. 12 Slope of breakdown voltage and misfire intensity

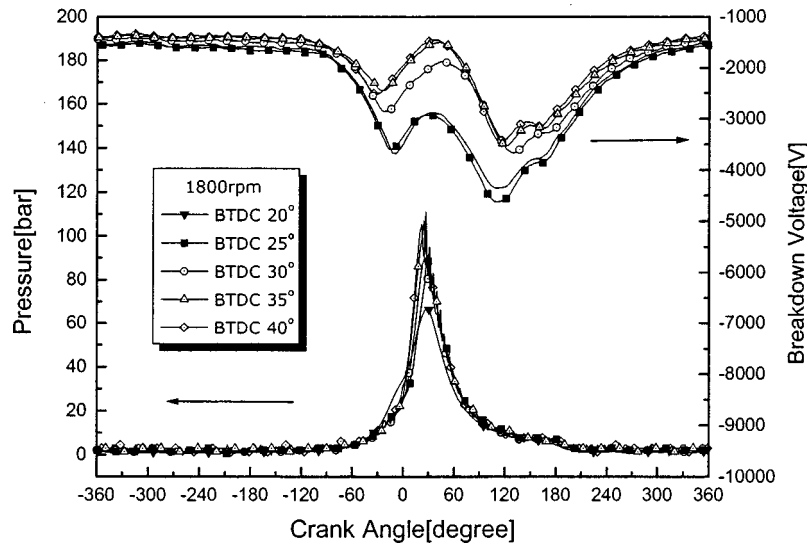


Fig. 13 Breakdown voltage and pressure according to crankangle at 1800 rpm

pression stroke, the value of BDV increases since it becomes more difficult for breakdown to occur between the electrodes due to higher pressure.

As shown in these figures, it is distinguishable that the slope of the BDV signal increases as fuel trim decreases during the exhaust stroke. In this study, this change is used for diagnosis of the misfire. We are interested in the exhaust stroke for misfire diagnosis, because the BDV has different value between normal combustion and misfire combustion in this region. As you can see in Figs. 4–9, the value of pressure is the same from the crank position of ATDC 180 but the value of BDV is different. That means temperature has changed at exhaust stroke because of misfire combustion. As a result, we can distinguish the difference between the misfire and normal combustion. Moreover, we can classify the intensity of misfire using the level of BDV value. As the fuel trim decreases, the slope of the BDV signal at the exhaust stroke increases. And the slope of the BDV becomes negative when fuel trim is -40 at the exhaust stroke. And, at this point, equivalence ratio is approximately 0.7, which is the value that can severely deteriorate the three-way converter.

To classify the misfire intensity, we defined the following equation and indicated the misfire intensity by fuel trim in Figs. 10 and 11. We set the difference between IMEP of normal combustion and IMEP of total misfire (fuel cut) to 100 percent. On the basis of this, we measured the difference between IMEP of normal combustion and IMEP of measured. By this principle, we defined the misfire intensity. When the misfire intensity is increased, it means the incomplete combustion is increased. And the misfire intensity reaching 100 percent means there is no combustion in the cylinder.

$$\text{misfire}(\%) = \left(\frac{\text{IMEP}_{\text{normal}} - \text{IMEP}_{\text{measured}}}{\text{IMEP}_{\text{normal}} - \text{IMEP}_{\text{fuelcut}}} \right) \cdot 100 \quad (2)$$

In this experiment, we decided the -40 of fuel trim value to be the misfire criterion, and it is known that the misfire intensity is 80 percent at this point.

Figure 12 shows the slope and intensity of the BDV signal, and the slope of the BDV signal is negative when the intensity of the misfire is more than 80 percent. From these results, we defined the

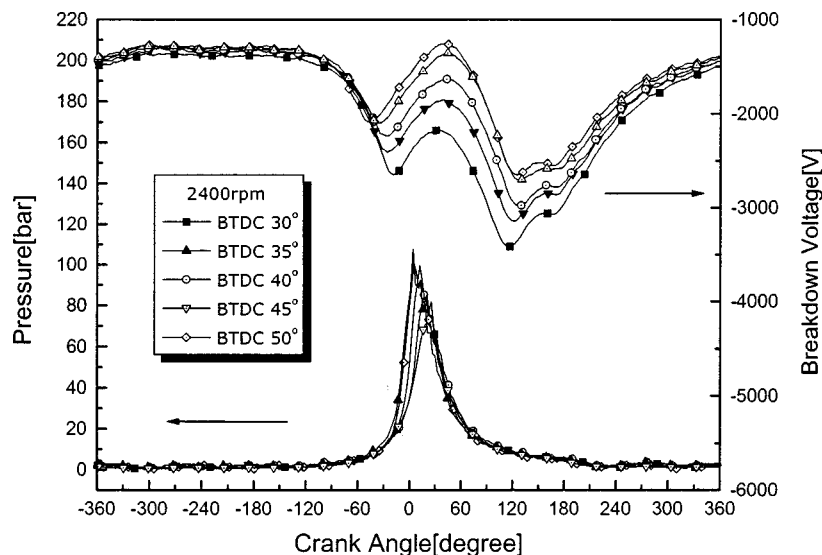


Fig. 14 Breakdown voltage and pressure according to crankangle at 2400 rpm

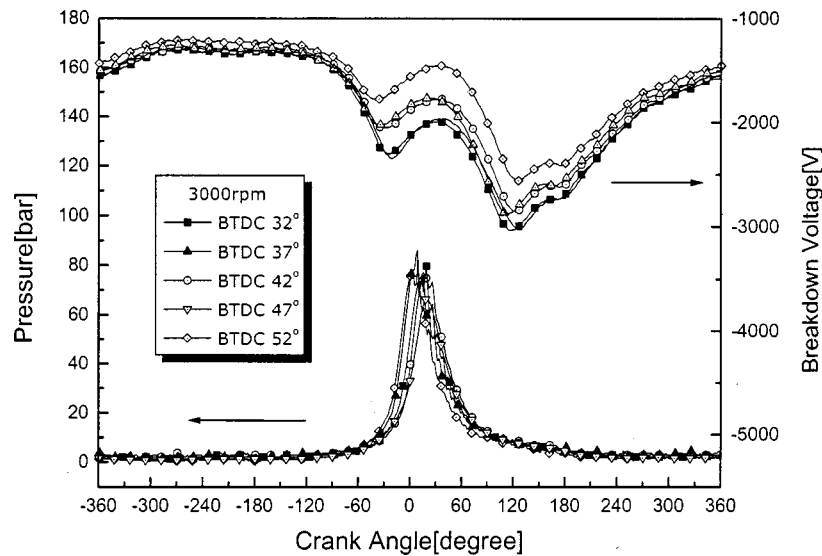


Fig. 15 Breakdown voltage and pressure according to crankangle at 3000 rpm

misfire is more than 80 percent. From these results, we defined the misfire criterion to be the point at which the slope of BDV signal becomes zero value. So, the larger the negative slope of the BDV signal, the stronger the intensity of misfire.

Figure 13 shows the breakdown voltage and pressure by crank angle at the state of MBT (maximum brake torque) and 1800 rpm. When the knock happens and becomes stronger by the ignition timing advance, the characteristic of the breakdown voltage signal and pressure signal is considered. As the ignition timing increases, the pressure increases and the breakdown voltage decreases in the region of combustion.

The region of ATDC 0–ATDC 60 is defined as the diagnostic field for knock detection because the characteristic pressure wave which shows the knock phenomenon occurs in this region ([10]). In this figure, as the knock intensity increases (by ignition timing advance), breakdown voltage decreases. In general, it is known that the gas temperature in the cylinder abruptly increase to three or four times when the knock occurs ([10]). And the breakdown voltage is inversely proportional to the gas temperature, so break-

down voltage abruptly decreases when the gas temperature increases. Actually, the pressure increases as well when knock occurs. But it just increases to 0.5 times at most. So the effect of temperature is greater than the effect of pressure. That's the reason we mainly mention the temperature to interpret the BDV when knock occurs in the cylinder. In this study, breakdown voltage characteristic like this is utilized for knock detection.

Figures 14 and 15 also show the breakdown voltage and pressure by crank angle at the state of 2400 rpm and 3000 rpm. In these figures, we can see the same tendency; breakdown voltage decreases as the knock intensity increases. From these results, we came to the conclusion that it is possible to detect the knock phenomenon regardless of the engine speed.

Figure 16 shows the breakdown voltage when knock occurs (lower curve) and when misfire occurs (upper curve). And it is clear that the diagnostic region is different in each case. When knock happens, it is focused on the combustion region, and when misfire happens, it is focused on the exhaust region. So it is pos-

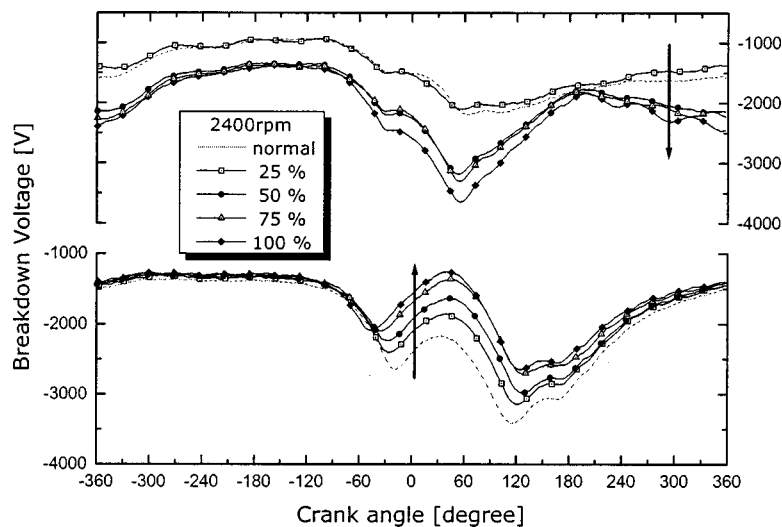


Fig. 16 Breakdown voltage and pressure as a function of crankangle

sible to detect the knock and misfire with the same diagnostic system.

Conclusions

1 A four channel breakdown voltage (BDV) measurement system which generates high-bias voltage (30 kV) to detect misfire and knocking in a gasoline engine and successfully detect misfire and knocking regardless of engine rpm & load has been demonstrated.

2 There is a difference between misfire and normal combustion in temperature at the exhaust stroke, so this difference can be utilized for classification of the intensity of misfire. Moreover, the slope of BDV signal changes according to temperature, so it is possible to do quantitative analysis on misfire.

3 The criterion of misfire can be defined as the point at which the slope of the BDV signal during an exhaust stroke becomes zero when the value of fuel trim is -40 and the fuel quantity injected to the combustion chamber is smaller than the normal combustion by 30%.

4 There is a difference between knocking and normal combustion in temperature at the combustion stroke, which makes the difference in the BDV. This difference is utilized for detection of the knocking phenomenon.

5 The diagnostic region is different for misfire and knocking, so it is possible to detect these abnormal combustion phenomena by the same detection system.

References

- [1] Williams, J., 1996, "An Overview of Misfiring Cylinder Engine Diagnostic Techniques Based on Crankshaft Angular Velocity Measurement," SAE Paper 960039.
- [2] Nonomura, N., Sugiyama, J., Tsukada, K., and Takeuchi, M., 1987, "Measurement of Engine Torque With the Inter-Bearing Torque Sensor," SAE Paper 870472.
- [3] Reinmann, R., Saitzkoff, A., and Mauss, F., 1997, "In-Cylinder Pressure Measurement Using the Spark Plug as an Ionization Sensor," SAE Paper 970857.
- [4] Eriksson, L., Nielsen, L., and Glavenius, M., 1997, "Closed Loop Ignition Control by Ionization Current Interpretation," SAE Paper 970854.
- [5] Auzins, J., Johansson, H., and Nytomt, J., 1995, "Ion-Gap Sense in Misfire Detection, Knock and Engine Control," SAE Paper 950004.
- [6] Raizer, Y. P., 1991, *Gas Discharge Physics*, Springer-Verlag, New York.
- [7] Meek, J. M., and Craggs, J. D., 1978, *Electrical Breakdown in Gases*, John Wiley and Sons, New York.
- [8] Martychenko, A. A., Park, J. K., Ko, Y. S., and Chae, J. O., 1999, "A Study on the Possibility of Estimation of In-Cylinder Pressure by Means of Measurement of Spark Gap Breakdown Voltage," SAE Paper 1999-01-1115.
- [9] Park, J. K., Martychenko, A. A., Ko, Y. S., Jo, M. S., and Chae, J. O., 1999, "The Misfire Detection and Intensity Interpretation Using Breakdown Voltage Characteristics," SAE Paper 1999-01-2934.
- [10] Heywood, J. B., 1988, *Internal Combustion Engine Fundamental*, McGraw-Hill, New York.

Combustion and Emission Characteristics of Direct-Injection Compression Ignition Engines by Means of Two-Stage Split and Early Fuel Injection

K. Yamane

e-mail: yamane@mech.usp.ac.jp

Y. Shimamoto

Department of Mechanical Systems Engineering,
The University of Shiga Prefecture,
2500 Hassaka, Hikone,
Shiga 522-8533, Japan

The objective of this study was to experimentally clarify the effect of two-stage split and early injection on the combustion and emission characteristics of a direct-injection (DI) diesel engine. Engine tests were carried out using a single-cylinder high-speed DI diesel engine and an injection system, combining an ordinary jerk pump and an electronically controlled high-pressure injection system, KD-3. In these experiments to compare the combustion and exhaust emission characteristics with two-stage split and early injection, a single-stage and early injection was tested. The FT-IR exhaust-gas analyzer simultaneously measured the exhaust emissions of 26 components. The results showed that HCHO, CH₃CHO, and CH₃COOH were emitted during the very early stage of both single injection and two-stage injection. These concentrations were higher than those from diesel combustion with ordinary fuel injection timings. These exhaust emissions are characteristic components of combustion by premixed compression ignition with extremely early injection. In particular, the HCHO concentration in exhaust was reduced with an increase in the maximum rate of heat release after cool flame due to pre-reaction of pre-mixture. At extremely early injection, the NO_x concentration was extremely low; however, the indicated specific fuel consumption (ISFC) was higher than that of ordinary diesel combustion. In the case of two-stage injection, the degree of constant volume is increased, so that ISFC is improved. These results also demonstrated the possibility of reducing HCHO, NO_x, and smoke emissions by means of two-stage split and early injection. [DOI: 10.1115/1.1473157]

Introduction

Premixed compression ignition combustion, such as that accomplished by homogeneous charge compression ignition (HCCI) (Ryan III et al. [1]) or by premixing at extremely early stages of compression stroke by direct-injection (Takeda et al. [2]) has the potential to achieve ultra-low exhaust emissions. However, although such combustion can sharply reduce NO_x emissions, it is still characterized by a number of lingering problems. For example, it is difficult to control the ignition timing and the operating region is limited to lower engine loads. In addition, premixed compression ignition combustion is characterized by high THC and CO concentrations and high fuel consumption. For this reason, a new combustion concept based on compression ignition of a lean pre-mixture using multiple injection with a single injector (Yokota et al. [3]) and a two-stage split injection with multiple injector and injection systems (Hashizume et al. [4]) have been proposed. The aim of both combustion systems is to obtain lower NO_x and particulate emissions by compression ignition of a lean pre-mixture derived from preliminary injection at partial load and by ordinary diesel combustion under lower concentration of oxygen by second-stage injection at higher engine load.

The combustion system proposed in the present study can be outlined as follows. NO_x concentration is reduced by combustion of a over lean-mixture formed by the first-stage injection. Most of pre-mixture is combusted by second-stage injection, and thus the

amount of second-stage injection controls the engine load. This combustion system is based on a hybrid of premixed compression ignition combustion and ordinary diesel combustion. The over lean pre-mixture is formed by the first-stage injection between the early and middle stages of the compression stroke, and then a portion of that pre-mixture is combusted by compression ignition, and the remainder by second-stage injection. In this study, we investigate exhaust emissions, and particularly the emission of HCHO derived from premixed combustion such as that in spark ignition engines, and we clarify the relationship between combustion and emission characteristics.

Experimental Apparatus and Procedures

Test Engine and Operating Conditions. The experiments were carried out on a single-cylinder, horizontal-type, four-stroke-

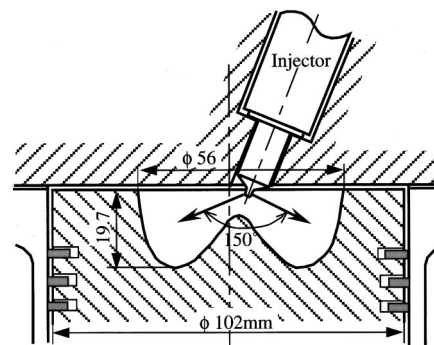


Fig. 1 Combustion chamber configuration

Contributed by the Internal Combustion Engine Division of THE AMERICAN SOCIETY OF MECHANICAL ENGINEERS for publication in the ASME JOURNAL OF ENGINEERING FOR GAS TURBINES AND POWER. Manuscript received by the ICE Division, July 13, 2000; final revision received by the ASME Headquarters, December 5, 2001. Editor: D. N. Assanis.

Table 1 Main specifications of a test engine and injection systems

Engine type	Direct-injection diesel engine
Bore \times stroke	Single cylinder, water-cooled 102 mm \times 105 mm
Displacement	0.857 liters
Compression ratio	17.8:1
Swirl ratio	2.4
Combustion chamber	Toroidal
Fuel injection system	KD-3 (plunger dia.=6.5 mm) PFR-1 (plunger dia.=9 mm)
Injection nozzle	DLLA150P224

cycle DI diesel engine (Yanmar NFD170) that was naturally aspirated and water cooled. Table 1 shows the main specifications of the test engine and injection systems. A toroidal-type piston cavity as shown in Fig. 1 was used. The engine was operated at 1800 rpm and at a fixed cooling-water temperature of 80°C.

A nozzle orifice diameter of 0.22 mm was employed in this experiment. An injection nozzle orifice was fixed for all experiments to compare combustion and emission characteristics under ordinary combustion chamber shape and nozzle orifice. Therefore, the injection nozzle orifice is not an optimum one to attain best efficiency and lowest exhaust emission at the two-stage split and early injection.

Injection System and Method of Split Injection. To realize the two-stage split and early injection (SPEI), two injection systems connected with a check valve were used as shown in Fig. 2. The first-stage injection between the early and middle stages of the compression stroke was achieved by an electromagnetic controlled high-pressure injection system, KD-3, as shown Fig. 3. This injection system is applied oil-hammering in a convergent injection pipeline, which was developed by one of the authors (Ikegami et al. [5]). The injection timings of the first-stage injection were changed by this system, and the injection quantity was fixed. To change the engine load, the injection quantity at the second-stage injection was changed by means of a jerk-type pump installed with an engine camshaft, and the injection timing was fixed at TDC. To compare the combustion and emission characteristics with SPEI, a single-stage and early injection (EI) was tested by using a KD-3 injection system.

Under engine-firing conditions, the injection fuel quantity was measured by integration of an injection rate waveform which was determined by applying a partial computer simulation technique. This method uses the measured pressure at the nozzle holder-inlet, the measured nozzle needle-lift, and the measured cylinder pressure as input signal data. The maximum injection pressure at the

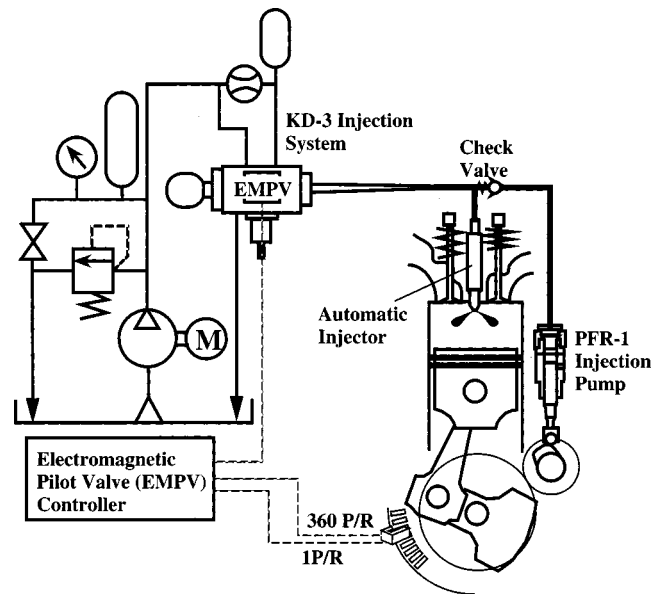


Fig. 2 Layout of second-stage injection system

nozzle holder-inlet was controlled to 30 MPa to form a locally rich-mixture for SPEI, and for EI it was elevated to 70 MPa to realize the combustion by compression ignition with premixed lean mixture.

Measurement of Exhaust Gas Emissions. Smoke density was measured by a Bosch-type smoke meter, and exhaust gas emissions of 26 components, including NO, NO₂, lower HCs, and unregulated components, i.e., HCHO, etc., as shown in Table 2, were simultaneously measured by an FT-IR exhaust gas analyzer (Horiba MEXA-4000FT).

Experimental Results and Discussion

Effect of First-Stage Injection Timings on Combustion and Emission Characteristics. Figure 4 shows the effect of first-stage injection timings, θ_{j1} , on indicated specific fuel consumption, b_i , indicated mean effective pressure, p_i , degree of constant volume, η_{glh} , combustion efficiency, η_i , NO_x, smoke HC(C₁–C₇), HCHO, CH₃CHO, and HCOOH for both the SPEI and EI at fixed engine speed of 1800 rpm and equivalence ratio of $\phi=0.4$. For SPEI, the amount of fuel injected at the first-stage injection maintained at six times that of the amount injected at the

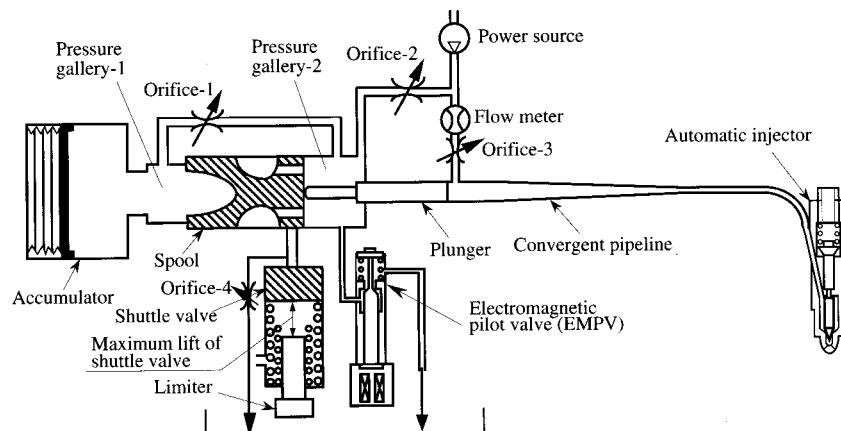


Fig. 3 Schematic illustration of a high-pressure injection system using oil-hammering in a convergent pipeline, KD-3 (Ikegami et al. [5])

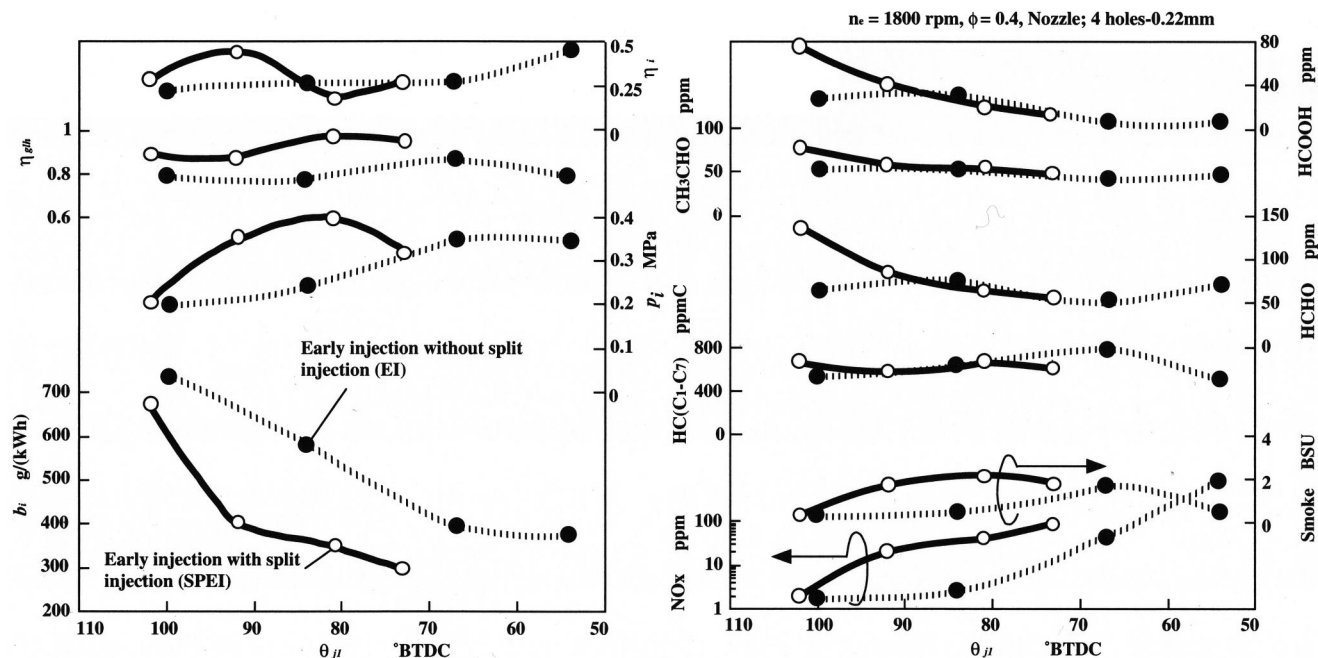


Fig. 4 Effect of first-stage injection timings, θ_{ji} , on indicated specific fuel consumption, b_i , indicated mean effective pressure, p_i , degree of constant volume, η_{glh} , combustion efficiency, η_i , concentrations of NO_x , smoke, $\text{HC}(\text{C}_1-\text{C}_7)$, HCHO , CH_3CHO , and HCOOH

second-stage injection. η_i was calculated as the ratio of the amount of heat release at the combustion end derived from measured cylinder pressure to theoretical amount of heat release estimated from amount of injected fuel per one stroke, and η_{glh} was calculated as the ratio of the product of rate of heat release and Otto cycle thermal efficiency for small division in crank angle to an integrated amount of heat release derived from measured cylinder pressure.

We can see in this figure that concentration of NO_x is a very low level of less than 100 ppm for both of SPEI and EI at earlier injection timing of 70°BTDC. The smoke number ranges from 1 to 2. It appears that this smoke resulted from the low injection pressure of the second-stage injection, and thus that this smoke would be reduced by the second-stage injection with high injection pressure (Yamaneet al. [6]). The concentrations of gas components, HCHO , CH_3CHO , and HCOOH for both of SPEI and EI were remarkable high in the combustion. All three of these concentrations were clearly higher than the corresponding concentrations in ordinary diesel combustion. The pre-mixture formed by extremely early injection is oxidized at lower temperature, then HCHO is formed. The mixture with the oxidation reaction reaches at cylinder wall layer and its reaction is quenched by wall layer and ambient air, because wall temperature and ambient air are lower than the mixture with oxidation reaction. As the result, exhaust gas concentration of HCHO indicates high level.

Figure 5 shows the courses of cylinder pressure, p , net rate of heat release, \dot{q} , mean gas temperature, T_g , which is calculated from measured cylinder pressure thermodynamically, and lift of nozzle needle, h_z , at different first-stage injection timings. In this figure it is shown that there are two peaks in the rate of heat

release. The first peak results from the cool-flame caused by the pre-reaction of pre-mixture and corresponding generation of formaldehyde, i.e., HCHO (Yanagihara [7]). The second peak of \dot{q} represents a hot flame of pre-mixture combustion. This peak at the retarded injection timings is higher than that at the advanced injection timings. At SPEI, it drops before TDC and links with that by diffusion combustion by a second-stage injected fuel. It lasts to expansion stroke after TDC. Thus the indicated mean effective pressure, p_i , goes down at the late injection timing. In the case of the late injection timings that the peak of hot-flame shows high level in both EI and SPEI, unstable ignition occurs and combustion control is difficult.

In the case of the latest injection timing of EI, an event of \dot{q} by cool and hot-flame is exhibited at a little earlier crank angle than that at other injection timings. This will be because the injected spray impinges at the top-land of piston and pre-mixture is formed more quickly. However, in the present study the spray penetration and piston cavity shape on the formation and ignition of pre-mixture are not clear, because of not changing spray nozzle orifices and piston cavity shapes.

The maximum of \dot{q} in both peaks at SPEI is lower than that at EI. This is because the injection pressure for the first-stage injection at SPEI is lower than that at EI. For this reason, the degree of mixing of fuel and air is deteriorated and the rich mixture is formed locally. As a result, the amount of combustible mixture decreases and the degree of pre-reaction is controlled. For SPEI, the rich mixture formed by the first-stage injection will be quickly burnt in a diffusion combustion with the fuel injected at second-stage injection. As a result, η_{glh} in the case of SPEI was improved. For this reason, it is seen that p_i became higher and b_i became lower than in the case of EI.

Figure 6 indicates the effects of first-stage injection timings, θ_{ji} , on the concentration of exhaust gas emissions including unregulated species measured by FT-IR. It is shown that the characteristic components in the exhaust gas species were HCHO , CH_3CHO , CH_4 , and C_2H_6 for both SPEI and EI. This indicates that the pre-mixture formed by the first-stage injection undergoes

Table 2 Gas components measured by FT-IR exhaust gas analyzer

CO , CO_2 , NO , NO_2 , N_2O , H_2O , NH_3 , SO_2 , HCHO , CH_3CHO , CH_3OH , CH_3COCH_3 , $(\text{CH}_3)_2\text{COCH}_3$, HCOOH , CH_4 , C_2H_4 , C_2H_6 , C_3H_6 , C_3H_8 , $1,3\text{-C}_4\text{H}_6$, $\text{iso-C}_4\text{H}_8$, $n\text{-C}_4\text{H}_{10}$, $\text{iso-C}_4\text{H}_{10}$, C_6H_6 , C_7H_8 , $\text{NO}+\text{NO}_2$

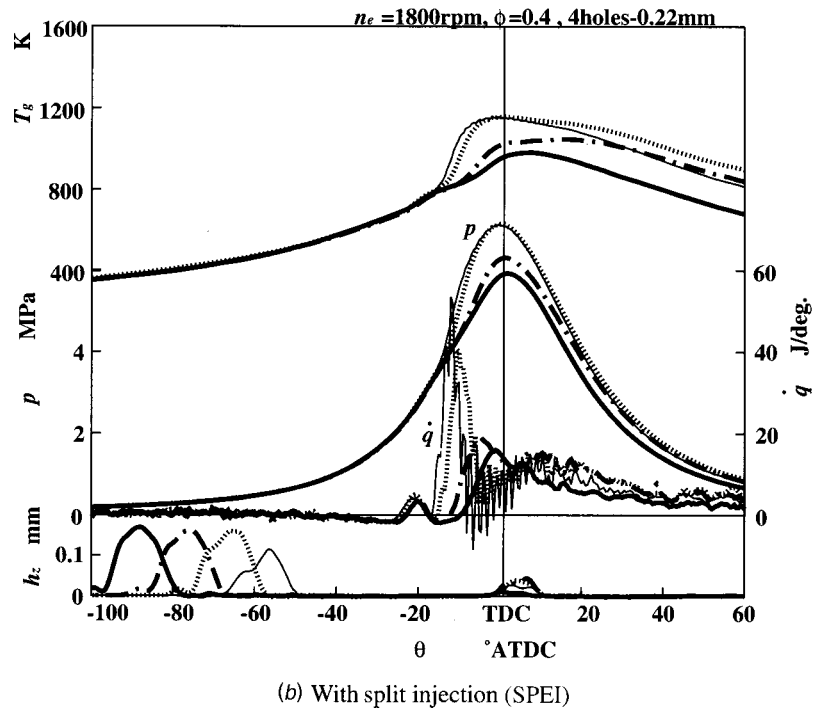
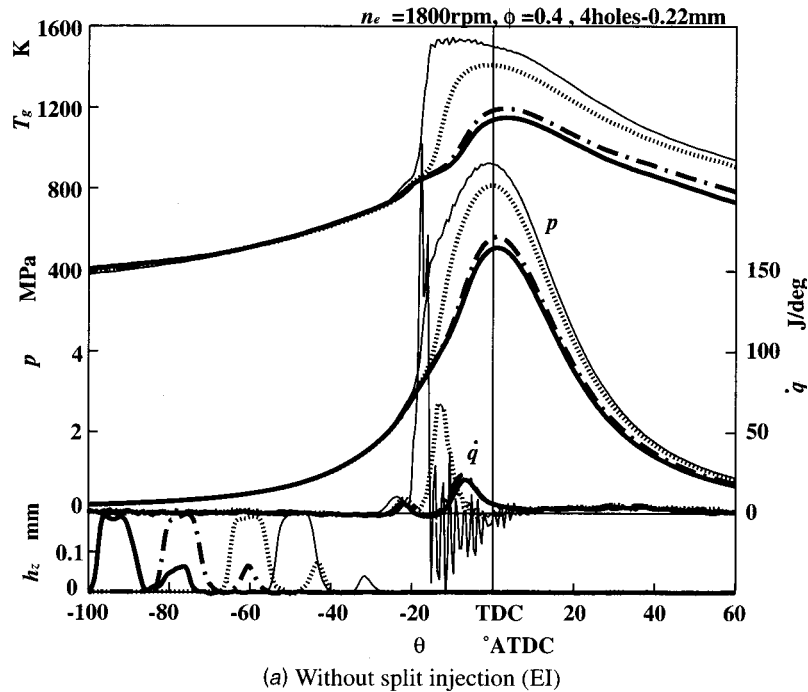


Fig. 5 Courses of cylinder pressure, p , rate of heat release, \dot{q} , mean gas temperature, T_g , and lift of nozzle needle, h_z , at different first-stage injection timings ($n_e=1800$ rpm, $\phi=0.4$)

a lower temperature oxidation reaction with cracking of hydrocarbons, simultaneously, and these species are stored in the quenching zone; wall layer.

In generally, the chemical species of HCHO, which is one of the species of ignition, is emitted and stored by an oxidation chemical reaction referred to as a cool-flame reaction and characterized by lower temperature and sufficient reaction time. The HCHO results in a quick oxidation reaction referred to as a hot-flame at high pressure. Then, the HCHO is consumed. In Fig. 4 it

is found that a higher concentration of HCHO is emitted in the exhaust. This result suggests that all molecule of HCHO do not always transit to hot-flame. This is because the cool-flame with HCHO is quenched at the wall region with lower temperature, and HCHO is emitted with unburned hydrocarbons.

Effect of Equivalence Ratio on Combustion and Emission Characteristics. Figure 7 shows the effect of equivalence ratio, ϕ , on combustion characteristics and exhaust emissions at SPEI

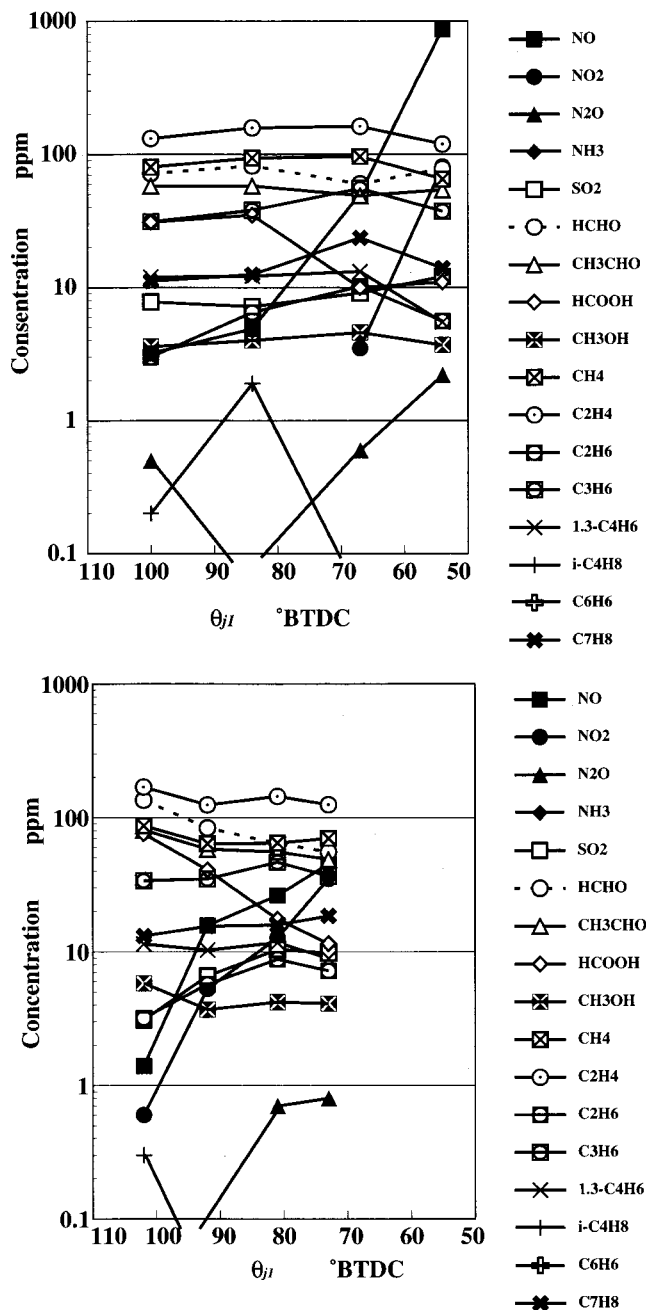


Fig. 6 Concentrations of exhaust gas emissions including unregulated species analyzed by FT-IR for different first-stage injection timings, θ_{11} ($n_e=1800$ rpm, $\phi=0.4$)

and ordinary diesel combustion. Equivalence ratio, ϕ , was changed by the amount of fuel injected at the second-stage injection of SPEI, and the first-stage injection timing, θ_{11} , was fixed at 82 deg BTDC. The amount of first-stage injected fuel to that of second-stage was the same with the case of $\phi=0.4$ in Fig. 4 which a stable combustion was obtained. The ordinary diesel combustion was realized by using a KD-3 injection system. In this case, an injection timing was fixed at 6 deg BTDC. The best thermal efficiency was indicated in this engine speed and this injection timing by employed injection and combustion system in experiments. For this reason we fixed the injection timing to 6 deg BTDC. Figure 8 shows the courses of p , \dot{q} , T_g and h_z at different equivalence ratios for SPEI, and for KD-3 the courses of p , \dot{q} , $T_g h_z$ and pressure in the nozzle inlet, p_N , are shown in Fig. 9. In

Fig. 8, rate of heat release, \dot{q} , before the start of the second-stage injection is slightly changed. This is due to the pressure fluctuation of first-stage injection. This fluctuation little affected combustion and emission characteristics in this experiment.

From Fig. 7, it is found that the engine performance b_i , p_i , η_{g1h} by SPEI is worse than those by the ordinary diesel combustion. However, concentration of NO_x is especially lower than that of ordinary diesel combustion, which is below 100 ppm. And smoke density is lower than that of the ordinary diesel combustion under the range of lower equivalence ratio. Under higher equivalence ratio, smoke density in the case of ordinary diesel combustion reaches high in spite of high-pressure injection of 70 MPa. This may be due to the secondary injection as shown in the courses of needle lift h_z in Fig. 9. There is a tendency for HCHO, CH_3CHO , and HCOOH to be reduced with an increase in equivalence ratio. This result suggests that HCHO with high concentration is consumed and decomposed by diffusion combustion of fuel injected at the second-stage injection.

At lower equivalence ratio, the concentration of unburned hydrocarbon HC ($\text{C}_1\text{--C}_7$) shows a high level, and b_i increases remarkably. This is because that amount of fuel injected at second stage is less. For this reason, most of the pre-mixture formed by first-stage injection does not burn and remains.

From Fig. 7 it is seen that degree of constant volume η_{g1h} decreases with an increase in equivalence ratio ϕ in the case of SPEI. This is because the combustion period is elongated to later crank angle with an increase in amount of fuel injected at second-stage as shown in Fig. 8.

Figure 10 indicates a relationship between HCHO concentration in exhaust and the maximum rate of heat release, \dot{q}_{\max} . It is clear that HCHO concentration is greatly reduced with an increase in \dot{q}_{\max} . This shows that decomposition of HCHO strongly depends on the appearance of hot-flame linked diffusion flame. And it is found that the slope falls quickly, as shown in Fig. 10. This suggests that the oxidation rate of HCHO in the transition from cool-flame to hot-flame is very high.

At a higher maximum rate of heat release, that is, at \dot{q}_{\max} of over 50 J/deg, HCHO concentration increases. In this case, the first-stage injection timing was retarded at EI. This result indicates that the amount of HCHO quenched and stored at the cylinder wall increases with the retardation of injection timings, and due to the combustion without diffusion flame for EI the amount of HCHO decomposition is limited. Hence, it is important to reduce the maximum rate of heat release due to hot-flame in order to reduce the concentration of HCHO in the exhaust.

Relationship Between NO_x , Smoke, and Indicated Specific Fuel Consumption (ISFC). This section shows a present view about the possibility of SPEI to reduce emission and fuel consumption by comparing ordinary diesel combustion in a limited engine operating range of present experiments.

Figure 11 shows the relationship between smoke, NO_x , and ISFC at the first-stage injection timing changes and fixed the second-stage injection timing, TDC for SPEI and EI, and the injection timing changes for ordinary diesel combustion. It can be seen that the relationships between smoke and NO_x , ISFC, and NO_x in the case of retarding injection timing for the SPEI and EI is on the opposite relation of that in the ordinary diesel combustion. In the case of the SPEI and EI, and smoke density reduces with a decrease in NO_x concentration with extremely advancing first-stage injection timing. This is because the pre-mixture over lean-limit is formed and is quenched at the region of cylinder wall. As the first-stage injection timing retards, smoke and NO_x concentrations increase. This is considered that a portion of that lean pre-mixture becomes hot flame, then this flame heats the quenched mixture reached at the wall region. For this reason, soot is formed at the wall region and is emitted. But NO concentration does not reach a high level because of a lean combustion without a rapid pressure rise.

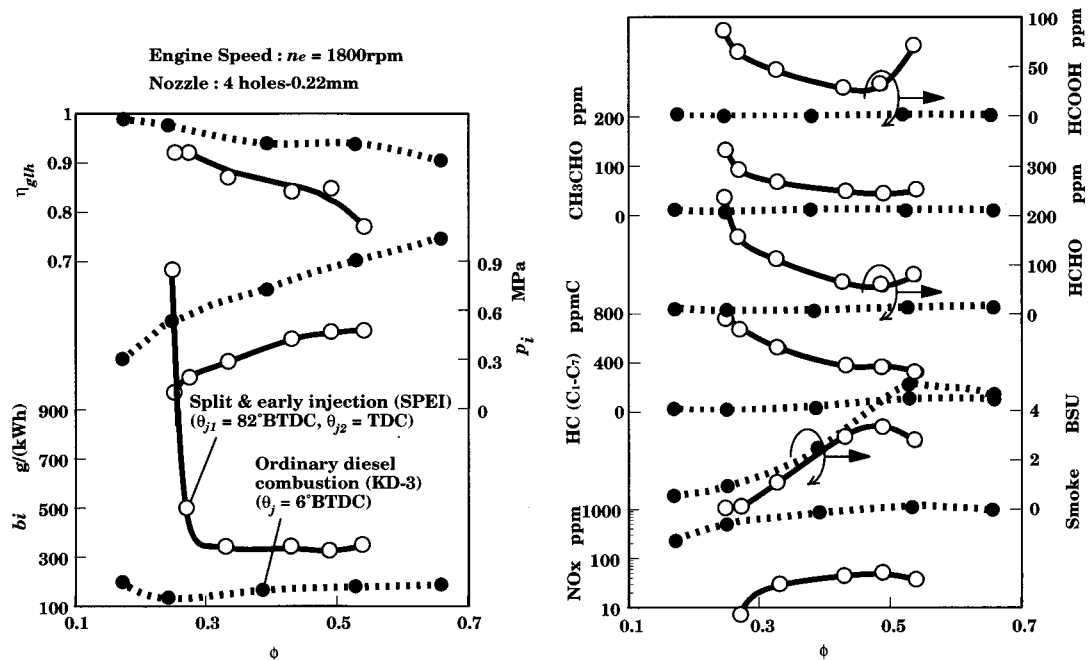


Fig. 7 Effect of equivalence ratios, ϕ , on engine performance and exhaust gas emissions at SPEI and ordinary diesel combustion obtained by KD-3 injection system

At the later injection timing of both EI and SPEI there is a tendency to smoke reduction. This will be because the amount of lean flammable pre-mixture grows, most of their mixture quickly burns, and the rapid pressure rise with a fluctuation in a tail of the heat release rate curve occurs as shown in Fig. 5. For this reason, combustion temperature rapidly goes up and its burnt gas is kept at higher temperature. Especially at EI, NO_x concentration be-

comes high. But due to the excess air in the mixture, smoke density does not becomes high.

In the case of the ordinary diesel combustion, smoke and NO_x concentrations are reduced at extremely retarded injection timing. This is because the ignition delay becomes long and a larger amount of pre-mixture is formed. Due to lower gas temperature by expansion stroke, smoke and NO_x are reduced.

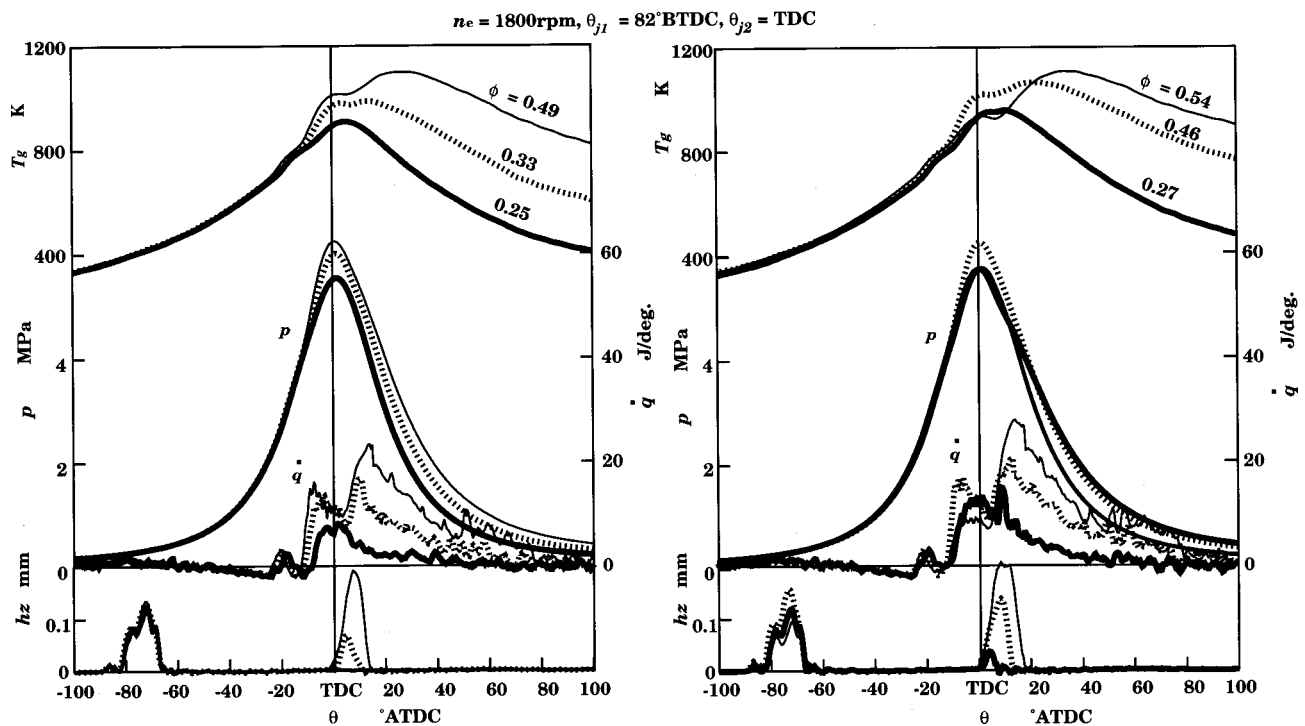


Fig. 8 Courses of p , \dot{q} , T_g , and h_z for different equivalence ratio ϕ

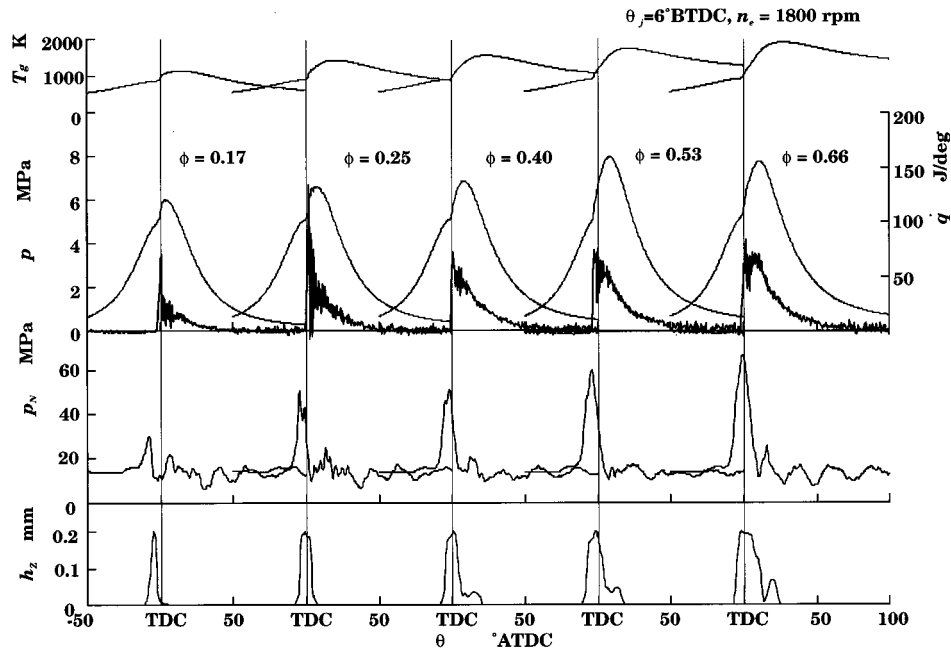


Fig. 9 Courses of p , q , T_g , h_z and the pressure in nozzle holder-inlet, p_N , for different equivalence ratio, ϕ , by using a KD-3 injection system

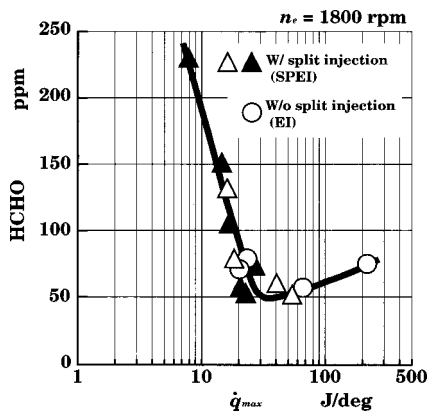


Fig. 10 Relationship between HCHO from exhaust and maximum of rate of heat release \dot{q}_{\max}

There is a tradeoff relationship between ISFC and NO_x for SPEI, EI and ordinary diesel combustion. At ordinary diesel combustion as the injection timing retards NO_x decreases and ISFC increases. At SPEI and EI, as the first-stage injection timing retards, NO_x increases and ISFC decreases. At a late injection timing of first-stage injection, the level of ISFC at SPEI is lower than that at EI, and that curve approaches a curve at ordinary diesel combustion. But this ISFC level is approximately 50% higher than that of the ordinary diesel combustion. This is due to a long combustion duration. This problem will be improved by reduction of combustion duration by means of the second-stage injection with higher pressure. Therefore, SPEI has the possibility to improve ISFC at a late injection timing of first-stage injection. However, to control the timing and intensity of the occurring of hot-flame is indispensable.

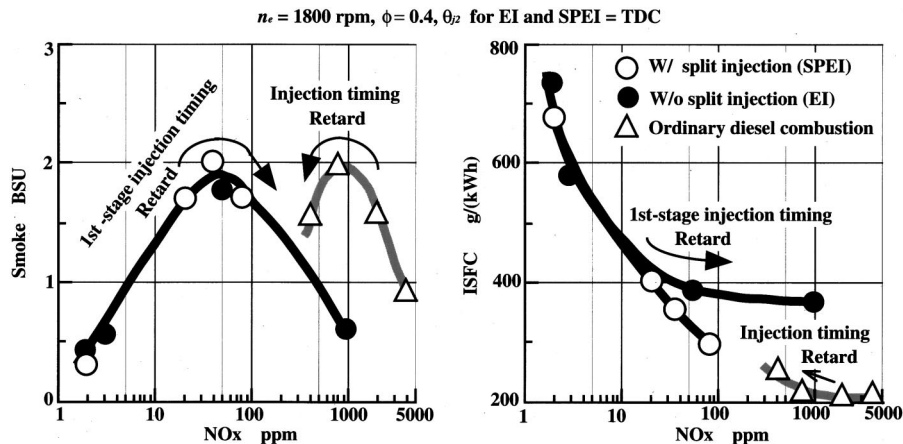


Fig. 11 Relationship between smoke density, indicated specific fuel consumption ISFC, and NO_x concentration obtained from experimental results by first-stage injection timing changes for SPEI and EI, and injection timing changes for ordinary diesel combustion

Conclusion

This study experimentally investigated the effects of second-stage split and early injection (SPEI) on the combustion and emission characteristics of a DI diesel engine. The results showed that HCHO, CH₃CHO, and CH₃COOH were emitted during the very early stage of both single injection (EI) and second-stage injection (SPEI). In particular, the HCHO concentration in exhaust was reduced with an increase in the maximum rate of heat release after cool-flame due to pre-reaction of pre-mixture. The NO_x concentration of EI and SPEI was extremely low at extremely advanced timing of the first-stage; however, the indicated specific fuel consumption (ISFC) was higher than that of ordinary diesel combustion. SPEI have a possibility to approach ISFC to that of ordinary diesel combustion at a retarded timing of first-stage injection. Also SPEI can extend the engine operating region; changing engine loads, which is one of the problems in the premixed compression ignition combustion. However, at higher engine load, a high injection pressure of over 100 MPa, for the second-stage injection, will be needed to greater reduce the smoke density and the fuel consumption.

References

- [1] Ryan, T. W. III, and Callahan, T. J., 1996, "Homogeneous Charge Compression Ignition of Diesel Fuel," SAE Technical Paper 961160.
- [2] Takeda, Y., Nakagome, K., and Niimura, K., 1996, "Emission Characteristics of Premixed Lean Diesel Combustion With Extremely Early Staged Fuel Injection," SAE Technical Paper 961163.
- [3] Yokota, H., Kudo, Y., Nakajima, H., Kakegawa, T., and Suzuki, T., 1997, "A New Concept for Low Emission Diesel Combustion," SAE Technical Paper 970891.
- [4] Hashizume, T., Akagawa, H., and Tsujimura, K., 1997, "Emission Reduction Using Multiple Stage Diesel Injection," *Proc. of The 14th Internal Combustion Engine Symposium*, SAE of Japan, Tokyo, pp. 259–264 (in Japanese).
- [5] Ikegami, M., Yamane, K., Neichi, T., and Zhu, Q. M., 1993, "A High-Pressure Diesel Fuel Injection System Using Spool Acceleration and Oil Hammering," SAE Trans., **102**, pp. 743–754.
- [6] Yamane, K., and Shimamoto, Y., 1999, "Prediction of NO and Soot From Diesel Engines With Fuel Injection Rate Shaping Using Multidimensional Engine Simulation," *Proc. of The 15th Internal Combustion Engine Symposium (International)*, SAE of Japan, Tokyo, pp. 489–495.
- [7] Yanagihara, H., Sato, Y., and Mizuta, J., 1996, "A Study of DI Diesel Combustion Under Uniform-Higher Dispersed Mixture Formation," *Proc. of The 13th Internal Combustion Engine Symposium*, JSME, Tokyo, pp. 365–371 (in Japanese).

G. M. Bianchi¹

Department of Mechanical Engineering,
Diem—University of Bologna,
Viale Risorgimento 2,
Bologna 40136, Italy

G. Cantore

P. Parmeggiani

Department of Mechanical Engineering,
University of Modena,
Via Vignolese 905,
Modena 41100, Italy

V. Michelassi

Department of Mechanical and
Industrial Engineering,
University of Roma Tre,
Via di tor Vergata,
Rome 00100, Italy

On Application of Nonlinear k - ε Models for Internal Combustion Engine Flows

The linear k - ε model, in its different formulations, still remains the most widely used turbulence model for the solutions of internal combustion engine (ICE) flows thanks to the use of only two scale-determining transport variables and the simple constitutive relation. This paper discusses the application of nonlinear k - ε turbulence models for internal combustion engine flows. Motivations to nonlinear eddy viscosity models use arise from the consideration that such models combine the simplicity of linear eddy-viscosity models with the predictive properties of second moment closure. In this research the nonlinear k - ε models developed by Speziale in quadratic expansion, and Craft et al. in cubic expansion, have been applied to a practical tumble flow. Comparisons between calculated and measured mean velocity components and turbulence intensity were performed for simple flow structure case. The effects of quadratic and cubic formulations on numerical predictions were investigated too, with particular emphasis on anisotropy and influence of streamline curvature on Reynolds stresses. [DOI: 10.1115/1.1454115]

Introduction

The modeling of turbulence is still one of the most challenging and controversial matter of engineering and physics, although the enormous improvements in computer and measurement instruments. Direct numerical simulation (DNS) allowed insight into the detailed physics of very simple flow providing an enormous and accurate statistically resolved data for turbulence model validation and calibration. Unfortunately, practical engine flows are much more complex than those used for model calibration. Flow curvature, acceleration, separation, and wall effects strongly determine turbulence characteristics. Even more difficulties arise when chemical reaction or multiphase flow have to be considered.

Turbulence modeling of internal combustion engines (ICE) is one of the most difficult challenges due to the complexity of in-cylinder flows and the lack of detailed measurements under practical geometrical and operating conditions (Arcoumanis et al. [1], Bo et al. [2], Burgess and O'Rourke [3], and Corcione and Valentino [4]). The need to improve turbulence simulation accuracy in ICE area is driven by the evidence that fuel evaporation and mixing processes as well as flame propagation and spray dynamics are influenced by in-cylinder flow turbulence features (El Thary and Haworth [5], Gosman and Watkins [6], and Celik and Yavuz [7]). Turbulence is primarily generated during induction by the interaction between the intake-jet, the valves and the combustion chamber walls. Another common source of turbulence is the shear in the mean flow: as is well known, the in-cylinder large-scale rotating flow structures are generated during the intake process (i.e., swirl, tumble, and cross tumble) and decay during compression stroke transferring energy to turbulence eddies (see Arcoumanis et al. [8]). The energy transfer rate is affected by mean strain levels and flow curvature and it usually occurs under nonequilibrium conditions (Han et al. [9], Borgnakke and Xiao [10], Burgess and Amsden [11], Tanner and Reitz [12], and Morel and Mansour [13]). Tumbling motion is the best source of turbulence because it is stretched by piston motion during compression and therefore it greatly increases its shear levels promoting turbu-

lence production (Arcoumanis et al. [8]). Experiments show that the shear in the mean flow can be also generated by swirl motion and by squish motion at the end of the compression stroke. The picture can be even more complex if one considers the contribution to shear of liquid jet injected at high velocity.

How the engine in-cylinder unsteady, anisotropic, and nonequilibrium turbulence can be simulated at a relatively low computational cost is the purpose of this paper.

It is well known that DNS is limited to simple flows at relatively low Reynolds numbers due to its extremely high computational cost. This makes DNS far from being feasible in the near future for practical engines flows due to their very wide range of length and time scales.

The semi-direct approach of the large eddy simulation (LES) solves the larger scales of flow, modeling the effect of the smaller scales on them, but it still requires some gross approximations in the near-wall region. LES implies high CPU requirements and it is currently faced with many problems in engineering practical flows (i.e., subgrid scale modeling, high sensitivity to grid quality).

The feasible alternative to DNS and LES is to solve the Reynolds-averaged Navier-Stokes equations (RANS) in conjunction with a turbulence model. The several turbulence models available in the open literature differ from the underlying concepts, complexity, and accuracy in capturing flow characteristics. The literature clearly indicates that none of the turbulence models developed up to now, even the most complex ones, can return satisfactory accuracy over a wide range of flow conditions. Usually the lower is the physical fundament, and the lower is the range of applicability even if empirical constants are used and tuned case by case. On the other hand, the higher is the physical background, and the higher are the computational requirements. Therefore compromises are made, and also the most complex and potentially most valid turbulence models bring omissions or empirical assumptions. Neglecting the simplest and less general one-equation turbulence models, the two-equation linear eddy viscosity models (in the following they will be simply referred as EVM) offer a good compromise between accuracy and computational cost. EVM are based on the linear Boussinesq stress-strain relationship by using an isotropic eddy viscosity, which is related to turbulence flow conditions. Among the EVM, the linear k - ε turbulence model is the most widely adopted in ICE simulations (Amsden et al. [14], El-Thary [15], Bo et al. [2], Morel and Man-

¹To whom all correspondence should be addressed.

Contributed by the Internal Combustion Engine Division of THE AMERICAN SOCIETY OF MECHANICAL ENGINEERS for publication in the ASME JOURNAL OF ENGINEERING FOR GAS TURBINES AND POWER. Manuscript received by the ICE Division, July 1999; final revision received by the ASME Headquarters, August 2001. Editor: D. N. Assanis.

sour [13], Han et al. [9], Celik and Yavuz [7], and Computational Dynamics Ltd., [16]). As is well discussed by Wilcox and Rubesin [17], Bradshaw et al. [18], and Leschziner [19], one of the weak point of the Boussinesq relationship is the assumption that turbulence stresses react to the mean strain rate immediately in a manner similar to Newtonian molecular response. This is true only in thin shear flows where the shear stress is the relevant stress and it can be assumed that the shear stress is proportional to the mean velocity gradient via the turbulent viscosity. By contrast, this link between stress and strain cannot be extended to more complex flows where misalignment of stress and strain tensor occurs and stress and strain develop at different rates. As a consequence, linear k - ε models are found to work quite well in steady incompressible two-dimensional shear flows or more generally in thin shear flows. Conversely they fail in complex flows as those evolving in ICE combustion chambers (Burgess and Amsden [11], Morel and Mansour [13], El-Thary [15], Han et al. [9], and Ramos [20]). Moreover, the eddy viscosity concept is unable to resolve turbulence stress anisotropy as well as effects of energy distribution among the normal stresses since it misses pressure correlation terms which cancel out in the turbulent kinetic energy equation. The latter defect leads to the neglect of countergradient diffusion that is found to be responsible for the growth of normal stresses across the flame, as shown by Bray et al. [21]. Finally, poor predictions in flows with strong curvature have been showed by many researchers (see Burgess and Amsden [11], Ramos [20], and Moryoshi et al. [22]). In particular, attempts to take into account the effect of swirl on the turbulence dissipation rate were made by modifying the ε equation (see Coleman and Mansour [23] and Moryoshi et al. [22]) or by accounting for the role of irrotational strains (Hanjalic and Launder [24]).

The most complete RANS closure methods, which are also the most expensive ones, are the second-moment closure models (i.e., Reynolds stress models (RSM)). In the RSM, a constitutive relation as in linear EVM does not force the relation between Reynolds stress and mean velocity gradient. Another feature of the RSM is that they also allow accounting for history effects, curvature influence, and pressure correlation. In spite of that, also RSM suffer from closure assumptions and approximations that could limit their accuracy: in particular, anisotropic dissipation, stress diffusion, and pressure-strain correlation term modeling still represent a challenge. These limits, combined with the very demanding RSM computational resource, led to the development of the nonlinear EVM. This kind of model wants to join the physical fundamentals of the second-moment closure with the relatively low computational cost and mathematical complexity of the second-moment closures.

Although nonlinear eddy viscosity models imply higher computational cost and are affected by stronger numerical problems than the linear EVM, their use is motivated by the capability to capture anisotropy and curvature effects that are one of the most important features of ICE flows.

Contribution of the Present Work

The focus of this work is to assess the predictive capability of nonlinear k - ε models in solving ICE flows. This work aims to show the main features and possible advantages of NLVM when applied to complex rapidly distorted and nonequilibrium flows. The purpose is to demonstrate that nonlinear k - ε models are well suited to capture anisotropy and effects of flow curvature on Reynolds stress. In this research the nonlinear k - ε models developed by Speziale [25] in quadratic expansion, and by Craft et al. [26], in cubic expansion, have been applied to the simulation of practical tumble engine flows during motored compression stroke. Two different flow configurations characterized by a weak and an intense tumble motion at intake valve closure (IVC) have been investigated.

Linear k - ε Model in Internal Combustion Engine (ICE) Simulations

The linear k - ε model was developed and tested with success in thin shear steady incompressible flows characterized by one characteristic time scale and one characteristic length scale (see Launder and Spalding [27], Leschziner [28], and Rodi [29]). Over the last 20 years, many workers spent efforts to modify the transport equations of k and ε to suit engine applications from those used in steady incompressible shear flows. In particular, looking for improvements, researchers' attention was focused on modifications to the ε -equation since the transport equation for ε has a less certain ground than the k -equation.

Gosman and Watkins [6] extended the application of the standard k - ε model to compressible flow by including the effect of density variations through the use of the dilation term D . Later, Reynolds [30] modified the form of the dissipation equation proposed by Gosman and Watkins in order to capture rapid spherical compression or expansion introducing the constant C_3 in the ε -equation. The most widely adopted form of the k - ε model for ICE simulations is

$$\frac{Dk}{Dt} = P - \varepsilon + Diff_k \quad (1)$$

$$\frac{D\varepsilon}{Dt} = C_1 \cdot \frac{\varepsilon}{k} \cdot P - C_2 \cdot \frac{\varepsilon^2}{k} + (1 - C_3)D\varepsilon + Diff_\varepsilon \quad (2)$$

where

$$P = \left[2\nu_t \left(S_{ij} - \frac{1}{3}D\delta_{ij} \right) - \frac{2}{3}k\delta_{ij} \right] \cdot S_{ij} \quad (3)$$

$$S_{ij} = \frac{1}{2} \left(\frac{\partial U_i}{\partial x_j} + \frac{\partial U_j}{\partial x_i} \right) \quad D = \nabla \cdot \mathbf{U} = S_{kk}$$

$$\nu_t = c_\mu \frac{k^2}{\varepsilon} \quad (4)$$

where S_{ij} is the strain tensor. The constitutive relationship is given by the linear stress-strain relationship proposed by Boussinesq:

$$\tau_{ij} = 2\mu_t \left(S_{ij} - \frac{1}{3}S_{ll}\delta_{ij} \right) - \frac{2}{3}\rho k\delta_{ij}. \quad (5)$$

As previously mentioned, many authors worked on constants C_1 , C_2 , and C_3 in order to improve the modeling of turbulence dissipation by including nonequilibrium viscosity change and rapid compression influence. In this work, we used the following values of the model constants in Eqs. (2) and (4): $c_\mu = 0.09$, $C_1 = 1.44$, $C_2 = 1.92$, and $C_3 = (7 - C_1)/3$.

Nonlinear k - ε Models in ICE Simulations

The linear EVM have been extensively criticized because of their lack of physical ground of both the constitutive relationship and ε -transport equation. In the ICE simulations area, many workers have moved toward second-order closures like Borgnakke and Xiao [10], who applied the RSM in compressible ICE flows, and Burgess and Amsden [11] who applied the Launder, Reece and Rodi (LRR) model to a swirling flow. As previously pointed out, the second-moment closures provide a higher level of accuracy with severe additional computational costs as well as unresolved uncertainties in modeling turbulence dissipation (Leschziner [28] and Durbin and Speziale [31]) and the effects of flow curvature (Burgess and Amsden [11]).

A very interesting compromise between the second-moment closures and the linear EVM may be represented by the nonlinear EVM, which are based on a nonlinear stress-strain relationship. The nonlinear EVM constitutive relation allows linking the sim-

plicity of EVM formulations with the superior physical ground of the second-moment closures with low additional computational costs.

The foundations of nonlinear EVM were laid by Pope [32] who proposed a general explicit relation between Reynolds stress tensor and mean strain

$$a_{ij} = \sum G^\lambda T_{ij}^\lambda \quad (6)$$

where T_{ij}^λ is a tensorial power expansion in the strain and vorticity tensors, S_{ij} and Ω_{ij} , respectively. The vorticity tensor is expressed as

$$\Omega_{ij} = \frac{1}{2} \left(\frac{\partial U_i}{\partial x_j} - \frac{\partial U_j}{\partial x_i} \right) \quad (7)$$

and G^λ are coefficients which are in the strain and vorticity invariants, \tilde{S} and $\tilde{\Omega}$, respectively, given by

$$\tilde{S} = \frac{k}{\varepsilon} \sqrt{S_{ij} S_{ij}} \quad (8)$$

$$\tilde{\Omega} = \frac{k}{\varepsilon} \sqrt{\Omega_{ij} \Omega_{ij}}. \quad (9)$$

Speziale [25] took G^λ as powers of the eddy turnover time scale $\tau = k/\varepsilon$ in order to achieve dimensional consistency.

The nonlinear EVM (NLEVM) developed and available in the open literature comes from different routes and they are *quadratic* (Speziale [25] and Shi and Zhu [33]), *cubic* (Lien et al. [34], Craft et al. [26,35], and Apsley and Leschziner [36]), and even *quartic* (Gatski and Speziale [37]). This difference in order leads to different capability in modeling turbulence: In particular, quadratic terms allow accounting for anisotropy while cubic terms allow capturing the effect of flow curvature on turbulence.

In this work the quadratic and the cubic nonlinear k - ε models proposed for incompressible flows by Speziale [25] and by Craft et al. [26] respectively, have been used. A two-scale transport equation approach has been used. Both models were extended to ICE applications by including the compressibility effects. In order to achieve numerical convergence and avoid numerical instabilities, the extension of the NLEVM to the highly unsteady and very complex engine flows has required further modifications to the expression of the model constants.

Quadratic Nonlinear k - ε Model. This research examines a modified version of the model derived by Speziale [25] and is based on the Taylor expansion using invariance considerations. The stress-strain constitutive relation, modified in order to account for compressibility, is expressed as

$$\begin{aligned} \tau_{ij} = & -\frac{2}{3} \rho k \delta_{ij} + 2 \rho c_\mu \frac{k^2}{\varepsilon} \left(S_{ij} - \frac{1}{3} S_{mm} \delta_{ij} \right) \\ & + \gamma_1 \left(S_{im} S_{mj} - \frac{1}{3} S_{mn} S_{mn} \delta_{ij} \right) + \gamma_2 \left(\dot{D}_{ij} - \frac{1}{3} \dot{D}_{mm} \delta_{ij} \right) \end{aligned} \quad (10)$$

where

$$\gamma_1 = 4 C_D c_\mu^2 \rho \frac{k^3}{\varepsilon^2} \quad \text{and} \quad \gamma_2 = 4 C_E c_\mu^2 \rho \frac{k^3}{\varepsilon^2}.$$

C_D and C_E are nondimensional coefficients. The term

$$\dot{D}_{ij} = \frac{\partial S_{ij}}{\partial t} + \bar{v} \cdot \nabla S_{ij} - \frac{\partial U_i}{\partial x_k} S_{kj} - \frac{\partial U_j}{\partial x_k} S_{ki} \quad (11)$$

is the Oldroyd derivative of S_{ij} . The extension to ICE applications required overcoming numerical problems. This suggested omitting completely in our formulation the Oldroyd derivative in order to obtain numerical stability. This choice has been also partially performed also by Sarkar and Speziale [38]. Our concern is

that omitting this term may lead to lack of rigor in unsteady flow conditions since it represents a time derivative. In order to account for the presence of large strain the term γ_1 has been redefined. The form of the quadratic nonlinear constitutive relation used in this research is finally

$$\begin{aligned} \tau_{ij} = & -\frac{2}{3} \rho k \delta_{ij} + 2 \rho c_\mu \frac{k^2}{\varepsilon} \left(S_{ij} - \frac{1}{3} S_{mm} \delta_{ij} \right) \\ & + \gamma_1 \left(S_{im} S_{mj} - \frac{1}{3} S_{mn} S_{mn} \delta_{ij} \right). \end{aligned} \quad (12)$$

When constructing the coefficient γ_1 the “weak” realizability constraint (i.e., positiveness of turbulent kinetic energy k) has been used. The resulting coefficient is $\gamma_1 = 4 C_D / \tilde{S} c_\mu^2 \rho k^3 / \varepsilon^2$. The constant C_D has been set in order to fit experimental data of velocity profile (see later) as well as trying to keep the same weight given by Speziale to quadratic terms in order to reproduce the turbulent channel flow experimental data. The value $C_D = 5.0$ has been found to match this goal. Speziale [25] reproduced in simulation the exact development of turbulence-driven secondary flows in noncircular duct thanks to the use of the second-order NLEVM turbulence model.

Cubic Nonlinear k - ε Model. The expansion to second order is not enough if flow curvature effects have to be considered. In order to capture the influence of flow curvature on Reynolds stresses, cubic terms have to be included in the stress-strain relationship. If we retain up to cubic terms, the most general stress-strain relationship for compressible flow gives

$$\begin{aligned} a_{ij} = & \frac{\overline{u_i u_j} - 2/3 \delta_{ij} k}{k} \\ = & -2 \frac{\nu_t}{k} \left(S_{ij} - \frac{1}{3} S_{ll} \delta_{ij} \right) + c_1 \frac{\nu_t}{\varepsilon} \left(S_{ik} S_{jk} - \frac{1}{3} S_{kl} S_{kl} \delta_{ij} \right) \\ & + c_2 \frac{\nu_t}{\varepsilon} (\Omega_{ik} S_{jk} + \Omega_{jk} S_{ik}) + c_3 \frac{\nu_t}{\varepsilon} \left(\Omega_{ik} \Omega_{jk} - \frac{1}{3} \Omega_{kl} \Omega_{kl} \delta_{ij} \right) \\ & + c_4 \frac{\nu_t k}{\varepsilon^2} (S_{ki} \Omega_{lj} + S_{kj} \Omega_{li}) S_{kl} \\ & + c_5 \frac{\nu_t k}{\varepsilon^2} \left(\Omega_{il} \Omega_{lm} S_{mj} + S_{il} \Omega_{lm} \Omega_{mj} - \frac{2}{3} S_{lm} \Omega_{mn} \Omega_{nl} \delta_{ij} \right) \\ & + c_6 \frac{\nu_t k}{\varepsilon^2} (S_{ij} S_{kl} S_{kl}) + c_7 \frac{\nu_t k}{\varepsilon^2} (S_{ij} \Omega_{kl} \Omega_{kl}). \end{aligned} \quad (13)$$

The constitutive relation of Eq. (13) allows accounting for anisotropy as well as for stabilizing/destabilizing effects of mean streamline curvature in thanks to the contribution of the cubic terms. Stable curvature has a tendency in reducing turbulent energy and occurs when $\tilde{S}^2 - \tilde{\Omega}^2 < 0$. If $c_7 - c_5$ is chosen positive, the shear stress will decrease when $\tilde{S}^2 - \tilde{\Omega}^2 < 0$, the opposite behavior occurring when $\tilde{S}^2 - \tilde{\Omega}^2 > 0$. It must be also pointed out that in two-dimensional flow the quadratic terms have no direct influence on turbulence production and with a proper choice of constant c_5 , c_6 , c_7 (i.e., $c_6 + c_7 - c_5 = 0$) the cubic terms play no role in simple shear.

The cubic nonlinear models available in the open literature are based on Eq. (13) and differ mainly for the value of the coefficient c_i and the determination of c_μ and the form of the dissipation equation. Almost all studies recommend coefficient values by considering the prediction of shear flow and one other flow condition. As a consequence the coefficients depend on what flow or flow features have to be predicted. It must be pointed out that among the different models the form of c_μ depends on strain and vorticity invariants. In the present work, the coefficients c_i are assumed to be strain-invariant dependent and they are derived with modifica-

Table 1 Coefficients of nonlinear cubic EVM for ICE applications

c_1	c_2	c_3	c_4	c_5	c_6	c_7
$-1/\sqrt{S}$	$1/\sqrt{S}$	0	$-5/\sqrt{S}$	0	$-5/\sqrt{S}$	$5/\sqrt{S}$

tions from those suggested by Craft et al. [26]. In particular, the values of c_i derived from optimization in ICE flow application, are given in Table 1.

It must be pointed out that the cubic model used is formally identical in the linear and quadratic part to that proposed by Craft et al. [26] except for the term $(\Omega_{ik}\Omega_{jk} - \frac{1}{3}\Omega_{kl}\Omega_{kl}\delta_{ij})$. The latter has been criticized by Gatski and Speziale [37] since it produces anisotropy under solid-body rotation from initial isotropic turbulence flow condition. The modification to constants has been conducted by verifying that in simple shear flows the model is able to return anisotropy as well as making the linear term the only contribution to the shear stress (i.e., from the choice $c_7 = -c_6$ and $c_5 = 0$). Specific tuning has been based on ICE experimental velocity measurements. The expression for c_μ is taken as in Craft et al. [26]

$$c_\mu = \frac{0.3}{1 + 0.35(\max(\tilde{S}, \tilde{\Omega}))^{1.5}} \cdot \left(1 - \exp\left[\frac{-0.36}{\exp(-0.75\max(\tilde{S}, \tilde{\Omega}))} \right] \right) \quad (14)$$

This functional form of c_μ proposed by Craft et al. [26] allows achieving in a homogeneous shear prediction in good agreement with DNS data and experiments of the variation of the stress anisotropies with strain rate.

Validation

The aim of this work is to demonstrate that, in the case of complex flows with strong curvature, the nonlinear formulations determine different predictions of large-scale flow structure and normal turbulent stresses. Our intention was to demonstrate this hypothesis by simulating the motored compression stroke of an optical accessible engine with the CFD code KIVA 3.0. The linear and cubic $k-\varepsilon$ models were compared by simulating the compression stroke of an optical accessible engine with the KIVA 3.0 code. Computations start at IVC and they end at TDC. Details about the CFD code KIVA 3.0 can be found in Amsden et al. [14] and O'Rourke and Amsden [39].

Numerical Method. An arbitrary Lagrangian-Eulerian finite volume method has been used. A block structured approach was adopted for building computational domain. An implicit method was used for a marching solution of discretized governing equations in time. The conjugate residual method with a technique very similar to SIMPLE algorithm was adopted for solving coupled implicit equations. Convective terms were solved by a quasi-second-order (QSOU) accurate scheme based on Van Leer's scheme.

Engine Specifications. The engine used in this research is a two-valve engine with a flat piston and a flat head, experimentally characterized by Vafidis [40] (Fig. 1) at a full load and 1000 rev/min engine speed as the operating condition. Detailed specifications of the engine are summarized in Table 2.

The instantaneous axial component of the velocity was measured by an LDV system. The axial mean velocity and intensities were computed by ensemble averaging the experimental data on 1500 consecutive cycles, and *rms* velocity carried out at seven locations P_i (see Fig. 2) on the symmetry plane, 5 mm below engine head.

The discretization in space has been carried out by using a 180-deg Cartesian grid having a cell size of $1 \times 1 \text{ mm}^2$ over planes

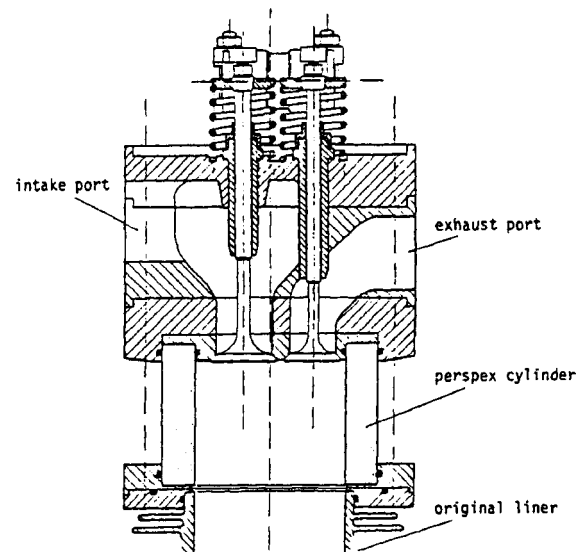


Fig. 1 (Vafidis, [40]): engine layout

normal to the cylinder axis. The cell size along the axial direction is adjusted during compression and therefore varies from 2 mm at IVC to 1 mm at TDC. This resolution has been demonstrated to given grid-independent results (see Bianchi [41]).

Table 2 Engine specifications

Bore	7.35 cm
Stroke	7.00 cm
Squish clearance	1.09 cm
Conrod	13 cm
Cylinder displacement	297 cm^3
Compression ratio	7.4:1
Intake valve closure (IVC)	100 c.a. deg BTDC

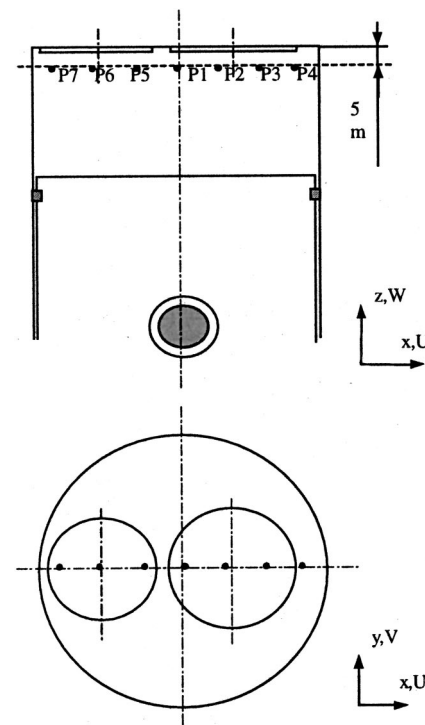


Fig. 2 Engine measurement locations

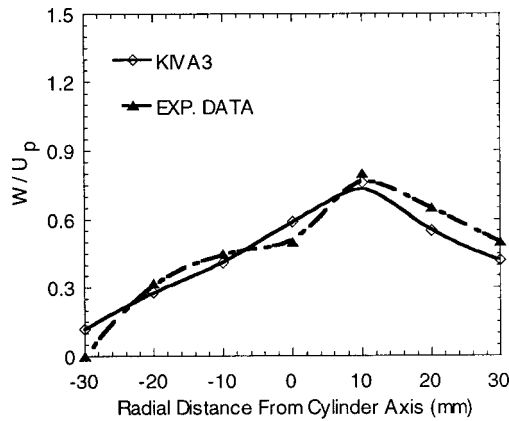


Fig. 3 Initial velocity profile—mean velocity axial component on the symmetry plane—locations at 2 cm below cylinder head

Flow Conditions at Intake Valve Closure (IVC). In order to test the capability of the $k-\varepsilon$ nonlinear models to capture anisotropy and the influence of flow curvature on turbulence stresses two different tumble ratios at IVC have been considered.

The first case, referred as the *low-tumble case*, was experimentally investigated by Vafidis [40] and it is characterized by an initial tumble ratio $RT_{xz}=0.1$. The initial mean flow was defined in order to match the measured velocity profile at IVC by using two counterrotating vortices, which represent a typical flow structure in practical engines (Fig. 3). The axis of rotation of these tumble vortices is normal to the $x-z$ plane. Swirl and cross-tumble have been neglected based on experimental evidence. Details about RT_{xz} evaluation can be found in the Appendix. Since cross-tumble is not considered, in the following RT_{xz} will be simply indicated as RT . This weak tumble motion at IVC makes this flow condition to be well representative of uniaxial compression.

In order to investigate the performance of the three models when faced with strong anisotropy and flow curvature effects, the tumble ratio has been increased to the value $RT=1.0$, typical of a practical high-tumble engine induction system. No experimental data were available for comparison. In the following, this flow condition will be referred as the *high-tumble case*. As in the former case we initialized the flow field by using two counterrotating axial vortices.

Results and Discussion

The *low-tumble case* is now analyzed and the behavior of the three models is discussed when the flow curvature effects are negligible. This allows one to investigate the capability of the turbulence models examined in capturing anisotropy. Figure 4 compares the numerical predictions of the tumble ratio during the compression stroke. In Figs. 5 and 6 the turbulence model predictions of axial mean velocity component and axial turbulence intensity w' at measurement points at TDC are compared with the experimental data. According to the constitutive relation, for linear $k-\varepsilon$ model w' is evaluated as $w'=\sqrt{2k/3}$, being $u'=v'=w'$.

When the low tumble ratio case is considered, the three models provide about the same predictions of both tumble ratio (Fig. 4) and axial mean velocity profile (Fig. 5), which is also in good agreement with measurements. A deep insight has been carried out by looking at the prediction of the axial turbulence intensity on the symmetry plane at the measurement points (Fig. 6) as well as at the invariant A at location P3 (Fig. 7). The invariant A is defined as

$$A = 1 - \frac{9}{8}(A_2 - A_3) \quad (15)$$

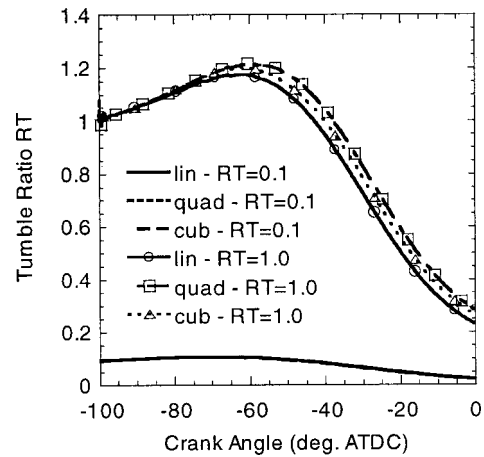


Fig. 4 Effect of constitutive relation on tumble ratio

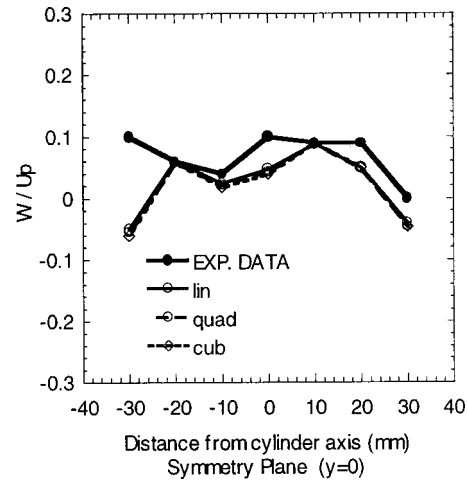


Fig. 5 Effect of constitutive relation on axial mean velocity profile at TDC— $RT=0.1$

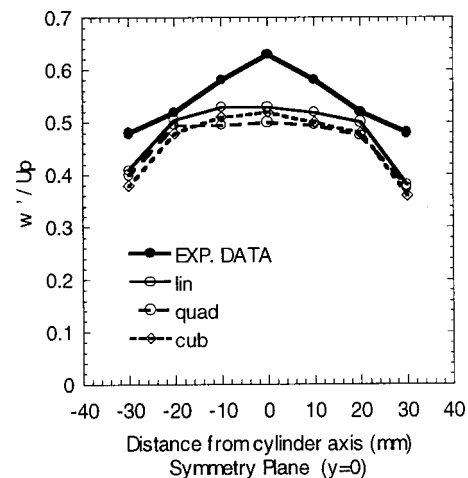


Fig. 6 Effect of constitutive relation on axial turbulence intensity at TDC— $RT=0.1$

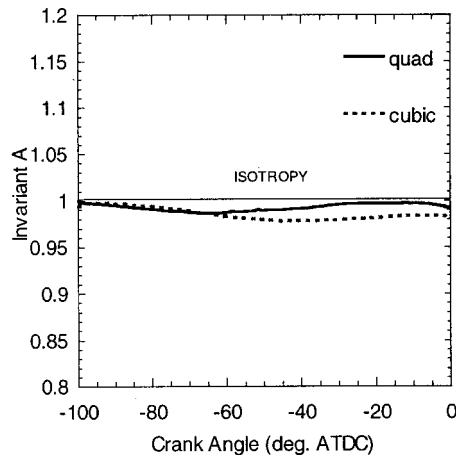


Fig. 7 Effect of constitutive relation on anisotropy levels prediction—location P3— $RT=0.1$

where $A_2 = a_{ij} a_{ij}$ and $A_3 = a_{ij} a_{jk} a_{ki}$ being a_{ij} the anisotropy tensor expressed as

$$a_{ij} = \frac{u_i u_j}{k} - \frac{2}{3} \delta_{ij}. \quad (16)$$

Invariant A gives an order of magnitude of anisotropy levels which increase as A departs far away from one.

The first interesting point of the analysis is that both quadratic and cubic formulations return lower levels of turbulence intensity with respect to the linear EVM, as one can see looking at Fig. 6. The excessive return of turbulence energy is typical of the linear EVM models when applied to strong compressive strains (see Leschziner [28]) as in the present case. Despite this improvement, the use of nonlinear constitutive relationship does not improve the agreement of the axial turbulence intensity predictions with respect to experimental data. The reasons for this have been extensively discussed by Han et al. [9], Bianchi et al. [41], and Tanner and Reitz [12] who have demonstrated that for ICE nonequilibrium flows undergoing rapid compression and subjected to rapid mean flow distortion, the form of the ε -equation may not be adequate. This because it represents an equation for the energy transfer from the larger scales to smaller scales rather than a budget rate of the turbulence energy transfer into heat assuming equilibrium between these two rates. Therefore, modifications to the stress-strain relationship cannot help eliminating the uncertainties involved in turbulence dissipation modeling.

The second interesting point of the analysis is represented by the fact that the addition of quadratic and cubic terms allows accounting for anisotropy, as one can verify by looking at Fig. 7. In particular, the cubic formulation seems to return higher levels of anisotropy than the quadratic one. It must be pointed out that the slightly low compression ratio of the engine and the weak tumble motion at IVC do not allow inducing high anisotropy levels at the end of the compression stroke. Despite this fact, Fig. 7 reveals the capability of both models in capturing this feature.

Dealing with the mass-averaged evolution of k and ε , shown in Figs. 8 and 9, respectively, no appreciable differences characterize the predictions given by the three models. In all cases, the low strain generated in the mean flow during compression cannot sustain turbulence that constantly decays. The absence of differences in the predictions among the three formulations can be explained by the very weak tumble structure at IVC, which determines low strains in the mean flow during compression when the tumble vortices are stretched by piston motion. As a consequence, the higher-order terms in the constitutive relation of turbulence stresses are negligible with respect to the first-order terms, at least for the case under investigation.

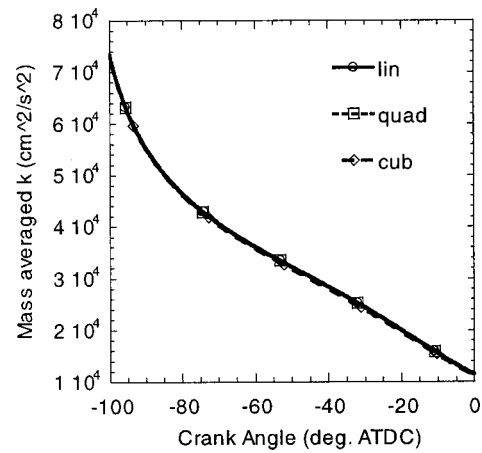


Fig. 8 Effect of constitutive relation on mass averaged k — $RT=0.1$

As the strength of the initial tumble motion is increased (*high-tumble* case), the analysis of the numerical predictions returns more significant differences among the three models since the higher-order term influence becomes stronger. As far as mass-averaged k is concerned (Fig. 10), one can note that both nonlin-

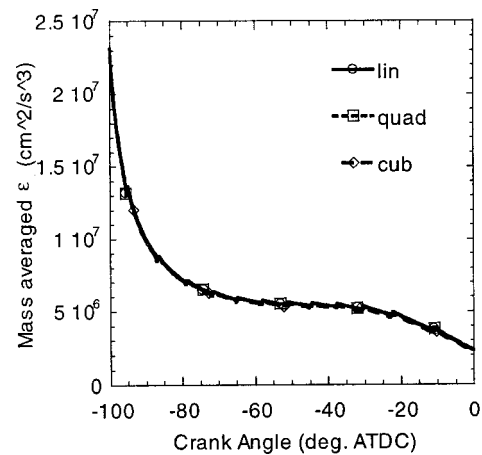


Fig. 9 Effect of constitutive relation on mass averaged ε — $RT=0.1$

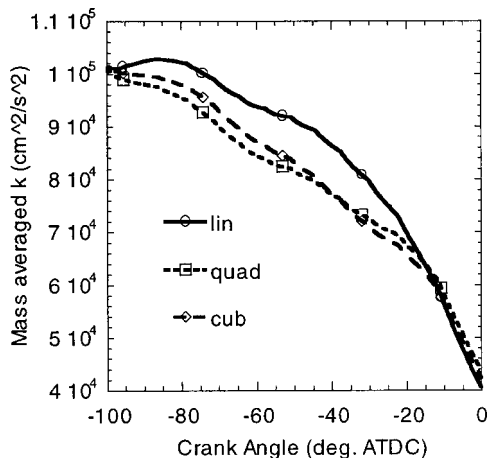


Fig. 10 Effect of constitutive relation on mass averaged k — $RT=1.0$

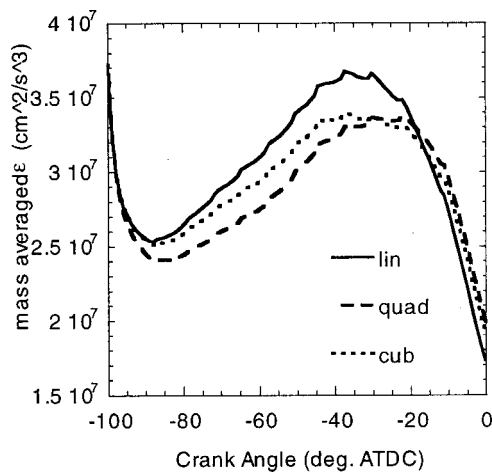


Fig. 11 Effect of constitutive relation on mass averaged ε — $RT=1.0$

ear k - ε models return much lower turbulence kinetic energy than the linear formulation until about 20 c.a. deg ATDC when the opposite trend occurs. In the *low-tumble* case this feature was detected only at TDC in the axial turbulence intensity profile at measurement locations and not in the mass-averaged k and ε evolutions. Also the mass-averaged ε predictions, presented in Fig. 11, are strongly affected by the constitutive relationship. This larger difference in the behavior of the three models can be attributed to the higher anisotropy levels induced by the more complex and stronger initial tumble motion. This is evident by comparing Figs. 7 and 12, where the evolution of invariant A at location P3 for the quadratic and cubic formulations is presented for the *low* and *high-tumble* cases, respectively. As in the *low-tumble* case, also in the *high-tumble* case the cubic model return higher levels of anisotropy.

How this is connected to mean flow features can be derived by looking at Fig. 4, where the numerical evolution of the tumble ratio is compared for the three models in the *low* and *high tumble* cases. As initial RT is increased, all the models predict the typical behavior experimentally shown in large bore-to-stroke-ratio engines during compression.

In the very first period from IVC, the reduction of momentum inertia coupled with low strain in mean flow determines the increase of RT until reaching a maximum around 60 c.a. deg BTDC (tumble spinning-up). Then, the further reduction of inertia mo-

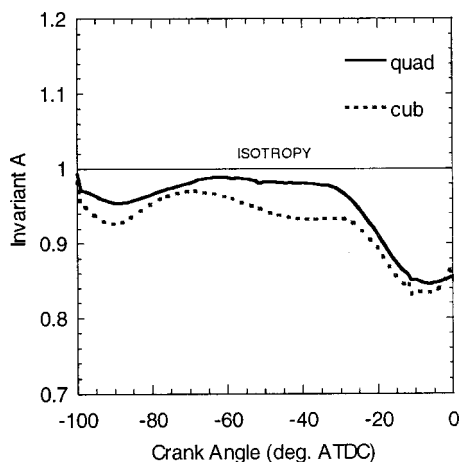


Fig. 12 Effect of constitutive relation on anisotropy levels prediction—location P3— $RT=1.0$

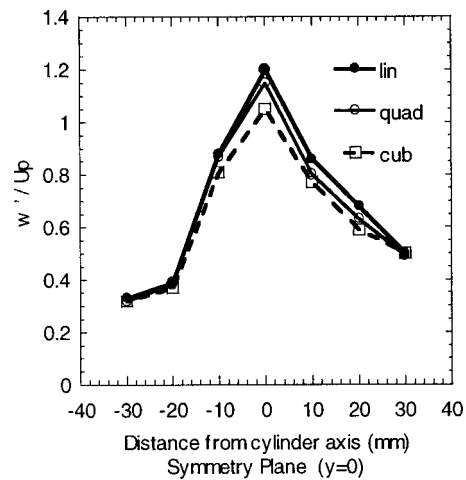


Fig. 13 Effect of constitutive relation on axial turbulence intensity at TDC— $RT=1.0$

mentum and the sharp increase in mean strain induced by piston motion, which reduces the vortex characteristic dimension, cause the transfer of energy to turbulence motion and therefore the decrease of RT in the latter part of the compression stroke. The nonlinear models predict higher tumble ratio (i.e., this means that the mean flow is storing higher energy levels). The lower turbulence kinetic energy levels and the higher RT seen when using nonlinear models indicate that the cubic and quadratic formulations predict a lower transfer rate of energy from the mean flow into turbulence. From the analysis of Fig. 4, it is seen also that the larger is the tumble ratio and the bigger is the difference between the cubic and quadratic model results, proving that the cubic terms play an important role in flows with strong curvature.

The influence of the constitutive relationship is particularly visible in measurement locations at TDC in terms of both axial turbulence intensity (Fig. 13) and axial mean velocity component (Fig. 14). Analysis of Fig. 13 confirms that nonlinear models predict lower turbulence levels. A deep insight into Fig. 13 and Fig. 14 show the important role played by cubic terms. As one can see, the quadratic formulation provides about the same levels of w' as those given by linear k - ε model. By contrast, the cubic k - ε model predicts 20 percent lower axial turbulence intensity than linear and quadratic models. These differences become lower moving from the center of the combustion chamber to the periphery. The

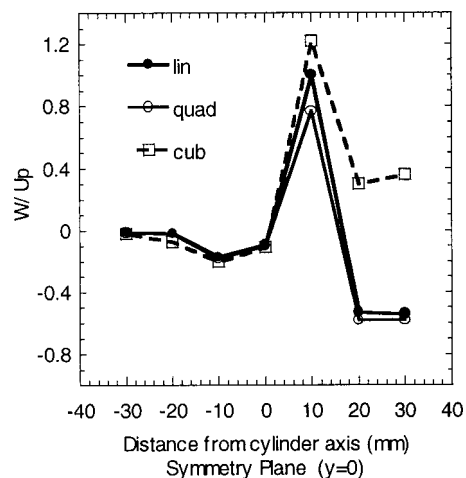


Fig. 14 Effect of constitutive relation on axial mean velocity profile at TDC

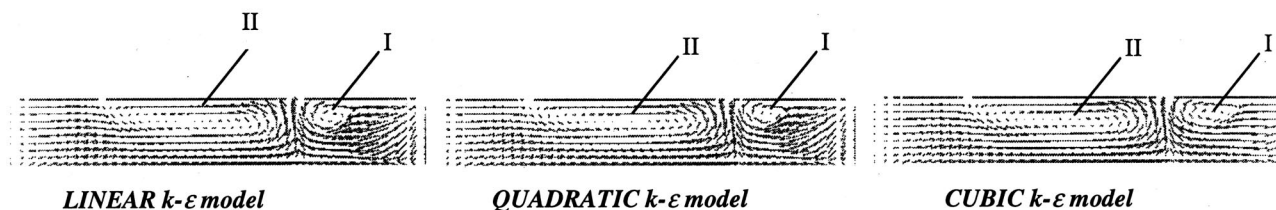


Fig. 15 Mean flow structure on symmetry plane—10 c.a. deg BTDC— $RT=1.0$

same conclusions can be drawn about the axial mean velocity prediction (Fig. 14). Beyond a distance of 10 mm from the cylinder axis, cubic formulation predicts a positive mean axial velocity component while quadratic and linear formulation predict a negative axial velocity component.

If the influence of the form of the $k-\varepsilon$ model constitutive relation on the mean flow structure predictions is very weak for the low tumble case, it is significant as the tumble ratio is increased. Figures 15 and 16 compare the mean flow field predictions of the three models at 10 c.a. deg. BTDC on the symmetry plane and on a plane normal to cylinder axis and located 5 mm below cylinder head, respectively.

During the compression, the initial two tumble vortices develop in a more complex whirling structure as the piston approaches TDC. The flow field on the symmetry plane (Fig. 15) is always characterized by the residual presence of the two initial tumble vortices. On the contrary, the mean flow pattern close to TDC is characterized by the growth of several and intense vortices (which are absent at IVC) on planes normal to the cylinder axis, as one can note in Fig. 16. Comparing the numerical predictions of the two models, it can be seen that the nonlinear formulation predictions differ from those by linear EVM in the flow structures. Fig-

ure 15 shows that the three models give different predictions of the shape of vortex I, which lies in a high strain region. In particular, the more significant difference can be detected in the cubic formulation predictions, since quadratic and linear models lead to a substantially similar vortex structure. This behavior was previously detected also in Fig. 14.

Figure 16 gives further proof of the role played by cubic terms in flow with strong curvature. As one can note, the cubic model predicts a different shape and location of vortex II and III. The analysis of Figs. 17 and 18 is useful to understand the influence of the cubic terms on turbulence stress predictions. The distribution of the anisotropic stress components a_{11} , and a_{33} , respectively, is compared for the quadratic and cubic models on a plane normal to the cylinder axis and located 5 mm below the cylinder head.

The high-tumble flow configuration at IVC promotes the growth of a_{11} and a_{33} . Hence, dU/dx and dW/dz are much greater than dV/dy , which determines a_{22} intensity. Because of negligible differences among models, the distribution of a_{22} is omitted. Dealing with a_{11} and a_{33} , differences in both distribution and values characterize their numerical predictions. It can be seen in Fig. 17 that cubic $k-\varepsilon$ model predicts a lower minimum of a_{11} and locates it in a more narrow region than quadratic formulation

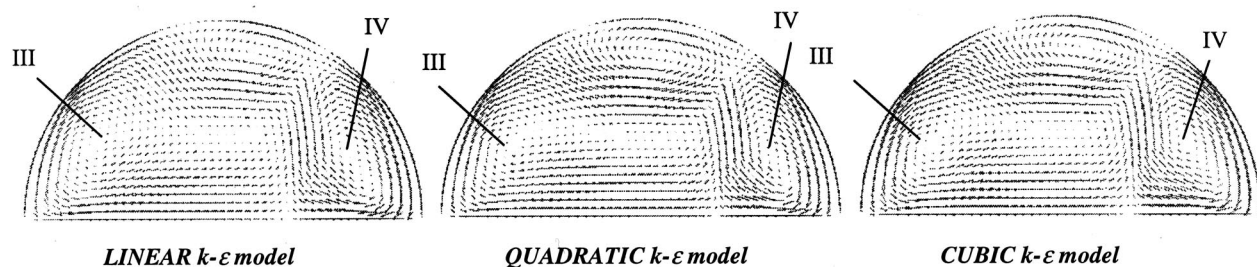


Fig. 16 Mean flow structure on a plane normal to cylinder axis and located 5 mm below cylinder head 10 c.a. deg BTDC— $RT=1.0$

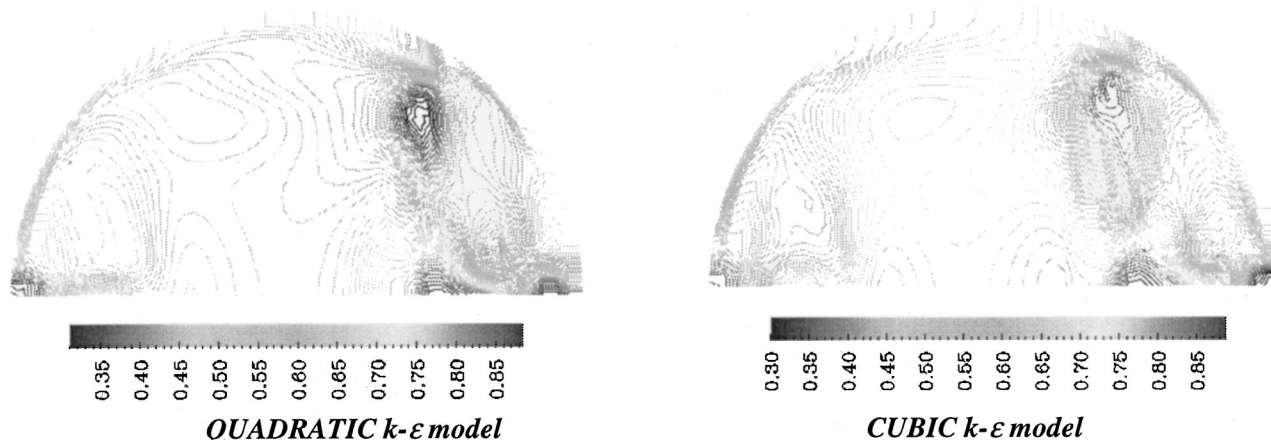


Fig. 17 Effect of constitutive nonlinear relationship on a_{11} —10 c.a. deg BTDC— $RT=1.0$

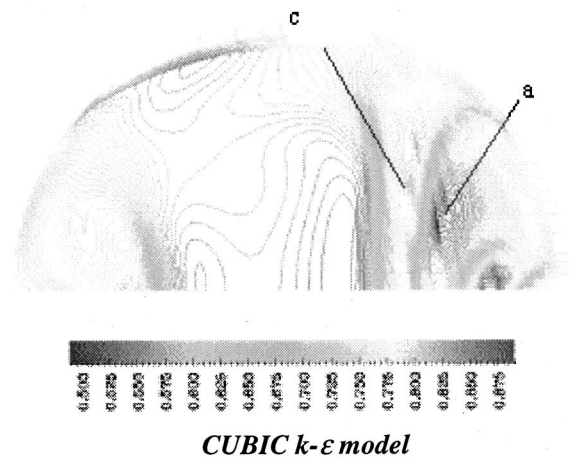
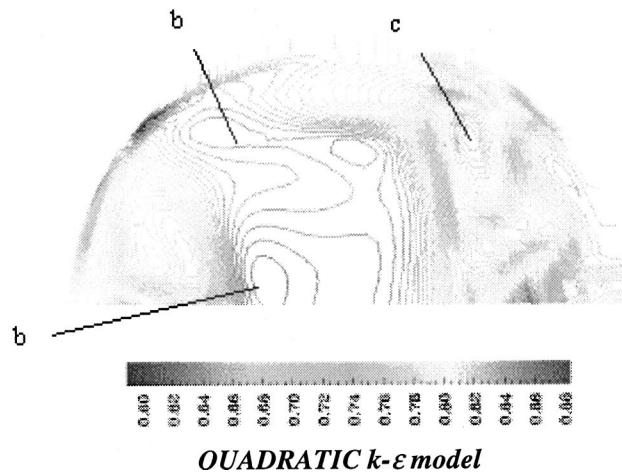


Fig. 18 Effect of constitutive nonlinear relationship on a_{33} —10 c.a. deg BTDC— $RT=1.0$

does. Moreover, a_{11} is about 10 percent lower for the quadratic model in the middle of the plane. It is interesting to note that both quadratic and cubic models give about the same maximum values of a_{11} . On the other hand, Fig. 18 shows that quadratic and cubic models determine different predictions of the distribution of the stress a_{33} on the plane considered. The cubic model locates the minimum of a_{33} in region (a), while the quadratic formulation predicts a minimum that is 10 percent higher and it is located in the wider region (b) on the opposite side with respect to region (a). Moreover, the cubic formulation predicts a maximum of a_{33} that is about 20 percent higher than that predicted by the quadratic model and it is located in about the same position. Differences can be also observed at the interfaces of the two vortices III and IV (region (c)), where the cubic formulation predicts a narrow and long island characterized by higher values of a_{33} . By contrast, the quadratic one locates region (c) in a smaller island toward the periphery of the chamber. This capability in capturing anisotropic effects could reveal important in spray modeling and in particular in droplet dispersion due to gas phase turbulence, as discussed by Bianchi [41].

At the end of the analysis it may be concluded that linear k - ε model can give only gross indications on turbulence features of ICE flows failing to capture curvature effects and anisotropy. On the other hand, nonlinear models may represent a significant step forward to accurate predictions of Reynolds stresses that play a critical role in spray dynamics, air-fuel mixing, and combustion processes. In particular, among the nonlinear models, the cubic formulations seems more tailored than quadratic one since it is able to capture simultaneously anisotropy and curvature effects. It must be remarked that all these conclusions are valid within the intrinsic limit of RANS approach applied to the typical transient nature of ICE flows.

Concluding Remarks

The present paper has discussed the application of *nonlinear* k - ε turbulence models for internal combustion engine flows. Motivations to nonlinear eddy viscosity models use arise from the consideration that such models combine the simplicity of linear eddy-viscosity models with the predictive properties of second moment closure.

Numerical results have been demonstrated that the nonlinear terms play a negligible influence in simple flows while they play a fundamental role in complex and rapidly distorted flows characterized by large strains.

The results in the *high-tumble* case, marked by larger values of the mean velocity gradient, seem to validate our hypothesis. In

particular the mean velocity field predicted by cubic k - ε model displays different whirling structures compared to the quadratic and linear k - ε model.

Despite the fact that encouraging results have been achieved, further validation still needs. Future work will be aimed to investigate the performance of nonlinear EVM models by applying cubic k - ε turbulence models in simulations of induction.

Nomenclature

- $\bar{\Omega}$ = mean rate of vorticity (vorticity invariant)
- Ω_{ij} = component of vorticity tensor
- γ_i = constants in quadratic nonlinear EVM
- ε = turbulent kinetic energy dissipation rate—rate transfer of energy from larger scales to smaller scales
- ε_T = rate transfer of energy from smaller scales into heat
- λ = Taylor length scale
- μ = molecular dynamic viscosity
- μ_t = turbulence dynamic viscosity
- ν = molecular kinematic viscosity
- ν_t = turbulence kinematic viscosity
- ρ = density
- τ = turbulence time scale $\tau=k/\varepsilon$
- ω = Enstrophy
- A = anisotropic invariant
- A_2 = anisotropic invariant
- A_3 = anisotropic invariant
- ATDC = after top dead center
- BTDC = before top dead center
- C_1 = k - ε turbulence model constant
- C_2 = k - ε turbulence model constant
- C_3 = k - ε turbulence model constant
- D = divergence
- Diff_ε = diffusion term in transport equation for ε
- Diff_k = diffusion term in transport equation for k
- HSDI = high speed direct injection
- IVC = inlet valve closing
- P = production term in transport equation for k measurement location in ENGINE A
- $\text{Pr}_\varepsilon - C1$ = production term by normal stresses in transport equation for k
- P_{nor} = production term by normal stresses in transport equation for k
- P_{shr} = production term by shear stresses in transport equation for k
- Re_T = turbulence Reynolds number
- RT = tumble ratio

\bar{S} = mean rate of strain or strain invariant
 S_{ij} = component of strain tensor
 T = temperature
 TDC = top dead center
 U = mean velocity
 U_p = mean piston speed
 a_{ij} = anisotropic stress component
 c_i = Cubic $k-\varepsilon$ turbulence model constant
 C_D = quadratic $k-\varepsilon$ turbulence model constant
 C_E = quadratic $k-\varepsilon$ turbulence model constant
 c_μ = $k-\varepsilon$ turbulence model constant
 k = turbulence kinetic energy
 u' = turbulence intensity
 x = Cartesian coordinate
 y = Cartesian coordinate
 z = Cartesian coordinate (axial direction)

Subscripts

i, j, k = Cartesian directions

Acknowledgments

MURST and CNR have supported this work.

Appendix

In-cylinder air motion is characterized by defining various non-dimensional parameters such as the swirl ratio and the tumble ratio. In the present paper tumble ratio RT is defined as the ratio of the integral of angular momentum about the y -axis, respectively, to solid body rotation of the entire cylinder charge mass at crank shaft speed about a center of rotation. The center of rotation is assumed to be the center of the mass. In the numerical implementation the integrals were replaced by the following.

Tumble Ratio RT

$$RT = \frac{\sum_{i=1}^{nverts} [(x_i - x_c) \cdot W_i - (z_i - z_c) \cdot U_i]}{\omega \cdot \sum_{i=1}^{nverts} \bar{m}_i \cdot s_{i,y}^2} \quad (A1)$$

where $nverts$ is the number of vertices in the mesh, ω is the crankshaft rotational speed; \bar{m}_i are the vertex masses; x_i , y_i , and z_i are the Cartesian coordinates of the generic node i , and x_c , y_c , and z_c are the Cartesian coordinates of the Center of the mass. U_i , V_i , and W_i are the mean velocity component of the generic node i along about x , y , and z -axes, respectively. Finally, $s_{i,x}^2$, $s_{i,y}^2$, and $s_{i,z}^2$ are defined as

$$s_{i,y}^2 = (x_i - x_c)^2 + (z_i - z_c)^2. \quad (A2)$$

References

- [1] Arcoumanis, C., Whitelaw, J. H., Hentschel, W., and Schindler, K.-P., 1994, "Flow and Combustion in a Transparent 1.9 Liter Direct Injection Diesel Engine," *Proc. Inst. Mech. Eng., Part D (J. Automob. Eng.)*, **208**, pp. 191–205.
- [2] Bo, T., Clerides, D., Gosman, A. D., and Theodossopoulos, P., 1997, "Prediction of the Flow and Spray Processes in an Automobile DI Diesel Engine," SAE Paper 970882.
- [3] Burgess, D. E., and O'Rourke, P. J., 1993, "Modeling Turbulence in Flows With a Strong Rotational Component," Los Alamos National Laboratory, Report No. LA-12552-MS.
- [4] Corcione, F. E., and Valentino, G., 1990, "Turbulence Length Scale Measurements by Two-Probe-Volume LDA Technique in a Diesel Engine," SAE Paper 902080.
- [5] El-Thary, S. H., and Haworth, D. C., 1992, "Directions in Turbulence Modeling for In-Cylinder Flows in Reciprocating Engines," *J. Propul. Power*, **8**, No. 5, pp. 1040–1048.
- [6] Gosman, A. D., and Watkins, P., 1977, "A Computer Prediction Method for Turbulent Flow and Heat Transfer in Piston/Cylinder Assemblies," *Proceedings of a Symposium on Turbulent Shear Flows*, Pennsylvania State University, pp. 5.23–5.30.
- [7] Celik, I., and Yavuz, I., 1997, "An Assessment of Turbulence Scales Relevant to IC Engines," ASME Paper No. 97-ICE-5.
- [8] Arcoumanis, C., Whitelaw, J. H., Vafidis, C., and Hu, Z., 1990, "Tumbling Motion: A Mechanism for Turbulence Enhancement Spark Ignition Engines," SAE Paper 900060.
- [9] Han, Z., Reitz, R. D., Corcione, F. E., and Valentino, G., 1996, "Interpretation of $k-\varepsilon$ Computed Turbulence Length-Scale Prediction for Engine Flows," *Proceed. 26th. Symposium on Combustion*, The Combustion Institute, Pittsburgh, PA, pp. 2717–2723.
- [10] Borgnakke, C., and Xiao, Y., 1991, "Compressible Turbulence Predicted by Reynolds Stress Models," SAE Paper 910260.
- [11] Burgess, D. E., and Amsden, A. A., 1993, "Modelling Turbulence in Flows With a Strong Rotational Component," Los Alamos National Laboratory, Report No. LA-12552-MS.
- [12] Tanner, F. X., and Reitz, R. D., 1999, "Scaling Aspects of the Characteristic Time Combustion Model in the Simulation of Diesel Engine," SAE Paper 1999-01-1175.
- [13] Morel, T., and Mansour, N. N., 1982, "Modeling of Turbulence in Internal Combustion Engines," SAE Paper 820040.
- [14] Amsden, A. A., O'Rourke, P. J., and Butler, T. D., 1989, "KIVA 2: A Computer Program for Chemically Reactive Flows With Sprays," Los Alamos National Labs, NTIS.
- [15] El-Tahry, S. H., 1983, "k- ε Equation for Compressible Reciprocating Flows," *J. Energy*, **7**, No. 4.
- [16] Computational Dynamics Limited, 1998, "STAR-CD User Manual," *CD—Computational Dynamics Limited/Analysis and Design*, London.
- [17] Wilcox, D. C., and Rubesin, M. W., 1980, "Progress in Turbulence Modeling for Complex Flow Fields Including Effects of Compressibility," NASA Technical Paper 1517.
- [18] Bradshaw, P. B., Launder, E., and Lumley, J., 1991, "Collaborative Testing of Turbulence Models," *ASME J. Fluids Eng.*, **113**, pp. 3–4.
- [19] Leschziner, M. A., 1997, "Turbulence Modelling for Complex Flows—Necessary and Avoidable Compromises," *Proceedings 7th Symposium on CFD*, Beijing.
- [20] Ramos, J. I., 1989, *Internal Combustion Engine Fundamentals*, Hemisphere, Washington, DC.
- [21] Bray, K. N. C., et al., 1981, "Turbulence Production in Premixed Turbulent Films," *Combust. Sci. Technol.*, **25**, pp. 127–140.
- [22] Moriyooshi, Y., Kobayashi, H., and Kamamoto, T., 1989, "Experimental Evaluation of the Turbulence Model in Numerical Simulation of In-Cylinder Air Motion," *JSAE Rev.*, **10**, No. 2.
- [23] Coleman, G. N., and Mansour, N. N., 1991, "Modeling the Rapid Spherical Compression of Isotropic Turbulence," *Phys. Fluids*, **3**, No. 9, pp. 2255–2259.
- [24] Hanjalic, K., and Launder, B. E., 1980, "Sensitizing the Dissipation Equation to Irrotational Strains," *ASME J. Fluids Eng.*, **102**, pp. 34–40.
- [25] Speziale, C. G., 1987, "On Non-Linear $k-l$ and $k-\varepsilon$ Models of Turbulence," *J. Fluid Mech.*, **178**, pp. 459–475.
- [26] Craft, T. J., Launder, B. E., and Suga, K., 1996, "Development and Application of a Cubic Eddy-Viscosity Model of Turbulence," *Int. J. Heat Fluid Flow*, **17**, pp. 108–115.
- [27] Launder, B. E., and Spalding, D. B., 1972, *Mathematical Models of Turbulence*, Academic Press, San Diego, CA.
- [28] Leschziner, M. A., 1998, "Advances in Modeling Physically Complex Flows With Anisotropy-Resolving Closure and Related Validation," *Proceedings of ASME Fluids Engineering Division Summer Meeting*, Washington, DC, ASME, New York.
- [29] Rodi, W., 1987, "Turbulence Model for Practical Applications," von Karman Institute for Fluid Dynamics, Lecture Series 1987-06.
- [30] Reynolds, W. C., 1980, "Modeling of Fluid Motions in Engines: An Introductory Overview," *Symposium on Combustion Modeling in Reciprocating Engines*, Plenum Press, New York, pp. 131–155.
- [31] Durbin, P. A., and Speziale, C. G., 1991, "Local Anisotropy in Strained Turbulence at High Reynolds Numbers," *ASME J. Fluids Eng.*, **113**, pp. 707–709.
- [32] Pope, S. B., 1975, "A More General Effective-Viscosity Hypothesis," *J. Fluid Mech.*, **72**, Part 2, pp. 331–340.
- [33] Shi, T. H., and Zhu, J., 1995, "Calculations of Diffuser Flows With an Anisotropic $k-\varepsilon$ model," NASA ICOMP-95-21.
- [34] Lien W., Chen, W. L., and Leschziner, M. A., 1996, *Engineering Turbulence Modelling and Measurements—3*, **91**, Elsevier, New York.
- [35] Craft, T. J., Launder, B. E., and Suga, K., 1993, "Extending the Applicability of Eddy-Viscosity Model Through the Use of Deformation Invariant and Non-linear Elements," *Proc. 5th Symposium Refined Flow Modelling and Turbulence Measurements*, p. 125.
- [36] Apsley, A. D., and Leschziner, M. A., 1997, "A New Low-Re Non-linear Two-Equation Turbulence Model for Complex Flows," *Proceedings 11th Symposium on Turbulent Shear Flows*, Grenoble.
- [37] Gatski, T. B., and Speziale, C. G., 1993, "On Explicit Algebraic Stress Models for Complex Turbulent Flows," *J. Fluid Mech.*, **254**, pp. 59–78.
- [38] Sarkar, S., and Speziale, C. G., 1997, "Nonlinear and Anisotropic Turbulence Models," von Karman Institute for Fluid Dynamics, Lecture Series 1997-03.
- [39] Amsden, A. A., O'Rourke, P. J., and Butler, T. D., 1993, "KIVA-3: A KIVA Program With Block-Structured Mesh for Complex Geometries," Los Alamos National Labs, Report No. LA-12503-MS.
- [40] Vafidis, C., 1986, "Aerodynamics of Reciprocating Engines," Ph.D. thesis, Imperial College of Science & Technology, Thermo-Fluids Section, London.
- [41] Bianchi, G. M., 1999, "Diesel-Spray Break-Up in Turbulent Flows," Ph.D. thesis, University of Bologna, - Polytechnic of Bari, Bari, Italy.

Development of the Tracer Gas Method for Large Bore Natural Gas Engines—Part I: Method Validation

D. B. Olsen
G. C. Hutcherson¹
B. D. Willson
C. E. Mitchell

Engines and Energy Conversion Laboratory,
Department of Mechanical Engineering,
Colorado State University,
Fort Collins, CO 80523

The tracer gas method is investigated as a means to study scavenging in fuel-injected large-bore two-stroke cycle engines. The investigation is performed on a Cooper-Bessemer GMV-4TF natural gas engine, with a 36-cm bore and a 36-cm stroke. Two important parameters are evaluated from the tracer gas measurements, which are scavenging efficiency and trapped A/F ratio. Measurements with the tracer gas method are compared with in-cylinder sampling techniques to evaluate the accuracy of the method. Two different tracers are evaluated, monomethylamine and nitrous oxide. Monomethylamine is investigated because of its common use historically as a tracer gas. Nitrous oxide is a new tracer gas that overcomes many of the difficulties experienced with monomethylamine. The tracer gas method with nitrous oxide is determined to be accurate for evaluating scavenging efficiency and trapped A/F ratio in comparison to the in-cylinder sampling techniques implemented. [DOI: 10.1115/1.1454116]

Introduction

The tracer gas method (TGM) provides a means to directly measure trapping efficiency. Trapping efficiency is key to accurate evaluations of scavenging efficiency and trapped air/fuel (A/F) ratio in fuel-injected two-stroke cycle engines. The trapped A/F ratio is the parameter that perhaps has the greatest influence on emissions. It is the ratio of the mass of air to the mass of fuel in the engine cylinder when the intake valves or ports close. This is the air and fuel mixture that is actually burned in the cylinder. The overall A/F ratio, which may be significantly different, is the A/F ratio that reflects the total supply of air and fuel to the engine. The trapped A/F ratio is commonly expressed as the trapped equivalence ratio, or simply equivalence ratio, and is defined as

$$\phi = \frac{(A/F)_{stoic}}{(A/F)_{tr}} \quad (1)$$

where

$(A/F)_{tr}$ = mass-based air/fuel ratio trapped in the engine cylinder

$(A/F)_{stoic}$ = stoichiometric mass-based air/fuel ratio.

Expressing the A/F ratio as equivalence ratio provides a means to compare performance and emissions from engines that run on different fuels. The strong influence that trapped equivalence ratio has on the criteria emissions, total CO, THC (total hydrocarbon), and NO_x is well established. Thus, the characterization of trapped A/F ratio is vital in studying emissions from IC engines.

The scavenging efficiency provides an indicator of how effective the scavenging system is at removing combustion products and filling the cylinder with fresh charge. It is defined as

$$\eta_{sc} = \frac{m_{ret}}{m_{tr}} \quad (2)$$

where

m_{tr} = trapped mass in the cylinder, including residual combustion products from the previous cycle

m_{ret} = mass of delivered air or air/fuel mixture trapped per cycle.

The scavenging efficiency is an important quantity because it is directly proportional to indicated power per cylinder for two-stroke cycle engines, which can be written as

$$P = \eta_f \eta_{sc} N V_{pc} Q_{HV} \rho_{a,i} (F/A)_{tr} \quad (3)$$

where

η_f = fuel conversion efficiency

N = crankshaft rotational speed in revolutions per second

V_{pc} = total cylinder volume at port closure

Q_{HV} = fuel heating value

$\rho_{a,i}$ = inlet air density.

The TGM investigated is an experimental technique that directly measures trapping efficiency. The trapping efficiency denotes the fraction of gas flowing through an engine that can be utilized in the combustion process, defined as

$$\eta_{tr} = \frac{m_{ret}}{m_{del}} \quad (4)$$

where

m_{del} = total mass of delivered air or air/fuel mixture per cycle.

The fraction of the charge that cannot be utilized in the combustion process is referred to as the short-circuited fraction, which is simply

$$f_{sc} = 1 - \eta_{tr} \quad (5)$$

The short-circuiting process generally occurs during scavenging and is often called scavenged short-circuiting. A simple representation of this process is shown in Fig. 1. Another important parameter is the delivery, or scavenging, ratio which is defined as

$$\Lambda = \frac{m_{del}}{m_{ref}} \quad (6)$$

where m_{ref} is a reference mass. Typically, the trapped cylinder mass is used as the reference mass. Defining the reference mass in this way, the scavenging efficiency can be expressed as

¹Presently at Enginuity, Inc.

Contributed by the Internal Combustion Engine Division of THE AMERICAN SOCIETY OF MECHANICAL ENGINEERS for publication in the ASME JOURNAL OF ENGINEERING FOR GAS TURBINES AND POWER. Manuscript received by ICE Division, July 2000; final revision received by the ASME Headquarters August 2000. Editor: D. N. Assanis.

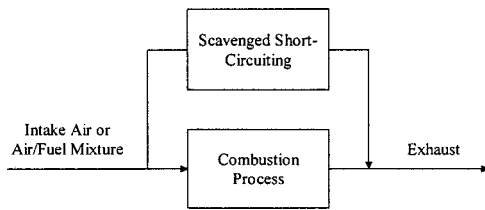


Fig. 1 Short-circuiting process

$$\eta_{sc} = \Lambda \eta_{tr} \quad (7)$$

Thus, the scavenging efficiency can be evaluated upon measuring the necessary parameters to calculate the delivery ratio and measuring the trapping efficiency with the TGM. The trapped A/F ratio is also calculated from the trapping efficiency with the equation

$$(A/F)_{tr} = (A/F)_{ov} \eta_{tr} \quad (8)$$

where

$(A/F)_{ov}$ = mass-based overall air/fuel ratio.

Historically, trapping efficiency has been a difficult parameter to measure. This is because trapping efficiency varies with the level of in-cylinder mixing, gas velocities, exhaust tuning, and other physical phenomena that are difficult to predict. Numerous techniques involving in-cylinder sampling have been successfully implemented to measure trapping efficiency ([1]). Although these techniques have proven to be reliable given that a significant portion of the cylinder contents is removed, or represented with each sample, it generally requires major engine modification and a laboratory environment. In-cylinder sampling can be intrusive to the combustion process and is costly to carry out. The engine cylinder typically must be physically modified to accommodate a sample valve. The biggest advantage of the TGM is that it does not require major engine modification to execute. Additionally, it is adaptable to field applications. The experimental setup is external to the engine, eliminating the need for major engine modification.

In the TGM a small amount of tracer is continuously fed into and mixed with the intake air or fuel/air mixture. The tracer that is trapped in the cylinder is destroyed during combustion and the short-circuited portion survives in the exhaust. Ideally, the tracer is completely destroyed at combustion temperatures and stable at exhaust temperatures. The short-circuited fraction and trapping efficiency are quantified by comparing tracer mole fraction in the intake to that in the exhaust.

This paper is Part I, "Method Evaluation," of a two-part series on the TGM. The focus of Part I is to address the issue of whether the method is accurate and practical for large-bore two-stroke cycle engines. It also, however, provides a recipe for implementation. Part II, "Measurement of Scavenging Characteristics," is an application of the TGM to the Cooper-Bessemer GMV-4TF large-bore natural gas engine.

Tracer Gas Selection

Selecting the appropriate tracer gas for a particular application is critical to obtaining accurate results. Schweitzer and DeLuca [2] originally developed the TGM in 1942 for measuring the trapping efficiency of large diesel engines. Although the TGM has been available for over half a century, the use of the technique does not appear to be common. Only six references were found where trapping efficiency measurements with the TGM were performed ([3–7]). This is probably due to difficulties experienced with the technique. Among these difficulties were the requirement of a wet chemistry method to detect monomethylamine (CH_3NH_2), which has been the tracer predominantly used, and monomethylamine consumption in the exhaust system. In hindsight, the use of

monomethylamine may not have been optimal. Other tracers that have been used are butane, carbon monoxide, and oxygen. These tracers are reactive at typical exhaust temperatures as well. Additionally, they are all typically found in significant quantities in combustion products, which presents the problem of separating the combustion product and the short-circuited fraction contributions to the tracer measured in the exhaust. A new tracer gas, nitrous oxide, has been introduced at the Engines and Energy Conversion Laboratory at Colorado State University for use in the TGM. Nitrous oxide overcomes many of the short-comings of previously used tracers.

The characteristics of an *ideal tracer gas*, adapted from Schweitzer and DeLuca, are

- 1 easy and safe to handle,
- 2 readily detectable by common gas analyzers,
- 3 completely destroyed when exposed to combustion temperatures in the cylinder,
- 4 stable in the intake, exhaust, and sample systems, and
- 5 not present in significant quantities in the combustion products.

Monomethylamine. Monomethylamine occurs in herring brine, in urine of dogs after eating meat, in certain plants such as *Mentha aquatica*, and in crude methanol together with di- and trimethylamine ([8]). It is a flammable gas at standard temperature and pressure. Monomethylamine is irritating to the eyes, skin, and respiratory tract. It has an odor similar to ammonia. Monomethylamine is sold in liquefied form as a 33 percent aqueous solution; it is a good solvent for many organic substances. Monomethylamine has recently become more difficult to obtain. It is now regulated by the U.S. Government as a controlled substance because of its use in the illegal manufacturing of amphetamines.

The monomethylamine reaction rate has a strong dependence on temperature. This makes it possible for the third and fourth characteristics given above to be satisfied. Monomethylamine is measurable by Fourier transform infra-red (FTIR) analyzers. The vapor pressure is low enough so that it can be conveniently stored as a liquid at room temperature, but high enough to be used for direct injection into the intake air stream. It is not a normal constituent in the exhaust or intake gas for engines running on common fuels (i.e., gasoline, natural gas, propane, diesel, etc.).

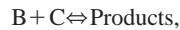
Nitrous Oxide. Nitrous oxide is a constituent of the earth's atmosphere, about 0.00005 percent by volume ([8]). It is a colorless gas with a slightly sweetish odor. It is very stable and rather inert chemically at room temperatures. Nitrous oxide is sold as a compressed liquid with a vapor pressure of about 5600 kPa at room temperature. It is used to oxidize organic compounds at temperatures above 570 K, to make nitrites from alkali metals at their boiling points, in rocket fuel formulations, and in preparing of whipped cream. Nitrous oxide is a narcotic in high concentrations. It is less irritating to the skin than other oxides of nitrogen.

Nitrous oxide is well known for its power enhancement in high-performance racing engines. It is safe to handle, stable at room temperature, and, because of its regular use for high-performance applications, is readily available. The role of nitrous oxide in power enhancement has generally been attributed to its oxygen content, which is 50 percent higher than air by weight, and its low inlet temperature caused by high throttling pressure drops. In fact, the limited literature available on nitrous oxide behavior shows that its decomposition is exothermic at high temperature, thereby providing a power-enhancement mechanism in addition to the increased oxygen concentration. Less than 5 ppm of nitrous oxide is found in most product gases from combustion systems. Fluidized bed coal combustors are the exception, yielding nitrous oxide levels of around 50 ppm ([9]). The higher nitrous oxide level is due to lower combustion temperatures and fuel-bound nitrogen.

Nitrous oxide is easy and safe to handle and detectable with an FTIR spectrometer. The infra-red absorption spectrum of nitrous oxide is fairly isolated and does not interfere with other exhaust

constituents. Conversely, monomethylamine absorbs infra-red radiation at many of the same wavelengths as water does. The end result is that the mole fraction of monomethylamine in exhaust can be measured with an FTIR spectrometer, but not as accurately as nitrous oxide. Neither monomethylamine nor nitrous oxide is present in significant quantities in the exhaust of the GMV-4TF engine. Under typical operating conditions, trace amounts of nitrous oxide (0.5–3 ppm) are measured in the exhaust of the GMV-4TF, but not enough to affect the TGM measurement.

Tracer Gas Global Chemical Kinetics. The most prevalent difficulty with previously used tracers is the reaction of the tracer in the exhaust system between the exhaust ports, or valves, and the sample tap. Clearly, a tracer more stable at exhaust temperatures is needed. One way to compare the stability of different tracers is through the use of an Arrhenius plot. The plot compares the natural log of the global rate constant for one or more reactions through a temperature range of interest. For a bimolecular reaction of



the consumption of B can be represented by the rate expression

$$\frac{d[B]}{dt} = k[B][C], \quad (9)$$

where the brackets represent concentration in moles per unit volume and t is time. The order with respect to each of the reactants is assumed to be unity. The rate constant, k , is defined by the Arrhenius equation

$$k = AT^n e^{-E_a/RT} \quad (10)$$

where T is temperature, E_a is the activation energy, A is the frequency factor, n is the temperature coefficient, and R is the universal gas constant. Figure 2 shows a comparison of the natural log of k versus inverse temperature for three different tracers. The sources for the activation energy and frequency factor are given on the plot ([10–13]). The order of reaction with respect to the reactants is assumed to be unity for all cases, as shown in Eq. (9). The temperature coefficient, n , is assumed to be zero. The plot does not take into account variations in concentrations; however, this effect is generally small compared to the influence of temperature. The desired behavior is to have a steep, temperature-sensitive curve, sloping downward to the right, and positioned so

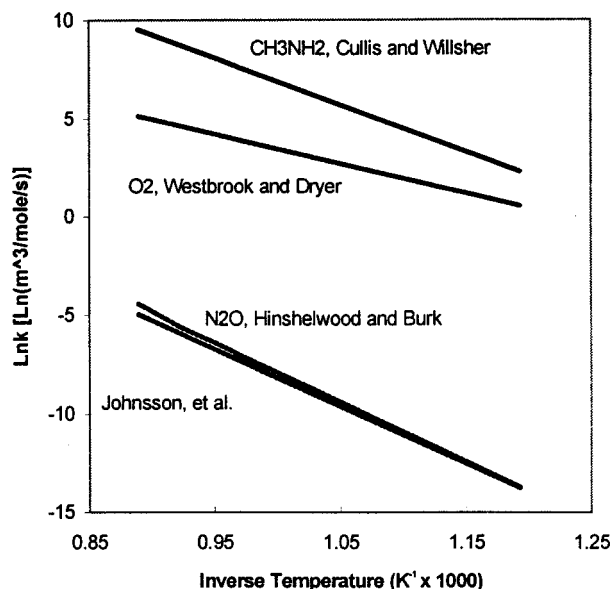


Fig. 2 Arrhenius plot comparison of tracer gases

that the tracer is reactive at combustion temperatures and stable at exhaust temperatures. Nitrous oxide and monomethylamine both have relatively steep curves, whereas the oxygen curve is more gradual. Oxygen, sometimes used as a tracer in four-stroke engines that burn a stoichiometric or rich A/F ratio, is included for comparison.

The purpose of this plot is qualitative rather than quantitative. Simplified mechanisms are, in general, not very accurate unless the concentration, temperature, and pressure ranges are the same as those for the original data. However, it is evident from the plot that nitrous oxide has a significantly smaller rate constant in the temperature range shown on the plot (800 to 1100 K). Thus, it is likely that nitrous oxide will be more stable in the exhaust system than monomethylamine.

Tracer Gas Analysis

In this work three quantifiable, potential nonideal tracer effects are identified in the TGM, which are incomplete reaction in the cylinder during combustion, tracer destruction in the exhaust, and the effects of engine misfire. Engine misfire for convenience is included in the nonideal tracer effects because during a misfire the tracer generally does not react in the cylinder. However, this is actually indicative of unstable combustion rather than a negative characteristic of the tracer. Three parameters are defined to account for these effects, which are

Cylinder reaction efficiency:

$$\eta_{cr} = [\text{mass of tracer reacted}] / [\text{mass of tracer retained in cylinder}]$$

Exhaust reaction:

$$\varepsilon_r = [\text{mass of tracer reacted in exhaust}] / [\text{mass of tracer entering exhaust}]$$

Misfire fraction:

$$f_{mf} = [\text{number of misfires}] / [\text{total number of cycles sampled}].$$

If these effects are insignificant, then analyzing the tracer gas data is simplified considerably. This assumption is termed the “ideal tracer assumption.” When this assumption is made, a simple relationship can be developed to calculate trapping efficiency in terms of measured quantities. The derivation is performed in another publication ([14]). The resulting equation is

$$\eta_{tr} = 1 - \frac{X_{t,e} \{1 + (F/A)_{ov}\}}{X_{t,i} SG_e} \quad (11)$$

where

$$\begin{aligned} X_{t,e} &= \text{mole fraction of tracer in exhaust,} \\ X_{t,i} &= \text{mole fraction of tracer in intake air,} \\ (F/A)_{ov} &= \text{mass based overall fuel air ratio, and} \\ SG_e &= \text{specific gravity of exhaust} = MW_e / MW_a. \end{aligned}$$

If the non-ideal tracer effects are significant, then they should be evaluated and used as corrections in calculating trapping efficiency from measured tracer gas data. An equation for trapping efficiency that includes the non-ideal tracer effects is derived in previous work ([14]) which is

$$\eta_{tr} = 1 - \frac{\{1 + (F/A)_{ov}\} X_{t,e}}{(1 - \varepsilon_r)(\eta_{cr} - f_{mf}) SG_e X_{t,i}} + \frac{1 - \eta_{cr} + f_{mf}}{\eta_{cr} - f_{mf}}. \quad (12)$$

Equations and discussion on evaluating the nonideal tracer effects are also discussed in a prior publication ([14]).

Test Apparatus

A test schematic of the tracer gas injection system including the main components is shown in Fig. 3. The tracer gas injection

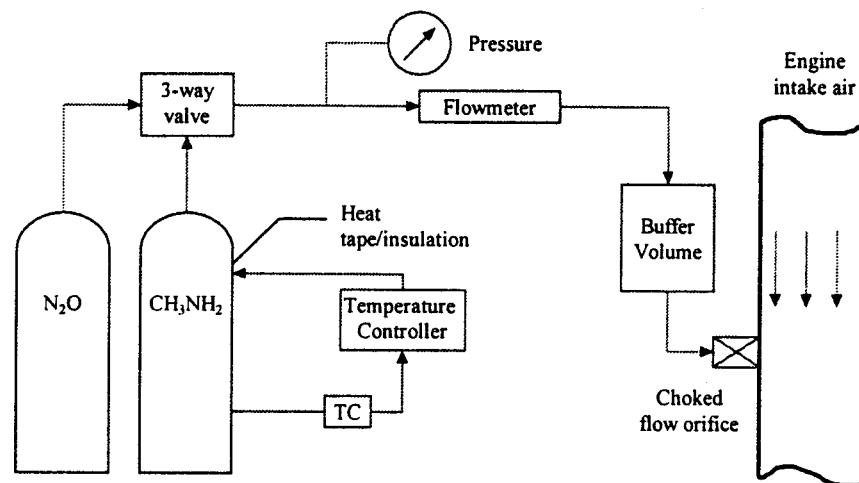


Fig. 3 Test schematic for two-stroke cycle engine testing

system accommodates both tracers, monomethylamine and nitrous oxide. Both tracers are purchased in liquid form and the liquid vapor pressure is utilized as the source pressure for injection. Monomethylamine has a vapor pressure of about 400 kPa at room temperature and nitrous oxide has a vapor pressure of about 6000 kPa at room temperature. The monomethylamine bottle is wrapped with heat tape and insulation and instrumented with a thermocouple and a temperature controller. This provides the ability to increase the monomethylamine source pressure by increasing the temperature of the bottle. The nitrous oxide vapor pressure at room temperature is high enough so that temperature control is not necessary. The test setup includes a three-way ball valve to switch between tracers. The tracer regulators (not shown) and injection lines are heated to prevent tracer condensation due to throttling temperature drops through the regulators or other restrictions. The tracer injection pressure is controlled with a precision regulator to minimize inlet tracer mole fraction fluctuations. Both gases can be corrosive, and liquid condensation accelerates the corrosion process. The tracer injection pressure and flowrate are measured, primarily to make it easier to duplicate data points. The tracer intake mole fraction is recorded with an FTIR spectrometer. A buffer volume is installed near the tracer injection orifice to attenuate any pressure fluctuations in the system.

The tracer enters the intake air stream via a choked flow orifice. It is important that the flow is choked, because in that case the mass flow rate depends only on upstream stagnation pressure and temperature. This eliminates the impact of pressure fluctuations in the intake air pipe. The tracer injection orifice is sized so that the jet centerline velocity is reduced to a value approximately equal to the average intake air velocity before it reaches the opposite side of the intake air pipe. This analysis is performed using axisymmetric turbulent jet equations developed in Turns [15]. For the 20 cm I.D. intake air pipe, this results in an orifice diameter of about 1.6 mm. The tracer injection orifice is located 10 to 12 meters upstream of the intake manifold. A characteristic mixing time is evaluated to ensure that the distance between the location of the tracer injection orifice and the intake manifold is sufficient for uniform mixing to occur. This analysis follows the work of Abraham et al. [16] Based on the characteristic mixing time and the average air velocity in the pipe, the tracer is well mixed in less than 1 m of pipe length. Thus, the length of pipe allotted for the tracer to mix with the intake air is more than adequate. The intake air tracer mole fraction is measured approximately 2 m upstream of the intake manifold. The tracer exhaust mole fraction is nominally measured from the stack, about 6 m downstream of the exhaust manifold.

Evaluation of Nonideal Tracer Effects

Combustion Misfire. Combustion misfires were detected with in-cylinder pressure measurements and accounted for in all the tracer gas calculations, where applicable. To account for combustion misfire all the tracer in the cylinder during a misfire was assumed to survive and be emitted to the exhaust system. The validity of this assumption was addressed numerically in other work ([14]). Chemical kinetic modeling was carried out of the reaction of monomethylamine and nitrous oxide during a complete misfire in the cylinder of the GMV-4TF at nominal operating conditions, which were 300 rpm and a brake power of 330 kW (440 hp). The result was both tracers were stable during a complete misfire.

Tracer Exhaust Reaction. Exhaust sampling was carried out at various locations along the exhaust pipe downstream of the exhaust manifold. The residence time in the exhaust manifold for the GMV-4TF is relatively large. The exhaust gas spends about half the time in the manifold and half in the pipe. As a result the exhaust constituents are well mixed and the gas temperature is significantly lower than cylinder exit temperature before they get to the first sample tap location. Therefore, any tracer exhaust reaction that takes place is expected to occur primarily in the manifold. The distance between the exhaust manifold and the stack is approximately 5.2 meters. Tracer mole fraction measurements were taken along the exhaust pipe under nominal engine operating conditions. The results are shown in Fig. 4. Short-circuited fraction values, calculated from Eqs. (5) and (12) assuming $\varepsilon_r = 0$ and $\eta_{cr} = 1$, are presented instead of raw mole fraction measurements. The short-circuited fraction is proportional to the tracer mole fraction in the exhaust pipe, yet the calculation accounts for variations in misfire fraction and intake tracer mole fraction variations between data points. Temperatures at each sample tap are not presented. Typical stack temperatures (the sample tap furthest from the exhaust manifold) are around 600 K.

The data shows a large difference between the average short-circuited fractions measured with N_2O and with CH_3NH_2 . This discrepancy will be discussed later in detail. If there is no tracer reaction in the exhaust the data should form horizontal straight lines. Nitrous oxide appears to be very stable in the exhaust pipe, forming a fairly straight, horizontal line. Monomethylamine short-circuited fractions show a gradual decreasing trend as the distance down the exhaust pipe increases. The data indicates that approximately 6 percent of the monomethylamine is destroyed in this section of the exhaust system.

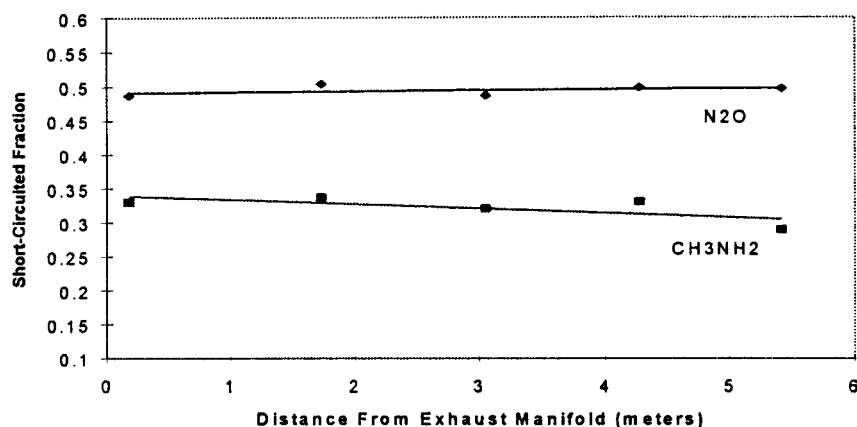


Fig. 4 Tracer short-circuited fraction in exhaust system

This test data provides information on the exhaust stability of N_2O and CH_3NH_2 in the portion of the exhaust system downstream of the exhaust manifold. For CH_3NH_2 it suggests that the reaction in the exhaust manifold is probably substantial, because gas temperatures in the exhaust manifold are significantly higher than those downstream in the exhaust pipe and the residence time in the exhaust manifold is large. Since there is some indication of CH_3NH_2 exhaust reaction downstream of the manifold, it is likely that significant destruction takes place in the exhaust manifold. The apparent large monomethylamine exhaust reaction could explain most of the difference between the nitrous oxide and monomethylamine average short-circuited fractions. However, there is no way to draw any definitive conclusions about the stability of the tracers in the exhaust manifold based on this data alone. Since the exhaust manifold is not equipped with sample taps, the exhaust reaction for the entire exhaust system cannot be determined from direct exhaust sampling. Instead, the exhaust reaction is calculated based on direct measurements of cylinder reaction efficiency and trapped A/F ratio through the use of in-cylinder and exhaust port sampling.

Cylinder Reaction Efficiency. The calculation of cylinder reaction efficiency from in-cylinder sampling valve and/or port checkvalve data is discussed in an earlier publication ([14]). The in-cylinder sampling valve is mounted in the air-start port in the cylinder head of cylinder #2 in the GMV-4TF. Cylinders 2 and 4 are located on the same side (referred to as the 2–4 bank) of the engine. The exhaust sample tap is located on the 2–4 bank side of the exhaust elbow just downstream of the exhaust manifold. The exhausts from the two sides of the engine remain separate until they pass through the exhaust elbow. The piston motions are slightly different between the 1–3 and 2–4 banks, primarily because of the articulated geometry in the crankshaft kinematics. The end result is that the exhaust and intake ports for cylinders 1 and 3 are open 3.9 and 4.4 percent longer, respectively, than cylinders 2 and 4. This causes a significant difference in the scavenging between the two sides, and consequently the 2–4 bank A/F mixture, both trapped and overall. The 2–4 bank mixture is richer

than for the 1–3 bank. Thus, the in-cylinder sampling results must be correlated to the exhaust measurements from the same side of the engine.

In-cylinder sampling was performed using two different valves, a large electro-hydraulically actuated sample valve located in the air-start port in the cylinder head and a checkvalve located in the center exhaust port. Both valves were mounted on cylinder #2. The large sample valve was actuated either during compression or expansion. Compression samples were extracted using an opening crank angle of 83 deg BTDC and a duration of 80 deg. This resulted in 40–55 percent of the cylinder mass being removed during each compression sample. Expansion samples were removed utilizing an opening crank angle of 30 deg ATDC with a duration of 60 deg. This resulted in 10–20 percent of the cylinder mass being removed during expansion. The checkvalve in the center exhaust port was designed to sample the blowdown pulse. A more complete description of the in-cylinder sampling techniques is provided in other publications ([14,17]).

Cylinder reaction efficiency evaluations based on in-cylinder sampling are presented in Table 1 for two different boost levels. Cylinder reaction efficiency evaluations for monomethylamine are not given. It was presumed that monomethylamine reaction in the exhaust manifold would make it difficult to achieve repeatable trapping efficiency measurements. Thus, adequate testing time was not allotted for this evaluation. The exhaust reaction of monomethylamine is discussed more in the following section. The average cylinder reaction efficiency for nitrous oxide is about 0.96. This is very good considering that it appears to be stable in the exhaust system. The exhaust port checkvalve was also used to sample combustion products when tracer was flowing through the engine. No nitrous oxide was detected through the exhaust port checkvalve at any of the boost levels tested. This result can be interpreted two ways. Either the exhaust port checkvalve samples a region where tracer is completely consumed, or the tracer detected with the in-cylinder sample valve during expansion is con-

Table 1 Evaluation of cylinder reaction efficiency through in-cylinder sampling at nominal speed and load

TRACER	EXH. MAN. PRESSURE, kPag	COMPRESSION SAMPLE, ppm	EXPANSION SAMPLE, ppm	CYLINDER REACTION EFFICIENCY, η_{cr}
N_2O	4.99	762	34.1	0.956
N_2O	10.5	756	20.5	0.973

sumed during the latter part of the expansion stroke. In light of this, the average nitrous oxide cylinder reaction efficiency of 0.96 should be considered a conservative value.

Comparison of Tracer Gas Method with In-Cylinder Sampling

In-cylinder sampling during compression and expansion and exhaust blowdown sampling with the checkvalve allowed the evaluation of the trapped equivalence ratio by several different techniques. One of the techniques has not been discussed, which involves the analysis of a tracer seeded in-cylinder compression sample to evaluate the scavenging efficiency. The calculation of scavenging efficiency is adapted from the technique of Kannappan [18] to include an adjustment for incomplete tracer destruction in the cylinder. The resulting equation is

$$\eta_{sc} = \frac{X_{t,tr} \eta_{cr}}{X_{t,a} SG_{tr} - X_{t,tr}(1 - \eta_{cr})} \quad (13)$$

where

- $X_{t,tr}$ = mole fraction of tracer trapped in cylinder before fuel addition,
- $X_{t,a}$ = mole fraction of tracer in intake air, and
- SG_{tr} = specific gravity of the tracer.

Any fuel present in the sample is mathematically removed before applying Eq. (13). This removes the effects of incomplete fuel and air mixing, and only requires that the air delivered be well mixed with the residual cylinder gases at the time the sample is taken. The scavenging efficiency is multiplied by the trapped mass to get the mass of air delivered. The mass of fuel delivered to each cylinder per cycle is evaluated from an orifice flowmeter fuel flow measurement. It is assumed that the fuel delivered to each cylinder is the same, which is a good assumption based on the inspection of the input voltage profiles to the fuel injector drivers. The air delivered is then divided by the fuel delivered to calculate the trapped A/F ratio.

The possibility of deriving an in-cylinder A/F ratio from the concentration of fuel in the cylinder was considered. To get a relatively large sample the valve had to be open for most of the compression stroke duration. Although the sample valve did not open until after the fuel injection event was finished, analysis of the samples revealed that the A/F ratio calculated in this manner

was extremely lean, below the flammability limit. This indicated that the fuel was not well mixed with the air when the sample was extracted.

Trapped Equivalence Ratio Comparison. Figure 5 presents trapped equivalence ratio and delivery ratio vs. exhaust manifold pressure for the various techniques that have been discussed. Calculation of trapped A/F ratio based on the perfect mixing model is included for comparison. The perfect mixing model appears in many textbooks on two-stroke cycle engines, including Heywood [19]. Scavenging efficiency values are not presented because they are calculated using nearly the same measured quantities. General conclusions on the relative accuracy of the various techniques do not change when comparing scavenging efficiency. The trapped equivalence ratios from the exhaust port check valve and large sample valve expansion samples are arrived at through standard exhaust gas analysis of constituent mole fractions measured with the FTIR spectrometer. The data show that as the exhaust manifold pressure increases the charge gets progressively leaner, with a slight leveling trend at the larger pressures. Note that the curve fit to the nitrous oxide tracer gas method (TGM) data passes through each group of data points with some occurring above and some below. The location of data from a particular technique with respect to the nitrous oxide TGM curve is fairly consistent. For example, all of the equivalence ratios from exhaust analysis of in-cylinder samples taken during expansion appear below the nitrous oxide TGM curve, at significantly leaner equivalence ratios. This could be explained by stratification of the fuel in the cylinder. The in-cylinder samples during expansion extracted only 10 to 20 percent of the cylinder mass per cycle. If a region richer than the bulk charge exists near the bottom of the cylinder and a leaner region is present near the top, the sample extracted by the valve will be leaner than the bulk charge.

The exhaust port checkvalve and the nitrous oxide TGM data are very close to each other for nearly all of the boost levels. The exhaust port checkvalve extracts a relatively small sample each cycle because it has a smaller flow area. However, with regard to mixing of trapped cylinder gases, the location of the exhaust port checkvalve is optimal. When the exhaust ports open the trapped cylinder gases are as uniform as they will ever get before being mixed with scavenging air from the previous cycle, which occurs just downstream of the exhaust ports. Thus, the increased level of mixing in the port checkvalve samples may help compensate for smaller sample sizes. Additionally, the exhaust port checkvalve is

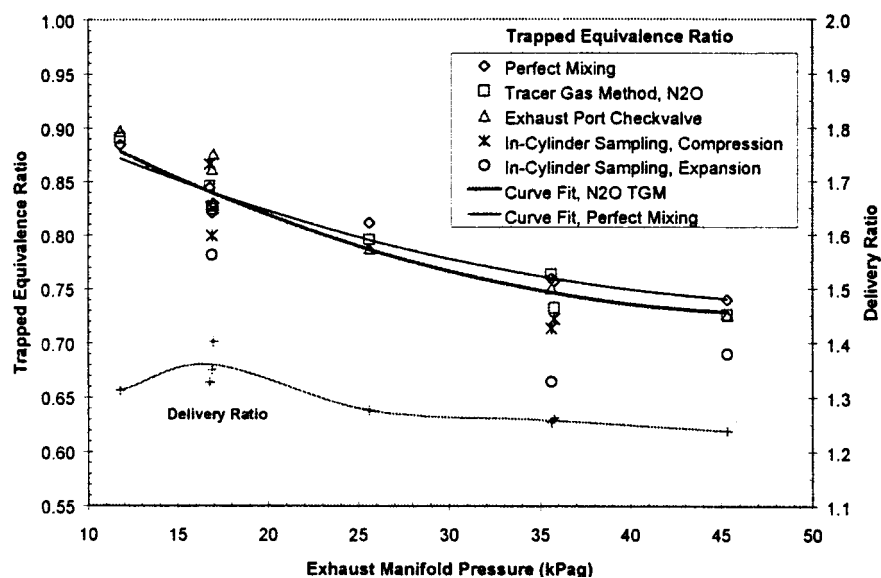


Fig. 5 Trapped equivalence ratio and delivery ratio versus exhaust manifold pressure

open during the entire blowdown event, when a significant portion of the cylinder pass flows past the checkvalve. Therefore, the sample may be representative of a large amount of mass than actually flows through the check valve.

One monomethylamine TGM data point (not shown) was taken at exhaust manifold pressure of 36 kPag during the method comparison testing. The monomethylamine cylinder reaction efficiency was assumed to be 1.0. The measured trapping efficiency was 0.79. The scavenging efficiency evaluated from this was 0.94, which is unrealistically high. In earlier monomethylamine TGM measurements scavenging efficiencies were greater than one, which is impossible. The resulting trapped equivalence ratio from the 36 kPag monomethylamine point was 0.57, which is near the flammability limit and approximately 24 percent leaner than the exhaust port checkvalve point at the same exhaust manifold pressure. The exhaust port checkvalve point was used for comparison because it is located near the center of the other data at the same boost.

Excessive destruction of monomethylamine in the exhaust accounts for the apparent error in the monomethylamine TGM measurement. To quantify the amount of monomethylamine destroyed in the exhaust the actual trapped equivalence ratio is assumed to be equal to the trapped equivalence ratio evaluated from the exhaust port checkvalve technique. The fraction destroyed in the exhaust is then solved for, which results in a value of $\varepsilon_r = 0.44$. Hence, for this boost level, nearly 50 percent of the monomethylamine reacts in the exhaust. This is much higher than the 6 percent monomethylamine destruction in the exhaust shown in Fig. 4. As expected, it appears that the majority of the monomethylamine exhaust reaction occurs in the exhaust manifold. To accurately measure scavenging characteristics and trapped equivalence ratio with the monomethylamine TGM, the fraction destroyed in the exhaust would need to be characterized for each operating condition to be tested. Consequently, the usefulness of monomethylamine as a tracer is severely limited for this application.

The trapped equivalence ratio is also evaluated using the perfect mixing model. The perfect mixing model predicts trapped equivalence ratio well for this engine design. The perfect mixing model assumes that no blowdown of pure combustion products or short-circuiting of scavenging air occurs. If the effects of these two assumptions offset, then the model can make accurate predictions. Apparently this is the case in the GMV-4TF engine. However, it is not likely to be the case for other two-stroke cycle engine designs. For other engine designs, ideally, the perfect mixing model should be compared to other techniques, such as the nitrous oxide TGM, before using it to predict scavenging characteristics.

The nitrous oxide TGM data is corrected for incomplete cylinder reaction using the average of the measured nitrous oxide cylinder reaction efficiencies given in Table 1, but the exhaust reaction is assumed to be negligible. The nitrous oxide TGM compares quite well with the other measurement techniques. Within the accuracy of the data, it appears that there is no significant consumption of nitrous oxide in the exhaust system. The other techniques for evaluating trapped equivalence ratio, in-cylinder sampling and exhaust port checkvalve sampling, have errors associated with them. However, they are often referred to in the literature as "direct measurements." The main error associated with in-cylinder sampling and exhaust port checkvalve sampling is the extraction of a sample that is not representative of the entire cylinder mass due to incomplete mixing. Actually, the TGM is the only one of the techniques presented that is a true bulk measurement. Based on the data it appears to be as accurate, if not more accurate, than the "direct measurement" techniques.

Error Analysis. The accuracy of determining scavenging parameters using the tracer gas method is dependent on instrument measurement uncertainties and accounting for non-ideal tracer effects. The overall instrument measurement uncertainty can be evaluated using standard error analysis techniques ([20]). Mea-

Table 2 Estimates for measurement uncertainty with and without the uncertainty in cylinder reaction efficiency

Scavenging Parameter	Uncertainty (\pm %) Instrument Measurement Uncertainty Only	Uncertainty (\pm %) Including Uncertainty in η_{cr}
Trapping Efficiency	1.5	3.4
Trapped A/F Ratio	1.6	3.5
Delivery Ratio	0.39	0.39
Scavenging Efficiency	1.9	3.8

surement uncertainties for the various instruments such as thermocouples, pressure transducers, and gas analyzers are obtained from the manufacturer's specifications. Estimates for overall measurement uncertainty for various scavenging parameters are given in Table 2. Estimating the measurement uncertainty from nonideal tracer gas effects is nontrivial. This uncertainty is dependent on how significant these effects are and, if significant, how effectively they are evaluated. Whether or not the nonideal tracer effects are important depends on the operating characteristics of the engine to which the tracer gas method is being applied. In this case the exhaust reaction is insignificant. The misfire fraction is small, although it is measured and accounted for. There is, however, significant uncertainty in the measurement of cylinder reaction efficiency. In-cylinder sampling measurements showed a worst-case cylinder reaction efficiency for N_2O of 0.96, while exhaust port check valve sampling resulted in a cylinder reaction efficiency of 1.0. Using the worst-case scenario, the potential error that is introduced is ± 1.9 percent. The potential measurement error for the various scavenging parameters is reevaluated, including the reaction efficiency uncertainty, and provided in the last column of Table 2.

Summary and Conclusions

An investigation into applying the tracer gas method to two-stroke cycle large bore natural gas engines was carried out. A set of equations for evaluating trapping efficiency, scavenging efficiency, and trapped A/F ratio from tracer gas data was developed. The tracer gas method selection criteria was discussed. Two tracer gases were considered, monomethylamine and nitrous oxide. Tracer gas method measurements were compared to in-cylinder sampling results and the perfect mixing model.

Conclusions arrived at during this work are specific to the engine that was tested. However, similar results are expected for other engines that operate under similar combustion regimes and have comparable exhaust temperatures. The conclusions are as follows.

- Nitrous oxide is an excellent choice for a tracer gas.
- The use of monomethylamine as a tracer gas is severely limited by excessive reaction in the exhaust system.
- Evaluation of scavenging efficiency and trapped A/F ratio with the nitrous oxide tracer gas method is comparable in accuracy to in-cylinder sampling techniques
- The perfect mixing model makes accurate predictions of scavenging characteristics and trapped A/F ratio for the scavenging configuration tested.
- The tracer gas method experimental setup is external to the engine, making it a reasonable technique to carry out on field engines.

Acknowledgments

The authors express their appreciation to Kevin Johnson and Stephanie Mick for the important roles that they played in acquir-

ing the test data. This research was sponsored by the Pipeline Research Council International of the American Gas Association and the Gas Research Institute. Enginuity International, Inc., the prime contractor, provided project management. The in-cylinder sample valve was designed by Optimal Engineering, Inc., and manufactured by the Woodward Governor Company.

References

- [1] Nuti, M., and Martorano, L., 1985, "Short-Circuit Ratio Evaluation in the Scavenging of Two-Stroke S. I. Engines," SAE 850177.
- [2] Schweitzer, P. H., and DeLuca, F., Jr., 1941, "The Tracer Gas Method of Determining the Charging Efficiency of Two-Stroke-Cycle Diesel Engines," National Advisory Committee for Aeronautics (NACA), Technical Note No. 838.
- [3] Irish, J. S., Karl, R. D., Keller, H. B., and Waldron, A. L., 1949, "Measurement of Scavenging Efficiency in the Two Stroke Engine: A Comparison and Analysis of Methods," Thesis, Massachusetts Institute of Technology, Cambridge, MA.
- [4] Isigami, S., Tanaka, Y., and Tamari, M., 1963, "The Trapping Efficiency Measurement of Two Stroke Cycle Diesel Engine by Tracer Gas Method," JSME, **6**, No. 23.
- [5] Huber, E. W., 1971, "Measuring the Trapping Efficiency of Internal Combustion Engines Through Continuous Exhaust Gas Analysis," SAE 710144.
- [6] Bazika, I. V., and Rodig, J., 1963, "A New Method of Determining the Scavenging Efficiency of Oil-Engine Cylinders," Eng. Digest, **24**, No. 3.
- [7] Wallace, F. J., and Cave, P. R., 1971, "Experimental and Analytical Scavenging Studies on a Two-Cycle Opposed Piston Diesel Engine," Society of Automotive Engineers, Paper No. 710175.
- [8] Budavari, S., et al., 1989, *The Merck Index: An Encyclopedia of Chemicals, Drugs, and Biologicals*, Merck & Co., Inc.
- [9] Hayhurst, A. N., and Lawrence, A. D., 1992, "Emissions of Nitrous Oxide from Combustion Sources," Prog. Energy Combust. Sci., **18**, pp. 529–552.
- [10] Cullis, C. F., and Willsher, J. P., 1951, "The Thermal Oxidation of Methylamine," Proc. R. Soc. London, Ser. A, **A209**, pp. 218–238.
- [11] Westbrook, C. K., and Dryer, F. L., 1984, "Chemical Kinetic Modeling of Hydrocarbon Combustion," Prog. Energy Combust. Sci., **10**, pp. 1–57.
- [12] Hinshelwood, C. N., 1924, "The Homogeneous Thermal Decomposition of Nitrous Oxide," Proc. R. Soc. London, Ser. A, **106**.
- [13] Johnsson, J. E., Glarborg, P., and Dam-Johansen, K., 1992, "Thermal Dissociation of Nitrous Oxide at Medium Temperatures," *Twenty-Fourth Symposium (International) on Combustion*, The Combustion Institute, Pittsburgh, PA, pp. 917–923.
- [14] Olsen, D. B., 1999, "Experimental and Theoretical Development of a Tracer Gas Method for Measuring Trapping Efficiency in Internal Combustion Engines," Ph.D. Dissertation, Colorado State University.
- [15] Turns, S. R., 1996, *An Introduction to Combustion*, McGraw-Hill, New York, Inc.
- [16] Abraham, J., Maggi, V., Macinnes, J., and Bracco, F. V., 1994, "Gas Versus Spray Injection: Which Mixes Faster?" SAE 940895.
- [17] Olsen, D. B., Holden, J. C., Hutcherson, G. C., and Willson, B. D., 2001, "Formaldehyde Characterization Utilizing In-Cylinder Sampling in a Large Bore Natural Gas Engine," ASME J. Eng. Gas Turbines Power, **123**, pp. 669–676.
- [18] Kannappan, A., "A New Method for Evaluating the Scavenging Performance of Two-Stroke Diesel Engines," Society of Automotive Engineers, Paper No. 640370.
- [19] Heywood, J. B., 1988, *Internal Combustion Engine Fundamentals*, McGraw-Hill, New York.
- [20] Berlin, H. M., and Getz, F. C., Jr., 1988, *Principles of Electronic Instrumentation and Measurement*, Merrill Publishing Company.

Development of the Tracer Gas Method for Large Bore Natural Gas Engines—Part II: Measurement of Scavenging Parameters

D. B. Olsen

G. C. Hutcherson¹

B. D. Willson

C. E. Mitchell

Engines and Energy Conversion Laboratory,
Department of Mechanical Engineering,
Colorado State University,
Fort Collins, CO 80523

In this work the tracer gas method using nitrous oxide as the tracer gas is implemented on a stationary two-stroke cycle, four-cylinder, fuel-injected large-bore natural gas engine. The engine is manufactured by Cooper-Bessemer, model number GMV-4TF. It is representative of the large bore natural gas stationary engine fleet currently in use by the natural gas industry for natural gas compression and power generation. Trapping efficiency measurements are carried out with the tracer gas method at various engine operating conditions, and used to evaluate the scavenging efficiency and trapped A/F ratio. Scavenging efficiency directly affects engine power and trapped A/F ratio has a dramatic impact on pollutant emissions. Engine operating conditions are altered through variations in boost pressure, speed, back pressure, and intake port restriction.

[DOI: 10.1115/1.1454117]

Introduction

The natural gas industry uses over 8000 large bore (bore ≥ 36 cm), two-stroke cycle, slow speed (speed < 300 rpm) natural gas engines for compression and power generation in the U.S. These engines typically operate at high utilization factors, and produce more than 110 billion kW-hours of annually. As extensive as this engine population is, there is no standardized technique for evaluating scavenging efficiency and trapped air/fuel (A/F) ratio. Typically these parameters are not accurately known in fuel-injected two-stroke cycle engines. Often these parameters are calculated based on simple scavenging models, such as the perfect mixing model, which are not likely to model the scavenging process accurately. The tracer gas method (TGM) provides an experimental technique, external to the engine, to evaluate the scavenging efficiency and trapped A/F ratio in two-stroke cycle engines.

The importance of scavenging efficiency and trapped A/F ratio on the performance of two-stroke cycle engines is discussed in detail in a companion paper, Part I—Method Validation ([1]). The analysis involved in evaluating these parameters using the tracer gas method is also outlined. Scavenging efficiency directly impacts engine power, and the trapped A/F ratio has a marked influence on pollutant emissions. The ability to measure these parameters is crucial for future development of advanced two-stroke engine technologies aimed at increasing engine efficiency and decreasing pollutant emissions.

In this program scavenging parameters are studied using the tracer gas method with nitrous oxide as the tracer gas. The tracer gas method is described in Part I [1]. The testing is performed on a four-cylinder fuel injected, two-stroke cycle, natural gas engine with a 36-cm bore and a 36-cm stroke, manufactured by Cooper-Bessemer (model GMV-4TF). Scavenging parameters are investi-

gated at a number of different operating conditions, which are varied by changing engine boost pressure, speed, back pressure, and intake port restriction.

Test Apparatus

Engine Description. The characteristics of the Cooper-Bessemer GMV-4TF engine are summarized in Table 1. A ten-cylinder version of this engine, the GMV-10TF, is also produced and is common in the field. It has identical cylinder, port, and manifold geometry. When new the GMV-4TF was piston scavenged. It is now equipped with a turbocharger simulation package, which allows the engine to be tested with a wide range of intake manifold (boost) and exhaust manifold (back) pressures. The nominal ignition source is spark, although the engine accommodates other ignition sources such as multi-strike and precombustion chamber ignition. The nominal engine configuration is emphasized in this test program. The fuel delivery is with electro-hydraulic gas admission valves that operate at an injection pressure of about 280 kPa. Again, other fuel delivery configurations are possible but the nominal configuration is the one that is tested. Nominal operating conditions are given in Table 2.

Scavenging Configuration. The classification of the scavenging configuration of the GMV-4TF is not obvious. Generally

Table 1 GMV-4TF engine characteristics

Manufacturer	Cooper-Bessemer
Displacement	141 liters
Bore	35.6 cm
Stroke	35.6 cm
Number of cylinders	4
Scavenging	Curtis
Air delivery	Supercharger
Ignition	Spark
Fuel delivery	Fuel injection

¹Presently at Enginuity, Inc.

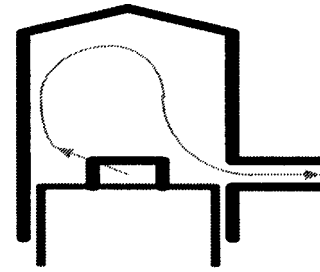
Contributed by the Internal Combustion Engine Division of the THE AMERICAN SOCIETY OF MECHANICAL ENGINEERS for publication in the ASME JOURNAL OF ENGINEERING FOR GAS TURBINES AND POWER. Manuscript received by the ICE Division, July 2000; final revision received by the ASME Headquarters, August, 2001. Editor: D. N. Assanis.

Table 2 GMV-4TF nominal engine operating conditions

Brake power	330 kW
Torque	10 kN-m
Brake mean effective pressure	1.9 MPa
Average peak cylinder pressure	3.4 MPa
Average location of peak pressure	19° ATC
Engine speed	300 rpm
Brake specific fuel consumption	220 g/kW-hr
Ignition timing	10° BTC
Overall A/F ratio (carbon balance)	43
Air mass flowrate	0.86 kg/s
Fuel mass flowrate	0.020 kg/s
Intake manifold pressure	25 kPag
Exhaust manifold pressure	17 kPag
Exhaust O ₂	14%, dry
Exhaust THC	770 ppm, dry
Exhaust NO _x	800 ppm, dry
Exhaust CO	81 ppm, dry
Exhaust CO ₂	4.2%, dry
Intake manifold temperature	320 K
Exhaust stack temperature	600 K
Average cooling water temperature	340 K

scavenging arrangements on engines are lumped into three broad categories, which are cross, loop, and uniflow scavenging. An illustration of each is shown in Fig. 1. The GMV-4TF scavenging port configuration has been labeled as loop scavenged by the engine manufacturer, Cooper-Bessemer [2] although the design contains features of both loop and cross scavenging. The subcategory of loop scavenged configurations that it falls under is the Curtis type.

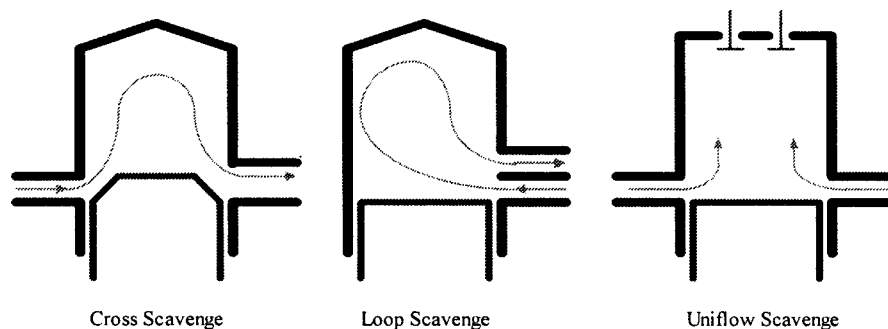
In 1920 Schnürle discovered a method by which the use of the troublesome deflector piston in cross scavenged engines could be eliminated. Instead of the single scavenging (intake) port diametrically opposed to the exhaust port, a pair of ports was located symmetrically around the exhaust port and on the same level, as shown in Fig. 2. The scavenging flow was directed upward and away from the exhaust port. Curtis developed this idea further by adding more scavenging ports opposite the exhaust port. The configuration has been classified as loop scavenged because the flow path, at least from the “Schnürle” ports, prescribes a loop rather than flowing across the cylinder. In the GMV-4TF there are eight scavenging ports and five exhaust ports located across from each other. The exhaust port length spans the bottom 29 percent of the stroke (approximately 10 cm), and the intake port length covers the bottom 21 percent of the stroke (approximately 7.5 cm). The intake ports wrap around the cylinder, covering approximately 210 deg. The intake ports opposite the center exhaust port are directed upward and across the cylinder. The intake ports that wrap around the cylinder are “Schnürle” ports and are directed upward toward the opposite side of the cylinder from the center

**Loop Scavenge (Schnürle Type)****Fig. 2 Schnürle-type loop scavenging: intake flow is directed upward and away from the exhaust port**

exhaust port. The exhaust ports wrap around the cylinder as well, covering approximately 120 deg. The piston cross section is M-shaped, so when the ports are partially covered it acts like a deflector piston. The deflector piston and the fact that some exhaust ports are opposite intake ports are characteristics of the cross scavenge configuration. The direction of the entering scavenging flow and the piston shape work to scavenge the upper portion of the cylinder more effectively. A drawing showing the geometry of the cylinder, ports, and head for the GMV-4TF is provided in another paper ([3]).

The scavenging flow for this cylinder was studied with Schlieren photography by Boyer et al. [2]. An interesting conclusion that was made was that the scavenging air enters the cylinder through the intake ports in turbulent jets. The flow penetrates the combustion products rather than entraining them, and initially resides near the cylinder head. Conversely, the gas flow that exits the cylinder is characterized by laminar flow streamlines. The authors describe this as a desirable situation for this port design, because the scavenging air tends to accumulate behind the combustion products and subsequently pushes them out like a laminar gas piston.

Instrumentation. The exhaust composition and tracer concentrations were measured using a Rosemount 3000 five-gas emission analyzer (criteria pollutants, O₂, and CO₂) and a Nicolet REGA Fourier transform infrared spectrometer (tracer and most exhaust constituents). The inlet air and exhaust flowrates were measured using Dietrich Standard Diamond II Annubars. The Annubar™ is a differential pressure device that operates as a self-averaging Pitot tube. The natural gas fuel flowrate was measured with an AGA (American Gas Association) standard orifice flowmeter. Orifice flowmeters are generally more accurate than Annubar™ flowmeters, but come with the penalty of larger pressure losses. The engine and support hardware was instrumented with numerous pressure sensors and thermocouples. A comprehensive description of the engine test bed and instrumentation is given by Schoonover [4] and Potter [5].

**Fig. 1 Methods of scavenging two-stroke engines.**

Results And Discussion

Tracer Gas Method (TGM) Trapping and Scavenging Efficiency Evaluations. Trapping efficiency measurements are presented for the GMV-4TF engine using the tracer gas method with nitrous oxide. The TGM provides a direct measurement of the trapping efficiency. To calculate the scavenging efficiency from the trapping efficiency, an evaluation of the delivery ratio is required. The delivery ratio is calculated, in terms of measured parameters, using the equation

$$\Lambda = \frac{dm_{del}/dt}{V_{pc}\rho_{pc}N_{cyl}\omega}$$

where

- dm_{del}/dt = measured air mass flow through engine,
- V_{pc} = cylinder volume at exhaust port closing,
- ρ_{pc} = calculated charge density at exhaust port closing using exhaust manifold pressure and intake manifold temperature,
- N_{cyl} = number of cylinders, and
- ω = engine speed in revolutions per second.

The overall A/F ratio is determined by exhaust gas analysis,

described by Fanick et al. [6], commonly referred to as the carbon balance method. The mass flow of air through the engine is evaluated from the overall A/F ratio and the fuel flow measurement with the orifice flowmeter. The charge density at port closure was evaluated using the ideal gas law, the exhaust manifold pressure, the molecular weight of air, and the intake air manifold pressure. The delivery ratio is an important parameter in the scavenging process because it reflects the air flow through the cylinder per cycle relative to the trapped cylinder mass. Increasing this ratio generally results in more effective scavenging.

For the scavenging measurements presented in this section, the misfire fraction and incomplete tracer destruction in the cylinder were compensated for. The misfire fraction is evaluated by looking at the pressure-time histories for approximately 1000 cycles, and recording the number of cycles where the pressure did not rise higher than 110 percent of peak motored pressure. An average cylinder reaction efficiency of 0.96 was used to account for incomplete tracer reaction in the cylinder. An error analysis for evaluation of scavenging parameters with the tracer gas method is provided elsewhere ([1]).

Speed Variations. Large-bore natural gas engines are, in general, constant speed engines. Therefore, the potential variations in speed are not large. However, the range of speed variations do

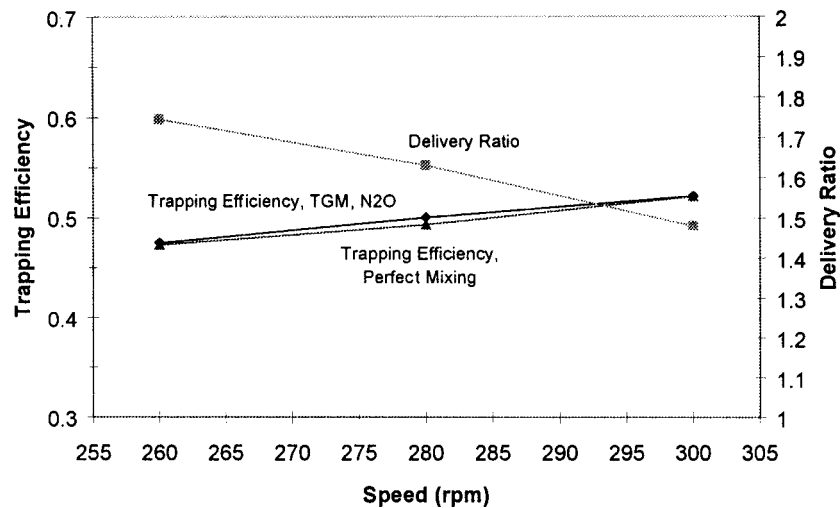


Fig. 3 Trapping efficiency versus speed

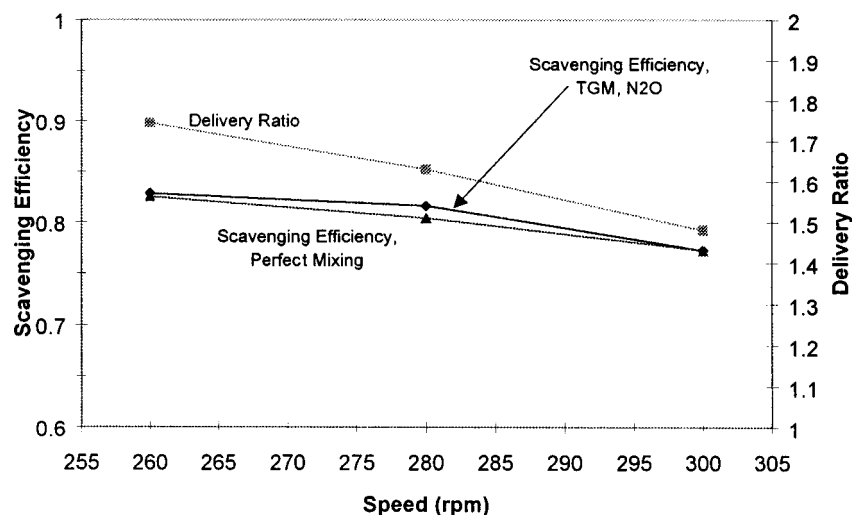


Fig. 4 Scavenging efficiency versus speed

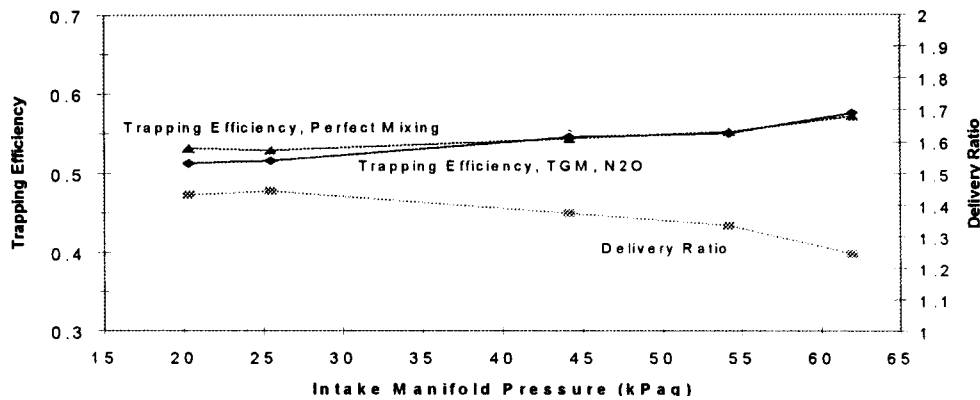


Fig. 5 Trapping efficiency versus intake manifold pressure

significantly change delivery ratio and consequently the scavenging characteristics. Figures 3 and 4 show how trapping and scavenging efficiency change with speed. Calculations based on perfect mixing are presented with the nitrous oxide TGM data for comparison. Recall that the perfect mixing model is not an ideal case. Actual scavenging can be better or worse than that predicted by perfect mixing. Delivery ratios are plotted on the second y-axis. Throughout the speed map the intake manifold pressure is constant at 25 kPa. Torque control is achieved by reducing the fuel flow to the engine as speed decreases, maintaining constant torque at about 9 kN-m. The trapping efficiency is seen to increase nearly linearly with speed and the scavenging efficiency decreases with speed for both evaluation methods. As speed increases, the airflow through the engine remains approximately constant because the effective port flow area does not change. The decrease in scavenging efficiency with increasing speed can be attributed to two factors, (1) the mass of combustion products per cycle to be scavenged increases with increasing speed due to increased fuel flow and (2) the time for the scavenging air to remove combustion products from the cylinder per cycle decreases with increasing speed.

The nitrous oxide TGM scavenging efficiencies are generally higher than those evaluated with the perfect mixing model, but not by very much. In looking in the literature for data to compare with, recall that the scavenging configuration of the GMV-4TF possesses characteristics of both loop and cross scavenging. Data from large two-stroke diesel engines by Gyssler [7], delivery ratios from 1.2 to 1.4, show scavenging efficiencies from loop scav-

enged engines slightly above perfect mixing (0.01 to 0.1 above) and cross scavenged engines slightly below perfect mixing (0.05 to 0.1 below). In other published data by Houtsma [8] scavenging efficiencies from loop scavenged engines are reported as being about 0.05 to 0.1 lower than perfect mixing for delivery ratios 0.8 to 1.4. The scavenging efficiencies measured with the nitrous oxide TGM for the speed map range from coincident to 0.03 above perfect mixing. Therefore, the measured scavenging performance of the GMV-4TF falls within boundaries defined by the range of the test data from these sources.

Intake Manifold Pressure (Boost) Variations. The trapping and scavenging efficiencies are plotted versus intake manifold pressure in Figs. 5 and 6. Bear in mind that the intake manifold pressure is the parameter that is varied, but it is the exhaust manifold pressure that most directly affects engine performance. Delivery ratios are plotted on the second y-axis. In general the pressure drop across the engine is kept constant throughout the boost map, so increases in intake manifold pressure are accompanied by increases in exhaust manifold pressure. The pressure drop across the engine is maintained constant at about 8.5 kPa via a motorized exhaust butterfly valve. The intake manifold pressure more than tripled during the test, though the delivery ratio did not change proportionately. Therefore, only small changes in scavenging characteristics were seen. Based on the nitrous oxide TGM measurements, general trends of increasing trapping efficiency with intake manifold pressure and decreasing scavenging efficiency with intake manifold pressure are observed. The exception to both

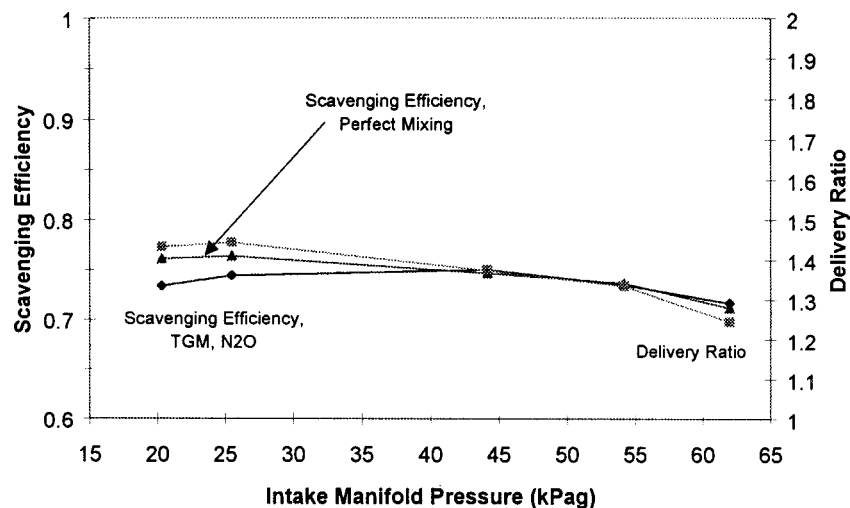


Fig. 6 Scavenging efficiency versus intake manifold pressure

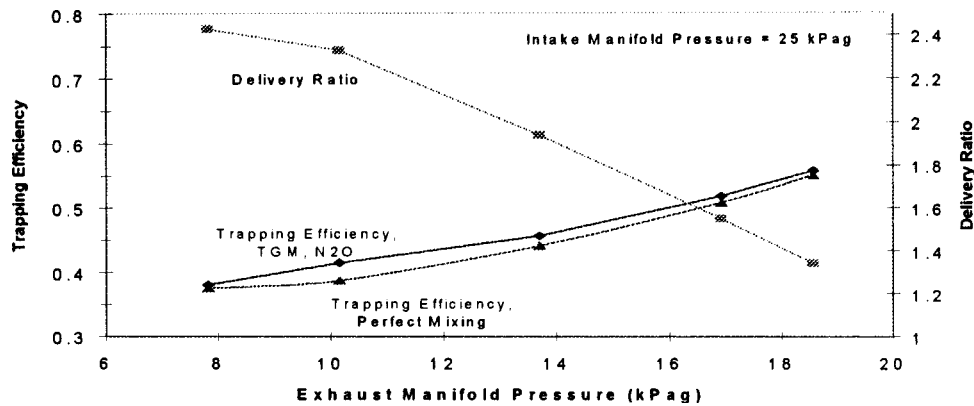


Fig. 7 Trapping efficiency versus exhaust manifold pressure for back pressure valve variations at constant intake manifold pressure (25 kPag)

of these trends is at the lowest intake manifold pressure. It appears that a maximum in delivery ratio occurs at an intake manifold pressure of about 25 kPag, the nominal boost for the engine. The best scavenging efficiencies occur at the nominal intake manifold pressure (25 kPag) and at 44 kPag where the nitrous oxide TGM scavenging efficiencies are 0.74 and 0.75, respectively. As with the speed map, the nitrous oxide TGM data is very close to the data evaluated using the perfect mixing model. The largest discrepancy occurs at the lowest intake manifold pressure, where the perfect mixing model is about 0.03 higher than the nitrous oxide TGM data.

Backpressure Variations. The exhaust backpressure was varied by changing the backpressure butterfly valve setting in the exhaust pipe at constant boost. This influenced the delivery ratio the most, and consequently had the strongest impact on scavenging. Backpressure maps were performed at two boost levels, 25 kPag and 34 kPag. Torque was held constant at the nominal value, 10 kN-m. The fuel flow to the engine was adjusted to control torque. However, the fuel flow did not need to be adjusted much because in all cases a lean trapped A/F ratio was burned, which provides ample oxygen to burn the injected fuel. Improvements to scavenging using the exhaust backpressure valve are interesting, but not necessarily realistic. This is because the valve is designed to simulate the pressure drop across the exhaust turbine of a turbocharger and on real turbochargers this is not adjustable.

Figures 7, 8, 9, and 10 show trapping and scavenging efficiency versus exhaust manifold pressure for variations in the backpressure valve setting at two different boost levels. The delivery ratio is plotted on the second y-axis. The exhaust manifold pressure is a measure of the pressure drop across the backpressure butterfly valve. It can be seen on all four graphs that the exhaust backpressure has a dramatic effect on delivery ratio, which nearly doubled as the backpressure was reduced. The general trends of increasing trapping efficiency with increasing exhaust manifold pressure and decreasing scavenging efficiency with increasing exhaust manifold pressure are observed. These trends are directly related to the effect that the backpressure has on delivery ratio. The nitrous oxide TGM trapping efficiency and scavenging efficiency values are generally larger than those evaluated with perfect mixing. The trapping efficiency data tends to be closer to perfect mixing than the scavenging efficiency data. The nitrous oxide TGM trapping efficiencies range from 0.38 to 0.56 for a boost pressure of 25 kPag, and 0.41 to 0.57 for a boost pressure of 34 kPag. The nitrous oxide TGM scavenging efficiencies range from 0.75 to 0.97 for the 25 kPag boost pressure case, and 0.72 to 0.93 for the 34 kPag boost pressure case. There is very little difference in the trapping and scavenging efficiencies for the two different boost cases. Note that for high scavenging efficiencies the trapping efficiency is low. Hence, much of the airflow is short circuited and is not utilized in the combustion process. This results in a penalty of excess blower power. Conversely, when the trap-

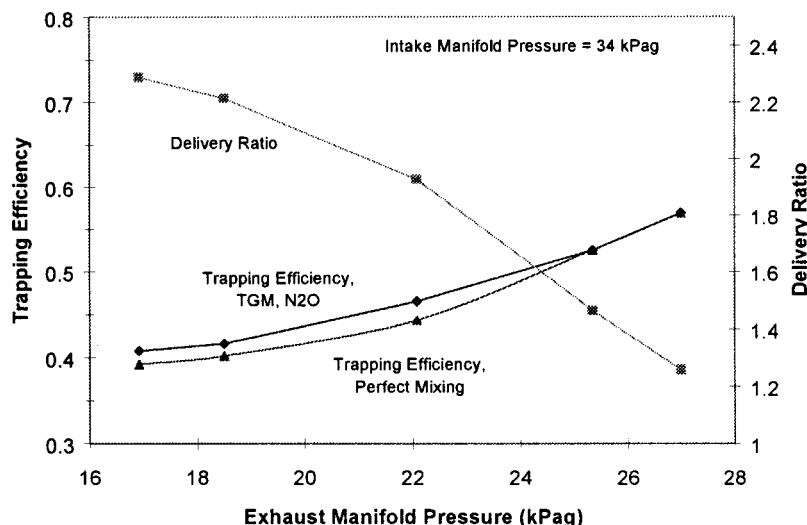


Fig. 8 Trapping efficiency versus exhaust manifold pressure for back pressure valve variations at constant intake manifold pressure (34 kPag)

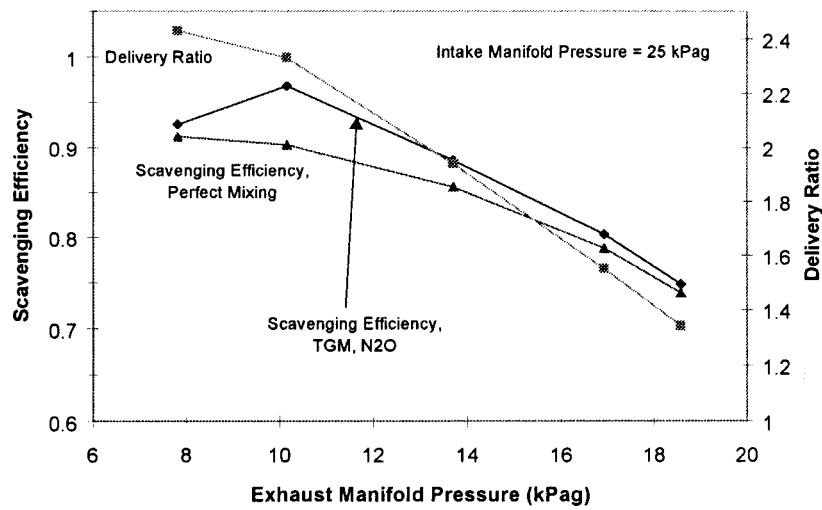


Fig. 9 Scavenging efficiency versus exhaust manifold pressure for back pressure valve variations at constant intake manifold pressure (25 kPag)

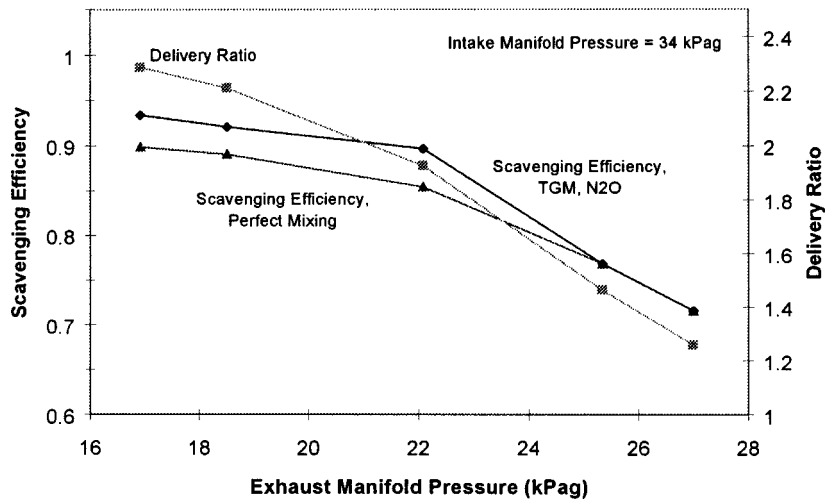


Fig. 10 Scavenging efficiency versus exhaust manifold pressure for back pressure valve variations at constant intake manifold pressure (34 kPag)

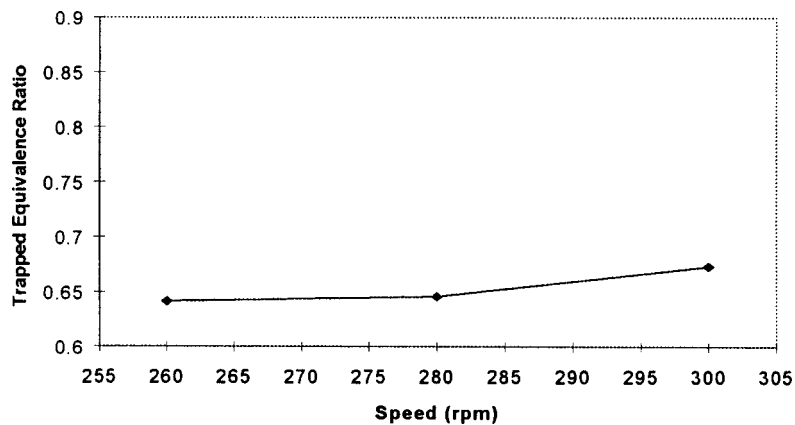


Fig. 11 Nitrous oxide TGM trapped equivalence ratios for variations in speed

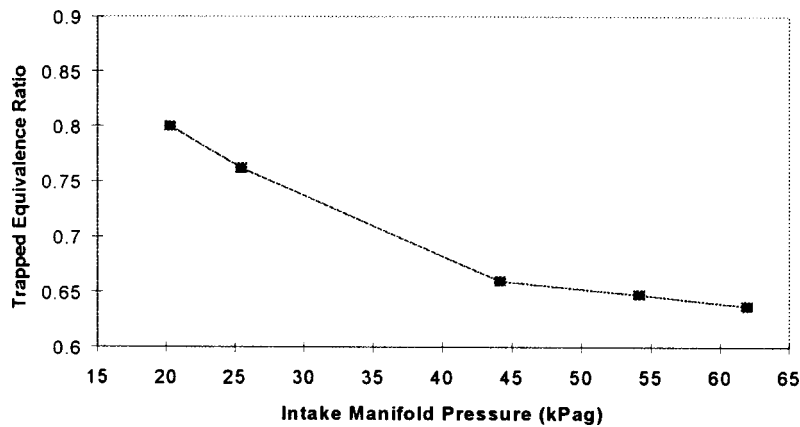


Fig. 12 Nitrous oxide TGM trapped equivalence ratios for variations in intake manifold pressure

ping efficiency is high the scavenging efficiency is low. In this case the blower power is low, but the engine may suffer from low power output and poor efficiency due to decreased scavenging efficiencies.

TGM Trapped Equivalence Ratio Evaluations. One of the main reasons to implement the tracer gas method is the information gained about the trapped equivalence ratio. The trapped equivalence ratio is calculated from the stoichiometric A/F ratio, the measured trapping efficiency, and overall A/F ratio calculated from exhaust gas analysis. Figures 11–13 show the trapped equivalence ratios evaluated from the nitrous oxide TGM measurements utilizing nitrous oxide as the tracer. Trapped equivalence ratio maps are presented for speed, boost, and back pressure.

Figure 11 shows a gradual trend of the trapped mixture getting richer as speed is increased. The testing showed a gradual decrease in scavenging efficiency as speed increased (Fig. 4). This explains the increase in the trapped equivalence ratio. As speed increases a smaller fraction of the cylinder mass at port closure is fresh air, increasing the trapped equivalence ratio. Boost has a much stronger influence on trapped equivalence ratio (Fig. 12) than speed. Increasing the boost at constant torque tends to decrease the equivalence ratio, resulting in a leaner mixture. The data show a significant decrease in trapped equivalence ratio as the boost increases, with a flattening trend at the higher boost levels. Referring to Fig. 6, the scavenging efficiency actually goes down with increasing boost. Therefore, at boost levels higher than 25 kPag (nominal) the scavenging process is less effective at removing combustion products and refilling the cylinder with fresh charge. Although there is a smaller fraction of fresh charge in the cylinder at port closure, the total mass of fresh air in the cylinder is larger at boosts above nominal. That is why the charge gets leaner with increasing boost, while the scavenging efficiency decreases. Changes in fuel flow can also affect trapped equivalence ratio. Throughout the boost map the fuel flow increases with boost, which cannot explain the observed trend. In fact, increasing the fuel flow increases trapped equivalence ratio. The increase in fuel flow is probably necessary to maintain constant torque to compensate for increased misfires and incomplete combustion that can be characteristic of a leaner and higher pressure charge.

The general trend seen in the backpressure maps (Fig. 13) is one of decreasing trapped equivalence ratio with decreasing exhaust manifold pressure. Referring to Figs. 9 and 10, the general trend is increasing scavenging efficiency with decreasing exhaust manifold pressure. As the back pressure is reduced the scavenging efficiency increases by about 29 percent, from 0.75 to 0.97, for the back pressure map at 25 kPag boost; however, the final reduction in back pressure decreases the scavenging efficiency to 0.93. For the back pressure map at 34 kPag boost, the scavenging efficiency

increases by about 30 percent, from 0.72 to 0.93. Thus, the fraction of fresh charge in the cylinder at port closure is generally greater at lower back pressures. The back pressures. The fuel flow remained relatively constant throughout the test, so the effect of increasing the fraction of fresh charge is the likely cause of the reduced trapped equivalence ratios. As the back pressure drops, the trapped mass at port closure goes down and, if scavenging efficiency is constant, the mass of fresh intake air goes down as well. For a constant fuel flow, this tends to increase trapped equivalence ratio, competing with the effect of increasing the scavenging efficiency. Apparently the effect of increasing the scavenging efficiency is dominant for most of these test points, the main exception being the 8 kPag point in Fig. 13.

The Effect of Intake Port Restriction on Scavenging and Trapped Equivalence Ratio.

A test was carried out to simulate the reduction in port flow area due to carbon deposit build-up. The nitrous oxide TGM was implemented to measure the effects of port restriction on scavenging and trapped equivalence ratio. On the GMV-4TF engine the intake ports are on the outside and are much more accessible than the exhaust ports, so the area of the intake ports was reduced instead of the area of the exhaust ports. Though carbon deposit buildup typically occurs in the exhaust ports, one of the primary effects is to restrict the overall effective flow area. This can be accomplished by reducing the flow area of either set of ports. Reducing the flow area also alters gas flow patterns in the cylinder, which can affect scavenging. This is a

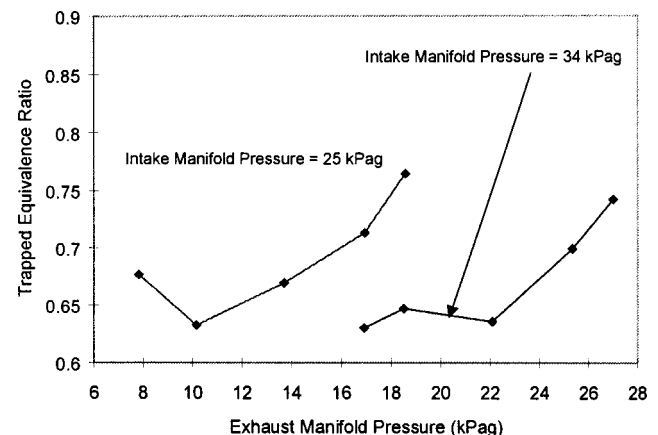


Fig. 13 Nitrous oxide TGM trapped equivalence ratios for variations in exhaust back pressure at two boost levels

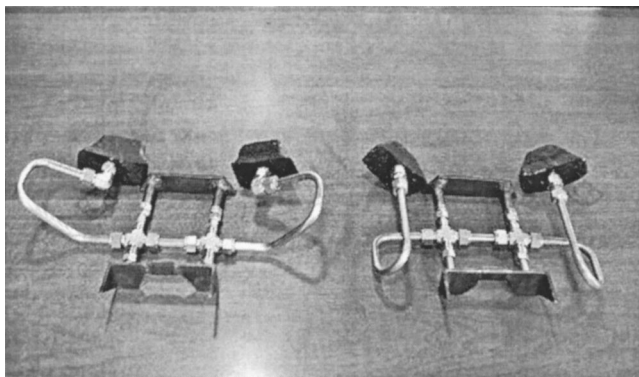


Fig. 14 Fixture implemented to block one or two of the intake ports

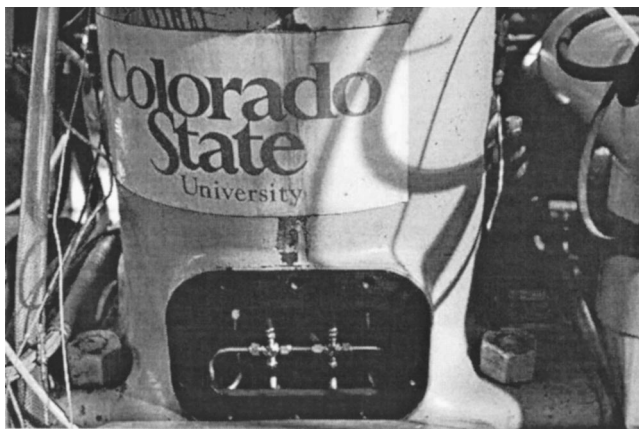


Fig. 15 Port blockage fixture installed in cylinder

more complex problem. No attempt was made to try and separate the effects of decreased effective flow area and the change in gas flow patterns.

A fixture for plugging the intake ports was developed. The fixture was designed to plug either one or two intake ports on a particular cylinder. The design of the fixture was simplified considerably by plugging a whole port, rather than reducing the area

of each port. The fixture that was built is shown in Fig. 14. Figure 15 displays the fixture installed in an engine cylinder. Since there are eight intake ports, the fixture reduced the intake port area to either 7/8 or 3/4 of the original area. The test was performed on the 2–4 bank of the engine only. Thus, exhaust measurements were taken from the 2–4 bank exhaust elbow rather than the stack.

Some results of the testing are presented in Figure 16. This data is at a constant intake manifold pressure (46 kPag) and pressure drop across the engine (10 kPag). The pressure drop across the engine is controlled with the exhaust backpressure butterfly valve, as described earlier. As the level of intake port area blockage increases, the delivery ratio for the 2–4 bank decreases. This is due to an overall decrease in airflow through the engine, and a decrease in the fraction of overall airflow that flows through the 2–4 bank. The decrease in delivery ratio decreases the scavenging efficiency and increases the equivalence ratio of the 2–4 bank, resulting in a richer mixture being burned. THC and CO emissions do not change significantly; however, CH_2O (formaldehyde) and NO_x emissions do. CH_2O emissions increase by 8 percent and NO_x emissions increase by 54 percent. There are many things that can cause significant changes in exhaust emissions, such as ambient air conditions (humidity, temperature, etc.), fuel composition, piston ring wear, and, as illustrated here, port blockage. The tracer gas method provides an additional tool for resolving emissions problems in field engines. Implementing the tracer gas method allows the scavenging characteristics to be isolated from other factors that can affect emissions.

Summary And Conclusions

Scavenging parameter investigations were performed on the GMV-4TF engine using the nitrous oxide TGM for variations in engine operating conditions. For comparison purposes, perfect mixing evaluations were carried out in parallel. The nitrous oxide TGM results were compared to data in the literature for loop scavenged and cross scavenged engines. The scavenging performance of the GMV-4TF falls within boundaries defined by the range of the test data reviewed.

- Increasing speed at constant torque decreases scavenging efficiency and increases trapped equivalence ratio, resulting in a richer mixture being burned.
- At constant torque increasing boost from the nominal value decreases scavenging efficiency, but decreases trapped equivalence ratio because of the added cylinder fresh air mass.

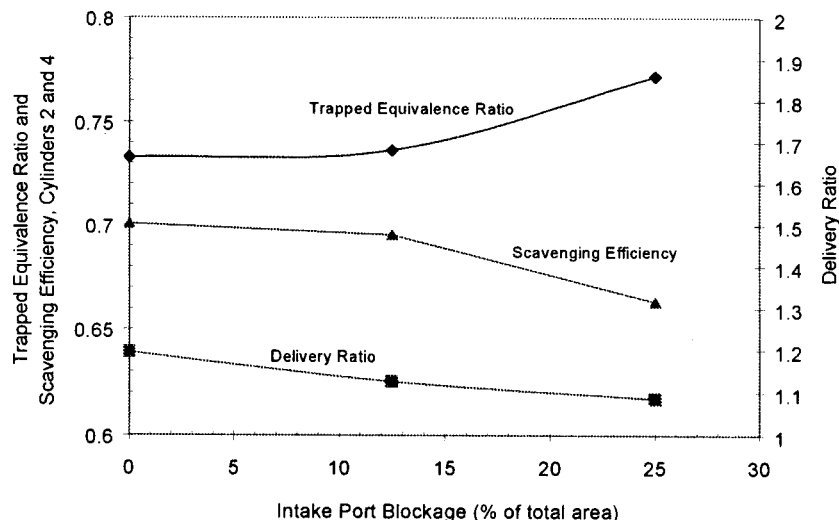


Fig. 16 Nitrous oxide TGM measurements of trapped equivalence ratio and scavenging efficiency versus percent of intake port blockage

- Changes in exhaust manifold pressure, or backpressure, have the largest impact on scavenging characteristics. As backpressure is decreased at constant boost, the scavenging efficiency increases and the trapped equivalence ratio decreases as a result of large increases in delivery ratio. This highlights the importance of minimizing exhaust turbine pressure drop at a given boost in designing turbochargers.

- The nitrous oxide TGM is a useful tool in resolving emissions problems because it isolates scavenging problems, such as port restrictions.

Acknowledgments

The authors express their appreciation to Jason Holden, Kevin Johnson, and Stephanie Mick for the important roles that they played during testing. This research was sponsored by the Pipeline Research Council International of the American Gas Association and the Gas Research Institute. Enginuity International, Inc., the prime contractor, provided project management.

References

- [1] Olsen, D. B., Hutcherson, G. C., Willson, B. D., and Mitchell, C. E., 2000, "Development of the Tracer Gas Method for Large Bore Natural Gas Engines: Part 1—Method Validation," *Proceedings ASME Spring Technical Conference, ICE-Vol. 34-1*, Paper No. 2000-ICE-255.
- [2] Boyer, R. L., Craig, D. R., and Miller, C. D., 1953, "A Photographic Study of Events in a 14-in. Two-Cycle Gas-Engine Cylinder," *Trans. ASME*, Paper No. 53-S-45.
- [3] Olsen, Daniel B., Holden, Jason C., Hutcherson, Gary C., and Willson, Bryan D., 2001, "Formaldehyde Characterization Utilizing In-Cylinder Sampling in a Large Bore Natural Gas Engine," *ASME J. Eng. Gas Turbines Power*, **123**, 669–676.
- [4] Schoonover, R. C., 1995, "Development of a Turbocharger Simulation Package and Applications to Large Bore Engine Research," Masters thesis, Colorado State University.
- [5] Potter, C. R., 1995, "The Design and Development of an Independent Large Bore, Natural Gas, Engine Test Facility," Masters thesis, Colorado State University.
- [6] Fanick, E. R., Dietzmann, H. E., and Urban, C. M., 1988, "Emissions Data for Stationary Reciprocating Engines and Gas Turbines in Use by the Gas Pipeline Transmission Industry," American Gas Association, Report No. PR-15-613.
- [7] Gyssler, G., 1965, "Problems Associated With Turbocharging Large Two-Stroke Diesel Engines," *Proc. CIMAC*, Paper B.16.
- [8] Houtsma, C. G., et al., 1950, "Correlation of Scavenging Ratio and Scavenging Efficiency in 2-Stroke Compression-Ignition Engine," Thesis, Massachusetts Institute of Technology, Cambridge, MA.

Multicode Prediction of the Influence of the Exhaust System on the Performance of a Turbocharged Engine

G. Chiatti
O. Chiavola

Department of Mechanical and Industrial
Engineering,
University "Roma Tre,"
Via della Vasca Navale, 79,
00146 Rome, Italy

A multicode approach, based on the simultaneous use of zero-dimensional, one-dimensional, and three-dimensional models, has been developed and tested, and is here applied to predict the thermodynamic and fluid dynamic phenomena that characterize the unsteady gas flow propagation along the exhaust system of a turbocharged four-cylinder engine. The investigation is carried out by applying each model in a different region of the geometry, allowing to obtain detailed information of the flow behavior in complex elements, such as junctions, avoiding the significant limitations that a one-dimensional scheme always introduces, as well as fast processing typical of one-dimensional and zero-dimensional models, devoted to the analysis of ducts and volumes. The effect of the influence of different configurations of the exhaust system on the engine performance is analyzed. [DOI: 10.1115/1.1455640]

Introduction

In the design procedure of turbocharged internal combustion engine the selection of the most effective exhaust system configurations is of paramount importance since the engine performances are greatly affected by the gas flow unsteadiness. Within this optimization process, the numerical simulation plays an important role aimed to predict the unsteady compressible flow caused by the periodic opening and closing of the valves in order to assess the influence of the geometrical configuration on engine performance and to select the system that ensures better tuning between the exhaust system and the engine.

Nowadays different kinds of approaches, based on a zero-dimensional, one-dimensional, or three-dimensional analysis are generally adopted. Each method retains advantages and disadvantages, as assumptions of different levels of the physical behavior of the flow are always introduced in the modeling of the system. One-dimensional nonlinear gas dynamic models are based on the hypothesis of uniformly distributed thermodynamic quantities over each cross-sectional area of the geometry. They are able to analyze the unsteady compressible flow in engine inlet and exhaust systems acting as a set of ducts, including charge of the pipe cross-sectional area, wall friction, and wall heat transfer effects. Zero-dimensional models are generally adopted to solve the thermodynamics in geometries where the performance can be adequately described by averaged quantities without taking into account the wave action. One-dimensional fluid dynamic models allow rapid calculation and may be easily matched with zero-dimensional models able to simulate the cylinder or other volumes. These approaches are basically incapable of accounting for the effects of multidimensional propagation. More realistic three-dimensional models are able to describe in detail the fluid behavior of complex geometries, taking account for phenomena such as the coupling effects of the mean flow pattern and turbulence dissipation, but they are more expensive and time-consuming.

A new kind of methodology, based on the simultaneous use of zero-dimensional, one-dimensional, and three-dimensional models, has been set up.

The multicode approach retains the advantages of all methods: detailed information of the flow behavior as it is able to accurately predict, with the three-dimensional scheme the propagation of the pressure waves through complex elements, such as junctions, avoiding the significant limitations that a one-dimensional schematization always introduces, as well as fast processing typical of one-dimensional and zero-dimensional schemes devoted to the analysis of ducts and volumes.

The developed methodology, tested on a simple geometry, has been then applied to predict the thermodynamic and fluid dynamic phenomena that characterize the unsteady gas flow propagation along the exhaust system of a turbocharged 4-cylinder engine and to analyze the effect of the influence of different configurations of the system on the engine performance.

Turbocharging

The power output of an internal combustion engine can be increased if turbocharging is used. To this aim two different systems are generally adopted. In the first one the exhaust gases coming from all cylinders flow into a common exhaust manifold, whose volume is sufficiently large to damp down the unsteady flow, and then feed one single-entry turbine.

The fluctuating gas flow ([1,2]) from the cylinders is damped so that the conditions at the turbine entry are essentially steady with time, providing a nearly constant pressure turbocharging.

As the mass flow is relatively constant, high efficiency of the turbine is achieved; the disadvantage of this kind of turbocharging is the high kinetic energy of the exhaust gases leaving the cylinders is not fully utilized; the frictional losses, due to the mixing process between exhaust flow, coming from different cylinders, decrease the available kinetic energy, too.

A better utilization of the exhaust kinetic energy can be ensured by adopting a pulse system turbocharging ([3,4]), in which the available energy at the turbine is increased as regards the constant pressure architecture. Short and narrow pipes characterize the configuration, the gas flow into the turbine is highly unsteady and the turbine operates under variable conditions. Flow unsteadiness

Contributed by the Internal Combustion Engine Division of THE AMERICAN SOCIETY OF MECHANICAL ENGINEERS for publication in the ASME JOURNAL OF ENGINEERING FOR GAS TURBINES AND POWER. Manuscript received by the ICE Division July 2000; final revision received by the ASME Headquarters August 2001. Associate Editor: D. Assanis.

can be reduced by grouping together several cylinders in a common exhaust pipe and by adopting a pulse converter.

The choice between pulse, pulse converter, and constant-pressure turbocharging systems depends on the application for which the engine is designed and on the efficiency of the turbocharging system at the normal rating of the engine ([5,6]).

In the preliminary system design process the comparison between different geometrical solutions of ducts and of turbines (number of inlets and entry area) is very useful ([7,8]). A simulation tool, able to take care, in simple way, of the effects due to the exhaust process of the cylinder and to different duct diameter and length (zero-dimensional and one-dimensional models) ([9–12]) and high accuracy model to adequately investigate junctions and nozzle (three-dimensional models), has to be adopted. To this aim the proposed methodology has been set up and two different exhaust system configurations applied to a 4-cylinder turbocharged engine have been investigated; in the former case two pairs of cylinders feed two separate exhaust manifold branches and a twin-entry turbine, realizing a pulse turbocharging. In the latter one the four cylinders are connected to one single manifold system and to one single-entry turbine, in this way a constant pressure system is achieved.

Multicode Approach

At present, in intake and exhaust systems of high-performance engines, complex components are always included. The analysis of the unsteady gas flow in such complex elements requires a multidimensional simulation in order to take into account the three-dimensional flow structure strongly affected by the shape of the cross section of the ducts and the angle between the branches, as one-dimensional model is not appropriate to accurately predict the complex behavior of the flow.

An accurate multidimensional investigation of some parts can not be carried out without taking into account for the influence that all the other parts of the intake and exhaust system and the engine give rise to, as the behavior of each element is strongly affected by the mutual interactions between different component parts. For this reason the analysis of engine breathing process can be carried out only if the complete engine system is considered.

In order to provide realistic boundary conditions (accounting for the complete system) to perform the three-dimensional calculation, it has to be considered that in the intake and exhaust systems the complex elements are usually connected by means of ducts. These elements, characterized by constant or slowly variable cross-sectional area, do not require an accurate three-dimensional description, as they can be adequately analyzed by a one-dimensional simulation.

A coupling procedure between three-dimensional and one-dimensional methods can be adopted: some parts of the system can be investigated by means of the three-dimensional method and other parts can be schematized as one-dimensional domains.

In this way the one-dimensional code may be seen as an efficient provider of boundary conditions necessary to perform the three-dimensional calculation.

As cylinders represent the excitation source for the intake and exhaust system, the simulation of the thermodynamic cycle in the cylinder during both the closed and the opened valve periods has to be performed. To this aim a zero-dimensional model can be adopted, so that the evaluation of the thermofluid dynamic quantities inside the cylinders provides the physical boundary conditions for one-dimensional domain calculation.

By adopting a three-dimensional description coupled with one-dimensional and zero-dimensional models, the complete intake and exhaust system can be simulated and high accuracy as well as fast processing and high flow pattern resolution can be achieved.

The simultaneous solution of the governing equations inside the cylinders and the components of the complete system guarantees that the interaction between the different components and the engine is taken into account.

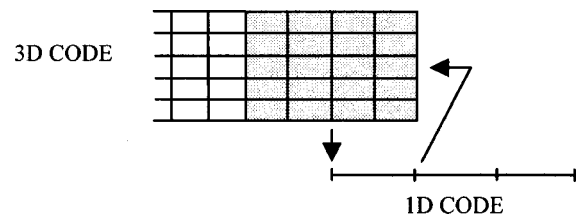


Fig. 1 Coupling procedure ([19])

Models and Coupling Procedure

The self-developed one-dimensional model is based on a refinement of the method of characteristics, proposed by Moretti [13], to solve the nonlinear hyperbolic system of equations that describe the gas flow in pipes including the effects of duct wall friction, heat transfer, and duct area gradient.

It is a λ -scheme explicit difference method, organized on a two-level calculation, characterized by a second order accuracy both for time and space.

The model allows to deal with contact discontinuity caused by the interaction between hot gas discharged by the cylinder and cold gas lain in the duct. It is a separation front through which velocity and pressure are continuous, while temperature, sound velocity, and entropy are discontinuous. The propagation of the discontinuity along the system is provided.

The one-dimensional model is matched with a lumped parameter scheme that is able to perform the behavior of the cylinder both for the opened valve and the closed valve periods.

It incorporates a multizone model to analyze the combustion process (the cylinder is divided in zones, in which unburned gas and burned products are in thermodynamic equilibrium). At each time step all variables are evaluated by means of conservation equations applied to the different zones and to the overall volume.

The zero-dimensional and one-dimensional models have been validated by comparing the predicted results with experimental ones and those belonging to other numerical schemes ([13,14]).

The three-dimensional code used is the CFD package FIRE ([15]) developed by AVL. It is based on a finite volume method adopting an implicit scheme to solve the governing equations (SIMPLE algorithm).

The hybrid approach combines the thermo dynamic and the gas dynamic one-dimensional model with the three-dimensional FIRE scheme: They are simultaneously applied to different regions of the same geometry. The complete engine system is divided into calculation domains and in each one it is adopted the most suitable model, according to the involved phenomena. Since one-dimensional model is unable to consider spatial flow distribution within the cross section of the duct (no appreciable three-dimensional behavior can appear in that cross section), the choice of the position where locate the interface region between one-dimensional and three-dimensional domains has to be carefully planned.

The interface procedure and the related interpolation technique adopted to model one-dimensional and three-dimensional connections is of primary importance, since they deeply affect the predicted results.

At each one-dimensional to three-dimensional connection an overlapping region is defined (Fig. 1).

In the one-dimensional domain, an additional pipe of one cell length is considered; it corresponds to the three-dimensional region used to link the different models. One-dimensional and three-dimensional geometries are simultaneously analyzed to guarantee a correct evaluation of the system's behavior avoiding numerical mismatch at boundaries, that may led to erroneous results: for this reason the transfer of data from one-dimensional to three-dimensional regions and vice versa takes place whenever the codes are in synchronism.

Focusing on a particular time step, the averaged FIRE quantities in the overlapping region are transferred to the additional pipe and they are used to prescribe the boundary conditions necessary to one-dimensional model. As it uses an explicit scheme to solve the governing equations, the time step can be calculated.

The obtained one-dimensional thermofluid dynamic quantities are then prescribed as boundary conditions to perform the three-dimensional calculation. In order to choose the type of boundary conditions to apply at the three-dimensional interfaces, some tests have been carried out, in which pressure and temperature of mass flow and temperature have been assigned to the connection region between one-dimensional and three-dimensional domains. To enforce the conservation of mass flow at interface, it has been chosen to assign mass flow and temperature. These quantities are determined by one-dimensional code and afterwards they are imposed on interface as FIRE boundary conditions. The gas composition is taken into account, and, depending on the velocity sign, the turbulent quantities are either imposed or extrapolated ([14,16–19]).

Aimed at imposing no uniform profiles as FIRE boundary conditions, the averaged quantities determined by one-dimensional code are modified according to the profiles obtained by three-dimensional calculations, and are then used in the subsequent three-dimensional time-step analysis.

The hybrid methodology with the interface procedure has been applied at first to a simple geometry and the overall developed procedure has been validated ([13,14,16,17]).

Test Case

To show the capability of the multicode approach to predict the unsteady flow caused by the periodic opening and closing of the valves, the exhaust system of one cylinder four-stroke Diesel engine, whose main specifications are reported in Table 1, has been modeled and the results have been compared with those of experimental tests and another numerical technique. The configuration has been simulated by adopting zero-dimensional, one-dimensional, and three-dimensional models, used in different parts of the geometry, according to the scheme of Fig. 2.

The three-dimensional model as been used to investigate the behavior of the regions in which abrupt cross-sectional variations occur, giving rise to multidimensional phenomena. Only a three-dimensional modeling of such geometry allow to obtain realistic and accurate results, since the one-dimensional simulation is basically unable to account for the complex wave propagation.

Table 1 Main specifications of the investigated engine

Swept volume	426 cm ³
Bore	85 mm
Stroke	75 mm
Connecting rod length	117.5 mm
Compression ratio	19:1
Valve timing	e.v.o. 130 deg–e.v.c. 370 deg i.v.o. 350 deg–i.v.c. 590 deg

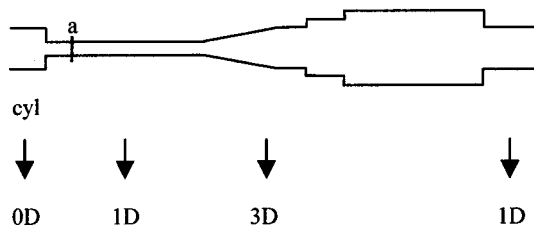


Fig. 2 Scheme of the simulated exhaust system

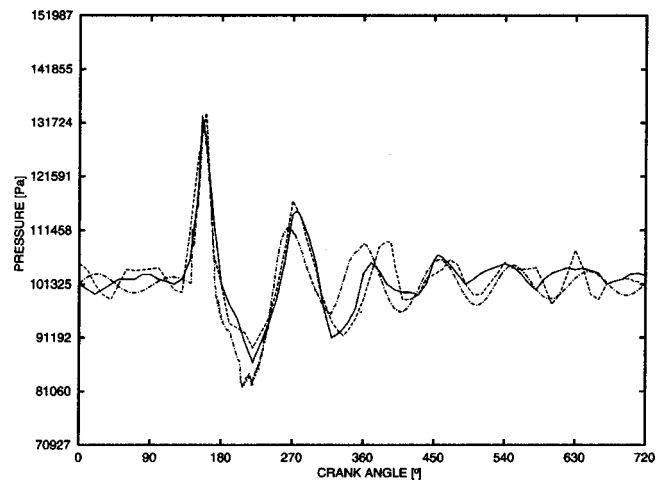


Fig. 3 Comparison between predicted and measured pressure histories at location a; engine speed 3140 rpm; computed (---), measured ([20]) (—), computed ([20]) (· · ·)

In Fig. 3 the pressure-crank angle history, referred to location a of the exhaust system (Fig. 2), is compared with the experimental measurements and the numerical simulation presented by Onorati [20]. In such one-dimensional simulation some corrective lengths have been used aimed at allowing a better prediction of the complex wave interaction at discontinuities and then at taking into account for the effective position of the plane of wave reflection.

Some amplitude differences appear in the graph, due to the influence of different loss coefficients adopted in both one-dimensional numerical approaches; these coefficients haven't been modified or tuned in order to ensure a better agreement with measured data since the aim of the present paper was not to reproduce the particular result but to assess the capability of the code to catch the main aspects of unsteady propagation which affect the engine performance, such as the pressure time history at the exhaust valve.

From the comparison between the simulated results, it is highlighted that the one-dimensional model, in which corrective

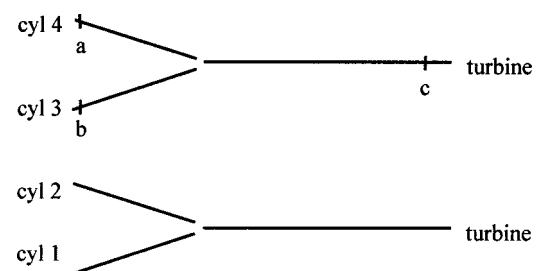


Fig. 4 Two-pulse exhaust system scheme

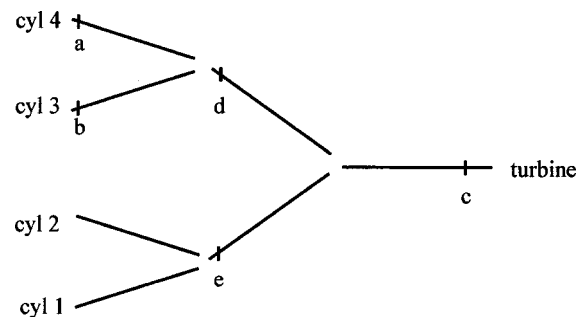


Fig. 5 Constant pressure exhaust system scheme

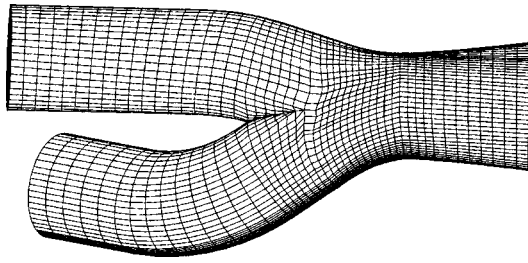


Fig. 6 Junction modeled as three-dimensional domain

lengths are included, is able to reproduce the results obtained by means of the hybrid scheme in the crank angle range where the pressure disturbances are characterized by peaks of larger value.

Simulation of a Turbocharged Engine

Two different exhaust system configurations of a four-cylinder turbocharged four-stroke, spark ignition engine have been investigated by adopting the multicode approach: two-branch junctions equipped with a twin-entry turbine (two-pulse scheme) and three two-branch junctions with a single entry turbine (constant pressure system).

The scheme of the former configuration is depicted in Fig. 4, while the latter one is represented in Fig. 5; the same size turbine housing has been applied to the two different exhaust systems and the same engine running conditions have been investigated (4200 rpm).

In both cases the thermodynamics in the turbine and cylinders has been analyzed by means of zero-dimensional models.

All ducts connecting the cylinders with the junctions and the junctions with the turbines have been investigated by using the one-dimensional method.

The analysis of the junctions by means of lumped parameter schemes allows to obtain global results but, due to the underlying hypotheses, a masking of the local behavior is produced. Therefore, one-dimensional investigations are not appropriate for assessing the effects of geometry (shape of the cross section, angle, and location of the junction, etc.) ([21]) in order to optimize the engine performance or require preliminary experimental tests to measure the loss coefficients that are deeply influenced by the geometry of the junction and the operative conditions (flow split ratio, inlet flow rate) ([22]).

Accurate predictions of the complex unsteady phenomena occurring inside such systems during the different parts of the engine cycle may be obtained by means of three-dimensional turbu-

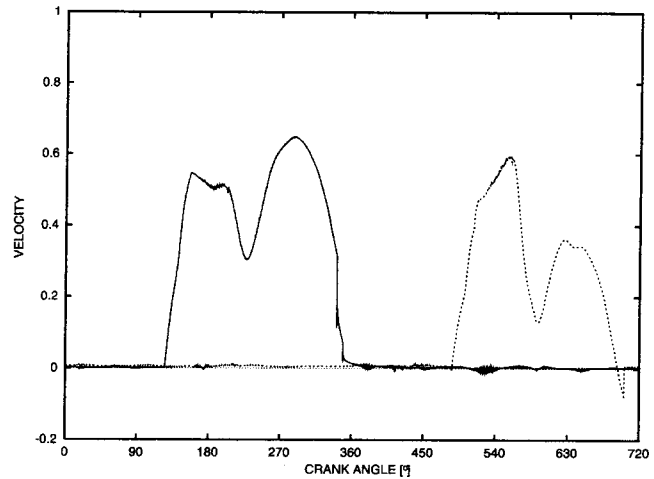


Fig. 8 Velocity traces at locations *a* — and *b* · · · (Fig. 4)

lent modeling of the flow. In [21,22], the comparison between experimental data and numerical predictions has demonstrated both the necessity and the capability of the three-dimensional model to simulate such complex geometries.

Following the previous considerations, all junctions have been modeled as three-dimensional domains, as depicted in Fig. 6.

Fixed monitoring positions along the simulated system, located next to cylinders, at the two-branch junctions, and in the duct connecting the junctions with the turbine inlet, have been considered. The related pressure and velocity versus crank angle histories are presented to point out how the different configurations affect the scavenging process in the cylinders and the turbine efficiency.

Monitoring positions *a* and *b* are placed next to cylinders 4 and 3, while *c* is placed in the duct connecting the junction with the turbine, close to the turbine inlet, as depicted in Figs. 4 and 5.

Figures 7 and 8 show the pressure and the velocity crank angle histories related to locations *a* and *b* next to cylinders 4 and 3, respectively, of the two-pulse system.

From the graphs, the mass flow coming from the cylinders during the exhaust period can be deduced and therefore the quality of

the scavenging process and the effect on the quantity of the discharge gas remaining in the cylinders after the exhaust valve closing can be evaluated.

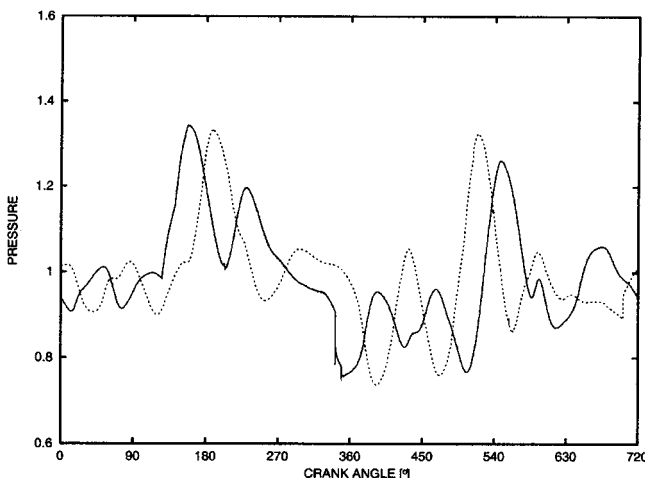


Fig. 7 Pressure traces at locations *a* — and *b* · · · (Fig. 4)

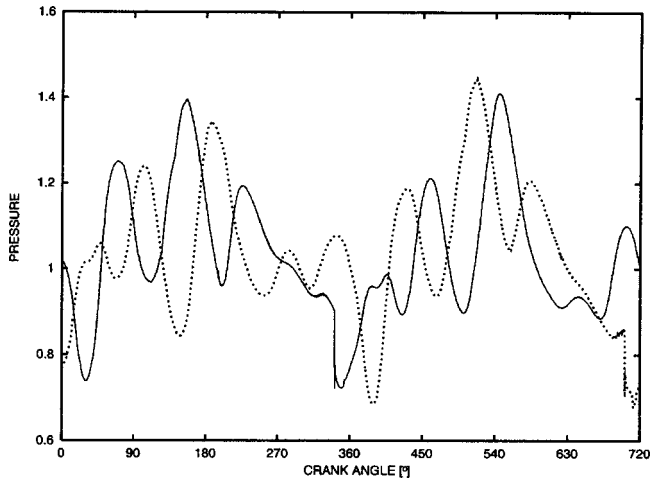


Fig. 9 Pressure traces at locations *a* — and *b* · · · (Fig. 5)

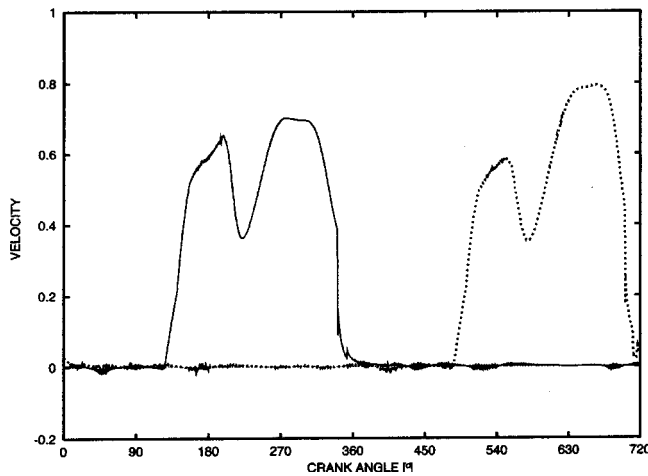


Fig. 10 Velocity traces at locations *a* — and *b* ··· (Fig. 5)

Such a value can be related to the exhaust system geometry and to the turbine opening, and can then be considered in order to optimize the exhaust configuration.

A comparison between Figs. 7 and 8 with the corresponding Figs. 9 and 10 highlights that in the wider configuration charac-

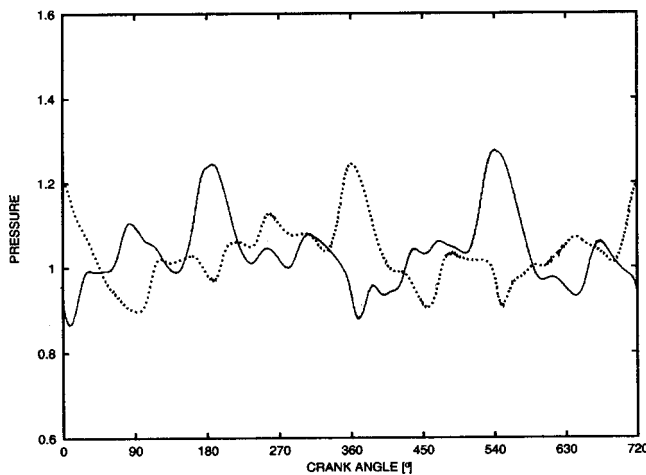


Fig. 11 Pressure traces at locations *d* — and *e* ··· (Fig. 5)

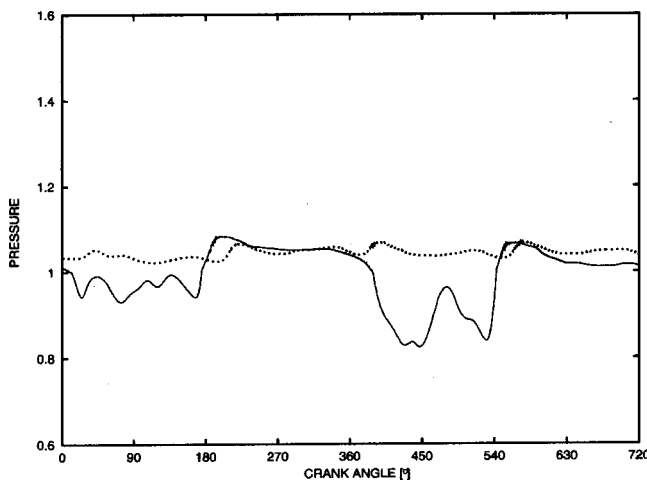


Fig. 12 Pressure traces at location *c* of Figs. 4 — and 5 ···

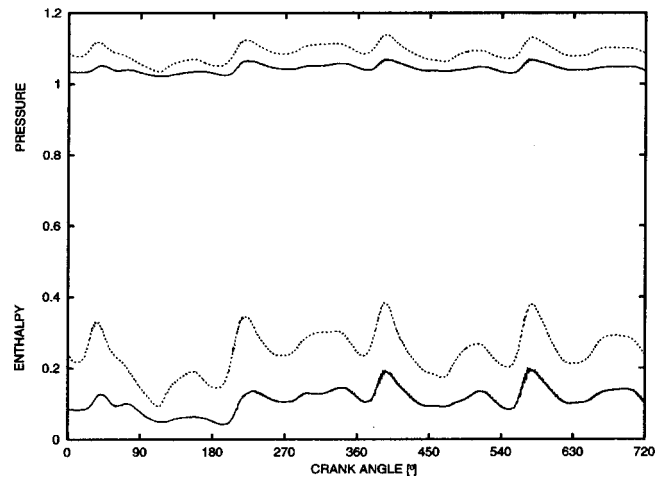


Fig. 13 Pressure and turbine isentropic specific enthalpy drop traces for constant pressure system in the basic configuration (—) and with a reduction of turbine inlet area (···), respectively

terizing the constant pressure system, the exhaust process of cylinder 3 is less affected by the discharge process of cylinder 4, as their crank angle traces are quite similar.

In Fig. 11 the pressure crank angle histories at locations *d* and *e*, near the two 2-branch junctions of the constant pressure system are plotted, pointing out the behavior of the engine blocks as each position exhibits peaks referred to the cylinder belonging alternately to one of the two engine blocks.

Figure 12 shows the pressure histories related to location *c* of Figs. 4 and 5 representing the flow conditions upstream the turbine and therefore it can be used to evaluate, together with the similar entropy history, the enthalpy level available in the turbine and then its performance, by means of thermodynamic models for both the exhaust systems configurations: the two-pulse and the constant pressure scheme. By adopting the latter one it appears that the conditions at the turbine entry, although not steady, exhibit less severe fluctuations with time than those one obtained with the former scheme, thus all the losses in the turbine resulting from unsteady flow are reduced, and high average turbine efficiency can be reached.

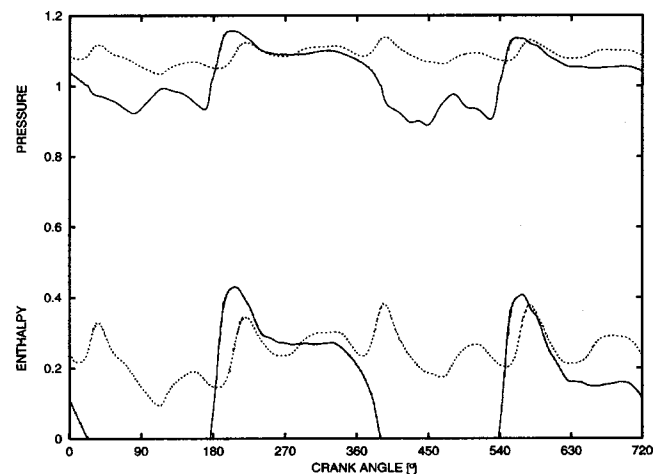


Fig. 14 Pressure and turbine isentropic specific enthalpy drop traces for two-pulse scheme (—) and constant pressure system (···), respectively

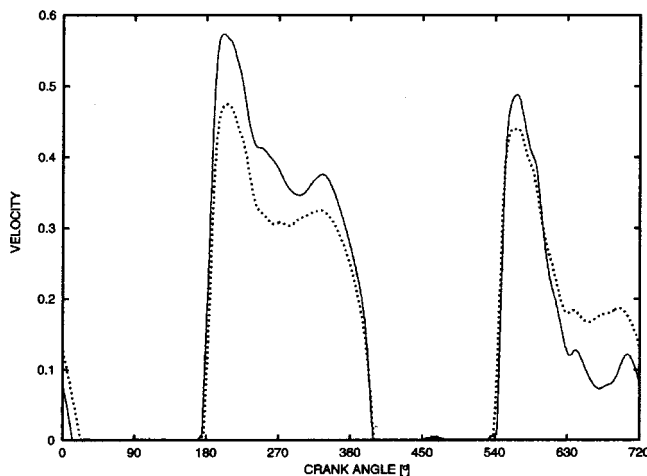


Fig. 15 Velocity traces at location c of Figs. 4 in the basic configuration (—) and with a reduction of turbine inlet area (· · ·), respectively

The disadvantage of the constant pressure system is due to the inability to suddenly follow the variation of the engine load or speed, as the available energy at the turbine increases only gradually due to the larger volumes.

The same exhaust system configuration depicted in Figs. 4 and 5 has been investigated by considering turbochargers with differ-

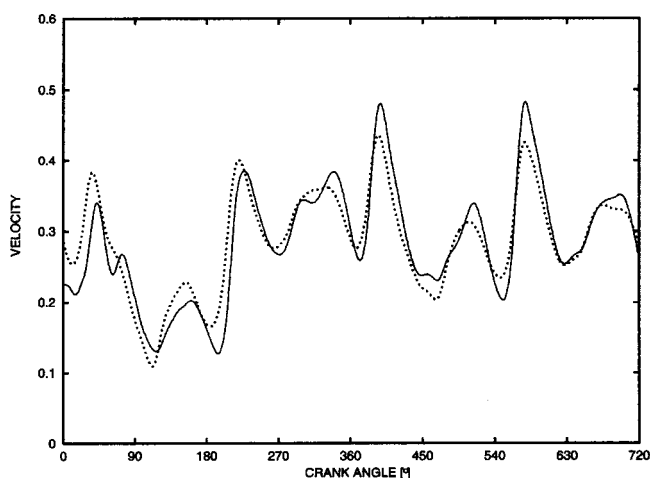


Fig. 16 Velocity traces at location c of Figs. 5 in the basic configuration (—) and with a reduction of turbine inlet area (· · ·), respectively

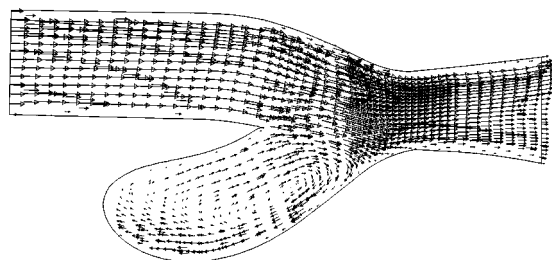


Fig. 17 Velocity field in the 2-branch junction during the discharge period of cylinder 4

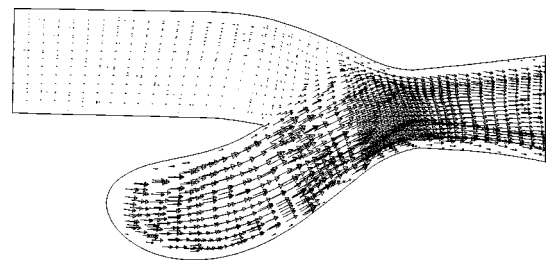


Fig. 18 Velocity field in the 2-branch junction during the discharge period of cylinder 3

ent inlet housings. The adoption of a turbine area closer than the basic configuration analyzed at the beginning, creates an increase of the back pressure that hinders the exhaust process from the cylinders but, increasing the exhaust manifold pressure and hence the pumping work during the exhaust process, increases the available energy at the turbine. This feature can be highlighted from Fig. 13 in which a comparison between pressure traces at the turbine inlet section and available isentropic specific enthalpy drop across the turbine are shown for the constant pressure system equipped with two different turbine areas.

In Fig. 14 the same thermodynamic quantities are depicted, referred to constant pressure and two-pulse exhaust system configuration, both equipped with the same size of turbine housing (area closer than the basic configuration). In the bottom of the figure the trace of the isentropic specific enthalpy drop of the pulse configuration is only referred to a single port.

Figures 15 and 16 show the flow velocity crank angle histories referred to the turbine inlet section, respectively, for the two-pulse and the constant pressure exhaust system configuration. In each figure a comparison between the traces due to different size of turbine area is reported.

It has to be noted that in the former diagram the velocity predictions do not overlap with each other, as they are referred only to a single port of the turbine.

The multicode investigation allows to visualize the complex three-dimensional fluid dynamic fields. The analysis of the velocity fields in the two-branch junction for different operating conditions, depicted in Figs. 17 and 18, provides useful information about the way of increasing the performance of the junction, in terms of both pressure drop reduction and filter effect for the backflow towards the cylinder, while it is going to complete the discharge period, altering its effectiveness.

All presented diagrams are dimensionless: pressure, enthalpy and velocity crank angle histories are referred to reference values.

Conclusions

The paper presents the potentiality of the hybrid scheme, based on the simultaneous use of different simulation schemes adapted to specific geometries, to analyze complete exhaust systems organized in any complex architecture.

Both zero-dimensional and one-dimensional models have been developed by the authors, while as three-dimensional code, the commercial package FIRE has been adopted; the validity of the proposed method is general, since it does not depend on the particular kind of multi-dimensional code used.

The hybrid methodology retains the advantages of detailed information of flow behavior as it is able to accurately predict, with the three-dimensional scheme, the propagation of the pressure waves through complex geometry, avoiding the significant limitations that a one-dimensional schematization always introduces, as well as fast processing typical of one-dimensional and zero-dimensional schemes devoted to the analysis of ducts and volumes.

Within the simulation of the exhaust systems of turbocharged engine, the hybrid approach, able to reduce both cost and time and

to analyze the overall system as sequence of regions, allows to easily deal with two different optimization procedures:

- of the system (length and diameter of ducts, different configuration and opening of turbine);
- of the junction geometry, to minimize the negative influence of the pressure wave on the scavenging process of cylinders.

The procedure may be furthermore applied in setting up and performing parametric analysis of the entry turbine housing, by simulating with the three-dimensional model the corresponding domain coupled with an easy and simple schematization of the complete exhaust system together with the engine.

References

- [1] Capobianco, M., Gambarotta, A., and Cipolla, G., 1989, "Influence of the Pulsating Flow Operation on the Turbine Characteristics of a Small Internal Combustion Engine Turbocharger," *I. Mech. E.*, Paper No. C372/019.
- [2] Capobianco, M., Gambarotta, A., and Cipolla, G., 1990, "Effect of Inlet Pulsating Pressure Characteristics on Turbine Performance of an Automotive Wastegated Turbocharger," *SAE Paper No.* 900359.
- [3] Capobianco, M., and Gambarotta, A., 1993, "Performance of a Twin-Entry Automotive Turbocharger Turbine," *ASME Paper No.* 93-ICE-2.
- [4] Yeo, J. H., and Baines, N. C., 1990, "Pulsating Flow Behavior in a Twin-Entry Vaneless Radial-Inflow Turbine," *I. Mech. E.*, Paper No. C405/004.
- [5] Capobianco, M., Gambarotta, A., and Zamboni, G., 1996, "Experimental Characterization of Turbocharging and EGR Systems in an Automotive Diesel Engine," *I. Mech. E.*, Paper No. C517/027.
- [6] Capobianco, M., Gambarotta, A., and Zamboni, G., 1998, "Controlling Turbocharging and EGR System to Improve Exhaust Aftertreatment Conditions in an Automotive Diesel Engine," *I. Mech. E.*, Paper No. C554/004.
- [7] Trenc, F., Bizjan, F., and Hribernik, A., 1998, "Influence of the Exhaust System on Performance of a 4-Cylinder Supercharged Engine," *ASME J. Eng. Gas Turbines Power*, **120**, pp. 855–860.
- [8] Rakopoulos, C. D., Andritsakis, E. C., Hountalas, D. T., 1995, "The Influence of the Exhaust System Unsteady Gas Flow and Insulation on the Performance of a Turbocharged Diesel Engine," *Heat Recovery Syst. CHP*, **15**, No. 1, pp. 51–72.
- [9] Onorati, A., Winterbone, D. E., and Pearson, R. J., 1993, "Comparison of the Lax-Wendroff Technique and the Method of Characteristics for Engine Gas Dynamic Calculations Using Fast Fourier Transform Spectra Analysis," *SAE Paper No.* 930428.
- [10] Winterbone, D. E., Nikpour, B., and Frost, H., 1991, "A Contribution to the Understanding of Turbocharger Turbine Performance in Pulsating Flow," *I. Mech. E.*, Paper No. C433/011.
- [11] Benson, R. S., 1974, "Nonsteady Flow in a Turbocharger Nozzleless Radial Gas Turbine," *SAE Paper No.* 740739.
- [12] Chen, H., and Winterbone, D. E., 1990, "A Method to Predict Performance of Vaneless Radial Turbines Under Steady and Unsteady Flow Conditions," *I. Mech. E.*, Paper No. C405/008.
- [13] Chiavola, O., 1999, "Sviluppo di modelli di simulazione delle prestazioni fluidodinamiche ed acustiche dei condotti di aspirazione e scarico di motori a combustione interna alternativi," Ph.D. thesis, University 'La Sapienza,' Rome.
- [14] Chiatti, G., and Chiavola, O., 1999, "Exhaust Flow Modelling in Multicylinder Engine by Coupling 3D FIRE With 1D Gasdynamic Code," *CDF User Meeting*, AVL LIST GmbH, Graz.
- [15] *FIRE Manual*, 1997, version 6.2.b, AVL LIST, GmbH Graz.
- [16] Chiatti, G., and Chiavola, O., 1999, "Integrated 3D and 1D Modelling of Ice Exhaust Systems Flow," *5th International Conference on High Tech Cars and Engine*, Modena.
- [17] Chiatti, G., and Chiavola, O., 1999, "Coupling 1D and 3D Gasdynamic Schemes to Model Engine Intake and Exhaust Systems," *ISABE XIV*, Florence.
- [18] Mouro, J., and Raulot, A., 1997, "Coupling of a 1D Gasdynamics Code With FIRE," *Proceedings of 3rd International FIRE User Meeting*, AVL LIST GmbH, Graz.
- [19] Prenninger, P., and Bartsch, P., 1997, "Application of AVL-BOOST-FIRE-Hybrid Calculation in Engine Optimization," *Proceedings of 3rd International FIRE User Meeting*, AVL LIST GmbH, Graz.
- [20] Onorati, A., 1995, "Numerical Simulation of Exhaust Flows and Tailpipe Noise of a Small Single Cylinder Diesel Engine," *Proceedings of the SETC*, Mecca, Milwaukee, WI.
- [21] Fu, H., Tindal, M. J., Watkins, A. P., and Yianneskis, M., 1992, "Computation of Three-Dimensional Turbulent Flows in a Pipe Junction With Reference to Engine Inlet Manifolds," *Proc. Inst. Mech. Eng.*, **206**, pp. 285–296.
- [22] Gori, A., Sassi, L., and Bidini, G., 1995, "Analisi 3D del flusso in giunzioni di condotti di scarico," *ATA vol.* **48**, No. 10, pp. 508–515.

Use of Detailed Chemical Kinetics to Study HCCI Engine Combustion With Consideration of Turbulent Mixing Effects

S.-C. Kong
Research Scientist

R. D. Reitz
Professor

Engine Research Center,
Department of Mechanical Engineering,
University of Wisconsin-Madison,
1500 Engineering Drive,
Madison, WI 53706

Detailed chemical kinetics was used in an engine CFD code to study the combustion process in HCCI engines. The CHEMKIN code was implemented in KIVA such that the chemistry and flow solutions were coupled. The reaction mechanism consists of hundreds of reactions and species and is derived from fundamental flame chemistry. Effects of turbulent mixing on the reaction rates were also considered. The results show that the present KIVA/CHEMKIN model is able to simulate the ignition and combustion process in three different HCCI engines including a CFR engine and two modified heavy-duty diesel engines. Ignition timings were predicted correctly over a wide range of engine conditions without the need to adjust any kinetic constants. However, it was found that the use of chemical kinetics alone was not sufficient to accurately simulate the overall combustion rate. The effects of turbulent mixing on the reaction rates need to be considered to correctly simulate the combustion and heat release rates. [DOI: 10.1115/1.1413766]

Introduction

In the homogeneous charge compression ignition (HCCI) engine, a homogeneous mixture is formed in the combustion chamber and the mixture is compression-ignited. The HCCI engine is an alternative to the conventional gasoline or diesel engines. In fact, HCCI could be regarded as a type of operating mode rather than a type of engine. The HCCI mode can be obtained in a conventional two or four-stroke gasoline or diesel engines to run in a full-time or part-time HCCI mode.

The main objective of HCCI combustion is to reduce soot and NO_x emissions while maintaining high fuel efficiency at part-load conditions ([1]). In HCCI engines, the mixture auto-ignites in multiple spots and then is consumed quickly without discernable flame propagation ([2,3]). The mixture is both lean and homogeneous so that little NO_x and soot are formed.

However, there are still challenges associated with the successful operation of HCCI engines. The challenges include the control of ignition and combustion phasing, reduction of high HC and CO emissions, and the utilization of EGR, etc. Nonetheless, the fundamental understanding of the combustion process in HCCI engines is still limited, and there has been increasing number of research papers on HCCI ([4]).

Due to the fact that the HCCI mixture is not burned by a discernable flame, the physics of flow-combustion interactions in a typical burning flame are considered to be absent. However, experiments still indicated the local fluctuations recorded by Raman scattering due to the local fuel inhomogeneity ([3]). The features of inhomogeneity could become important in the high EGR cases. In fact, it has not been successful to use chemical kinetics alone to simulate the combustion by assuming a uniform temperature distribution, i.e., the single-zone model. The high temperatures in the center of the chamber are responsible for the ignition. To account for the temperature stratification, a multizone model was used which divided the entire mixture into several groups ([5,6]). The effects of engine flow field on combustion are still not considered. On the other hand, due to the possible inhomogeneity in mixture

and temperature distribution, it has been suspected that the turbulence also has effects on the combustion rates ([7,8]). It is still a question whether the mixture is completely homogeneous and the turbulent mixing has no effect on the heat release rates.

This paper presents a model to simulate the HCCI combustion by combining detailed chemical kinetics and engine CFD computations. The present model allows to investigate the interactions between chemical kinetics and engine flows in the HCCI engine.

Model Formulation

The CHEMKIN chemistry solver ([9]) is integrated into the KIVA code ([10]) for solving the detailed chemistry during multidimensional engine simulations. The KIVA code provides CHEMKIN the species and thermodynamic information of the computational cells, and the CHEMKIN code returns the new species information and energy release after solving the chemistry. The chemistry and flow solutions are then coupled.

In the current model, if the CHEMKIN solutions were solely used in the KIVA code, the species conversion rates would be regarded as *kinetics-controlled*. However, the use of kinetics-controlled reactions usually results in a very fast combustion rate ([7,8]). It is suspected that there are inevitable inhomogeneities in the mixture, and in the actual engine process the fuel and the oxidizer do not have enough time to mix down to the molecular level. Therefore, the reactions could be partly controlled by the breakup of turbulent eddies which results in a slower reaction rate.

In this paper, a new reaction rate for each species has been formulated which incorporates the effects of both chemical kinetics and turbulent mixing. The premise of the model is that the reaction rate is mainly determined by a kinetic timescale and a turbulent timescale. The kinetic timescale is the time needed for a species to reach its equilibrium state under perfectly mixed conditions. The turbulent timescale is the time of eddy breakup in order to mix both the fuel and oxidizer supposing that inhomogeneities exist in the mixture. In fact, the inhomogeneities could be caused by the partial mixing of combustion radicals and products but not only the fuel and oxidizer themselves. The kinetic timescale is different for each species while the turbulent timescale is the same for all species. The unknowns include the equilibrium concentration and the kinetic timescale of each species and the model is expressed as

Contributed by the Internal Combustion Engine Division of THE AMERICAN SOCIETY OF MECHANICAL ENGINEERS for publication in the ASME JOURNAL OF ENGINEERING FOR GAS TURBINES AND POWER. Manuscript received by the ICE Division, Sept. 2000; final revision received by the ASME Headquarters, Mar. 2001. Editor: D. N. Assanis.

$$\omega_i = \frac{Y_i^* - Y_i}{\tau_{\text{kin},i} + \tau_{\text{turb}}} \begin{cases} Y_i : \text{current concentration} \\ Y_i^* : \text{equilibrium concentration} \\ \tau_{\text{kin},i} : \text{kinetic timescale} \\ \tau_{\text{turb}} : \text{turbulent timescale} \sim k/\varepsilon. \end{cases} \quad (1)$$

If turbulent effects on the reaction rate are excluded, Eq. (1) can be simplified to a kinetics-controlled reaction rate, $\omega_{\text{kin},i}$, as

$$\omega_{\text{kin},i} = \frac{Y_i^* - Y_i}{\tau_{\text{kin},i}}. \quad (2)$$

The kinetics-controlled reaction rate can be rewritten in terms of the CHEMKIN solutions as

$$\omega_{\text{kin},i} = \frac{Y'_i - Y_i}{dt} = \frac{\Delta Y_i}{dt} \quad (3)$$

where dt is the numerical timestep, and Y_i and Y'_i are the species concentrations before and after the CHEMKIN model is called, respectively. A relation between the kinetic timescale and the equilibrium concentration of each species is then obtained by equating Eqs. (2) and (3).

$$\tau_{\text{kin},i} = \frac{Y_i^* - Y_i}{\Delta Y_i} dt \quad (4)$$

However, it is impractical to solve the equilibrium concentration and the kinetic timescale for each individual species considering that the reaction mechanism may involve hundreds of species and reactions. Two assumptions are made to help solve the equation. First, the kinetic timescale for all the species is assumed to be equal to that of the fuel. Second, the equilibrium concentration of the fuel is assumed to be zero since the fuel is likely to react into intermediate species soon after the reaction has started even in rich conditions. Therefore, the kinetic timescale and equilibrium concentration of each species can be derived in terms of the CHEMKIN solutions as

$$\left. \begin{matrix} \tau_{\text{kin},i} = \tau_{\text{kin,fuel}} \\ Y_f^* \rightarrow 0 \end{matrix} \right\} \Rightarrow \begin{cases} \tau_{\text{kin}} = (-Y_f/\Delta Y_f)dt \\ Y_i^* - Y_i = (-Y_f/\Delta Y_f)\Delta Y_i. \end{cases} \quad (5)$$

Notice that the terms ΔY_f and ΔY_i are the concentration changes of the fuel and species i , respectively, obtained from CHEMKIN calculations. However, in the case of fuel concentration approaching to zero, the kinetic timescale of CO is used as the rate limiting kinetic time since CO is transformed to CO_2 and contributes significantly to the energy release after fuel consumption is completed. In two-stage auto-ignition process, excitation will occur after fuel consumption is completed and zero fuel concentration will predict infinite fast kinetics. In terms of model formulation, the maximum of the kinetic timescales of fuel or CO is taken as the resulting kinetic timescale.

By combining Eqs. (1) and (5), a new formula to compute the new species at the current time-step, Y_i^{n+1} , can be obtained as

$$Y_i^{n+1} - Y_i^n = \omega_i dt = \frac{(-Y_f/\Delta Y_f)\Delta Y_i}{\tau_{\text{kin}} + \tau_{\text{turb}}} dt = \frac{\tau_{\text{kin}}}{\tau_{\text{kin}} + \tau_{\text{turb}}} \Delta Y_i. \quad (6)$$

The formula includes the effects of both chemical kinetics and flow turbulence on the reaction rate. The model is also formulated such that the turbulence starts to have effects after ignition has occurred. Ignition occurs at the molecular level and the turbulence will not have effects on the combustion until the reaction zones grow to a size comparable to that of the turbulent eddy. From Eq. (6), if the turbulent timescale is neglected, the solutions remain kinetics-controlled.

The CHEMKIN utilities are used for every computational cell at every time-step. The present model does not require the empiricism as in the multizone model such as determining the mass percentage of each reaction zone and the interactions between zones ([6]). The thermal stratification has been considered by the nature of multidimensional KIVA computations. It should also be

noticed that the interactions of engine turbulence and combustion have already been considered by integrating CHEMKIN to KIVA. The turbulence affects combustion by flow motion, property transport, heat transfer, etc. The emphasis of Eq. (6) is the incorporation of the mixing concept in the reaction rate in addition to the chemical kinetics itself.

The computations started at intake valve closure and assumed a uniform distribution of mixture properties. The initial mixture temperature was adopted from the results of engine heat release rate analysis. The RNG k - ε model was used for turbulence modeling and the piston-ring crevice flow were also modeled. For the direct-injection diesel case, the fuel spray atomization was modeled using the WAVE breakup model ([11]).

Results

CFR HCCI Engine. The current model was first applied to simulate a premixed CFR engine running in HCCI mode with the operating conditions listed in Table 1 ([12]). The intake charge was heated to ensure successful autoignition. An ethylene (C_2H_4) reaction mechanism consisting of 69 species and 387 reactions was used ([13]).

First, the simulations excluded the effects of turbulent mixing on the reaction rates. The results are shown in Figs. 1 and 2 as the cases denoted “kinetics.” As can be seen, the computations gave a steep rise in cylinder pressure, indicating that the kinetics-controlled reaction rates results in a faster combustion rate. Effects of turbulent mixing on reaction rates were then considered as shown in the cases denoted “mixing effects.” Ignition timings were not changed as they were determined by the chemical kinetics alone. As can be seen, better agreement in the combustion phasing was obtained with the incorporation of mixing effects in the reaction rates.

Table 1 Conditions of the CFR engine under HCCI mode

Engine Specifications	Bore x Stroke: 83.1 x 114.3 mm Conn. Rod Length: 254 mm Intake Valve Closure: 130 BTDC Fuel: C_2H_4	
	Case 1	Case 2
rpm	600	1200
ϕ	0.40	0.24
CR	6.3	10.5
Swirl Ratio	1.8	8.0
Inlet Temperature	703 K	688 K

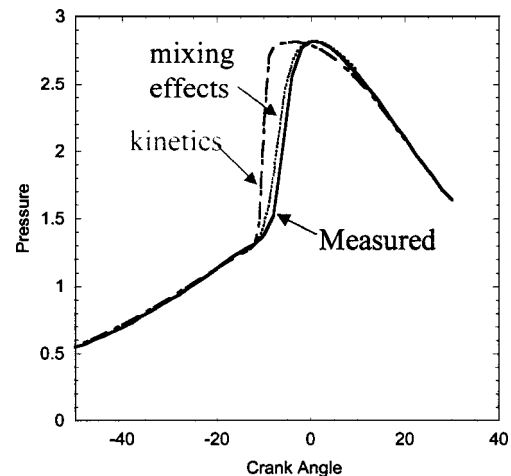


Fig. 1 Results of Case 1 for the CFR HCCI engine in Table 1

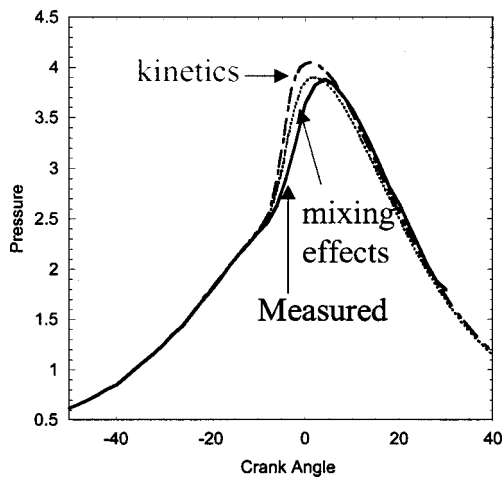


Fig. 2 Results of Case 2 for the CFR HCCI engine in Table 1

The computed in-cylinder temperature contours of Case 1 around the time of ignition are shown in Fig. 3. Ignition was observed to occur in the middle of the combustion chamber where the temperatures were relatively high. The results agree with the common understanding of the HCCI combustion. It should be noted that no modification to the kinetics constants was needed for both cases.

Volvo-Converted HCCI Engine. A six-cylinder Volvo TD100 series diesel engine was converted to operate only on a single cylinder at the HCCI mode ([14]). A flat-top piston was used to give a simple pancake combustion chamber. The engine was supercharged to give a high in-cylinder pressure and temperature to ensure autoignition. The engine conditions included three different boost pressures. The intake air was preheated with an electrical heater and the temperature was adjusted to give a reasonable combustion phasing. The fuel was natural gas which, however, also contained a non-negligible content of other higher hydrocarbon fuels. The fuel composition and engine conditions are listed in Table 2.

Since the natural gas contained other higher order of hydrocarbons up to n-butane, a reaction mechanism including reactions up to C_4 was used. The reaction mechanism contained 211 species and 1174 reactions ([13]). The computations used a two-dimensional mesh and started from intake valve closure assuming a homogeneous distribution of temperature and mixture initially.

Results of the naturally aspirated case are shown in Figs. 4 and 5. It can be seen that the cylinder pressure and heat release rate were predicted reasonably well by the current model and reaction

Table 2 Conditions of Volvo-converter HCCI engine

Engine Specification	Volvo TD 100 Series Diesel		
	Bore x Stroke: 120.65 x 140 mm		
	Conn. Rod Length: 260 mm		
	Displacement Vol: 1600 c.c.		
	Compression Ratio: 19		
	Intake Valve Closure: 13 ABDC		
	Speed: 1000 rpm		
Fuel—Natural Gas	Composition	Vol. %	Mass %
	Methane	91.1	81.0
	Ethane	4.7	7.9
	Propane	1.7	4.2
	n-Butane	1.4	4.7
	Nitrogen	0.6	0.9
	CO ₂	0.5	1.2
Boost Pressure	0 bar	1 bar	2 bar
Intake Temperature	151 C	79 C	50 C
ϕ	0.379	0.292	0.260

mechanism. However, the kinetics-controlled reactions still gave a faster combustion rate than the measurements. A better level of agreement was obtained if the effects of turbulent mixing were used to modify the reaction rates.

Results of the boosted cases are shown in Figs. 6–9. The computed results also indicate that the mixing effects need to be considered in the reaction rates to give a better combustion phasing prediction. It should be noted that none of the kinetic constants needed to be adjusted from the original mechanism for all three cases. It is apparent that a good reaction mechanism is essential to the correct prediction of the ignition.

Caterpillar-Converted HCCI Engine. The model was further applied to simulate HCCI combustion in a Caterpillar single-cylinder engine using early injection scheme ([15]). The engine is a direct-injection heavy-duty diesel engine as described in Table 3. Advanced injection timing was used to ensure a homogeneous mixture at the time of combustion.

A three-dimensional 60-deg computational sector was used considering that the injector had six nozzle holes. The computations started from intake valve closure with the initial conditions obtained from the one-dimensional cycle simulation results. The reactions used an n-heptane mechanism consisting 40 species and 165 reactions which has been validated in constant pressure ignition delay predictions for diesel fuels ([16]).

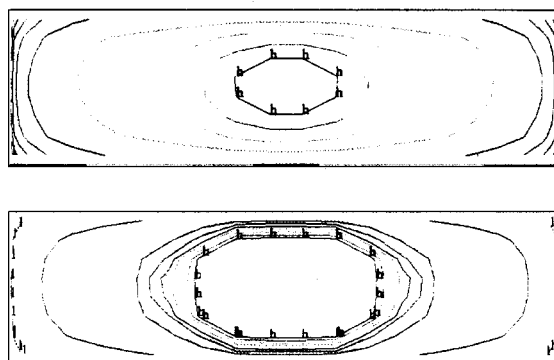


Fig. 3 Computed in-cylinder temperature contours of Case 1 around the ignition timing

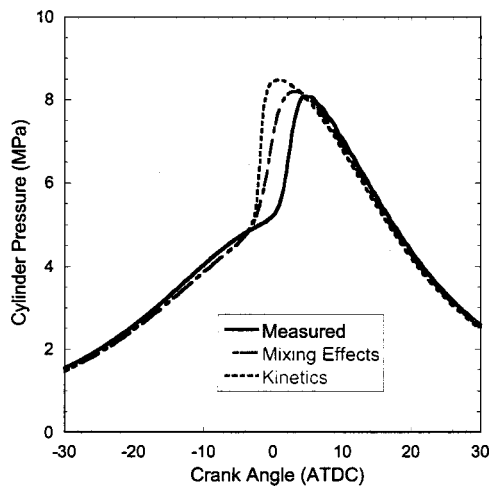


Fig. 4 Comparisons in cylinder pressure for the 0-bar boost case

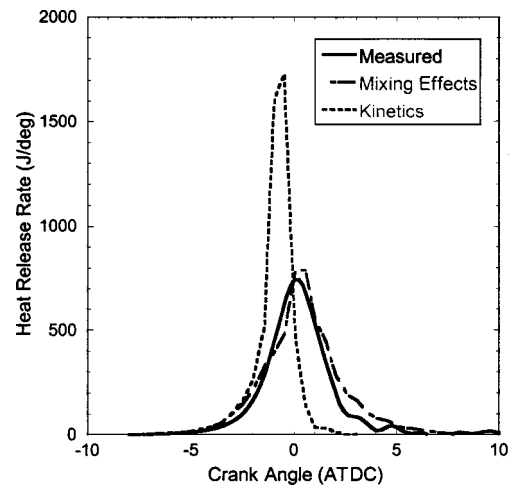


Fig. 7 Comparisons in heat release rate for the 1-bar boost case

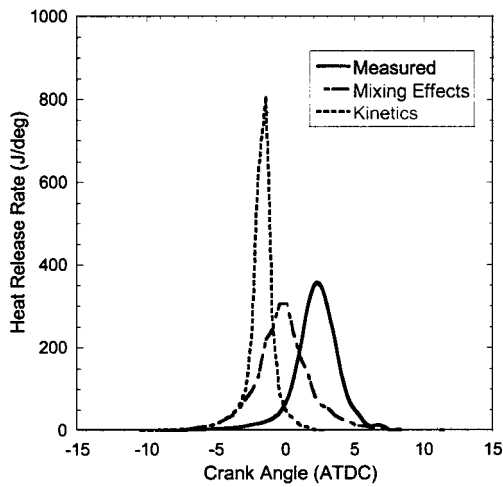


Fig. 5 Comparisons in heat release rate for the 0-bar boost case

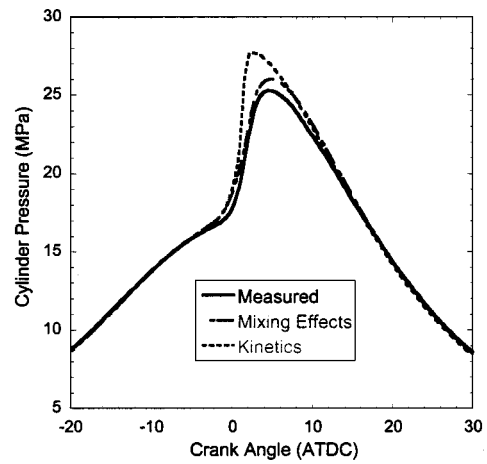


Fig. 8 Comparisons in cylinder pressure for the 2-bar boost case

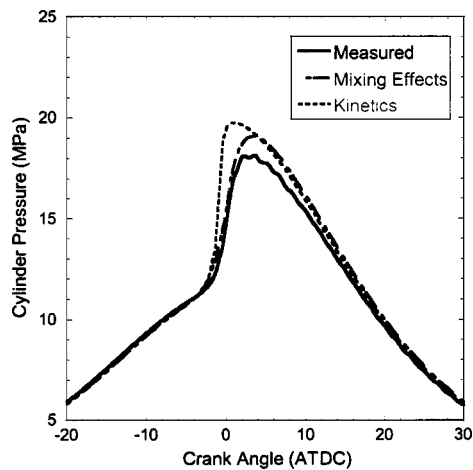


Fig. 6 Comparisons in cylinder pressure for the 1-bar boost case

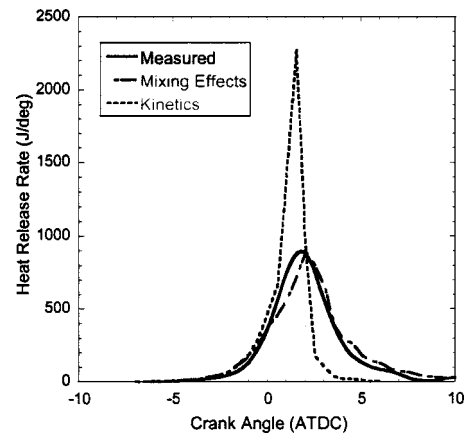


Fig. 9 Comparisons in heat release rate for the 2-bar boost case

Table 3 Caterpillar engine specifications

Engine Specification	Caterpillar SCOTE (single-cylinder oil test engine) Bore x Stroke: 137.2 x 165.1 mm Conn. Rod Length: 263.0 mm Compression Ratio: 15.6 Displacement: 2.44 liters Quiescent Chamber
Injection system	Common Rail
Injection Pressure	90 MPa
Load	25%
SOI	-44 ATDC
Speed	821 rpm
Intake Temperature	39 C
Intake Pressure	14.9 psia

The computed results are compared to the experimental measurements in Figs. 10 and 11. The results show that the ignition timing was predicted correctly without the need to modify any kinetic constants in the original reaction mechanism. Two-stage ignition characteristics were also predicted by the model as can be seen from the early rise in both the pressure and heat release rate curves. However, as in the previous engine comparisons, the use of kinetics-controlled reaction rates still results in too fast combustion. The effects of turbulent mixing on the reaction rates need to be considered to achieve better agreement in the combustion phasing.

In this case ($\text{SOI} = -44\text{ATDC}$), since the fuel was injected very early when the in-cylinder gas temperature was relatively low, most of the liquid fuel impinged on the piston crown before they vaporized. The spray drops and fuel vapor distributions would determine the ignition location and subsequent combustion process. Figure 12 shows the in-cylinder temperature and droplet distributions on the midplane of the fuel spray at -10ATDC when combustion already started. It can be seen that the mixture is not as homogeneous as expected for this particular advanced injection case. Other injection schemes may need to be explored to achieve a more adequate HCCI combustion mode.

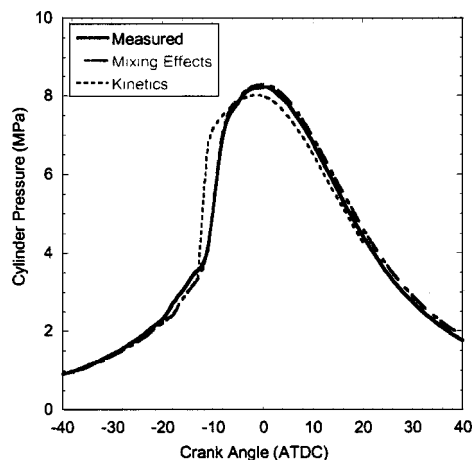


Fig. 10 Cylinder pressure results of the Caterpillar engine at HCCI mode

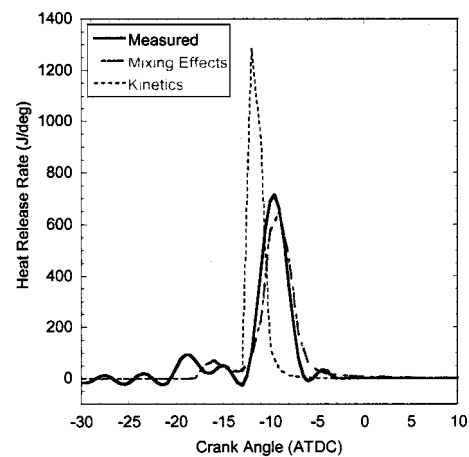


Fig. 11 Heat release rate data of the Caterpillar engine at HCCI mode

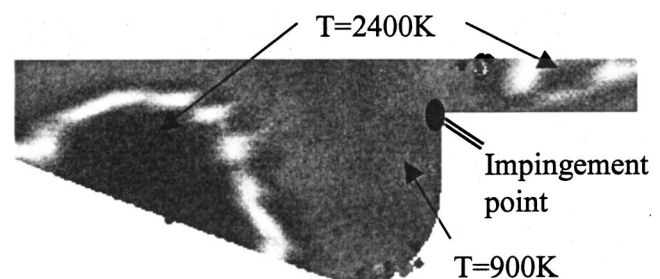


Fig. 12 In-cylinder droplet distribution and temperature contours at the midplane of the fuel spray at -10ATDC

Summary

Detailed chemical kinetics was implemented into an engine CFD code to simulate HCCI combustion. The engine turbulence and chemical reactions are coupled by incorporating the CHEMKIN code into the KIVA code. Reaction mechanisms developed from fundamental chemistry studies were used unmodified in the present study.

Computed cylinder pressures and heat release rates were compared to experimental measurements. The results show that the ignition timings were predicted correctly using the detailed chemistry without the need to adjust model constants. However, the kinetics-controlled reaction rates resulted in too fast combustion, and the effects of turbulent mixing needed to be considered to give a better agreement in the combustion phasing with the experiments.

The present study also shows that two-dimensional simulations are adequate for cases in which a homogeneous mixture is introduced into the cylinder. For direct-injection configurations, the spray dynamics need to be modeled in a truly three-dimensional manner to better account for the mixture distribution which, in turn, will greatly affect the subsequent ignition location and combustion process.

Acknowledgments

The authors thank the financial support of DOE/Sandia National Laboratories and the Army Research Office. The experimental data provided by M. Christensen and B. Johansson at the Lund Institute of Technology and by C. Marriott at the University of Wisconsin-Madison are very much appreciated.

References

- [1] Thring, R. H., 1989, "Homogeneous-Charge Compression-Ignition (HCCI) Engines," SAE Paper 892068.
- [2] Aoyama, T., Hattori, Y., Mizuta, J., and Sato, Y., 1996, "An Experimental Study on Premixed-Charge Compression-Ignition Gasoline Engine," SAE Paper 960081.
- [3] Richter, M., Franke, A., Alden, M., Hultqvist, A., and Johansson, B., 1999, SAE 1999-01-3649.
- [4] Stanglmaier, R. H., and Roberts, C. E., 1999, "Homogeneous Charge Compression Ignition (HCCI): Benefits, Compromises, and Future Engine Applications," SAE Paper 1999-01-3682.
- [5] Flowers, D., Aceves, S., Smith, R., Torres, J., Girard, J., and Dibble, R., 2000, "HCCI in a CFR Engine: Experimental and Detailed Kinetic Modeling," SAE Paper 2000-01-0328.
- [6] Aceves, S. M., Flowers, D. L., Westbrook, C. K., Smith, J. R., Pitz, W., Dibble, R., Christensen, M., and Johansson, B., 2000, "A Multi-Zone Model for Prediction of HCCI Combustion and Emissions," SAE Paper 2000-01-0327.
- [7] Kong, S. C., Ayoub, N. A., and Reitz, R. D., 1992, "Modeling Combustion in Compression Ignition Homogeneous Charge Engines," SAE Paper 920512.
- [8] Maigaard, P., Mauss, F., and Kraft, M., 2000, "Homogeneous Charge Compression Ignition Engine: A Simulation Study on the Effects of Inhomogeneities," ASME Paper 2000-ICE-275.
- [9] Kee, R. J., Rupley, F. M., and Miller, J. A., 1989, "CHEMKIN-II: A Fortran Chemical Kinetics Package for the Analysis of Gas-Phase Chemical Kinetics," Sandia Report, SAND 89-8009.
- [10] Amsden, A. A., 1997, "KIVA-3V: A Block-Structured KIVA Program for Engines With Vertical or Canted Valves," Los Alamos Report LA-13313-MS.
- [11] Patterson, M. A., and Reitz, R. D., 1998, "Modeling the Effects of Fuel Spray Characteristics on Diesel Engine Combustion and Emissions," SAE Paper 980131.
- [12] Boggs, D. L., and Borman, G. L., 1991, "Calculation of Heat Flux Integral Length Scales From Spatially-Resolved Surface Temperature Measurements in an Engine," SAE 910721.
- [13] Curran, H. J., Gaffuri, P., Pitz, W. J., and Westbrook, C. K., 1998, "A Comprehensive Modeling Study of N-Heptane Oxidation," *Combust. Flame*, **114**, pp. 149–177.
- [14] Christensen, M., Johansson, B., AmnJus, P., and Mauss, F., 1998, "Supercharged Homogeneous Charge Compression Ignition," SAE Paper 980787.
- [15] Marriott, C., 2000, master research project, University of Wisconsin-Madison, in progress.
- [16] Nordin, N., 1998, "Numerical Simulations of Non-Steady Spray Combustion Using a Detailed Chemistry Approach," thesis for the degree of Licentiate of Engineering, Department of Thermo and Fluid Dynamics, Chalmers University of Technology, Goteborg, Sweden.

P. A. Lakshminarayanan

N. Nayak

S. V. Dingare

A. D. Dani

Kirloskar Oil Engines Ltd.,
Research and Engineering Department,
L. Kirloskar Road,
Pune-411003,
Maharashtra, India

Predicting Hydrocarbon Emissions From Direct Injection Diesel Engines

Hydrocarbon (HC) emissions from direct injection (DI) diesel engines are mainly due to fuel injected and mixed beyond the lean combustion limit during ignition delay and fuel effusing from the nozzle sac at low pressure. In the present paper, the concept has been developed to provide an elegant model to predict the HC emissions considering slow burning. Eight medium speed engines differing widely in bores, strokes, rated speeds, and power were studied for applying the model. The engines were naturally aspirated, turbocharged, or turbocharged with intercooling. The model has been validated by collecting data on HC emission, and pressures in the cylinder and in the fuel injection system from the experimental engines. New coefficients for the correlation of HC with operating parameters were obtained and these are different from the values published earlier, based on single-engine experiments. [DOI: 10.1115/1.1456091]

Introduction

Hydrocarbon (HC) emissions from diesel engines are due to several factors. The fuel leaned beyond flammability limits (Greeves et al. [1]) bulk quenching during expansion, fuel effusing from nozzle sac after completion of injection (Yu et al. [2]) are the most important reasons. Wall wetting, cyclic misfire, and local undermixing influence the HC ([2]) only under extreme operating conditions like long idling or cold starting. On the other hand, in spark ignition engines, the emission of HC (Dent and Lakshminarayanan, [3]) is mainly due to quenching near the cylinder walls and crevices like adsorption and desorption by oil film on the cylinder walls, and quenching. The earliest detailed work of Yu et al. [2] on diesel engines dealt with design parameters that have decisive influence on the HC. The mechanism of HC formation was studied by looking at the structure of spray, in an engine of bore of 140 mm. In their work, systematic experiments were conducted to compare the experimental results with the estimated HC. Except for the effect of engine speed, influence of all the operating parameters was satisfactorily explained. The temporal factor due to speed was not having any effect in the model as opposed to the experimental results because reaction of overmixed fuel was not considered. Ikegami et al. [4] carried out a schematic study of particulate and hydrocarbon from a direct injection diesel engine by sampling from a mini dilution tunnel. Results show that HC concentrations are greatly affected by ignition delay or by temperature in the engine cylinder. Nakayama et al. [5] studied the effects of valve timings and valve lift systems on HC in a cold start condition on an engine of bore 85 mm. Tsunemoto et al. [6] studied the effects of combustion and injection systems on HC and particulate emissions on an engine of bore 102 mm. Detailed parametric studies were made by varying the aspect ratio of the piston cavity, the swirl at top dead center (TDC), the start of injection, and the excess air fuel ratio. HC emissions were found invariant for swirl and the shapes of the cavity if they were optimized for smoke and fuel consumption. Most importantly, a good empirical correlation was arrived at between the particulate matter and the Bosch smoke number. An interesting work by Dent [7] considered the influence of the mixing scale of the shear flow generated by the spray, on HC emissions. All the above work

showed that for the usual operating conditions of speed and load, HC emissions from a reasonably optimized engine depends on the fuel injected and overmixed during ignition delay. The fuel evaporating from the sac (Greeves et al. [1]) after injection and reacting slowly during expansion stroke adds to the HC emissions.

In the present work, data were collected from a variety of engines of different bores and strokes at widely ranging operating conditions of speed and load. These engines were naturally aspirated, or turbocharged, or turbocharged with aftercooling. A semi-empirical phenomenological study was successfully made for HC emissions from a direct injection diesel engine. The unburned HC was correlated with the overmixed fuel during the ignition delay and the fuel effusing from the sac that undergoes slow burning in the expansion stroke. The overmixed fuel is calculated from the measured instantaneous pressures in the nozzle and in the cylinder in conjunction with the effective flow area derived from the measured needle lift. Slow reaction of the overleaned fuel was considered during the characteristic time of ignition delay. The ratio of observed raw HC emissions in the exhaust to the total quantity of fuel injected is defined as the exhaust indicated hydrocarbons, EIHC or specific hydrocarbon, SHC.

Experiments

Experimental Setup. A schematic diagram of the experimental setup is shown in Fig. 1. The cylinder pressure was measured using an uncooled AVL piezoelectric pressure transducer of type GM11D in engines A to D. Here the length of the duct leading the pressure from the cylinder to the transducer was very short. In the engines E and F the duct was 2 mm in diameter and about 5 cm long and the AVL cooled pressure transducer of type GM32D was used. The line pressure was measured using a strain gage type pressure transducer from AVL of type 31DP2000-2.0, GG0443. The needle lift was measured using by building in a linearly variable differential transformer (LVDT) in the injector at the fuel injection equipment manufacturer, MICO, Bangalore. The crank angle position was sensed using an AVL encoder of type 364-angle encoder. Here, a disk divided into 360 parts, and infrared light sources with an optical sensor are in a sealed housing with the shaft extending from the encoder. The stator of the encoder is fixed to the engine crankcase rigidly and the shaft is coupled to the crank pulley. Each degree of crank angle is further divided into four equal parts electronically to increase the resolution. The engine is loaded using an eddy current brake. All the transient signals from different transducers and the encoder are fed into an

Contributed by the Internal Combustion Engine Division of THE AMERICAN SOCIETY OF MECHANICAL ENGINEERS for publication in the JOURNAL OF ENGINEERING FOR GAS TURBINES AND POWER. Manuscript received by the ICE Division, July 2000; final revision received by the ASME Headquarters, October 2001. Editor: D. N. Assanis.

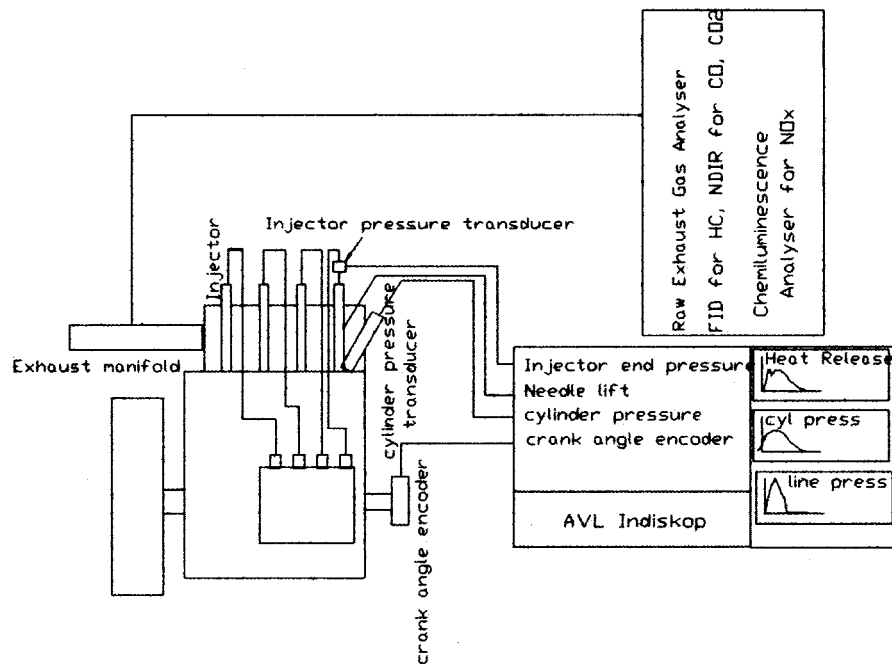


Fig. 1 Experimental setup

AVL Indiskop of type 647 version MIP A/E 7.0. Here there are signal conditioners and amplifiers and a computer to process all the signals for calculating thermodynamics like heat release rate and other details like the duration of injection, ignition delay and peak values of various pressures.

The raw exhaust gas is sampled and led by a heated line to the AVL exhaust gas analysis system consisting of NGA 2000 FID HHC analyzer, NGA 2000 Chemiluminescent HNO/HNO_x analyzer, and NGA 2000 NDIR CO analyzer. The unburned hydrocarbon is measured using a flame ionization detector (FID). Here the exhaust gas is burned in a clean hydrogen flame. The current due to carbon ions in the flame between two electrodes is detected and correlated against the current measured when a sample of air with known propane composition was passed through the FID.

Injection Characteristics and the Indicated Diagrams. Engines A to G in Table 1 were fully instrumented for needle lift, pressures in the injection line and in cylinder. Table 2 explains the details of FIE used on the engine. To cover a wide range of engines in the study of HC emissions, the engine used by Yu et al. [2] was also studied using the integrated parameters such as ignition delay, nozzle hole size, and injected quantity. In Tables 1, 2, and 3, it is mentioned as engine H. Figure 2 shows typical traces

of line pressure, cylinder pressure, needle lift, and apparent heat release of the turbocharged engine, B at 90 percent load.

All the engines from A to G were of modern type designed for low emissions of NO_x and hydrocarbons. The compression ratio was relatively higher to enable injection delayed with respect to the previous generation of engines to which engine G belongs. The decrease in ignition delay in such engines resulted in lower premixed burning fraction and hence the sharp first peak is missing in the heat release diagrams (Chmela and Orthaber [8]). Further, to filter out the fluctuations in pressure due to physical effects in the cylinder, and the duct leading the pressure to the transducer, a moderate smoothening of the pressure diagram is optionally carried out using the moving average software in the AVL Indiskop.

The pressure-time diagram was smoothened by taking a moving average over 2-deg crank angle by using the smoothening feature available in the AVL Indiskop. However, the missing of the first sharp peak in the heat-release rate curve is more due to higher compression ratio and low ignition delay in the modern engine than due to smoothening of the data.

Flame Ionization Detector. The output of the FID is the carbon atom count. As the equipment is calibrated using propane, the corresponding unburned diesel will be proportional to the ratio of the molecular weights of diesel and propane and hence about 1.1 times the indicated value.

HC Model

In the theoretical approach of Yu et al. [2], the effects of fuel-air mixing are isolated from the effect of injection system characteristics, misfire, and other sources. The contribution to hydrocarbon emissions from fuel-air mixing is calculated using a transient spray model.

Table 1 Engine specifications

Engine	Aspiration	Cylinders	Bore	Stroke	Rated Power	Rated speed	Nozzle holes x diameter	Sac volume
			mm	mm	hp/rpm			mm ³
A	Natural	4	105	120	76	2200	5x0.200	0.59
B	Turbocharged	4	105	120	105	2200	5x0.240	0.38
C	Turbocharged	4	110	116	90	2200	5x0.200	1.37
D	Natural	3	100	110	32	2000	5x0.200	1.37
E	Turbocharged and after-cooled	6	118	135	150	1500	4x0.350	0.60
F	Natural	6	100	120	112	2500	4x0.290	0.59
G	Turbocharged and after-cooled	6	102	120	160	2500	6x0.260	0.00
H	Natural	1	140	152	-	1500	8x0.203	0.62

Table 2 Details of FIE

A to G	Bosch type Jerk injection system
H	PT injection system

Table 3 Experimental data on HC emissions

Engine	Speed	Power	Fuel injected, mg		HC measured		Air-fuel ratio	delay
			per cycle	during delay	ppm	mg/cycle/cylinder		
A	1400	39.7	43.70	13.10	250	0.12	21.58	0.71
	1400	31.0	37.90	17.00	212	0.11	24.88	0.77
	1400	20.7	27.00	17.30	211	0.11	34.93	0.77
	1500	42.5	46.90	13.90	238	0.12	19.88	0.56
	1500	33.1	32.70	14.30	225	0.11	28.51	0.56
	1500	22.1	30.30	20.30	205	0.10	30.77	1.22
	2200	55.5	43.50	14.10	307	0.15	21.13	0.45
	2200	38.8	31.00	14.90	252	0.12	29.65	0.38
	2200	26.7	16.90	10.20	263	0.13	54.39	0.53
	2200	4.9	10.40	8.50	346	0.17	88.38	0.64
	2300	56.1	45.70	16.80	206	0.10	19.88	0.54
	2300	38.0	29.60	12.30	237	0.12	30.69	0.62
	2300	25.4	16.50	9.40	266	0.13	55.05	0.36
	2300	4.9	12.20	8.30	387	0.19	74.46	0.54
	2500	56.8	40.90	12.50	208	0.10	21.95	0.47
	2500	27.6	16.70	10.20	258	0.12	53.75	0.53
	2500	5.5	11.40	10.40	384	0.18	78.74	0.73
B	2200	48.5	47.32	5.49	190	0.13	30.30	0.53
	2200	72.8	67.28	4.32	162	0.12	24.60	0.46
	1500	60.6	72.88	3.54	121	0.10	23.20	0.56
	1500	49.6	57.80	3.96	149	0.11	28.80	0.67
	1500	33.0	40.60	6.75	168	0.11	37.70	0.78
	1500	11.0	15.92	3.40	193	0.11	59.40	0.78
C	2210	60.6	64.10	32.20	305	0.27	22.66	1.02
	2211	46.6	49.80	34.80	383	0.31	29.17	1.13
	2207	31.6	34.90	31.00	405	0.30	41.62	1.10
	2204	0.0	16.40	16.40	646	0.40	50.24	1.21
	1508	46.1	70.20	36.50	346	0.26	19.15	1.33
	1507	35.8	53.90	38.70	374	0.26	24.94	1.38
	1500	24.3	41.60	39.10	361	0.23	32.31	1.50
	610	0.0	78.60	78.60	447	0.22	15.39	4.37
D	2000	23.1	32.50	25.80	560	0.22	23.69	1.04
	2000	17.6	26.60	22.30	520	0.20	28.95	0.92
	2000	11.8	24.00	19.50	480	0.18	32.08	1.04
	2000	5.9	21.10	18.20	620	0.23	36.49	0.92
	1319	8.7	29.10	22.80	480	0.19	26.63	0.95
	1298	17.8	48.70	36.70	690	0.29	15.91	1.28
	1300	12.9	28.50	24.70	540	0.22	27.19	0.83
E	1500	86.2	50.80	27.50	113	0.23	28.10	1.11
	1500	57.6	34.10	27.90	136	0.24	34.80	1.28
	1500	29.7	21.60	21.40	208	0.33	50.00	1.39
	1500	8.6	12.20	12.10	232	0.34	72.50	1.44
F	1500	39.0	27.90	23.00	565	0.24	26.70	1.28
	1500	25.8	20.30	19.50	583	0.25	38.60	1.33
	2500	78.7	39.40	26.70	214	0.09	19.02	0.53
	2500	37.7	20.70	15.80	473	0.20	37.40	0.57
	2500	9.0	8.30	8.00	470	0.20	78.20	0.60
G	1600	90.4	65.00	14.30	65	0.05	21.61	1.33
	2500	115.4	86.00	3.10	60	0.06	13.95	0.67
H	700	-	17.14	15.00	400	0.46	138.90	2.02
	1300	-	17.17	15.00	500	0.57	138.90	1.47
	1300	-	17.18	14.00	400	0.46	138.80	1.41
	1300	-	17.17	9.00	150	0.17	138.80	1.09
	1300	-	17.17	13.00	250	0.29	138.80	1.35
	1300	-	17.17	15.00	450	0.52	138.80	1.47
	1300	-	17.17	14.00	510	0.59	138.80	1.46
	1300	-	25.13	10.00	200	0.23	95.00	1.31

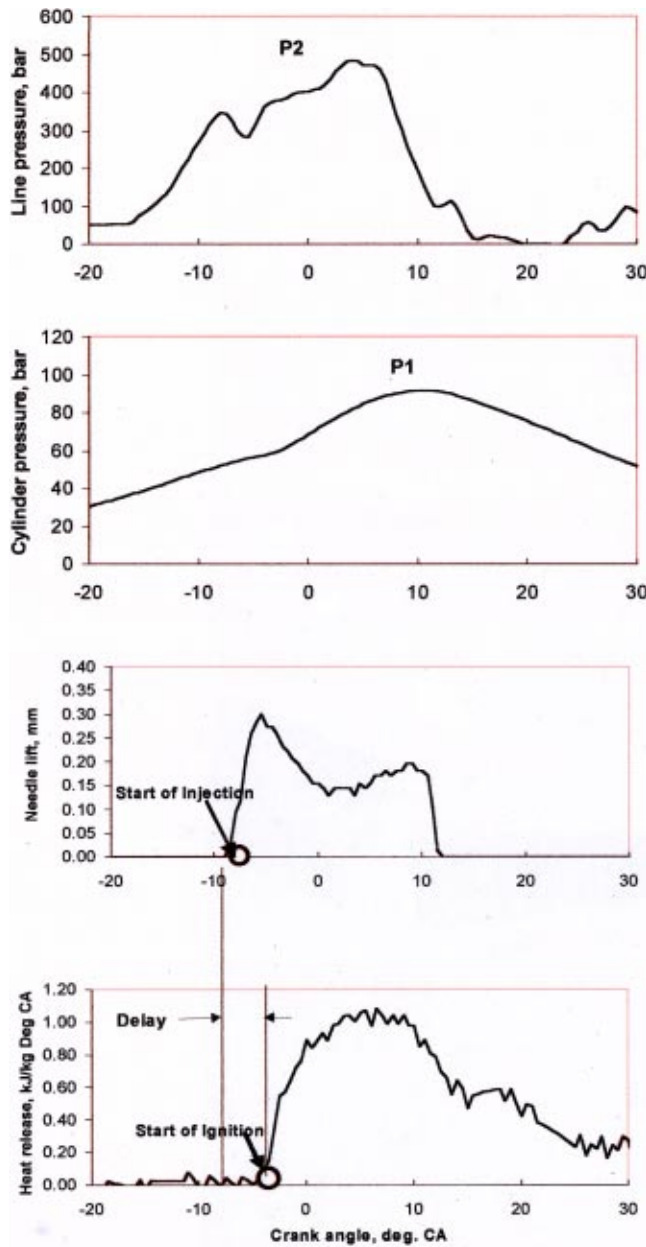


Fig. 2 Injector and in-cylinder characteristics of turbocharged engine b at 90 percent load

In the present work, the spray structure in all types of engines was found similar during the small period of ignition delay and hence they could be represented by simple numbers.

Spray Structure. The spray mixing model and spray characteristics are determined by equations of spray penetration and growth of spraywidth. A schematic behavior of the transient vaporizing spray is shown in Fig. 3 before detachment of the spray and in Fig. 4 after detachment (Lakshminarayanan and Dent [9]). The transient evaporating process can be considered as the introduction of successive packets of fuel along many streamlines radiating from a virtual origin of the spray located inside the nozzle at a distance from the mouth. Let us suppose the injection duration is $5\Delta t$ and for discussion, and let us take a streamline coincident with the jet axis.

Before Detachment of the Jet. Each packet is made up of a number of elemental packets. If it is assumed that the injection

period is $5\Delta t$ say, then 0, 1, 2... 5 in Fig. 3 represent the distribution of mixture packets injected at times 0, Δt , $2\Delta t$... $5\Delta t$. Because of shear and turbulent diffusion, the subpackets and the distribution of vaporizing droplets and vapor along the axis have the form shown in Fig. 3. Packet 4, for example, was at $t - \Delta t$, in the same state as packet 5 at t . The change in vapor concentration in packet 4 in the time interval Δt , from $t - \Delta t$ to t is due to the combined effects of dilution by entrained air (path B) and increase in concentration due to vaporization (path C).

The time history of packet 4 between $t - \Delta t$ and t is shown by paths ABC (Fig. 3). Point 3 represents the packet with the maximum vapor concentration and it is at x_0 from the nozzle tip.

For most cases of the load and speed, the diesel spray in a DI diesel engine has still not reached the wall during the ignition delay period. In addition, during this period the momentum of fuel is still far higher than the momentum of the swirling air, as the penetration is small from the cylinder center. Therefore, Eq. (1) to (6) are applicable to the spray during the delay to describe the concentration of vapor in the spray.

A Mathematical Model for the Spray Structure Before Detachment. In Fig. 5, notations of the free axisymmetric spray (Lakshminarayanan and Dent [9]) are shown, with profiles of concentration along the axis and radius. The equivalent diameter of the spray hole for a vapor jet d_e is defined.

$$d_e = d_o(\rho_f/\rho_a)^{1/2} \quad (1)$$

The virtual source of the evaporating jet is inside the orifice at a distance δ from the nozzle tip.

$$\delta = 2.3 d_e \quad (2)$$

Along the axis, the concentrations of fuel vapor decreases hyperbolically (Fig. 3) from the virtual origin where x is the distance from the mouth of the nozzle.

$$C_{f \max x} = 5.2 d_e / (x + \delta) \quad (3)$$

Equation (4) is singular at the virtual source. Experiments have shown that the vapor concentration increases linearly from the virtual origin to a fixed position, x_0 , until the jet detaches. The distance can be considered as the length of the liquid core in the spray.

$$x_0 = 7d_e = \text{a constant before detachment} \quad (4)$$

The singularity near the origin is resolved by the following relationship, up to $7d_e$, i.e., if $x/d_e < x_0/d_e = 7$.

$$C'_{f \max x} = C_{f \max x_0} [(x + \delta)/(x_0 + \delta)] \quad (5)$$

Along the radius, the distribution of the vapor concentration is Gaussian type. However, near the core of the spray, the concentration is limited to the maximum vapor concentration described above (Fig. 5).

$$C_{f \max r} = C_{f \max x_0} \exp\{-203(r/(x + \delta))^2\} \\ = C'_{f \max x} \text{ whichever is less} \quad (6)$$

After Detachment. For instants in time greater than the injection period, $t > 5\Delta t$, the center line concentration is shown schematically in Fig. 5. Point 3 seems to penetrate similar to the tip of the jet, however slowly (Lakshminarayanan and Dent [9]). The jet-like structure is still maintained, and turbulent mixing occurs entraining air into the jet-like plume, but packets of fuel are not replenished by the nozzle. Therefore, regions near the nozzle tip will be leaner than at the instant injection was complete i.e., $5\Delta t$. Subpackets on the centerline will still move downstream at a faster rate than those near the edges of the plume. Furthermore, no appreciable increase in jet width was observed (Lakshminarayanan and Dent, [9]). Therefore, the concentration profile across the plume near the nozzle tip is very flat in the central regions as shown in Fig. 6, even after the end of injection. As discussed before, during the delay period, the detachment or wall wetting is not observed in most of the load and speed cases of a normally

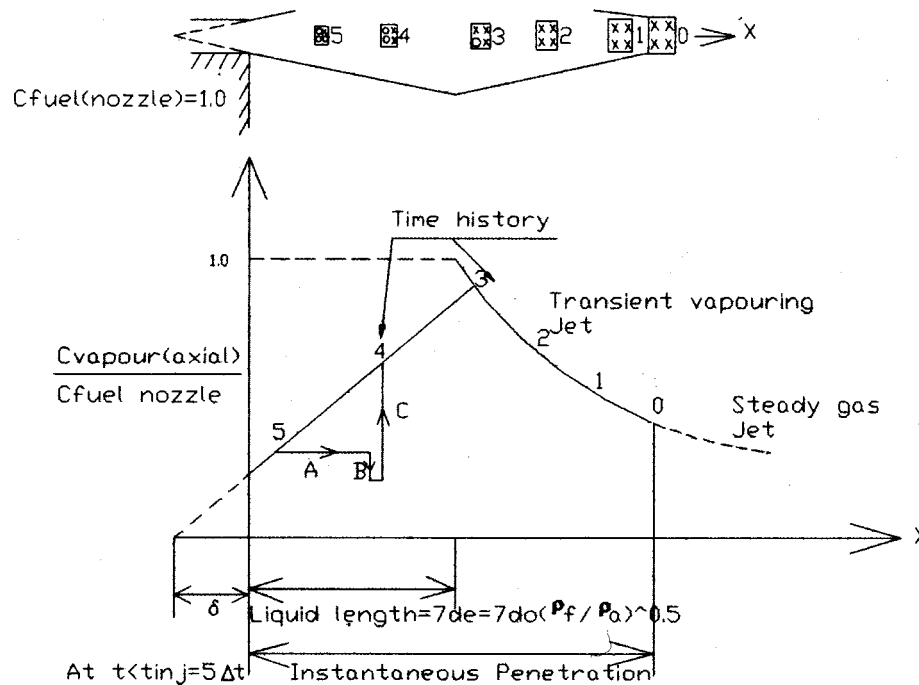


Fig. 3 Vaporization along the axis—before jet detachment

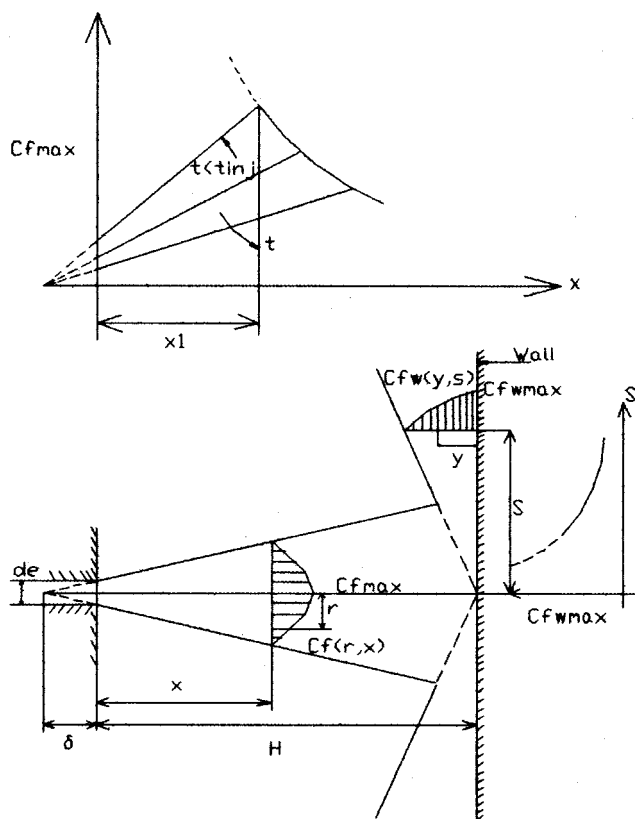


Fig. 4 Vaporization along the axis after jet detachment

operating the engine. In very few cases where it happens, the equations given in [9] were used. For brevity, the equations are not given in this paper.

Ignition Delay

Theoretical Estimation. Ignition delay (ID) is the time elapsed between the start of injection to the ignition. The time taken for visible fire to appear in the premixed zone of spray is a strong function of pressure and temperature of the ambient. In addition, the physical properties like the Cetane number, viscosity of fuel, nozzle hole size, injected quantity and injection pressure contribute to the delay phenomenon in diesel engines (Chandorkar et al. [10]). However, for diesel fuels a reasonable estimate of the delay, ID, is achieved by Wolfer (Watson and Pilley, [11]).

$$ID = 3.45 \exp(2100/T_m) p_m^{-1.02} \quad (7)$$

where T_m , p_m are the mean temperature and pressure of the ambient during ignition delay.

Experimental Estimation. Alternatively, the delay could be measured using the experimental pressure and needle lift traces (Fig. 2). Using the first law of thermodynamics, the apparent heat release rate could be calculated from the pressure crank-angle diagram. The ignition delay is measured as the time from the point of needle lift to the start of heat release. However, the measurement noise does not allow us to pick the two points clearly from experimental data. Therefore, the needle opening is assumed to be at a threshold of ten percent of the maximum lift and the time when five percent of cumulative heat release is reached is considered the start of burning.

The ignition delay of engines A to G was satisfactorily predicted using Eq. (7) and the results matched with the delay obtained from the pressure and needle lift traces.

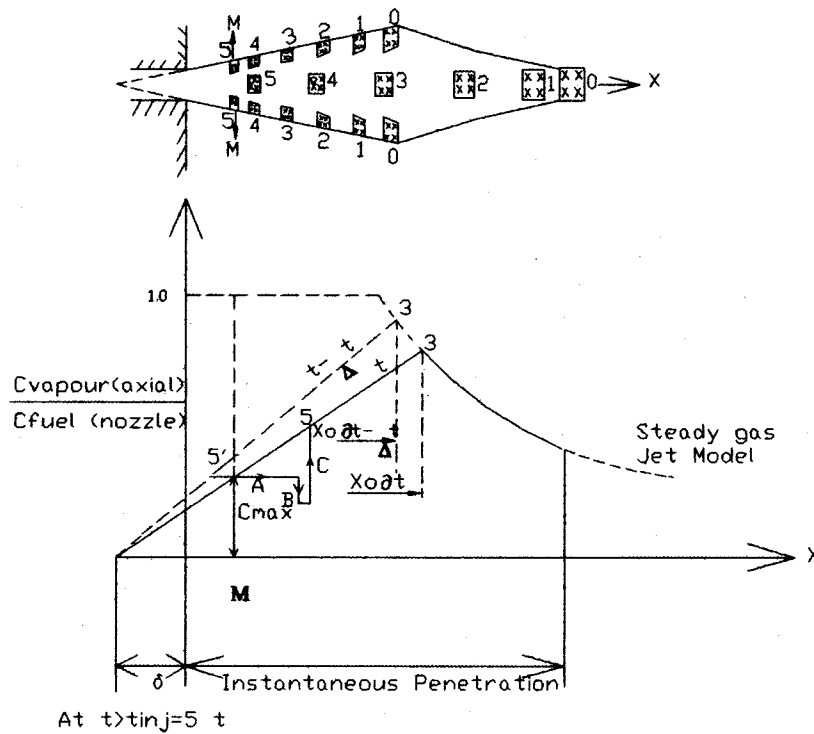


Fig. 5 Notations used in the paper for the axisymmetric spray model

Fuel Injected During Delay. The flow area of the nozzle holes, A , is calculated using the series of resistances, namely the gap between the needle seat, the seat in the needle, and spray holes by treating them as a series of orifices. A flow coefficient, c_d of 0.8 is reasonable for the spray holes. The instantaneous injection rate, dq/dt is given by the pressures before the nozzle, p_2 , and in the cylinder, p_1 , and instantaneous flow area.

$$dq/dt = c_d \rho_f A \sqrt{2(p_2 - p_1)/\rho_f} \quad (8)$$

where

$$\rho_f = \text{density of fuel.}$$

Since the value of p_1 and p_2 change during the delay period, their mean values are considered in the equation.

The amount of fuel injected during the delay period of the combustion process Q_{del} is obtained from the delay period and the rate of injection.

$$Q_{del} = ID \cdot dq/dt \quad (9)$$

Over-Leaned Fuel Air Mixture. Considering the structure of the nascent spray during the ignition delay, the fuel-air mixture beyond the lean combustion limit of relative air-fuel ratio, ϕ_L will not burn efficiently, as it is overleaned. It will be emitted as unburned HC by the engine. The value of ϕ_L lies between 3.0 and

5.0, for most of the operating and injection parameters (Yu et al. [2]). In the present work a lean limit of 5.0 is used.

The concentration profiles along the axis and radius of conical spray is self-preserving except for the rich core containing liquid spray (Lakshminarayanan and Dent [9]). The zone of lean fuel-air mixture lies on the periphery of the cone and hence the simplified laws of similarity for concentration profiles are valid. Hence, in principle, with the help of Eqs. (1) to (6) it is possible to estimate the fuel mass leaned beyond the flammability limit, ϕ_L . Equations (1) to (6) and those given in [9] allow the calculation of overleaned fuel at the end of ignition. The fuel integrated over the spray volume using Eq. (6) is not finite. Therefore, the overleaned fuel is calculated as the difference between the fuel injected during the delay using Eq. (9) and that integrated from zero radius to the radius of ϕ_L .

Overleaning Factor. The detailed calculations of a number of cases given in Table 3 for various engines showed that the overleaned fuel can be expressed as a fraction of the fuel injected during the delay period and that the fraction is a constant. The value of the fraction was roughly equal to 0.01, if either the delay or the injected quantity during the delay is not large and dealt with in detail later in the paper. The fraction is defined as the overleaning factor.

Fuel Effusing the Injector Sac. The liquid fuel remaining in the sac after the needle closed is at a pressure equal to that in the engine cylinder. However, the heat transferred from the hot combustion gases to the sac vaporizes a part of the fuel components. The vapor comes through the holes at velocities too low to mix sufficiently with air and burn in the short period available during the expansion. The residue remains in the sac to be injected normally in the next cycle.

The actual formation of hydrocarbons from the fuel in the sac is a function of the time and the rate at which the fuel discharges from the sac volume (Greeves et al. [1]). Therefore, the hydrocarbon emission, HC_v , due to sac volume is

$$HC_v = V_s \rho_f y. \quad (10)$$

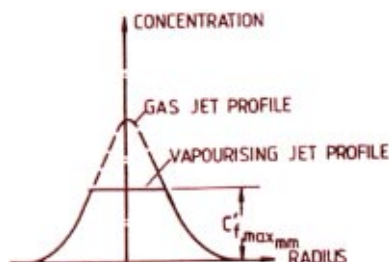


Fig. 6 Radial profile of concentration for a vaporizing jet

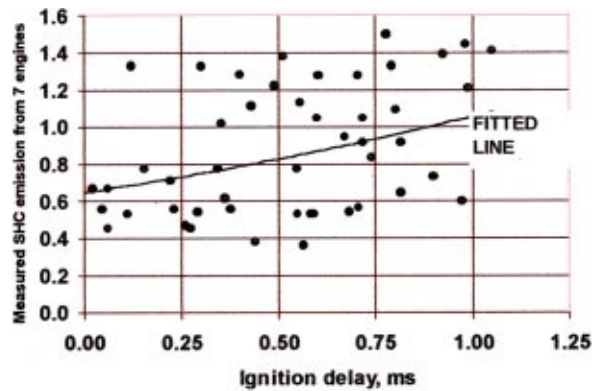


Fig. 7 Correlation of exhaust indicated hydrocarbon with ignition delay

Here, y refers to the yield or the fraction of fuel evaporated from the sac of volume V_s and ρ_f is the density of fuel.

Other Sources of Hydrocarbons. The engine coolant temperature and lubricating oil could influence hydrocarbon emissions as well. However, in the present model, the engine is considered warmed up sufficiently so that the two factors have negligible effect on HC emissions.

Formation of Unburned Hydrocarbons. After the ignition delay, the combustible mixture of air and fuel within limits of combustion burns explosively to form equilibrium combustion products. The fuel beyond the lean limit of combustion burns slowly or partially decomposes to lighter fractions, or recombines to heavier hydrocarbon molecules resulting in exhaust hydrocarbons. This phenomenon is modeled according to a global slow burning rate.

Global Slow Burning Rate. The diesel combustion is heterogeneous in nature, where the fuel evaporates and the burned and unburned gases mix during expansion. Hence, many processes contribute to hydrocarbon emissions from a diesel engine.

Greeves et al. [1] and Yu et al. [2] explain the phenomenon of bulk quenching as a physical process, related to the incomplete combustion of the combustible mixture due to volume expansion.

The leaned out fuel finds it difficult to support a propagating flame in the expansion stroke as the reaction rate is very slow by virtue of low concentration of fuel. In the present work, quenching is modeled using a global slow rate of reaction.



$$\text{mean reaction rate} = A C_a^n C_f^m \exp(-E/RT) \quad (12)$$

where

$$A = 150 \text{ to } 210$$

$$C_a = \text{mean concentration of air in the lean zone} \\ = 1, \text{ approximately}$$

$$C_f = \text{mean concentration of fuel leaned out and effused from the sac}$$

$$n = 18$$

$$m = 1$$

$$E/R = 2100 \text{ K}$$

The equation for slow reaction is validated for the ignition delay period in an earlier work of the authors (Chandorkar, Dani, and Lakshminarayanan [10]). The dilution of the leaned out fuel after a characteristic period will be too low even to continue the slow reaction. The typical period scales with the delay period. The quantity of slow burnt fuel is given by the mean reaction rate and a characteristic ignition delay.

$$\text{slow burnt fuel} = \text{reaction rate} \times \text{ignition delay} \quad (13)$$

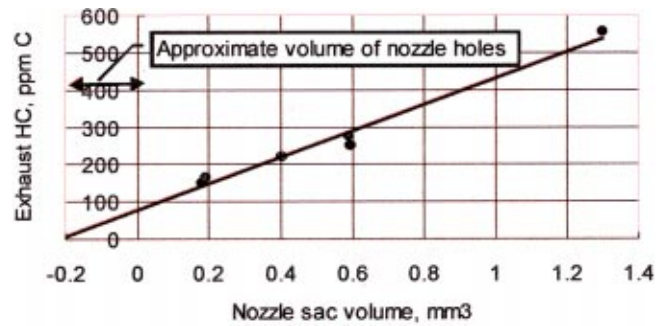


Fig. 8 Effect of nozzle sac volume on HC concentrations and yield value of 0.21 ([1]) for one type of engine and one operating condition

Predicting HC in the Exhaust

Definition of Specific Hydrocarbon or Exhaust Indicated Hydrocarbon. In the present work, specific HC in the exhaust (SHC) or the exhaust indicated hydrocarbon (EIHC) is defined as the ratio of mass emission of HC in the exhaust to the quantity of fuel injected during the delay.

Analysis of Experimental Data

Relating HC to Ignition Delay. The measured specific HC is plotted against the ignition delay as given by Greeves et al. [1], Fig. 7. Their correlation seems to be valid for a given engine and at one condition of speed and load. For a wide variety of engines and operating conditions, the correlation coefficient is as low as 0.3.

Relationship of HC Emissions and Sac Volume. Figure 8 shows (Greeves et al. [1]) the effect of sac volume alone on HC at a particular condition of load and speed for the engine studied. The negative intercept on the horizontal axis corresponds to the volume of holes. The yield value could be estimated as 0.21.

On the other hand, insignificant correlation was found between the observed mass of HC emissions and the sac volume for various engines at different operating conditions (Fig. 9).

HC and Fuel-Injected During Delay. As a first step, the observed HC was plotted against the ratio of fuel injected during ignition delay to the total fuel injected in Fig. 10, without considering the emissions from the sac. The regression coefficient was 0.93 showing the important effect of the quantity of fuel injected during ignition delay, Q_{del} on HC emissions from a diesel engine. The straight-line relationship in a semi-log plot showed that with increasing amount of fuel injected during delay, the emissions increased exponentially (Fig. 10). Figure 11 shows a good nonlinear relationship in a Cartesian coordinate system.

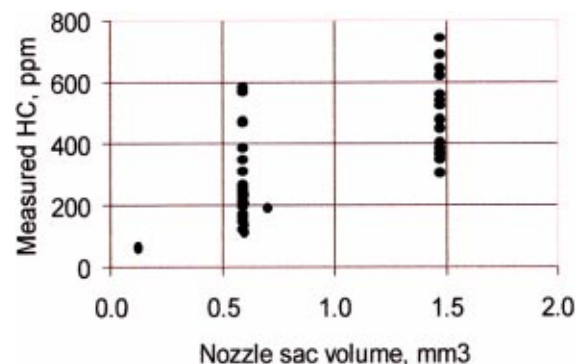


Fig. 9 Effect of nozzle sac volume on HC

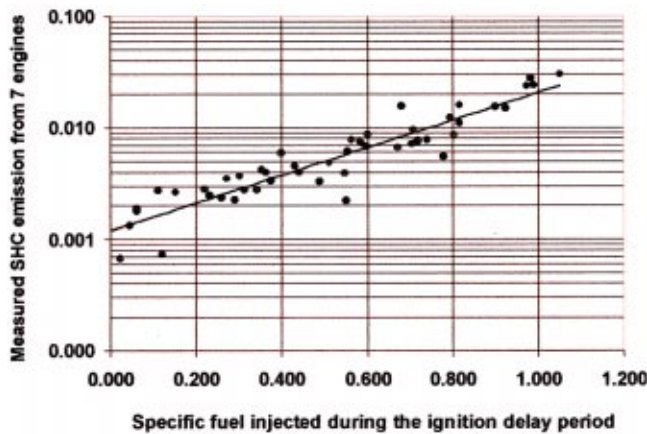


Fig. 10 Semi-log plot of specific mass of fuel injected during the ignition delay and HC

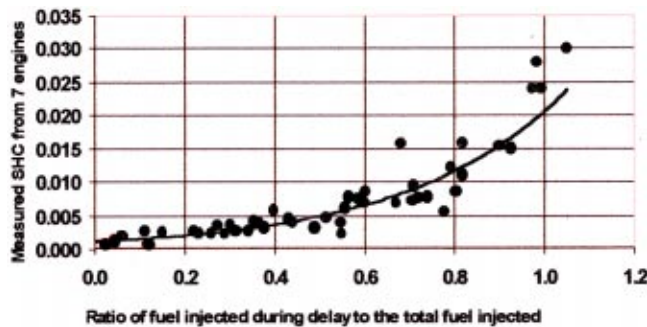


Fig. 11 Specific fuel injected during the ignition delay period

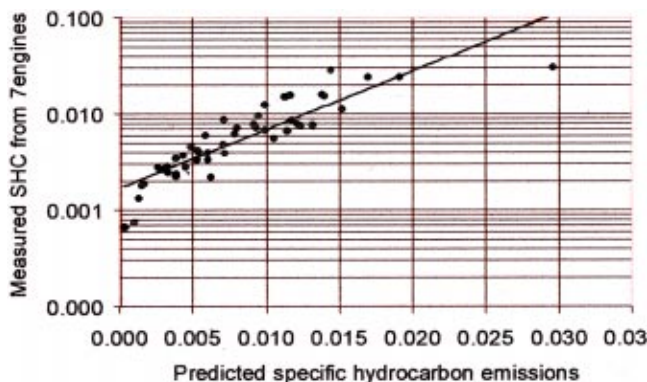


Fig. 12 Semi-log plot of specific mass of fuel and HC considering sac and an overleaning factor was 0.008

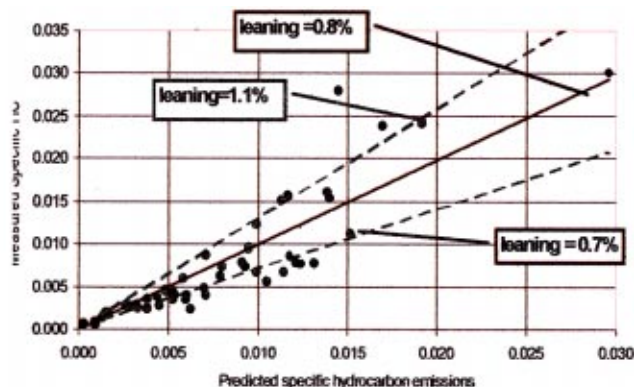


Fig. 13 Specific mass HC considering overleaning and sac

$$HC/m_f = 0.0012 \exp(2.86Q_{del}/\text{total fuel injected}) \quad (14)$$

However, the fuel injected during the delay period is many times higher than the observed HC emissions. Further, the exponential relationship suggests that more time is available for the fuel to lean out when the delay increases. Therefore, considering an overleaning factor and the effect of sac volume will improve the correlation quantitatively.

Specific HC in the Exhaust. The specific HC could be modeled using the expression given below.

$$\begin{aligned} \text{EIHC in the exhaust} &\propto [(\text{fuel injected during delay from} \\ &\quad \text{Eq. (9)} \times \text{fuel overleaning factor} \\ &\quad + \text{sac volume} \times \text{yield}) \\ &\quad - \text{slow-burnt fuel from Eq. (13)}] / m_f \\ &= m_{cal} / m_f \end{aligned} \quad (15)$$

Phenomenological Model. The relationships with important parameters, namely the sac volume and fuel injected during the delay, suggest that the correlation will not predict HC if the two parameters are considered individually. Incorporating the overleaning factor and the unburnt fuel yielded by the sac volume lead to a phenomenological model. The suitable yield from the sac was found to be 12 percent.

An average overleaning factor of 0.008 could be obtained from the thick jet structure of a diesel spray given in Eqs. (1) to (6), during the ignition delay period. The measured specific HC was plotted against the EIHC calculated using this factor in Eq. (15) on a semi-log paper in Fig. 12 and on a linear graph paper in Fig. 13. Here, the coefficient of the fit was better than 0.9 validating the proposed model for predicting HC emissions, quantitatively.

Discussions

The fuel injected during the ignition delay is cold and is dispersed into various packets of different air fuel ratios. The fuel leaned beyond an air excess ratio of 5.0 exits the engine as unburnt hydrocarbon emissions. By studying the spray structure, the overmixed fuel is estimated to lie between 0.007 and 0.011 of the fuel injected during the delay period in direct-injection diesel engines (Fig. 13). The lower value of leaning factor is valid when the ignition delay is relatively less. The HC emissions are augmented by fuel effusing from the sac. The yield from the sac is about 0.12. The overleaned fuel-air mixture burns slowly along with the fuel leaked from the sac during a characteristic period. The reaction rate could be described by Arrhenius-type relationship.

Summary

A strong relationship of HC exists with the sum of leaned-out fuel during the ignition delay and fuel yielded by the sac. Detailed consideration of overleaning factor enables prediction of exhaust indicated HC for any DI diesel engine over a wide range of speeds and loads irrespective of the nature of aspiration, after reasonable warmup of the engine. The model considers the chemical effect of fuel on HC emissions indirectly in the ignition delay term.

Nomenclature

- A = area of orifice, m^2
- C = concentration (mass) of vapor
- CN = Cetane number
- c = coefficient
- D = diameter, m
- E = activation energy = $618840/(CN+25)$, J/mol ([12])
- H = distance between impingement plate and nozzle

HC = hydrocarbon
 ID = ignition delay
 m = mass
 p = cylinder pressure, bar
 Q = flow rate, kg/s
 dq/dt = instantaneous injection rate
 R = universal gas constant, J/mol K
 RHS = right-hand side
 s, S = radius of a point in the wall jet, m
 V = sac volume, m³
 T = cylinder temperature, K
 t = time, sec
 x = distance from nozzle
 y = height from plate, m
 ρ = density, kg/m³
 δ = distance between nozzle hole and virtual origin, m
 ϕ = excess air ratio

Subscripts

a = air
 c = carbon atoms in fuel
 cal = calculated using Eq. (15) for a given overleaning factor 0.8 percent
 d = discharge
 del = delay
 e = equivalent
 f = fuel
 inj = injected
 L = lean limit of combustion
 m = mean
 Max = maximum
 s = sac
 r = radial position
 v = due to sac volume

w = pertaining to wall jet
 x = axial distance
 o = point where the effect of detachment is felt; nozzle
 1 = cylinder pressure
 2 = line pressure

References

- [1] Greeves, G., Khan, I. M., Wang, C. T. H., and Fenne, I., 1977, "Origins of Hydrocarbon Emissions From Diesel Engines," SAE Paper 770259.
- [2] Yu, R. C., Wong, V. W., and Shahed, S. M., 1980, "Sources of Hydrocarbon Emissions From Direct Injection Diesel Engines," SAE Paper 800048.
- [3] Dent, J. C., and Lakshminarayanan, P. A., 1983, "A Model for Absorption and Desorption of Fuel Vapor by Cylinder Lubricating Oil Films and Its Contribution to Hydrocarbon Emissions," SAE Paper 830652.
- [4] Ikegami, M., Li, X.-H., Nakayama, Y., and Keimiwa, 1983, "Trend and Origins of Particulate and Hydrocarbon Emission From Direct Injection Diesel Engine," SAE Paper 831290.
- [5] Nakayama, Y., Maruya, T., Oikawa, T., Fujiwara, M., and Kawamata, M., 1994, "Reduction of HC Emission From VTEC Engine During Cold Start Condition," SAE Paper 940481.
- [6] Tsunemoto, H., Ishitani, H., and Konno, A., 1992, "The Increase of HC Emissions From a Direct Injection Diesel Engine During Long Idling Operation," SAE Paper 922227.
- [7] Dent, J. C., 1980, "Turbulent Mixing Rate—Its Effect on Smoke and Hydrocarbon Emissions From Diesel Engines," SAE Paper 800092.
- [8] Chmela, F. G., and Orthaber, G. C., 1999, "Rate of Heat Release Prediction for Direct Injection Diesel Engines Based on Purely Mixing Controlled Combustion," SAE Paper 1999-01-0186.
- [9] Lakshminarayanan, P. A., and Dent, J. C., 1983, "Interferometric Studies of Vaporizing and Combusting Sprays," SAE Paper 830244.
- [10] Chandorkar, S. B., Dani, A. D., and Lakshminarayanan, P. A., 1988, "Effects of Injection Parameters, Fuel Quality and Ambient on the Ignition Delay and the Location of the Flame Kernel in a Diesel Spray in a Quiescent Chamber," SAE Paper 881227.
- [11] Watson, N., and Pilley, A. D., 1980, "A Combustion Correlation for Diesel Engine Simulation," SAE Paper 800029.
- [12] Heywood, J. B., 1988, *A Textbook on Internal Combustion Engine Fundamentals*, McGraw-Hill, New York.

A Model for Multicomponent Spray Vaporization in a High-Pressure and High-Temperature Environment

Y. Zeng

C. F. Lee

e-mail: cflee@uiuc.edu

Department of Mechanical and Industrial Engineering,
University of Illinois at Urbana-Champaign,
140 Mechanical Engineering Building,
1206 West Green Street,
Urbana, IL 61801

A multicomponent droplet vaporization model including both gas and liquid phase transport processes was developed for multidimensional spray computations. This paper focuses on two effects altering vaporization in a high-pressure and high-temperature environment. One effect is on droplet surface regression caused by a higher vaporization rate. This effect is well characterized by the Lewis number and the Peclet number with the regression velocity. Formulas based on the two numbers were included to improve model accuracy. The other effect is on the nonideal behavior and was covered in the model by using the Peng-Robinson equation of state to determine phase equilibrium at the droplet surface. The model was validated by the results from an accurate simplified vortex model and experimental measurements, and excellent agreements were demonstrated. Further comparisons against the model without the two effects and an infinite diffusion model show that significant improvement was achieved by the model for single-droplet and spray computations. [DOI: 10.1115/1.1456094]

Introduction

Droplet vaporization is an important phenomenon in applications powered by liquid fuel, such as internal combustion engines, gas turbines, and rockets. For multicomponent droplets, the differences in volatility result in the differences in vaporization rates for components. Since vaporization occurs only at the interface and the liquid mass deep inside the droplet cannot reach the surface quickly enough due to the mass diffusional resistance, the mass fraction of the more volatile component decreases at the droplet surface while that of the less volatile component increases with time. This leads to an unsteady nonuniform distribution of mass fractions inside the droplet (i.e., preferential vaporization).

In the past few decades, the modeling of droplet vaporization has been extensively investigated. Several kinds of models, with different accuracies and computational resource requirements, were developed to describe the unsteady transport of the liquid phase flow within the droplet.

The transport inside the droplet is due to a combination of molecular diffusion and convective motion. If a relative velocity between the droplet and the ambient gas is low, molecular diffusion is the primary transport mode. For the high relative velocity environment, however, the vortex motion (internal circulation) generated by the shear stress at the interface promotes the convective transport significantly ([1]).

The computational complexity of available models for the liquid phase transport process ranges from zero-dimensional to two-dimensional. In the most detailed models (vortex models), two-dimensional axisymmetric equations for mass, momentum and energy conservation are used to describe the transient evolution of the temperature and mass fractions within the droplet. The vortex motion inside the droplet is described by vorticity and stream function equations ([2]) or analytical solutions ([3]). However, the high computational cost of these models is prohibitive for most multidimensional spray computations. At the opposite extreme, the infinite diffusion (zero-dimensional) model assumes that the

transport processes of mass and heat occur so quickly that the physical properties and chemical composition are always uniform inside the droplet. Between these two extremes, both the pure diffusion model and the simplified vortex model use one-dimensional governing equations. The simplified vortex model includes more physics than the pure diffusion model. In the pure diffusion model ([4]) the effect of internal circulation is neglected. In contrast, simplified vortex models represent the internal circulation by artificially enlarged diffusivities ([3,5]) or by using a similarity transformation ([6]). Both approaches were found to be effective and yielded results similar to those of the detailed vortex models ([3,6]). Some zero-dimensional models were also formulated. Tong and Sirignano [7] simplified the partial differential equations to a set of ordinary differential equations by using similarity transformations and an integral approach based on the Green function and the eigenvalue methods, which captured the transient variations of surface temperature and mass fractions. Rensizbulut et al. [8] related the differences between the surface and average values (e.g., temperature or mass fractions) to the mass or heat flux at the droplet surface by using the Sherwood and Nusselt numbers, which are both functions of the Fourier number. Abraham and Magi [9] proposed a phenomenological model based on the concept that components with higher volatility and lower latent heat vaporize faster. These zero-dimensional models are preferred in multidimensional spray computations due to their low computational cost, since for a spray, thousands of parcels need to be traced with each parcel representing a collection of droplets that have the same properties.

Internal combustion engines typically feature high-pressure and high-temperature environments, in which the ideal behavior for phase equilibrium is no longer valid and the surface regression will significantly affect the mass and energy transport inside the droplet due to the high vaporization rate. Cubic equations of state were found to be appropriate for high-pressure environments. For example, Jin and Borman [5] used the Redlich-Kwong equation of state to construct a high-pressure droplet vaporization model. Some similar approaches can also be found in the references [10–13]. Two other practical topics on spray vaporization are on dense sprays and fuel representation. For dense sprays, the interaction among droplet arrays typically decreases the vaporization rate of

Contributed by the Internal Combustion Engine Division of THE AMERICAN SOCIETY OF MECHANICAL ENGINEERS for publication in the ASME JOURNAL OF ENGINEERING FOR GAS TURBINES AND POWER. Manuscript received by the ICE Division, July 2000; final revision received by the ASME Headquarters, November 2001. Editor: D. N. Assanis.

the droplet compared to an isolate droplet. Theoretical studies on this phenomenon have been performed, and some correction factors were developed ([14,15]). For fuel representation, conventionally, several components are used to simulate a practical fuel. Continuous representation, however, employs a two-parameter probability density function to simulate the wide volatility distribution of the real fuel ([16]).

Recently, the authors [17] developed a zero-dimensional multi-component vaporization model. The unique feature of this model is that the difference between surface and average variables (e.g., mass fractions or temperature) are traced by a set of ordinary differential equations to account for the nonuniform distributions of temperature and mass fractions inside the droplet. The effect of internal circulation is also taken into consideration by using the effective diffusivity to replace the physical diffusivity. This model was further improved and is presented in this paper by including the effects of surface regression and nonideal behavior due to high pressure and high temperature, however, under subcritical conditions. The rest of this paper will first give the basic framework for determining the droplet vaporization rate and the heat flux to the droplet followed by a brief description of our previous model ([17]). Then the methods accounting for the effects of surface regression and high pressure will be described. Finally, the results and the performance of the present model will be discussed.

Vaporization Rate and Heat Flux To Droplet

With parcel representation for sprays, point-volume methods are used to account for the two-way coupling between parcels and the continuous gas phase, and the momentum, heat and mass transfers between two phases are determined by semi-empirical correlations for drag, the Nusselt number, and the Sherwood number ([18]). Renksizbulut et al. [8] showed that this approach has sufficient accuracy if the properties at the droplet surface are well determined and the one-third rule is used to calculate the properties of the film gas around the droplet.

The correlations in reference [5] were used in this study. The species vaporization rate is given by [5].

$$w_i = \frac{\Gamma}{2R} Sh_i \xi_i B_i \quad (1)$$

where the Sherwood number of component i is given by

$$Sh_i = 2 + 0.555 Re^{1/2} Sc_{gi}^{1/3} [1 + 1.232 / (Re Sc_{gi}^{4/3})]^{-1/2} \quad (2)$$

for force convection. In Eq. (1), the transfer number of component i is given by [5],

$$B_i = \frac{Y_{gis} - Y_{i\infty}}{1 - Y_{gis}(\sum_j w_j)/w_i}, \quad (3)$$

where $Y_{i\infty}$, the gas phase mass fraction of component i in the surroundings, is evaluated as the value of the computational cell where the droplet is located. The gas phase mass fraction of component Y_{gis} at the droplet surface is determined by the thermodynamic phase equilibrium at the droplet surface. If the pressure is relatively low, the Raoult's law, which assumes ideal mixing behavior, can be applied. Thus, the gas phase and the liquid phase mole fractions can be related by

$$P_\infty X_{gis} = X_{lis} P_{sat}(T_s). \quad (4)$$

The determination of phase equilibrium in a high-pressure environment will be discussed in detail later.

The heat flux to the droplet is given by [5],

$$q = h_i(T_\infty - T_s) - \sum w_i h_{vi}, \quad (5)$$

where the heat transfer coefficient from the ambient gas to the droplet h_i is given by

$$h_i = Nu \frac{k_g}{2R} \xi_T. \quad (6)$$

For force convection, the Nusselt Number, Nu , is given by [5],

$$Nu = 2 + 0.555 Re^{1/2} Pr_g^{1/3} [1 + 1.232 / (Re Pr_g^{4/3})]^{-1/2}. \quad (7)$$

In Eqs. (1) and (7), ξ_i and ξ_T account for the effect of vaporization on the mass and heat transfers ([5]). In the case of nature convection, the Reynolds number is replaced by the square root of the Grashof number for Eqs. (2) and (7).

In the above semi-empirical correlations, the properties at the droplet surface are frequently used. Since most properties are temperature and composition-dependent, sufficiently accurate surface temperature and mass fractions are needed. Due to the thermal and mass diffusional resistance, the temperature and mass fraction distributions are not uniform in general. Appropriate equations are required to solve for the distributions inside the droplet. Recently, the authors developed an approach in which only ordinary differential equations are needed to solve for the distributions ([17]), and a brief description is given in the following section and this approach is referred to as the previous model in the remaining text.

Previous Model

The previous model ([17]) starts from the model developed by Jin and Borman [5]. The typical flow field inside the droplet consists of two symmetric vortices induced by the shear stress between the droplet and surface (i.e., internal circulation). Due to the presence of this internal circulation, proper description of the flow inside the liquid phase requires an equation that is at least two-dimensional. Jin and Borman [5] reduced the equation to a set of one-dimensional governing equations by introducing the concept of effective diffusivity, which accounts for the effect of internal circulation by using an enlarged diffusivity. Zeng and Lee [17] obtained a quasi-analytical solution for this one-dimensional equation, and the derived solution is in an ordinary differential form.

The overall species mass conservation and energy conservation equations in the infinite diffusion model are first used to find mean values of the temperature and mass fractions. In order to find values at the droplet surface, an ordinary differential equation describing the evolution of the difference between surface and average values is solved as

$$\frac{\partial \Phi_d}{\partial t} = \frac{0.2 \phi R / D - \Phi_d}{R^2 / s_1^2 D} \quad (9)$$

where $s_1 = 4.4934$. Φ_d is either the difference between the surface and average temperatures or the difference between the surface and average mass fractions. For temperature, D is the thermal diffusivity, and $\phi = qD/k_l$. For the mass fractions, D is the mass diffusion coefficient and $\phi = [w_i - (\sum w_j)y_{im}]/\rho_l$. The integration of Eq. (9) with respect to time gives the difference between surface and average values. Thus, the surface values can be found by simple algebra operation. Compared to the infinite diffusion model, the only additional work is solving Eq. (9). Since Eq. (9) is an ordinary equation, the solution procedure only accounts for a small portion of the total required computational time (in the order of 1 percent). Notice should be made that on the right-hand side of Eq. (9), the first term in the numerator represents the equilibrium value, and the denominator represents the time constant of the transient process. Similar in manner to the dynamical relations often used for chemical reaction rates, the time rate of change is proportional to the deviation from the equilibrium value and inversely proportional to the time constant.

In Eq. (9), the effective diffusivities rather than the physical diffusivities are used to account for the effect of internal circulation. The following two equations give the ratio of effective diffusivity to physical diffusivity ([3]),

$$\begin{cases} \frac{k_l^e}{k_l} = 1.86 + 0.86 \tanh[2.245 \log_{10}(\text{Re Pr}_{li}/30)] \\ \frac{\Gamma_{li}^e}{\Gamma_{li}} = 1.86 + 0.86 \tanh[2.245 \log_{10}(\text{Re Sc}_{li}/30)] \end{cases} \quad (10)$$

Surface Regression

In the development of the previous model, the effects of surface regression on the distribution of temperature and mass fractions are neglected. It is a reasonable assumption when the vaporization rate is slow compared to the diffusion flux inside the droplet. However, it may cause severe errors when the vaporization rate is very high. Higher vaporization rates tend to make the steady profiles of temperature and mass fractions deviate significantly from those at a lower vaporization rate or at a process dominated by diffusion. A method is developed and presented below to account for this deviation, and a nondimensional variable characterizing this deviation will be introduced.

For temperatures inside the droplet, the governing equation is

$$\begin{cases} \frac{\partial T}{\partial t} = \frac{\partial}{\partial r} \left(\alpha_l^e \frac{\partial T}{\partial r} \right) \\ \left. \frac{\partial T}{\partial r} \right|_{r=0} = 0, \quad \left. \frac{\partial T}{\partial r} \right|_{r=R} = \frac{q}{k_l^e} \end{cases} \quad (11)$$

By choosing the droplet radius R as the characteristic length, R^2/α_l^e as the characteristic time, qR/k_l^e as the characteristic temperature, Eq. (11) can be normalized as

$$\begin{cases} (1 + 2\tau\text{Pe}_V) \frac{\partial \theta}{\partial \tau} + \left(\text{Pe}_V - \frac{2}{s} \right) \frac{\partial \theta}{\partial s} - \frac{\partial^2 \theta}{\partial s^2} = 0 \\ \left. \frac{\partial \theta}{\partial s} \right|_{s=0} = 0, \quad \left. \frac{\partial \theta}{\partial s} \right|_{s=1} = 1 \end{cases} \quad (12)$$

In Eq. (12), the nondimensional variable Pe_V is defined as

$$\text{Pe}_V = - \frac{R \partial R / \partial t}{\alpha_l^e} \quad (13)$$

which represents the ratio of the thermal diffusion time scale to the surface regression time scale. It serves as a representative scalar for the effect of surface regression on the temperature profile. Pe_V is mainly a function of droplet surface temperature, and the droplet diameter has little effect on the magnitude of Pe_V since $\partial R / \partial t$ is inversely proportional to R as in Eq. (1). Except during a very short initial period when a droplet is introduced into a thermally nonequilibrium environment, $\partial \theta / \partial \tau$ will only be the function of time (i.e., it is uniform spatially). Hence the following solution can be found for Eq. (12) at infinite time:

$$\frac{\partial \theta}{\partial s} = \left[C_1 \int_0^s s^2 \exp\left(-\frac{\text{Pe}_V}{2} s^2\right) ds \right] s^{-2} \exp\left(\frac{\text{Pe}_V}{2} s^2\right) \quad (14)$$

where C_1 is constant and is given by

$$C_1 = \left[\int_0^1 s^2 \exp\left(-\frac{\text{Pe}_V}{2} s^2\right) ds \right]^{-1} \exp\left(-\frac{\text{Pe}_V}{2}\right). \quad (15)$$

Through the integration of Eq. (15), the temperature profile and the relation between the heat flux to the droplet and the difference between surface and average temperatures can be determined. Figure 1 gives the normalized temperature profiles at different Pe_V . When Pe_V is less than unity, the distribution is quadratic. With increasing Pe_V , the distribution shows the structure similar to that of the boundary layer flow, with decreasing boundary layer thickness. The normalized difference $E(\text{Pe}_V)$ between the surface and average temperature variations versus Pe_V are plotted in Fig. 2, with $E(\text{Pe}_V)$ normalized to 1.0 at $\text{Pe}_V=0$. With increasing Pe_V ,

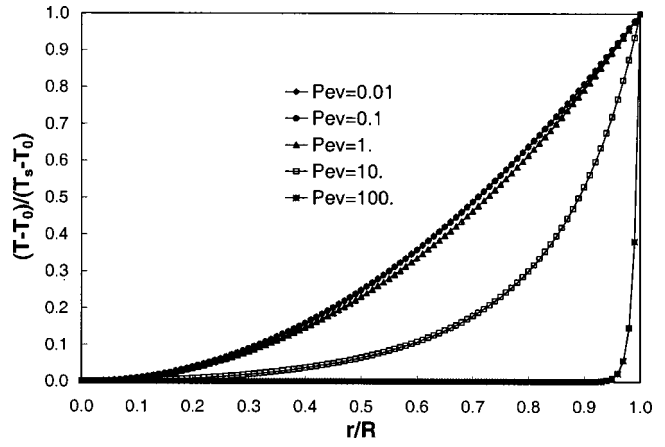


Fig. 1 The normalized temperature profiles at different Pe_V

the normalized difference decreases in a nearly linear manner. In order to account for this trend, Eq. (9) was modified to

$$\frac{\partial \Phi_d}{\partial t} = \frac{0.2E(\text{Pe}_V)\phi R/D - \Phi_d}{E(\text{Pe}_V)R^2/s_1^2 D}. \quad (16)$$

For mass fractions, the same formula as that for temperature in Eq. (16) can be obtained by similar procedures. The only difference is that Pe_V is replaced by $\text{Le} \cdot \text{Pe}_V$ and $\phi = [w_i - (\sum w_i)y_{is}]/\rho_l$.

Vaporization Regimes

With the present model, three extreme vaporization regimes are identified: First, if $\text{Pe}_V \ll 1$, $\Phi_d \ll 1$, thus the distribution of Φ is nearly uniform and the combined effect of preferential vaporization and finite diffusion and the effect of surface regression are negligible (i.e., distillation limit, see [19]); second, if $\text{Pe}_V \sim 1$, $E(\text{Pe}_V) \sim 1$, only the effect of surface regression is negligible; lastly if $\text{Pe}_V \gg 1$, $0.2\text{Pe}_V E(\text{Pe}_V) \sim 1$, it was found that the vaporization rate distribution among components is proportional to the mean mass fractions of the liquid phase, and thus the mean mass fractions of the droplet is essentially frozen (i.e., diffusion limit, in [19]). A typical value of Pe_V is in the order of 10 for mass diffusion and in the order of 1 for thermal diffusion, and both finite diffusion and surface regression effects are important within this range.

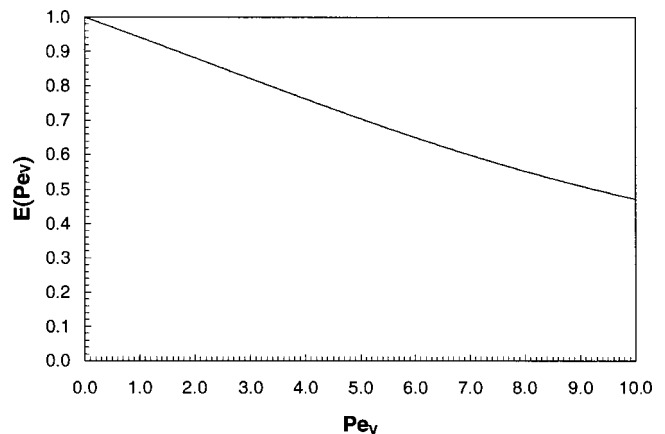


Fig. 2 The normalized temperature difference at different Pe_V

High Pressure

In a high-pressure environment, the assumption of ideal gas behavior is invalid. Consequently, the Raoult's law does not give the appropriate thermodynamical phase equilibrium relation at the droplet surface. To account for the effect of nonideal behavior at high pressure, the Peng-Robinson equation of state was used to calculate the compressibility factor and fugacity for the gas phase and liquid phase ([20]),

$$Z^3 - (1 - B)Z^2 + (A - 3B^2 - 2B)Z - (AB - B^2 - B^3) = 0 \quad (17)$$

$$\ln\left(\frac{f_i}{x_i P}\right) = \frac{b_i}{b}(Z - 1) - \ln(Z - B) - \frac{A}{2\sqrt{2}B} \left(\frac{2\sum x_i a_{ik}}{a} - \frac{b_i}{b} \right) \ln\left(\frac{Z + 2.414B}{Z - 0.414B}\right) \quad (18)$$

The expressions for A , B , a , b , a_{ij} , and b_i can be found in reference [20]. In Eq. (17), Z is the compressibility factor, f_i the fugacity of species i , x_i the mole fraction of species i , and P the ambient pressure. For a given state (T, P, x_i) , Eq. (17) will yield three solutions for Z . Among the solutions, either one is real or all of them are real. The largest real solution corresponds to the gas phase while the smallest real solution corresponds to the liquid phase. By equating the species fugacities of liquid and gas phases and coupled with Eq. (9), the phase equilibrium relation can be determined. The inclusion of the above model does not significantly increase the computation time. For typical spray computations, the time increase is about three percent comparing to the infinite diffusion model.

Results and Discussions

The proposed model was implemented into a modified version ([17]) of KIVA-3V ([18]), which is a comprehensive multidimensional CFD code. The partial-donor-cell (PDC) fluxing scheme is used in this study to gain second order accuracy spatially. The overall accuracy in time is first order. For vaporization, the liquid phase flow and the gas phase flow are coupled at the interface, and iterative approaches are used to determine temperature and mass fractions at the droplet surface by checking whether the continuity requirements for mass and heat flux at the interface are met.

In order to verify the performance of the present model, the vaporization of a multicomponent droplet was first computed and the results were compared with those using a one-dimensional and two zero-dimensional liquid phase models. Then three sets of computations for the vaporization of a single droplet were made and compared with the experimental measurement. Finally, the model was applied to study the vaporization of a hollow-cone spray typically used in gasoline direct injection (GDI) engines. Two cases were computed to highlight the effect of nonideal behavior at high-pressure environments. Detailed discussions of the results will be presented.

Comparisons With Other Models. A one-dimensional simplified vortex model for the liquid phase originally developed by Jin and Borman [5] was used to verify the present zero-dimensional model. In this simplified vortex model, semi-empirical correlations are used to determine the vaporization rate and the heat flux to the droplet from the surrounding gas while the liquid phase flow is described by mass and energy conservation equations. The effect of internal circulation is accounted for by using a newer version of effective diffusivities (Eq. (10) in [3]) instead of that used by Jin and Borman [5]. In summary, the applied one-dimensional model and the present model are the same except for the description of the liquid phase flow. This exception results in that the simplified vortex model takes about 25 times more computational time than the present model since the simplified vortex model uses 100 grid points in each droplet and also requires more cycles to converge at each time step.

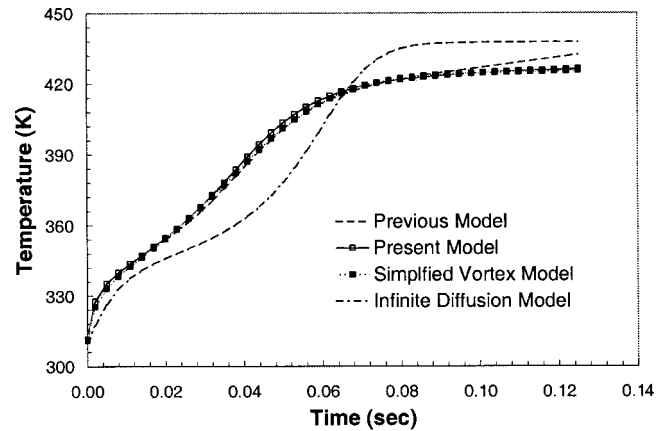


Fig. 3 Droplet surface temperature variation versus time

In the test case, the computed droplet consists of 50 percent C_5H_{12} and 50 percent C_6H_{14} in terms of mass, the initial velocity is 10 m/sec, and the initial temperature is 300 K. The ambient gas is pure nitrogen with zero velocity, an initial temperature of 500 K and an initial pressure of 100 kPa. Again, the grid used in the simplified vortex model consists of 30 grid points inside the droplet. For comparison, the infinite diffusion model ([21]) and the previous model ([17]) developed by the authors were also applied. The predicted surface temperature and mass fraction of C_6H_{14} by four models are shown in Figs. 3 and 4, respectively. Overall, the present model agrees better with the simplified vortex model than the previous model for predicted surface variables, especially during the later part of the droplet lifetime. In contrast, the infinite diffusion model yields a lower surface temperature initially and a higher temperature at later times. Figure 5 shows that the four models yield similar results for droplet radius square. Interestingly, the infinite diffusion model gives a slightly lower vaporization rate initially due to lower predicted surface temperature as shown in Fig. 3. However, the higher vaporization rate at later times due to higher surface temperature compensates for the initially lower vaporization rate to produce droplet radius results similar to the other models.

The temporal history of mass fractions of C_6H_{14} is shown in Fig. 6. Initially, the four models yield similar results because the droplet temperature is low and the vaporization rate in turn is slow. Consequently, the effects of preferential vaporization and surface regression, both of which are proportional to the droplet vaporization rate, are not significant initially. However, with increasing time and surface temperature, the effect of preferential

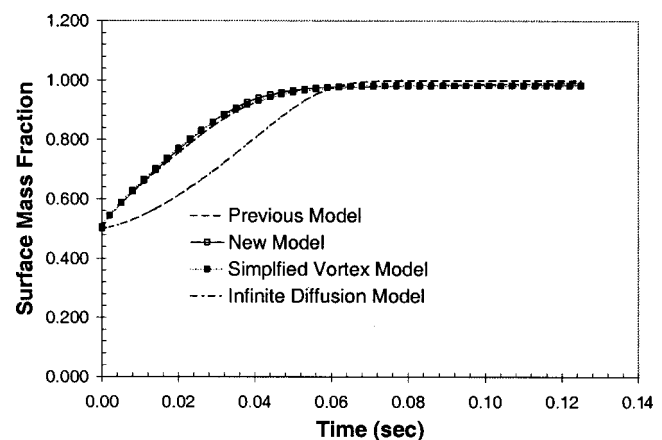


Fig. 4 C_6 surface mass fraction variation versus time

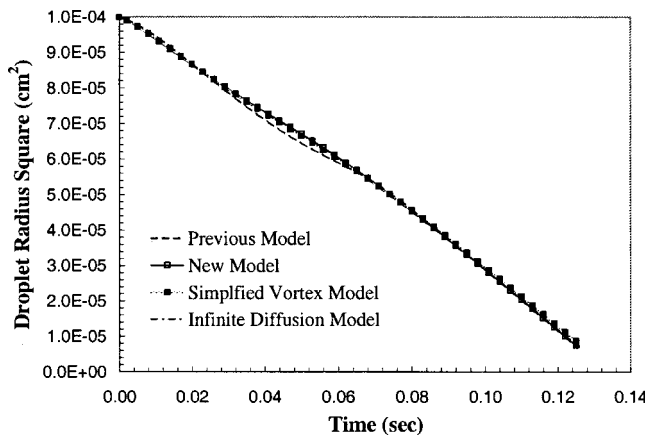


Fig. 5 Droplet radius square variation versus time

vaporization becomes more important, which is indicated by the discrepancy between the results of the infinite diffusion model and those of the other models. Shortly after the effects of preferential vaporization become apparent, the effects of surface regression also become more important. The previous model overpredicted the mass fraction of the C_6H_{14} . This overprediction becomes more severe at later times. The present model gives satisfactory agreement with the simplified vortex model. The magnitude of $Pe_V \cdot Le$ versus time is plotted in Fig. 7. The maximum value is close to 10, and at this point, the difference between the surface and average values is only about half of the difference at $Pe_V \cdot Le = 0$ (i.e., no surface regression rate). From numerical experiments, it was found that the infinite diffusion model can give a reasonably good result when $Pe_V \cdot Le < 1$. The previous model extends this limit to $Pe_V \cdot Le < 4$, and the present model further extends beyond this limit. As shown in this case, when $Pe_V \cdot Le \sim 10$, the present diffusion model can still yield a result similar to that of the simplified vortex model.

Comparisons With Experimental Data. The first computation examines the present model performance at low-pressure environments for a single component droplet. One set of data in an experimental investigation on single droplet vaporization ([22]) was used here. The droplet with an initial diameter of 2 mm and an initial velocity of 1.1 m/s vaporizes at a low pressure (1 atm) and high temperature (1000 K) environment. Figure 8 shows the comparison between the computed and experimental droplet radius variations versus time. A good agreement is observed between the measured data and the computation results. The corresponding surface temperature temporal history is shown in Fig. 9

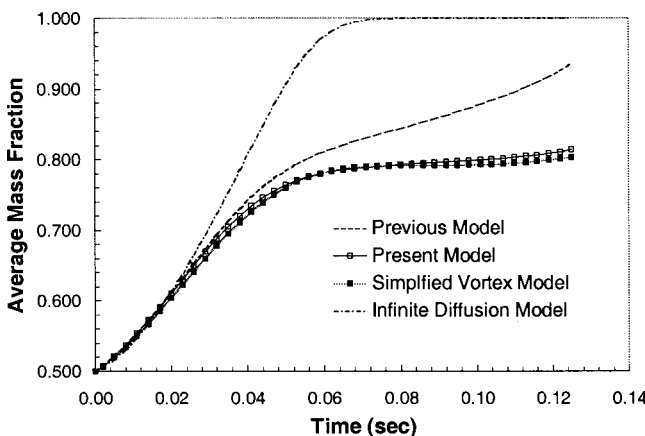


Fig. 6 C_6 average mass fraction variation versus time

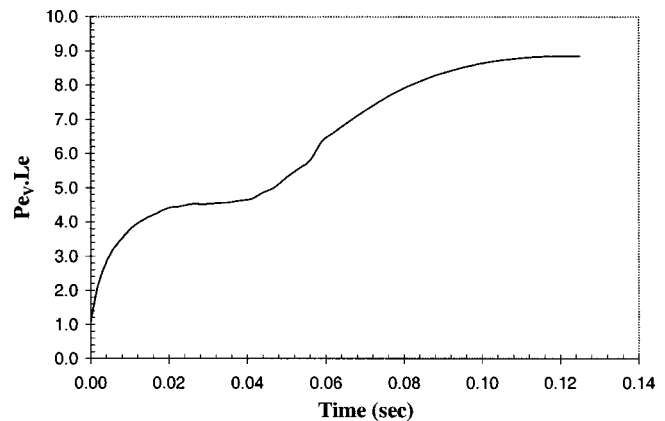


Fig. 7 $Pe_V \cdot Le$ variation versus time

where the computational result of Hohmann et al. [12] is also plotted. The present computation agrees very well with that of Hohmann et al. [12]. It is worthy to point it out that Hohmann et al. [12] used a one-dimensional liquid phase model similar to the model proposed by Jin and Bormann [5] whose computational cost is much more expensive than the present model. For illustration, the average temperature variation versus time is also plotted in Fig. 9. Due to the relatively high thermal resistance of the liquid, a large temperature gradient inside the droplet exists. This is indicated by the difference of the surface and average temperatures. Since the infinite diffusion model assumes uniform distribution and calculates temperatures equivalent to average temperatures, it cannot be expected to be accurate enough.

The second computation is for the vaporization of a multicomponent droplet of 75 percent C_7H_{16} and 25 percent $C_{10}H_{22}$. The computational parameters were taken from the ref. [23]. The droplet initially has a radius of 0.675 mm, a temperature of 294 K. The ambient air was initially in a quiescent state and accelerated to 3.1 m/sec at $t = 2$ sec. The computed and measured droplet surface temperatures were shown in Fig. 10, and the results for radius squared were shown in Fig. 11. Good agreement between computation and measurements is obtained.

In order to validate the present model performance at high-pressure environments, a droplet vaporizing at a low ambient pressure (1 atm) and a high ambient pressure (51 atm) were computed, respectively. The data were taken from the experiment of Kadota and Hiroyasu [10]. Initially, the droplet has a diameter of 1.8 mm and a temperature of 293 K, and the ambient gas has a temperature of 373 K. The droplet was fixed at a glass fiber, so

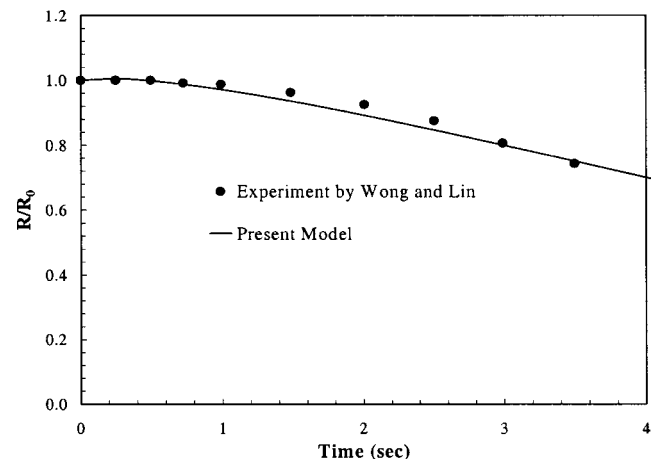


Fig. 8 Droplet radius variation versus time

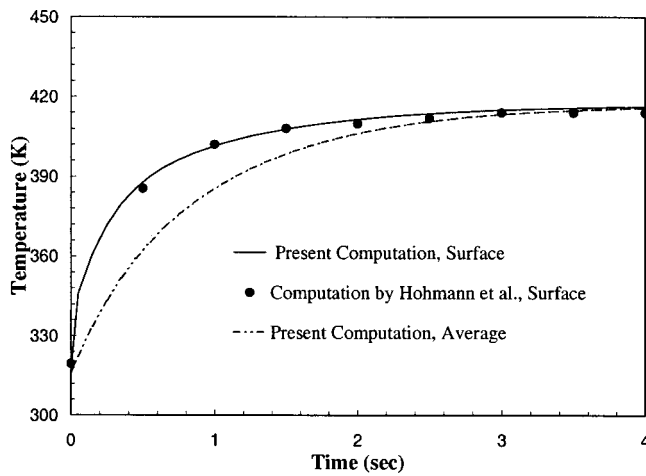


Fig. 9 Droplet temperature variation versus time

there was no forced convection. However, the natural convection existed ([10]). Figure 12 shows the nondimensional computed and experimental droplet radius (normalized by initial radius) history. For comparison, the results of both ideal gas model and high-pressure model are shown. A good agreement is obtained between the experimental data and the results of the high-pressure model. In contrast, the ideal gas model gives a significantly smaller vaporization rate at higher-pressure environments.

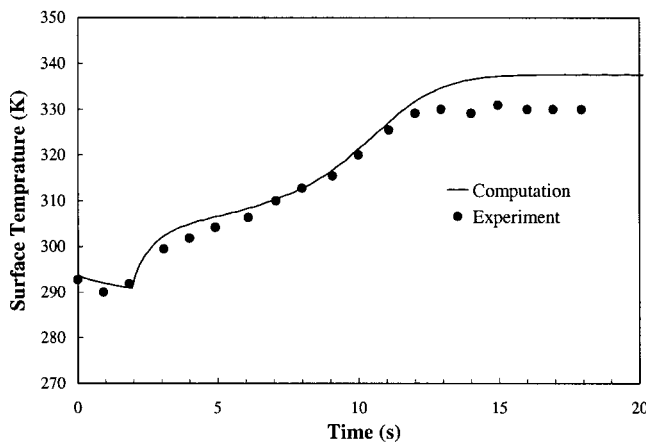


Fig. 10 Droplet surface temperature variation versus time

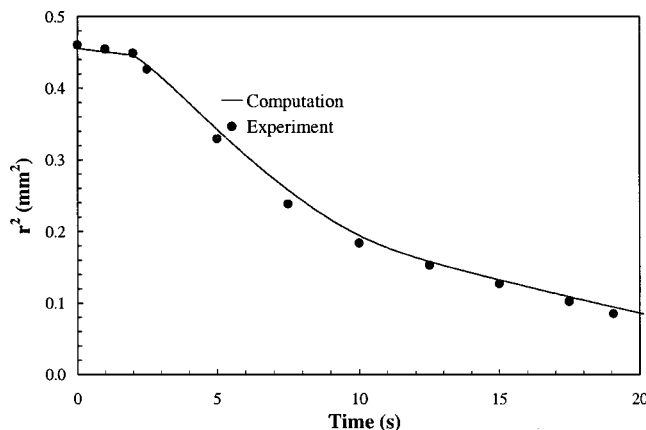


Fig. 11 Droplet radius squared variation versus time

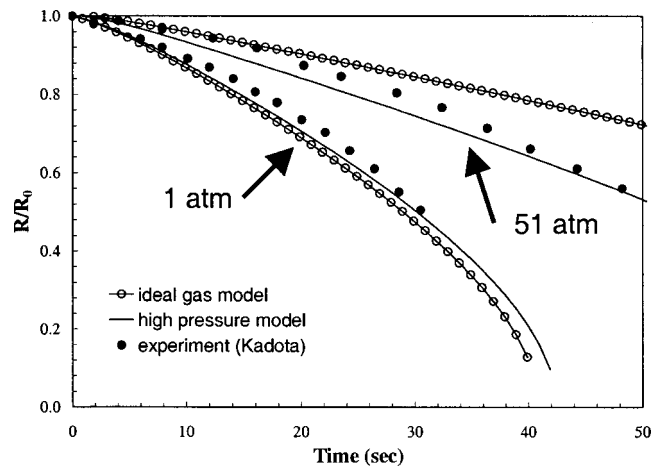


Fig. 12 Droplet radius variation versus time

Hollow-Cone Spray. The vaporization of a hollow-cone spray was computed to evaluate the feasibility of applying the present model to a realistic spray. The computational parameters were chosen to simulate the conditions in the GDI engine during late injection. The ambient gas has a high temperature of 500 K and a high pressure of 15 atm. The main parameters of the spray are listed in Table 1. The computational domain is a cylindrical column with a radius of 4 cm and a height of 10 cm. For computational efficiency, a two-dimensional axisymmetrical grid was used with 50 grid points in the axial direction and 30 grid points in the radial direction.

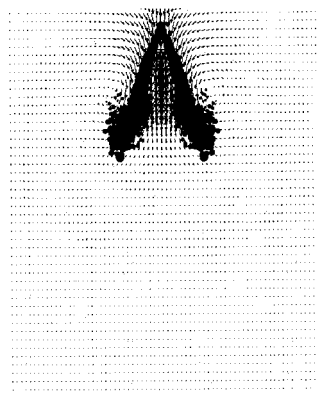
In the computation, the fuel is composed of 15 percent isopentane, 20 percent hexane, 45 percent isooctane, and 20 percent decane by mass, and it produces a distillation curve similar to that of a California Phase II gasoline ([24]). The plots of droplet position and gas velocity vector at several instants are shown in Fig. 13. Due to the strong entrainment induced by the spray and the high-density gas, a circulation of the gas flow is developed surrounding the droplets, and the spray collapses toward the axis. At later times, larger droplets tend to stay at the edge of the spray while smaller droplets tend to stay near the inside of the cone. Figure 14 shows the corresponding equivalence ratio distribution, and a richer region along the symmetry axis exists. To illustrate the importance of considering the nonideal behavior in high-pressure environments, a computation for this spray was made using the ideal gas law for thermodynamic phase equilibrium (i.e., without the high pressure effect). The vaporization history with and without high-pressure effects is shown in Fig. 15 where the species fuel mass is normalized by its total injection mass. Clearly, using the ideal gas law will lead to lower vaporization rates for both light (C_5H_{12}) and heavy (C_8H_{18}) components for it underestimated the mass fractions of the gas phase at the droplet surface.

Summary

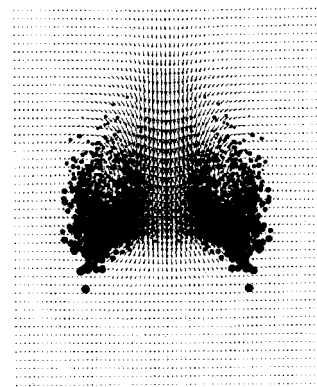
A preferential model for multicomponent droplets and sprays with zero-dimensional complexity was developed. It takes into account important mechanisms including nonuniform mass fraction and temperature distribution, internal circulation, surface regression, and nonideal behavior in high-pressure environments. The model was verified through comparison with three experi-

Table 1 Injection parameters

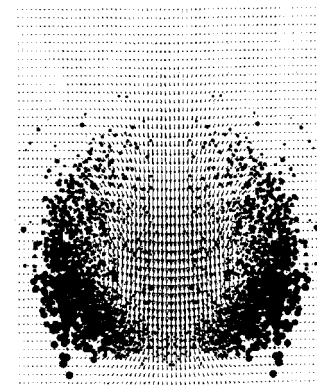
Injected mass	1.40 mg	Injection duration	1.3 ms
Injection velocity	25 m/s	SMD	30 μ m
Spray cone angle	45 deg	Spray thickness	10 deg



$t = 0.8 \text{ ms}$



$t = 2.2 \text{ ms}$

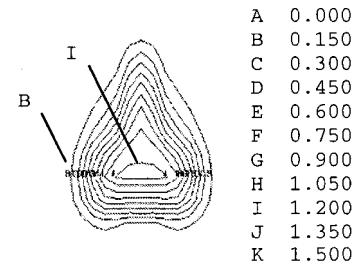


$t = 3.8 \text{ ms}$

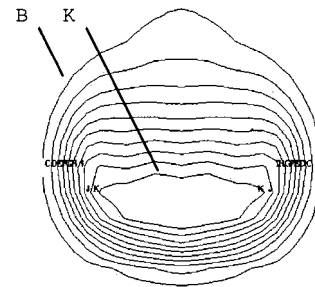
Fig. 13 Plot of droplet position and gas phase velocity vector

mental data and a simplified vortex (one-dimensional) model and two other zero-dimensional models (infinite diffusion model, the previous model developed by the authors). The present model was also applied to a hollow-cone spray typically used in gasoline direction engines. The results of the validation and application can be summarized as follows.

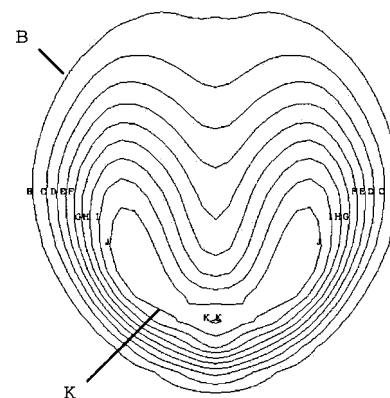
1 The defined nondimensional variables Pe_V and $Pe_V \cdot Le$ are appropriate variables representing the effects of preferential vaporization and surface regression. When $Pe_V \cdot Le < 4$, the effect of surface regression is negligible, and when $Pe_V \cdot Le < 1$, the effect of preferential vaporization is also negligible.



$t = 0.8 \text{ ms}$



$t = 2.2 \text{ ms}$



$t = 3.8 \text{ ms}$

Fig. 14 Plot of equivalence ratio contour

2 The comparison of three zero-dimensional models with the simplified vortex model for computations of a single droplet shows that the accuracy of the present model is the best among three models because it considers the effects of preferential vaporization and surface regression. In contrast, the accuracy of the infinite diffusion model is the worst because it ignores these two effects.

3 It was concluded from spray computations that using the ideal gas equation for phase equilibrium in high-pressure environments results in a lower vaporization rate than using the nonideal gas formulation.

Acknowledgments

This work was supported in part by the National Science Foundation under grant No. CTS-9734402, with Farley Fisher as tech-

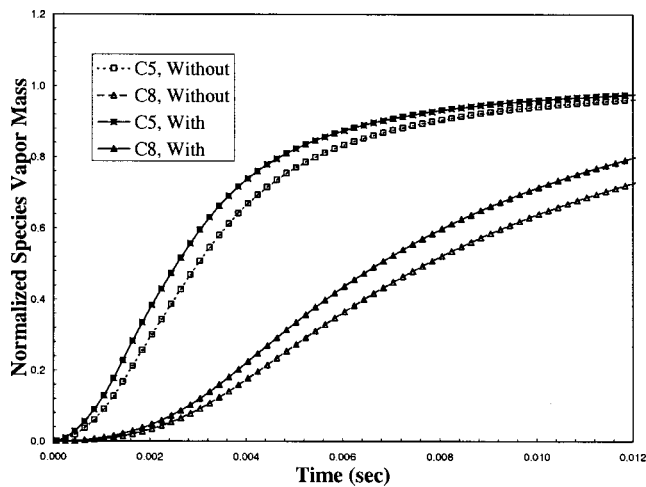


Fig. 15 Comparison of vaporization history with and without high pressure effect

nical monitor, and by Ford Motor Company. We also thank Dar-Lon Chang and Yu-Yu Lee for their assistance in preparing the manuscript.

Some of the results of this paper were presented at the 1999 Fall Technical Conference of ASME Internal Combustion Engine Division, Ann Arbor, MI, Oct. 1999.

Nomenclature

C_p	= heat capacity
D	= diffusion coefficient
E	= ratio between the difference of surface and average values and that at $Pe_V=0$
h_t	= heat transfer coefficient
h_v	= vaporization enthalpy
k	= heat conductivity
Nu	= Nusselt Number
P	= pressure
Pr	= Prandtl number
q	= heat flux
R	= droplet radius
Re	= Reynolds number
r	= radius coordinate
Sc	= Schmidt number
Sh	= Sherwood number
T	= temperature
t	= time
V	= velocity
X	= mole fraction
Y	= mass fraction
w	= vaporization rate
ρ	= density
Φ	= diffusion variable
α	= thermal diffusivity
Γ	= mass diffusion coefficient
θ	= nondimensional temperature
τ	= nondimensional time
ϕ	= variable in boundary conditions
ζ	= nondimensional radial coordinate
ξ_i	= correction factor for the effect of Stephan flow on mass transfer

Subscripts

d	= difference between the surface and mean values
g	= gas phase
i	= species index
m	= average value
s	= surface value
sat	= property at saturated state
o	= initial value
l	= liquid phase
∞	= ambient value

Superscript

e	= effective transport coefficient
-----	-----------------------------------

References

- [1] Sirignano, W. A., 1978, "Theory of Multicomponent Vaporization," *Arch. Thermodyn. Combust.*, **9**, pp. 231–247.
- [2] Megaridis, C. M., and Sirignano, W. A., 1990, "Numerical Modeling of a Vaporizing Multicomponent Droplet," *23rd Symposium (International) on Combustion*, The Combustion Institute, Pittsburgh, PA, pp. 1413–1421.
- [3] Abramzon, B., and Sirignano, W. A., 1989, "Droplet Vaporization Model for Spray Combustion Calculations," *Int. J. Heat Mass Transf.*, **32**, pp. 1605–1618.
- [4] Law, C. K., 1978, "Internal Boiling and Superheating in Vaporizing Multicomponent Droplets," *AIChE J.*, **24**, pp. 626–632.
- [5] Jin, J. D., and Borman, G. L., 1985, "A Model for Multicomponent Droplet Vaporization at High Ambient Pressures," *SAE Technical Paper 850264*.
- [6] Tong, A. Y., and Sirignano, W. A., 1986, "Multicomponent Droplet Vaporization in a High Temperature Gas," *Combust. Flame*, **66**, pp. 221–235.
- [7] Tong, A. Y., and Sirignano, W. A., 1986b, "Multicomponent Transient Droplet Vaporization with Internal Circulation: Integral Equation Formulation and Approximate Solution," *Numer. Heat Transfer*, **10**, pp. 253–278.
- [8] Renksizbulut, M., Bussmann, M., and Li, X., 1992, "A Droplet Vaporization Model for Spray Calculations," *Part. Part. Syst. Charact.*, **9**, pp. 59–65.
- [9] Abraham, J., and Magi, V., 1998, "A Model for Multicomponent Droplet Vaporization in Sprays," *SAE Technical Paper 980511*.
- [10] Kadota, T., and Hiroyasu, H., 1976, "Evaporation of a Single Droplet at Elevated Pressure and Temperature," *Bull. JSME*, **19**, pp. 1515–1521.
- [11] Ayoub, N. S., and Reitz, R. D., 1997, "Multidimensional Modeling of Fuel Effects and Split Injections on Diesel Engine Cold-Starting," *J. Propul. Power*, **13**, pp. 123–130.
- [12] Hohmann, S., Klingsporn, M., and Renz, U., 1996, "An Improved Model to Describe Spray Evaporation Under Diesel-Like Conditions," *SAE Technical Paper 960630*.
- [13] Aggarwal, S. K., and Shu, Z., "Multicomponent and Single-Component Fuel Droplet Evaporation under High Pressure Conditions," *AIAA Paper 98-3833*.
- [14] Annamalai, K., and Chandra, S., 1992, "Evaporation of Multicomponent Drop Arrays," *Emerging Energy Technology*, PD-Vol. 41, ASME, New York.
- [15] Jiang, T. L., and Chiang, W. T., 1994, "Droplet Vaporization in Expandable Dense Sprays at Sub- and Supercritical Conditions," *Atomization Sprays*, **4**, pp. 523–549.
- [16] Lippert, A. M., and Reitz, R. D., 1997, "Modeling of Multicomponent Fuels Using Continuous Distributions With Application to Droplet Evaporation and Sprays," *SAE Paper 972282*.
- [17] Zeng, Y., 2001, "Modeling of Multicomponent Fuel Vaporization in Internal Combustion Engines," Ph. D. thesis, University of Illinois at Urbana-Champaign, Urbana, IL.
- [18] Amsden, A., 1997, "KIVA-3V: A Block-Structured KIVA Program for Engines With Vertical or Canted Valves," *Los Alamos National Laboratory Report LA-13313-MS*.
- [19] Law, C. K., 1982, "Recent Advance in Droplet Vaporization and Combustion," *Prog. Energy Combust. Sci.*, **8**, pp. 171–201.
- [20] Reid, R. C., Prausnitz, J. M., and Poling, B. E., 1987, *The Properties of Gases and Liquids*, 4th Ed., McGraw-Hill, New York.
- [21] Law, C. K., 1976, "Multicomponent Droplet Combustion With Rapid Internal Mixing," *Combust. Flame*, **26**, pp. 219–233.
- [22] Wong, S. C., and Lin, A. C., 1992, "Internal Temperature Distributions of Droplets Vaporizing in High Temperature Convective Flows," *J. Fluid Mech.*, **237**, pp. 671–687.
- [23] Daif, A., Bouaziz, M., Chesneau, X., and Ali Cherif, A., 1998, "Comparison of Multicomponent Fuel Droplet Vaporization Experiments in Forced Convection With the Sirignano Model," *Exp. Therm. Fluid Sci.*, **18**, pp. 282–290.
- [24] Kelly-Zion, P. L., Styron, J. P., Lee, C. F., Lucht, R. P., Peters, J. E., and White, R. A., 1998, "Multicomponent Liquid and Vapor Fuel Measurements in the Cylinder of a Port Injected, Spark Ignition Engine," *27th Symposium (International) on Combustion*, The Combustion Institute, Pittsburgh, PA, pp. 2111–2117.

J. F. Kikstra¹

NRG,
P. O. Box 25,
1755 ZG Petten,
The Netherlands
e-mail: J.F.Kikstra@nrg-nl.com

A. H. M. Verkooijen

Faculty of Mechanical Engineering,
Delft University of Technology,
P. O. Box 5073,
2600 AG Delft, The Netherlands
e-mail: A.H.M.Verkooijen@iri.tudelft.nl

Dynamic Modeling of a Cogenerating Nuclear Gas Turbine Plant—Part I: Modeling and Validation

The high-temperature gas-cooled reactor is a promising concept for inherently safe nuclear power generation. This article deals with dynamic modeling of a combined heat and power plant, based on a helium-cooled reactor in combination with a closed-cycle gas turbine system. A one-dimensional flow model describing the helium flow and the two-phase water flow is used through the whole plant, with different source terms in different pieces of equipment. A stage-by-stage model is produced for the radial compressor and axial turbine. Other models include the recuperator, water/helium heat exchangers, a natural convection evaporator, valves, etc. In Part II the model will be used to analyze the dynamic behavior and to design a control system. [DOI: 10.1115/1.1426086]

1 Introduction

In the light of the depletion of fossil fuel resources, alternative energy sources should be considered. The main drawback of nuclear energy hitherto has been its safety problems which lead to expensive security measures, thus adversely affecting economic performance and public acceptance. The high-temperature gas-cooled reactor (HTGR) is a nuclear reactor which is inherently safe. Due to the use of small coated fuel particles in a graphite fuel element, combined with low power densities, a core meltdown is impossible. The reactor is cooled with helium, which is nuclearly and chemically inert. Even if there is no active cooling or even if no cooling gas is present in the core, the heat removal by radiation and natural convection keeps the temperature below the level at which radioactive compounds are released from the fuel. This safety characteristic can only be obtained with a small scale reactor, typically up to 250 MWth. The HTGR technology has been proven in practice; several plants have operated successfully ([1]). In those plants, a steam cycle was used to produce electricity. This led to poor economics due to the low efficiency. Better performance can be obtained when the gas is directly used in a closed-cycle gas turbine (CCGT) system. The low power level and high temperature makes the nuclear gas turbine a suitable candidate for CHP.

2 Plant Layout

The layout of the system for the considered ACACIA plant (advanced atomic cogenerator for industrial applications) is shown in Fig. 1 ([2]). The helium stream is first compressed in a five-stage radial compressor, (1), and is heated by the exhaust flow from the turbine in a recuperator, (2). After the recuperator, the helium passes through the core of the HTGR, (3), where it is heated. The core is a bed of graphite pebbles (6-cm diameter), which are loaded with a large number of small fuel particles. The helium then expands in the seven-stage axial turbine, (4), which drives the compressor and the generator at a speed of 12,000 rpm. Power electronics convert the electric energy (ca. 200 Hz) to 50 Hz grid frequency. Because of the converter, the shaft speed can freely vary. Helium from the turbine is cooled, first in the recuperator and subsequently in the precooler, (5). In the precooler, heat is transferred to an intermediate helium circuit. The purpose of the intermediate stream is to avoid ingress of water in the primary system, which can lead to reactivity and corrosion problems. The intermediate loop is kept at a higher pressure than the primary system and the steam system, so that in case of a leak secondary helium flows into the primary loop or into the steam circuit. In the steam generator, part of the intermediate helium flows through a superheater, (6). The bulk of the flow bypasses this heat exchanger, because the steam has to be only slightly superheated. Then the helium flows through a natural convection evaporator, (7), and an economizer, (8). The steam is exported to an industrial customer. The intermediate flow is subsequently cooled in the final cooler, (9), and compressed in the blower, (10). Table 1 summarizes the ACACIA operating conditions.

3 Dynamic Model

3.1 Goal and Structure. The main reasons for the development of the dynamic model of the ACACIA plant are (1) to investigate the interaction between design and dynamics, (2) to develop and test a control structure, (3) to determine the consequences of disturbances and accidents, and (4) to establish startup and shutdown procedures.

(1) *Investigation of Interaction Between Design and Dynamics.* Some design decisions strongly affect the system dynamics. Examples are the size of equipment, volumes between equipment, choice for single-shaft or multishaft system, and the position of control valves. With the dynamic model the influence can be checked with some typical transients. In order to easily change the configuration, the model must be modular.

(2) *Development and Testing of a Control Structure.* A dynamic model can be used to predict the responses of controlled variables (temperatures, pressures, etc.) on changes of process input-variables like valve positions, pump speeds, etc. When these interactions are mapped, a scientifically justified approach to the control system design can be followed. The control system can subsequently be implemented in the model, so that it can be tested and tuned to give stable and robust control. Therefore it is necessary to have a dynamic model which closely predicts the behavior of the plant in its normal operating region.

(3) *Establishing Startup and Shutdown Procedures.* In order to establish startup and shutdown procedures it is necessary to

¹Current address: Cargill R&D Europe, P.O. Box 34, 4600 AA Bergen op Zoom, The Netherlands. e-mail: Jan_Foeke_Kikstra@Cargill.com

Contributed by the Nuclear Division of THE AMERICAN SOCIETY OF MECHANICAL ENGINEERS for publication in the ASME JOURNAL OF ENGINEERING FOR GAS TURBINES AND POWER. Manuscript received by the C&F Division, Oct. 2000; final revision, Apr. 2001. Editor: R. Duffey.

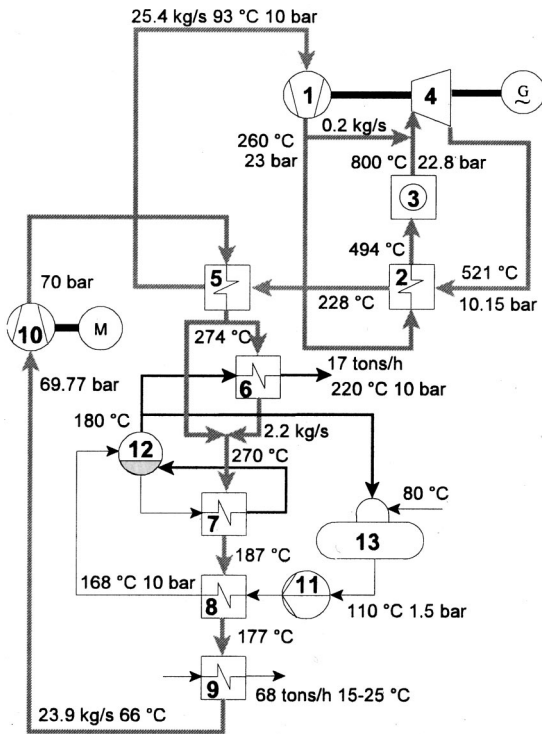


Fig. 1 ACACIA plant layout

model the process behavior in a larger operating region. The model should then be valid for low flows as well as for normal flows.

(4) *Determining the Consequences of Disturbances and Accidents.* In nuclear plants it is of high importance to be able to predict the consequences of accidents, since it has to be guaranteed that accidents will not lead to release of radioactivity. The accident transients that have to be calculated are

1. load rejection, sudden disconnection from the grid;
2. shaft break of turbomachinery;
3. compressor surge and stall problems;
4. helium leakage, leading to reverse flow or complete depressurization; and
5. withdrawal of control rods.

To calculate the consequences of incidents the model should be able to predict the plant behavior for negative flows.

3.2 Simplifying Assumptions. The most important assumptions used to simplify the rigorous model described above, have been listed in Table 2 and are discussed below. Of course, many more assumptions have to be made regarding the effects simulated or discarded in models of different components. These assumptions are discussed in the description of the component model.

(1) *One-Dimensional Treatment of Flowpaths.* Under normal operating conditions, the flow is turbulent through the whole system, therefore radial differences are not very important. If the flow becomes laminar, calculations of properties like, e.g., heat transfer coefficients and friction factors can nevertheless be based on radially averaged fluid properties. Because the rate of change of fluid properties perpendicular to the streamline is small compared to the rate of change along the streamline, the flow through the system can be modeled as one-dimensional, which means that all fluid properties are assumed to be uniform over any cross section. A one-dimensional treatment of course does not capture precisely what happens inside all the different components. This is

Table 1 Key parameters of ACACIA plant

Reactor		Compressor	
Power	40 MW	Inlet pressure	10 bar
Pressure	23 bar	Inlet temp.	93 °C
He temperatures	494-800 °C	Mass flow	25.4 kg/s
Secondary cycle		Steam production	
Medium	He	Mass flow	17 ton/h
Pressure	70 bar	Inlet pressure	3 bar
Mass flow	23.8 kg/s	Inlet temp.	80 °C
Temperatures	68-276 °C	Outlet pressure	10 bar
		Outlet temp.	220 °C
Cycle performance			
Electric eff.	32%	Total eff.	62%

not a problem, since the model focuses on the interaction of components rather than on the detailed behavior of a component.

(2) *Discretization of Flowpath With Staggered Grid and Method of Lines.* Instead of solving the microscopic balance equations, the flowpath will be divided in sections for which macroscopic alternatives will be solved. The flow path in the different components (recuperator, reactor, compressor, etc.) is divided into a number of so-called thermal nodes, which are small volumes, assumed to be perfectly mixed and to have a constant cross-sectional area. For these thermal nodes, the mass and energy balances are solved. The mass flow between these volumes is determined by solving the momentum balance for a so-called flownode, which consists of the two halves of neighboring thermal nodes. This staggered grid ([3]) is chosen because of its numerical stability.

(3) *Point-Kinetic Neutronics Model.* The behavior of the reactor is only of interest as far as it influences the energy conversion system. Only the relation between input conditions, control rod-positions, and outlet temperature needs to be modeled. This has been done with a zero-dimensional point kinetic. The parameters of this simplified model have been derived from a rigorous model built with the three-dimensional neutronics and thermal hydraulics code PANTHER. The difference between the prediction of these two models for typical operational transients is within two percent ([4]).

Table 2 Simplifying assumptions

Modeling Assumptions	
1	One-dimensional treatment of flowpaths
2	Discretization of flowpath with staggered grid and method of lines
3	Point-kinetic neutronics model
4	Nonhomogenous two-phase flow with single momentum balance

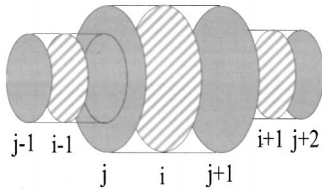


Fig. 2 Flowpath divided in thermal node $i-1$, i and $i+1$ and flownodes j and $j+1$

(4) *Nonhomogenous Two-Phase Flow With Single Momentum Balance.* At the pressures for which water/steam subsystem model should be valid (1 to 20 bar), a water/steam mixture cannot be modeled as a homogenous fluid, since there can be a considerable difference in velocity between the two phases. An alternative is to solve the balances for each phase separately, but in that case it will be difficult to describe the momentum exchange between the phases. A frequently used alternative is to assume thermodynamic equilibrium, to solve the momentum balance for the two-phase mixture and to add an empirical relation between the relative velocities of both phases ([5]).

3.3 Structure of the Model. In order to make a process model which can easily be adopted to changes in the process, it is necessary to build a generic model. In that way, changes in geometry, sizes, or layout can easily be incorporated in the model. To develop such a model, the process is divided into components and subsystems which can be described with a modular model.

The division of the total plant into components, which are interconnected with few relations, is analogous to the different pieces of equipment. Modeled components are compressor, recuperator, reactor, turbine, shaft, etc. Within each component there exist subsystems which behave similarly in different components. These subsystems are

1. one-phase flow,
2. two-phase flow,
3. neutronics, and
4. solid structure.

First a general model for these subsystems will be developed, then the component specific source terms will be modeled. The one-phase flow model is discussed underneath; the two-phase model is very similar. The model of the neutronics of the reactor is described by Verkerk [4]. The model of the solid structure allows for heat transport by conduction in two dimensions, heat transfer to a fluid and internal heat generation (from the nuclear reaction).

3.4 Flow Model. In Fig. 2 the staggered grid, the division of the flowpath in ideally mixed thermal nodes and flownodes consisting of two half thermal nodes, is illustrated. The mass balance for thermal node i between the cross sections j and $j+1$ in Fig. 2 is

$$V_i \frac{d\rho_i}{dt} = \phi_j - \phi_{j+1}. \quad (1)$$

Using the simplification of negligible axial diffusion of heat, the total energy balance (including internal, kinetic, and potential energy) for the same element can be written as

$$V_i \frac{d(\rho_i E_i)}{dt} = \phi_j (H + K + \Phi)_j - \phi_{j+1} (H + K + \Phi)_{j+1} + Q_i + W_i. \quad (2)$$

The total enthalpy ($H + K + \Phi$) of a stream crossing the cell border is assumed to be equal to the value in the thermal node which lies upstream:

$$(H + K + \Phi)_j = \begin{cases} (H + K + \Phi)_{i-1} & \phi_j \geq 0 \\ (H + K + \Phi)_i & \phi_j < 0. \end{cases} \quad (3)$$

The momentum balance for flownode j consisting of half of thermal node $i-1$ and half of thermal node i is

$$\frac{d \left(\frac{\Delta x_{i-1} + \Delta x_i}{2} \phi_j \right)}{dt} = \phi_{i-1} v_{i-1} - \phi_i v_i + A_{i-1} p_{i-1} - A_i p_i \\ + F_{\text{friction } ji-1} + F_{\text{friction } ji} + \frac{F_{\text{rot } i-1} + F_{\text{rot } i}}{2} \\ + \frac{F_{\text{grav } i-1} + F_{\text{grav } i}}{2} + F_{\text{area change } j}. \quad (4)$$

$F_{\text{area change}}$ is a force which compensates the pressure and forces of rotating equipment and gravity in case of a change of cross-sectional area ($A_{i-1} \neq A_i$). In order to conserve the numerical stability of the staggered grid, the friction force has to be calculated from the mass flow at the inlet and outlet, and not at the center of a volume. For the friction force apply

$$F_{\text{friction } ji} = - \frac{e_v |\phi_j| \phi_j}{4 A_i \rho_i} \quad F_{\text{friction } j+1i} = - \frac{e_v |\phi_{j+1}| \phi_{j+1}}{4 A_i \rho_i} \quad (5)$$

using the friction loss factor e_v which can be calculated from the Fanning friction factor f , flow length Δx , and equivalent hydraulic diameter D_e .

$$e_v = \frac{4 f_i \Delta x_i}{D_{ei}}. \quad (6)$$

These balances can be used to describe the behavior of both gas and compressible liquid, only the equation of state and the relation between enthalpy, pressure, and temperature have to be added. The relations used for helium are given by Yan [6], those for water are given by Wagner [7]. The set of equations will be closed when correlations for e_v , $Q F_{\text{rot}}$ and W are added. These relations differ from component to component and will be described in the component models.

The method described above can be viewed as modeling of a flow through a sequence of perfectly mixed tanks. Another view is to consider it as a continuous system solved with the method of lines, in which the energy balance is solved with a first-order upwind scheme and the mass and momentum balances are solved with second-order central schemes. This discretization is a valid approximation as long as the velocities stay well below the velocity of sound. If sonic or supersonic gas velocities are reached, only information of the upstream node can influence the flow in a given node. In this case the central difference scheme is no longer applicable. In the primary helium flow the highest Mach number is 0.4 (in the compressor). In valves connecting high and low pressure plenums choked flow can occur, therefore an alternative model is used in these valves.

3.5 Compressor Model. In order to simulate the compressor behavior, relations have to be found between the source terms (forces on, heat transport to, and work done on the fluid), the inlet conditions and mass flow, the speed, and the geometry of each stage. These relations have to be valid during normal operation, stalled operation, and backflow (as it occurs in surge). In normal operation, the source terms are calculated from the changes in direction and magnitude of the velocity of the gas flow, using a method based mainly on the work of Gravdahl [8]. In the stalled region and for backflow a empirical relation based on the work of Greitzer [9] is used for the calculation of the forces on the gas. The compressor flowpath is discretized with two thermal nodes for each stage: one for the impeller and the other for the diffuser and volute.

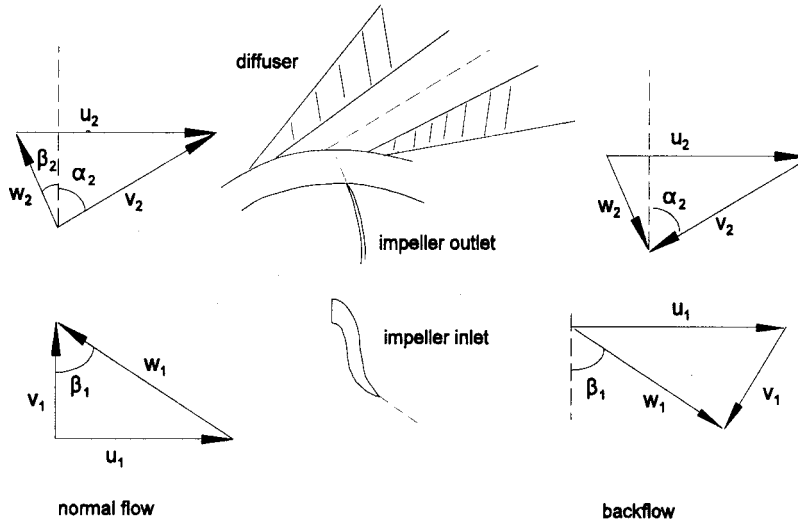


Fig. 3 Velocity triangles in the radial compressor

Figure 3 shows the velocity triangles at the impeller and diffuser inlet for positive and negative flow. v , w , and u denote the absolute, relative, and impeller velocity, respectively. The enthalpy rise ΔH over the impeller flowpath can be calculated from the Euler equation:

$$\Delta H = u_{\text{entr}} v_{\text{tang entr}} - u_{\text{ex}} v_{\text{tang ex}} \quad (7)$$

For forward flow $v_{\text{tang entr}}$ is zero. The tangential gas velocity at the impeller outlet is calculated from the impeller velocity, the backswept angle of the blades, and the slip losses, which are calculated with a correlation given by Japikse [10]. For backflow it is assumed that the gas flow leaves the diffuser and impeller with the angles α_2 and β_1 equal to the wall angles. This is a fair approximation, since an exact prediction of the enthalpy rise is not very important in backflow transients. The work done on the fluid (W) is calculated from the Euler enthalpy rise ΔH and the disk friction work, for which a correlation given by Pantell [11] is used.

The isentropic enthalpy gain ΔH_{isen} over the impeller is obtained when a number of loss terms are deducted from the Euler enthalpy rise. The modeled losses are incidence losses $\Delta H_{\text{inc eye}}$ and $\Delta H_{\text{inc tip}}$ (due to a discrepancy between blade and gas angle at the impeller and diffuser inlet), clearance losses ΔH_{cl} (due to a leakage over the blades in the gap between impeller and house) and backflow losses $\Delta H_{\text{backflow}}$ (due to reinjection of gas into the impeller because of the pressure gradients in the impeller tip region).

$$\Delta H_{\text{isen}} = \Delta H - \Delta H_{\text{inc eye}} - \Delta H_{\text{inc tip}} - \Delta H_{\text{cl}} - \Delta H_{\text{backflow}} \quad (8)$$

The force on the gas in the impeller are then calculated from ΔH_{isen} using

$$\left(\frac{p_{\text{in}} + F_{\text{rot}}/A_{\text{imp av}}}{p_{\text{in}}} \right) = \left(\frac{T_{\text{in}} + \Delta H_{\text{isen}}/C_p}{T_{\text{in}}} \right)^{\kappa/(\kappa-1)} \quad (9)$$

The incidence losses are calculated according to the “NASA shock loss theory” ([10]). It is based on the assumption that the kinetic energy associated with the tangential component of the “mismatch” in velocity, $1/2 \Delta v_{\text{tang}}^2$, is dissipated as illustrated for the diffuser inlet in Fig. 4. Insertion of trigonometric relations yields

$$\Delta H_{\text{inc eye}} = \frac{(u_1 - v_1 \tan \beta_1 \text{ blade})^2}{2} \quad (10)$$

$$\Delta H_{\text{inc tip}} = \frac{(v_{\text{tang 2}} - v_{\text{rad 2}} \tan \alpha_2 \text{ diff})^2}{2}$$

The clearance loss and backflow loss are assumed to be a constant fraction of the enthalpy gain. The friction losses could be taken into account in the same manner. However, in the approach followed here, the friction forces (calculated from the friction loss factor e_v) are used in the momentum balance. In order to calculate the friction losses in the impeller, diffuser and volute, the friction factor Reynolds relation for a smooth pipe is used. Moreover, the three 90-deg bends in the volute give and the deswirl vanes give extra pressure losses, which are modeled with relations given by Fox [12].

When the isentropic and total enthalpy rise are nondimensionalized through division by the square impeller velocity (yielding ψ and λ) and plotted against ϕ , the ratio of gas and impeller velocity, the curves approximately collapse on one line for a wide range of input conditions and shaft speeds ([13]). This is shown in Fig. 5.

$$\phi = \frac{v_{\text{inlet}}}{u} \quad \lambda = \frac{\Delta H}{u^2} \quad \psi = \frac{\Delta H_{\text{isen}}}{u^2} \quad (11)$$

The calculational method described above also gives a prediction in the stall region (dotted in Fig. 5). Due to the separation of the flow from the blades and local circulating flows, the calculation overestimates ψ . Therefore, an empirical fit measured by Greitzer [9] is used for the stall and backflow region. The parabolic fit used is shown as a dashed line.

In the stall region, the steady-state characteristic cannot be used directly, because there is a delay induced by the development of stall cells in the stages. The time constant τ_{stall} for this phenomenon is related to the rotational speed, a typical τ_{stall} corresponds to two revolutions ([9]). The applied force is therefore calculated from

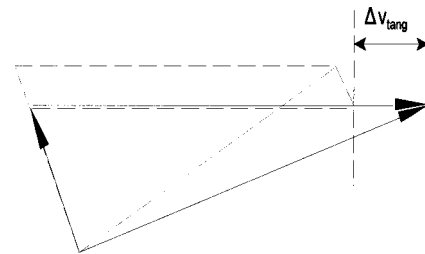


Fig. 4 Incidence loss at impeller tip (dotted: design velocities, drawn: actual velocities)

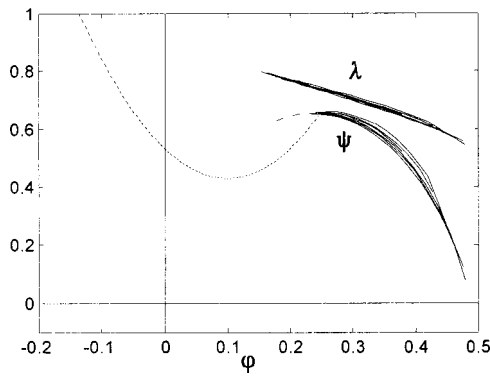


Fig. 5 Dimensionless stage curves with extension for stall and backflow

$$\frac{dF_{rot}}{dt} = \frac{1}{\tau_{stall}} (F_{rot,ss} - F_{rot}) \quad \tau_{stall} = \frac{2}{\omega} \quad (12)$$

In order to test the model, first the compressor map (shown in Fig. 6) has been calculated. The most striking feature is that the design point (marked with an asterisk) does not have the highest efficiency. Because the friction losses are high compared to the incidence losses, a higher efficiency is reached at lower mass flows. The dynamic behavior is tested in a configuration in which the compressor is connected with a plenum and a valve as shown in Fig. 7. In the transient the valve is closed further, so that the surge line is passed. The predicted oscillations of the compressor flow for two plenum sizes are shown in Figs. 8 and 9. The transition from stall, to classical surge and deep surge follows Greitzer's theory. The chaotic pattern in Fig. 8 is due to the interaction between the different stages. Unfortunately these predictions could not be verified with experimental results. However, the qualitative behavior is plausible, which is good enough for the purpose for which the model will be used.

3.6 Turbine Model. The turbine model is based on the two-dimensional gas path at the mean diameter. The source terms are calculated from the changes in direction and magnitude of the gas velocity using a first-principle model based on the work of Zehner [14]. φ , λ , and ψ (as defined in Eq. (11)) are related by the stage

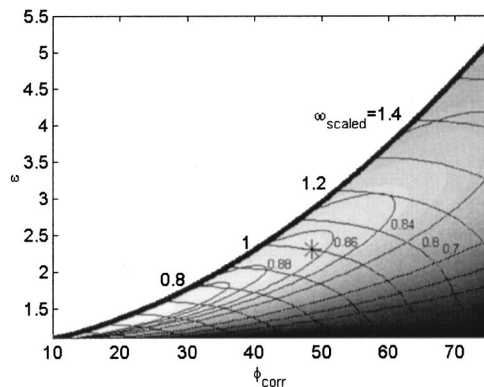


Fig. 6 Compressor map



Fig. 7 Compressor surge test configuration

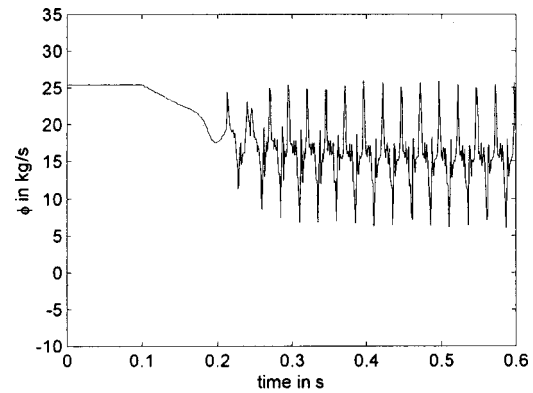


Fig. 8 Compressor flow during classical surge ($V_{plenum}=0.1 \text{ m}^3$)

efficiency and angles and magnitude of the velocities in stator and rotor, for both positive and negative flow. It is assumed that the gas leaving a row has the same angle as the blades at the outlet, for forward as well as for backward flow. For forward flow, this is a valid approximation. For backward flow, it is not as accurate because of the blunt blade shape at the outlet (normally inlet). However, backflow will only be encountered in very rare break accidents. For these accidents an approximation of the turbine behavior is good enough, since other effects which cannot be predicted (like size of the break) will have a stronger influence.

Using the angles and velocities as defined in Fig. 10 for forward flow the following φ - λ and φ - ψ relations can be obtained:

$$\lambda = \varphi (\cot \alpha_1 - \cot \beta_2) - 1 \quad (13)$$

$$\psi = \frac{\varphi}{2} \left[\frac{\varphi}{\sin^2 \alpha_1} \left(\frac{1}{\eta_{stator}} - 1 \right) + \varphi \left(\frac{1}{\eta_{rotor} \sin^2 \beta_2} - \frac{1}{\sin^2 \beta_0} \right) - 2(\cot \beta_0 - \cot \alpha_1) \right] - 1 \quad (14)$$

with η as a row efficiency. Similar results can be obtained for backflow.

The row efficiency is known from primary losses, secondary losses, and clearance losses, which are calculated using theoretical and empirical relations by Zehner [14] and Traupel [15].

$$\eta = 1 - (\zeta_{prim} + \zeta_{sec} + \zeta_{cl}). \quad (15)$$

For low flows this approach leads to nonphysical behavior, therefore in this region a parabolic fit is used. For zero flow the forces on the fluid are assumed zero, since no correlation for this small force could be found. The work input for zero flow is equal to the windmilling losses correlated as suggested by Schobeiri [16].

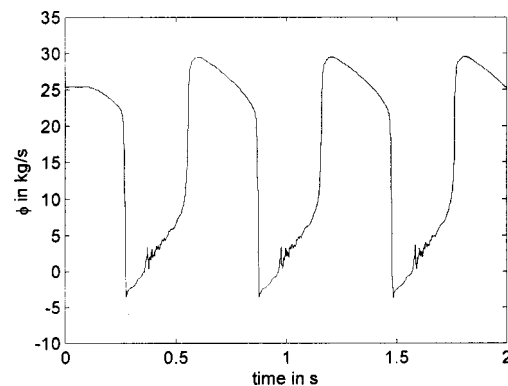


Fig. 9 Compressor flow during deep surge ($V_{plenum}=10 \text{ m}^3$)

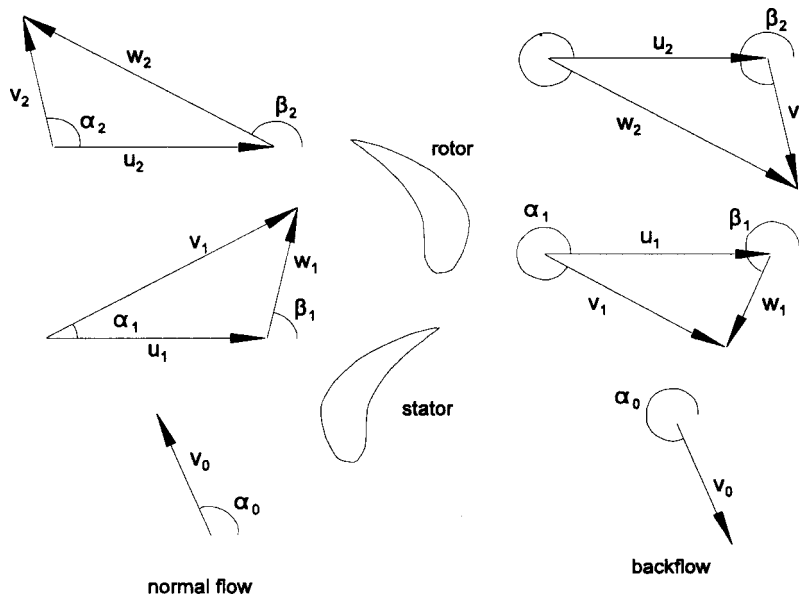


Fig. 10 Velocity triangles in the turbine stage

Figures 11 and 12 show the comparison between the model described here and a simple model based on Stodola's law ([15]) with a parabolic fit of efficiency versus dimensionless speed parameter ([17]). The flow ϕ and isentropic efficiency η_{isen} are plotted against the pressure ratio ε for different rotational speeds ω . The mass flow of the simple model is hardly dependent on the rotational speed. This is consistent with the expectations, since the mass flow is calculated from an expression based on the similarity with a nozzle, in which there is no rotational speed. The stage-by-stage model does not correctly model choking; the mass flow does not level off at high pressure ratios. This was to be expected, since the discretization scheme cannot be used for choked flow. The "nozzle" model, of course, correctly predicts the choking. If a correct prediction of choking in the dynamical model is necessary, then a choking valve (discussed later) can be placed directly after the turbine. The efficiency curves are again similar but not the same. The simple model assumes a quicker decline of efficiency at off-design conditions than the stage-by-stage model. If the parabolic fit for off-design efficiency is tuned to the results of the stage-by-stage model, the results would be more similar.

The turbine and compressor are connected with a shaft model in which the mechanical inertia is used to predict the shaft speed

from the rotational energy balance. The mechanical and electric losses are assumed to be a constant fraction of the electricity production.

3.7 Heat Exchanger Model. The core model of all one-phase heat exchangers consists of a hot flow, a cold flow, and a wall in between shown in Fig. 13. The wall model describes the heat storage in the wall and axial conduction. For proper counter-flow behavior each flow is divided in a number of thermal nodes (and flownodes) and the wall is divided in the same number of elements. 5 to 20 nodes were used for different heat exchangers. The discretization mesh has been assessed by comparison of typical transient results calculated with an increasing number of nodes. Since the thermal inertia of the wall is the most important dynamic feature, a low number of nodes gives almost the same results as an "infinite" number of nodes. In order to reach closure of the equations describing the flow through the core relations have to be obtained for friction-factor f and the heat exchange with the wall Q for both sides.

Q can be written as

$$Q = \Omega \alpha S (T_{wall} - T_{fluid}). \quad (16)$$

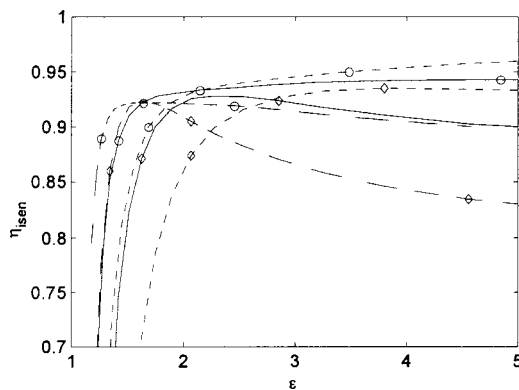


Fig. 11 Efficiency comparison of simple and stage-by-stage model

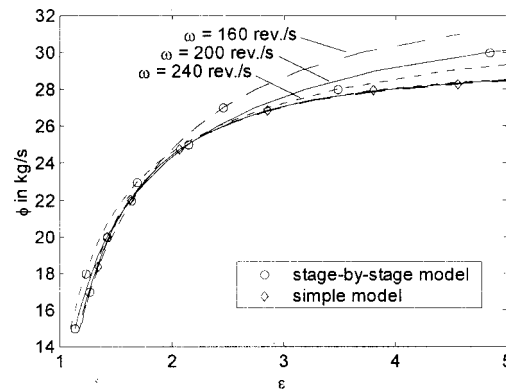


Fig. 12 Mass flow comparison of simple and stage-by-stage model

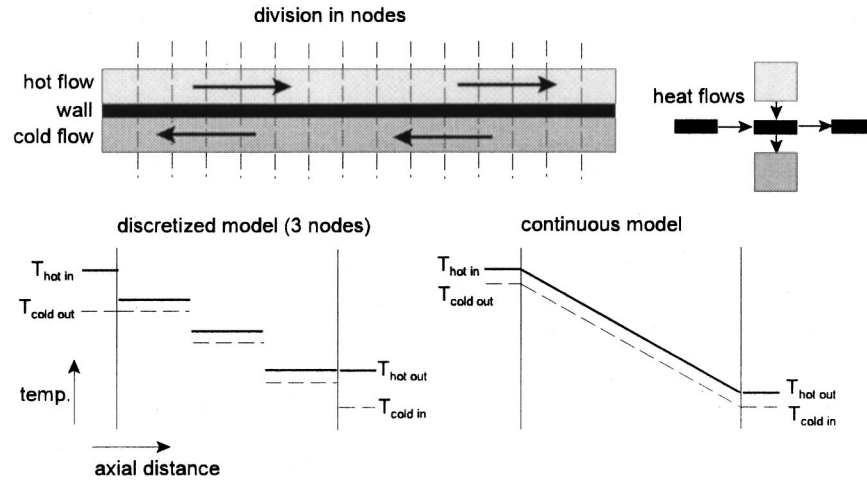


Fig. 13 Heat exchanger discretization

The correction factor Ω is used to adjust for the lower heat transfer due to the modeling with a number of ideally mixed nodes instead of a continuous model. The efficiency of a counter-flow heat exchanger is considerably higher than the efficiency of a small number of ideally mixed heat exchangers with the same area and heat transfer coefficients. This is clarified in Fig. 13. With a ΔT in each node which is equal to that in the continuous model, the difference between the outlet temperatures of the discretized model is considerably larger than that of the continuous model. A correction can be made by enlarging the driving force with a factor Ω . The value of Ω is highly dependent on the number of mixed volumes which represent the heat exchanger; for small numbers no Ω can be found, whereas for large numbers Ω tends to one. An analytical expression for Ω can be found using the definition of heat exchanger efficiency η ([18]).

$$\Omega = \frac{\eta}{NTU \left(1 - \eta \frac{C_{\min}}{C_{\max}} \right)} \quad NTU = \frac{\alpha S}{C_{\min}} \quad \eta = \frac{Q_{\text{transf}}}{Q_{\text{transf } S=\infty}} \quad (17)$$

NTU stands for number of transfer units and C_{\min}/C_{\max} is the ratio of heat capacities of the flows. η is a function of C_{\min}/C_{\max} , NTU, and the flow arrangement, therefore it can be plotted against C_{\min}/C_{\max} and NTU for a counterflow arrangement. This is shown in Fig. 14.

The pressure and heat transfer coefficients for each node are related to the flow conditions with empirical relations between the friction factor and the Reynolds number and between the Stanton-Prandtl^{2/3} group and the Reynolds number.

The heat exchanger dynamics have been verified with the energy balance of the transient following a step change of 100°C on the cold flow inlet temperature of recuperator. The response of the inlet and outlet temperatures are given in Fig. 15, while Fig. 16 shows the heat flow to the heat exchanger body:

$$Q_{\text{to steel}} = C_p [\phi_{\text{hot}} (T_{\text{hot in}} - T_{\text{hot out}}) + \phi_{\text{cold}} (T_{\text{cold in}} - T_{\text{cold out}})] \quad (18)$$

Integration of $Q_{\text{to steel}}$ gives the enthalpy difference of steel, from this the average steel temperature rise can be calculated.

$$\int_0^t Q_{\text{to steel}} = \Delta h_{\text{steel}}(t) = MC_p \Delta T(t) \rightarrow \Delta T(\infty) \approx \Delta T(100 \text{ s}) = 50^\circ\text{C} \quad (19)$$

The mean wall temperature rise is again calculated to be 50°C from comparison of the average wall temperature before and after

the transient. This is also the expected behavior when the inlet temperature on one side is raised with 100°C while the other inlet temperature is kept constant.

3.8 Valve Model. In valves connecting high and low-pressure plenums, choked flow can occur. In order to correctly predict the behavior in both choked and unchoked condition, the valve is modeled as a series connection of an isentropic nozzle and a resistance, as proposed by Pool [19]. The minimum area of the nozzle and friction loss factor of the resistive element are related to the stem position. From these two and the pressure difference the mass flow is calculated. This mass flow is then

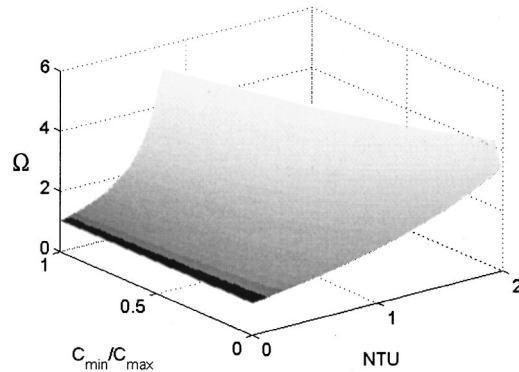


Fig. 14 Correction factor Ω

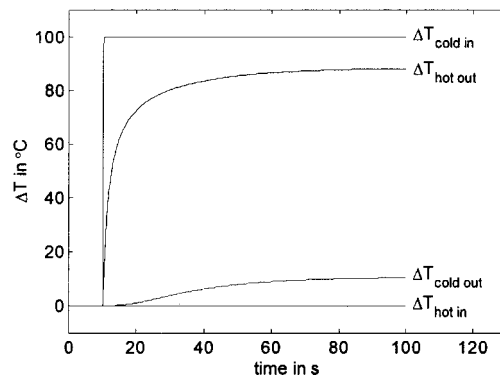


Fig. 15 Response on temperature step

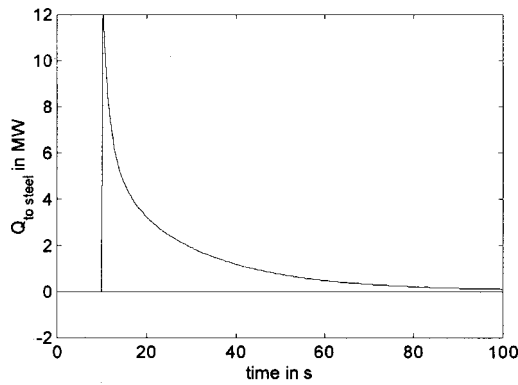


Fig. 16 Heat flow to recuperator steel

established by adjusting a fictional friction loss factor which is used in the momentum balance. The cross-sectional area of the thermal node is much larger than the nozzle area, so choked flow in the nozzle does not lead to choked flow in the thermal node. The valve model is tested by applying a varying positive and negative pressure drop over an open valve. In Fig. 17 the steady-state results are compared with the analytical solutions for a low pressure drop and choked positive and negative flow.

3.9 Complete Plant Model. In order to simulate the complete flowsheet shown in Fig. 1, several other models have been produced. These include models for the two-phase flow in the evaporator, like a correlation for the velocity ratio of water and steam in the natural convection loop and correlations for two-phase friction losses and heat transfer. Moreover, fairly simple models have been produced for the feedwater pump, secondary helium blower, deaerator, and steam drum ([20]).

The models have been implemented in the simulation tool Aspen Custom Modeler [21]. All the component models can be combined in a graphical environment, thus allowing the user to build a flowsheet, reusing the predefined models. ACM solves the implicitly formulated set of the algebraic and differential equations. The complete plant model contains approximately 60,000 variables and 1000 state variables. Because of the implicit formulation, the model can also easily be used for design. For example, instead of calculating the compressor performance from its geometry, the geometry needed to achieve a certain pressure ratio can be found.

In order to validate not only the component behavior, but also the transient behavior of the complete primary cycle, another model has been produced using the RELAP5 transient code for nuclear power plant simulation. Predictions of load-following and load-rejection transients are slightly different in numerical results,

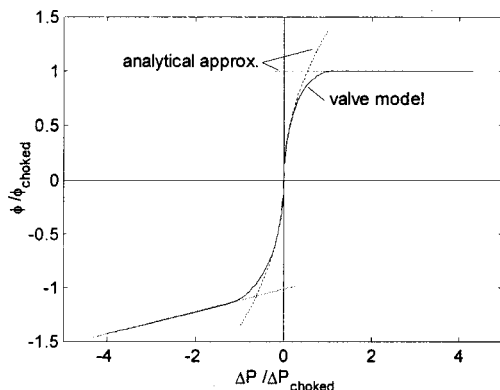


Fig. 17 Pressure flow relation of valve

the qualitative behavior is the same. The differences can all be attributed to the poor representation of the compressor and the turbine in RELAP5 ([4,20]).

4 Conclusions

A dynamic model of the cogenerating nuclear gas turbine plant has been produced. It is capable of describing a wide range of operating conditions, thus making it a powerful tool both for design and optimization of a control structure and incident analysis. Its level of detail surpasses any model described in the literature. The setup of the code allows also for use as a design code. Because of its modular approach it can easily be used for other power plants. If thermodynamic properties of air, fuel, and off-gas are added, one can easily model a complete conventional power plant.

It is impossible to prove that a dynamic model correctly predicts the transient behavior under all conditions. However, by logical tests and comparison with analytical solutions and other models and codes, it is made plausible that the model developed gives a correct estimation of the system dynamics over a time scale varying from fractions of a second to several days.

Nomenclature

- A = cross-sectional area in m^2
- C = heat capacity in J K^{-1}
- C_p = specific heat in $\text{J kg}^{-1} \text{K}^{-1}$
- D_e = equivalent hydraulic diameter in m
- e_v = friction loss factor
- $E = U + K + \Phi$ = specific total energy in J kg^{-1}
- F = force in N
- $g = 9.81$ = gravitational acceleration in m s^{-2}
- h = height in m
- $H = U + p/\rho$ = specific enthalpy in J kg^{-1}
- $K = 1/2 v^2$ = specific kinetic energy in J kg^{-1}
- M = mass in kg
- p = pressure in Pa
- Q = heat flow in J s^{-1}
- S = surface for heat transfer in m^2
- t = time in s
- T = temperature in K
- u = rotor velocity in m s^{-1}
- U = specific thermal energy in J kg^{-1}
- v = absolute velocity in m s^{-1}
- $V = A \Delta x$ = volume in m^3
- w = relative velocity in m s^{-1}
- W = work in J s^{-1}
- α = absolute angle in rad or heat transport coefficient in $\text{J m}^{-2} \text{K}^{-1} \text{s}^{-1}$
- β = relative angle in rad
- Δx = thermal node flow length in m
- ε = pressure ratio
- ζ = row losses
- η = efficiency
- $\kappa = C_p/C_v$ = ratio of specific heats
- λ = work coefficient
- ρ = density in kg m^{-3}
- τ = time-constant in s
- ϕ = mass flow in kg s^{-1}
- Φ = specific potential energy in J kg^{-1}
- ψ = isentropic work coefficient
- ω = rotor speed in revolution s^{-1}
- Ω = correction for heat exchanger efficiency
- φ = flow coefficient
- av = average
- $entr$ = entrance
- ex = exit
- cl = clearance
- $diff$ = in diffuser
- imp = in impeller

inc = incidence
 isen = isentropic
 NTU = number of transfer units
 sec = secondary
 ss = steady-state
 tang = tangential
 tranf = transferred
 rot = in rotating equipment

References

- [1] Kugeler, K., and Schulten, R., 1989, *Hochtemperatur-reaktortechnik*, Springer, Berlin.
- [2] Kikstra, J. F., and Verkooijen, A. H. M., 2000, "Conceptual Design for the Energy Conversion System of a Nuclear Gas Turbine Cogeneration Plant," *J. Energy Power*, **214**, Part A, pp. 401–411.
- [3] Patankar, S. V., 1980, *Numerical Heat Transfer and Fluid Flow*, Hemisphere, Washington, DC.
- [4] Verkerk, E. C., 2000, "Dynamics of the Pebble-Bed Nuclear Reactor in the Direct Brayton Cycle," Ph.D. thesis, Delft University of Technology.
- [5] Bourne, J. A., 1987, "Two-Phase Flow Models: the Closure Issue," *Multi-phase Science and Technology*, Vol. 3, G. F. Hewitt et al., eds., Hemisphere, Washington, DC.
- [6] Yan, X. L., 1990, "Dynamic Analysis and Control System Design for an Advanced Nuclear Gas Turbine Power Plant," Ph.D. thesis, MIT, Cambridge, MA.
- [7] Wagner, W., and Kruse, A., 1998, *Properties of Water and Steam, IAPWS-IF97*, Springer, Berlin.
- [8] Gravdahl, J. T., and Egeland, O., 1999, *Compressor Surge and Rotating Stall: Modeling and Control*, Springer, London.
- [9] Greitzer, E. M., 1976, "Surge and Rotating Stall in Axial Flow Compressors, Part I: Theoretical Compression System Model," *ASME J. Eng. Gas Turbines Power*, **98**, pp. 190–198.
- [10] Japikse, D., 1996, *Centrifugal Compressor Design and Performance*, Wilder, Vermont.
- [11] Pantell, K., 1949, "Versuche über Scheibenreibung," *Forsch. Geb. Ingenieurwes.*, **16**, No. 4.
- [12] Fox, R. M., and McDonald, A. T., 1994, *Introduction to Fluid Dynamics*, John Wiley and Sons, New York.
- [13] Casey, M. V., and Marty, F., 1986, "Centrifugal Compressors—Performance at Design and Off-Design," *Proc. Inst. Refrig.*, Surrey, **82**, pp. 71–82.
- [14] Zehner, P., 1980, "Vier-Quadranten Charakteristiken Mehrstufiger Axialer Turbines," *Fortschritt-Berichte der VDI Zeitschriften*, Reihe 6, **75**.
- [15] Traupel, W., 1982, *Thermische Turbomachinen*, Springer, Berlin.
- [16] Schobeiri, T., and Abouelkheir, M., 1992, "Row-by-Row Off-Design Performance Calculation Method for Turbines," *AIAA J. Propul. Power*, **8**, pp. 823–828.
- [17] Attia, M. S., 1995, "Development of Axial Compressor and Turbine Simulation Modules for Integration into the Dynamic Simulation Code GETRAN," Ph.D. thesis, Texas A&M University, College Station, TX.
- [18] Kays, W. M., and London, A. L., 1985, *Compact Heat Exchangers*, McGraw-Hill, New York.
- [19] Pool, E. B., 1982, "Friction Area and Nozzle Area for Valves and Fittings as New All-Purpose Flow Parameters," *Lyons' Valve Designer's Handbook*, J. L. Lyons, eds., Van Nostrand Reinhold, New York.
- [20] Kikstra, J. F., 2001, "Modelling, Design and Control of a Cogenerating Nuclear GasTurbine Plant," Ph.D. thesis, Delft University of Technology.
- [21] Aspen Custom Modeler 10.1 User Manual, 1999, Cambridge MA.

Dynamic Modeling of a Cogenerating Nuclear Gas Turbine Plant—Part II: Dynamic Behavior and Control

J. F. Kikstra

NRG,
P.O. Box 25,
1755 ZG Petten,
The Netherlands
e-mail: J.F.Kikstra@nrg-nl.com

A. H. M. Verkooijen

Faculty of Mechanical Engineering,
Delft University of Technology,
P.O. Box 5073,
2600 GA Delft, The Netherlands
e-mail: A.H.M. Verkooijen@iri.tudelft.nl

Using the dynamic model of the cogenerating nuclear gas turbine plant developed in Part I of this article, the dynamic behavior of this plant is analyzed and a control structure is designed. First it is determined how several design choices affect the system dynamics. Then the requirements and options for a control system design are investigated. A number of possible control valve positions in the flowsheet are tested with transients in order to make an argued choice. The model is subsequently used to determine the optimal working conditions for different heat and power demands, these are used as set-points for the control system. Then the interaction between manipulated and controlled variables is mapped and based on this information a choice for coupling them in decentralized feedback control loops is made. This control structure is then tuned and tested. It can be concluded that both heat and power demand can be followed with acceptable performance over a wide range. [DOI: 10.1115/1.1426087]

1 Introduction

In Part I of this paper the ACACIA plant (advanced atomic cogenerator for industrial applications) is introduced and a model describing its transient behavior is developed. This paper describes the use of the model for various purposes. First the effect of the turbomachinery design on the dynamic response is investigated, a/o the off-design and dynamic behavior of the proposed single-shaft configuration is compared with an alternative design with free-running power turbine. Then the requirements and different options for control of the plant are discussed. In the literature, several control structures have been proposed for nuclear gas turbine plants for electricity production ([1,2]) but no previous studies for cogeneration plants exist. With some open-loop tests, different bypass and throttle control valve positions in the flowsheet are assessed.

The plant should be able to meet both heat and power demands. A two-dimensional field of possible combinations with its optimal conditions is found. These values are used as set-points in the control system. In order to pair the manipulated and controlled variables in a decentralized control system, a dynamic relative gain analysis is performed. With the results a control scheme is chosen. This control system is then tuned and tested with typical load-following transients.

2 Influence of Design on Dynamics

An alternative for the single shaft design presented in Part I is a two-shaft system with a free-running power turbine ([3]). With the turbine split in two sections, each part can run at its optimal speed. When the power turbine rotational speed can be decreased to 50 or 60 rev/s a synchronous generator can be used. This choice does not only affect the steady-state efficiency, the off-design and dynamic behavior is completely different.

In Fig. 1 the steady-state relation between the generator rotational speed and the electricity produced is shown for both the

single-shaft and the two-shaft system. The results are produced with a constant compressor and turbine inlet temperature and constant helium inventory. For the single-shaft plant, the electricity production shows a maximum to the left of its design point. At this speed the system works less efficient because the turbomachinery does not operate at the design point and because the recuperator effectiveness decreases with the increased mass flow. However, the electricity production increases since the larger mass flow transports more energy from the reactor to the energy conversion system. These counterbalancing effects yield a maximum power production at a shaft speed of approximately 230 rev/s. The nuclear gas turbine is in this respect completely different from a conventional gas turbine in which the energy input (by injection of fuel in the combustion chamber) is totally unaffected by the shaft speed.

At shaft speeds lower than the maximum no stable operation is possible without an active control system. If the electricity demand is not met, the shaft decelerates, since kinetic energy is consumed to produce electricity. At the lower shaft speed even less power is produced, so the shaft will decelerate until its speed is zero. If the shaft accelerates from its design speed, more work will be done in the turbine, which will further accelerate the shaft, until the maximum of the curve is reached. With a bypass valve opened or with different temperatures and pressures, the position of the top of the curve changes. However, there will always be an unstable left half of the working line. The control system must stabilize the system. This can easily be achieved with a control loop using the electricity as the manipulated variable.

An increase of turbine speed in case of the two-shaft system does not lead to an increase of energy withdrawal from the reactor, because the compressor speed and thus mass flow remain unchanged. Since the two-shaft characteristic is extremely flat around the operating point, a small change of electricity demand has an enormous effect on the shaft speed. This is because there is no change of compressor load associated with the change of generator speed. Moreover, the asynchronous generator precludes the electrical network from limiting the speed. The only effect which reduces the power of the free-running turbine, is its decreased efficiency. This makes it very difficult to control the two-shaft system. One can read from the figure that in case of a load rejection (electricity production equals zero) the single shaft system

Contributed by the Materials, Manufacturing, and Metallurgy Division of THE AMERICAN SOCIETY OF MECHANICAL ENGINEERS for publication in the ASME JOURNAL OF ENGINEERING FOR GAS TURBINES AND POWER. Manuscript received by the MM&M Division, Oct. 2000; final revision received by the ASME Headquarters Apr. 2001. Associate Editor: R. Duffey.

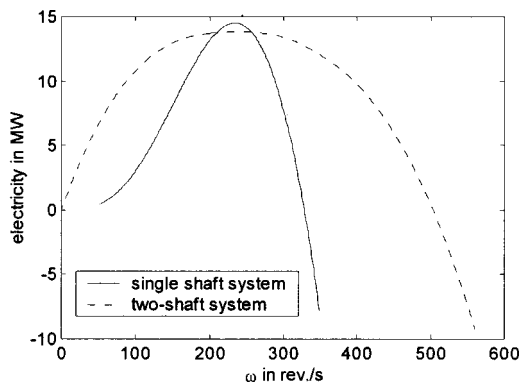


Fig. 1 Steady-state relation

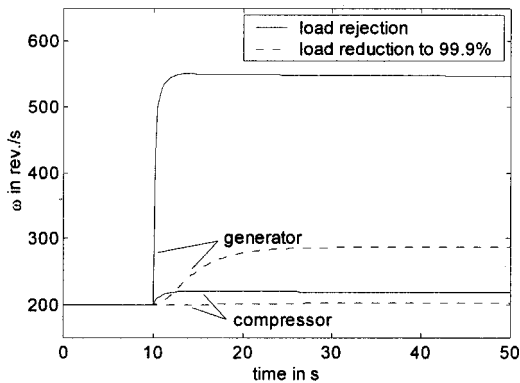


Fig. 2 Effect on shaft speeds of large and small load reduction

will speed up to 320 rev/s, while the final rotational speed of the two-shaft system is over 500 rev/s. Figure 2 shows the dynamic response of the two-shaft system on a load rejection and on a load change with only 0.1 percent. This minor fluctuation already gives an unacceptable high shaft speed.

Helium has a very high acoustic velocity due to its low molecular weight. Therefore the turbomachinery operates far removed from the choking limit, unlike most air-breathing gas turbines. However, when the outlet of the compressor or turbine is made sufficiently small, the system works close to choking. In that case mass flow cannot rise too much, which will limit the maximum shaft speed in a passive manner. Moreover, during a load rejection the increase of pressure ratio will lead to a strong decrease of turbine outlet temperature (its inlet temperature is constant by virtue of the large heat capacity of the reactor core). The tempera-

ture swing will give a thermal shock to the recuperator. With a choked turbine the extra pressure drop takes place in the choked section which does not affect the temperature. The shaft speed and compressor and turbine outlet temperature during a load rejection are shown in Fig. 3. The diffuser losses will of course increase in this configuration. Unfortunately, it does not help to operate the turbine close to choking when bypass valves are used. The bypass valves reduce the turbine flow, which precludes choking.

Changing the mechanical inertia of the shaft shows that this parameter has a predominate impact on the time-constant of transients involving a change of shaft speed. The time-lags associated with the redistribution of helium over high and low pressure plenums in case of a change of pressure ratio are almost negligible, due to the small helium inventory. The steepness of the compressor speed lines has also been altered to investigate the influence of the compressor design on the system dynamics. Its influence on a transient in which the load and shaft speed change is very small, since the ratio of gas and rotor velocity and thus the operating point in a dimensionless compressor map is almost constant during the transient.

3 Control System: Goals and Options

A cogeneration plant should be able to meet a range of heat and power demands independently, preferably while maintaining a high efficiency. The variables that have to be controlled and all possible control elements are indicated in Fig. 4. An asset of the closed cycle is that high part-load efficiency can be obtained by reducing the helium inventory. If at part load the pressure is halved and all temperatures are kept constant, the gas velocities are the same as at full load. The mass flows and the power are also halved, the efficiency stays high. The pressure losses are reduced and the heat exchanger efficiency increases, thus giving a slightly higher efficiency than at full load. The helium inventory can be increased or decreased without need for an extra compressor, if a number of parallel inventory vessels with a pressure between the lower and upper primary system pressure is used. In most designs, the helium inventory is rather large, therefore filling and emptying the system is a slow process ([2]). In order to quickly adjust the electricity production the turbine can be bypassed, for this a number of valve positions is conceivable. The mixing with either hot or cool helium when a bypass valve is opened will give a strong and fast change of turbine outlet temperature. This results in a thermal shock of the recuperator which can lead to fatigue or direct failure ([4,5]). A countermeasure could be to use two bypass valves: bypass one (see Fig. 4) to control the shaft speed and bypass two to control the temperature ([6]). A bypass flow gives a dramatic decrease of efficiency, therefore the bypass valves should be almost closed during prolonged operation at a certain heat and power demand. An alternative for bypass control is to throttle the

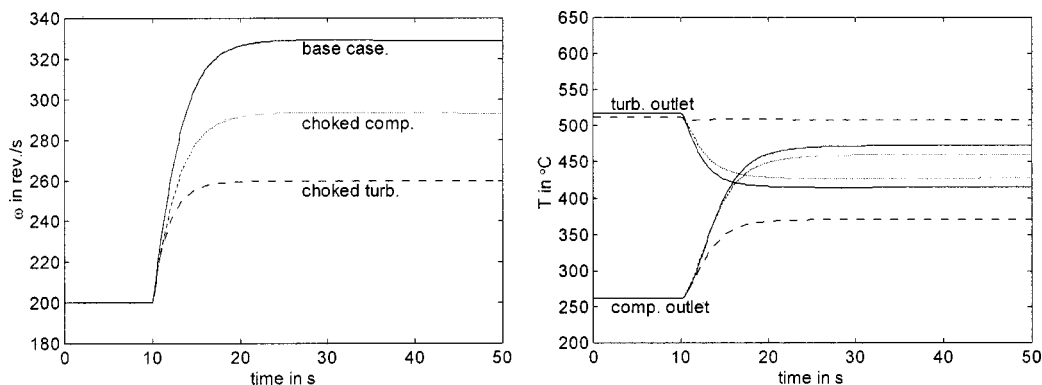


Fig. 3 Load rejection with choked turbomachinery

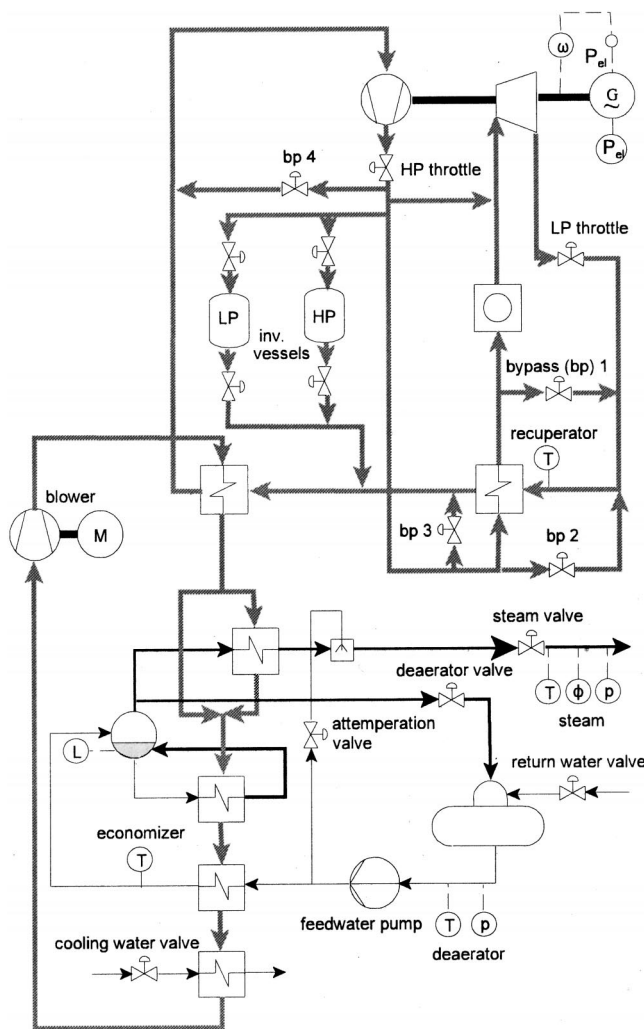


Fig. 4 Controlled variables and possible manipulated variables

primary flow ([7]). The main disadvantages of throttle valves is that they have to be much larger and give a pressure drop and thus a decreased efficiency even when fully opened. Since the generator is asynchronous, the shaft speed must be actively controlled. The fastest and easiest option is to use the electric load as manipulated variable. The turbine inlet temperature is left uncontrolled, since it is passively controlled by the reactor neutronics. A rise of reactor inlet temperature has a negative impact on the neutron economy which leads to power reduction, so that the reactor outlet temperature is kept fairly constant.

An inventory reduction with constant temperatures in the primary cycle gives an unchanged heat-to-power ratio. In order to increase the heat-to-power ratio, the temperature in the precooling has to be increased. This can be done by reducing the cooling water flow. In order to efficiently transport the energy from the precooling to the steam generator and final cooler the blower speed must also be adjusted. The temperature and pressure of the industrial steam of course have to be controlled. For temperature control a spray attemperator can be used without a penalty on the system efficiency, because the pinch point in the steam generator lies at the evaporator water inlet. Moreover, the economizer should always remain subcooled, therefore its outlet temperature must be controlled. The drum level and deaerator conditions also

have to be controlled, this can be achieved by manipulating the feedwater pump speed and the valves in the steam and water pipe to the deaerator.

4 Control Valve Positions

In Fig. 4, a number of alternative bypass and throttle valves are shown. Valves 1 and 2 are proposed in similar designs ([2,6]). Valve one is used to reduce the shaft speed, opening leads to a temperature rise of the turbine outlet. To compensate for this temperature rise valve two is opened, which leads to a reduction of the turbine outlet temperature. The bypass valve is situated in a high temperature environment, which might complicate the design. An alternative position for the bypass valve would be between the cold (instead of the hot) inlet and outlet of the recuperator (valve 3). Yet another possible position is between compressor outlet and inlet (valve 4). Two possible throttle valves are conceivable, either positioned in the high pressure (HP) or low pressure (LP) side.

The influence of these valves is tested with a model of the primary system only in which the shaft speed is reduced to its nominal speed after a load rejection. The system is operated with constant compressor inlet temperature. In order to assess the different control possibilities a number of output parameters have been monitored. The shaft speed must be reduced with as little overshoot as possible. Figure 5 shows the transients of the shaft speed during 50 s. Figure 6 shows the original temperature profile of the recuperator (hot and cold helium temperature) dotted while the profile at the end of the transient (after 50 s) is drawn. The heat transport to and from the primary helium flow in the reactor, respectively, is the precooling plotted in Fig. 7. In order to minimize the disturbance of the secondary system, both the heat flow to it and the precooling hot inlet (recuperator hot outlet) temperature must be as constant as possible. The heat from reactor be-

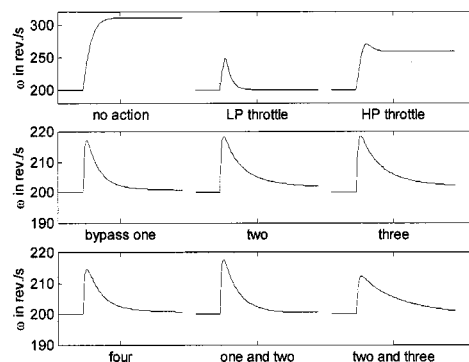


Fig. 5 Shaft speed response on different control actions

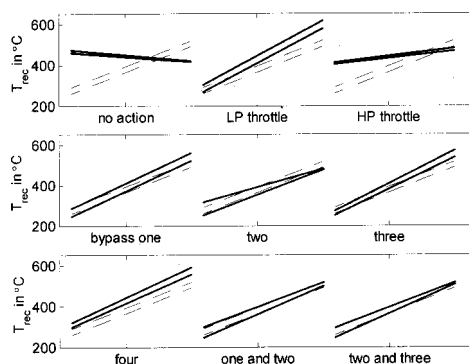


Fig. 6 Recuperator temperature profile response on different control actions, dotted: profile before transient, drawn: after transient

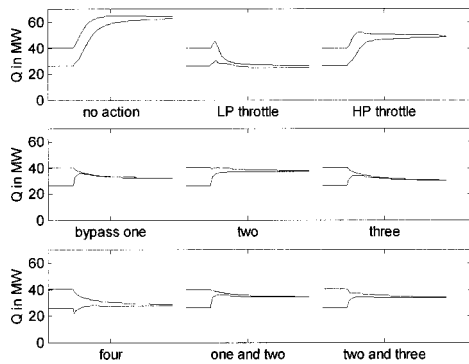


Fig. 7 Heat flow response on diff. control actions, upper: heat to primary system in reactor, lower: heat to secondary system

comes equal to the heat supplied to the secondary system, the difference is used to heat the recuperator and precool core. A small and short deviation between both heat flows proves that the heat exchangers operate at constant temperature.

It can be seen that in case of a load rejection without control the recuperator actually cools the low pressure flow instead of heating it. The heat flow to the secondary cycle becomes too large, due to the fact that the compressor inlet temperature is constantly kept low, leading to a poor efficiency. The strong increase of the pre-cooler hot inlet temperature will normally also lead to a rise in compressor temperature and thus to a decrease of the heat transport. If necessary, the temperature can be increased further by reduction of the cooling flow.

With the LP throttle (in the turbine outlet) the mass flow is reduced to 23 kg/s. This leads to a hardly changed energy transport to the secondary cycle and a well-controlled shaft speed. The HP throttle can only limit the increase of mass flow to 29 kg/s. (No control gives an increase from 25.4 to 33 kg/s.) Throttling

further brings the system in an unstable operating point. The increased recuperator hot outlet temperature gives a strong increase of heat transport to the intermediate helium loop.

Opening of the bypass valves has hardly any effect on the recuperator cold inlet temperature for valves 1, 2, and 3. The reason is that the compressor inlet temperature is kept constant with the large secondary flow through the pre-cooler (simulating perfect control of the secondary loop) and the pressure ratio over the compressor does not change very much. When valve 4 is opened hot helium is mixed with the compressor inlet flow so the compressor outlet temperature rises. This rise could also be accomplished by decreasing the final cooler water flow. The increase of temperature leads to a decrease of heat transport from the reactor.

For valves 1, 2, and 4 the mass flow on both sides of the recuperator is equal. This keeps the temperature lines parallel, which is favorable because it keeps the temperature difference and thus the thermal stresses perpendicular to the flow direction small. Opening of valves 1, 3, and 4 lead to an increase of the turbine outlet temperature. This increase is the smallest with valve one. A load decrease with opening of valve 2 leads to a decrease of the recuperator hot inlet temperature. This shows that the combination of the bypass and attemperature valve can be used to keep the temperature constant.

Finally the results are shown for a transient in which two bypasses (valve 1 and 2, respectively, 1 and 3) are opened simultaneously. This can lead to a hardly changed recuperator temperature profile. Figure 7 shows that the energy transport to the secondary cycle is still too high. It can be reduced further with an increase of the compressor inlet temperature. This will again raise the temperature at the cold side of the recuperator. The combination of valve 2 and 3 is chosen since it gives good performance with small valves operating at low temperatures.

5 Optimal Operating Conditions

The dynamic model can also be used to calculate the optimal steady-state situation for a given heat and power demand. The

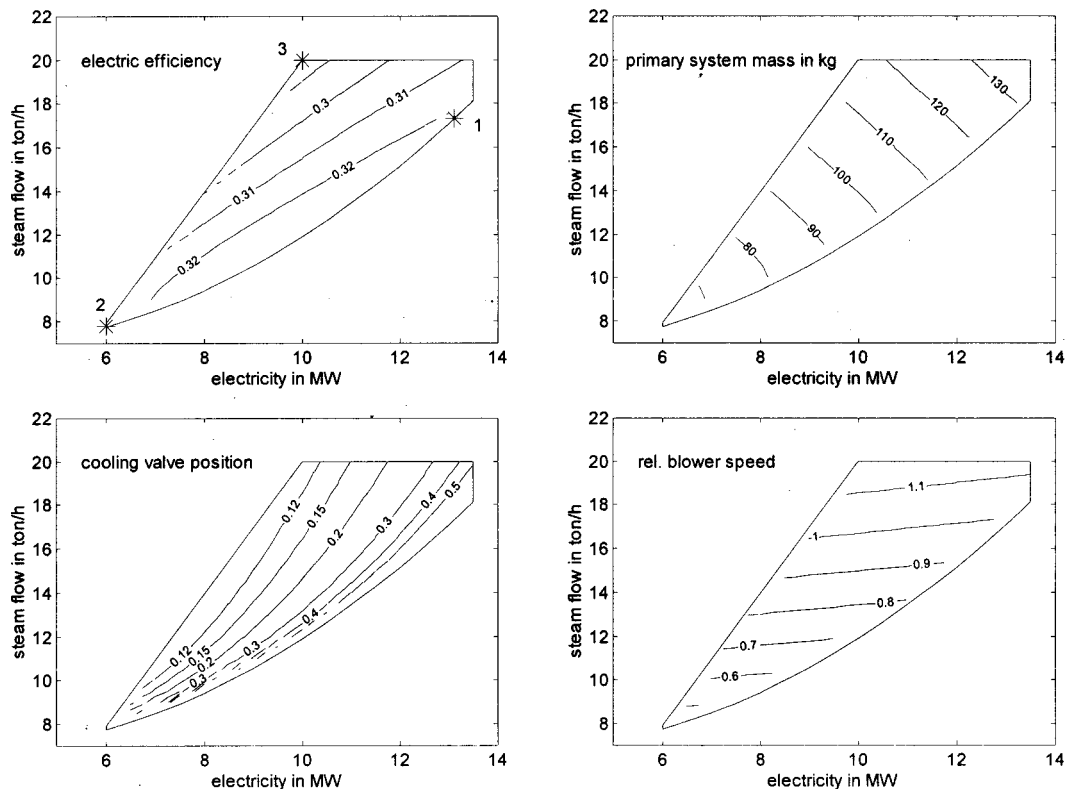


Fig. 8 Optimal operating conditions for different heat and power demands

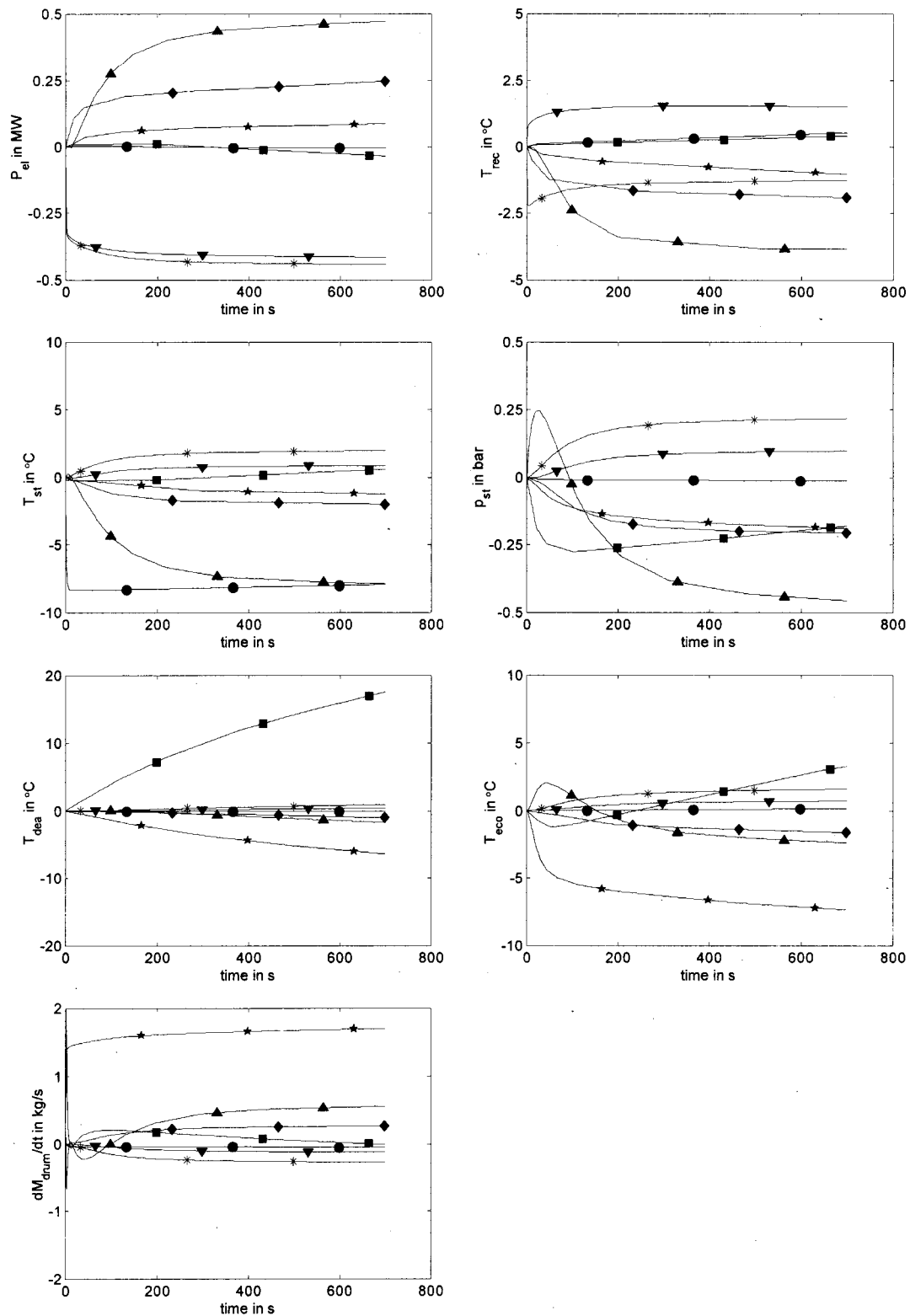


Fig. 9 Response on "unit" step of manipulated variables under normal operating conditions * bypass valve two +1 percent, ▼ bypass valve three +1 percent, ▲ blower +10 percent, ● attemperation valve +30 percent, ★ feedwater pump +10 percent, ■ deaerator valve +40 percent, ◆ cooling valve +20 percent

operational region with optimal conditions are shown in Fig. 8. At high electricity and heat production the area is bounded because otherwise the helium inventory and thus the pressure is too high. The "left" and "right" boundaries are due to saturation of the

cooling valve; at the left boundary the valve is fully closed, whereas it is fully opened at the right boundary. In order to achieve the highest efficiency, the bypass valves should be closed. With the bypass valves open, the plant can operate to the left of

the region shown. One can see that the electric efficiency stays high over the operating region. If the inventory is reduced, the both steam and power production decrease proportionally. When the cooling valve is opened, less steam can be produced, but the electric efficiency rises. In order to keep the correct temperature profile in the steam generator (a/o to keep the economizer water outlet slightly subcooled) the blower speed is varied almost proportional to the steam flow.

6 Control System Design

6.1 Step Responses. In order to map the interaction between the possible manipulated and controlled variables, step responses have been produced in the three operating points marked with an asterisk in Fig. 8. The shaft speed is controlled using the electric load, in order to obtain a stable response. With all other inputs constant, a small step is applied to one input, after which the output is monitored for 700 s. Results are shown in Fig. 9. The inventory valves and the return water valve have been omitted in this analysis, the first because it is the only input to influence the primary helium mass and the latter because if it is used to control the deaerator pressure it has hardly any interaction with the rest of the system. The steam valve is operated by the customer, so it is a disturbance instead of a manipulated variable for the control system. Instead of the drumlevel, the time differential of the drum mass is monitored. This gives easier insight since the drumlevel is a pure integrator.

All manipulated variables influence a number of controlled variables, with the exception of the attemperation and deaerator valve, which mainly influence the steam and deaerator temperature, respectively. The responses of the steam pressure and economizer output temperature on the blower speed show nonminimum phase behavior. Changing the secondary mass flow changes the temperature profiles in all heat exchangers in the loop. The speed at which a heat exchanger reaches a new steady-state depends on its thermal inertia. This thermal inertia and the sign of the response are different for different heat exchangers. Directly after an increase of blower speed more heat is transported from the pre-cooler to the evaporator, leading to a pressure rise, because more water is evaporated. After a while more heat is removed in the final cooler, which has the opposite effect.

Figures 10 and 11 show some important step responses in the other two operating points. A strong nonlinearity over the operational region exists. The nonlinearity of the response on a step-change in blower speed is due to the counterbalancing effects of the changed temperature profiles in the heat exchangers. The effect of blower speed on the temperatures and pressure is dependent on the ratio of duties of the heat exchangers. The magnitude of the step response on the cooling water flow strongly depends on the initial valve position. When the valve is almost closed (in operating point 3), a small absolute change gives a fairly large relative change which gives the response a high gain. The nonlinearity complicates the control system design.

6.2 Relative Gain Analysis. More insight into the optimal choice of input-output pairing for a SISO feedback control struc-

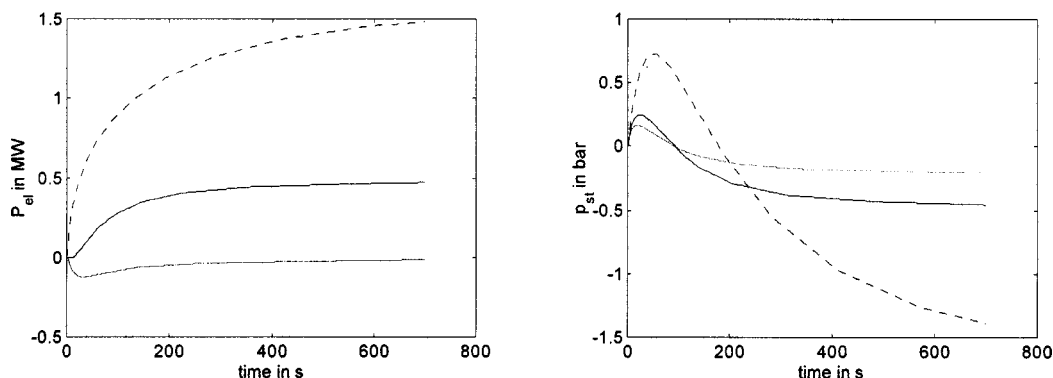


Fig. 10 Response to step on blower speed, drawn: at normal operating conditions (point 1), dotted: at operating point 2, dashed: at operating point 3

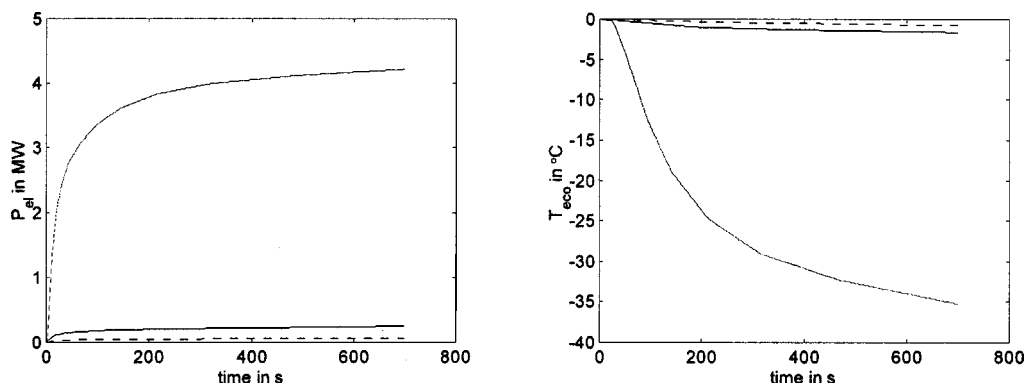


Fig. 11 Response to step on cooling water valve position, drawn: at normal operating conditions (point 1), dotted: at operating point 2, dashed: at operating point 3

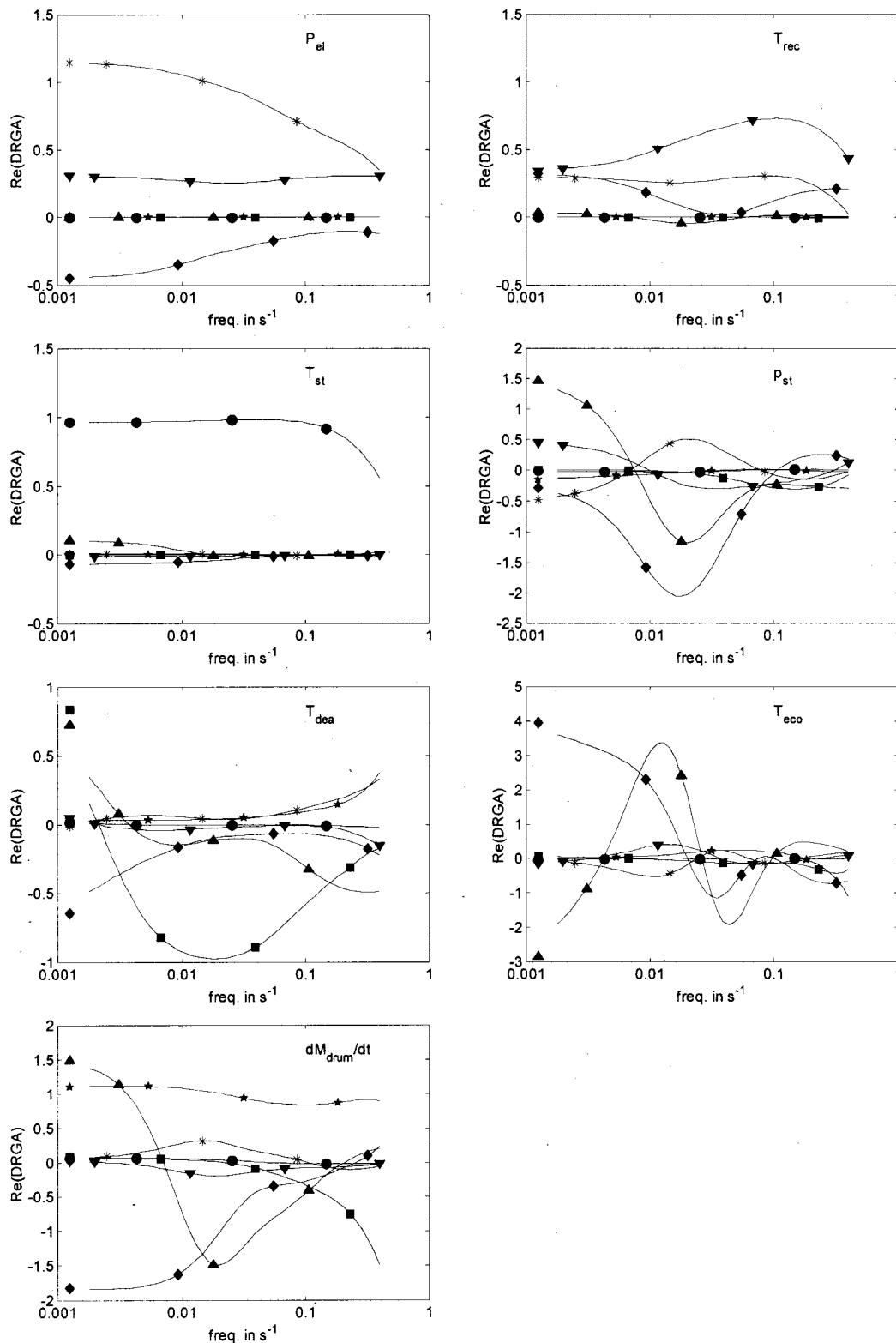


Fig. 12 Dynamic relative gain analysis, * bypass valve 2, ▼ bypass valve 3, ▲ blower, ● attenuation valve, ★ feedwater pump, ■ deaerator valve, ♦ cooling valve

ture can be made based on analysis of the Bristol Relative Gain Array ([8]). The RGA matrix has as its elements the ratio of open loop gain with all other loops open and open loop gain with all other loops closed for every input-output combination. One element of a column close to one with all the other elements close to zero indicates that this is a good input-output pair; the control

loop shows little interaction with other loops. Negative elements indicate that a difference of sign between the response with the other loops open or closed, which of course complicates the use of this pair for control. The RGA at operating point 1 is shown underneath. The elements indicating strong interaction have been underlined.

	bp. v. 3	bp. v. 2	att. v.	blower	pump	cool. v.	dea. v.
P_{el}	1.1435	0.3023	-0.0001	0.0024	-0.0001	-0.4473	-0.0006
T_{rec}	0.2955	0.3417	0.0012	0.0379	0.0000	0.3224	0.0013
T_{st}	0.0092	-0.0129	0.9618	0.1051	-0.0010	-0.0680	0.0058
P_{st}	-0.4811	0.4579	-0.0123	1.4716	0.0027	-0.2838	-0.1550
T_{dea}	-0.0159	0.0500	0.0178	0.7237	0.8341	-0.6456	0.0359
T_{eco}	-0.0149	-0.1546	-0.0373	-2.8260	0.0733	3.9454	0.0141
dM_{drum}/dt	0.0638	0.0156	0.0688	1.4854	0.0910	-1.8231	1.0985

The RGA does not show dynamic interaction. Dynamic relative gain analysis ([9]) is an extension which overcomes this shortcoming. Assuming perfect control, the frequency response at different frequencies can be calculated from the transfer function or a state-space model. This state-space model is obtained from a model reduction using Hankel singular value decomposition based on the stepweights ([10]) obtained from Fig. 9. Using input and output scaling, a tenth order state-space realization could be obtained of the model with 700 stepweights (sample time one second) for each input-output pair. Figure 12 shows the real part of the response at different frequencies. At the low frequency end an extra symbol indicates the RGA at zero frequency.

The only loop which shows no interaction with the rest of the system, is the steam temperature control with the attenuation valve. The two topmost figures suggest that the best pairing for the bypass valves is the control of electric power with valve three and recuperator temperature with valve two. However, the goal of the control structure is not to keep the temperature constant, but only to limit the rate of change of the temperature. Trying to keep the temperature constant will lead to an unnecessarily opened bypass which reduces the efficiency. Moreover, a temperature above the set-point can still not be corrected because the valve is closed during normal full power operation, in other words, the controller operates very close to saturation. Therefore the electricity production is controlled with valve 3 and valve 2 is operated in ratio with valve 3.

The blower speed shows interaction with almost all output variables. Moreover, as expected from the nonminimum phase behavior, the sign of response changes with frequency. Some tests proved that closed-loop control using the blower speed is extremely difficult, if not impossible, due to the slow nonminimum phase behavior. If the steam pressure is tightly controlled, the economizer temperature will not change much either. Even without a closed-loop temperature control the economizer remains subcooled, therefore this control loop can be omitted. This leaves the cooling water valve as the remaining manipulated variable for steam pressure control. The a priori guess of using the feedwater pump for drumlevel control and the deaerator valve for control of the deaerator temperature is plausible.

6.3 Control Structure. In Fig. 13 the control structure is depicted. The customer gives a set-point for the electric power P_{el} and steam flow ϕ_s . Using Fig. 8 the optimal blower speed and primary helium mass are found. The blower speed is directly adjusted. If the helium inventory is directly adjusted to its optimal steady-state value after a change in electric load, the heat input to the secondary cycle changes quickly. The heat removal in the final cooler cannot be adjusted equally fast, due to its thermal inertia. This results in unacceptably large swings in steam pressure during load changes. The problem can be overcome by first adjusting the helium inventory to such a value that the primary mass flow through the precoolers is kept constant. Since the temperatures are also fairly constant due to the operation of bypass valves, the heat flow to the secondary cycle remains in balance. In case of opening of the bypass valve in order to reduce the electricity production, the compressor flow and thus the primary precoolers flow in-

creases. To counterbalance this effect the inventory is reduced. This is accomplished by ramping up or down the set-point simultaneously with the electricity demand. Subsequently the inventory can be very slowly reduced to the optimal value shown in Fig. 8, this is done with a 1000 s ramp. The reduction in heat input into the secondary cycle leads to a steam pressure reduction, which lets the controller close the cooling water valve. The compressor inlet temperature rises which through an increased power consumption of the compressor gives a reduced electricity production. This is balanced by closing the bypass valves, thus raising the efficiency. The set-point for the inventory M_{system} is compared with a value calculated from the helium mass in the vessels, which is known from temperature and pressure measurements. A PI con-

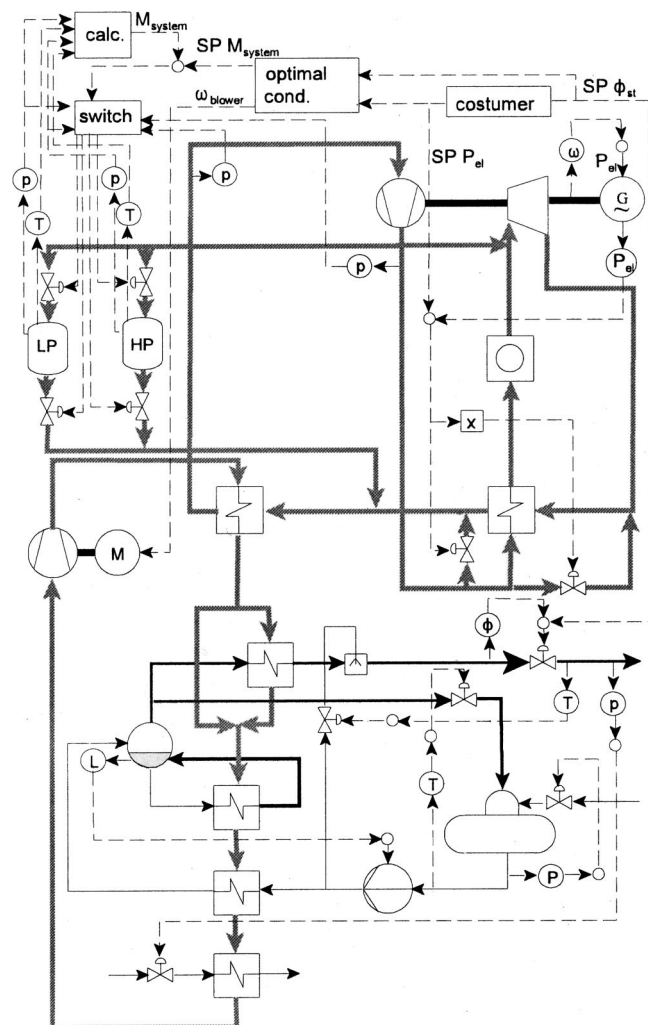


Fig. 13 Control structure of the ACACIA plant

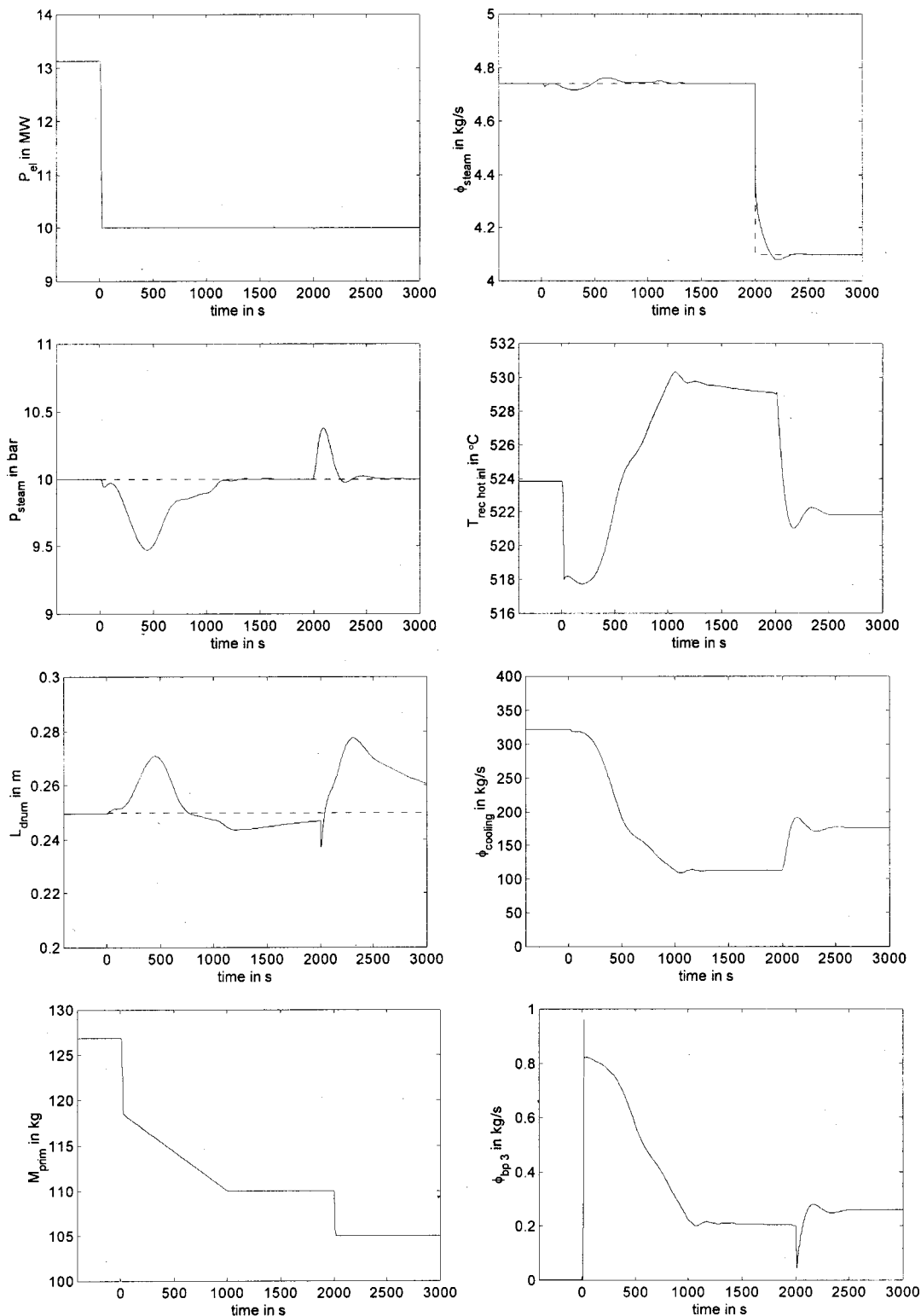


Fig. 14 Results of ACACIA control system test transient

troller sends a signal to a logic switch which operates the inlet or outlet valve of the LP or HP vessel, dependent on the system upper and lower pressure and the sign of the error. All the controllers use PI feedback, they have been tuned heuristically with a number of transients.

The results of a transient in which both power and heat demand are changed is shown in Fig. 14. Starting at $t=10$ s the electricity demand is ramped down with 25 percent in 10 s. As a result, the

inventory is directly adjusted and during the next 1000 s ramped down to its optimal value. At $t=2000$ s the heat demand is decreased with 15 percent.

The electricity production exactly meets the demand, while the steam flow and pressure show only small deviations from their set-point (shown as dotted line). The steam temperature and the deaerator conditions are almost the same as their set-points and therefore omitted in Fig. 14. Ratio control of bypass valve two

cannot keep the recuperator temperature completely constant, but the changes are small. The drumlevel is kept in the middle of the drum. The controller is not set very aggressively since that would lead to short and large deviations of the steady-state pump speed, which would unnecessarily upset the system. Because of the integrating nature of the drumlevel response to both the pump speed and disturbances, longer small differences in pump speed work equally well. The bypass valves are almost closed during the heat load following transient. If they are completely closed (as could happen in larger load swings), either the electricity set-point cannot be attained, or the inventory must be adjusted to secure the electricity production.

7 Conclusions

The dynamic model has proven to be a valuable tool in the system and control system design. It can be used for the assessment of alternative designs and control options and for optimization of steady-state and dynamic performance. The ACACIA plant can meet a large field of heat and power demands with high efficiency. Its control system can track the set-points quickly, without too large temperature swings in the recuperator.

Nomenclature

L	=	drumlevel in m
M	=	mass in kg
P	=	power in MW
p	=	pressure in bar
Q	=	heat in MW
T	=	temperature in °C
ϕ	=	mass flow in kg/s
ω	=	rotational speed in rev/s
bp	=	bypass

dea	=	deaerator
eco	=	economizer
el	=	electric
HP	=	high pressure
inv	=	inventory
LP	=	low pressure
SP	=	set-point
st	=	steam
rec	=	recuperator

References

- [1] Bardia, A., 1980, "Dynamics and Control Modeling of the Closed-Cycle Gas Turbine (GT-HTGR) Power Plant," *Proceedings of the Fourth Power Plant Dynamics, Control and Testing Symposium*, E. M. Katz, ed., Mar., TN.
- [2] Yan, X. L., 1990, *Dynamic Analysis and Control System Design for an Advanced Nuclear Gas Turbine Power Plant*, Cambridge MA.
- [3] Op het Veld, R., and Buijtenen, J. P. van, 1998, "An Empirical Approach to the Preliminary Design of a Closed Cycle Gas Turbine," ASME Paper No. 98-GT-393.
- [4] Nakaoka, T., et al., 1996, "Evaluation of Fatigue Strength of Plate-Fin Heat Exchanger Under Thermal Loading," *Proceedings of the ASME International Conference on Pressure Vessel Technology*, Vol. 1, ASME, New York.
- [5] Carter, P., et al., 1996, "Failure Analysis and Life Prediction of a Large, Complex Plate Fin Heat Exchanger," *Eng. Fail. Anal.*, **3**, No. 1.
- [6] Simon, W. A., Neylan, A. J., and Silady, F. A., 1993, "Design Features of the Gas Turbine Modular Helium Reactor (GT-MHR)," *Technical Report GA-A21351*, General Atomics, San Diego, CA.
- [7] Adams, R., 1994, Adams Atomic Engines, Inc., U.S. Patent number 5,309,492.
- [8] Stephanopoulos, G., 1984, *Chemical Process Control: An Introduction to Theory and Practice*, Prentice-Hall, Englewood Cliffs, NJ.
- [9] Maciejowski, J. M., 1989, *Multivariable Feedback Design*, Addison-Wesley, Wokingham, UK.
- [10] Zee, G. A. van, and Bosgra, O. H., 1979, "The Use of Realization Theory in the Robust Identification of Multivariable Systems," *Proceedings of the Fifth IFAC Symposium on Identification and Parameter Estimation*, Darmstadt, Germany.